V International Conference on Particle-based Methods. Fundamentals and Applications

PARTICLES 2017

26 - 28 September 2017, Hannover, Germany

P. Wriggers, M. Bischoff , E. Oñate, D.R.J. Owen and T. Zohdi (Eds.)

V International Conference on
PARTICLE-BASED METHODS. Fundamentals and Applications
PARTICLES 2017

26 – 28 September 2017
Hannover, Germany

A publication of:

International Center for Numerical Methods in Engineering (CIMNE)
Barcelona, Spain

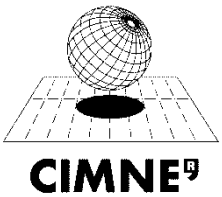

ISBN: 978-84-946909-7-6

TABLE OF CONTENTS

PREFACE

This volume contains the Technical Programme of the papers accepted for presentation at the V International Conference on Particle-based Methods (PARTICLES 2017), held in Hannover on 26 - 28 September, 2017. The four previous conferences of the series were held in Barcelona, Spain, in the years 2009 and 2011, in Stuttgart, Germany, in September 2013, and in Barcelona on 2015.

PARTICLES 2017 will address both the fundamental basis and the applicability of state-of-the-art particle-based computational methods that can be effectively used for solving a variety of problems in engineering and applied sciences.

The denotation "Particle-Based Methods" basically stands for two different computational models in solid and fluid mechanics.

On the one hand it represents *discretization concepts* in which the response of a continuum is projected onto "particles" carrying the mechanical information during deformations. Typical representatives are Meshless Methods, Smoothed Particles Hydrodynamics (SPH), Moving Particle Simulation (MPS), Particle Finite Element Method (PFEM), Material Point Method (MPM) and the Lattice-Boltzmann-Method (LBM).

The conference is held under the auspices of the European Community on Computational Methods in Applied Sciences (ECCOMAS) and the International Association for Computational Mechanics (IACM). The organizers would like to thank all the participants and the supporting organizations for their help in making PARTICLES 2017 possible.

PARTICLES 2017 Organizers

P. Wriggers (Chair)
Leibniz Universität Hannover, Germany

M. Bischoff
Universität Stuttgart, Germany

E. Oñate
CIMNE / Universitat Politècnica de Catalunya,Barcelona, Spain

D.R.J. Owen
Swansea University, United Kingdom

T. Zohdi
University of California, Berkeley, USA

ACKNOWLEDGEMENTS

The conference organizers acknowledge the support towards the organization of PARTICLES 2017 to the following organizations:

Leibniz Universität Hannover

International Center for Numerical Methods in Engineering (CIMNE)

Universitat Politècnica de Catalunya (UPC)

European Community on Computational Methods in Applied Sciences (ECCOMAS)

International Association for Computational Mechanics (IACM)

Computational Particle Mechanics, a Springer Journal

We thank the **Plenary Speakers**, the **Invited Sessions Organizers** and the **Authors** for their help in the setting up of a high standard Scientific Programme.

SUMMARY

CONTENTS

INVITED SESSIONS

IS - Advanced Particle Methods for Continuum Mechanics

IS - Complex Particle Suspensions

IS - Discrete Modelling in Cell and Tissue Mechanobiology

IS - Fracture and Fragmentation with DEM

IS - Granular Plasticity

IS - Micro-macro: From Discrete Particles to Continuum Models of Granular Mechanics

IS - Models and Tools for Particulate Flows undergoing Phase Change or Reactions

IS - Multiscale Numerical and Experimental Analysis of Particle Systems (T-MAPPP Symposium)

IS - Parallel High Performance Simulation within the Framework of Particle-Based Methods

IS - Particle-based Methods for Fluids and Fluid-Structure Interaction Problems

IS - Segregation in Granular Systems

IS - XDEM - A Software Platform for Advanced Multi-Physics Simulation Technology

CONTRIBUTED SESSIONS

Bio-Medical and Pharmaceutical Processes

Concrete Material and Structures

Discrete Element Method (DEM)

Forming Processes

Free Surface Flows

Geomechanics

Granular Materials and Structures

High Performance Computing

Industrial Applications

Lattice-Boltzmann-Method (LBM)

Material Modelling and Characterization

Material Point Method (MPM)

Meshless Methods

Molecular Dynamics (MD)

Multi-physics Problems

Multiphase and Particulate Flows

Railway Ballast

Smoothed Particles Hydrodynamics (SPH)

V International Conference on Particle-based Methods – Fundamentals and Applications
PARTICLES 2017
P. Wriggers, M. Bischoff, E. Oñate, D.R.J. Owen, & T. Zohdi (Eds)

MODELLING OF THE DISPERSED PHASE MOTION IN FREE-SURFACE FLOWS WITH THE TWO-FLUID SMOOTHED PARTICLE HYDRODYNAMICS APPROACH

Michał Olejnik*, Kamil Szewc, Jacek Pozorski

Institute of Fluid Flow Machinery, Polish Academy of Sciences
Fiszera 14, 80-231 Gdańsk, Poland
*email: michal.olejnik@imp.gda.pl

Key words: Sedimentation, Free-surface Flow, Meshless Methods, Two-fluid Approach

Abstract. The sediment transport is an important problem in hydro-engineering. Accurate numerical modelling of this complex phenomenon remains a challenging task. In the present study we employ the Smoothed Particle Hydrodynamics (SPH) approach in the two-fluid formulation to compute the interactions between the carrier and dispersed phases. The main goal is to test this rather uncharted SPH variant for simple cases and to find problematic points that require further improvement. We present initial results of validation with experiment involving a vertical sheet of sand entering the water tank through free surface, as well as results from a simplified quasi-2D study of sedimentation.

1 INTRODUCTION

The phenomena involving interaction of the carrier fluid and dispersed phase are object of active research. In environmental sciences, transport of sediment (sand) in the coastal areas is a complex process of particular interest in hydro-engineering. Numerical predictions require advanced models able to handle physics of multiphase and free-surface flow. While some grid-based approaches to tackle this issue exist, they suffer from problems related to their Eulerian character. Lagrangian methods, such as Smoothed Particle Hydrodynamics (SPH), are surfacing as an interesting and promising alternative. Although initially the SPH method was developed for astrophysical computations, over the years it was successfully applied to a wide range of CFD problems, including both free-surface and multiphase flows [1, 2].

The present work is a part of ongoing development of entirely SPH-based solver capable of computing the free-surface flow, its interaction with deformable seabed [3], as well as transport of sand carried by water. In the following we focus on the last aspect. For this purpose we employ the so-called two-fluid SPH formulation, initially developed for calculations of dust motion within gaseous medium [4], recently adapted for sedimentation

problems [5]. Basing on the results for the case of sand entering water through the free surface, as well as sedimentation problem, we outline main difficulties encountered.

2 GOVERNING EQUATIONS

2.1 Two-fluid model

The essence of the two-fluid modelling of multiphase flows is to treat the dispersed phase and the carrier fluid as two separate continuous phases, interpenetrating and interacting with each other. As a consequence the conservation equations for both phases, including interaction terms between them, are solved. The idea of this approach can be found in [6]. In this work we consider liquid L and dispersed phase (dust) D. Their volume densities are defined as

$$\hat{\varrho}_L = \theta_L \varrho_L, \tag{1}$$

$$\hat{\varrho}_D = \theta_D \varrho_D, \tag{2}$$

where θ and ϱ denote the volume fraction and material density, respectively. The volume fractions need to satisfy the condition

$$\theta_L + \theta_D = 1. \tag{3}$$

The mass conservation equation for each phase is given as

$$\frac{d\hat{\varrho}_L}{dt} = -\hat{\varrho}_L \nabla \cdot \mathbf{u}_L, \tag{4}$$

$$\frac{d\hat{\varrho}_D}{dt} = -\hat{\varrho}_D \nabla \cdot \mathbf{u}_D, \tag{5}$$

and the momentum conservation equations are

$$\frac{d\mathbf{u}_L}{dt} = -\frac{\nabla p}{\varrho_L} - \frac{K}{\hat{\varrho}_L}(\mathbf{u}_L - \mathbf{u}_D) + \frac{1}{\varrho_L}(\nabla \mu \cdot \nabla)\mathbf{u}_L + \mathbf{f}, \tag{6}$$

$$\frac{d\mathbf{u}_D}{dt} = -\frac{\nabla p}{\varrho_D} - \frac{K}{\hat{\varrho}_D}(\mathbf{u}_D - \mathbf{u}_L) + \mathbf{f}, \tag{7}$$

where $\mathbf{f}$ and K denote the mass force and the drag factor, respectively; μ is the dynamic viscosity. An example of the two-fluid approach calculations within Eulerian-Eulerian framework for problem of a dust sedimentation can be found in [7]. Since our long-term aim is to include the effect of surface waves on the dispersed phase, as well as the specific model of the bottom layer [3], we decided to apply the Lagrangian-Lagrangian two-fluid model, based on a particle method, namely SPH.

2.2 SPH formulation

The general idea behind SPH lies in interpolation theory. Let us consider any scalar (for simplicity) field A. The integral formula

$$A(\mathbf{r}) = \int_{\Omega} A(\mathbf{r}')\delta(\mathbf{r} - \mathbf{r}')\mathbf{dr}', \tag{8}$$

where $\delta(\mathbf{r})$ is the Dirac delta function, can be used to express the field value at the point $\mathbf{r}$ in space Ω. To obtain SPH approximation, first we replace $\delta(\mathbf{r})$ with the weighting kernel function $W(\mathbf{r}, h)$ which should be normalised, symmetrical and converge to $\delta(\mathbf{r})$ with $h \to 0$ [1]. Argument h is the so-called smoothing length and it determines the interpolation range. In our work we use the Wendland kernel [8], as the one guaranteeing good stability of computations [9].

The second step consists in discretisation of space into a set of particles of volume $\Omega_b = m_b/\varrho_b$, where m_b is the mass and ϱ_b is the density of particle b. As a result the integral from Eq. (8) is approximated by a sum, i.e.

$$A(\mathbf{r}) \simeq \sum_b A(\mathbf{r}_b)W(\mathbf{r} - \mathbf{r}_b, h)\Omega_b. \tag{9}$$

In the shorthand notation, the SPH approximation $\langle A\rangle_a$ of field A at any point a is defined as

$$\langle A\rangle_a = \sum_b A_b W_{ab}(h)\Omega_b, \tag{10}$$

where $A_b = A(\mathbf{r}_b)$ and $W_{ab}(h) = W(\mathbf{r}_a - \mathbf{r}_b, h)$. Thanks to the properties of $W(\mathbf{r}, h)$ differentiation can be shifted from the field to the kernel function yielding

$$\langle \nabla A\rangle_a = \sum_b A_b \nabla W_{ab}(h)\Omega_b. \tag{11}$$

Further derivatives can be obtained in a similar way. Using Eqs. (10) and (11) differential equations can be rewritten in SPH formalism and solved by calculating interaction between particles. The detailed derivation of the SPH method for fluid-flow problems can be found in [2].

Now, we will briefly recall the two-fluid SPH formulation used in the present study. In this approach both phases are described by separate sets of SPH particles. Following the original work by Monaghan and Kocharyan [4] we denote liquid particles with indices a and b, while i and j are used for the dust particles. We recall that the "dust particles" are understood here as parts of the continuum, and not the real physical particles. Since cases considered in this research involve free-surface flows, we decided to use SPH formalism proposed by Colagrossi and Landrini [10], well suited for the task [11]. In this formulation Eqs. (4) and (5) will become

$$\frac{d\hat{\varrho}_a}{dt} = -\hat{\varrho}_a \sum_b \frac{m_b}{\hat{\varrho}_b}\mathbf{u}_{ab} \cdot \nabla_a W_{ab}, \tag{12}$$

$$\frac{d\hat{\varrho}_i}{dt} = -\hat{\varrho}_i \sum_j \frac{m_j}{\hat{\varrho}_j} \mathbf{u}_{ij} \cdot \nabla_i W_{ij}, \tag{13}$$

where $\mathbf{u}_{ab} = \mathbf{u}_a - \mathbf{u}_b$. Equations (6) and (7) are taken as

$$\begin{aligned} \frac{d\mathbf{u}_a}{dt} = \sum_b m_b \left(\frac{\theta_a p_a + \theta_b p_b}{\hat{\varrho}_a \hat{\varrho}_b} + \Pi_{ab} \right) \nabla_a W_{ab} - \sum_j m_j \frac{\theta_j p_a}{\hat{\varrho}_a \hat{\varrho}_j} \nabla_a W_{aj} + \\ -\sigma \sum_j m_j \frac{K_{aj}}{\hat{\varrho}_a \hat{\varrho}_j} (\mathbf{u}_{aj} \cdot \hat{\mathbf{r}}_{aj}) \hat{\mathbf{r}}_{aj} W_{aj} + \mathbf{f}, \end{aligned} \tag{14}$$

$$\begin{aligned} \frac{d\mathbf{u}_i}{dt} = \sum_j m_j \left(\frac{\theta_i p_i + \theta_j p_j}{\hat{\varrho}_a \hat{\varrho}_b} \right) \nabla_i W_{ij} - \sum_b m_b \frac{\theta_i p_b}{\hat{\varrho}_i \hat{\varrho}_b} \nabla_i W_{ib} + \\ -\sigma \sum_b m_b \frac{K_{ib}}{\hat{\varrho}_i \hat{\varrho}_b} (\mathbf{u}_{ib} \cdot \hat{\mathbf{r}}_{ib}) \hat{\mathbf{r}}_{ib} W_{ib} + \mathbf{f}, \end{aligned} \tag{15}$$

where σ (2 or 3) is the dimensionality of the problem. The first two r.h.s. terms in the above equations are the pressure terms, with Π being the viscous stress tensor for liquid phase. The third term is the drag term. To calculate the drag coefficient, Gidaspow's drag model [12] is used in which

$$K = \begin{cases} 150 \frac{\theta_D^2}{\theta_L^2} \frac{\mu}{d^2} + 1.75 \frac{\theta_D}{\theta_L} \frac{\varrho_L}{\varrho_D} |\mathbf{u}_{LD}| & \text{when} \quad \theta_L < 0.8 \\ \frac{3 \varrho_L \theta_L \theta_D C_D}{4d} |\mathbf{u}_{LD}| \theta_L^{-2.65} & \text{when} \quad \theta_L \geq 0.8 \end{cases}. \tag{16}$$

where d is the diameter of solid particle and C_D is drag coefficient taken as [13]

$$C_D = \frac{24}{Re_p} \left(1 + \frac{3}{16} Re_p \right)^{0.5}, \tag{17}$$

and $Re_p = d|\mathbf{u}_{LD}|/\nu$. The slip velocity $\mathbf{u}_{LD}$ is defined as $\mathbf{u}_{LD} = \mathbf{u}_L - \mathbf{u}_D$. The liquid-dust interactions used in the evaluation of drag term are calculated using a double-hump-shaped kernel

$$W(q) = \frac{63}{320\pi} q^2 (1 + 2q)(2 - q)^4, \tag{18}$$

where $q = |\mathbf{r}|/h$, $q \leq 2$. The liquid volume fraction is calculated from

$$\frac{d\theta_a}{dt} = -\frac{1}{\varrho_D} \sum_j m_j \mathbf{u}_{aj} \cdot \nabla_a W_{aj}, \tag{19}$$

and Eq. (2) for the dispersed phase [5]. The set of governing equations for fluid flow is closed with the state equation in the form

$$p_a = \frac{s^2 \varrho_0}{\gamma} \left[\left(\frac{\varrho_a}{\varrho_0} \right)^\gamma - 1 \right], \tag{20}$$

Figure 1: Left picture: test of the sand dispenser (the mass flux measurement in "dry" conditions). Right picture: the laser-lit sand sheet falling in the water tank; the upper edge marks the free surface and the white dashed line indicates the border of the sand-laden area; the sand bottom visible as lighter-gray region. Experimental data, courtesy of B. Stachurska (IBW PAN).

where s is a numerical speed of sound, γ is a constant and ϱ_0 is a reference density. In the present work, we deal with small volume fractions of dispersed phase, i.e. $\theta_D \leq 0.2$, hence we assumed $p_i = 0$ for all dust particles.

Note that, contrary to the original works where this model was developed [5, 14], all interactions are calculated using constant smoothing length. Additionally we use equation for mass evolution

$$\frac{dm_a}{dt} = m_a \sum_b \frac{m_b}{\hat{\varrho}_b} \mathbf{u}_{ab} \cdot \nabla_a W_{ab}, \tag{21}$$

to correct possible issues generated by changing volume densities, for details see [11].

3 RESULTS

3.1 Validation with the experiment

Since the model was tested for the cases of sedimentation in static and stirred tank [5, 14], we decided to proceed with validation with experiment designed and conducted specially for this task. The main goal was to deliver results that could serve as reference data for 2D numerical simulation. For that purpose, a simple wooden box with a thin outlet slit was constructed to form the curtain of sand with the width of 400 mm and the nominally constant thickness, in practice varying from 3 to 5 mm, see left panel of Fig. 1. The sand used had density of 2650 kg/m^3 and the mean grain diameter of 0.26 mm, and the measured mass flux was 148 ± 7 g/s. In the experiment, the sand sheet was vertically poured into the water tank, large enough to neglect the influence of vertical walls. Particle image velocimetry (PIV) measurements of the velocity field were performed with sand grains as tracers. A single experimental run lasted 10 seconds, measured from

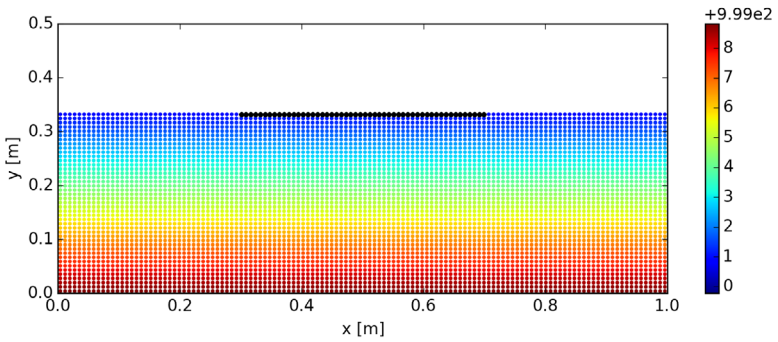

Figure 2: Computational domain at $t = 0\,\mathrm{s}$. Fluid particles are coloured with their densities set to match the hydrostatic pressure; black particles represent the sand.

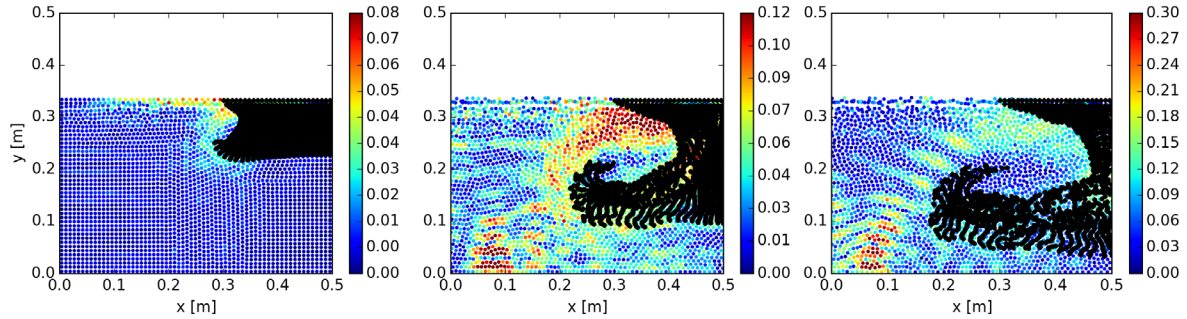

Figure 3: The SPH computation at $t = 2.5\,\mathrm{s}$ (left), $t = 5\,\mathrm{s}$ (middle) and $t = 6\,\mathrm{s}$ (right). Fluid particles are coloured with their velocities, black particles represent the sand; only the left half of domain is shown since the flow case was symmetric in practice, see Fig. 4.

the opening of the sand source to its closure. While the whole setup was designed to be treated as 2D case, dispersion of sand in direction perpendicular to the curtain's width was inevitable, making it in fact a 3D problem.

To reconstruct the experimental setup within the numerical simulation we used a square computational domain with periodic boundary conditions in the horizontal direction and no-slip boundary modelled with ghost particles at the bottom for the liquid phase. In the case considered, the initial water level was set to 33 cm, with one row of the dust particles at the free-surface, see Fig. 2. Initial velocity of dust was set to $u_0 = 25\,\mathrm{cm/s}$ as in the experiment. The new row of particles was added at the same place every 0.1 s with their velocities set to u_0. Due to the lack of proper boundary conditions at the bottom for dispersed phase, the dust particles were made to stop after reaching it.

The main problem in reconstructing the experimental conditions lies in setting θ_D, so that its value and the mass flux of sand are the same as in experiment. As a temporary remedy we tried to set θ_D, so that the mass flux is match, i.e. after 1 s mass of sand in the domain is equal to 148 g, which corresponds to $\theta_D = 0.00176$ at the resolution of

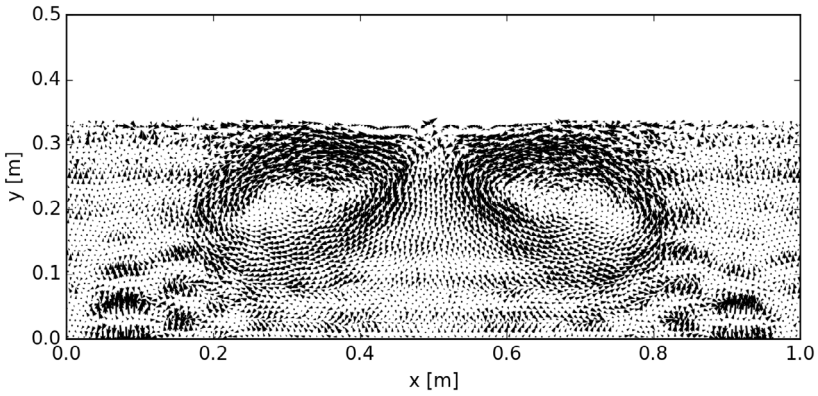

Figure 4: Velocity field of the liquid phase at $t = 5\,\mathrm{s}$ (see Fig. 3).

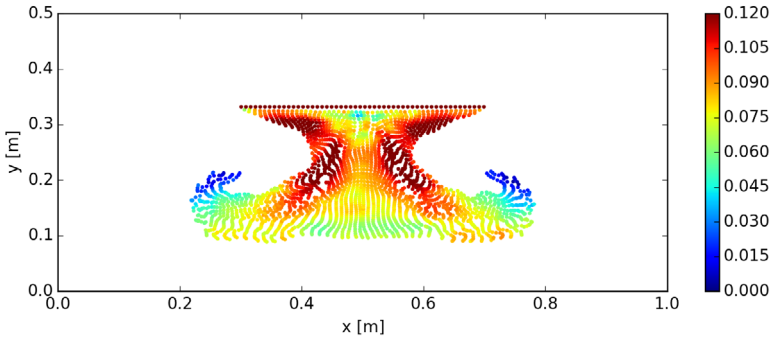

Figure 5: Velocity magnitude of dust particles at $t = 5\,\mathrm{s}$ (see Fig. 3).

$L/h = 64$ and $h/\Delta r = 2$. This turned out to be not the best solution, since such a low volume fraction of the dispersed phase had barely any effect on the liquid and general outcome was much different from the experimental one.

Setting θ_D to 0.0176 yielded more interesting results. Obviously, the mass flux was too high ($1.48\,\mathrm{kg/s}$), but this volume fraction was enough to stir the fluid, see Fig. 3. This resulted in two vortices appearing at the edges of sedimenting sand curtain, see Fig. 4. Note, that the velocity field within the liquid was rather noisy, especially in later stages of simulation.

It is hard to compare these results with the reference data, since the initial conditions were not reproduced perfectly. For the case of higher θ_D the behaviour of sand, i.e. bending of sand sheet near the free surface into a triangular shape and later expansion, was similar to the observations made in experiment, see right panel of Fig. 1. Furthermore, PIV measurements showed that sedimentation velocity was higher in the outer parts of sand curtain. This effect was also reproduced in SPH simulation, as shown in Fig. 5. It is important to note that rough estimations of θ_D in the experiment point towards

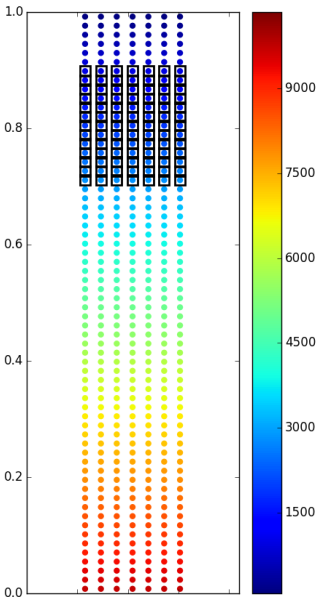

Figure 6: Computational domain at $t = 0$ s for quasi-2D simulation. Liquid particles are coloured with the hydrostatic pressure, dust particles are marked with black squares.

values around 0.1; however, reproducing this in calculations would require much higher resolution to reproduce mass flux correctly.

3.2 Quasi-2D study of sedimentation

Not satisfied with noisy velocity field within the liquid phase, see Fig. 3, we decided to investigate the model in more detail. For that purpose we used the validation case described by Kwon and Monaghan, 2015 [5], i.e. the infinitely long layer of sediment of thickness $0.2H$ falling due to the gravity within a hydrostatic tank of height H. Usually, periodic boundary conditions would be used, but since there is no motion in the x direction, governing equations can be solved with only y component. To avoid deriving the 1D SPH formulation, we considered 7 columns of particles, and solved governing equations for the middle one; for the initial setup see Fig. 6. Thanks to the compact support of the weighting kernels used, interactions with particles further away would return zero values. After the advection step, the fields' values and particle positions are rewritten row by row with those from the 4th column, hence quasi-2D. The sediment is placed between $0.7H$ and $0.9H$. Due to the gravity it should start falling and after short time reach constant settling velocity v_{ref}, known from the analytical solution of the problem. The results reported in this paper were obtained for $\theta_D = 0.02$ in the area occupied initially by dust; similar outcomes and conclusions were obtained for higher values of this parameter, however, we omitted them in the following for clarity.

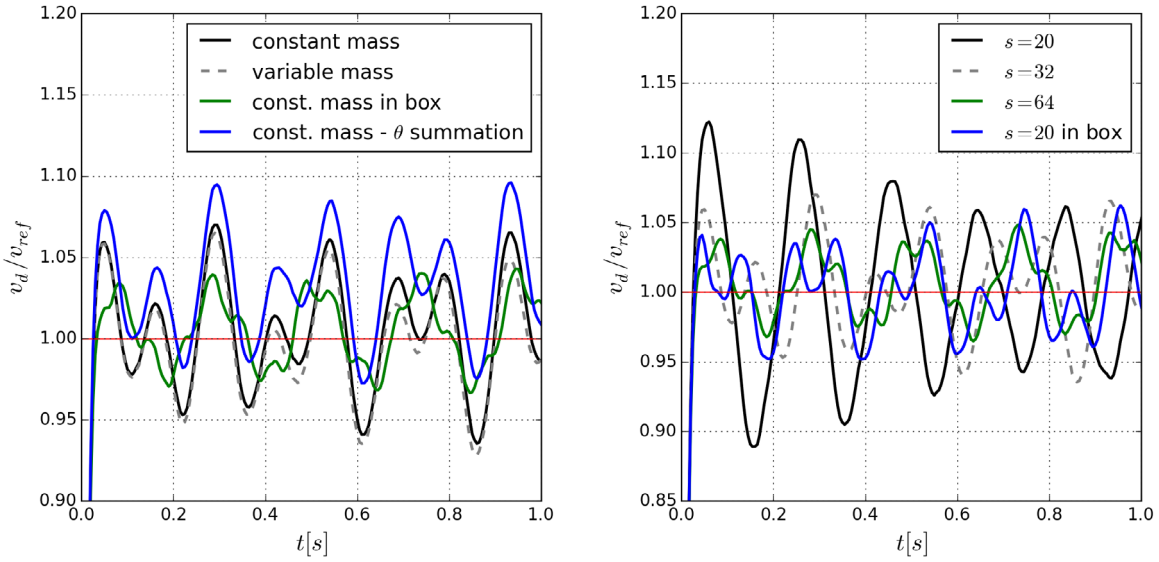

Figure 7: Evolution of the mean settling velocity for different variants of the model with $s = 32$ m/s (left) and influence of this parameter for the constant mass one (right).

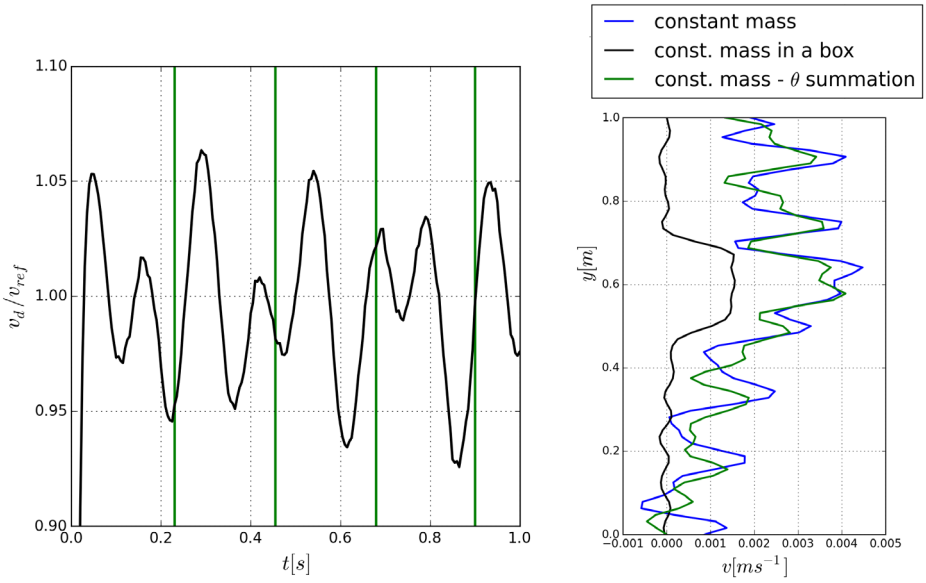

Figure 8: Evolution of the mean settling velocity for the middle row of dust particles with horizontal lines marking timesteps at which they are passing right through liquid particles (left) and comparison of the liquid phase velocity profiles (right).

For the sake of comparison we tested different variants of the model, namely:

1) "constant mass" - model presented in Section 2.2 without Eq. (21),

2) "variable mass" - model presented in Section 2.2 with Eq. (21),

3) "constant mass in box" - the same as the 1st one but with domain closed with wall instead of free surface,

4) "constant mass - θ summation" - the same as the 1st one but with summation formula for θ_L

$$\theta_a = 1 - \frac{1}{\varrho_D} \sum_j m_j W_{aj}, \tag{22}$$

instead of Eq. (19).

The result for the evolution of settling velocity v_d averaged over all dust particles is shown in Fig. 7. The velocity, instead of reaching a constant value, oscillates around the analytical prediction. Using Eq. (21) does not improve the results significantly, while the variant with evolution equation for θ_L gives slightly more accurate result. The magnitude of oscillations is lowered by increasing the speed of sound in Eq. (20), but without affecting their frequency. Closing the domain with the upper wall, however, improves outcomes in most visible way. It reduces the magnitude of oscillations, even for the lowest value of s tested. One of the possible reasons for this oscillations could be interaction of two sets of particles passing through each other, however, as presented on the left plot of Fig. 8, there is now correlation between extrema of the value of v_d and moments when dust particles are positioned exactly at spots occupied by the liquid particles. Furthermore, comparison of velocity profiles of water, see right plot of Fig. 8, shows that closing domain with the lid significantly reduces noise. This solution, while simple, is not very practical since it restricts simulations only to internal flows. The reason for oscillations in sedimentation velocity is hard to be pin-pointed, however, the fact that closed domain improves the results implies that the "liquid" part of the two-fluid SPH formulation requires some improvement for the free-surface flows.

4 CONCLUSIONS

In the paper the performance the two-fluid SPH model was assessed. The comparison with experiment was not complete due to difficulties in exact reproduction of the initial conditions within numerical simulation. The qualitative results, however, showed that the motion of the sand within a water computed with SPH was very similar to that observed in experiment. The analysis of the results for sedimentation in the quasi-2D setup showed that, apart from hard to explain oscillations in dust settling velocity, the formulation used for calculations requires a further extension of the model to treat free-surface flows. Using some variation of the δ-SPH scheme [15] might be one of the possible solutions.

Nevertheless, the perspective is promising, especially considering recent advancements in SPH for granular flows [3] and possible coupling of different SPH formalisms for hydro-engineering calculations.

Acknowledgements

This research was supported by the National Science Centre, project No. 2013/11/B/ST8/03818. We would like to thank Barbara Stachurska and Professor Ryszard Staroszczyk from Institute of Hydroengineering, Polish Academy of Sciences (IBW PAN) for providing the experimental data.

REFERENCES

[1] Monaghan, J.J., Smoothed Particle Hydrodynamics, *Annu. Rev. Astron. Astrophys.*, 30, pp. 543-574, 1992.

[2] Violeau, D. *Fluid Mechanics and the SPH Method: Theory and Applications*. Oxford University Press (2012).

[3] Szewc, K. Smoothed particle hydrodynamics modelling of granular column collapse. *Granul. Matter* (2017) **19:3**:1-13.

[4] Monaghan, J.J. and Kocharyan, A. SPH simulation of multi-phase flow. *Comp. Phys. Comm.* (1995) **87**:225-235.

[5] Kwon, J. and Monaghan, J.J. Sedimentation in homogeneous and inhomogeneous fluids using SPH. *Int. J. Multiphase Flow* (2015) **72**:155-164.

[6] Brennen, C.E. *Fundamentals of Multiphase Flows*. Cambridge University Press (2005).

[7] Bergantz, G.W. and Ni, J. A numerical study of sedimentation by dripping instabilities in viscous fluids. *Int. J. Multiphase Flow* (1999) **25**:307-320.

[8] Wendland, H. Piecewise polynomial, positive definite and compactly supported radial functions of minimal degree. *Adv. Comput. Math.* (1995) **4**:389-396.

[9] Szewc, K., Pozorski, J., and Minier, J.-P., Analysis of the incompressibility constraint in the SPH method, *Int. J. Numer. Meth. Eng.*, (2012) **92**:343-369.

[10] Colagrossi, A. and Landrini, M. Numerical simulation of interfacial flows by smoothed particle hydrodynamics. *J. Comput. Phys.* (2003) **191**:227-264.

[11] Szewc, K. Fluid-granular media multiphase modelling using the Smoothed Particle Hydrodynamics method. *9th International Conference on Multiphase Flow*, Florence, Italy, May 22-27, 2016, paper no. **1098**, Proceedings on a USB.

[12] Gidaspow, D. *Multiphase Flow and Fluidization: Continuum and Kinetic Theory Description*. Academic Press, San Diego (1994).

[13] Olson, R.M. *Essentials of Engineering Fluid Mechanics*. International Textbook Company, Scranton, Pennsylvania (1960).

[14] Kwon, J. and Monaghan, J.J. A novel SPH method for sedimentation in a turbulent fluid. *J. Comp. Phys.* (2015) **300**:520-532.

[15] Molteni, D. and Colagrossi, A. A simple procedure to improve the pressure evaluation in hydrodynamic context using the SPH. *Comp. Phys. Comm.* (2009) **180**:861-872.

V International Conference on Particle-based Methods – Fundamentals and Applications
PARTICLES 2017
P. Wriggers, M. Bischoff, E. Oñate, D.R.J. Owen, & T. Zohdi (Eds)

CROSS-FLOW OF AIR THROUGH SEALED ELEVATOR ENCLOSURES

O. A. AVERKOVA[1], I.N. LOGACHEV[1] , K.I. LOGACHEV[1] AND O.N. ZAYTSEV[2]

[1] Belgorod State Technological University named after V.G. Shukhov
(BSTU named after V.G. Shukhov),
Kostukova str., 46, Belgorod, Russia, 308012
e-mail: kilogachev@mail.ru, web page: http://www.bstu.ru

[2] V.I. Vernadsky Crimean Federal University (Vernadsky CFU),
4 Vernadskogo Prospekt, Simferopol, Russia, 295007
e-mail: zon071941@mail.ru, web page: http://www.eng.cfuv.ru

Key words: Granular Materials, Bulk Material Transfer, Air Suction, Local Exhaust Ventilation.

Abstract. Both the direction and the flow rate of ejected air in bucket elevator [1,2] enclosures that feature a separate arrangement of carrying and idle conveyor runs would depend on the ratio between ejection heads and the difference between static pressures inside the enclosures of elevator head and elevator boot. A forward motion of air (along the bucket travel direction) arises inside the enclosure of the carrying run when ejection forces prevail and inside the return run enclosure at any ejection forces differential pressures. A counterflow of air is only possible in a single enclosure.

Relative velocities and flow rates of air inside the elevator enclosures depend on two parameters, *t* and *g*, representing the ratio of differential pressures and resistances of enclosures to ejection forces.

When pressures inside the upper and lower elevator enclosures are equal. With ejection forces large enough air velocities become equal to the velocity of traveling elevator buckets.

Absolute velocities of airflows inside enclosures are dependent not only on the velocity of moving buckets but also on the differential pressure, head resistance of elevator buckets and aerodynamic drag of enclosures, as well as spillage of particles.

In the case of a forward flow pattern, air flow rate inside the return run enclosure is greater than the one inside the carrying run enclosure of the elevator conveyor. The explanation is that ejection forces arise in an opposite direction to forces caused by differential pressure inside the carrying run enclosure (both forces act in the same direction inside the return run, thus intensifying the air ejection process and boosting additional ejection forces which occur when buckets are unloaded, producing streams of spilled particles), as well as different values of the drag coefficient for empty and laden buckets.

When air moves in a counterflow pattern, ejection forces of buckets create additional drag and therefore the absolute flow rate of ascending air inside the return run enclosure, as well as descending air inside the carrying run enclosure, increase less markedly than in the forward flow case.

1 INTRODUCTION

Consider the most common case of an elevator with two buckets. Let the carrying and return runs of the elevator with buckets be located in separate sealed enclosures that will not experience cross-flows of air over their entire length. These enclosures are aerodynamically coupled only in their bottom (loading) and top (unloading) parts.

2 THE RESULTS OF THE STUDY

Let static pressure p be maintained in these parts respectively at p_k and p_n, additionally assuming that

$$p_k < p_n . \tag{1}$$

In this case air will arrive from the upper into the lower zone through the return run enclosure but will only pass through the carrying run enclosure when ejection head caused by laden buckets is lower that differential static pressure.

$$\Delta p_e \le p_n - p_k , \tag{2}$$

Then, the limit case (at $v = 0$) owing to (7.65) and (7.66) will be written as:

$$p_n - p_k > \zeta_1 \frac{v_e^2}{2} \rho \tag{3}$$

or the following inequality can be used to describe the trigger condition for ejection properties of the carrying run:

$$h_a = \frac{p_n - p_k}{\frac{v_e^2}{2} \rho} > \zeta_1 \tag{4}$$

or

$$t_1 = \frac{h_a}{M_1} \ge 1 . \tag{5}$$

Hereinafter a subscript “1” will continue to denote characteristic parameters of airflow inside the enclosure of conveyor carrying run (i.e. “1” will be substituted for index $'v'$, e.g. longitudinal air velocity u_1 instead of v, ζ_1 instead of ζ_v, M_1 instead of M_v etc.), whereas subscript “2” will denote longitudinal airflow in the return run enclosure (airflow velocity u_2 instead of u, parameter ζ_2 instead of ζ_u, M_2 instead of M_u etc.)

Generally (when p_n may also be less than p_k), two patterns of air cross-flows through bucket elevator enclosures are possible: a direct-flow pattern with positive velocities u_1 and u_2 and air moving in the same direction with buckets, and a combined pattern whereby airflow and bucket traveling directions are the same in one enclosure but opposite in the other (Fig. 1).

Let's determine air flow rates Q_1 and Q_2 as well as their difference:

$$\Delta Q = Q_2 - Q_1 .$$

Air flow rates can also become negative, depending on the sign and magnitude of velocity vectors u_1 and u_2.

First we'll determine the flow rate Q_2. Dynamics equation (7.43) will be used to find out the flow rate in the return run enclosure. In this case static pressure at inlet and outlet of the enclosure will be expressed through pressures p_n and p_k using local resistance coefficients for air entering the enclosure (ζ_{2n}) and leaving the enclosure (ζ_{2k}).

$$p_2(0) = p_n - \zeta_{2n} \frac{u_2^2}{2} \rho , \tag{6}$$

$$p_2(l) = p_k + \zeta_{2k} \frac{u_2^2}{2} \rho . \tag{7}$$

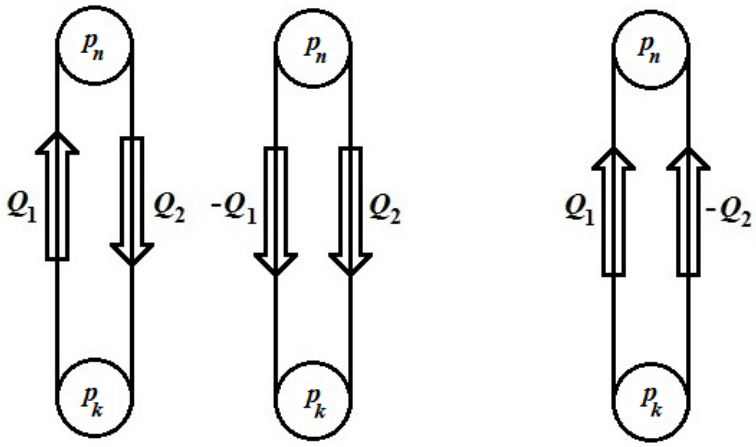

a) At $p_n > p_k$ b) At $p_n < p_k$

Figure 1: Aerodynamic diagrams for cross-flows of air in two sealed enclosures of a bucket elevator

In view of the accepted conditions we'll rewrite equation (7.43) and expand the values of E_k and E_p based on (7.47), (7.48) and (7.52),

$$p_k - p_n + \sum \zeta_2 \frac{u_2^2}{2} \rho = M_2 \frac{|v_e - u_2|(v_e - u_2)}{2} \rho , \tag{8}$$

where $\sum \zeta_2$ is the sum total of LRCs of the enclosure.

$$\sum \zeta_2 = \zeta_{2n} + \lambda_w \frac{l}{D_w} + \zeta_{2k} , \tag{9}$$

M_2 is a parameter describing the ejection capacity of the return run of the conveyor and flow of spilled material (in accordance with formula (7.78)).

If both sides of the equation are divided by $\rho\frac{v_e}{2}$, a dimensionless equation would result:

$$-h_a + \sum\zeta_2\varphi_2^2 = M_2\left|1-\varphi_2\right|\left(1-\varphi_2\right), \tag{10}$$

where $\varphi_2 = \frac{u_2}{v_e}$;

$$h_a = \frac{p_n - p_k}{\rho\frac{v_e^2}{2}} = \frac{h_k - h_n}{\rho\frac{v_e^2}{2}}, \tag{11}$$

where h_k is the negative pressure maintained inside an aspirated cowl of elevator boot by an aspiration system fan (Pa); h_n is the sustained negative pressure occurring inside an unaspirated cowl of the bucket elevator head as a result of air cross-flow through the unloading chute and elevator enclosures (Pa).

The sought flow rate Q_2 is determined by an obvious relation

$$Q_2 = \varphi_2 v_e S, \tag{12}$$

where $S = a \cdot b$.

The value of φ_2 is determined with equation (10) which, owing to random nature of h_a, can be written as the following dimensionless equation:

$$h_a + M_2\left|1-\varphi_2\right|\left(1-\varphi_2\right) = \sum\zeta_2\varphi_2\left|\varphi_2\right|, \tag{13}$$

or

$$t_2 = g_2\varphi_2\left|\varphi_2\right| - \left|1-\varphi_2\right|\left(1-\varphi_2\right), \tag{14}$$

where dimensionless numbers have been introduce to dispense with some determinant parameters:

$$t_2 = \frac{h_a}{M_2}, \tag{15}$$

$$g_2 = \frac{\sum\zeta_2}{M_2}, \tag{16}$$

representing a ratio of the available pressure and pressure losses to the total resistance that the enclosure poses to ejection head created by the bucket elevator [1].

Expanding signs of absolute values reduces equation (14) to the following three combined equations:

$$t_2 = g_2\varphi_2^2 - \left(1-\varphi_2\right)^2 \quad \text{at } 1 \ge \varphi_2 \ge 0; \tag{17}$$

$$t_2 = -g_2\varphi_2^2 - \left(1-\varphi_2\right)^2 \quad \text{at } -\infty < \varphi_2 \le 0; \tag{18}$$

$$t_2 = g_2\varphi_2^2 + \left(1-\varphi_2\right)^2 \quad \text{at } +\infty > \varphi_2 \ge 1. \tag{19}$$

[1] One should keep in mind that the parameter g_2 may change as a result of possible changes in $\sum\zeta$ when the sign of φ_2 reverses.

The single-valued function $\varphi_2 = f(t_2)$ is plotted as a joint set of three parabolic arcs (Fig. 2):

$$y_1 \equiv t_2 = -\varphi_2(g_2+1) + 2\varphi_2 - 1 \text{ at } -\infty < \frac{\varphi}{2} \le 0; \tag{20}$$

$$y_2 \equiv t_2 = -\varphi_2^2(1-g_2) + 2\varphi_2 - 1 \text{ at } 1 \ge \varphi_2 \ge 0; \tag{21}$$

$$y_3 \equiv t_2 = -\varphi_2^2(1+g_2) - 2\varphi_2 + 1 \text{ at } \infty > \varphi_2 \ge 1. \tag{22}$$

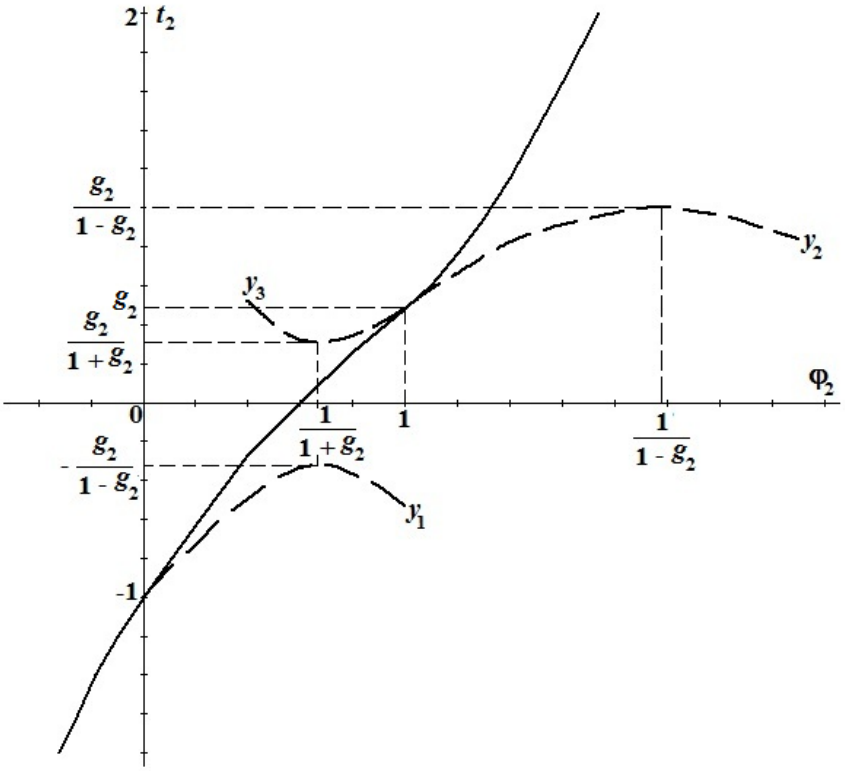

Figure 2: Variation in relative flow rate of air transferred the enclosure of elevator conveyor return run as a function of pressure transitions (solid curve – plot of single-valued function $\varphi_2 = f(t_2)$)

In order to obtain a single value for dimensionless flow rate φ_2 across the entire variation range of the parameter t_2, roots of the following equations have to be found:

$$-\varphi_2^2(1+g_2) + 2\varphi_2 - (1+t_2) = 0 \text{ at } -\infty < t_2 < -1; \tag{23}$$

$$-\varphi_2^2(1-g_2) + 2\varphi_2 - (1+t_2) = 0 \text{ at } g_2 > t_2 > -1; \tag{24}$$

$$\varphi_2^2(1+g_2) - 2\varphi_2 + (1-t_2) = 0 \text{ at } \infty > t_2 > g_2. \tag{25}$$

As a result (at $g_2 < 1$),

$$\varphi_2 = \frac{1}{1+g_2}\left[1 - \sqrt{1-(1+t_2)(1+g_2)}\right] \quad \text{at } -\infty < t_2 \le -1; \tag{26}$$

$$\varphi_2 = \frac{1}{1-g_2}\left[1-\sqrt{1-(1+t_2)(1-g_2)}\right] \quad \text{at } g_2 > t_2 \geq -1; \tag{27}$$

$$\varphi_2 = \frac{1}{1+g_2}\left[1+\sqrt{1-(1-t_2)(1+g_2)}\right] \quad \text{at } \infty > t_2 > g_2. \tag{28}$$

Thus, forward airflow arises in the enclosure of the return run at $t_2 > -1$ i.e. at

$$M_2 > -h_a\,. \tag{29}$$

Otherwise, at

$$M_2 < -h_a\,, \tag{30}$$

a countercurrent of air is promoted by a significant negative pressure in the upper cowl at

$$h_n > h_k + M_2 \frac{v_e^2}{2}\rho\,. \tag{31}$$

Absent differential pressure $(h_n = h_k)$, φ_2 reaches its limit value:

$$\lim_{t_2 \to 0} \varphi_2 = \varphi_{2pr} = \frac{1}{1+\sqrt{g_2}}\,, \tag{32}$$

which converges toward one with increasing ejection forces

$$\varphi_{2pr} \approx 1\,, \text{ at } M_2 >> \sum\zeta_2\,, \tag{33}$$

i.e. the velocity of air inside the return run conveyor belt enclosure of the elevator reaches the velocity of the belt only with significant ejection forces.

Let's now determine air flow rate inside the enclosure of the carrying run of the bucket elevator. To that end we'll put forward an equation for the dynamics of air in this enclosure with a compound effect of differential pressure $\Delta p = p_n - p_k$ and of ejection head created by a belt with laden buckets. It will be recognized that air velocity u_1 may turn negative at significant differential pressures. The dynamics equation for airflow in this enclosure will be put down as follows[2]:

$$M_1\left|1-\varphi_1\right|(1-\varphi_1) - h_a = \sum\zeta_1\varphi_1\left|\varphi_1\right| \tag{34}$$

or

$$t_1 = \left|1-\varphi_1\right|(1-\varphi_1) - g_1\varphi_1\left|\varphi_1\right|\,, \tag{35}$$

where

$$t_1 = \frac{h_a}{M_1}\,;\; g_1 = \frac{\sum\zeta_1}{M_1}\,. \tag{36}$$

An expansion of the signs at absolute values breaks down the equation (35) into three separate ones:

[2] It should be noted that, generally, a reversal of airflow inside elevator enclosure will also change $\sum\zeta_1$ and $\sum\zeta_2$ ($\sum\zeta_1 \uparrow \neq \sum\zeta_1 \downarrow$; $\sum\zeta_2 \downarrow \neq \sum\zeta_2 \uparrow$, arrows indicate downward ($\downarrow$) and upward ($\uparrow$) airflow direction).

$$t_1 = (1-\varphi_1)^2 + g_1\varphi_1^2 \qquad \text{at } -\infty < \varphi_1 \le 0; \tag{37}$$

$$t_1 = (1-\varphi_1)^2 - g_1\varphi_1^2 \qquad \text{at } 1 \ge \varphi_1 \ge 0; \tag{38}$$

$$t_1 = -(1-\varphi_1)^2 - g_1\varphi_1^2 \qquad \text{at } +\infty > \varphi_1 \ge 1. \tag{39}$$

The first of these equations describes the balance of dimensionless forces in the case of downward (from top to bottom) motion of air arising as a result of a significant difference in the available static differential pressure ($\Delta p = p_n - p_k$). The ejection head of a bucket-carrying belt reduces airflow, further hindering the downward motion. When the available differential pressure is small enough (the second and third equations), an upward airflow (from bottom to top) arises. In this case it is counteracted not only by the drag of enclosure walls but also by differential pressure Δp.

The single-valued function $\varphi_1 = f(t_1)$ is plotted as a joint set of three parabolic arcs[3] (Fig. 3):

$$y_1 \equiv t_1 = (1+g_1)\varphi_1^2 - 2\varphi_1 + 1 \text{ at } -\infty < \varphi_1 \le 0; \tag{40}$$

$$y_2 \equiv t_1 = (1-g_1)\varphi_1^2 - 2\varphi_1 + 1 \text{ at } 1 \ge \varphi_1 \ge 0; \tag{41}$$

$$y_3 \equiv t_1 = -(1+g_1)\varphi_1^2 + 2\varphi_1 - 1 \text{ at } +\infty > \varphi_1 \ge 1. \tag{42}$$

Single-valued functions of dimensionless air velocity φ_1 inside the enclosure of the carrying run of the conveyor within the entire range of variations in the parameter t_1 are determined by roots of the following equations:

$$(1+g_1)\varphi_1^2 - 2\varphi_1 + (1-t_1) = 0 \text{ at } \infty > t_1 \ge 1; \tag{43}$$

$$(1-g_1)\varphi_1^2 - 2\varphi_1 + (1-t_1) = 0 \text{ at } -g_1 \le t_1 \le 1; \tag{44}$$

$$(1-g_1)\varphi_1^2 - 2\varphi_1 - (1+t_1) = 0 \text{ at } -\infty < t_1 \le -g_1, \tag{45}$$

which gives (at $g_1 < 1$):

$$\varphi_1 = \frac{1}{1+g_1}\left[1 + \sqrt{1-(1+t_1)(1+g_1)}\right] \qquad \text{at } -\infty \le t_1 \le -g_1; \tag{46}$$

$$\varphi_1 = \frac{1}{1-g_1}\left[1 - \sqrt{1+(t_1-1)(1-g_1)}\right] \qquad \text{at } 1 \ge t_1 \ge -g_1; \tag{47}$$

$$\varphi_1 = \frac{1}{1+g_1}\left[1 - \sqrt{1+(t_1-1)(1+g_1)}\right] \qquad \text{at } \infty > t_1 \ge 1. \tag{48}$$

[3] Parabola sections outside of the range of single-valued function $t = f(\varphi)$ are shown on Fig. 3.6 as dotted lines.

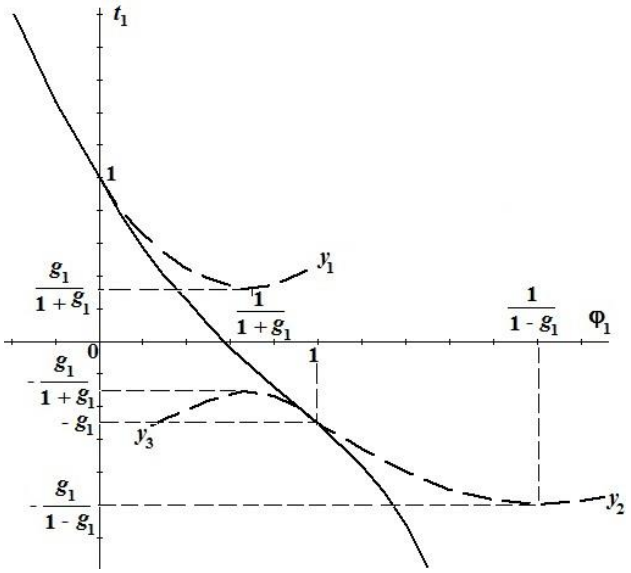

Figure 3: Variation in relative flow rate of air flowing over the enclosure of elevator conveyor carrying run as a function of differential pressure (solid curve – plot of single-valued function $\varphi_1 = f(t_1)$)

As is evident from these results, counterflow of air $(\varphi_1 < 0)$ inside the enclosure of conveyor belt carrying run may only arise at greater values of the parameter t_1, i.e. at

$$t_1 > 1, \quad h_k > h_n + M_1 \frac{v_e^2}{2} \rho . \tag{49}$$

The limit value of dimensionless air velocity (flow rate) inside the enclosure of the conveyor carrying run (at $h_k = h_n$) is

$$\lim_{t_1 \to 0} \varphi_1 = \varphi_{1pr} = \frac{1}{1+\sqrt{g_1}} \tag{50}$$

and air velocity u_1 reaches the velocity of buckets v_e

$$\varphi_{1pr} = 1 \text{ at } M_1 >> \sum \zeta_1 . \tag{51}$$

When static differential pressure is small $(t_1 < 1)$ only the forward airflow pattern may arise inside enclosures. Airflow follows the traveling conveyor belt inside enclosures of the bucket elevator. Additionally, as a rule,

$$Q_2 > Q_1 .$$

This is explained by the influence of ejecting capacity of spillage when grain is unloaded from buckets in the upper part of elevator, and by the difference between the drag of an empty bucket and a grain-laden bucket. In addition the available differential pressure promotes airflow inside return run enclosures while hindering it in the carrying run enclosure. The latter explains the fact that, given equal ejection forces ($M_1 = M_2$) and aerodynamic drag forces (

$\sum\zeta_1 = \sum\zeta_2$), velocities (airflows in bucket elevator enclosures) fail to equalize (Fig. 4).

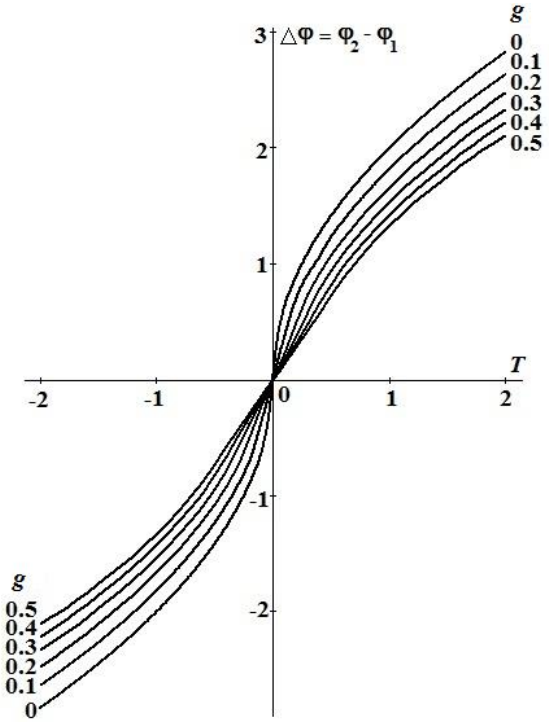

Figure 4: Changes in relative flow rate of air transferred through bucket elevator enclosures (at $t_1 = t_2 = t$, $g_1 = g_2 = g$)

In this case the difference between airflows

$$Q_2 - Q_1 = (\varphi_2 - \varphi_1) v_e S \tag{52}$$

will be either positive (at $t > 0$) or negative (at $t < 0$) and will increase in its absolute value with increasing parameter t.

Tables 1 and 2 summarize calculated values of relative air flow rates inside bucket elevator enclosures. These values have been determined using formulas (26–28) and (46–48).

These findings reveal that, within the range of low available pressures (at $t < 1$), flow rate of ascending air inside the return run enclosure declines both with increasing parameter t_2 and decreasing parameter g_2. Within the range of high available pressures (at $t_2 > g_2$), air velocity $u_2 > v_e$. In this case the ejecting capacity of empty buckets poses additional resistance and therefore relative flow air φ_2 would decrease with increasing M_2 at unchanged Δp (and decreasing t_2).

The relative flow rate of ascending air decreases with increasing Δp inside the enclosure of the carrying run of the conveyor, and a downward airflow arises at $t_1 > 1$ (φ_1 is negative). Higher values of M_1 (decreasing t_1) result in decreased flow rate φ_1.

Table 1: Relative air flow rate φ_2 inside the enclosure of bucket elevator return run

t_2 \ g_2	0	0.1	0.2	0.3	0.4	0.5
-2.0	-0.4142	-0.4083	-0.4027	-0.3974	-0.3923	-0.3874
-1.9	-0.3784	-0.3733	-0.3685	-0.3639	-0.3595	-0.3553
-1.8	-0.3416	-0.3374	-0.3333	-0.3295	-0.3257	-0.3222
-1.7	-0.3036	-0.3004	-0.3971	-0.2939	-0.2908	-0.2879
-1.6	-0.2649	-0.2622	-0.2596	-0.2571	-0.2546	-0.2523
-1.5	-0.2247	-0.2227	-0.2208	-0.2189	-0.2170	-0.2153
-1.4	-0.1832	-0.1818	-0.1805	-0.1791	-0.1779	-0.1766
-1.3	-0.1402	-0.1393	-0.1385	-0.1377	-0.1369	-0.1361
-1.2	-0.0954	-0.0950	-0.0946	-0.0942	-0.0938	-0.0935
-1.1	-0.0488	-0.0487	-0.0486	-0.0485	-0.0484	-0.0483
-1.0	0.000	0.000	0.000	0.000	0.000	0.000
-0.9	0.0513	0.0512	0.0510	0.0509	0.0508	0.0506
-0.8	0.1056	0.1050	0.1044	0.1038	0.1032	0.1026
-0.7	0.1633	0.1618	0.1603	0.1588	0.1574	0.1561
-0.6	0.2254	0.2222	0.2192	0.2164	0.2137	0.211
-0.5	0.2929	0.2871	0.2818	0.2768	0.3722	0.2679
-0.4	0.3675	0.3575	0.3486	0.3406	0.3333	0.3267
-0.3	0.4523	0.4352	0.4208	0.4084	0.3974	0.3875
-0.2	0.5528	0.5232	0.5000	0.4810	0.4648	0.4508
-0.1	0.6838	0.6268	0.5886	0.5596	0.5363	0.5168
0	1.000	0.7597	0.6910	0.6461	0.6126	0.5858
0.1	1.3162	1.000	0.8170	0.7435	0.6948	0.6584
0.2	1.4472	1.2240	1.000	0.8511	0.7847	0.7351
0.3	1.5477	1.3451	1.1667	1.000	0.8849	0.8168
0.4	1.6325	1.4392	1.2743	1.1300	1.000	0.9046
0.5	1.7071	1.5189	1.3604	1.2243	1.1055	1.000
0.6	1.7746	1.5894	1.4343	1.3022	1.1881	1.0883
0.7	1.8367	1.6535	1.5000	1.3700	1.2583	1.1611
0.8	1.8944	1.7120	1.5598	1.4309	1.3204	1.2244
0.9	1.9487	1.7667	1.6151	1.4867	1.3767	1.2813
1.0	2.0000	1.8182	1.5667	1.5385	1.4286	1.3333
1.1	2.0488	1.8669	1.7153	1.5869	1.4769	1.3816
1.2	2.0954	1.9132	1.7613	1.6357	1.5224	1.4268
1.3	2.1402	1.9575	1.8052	1.66761	1.5655	1.4694
1.4	2.1832	2.0000	1.8471	1.7176	1.6064	1.5099
1.5	2.2247	2.0409	1.8874	1.7573	1.6456	1.5486
1.6	2.2649	2.0804	1.9262	1.7955	1.6832	1.5856
1.7	2.3038	2.1186	1.9637	1.8323	1.7194	1.6212
1.8	2.3416	2.1556	2.0000	1.8679	1.7543	1.6555
1.9	2.3784	2.1915	2.0354	1.9024	1.7881	1.6886
2	2.4142	2.2265	2.0694	1.9358	1.8209	1.7208

Table 2: Relative air flow rate φ_1 inside the enclosure of bucket elevator carrying run

t_1 \ g_1	0	0.1	0.2	0.3	0.4	0.5
-2.0	2.4142	2.2265	2.0694	1.9358	1.8209	1.7208
-1.9	2.3784	2.1915	2.0354	1.9024	1.7881	1.6886
-1.8	2.3416	2.1556	2.0000	1.8679	1.7543	1.6555
-1.7	2.3038	2.1186	1.9637	1.8323	1.7194	1.6212
-1.6	2.2649	2.0804	1.9262	1.7955	1.6832	1.5856
-1.5	2.2247	2.0409	1.8874	1.7573	1.6456	1.5486
-1.4	2.1832	2.0000	1.8471	1.7176	1.6064	1.5099
-1.3	2.1402	1.9575	1.8052	1.6761	1.5655	1.4694
-1.2	2.0954	1.9132	1.7613	1.6357	1.5224	1.4268
-1.1	2.0488	1.8669	1.7153	1.5869	1.4769	1.3816
-1.0	2.0000	1.8182	1.5667	1.5385	1.4286	1.3333
-0.9	1.9487	1.7667	1.6151	1.4867	1.3767	1.2813
-0.8	1.8944	1.7120	1.5598	1.4309	1.3204	1.2244
-0.7	1.8367	1.6532	1.5000	1.3700	1.2583	1.1611
-0.6	1.7746	1.5894	1.4343	1.3022	1.1881	1.0883
-0.5	1.7071	1.5189	1.3604	1.2243	1.1055	1.000
-0.4	1.6325	1.4392	1.2743	1.1300	1.000	0.9046
-0.3	1.5477	1.3451	1.1667	1.000	0.8849	0.8168
-0.2	1.4472	1.2240	1.000	0.8511	0.7847	0.7351
-0.1	1.3162	1.000	0.8170	0.7435	0.6948	0.6584
0	1.000	0.7597	0.6910	0.6461	0.6126	0.5858
0.1	0.6838	0.6268	0.5886	0.5596	0.5363	0.5168
0.2	0.5528	0.5232	0.5000	0.4810	0.4648	0.4508
0.3	0.4523	0.4352	0.4208	0.4084	0.3974	0.3875
0.4	0.3675	0.3775	0.3486	0.3406	0.3333	0.3267
0.5	0.2929	0.2871	0.2818	0.2768	0.3722	0.2679
0.6	0.2254	0.2222	0.2192	0.2164	0.2137	0.2111
0.7	0.1633	0.1618	0.1603	0.1588	0.1574	0.1561
0.8	0.1056	0.1050	0.1044	0.1038	0.1032	0.1026
0.9	0.0513	0.0512	0.0510	0.0509	0.0508	0.0506
1.0	0.000	0.000	0.000	0.000	0.000	0.000
1.1	-0.0488	-0.0487	-0.0486	-0.0485	-0.0484	-0.0483
1.2	-0.0954	-0.0950	-0.0946	-0.0942	-0.0938	-0.0935
1.3	-0.1402	-0.1393	-0.1385	-0.1377	-0.1369	-0.1361
1.4	-0.1832	-0.1818	-0.1805	-0.1791	-0.1779	-0.1766
1.5	-0.2247	-0.2227	-0.2208	-0.2189	-0.2170	-0.2153
1.6	-0.2649	-0.2622	-0.2596	-0.2571	-0.2546	-0.2523
1.7	-0.3036	-0.3004	-0.3971	-0.2939	-0.2908	-0.2879
1.8	-0.3416	-0.3374	-0.3333	-0.3295	-0.3257	-0.3222
1.9	-0.3784	-0.3733	-0.3685	-0.3639	-0.3595	-0.3553
2	-0.4142	-0.4083	-0.4027	-0.3974	-0.3923	-0.3874

CONCLUSIONS

- Both the direction and the flow rate of ejected air in bucket elevator enclosures that

feature a separate arrangement of carrying and idle conveyor runs would depend on the ratio between ejection heads and the difference between static pressures inside the enclosures of elevator head and elevator boot. A forward motion of air (along the bucket travel direction) arises inside the enclosure of the carrying run when ejection forces prevail (at $\Delta\overline{p} < M_1$, $t_1 < 1$ and $\Delta\overline{p} < M_2$) and inside the return run enclosure at any ejection forces differential pressures (at $\Delta\overline{p} > -M_2$, $t_2 > -1$). A counterflow of air is only possible in a single enclosure: within the carrying run enclosure at $\Delta\overline{p} > M_1$ or within the return run enclosure at $\Delta\overline{p} < -M_2$. The other enclosure would experience a forward flow of air in this case.

- Relative velocities and flow rates of air inside the elevator enclosures depend on two parameters, t and g (14) and (35), representing the ratio of differential pressures and resistances of enclosures to ejection forces. Single-valued variables φ_1 and φ_2 within a wide range of differential pressures ($-\infty < t_1 < \infty$; $-\infty < t_2 < \infty$) can be determined using formulas (46 … 48) and (26 … 28).

When pressures inside the upper and lower elevator enclosures are equal, relative velocities reach their maxima determined by relations (50) and (32). With ejection forces large enough ($M_1 >> \sum\zeta_1$ and $M_2 >> \sum\zeta_2$) air velocities become equal to the velocity of traveling elevator buckets.

Absolute velocities of airflows inside enclosures are dependent not only on the velocity of moving buckets but also on the differential pressure, head resistance of elevator buckets and aerodynamic drag of enclosures, as well as spillage of particles.

- In the case of a forward flow pattern, air flow rate inside the return run enclosure is greater than the one inside the carrying run enclosure of the elevator conveyor. The explanation is that ejection forces arise in an opposite direction to forces caused by differential pressure inside the carrying run enclosure (both forces act in the same direction inside the return run, thus intensifying the air ejection process and boosting additional ejection forces which occur when buckets are unloaded, producing streams of spilled particles), as well as different values of the drag coefficient for empty and laden buckets.

When air moves in a counterflow pattern, ejection forces of buckets create additional drag and therefore the absolute flow rate of ascending air inside the return run enclosure, as well as descending air inside the carrying run enclosure, increase less markedly than in the forward flow case (Tables 1 and 2).

The work has been carried out with the financial support of the Grant Council of the President of the Russian Federation (project MD-95.2017.8) and RFBR (research project No. 16-08-00074a).

REFERENCES

[1] I. N. Logachev and K.I. Logachev. Industrial Air Quality And Ventilation: Controlling Dust Emissions. Boca Raton: CRC Press, 2014.

[2] I. N. Logachev, K. I. Logachev and O.A. Averkova. Local Exhaust Ventilation: Aerodynamic Processes and Calculations of Dust Emissions. Boca Raton: CRC Press, 2015.

V International Conference on Particle-based Methods – Fundamentals and Applications
PARTICLES 2017
P. Wriggers, M. Bischoff, E. Oñate, D.R.J. Owen, & T. Zohdi (Eds)

EJECTING PROPERTIES OF A BUCKET ELEVATOR

O. A. AVERKOVA[1], I.N. LOGACHEV[1] , K.I. LOGACHEV[1] AND O.N. ZAYTSEV[2]

[1] Belgorod State Technological University named after V.G. Shukhov
(BSTU named after V.G. Shukhov),
Kostukova str., 46, Belgorod, Russia, 308012
e-mail: kilogachev@mail.ru, web page: http://www.bstu.ru

[2] V.I. Vernadsky Crimean Federal University (Vernadsky CFU),
4 Vernadskogo Prospekt, Simferopol, Russia, 295007
e-mail: zon071941@mail.ru, web page: http://www.eng.cfuv.ru

Key words: Granular Materials, Bulk Material Transfer, Air Suction, Local Exhaust Ventilation.

Abstract. Air inside the enclosure of a belt elevator may be brought into motion both by moving bucket belt and by spillage flows during loading and unloading of buckets. Initial findings from studies performed to evaluate air motion in ducts with mobile partitions have been published in our earlier monographs [1-3]. Here we'll consider the process of air ejection in bucket elevators from the standpoint of classical laws of change in air mass and momentum. Direction of airflow inside enclosures of the carrying and return runs of a bucket elevator is determined by the drag of buckets and moving conveyor belt as well as ejection head created by a stream of spilled particles when buckets are unloaded. As a result of these forces acting together inside an enclosure, differential pressure arises. This differential pressure is equal to the sum total of ejection heads created by conveyor belt with buckets E_k and flow rate of spilled material E_p minus aerodynamic drag of enclosure walls.

The ejection head E_k created by a bucket-carrying conveyor belt is determined by aerodynamic coefficient c_{ek} (proportional to the number of buckets, their head resistances and squared mid-sectional dimensions) together with an absolute value and the direction of bucket velocity relative to the velocity of airflow inside the enclosure. Ejection head of spilled particles E_p depends on the drag coefficient of particles, their size and flow rate, as well as the enclosure length, enclosure cross-section and relative flow velocity of particles.

When both the carrying and return runs of the conveyor belt are located in a common enclosure, the velocity of forward airflow varies over its length as a result of cross-flows of air through gaps between the conveyor runs and enclosure walls. Cross-flows are caused by a differential pressure between the carrying and return run enclosures and is dependent on the drag of the gap. Cross-flow direction depends on the ratio between p_v and p_u.

Given identical size of elevator enclosures, change in absolute values of longitudinal velocities is identical and depends on absolute values of cross-flow velocities and geometrical dimensions of the gap, as well as enclosure cross-section. The momentum of longitudinal

airflow in this case is determined by variable magnitudes of aerodynamic forces of buckets due to changes in their relative motion velocities.
The flow rate of air in enclosures may be determined by numerically integrating three dimensionless combined differential equations.

1 INTRODUCTION

Let's now consider ejection properties of a bucket-belt elevator. Air inside the enclosure of a belt elevator may be brought into motion both by moving bucket belt and by spillage flows during loading and unloading of buckets. Initial findings from studies performed to evaluate air motion in ducts with mobile partitions have been published in our earlier monographs [1-3]. Here we'll consider the process of air ejection in bucket elevators from the standpoint of classical laws of change in air mass and momentum.

2 THE RESULTS OF THE STUDY

Let's begin with considering airflow in a duct of elevator return line of length dx (Fig. 1). For this area we can a momentum conservation equation can be written in projections onto axis $0x$ directed vertically downwards. We'll formulate a one-dimensional problem assuming that the velocity of ejected air is directed downwards and is equal to the cross-sectional average:

$$u = \frac{Q}{S}; \quad S = ab, \tag{1}$$

where Q is the flow rate of air ejected inside the duct (m^3/s); a, b are cross-sectional dimensions of the duct (m)

The tangential frictional stress on the surface of a moving belt is equal to

$$\tau_l = c_l \frac{(v_e - u)|v_e - u|}{2}\rho, \tag{2}$$

where c_l is a dimensionless resistance coefficient, v_e is the velocity of elevator belt (m/s).

Similarly, tangential frictional stress on the surface of enclosure walls is

$$\tau_w = c_w \frac{u|u|}{2}\rho, \tag{3}$$

where c_w is a dimensionless resistance coefficient of enclosure walls.

It is known that coefficients c_l, c_w are related to friction coefficients in the Darcy-Weisbach equation for determining pressure losses in straight pipe sections

$$c_l = \frac{\lambda_l}{4}; \; c_w = \frac{\lambda_w}{4},$$

where λ_l is the hydraulic friction coefficient of the belt; λ_w is the hydraulic friction coefficient of enclosure walls.

The aerodynamic force of a bucket, expressed similarly to the aerodynamic force of particles, is

$$R_k = c_k F_k \frac{(v_e - u)|v_e - u|}{2} \rho\,, \tag{4}$$

where F_k is the mid-section area of a bucket $\left(F_k = A_k B_k\right)$ (m^2), c_k is the drag coefficient of an empty bucket.

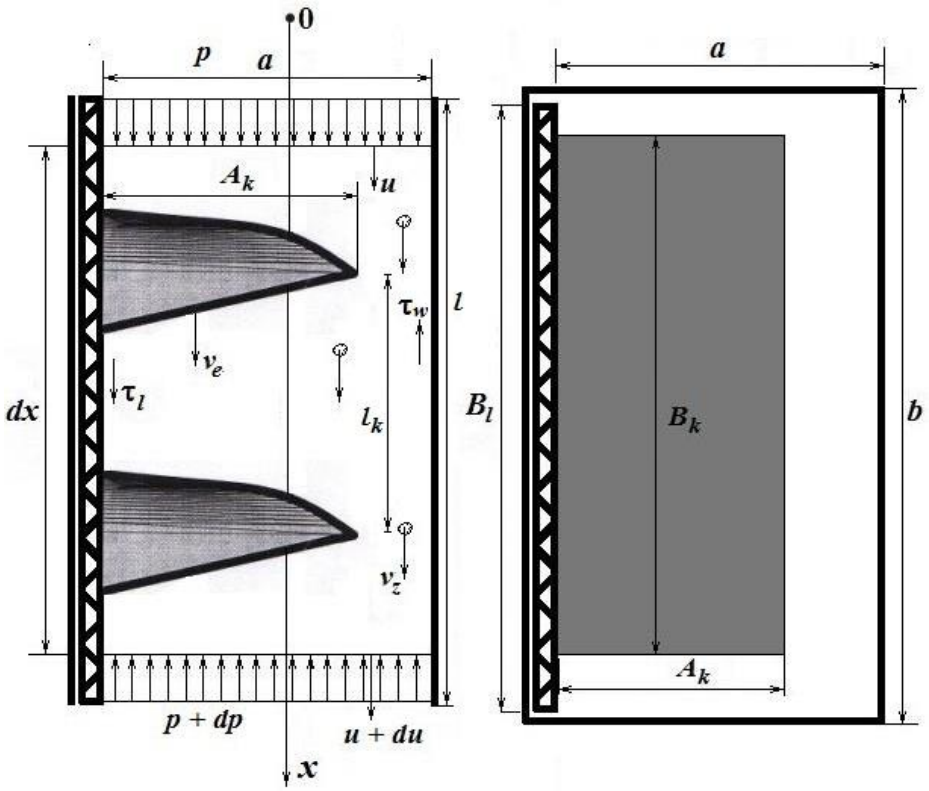

Figure 1: Diagram of forces acting on an element of elevator return run enclosure with a length dx

In this case the equation for change in momentum would appear as:

$$\rho u S(-u) + \rho(u+du)S(u+du) =$$
$$= pS - (p+dp)S - \tau_w(b+2a)dx + \tau_l B_l dx + R_k \frac{dx}{l_k} + R_z \frac{\beta dx S}{V_p}\,, \tag{5}$$

where l_k is the spacing of buckets on the belt (m); β is volumetric concentration of grain spillage, equal to

$$\beta = \frac{G_p}{\rho_z S v_z}\,; \tag{6}$$

G_p is the mass flow rate of grain spillage during bucket unloading (kg/s)

ρ_z is grain density (kg/m^3)

v_z is the fall velocity of grain (m/s)

V_p is the volume of an individual particle (m^3)

R_z is the aerodynamic force of a single particle of spilled material,

$$R_z = \psi_z F_z \frac{|v_z - u|(v_z - u)}{2}\rho; \tag{7}$$

F_z is the mid-section area of a particle (m^2)

$$F_z = \frac{\pi d_e^2}{4}; \tag{8}$$

d_e is equivalent grain diameter (m).

Considering that, in this case,

$$u = \text{const}, \tag{9}$$

after a trivial transformation of equation (5), ignoring infinitesimal second-order terms, we'll obtain the following relation for determining differential pressure inside the enclosure of the return run of the elevator:

$$p(0) - p(l) + E_k + E_p = p_w, \tag{10}$$

where $p(0), p(l)$ are static pressures at the inlet/outlet of the enclosure (Pa)

p_w is aerodynamic drag of enclosure walls (Pa)

$$p_w = \int_0^l \lambda_w \frac{2a+b}{4S}\frac{u^2}{2}\rho dx, \tag{11}$$

equal at $u = \text{const}$ and $S = \text{const}$

$$p_w = \lambda_w \frac{l}{D_w}\frac{u^2}{2}\rho, \tag{12}$$

$$D_w = \frac{4S}{b+2a}, \tag{13}$$

l is the total length of elevator enclosure (distance between the axes of driving and return drums along the belt of the bucket elevator) (m); E_k is ejection head created by a conveyor belt with buckets:

$$E_k = \frac{1}{S}\int_0^l \left(c_k \frac{F_k}{l_k} + \frac{\lambda_l}{4} B_l \right) \frac{|v_e - u|(v_e - u)}{2}\rho dx, \tag{14}$$

which, at constant relative velocity, is equal to

$$E_k = c_{ek} \frac{|v_e - u|(v_e - u)}{2}\rho; \tag{15}$$

c_{ek} is aerodynamic coefficient of the return run of elevator belt (with account of empty buckets and conveyor belt carrying them):

$$c_{ek} = \frac{l}{S}\left(c_k \frac{F_k}{l_k} + \frac{\lambda_l}{4} B_l \right), \tag{16}$$

E_p is the ejection head created by a flow of spilled grain during unloading of elevator buckets:

$$E_p = \frac{1}{S}\int_0^l \psi_z K_m \varepsilon G_p \frac{|v_z - u|(v_z - u)}{2} \frac{dx}{v_z}, \tag{17}$$

which, for a constantly accelerated vertical flow of particles at $\psi_z = \text{const}$, equals:

$$E_p = \frac{\psi_z K_m \varepsilon}{2} \frac{G_p}{Sg} \frac{|v_k - u|^3 - |v_n - u|^3}{3} \tag{18}$$

or, for a uniformly accelerated flow of particles at $v_z = v_e = \text{const}$; $u = \text{const}$,

$$E_p = \frac{\psi_z K_m \varepsilon}{2} \frac{G_p}{S} \frac{l}{v_e} \left[|v_e - u|(v_e - u) \right], \tag{19}$$

where K_m is the ratio of mid-sectional area of a particle to its volume (1/m); ε is the ratio of air density to particle density.

Let's now consider a more complex case with carrying and return runs of a bucket elevator both located in a common enclosure (Fig. 2). In this case air may flow laterally from one part of the enclosure (for example, the one with grain-laden buckets running) to another (with empty buckets running). The velocity of air cross-flow in the gap between the belt and enclosure walls will be designated as ω. Parameters of airflow in the right-hand side of the enclosure (where empty buckets run and spilled particles fall) will be denoted with a subscript u (from the designation of air velocity in the return run) while those in the left-hand side will be denoted respectively with v (from the designation of air velocity in the carrying run of the conveyor).

The cross-flow velocity is determined by differential pressure and aerodynamic drag of gaps:

$$\Delta p = p_v - p_u = \zeta_z \frac{w|w|}{2} \rho, \tag{20}$$

where p_v, p_u are the respective excess static pressures in the left-hand and right-hand sides of the enclosure (Pa); ζ_z is the total local resistance coefficient (LRC) for two gaps between chute walls and the end sides part of carrying and return runs of the conveyor.

The sign of the absolute value in the right-hand side was introduced to ensure universality of the relation which in this case would be just as good for the case of a reverse flow (with $p_u > p_v$). The velocity w in such "vector" case will be negative, that is, velocity vector will be directed oppositely (from right to left). This vector is represented with a dotted line on Fig.2.

Due to the presence of lateral cross-flow of air, velocities u and v will not be constant but rather would change along the height of the elevator enclosure.

Now we'll write an airflow conservation equation while still assuming velocities u and v to be averaged throughout cross-section and the positive direction of these velocities to coincide with bucket traveling direction:

$$uab = (u + du)ab - w(b - B_l)dx, \tag{21}$$

$$vab = (v + dv)ab - w(b - B_l)dx. \tag{22}$$

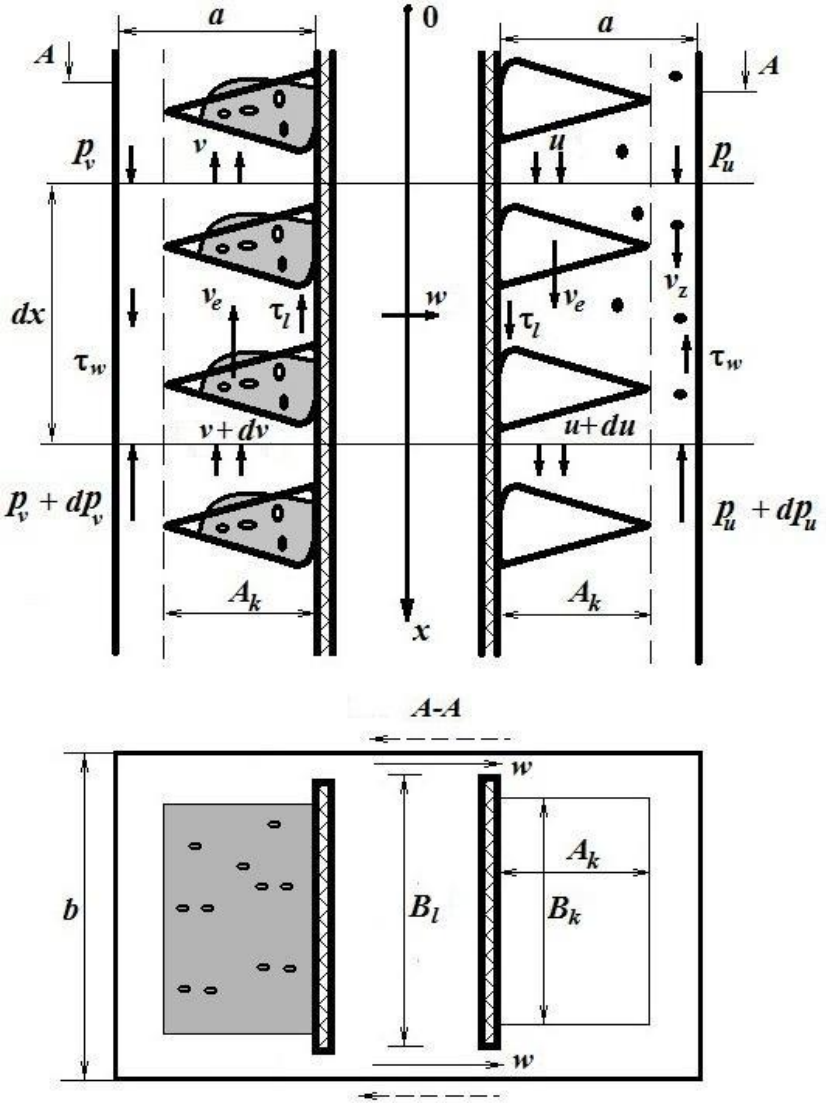

Figure 2: Longitudinal airflow diagram for return and carrying runs both located in a common elevator enclosure

It can be seen from here that change in the absolute value of dilatational velocities is equal:

$$\frac{du}{dx} = w\frac{b - B}{ab}, \qquad \frac{dv}{dx} = w\frac{b - B}{ab}. \tag{23}$$

And the difference of these velocities does not vary along the enclosure

$$u - v = k = \text{const}. \tag{24}$$

Let's now write a motion preservation equation for the chosen element of enclosure of length dx. For the right-hand (downward) airflow the momentum conservation equation in the projection onto axis $0x$ does not differ in any way from equation (5). Trivial transformations would yield the following differential equation for the dynamics of the air current at hand:

$$2\rho u\frac{du}{dx} = -\frac{dp_u}{dx} - \frac{\lambda_w}{D_w}\frac{u^2}{2}\rho + \zeta_u\frac{|v_e - u|(v_e - u)}{2}\rho + A_n\frac{|v_e - u|(v_e - u)}{2v}\rho, \tag{25}$$

with the following notational simplification:

$$\zeta_u = \frac{\lambda_l}{4}\frac{B_l}{ab} + c_k\frac{A_k B_k}{abl_k}, \tag{26}$$

$$A_n = \frac{1.5}{d_e}\frac{G_p}{\rho_z}\frac{\psi_e}{ab}. \tag{27}$$

For the left-hand (upward) airflow we'll first write the momentum preservation equation in differentials:

$$-\rho v v ab - \rho(v + dv)ab(-v - dv) = p_v ab - (p_v + dp_v)ab + \tau_w(b + 2a)dx - \tau_l B_l dx - R_k\frac{dx}{l_k}, \tag{28}$$

where

$$\tau_w = \frac{\lambda_w}{4}\frac{v|v|}{2}\rho; \tag{29}$$

$$\tau_l = \frac{\lambda_l}{4}\frac{(v_e - v)|v_e - v|}{2}\rho; \tag{30}$$

$$R_k = c_{kz}A_k B_k\frac{(v_e - v)|v_e - v|}{2}\rho; \tag{31}$$

c_{kz} is a dimensionless coefficient of aerodynamic drag of a grain-laden bucket.

After trivial transformations equation (28) would appear as follows:

$$2\rho v\frac{dv}{dx} = -\frac{dp_v}{dx} + \frac{\lambda_w}{D_w}\frac{v^2}{2}\rho - \zeta_v\frac{|v_e - v|(v_e - v)}{2}\rho, \tag{32}$$

$$\zeta_v = \frac{1}{ab}\left(\frac{\lambda_l B_l}{4} + c_{kz}\frac{A_k B_k}{l_k}\right). \tag{33}$$

Thus, longitudinal airflow in case of co-location of the carrying and return runs in the same enclosure can be described with combined equations:

$$2\rho u\frac{du}{dx} = -\frac{dp_u}{dx} + f_u, \tag{34}$$

$$2\rho v\frac{dv}{dx}=-\frac{dp_v}{dx}+f_v, \tag{35}$$

$$\frac{du}{dx}=w\frac{b-B_l}{ab}; \tag{36}$$

$$v=u-k; \tag{37}$$

$$\Delta p=\zeta_z\frac{w|w|}{2}\rho;\quad \Delta p=p_v-p_u, \tag{38}$$

with the following assignments for brevity:

$$f_u=-\frac{\lambda_w}{D_w}\frac{u|u|}{2}\rho+\zeta_u\frac{|v_e-u|(v_e-u)}{2}\rho+A_n\frac{|v_z-u|(v_z-u)}{2v_z}\rho, \tag{39}$$

$$f_v=\frac{\lambda_w}{D_w}\frac{v|v|}{2}\rho-\zeta_v\frac{|v_e-v|(v_e-v)}{2}\rho. \tag{40}$$

Newly-introduced functions f_u and f_v can be written in a more convenient (symmetric) form. First of all let's assume that spillage velocity is equal to the velocity of the return run (considering that gap between buckets and enclosure walls is rather narrow, particles would first impinge on the bottom of a bucket and then accelerate gravitationally and "catch up" with uniformly moving buckets):

$$v_z\approx v_e. \tag{41}$$

Then,

$$f_u=-\xi_u\frac{\mathrm{T}}{l}\frac{\rho u^2}{2}+\gamma_u\frac{M_u}{l}\frac{\rho(v_e-u)^2}{2}, \tag{42}$$

$$f_v=\xi_v\frac{\mathrm{T}}{l}\frac{\rho v^2}{2}-\gamma_v\frac{M_v}{l}\frac{\rho(v_e-v)^2}{2}, \tag{43}$$

where T, M_u and M_v are dimensionless parameters:

$$\mathrm{T}=\lambda_w\frac{l}{D_w}; \tag{44}$$

$$M_u=\lambda_l\frac{l}{D_l}+c_k\frac{l}{l_k}\frac{A_kB_k}{S}+1.5\psi\frac{l}{d}\beta_e; \tag{45}$$

$$M_v=\lambda_l\frac{l}{D_l}+c_{kz}\frac{l}{l_k}\frac{A_kB_k}{S}; \tag{46}$$

$$D_w=\frac{4S}{b+2a};$$

$$D_l=\frac{4S}{B_l}; \tag{47}$$

$$\beta_e = \frac{G_p}{\rho_z v_e S}; \tag{48}$$

$$\xi_u = \text{signum}(u),\ \xi_v = \text{signum}(v) = \text{signum}(u-k); \tag{49}$$

$$\gamma_u = \text{signum}(v_e - u); \quad \gamma_v = \text{signum}(v_e - v) = \text{signum}(v_e + k - u). \tag{50}$$

Combined equations (34 … 38) can be simplified significantly. Cross-flow velocity of a lateral flow can be derived from (38):

$$w = \delta\sqrt{\frac{2|\Delta p|}{\zeta_z \rho}}, \quad \Delta p = p_v - p_u, \tag{51}$$

where

$$\delta = \text{signum}(\Delta p). \tag{52}$$

Substitution of (51) into (36) yields

$$\frac{du}{dx} = \delta\frac{L}{l}\sqrt{\frac{2|\Delta p|}{\rho}}, \tag{53}$$

where

$$L = \frac{l(b-B)}{S\sqrt{\zeta_z}}. \tag{54}$$

By subtracting relation (35) from the equation (34) and considering $\frac{dv}{dx} = \frac{du}{dx}$ in view of (37) we'll get:

$$2\rho k\frac{du}{dx} = \frac{d\Delta p}{dx} - \xi_u\frac{T}{l}\frac{u^2}{2}\rho + \gamma_u\frac{M_u}{l}\frac{(v_e-u)^2}{2}\rho - \xi_v\frac{T}{l}\frac{v^2}{2}\rho + \gamma_v\frac{M_v}{l}\frac{(v_e-v)^2}{2}\rho \tag{55}$$

or, in view of (53),

$$-\frac{d\Delta p}{dx} = -2\delta k\rho\frac{L}{l}\sqrt{\frac{2|\Delta p|}{\rho}} - \xi_x\frac{T}{l}\frac{u^2}{2}\rho + \gamma_u\frac{M_u}{l}\frac{(v_e-u)^2}{2}\rho - \xi_v\frac{T}{l}\frac{v^2}{2}\rho + \gamma_v\frac{M_v}{l}\frac{(v_e-v)^2}{2}\rho. \tag{56}$$

Equation (56) can be supplemented with (34) in view of (42) and (53):

$$\frac{dp_u}{dx} = -2\rho u\delta\frac{L}{l}\sqrt{\frac{2|\Delta p|}{\rho}} - \xi_u\frac{T}{l}\frac{u^2}{2}\rho + \gamma_u\frac{M_u}{l}\frac{(v_e-u)^2}{2}\rho. \tag{57}$$

This, in view of (53), yields a familiar combined set (considering (37)) of three differential equations (57), (56) and (53) describing the process of averaged longitudinal airflows in an enclosure with co-location of the carrying and return runs of bucket elevator inside it.

Changes in the velocity u can be found from (55) using (53) which can be written as follows:

$$\Delta p = A\left(\frac{du}{dx}\right)^2 \frac{\rho}{2}\left(\frac{l}{L}\right)^2, \tag{58}$$

where

$$A = \text{signum}\left(\frac{du}{dx}\right).$$

A substitution of (58) into (55) using the relation (37) results in a 2nd order non-linear equation relative to the sought function u:

$$\begin{aligned} -A\rho\left(\frac{l}{L}\right)^2 \frac{d^2u}{dx^2}\frac{du}{dx} + 2\rho k\frac{du}{dx} = -\xi_u \frac{T}{l}\frac{u^2}{2}\rho + \gamma_u \frac{M_u}{l}\frac{(v_e-u)^2}{2}\rho - \\ -\xi_v \frac{T}{l}\frac{(u-k)^2}{2}\rho + \gamma_v \frac{M_v}{l}\frac{(v_e+k-u)^2}{2}\rho. \end{aligned} \tag{59}$$

We'll use a dimensionless differential equation formula to facilitate our numerical integration of the resulting dimensional equations. It will enable us to reduce the number of constants. The following quantities will be considered as basic values:

– elevator belt velocity v_e

– elevator enclosure length or height l;

– dynamic pressure $\rho v_e^2/2$.

Thus, let

$$p_u = p\frac{v_e^2\rho}{2}; \quad \Delta p = R\frac{v_e^2\rho}{2}; \quad u = u^* v_e; \quad k = m^* v_e; \quad x = zl, \tag{60}$$

then, after we substitute accepted conventions into equations (34 (56) (53) and perform certain trivial transformations, the following system of dimensionless differential equations will result:

$$\frac{dp}{dz} = -\delta u^* 4L\sqrt{|R|} - \xi_u T\left(u^*\right)^2 + \gamma_u M_u\left(1-u^*\right)^2; \tag{61}$$

$$\frac{dR}{dz} = 4\delta m^* L\sqrt{|R|} + \xi_u T\left(u^*\right)^2 - \gamma_u M_u\left(1-u^*\right)^2 + \xi_v T\left(u^*-m^*\right)^2 - \gamma_v M_v\left(1+m*-u^*\right)^2; \tag{62}$$

$$\frac{du^*}{dz} = \delta L\sqrt{|R|}, \tag{63}$$

where

$$\delta = \text{signum}(R), \quad \xi_u = \text{signum}(u^*), \quad \xi_v = \text{signum}(u^*-m^*), \tag{64}$$

$$\gamma_u = \text{signum}(1-u^*), \quad \gamma_v = \text{signum}(1+m^*-u^*). \tag{65}$$

Similarly, (59) will now appear as:

$$\left(-A_3\frac{2}{L^2}\frac{d^2u^*}{dz^2}+4m^*\right)\frac{du^*}{dz}= \\ =-\xi_u T\left(u^*\right)^2+\gamma_u M_u\left(1-u^*\right)^2-\xi_v T\left(u^*-m^*\right)^2+\gamma_v M_v\left(1+m^*-u^*\right)^2, \tag{66}$$

where

$$A_3=\text{signum}\left(\frac{du^*}{dz}\right). \tag{67}$$

CONCLUSIONS

- Direction of airflow inside enclosures of the carrying and return runs of a bucket elevator is determined by the drag of buckets and moving conveyor belt as well as ejection head created by a stream of spilled particles when buckets are unloaded. As a result of these forces acting together inside an enclosure, differential pressure (10) arises. This differential pressure is equal to the sum total of ejection heads created by conveyor belt with buckets E_k (14) and flow rate of spilled material E_p (17) minus aerodynamic drag of enclosure walls (11).
- The ejection head E_k created by a bucket-carrying conveyor belt is determined by aerodynamic coefficient c_{ek} (16) (proportional to the number of buckets, their head resistances and squared mid-sectional dimensions) together with an absolute value and the direction of bucket velocity relative to the velocity of airflow inside the enclosure.
- Ejection head of spilled particles E_p (19) depends on the drag coefficient of particles, their size and flow rate, as well as the enclosure length, enclosure cross-section and relative flow velocity of particles.
- When both the carrying and return runs of the conveyor belt are located in a common enclosure, the velocity of forward airflow varies over its length as a result of cross-flows of air through gaps between the conveyor runs and enclosure walls. Cross-flows are caused by a differential pressure between the carrying and return run enclosures and is dependent on the drag of the gap (20). Cross-flow direction depends on the ratio between p_v and p_u.
- Given identical size of elevator enclosures, change in absolute values of longitudinal velocities is identical and depends on absolute values of cross-flow velocities and geometrical dimensions of the gap, as well as enclosure cross-section (23, 24). The momentum of longitudinal airflow in this case is determined by variable magnitudes of aerodynamic forces of buckets due to changes in their relative motion velocities.
- The flow rate of air in enclosures may be determined by numerically integrating three dimensionless combined differential equations (61) – (63).
- The work has been carried out with the financial support of the Grant Council of the President of the Russian Federation (project MD-95.2017.8) and RFBR (research project No. 16-08-00074a).

REFERENCES

[1] O. D. Neikov and I.N. Logachev. *Suction and air dedusting in production of powders*. Moscow: Metallurgiya, 1981. 124 p.

[2] I. N. Logachev. Aspiration in loose-matter handling systems of agglomeration shops // *Local exhaust ventilation*. Moscow, Moscow House for Research and Engineering Information (MDNTI), 93–106 (1969).

[3] I.N. Logachev and K.I. Logachev. *Industrial Air Quality And Ventilation: Controlling Dust Emissions*. Boca Raton: CRC Press, 2014.

V International Conference on Particle-based Methods – Fundamentals and Applications
PARTICLES 2017
P. Wriggers, M. Bischoff, E. Oñate, D.R.J. Owen, & T. Zohdi (Eds)

PATTERN FORMATION IN LAMINAR FLOW OF SUSPENSIONS THROUGH SQUARE CHANNELS

PHILIPPE SEIL[1], STEFAN PIRKER[2] AND THOMAS LICHTENEGGER[3]

[1] CD Laboratory for Multi-Scale Modelling of Multiphase Processes, Johannes Kepler University Linz
Altenbergerstrasse 69, 4040 Linz, Austria
philippe.seil@jku.at

[2] Department for Particulate Flow Modelling, Johannes Kepler University Linz

[3] Linz Institute of Technology (LIT), Johannes Kepler University Linz

Key words: Lateral Migration, Channel Flow, Suspensions, Lattice Boltzmann Method, Discrete Element Method

Abstract. The study of particulate suspensions flowing through narrow channels has received much attention in the last decades, especially with advance in the field of microfluidics devices. In square channels, it is known that particles in dilute suspensions migrate to equilibrium positions at the channel faces, and also at the channel corners for a channel Reynolds number above 260. However, most studies focused on very dilute systems, excluding particle-particle interactions. In this paper, we present simulations of suspensions with solid fractions up to 3%. In these simulations, we find two new patterns: at $\mathrm{Re}_{\mathrm{ch}} < 260$, the equilibrium positions split up and particles assume a staggered position, and at $\mathrm{Re}_{\mathrm{ch}} > 260$, the fraction of particles moving to the corner equilibrium positions increases with solid fraction. We present a characterization of these two effects and speculate about possible mechanisms leading to the formation of both patterns.

1 INTRODUCTION

The dynamics of particulate suspension flow through narrow channels features a broad variety of non-trivial phenomena. Over half a century ago, Segré and Silberberg [1] discovered that a neutrally buoyant, spherical particle in pipe flow migrates to an off-center equilibrium position located at $\approx 0.62 R_{\mathrm{pipe}}$ away from the pipe axis.

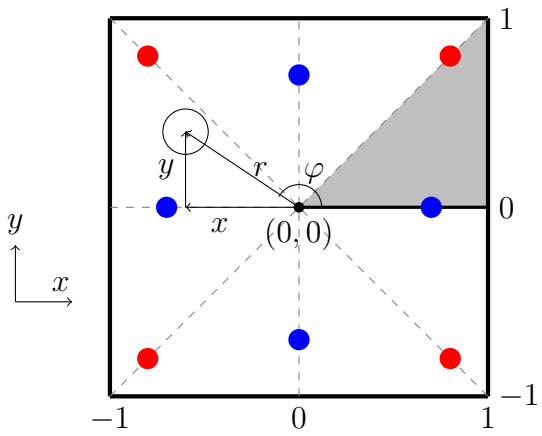

Figure 1: A sketch of the coordinate conventions used in the simulations. All results are given in coordinates normalized by $D/2$. In figs. 3 and 4, all final positions are mapped to the grey triangle. The dots indicate approximate locations of face (blue) and corner (red) equilibrium positions.

A similar effect exists for rectangular and square channels, where due to reduced symmetry only eight equilibrium positions are possible: four close to the channel corners, and four close to the channel faces (see fig. 1). Using simulations, Chun and Ladd [2] predicted that in a square channel at $\mathrm{Re}_{\mathrm{ch}} < 500$ particles move to all eight positions, while at $\mathrm{Re}_{\mathrm{ch}} \geq 500$ only the corner positions remain stable. However, through experiments, Di Carlo et al. [3, 4] found that at $\mathrm{Re}_{\mathrm{ch}} < 100$ only the face positions are stable. Miura et al. [5] examined cases with $\mathrm{Re}_{\mathrm{ch}} = 100 - 1000$, and found that the corner equilibrium positions only become stable above $\mathrm{Re}_{\mathrm{ch}} = 260$. All these experiments were done using very dilute systems, thus not much is known about denser systems. Matas et al. [6] investigated denser suspensions in pipe flow, and found trains of particles with an average spacing of $1.5 - 4.5 d_{\mathrm{p}}$ depending on the particle Reynolds number Re_{p}. Humphry et al. [7] and Kahkeshani et al. [8] also studied particle trains and preferred interparticle spacings, although in rather confined geometries. In this paper, we present simulations of flow of particulate suspensions through square channels. We investigate the influence of $\mathrm{Re}_{\mathrm{ch}}$ and solid fraction f_{s} on pattern formation, and present assumptions about possible underlying mechanisms.

2 METHODS AND SETUP

2.1 Computational Methods

We used a fully resolved[1] coupled approach between the lattice Boltzmann method (LBM) [9] and the discrete element method (DEM) [10] for our simulations. Using the method of Noble and Torczinsky [11], we have implemented, validated, and released this approach in the software *LBDEMcoupling* [12, 13]. Therefore, we give only a brief discussion of the numerical methods. For more thorough explanations, the reader is directed to the book by Krüger et al. [14] for the LBM and coupling methodology, and to the book by Pöschel and Schwager [15] for the DEM.

In the LBM, the fluid flow is simulated by solving the *LBGK* equation

$$f_i(\vec{x}+\vec{c}_i\Delta t, t+\Delta t) - f_i(\vec{x},t) = -(1-B)\underbrace{\frac{1}{\tau}\left(f_i(\vec{x},t) - f_i^{(eq)}(\vec{u},\rho)\right)}_{\text{BGK coll.}} + B\underbrace{\Omega_i^s(\vec{u}_s)}_{\text{solid coll.}} \quad (1)$$

on a regular grid for a set of particle distributions $\{f_i\}$. The $\{\vec{c}_i\}$ are a set of vectors to adjacent grid cells. In the present simulations, the *D3Q19* discretization scheme was chosen, which consists of six vectors to the nearest neighbours, twelve vectors to the second-next neighbours, and a zero vector. A timestep consists of two parts: collision and streaming. In the collision step, the left hand side of eq. (1) is applied to the $\{f_i\}$. This represents a tendency towards a local equilibrium distribution $f_i^{(eq)}(\vec{u},\rho)$ occurring at a timescale given by the relaxation time τ. In the streaming part, each population $f_i(\vec{x})$ is copied to the location $\vec{x}+\vec{c}_i$, which now has a set of off-equilibrium populations, and the simulation continues with the next collision step. Local density and velocity are given by

$$\rho = \sum_i f_i \qquad ; \qquad \rho\vec{u} = \sum_i \vec{c}_i f_i \quad (2)$$

and the pressure equation is solved by allowing for a slight compressibility: pressure differences are proportional to density differences. In eq. (1), the interaction with a solid covering a fraction B of the cell and moving at velocity $\vec{u}_s$ has also been included by blending between the BGK collision and an additional collision operator Ω_i^s [11].

[1] grid spacing $\Delta x <$ particle diameter d_p

The DEM [10] originates in molecular dynamics and is able to model the dynamics of systems consisting of single particles by integrating Newton's second law

$$m_i \ddot{\vec{x}}_i = \sum_{j \neq i} \vec{F}_{ij} + \vec{F}_i^{ext} \tag{3}$$

where $\vec{F}_{ij}$ is the interaction force between particles i and j, and $\vec{F}_i^{ext}$ are external forces due to gravity, hydrodynamic interactions, or other external influences. In the case of granular material, spring-dashpot interaction potentials of Hertz type are commonly used to model the particle-particle interaction. In this study, we used the model of Tsuji [16] and Antypov and Elliot [17]. Additional models for sliding [10] and rolling friction [18] were used to accurately depict the dynamics of interparticle collisions.

2.2 Simulation Setup

To ensure comparability to experiments, we chose a simulation setup that closely mimics the experiments of Miura et al. [5]. They used a square channel with edge length $D = 6\text{mm}$ and $L = 4\text{m}$. Consequently, we adopted the edge length and used periodic boundary conditions to create an infinite channel. A pressure gradient was applied using the periodic pressure boundary condition of Zhang and Kwok [19]. The particle diameter was $d_\text{p} = 650\mu\text{m}$, resulting in $\frac{D}{d_\text{p}} = 9.23$. Additional fluid parameters were kinematic viscosity $\nu = 1.6 \cdot 10^{-6}\text{m}^2/\text{s}$ and density $\rho = 1053\text{kg}/\text{m}^3$.

We used a resolution of $100 \times 100 \times 800$ grid cells for the simulation, resulting in a particle diameter of $10.8\Delta x$. A similar resolution was found to produce acceptable results in our validation tests [13]. We made sure that the Mach number did not exceed $\text{Ma} = 0.05$ to avoid compressibility errors in the LBM. The channel Reynolds number was defined as

$$\text{Re}_\text{ch} = \frac{D\bar{U}}{\nu} \tag{4}$$

with $\bar{U}$ being the average streamwise flow velocity. $\bar{U}$ was controlled by setting the pressure difference Δp between inlet and outlet. The channel was initialized to a product of two Poiseuille parabolas (in x and y direction) and a streamwise (z) linear pressure decrease. We investigated solid fractions of $f_\text{s} = 0.017\% \ldots 3\%$ ($N_\text{p} = 2 - 363$ particles) at $\text{Re}_\text{ch} = 60$, 190 and $f_\text{s} = 0.017\% \ldots 1\%$ ($N_\text{p} = 2 - 121$) at $\text{Re}_\text{ch} = 310$, 500. For each combination of Re_ch and f_s, between two and eight simulations with randomly generated initial configurations were carried out to achieve

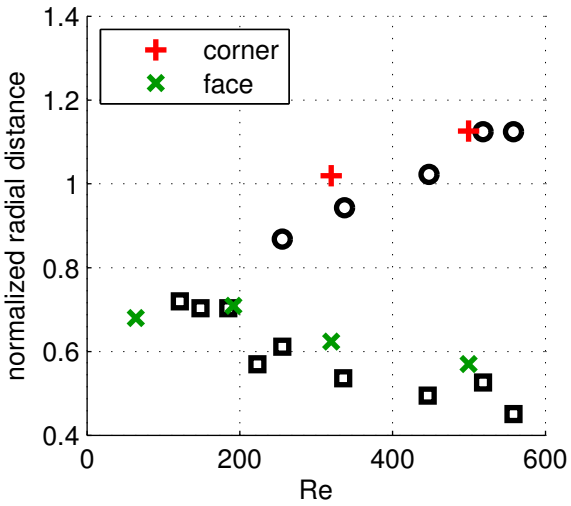

Figure 2: Radial distance of equilibrium positions from the channel centerline. Black circles and squares are corner and face positions found by Miura et al. [5]. Green "x" (face) and red "+" (corner) are our simulation results. Distance is normalized to $D/2$.

proper statistics.

3 RESULTS AND DISCUSSION

Just as in the experiments, the particles migrated to the two sets of equilibrium positions, except for the most dense cases ($f_s \geq 1\%$) where pattern formation broke down due to the high amount of interaction. Generally, migration happened in two stages: First, the particles moved out radially. Then, they tangentially migrated to their final positions. Typically, the second part of migration took longer than the first part. Our results are presented in more detail below. First, to give some validation, the most dilute cases are compared to experimental results. Then, we present two patterns found in denser cases.

3.1 Comparison to previous results

We now compare equilibrium positions found in the most dilute systems simulated to results by Miura et al. [5]. The experiments in ref. 5 were performed at solid fractions of $0.016-0.023\%$, while our most dilute systems had $f_s = 0.017\%$ ($N_p = 2$). In agreement with the experiments, we found that at $\mathrm{Re}_{ch} = 60$, 190 only the face equilibrium positions were stable, while at $\mathrm{Re}_{ch} = 310$, 500 particles also migrated

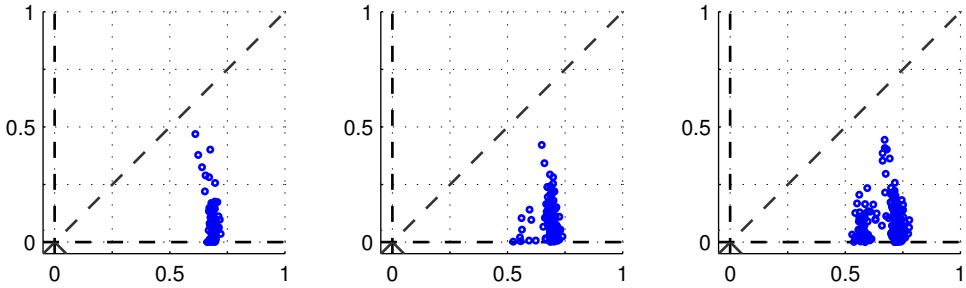

Figure 3: Equilibrium positions for $\mathrm{Re}_{\mathrm{ch}} = 60$ for $f_\mathrm{s} = 0.1\%$, 0.3%, 0.6% (left to right) folded to the grey triangle in fig. 1.

to the corner equilibrium positions. Figure 2 shows the average radial positions at the end of the simulations for the four $\mathrm{Re}_{\mathrm{ch}}$ investigated at $f_\mathrm{s} = 0.017\%$. Both corner and face positions follow the same trend as in the experiments, albeit with a slight overprediction of radial distance in our simulations. Due to the random initialization procedure, an exact determination of a focusing time was not possible. However, estimates can be made. We find focusing times of $6500 - 15000 t_\mathrm{s}$ where

$$t_\mathrm{s} = \frac{D\bar{U}}{\nu} \tag{5}$$

is the Stokes time. This is in agreement with the durations reported by Chun and Ladd [2]. Assuming that a particle travels with $\bar{U}$, the required channel lengths for full focusing range from 2.12m ($\mathrm{Re}_{\mathrm{ch}} = 500$) to 4.88m ($\mathrm{Re}_{\mathrm{ch}} = 60$), which is in good agreement with the channel length used by Miura et al. (4m).

3.2 Multi-Particle Effects

As already mentioned above, two new patterns were found in the simulations: At $\mathrm{Re}_{\mathrm{ch}} = 60$, 190, each face equilibrium position splits up in two equilibrium positions. This is shown in fig. 3. At $\mathrm{Re}_{\mathrm{ch}} = 310$, 500, a higher fraction of the particles is found at the corner equilibrium positions with increasing f_s, as illustrated in fig. 4.

3.2.1 Split equilibrium positions

At $\mathrm{Re}_{\mathrm{ch}} = 60$, 190, the equilibrium positions at the face centers split up in two equilibrium positions with increasing f_s. Figure 5 shows histograms of particles' radial distance from the channel center for these $\mathrm{Re}_{\mathrm{ch}}$. At $f_\mathrm{s} = 0.1\%$, there is only a single peak, but at $f_\mathrm{s} = 0.3\%$ a secondary peak closer to the axis appears for both

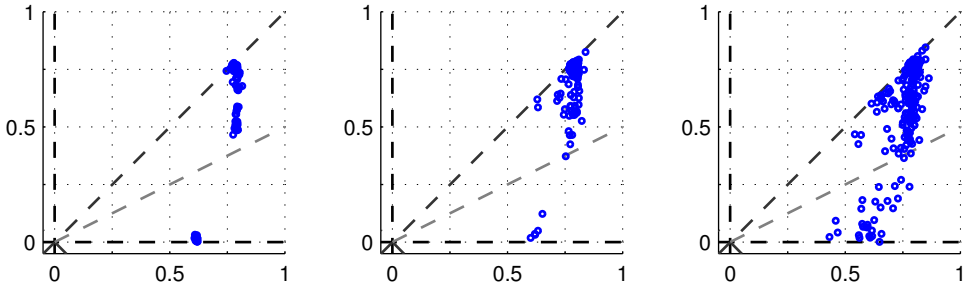

Figure 4: Equilibrium positions for $\mathrm{Re}_{\mathrm{ch}} = 310$ for $f_\mathrm{s} = 0.1\%$, 0.3%, 0.6% (left to right) folded to the grey triangle in fig. 1. Particles below the additional gray line are considered to be at the face equilibrium positions, while particles above are at the corner equilibrium positions.

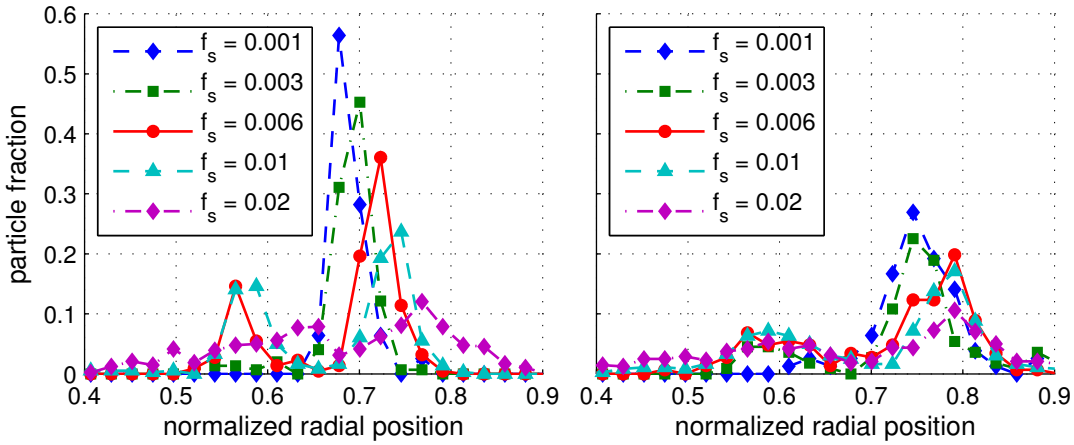

Figure 5: Normalized histograms of radial distance to the channel axis for $\mathrm{Re}_{\mathrm{ch}} = 60$ (left) and $\mathrm{Re}_{\mathrm{ch}} = 190$ (right).

$\mathrm{Re}_{\mathrm{ch}}$. The particles align in a staggered configuration as shown in fig. 6. This hints at a possible mechanism for the emergence of split equilibrium positions: Kahkeshani et al. [8] found that the preferred axial spacing between particles is smaller for staggered configurations than for particles forming a train ($2.5d_\mathrm{p}$ compared to $5d_\mathrm{p}$ in their experiments), and Humphry et al. [7] found that with increasing particle concentration, a single train in a rectangular channel will split up in two parallel trains. So, with increasing N_p, a single train becomes unstable. Due to the nature of the flow, particles are focused at the four face equilibrium positions. If now the particle density exceeds a stability limit, the average interparticle spacing goes down. To accommodate more particles in the train, a staggered configuration that allows for lower interparticle spacings is formed. We will thoroughly test this assumption

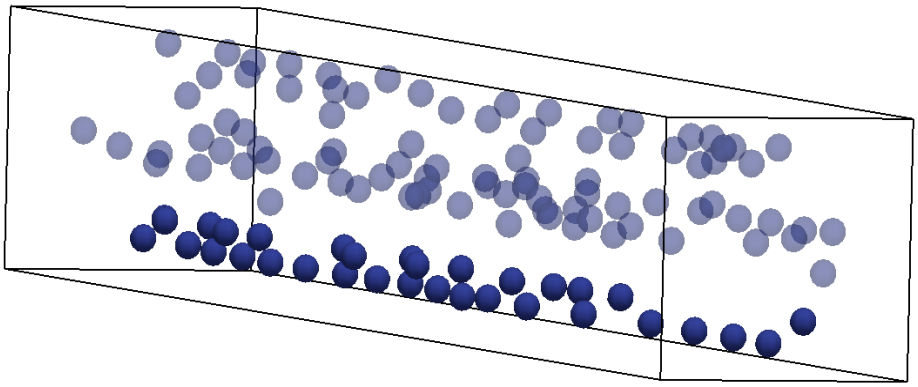

Figure 6: Illustration of the staggered configuration at $\mathrm{Re}_{\mathrm{ch}} = 60$, $f_{\mathrm{s}} = 1\%$ at the lower channel wall. Other particles have been reduced in opacity for clarity.

and publish the results in the future.

3.2.2 Instability of face equilibrium position

At $\mathrm{Re}_{\mathrm{ch}} = 310, 500$, another novel feature was found: When the number of particles in the channel was increased, a higher fraction of particles moved to the corner equilibrium position. Figure 7 (left) shows the fraction of particles at the corner equilibrium positions over f_{s}. There is a maximum at $f_{\mathrm{s}} = 0.3\%$ for $\mathrm{Re}_{\mathrm{ch}} = 310$ and at $f_{\mathrm{s}} = 0.6\%$ for $\mathrm{Re}_{\mathrm{ch}} = 500$. The minimum for $\mathrm{Re}_{\mathrm{ch}} = 500$, $f_{\mathrm{s}} = 0.03\%$ most likely comes from having not enough samples at this solid fraction. This will be investigated in the future. The patterns form in two steps: First, the particles migrate close to the equilibrium positions where they would be expected. Then, over time, particles at the face positions get pushed away and migrate to the corners, where they remain. Figure 7 (right) shows the radial positions of particles over time. Again, at the moment we can only speculate about the mechanisms leading to this effect. Nakagawa et al. [20] found that for $\mathrm{Re}_{\mathrm{ch}} > 260$ a separatrix between corner and face equilibrium positions exists, that single particles do not cross. Therefore, the initial position of a particle determines to which equilibrium position it will migrate. In the case of multiple particles, the particles travel at different velocities and constantly pass each other. When a particle passes another, there is a lateral repulsive force between the two. This lateral force could push one of the two particles over the separatrix, causing migration to another equilibrium position. It is assumed that this effect does not bring particles back to the face equilibrium positions because the corner equilibrium positions are more geometrically confined.

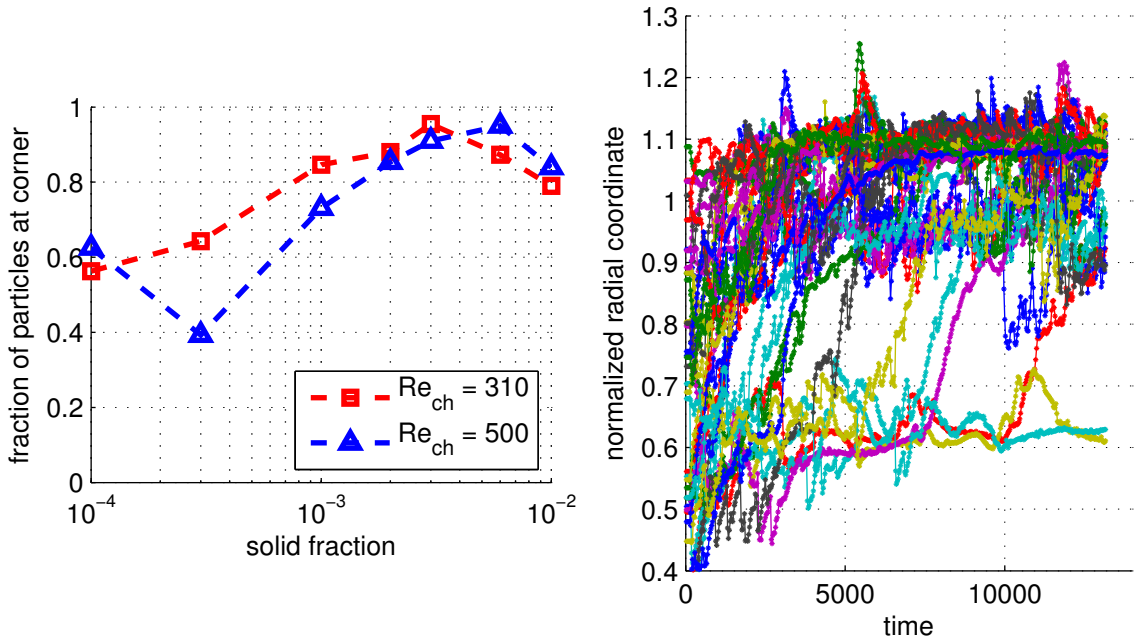

Figure 7: **Left:** Fraction of particles found at the corner equilibrium positions over $f_s$for $\mathrm{Re}_{ch} = 310, 500$. **Right:** Radial position of particles at $\mathrm{Re}_{ch} = 310$, $f_s = 0.3\%$. Time is given in multiples of Stokes time eq. (5). A radial position of ≈ 0.6 corresponds to the face equilibrium position, and a radial position of ≈ 1.1 is the corner equilibrium positions. Over time, particles migrate from the former to the latter, but not in the other direction.

4 SUMMARY AND OUTLOOK

We have looked at lateral migration phenomena in suspension flow through square channels. After making sure we match experiments for dilute cases, we increased the solid fraction. There, we found two effects: at lower Re_{ch}, a secondary equilibrium position right "on top" of the primary one appears. At $\mathrm{Re}_{ch} = 310, 500$, increasing solid fraction leads to lower occupation at the face equilibrium positions. To the best of the authors' knowledge, these effects have not been reported anywhere. A more thorough analysis of these patterns will be published soon, and we hope for independent testing of these findings, either through experiments or through numerical studies.

References

[1] G. Segré and A. Silberberg. Behaviour of macroscopic rigid spheres in poiseuille flow part 2. experimental results and interpretation. *Journal of Fluid Mechanics*, 14:136–157, 1962.

[2] B Chun and AJC Ladd. Inertial migration of neutrally buoyant particles in a square duct: An investigation of multiple equilibrium positions. *Physics of Fluids*, 18:031704, 2006.

[3] Dino Di Carlo, Daniel Irimia, Ronald G. Tompkins, and Mehmet Toner. Continuous inertial focusing, ordering, and separation of particles in microchannels. *Proceedings of the National Academy of Sciences*, 104(48):18892–18897, 2007.

[4] Dino Di Carlo, Jon F. Edd, Katherine J. Humphry, Howard A. Stone, and Mehmet Toner. Particle segregation and dynamics in confined flows. *Phys. Rev. Lett.*, 102:094503, Mar 2009.

[5] Kazuma Miura, Tomoaki Itano, and Masako Sugihara-Seki. Inertial migration of neutrally buoyant spheres in a pressure-driven flow through square channels. *Journal of Fluid Mechanics*, 749:320–330, 6 2014.

[6] Jean-Philippe Matas, Virginie Glezer, Élisabeth Guazzelli, and Jeffrey F Morris. Trains of particles in finite-reynolds-number pipe flow. *Physics of Fluids (1994-present)*, 16(11):4192–4195, 2004.

[7] Katherine J Humphry, Pandurang M Kulkarni, David A Weitz, Jeffrey F Morris, and Howard A Stone. Axial and lateral particle ordering in finite reynolds number channel flows. *Physics of Fluids*, 22(8):081703, 2010.

[8] Soroush Kahkeshani, Hamed Haddadi, and Dino Di Carlo. Preferred interparticle spacings in trains of particles in inertial microchannel flows. *Journal of Fluid Mechanics*, 786:R3, 2016.

[9] Guy R McNamara and Gianluigi Zanetti. Use of the boltzmann equation to simulate lattice-gas automata. *Physical Review Letters*, 61(20):2332–2335, 1988.

[10] Peter A Cundall and Otto DL Strack. A discrete numerical model for granular assemblies. *Geotechnique*, 29(1):47–65, 1979.

[11] D. R. Noble and J. R. Torczynski. A lattice-Boltzmann method for partially saturated computational cells. *International Journal of Modern Physics C*, 09(08):1189–1201, 1998.

[12] P. Seil and S. Pirker. LBDEMcoupling: Open-source power for fluid-particle systems. *Proceedings of the DEM7*, 2016.

[13] Philippe Seil, Stefan Pirker, and Thomas Lichtenegger. Onset of sediment transport in mono- and bidisperse beds under turbulent shear flow. *Computational Particle Mechanics*, May 2017.

[14] Timm Krüger, Halim Kusumaatmaja, Alexandr Kuzmin, Orest Shardt, Goncalo Silva, and Erlend Magnus Viggen. *The Lattice Boltzmann Method: Principles and Practice*. Springer, 2016.

[15] Thorsten Pöschel and Thomas Schwager. *Computational granular dynamics: models and algorithms*. Springer Science & Business Media, 2005.

[16] Yutaka Tsuji, Toshitsugu Tanaka, and T Ishida. Lagrangian numerical simulation of plug flow of cohesionless particles in a horizontal pipe. *Powder technology*, 71(3):239–250, 1992.

[17] D Antypov and JA Elliott. On an analytical solution for the damped hertzian spring. *EPL (Europhysics Letters)*, 94(5):50004, 2011.

[18] YC Zhou, BH Xu, AB Yu, and P Zulli. An experimental and numerical study of the angle of repose of coarse spheres. *Powder technology*, 125(1):45–54, 2002.

[19] Yunfeng Zhang and Daniel Y. Kwok. Pressure boundary conditions of the lattice boltzmann method for fully developed periodic flows. *Phys. Rev. E*, 73:047702, 2006.

[20] Naoto Nakagawa, Takuya Yabu, Ryoko Otomo, Atsushi Kase, Masato Makino, Tomoaki Itano, and Masako Sugihara-Seki. Inertial migration of a spherical particle in laminar square channel flows from low to high reynolds numbers. *Journal of Fluid Mechanics*, 779:776–793, 9 2015.

V International Conference on Particle-based Methods – Fundamentals and Applications
PARTICLES 2017
P. Wriggers, M. Bischoff, E. Oñate, D.R.J. Owen, & T. Zohdi (Eds)

METHODS FOR SIMULATING ACTIN FILAMENT DYNAMICS IN MCELL

Kadri Pajo[1,2] and Melanie I. Stefan[2]

[1] Department of Physiology and Pharmacology
Karolinska Institutet
von Eulers väg 8, Stockholm, Sweden

[2] Centre for Integrative Physiology
Edinburgh Medical School: Biomedical Sciences
University of Edinburgh, EH8 9XD, UK
*e-mail: mstefan@exseed.ed.ac.uk, web page: `http://www.stefanlab.net`

Key words: actin, cytoskeleton, dendrites, MCell

Abstract.

Learning is mediated by activity-dependent changes in synaptic strength that rely on Calcium-dependent signalling in the postsynaptic neuron. In the hippocampus, synapses are located on dendritic spines, small mushroom-like structures that grow from the dendrite. Dendritic spines form micro-compartments that are - to some extent - chemically isolated from the rest of the dendrite due to the long and narrow spine neck limiting diffusion in and out. The shape and the physical structure of a dendritic spine are determined by the actin filaments that form the cellular cytoskeleton. Long-term potentiation (LTP) of the synapse leads to remodelling of the polymeric actin cytoskeleton, which increases the size of the dendritic spine. This process is regulated by interactions between actin and other postsynaptic proteins [1]. Here, addressing the lack of spatiotemporal models that combine structure with biochemical signalling, we present a set of methods that allows the modelling of the biochemistry and spatial dynamics of actin filament remodelling using the spatial stochastic simulator MCell [2, 3, 4]. These methods allow us to recapitulate the main events relevant for actin filament remodelling, including polymerisation, depolymerisation, branching and severing followed by filament displacement in space. They rely on the ability of MCell to model multi-state complex molecules [5] and on a system of virtual tags to label states of actin subunits. The "complex molecule" feature of MCell 3.3 was utilised by defining an immobile three-dimensional matrix with 8000 subunits, each belonging to one of the defined states. This provides a frame in which some of the subunits are occupied by actin monomers representing the cytoskeleton, while the rest are vacant. In response to biochemical reactions with freely diffusing modifier proteins, the state of the subunits can be changed allowing the rearrangement of the filaments. In addition, with the help of a tagging system for subunits, the monomers

forming a single filament can change their location inside the immobile matrix in corpore by occupying previously vacant slots. In the future, the model could be extended by incorporating more elements from signalling pathways and modelling filament bundles present in non-stimulated synapses. As such, the model can provide insights into how the actin cytoskeleton interacts with postsynaptic proteins that mediate LTP.

1 INTRODUCTION

Long-term changes in synaptic strength are thought to underlie many forms of learning and memory (reviewed in [6]). In the hippocampus, synapses terminate on specialised structures called dendritic spines. These serve as small diffusion-limited compartments that organise the postsynaptic molecular machinery in space (reviewed in [7]). Disruptions in the structure and function of dendritic spines have been linked to a wide range of diseases, from intellectual disabilities [8] and autism-spectrum disorders [9] to psychiatric conditions [10].

Within the dendritic spine, there is a complex interplay between biochemical signalling and structural change. Actin filaments provide structural stability and determine the size and physical shape of a spine. Other postsynaptic proteins interact with the actin cytoskeleton in an activity-dependent manner. Induction of long-term potentiation (LTP), for example, leads to actin cytoskeleton remodelling, which allows the dendritic spine head to change in size and shape [1, 11].

Actin is present both as free monomers termed G-actin (globular) and microfilaments called F-actin (filamentous). Filaments are formed from actin polymers that bundle together to give the cell its shape. Filaments are polar, with the end that faces the spine head ("barbed" end) growing more rapidly than the opposite end ("pointed" end) [12].

Both G-actin and F-actin monomers bind adenine nucleotides. G-actin monomers marked with ATP are incorporated into growing filaments. ATP is slowly hydrolysed into ADP which serves as the molecular tag of an ageing filament. Filament regions rich in F-actin-ADP monomers are subject to severing by cofilin. Severing into shorter filaments is vital for actin remodelling as it generates more ends for polymerisation and depolymerisation. Another way of generating barbed ends is branching. This is mediated by the Arp2/3 complex which nucleates new filaments from the sides of existing filaments, forming a branched network [12].

So far, most models of the dynamics of actin or other cytoskeletal proteins have taken one of two directions: Some have focused on the biochemical reaction network important for cytoskeletal dynamics, without explicitly considering the spatial arrangement of subunits (e.g. [13, 14]). Others have provided mechanical models of the cytoskeleton that predict the changes in cellular shape in response to stimulation. These models, however, focus on the intracellular force distributions and ignore many of the biochemical constituents of the cytoskeleton (reviewed in [15]). Therefore, there is currently a need for

spatiotemporal biochemical models of actin dynamics that are able to combine structural aspects with biochemical signalling.

Here, we present a method for achieving this using the particle-based spatial stochastic simulator MCell [2, 3, 4]. MCell 3.3 provides a syntax for multi-subunit complexes that allows users to specify both macromolecular complexes and molecules that can adopt a large number of biological states (reviewed in [5]). We use this syntax and a system of subunits and tags to model actin cytoskeleton remodelling, including actin polymerisation and depolymerisation, branching of actin filaments, and filament severing and shifting. Our model includes a relatively small number of molecular species and biochemical interactions, but can be extended to include more components of the postsynaptic proteome in the future.

2 METHODS

We used MCell 3.3 [2, 3, 4]. MCell enables users to track the trajectory and state of every single molecule in a reaction compartment, making it possible to model molecules that can exist in many different states [5]. MCell also allows the use of immobile complex molecules which can consist of any desired number of subunits with defined states and orientations in space relative to each other. Here, we used this feature to create a 3D matrix of "subunits" as a frame for the cytoskeleton, and to develop a system with rule sets which would represent actin remodelling, as explained below.

MCell simulation files were written in GNU Emacs text editor and the definition of the 3D matrix cube with 8000 ($20 \times 20 \times 20$) subunits was written into a separate file using a C script. MCell simulations were run on standard laptop and desktop computers and took a few hours to complete for 10^7 simulations (1 s of model time). Results were visualised using the CellBlender add-on for Blender 2.78.

The biochemical components of the model are simplified and include the free monomeric molecules Arp2/3, cofilin, and G-actin (bound to either ADP or ATP). In addition, filamentous (F) actin exists as part of a macromolecular complex that interacts with the monomeric molecular components as described below. At the beginning of the simulation, 39 molecules of ADP-bound G-actin, and four molecules each of Arp2/3 and cofilin were released into the simulation volume. In addition, the simulation volume was seeded with a short, branched F-actin filament consisting of 15 subunits. We use a simplified representation that disregards the double-helical nature of actin filaments for the purpose of easier spatial representation.

Where possible, we took reaction parameters from previous models [14, 16]. However, since the focus of this work was to establish a general method to model filament dynamics in MCell, we did not work on refining estimates for unknown parameters or on determining parameter robustness.

The model files are available on github under the following link: `https://github.com/MelanieIStefan/actin_model`.

3 RESULTS

3.1 Model of actin filament structure using virtual subunits

As the MCell complex molecule feature has so far not been used for filament remodelling, the main focus was to develop a set of rules to model actin filament dynamics in MCell.

Whilst MCell allows users to specify multi-subunit complexes, the size and number of subunits of those complex needs to be specified from the start. We thus pre-defined a "virtual complex" of potential actin subunits. This was done by specifying a $20 \times 20 \times 20$ matrix, which represented possible sites for actin filament growth. This spanned the entire reaction volume. At the start of the simulation, only 15 of those sites were occupied with actual F-actin subunits (bound to either ATP or ADP). All other sites were occupied by "virtual subunits" (named "empty" in our simulation) and were hidden in CellBlender visualisations. Since subunits occupy no actual space in MCell, those virtual subunits do not impact the diffusional properties of other molecules. They can, however, undergo reactions to change, for instance, from an "empty" (virtual) subunit into an F-actin subunit, thus representing extension of the actin filament into a previously empty unit of space.

The outermost subunits of the "virtual complex" received a special designation as "border", in order to prevent errors that might arise from trying to extend filaments outside the original bounds of the $20 \times 20 \times 20$ matrix.

3.2 Actin polymerisation and depolymerisation

The actin filament matrix has directionality and the subunits were defined using x, y and z coordinates. To simplify modelling, the filaments were represented as linear strands of monomers growing upwards at a 45° in four directions: +x (right) and -x (left) on the xy-plane, and +z (forward) and -z (backward) on the yz-plane.

In our model, actin polymerisation and depolymerisation are taking place independently with defined kinetic parameters. Polymerisation occurs when a freely diffusing G-actin-ATP molecule collides with an "empty" subunit that is on the tip of a filament. As a result, a previously "empty" subunit will become occupied by an F-actin-ATP molecule. In order to avoid filament collisions, a polymerisation reaction can only occur when no other molecules occupy subunits in the immediate vicinity of the growing end. In contrast, depolymerisation occurs spontaneously from pointed ends that are occupied by an F-actin-ADP subunit. In this reaction, a previously occupied subunit becomes "empty" and one molecule of freely diffusing G-actin-ADP will be released. To simplify the model, G-actin-ADP molecules will spontaneously be phosphorylated with a defined kinetic parameter in order to be reused for filament growth. This scheme is illustrated in Figure 1 (left panel).

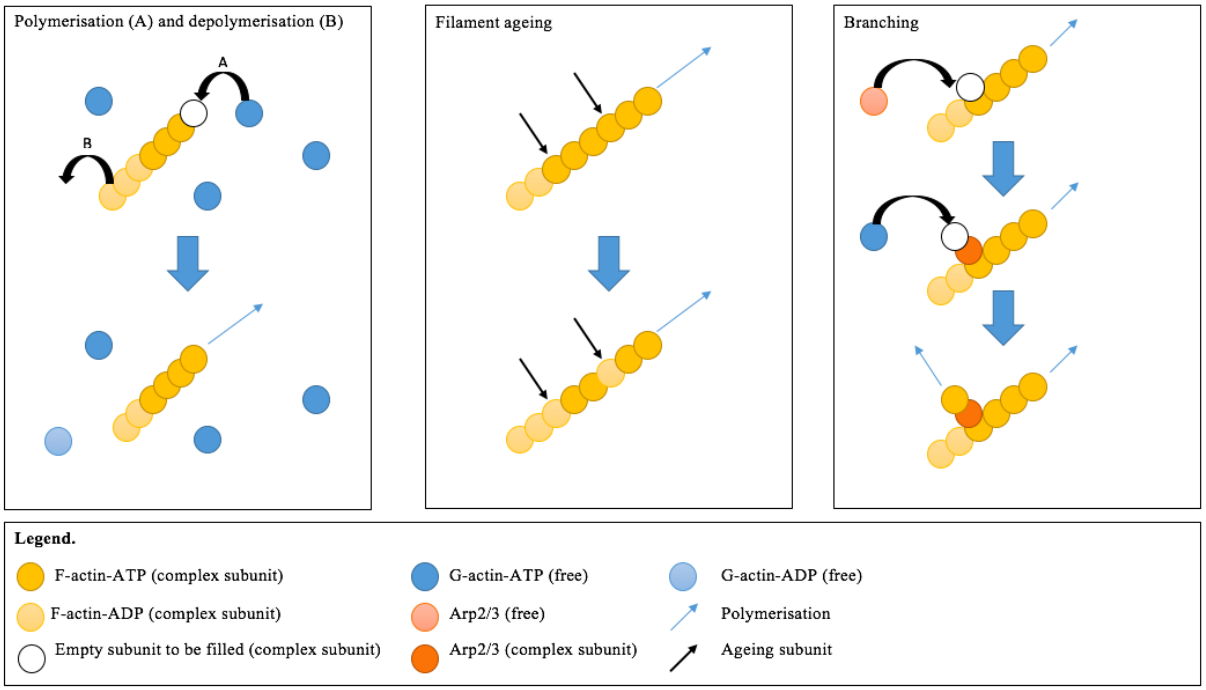

Figure 1: Method for modelling actin polymerisation and depolymerisation (left panel), ageing of actin filaments (middle panel) and branching of actin filaments (right panel).

3.3 Filament ageing

Filament ageing (middle panel of figure 1) involves the hydrolysis of ATP into ADP. In our model, this takes place with three different kinetic parameters depending on the subunit composition of the region. If a monomer is surrounded by F-actin-ADP monomers on both sides, then hydrolysis is taking place with the fastest parameter. If it is surrounded by F-actin-ATP and F-actin-ADP, then the kinetic parameter governing that reaction is half of the previous one. Lastly, if the monomer is surrounded by F-actin-ATP on both sides, then the speed is half of the intermediate speed. This ensures that hydrolysis is more likely to happen around subunits that are already hydrolysed, i.e. the parts of the filament that are older and closer to the pointed end. This is necessary since in memoryless stochastic models the reaction probability does not increase with time and hydrolysis would otherwise take place with similar kinetics throughout the filament.

3.4 Filament branching

Branching of actin filaments takes place when a freely diffusing Arp2/3 molecule collides with an "empty" subunit that is on the side of a filament that faces the spine head. Arp2/3 nucleation is followed by G-actin-ATP monomer binding to either of the three upward directions that are not parallel with the mother filament. After nucleation, polymerisation of the daughter filament continues in a similar manner to the mother filament (see figure 1, right panel). One filament can be branched from different locations and in different directions, resulting in the formation of a 3D network.

3.5 Filament severing and shifting

Another crucial event in cytoskeletal remodelling is the dislocation of parts of a filament. In this model, the concept of shifting involves vacating of the original set of positions in the matrix and instantly occupying neighbouring empty slots further away while maintaining the original structure. This required the development of a rule set for monomer tagging that allowed for full filament shift. We first developed a set of rules governing severing events. Severing divides filaments into two providing more barbed ends for polymerisation as well as more pointed ends for depolymerisation. Filament severing is mediated by cofilin and is preferably taking place in the older parts of the filament. Here, it is modelled as a reaction between freely diffusing cofilin and F-actin-ADP, whereupon F-actin-ADP instantly receives a tag (tag 1), which marks it for severing (figure 2). The tag is instantly transmitted to all neighbouring F-actin subunits towards the pointed end, regardless of their nucleotide phosphorylation status, until the tagging chain reaches Arp 2/3. An Arp2/3 molecule that is in the immediate vicinity of a subunit with tag 1 is instantly tagged as well. The untagged subunits from another branch next to the tagged Arp2/3 molecule will then be instantly tagged with tag (2) and now, tagging can take place in both directions and will also include all the other branches attached to tagged monomers. This ensures that only the parts below the site of severing will shift, leaving

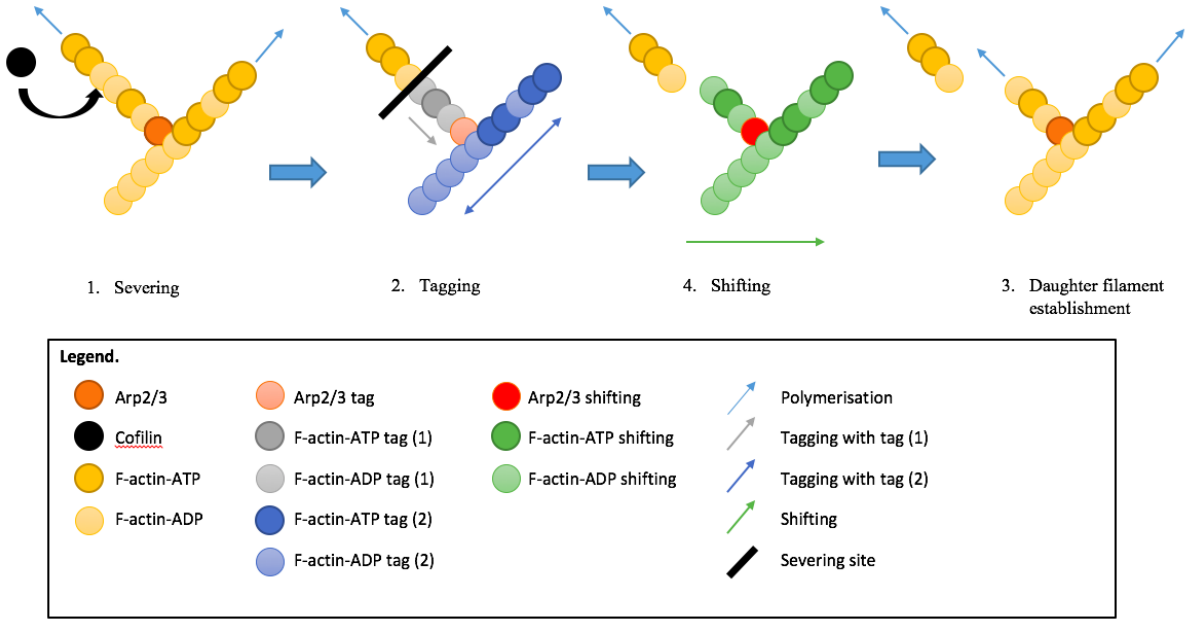

Figure 2: Method for modelling actin filament severing and shifting.

the upper part of the filament in its place.

The kinetic parameter for the tagging reaction is a large arbitrary number, chosen to be faster than any other reaction in the simulation. This is to prevent all the other possible changes that could take place within the filament during the same short time window. Once a molecule receives a tag, it cannot be subject to any other reaction events besides shifting. However, in order to avoid errors, the rule set includes rules that ensure that no other molecule is occupying the subunits through which shifting will take place. In current models, molecules are only shifting in the +x direction. Therefore, each subunit will only shift if the next slot in +x direction is unoccupied.

The kinetic parameter for shifting is also very fast but slightly slower than the tagging speed to ensure that no movement occurs before the whole filament is tagged. Briefly after the shifting intermediate is generated and labelled with a shifting tag, the original subunit disappears by being tagged as "empty".

The next step shifts the subunit by one more slot in the +x direction and converts it back to its original molecular state (e.g. F-actin-ATP). The shifting intermediate is again converted back to vacant subunits. This ensures that the original filaments and the part that shifted away from it are two subunits away from each other to allow polymerisation from the newly generated barbed end.

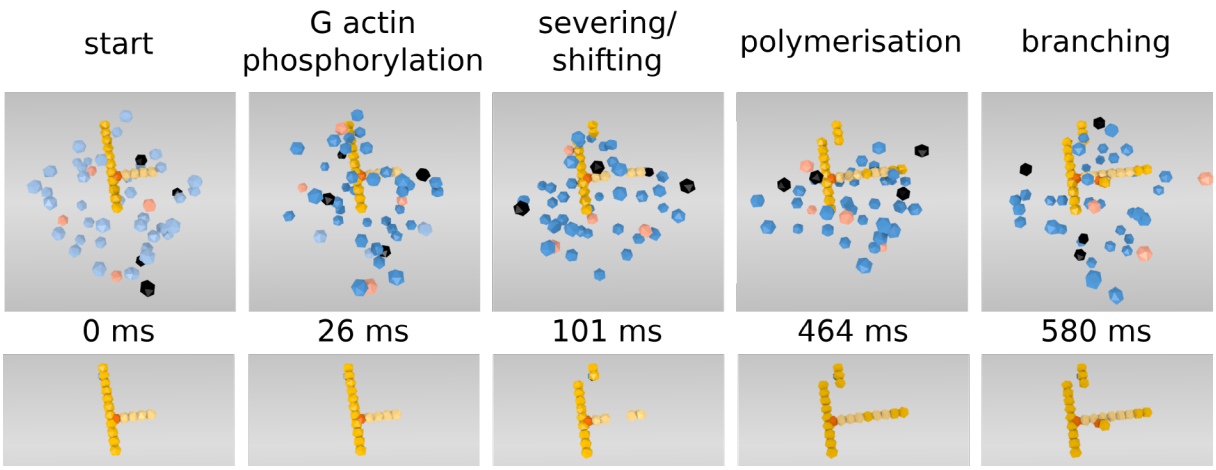

Figure 3: Stills from an MCell simulation showing G-actin phosphorylation, filament severing/shifting, polymerisation and branching.

3.6 Simulation results

In order to test the implementation of our rule set in MCell, we ran 10 simulations using different random seeds. Simulations were run with a time interval of 10^{-7} s, for a total of 1 s each. Within this time frame, we were typically able to observe one or several instances of filament severing and shifting, branching, and elongation. Filament ageing and depolymerisation have much slower reaction rates, and are therefore not observed in this time frame. As an example, still images from one of the simulations (using random seed 4) are shown in figure 3.

4 DISCUSSION

This work presents a proof of concept that the "complex molecule" syntax in MCell 3.3 [2, 3, 4] can be used to model actin cytoskeleton dynamics and, more generally, assembly, disassembly and movement of any type of biopolymer. Thus, the particle-based simulator MCell can act as a bridge between structure-based models of biopolymer assembly and models of cellular biochemical pathways.

Our present model is an implementation of the methods we have developed to model different aspects of actin dynamics in MCell and serves as a prototype. The representation of actin filament dynamics could be extended, e.g. by allowing shifting of severed polymers over wider ranges. There is also work to be done in determining and refining the parameters governing all reactions in order to create a model that closely matches results from previous experiments.

Finally, the model can be combined with models of biochemical pathways within the dendritic spine. We have previously worked on Calcium-dependent signalling pathways in dendritic spines [17, 18, 19]. For instance, Calcium signalling leads to activation of CaMKII, a key protein for initiating synaptic long-term potentiation [6]. CaMKII inter-

acts with the actin cytoskeleton and thereby regulates its ability to remodel and to regulate spine structure. Combining our model of actin dynamics with a model of CaMKII activation could give a unique insight into how biochemical regulation and structural changes interact to regulate the synaptic machinery that controls learning and memory.

REFERENCES

[1] Bosch, M. and Hayashi, Y. Structural plasticity of dendritic spines. *Current Opinion in Neurobiology* (2012) **22**:383-388.

[2] Stiles, J.R.; Helden, D.V.; Bartol, T.M.; Salpeter, E.E. and Salpeter, M.M. Miniature endplate current rise times less than 100 microseconds from improved dual recordings can be modeled with passive acetylcholine diffusion from a synaptic vesicle. *Proc Natl Acad Sci USA* (1996) **93**:5747–5752.

[3] Stiles, J. and Bartol, T. Monte Carlo methods for simulating realistic synaptic microphysiology using MCell. In: De Schutter, E. (Ed.) *Computational Neuroscience: Realistic Modeling for Experimentalists*. CRC Press, Boca Raton, (2001).

[4] Kerr, R.A.; Bartol, T.M.; Kaminsky, B.; Dittrich, M.; Chang, J.-C.J.; Baden, S.B.; Sejnowski, T.J. and Stiles, J. R. Fast Monte Carlo Simulation Methods for Biological Reaction-Diffusion Systems in Solution and on Surfaces. *SIAM J Sci Comput* (2008) **30**:3126.

[5] Stefan, M.I.; Bartol, T.M.; Sejnowski, T.J. and Kennedy, M.B. Multi-state Modeling of Biomolecules. *PLoS Comput Biol* (2014) **10**:e1003844.

[6] Lisman, J.; Yasuda, R. and Raghavachari, S. Mechanisms of CaMKII action in long-term potentiation. *Nature Reviews Neuroscience* (2012).

[7] Chazeau, A. and Giannone, G. Organization and dynamics of the actin cytoskeleton during dendritic spine morphological remodeling. *Cell Mol Life Sci* (2016) **73**:3053–3073.

[8] He, C.X. and Portera-Cailliau, C. The trouble with spines in fragile X syndrome: density, maturity and plasticity. *Neuroscience* (2013) **251**:120–128.

[9] Phillips, M. and Pozzo-Miller, L. Dendritic spine dysgenesis in autism related disorders. *Neurosci Lett* (2015) **601**:30–40.

[10] Robison, A.J. Emerging role of CaMKII in neuropsychiatric disease. *Trends Neurosci* (2014) **37**:653–662.

[11] Kim, K.; Lakhanpal, G.; Lu, H.; Khan, M.; Suzuki, A.; Kato Hayashi, M.; Narayanan, R.; Luyben, T.; Matsuda, T.; Nagai, T. et al. A Temporary Gating

of Actin Remodeling during Synaptic Plasticity Consists of the Interplay between the Kinase and Structural Functions of CaMKII. *Neuron* (2015) **87**:813-826.

[12] Pollard, T.D.; Blanchoin, L. and Mullins, R.D. Molecular Mechanisms Controlling Actin Filament Dynamics in Nonmuscle Cells. *Annual Review of Biophysics and Biomolecular Structure* (2000) **29**:545-576.

[13] Ruiz-Martinez, A.; Bartol, T.; Sejnowski, T. and Tartakovsky, D. Efficient Multiscale Models of Polymer Assembly. *Biophysical Journal* (2016) **111**:185-196.

[14] Rangamani, P.; Levy, M.G.; Khan, S. and Oster, G. Paradoxical signaling regulates structural plasticity in dendritic spines. *Proceedings of the National Academy of Sciences* (2016) **113**:E5298-E5307.

[15] Chen, T.-J.; Wu, C.-C. and Su, F.-C. Mechanical models of the cellular cytoskeletal network for the analysis of intracellular mechanical properties and force distributions: A review. *Medical Engineering and Physics* (2012) **34**:1375-1386.

[16] Tania, N.; Condeelis, J. and Edelstein-Keshet, L. Modeling the Synergy of Cofilin and Arp2/3 in Lamellipodial Protrusive Activity. *Biophysical Journal* (2013) **105**:1946-1955.

[17] Stefan, M.I.; Edelstein, S.J. and Le Novère, N. An allosteric model of calmodulin explains differential activation of PP2B and CaMKII. *Proc Natl Acad Sci USA* (2008) **105**:10768–10773.

[18] Li, L.; Stefan, M.I. and Le Novère, N. Calcium Input Frequency, Duration and Amplitude Differentially Modulate the Relative Activation of Calcineurin and CaMKII. *PLoS One* (2012) **7**:e43810.

[19] Stefan, M.I.; Marshall, D.P. and Le Novère, N. Structural analysis and stochastic modelling suggest a mechanism for calmodulin trapping by CaMKII. *PLoS One* (2012) **7**:e29406.

V International Conference on Particle-based Methods – Fundamentals and Applications
PARTICLES 2017
P. Wriggers, M. Bischoff, E. Oñate, D.R.J. Owen, & T. Zohdi (Eds)

BRAZILIAN TEST - A MICROSCOPIC POINT OF VIEW ON TENSILE FRACTURE GENERATION

P. Klejment, W. Debski

Affiliation
Institute of Geophysics PAS, Warsaw, Poland
pklejment@igf.edu.pl
debski@igf.edu.pl
www.private.igf.edu.pl/ debski

Key words: Brazilian test, DEM, ESyS-Particle

Abstract. The tensile strength of solid materials is one of the most important parameter describing a behavior of the material under external mechanical loading and thus its knowledge is of great practical importance. However, the direct measurement of tensile strength especially for brittle materials is quite difficult and only limited results are available. To cope with this situation various methods of indirect measurements have been proposed among others the, so called Brazilian test is the most popular. The method relies on diametrically loading of disc-like sample of the brittle material until it splits apart due to a induced tensile stress. In this paper we report our effort of describing the fracturing process during the Brazilian test from the "microscopic"point of view. For this purpose we use an advanced implementation of the Discrete Element Method - the ESyS-Particle software. We represent rock specimen as a set of interacting spherical particles which mimic grains of real rock material. We have observed that the maximum loading force which sample can withstand almost linearly scales up with a ratio of maximum-to-minimum particles diameters.

1 INTRODUCTION

The tensile strength of solid materials is one of the most important parameter describing a behavior of the material under mechanical load and thus its knowledge is of great practical importance. However, the direct measurement of tensile strength, especially for brittle materials is quite difficult and thus only limited results are available. To cope with this situation [3] have proposed an indirect method of estimation of the tensile strength know as the *Brazilian test*. The method relies on diametrically loading of disc-like sample of the brittle material until it splits apart due to induced tensile stress as sketched in Fig. 1. Due to its simplicity and low cost of sample preparation it became very popular and has got a recommendation of the International Society for Rock Mechanics Commission as the standard method of the tensile strength estimation [9]. The justification of

the method comes from theory of elasticity which predicts that for an ideal homogeneous elastic cylinder of Radius R and length L subjected to a diametrically linear loading P the stress inside the body reads [11]:

$$\begin{aligned}
\sigma_x &= \frac{P}{\pi RL} - \frac{2P}{\pi L}\left(\frac{x^2(R-y)}{[x^2+(R-y)^2]^2} + \frac{x^2(R+y)}{[x^2+(R+y)^2]^2}\right) \\
\sigma_y &= -\frac{P}{\pi RL} - \frac{2P}{\pi L}\left(\frac{(R-y)^3}{[x^2+(R-y)^2]^2} + \frac{x(R+y)^2}{[x^2+(R+y)^2]^2}\right) \\
\tau_{xy} &= \frac{2P}{\pi L}\left(\frac{x(R-y)^2}{[x^2+(R-y)^2]^2} - \frac{x(R+y)^2}{[x^2+(R+y)^2]^2}\right)
\end{aligned} \tag{1}$$

where $x,\ y$ refer to coordinates shown in Fig. 1. As it follows from above, at the loading plane ($x = 0$) the σ_x and σ_y are normal stresses ($\tau_{xy} = 0$) perpendicular and parallel to the loading plane, the tensile stress σ_x is constant and reads

$$\sigma_T = \frac{P}{\pi RL} \tag{2}$$

while the compressional stress σ_y increases from $3\sigma_x$ at the center of the disc to infinity at the loading point.

These formulas have been extended to a more realistic laboratory situations taking into account loading over a finite, bended surface, non-homogeneity and anisotropy of the material, to name a few extensions. The usefulness and simplicity of the Brazilian test follows directly from Eq. 2 which predicts that tensile is proportional to the loading. Thus, assuming that splitting of the samples occurs when tensile stress reaches the material tensile strength, it can easily be estimated from Eq. 2 by recording the loading force when sample crushes.

The Brazilian test method has gain a lot of popularity not only because of simplicity of its application but also due to more fundamental questions concerning mechanisms of creation and development of the tensile fractures under a simple initial and boundary conditions. However, it has received also a lot of criticism due to lack of robustness and proximity. This last issue arises from the fact that the Brazilian test results show a systematic overestimation of the tensile toughness with respect to values obtained in direct measurements. Thus, there is a lot of ongoing discussion on reasons of this discrepancies. There is also still an open question about dynamics of nucleation and development of the main tensile and secondary cracks resulting in a final breaking apart of the specimen. The classical theory predicts creation of such crack in a center of the sample where compressing stress is the smallest. After nucleation the crack is expected to propagate along the loading plane outwards. However, in many experiments the crack was observed to nucleate not in center but close to sample surface [12]. Wings-type and secondary cracks have also been observed [5]. Another open question is which criterion should be used for estimation of the tensile strength. The most popular approach is based on the stress criterion according to which the material breaking occurs when *tensile stress* reaches the critical value and

Eq. 2 is then directly used. However, this is fully arbitrary choice. Another, physically justified the *strain criterion* was proposed by [17]. Both criteria are equivalent (at least from mathematical point of view) for perfectly elastic media but not if large deformation effects are taken into account.

Theoretical analysis of the Brazilian test method are based mainly on the classical continues mechanics [6, 8, 14] and are limited to the simplest cases. Analysis of more realistic cases can be done only numerically. Authors of such studies use most often different variants of the Finite and/or Boundary Element Methods [15, 4, 18]. Only recently, a simple but very interesting analysis based on the Fiber Bundle Method has been presented [13]. In this paper we analyze some of the above mentioned issues from a "molecular" point of view using an advanced implementation of the Discrete Element Method (DEM) [2]. The method represents the medium as a set of interacting elements "molecules" and is particularly convenient for describing process of medium fragmentation. Moreover, it has been argued [16] that such representation is more natural for describing rock materials than methods based on the continuous mechanics. The used EsyS-Particle software allows a full 3D analysis of stress and displacement evolution in the sample under external loading, takes into account possible large deformations like the classical Finite Element approach and supports description of the material fragmentation and thus cracks nucleation and its temporal evolution [1].

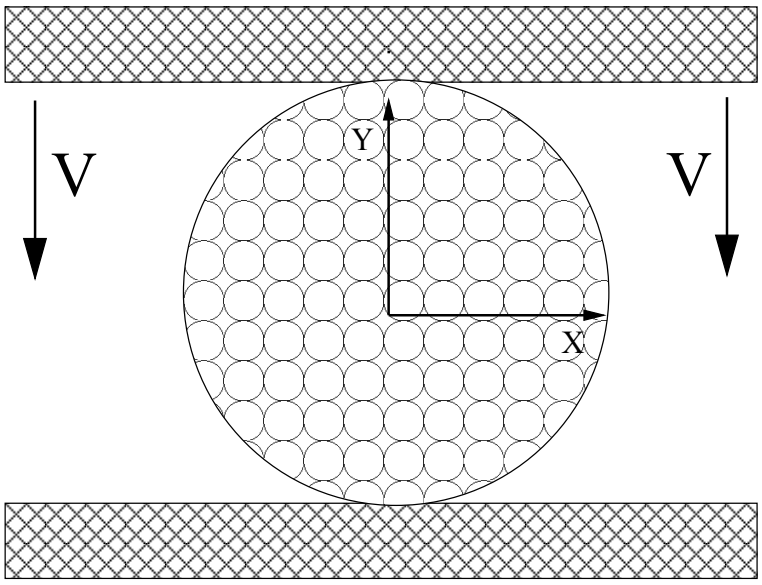

Figure 1: The sketch of the simulation setup used in numerical simulations. The horizontal loading plates are assumed to be perfectly rigid. The lower plate is fixed while the upper one moves downwards with constant velocity V providing the diameter loading of the disc.

2 DEM SIMULATIONS

2.1 Simulation setup

We have performed a number of numerical simulations of Brazilian test experiment considering the specimen in a form of disc (cylinder) of diameter 10 mm and thickness 5 mm, diametrically loaded as it is shown in Fig. 1. The sample was build of spherical particles of varying size within predefined ranges. The maximum radius of used particles was always kept fixed and equal to $R_{max} = 0.2$ mm. The minimum radii were varying among simulations in a range from 0.027 mm up to 0.1 mm. The external load was supplied by two perfectly rigid plates. The lower plate was fixed while the upper one moved downward with constant velocity V=4mm/sec. Simulations ended when the vertical displacement of the upper plate reached the predefined level of 0.2 mm, selected as a large enough to include the sample breaking and a beginning of the post failure stage. In Fig. 2 examples of the facial views of one of the sample prior and after creating a main tensile crack (but still before complete breaking of the sample) are shown. During loading we have recorded at each time step the vertical position of the upper plate and total vertical force acting on it, so a stress - strain relation was continuously monitored. Besides that, we have also recorded total kinetic energy of particles and total potential energy of inter-particles interactions.

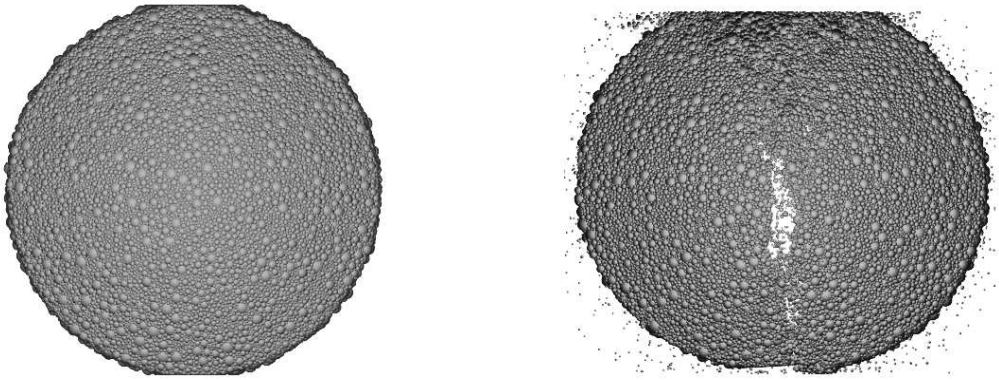

Figure 2: An example view of the sample face prior to loading (left) and after creating a tensile crack (right) in the middle of the sample.

The most nontrivial element of any DEM simulation is defining the particle interactions and breaking conditions. We have used the model of "elastic-brittle interactions" supported by ESyS-Particle and illustrated in Fig. 3.
In this model the near-neighborhood particles interact with each other with repulsive/cohesive radial forces and non-radial "shearing" ones. If interacting particles separate by fixed distance (in terms of percentage of their radii) the interacting bond is broken and interaction is reset to zero. Breaking of shearing forces is based on the Coulomb-Mohr criterion [2]. Under these assumptions our specimen represents a medium which for small external load-

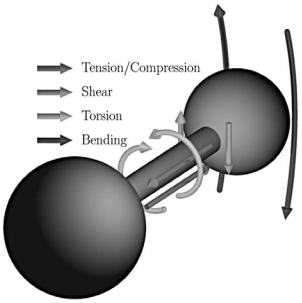

Figure 3: A sketch of forces and moments between particles interacting according to used the advanced interaction model implemented in ESyS-Particle (after [2]).

ing behaves as an ideal elastic body. For larger loads, when some inter-particles bonds break and particles can significantly move away from their initial location the material exhibits some plasticity. Finally, in a large stress concentration regions the particles can separates "en bloc" due to a significant stress redistribution when interaction bonds break (a similar effect is observed in soft-clamp Fiber Bundle Model [10] which finally leads to an initiation and development of cracks. This way, with this simple setup we can simulate behavior of a variety of solid materials.

In the current simulations we have concentrated on a question how size of particles building the sample influences simulation results. For this reason we have kept particle interactions fixed and also the loading rate was kept constant. The build disc samples consisted from about $5 \cdot 10^4$ up to almost $2 \cdot 10^6$ particles and typical $5 \cdot 10^4$ time steps were required to break the samples apart. The time step we have used for the temporal integration (evolution) have been chosen as the compromise between numerical stability and computational time and reads $dt = 5 \cdot 10^{-6}$. With this simulation setup computational time on 10 cores CPU workstation ranged between 6 and 90 hours.

2.2 Simulation results

Let us begin the discussion of obtained results from the analysis of a relation between applied load and vertical displacements (strain) of the sample. The scaled together (for presentation purpose) strain-stress relations for five simulations are shown in Fig. 4 and few particular features are clearly visible in this figure.

Firstly, the maximum attained values of load P_{max}, at which samples break apart strongly depend on the minimum size R_{min} of particles building the sample. On the contrary, the critical strain d_c at which $fmax$ is reached feeble depends on R_{min} ranging from about 0.1 mm up to 0.12 mm. In the consequence the slope of the initial part of the strain-stress curves also significantly varies with R_{min}. Secondly, for small strains the response of the sample to the load is essentially elastic, manifesting itself in an almost linear strain-stress dependences. The visible undulation of the curve is partially due to an acoustic wave generated at the beginning of loading when the upper plate "hits" the

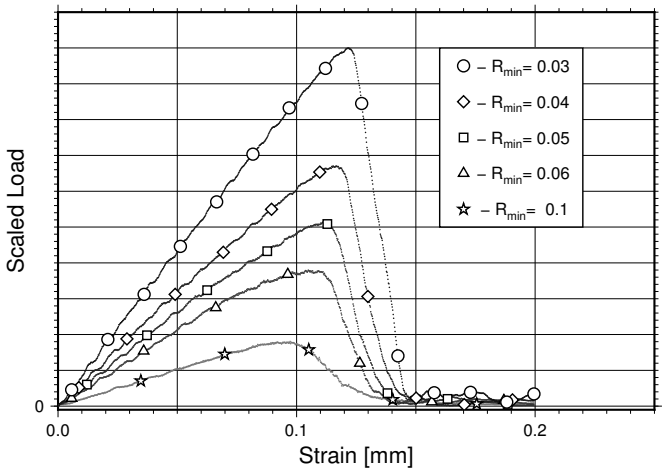

Figure 4: The load against the vertical displacement (strain) for five different samples composed of particles with different minimum radii R_{min}. The maximum radius was fixed for all samples $R_{max} = 0.2$ mm. The weak undulation in first part of curve is mainly due to acoustic waves generated by abrupt beginning of loading of the samples.

sample with the constant speed and partially due to a numerical noise. Only for very small strains (less than 0.01mm) this linearity is broken and a "flattening" of the stress-strain curves is observed. This is a purely numerical effect connected to a non-optimum initial packing of particles in the samples. Thirdly, a departure from the elastic behavior appears at larger strains and manifest itself as a flattening of the curves. This plastic regime starts earlier for samples built of larger particles. In case of samples with $R_{min} = 0.03$ mm it appears just before reaching the maximum withstand load, while for samples built of particles with $R_{min} \sim 0.1 \sim 0.06$ mm it starts almost in half of the strain value at given sample breaks. Finally, in the post failure stage the stress drop rate is smaller for samples built of larger particles. It is interesting to note, that the post failure stress reaches minimum (complete breakage of the sample) for similar values of strain in all cases. To summarize, we have observed a significant mechanical strengthening for samples composed of smaller particles with respect to softer samples build of larger particles. However, the vertical deformation at which samples break apart only weakly depends on R_{min}.

In the next step we have analyzed variation of number of broken inter-particle bonds with progressing load. The results are shown in Fig. 5 where separately scaled number of broken bonds for five considered samples are shown together. The behavior of plotted curves is very similar in a narrow vicinity of critical strain d_c when samples start to break for all but one cases . An abrupt increase of bonds breaking starts just around reaching critical load P_{max} and continue until the sample fully breaks and load reaches minimum value. Only for the very soft sample ($R_{min} = 0.1$) inter-particle bonds start to break massively earlier and the process goes smoother through larger range of sample

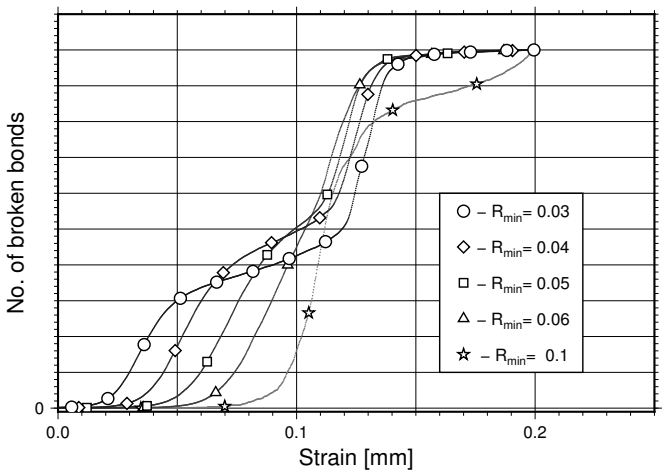

Figure 5: Number of broken inter-particle bonds as the function of the sample vertical deformation.

deformations. The particle composition of the samples influences significantly the initial part of curves corresponding to elastic behavior of samples. For deformations smaller than 0.1 mm we clearly see in Fig. 5 that smaller particles are used to build the sample, sooner inter-particle bonds starts to break. Simultaneously, smaller R_{min} is, larger hardening of a sample before the final breakage is observed. This effect manifests itself by flattening of curves when strain approaches 0.1 mm. Since during the simulations interaction bonds were not allowed to re-heal after breaking, the observed initial increase of bonds breaking can be interpreted as beginning of a visco-plastic deformation of the samples. Let us note, that this effect is quite feeble and can hardly be visible in strain-stress curves in Fig. 4. The degree of this induced viscosity significantly depends on the particles size. From a physical point of view this observation suggests, that at intermediate values of loading some dislocations are induced in the samples. Indeed, such dislocations are more probable for smaller particles and for this reason viscous behavior would start earlier for samples with smaller R_{min}. Moreover, the particle rearrangement by dislocations very soon leads to denser particle packing and in the consequence to the hardening of samples. Finally, for the very small deformation we observe no particle bonds breaking. This is a perfectly elastic regime.

Next, let us consider the change in the potential energy of particle interaction and the particles kinetic energy (without rotational energy) with progressing vertical deformation. The results are shown in Fig. 6.

In the first approximation one can assume that an external compressional load induces harmonic repulsive forces between interacting particles. In consequence, a change of total potential energy should be proportional to the squared sample deformation. Such a behavior is indeed visible in the right panel in Fig. 6 for small and intermediate deformations. For larger deformations when the rupture process nucleate potential energy starts to be

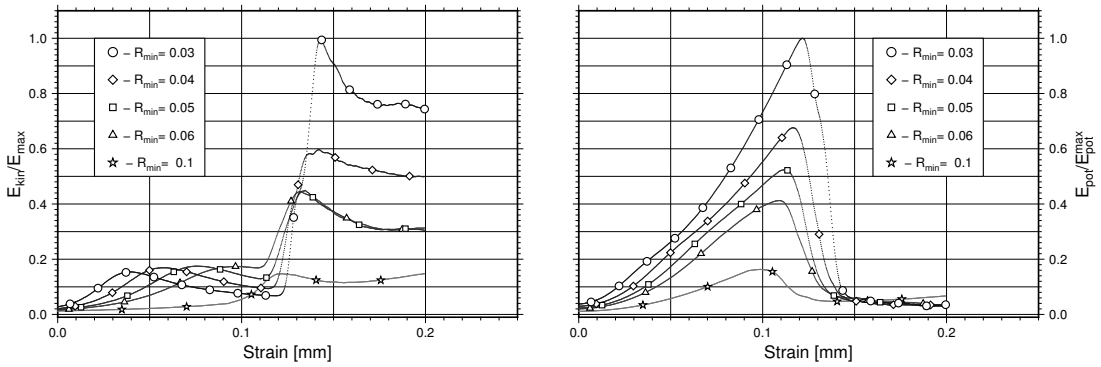

Figure 6: The absolute value of the kinetic (left) and potential energy of particles interactions (right) scaled to the maximum value obtained in all simulations.

released and diminishes. Besides these changes of the potential energy with deformation is different for samples with different R_{min}. It increases most rapidly for samples build of smaller particles and reaches larger values, as expected. The samples build of smaller particle can accumulate larger elastic deformation (potential) energy. In consequence, taking into account that the breaking (critical) strain d_c only slightly increases with decreasing R_{min} and deformation at which samples breaks apart is almost the same for all samples the potential energy released is more abrupt for samples with smaller R_{min}. Thus, we can expect that breaking process will go faster for samples build of smaller particles.

As far as the kinetic energy E_{kin} is concerned we can see in the left panel of Fig. 6 that it is quite stable in the first phase of loading. Some increase and variations of E_{kin} at the intermediate loading can be attributed to the dislocations processes discussed above. During the breaking stage it increases significantly due to a release of potential energy. The changes (mostly decrease) of E_{kin} in the post-failure stage are more complex due to a possible secondary cracking of the samples [5]. However, at this stage, the behavior of E_{kin} is also strongly influenced by a numerical dumping implemented in the used code and thus include a non-physical component. For this reason we do not analyze this stage any more.

Considering energy transformations during the loading and breaking stage of the process we have analyzed the difference between work of the external load and sum of the kinetic and potential energies. The obtained results are shown in Fig. 7

For small, elastic deformations the work of the loading force (ΔW) fully converts into the elastic ($E_T = E_{kin} + E_{pot}$) energy. In consequence $\Gamma = \Delta W - E_T$ vanish. At the intermediate loading stage we observe a monotonic increase of Γ with the sample deformation. This is a signature of non-elastic transfer of external energy. We attache it to breaking of inter-particle interactions bonds and particle dislocations. In real materials at this stage the external energy is also efficiently transformed into the heat. However our

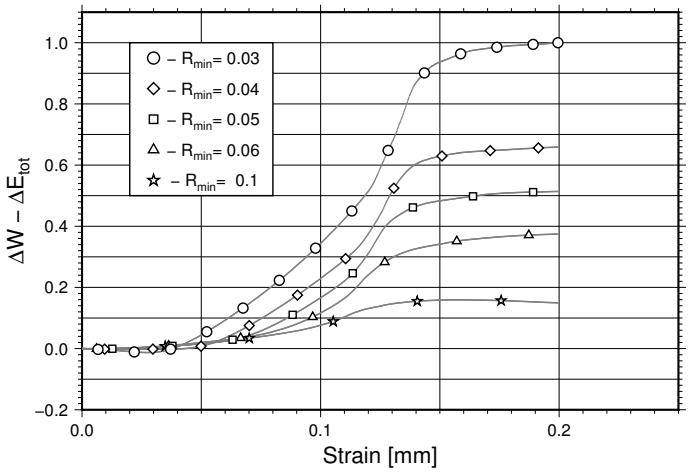

Figure 7: The difference between external load work (ΔW) and sum of kinetic and potential energy. The obtained values were scaled by the largest value obtained in all simulations.

simulations do not take into account thermal effects yet. It is interesting to observe that at this stage Γ exhibits a strong dependences on particle size (R_{min}). During the braking stage ($0.11 < dl < 0.14$) Γ further increases and finally saturates, as expected.

2.3 Scaling

Discussing results shown in Fig. 4 we have noticed that the maximum load the sample can withstand depends significantly on R_{min}. To analyze this issue more in depth we have plotted in Fig. 8 the maximum loads P_{max}, d_c, and the potential energy at the d_c strain for all considered samples.

The obtained results show that the dependence of P_{max} on inverse of R_{min} is almost perfectly linear. Very similar behavior exhibits potential energy calculated for the strain when load reaches its maximum value. The critical strain d_c also almost linearly but, much weaker depends on the R_{max}/R_{min} ratio. At the moment we have no explanation of this observed P_{max} (potential energy) scaling. Actually, a preliminary analysis carried out for a larger set of samples with different R_max confirmed that with a quite good approximation P_{max} depends only on the ratio R_{max}/R_{min} and thus the reported scaling holds.

3 CONCLUSIONS

With the performed numerical simulations we have reached a few goals. From the technical point of view we have proved that ESyS-Particle software is working correctly with this type problems provided the most advanced particle interaction model is used. The obtained results are in a full agreement with similar results obtained both analytically as well as by a more traditional FEM methods. We have also demonstrated exceptional

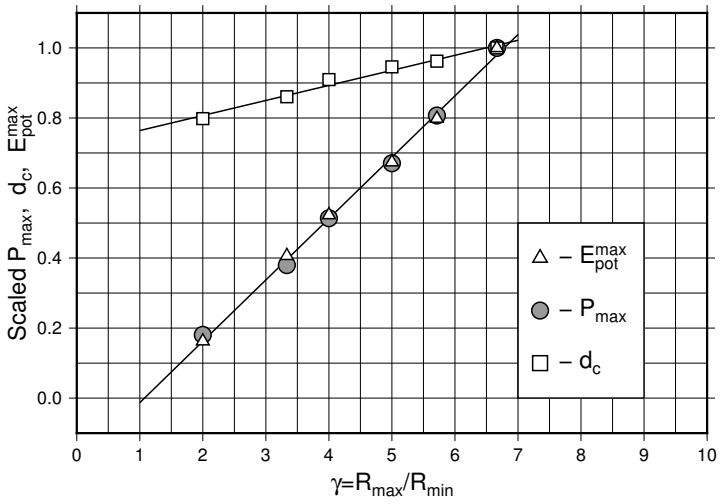

Figure 8: The maximum critical load, critical strain d_c and potential energy at d_c strain as the function of $\gamma = R_{max}/rmin$.

abilities of the DEM method with solving problems including sample fragmentation. The method has allowed a detailed monitoring of internal microscopic state of loaded sample including changes of particles kinetic and potential energies to name a few. From the physical point of, we have got an insight into creation of the tensile crack under the simulated laboratory conditions. We were able to monitor a nucleation and temporal evolution of tensile crack which finally lead to breaking apart of Brazilian test samples. Following an evolution of the total kinetic and potential energies during lading we were able to identify a few stages in a response of the samples to constant speed loading. At the beginning of loading the elastic response of the samples was clearly visible. For the intermediate loading the samples exhibited a visco-elastic properties due to inducing particles dislocations. At the end of this stage large dislocation occurring *en block* resulted in a visible plastic behavior of the samples and finally lead to crack nucleation and breaking the sample apart. The most interesting is, however, observing how size of used particles influenced each of the above stage. Although we used relatively small range of particle sizes the obtained results clearly shows that the most sensitive to the material composition is the intermediate loading stage when dislocations start to change the properties of materials and lead to a crack nucleation. On the other hand, the rather weak dependence of the critical strain and the strain when the crack fully breaks the sample into two pieces shows that this failure stage is rather insensitive to the material composition. However, in our judgement, the most important result of the performed simulations is reporting of the scaling of the critical load which the sample can withstand with inverse of the size of the smallest particles building the sample. This unexpected observation is further investigating and results will soon be published elsewhere. At this time we have no

physical explanation of the observed scaling.

4 ACKNOWLEDGEMENTS

Author (WD) would like to thank A. Hansen and S. Pradham for many discussions on Fiber Bundle Models, and T. Yanagidani for introduction into the Brazilian test method during a visit of Kobe University. A. Kosmala is acknowledge for help during manuscript preparation. This paper was partially supported by research grant No. 2015/17/B/ST10/01946 of NCN, Poland and internal grant of IGF PAS for young scientists No. 5f/IGF PAN/2016ml

REFERENCES

[1] S. Abe, S.H. van Gent, and J.L. Urai. DEM simulation of normal faults in cohesive materials. *Tectonophysics*, 512,(1):12–21, 2011. doi: 10.1016/j.tecto.2011.09.008.

[2] Abe S., Boros V., Hancock W., Weatherley D., ESyS - Particle Tutorial and User's Guide Version 2.3.1. 2014.

[3] T. Akazawa. New test method for evaluating internal stress due to compression of concrete: the splitting tension test. *J Japan Soc Civil Eng.*, 29:777–787, 1943.

[4] M. Cai and P.K. Kaiser. Numerical Simulation of the Brazilian Test and Tensile Strength of Anisotropic Rocks and Rocks with Pre-existing Cracks. *Int. J. Rock Mech. Min. Sci & Geomech. Abstr.*, 41(3):2B03, 2004.

[5] M. Cai. Fracture Initiation and Propagation in a Brazilian Disc with a Plane Interface: a Numerical Study. *Rock Mech Rock Eng*, 46:289–302, 2013. doi: 10.1007/s00603-012-0331-1.

[6] J. Claesson and B. Bohloli. Brazilian test: stress field and tensile strength of anisotropic rocks using an analytical solution. *Int. J. Rock Mech. Min. Sci & Geomech. Abstr.*, 39(8):991–1004, 2002. doi: 10.1016/s1365-1609(02)00099-0.

[7] P.A. Cundall and O.D.L. Strack. A discrete numerical model for granular assemblies,. *Geotechnique*, 29(1):47–65, 1979. doi: 10.1680/geot.1979.29.1.47.

[8] G.E. Exadaktylos and K.N. Kaklis. Applications of an explicit solution for the transversally isotropic circular disc compressed diametrically. *Int. J. Rock Mech. Min. Sci & Geomech. Abstr.*, 38(2):227–243, 2001. doi: 10.1016/s1365-1609(00)00072-1.

[9] Int. Soc for Rock Mech. Commission on Standardization of Laboratory and Field Tests. Suggested Methods for Determining Tensile Strength of Rock Materials. *Int. J. Rock Mech. Min. Sci& Geomech. Abstr.*, 15(3):99–103, 1978. doi: 10.1016/0148-9062(78)90003-7.

[10] A. Hansen, P.C. Hemmer, and S. Pradhan. *The fiber Bundle Model*. Viley-VCH, Veinheim, 2015.

[11] D.W. Hobs. The tensile strength of rocs . *Int. J. Rock Mech. Min. Sci. & Geomech. Abstr.*, 1(3):385–396, 1964. doi: 10.1016/0148-9062(64)90005-1.

[12] J.A. Hudson, E.T. Brown, and F. Rummel. The controlled failure of rock disc and rings loaded in diametral compression. *Int. J. Rock Mech. Min. Sci. & Geomech. Abstr.*, 9(2):241–248, 1972. doi: 10.1016/0148-9062(72)90025-3.

[13] S. Kundu, A. Stroisz, and S. Pradhan. A simple discrete-element-model of Brazilian test. *The European Phys. J. B*, 89:130–137, 2016. doi: 10.1140/epjb/e2016-60915-y.

[14] A. Lavrov and A. Vervoort. Theoretical treatment of tangential loading effects on the Brazilian test stress distribution. *Int. J. Rock Mech. Min. Sci & Geomech. Abstr.*, 39(2):275–283, 2002. doi: 10.1016/s1365-1609(02)00010-2.

[15] E. Onate and T. Rojek. Combination of discrete element and finite element methods for dynamic analysis of geomechanics problems. *Computer methods in applied mechanics and engineering*, 193:3087–3128, 2004.

[16] D. Potyondy and P. Cundall. A bonded-particle model for rock. *Int. J. Rock Mech. and Min. Sci.*, 41(8):1329–1364, 2004. doi: 10.1016/j.ijrmms.2004.09.011.

[17] T.R. Staccey. A simple extension strain criterion for fracture of brittle rock. *Int. J. Rock Mech. Min. Sci & Geomech. Abstr.*, 18(6):469–474, 1981. doi: 10.1016/0148-9062(81)90511-8.

[18] W.C. Zhu and C.A. Tang. Numerical simulation of Brazilian disk rock failure under static and dynamic loading. *Int. J. Rock Mech. Min. Sci & Geomech. Abstr.*, 43: 236–252, 2006.

Does shape matter? FEMDEM estimations of strength and post failure behaviour of catalyst supports

A. Farsi[1], J. Xiang[1], J. P. Latham[1], M. Carlsson[2], E. H. Stitt[2], M. Marigo[2]

[1]Applied Modelling and Computation Group (AMCG),
Department of Earth Science and Engineering
Imperial College London, South Kensington Campus,
London SW7 2AZ, United Kingdom

[2]Johnson Matthey, P.O. Box 1, Belasis Avenue,
Billingham, Cleveland, TS23 1LB, United Kingdom

ABSTRACT

The combined finite-discrete element method (FEMDEM) implemented in Solidity is employed to simulate the effects of geometrical features and loading orientation on the pre- and post-failure behaviour of catalyst supports. In this paper, a comparison with experimental results and a mesh sensitivity analysis for the numerical simulations of uniaxial compression tests on cylindrical pellets are presented and discussed. The structural strength of complex-shaped pellets under simplified loading conditions is investigated with numerical simulations. Some preliminary results that give an insight into the relation between the shape of catalyst supports and their mechanical performance are also presented and discussed.

1 Introduction

The catalysts typically employed for fixed-bed reactors in steam reformers contain an active metal component supported on porous materials with a high surface area, most commonly alumina (aluminium oxide, Al_2O_3). To maximise the available surface area and increase heat transfer, these supports can be shaped as cylindrical pellets, balls or more complex configurations. In conventional reforming processes, reaction temperatures in the 450-950 °C range are required depending on the application [1]. For this reason the bundles of tubes are suspended in a heated chamber, as shown in Figure 1.

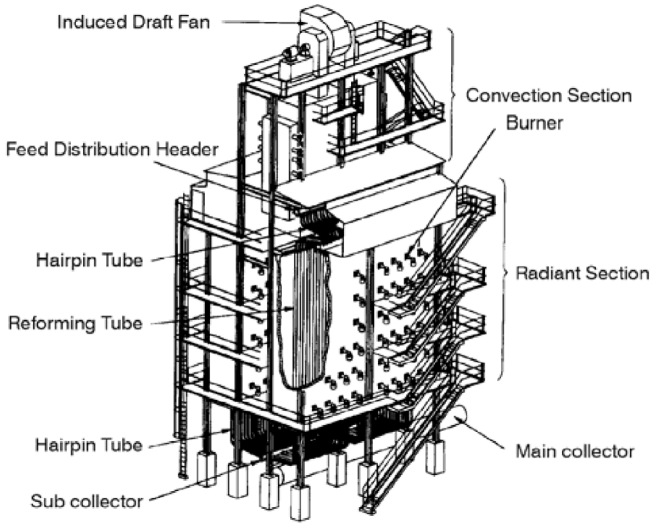

Figure 1: Topsoe reformer with burners placed on side walls [1].

A better understanding of fracture propagation in packed structures of ceramic bodies is crucial to the development of new strategies to reduce the accumulation of catalyst fragments and to extend the lifetime of reactors, and further innovations in fixed-bed reactor technology.

In this work, the effects of the catalyst support shapes on their final strength and fragmentation behaviour are investigated through controlled experiments and numerical simulations. Uniaxial compression tests and high-speed video recordings are employed to estimate strengths and pellet crushing behaviours. The combined finite-discrete element method (FEMDEM) implemented in Solidity [2] is employed to simulate the effects of geometrical features and loading orientation on the pre- and post-failure behaviour of catalyst supports. In this paper, a comparison with experimental results and a mesh sensitivity analysis for the numerical simulations of uniaxial compression tests on cylindrical pellets are presented and discussed. The structural strength of complex-shaped pellets under simplified loading conditions is investigated with numerical simulations and some preliminary results are also presented and discussed.

2 Uniaxial compression

The uniaxial compression test apparatus was mounted an actuators to apply a uniaxial load, as described in [3]. The loading plates and the tested samples have been modelled with 2D Solidity FEMDEM simulations. Both tests and simulations have been performed on discs with and without holes. In this work, two sets of specimens (Set 1 and 2) with different diameters (D), holes diameters (d), thicknesses (t) and mechanical properties have been considered. The geometries are summarised in Table 1.

Table 1: Average of the measured dimensions and bulk density of the tested specimens.

Set		D [mm]	d [mm]	t [mm]	Bulk density [g/cm^3]
1	Disc	18.56 ± 0.01	-	19.16 ± 0.01	2.32
	4-hole	18.39 ± 0.01	5.14 ± 0.01	12.54 ± 0.01	2.31
2	Disc	17.69 ± 0.01	-	18.36 ± 0.01	2.69
	4-hole	17.56 ± 0.01	4.88 ± 0.01	12.00 ± 0.01	2.64

The mesh and boundary conditions are shown in Figure 2(a) and 4(a), 4(c) respectively. The experiments were also recorded with a high-speed camera to determine the fracture paths and pellet crushing behaviours. In the numerical simulations, the bottom plate is fixed and the top loading plate is constrained with constant velocity. The velocity of the constraint is set to 0.01 m/s, which is the loading rate that was set in the laboratory experiments. To reduce the calculation time, when the simulation starts, the top plate is in contact with the specimen and for this reason an initial velocity equal to the one applied to the constraint is imposed on the loading plate. The specimen is discretised with an unstructured fine mesh to better represent both the de-bonding stress during the opening of the cracks and the fracture path along the element boundaries. The total number of elements employed in the simulations of discs with and without holes is about 37,000 and 53,000 respectively. The material properties used to describe the loading plates are E_s=210 GPa, ν_s=0.3 and ρ_s=7850 kg/m^2, where E_s is the Young's modulus, ν_s is the Poisson's ratio and ρ_s is the density. The material properties used for the specimens vary depending on the bulk density of the tested sample. Figure 2 shows the simulation results of a disc with no holes from Set 1, with E_c=40.05 GPa, ν_c=0.17, ρ_c=2310 kg/m^2, f_t=5.07 MPa and G_I=0.2 J/m^2. Since a value of fracture toughness was not available for the cylindrical samples, values G_I have been optimised for the sets of sample to obtain the correct failure mechanism for the uniaxial compression of a disc. In other words G_I

has been selected from the simulation showing a fracture initiating from the centre of the disc and propagating to the two contact points. The same values of energy release rate have been used for the simulations of uniaxial compression of pellets with four holes with the same bulk density. Figure 5 compares of the simulation results for discs with four holes from Set 1, with the corresponding results for samples from Set 2 with E_c=50.08 GPa, ν_c=0.17, ρ_c=2690 kg/m^2, f_t=10.62 MPa and G_I=0.4 J/m^2.

3 Results and discussion

Figure 2(b) shows the horizontal stresses reaching the value of tensile stress (red) in the centre of the disc before failure. After that point, a fracture initiates from the centre and propagates diametrically to the two points of contacts, as shown in Figure 2(c). While the fracture reaches the two points of contact, also the applied load drastically decreases and the two halves of the disc fragment under the action of the two loading plates as shown in Figure 2(d). The simulation results can be compared with two frames obtained from the high-speed video recordings of the test of a disc with no holes from Set 1 shown in Figure 2(e) and 2(f). Assuming an elastic response of the disc to a linearly increasing load, and that the applied load is transmitted by each loading plate on a flat 200 μm portion of the disc surface (i.e. an angle $\alpha = 0.6°$ between the centre of the loading plate, the centre of the disc and the extreme point of the contact surface between the disc and the plate), an approximate solution for the relation between the plate displacement (d) and applied load during the test (P) can be defined in equation (1) [4].

$$d = -\frac{2P}{\pi\ E\ t}[(1-\mu) - log(1+\frac{4}{sin^2(\alpha)})]\frac{\alpha}{sin(\alpha)} \tag{1}$$

In Figure 3 the load-displacement curve calculated in the numerical simulation is compared with the approximated experimental curve calculated with equation (1). The maximum value for the contact force is slightly higher in the numerical results than in the theoretical prediction. This could be because the mesh elements are not all perfectly aligned across the vertical plane where the stress field develops its maximum tension.

Numerical simulations of the uniaxial compression tests on the disc with four holes have been carried out loading specimens with different orientations, i.e. with respect to the angles between the line of the contact points and the symmetry axes of the discs created by the four hole locations. When the two hole centres lie directly in line with the loading points, this is called the 'weak orientation'. Whereas, when the two hole centres lie perpendicularly to line with the loading points, this is called the 'strong orientation'. Loading orientations at intervals of 5° have been considered between the weak (0°) and the strong (45°) orientation configuration of the four-hole disc. Figure 4 shows the loading conditions and load-displacement curves obtained from uniaxial compressive test simulations on the four-hole specimens from Set 1. The load that makes the first fracture initiating within the pellet (i.e. when the first joint element in the FEMDEM discretisation breaks [5]) is determined by inspecting the fracture walls in the numerical results. In Figure 5 the load at failure calculated in the numerical simulation for the different orientations of pellets with four holes from Set 1 and 2 is compared. The values of load have been normalised with respect to the strength of an equivalent cylinder of identical geometry and mechanical properties without holes. This normalisation allows to clearly visualise and compare the interaction of internal geometrical features and loading orientations on samples with different sizes and mechanical properties. This would have been otherwise impossible as the failure loads may differ of orders of magnitude. Figure 5 shows a good agreement between the two normalised curves, demonstrating a similar trend of the structural strengths for the two sets of samples. Figure 5 shows also that the structural strength of pellets that are loaded on their strong orientations is consistently almost five times greater than the structural strength

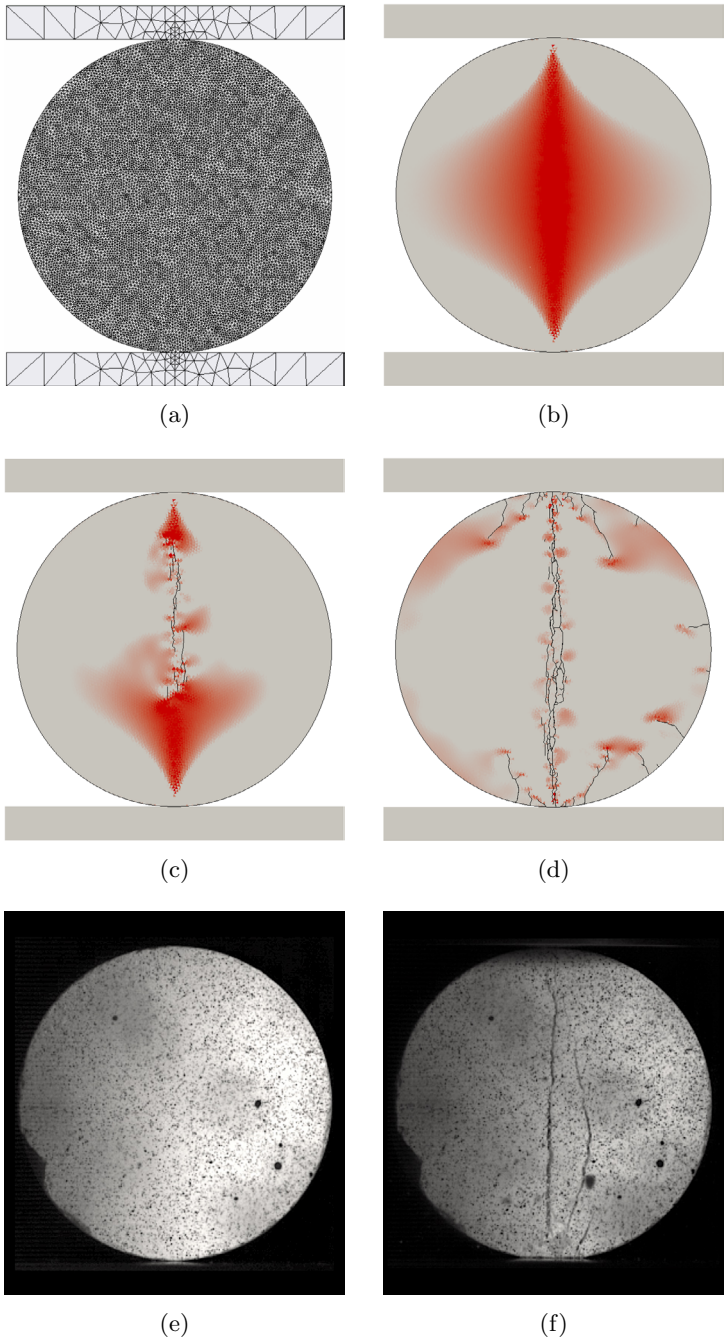

Figure 2: Simulation of the uniaxial compressive test on a cylinder without holes from Set 1: (a) triangular mesh discretisation of the specimen and loading plates. (b) Horizontal tensile stress field before failure reaching the value of tensile strength in the centre of the disc. (c) Crack propagating from the centre of the disc to the two sides and (d) splitting of the two sides of the disc and post failure fragmentation. Two frames from the video recording of the uniaxial compressive test on a cylinder without holes from Set 1: (e) before and (f) after failure.

for the weak orientations.

A mesh sensitivity analysis has been carried out for the uniaxial compression test simulations. The disc without holes from Set 1 has been discretised with four different realisations of a 150 μm element size mesh (Figure 8) obtained with three different values for the rigid rotation about the centre of the disc. With the same process, four different realisations of a 100 μm element size mesh have also been obtained, as shown in Figure 9. The load-displacement curves for the four realisations of a 150 μm element size mesh are shown in Figure 6. Figure 7 shows the load-

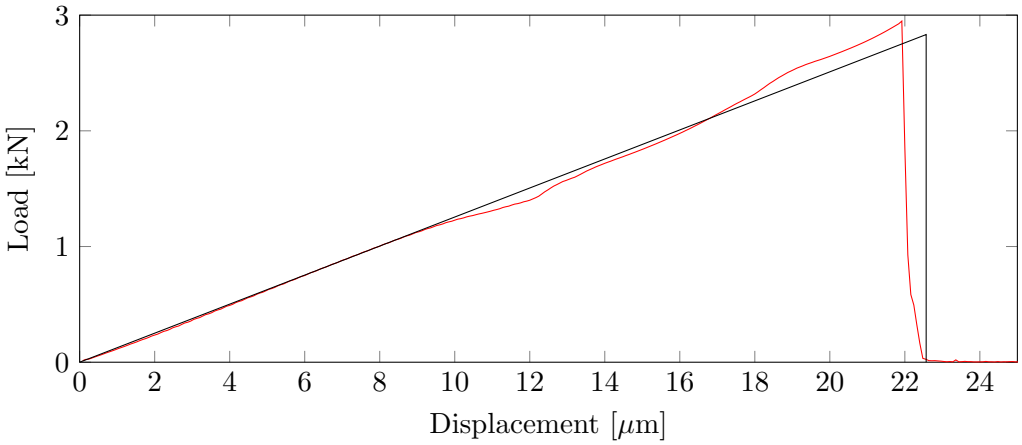

Figure 3: Load-displacement curve for the uniaxial compressive test on a cylinder without holes from Set 1: comparison between the numerical results (red) and the the approximated experimental curve (black) calculated with equation (1).

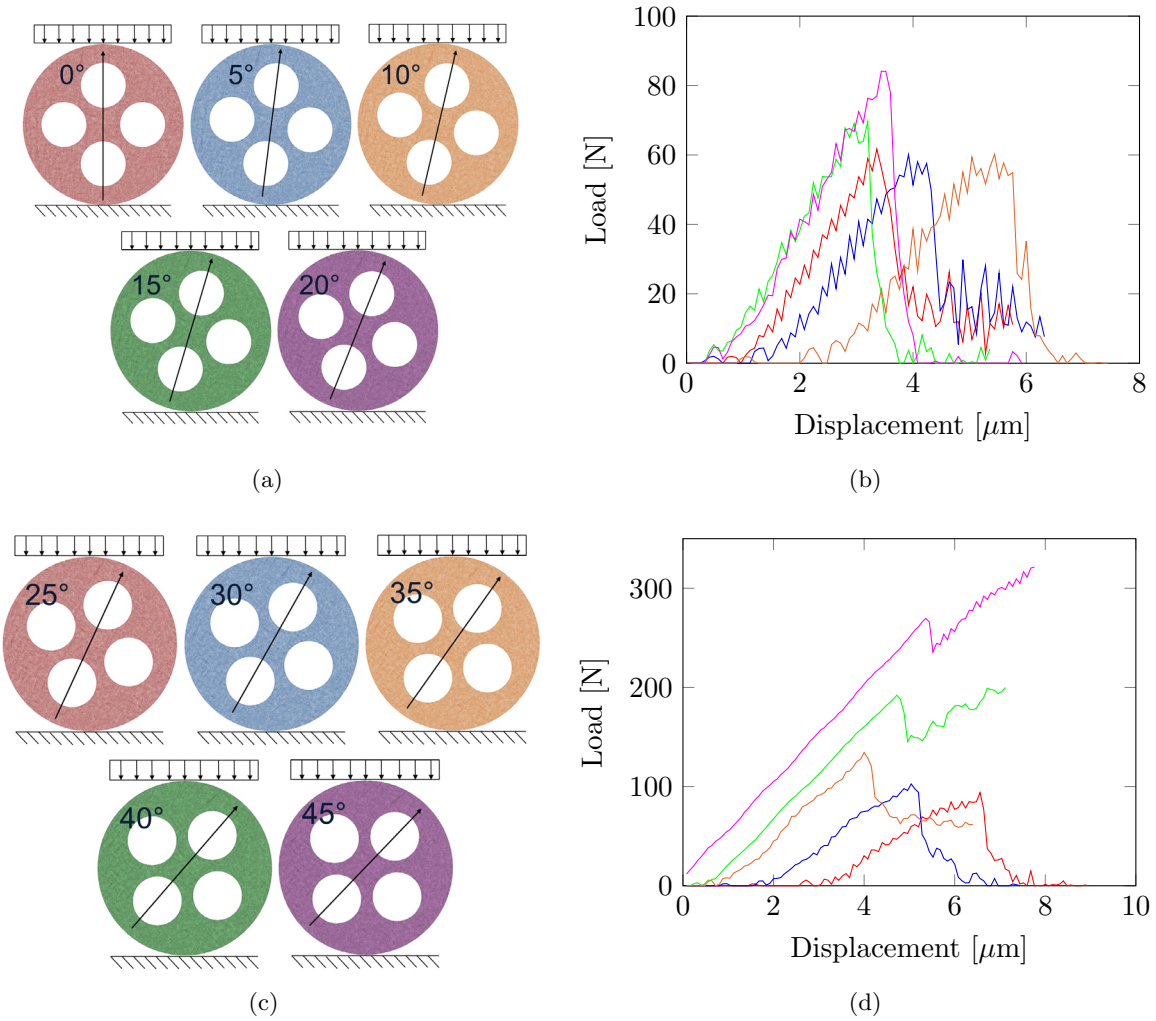

Figure 4: Boundary conditions and load-displacement curves obtained from uniaxial compressive test simulations on the four-hole specimens from Set 1 for orientation angles: (a,b) 0° (red), 5° (blue), 10° (orange), 15° (green), 20° (magenta) and (c,d) 25° (red), 30° (blue), 35° (orange), 40° (green) and 45° (magenta).

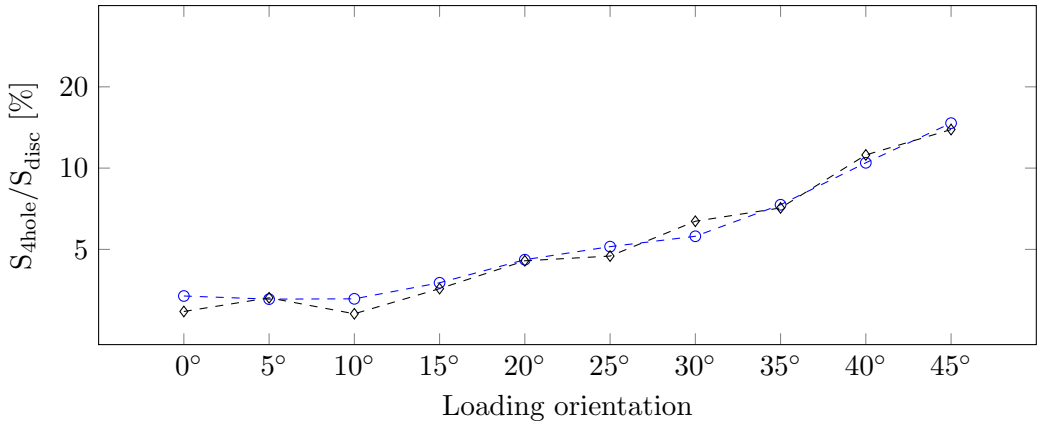

Figure 5: Relation between the loading orientation and the structural strength of four-hole pellets, normalised with respect to the strength of an equivalent cylinder without holes. Numerical results for Set 1 (blue) and Set 2 (black).

displacement curves for the four realisations of a 100 μm element size mesh. The initial part of the plots show the load take up with displacement is sensitive to the initial contact condition of the specimen with the two loading plates, which varies in due to the rigid rotation of the mesh. This causes small fluctuations in the load-displacement curves in Figure 7. The peak values of the load for the 8 realisations of the 150 μm and 100 μm element size are consistent with the theoretical peak load values also plotted in the figures, suggesting there are no significant unintended anisotropies in stiffness and strength imposed by the unstructured meshing tool employed.

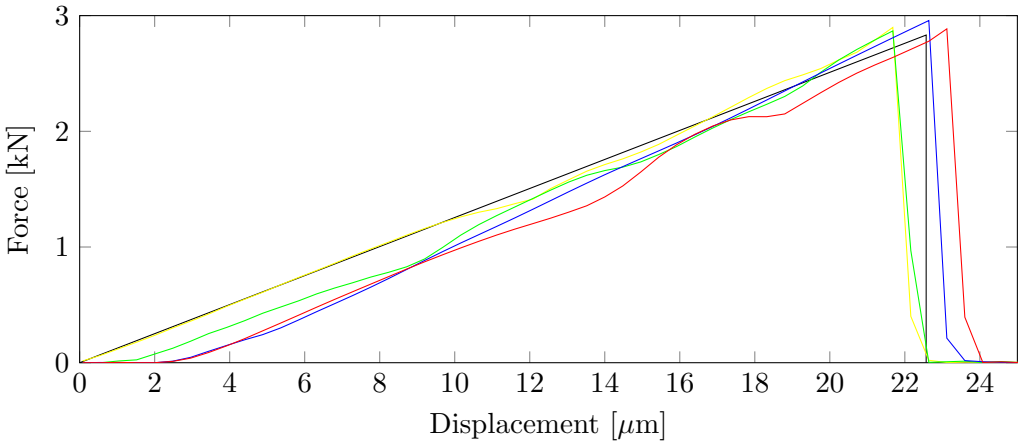

Figure 6: Mesh sensitivity analysis for the uniaxial compression test simulations: comparison of the load-displacement curve calculated in the numerical simulations for the 150 μm mesh obtained with 0° (yellow), 10° (green), 20° (blue) and 30° (red) rotation of the original mesh of the disc. The approximated experimental curve for Set 1 (black) is also plotted.

4 Conclusions

The numerical results of uniaxial compressive tests on cylinders without holes (Brazilian disc tests) have been presented. The contact force extrapolated from the numerical simulations has been compared to corresponding approximated experimental curves, giving further confirmations [3] of a correct simulation of mode I fracture in porous ceramic pellets. A mesh sensitivity analysis has also been carried out for the uniaxial compression test simulations, suggesting that there are no significant unintended anisotropies in stiffness and strength imposed by the unstruc-

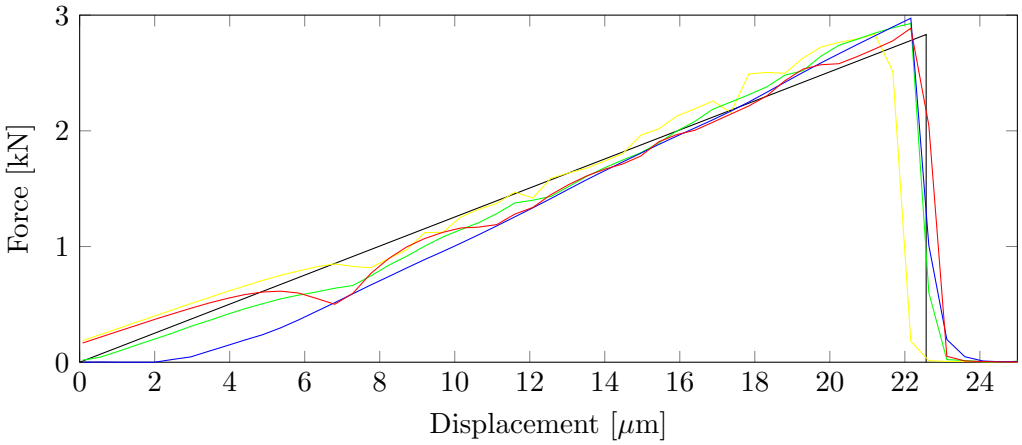

Figure 7: Mesh sensitivity analysis for the uniaxial compression test simulations: comparison of the load-displacement curve calculated in the numerical simulations for the 100 μm mesh obtained with 0° (yellow), 10° (green), 20° (blue) and 30° (red) rotation of the original mesh of the disc. The approximated experimental curve for Set 1 (black) is also plotted.

tured mesh employed in the FEMDEM simulations. The structural strength of complex-shaped pellets under simplified loading conditions was also investigated with numerical simulations. Loading orientations at intervals of 5° have been considered between the weak and the strong orientation configuration of the four-hole discs. The load at failure calculated in the numerical simulations for the different orientations of pellets from two sets of samples have been compared. The values of normalised load with respect to the strength of an equivalent cylinder of identical geometry and mechanical properties without holes have been shown to be in good agreement for two sets of samples with different sizes and mechanical properties. This provides a consistent relation between simplified loading conditions and the structural strength of four-hole discs, also giving an insight into the relation between the shape of catalyst supports and their mechanical performance. First confirmations of the Solidity FEMDEM code capabilities in representing realistic contact forces between complex-shaped catalyst pellets has been provided in previous works [6, 7]. Future research will be undertaken to compare the numerically inferred structural strengths with values obtained from real experiments on cylindrical pellets with four holes and to investigate other shape related catalyst performance properties, such as fragment size distributions of crushed pellets.

REFERENCES

[1] J. R. Rostrup-Nielsen and T. Rostrup-Nielsen, "Large-scale hydrogen production," *CATTECH*, vol. 6, no. 4, pp. 150–159, 2002.

[2] Applied Modelling and Computation Group (AMCG) at Imperial College London, "Solidity FEMDEM code," *www.solidityproject.com*.

[3] A. Farsi, J. Xiang, J. P. Latham, A. D. Pullen, M. Carlsson, E. H. Stitt, and M. Marigo, "An application of the finite-discrete element method in the simulation of ceramic breakage: methodology for a validation study for alumina specimens," in *IV International Conference on Particle-based Methods Fundamentals and Applications PARTICLES 2015*, no. November, pp. 1–12, 2015.

[4] Q. Z. Wang, X. M. Jia, S. Q. Kou, Z. X. Zhang, and P. a. Lindqvist, "The flattened Brazilian disc specimen used for testing elastic modulus, tensile strength and fracture toughness of brittle rocks: Analytical and numerical results," *International Journal of Rock Mechanics and Mining Sciences*, vol. 41, no. 2, pp. 245–253, 2004.

[5] A. Munjiza, *The Combined Finite-Discrete Element Method*. Wiley, 2004.

[6] A. Farsi, J. Xiang, J.-P. Latham, M. Carlsson, E. H. Stitt, and M. Marigo, *Simulation and Characterisation of Packed Columns for Cylindrical Catalyst Supports and Other Complex-Shaped Bodies*, pp. 397–406. Singapore: Springer Singapore, 2017.

[7] J. Xiang, J. Latham, and A. Farsi, *Algorithms and Capabilities of Solidity to Simulate Interactions and Packing of Complex Shapes*, pp. 139–149. Singapore: Springer Singapore, 2017.

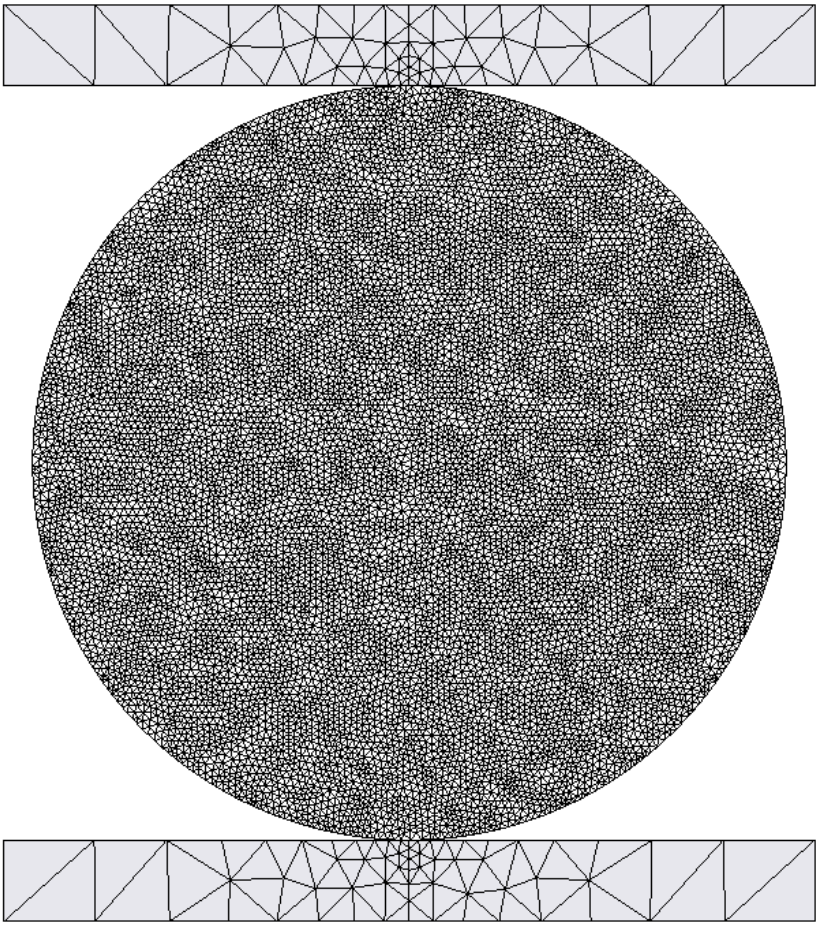

Figure 8: Mesh sensitivity analysis for the uniaxial compression test simulations: triangular mesh discretisation of the test setup for the 150 μm mesh. The mesh is then rotated of 10°, 20° and 30° to preform a comparison of four different mesh realisations with the same element size.

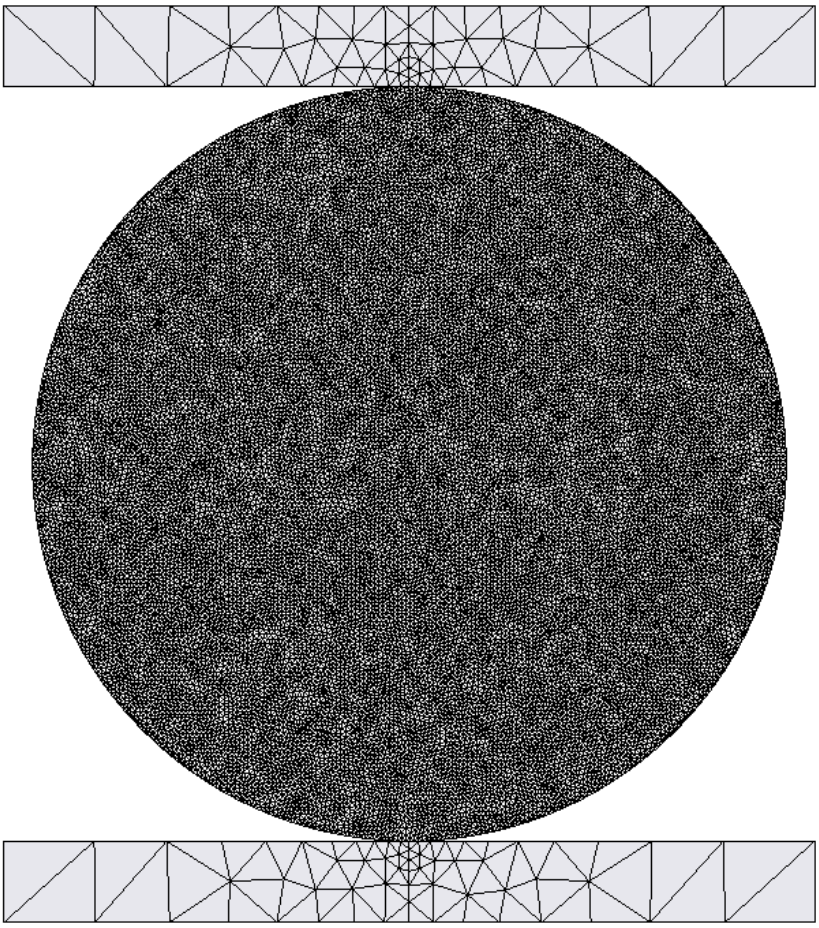

Figure 9: Mesh sensitivity analysis for the uniaxial compression test simulations: triangular mesh discretisation of the test setup for the 100 μm mesh. The mesh is then rotated of 10°, 20° and 30° to preform a comparison of four different mesh realisations with the same element size.

V International Conference on Particle-based Methods – Fundamentals and Applications
PARTICLES 2017
P. Wriggers, M. Bischoff, E. Oñate, D.R.J. Owen, & T. Zohdi (Eds)

VGCM3D - A 3D RIGID PARTICLE MODEL FOR ROCK FRACTURE FOLLOWING THE VORONOI TESSELLATION OF THE GRAIN STRUCTURE: FORMULATION AND VALIDATION

M. CANDEIAS[1], N. MONTEIRO AZEVEDO[2] M. L. BRAGA FARINHA[3]

[1] Laboratório Nacional de Engenharia Civil (LNEC)
Av. do Brasil 101, 1700-066 Lisboa, Portugal
E-mail marilinecandeias@gmail.com, web page: http://www.lnec.pt/organizacao/dbb

[2] Laboratório Nacional de Engenharia Civil (LNEC)
Av. do Brasil 101, 1700-066 Lisboa, Portugal
E-mail nazevedo@lnec.pt, web page: http://www.lnec.pt/organizacao/dbb

[3] Laboratório Nacional de Engenharia Civil (LNEC)
Av. do Brasil 101, 1700-066 Lisboa, Portugal
E-mail lbraga@lnec.pt, web page: http://www.lnec.pt/organizacao/dbb

Key words: Fracture, rock, particle shape, calibration.

Abstract. Detailed particle models by taking into account the material grain structure explicitly consider the material randomness, including a size limiter for damage localization. A VGMC3D contact model is presented that considers the polyhedral particle shape in an approximate way. The VGCM3D flexible contact model is validated against known experimental data on a granite rock, namely triaxial tests and Brazilian tests.

1 INTRODUCTION

Detailed rigid particle models were introduced in the study of fracture of quasi-brittle materials such as concrete, rock and asphalt concrete in the 1990s [1, 2, 3, 4]. More recently, 3D rigid spherical particle models have been proposed both for rock [5, 6, 7, 11] and for concrete, [8, 9, 10].

Particle models are conceptually simpler than a continuum approach, and the development of cracks and rupture surfaces appears naturally as part of the simulation process given its discrete nature. Assemblies of discrete particles connected through simple interaction laws are able to capture the global behaviour of quasi-brittle macro-material, such as concrete or rock. In rock fracture studies the bonded particle model, BPM [6], has received considerable attention given its known ability to model rock complex behaviour, namely in uniaxial compression. The BPM model, as presented in [6], does not match the ratio of the compressive strength to tensile strength that occurs in rock. In addition, the macroscopic friction angle obtained with this model in triaxial testing is much lower than the known hard rock experimental values.

Wang et Tonon [12] proposed a 3D spherical particle model that gives a good agreement with the triaxial failure envelope obtained in Lac du Bonnet granite rock. It is shown that the

inclusion of a frictional term for the contact shear strength has a significant effect in the increase of the macroscopic friction angle. However, the ratio of compressive to tensile strength of Lac du Bonnet granite was not well reproduced. A 3D particle contact model that allows moment transmission at the contact level and adopts a Delaunay 3D edge criteria for particle interaction [7] was presented. This model is shown to be able to predict the failure envelopes and the compressive to tensile strength ratio of a hard rock such as Lac du Bonnet granite. Scholtès and Donzé [11] introduced an interaction range parameter that controls the grain interlock. The particle model proposed by the authors is shown to be able to predict high ratios of tensile to compression strength.

Particle models based on polyhedral particles, either rigid or deformable [13, 14] are computationally more demanding than those based on rigid spherical particles, limiting the number of particles to be modelled or demanding parallelization techniques.

In this paper a 3D rigid particle model is proposed which takes into account the effect of polyhedral shape particles but still keeps the simplicity of spherical particle models and does not require a significant increase in the computational effort. With this purpose, a particle generation algorithm is adopted that generates polyhedral shape particles based on the Laguerre Voronoi diagrams [15]. The Voronoi structure is the dual structure of the weighted Delaunay tetrahedralization of the spherical particle gravity centres. A polyghedral particle model is then approximated by spherical particles that interact with each other through a multiple local contact scheme [7] being the contact area and the contact location given by the common inter-particle Laguerre Voronoi facet. A similar model has been recently proposed for 2D particle models [16]. The model is validated against known results of triaxial and Brazilian tests of a granite rock, showing a good agreement.

FORMULATION

2.1 Fundamentals

In the DEM, the domain is replaced by an assembly of discrete entities that interact with each other through contact points or contact interfaces. The set of forces acting on each particle are related to the relative displacements of the particle with respect to its neighbours. At each step, given the applied forces, Newton's second law of motion is invoked to obtain the new position of the particle. The equations of motion, including local non-viscous damping, of a particle may be expressed as:

$$F_i(t) + F_i^d(t) = m\ddot{x}_i \tag{1}$$

$$M_i(t) + M_i^d(t) = I\dot{\omega}_i \tag{2}$$

where $F_i(t)$ and $M_i(t)$ are, respectively, the total applied force and moment at time t including the exterior contact contribution, m and I are respectively, the particle mass and moment inertia, $\ddot{x}_i$ is the particle acceleration. The damping forces using a local damping formulation are given by:

$$F_i^d(t) = -\alpha|F_i(t)|sign(\dot{x}_i) \tag{3}$$

$$M_i^d(t) = -\alpha|M_i(t)|sign(\omega_i) \tag{4}$$

being $\dot{x}_i$ the particle velocity, ω_i the angular velocity and α the local non-viscous damping parameter and the function $sign(x)$ given by:

$$sign(x) = \begin{cases} +1, & x > 0 \\ -1, & x < 0 \\ 0, & x = 0 \end{cases} \tag{5}$$

2.2 Voronoi-generalized contact model (VGCM-3D)

The 3D Voronoi-generalized contact model (VGCM-3D) is based on the GCM-3D contact model that considers on a given circular surface a discrete number of local contact points that are able to transfer normal and shear forces [7]. Figures 1 a) and b) show the GCM-3D local contact point position for a 4 local contact point scheme. In the VGCM-3D contact model the contact surface and the contact point location are defined by the Voronoi tessellation. The common Voronoi facet is considered to be the contact surface and the vertexes of the Voronoi facet including the gravity centre of the Voronoi facet are considered to be the local contact point location, Figure 1 c) and d). In the GCM-3D contact models, the contact unit normal is defined given the particles centre of gravity and the inter-particle distance:

$$n_i = \frac{x_i^{[B]} - x_i^{[A]}}{d} \tag{6}$$

The contact overlap for the reference contact point and its location, are given by:

$$U^n = R^{[A]} + R^{[B]} - d \tag{7}$$

The VGCM-3D contact model reference contact point, $x_i^{[0]}$, is defined at the associated Voronoi cell facet using:

$$x_i^{[0]} = x_i^{[A]} + \left(R^{[A]} - \frac{1}{2}U^n - d_v\right) n_i \tag{8}$$

where d_v is the distance along the contact normal between the PCM geometric contact plane, Figure 1 a), of the two spherical particles in contact and the adopted contact plane as defined by the corresponding Voronoi cell facet, Figure 1 c).

The local contact point position ($x_i^{[J]}$) in global coordinates is defined relative to the reference local contact point. A local (t, s) axis centred at the reference local contact point is adopted and the relative position of the local points in the local axes, Figures 1 b) and d), are defined at the beginning of the calculation. The contact point position of each local point is then defined in global coordinates using:

$$x_i^{[J]} = x_i^{[0]} + s^{[J]} x_i^{[s]} + t^{[J]} x_i^{[t]} \tag{9}$$

where: $x_i^{[s]}$ and $x_i^{[t]}$ are the local s axes and local t axes, respectively, expressed in global coordinates, assuming that $\vec{s} \times \vec{t} = \vec{n}$. The contact forces that are acting at each local contact

point can be decomposed into its normal and shear component with respect to the contact plane:

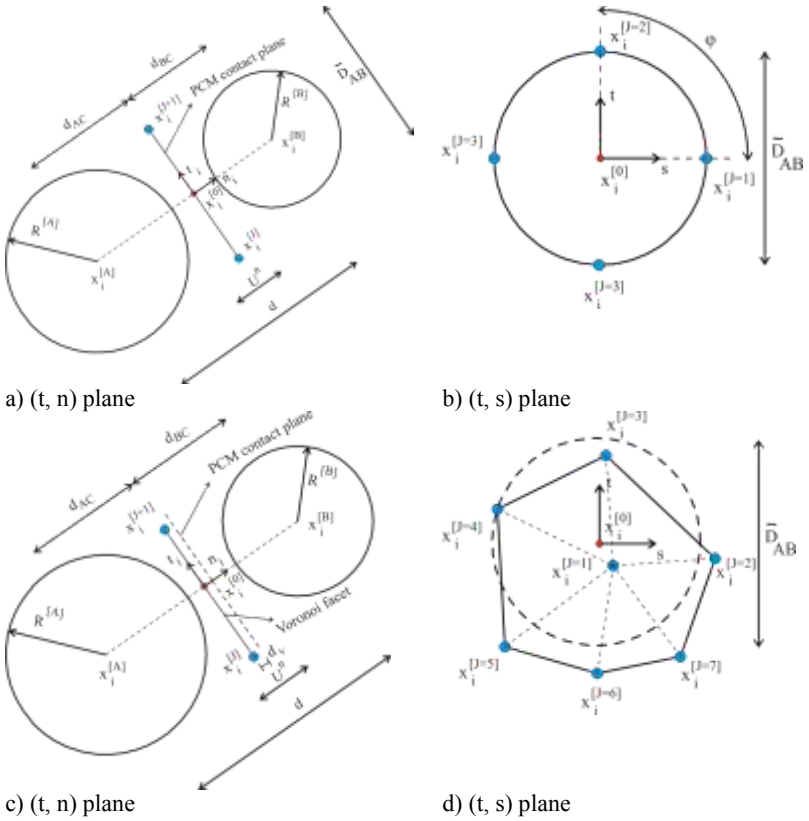

a) (t, n) plane b) (t, s) plane

c) (t, n) plane d) (t, s) plane

Figure 1: GCM-3D contact model with 4 local points considering an approximated circular contact surface a) and b) and VGCM-3D contact model with variable number of local points given by the Voronoi facet vertexes and gravity centre c) and d)

$$F_i^{[J]} = F_i^{[n,J]} + F_i^{[s,J]} \tag{10}$$

The contact velocity of a given local contact point, which is the velocity of particle B relative to particle A, at the contact location is given by:

$$\dot{x}_i^{[J]} = \left(\dot{x}_i^{[J]}\right)_B - \left(\dot{x}_i^{[J]}\right)_A \tag{11}$$
$$= \left(\dot{x}_i^{[B]} + e_{ijk}\omega_j^{[B]}\left(x_k^{[J]} - x_k^{[B]}\right)\right) - \left(\dot{x}_i^{[A]} + e_{ijk}\omega_j^{[A]}\left(x_k^{[J]} - x_k^{[A]}\right)\right)$$

where, e_{ijk} is the permutation tensor. The contact displacement normal increment ($\Delta x^{[J,N]}$) stored as a scalar and shear increment ($\Delta x_i^{[J,S]}$) stored as a vector, are given by:

$$\Delta x^{[J,N]} = \left(\dot{x}_i^{[J]}\Delta t\right)n_i \tag{12}$$

$$\Delta x_i^{[J,S]} = \left(\dot{x}_i^{[J]}\Delta t\right) - \Delta x^{[J,N]}n_i \tag{13}$$

The local contact overlap is defined incrementally for the local points based on the current contact velocity time step (Δt):

$$U^{J,n} = U^{J,n\ old} + \left(\dot{x}_i^{[J]}n_i\right)\Delta t \tag{14}$$

Given the normal and shear stiffness of the local contact point, the normal and shear forces increments are obtained following an incremental linear law:

$$\Delta F^{[J,N]} = -k_n^{[J]}\Delta x^{[J,N]} \tag{15}$$

$$\Delta F_i^{[J,S]} = -k_s^{[J]}\Delta x_i^{[J,S]} \tag{16}$$

The predicted normal and shear contact forces acting at the local contact point are then updated by applying the following equations:

$$F^{[J,N\ new]} = F^{[J,N\ old]} + \Delta F^{[J,N]} \tag{17}$$

$$F_i^{[J,N\ new]} = F_i^{[J,S\ old2]} + \Delta F_i^{[J,S]} \tag{18}$$

Given the predicted normal and shear contact forces the adopted constitutive model is applied, if the predicted forces do not satisfy the constitutive model it is necessary to carry out adjustments. The resultant contact force at the local contact point is then given by:

$$F_i^{[J]} = F^{[J,N]}n_i + F_i^{[J,S]} \tag{19}$$

At the reference contact point the resultant contact force and contact moment are defined given the contribution from all contact points:

$$F_i^{[C]} = \sum_J F_i^{[J]} \tag{20}$$

$$M_i^{[C]} = -\sum_J e_{ijk}(x_j^J - x_j^0)F_k^J \tag{21}$$

The contact force and moment are then transferred to the centre of gravity of each particle in contact through:

$$F_i^{[A]} = F_i^{[A]} - F_i^{[C]} \tag{22}$$

$$F_i^{[B]} = F_i^{[B]} + F_i^{[C]} \tag{23}$$

$$M_i^{[A]} = M_i^{[A]} - e_{ijk}\left(x_j^{[0]} - x_j^{[A]}\right)F_k^{[C]} - M_i^{[C]} \tag{24}$$

$$M_i^{[B]} = M_i^{[B]} + e_{ijk}\left(x_j^{[0]} - x_j^{[B]}\right)F_k^{[C]} + M_i^{[C]} \tag{25}$$

2.3 Numerical stability

When only a steady state solution is sought, a mass scaling algorithm is adopted in order to reduce the number of timesteps necessary to reach the desired solution. The particle mass and inertia are scaled so that the adopted centred-difference algorithm has a higher rate of convergence for a given loading step. The particle scaled mass and inertia used in the calculations are set assuming a unit time increment ($\Delta t = 1$) given the particle stiffness at a given time through:

$$m_{scaled} = 0.25K_t \tag{26}$$

$$I_{scaled} = 0.25K_\theta \tag{27}$$

An upper bound expression for the total particle translation stiffness K_t and of the total rotational stiffness K_θ can be found in [7].

2.4 Local contact stiffness and local contact strength

The VGCM-3D model requires the user definition of the contact deformability parameters, namely the Young's modulus of the equivalent continuum material ($\bar{E}$) and the constant that relates the normal and the shear stiffness spring value (η). In this work the local contact normal and shear stiffness are given by:

$$k_n^{[J]} = \frac{\bar{E}}{d}A_c^{[J]} \tag{28}$$

$$k_s^{[J]} = \eta k_n^{[J]} \tag{29}$$

where, $A_c^{[J]}$ is the contact area associated with the local point J and d is the distance between the particles centre of gravity. In this work the contact geometry is equal to the 3D Voronoi facet [15]. In the VGCM-3D contact model the Voronoi facet is triangulated as indicated in Figure 1 d) and the contact area associated with the local contact point is defined by the sum of one third of the area of the associated triangles.

For the local inter-particle contacts the VGCM-3D model also requires the definition of the contact strength properties, the maximum contact tensile stress ($\sigma_{n.t}$), the maximum contact cohesion stress (τ) and the contact frictional term (μ_c). The maximum contact local tensile strength ($F_{n.max}^{[J]}$) and the maximum local contact shear strength ($F_{s.max}^{[J]}$) are defined given the user-specified contact strength properties and the current local contact normal force ($F_n^{[J]}$) as follows:

$$F_{n.max}^{[J]} = \sigma_{n.t}\, A_c^{[J]} \tag{32}$$

$$F_{s.max}^{[J]} = \tau\, A_c^{[J]} + F_n^{[J]}\, \mu_c = C_{max}^{[J]} + F_n^{[J]}\, \mu_c \tag{33}$$

where $C_{max}^{[J]}$ is the adopted maximum local contact cohesion strength. Figure 2 shows the adopted bilinear softening contact model under tension and shear, more details can be found in [7] regarding the model implementation.

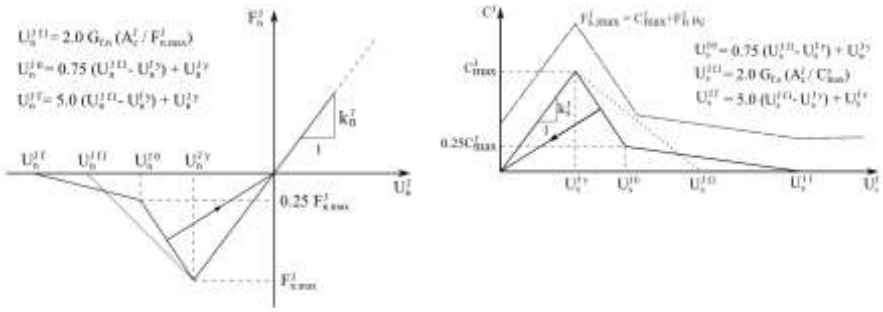

a) Normal direction b) Shear direction

Figure 2: Constitutive model with bilinear softening under tension and shear

2.5 Particle scheme generation

A particle generation scheme has been implemented which generates polyhedral shaped particles based on the Laguerre-Voronoi diagrams [15] using a weighted Delaunay tetrahedralization of the spherical particle gravity centres. A Laguerre tesselation is preferred to a traditional tessellation because it generates Voronoi diagrams with facets closer to the geometric PCM contact planes when considering two particles in contact. The initial particle assembly grain structure is constructed by first introducing spherical particles with half of their radius to ensure that the particles do not overlap with each other, Figure 3 a). Then the real particle radius is adopted, and a DEM cohesionless type solution is obtained, leading to a redistribution of the particle overlap throughout the assembly, Figure 3 b).

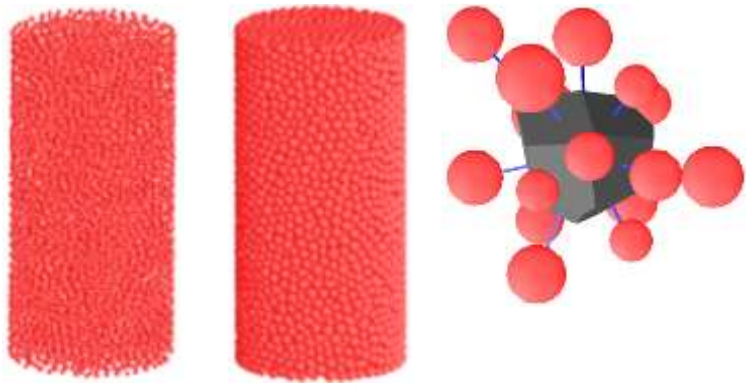

a) Half radius insertion b) Final assembly c) VGCM-3D (Voronoi facet)

Figure 3: VGCM-3D particle assembly and VGCM-3D inter-particle contact

3 TRIAXIAL AND BRAZILIAN TESTS IN A GRANITE ROCK

3.1 Numerical setup

The proposed VGCM-3D model is validated against known uniaxial, triaxial and Brazilian tests in a granite rock [17]. The numerical uniaxial tests, without lateral confinement pressure, and the triaxial tests with lateral confinement pressure are performed in cylindrical specimens with a diameter of 80 mm and a height of 160 mm. The Brazilian tests are performed in cylindrical specimens with a diameter of 80 mm and a thickness of 40 mm. For both geometries, a uniform diameter distribution ranging from 4 to 6 mm was adopted. The uniaxial and triaxial tests assemblies have on average 7988 particles, and the Brazilian tests have on average 1997 particles, Figure 4.

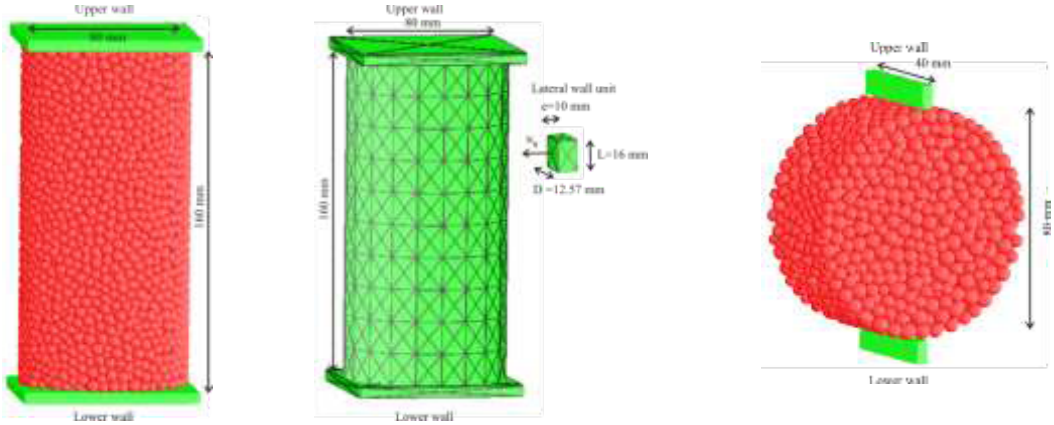

a) Uniaxial test (tensile and compression)

b) Triaxial test

c) Brazilian test

Figure 4: Discrete element model GCM-3D boundary conditions

3.2 Deformability parameters

The influence of the contact deformability parameters, the Young's modulus of the equivalent continuum material ($\bar{E}$) and the constant that relates the shear and normal stiffness spring value (η), on the elastic macroscopic properties, Young's modulus (E) and Poisson's coefficient (ν), are assessed. Two sets of tests were carried out. In the first set of tests the macro-properties were obtained by fixing constant values of $\bar{E}$ ($0.5\bar{E}$, $1.0\bar{E}$ and $2.0\bar{E}$) and varying the ratio of normal to shear stiffness. In the second set of tests the macro-properties were obtained by fixing constant values of η (0.0, 0.25, 0.50, 0.75 and 1.0) and varying the elastic contact constant $\bar{E}$. Assuming a $\bar{E}$ value equal to 48.8 GPa.

Figure 5 a) and c) shows that the material Young's modulus is related to both elastic contact model parameters, being more influenced by the ratio of normal to shear stiffness (η) for higher elastic contact values ($\bar{E}$). Figure 5 b) and d) shows that the material Poisson's coefficient is mainly influenced by the ratio of normal to shear stiffness. Similar results were found in [7, 12].

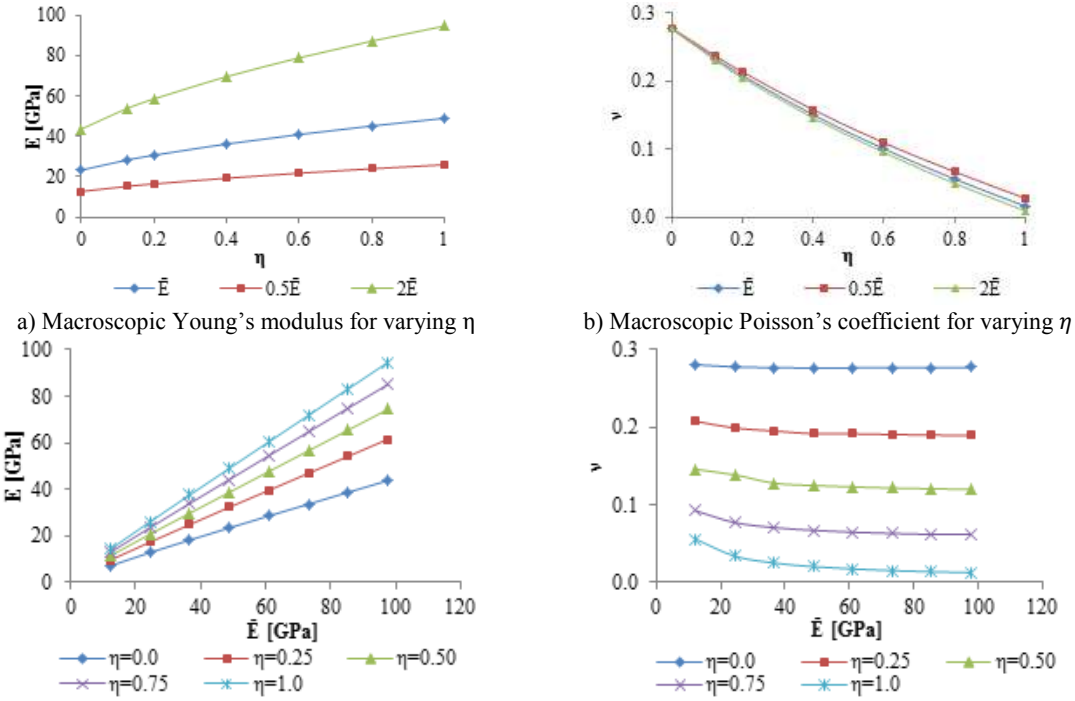

a) Macroscopic Young's modulus for varying η

b) Macroscopic Poisson's coefficient for varying η

c) Macroscopic Young's modulus for varying $\bar{E}$

d) Macroscopic Poisson's coefficient for varying $\bar{E}$

Figure 5: VGCM3D influence of the contact deformability parameters ($\bar{E}$ and η) on the elastic macroscopic properties (ν)

3.3 Calibrated brittle and bilinear softening models

The VGCM-3D with a brittle contact force displacement model (VGCM-3D G_{el}) and the VGCM-3D with a contact force model following a bilinear softening model (VGCM-3D $9.5G_{el}$) were calibrated in order to achieve the set of deformability and strength parameters that predicts numerical results closer to Augig granite experimental data. For the VGCM-3D $9.5G_{el}$, a contact fracture energy equal to 9.5 times the energy of the fracture branch was adopted in tension and shear. In the VGCM-3D G_{el} brittle model the contact energy adopted in tension and shear directions corresponds to the fracture energy associated with the elastic branch.

Table 1 summarizes the micro-properties adopted for each contact model and Table 2 presents the known macroproperties of the Augig Granite and the macroscopic numeric response. Figure 6 shows the strength envelope obtained with the VGCM-3D G_{el} and with the VGCM-3D $9.5G_{el}$ contact models. For both models, the vertical maximum stress-strain values with $0,\ 3, 6, 9$ and 12 MPa confinement pressures are presented. In the presented strength envelope, the plotted tensile strength values correspond to the indirect tensile strength values.

As shown in Table 2 and in Figure 6, the VGCM-3D particle model here proposed is capable of representing the failure envelope and the compressive to tensile strength ratio of a hard rock such as Augig granite. Further, it is shown that by including a bilinear softening law at the contact level (VGCM-3D $9.5G_{el}$), the particle model here presented is capable of predicting a direct tensile to indirect tensile ratio closer to that expected in rock (the indirect tensile strength is usually higher than the direct tensile strength value).

Table 1 – Calibrated Micro-properties adopted in VGCM-3D particle models

	$\bar{E}$ $[GPa]$	η	μ_c	$\sigma_{n.t}$ $[MPa]$	τ $[MPa]$	$G_{f.n}$ $[N/m]$	$G_{f.s}$ $[N/m]$
VGCM-3D G_{el}	48.8	0.125	0.05	35.5	106.5	6.8	3275.2
VGCM-3D 9.5G_{el}				11.4	88.5	64.6	3114.4

Table 2 - Augig granite macro-properties and numerical macro-properties

	E $[GPa]$	ν	q_u $[MPa]$	$\sigma_{t.dir}$ $[MPa]$	$\sigma_{t.ind}$ $[MPa]$	c $[MPa]$	φ [°]
Augig granite [17]	25.8	0.23	122.1	-	8.8	21.0	53.0
VGCM-3D G_{el} calibrated	25.8	0.23	125.2	16.4	8.9	27.1	43.2
VGCM-3D 9.5G_{el} calibrated			124.5	7.4	9.1	24.8	46.6

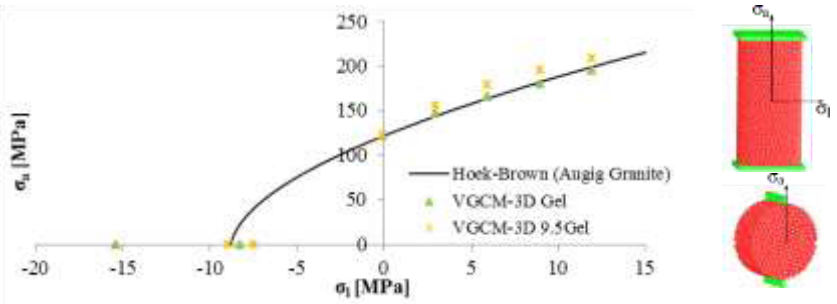

Figure 6: Strength Envelope: VGCM-3D G_{el} and VGCM-3D 9.5G_{el} contact models

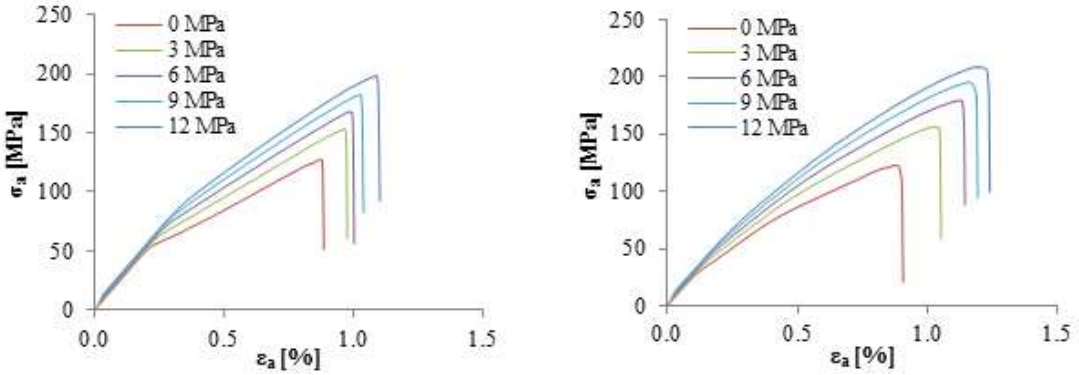

a) VGCM-3D G_{el} calibrated b) VGCM-3D 9.5G_{el} calibrated

Figure 7: Vertical stress-strain curves for the different confinement pressures

Figure 7 shows the axial stress–strain response for the uniaxial and the triaxials tests obtained with the VGCM-3D calibrated models for a lateral confinement of 3, 6, 9 and 12 MPa. As shown in Figure 7 the consideration of a bilinear softening law in tension and shear does not lead to an unrealistic ductile macroscopic response. It is verified that the GCM-3D G_{el} calibrated has an extremely brittle response, presenting an inflection point in the stress-strain curves. This inflection point reveals an unexpected loss in the material strength for

stress values lower than the ultimate vertical stress values. This behaviour is more pronounced for lower lateral confinement pressures (0 and 3 MPa). The increase in the lateral confinement pressures increases the ductility of the stress-strain curves. Comparing both models, the stress-strain curves obtained with the GCM-3D $9.5G_{el}$ calibrated model have a less brittle response when compared to the stress-strain curves obtained with the GCM-3D G_{el} calibrated model.

Figure 8 shows the crack patterns obtained in uniaxial compression, direct tensile, triaxial with confinement stress of 9 MPa and in an indirect tensile test (Brazilian) for the VGCM-3D $9.5G_{el}$ calibrated model. As can be seen, the crack patterns obtained for the different tests are accordingly to the expected. In the uniaxial compression test without friction between the horizontal walls and the particle assembly the development of vertical cracks, Figure 8 a). The increase of confinement stress leads to a development of shear surfaces with a given inclination, as observed in Figure 8 c). In the direct tensile test the rupture surface is perpendicular to the load direction, and in the indirect tensile test the rupture surface is parallel to the load direction.

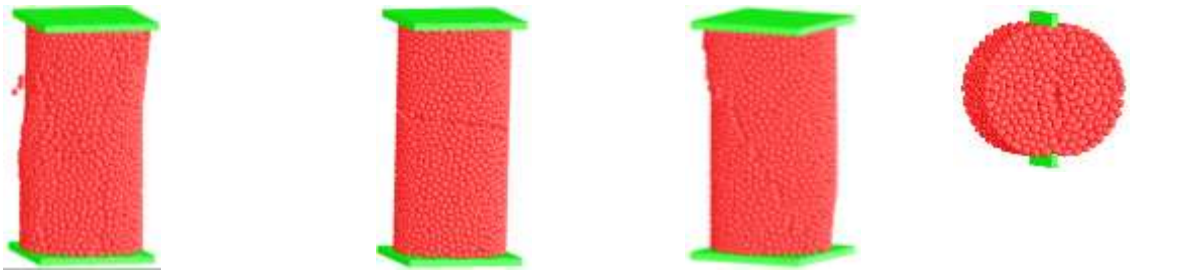

a) Uniaxial compression test b) Direct tensile test c) $\sigma_1 = 9$ MPa d) Brazilian test

Figure 8: VGCM-3D $9.5G_{el}$ calibrated final fracture patterns

4 CONCLUSIONS

A generalized 3D contact model, VGCM-3D, which enables moment transmission and contact discretizations with multiple local contact points is presented. The contact geometry and location are given by the Laguerre–Voronoi diagram facets, and the neighbouring particles are considered to interact if a common Voronoi facet is shared. By incorporating the VGCM-3D as described, the rigid particle model takes into account the polyhedral shaped particles in an approximate way, but still keeps the simplicity of spherical particle models and does not require a significant increase in the computational effort.

The results presented highlight the need to incorporate a bilinear softening constitutive model at the contact level to obtain a better agreement between the direct tensile strength and the indirect tensile strength. The latter ratio cannot be correctly predicted with a simple brittle model. It is also shown that particle assemblies with bilinear softening contact laws still predict a brittle macroscopic response under tensile, compression and biaxial state of stress. The bilinear contact model, for the level of contact fracture energy adopted, does not change significantly the fracture processes, it mainly slows down the rupture evolution and slightly induces a higher localization of the final crack patterns.

Finally the model shows a good agreement with known results of triaxial and Brazilian tests of a granite rock.

REFERENCES

[1] Meguro, K., Iwashita, K. and Hakuno, M. Fracture analyses of media composed of irregularly shaped regions by the extended distinct element method. *Structural Eng./Earthquake Eng.,* (1991) **8 (3)**:37-48.

[2] Potyondy, D., Cundall, P. and Lee C. Modelling rock using bonded assemblies of circular particles. In: Aubertin M. et al (eds) Proceedings of the 2nd North American Rock Mechanics Symposium, Rotterdam, Balkema, (1996), 1937-1944 .

[3] Schlangen, E. and Garboczi, E. Fracture simulation of concrete using lattice models: Computational aspects. *Engineering Fracture Mechanics,* (1997) **57(2/3)**:319-332.

[4] Chang, K.G. and Meegoda, J.N. Micromechanical simulation of hot mix asphalt. *Journal of Engineering Mechanics. ASCE.* (1997), 123(5):495-503.

[5] Matsuda, Y. and Iwase, Y. Numerical simulation of rock fracture using three-dimensional extended discrete element method. Earth Planets Space, (2002), **54(4)**: 367:378.

[6] Potyondy, D. and Cundall, P. A bonded-particle model for rock. *International Journal of Rock mechanics and Mining Sciences,* (2004) **41(8)**: 1329-1364.

[7] Monteiro Azevedo, N. and Lemos, J. A 3D generalized rigid particle contact model for rock fracture. *Engineering Computations*, (2013), **30(2)**:277-300.

[8] Lilliu, G. and Van Mier, M. 3D lattice type fracture model for concrete. *Engineering Fracture Mechanics*, (2003) **70(7-8)**:927-941.

[9] Hentz, S., Daudeville, L., Donzé, F.V. Identification and validation of a discrete element model for concrete. *Journal of Engineering Mechanics. ASCE.* (2004), **130(6)**:709-719.

[10] Cusatis, P., Bazant, Z. and Cedolin, L. Confinement-shear lattice CSL model for fracture propagation in concrete. *Computer Methods in Applied Mechanics and Engineering,* (2006) **195(52)**:7154-7171.

[11] Scholtès, L. and Donzé, F.V. A DEM model for soft and hard rocks: Role of grain interlocking. *Journal of the Mechanics and Physics of Solids.* (2013), **61(2)**:709-719.

[12] Wang, Y. and Tonon, F. Modeling Lac du Bonnet granite using a discrete element model. *International Journal of Rock mechanics and Mining Sciences*, (2009), **46(7)**: 1124:1135.

[13] Gao, F. and Stead, D., The application of a modified Voronoi logic to brittle fracture modelling at the laboratory and field scale. *International Journal of Rock Mechanics and Mining Sciences*, (2014), **68**: 1:14.

[14] Ghazvinian, E., Diederichs, M. and Quey, R., 3D Random Voronoi grain-based models for simulation of brittle rock damage and fabric-guided micro-fracturing. *Journal of Rock Mechanics and Geotechnical Engineering*, (2014), **6(6)**: 506:521.

[15] Okabe, A., Boots, B. and Sugihara, K. *Spatial tesselations. Concepts and applications of Voronoi diagrams*, John Wiley & Sons (1992).

[16] Monteiro Azevedo, N., Candeias, M. and Gouveia, F., A rigid particle model for rock fracture following the Voronoi tessellation of the grain structure: Formulation and Validation, *Rock mechanics and Rock Engineering,* (2015), **48(2)**:535-557.

[17] Kazerani, T. and Zhao, J. Micromechanical parameters in bonded particle method for modelling of brittle material failure, *International Journal for Numerical and Analytical Methods in Geomechanics*, (2010), **34(18)**:1877-1895.

V International Conference on Particle-based Methods – Fundamentals and Applications
PARTICLES 2017
P. Wriggers, M. Bischoff, E. Oñate, D.R.J. Owen, & T. Zohdi (Eds)

INSTABILITIES OF A SAND LAYER SUBJECTED TO AN UPWARD WATER FLOW BY A 2D COUPLED DISCRETE ELEMENT - LATTICE BOLTZMANN HYDROMECHANICAL MODEL

MOULOUD MANSOURI[1], MOULAY S. EL YOUSSOUFI [2,3] AND FRANÇOIS NICOT[4]

[1] Département de Génie Civil, Université Ferhat Abbas Setif 1
19000, Setif, Algeria
email : mansouri.mouloud@univ-setif.dz

[2] LMGC - UMR 5508, Université de Montpellier - CC048
163 rue Auguste Broussonnet, 34090 Montpellier, France
[3] Laboratoire de Micromécanique et d'Intgrité des Structures (MIST)
IRSN-CNRS-Université de Montpellier, France
email : moulay-said.el-youssoufi@umontpellier.fr

[4] Université Grenoble-Alpes, IRSTEA, Unité de Recherche ETNA
Domaine Universitaire, BP 76, F38402 - Saint Martin d'Hères, France
email : francois.nicot@irstea.fr

Key words: Discrete Element Method, Lattice Boltzmann, quicksand

Abstract. This work deals with the numerical simulation of the instabilities occurring in a sand layer subjected to an upward water flow. A coupled Discrete Elements - Lattice Boltzmann hydromechanical model is used for this end. After a brief presentation of the numerical model, simulations of an upward fluid flow through granular deposits are performed for two cases namely under controlled hydraulic gradients and under controlled volumetric flow rates. In the first case i.e. under controlled hydraulic gradient, the simulations show that the quicksand condition is actually reached for a hydraulic gradient very close to the critical hydraulic gradient calculated from the global analysis of classical soil mechanics. The simulations point out moreover that the quicksand phenomenon could be produced locally under slightly lower gradients. In the second case i.e. under controlled volumetric flow rates, the simulations show that there are three levels of flow ; low flow rates that allow infiltration without any destabilization, medium flow rates that cause expansion of the deposit to increase its permeability and high flow rates which may cause the formation continuous tunnel between the upstream and the downstream sides as well as sand boils. It is shown also that under the controlled flow rate condition the hydraulic gradient remains in all cases less than the average critical hydraulic gradient.

1 INTRODUCTION

Quicksand condition can occur for a layer of sand subjected to an upward flow under a hydraulic gradient close to the critical hydraulic gradient. The latter corresponds to the state where the seepage force equals the submerged weight of the sand layer. Even if the classical soil mechanics allows to obtain the critical hydraulic gradient which defines the state of the beginning of soil uplift, it is not able to show the evolution of a soil layer subjected to upward flow before and after the quicksand condition is reached. Furthermore, it does not allow to define the size of the zone affected by the phenomenon, i.e. a restricted zone or a generalized uplift.

This work presents an analysis of the evolution of a sand layer subjected to an upward flow under two different conditions ; first under a gradually increased hydraulic gradient and second under a gradually increased volumetric flow rate. The analysis is carried out using a numerical model based on the coupling of a discrete method to model the sand grains with the Lattice Boltzmann method to model the water flow [1]. For the sake of simplicity, the analysis is carried using 2D simulations.

2 DISCRETE ELEMENT METHOD

The Discrete Element approach models the grains of a granular material by independent elements, each element interacts with its neighbors at the contact points. The overall deformation of the medium is mainly due to the relative movements of the grains assumed as rigid bodies. Therefore, the behavior of the medium can be described through the integration of the dynamic equations applied to each element. Such equations are written through Newton's second law by taking all external forces into account, such as the contact forces, the gravitational forces and the hydrodynamic forces. Since these forces can change abruptly with time, the integration should be performed in an incremental manner using small time steps.

The mollecular dynamics method originally proposed by Cundall and Strack [2] is implemented in this work. This method allows a slight overlap of the grains which is used to calculate the contact forces through explicit lows. We deal in this work with a 2D modeling where the grains are assumed circular, hence to detect the contacts at each time step the normal distance between any two grains i and j is examined. This distance is computed as : $D_n = \|\vec{x}_j - \vec{x}_i\| - r_j - r_i$, where $\vec{x}_i$, $\vec{x}_j$ are the i and j grains positions and r_i, r_j their radii respectively. The two grains are in contact if they overlap ($D_n \leq 0$). A contact force applied by a grain j on a grain i is decomposed into normal and tangential components. The normal force is calculated here using the viscoelastic linear model (Fig.1a), hence $\vec{F}_n = (-k_n D_n - \nu_n V_n).\vec{n}$, where V_n is the normal velocity of the grain j relative to the grain i, k_n and ν_n are the elastic and the viscous damping constants respectively and $\vec{n}$ is the unit vector pointing from i to j, i.e. : $\vec{n} = (\vec{x}_j - \vec{x}_i)/\|\vec{x}_j - \vec{x}_i\|$.

The tangential force is computed using the viscoelastic - frictional model (Fig.1b) as $\vec{F}_s = min\left(k_s D_s + \nu_s V_s, \mu F_n\right)\vec{s}$, where $\vec{s}$ is the tangential unit vector obtained by rota-

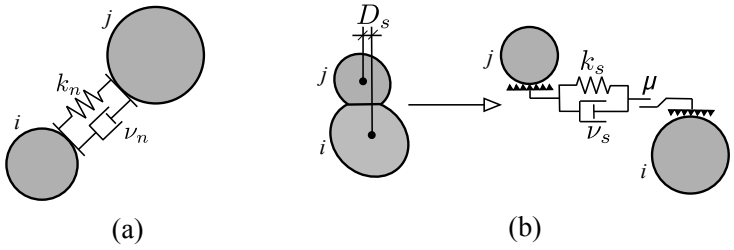

Figure 1: Modeling of the contact interaction forces ; (a) the normal force model, (b) the tagential force model.

tion of the normal vector $\vec{n}$ by an angle $\pi/2$ in the counterclockwise direction, V_s is the tangential velocity of the grain j relative to the grain i, D_s is the cumulative tangential displacement of the grain j relative to the grain i from the moment of contact initiation, μ is the Coulomb's coefficient of friction, k_s and ν_s are the tangential elastic and viscous damping constants respectively.

It should be noted that the choice of the elastic and the viscous damping constants (k_n and ν_n) is not arbitrary, in fact k_n must be high enough to avoid substantial overlap that affects the overall behavior, whereas ν_n that controls the damping in the material is selected such that the restitution coefficient ϵ_n defined as the ratio of the normal velocities at the start and the end of the contact is between 0 and 1.

Once the contact forces and the other external forces acting on a grain are obtained at a discrete time t, accelerations are calculated through the dynamic equations,then integrated to obtain the kinematic variables of the grain at time $(t + \Delta t)$. Considering that accelerations are not constant during a time increment Δt, special algorithms are used to predict accurately the kinematic variables, such as the Velocity-Verlet algorithm.

Finally, it is important to note that in order to correctly describe the evolution of the contact force, the time step Δt should be sufficiently small compared to the contact duration t_c. It is usually taken as $\Delta t \approx t_c/10$. For the viscoelastic model the contact duration can be approximated by $t_c = \pi\sqrt{m_{eff}/k_n}$, where $m_{eff} = m_i m_j/(m_i + m_j)$, m_i and m_j are the masses of the grains in contact. Therefore the maximum time step is computed as :

$$\Delta t_{max} \approx 0.1\pi\sqrt{m/k_n} \tag{1}$$

where m is the smallest effective mass in the system.

3 LATTICE BOLTZMANN METHOD

In the Lattice Boltzmann Method, one solves the kinetic equation for the particle distribution function $f(\vec{x}, \vec{\xi}, t)$, which depends on the spatial position $\vec{x}$, the velocity of particules $\vec{\xi}$, at the time t. The macroscopic quantities of interest such as mass density ρ and momentum density $\rho\vec{u}$ are weighted averages of the distribution function :

$$\rho = \int f d\vec{\xi} \qquad \text{(a)} \qquad\qquad \rho\vec{u} = \int \vec{\xi} f d\vec{\xi} \qquad \text{(b)} \tag{2}$$

A popular kinetic model adopted for the method is the so-called BGK (Bhatnagar, Gross and Krook) model. In this model the collisions term in the Boltzmann equation is simplified using the simple relaxation time approximation :

$$\frac{\partial f}{\partial t} + \vec{\xi}.\vec{\nabla} f = -\frac{1}{\lambda}(f - f^{(0)}) \tag{3}$$

where $f^{(0)}$ is the equilibrium distribution function (Maxwell-Boltzmann equilibrium function) and λ is the relaxation time. To solve for f numerically, Eq.(3) is discretized twice : a first discretization with respect to the time involving a time increment Δt and a second discretization based on the velocity space by chosing a finite set of velocity vectors that particles can have. The continuous particle distribution function $f(\vec{x}, \vec{\xi}, t)$ becomes therefore, a set of discrete distributions $f_i(\vec{x}, t)$ associated with the chosen velocity vectors $\vec{e}_i$. As an illustration, here is presented the D2Q9 model (2 Dimensions, 9 Velocity vectors) which is widely used for 2D simulations. Figure 2a, sketches the discrete velocity vectors in the D2Q9 model.

The discretizations lead to the LBGK (Lattice BGK) equation, that describes the incremental evolution of the discrete particle distributions f_i :

$$f_i(\vec{x} + \vec{e}_i \Delta t, t + \Delta t) - f_i(\vec{x}, t) = -\frac{1}{\tau}\left(f_i(\vec{x}, t) - f_i^{(eq)}(\vec{x}, t)\right) \tag{4}$$

where $f_i^{(eq)}$ is the discrete equilibrium distribution given as :

$$f_i^{(eq)} = \rho w_i \left[1 + \frac{3}{c^2}\vec{e}_i.\vec{u} + \frac{9}{2c^4}(\vec{e}_i.\vec{u})^2 - \frac{3}{2c^2}\vec{u}.\vec{u}\right] \tag{5}$$

where c is a characteristic speed of the model, w_i being the weighting factors; $w_0 = 4/9$, $w_{2,4,6,8} = 1/9$, $w_{1,3,5,7} = 1/36$, τ is the dimensionless relaxation time such as $\frac{1}{\tau} = \frac{\Delta t}{\lambda}$.

Equation (4) describes the incremental evolution of the discrete particle distributions f_i at the nodes of a regular lattice having a space step $\Delta x = c\Delta t$ (Fig. 2b). Hence if the space discretization's step is selected, the characteristic speed of the model is defined by $c = \frac{\Delta x}{\Delta t}$.

The fluid pressure p can be computed from the mass density through the equation of state $p = c_s^2 \rho$, where c_s is the sound speed of the model related to the lattice model's speed c as $c_s = c/\sqrt{3}$.

It is shown through the Chapman-Enskog analysis [3] that LB models recover the incompressible Navier-Stokes equations when the density fluctuation of the fluid is assumed to be negligible and the equivalent kinematic viscosity is given by :

$$\nu = \frac{1}{3}c\Delta x\left(\tau - \frac{1}{2}\right) \tag{6}$$

Therefore, in order to correctly simulate an incompressible fluid flow, one must ensure that the density fluctuation is sufficiently small. This can be achieved using a model with

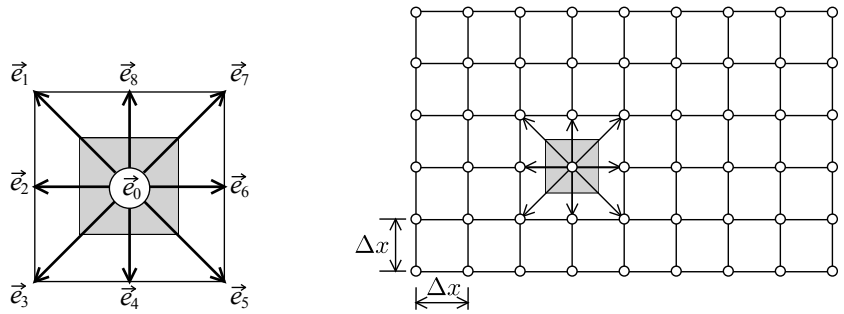

Figure 2: (a) D2Q9 model, (b) Flow domain discretization using the D2Q9 model

the sound speed c_s is larger enough than the maximum velocity of the simulated flow u_{max}, i.e. with a 'computational' Mach number defined as $M_a = \frac{u_{max}}{c_s}$ sufficiently small. In practice, M_a should be maintained, smaller than 0.1.

The discretization parameters are Δx, Δt and τ, if the viscosity of the fluid is given, only two of these parameters can be chosen independently since they are related through Eq. 6. In practice, it is often convenient to choose τ and Δx as two independent parameters and compute Δt from Eq. 6. This is due to the fact that τ is largely responsible for the numerical stability of LB simulations and Δx is often dictated by the space description precision. In practice τ is typically chosen in the range $]0.5\,,\,3]$.

4 COUPLED DISCRETE ELEMENT - LATTICE BOLTZMANN MODEL

4.1 Solid moving boundary treatment and hydrodynamic forces computation

The treatment of a solid moving boundary is decisive in granular materials hydromechanics. To model the fluid-solid no slip condition, we use in this work the interpolated bounce back scheme proposed by Bouzidi et al. [4]. For a linear interpolation, the post-collision distributions to be assigned to the solid boundary nodes before the streaming step are

$$\begin{cases} f_{\hat{i}}^{out}(\vec{x}_s,t) = 2q f_i^{out}(\vec{x}_f,t) + (1-2q) f_i^{out}(\vec{x}_{f'},t) + 6 w_i \rho_w \frac{\vec{e}_{\hat{i}}.\vec{u}_w}{c^2}, & q \leqslant \frac{1}{2} \\ f_{\hat{i}}^{out}(\vec{x}_s,t) = \frac{1}{2q} f_i^{out}(\vec{x}_f,t) + \frac{2q-1}{2q} f_{\hat{i}}^{out}(\vec{x}_{f'},t) + \frac{3}{q} w_i \rho_w \frac{\vec{e}_{\hat{i}}.\vec{u}_w}{c^2}, & q \geqslant \frac{1}{2} \end{cases} \tag{7}$$

where $\vec{e}_{\hat{i}}$ refers to the opposite direction of the direction $\vec{e}_i$ ($\vec{e}_{\hat{i}} = -\vec{e}_i$), $\vec{u}_w$ is the velocity of the boundary, ρ_w is the fluid mass density at the boundary and q defines the fraction of the boundary intersected link located in the fluid domain and calculated by referring to Figure 3 as $q = \frac{\|\vec{x}_f - \vec{x}_w\|}{\|\vec{x}_f - \vec{x}_s\|}$.

When a solid boundary moves, there are grid nodes that move from the solid region into the fluid region to become fluid nodes (indicated by □ in Fig. 3). Therefore one must specify the distribution functions applying to these nodes. In this work, unknown distri-

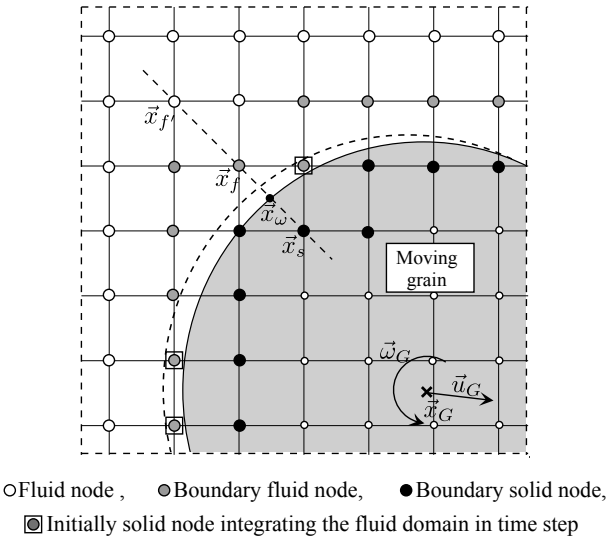

Figure 3: Representation of a moving grain on the lattice grid

butions are approximated as the equilibrium distributions computed using the averaged fluid's density in the whole system and the velocity of the solid particle at the specified node's position just before it leaves the solid region.

The hydrodynamic forces are computed in this work through the momentum exchange method [3].

4.2 Coupling procedure

As mentioned in the previous section, the time step in LBM (noted in the following Δt_{LB}) depends on the other discretization parameters and calculated from Eq. 6. Δt_{LB} is often larger than the maximum value DEM time step noted here Δt_{DEmax} and calculated from Eq. 1. Therfore, one should perform a number n_d of DEM computation steps then perform one LB computation step. This can be carried out by selecting the DEM time step $\Delta t_{DE} \leqslant \Delta t_{DEmax}$, such that $n_d \Delta t_{DE} = \Delta t_{LB}$, with the integer number n_d may be computed as $n_d = Int\left(\frac{\Delta t_{LB}}{\Delta t_{DEmax}}\right) + 1$, then the DEM time step is set :

$$\Delta t_{DE} = \frac{\Delta t_{LB}}{n_d} \tag{8}$$

Note finally that the static buoyancy force is taken into account by multiplying the gravitationnal acceleration by the coefficient $(1 - \rho_w/\rho_s)$, where ρ_w and ρ_s are the fluid and solid densities respectively.

5 2D SIMULATIONS OF AN UPWARD WATER FLOW THROUGH A SAND LAYER

It is worth noting that 2D discrete element modeling of a granular deposit produces a porous model with non interconnected pores. This completely changes the hydraulic properties of a saturated granular material. Therefore, the grains are maintained spaced, so that intergranular pores remain interconnected. The radii of grains are slightly increased in the discrete element modeling while kept equal to the actual radii in the Lattice-Boltzmann discretization. Thus the contact forces between the grains develop before the contact actually occurs. In this study, the distance added to the actual radius in the discrete elements modeling is set equal to one spatial step in the Lattice-Boltzmann discretization (Δx), consequently, the space between each two grains contains at least one node of the Lattice-Boltzmann grid.

The simulated deposit is composed of 300 polydisperse grains, with maximum and minimum diameters of 0.4 and $0.8\,mm$ respectively. Periodic conditions are used in the horizontal direction with a period length of $14.4mm$. The resulting average deposit height is about $8.8mm$. The unit weight and kinematic viscosity of water are taken as $\gamma_w = 10kN/m^3$ and $\nu = 10^{-6}m^2$ respectively while the unit weight of solid grains γ_s is set to $26kN/m^3$. The grains are first deposited under gravity then placed into a water column of the same section and of larger height and subjected to an upward water flow. The Lattice-Boltzmann discretization in the horizontal direction is $400\Delta x$, so that the smallest grain diameter is discretized into about $11\Delta x$.

Starting from its classical expression, the hydraulic gradient could be written as $i = \frac{\gamma'}{\gamma_w}\frac{\Delta pS}{W'}$. where γ' is the submerged unit weight of the soil, Δp is the pressure drop between the lower and upper horizontal surfaces of the deposit, S and W' are the horizontal section and the submerged weight of the deposit respectively. The product ΔpS is the resultant of external pressures applied to the deposit. With increasing Δp, the quicksand phenomenon triggers when the resultant of external pressures equals the submerged weight of the deposit i.e. $\Delta pS = W'$, therefore the critical hydraulic gradient is $i_c = \frac{\gamma'}{\gamma_w}$ and the applied hydraulic gradient could be written in terms of the critical hydraulic gradient as $i = i_c\frac{\Delta pS}{W'}$. As S and W' are fixed (characteristics of the deposit), it results that in order to impose a fraction of the critical hydraulic gradient, the only parameter to select is the pressure drop Δp.

5.1 Flow under constant hydraulic gradients

The deposit is subjected to an upward flow by imposing a hydraulic gradient. The hydraulic gradient is varied gradually from very low values up to values close to the critical gradient. It is found that for low values of the gradient ($i \leqslant 0,97i_c$) no uplift of the deposit is observed. For ($i \geqslant 0,97i_c$) the uplift is observed but in different ways depending on the applied hydraulic gradient. Figure 4 shows the deposit evolution over time for three applied hydraulic gradients $i = 0,97i_c$, $i = i_c$ and $i = 1,1i_c$.

These snapshots show that quicksand occurs in a similar manner for gradients $i \geqslant i_c$, in fact the deposit is fully raised initially, but for a low gradient ($i = i_c$) it loosens quickly while for a high gradient it may be raised like a shutter. This can be attributed to the high pressure applied at the bottom of the deposit which prevents loosening. Furthermore, it can be observed that the lifting is more quicker for the high gradient, since the grains reach the end of the column of water in a shorter time; $0.18s$ for $i = 1.1i_c$ against $0.18s$ for $i = i_c$. For the case $i = 0.97i_c$, the snapshots show that quicksand develops step by step ; first there is a grain rearrangement in some areas at the bottom of the deposit that allows the creation of large channels where there is no pressure drop (surrounded areas on the second snapshot). Accordingly, the hydraulic gradient in the area overlying the channel becomes larger. This increase in gradient initiates an uprising of this zone which leads to the loosening of the lower zone. This loosening grows progressively until the quicksand onset. It should be noted that in this case ($i = 0.97i_c$) the quicksand process is much slower than in the case with $i \geqslant i_c$ (in this case the total process time is $0.9s$), and the initial stage i.e. the grain rearrangement is the most time consuming stage.

5.2 Flow under constant volumetric flow rates

The deposit is subjected to an upward flow by imposing a controlled flow rate. The flow rate is incremented from zero to relatively high values gradually. i.e. it is increased only after a sufficient number of time steps. For small flow rates where the deposit remains stable the incrementation is then done after the establishment of the steady state under the previous flow rate. Figure 5 shows snapshots of the deposit for different flow rates. It may be noted that, depending on the behavior of the deposit, the flow rates could be classified as low, medium and high. For low flow rates, the deposit remains stable ($Q \leq 1.26 \times 10^{-5} m^3/s$ in our case). The medium flows induce a deposit dilation behavior ($1.26 \times 10^{-5} m^3/s \leq Q \leq 12.0 \times 10^{-5} m^3/s$ in our case). For the first flow rates causing a dilation, only a widening of some intergranular channels is observed as surrounded in the snapshot $Q = 1.32 \times 10^{-5} m^3/s$. Then, from a certain level of flow rate, the deposit becomes unstable, it is observed a development of unstable water pockets within the deposit which rise irregularly towards the surface. These pockets are larger for large flow rates. The high flow rates corresponds to the formation and the evolution of a continuous tunnel between the upstream and the downstream sides as well as sand boils, as shown in the snapshots $Q = 18 \times 10^{-5} m^3/s$ and $Q = 24 \times 10^{-5} m^3/s$.

For each value of the flow rate we measured the porosity as well as the resulting hydraulic gradient. For small flow rates where the deposit remains at rest, the porosity and the hydraulic gradient are measured after the steady state is established. However for high flow rates the deposit becomes unstable, the porosity and the hydraulic gradient are then taken as averages over a sufficient number of time steps. Figures 6 and 7 show the evolution of the average porosity and the average hydraulic gradient with the imposed flow rate respectively. In Fig. 7, the hydraulic gradient is normalized with respect to critical hydraulic gradient. Figure 6 shows that the porosity remains constant for the

low flow rates, it slightly decreases before increasing almost proportionally to the flow imposed. This indicates that the deposit can contract for the first flow rates that cause destabilization and after the destabilization the dilation is almost proportional to the flow imposed.

Figure 7 shows that for low flow rates the resulting hydraulic gradient is proportional the the imposed flow rate which is in good agreement with Darcy's law. This plot shows also that the hydraulic gradient remains in all cases less than the critical hydraulic gradient indicating that the engagement of instability prevents the increase of the hydraulic gradient. The curve indicates also that once the flow rate reaches the destabilization value ($Q = 1.32 \times 10^{-5} m^3/s$) the gradient evolution ceases to increase abruptly.

6 Concluding remarks

We investigated the quicksand instability using a coupled Lattice-Boltzmann-Discrete element hydromechanical model. Simulations of an upward fluid flow through granular deposits are performed for two cases namely under a gradually increased hydraulic gradient and under a gradually increased volumetric flow rate. In the first case i.e. under controlled hydraulic gradient, the simulations show that the quicksand condition is actually reached for a hydraulic gradient very close to the critical hydraulic gradient calculated from the global analysis of classical soil mechanics. The simulations point out moreover that the quicksand phenomenon could be produced locally under slightly lower gradients. In the second case i.e. under gradually increased volumetric flow rate, the simulations show that there are three levels of flow ; low flow rates that allow seepage without any destabilization, medium flow rates that cause expansion of the deposit to increase its permeability, such expansion is almost proportional to the flow imposed. And high flow rates which may cause the formation of continuous tunnel between the upstream and the downstream sides as well as sand boils. It is shown also that under the controlled flow rate condition the hydraulic gradient remains in all cases less than the critical hydraulic gradient.

REFERENCES

[1] Mansouri, M., El Youssoufi, M. S. and Nicot, F. Numerical simulation of the quicksand phenomenon by a 3D coupled Discrete Element - Lattice Boltzmann hydromechanical model. *Int. J. Num. Anal. Meth. Geomech.* (2017) **41(3)**:338–358.

[2] Cundall, P. and Strack O., A discrete numerical model for granular assemblies, *Geotechnique* (1979) **29(1)**:47–65.

[3] Luo L. S., Theory of the lattice Boltzmann method: Lattice Boltzmann models for nonideal gases, *Physical Review E* (2000); **62(4)** : 4982–4996.

[4] Bouzidi, M., Firdaouss, M., Lallemand, P. Momentum transfer of a Boltzmann-lattice fluid with boundaries, *Physics of Fluids* (2001) **13**:3452–3459.

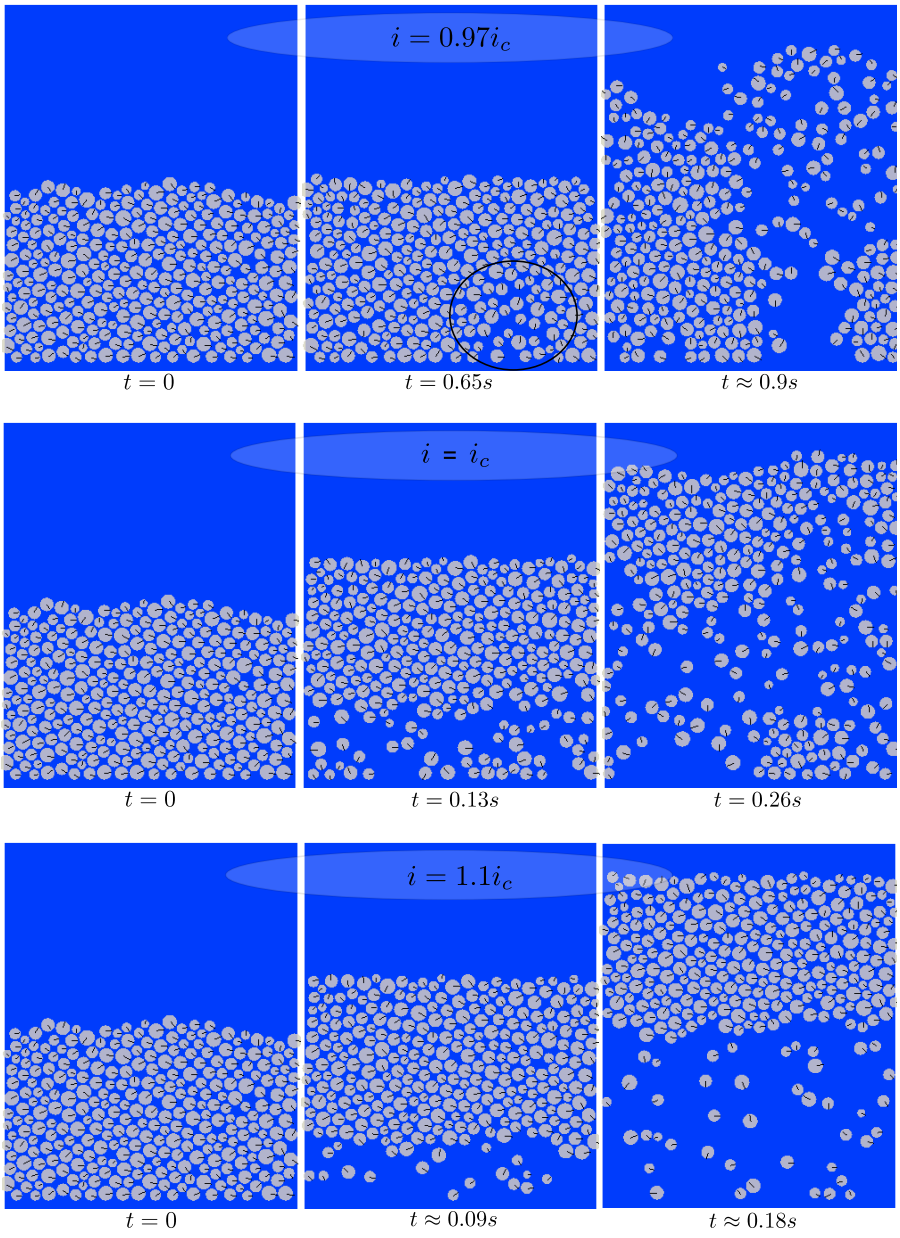

Figure 4: Snapshots in a chronological order, during the 2D simulation of the quicksand of a 300 grain deposit for imposed hydraulic gradients $i = 0.97i_c$, $i = i_c$ and $i = 1.1i_c$.

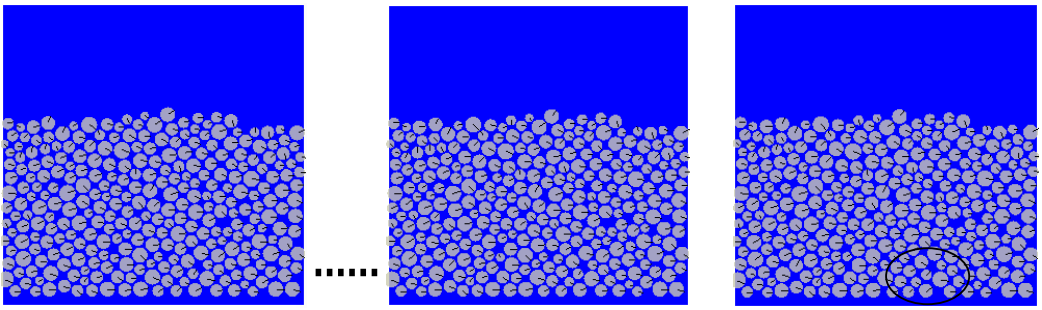

$Q = 0.0$ $Q = 1.26 \times 10^{-5} m^3/s$ $Q = 1.32 \times 10^{-5} m^3/s$

Snapshots of the deposit subjected to low flow rates

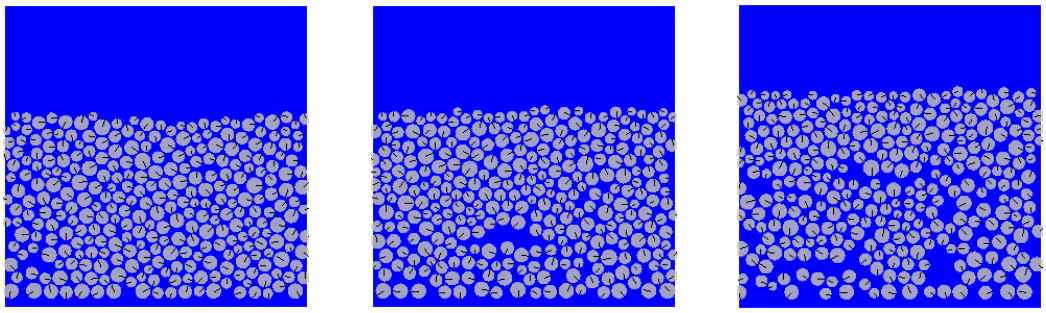

$Q = 2.4 \times 10^{-5} m^3/s$ $Q = 6.0 \times 10^{-5} m^3/s$ $Q = 12.0 \times 10^{-5} m^3/s$

Examples of snapshots of the deposit subjected to medium flow rates

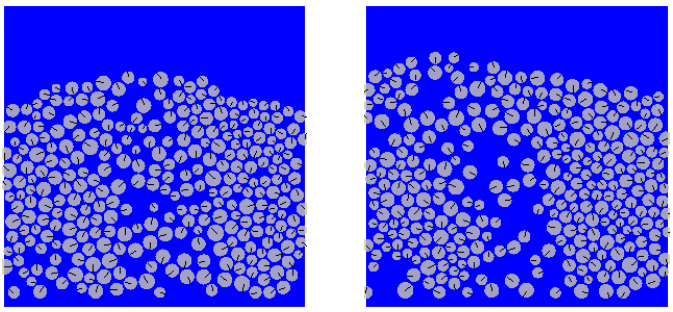

$Q = 18.0 \times 10^{-5} m^3/s$ $Q = 24.0 \times 10^{-5} m^3/s$

Examples of snapshots of the deposit subjected to high flow rates

Figure 5: Snapshots of the deposit subjected to an upward flow with different flow rates.

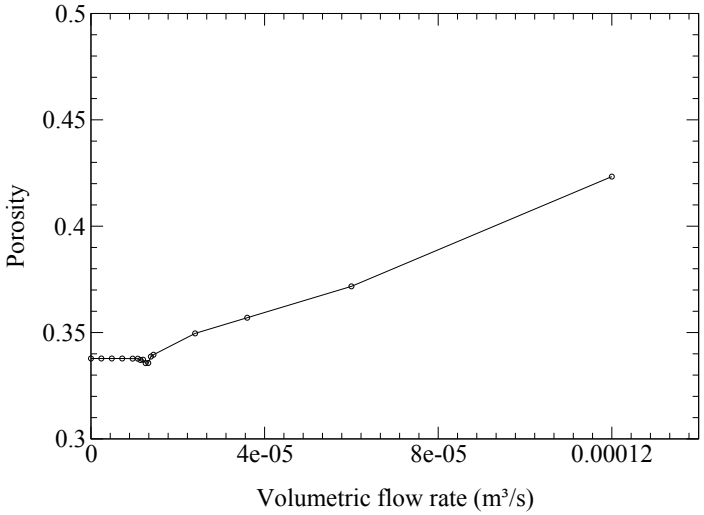

Figure 6: Evolution of the average porosity with the imposed flow rate

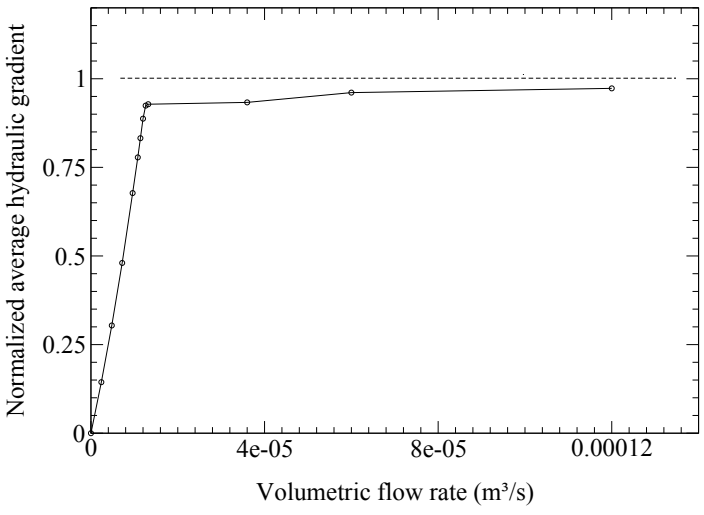

Figure 7: Evolution of the average hydraulic gradient with the imposed flow rate.

V International Conference on Particle-based Methods – Fundamentals and Applications
PARTICLES 2017
P. Wriggers, M. Bischoff, E. Oñate, D.R.J. Owen, & T. Zohdi (Eds)

MercuryDPM: Fast, flexible particle simulations in complex geometries Part II: Applications

Thomas Weinhart, Deepak R Tunuguntla, Marnix P van Schrojenstein Lantman, Irana FC Denissen, Christopher R Windows-Yule, Harmen Polman, Jonathan M F Tsang[2], Binbin Jin[2], Luca Orefice[3], Kasper van der Vaart[4], Sudeshna Roy, Hao Shi, Arianna Pagano[5], Wouter den Breeijen, Bert J Scheper, Ahmed Jarray, Stefan Luding, Anthony R Thornton

[1]Multiscale Mechanics, Engineering Technology, MESA+, University of Twente
PO Box 217, 7500 AE Enschede, Netherlands

[2]DAMTP, Centre for Mathematical Sciences, University of Cambridge
Wilberforce Road, Cambridge, CB3 0WA, United Kingdom

[3] Research Center Pharmaceutical Engineering GmbH,
Inffeldgaße 13, Graz, Austria

[4]Department of Civil and Environmental Engineering, Stanford University,
Stanford, CA 94305, USA

[5]Civil and Environmental Engineering, University of Strathclyde,
75 Montrose Street, Glasgow, G1 1XJ, United Kingdom

Key words: Granular Materials, DEM, *MercuryDPM*, Open-Source.

Abstract. *MercuryDPM* is a particle-simulation software developed open-source by a global network of researchers. It was designed *ab initio* to simulate realistic geometries and materials, thus it contains several unique features not found in any other particle simulation software. These features have been discussed in a companion paper published in the DEM7 conference proceedings; here we present several challenging setups implemented in *MercuryDPM*. Via these setups, we demonstrate the unique capability of the code to simulate and analyse highly complex geotechnical and industrial applications. The setups implemented include complex geometries such as (i) a screw conveyor, (ii) steady-state inflow conditions for chute flows, (iii) a confined conveyor belt to simulate a steady-state breaking wave, and (iii) a quasi-2D cylindrical slice to efficiently study shear flows. *MercuryDPM* is also parallel, which we showcase via a multi-million particle simulations of a rotating drum. We further demonstrate how to simulate complex particle interactions, including: (i) deformable, charged clay particles; and (ii) liquid bridges and liquid migration in wet particulates, (iii) non-spherical particles implemented via superquadrics. Finally, we show how to analyse and complex systems using the unique micro-macro mapping (coarse-graining) tool MercuryCG.

1 INTRODUCTION

MercuryDPM [1-3] is an open-source particle-simulation software written entirely in C++. Initially developed at the University of Twente, its developer/user community has grown rapidly, including researchers from the universities at Cambridge, Stanford, EPFL, Birmingham, Strathclyde, Sydney and Manchester. It was designed with the aim of allowing the simulation of realistic geometries and materials, found in industrial and geotechnical applications, and thus contains several unique features not found in any other particle simulation software: *(i)* a neighbourhood detection algorithm that can efficiently simulate *highly polydisperse packings*, which are common in industry [4]; (ii) an easy-to-use interface to define *complex walls*, making it easy to *exactly* model real industrial geometries [3]; and *(iii) MercuryCG* [5-8], a state-of-the-art analysis tool that extracts 3D continuum fields, providing accurate analytical/rheological information often not available from experiments or pilot plants. It further contains a *large range of contact models* to simulate complex interactions such as elasto-plastic deformation, sintering, breaking, wet and dry cohesion and liquid migration, all of which have important industrial applications. These features have been discussed in a companion paper published in the DEM7 conference proceedings [3]; here we present several challenging setups, implemented in *MercuryDPM*, that demonstrate those unique capabilities of the code.

2 COMPLEX GEOMETRIES

The following five applications demonstrate innovative geometries and boundary conditions that have recently been added to *MercuryDPM*.

2.1 Screw conveyor

Screw conveyors are mechanical devices ubiquitously used in the industry to transport material, generally in granular form. Despite its mechanical simplicity, the dynamics of the conveyed material inside of a screw feeder is complex, and strongly affected by the shape of the screw blade.

In most DEM solvers, the screw is implemented as a triangulated mesh: a collection of points on the screw surface is chosen and subdivided in triads, each of which will form a triangular tile covering the whole mapped surface. This way of implementing the surface of the screw, besides introducing artificial inaccuracies depending on the fineness of the mesh, can be problematic in the neighbourhood of sharp edges. In *MercuryDPM* both the helicoidal surface of a screw and a collision-detection algorithm between the screw and spherical particles is implemented analytically, which makes this approach more accurate and efficient.

The flow of a bi-disperse particle mixture inside a screw feeder is shown in Figure 2.1. The relative filling height (i.e. the height of the particle layer inside of the screw normalised by the screw diameter) is set to 0.35, while the screw rotates with an angular velocity of 2π rad/s. Figures a) and b) show that such devices trigger particle size segregation, due to both the shear between particles and screw components and the avalanching motion of the former. The rotation of the blade simultaneously lifts and pushes forward the particles, which are in a state of continuous avalanching, while the ones in contact with the external casing are greatly slowed by friction (see Figure 2.1c).

A better understanding of these complex dynamics might be useful for process optimization and design improvement, both of great importance in industrial processes. Applications of the model can range from pure DEM study of particle flow [22] to more complicated devices, such as roll compactors [23].

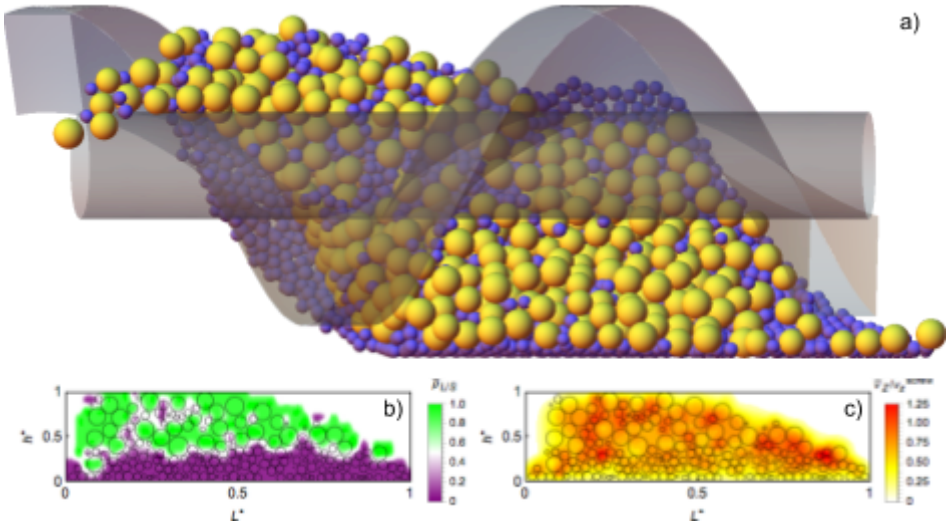

Figure 2.1 a) Snapshot of partially-filled screw feeder section transporting a bi-disperse particle mixture. Particles avalanche through the section, the screw surface being slightly shaded out for the sake of clarity. Particles coloured according to size. b) normalised coarse-grained density of big (green) and small particles (purple). The clear vertical separation shows particle size segregation. c) coarse-grained axial particle velocity normalized by screw axial velocity. The yellow particles in contact with the external casing are rotating with the screw, while particles in red are avalanching, triggering segregation.

2.2 Pressure-controlled periodic walls.

To model granular materials on a macroscopic scale, rheological relations are needed that describe the response of the material (i.e. the changes in density and stress) to externally applied shear and compression. For each material, these relations can be measured experimentally, e.g. a direct shear box for soils or shear cells for powders. However, to study the effect of specific material properties on the rheological response, it is more insightful to use simulations rather than experiments, as parameters can be changed easily – and individually – allowing for reliable parameter studies. In addition, simulations allow us to set up ideal homogeneous conditions, which is not possible in experimental studies where one is constrained by the external boundaries of the experimental device.

Here, we present a simulation setup for measuring the material's response under controlled, homogeneous strain and pressure conditions, shown in Figure 2: A user-defined shear is enforced by applying Lees-Edwards boundary conditions, and a horizontal driving force is applied to the particles to enforce homogeneous shearing. To control the confining pressure, the boundaries as well as the particle bulk are compacting/dilating each time step according to a servo control. This setup allows user to explore two variables (shear rate and pressure) at the same time, with a low computational cost for each simulation. Figure 2 shows a polydispersed granular system (mean diameter d) containing 4096 soft particles. The initial

length of each side is $L=16d$. At the center point in xy-plane (marked as O), one always has zero mean field shear velocity during the whole simulation. The pressure σ_{yy} is kept constant along the y-direction, mimicking the confining pressure applied in experimental conditions. The servo-control is applied to dilate/compact the sample along the y-direction, which smoothly reaches its steady state. In order to investigate the sheared granular flow behavior with different inertia and particle stiffness, we systematically vary the both the confined normal stress σ_{yy} and shear strain-rate $\dot{\gamma}$ such that the dimensionless stress/softness $\sigma_{yy}(d/k_n)$ ranges between 10^{-3} and 10^{-1} and the dimensionless shear strain-rate $\dot{\gamma}(\varrho_p d^3/k_n)^{1/2}$ is between 10^{-5} and 1.

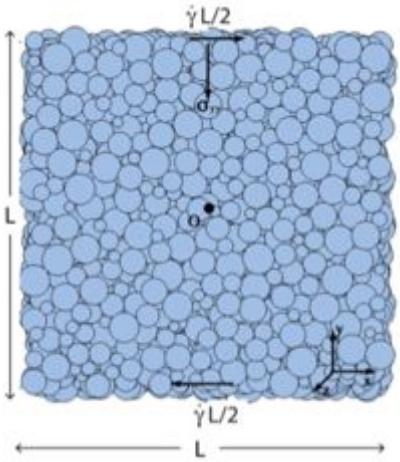

Figure 2.2 Representative volume element (RVE) with 4096 polydispersed particles subjected to a constant shear rate and confining stress.

2.3 Head formation in bidispersed avalanche flows

In the simple setup of an inclined plane with particles glued to the surface, it is a known result that flow-particles of different sizes segregate; the larger particles move towards the free surface, while the smaller particles sink to the bottom. Because the flow-speed is higher near the free surface than at the bottom, the large particles are transported towards the front. This leads to a flow front consisting of large particles, with a higher basal friction than the rest of the flow. This causes the front to be slower than the flow coming from behind, resulting in a bulbous head [14]. This bulbous head is much longer than it is high, so one needs many particles in order to be able to observe it in discrete particle simulations [15].

To implement this setup efficiently, we designed a Maser inflow boundary that produces a steady flow of particles, shown in Figure 2.3. The Maser boundary splits the domain into two parts: a small periodic chute with a steady flow, and the actual, much longer chute. Initially, the periodic chute runs until it reaches a steady state in both the flow- and segregation profile. Then, the Maser boundary is allowed to produce particles in the outflow domain: every particle in the periodic domain that crosses the downslope periodic boundary is both transported to the upslope boundary *and* copied into the outflow domain. One of the main advantages of this mechanism is that particles are only generated when needed: there is only a small number of 'extra' particles that need to be simulated at any given time, and one does not need to estimate the total number of particles in advance. The second advantage is that the Maser boundary generates a flow that is uniform and steady at the inflow; this reduces the distance in the flow has to travel before a steady bulbous head develops. Often a significant proportion of the simulation time goes into the inflow hopper or chute; the Maser removes the need to accurately simulate the inflow apparatus leading to a significant improvement in performance. In the future, we wish to use the Maser inflow boundary to generate data sets for full-scale chute flows, to investigate the use of flows over small periodic chutes and moving-bed channels as models for the full-scale chute flows.

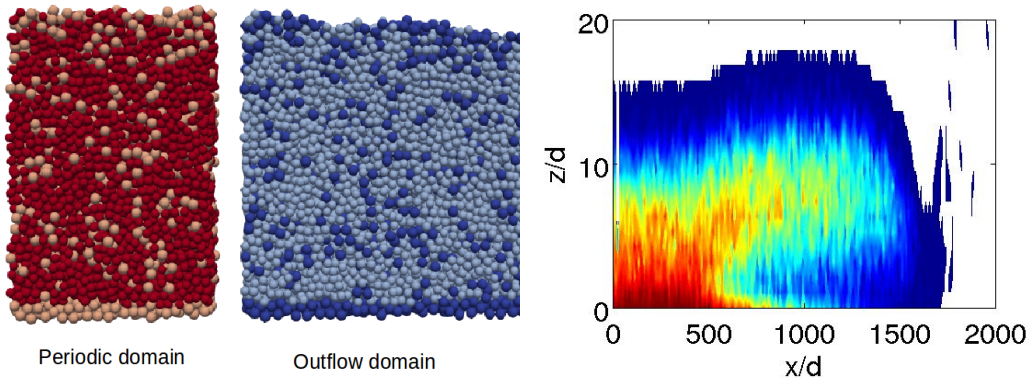

Figure 2.3: (a) Maser inflow boundary: the steady flow in the periodic domain generates particles for the full-scale chute flow in the outflow domain. Every time that a particle crosses the periodic boundary on the righthand side, it is simultaneously moved to the periodic boundary on the lefthand side and also copied in the outflow domain. (b) Bulbous head in shallow bidisperse chute flow. The colour-bar refers to the small-particle concentration: red is mostly small particles, blue is mostly large particles.

2.4 Breaking size-segregation waves in a moving-bed channel

As discussed in the previous section, size-segregation in a gravity-driven free-surface flow typically gives rise to the formation of a large-particle rich front and a small-particle rich tail. Separating these two regions is a recirculating structure where large particles, which have been deposited on the bed and overrun by the advancing flow front, are re-segregated to the free surface. At the same time small particles segregate to the bed in this region. This recirculating structure is referred to as a *breaking size-segregation* (BSS) *wave* [9, 10].

Simulating a BSS wave is challenging because of its time-dependent nature. BSS waves develop slowly, and after one has formed it travels close to the front of the flow. However, the BSS wave often travels slower than the front: as more large particles are carried to the front than are deposited on the bed, the large-particle front grows, thereby pushing the BSS wave back [11]. Thus, in order to study BSS waves in simulations, a very long chute is required to allow a steady BSS wave to emerge, and even then the BSS wave will be difficult to track. An alternate option is the use of a moving-bed channel [12,13]. In a moving-bed channel the bed is not rigid but consists of a moving conveyor belt that drags bottom layers of the flow upslope. At the same time the upper layers of the flow will still avalanche downslope. This creates a steady flow that remains stationary in the reference lab frame. A large-particle front and small-particle tail can develop in this flow configuration and thus also a BSS wave. Due to the compact setup of the moving-bed channel, the BSS wave reaches a steady-state position in a relatively short computational time. The particle positions, forces and velocities can then be time-averaged and coarse-grained for analysis.

Figure 2.4(a) shows a snapshot of a simulation of a bidisperse mixture of grains in a moving-bed channel. Large particles have accumulated at the downslope end of the channel (high x) while small particles have accumulated at the upslope end of the channel (low x). In between the tail and front exists a mixed region which is the BSS wave. Figure 2.4(b) shows a time- and width-averaged coarse grained field of the local small particle volume fraction φ_s. Here the structure of the BSS wave is more clearly visible. Note that φ_s is defined such that the small and large particle volume fraction sum to unity: $\varphi_s+\varphi_l=1$.

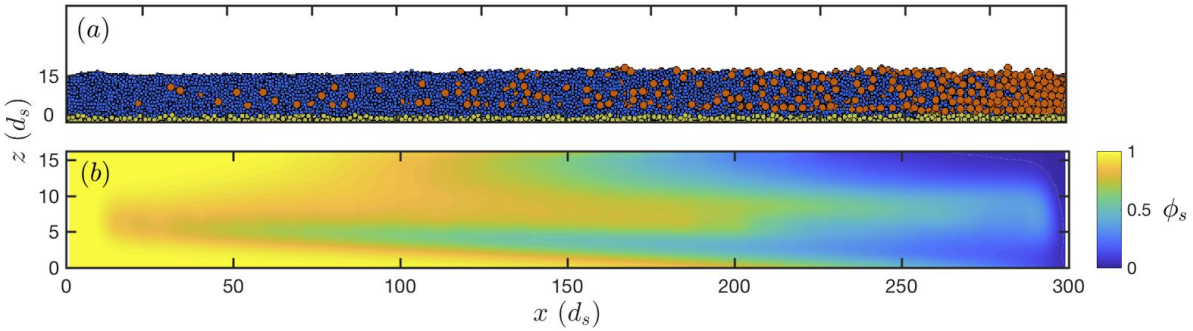

Figure 2.4: (a) Bidisperse granular mixture (d_l/d_s=2.4) in moving-bed channel geometry. The channel is inclined such that the mixture flows in x-direction. At the same time, the channel bed (yellow) moves in negative x-direction, dragging bottom layers of the flow upslope. This creates a steady granular flow. Size-segregation causes a large-particle rich front and a small-particle rich tail, separated by a breaking size-segregation wave. (b) Time- and width-averaged coarse-grained small-particle volume fraction.

2.5 Fingering instability in bidispersed avalanche flows

Under suitable circumstances, an avalanche of a bidisperse granular mixture is unstable to the *fingering instability* [16]. The avalanche is initially homogeneous in the cross-slope direction, but its front breaks into fingers, and the resulting flow has a longer runout distance than that of monodisperse avalanches of each separate species.

This instability is driven by granular segregation. For example, suppose the two species have different sizes but the same density. Segregation drives the larger species to the top of the avalanche. Being at the top, this species travels faster and ends up at the front of the avalanche. If the larger species is also more frictional, then this part of the front moves more slowly than the region of the avalanche behind it; consequently, the avalanche pushes through the front. For the instability to occur, the segregation should act quickly, and the larger species should be much more frictional than the smaller one, so that the front may become very slow.

We successfully realised examples of the fingering instability using *MercuryDPM*. We found that sliding friction does not sufficiently slow the motion of the larger species, even if the friction coefficient is increased to unphysically high levels. Laboratory experiments suggest that the friction of the larger species comes from the particles' angularity instead of an intrinsic friction of their material. This angularity can be captured in a simulation of spherical particles by introducing a rolling resistance.

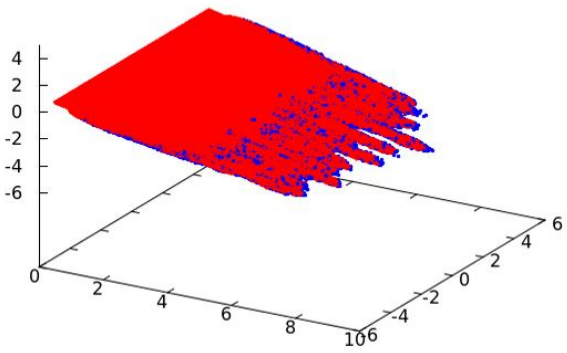

Future work will involve systematic comparisons of these simulations against laboratory experiments and continuum models. In particular, as the 'coefficient of rolling friction' in the Iwashita–Oda model [17] does not correspond to a physical quantity, it must be calibrated by looking at its effects on bulk friction angles.

Figure 2.5 Example of granular fingering in *MercuryDPM*. The blue particles are approximately twice the diameter of the red particles, and have higher coefficients of sliding and rolling friction.

3 FULLY PARALLELISED LARGE-SCALE SIMULATIONS

To enable large scale simulations, *MercuryDPM* is MPI-parallelised, which we showcase via a multi-million particle simulation of a long rotating drum.

3.1 Long rotating drums

Rotating drums or tumblers are widely used in a range of industrial sectors to process granular and particulate media. One of the most common applications of the rotating drum geometry is the mixing of two or more physically dissimilar 'species' of particulate. In granular systems as a whole, dissimilar particle species are prone to segregate when exposed to external excitation. In the rotating drum geometry, this can manifest itself as either *radial segregation* (whereby one species will segregate towards the radial centre of the system) or *axial segregation* (whereby the system will segregate along its axial length into distinct 'bands' of differing species).

While radial segregation can be observed in systems of almost any aspect ratio, axial segregation is typically observed to manifest itself only in systems with relatively great axial lengths. Simulating long drums is challenging, as a longer system will contain a greater number of particles and thus be significantly more computationally expensive to simulate.

The fully-parallelised nature of *MercuryDPM* means that, with access to an adequately large number of processors, it is possible to efficiently simulate systems of arbitrary length, and thus to gain valuable insight into the axial banding phenomenon, and indeed other behaviours which may only become significant in drums possessing large aspect ratios.

In Figure 3.1 we demonstrate the extent to which *MercuryDPM*'s parallel processing capability can expedite large simulations. By increasing the number of processors used by the code in proportion to the length of the drum (and hence the number of particles within the system), it is possible to maintain a near-constant simulation time, as opposed to the linearly increasing time required for a non-parallelised code. In other words, we can simulate systems containing of the order of 1,000 particles within a similar timeframe to a system containing many hundreds of thousands of particles.

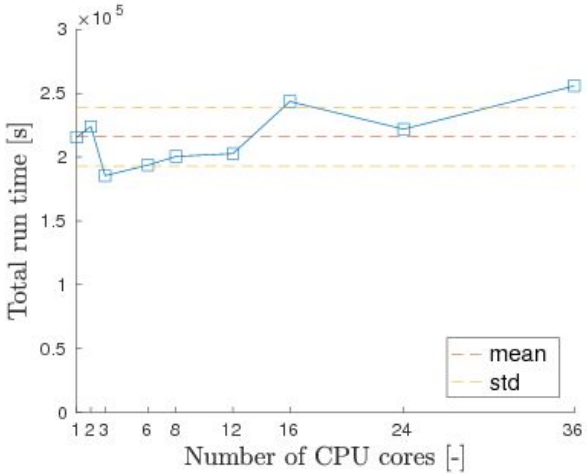

Figure 3.1. Computational run time required for 2.4 million timesteps of the rotating drum simulation. The number of particles per core is kept constant while increasing the number of cores. The computational cost is nearly constant, showing good parallel scalability.

4 COMPLEX PARTICLE AND CONTACT PROPERTIES

4.1 Modelling clay

Simulating clayey geomaterials using DPM is a great challenge, with many issues remaining to be solved. Firstly, physico-chemical microscopic interactions between particles have to be taken into account, as well as conventional mechanical interactions. Such interactions, mainly attributed to Coulomb repulsion/attraction and van der Waals forces, affect particles arrangement and are known to control the macroscopic behaviour of clays. On the other hand, the plate-like (3D) or rod-like (2D) shape of clay particles plays a key role in the interpretation of soil macroscopic behaviour and cannot be ignored during the analysis.

A modified contact model for simulating clayey geomaterials was implemented using *MercuryDPM* [20]. The first interaction is the conventional relationship between the overlap of particles in contact, δ_{ij}, and the repulsive contact force in the normal direction, f_{ij}, developing when overlapping occurs $(\delta_{ij}>0)$. The second interaction has to be defined as the relationship between the particles distance $(\delta_{ij}<0)$ and the attractive/repulsive force developing before the overlap occurs. These 'long range' forces are able to mimic the effect of Coulomb interactions, either repulsive or attractive, and van der Waals interaction, generally assumed to be attractive for clay particles. The total force acting on the particles is obtained by adding these three contributions together. A qualitative example of the implemented contact model is shown in Figure 4.1a.

Both rod-like and plate-like particles have been implemented, shown in Figure 4.1a/b. In addition to the previously mentioned contact law, an additional attractive interaction has been added that glues together particles belonging to the same rod or platelet.

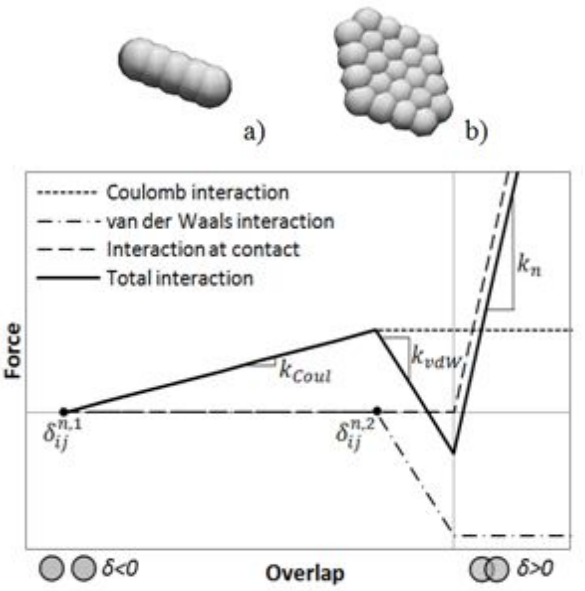

Figure 4.1 a) rod-like and b) plate-like particle shapes. c) Qualitative example of implemented contact model

4.2 Non-spherical particles

Besides utilising the multi-sphere approach shown in Sec. 4.1, *MercuryDPM* supports convex-shaped, superquadric particles, whose shape is described by the following equation:

$$f(x,y,z) = \left(\left|\frac{x}{a}\right|^{n_2} + \left|\frac{y}{b}\right|^{n_2}\right)^{n_1/n_2} + \left|\frac{z}{c}\right|^{n_1} - 1 = 0.$$

Note that (n_1, n_2, a, b, c) are the parameters defining the superquadric. For example, we get a cuboid with rounded-edges when $n_1 \gg 2, n_2 \gg 2$ and $a \neq b \neq c$. Other shapes can be defined similarly by changing the values of the exponents (blockiness parameters) and the axis-scales (half-lengths). As a result, it is now possible to have ellipsoids and rounded cubes in the same simulation. Hence, enabling simulations of complex realistic granular phenomena.

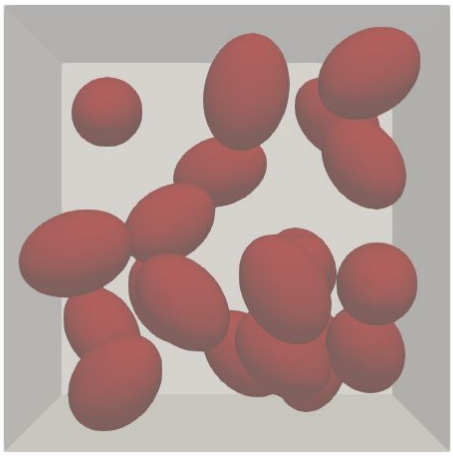

Figure 4.2: Example of free cooling of elliptical particles in a box. Ellipsoids are given an initial position and velocity and interact with each other and the side-walls.

4.3 Wet particles in a cylindrical shear cell

This simulation combines complex boundary conditions (a pie-shaped periodic boundary and moving walls) with a complex contact law (adhesive liquid bridge forces and liquid migration). Cylindrical shear cells are often used as rheometers as they allow the application of continuous shear. However, simulating a whole cell is expensive because of the large amount of particles involved. We therefore use the symmetry in angular direction and simulate only a slice, shown in Figure 4.3. For this, a special angular periodic boundary has been developed [18,19]. We use a phenomenological contact model combining a elastic repulsive force and a hysteretic liquid bridge capillary force based on the particle specifications, contact properties and liquid properties/ saturation in the system [19].

In our initial simulations, a simplistic situation is assumed where all contacts have liquid bridges of equal volume. In this case, the liquid in the system is not treated as a separate entity, rather the contact model takes accounts for the mean effect of liquid capillary bridges.

We then extended this model to account for liquid migration. The methodology is quite straight forward: liquid is transferred locally whenever contacts are formed or broken. Thus, the particles and the liquid are considered as two different entities in the system. Liquid is either associated with the particles as a thin liquid film, or with the contacts as liquid bridges. Film volumes are free to form new liquid bridges, whenever contacts are formed. Unlike film volumes, bridge volumes are bound to contacts till they are ruptured. When a liquid bridge is ruptured, bridge volumes are distributed neighbouring contacts and particles, as demonstrated in Figure 4.3. Total liquid conservation is ensured. The microscopic simulations of liquid migration allow the validation of a continuum scale model that describes the migration of liquid as shear-rate dependent diffusion.

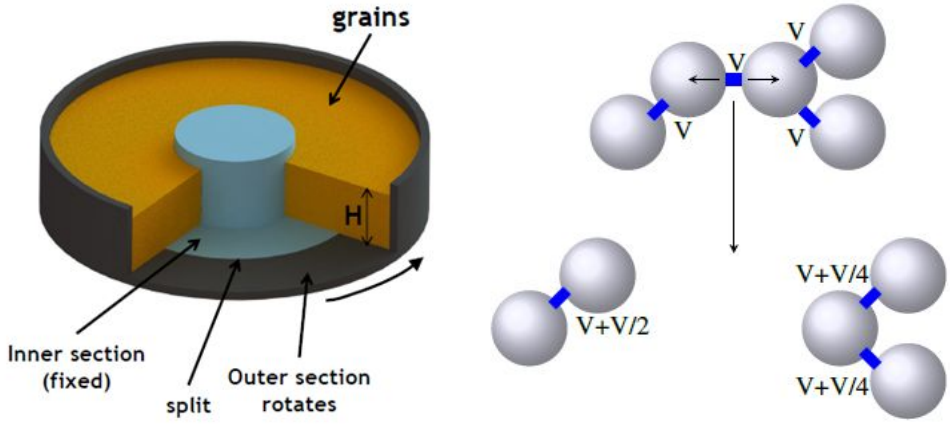

Figure 4.3 (a) Split bottom shear cell set-up (b) Bridge rupture according to liquid migration scheme [21]

5 COARSE-GRAINING ANALYSIS

In this final section, we demonstrate the capabilities of *MercuryCG*, our state-of-the-art analysis tool that extracts 3D continuum fields from particle simulations and experiments.

5.1 Silo Flow

The coarse-graining method implemented in *MercuryCG* [5-8] allows the calculation of continuum quantities (density, velocity, stress, and many more), even in regions with large spatial or temporal gradients. These measurements can then be used to characterise the macroscopic material properties (i.e. their rheology) and develop continuum models the describe the bulk behaviour. In [8], a silo flow model with a complex internal flow pattern was studied as a test case, where all three dense flow regimes are present, i.e.: (i) a stagnant zone, (ii) a highly localised shear band and (iii) a core zone with fast flow. The coarse-graining method was not only able to determine those zones (see Figure 8), but was further used to show the differences in rheological properties of the materials in each zone. This innovative use of continuum fields in the analysis of particle data may extend the range of validity of current rheological models, increasing their predictive capability.

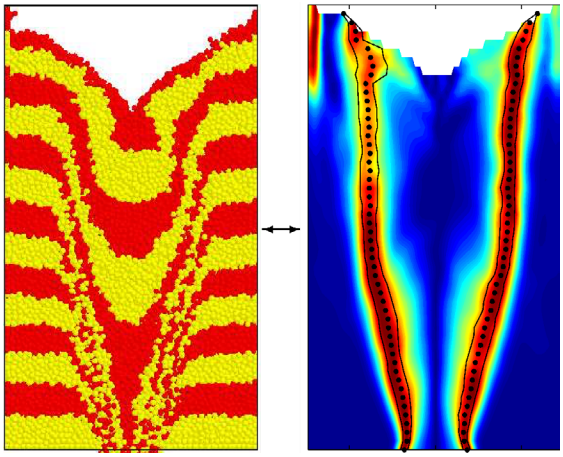

Figure 5.1: Silo flow in a quasi-2D geometry (left). The coarse-grained shear rate (right) can be used to distinguish three flow regimes: (i) a stagnant outer zone, (ii) a highly localised shear zone, and (iii) a fast-flowing core zone.

5.2 Experimental coarse-graining

Another key technology in the quest for characterisation of particles flow and dynamics is the particle tracking techniques. A particle tracking tool is being developed to convert data from experiments into data which can be read and post-processed by the coarse-graining method implemented in *MercuryCG*. This allows researchers and engineers to obtain quantitative and qualitative visualisation of the velocity gradient and distribution of particles. It can also be used to export multiple parameters of the particles flow. The tool is currently capable of tracking and processing optical data and Positron Emission Particle Tracking data (PEPT). In our development of this Tracking-MercuryCG tool, we aspire to extend its capability to track RIMS and NMRI data.

In Figure 5.2, we show a snapshot of a rotating drum filled with glass beads that rotates at 25 rpm. The flow of particles in this apparatus is an example of experimental data that can be processed using the Tracking-MercuryCG tool. In this case, slow motion video of a rotating drum is recorded using a MotionBLITZ EoSens high speed camera working at a speed of 460 frame/s (Figure 5.2 left). The video is then post-processed using the tracking tool where the dark glass beads in the drum are detected and tracked. Velocity gradient are afterward

generated using *MercuryCG*. In Figure 5.2 right, a coarse-grained velocity gradient of this experimental data is shown for dry and wet glass beads. In the upper part of the bed, the hot colours indicate areas where the local velocity of the particles is high, while cooler colours in the core of the bed indicate regions where the velocity of the glass beads is lower.

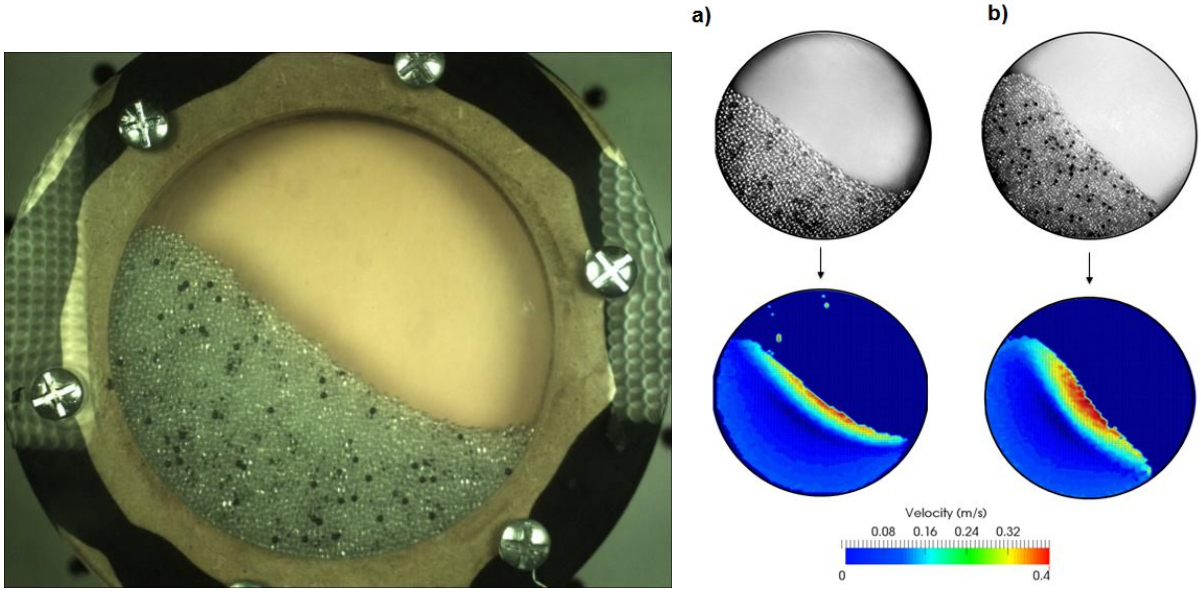

Figure 5.2 Left: Rotating drum apparatus: example for post-processing experimental data, using the particles tracking tool and coarse-graining. Right: Coarse-grained velocity gradient of the rotating drum at 25 rpm. a) Dry glass beads, b) Wet glass beads.

6 CONCLUSIONS

MercuryDPM is an open-source software based on a flexible, object-oriented framework, making it easy for users to customise the geometry and material properties to an extent not available in traditional particle simulation software. This has led to several innovative features such as complex in- and outflow conditions, curved walls, and pressure-controlled periodic walls. As the code is developed as an open-source project, users can merge their newly developed features into the publicly-available software, making it available to all *MercuryDPM* users. The codes presented here are available, or will be made available shortly, in the public *MercuryDPM* release, available at MercuryDPM.org; previews of the unreleased code are available in the current *MercuryDPM*-Alpha, which is available on request. A description of the files needed to run a specific application can be found at http://MercuryDPM.org/Documentation/Applications. We welcome you to use these features, give us feedback, and even become a developer should you choose to give back features to the *MercuryDPM* community. Just contact us via info@mercurydpm.org.

ACKNOWLEGEMENTS

We acknowledge the support of the following grants: NWO VICI 10828; NWO VIDI 13472; STW 11039; STW-DFG 12272; DFG SPP1482 B12; DFG LU 450/10.

REFERENCES

[1] Thornton, A.R., Krijgsman, D., te Voortwis, A., Ogarko, V., Luding, S., Fransen, R., Gonzalez, S. I., Bokhove, O., Imole, O. and Weinhart, T., A review of recent work on the Discrete Particle Method at the University of Twente: An introduction to the open-source package MercuryDPM, *Proc. 6th International Conference on Discrete Element Methods* (2013).

[2] Thornton, A.R., Krijgsman, D., Fransen, R., Gonzalez, S., Tunuguntla, D. R., ten Voortwis, A., Luding, S., Bokhove, O. and Weinhart, T., Mercury-DPM: Fast particle simulations in complex geometries, *EnginSoft Year 10(1)* (2013).

[3] Weinhart, T., Tunuguntla, D. R., van Schrojenstein Lantman, M., van der Horn, A. J., Denissen, I. F. C., Windows-Yule, C. R. K., de Jong, A. C. and Thornton, A. R., MercuryDPM: A fast and flexible particle solver Part A: Technical Advances, *Proc. 7th International Conference on Discrete Element Methods* (2016).

[4] Krijgsman, D., Ogarko, V. and Luding, S., Optimal parameters for a hierarchical grid data structure for contact detection in arbitrarily polydisperse particle systems, *Comp. Part. Mech. 1(3)*, (2014).

[5] Weinhart, T., Thornton, A.R., Luding, S. and Bokhove, O., From discrete particles to continuum fields near a boundary, *Granul. Matt. 14(2), 289-294* (2012).

[6] Tunuguntla, D. R., Thornton, A. R. and Weinhart, T., From discrete particles to continuum fields: Extension to bidisperse mixtures. *Comp. Part. Mech. 3(3), 349-365* (2016).

[7] Weinhart, T., Hartkamp, R., Thornton, A.R. and Luding, S., Coarse-grained local and objective continuum description of 3D granular flows down an inclined surface, *Phys. Fluids 25, 070605* (2013).

[8] Weinhart, T., Labra, C., Luding, S. and Ooi, J., Influence of coarse-graining parameters on the analysis of DEM simulation results, *Powder Technol. 293, 138-148* (2016). *Preprint*

[9] Thornton, A. R. and Gray, J. M. N. T., Breaking size segregation waves and particle recirculation in granular avalanches, *J. Fluid Mech. 596, 261–284* (2008).

[10] Gajjar, P., van der Vaart, K., Thornton, A. R., Johnson, C. G., Ancey, C. and Gray, J. M. N. T., Asymmetric breaking size-segregation waves in dense granular free-surface flows, *J. Fluid Mech., 794, 460–505* (2016).

[11] Gray, J. M. N. T. and Kokelaar, B. P., Large particle segregation, transport and accumulation in granular free-surface flows, *J. Fluid Mech. 652, 105–137* (2010).

[12] Davies, T. R. H., Debris-flow surges - experimental simulation, *J. Hydrology 29(1), 18–46* (1990).

[13] Chambon, G., Ghemmour, A. and Laigle, D.. Gravity-driven surges of a viscoplastic fluid: An experimental study, *J. Non-Newtonian Fluid Mech. 158(1), 54–62* (2009).

[14] Kokelaar, B.P., Graham, R.L., Gray, J.M.N.T. and Vallance, J.W., Fine-grained linings of leveed channels facilitate runout of granular flows, *Earth and Planetary Sci. Lett. 385, 172-180* (2014).

[15] Denissen, I. F. C., Weinhart, T., te Voortwis, A., Luding, S., Gray, J. M. N. T. and Thornton, A.R., Bulbous head formation in bidisperse shallow granular flow over an inclined plane. *J Fluid Mech.* (2017). *Under Review*

[16] Pouliquen, O. and Savage, S. B., Fingering in granular flows. *Nature 386* (1997).

[17] O'Sullivan, C. *Particulate Discrete Element Modelling: A Geomechanics Perspective*, CRC Press (2011).

[18] Roy, S., Luding, S. and Weinhart, T., A general(ized) local rheology for wet granular materials, *New J. Phys. 19, 043014* (2017).

[19] Roy, S., Singh, A., Luding, S. and Weinhart, T., Micro-macro transition and simplified contact models for wet granular materials, *Comp. Part. Mech. 3(4), 449–462* (2016).

[20] Pagano, A. G., Tarantino, A., Pedrotti, M., Magnanimo, V., Windows-Yule, C. R. K. and Weinhart, T. Micromechanics of non-active clays in saturated state and DEM modelling, *Proc. 8th International Conference on Micromechanics of Granular Media* (2017).

[21] This figure is taken from the presentation of Dr. Ken Kamrin, which was given at the KITP Conference on Complexity in Mechanics (2014), http://online.kitp.ucsb.edu/online/nonequil_c14/kamrin/

[22] Orefice, L. and Khinast J.G., DEM study of granular transport in partially filled horizontal screw conveyors, *Powder Technol. 305, 340-346* (2017).

[23] Mazor, A., Orefice, L., Michrafy, A., de Ryck, A. and Khinast, J.G., A combined DEM & FEM approach for modelling roll compaction process, *Powder Technol.* (2017). *In press*

DEVELOPMENT OF A FLUID-SOLID MULTIPHASE FLOW SIMULATOR BY A SPH-DEM COUPLED METHOD FOR SIMULATING A SEAWALL DESTRUCTION DUE TO SOIL FOUNDATION SCOUR

KENSUKE HARASAKI [1] AND MITSUTERU ASAI [2]

[1] Department of Civil Engineering, Graduate School of Engineering, Kyushu University
Motoka744, Nishi-ku, Fukuoka 819-0395, JAPAN
e-mail: harasaki@doc.kyushu-u.ac.jp,
web page: https://kyushu-u.wixsite.com/structural-analysis

[2] Ph.D., Associate Prof., Department of Civil Engineering, Graduate School of Engineering, Kyushu University
Motoka744, Nishi-ku, Fukuoka 819-0395, JAPAN
e-mail: asai@doc.kyushu-u.ac.jp,
web page: https://kyushu-u.wixsite.com/structural-analysis

Key words: Scouring, Seepage flow, Breakwater, SPH-DEM coupled method.

Abstract. In 2011, Tohoku-Kanto earthquake tsunami caused serious damage to the port and coastal structures such as breakwaters and seawalls. The damage mechanism of these structures has been studied in the past, and it is found that there are some causes. In this study, a new simulation tool taking account of the soil scouring and seepage flow phenomena is developed to represent and predict the collapse of the breakwater with SPH-DEM coupled method.

1 INTRODUCTION

In 2011, the huge tsunami induced by the Tohoku-Kanto earthquake caused very serious damages to the port structures, especially the coastal breakwaters. Damage mechanism of the breakwater has been studied in the past, and there are three main causes; (I) horizontal force due to the water level difference between the front and rear part of breakwater, (II) soil scouring behind the breakwater during overflow and (III) piping destruction associated with the decline of the soil durability by seepage flow. Fluid-Structure-Soil coupling simulation is desired for a systematic comprehension of the breakwater collapse mechanism as it may help to develop the next disaster prevention guidelines.

In our previous study, the analysis of free surface and seepage flow related to the third cause, (III) piping destruction, is conducted with the stabilized ISPH method proposed by M. Asai et al. [1]. However, this analysis is limited to the prediction of the breakwater destruction because the mound soil was not modelled. The modelling of the soil motion is needed to analyze the break water destruction and also the second cause, (II) soil scouring. In the scouring domain, water and soil are moving each other, thus the flow comes to be a multiphase flow.

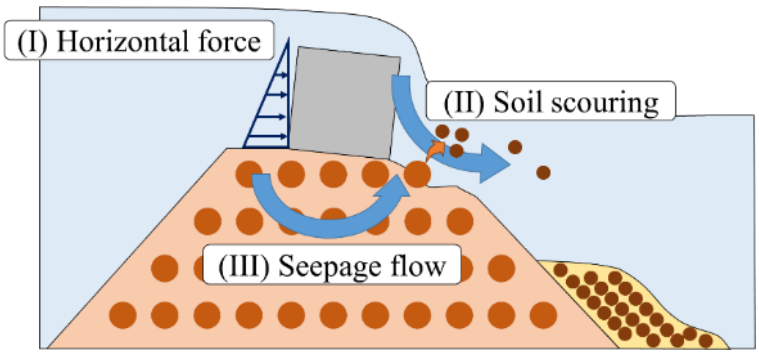

Figure 1: Main factors of the breakwater collapse

In this study, in addition to ISPH method for fluid analysis, Discrete Element Method (DEM) is selected to analyze the mound soil motion. In addition, this coupled method considering soil scouring and seepage flow is applied to the simple breakwater destruction analysis.

2 SPH-DEM COUPLING MODEL

A coupling model of ISPH method and DEM is the core in the multiphase flow analysis, and there are two models to couple ISPH method and DEM. One is the “Direct pressure model” we call. In general, a solid in fluid moves by receiving a pressure from fluid. In this method, a solid also moves in same way. However, if this method is adopted, the diameter of fluid particles need to be much smaller than the solid to calculate a force acting on the solid surface accurately. Therefore, the analysis cost is high to analyze a large scale model such as a breakwater collapse with this method. The other method is “Interaction force model”. In this method, a fluid particle can overlap with solid particles, and a fluid pressure don’t acts on a solid particle. Instead of a pressure, an interaction force acts on each particles, a resistance force on fluid and a drag force on solid. Furthermore, the diameter of fluid particle can be almost the same size with a solid

particle. This method can reduce the analysis cost compared than “Direct pressure model”, therefore “Interaction force model” is adopted to analyze.

3 ANALYSIS MEHOD

3.1 The unified governing equation

In the breakwater collapse analysis, a fluid flow will be regarded as a free surface flow in a fluid domain and a seepage flow in a mound. According to Akbari, H. [2], an unified governing equation for modelling both surface and seepage flows can be written as:

$$\frac{C_r(\varepsilon)}{\varepsilon}\frac{D\overline{\boldsymbol{v}}_f}{Dt} = -\frac{1}{\rho_f}\nabla P + \boldsymbol{g} + \nu_E(\varepsilon)\nabla^2\overline{\boldsymbol{v}}_f - a(\varepsilon)\overline{\boldsymbol{v}}_f - b(\varepsilon)\overline{\boldsymbol{v}}_f\left|\overline{\boldsymbol{v}}_f\right|, \tag{1}$$

$$\frac{D\bar{\rho}_f}{Dt} + \bar{\rho}_f\nabla\cdot\left(\frac{\overline{\boldsymbol{v}}_f}{\varepsilon}\right) = 0, \tag{2}$$

where ρ_f, $\boldsymbol{g}$, P and ε represent the original fluid density, the gravitational acceleration, the fluid pressure and the porosity. $\overline{\boldsymbol{v}}_f$ is the Darcy velocity which is understood as a spatially averaged velocity given by $\overline{\boldsymbol{v}}_f = \varepsilon\boldsymbol{v}_f$, $\boldsymbol{v}_f$ is the intrinsic fluid velocity. Here, $\bar{\rho}_f$ denotes the apparent density, which is given by $\bar{\rho}_f = \varepsilon\rho_f$. This relation regarding the apparent density is necessary to be employed in order to satisfy the volume conservation of fluid inside the porous medium. Some of the coefficient are defined as:

$$C_r(\varepsilon) = 1 + 0.34\frac{1-\varepsilon}{\varepsilon}, \tag{3}$$

$$\nu_E(\varepsilon) = \frac{\nu_w+\nu_T}{\varepsilon}, \tag{4}$$

$$a(\varepsilon) = \alpha_c\frac{\nu_w(1-\varepsilon)^2}{\varepsilon^3{d_s}^2}, \tag{5}$$

$$b(\varepsilon) = \beta_c\frac{(1-\varepsilon)}{\varepsilon^3 d_s}, \tag{6}$$

where $C_r(\varepsilon)$ is the inertial coefficient to evaluate the additional resistance force caused by the virtual mass, while $\nu_E(\varepsilon)$ is the effective viscosity including the kinematic viscosity of the fluid ν_w and the turbulent viscosity ν_T. The Smagorinsky model is adopted to define the eddy viscosity. $a(\varepsilon)$ and $b(\varepsilon)$ are the linear and non-linear coefficients, α_c and β_c in these equation are defined as the constant in our analysis. Moreover, d_s is the diameter of a solid particle. Here, the fourth and fifth terms in right side of Eq. (1) means the resistance force from the porous medium. This unified governing equation is proposed by Akbari to represent the seepage flow in a fixed porous medium with a low porosity. However, in the scouring domain, the soil as a porosity medium also moves and the porosity comes to be high. Therefore, the resistance force terms in Eq. (1) are modified referring to Wen and Yu [3], and the unified governing equation is rewritten as:

$$\frac{C_r(\varepsilon)}{\varepsilon}\frac{D\overline{\boldsymbol{v}}_f}{Dt} = -\frac{1}{\rho_f}\nabla P + \boldsymbol{g} + \nu_E(\varepsilon)\nabla^2\overline{\boldsymbol{v}}_f \begin{cases} -a(\varepsilon)\varepsilon\boldsymbol{v}_r - b(\varepsilon)\varepsilon^2\boldsymbol{v}_r|\boldsymbol{v}_r| & (\varepsilon < 0.8) \\ -\frac{3}{4}C_d\frac{(1-\varepsilon)\rho_f\boldsymbol{v}_r|\boldsymbol{v}_r|}{d_s}\varepsilon^{-2.7} & (\varepsilon \geq 0.8) \end{cases}. \tag{7}$$

Here, in considering the movement of the porous medium, the velocity in resistance force terms is changed to relative velocity $\boldsymbol{v}_r$ between fluid and solid which is given by $\boldsymbol{v}_r = \boldsymbol{v}_f - \boldsymbol{v}_s$. In taking a relative velocity, the fluid velocity must not be a spatially averaged velocity $\overline{\boldsymbol{v}}_f$ but an original velocity $\boldsymbol{v}_f$. Thus, the porosity ε is multiplied by the linear and non-linear coefficients.

In addition, the resistance force proposed by Wen and Yu for the high porosity domain ($\varepsilon \geq 0.8$) is considered. C_d is drag coefficient and defined with Reynolds number R_e as follows:

$$C_d = \frac{24\{1+0.15*{R_e}^{0.687}\}}{R_e} \qquad (R_e < 1000), \tag{8}$$

$$C_d = 0.43 \qquad (R_e > 1000), \tag{9}$$

$$R_e = \frac{\varepsilon \rho_f d_s |\boldsymbol{v}_f - \boldsymbol{v}_s|}{\nu_w}. \tag{10}$$

According to Eq. (7), the fluid flow outside the porous medium can be given by the Navier-Stokes equation with the porosity $\varepsilon = 1$. On the other hand, the fluid flow inside the porous medium can be described by including the resistance force. Eq. (2) represents the unified continuity equation for a compressible fluid.

The resistance force in Eq. (1) acts on fluid as a resistance force, and it needs to act on the porous medium as a drag force in the opposite sign as well to satisfy the action-reaction law. Thus, this resistance force can be considered as the interaction force between fluid and solid. The drag force as the interaction force for solid is described later.

3.2 The SPH method

In this study, the incompressible smoothed particle hydrodynamics (ISPH) method is adopted to solve the unified governing equation. The basic concept in SPH method is that for any function ϕ attached to particle "i" located at $\boldsymbol{x}_i$ is represented by the following volume summation:

$$\phi(\boldsymbol{x}_i) \approx \langle \phi_i \rangle := \sum_j \frac{m_j}{\rho_j} \phi_j W(r_{ij}, h), \tag{11}$$

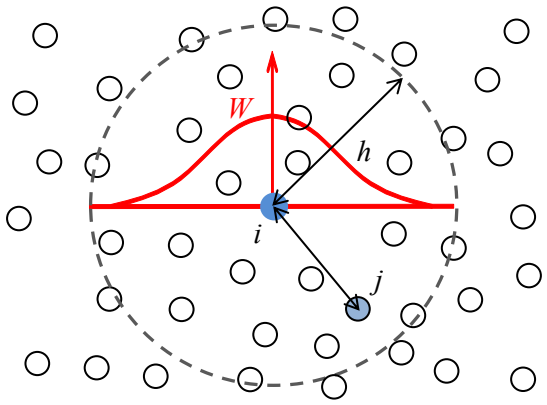

Figure 2: Particle placement and influence radius in the SPH method

where m and W are the representative volume of particle and a weight function known as the smoothing kernel function. j is a particle in the smoothing length h and r_{ij} is the length of the relative coordinate vector $\boldsymbol{r}_{ij}(= \boldsymbol{x}_j - \boldsymbol{x}_i)$. In this study, the smoothing length set to 2.4 times the initial diameter of the particle. The divergence $\nabla \cdot \phi$, the gradient $\nabla \phi$ and the Laplacian $\nabla^2 \phi$ can be written as:

$$\nabla \cdot \phi(\boldsymbol{x}_i) \approx \langle \nabla \cdot \phi_i \rangle = \frac{1}{\rho_i} \sum_j m_j (\phi_j - \phi_i) \cdot \nabla W(r_{ij}, h), \tag{12}$$

$$= \rho_i \sum_j m_j \left(\frac{\phi_j}{{\rho_j}^2} + \frac{\phi_i}{{\rho_i}^2} \right) \cdot \nabla W(r_{ij}, h), \tag{13}$$

$$\nabla \phi(\boldsymbol{x}_i) \approx \langle \nabla \phi_i \rangle = \frac{1}{\rho_i} \sum_j m_j (\phi_j - \phi_i) \nabla W(r_{ij}, h), \tag{14}$$

$$= \rho_i \sum_j m_j \left(\frac{\phi_j}{{\rho_j}^2} + \frac{\phi_i}{{\rho_i}^2} \right) \nabla W(r_{ij}, h), \tag{15}$$

$$\nabla^2 \phi(\boldsymbol{x}_i) \approx \langle \nabla^2 \phi_i \rangle = \sum_j m_j \left(\frac{\rho_i + \rho_j}{\rho_i \rho_j} \frac{\boldsymbol{r}_{ij} \cdot \nabla W(r_{ij}, h)}{{\boldsymbol{r}_{ij}}^2 + \eta^2} \right) (\phi_i - \phi_j). \tag{16}$$

Note that the triangle bracket $\langle \cdot \rangle$ indicates the SPH approximation of a particular function. η is the parameter to avoid division by zero and defined by the following expression $\eta^2 = 0.0001(h/2)^2$.

3.3 Formulation of the unified governing equation in the stabilized ISPH method

In ISPH method, the governing equation is discretized in time by the projection method based on the predictor and corrector scheme. In this method, the pressure is calculated implicitly and the velocity fields are updated explicitly. The unified governing equations, Eq. (2) and Eq. (7), are discretized as same way.

To begin with the discretization, $\overline{\boldsymbol{v}}_f$ at $n+1$ step is written as:

$$\overline{\boldsymbol{v}}_f^{n+1} = \overline{\boldsymbol{v}}_f^* + \Delta \overline{\boldsymbol{v}}_f^*, \tag{17}$$

where $\overline{\boldsymbol{v}}_f^*$ and $\Delta \overline{\boldsymbol{v}}_f^*$ are the predictor term and the corrector them respectively. Based on the projection method. Eq. (7) can be separated as:

$$\overline{\boldsymbol{v}}_f^* = \overline{\boldsymbol{v}}_f^n + \frac{\varepsilon \Delta t}{C_r(\varepsilon)} \left(\boldsymbol{g} + \nu_E(\varepsilon) \nabla^2 \overline{\boldsymbol{v}}_f^n - \boldsymbol{\gamma}^n \right), \tag{18}$$

$$\Delta \overline{\boldsymbol{v}}_f^* = \frac{\varepsilon \Delta t}{C_r(\varepsilon)} \left(-\frac{1}{\rho_f} \nabla P^{n+1} \right), \tag{19}$$

where $\boldsymbol{\gamma}$ summatizes the resistance terms in Eq. (7) as follows:

$$\boldsymbol{\gamma}^n = \begin{cases} -a(\varepsilon) \varepsilon \boldsymbol{v}_r^n - b(\varepsilon) \varepsilon^2 \boldsymbol{v}_r^n |\boldsymbol{v}_r^n| & (\varepsilon < 0.8) \\ -\frac{3}{4} C_d \frac{(1-\varepsilon) \rho_f \boldsymbol{v}_r^n |\boldsymbol{v}_r^n|}{d_s} \varepsilon^{-2.7} & (\varepsilon \geq 0.8) \end{cases}. \tag{20}$$

The pressure P^{n+1} in Eq. (19) is determined by the Pressure Poisson Equation as follows:

$$\nabla^2 P^{n+1} = \frac{C_r(\varepsilon) \rho_f}{\varepsilon \Delta t} \nabla \cdot \overline{\boldsymbol{v}}_f^*. \tag{21}$$

These equation are calculated with the concept of ISPH method. The position of a particle is updated at the end of each time step.

However, the particle density may change slightly from the initial value because the numerical particle density is calculated from the distribution of particles in the particle method. To avoid this change, the relaxation term is added to the original Pressure Poisson Equation in the stabilized ISPH method proposed by M. Asai et al.. With this concept, the Pressure Poisson Equation (Eq. (21)) is modified as follows:

$$\langle \nabla^2 P^{n+1} \rangle \approx \frac{C_r(\varepsilon)}{\varepsilon} \left(\frac{\rho_f}{\Delta t} \langle \nabla \cdot \vec{\boldsymbol{v}}_f^* \rangle + \alpha \frac{\bar{\rho}_f^n - \langle \bar{\rho}_f^n \rangle}{\Delta t^2} \right), \tag{22}$$

where α is called as the relaxation coefficient and is generally set to be much less than 1. In this study, α is set to 0.01. The analysis with the stabilized ISPH method can get good conservation of volume.

3.4 The equation of motion of soil in fluid

In this study, the soil motion is analyzed by a spherical Discrete Element Method (DEM). In general, the contact detection is done every time step and a DEM particle moves by receiving the contact forces in DEM. In addition to that, the fluid force also acts on the DEM particles in the fluid domain. There some kinds of the fluid forces, however the all of them don't influence the particle's motion. In this study, the buoyancy force and drag force are adopted to the fluid forces, the equation of motion of soil in fluid is written as follows with the contact force:

$$m_s \frac{d\boldsymbol{v}_s}{dt} = m_s \boldsymbol{g} - \nabla P V_s + \boldsymbol{F}_d + \sum \boldsymbol{F}_c, \tag{23}$$

where m_s, $\boldsymbol{v}_s$ and V_s are the mass, the velocity and the volume of a soil particle respectively. The second and third terms in right side are the fluid forces, the second is the buoyancy force and the third $\boldsymbol{F}_d$ is the drag force. $\boldsymbol{F}_c$ means the contact force between DEM particles. The equation of angular motion for the spherical DEM is given by:

$$I \frac{d\boldsymbol{\omega}}{dt} = \sum \boldsymbol{T}, \tag{24}$$

where $\boldsymbol{\omega}$ and $\boldsymbol{T}$ are the angular velocity and torque of contact forces. I is the moment of inertia and given as a constant value for a sphere.

The contact force between the particles or particle-wall is calculated by the intrusion of a particle with a spring-dashpot model in DEM. The contact force $\boldsymbol{F}_c$ is divided into two components, a repulsive force in the normal direction $\boldsymbol{F}_c^n$ and a friction force in the tangential direction $\boldsymbol{F}_c^t$, and described as:

$$\boldsymbol{F}_c = \boldsymbol{F}_c^n + \boldsymbol{F}_c^t , \tag{25}$$

where the superscript n and t represent normal and tangential direction. The each force $\boldsymbol{F}_c^n$ and $\boldsymbol{F}_c^t$ is written as:

$$\boldsymbol{F}_c^n = (-k\delta^n - \eta |\boldsymbol{v}_r^n|)\boldsymbol{n} , \tag{26}$$

$$\boldsymbol{F}_c^t = \begin{cases} (-k\delta^n - \eta |\boldsymbol{v}_r^t|)\boldsymbol{t} & |\boldsymbol{F}_c^t| < \mu |\boldsymbol{F}_c^n| \\ -\mu |\boldsymbol{F}_c^n| \boldsymbol{t} & |\boldsymbol{F}_c^t| \geq \mu |\boldsymbol{F}_c^n| \end{cases}, \tag{27}$$

where k, δ, η, $\boldsymbol{n}$ and $\boldsymbol{t}$ are the stiffness, the displacement, the damping coefficient, normal and tangential unit vector. The damping coefficient η is given by

$$\eta = -2\ln(e) \sqrt{\frac{k}{\ln^2(e) + \pi^2} \frac{2m_i m_j}{m_i + m_j}} , \tag{28}$$

where e is the coefficient of restitution. The torque is calculated from the tangential contact force.

$$\sum \boldsymbol{T} = \sum \boldsymbol{l} \times \boldsymbol{F}_c^t , \tag{29}$$

where $\boldsymbol{l}$ indicates the vector from the center of a particle to a contact point.

The drag force $\boldsymbol{F}_d$ has the same meaning as the interaction force. Therefore, the resistance force for fluid is adopted to the drag force for soil. The drag force acting on one particle is given by:

$$\boldsymbol{F}_d = \begin{cases} a(\varepsilon)\varepsilon\boldsymbol{v}_r + b(\varepsilon)\varepsilon^2\boldsymbol{v}_r|\boldsymbol{v}_r|\frac{V_s}{1-\varepsilon} & (\varepsilon < 0.8) \\ \frac{3}{4}C_d\frac{(1-\varepsilon)\rho_f\boldsymbol{v}_r|\boldsymbol{v}_r|}{d_s}\varepsilon^{-2.7}\frac{V_s}{1-\varepsilon} & (\varepsilon \geq 0.8) \end{cases}, \tag{30}$$

where d_s means the diameter of a soil particle.

4 ANALYSIS

4.1 Validation test

As a validation test, water and glass beads dam break flow analysis is implemented. This is already experimented by Xiaosong Sun et al. [4], and the analysis is validated by comparing with the experimental result. In this experiment, the glass beads are sphere. The dimension of the tank is shown in Fig 3, and the water and glass beads are steady in the tank initially. At time t = 0, the gate is pulled up in a vertical direction with 0.68m/s and the water and glass beads start to move. The computational parameters are shown in Table. 1. Time increment in this analysis is 0.0001s.

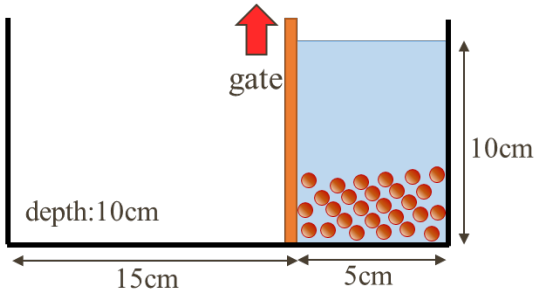

Figure 3: Analysis model of the dam break test

Table 1: Computational parameters

Fluid phase			
Particle number	Initial particle distance (cm)	Density (g/cm^3)	
13943	0.3	1.0	
Solid phase			
Particle number	Particle diameter (cm)	Density (g/cm^3)	Restitution coefficient
7920	0.3	2.5	0.9
Stiffness (N/m)		Friction coefficient	
1000		0.2	

As a qualitative comparison, the snapshots of analytical and experimental result are shown in Fig 4 for the instants of $t = 0.05$, 0.1, 0.15 and 0.2 sec. The analytical results show good agreement with the experiment.

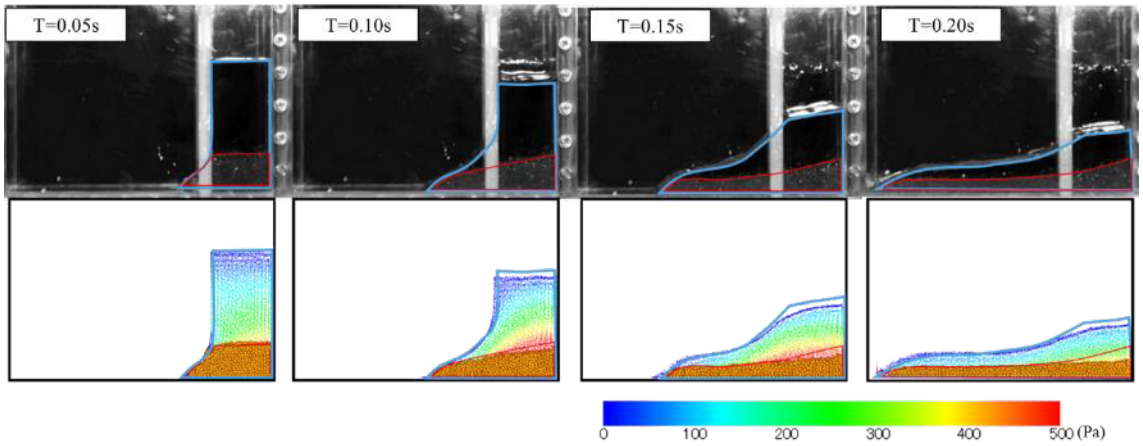

Figure 4: Comparison between experimental and analytical results
Blue and red lines highlights the water and glass beads domain respectively

As a quantitative comparison, the front position data of water and glass beads of the experiment measured by Xiaosong Sun et al. are compared with the analysis. The dimensionless number z^* and t^* are defined as by the tank size $a = 5cm$:

$$t^* = \mathrm{t}\sqrt{\frac{2g}{a}}, \tag{31}$$

$$z^* = \frac{z}{a}, \tag{32}$$

where z is the front positions of water and glass beads. The normalized positon of water and glass beads are plotted in Fig 5, the match between experiment and analysis for water and glass beads can be seen from it.

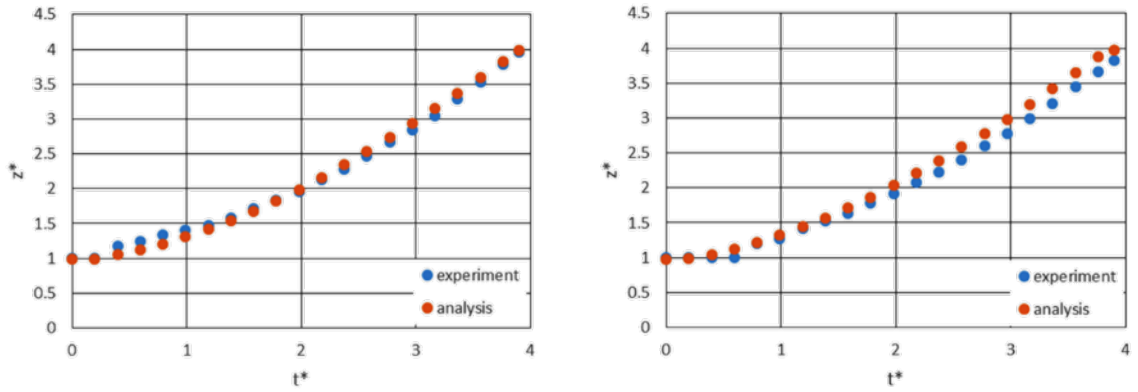

Figure 5: Comparison by the front position of water and glass beads

5 SCOURING AND PIPING ANALYSIS

The proposed SPH-DEM coupled method are validated by the dam break flow test. In this section, this method is applied to the scouring and seepage-induced piping analysis. In this

analysis, only the destruction of the mound is considered.

5.1 Validation test

In general, the breakwater mound is composed of soils, which moves individually. After the mound scouring is judged by our simulation result with the SPH method in the fluid domain, each soil's motion can be modeled by the DEM. However, the direct representation of the soil motion by the DEM induces high computational cost simulation in general. In this study, a macroscopic scouring and piping criterion are utilized to reduce the cost. The scouring and seepage-induced piping occur on the surface of the mound. Therefore, all the DEM particle is fixed in the original position, and only the surface soil DEM particle will be judged by the macroscopic empirical criterion. After the judgement of scouring and/or piping, the DEM soil particle will be moved by DEM manner. In this method, the number of analyzed DEM is much small and the cost is also lower. In addition, it is possible to distinguish whether the soil moves by the scouring of piping.

The criterion of the scouring is composed of active force F_a which moves the surface soil and resistance force F_r which is derived from friction force, if the active force is greater than the resistance force, the soil is judged as scoured.

$$F_a = \{\boldsymbol{F}_d + (\rho_s V_s \boldsymbol{g}) + \boldsymbol{F}_b\} \cdot \boldsymbol{t}, \tag{33}$$

$$F_r = \mu\{\boldsymbol{F}_d + (\rho_s V_s \boldsymbol{g}) + \boldsymbol{F}_b\} \cdot \boldsymbol{n}, \tag{34}$$

$$|F_a| > |F_r|. \tag{35}$$

The seepage-induced piping occurs when the hydraulic gradient defined as the gradient of the piezo water head excesses the critical hydraulic gradient. The hydraulic gradient $\boldsymbol{I}$ and the critical hydraulic gradient I_c can be calculated as follows:

$$\boldsymbol{I} = \frac{\nabla P}{\rho_f \boldsymbol{g}} + \nabla z, \tag{36}$$

$$I_c = \frac{G_s - 1}{1 + e}, \tag{37}$$

where z is the height from the arbitrary datum. G_s and e defined as $G_s = \rho_s/\rho_f$ and $e = \varepsilon/1 - \varepsilon$ respectively. However, the dimension of the hydraulic gradient and the critical hydraulic gradient are different. Therefore, the norm of the hydraulic gradient is utilized to compare these gradient. The criterion of the seepage-induced piping is given by:

$$|\boldsymbol{I}| > I_c. \tag{38}$$

However, this criterion can be applied to only a horizontal mound. The mound of the breakwater has the horizontal place but also the sloping place. Thus, the criterion of the piping is modified as:

$$|\boldsymbol{I}| > I_c n_y, \tag{39}$$

where n_y is the unit vector perpendicular to the slope.

5.2 Scouring and piping test

The analysis of the soil scouring and piping of the breakwater is done as a basic study. Here, the scouring and piping is analyzed individually.

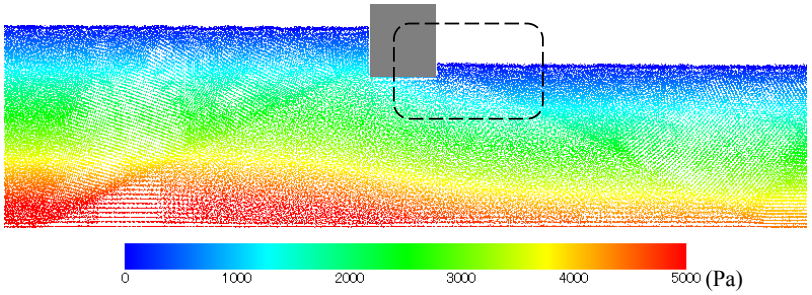

(a) Analysis result of water

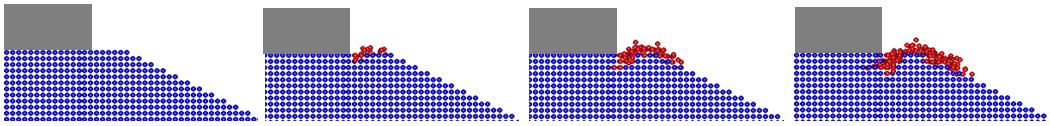

(b) Analysis result of soil
Judged particles are coloered red

Figure 6: The piping analysis result

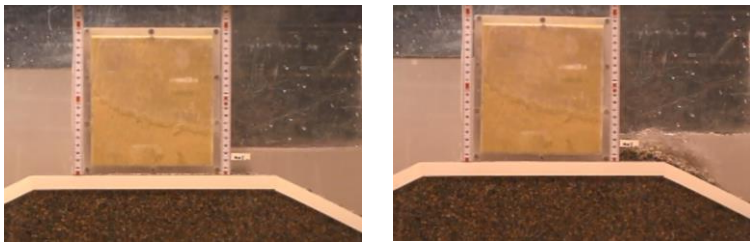

(a) Initial state (b) Piping occured

Figure 7: Snapshots of the piping experiment

At first, the piping analysis is shown in Fig 6. In this analysis, the seepage flow in the mound of breakwater occurs because of the water-level difference between the inside and outside of the port. From the soils' motion observed, this phenomena is similar to the experiment shown as Fig 7.

Next, the scouring analysis is shown in Fig 8 In this analysis, the soils are scoured along the flow.

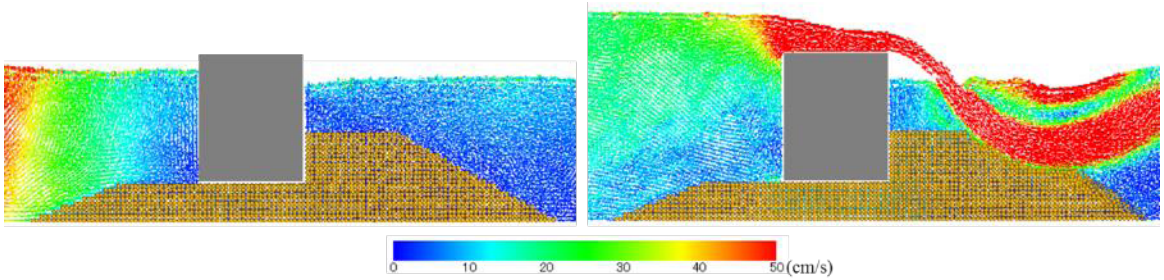

(a) Initial state (b) Piping occured

Figure 8: Analysis result of scouring

6 CONCLUSIONS

In this study, a SPH-DEM coupled method for the fluid-soil multiphase flow is developed to simulate the scouring and seepage-induced piping of breakwater. The interaction force between fluid and solid is considered to couple the SPH method for the fluid analysis and DEM for solid analysis, the unified governing equation including the interaction force based on Akbari and Wen and Yu is adopted for the fluid. For solid analysis, the interaction force is considered as the drag force. The water and glass beads dam break flow is analyzed to validate this method, and it shows a good agreement with experimental data. For scouring and seepage-induced piping, the criterion to estimate them is proposed. A good tendency is given from simple scouring and piping analysis. As the future works, a validation test will be conducted with experiment, finally this method would be expanded to simulate the collapse of a breakwater by Tsunami.

REFERENCES

[1] M. Asai, Aly, AM., Y. Sonoda and Y. Sakai, A stabilized incompressible SPH method by relaxing the density invariance condition, *Int. J. for Applied Mathematics*, Vol. 2012, Article ID 139583, 2012.

[2] Akbari, H., Modified moving particle method for modeling wave interaction with multi layered porous structures, *Coast. Eng*., Vol.89, pp.1-19, 2014.

[3] C. Wen. and Y. Yu., Mechanics of fluidization, *Chemical Engineering Progress Symposium Series 62*, 100, 1966.

[4] Xiaosong Sun, Mikio Sakai and Yoshinori Yamada, Three-dimensional simulation of a solid-liquid flow by the DEM-SPH method, *Journal of Computational Physics,* Vol.248, p.147-176, 2013.

Accelerated Heat Transfer Simulations Using Coupled CFD and DEM

Marina Sousani*, Andrew M. Hobbs[1], Adam Anderson[2], Richard Wood*

* DEM Solutions LTD, 49 Queen Street, Edinburgh, EH2 3NH
e-mail: marina.sousani@edemsimulation.com, web page: http://www.edemsimulation.com/

[1]Astec, Inc.
4101 Jerome Ave. Chattanooga, Tennessee, 37407, USA
e-mail: ahobbs@astecinc.com, web page: http://www.astecinc.com

[2]ANSYS UK Ltd.
Sheffield Business Park, 6 Europa View, Sheffield, S9 1XH, UK
e-mail: adam.anderson@ansys.com

Abstract

This work presents an accelerated simulation of heat and mass transfer by coupling Discrete Element Methodologies (DEMs) and Computational Fluid Dynamics (CFD), utilising Graphics Processing Unit (GPU) technology. The presented model is a continuation of previous work[1] and focuses on demonstrating the capabilities and effectiveness of implementing the GPU combined with the Central Processing Unit (CPUs) technologies to run a complex industrial simulation. A model of an aggregate drum dryer was used to produce hot mix asphalt and different configurations have been implemented to investigate the effect of GPU-CPU technology in such a complex simulation. Commercial codes from ANSYS and DEM-Solutions were coupled to simulate heat transfer from the hot gases to the aggregate particles. Fluid flow and particle-fluid interactions are solved by the CFD solver which exchanges information at regular intervals. The results showed that the coupled model captures accurately the convective heat transfer from the fluid to the solid phase and demonstrated significant improvement in terms of simulation time. The proposed model will have a significant impact in industrial applications as it describes a methodology to simulate large-scale applications rapidly and accurately.

Keywords: coupled DEM and CFD; GPU; aggregate dryer; heat and mass transfer

Introduction

Particle simulations have been well established as a means to model complex physical systems in a number of fields and are becoming increasingly more important in others. Much research has been done in a variety of areas such as molecular dynamics, plasma physics, fluid dynamics and rock mechanics [2-4], where particle simulations were coupled with Computational Fluid Dynamics (CFD)[5]. The Oil and Gas industries have been using CFD software for many years to model fluid behaviour in reservoirs, saturation of residual oil, well performance, fluidisation, sedimentation and others [6-11]. Lately the ability to simulate larger number of particles, especially for applications where particle-particle interaction and particles of different shape must be considered, has given a boost to the demand for more coupled DEM-CFD simulations.

Recently this type of modelling shows an increasing interest in the process manufacturing industry too. Hot mix asphalt (HMA) is the most common pavement surface in the U.S., which comprises around 94% of all roads. It is also increasingly popular in airport runways in the U.S. due to its efficiency on takeoffs and landings, its low maintenance and fast construction time. It has been approved by the

Environmental Protection Agency (EPA) and is thus considered a practical solution for water storage, flood control, erosion and hazardous-waste landfills worldwide [12-14]. HMA is a composite material that consists of mineral aggregates (sand and various sizes of crushed rock) mixed together with liquid asphalt cement binder (a product of crude oil), laid in layers and compacted. For an efficient mixing process, the asphalt binder must be heated at temperatures above 180ºC, to decrease its viscosity, and the aggregate must be dried prior to mixing [13]. Most aggregate is stored in stockpiles where the minimum moisture content will be that of the ambient air. A typical value for aggregate moisture content is 5% by mass meaning that for a nominal production rate of 320,000 kg/h of mix, 15,875 kg/h of H_2O must be removed. Typically, half of the total heat input is required to dry the aggregate making drying efficiency of critical importance [1].

The aggregate drying process is accomplished in a counter flow drum that is positioned on a 4.7º inclination and contains internal metal slats (flights). The drum is heated by a direct fire burner and the flights lift and veil the aggregate material through the hot gases to heat and dry the aggregate particles. Wet aggregate is fed into the uphill end and is moved along the drum towards the burner (Figure 1).

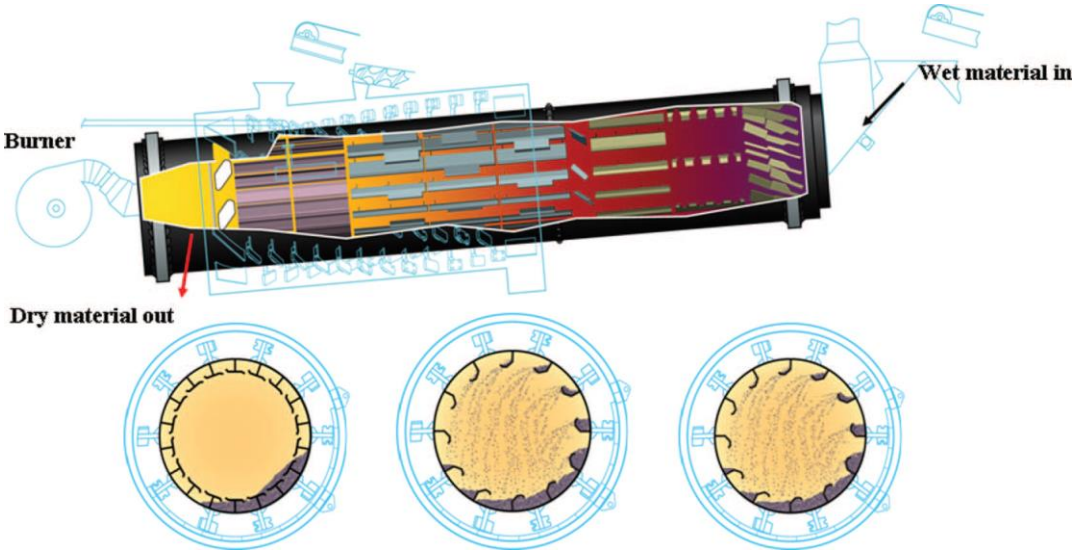

Figure 1 *Schematic of the Counter-flow aggregate dryer drum. Hobbs (2009).*

A key challenge associated with this process is the fact that veiling performance is tied to many different variables including flight shape, number of flights, drum rotational speed, and fill level. At the same time, direct observation of this phenomenon is impossible due to the harsh internal environment of the drum. Part of the aim of this work is to propose a methodology that enables not only the monitoring of the material's behaviour but the optimization of the flight design for increased drying efficiency. Furthermore, this paper presents an innovative way of accelerating such demanding simulations by performing DEM calculations in GPU mode while solving for the fluid in CPU mode.

Numerical methods

CFD is a very popular method amongst researchers that simulates fluid phenomena and provides qualitative prediction of fluid flows. A first appearance of CFD methods dates back to 1947 from the work of Kopal (1947) of supersonic flows on sharp cones and the first generation of CFD solutions the period between the 1950s and early 1960s [16-19]. Since then, the role of CFD in engineering predictions has been so strong that nowadays is considered a standard aspect in fluid dynamics, beyond the experimental and theoretical elements. A wide range of industrial applications employ CFD methods to study critical fluid phenomena and enhance their operations [1, 20-23]. There are commercial

software that have been used for modelling multiphase, combustion and heat transfer for particle flows including densely packed systems such as fluidized bed reactors. However, in some applications it is critical to account for the shape and the particle-particle interactions of the granular material, to provide a meaningful insight.

DEM is a method that describes the overall (macroscopic) mechanical behaviour of assemblies of particle systems as the result of the interaction of their constitutive individual elements. It allows displacements, rotations and complete separation of the discrete elements, and recognizes any new contacts that are developed during the simulation [24, 25]. Initially models, which were based on the particle-scale, were developed in order to simulate the micromechanical behaviour of soils and sands (non-cohesive materials) [26], but since then it has been widely utilised in a number of studies. DEM has been applied in several engineering fields, such as slope stability and mining to powder technology, minerals and process manufacturing [3, 4, 27-32], and is considered a very efficient engineering tool.

In nature particles rarely operate within systems that are fluid free, hence there is a need for a simulation methodology that can capture both the solid and the fluid mechanisms as well as the interaction between the two. Researchers have worked towards combining CFD techniques with the Newtonian particle methods used in DEM. Approaches that incorporate CFD with the DEM have been presented by Tsuji (1993), Tsuji (2008) and Xu and Yu (1997), where the interaction between the solid and gas phases have been modelled by solving Newton's second law of motion, with respect to the motion of the particles, and the Navier-Stokes equation with respect to the motion of the gas. However, the majority of the CFD-DEM approaches involve in-house codes making them inaccessible and expensive to industry. This paper presents an improved version of an existing commercial product that couples the CFD solver (ANSYS Fluent) with the DEM solver (EDEM) from DEM Solutions. The EDEM-CFD coupling is employed to simulate heat transfer from a reacting natural gas flame to the particle phase in an aggregate dryer.

Moreover, complex industrial applications that involve hundreds of thousands of particles are so computationally expensive that not even the most efficient couplings are able to support. This paper presents an innovative way of accelerating computationally intensive workloads by performing DEM calculations in GPU mode while solving for the fluid in CPU mode. The presented solver provides greatly reduced computational times compared to simulations on multi-core CPUs. This process has been performed with the use of the EDEM GPU solver engine, which has been created by DEM Solutions.

DEM – CFD Coupling Methodology

CFD

In previous work [1] particle positions and interactions were solved by the DEM solver, whereas the volume fraction, drag, and heat transfer were calculated by the coupling interface between the solvers. This required significant computation outside of the solvers making this approach less efficient for simulations that required large number of particles. Advantage has now been taken of developments in Fluent since the previous coupling and the latest Fluent solver presents a more sophisticated approach. Specifically, in the new Dense Discrete Phase Model (DDPM) coupling the EDEM particle data are converted into a Discrete Phase Model (DPM) injection and the volume fraction, drag, and heat transfer are calculated directly by Fluent, making for a more efficient calculation.

The volume fraction (the space occupied by each phase), in any given fluid cell, is calculated through an algorithm that utilises an octree method and detects those cells containing particles during the simulation. The flow of the fluid, around the particles, is then determined by the continuous phase flow while taken into account the blockage from the solid phase. Here, the volume fraction represents the space occupied by each phase, thus the laws of conservation of mass and momentum are satisfied by

each phase individually. The mass and momentum conservation equations for the particle phase p are given by:

$$\frac{\partial}{\partial t}(\alpha_p \rho_p) + \nabla \cdot (\alpha_p \rho_p \vec{V}_p) = \sum_{q=1}^{nphases} (\dot{m}_{fp} - \dot{m}_{pf}) \tag{1}$$

where subscripts p and f refer to the solid and fluid phase, respecively α_p is the volume fraction, ρ_p is the density of the individual phase, $\vec{V}_p$ is the velocity of the p phase and $\dot{m}_{pf}$ is the mass transfer from the p^{th} to f^{th} phase, respectively. Similarly, the momentum conservation equation for the solid phase is given by:

$$\begin{aligned} \frac{\partial}{\partial t}(\alpha_p \rho_p \vec{V}_p) + \nabla \cdot (\alpha_p \rho_p \vec{V}_p \vec{V}_p) \\ = -\alpha_p \nabla_p + \nabla \cdot \left[\alpha_p \mu_p \left(\nabla_{\vec{V}_p} + \nabla_{\vec{V}_p^T}\right)\right] + \alpha_p \rho_p \vec{g} + F_{vm,lift,user} \\ + \sum_{q=1}^{nphases} \left(\vec{K}_{pf}(\vec{V}_p - \vec{V}_f) + \dot{m}_{fp} \vec{V}_{fp} - \dot{m}_{pf} \vec{V}_{pf}\right) \\ + \vec{K}_{DPM}(\vec{V}_{DPM} - \vec{V}_p) + S_{DPM,explicit} \end{aligned} \tag{2}$$

where μ_p is the shear viscosity of the particle phase p, $\vec{K}_{fp}$ is the interphase momentum exchange coefficient between the fluid and particle phases, $F_{vm,lift,user}$ is a lift force (due to velocity gradients in the primary phase flow field), $\vec{V}_p$ and $\vec{V}_f$ are the particle and fluid velocities, respectively. $\vec{V}_{fp}$ is the interphase velocity and is dependent upon the mass transfer $\dot{m}_{fp}$. $S_{DPM,explicit}$ is the explicit component of the particle sink term, and $\vec{V}_{DPM}$ and $\vec{K}_{DPM}$ are the implicit terms of the particle averaged velocity of the considered discrete phase and interphase momentum exchange coefficient, respectively. Note that the equivalent mass/momentum conservation equations for the fluid phase follow the same logic.

The fluid-solid drag function follows the Gidaspow model [36] and is a combination of the Wen and Yu model [37] and the Ergun relation [38]. When the volume fraction, α_p is greater than 0.8 then the Wen-Yu equation is used, whereas when the volume fraction is less than 0.8 the Ergun relation is used [39]. Relevant modifications have been made by ANSYS for the Ergun relation (Eq.4). The fluid-solid exchange coefficient is given by:

α_p>0.8

$$K_{sl} = \frac{3}{4} C_D \frac{\alpha_S \alpha_f \rho_f |\vec{v}_f - \vec{v}_p|}{d_p} \alpha_l^{-2.65} \tag{3}$$

α_p<0.8

$$K_{sl} = 150 \frac{(1-\alpha_f)^2 \mu_f}{\alpha_p d_p^2} + 1.75(1-\alpha_f) \frac{\rho_f}{d_p} |\vec{v}_f - \vec{v}_p| \tag{4}$$

where C_D is the drag coefficient, d_p is the diameter of the particles in the solid phase, α_p and α_f are the volume fractions of the solid and fluid phases, respectively, and Re_s is the Reynold's number at the terminal settling condition for a single particle and is expressed as:

$$Re_s = \frac{\rho_f d_p |\vec{v}_p - \vec{v}_f|}{\mu_f} \tag{6}$$

where $\rho_f$and μ_f are the fluid density and the dynamic viscosity, respectively.

The drag coefficient C_D is directly dependent on the Reynolds number and it uses the following criteria:

$$C_D = \begin{cases} 24/Re_s & R_e < 0.55 \\ 24(1.0 + 0.15{Re_s}^{0.687})/Re_s & 0.55 < R_e \leq 1000 \\ 0.44 & R_e > 1000 \end{cases} \quad (7)$$

For the transfer of the DEM particle phase into a DPM injection, Fluent first checks the coordinates of each DEM particle with the fluid cells positions and applies the effects of the particle to the cell that is found to contain it. However, since the particle may overlap more than one fluid cell, a Node Based Averaging (NBA) algorithm is used to smooth the loading, distributing the particle's effects to neighbouring mesh nodes. This reduces grid dependency and computational instability by spreading the particle's effects smoother across the neighbouring cells.

Furthermore, as particles move through the fluid, thermal energy is also exchanged. The temperature change of each particle over time is calculated based on Equation (8). The summation of the convective and conductive heat fluxes [40] is given by:

$$m_P C_P \frac{dT}{dt} = \sum Q_{heat} \quad (8)$$

where m_P, C_P, and T are the mass, specific heat and temperature of the particle material, respectively.

$$\sum Q_{heat} = Q_{PF} + Q_{P1P2} \quad (9)$$

$$Q_{PF} = h_{PF} A_p \Delta T_{PF} \quad (10)$$

$$Q_{P1P2} = h_c \Delta T_{P1P2} \quad (11)$$

$$h_c = \frac{4k_{P1}k_{P2}}{k_{P1} + k_{P2}} \left(\frac{3F_N r^*}{4E^*}\right)^{1/3} \quad (12)$$

$$h_{PF} = \frac{k_F N_u}{d_p} \quad (13)$$

where, h_{PF} is the convective fluid-particle heat transfer coefficient, A_p is the particle surface area, ΔT_{PF} is the temperature difference between the fluid and the particles and Q_{P1P2} is the inter-particle heat flux, respectively. h_c is the conductive heat transfer coefficient between two particles and ΔT_{P1P2} is their temperature difference, k_P is the thermal conductivity of the particles, F_N is their normal force, r^* is the geometric mean of the particles radii and E^* is the effective Young's modulus. The bracketed term of the equation models the contact area between two particles. Finally, K_F is the gas thermal conductivity of the fluid, N_u is the Nusselt number, and d_p is the particle diameter. The presented model does not consider conductive heat transfer from the particles to the geometry.

The Nusselt number has been computed based on the results from Ranz and Marshall (1952) for R_e<200. Detailed information regarding the process can be found in Hobbs (2009). The Nusselt number is given by:

$$N_u = 2 + 0.6{R_e}^{1/2} Pr^{1/3} \qquad R_e < 200 \quad (14)$$

$$Pr = \frac{C\mu}{k} \tag{15}$$

where R_e is the Reynold's number based on the diameter of the individual phase and the relative velocity $|\vec{u}_p - \vec{u}_f|$ and the Pr is the Prandtl number for the subsequent phase.

DEM

In DEM simulations, the main computational challenge is the detection of contacts. To address this EDEM uses an algorithm that utilises a Cartesian grid to search for particle contacts. In particular, the domain is divided into grid cells of specified size, then the algorithm checks every cell but only analyses those that contain two or more elements (active cells). The idealized length of a grid cell is 2-6Rmin where R_{min} is the minimum particle radius in the simulation. This reduces the simulation time significantly, while the results remain unaffected by the number of grid cells. Furthermore, the EDEM solver utilises the Hertz–Mindlin contact model [42-44] to solve the contact forces (normal and tangential) between particles, including damping coefficients. For each identified contact the resultant force is calculated taking into consideration the body forces. Particle velocities and new positions, as a result of the forces acting on them, are updated using an explicit time marching scheme. The DEM detection algorithm and calculation cycle are shown in Figure 2(a) and (b), respectively.

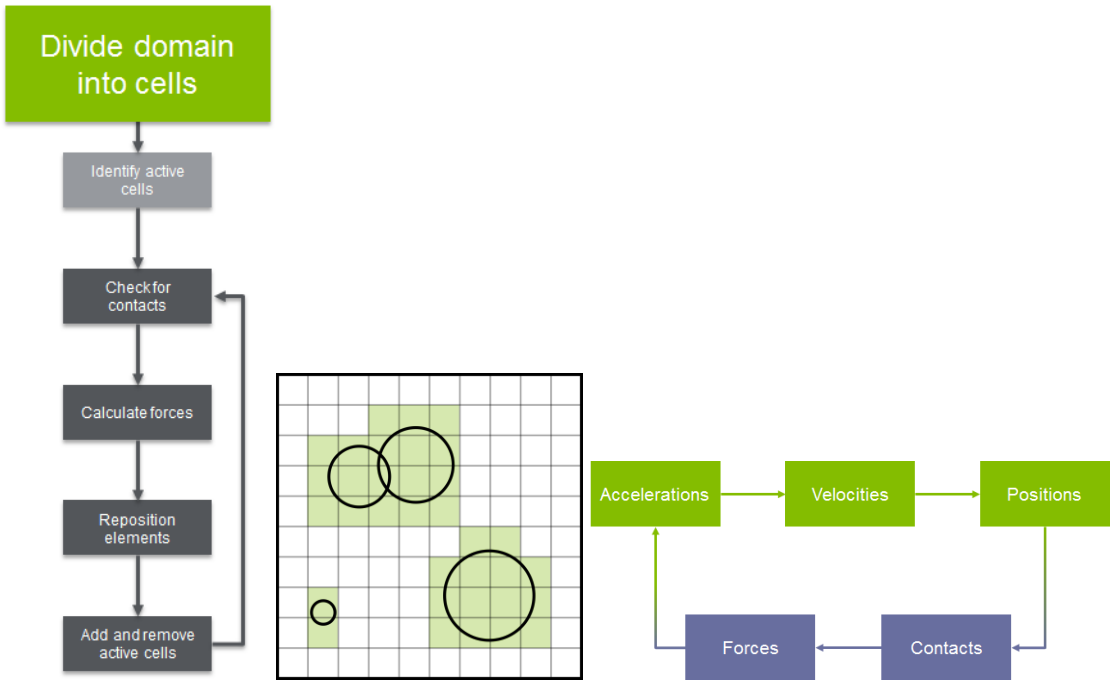

Figure 2 *Schematic of the detection algorithm steps applied on a representative 2D cell grid and the calculation cycle used in the DEM.*

Choosing the right time-step is critical when reducing the simulation time. In EDEM a time-step is chosen as a percentage of the Rayleigh time-step value, which refers to the time taken for a shear wave to propagate through a solid particle, and it is calculated based on the smallest particle of the simulation. The normal range is between 10-40% of the Raleigh time-step and is given by the following equation:

$$T_R = \frac{\pi R \left(\frac{\rho}{G}\right)^{1/2}}{(0.1631v + 0.8766)} \tag{16}$$

where R is the particle radius, ρ the particle density, G the shear modulus and v is the Poisson's ratio.

Figure 3(a) and (b) describe the full coupling methodology and sequence of actions between the two software. EDEM provides a Coupling Interface that includes all the relevant functions that exchange information with Fluent, while Fluent EdemUDF is a user defined function that is loaded into Fluent and handles all drag and heat transfer calculations. Specifically, after setting up the DEM model, EDEM calculates the particles positions and velocities and the DEM-CFD coupling initiates in which the Fluent UDF updates the particle properties taken from EDEM and converts them such that they are passed into Fluent. The latter calculates the volume fraction, drag forces and heat transfer, which are then passed back into EDEM through the UDF and the coupling interface. In general, the DEM time-step tends to be smaller than in CFD and can have a difference between 10 to 1000 times. Therefore, EDEM performs the necessary iterations in order to catch up with the next Fluent time-step and UDF repeats its calculations while passing the data back to Fluent.

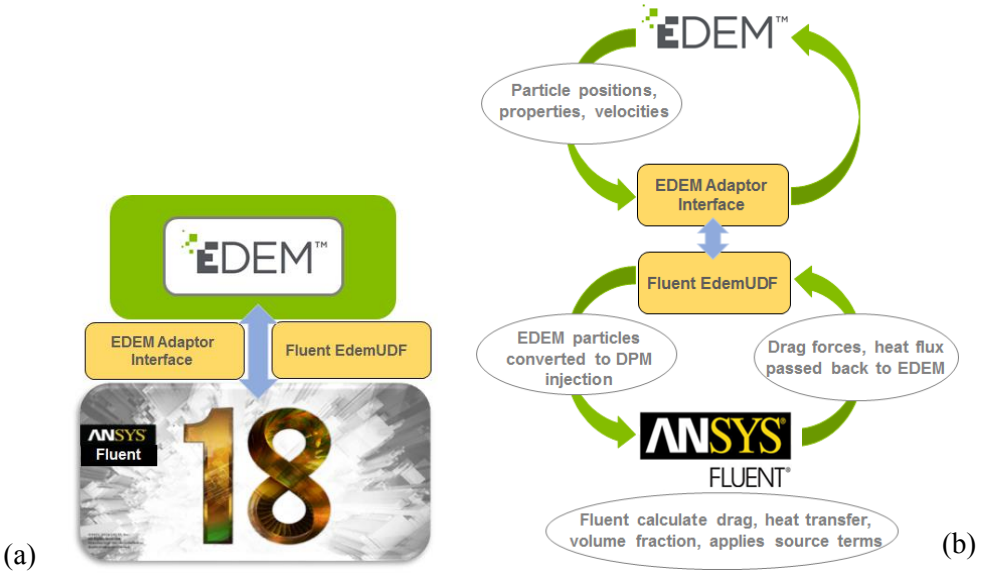

Figure 3 *Schematic of the EDEM-Fluent coupling logic.*

GPU Technology

This project presents an innovative way of accelerating large scale industrial simulations by performing DEM calculations in GPU mode while calculating fluid flow in CPU mode. The EDEM GPU solver provides higher clock speeds compared to simulations on multi-core CPUs.

The presented work has been performed with the use of the EDEM GPU solver engine, created and distributed by DEM Solutions LTD. The EDEM GPU simulation engine uses the Open Computing Language (OpenCL) [45] in combination with the AMD Radeon R9 Fury X graphics card for increased accuracy. OpenCL is an open industry language for general purpose parallel programming across CPUs, GPUs and other processors, that gives complete freedom to users. For example, using OpenCL allows a programmer to write general purpose programs that execute on GPUs without the need to map their algorithms onto a specific vendor's 3D graphics API. Finally, OpenCL creates an efficient programming interface, consisting of an API for coordinating parallel computation across heterogeneous processors, and a cross-platform intermediate language with a well specified computation environment.

Different parallel programming tools exist but the major advantage of using OpenCL is the fact that it fully supports all graphic cards, without tying the DEM user to a single GPU vendor. For example NVIDIA [46] is restricted in using CUDA [47], while OpenCL encapsulates NVIDIA, AMD, Intel Xeon Phi as well as CPUs under a common programming environment. The execution speed and accuracy of arithmetic operations in a computing unit is directly related to the precisión used. Most

computers use the floating-point format, which is an internal representation of numeric values stored in computer memory. This format can be categorized into the single and double precision, where the former requires 4 bytes (32 bits) and the latter 8 bytes (64bits). Even though increasing the number of bits results in increased accuracy, double precision models have much higher memory requirements. Thus, it is critical to select a fitting precision type for a specific application, so that a practical balance between accuracy and simulation time/memory is maintained. The presented results for both graphic cards used single precision.

The presented work uses both the EDEM GPU and CPU solver engines and has been repeated multiple times under different configurations but only selected combinations will be presented herein. The set of simulations, shown in Table 1, used 4CPU cores for the Fluent and 30, 40 CPU cores for EDEM, respectively. Moreover, the same simulation was repeated twice by using the EDEM GPU solver engine with single precision and two different graphics cards; the AMD Radeon R9 Fury X and the NVIDIA Quadro GP100.

Table 1 Configuration combinations for the coupled simulation with the use of the AMD Radeon R9 Fury X and the NVIDIA Quadro GP100 graphic cards.

CPU mode	**GPU mode**	
	AMD Radeon R9 Fury X	**NVIDIA Quadro GP100**
4 Fluent/30 EDEM	4 Fluent/4 EDEM	4 Fluent/4 EDEM
4 Fluent/40 EDEM		

Simulation setup

For this simulation the same geometry and similar setup has been used as presented in Hobbs (2009). Figure 4 demonstrates the 3D model of the aggregate dryer with its internal features (conveying screw flights, veiling flights, combustion flights). A CFD tetrahedral mesh was created by removing all the internal features and preserving mesh density in the burner and combustions zones, whereas a less dense mesh was used in the rest of the geometry.

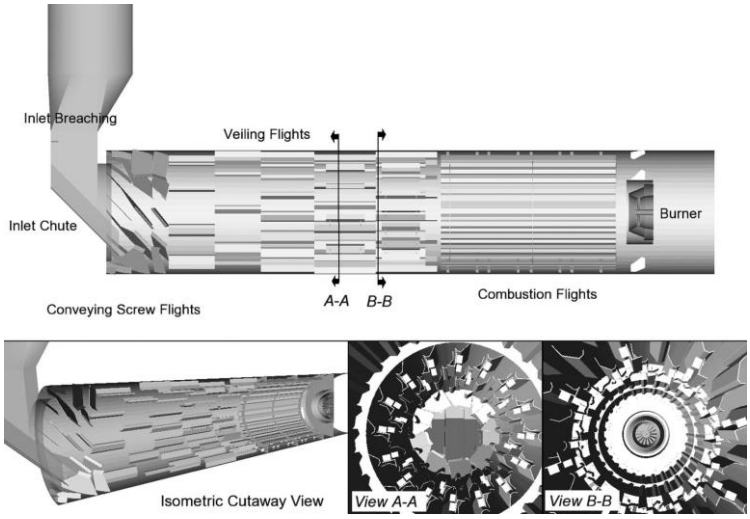

Figure 4 *CAD geometry of the aggregate dryer used for the coupled DEM-CFD simulation [1].*

The full set of the CFD input simulation parameters are shown in Table 2.

Table 2 CFD Input parameters

CFD Input parameters	
Type of fluid	Air
Fluid density (kg/m^3)	1.225
Fluid viscosity (Pa·s)	1.789E-05
Turbulence model	Standard k-ε
CFD cell type	Hybrid tetrahedral hexahedral
Cell number	7.2E+05
CFD time-step (sec)	0.02

The complete 3D drum dryer model was also imported into EDEM. A factory was defined that generated 539.942 discrete elements, comprised of bi-sphered particles of the same size, with a normal distribution and an initial temperature of 300K. The simulated results refer to 1 second of real physical time, after it had reached a quasi-static condition (100sec of run time). A number of trials were performed to determine the optimum time-step and simulating parameters, such as the cell size of the simulator grid. The full set of EDEM inputs are shown in Table 3.

Table 3 EDEM Input parameters

EDEM Input parameters	
Physics	Hertz-Mindlin contact model
Particle density (kg/m^3)	2900
Particle diameter (mm)	18
Particle Shear modulus (Pa)	1.38E+07
Particle Poisson's ratio	0.25
Geometry density (kg/m^3)	7800
Geometry Shear modulus (Pa)	7.50e+07
Geometry Poisson's ratio	0.30
Particle-Particle coefficient of restitution	0.45
Particle-Particle static friction coefficient	0.55
Particle-Particle rolling friction coefficient	0.05
Particle-Geometry coefficient of restitution	0.50
Particle-Geometry static friction coefficient	0.45
Particle-Geometry rolling coefficient	0.05
Particle generation rate (kg/sec)	80.64
EDEM time-step (sec)	1E-04
Cell size (mm)	31.49

Results and discussion

To post-process the CFD-DEM results, Ensight from CEI and EDEM Analyst were used. Figure 5 shows a side view of the aggregate dryer that demonstrates the swirling flow and the fluid-particle temperature distributions ranking 300-3000K and 300-1000K, respectively. The figure also includes

cross sections of the drum at specified points (A,B,C) showing the convective heat transfer. It can be observed that the neighbouring to the burner particles have higher temperatures and the fluid temperature is almost a 3-step decrease of flow. This indicates that as the particles are showered through the hot gases, thermal energy is exchanged and the heat is transferred from the fluid to the particles thus the fluid temperature drops. This particle-fluid behaviour is in very good agreement with the actual observations, validating the model.

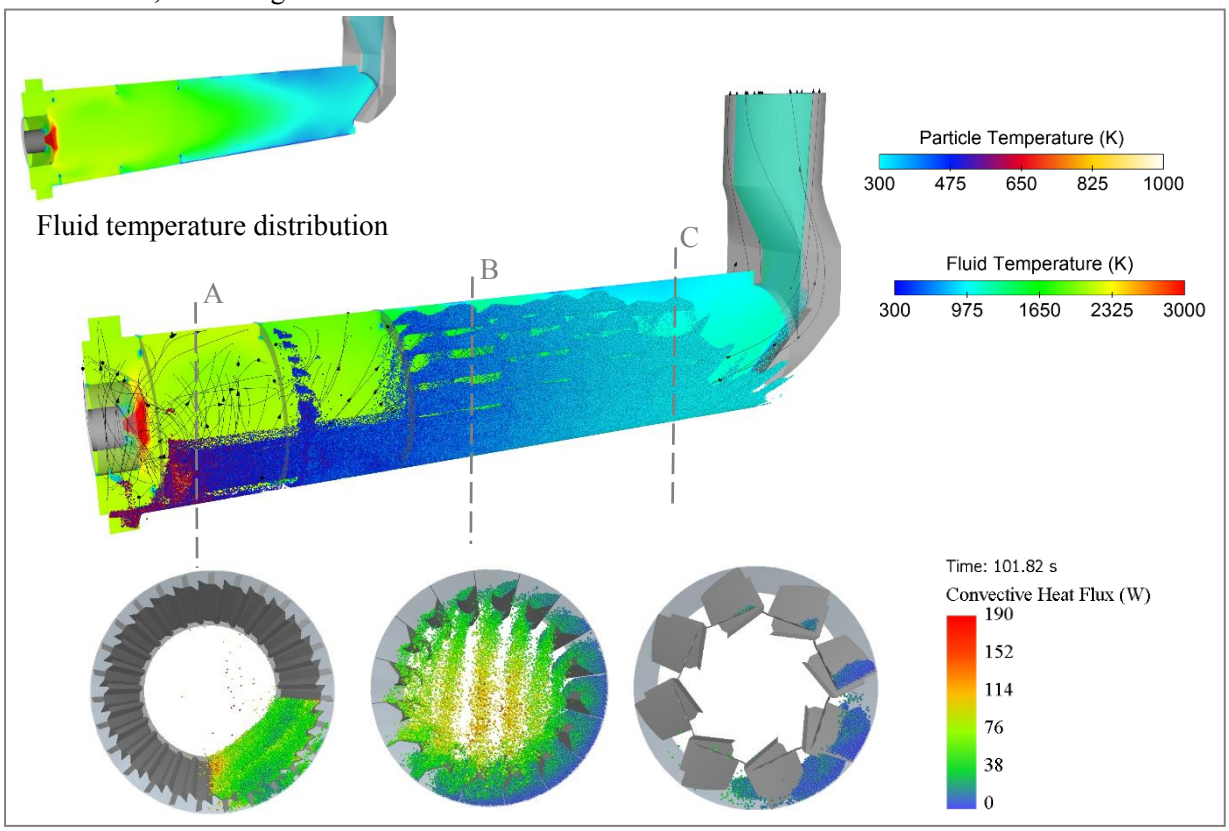

Figure 5 *Coupled CFD-DEM simulation of an aggregate dryer demonstrating the fluid - particle temperature distribution.*

Figure 6 demonstrates an inside view of the heat transfer from the fluid phase to the particle phase. It can be observed that the convective heat flux reaches a max value of around 190W and the simulated model accurately captures the dynamic state of the heat transfer along the length of the drum.

The following figures illustrate the net computational time, under different configurations, for both the EDEM/Fluent coupling and the EDEM part of the simulation. Some representative configurations have been selected for discussion. Figure 7 demonstrates the total computational time of the coupled simulation with and without the GPU solver. Specifically, the selected simulation results in CPU mode (grey columns) used 8, 12 and 32CPU cores for the Fluent part of the simulation and 30 or 40CPU cores for the corresponding EDEM part, respectively. It can be observed that in the first case the simulation took around 1.5 hours, while the simulation times dropped to 1.43 and 1.33 hours, respectively. This shows that even though a large number of cores have been selected, the overall simulation time is only slightly reduced. In contrast, the same simulation run in GPU mode with the use of the AMD Radeon R9 Fury X or the NIVIDIA Quadro GP100 graphic cards leads to reduced simulation times of 1.07 hours and 57minutes, respectively. This means that the NVIDIA Quadro GP100 simulation was 1.5 times faster on average, resulting in an average reduction time of 32%.

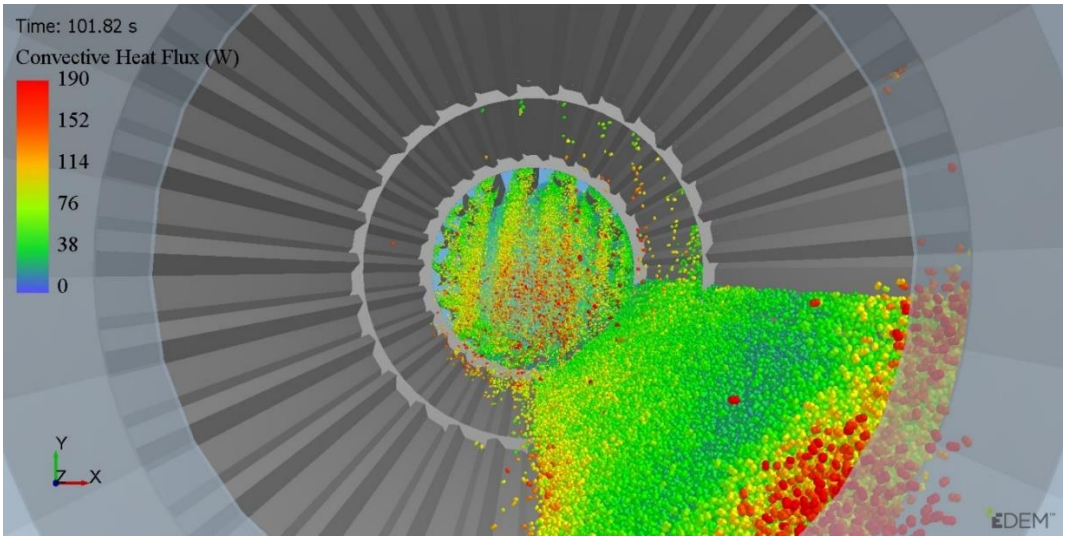

Figure 6 *Particle temperature distribution. Cross sections at the regions close to the burner (A), in the middle of the drum (B), and towards the inlet of the chute (C).*

Figure 8 follows the same logic as Figure 7 demonstrating the net computational time of the aforementioned configurations including only the EDEM part of the simulation. The grey columns show that it took between 39 and 39.25min to simulate the discrete phase for the 30 CPU (for EDEM) configuration and 38.88min for the 40 CPU (for EDEM) configuration. The selected configurations show a minor difference in terms of simulation time, whereas the same simulation took just over 6mins when run in GPU mode (orange column). This corresponds to an average 6.0 speed up demonstrating an average time reduction of 83% for the discrete calculations.

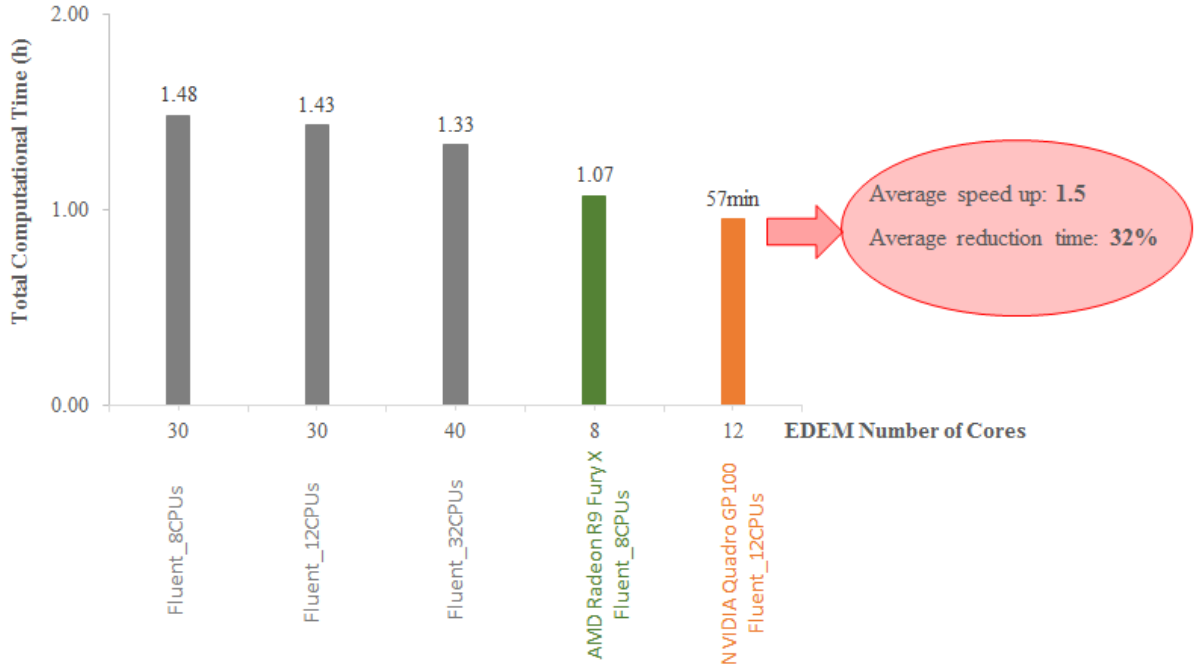

Figure 7 *Net computational time of the coupled simulation under different configurations in CPU mode (grey columns) using the AMD Radeon R9 Fury X graphic card (green), and using the NVIDIA Quadro GP100 (orange).*

Figure 8 *EDEM computational time of the coupled simulation under different configurations in CPU mode (grey columns) using the AMD Radeon R9 Fury X graphic card (green), and using the NVIDIA Quadro GP100 (orange).*

Conclusions

Many industrial applications involve discrete particle flows. Due to their transient nature, they often require extensive computational times and recalculation of the relevant particle physics, which makes such analyses impractical. Until recently the only option to run such simulations was the use of CPU technologies which put a barrier between efficiency and fast results. The current work demonstrates the capabilities and effectiveness of implementing an innovative GPU solver combined with multiple CPU cores to run a complex industrial simulation that models heat transfer within an aggregate drum dryer. The ANSYS Fluent CFD solver has being coupled with EDEM and run with and without the EDEM GPU solver engine.

The results show that the coupled model not only accurately captures the particle-fluid behaviour and the convective heat transfer between the two, but also features very fast simulation run times. With the use of one of the latest GPU graphic cards (NVIDIA Quadro GP100), the net computational time of the coupled DEM-CFD simulation was reduced by 32% corresponding to a 1.5 speed up. Furthermore, the DEM part of the simulation experienced the greatest reduction in computational time with a net computational time reduction of 83%, making the particle calculations 6.0 times faster. More simulations were run with less CPU cores, for both Fluent and EDEM, and the results showed even larger speed ups and time reductions. This indicates that the GPU technology could be very beneficial in cases where less powerful workstations are used for such simulations.

This work highlights the significance of using GPU technology for challenging coupled CFD-DEM calculations. This kind of analysis was previously difficult or even impossible to perform and thus has a major impact in large-scale industrial applications that require simulations of millions of particles.

References

1. Hobbs, A., *Simulation of an aggregate dryer using coupled CFD and DEM methods.* International Journal of Computational Fluid Dynamics, 2009. **23**(2): p. 199-207, http://dx.doi.org/10.1080/10618560802680971.

2. Hockney, R.W., *Computer Simulations Uning Particles*. 2nd ed. 1981, New-York: Routledge.

3. Donzé, F.V., V. Richefeu, and S.-A. Magnier, *Advances in discrete element method applied to soil, rock and concrete mechanics.* Electron J Geotech Eng, 2009. **8**: p. 1-44.

4. Stefanou, I. and I. Vardoulakis. *Stability assessment of SE/E rock corner slope of the Acropolis Hill in Athens*. in *5th GRACM International Congress on Computational Mechanics*. 2005.

5. Date, A.W., *Introduction to computational fluid dynamics*. 2005: Cambridge University Press.

6. Byrne, M.T., et al., *Computational Fluid Dynamics for Reservoir and Well Fluid Flow Performance Modelling*, in *SPE European Formation Damage Conference*. 2011, Society of Petroleum Engineers: Noordwijk, The Netherlands.

7. Wang, S., et al., *Simulation of Flow Behavior of Particles in a Liquid−Solid Fluidized Bed.* Industrial & Engineering Chemistry Research, 2010. **49**(20): p. 10116-10124, http://dx.doi.org/10.1021/ie101139h.

8. Qiu, L.-c. and C.-y. Wu, *A hybrid DEM/CFD approach for solid-liquid flows.* Journal of Hydrodynamics, 2014. **26**(1): p. 19-25, http://www.sciencedirect.com/science/article/pii/S1001605814600032.

9. Fayal, Z.F., B. Lakhdar, and N. Zoubir, *Horizontal Well Performance Flow Simulation CFD-Application*, in *SPE Production and Operations Conference and Exhibition*. 2010, Society of Petroleum Engineers: Tunis, Tunisia.

10. Afsharpoor, A., et al., *CFD modeling of the effect of polymer elasticity on residual oil saturation at the pore-scale.* Journal of Petroleum Science and Engineering, 2012. **94–95**: p. 79-88, http://www.sciencedirect.com/science/article/pii/S0920410512001696.

11. Weinlader, A., et al., *Prediction of the oil flow distribution in oil-immersed transformer windings by network modelling and computational fluid dynamics.* IET Electric Power Applications, 2012. **6**(2): p. 82-90.

12. National Asphalt Pavement Association, N.A.P.A. *History of Asphalt*. 2017. http://www.asphaltpavement.org/index.php?option=com_content&task=view&id=21&Itemid=41.

13. Asphalt Pavement Alliance, A.P.A. *Pavement Technologies*. Pavement Materials, 2017. http://driveasphalt.org/technologies.

14. National Asphalt Pavement Association *Asphalt for Environmental Liners (PS17)*. 1984. http://www.asphaltpavement.org/images/asphalt_environmental1.pdf.

15. Kopal, Z., *Tables of supersonic flow around cones*. 1947, Cambridge: Massachusetts Institute of Technology. 555.

16. Fay, J.A., *Theory of Stagnation Point Heat Transfer in Dissociated Air.* Journal of the Aerospace Sciences, 1958. **25**(2): p. 73-85, http://dx.doi.org/10.2514/8.7517.

17. Blottner, F.G., *Chemical nonequilibrium boundary layer.* AIAA Journal, 1964. **2**(2): p. 232-240, http://dx.doi.org/10.2514/3.2299.

18. Blottner, F.G., *Nonequilibrium laminar boundary-layer flow of ionized air.* AIAA Journal, 1964. **2**(11): p. 1921-1927, http://dx.doi.org/10.2514/3.2701.

19. Hall, H.G., Eschenroeder, A.Q., Marrone, P.V., *Blunt-Nose Inviscid Airflows With Coupled Nonequilibrium Processes.* Journal of the Aerospace Sciences, 1962. **29**(9): p. 1038-1051, http://dx.doi.org/10.2514/8.9690.

20. Biagioli, F., F. Guethe, and B. Schuermans, *Combustion dynamics linked to flame behaviour in a partially premixed swirled industrial burner.* Experimental Thermal and Fluid Science, 2008: p. Medium: X; Size: page(s) 1344-1353.

21. Dupont, V., et al., *The reduction of NOx formation in natural gas burner flames.* Fuel, 1993. **72**(4): p. 497-503, http://www.sciencedirect.com/science/article/pii/001623619390108E.

22. Griffiths, W.D. and F. Boysan, *Computational fluid dynamics (CFD) and empirical modelling of the performance of a number of cyclone samplers.* Journal of Aerosol Science, 1996. **27**(2): p. 281-304, http://www.sciencedirect.com/science/article/pii/0021850295005498.

23. Ma, L., D.B. Ingham, and X. Wen, *NUMERICAL MODELLING OF THE FLUID AND PARTICLE PENETRATION THROUGH SMALL SAMPLING CYCLONES.* Journal of Aerosol Science, 2000. **31**(9): p. 1097-1119, http://www.sciencedirect.com/science/article/pii/S0021850200000161.

24. Sousani, M., Ingham, D., Pourkashanian, M., Sheng, Y., Kenneth, I-I. E., *Simulation of the hydraulic fracturing process of fractured rocks by the discrete element method.* Environmental Earth Sciences, 2015. **73**(12): p. 8451-8469, http://dx.doi.org/10.1007/s12665-014-4005-z.

25. Sousani, M., Kenneth, I-I. E., Ingham, D., Pourkashanian, M., Sheng, Y., *Modelling of hydraulic fracturing process by coupled discrete element and fluid dynamic methods.* Environmental Earth Sciences, 2014. **72**(9): p. 3383-3399, http://dx.doi.org/10.1007/s12665-014-3244-3.

26. Cundall, P.A. and O.D.L. Strack, *A discrete numerical model for granular assemblies.* Géotechnique, 1979. **29**(1): p. 47-65, http://www.icevirtuallibrary.com/doi/abs/10.1680/geot.1979.29.1.47.

27. Kim, B.S., S.W. Park, and S. Kato, *DEM simulation of collapse behaviours of unsaturated granular materials under general stress states.* Computers and Geotechnics, 2012. **42**: p. 52-61, http://www.sciencedirect.com/science/article/pii/S0266352X11002047.

28. McKinnon, S.D. and I. Garrido de la Barra, *Stress field analysis at the El Teniente Mine: evidence for N–S compression in the modern Andes.* Journal of Structural Geology, 2003. **25**(12): p. 2125-2139, http://www.sciencedirect.com/science/article/pii/S0191814103000683.

29. Baird, A.F. and S.D. McKinnon, *Linking stress field deflection to basement structures in southern Ontario: Results from numerical modelling.* Tectonophysics, 2007. **432**(1–4): p. 89-100, http://www.sciencedirect.com/science/article/pii/S0040195106005476.

30. Pantaleev, S., et al., *An experimentally validated DEM study of powder mixing in a paddle blade mixer.* Powder Technology, 2017. **311**: p. 287-302, http://www.sciencedirect.com/science/article/pii/S0032591016309305.

31. Romuli, S., S. Karaj, and J. Müller, *Discrete element method simulation of the hulling process of Jatropha curcas L. fruits.* Biosystems Engineering, 2017. **155**: p. 55-67, http://www.sciencedirect.com/science/article/pii/S1537511016305499.

32. Johansson, M., et al., *Cone crusher performance evaluation using DEM simulations and laboratory experiments for model validation.* Minerals Engineering, 2017. **103–104**: p. 93-101, http://www.sciencedirect.com/science/article/pii/S0892687516303235.

33. Tsuji, Y., Kawaguchi, T.,Tanaka, T., *Discrete particle simulation of two-dimensional fluidized bed.* Powder Technology, 1993. **77**(1): p. 79-87, http://www.sciencedirect.com/science/article/pii/0032591093850107.

34. Tsuji, T., Yabumoto, K., Tanaka, T., *Spontaneous structures in three-dimensional bubbling gas-fluidized bed by parallel DEM–CFD coupling simulation.* Powder Technology, 2008. **184**(2): p. 132-140, http://www.sciencedirect.com/science/article/pii/S003259100700592X.

35. Xu, B.H. and A.B. Yu, *Numerical simulation of the gas-solid flow in a fluidized bed by combining discrete particle method with computational fluid dynamics.* Chemical Engineering Science, 1997. **52**(16): p. 2785-2809, http://www.sciencedirect.com/science/article/pii/S000925099700081X.

36. Gidaspow, D., Bezburuah, R., Ding, J., *Hydrodynamics of circulating fluidized beds: Kinetic theory approach*. Conference: 7th international conference on fluidization. 1991, Chicago, US: Illinois Instute of Techonology. 8.

37. Wen, C.Y., Yu, Y. H., *Mechanics of Fluidization.* The Chemical Engineering Progress Symposium Series, 1966. **62**(62): p. 100-111.

38. Ergun, S., *Fluid flow through packed columns.* Chemical Engineering Progress, 1952. **48**(2): p. 89-94, http://ci.nii.ac.jp/naid/10003393451/.

39. Benzarti, S., H. Mhiri, and H. Bournot, *Drag models for simulation gas-solid flow in the bubbling fluidized bed of FCC particles.* World Academy of Science, Engineering and Technology, 2012. **61**: p. 1138-1143.

40. Chaudhuri, B., F.J. Muzzio, and M.S. Tomassone, *Modeling of heat transfer in granular flow in rotating vessels.* Chemical Engineering Science, 2006. **61**(19): p. 6348-6360, http://www.sciencedirect.com/science/article/pii/S0009250906003393.

41. Ranz, W.E. and W.R. Marshall, *Evaporation from drops.* Chemical Engineering Progress, 1952. **48**(3): p. 141-146.

42. Hertz, H., *On the Contact of Rigid Elastic Solids and on Hardness.* Ch 6: Assorted Papers, 1882.

43. Mindlin, R.D., *Compliance of elastic bodies in contact.* J. Appl. Mech., 1949. **16**: p. 259-268.

44. Deresiewicz, H., Mindlin, R. D., *Elastic spheres in contact under varying oblique forces*. 1952, Columbia University, US: Department of Civil Engineering.

45. Khronos OpenCL Working Group, *The OpenCL Specification*, L. Howes, Editor. 2015.

46. nVIDIA. *NVIDIA'S INVENTION OF THE GPU*. [cited 2017 03 April]; Available from: http://www.nvidia.co.uk/object/about-nvidia-uk.html.

47. nVIDIA. *What is CUDA*. [cited 2017 03 April]; Available from: http://www.nvidia.com/object/cuda_home_new.html.

V International Conference on Particle-based Methods – Fundamentals and Applications
PARTICLES 2017
P. Wriggers, M. Bischoff, E. Oñate, D.R.J. Owen, & T. Zohdi (Eds)

PERFORMANCE OF LARGE SCALED TSUNAMI RUN-UP ANALYSIS USING EXPLICIT ISPH METHOD

Keita Ogasawara[1], Mitsuteru Asai[2], Mikito Furuichi[3] and Daisuke Nishiura[4]

[1] Department of Civil Engineering, Graduate School of Engineering Kyushu University
744 Motooka, Nishi-ku, Fukuoka , Japan
ogasawara@doc.kyushu-u.ac.jp

[2] Department of Civil Engineering, Graduate School of Engineering Kyushu University
744 Motooka, Nishi-ku, Fukuoka , Japan
asai@doc.kyushu-u.ac.jp

[3] Department of Mathematical Science and Advanced Technology,Japan Agency for Marine-Earth Science and Technology
3173-25, Showa-machi, Kanazawa-ku, Yokohama, 236-0001, Japan
m-furuic@jamstec.go.jp

[4] Department of Mathematical Science and Advanced Technology,Japan Agency for Marine-Earth Science and Technology
3173-25, Showa-machi, Kanazawa-ku, Yokohama, 236-0001, Japana
nishiura@jamstec.go.jp

Key words: stabilized EISPH, Tsunami run-up, parallel computing

Abstract. The tsunami run-up simulation by the particle method at city level needs to huge number of particle at least 1 billion particles. The conventional particle simulation method is not easy to solve these huge problem even on the premise of using supercomputer. Then, a new particle method 'fully explicit Incompressible SPH' is developed that takes into consideration both calculation efficiency and accuracy. Finally, we demonstrate the future plan how to use our simulation resultes for a practical 'Soft' disaster mitigation method through the evacuation education with the Virtual Reality(VR) system.

1 Introduction

On March 11, 2011, the huge tsunami caused by the great east Japan earthquake devastated many infrastructures in pacific coast of north eastern Japan. Particularly, the damage of outflow of bridge girders caused a traffic disorder and these collapse behaviours led to delay of recovery after the disaster. After 2011 tsunami, disaster prevention and mitigation techniques are actively developing in coastal infrastructures and establishing

prediction method for tsunami disaster is one of the severe issues toward the next millennium tsunami. After Tohoku earthquake 2011 Japan, our research group has been developed a three-dimensional tsunami run-up analysis tool using the stabilized ISPH[1] which is one of the semi-implicit Lagrangian particle method. The target site of simulation is Kochi city where huge tsunami disaster is anticipated with the next big Nankai Trough Earthquake. Tsunami run-up simulation in the urban area requires high resolution at least 2m in order to resolve the complicated tsunami flow through buildings and the other structures. It leads to the large scale problem, and the tsunami run-up simulation at Kochi city needs to at least 1 billion particles. It is difficult to simulate the conventional ISPH method even on the premise of using supercomputer. In this research, a new particle method 'fully explicit Incompressible SPH' is developed that takes into consideration both calculation efficiency and accuracy. Finally, we demonstrate the future plan how to use our simulation resultes for a practical 'Soft' disaster mitigation method through the evacuation education with the Virtual Reality(VR) system.

2 Analysis method

In the past, we adopted the stabilized ISPH method, but this method is a kind of implicit method and it is not suitable for large scale parallel calculation. Therefore, we have established a method corresponding to ultra large scale parallel computation by explicitizing the stabilized ISPH method.

2.1 Governing Equations of Fluid Analysis

To solve incompressible fluid problems , independent variables, flow velocity $\boldsymbol{u}$ and pressure p, should be obtained while satisfying the conservation law of mass and momentum. The governing equations in the Lagrange description are given by

$$\frac{D\rho}{Dt} + \rho\nabla\cdot\boldsymbol{u} = 0 \tag{1}$$

$$\frac{D\boldsymbol{u}}{Dt} = -\frac{1}{\rho}\nabla p + v\nabla^2\boldsymbol{u} + \boldsymbol{g} \tag{2}$$

where v is the coefficient of kinetic viscosity and $\boldsymbol{g}$ is the acceleration of gravity.

Based on the assumption that the density of water is constant, the mass conservation law eq.(1) is rewritten as

$$\nabla\cdot\boldsymbol{u} = 0 \tag{3}$$

Applying Eqs. (2) and (3) to particle i, we obtain

$$\frac{D\boldsymbol{u}_i}{Dt} \approx -\frac{1}{\rho_i}\langle\nabla p_i\rangle + v\langle\nabla^2\boldsymbol{u}_i\rangle + \boldsymbol{g}_i \tag{4}$$

$$\langle\nabla\cdot\boldsymbol{u}\rangle \approx 0 \tag{5}$$

The symbol of $\langle\cdot\rangle$ is the approximate value referring to the values of neighbor particles in the vicinity on the basis of the concept of the SPH method.

2.2 ISPH Method

In the particle method, density is calculated through the distribution of particles, therefor it leads to the problem of the conservation of volume. To solve this problem, the ISPH method, in which the velocity and pressure fields of the equations of motion are separated using the projection method to evaluate the pressure field implicitly and the velocity field explicitly, was proposed [2, 3]. Using the projection method, the velocity and pressure fields can be separated by defining a tentative state without considering the pressure gradient term in the Navier-Stokes equations of motion. In this section, the procedure for updating variables from time step n to $n+1$ is explained with the aim of applying the projection method to the SPH method. First, the time-derivative term in eq. (2) is subjected to forward difference approximation and the intermediate velocity $\boldsymbol{u}^*$ is defined in an intermediate state to separate the velocity as

$$\frac{D\boldsymbol{u}}{Dt} = \frac{\boldsymbol{u}^{n+1} - \boldsymbol{u}^n}{\Delta t} = \frac{\boldsymbol{u}^{n+1} - \boldsymbol{u}^*}{\Delta t} + \frac{\boldsymbol{u}^* - \boldsymbol{u}^n}{\Delta t} \tag{6}$$

Among the components of acceleration after separation, the intermediate velocity $\boldsymbol{u}^*$ is evaluated as follows assuming that the first and second terms on the right side of eq. (6) correspond to the pressure gradient term and other terms of eq. (2), respectively.

$$\begin{aligned} \frac{\boldsymbol{u}_i^* - \boldsymbol{u}_i^n}{Dt} &= v\langle\nabla^2\boldsymbol{u}_i^n\rangle + \boldsymbol{g}_i \\ \rightarrow (predictor)\ \boldsymbol{u}_i^* &= \boldsymbol{u}_i^n + \Delta t\left(v\langle\nabla^2\boldsymbol{u}_i^n\rangle + \boldsymbol{g}_i\right) \end{aligned} \tag{7}$$

The velocity from the intermediate state to the next time step is updated as follows assuming that the pressure is evaluated based on an appropriate method.

$$\begin{aligned} \frac{\boldsymbol{u}_i^{n+1} - \boldsymbol{u}_i^*}{\Delta t} &= -\frac{1}{\rho}\langle\nabla p_i^{n+1}\rangle \\ \rightarrow (corrector)\ \boldsymbol{u}^{n+1} &= \boldsymbol{u}^* + \Delta\boldsymbol{u}^* \end{aligned} \tag{8}$$

$$\Delta\boldsymbol{u}^* = -\Delta t\left(\frac{1}{\rho}\langle\nabla p_i^{n+1}\rangle\right) \tag{9}$$

As shown above, two-separated processes are implemented to update the state of velocity in ISPH method. The pressure is evaluated by solving the pressure Poisson equation given by

$$\begin{aligned} \langle\nabla^2 p_i^{n+1}\rangle &= -\frac{\rho^0}{\Delta t}\langle\nabla\cdot\Delta\boldsymbol{u}_i^*\rangle \\ &= \frac{\rho^0}{\Delta t}\langle\nabla\cdot\boldsymbol{u}_i^*\rangle \end{aligned} \tag{10}$$

2.3 A Modified Source Term to Relax the Incompressible Conditions

The original ISPH and our proposed stabilized ISPH are applied the same projection method in order to split velocity and pressure updates. In the projection method, an intermediate state is defined by excluding pressure gradient term in Navier-Stokes eqn. in (11). The difference between the original ISPH and the stabilized ISPH is the source term in the pressure Poisson equation (see [1]) for the detailed formulation of equations).

In the SPH method, the numerical density is evaluated by counting the number of neighbor particles. During the fluid dynamics simulation using the ISPH, the numerical density is changing in time. In other words, it is difficult to keep the constant numerical density value because of non-uniform particle distributions. Therefore, the modified source term has an important role to decrease the numerical error in the numerical density value.

$$\langle \nabla^2 p_i^{n+1} \rangle \approx \frac{\rho^0}{\Delta t} \langle \nabla \cdot \boldsymbol{u}_i^* \rangle + \alpha \frac{\rho_i^0 - \langle \rho_i^n \rangle}{\Delta t^2} \tag{11}$$

The pressure Poisson equation given by eq. (11) completely conforms to the formulation under a velocity divergence-free condition assuming that the relaxation parameter is zero. In addition, when the density instantaneously agrees with the initial density (or the density is negligibly small), the pressure Poisson equation and formulation are considered to be the same because the second term of the source term of the pressure Poisson equation is negligible. According to the formulation, the accumulated error related to the density produced during analysis is gradually canceled by the term of density difference, leading to a scheme with a good conservation of volume as a result of an almost constant density even for a long-term calculation.

2.4 Explicit pressure assessment scheme

Here, the stabilized ISPH method, which utilizes a semi-implicit time integration, is converted to an explicit version. The most time consuming part in the ISPH is the linear equation solver for the pressure Poisson eqn.. In addition, the linear equation solver is not so easy to get faster and to get a good parallel efficient in the supercomputers. The main purpose of the explicit version of the stabilized ISPH is to decreasing the total computational time in the supercomputer environments. The idea of the totally explicit ISPH method is proposed by Barcarolo[4] et al.. They just showed a couple of numerical examples without verification and validation. Therefore, we developed a modified EISPH method that satisfies accuracy and stability by explicitly solving the stabilized ISPH method that realized long term volume storability by referring the stabilized ISPH. In Eq.(11), it can be rewritten in a discrete approximation form for the left side, the following equation is obtained.

$$\langle \nabla^2 P_i^{n+1} \rangle = \sum_j m_j \frac{2}{\rho^0} \frac{r_{ij} \cdot \nabla W(r_{ij}, h)}{r_{ij}^2 + \eta^2} (P_i^{n+1} - P_j^{n+1}) \tag{12}$$

When Equation (12) is transformed, the following equation is obtained.

$$P_i^{n+1} = \frac{B_i + \sum_j A_{ij} P_j^{n+1}}{\sum_j A_{ij}} \tag{13}$$

For convenience of notation, the following section is used here.

$$A_{ij} = m_j \frac{2}{\rho^0} \frac{r_{ij} \cdot \nabla W(r_{ij}, h)}{r_{ij}^2 + \eta^2}, B_i = \frac{\rho^0}{\Delta t} + \alpha \frac{\rho_i^0 - \rho_i^n}{\Delta t^2}$$

In the equation (13), assuming that the pressure of the neighboring particles, which are originally unknown quantities, can be approximated by the pressure of the present time at minute time intervals from n steps to n+1 steps, Can be rewritten as follows.

$$P_i^{n+1} = \frac{B_i + \sum_j A_{ij} P_j^{n}}{\sum_j A_{ij}} \tag{14}$$

By using the expression (14) it is possible to make an explicit pressure assessment. The proposed method changes only the pressure evaluation in the conventional stabilized ISPH method, and does not need to change the other schemes. In this study, we call the above scheme a stabilized Explicit ISPH (EISPH) method.

3 Verification test

3.1 Simple dam break test

By using the stabilized EISPH method, it is possible to perform highly parallel calculation as compared with the calculation by the stabilized ISPH method. However, verification was conducted because verification of validity about calculation accuracy was insufficient. The verification problem was verified with the dam break problem shown in the Figure 1. We analyze by both EISPH method and ISPH method referred to as conventional method and verify the proposed method by comparing both analysis results. Other conditions related to analysis are as shown in Table 1, and both analyzes were carried out under the same conditions. Regarding time increment, both methods need to satisfy the CFL condition, so we decided to use the same value (0.0002 sec). However, with the EISPH method, which is a fully explicit method, the relationship between accuracy and time increment should be investigated separately in addition to the CFL condition. In order to verify focusing only on the accuracy of the EISPH method, the same conditions as the conventional method as semi-implicit method were used. The Figure. 2 shows the result at 6000 Step, and the color means the pressure contour, indicating that it shows a qualitatively good agreement. Figure. 3 is the time history of the pressure on the red dot in Figure. 1. This result also agrees well.

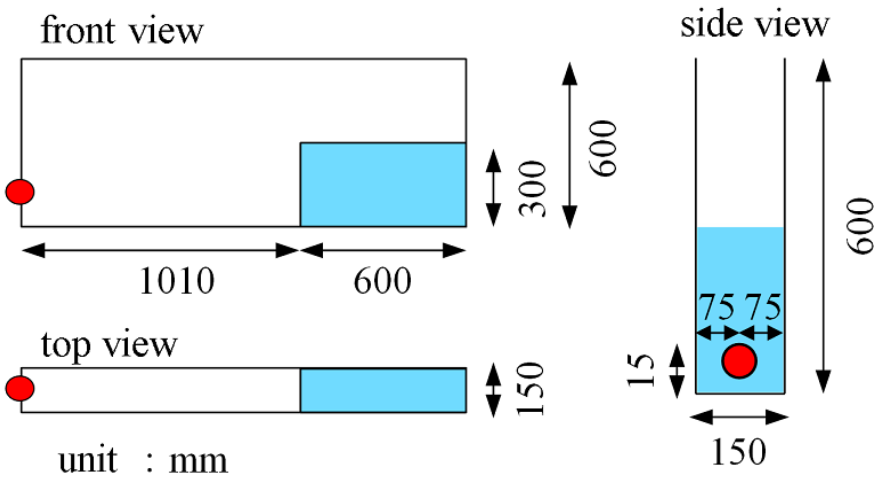

Figure 1: dam break model

Table 1: analysis conditions

particle diameter	number of particles	time increasement
10mm	214932	0.0002sec/step

3.2 Tsunami run-up simulation in a real city

A tsunami run-up simulation in a real city, Japan is conducted here. Figure. 4 shows the numerical model. The analysis conditions are as shown in Table 2, and the same value is used for time increment here as well. The color in the figure indicates the y-directional velocity. It also shows that this also shows a good agreement.

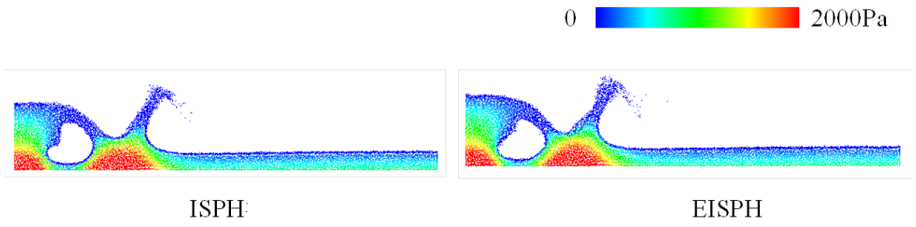

Figure 2: result(6000Step)

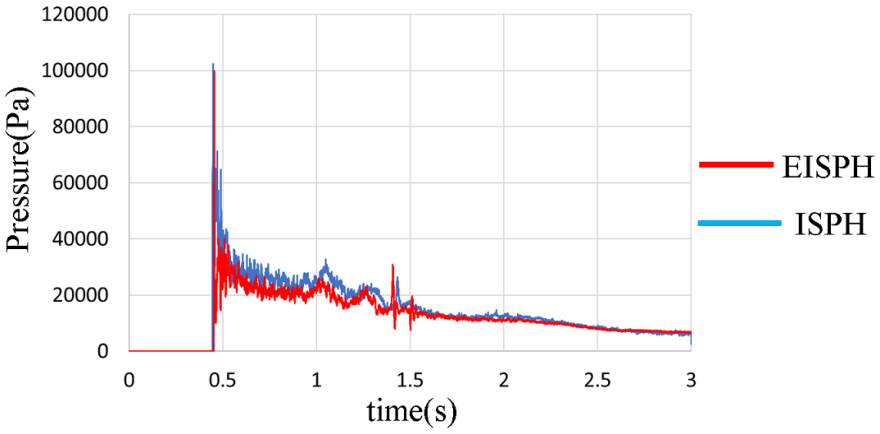

Figure 3: time history of th pressure

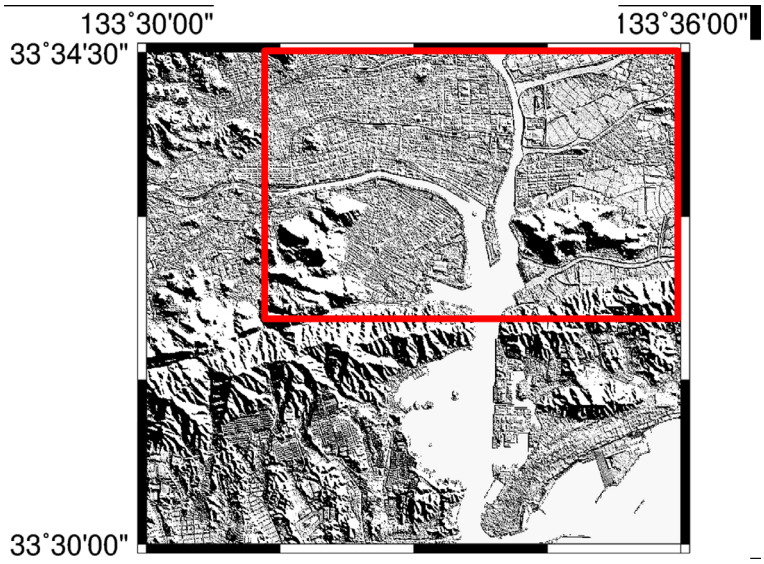

Figure 4: tsunami run-up area at Kochi city

Table 2: Analysis conditions

particle diameter	number of particles	time increasement
4m	33591333	0.05sec/step

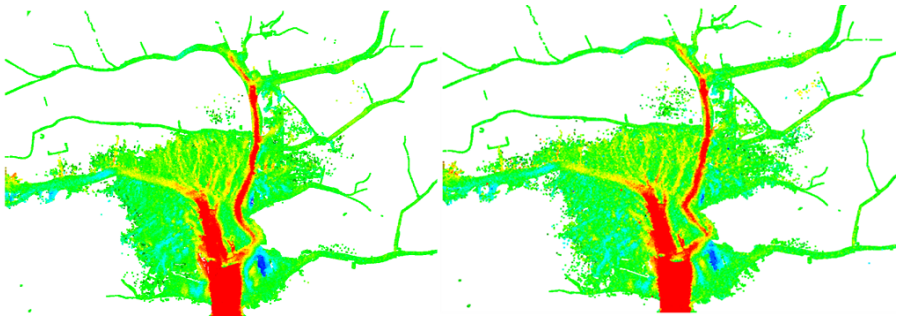

Figure 5: Results in EISPH method (left figure) and ISPH method (right figure)

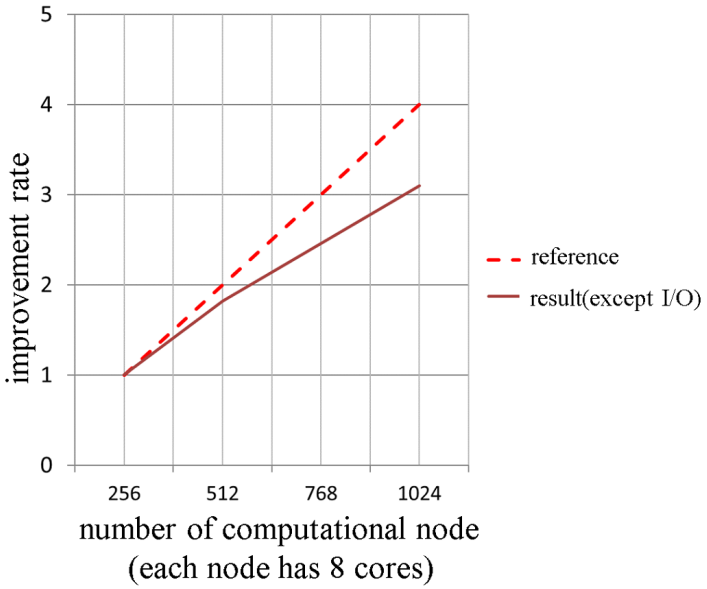

Figure 6: Parallelization efficiency

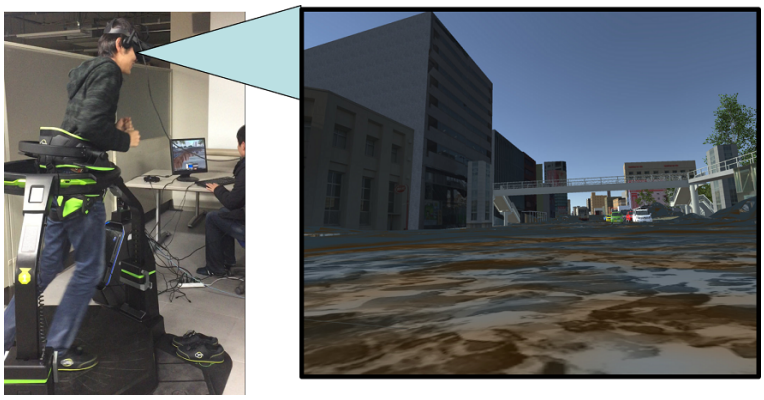

Figure 7: Virtual Reality usase example

3.3 Parallelization efficiency

By explicitization, it is not necessary to solve the pressure Poisson equation, which is the most time consuming part in the implicit version, and it is relatively easy to perform massively parallel calculations. The figure-6 is the calculation speed improvement rate in which parallel numbers are executed in 256 parallel, 512 parallel, 1024 parallel in the above-mentioned tsunami run-up analysis, respectively. For 256 parallels to 512 parallels, 91% of the ideal value shows good parallelization efficiency. In the 1024 parallel, 78% is not bad, but it tends to decline slightly, which seems to be overpowering as the number of parallels is excessive for this calculation.

3.4 Large scale parallelism and VR visualization

By enabling large-scale parallel computation, it is possible to calculate with resolution of several tens of centimeters in the tsunami run-up analysis. As a result of this, it becomes possible to accurately resolve the tsunami that moves up the block as described above, so that accurate calculation becomes possible, Even in visualization it makes it possible to draw waves through the road and it has big meaning. The authors made VR visualization and constructed a system for enlightenment etc. of the tsunami damage. Figure. 7 is a picture walking in the image with a walking controller with visualization of VR by computing only a specific area experimentally at 50 cm resolution. It is possible to walk not only inside the city block where the tsunami arrives but also in the VR image like the one on the right.

4 Conclusions

In this study, a stabilized EISPH method is proposed for the massively parallel computations for tsunami run-up simulation. We are trying to utilize the 3D tsunami run-up simulation results for the tsunami evacuation education through the VR systems. The

VR system is composed by the head mount display and walking controller. In the future, we plan to calculate the same tsunami run-up simulation with 50 cm resolution at the same city model.

REFERENCES

[1] M. Asai, A.M.Aly, Y.Sonoda, Y.Sakai, A Stabilized Incompressible SPH method by relaxing the Density invariance condition. *International Journal for Applied Mathematics*,No. 20130011,(2012)

[2] S.J.Cummins, M.Rudman, An SPH project method, *Journal Computational Phisics*,152.(2),(1990)

[3] A.Khayyer, H.Gotoh, S.Shao, Corrected incompressible SPH method for accurate water-surface tracking in breaking waves, *Coastal Engineering*,55, 236–250,(2008)

[4] D.A.Barcarolo, A.le Touze, F. de Vuyst, VALIDATION OF A NEW FULLY-EXPLICIT INCOMPRESSIBLE SMOOTHED PARTICLE HYDRODYNAMICS METHOD. *Blucher Mechanical Engineering Proceedings*, vol.1,num.1,(2014)

V International Conference on Particle-based Methods – Fundamentals and Applications
PARTICLES 2017
P. Wriggers, M. Bischoff, E. Oñate, D.R.J. Owen, & T. Zohdi (Eds)

NUMERICAL STUDY ON THE EFFECT OF PARTICLE SHAPE ON MIXERS

NICOLIN GOVENDER[1,2,5], DANIEL N. WILKE[3], RAJ K. RAJAMANI[4], PATRICK PIZETTE[4], JOHANNES KHINAST [5], and Benjamin J. Glasser [6]

[1] Research Center Pharmaceutical Engineering (RCPE) GmbH Graz , Austria
nicolin.govender@rcpe.at `www.rcpe.at`

[2] Centre for High Performance Computing (CHPC), Council for Scientific and Industrial Research (CSIR), Cape Town, South Africa
govender.nicolin@gmail.com `https://www.chpc.ac.za`

[3] Centre of Asset and Integrity Management, University of Pretoria, South Africa, 0086
wilkedn@gmail.com `http://www.up.ac.za/centre-for-asset-integrity-management`

[4] Metallurgical Engineering Department, University of Utah, USA
rajkrajamani@gmail.com `faculty.utah.edu`

[5] IMT Lille Douai, Univ. Lille, EA 4515 - LGCgE - Laboratoire de Génie Civil et géoEnvironnement, départment Génie Civil & Environnemental, F-59000 Lille, France
patrick.pizette@imt-lille-douai.fr and `http://www.lgcge.fr`

[6] Department of Chemical and Biochemical Engineering School of Engineering Rutgers, The State University of New Jersey, USA, bglasser@rutgers.edu and `http://cbe.rutgers.edu`

Key words: DEM, Graphical Processing Unit, Interactive Design, Interactive Simulation, Tumbling Mill, Numerical Multi-Fidelity Models

Abstract. Homogenization of particulate systems is a critical part in the processing of particulate materials to achieve consistency and ensure product quality. Homogenization is achieved by mixing, the aim is to obtain a final mixture that is homogeneous when mixing individual particulate constituents, in the sense of a uniform spatial mass distribution. Although there is always some measure of heterogeneity in a mixture this can be quantified by Gys sampling theory. This is critical for pharmaceutical industries in which it is essential that the variance of the active ingredients between tablets are within specified bounds. Although there have been numerous numerical studies on mixing using the Discrete Element Method (DEM), most studies to date have incorporated significant simplifications to reduce the computational time such as using mono-disperse size distributions, scaling up of particle size and spherical estimations of shape. The development of GPU based DEM simulations in the past few years significantly increased the number of spherical particles however most often at the expense of simplifying the physical

interaction between particles. This oversimplification of particle shape has much wider primary implications as primary contact mechanisms such as angularity and locking are omitted. This is important in the pharmaceutical industry where the feed powders are often made from crystalline solids in which the shape of the individual particles are polyhedral. As this study demonstrates, this is significant in that the underlining dynamics of polyhedral particles is vastly different to that of spherical particles, resulting in tighter packing fractions different flow patterns, and percolation. In this paper we use the GPU based DEM code BlazeDEM3D-GPU to study and quantify the effect of particle shape in a high shear blade mixer.

1 INTRODUCTION

Homogenization of particulate materials such as powders is critical in numerous industries ranging from civil engineering to pharmaceuticals to food processing. All these industries include homogenization which is the process of mixing various constituents to obtain a final product where each constituent is distributed uniformly. The homogeneity of the final product depends on both the quality of the constituents in terms of the heterogeneity of particle sizes (particle dispersity), shape uniformity, moisture content and the primary mixing method and device used. Particle dispersity between constituents results in segregation occurring due to percolation [16] which can drastically influence mixing of the constituents and compromise the final product. Consequently, in mixing there is an equilibrium point that limits stable homogenization due to segregation and other processes. This can have devastating consequences in pharmaceutical industries when the active ingredient is not uniformly dispersed throughout a mixture. It is paramount to understand the underlying dynamics of the particles and the effect of a particular mixing device. Influencing the physical properties such as particle shape of the constituents can help shift this equilibrium point to achieve better and more stable homogenization to reduce waste and consequently production costs. There has been limited success in improving the design of mixing devices via experimental means, owing to the difficulties in obtaining unbiased samples of a mixed product either due to the sampling technique or insufficient statistics. Furthermore detailed experimental information on the relationship between the particles with the mixer geometry and the particles themselves is difficult to obtain. Particulate materials exhibit of both solids and fluids behaviour in different flow regimes, making the prediction of the dynamics via empirical means also extremely difficult. Numerical modelling offers a means of investigating the problem, and in particular the potential effect of the various particle properties on mixing. Two numerical approaches are readily available to simulate particulate systems which are 1. continuum models [19], and 2. discrete element models[4]. Continuum models are computationally cheap to evaluate but offer no means to incorporate properties at particle scale naturally and reliably. Hence, although continuum methods can model problems at an industrial

scale their inability to accurately predict the macroscopic responses for variations at the particle-scale has only seen limited continuum solutions [20]. Limitations include, the failure to reliably predict the transitional flow regime in which both the collisional and frictional interactions drive flow behaviour [19], in addition to being unable to predict percolation which drives mixing. The underlying material models that are computationally tractable usually require re-characterization once particle scale properties are modified. In addition, the predictive capability of continuum models are limited to a small domain localized around which a solution has been calibrated and computed. The discrete element models are computationally expensive but readily allows for particle scale properties to be modified and investigated. In addition, the discrete element models are generally predictive over larger domains that continuum models [20]. The discrete element method is the only simulation approach that is capable of capturing microscopic and particle-scale effects to accurately predict the macro-scale of bulk behaviour but requires significant computational resources [12]. The discrete element method however is able to reliably predict all three flow regimes and in turn accurately quantifying mixing properties. As a result the discrete element method (DEM) has be- come the de facto standard to simulate particulate materials for which the discrete nature of particles and importance of quantifying particle-scale effects cannot be neglected. Consequently, the need for large scale discrete element simulations that can quantify the effect of particle-scale changes on the macro-scale response is becoming increasingly more important in industrial bulk material handling applications where simulations of lab-scale devices is not sufficient, poorly understood or not repeatable Ding et al. [23]. In addition, the demand to consider the poly-dispersed nature and shape non-uniformity of particulate systems in simulation has been well-established for a number of years by Clearly and Sawley [4], and recently reiterated by Höhner et al. [9] and Zhong et al. [22]. However, numerical studies to date that consider shape non-uniformity and polydispersity of polyhedral Figure 1 particle systems have been limited in scope due the large computational cost and lack of suitable codes to efficiently handle the associated geometrical complexity [6]. As a result the particle shape Figure 1 is often simplified as either spheres or by the multi-sphere approach that approximates a non-spherical particle as multiple spheres that are glued together [2], as depicted in Figure 1. Although the multi-sphere approximation is an improved description for complex particle shapes and allows for particle fragmentation to be taken into account [14], it is limited in the number of spheres that can be used to represent complex particle shapes, while being unable to accurately capture the particle angularity that may have a significant effect on the behaviour of the particulate system. Both the spherical and multi-spherical simplifications significantly reduce the complexity of inter-particle contact detection that results in a significant computational saving. In addition the constitutive models of interacting spheres has been well established and as a result has been used extensively simulations [18, 7]. Since the influence of particle shape and angularity on the mechanical behaviour of particle systems is well known [4, 10], the validity of approximate particle representations remains refutable [8, 13, 21]. To compute industrially

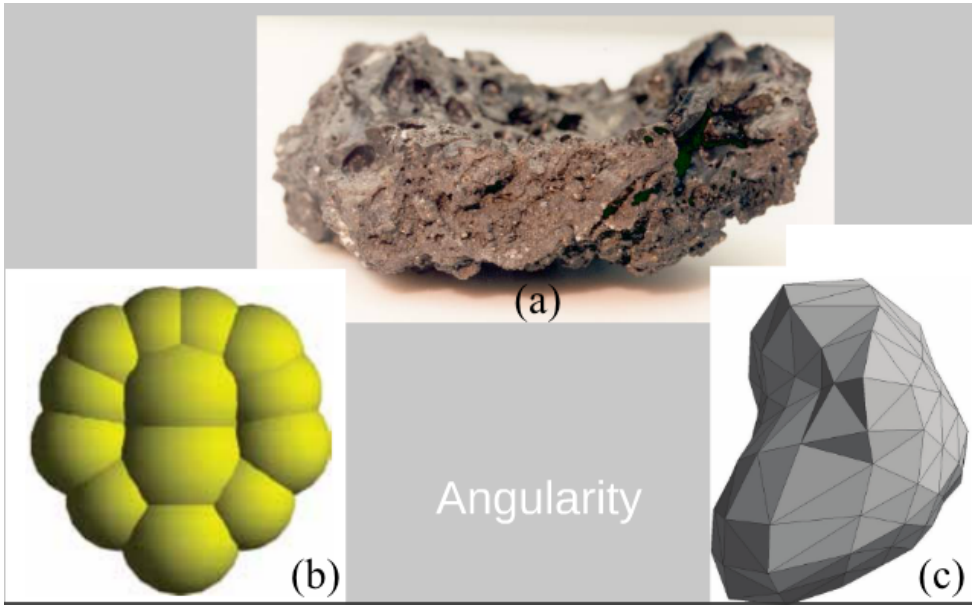

Figure 1: (a) Actual particle [1] represented using (b) a lumped sphere particle representation or (c) a polyhedron representation..

relevant discrete element simulations within a realistic time frame remains a challenging computational endeavour. Radeke et al. [15] performed the largest DEM simulation of a mixing device using 8 million spherical particles. This is still far from the hundreds of millions to billions of particles required for the simulation of industrially relevant mixing devices which have capacities of hundreds of litres. While the utilization of the Graphics Processing Units (GPU) in DEM simulations has resulted in simulations up to 50 million particles on a single computer and a billion particles using multiple computers with 256 GPUS, these simulations drastically oversimplify particle shape by modelling only spheres with simplistic contact models. In the case of Ge et al. the parallelization over multiple GPUs is highly problem specific.

2 OVERVIEW OF MIXING SIMULATIONS

The importance of considering particle shape in mixing has been demonstrated by Cleary et al. [5] for cubic salt particles being modelled as spherical particles. To correctly predict the mixing rate order and flow patterns required to consider the cubic salt particles as super-quadrics. The higher shear resistance of angular particles over spherical particles being the dominant reason for the observed differences. Laurent and Cleary [11] showed that approximating particles as spherical in a ploughshare mixer under-predicted the free surface angles, indicating again to lower shear resistance. In addition, particle shape can vary substantially between different types of particles and between particles from the same sample. Particle shape is known to be important to consider to accurately quantify

mixing of even rotating drums. Chandratilleke et al. [3] found that when fluidization of the bed occurs, the effect of air drag on the particles becomes important. As drag depends on particle shape the mixing and segregation may exhibit shape dependence. However, particle shapes are usually modelled as spheres and modifications to properties made due to the associated computational cost of non-spherical particle shapes. For example small values of rolling friction are often added in an attempt to account for mild departures from sphericity. However, Zhou et al. [23] showed that mixing kinetics were enhanced for low friction materials. Since, particle shape influences shear resistance it directly affects the ability to predict mixing. In addition, they reported that the particles flowing over the paddle was the mechanism responsible for segregation effects. The implication being again that particle shape directly influences the ability to predict and model segregation effects. However, to what extent particle shape needs to be considered remains poorly studied since most researchers simulate mixing processes in three dimensions use spherical particles citing computational expense as the primary limitation to investigate other particles shapes.

3 DETAILS OF CONTACT MODEL

Contact between spherical and polyhedral particles are resolved using a sliding-sticking friction model where the tangential force is coupled to the normal force through Coulomb's law. The initial tangential force is computed as the sum of the tangential spring force and a tangential viscous force

$$\mathbf{f}_0^t = -k_t \mathbf{L}^k - \gamma_t \mathbf{v}_t, \tag{1}$$

with $\mathbf{L}$ the tangential spring displacement from its equilibrium position, k_t the tangential spring parameter and γ_t the tangential dissipation parameter, and $\mathbf{v}_t$ the relative tangential velocity. For the static friction case, below the Coulomb limit, the tangential spring magnitude is incremented by

$$L^{k+1} = L^k + v_t \Delta t, \tag{2}$$

whereas for sliding friction

$$\mathbf{L}^{k+1} = -\frac{1}{k_t}(f_C^d \mathbf{n} + \gamma_t \mathbf{v}_t), \tag{3}$$

along the tangential unit vector $\mathbf{t} = \frac{\mathbf{f}_0^t}{\|\mathbf{f}_0^t\|}$. The contact volume is resolved for the polyhedral shaped particles as outlined in Figures 2(a)-(d). Specifically, a Kelvin-Voigt linear viscoelastic spring dashpot for rigid particles is considered. This results in an elastic force that stores energy and a dissipative Coulomb force that dissipates energy given by

$$\mathbf{F}_\mathrm{N} = (\mathrm{K_n} \Delta V)\mathbf{n} - \mathrm{C_n}(\mathbf{V}_\mathrm{R} \cdot \mathbf{n})\mathbf{n}, \tag{4}$$

where K_n is the volumetric spring stiffness ($\frac{N}{m^3}$), $\mathbf{n}$ the normal direction along which the force acts, C_n the damping coefficient ($\frac{Ns}{m}$) and $\mathbf{V_R}$ the relative velocity between the

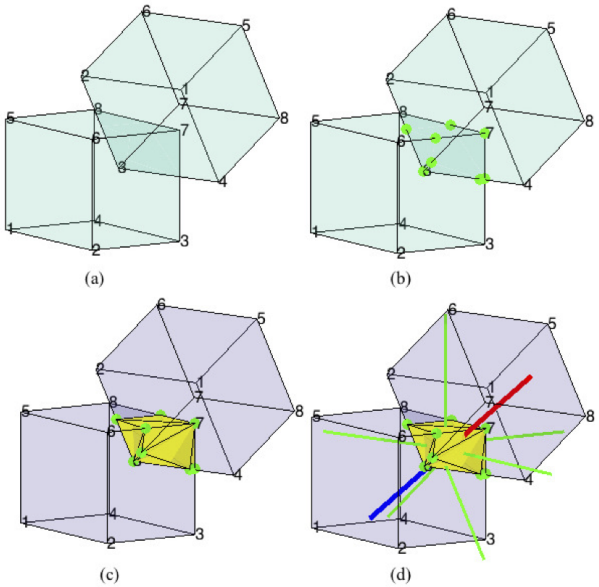

Figure 2: Contact resolution (a) between two intersection polyhedra by resolving the (b) contact points from which the (c) convex hull is constructed to compute the contact volume and (d) contact normals.

contacting particles. Given the overlap volume ΔV and contact normal that is resolved exactly for two polyhedral shaped particles as depicted in Figures 2(a)-(d).

In this study a normal spring stiffness of 100 N/m and tangential spring stiffness of $\frac{2}{7}$ of the normal stiffness is selected. In addition a coefficient of restitution (COR) of 0.9, friction coefficient of $\mu = 0.5$ and tangential viscous force of $\gamma_t = 0$ is selected.

4 SIMULATION OF A HIGH-SHEAR MIXER

The drum diameter is 13.5 cm with a single blade 0.80 cm high with a width of 0.10 cm as used by Sinnot et al. [17], the height of the particles is ≈2 cm. In this study two particles are considered, namely, spherical and tetrahedral shaped particles to fill a mixer volume of 100 cm^3 with a total mass of 240 g. In the high-shear mixer, mixing is done at 100 RPM for 10 seconds. The spherical particles are modelled as poly-dispersed by selecting 12 000 of the following diameters 0.14 cm, 0.1475 cm, 0.15 cm, 0.1525 cm and 0.155 cm for particles for a density of 2.5 g/cm^3. In turn , 60 000 truncated tetrahedral shaped particles are modelled using a particle volume of 0.001665 g/cm^3 and particle mass of 4.16×10^{-6} kg bounded with a radius of 0.0994 cm. The particle surface area is given by 0.08757 cm^2. The tetrahedral shaped particles are modelled with full angularity. The systems are colored initally in a left (green) right (red) split. The results for spherical shaped particles at various time instances is presented in Figures 3(a), (c) and (e), while the truncated tetrahedra is presented in Figures 3. The lower shear resistance of the spherical particles allowing for faster mixing to occur.

In order to quantify the mixing, the relative standard deviation (RSD) is reported as a function of time. $\sigma = \sqrt{\frac{1}{m_s - 1}\sigma_{m_s}(\bar{x} - x_{m_s})^2}$, mean value of $\bar{x}$, number of samples m_s and standard deviation σ. $RSD = \frac{\sigma}{\bar{x}}$. Evidently, the RSD reflects a higher mixing rate for the spherical particles than the truncated tetrahedra as presented in Figure 3. The spherical particle shapes tend to taper off around an (1-RSD) of around 0.92, while the truncated tetrahedra tapers off around (1-RSD) of 0.85 resulting in a difference of and RSD of 0.07 after 10 seconds. After 30s the values remained around these values and no further mixing occurred. The higher shear resistance that results from the angular truncated tetrahedra particle shape is evident and important to consider in that the rate of mixing achieved after 5 seconds with spheres is the maximum value acheived after 10 seconds for the polyhedra.

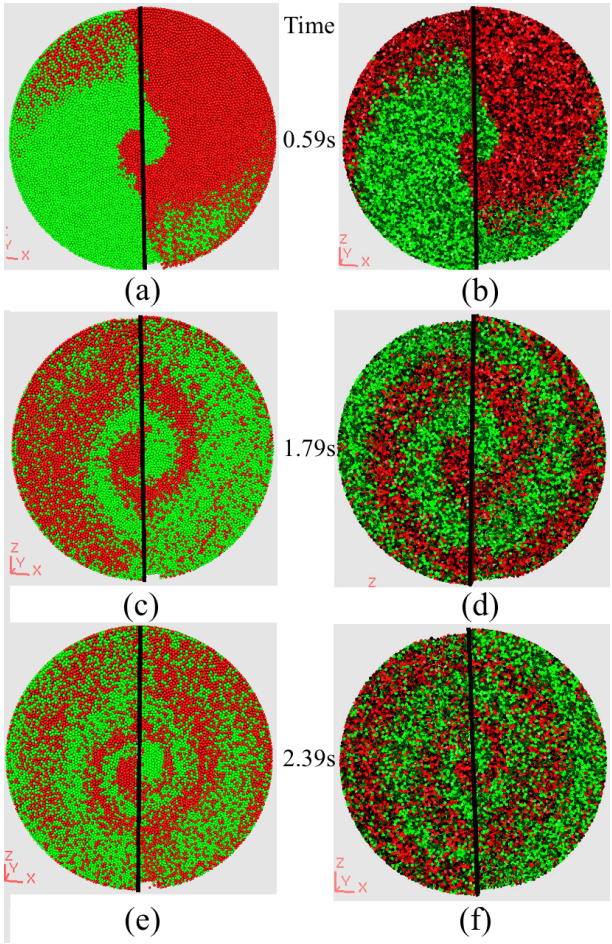

Figure 3: Mixing surfaces for the (a),(c),(e) spherical and (b),(d),(f) truncated tetrahedral particle shapes after 1 , 3 and 4 revolutions respectively.

One of the advantages of simulation over experiment which can greatly aid in the

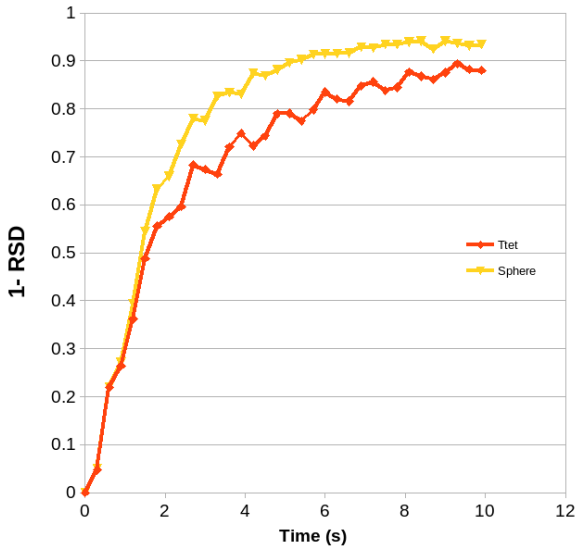

Figure 4: One minus the relative standard deviation as a function of time for the spherical and truncated tetrahedral shaped particles (1 rev = 0.60 s).

understanding mixers is that detailed information that would be tedious or difficult via experimental means is easily done in a computational environment. Consider Figure 5 which shows the RSD over a number of spatial cells, we see that while the average RSD indicates a fairly good mix for the truncated tetrahedral shaped particles, this mix is not as homogeneous in space as the spheres which is crucial for pharmaceuticals where differences of a few % leads to rejection of an entire batch due to regulatory requirements.

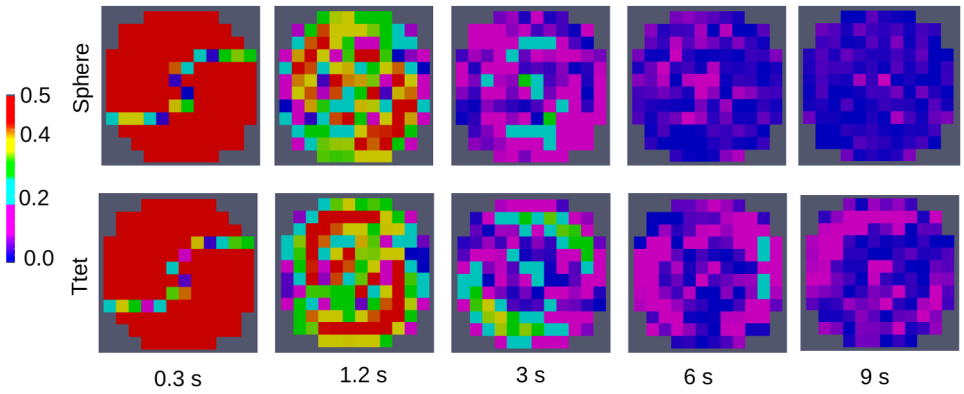

Figure 5: Relative standard deviation spatially distributed cells as a function of time for the spherical and truncated tetrahedral shaped particles (1 rev = 0.60 s).

Finally, Figure 6 depicts our current investigation of a semi-industrial scale simulation of a mixer in which 10 million truncated tetrahedral particles, are simulated on a single

computer using two GPUs at a rate of 1.5 s a day.

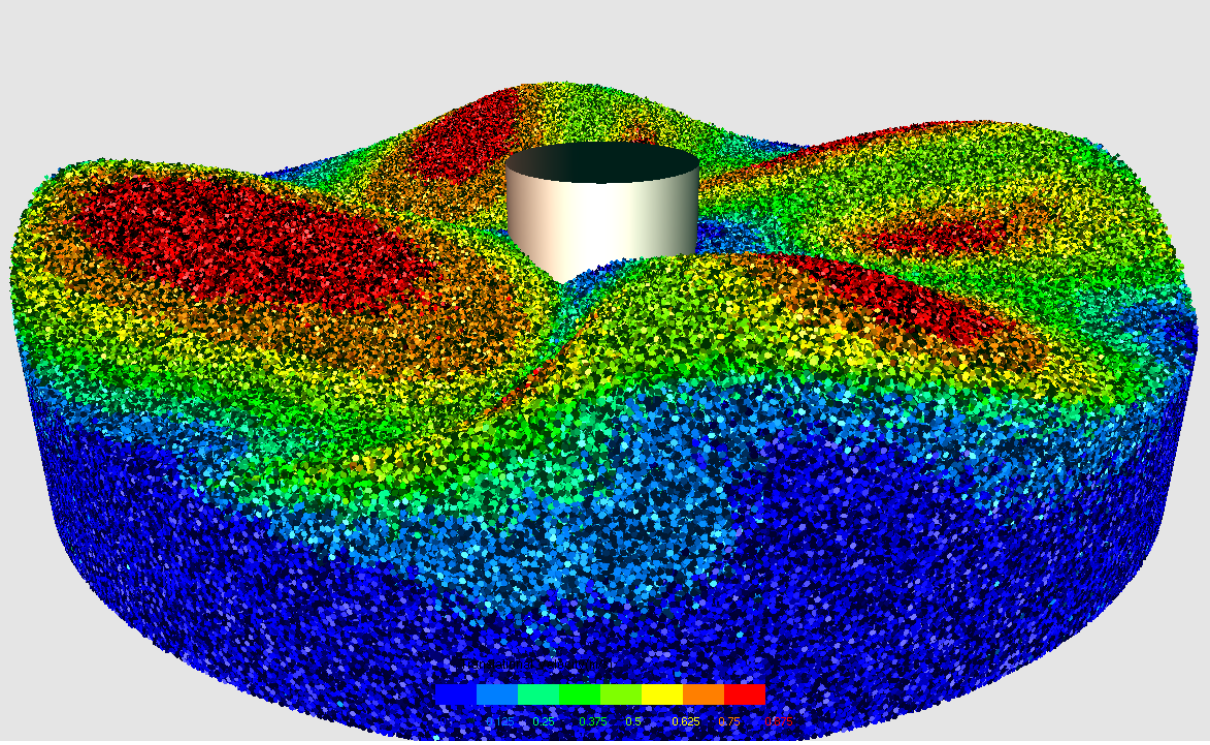

Figure 6: Semi-industrial scale simulation of a mixer using 10 million truncated tetrahedral particles.

5 CONCLUSIONS

This study quantified the difference in the relative standard deviation index of mixing between spherical particles and truncated tetrahedra. The importance of particle shape and angularity in the shear resistance of the particulate system is critical to consider as it has a significant effect on the mixing of the particulate system, highlighting again the importance of modelling particles with accurate geometry and angularity.

Acknowledgements

We gratefully acknowledge the support of NVIDIA Corporation with the donation of a Titan X Pascal GPU used for this research.

References

[1] URL `http://meteorites.wustl.edu/lunar/howdoweknow.htm`.

[2] H. Abou-Chakra, J. Baxter, and U. Tuzun. Three-dimensional particle shape de-

scriptors for computer simulation of non-spherical particulate assemblies. *Advanced Powder Technology*, 15:63–77, 2004.

[3] G. Chandratilleke, A. Yu, R. Stewart, and J. Bridgwater. Effects of blade rake angle and gap on particle mixing in a cylindrical mixer. *Powder Technology*, 193:303–311, 2009.

[4] P.W. Cleary and M.L Sawley. DEM modelling of industrial granular flows: 3D case studies and the effect of particle shape on hopper discharge. *Applied Mathematical Modelling*, 26:89–111, 2002.

[5] P.W. Cleary, G. Metcalfe, and K. Liffman. How well do discrete element granular flow models capture the essentials of mixing processes? *Applied Mathematical Modelling*, 22:995–1008, 1998.

[6] J.Q. Gan, Z.Y. Zhou, and A.B. Yu. A gpu-based dem approach for modelling of particulate systems. *Powder Technology*, 301:1172–1182, 2016.

[7] C. González-Montellano, Á. Ramírez, E. Gallego, and F. Ayuga. Validation and experimental calibration of 3d discrete element models for the simulation of the discharge flow in silos. *Chemical Engineering Science*, 66:5116–5126, 2011.

[8] D. Hohner, S. Wirtz, and V. Emden, H.K. Scherer. Comparison of the multi-sphere and polyhedral approach to simulate non-spherical particles within the discrete element method. *Powder Technology*, 208:643–656, 2011.

[9] D. Höhner, S. Wirtz, and V. Scherer. A numerical study on the influence of particle shape on hopper discharge within the polyhedral and multi-sphere discrete element method. *Powder Technology*, 226:16–28, 2012.

[10] J.P. Latham and A. Munjiza. The modelling of particle systems with real shapes. *Philosophical Transactions of the Royal Society of London, Series A: Mathematical, Physical and Engineering Sciences*, 362:1953–1972, 2004.

[11] B.F.C. Laurent and P.W. Cleary. Comparative study by pept and dem for flow and mixing in a ploughshare mixer. *Powder Technology*, 228:171–186, 2012.

[12] S. Mack, P. Langston, C. Webb, and York.T. Experimental validation of polyhedral discrete element model. *Powder Technology*, 214:431–442, 2011.

[13] D. Markauska. Investigation of adequacy of multi-sphere approximation of elliptical particles for DEM simulations. *Granular Matter*, 12:107–123, 2010.

[14] P. Pizette. Green strength of binder-free ceramic. *Journal of the European Ceramic Society*, 33:975–984, 2013.

[15] A.C. Radeke. Statistische und mechanische analyse der kraefte und bruchfestigkeit von dicht gepackten granularen medien unter mechanischer belastung, 2006.

[16] A.M. Scott and J. Bridgwater. Interparticle percolation: A fundamental solids mixing mechanism. *Ind. Eng. Chem. Fundamen.*, 14:22–27, 1975.

[17] M Sinnott and P Clearly. The effect of particle shape on mixing in a high shear mixer. *Computational Particle Mechanics*, 3:477–504, 2016.

[18] H. Tao, B. Jin, W. Zhong, X. Wang, B. Ren, Y. Zhang, and R. Xiao. Discrete element meth- od modeling of non-spherical granular flow in rectangular hopper. *Chemical En- gineering and Processing: Process Intensification*, 49:151–158, 2010.

[19] V. Vidyapati and S. Subramaniam. Granular flow in silo discharge: Discrete element method simulations and model assessment. *Industrial and Engineering Chemistry Research*, 52:13171–13182, 2013.

[20] Y. Wang and J.Y. Ooi. A study of granular flow in a conical hopper discharge using discrete and continuum approach. *Procedia Engineering*, 102:765–772, 2015.

[21] D. Zhao, E.G. Nezami, Y. Hashash, and Jamshid Ghaboussi.J. Three-dimensional discrete element simulation for granular materials. *Computer-Aided Engineering Computations: International Journal for Engineering and Software*, 23:749–770, 2006.

[22] Wenqi Zhong, Aibing Yub, Xuejiao Liu, Zhenbo Tong, and Hao Zhang. DEM/CFD-DEM modelling of non-spherical particulate systems: Theoretical developments and applications. *Powder Technology*, 302:108–152, 2016.

[23] Y. Zhou, A. Yu, R. Stewart, and J. Bridgwater. Microdynamic analysis of the particle flow in a cylindrical bladed mixer. *Chemical Engineering Science*, 59:1343–1364., 2004.

V International Conference on Particle-based Methods – Fundamentals and Applications
PARTICLES 2017
P. Wriggers, M. Bischoff, E. Oñate, D.R.J. Owen, & T. Zohdi (Eds)

POTENTIAL FOR INTERACTIVE DESIGN SIMULATIONS IN DISCRETE ELEMENT MODELLING

DANIEL N. WILKE[1], NICOLIN GOVENDER[2,3,4], PATRICK PIZETTE[4] and RAJ K. RAJAMANI[5]

[1] University of Pretoria
Centre of Asset and Integrity Management, University of Pretoria, South Africa, 0086
wilkedn@gmail.com http://www.up.ac.za/centre-for-asset-integrity-management

[2] Research Center Pharmaceutical Engineering
Research Center Pharmaceutical Engineering (RCPE) GmbH Graz , Austria
govender.nicolin@gmail.com www.rcpe.at

[3] Council for Scientific and Industrial Research (CSIR)
Centre for High Performance Computing (CHPC), CSIR, Cape Town, South Africa
govender.nicolin@gmail.com https://www.chpc.ac.za

[4] IMT Lille Douai, Univ. Lille, EA 4515 - LGCgE - Laboratoire de Génie Civil et géoEnvironnement, départment Génie Civil & Environnemental, F-59000 Lille, France
patrick.pizette@imt-lille-douai.fr and http://www.lgcge.fr

[5] University of Utah
Metallurgical Engineering Department, University of Utah, USA
rajkrajamani@gmail.com faculty.utah.edu

Key words: DEM, Graphical Processing Unit, Interactive Design, Interactive Simulation, Tumbling Mill, Numerical Multi-Fidelity Models

Abstract. This study investigates the potential for combining lower fidelity models with high performance solution strategies such as efficient graphical processing unit (GPU) based discrete element modelling (DEM) to not only do simulations faster but differently. Specifically this study investigates interactive simulation and design for which the simulation environment BlazeDEM-GPU was developed that allows researchers and engineers to interact with simulations. The initial results prove to be promising and warranting extensive research to be conducted in future which may allow for the development of alternative paradigms.

In addition to the design cycle, the role that this interactive simulation and design will play in education is invaluable as an in-house corporate training tool for young engineers to actively train and develop understanding for specific industrial processes. This would also allow engineers to conduct just-in-time (JIT) simulation based assessment of

processes before commencing on actual site visits, allowing for shorter and more focussed site excursions.

1 INTRODUCTION

Discrete element modelling gained momentum from the mid 90s when small industrial scale simulations of a couple of thousand spherical particles in two dimensions were analysed on a more regular basis. A decade later discrete element modelling simulations allowed for moderate industrial scale simulations of a few hundred thousand spherical particles [1]. Over the last five years the landscape of large scale industrial simulations started to emerge with the utilization of the graphical processing unit (GPU) [2]. It is now common to simulate a couple of million polyhedral shaped particles and tens of millions of spherical particles [2] within a couple of days. In addition, moderate scale industrial simulations can now be modelled within hours on a workstation instead of weeks or months on a cluster merely a decade ago. Combining the advances in high performance GPU based discrete element modelling with sound computational complexity reduction techniques such as discrete element simulations with varying fidelity of the physics or the numerics [13] and reduced order modelling [3] allows for the possibility of design optimization or design modification for industrial problems that involve granular flow. In design optimization the distinction between the need for *accurate analyses* and *accurate enough analyses* are seldom made although they can have significant impact on solution times when properly applied. Initially in the design optimization process the analyses only need to be *accurate enough* to capture the correct trends regarding an analyses. As a design converges the need for *accurate analyses* sometimes increases and then not even always. By clearly making a distinction between these two types of analyses has led to significant improvements of multi-fidelity design optimization approaches over the last decade [6, 7, 8, 9]. Here, multi-fidelity is used in the sense to imply fidelity of the physics or numerical computational fidelity of a simulation.

More importantly this allows for a new paradigm in design optimization and design modification that is distinct from the conventional design cycle. The design optimization cycle remains characterised by either the *analyse-wait-modify-analyse cycle* or more recently with cloud computing the *batch analyse-wait-modify-batch analyse cycle* utilizing mostly high fidelity numerical simulations as most design engineers or researchers do not distinguish between accurate solutions and solutions that give accurate trends during the design process. Combining a proper understanding between *accurate analyses* and *accurate enough analyses* that captures the consistent trends with a computationally efficient solution strategy for the discrete element method (DEM) allows for quick turn around times on feedback to the user. By incorporating this additional computational savings naturally allows us to extend the domain of application towards interactive design simulations in which low fidelity numerical models can be computed efficiently to give consistent

and responsive feedback to the user regarding the trends of various parameters during design modification. Consequently combining lower fidelity models with high performance GPU based DEM modelling is enabling a new and alternative paradigm denoted interactive simulation and design (ISD). The benefit of ISD is that engineers can explore the design domain independently to gain understanding of a process or even explore the design domain guided by a numerical optimization strategy which ultimately leads to better understanding of the optimal solution as opposed to the often black-box approach to design optimization in which the engineer is often detached in terms of understanding from the optimal solution.

BlazeDEM-GPU [2] is a GPU based DEM simulation environment designed with ISD in mind. BlazeDEM-GPU allows for changes to be made during a simulation in real time utilizing multiple GPUs to conduct a single simulation. This capability allows engineers to interactively engage with a simulation to study the effect of various model parameters. For example geometrical changes of the environment with which particles interact that includes the effect of lifter heights in a ball design as an example. Changes in the boundary conditions in steady state processes that include inter-particle cohesion or changes in flow rate of a continuous bulk material handling process. This would allow engineers to interact with the simulation to both quantitatively and qualitatively engage with a design problem or granular material process, allowing for formalized and intuitive understanding of the factors that influence granular flow to ultimately drive towards an enhanced understanding of optimal design solutions.

In addition to ISD, the role that this paradigm will play in education is invaluable as an in-house corporate training tool for young engineers to actively train and develop understanding for specific industrial processes. This also allows engineers to conduct just-in-time (JIT) simulation based assessment of processes before commencing on actual site visits, allowing for shorter and more focussed site excursions. Ultimately, this would allow experienced engineers to explore new processes and solidify the understanding behind experiential experience that is becoming ever more important in our dynamic modern environment.

2 EXPLANATORY EXAMPLE FOR NUMERICAL FIDELITY

As an explanatory example to explore the concepts behind numerical fidelity of a model, consider the coupled first order non-linear system of differential equations (Lokta-Volterra equations [10] given by

$$\frac{dx(t)}{dt} = \alpha x(t) - \beta x(t)y(t) \tag{1}$$

$$\frac{dy(t)}{dt} = \delta x(t)y(t) - \gamma y(t), \tag{2}$$

with two initial conditions on $x(0) = x_0$ and $y(0) = y_0$ that completes the formulation. For illustrative purposes consider the one dimensional least squares problem for which we

choose $\beta = \frac{1}{3}$, $\delta = \gamma = 1$ and $x_0 = y_0 = 0.9$. The aim is to find α that best matches $x(t)$ and $y(t)$ after $t = 8$ seconds. We compute the desired response $\mathbf{d}^*$ for $\alpha^* = 0.8$ using the forward Euler integration scheme using 1000 equal time steps between 0 and 8 seconds. Hence, the solution $\mathbf{d}^*$ is known which allows us to quantify our predicted solutions using a numerically lower fidelity model. Given some estimated response $\mathbf{d}_m(\alpha)$ using a lower fidelity model that depends on the following model parameter α. The difference between the known response and the model response is then given by

$$\mathbf{E}(\alpha) = (\mathbf{d}_m(\alpha) - \mathbf{d}^*), \tag{3}$$

which can be reduced to a scalar $f(\alpha)$ by the following ordinary least square projection

$$f(\alpha) = \mathbf{E}^T(\alpha)\mathbf{E}(\alpha). \tag{4}$$

Consider a lower numerical fidelity model using a random number of time steps between 290 and 350 for each computed α. By choosing a random number of integration time steps for each α allows us to quantify the variation in response between designs. The least squares error is depicted in Figure 1(a), while the derivative of the least squares error w.r.t. the variable α is depicted in Figure 1(b). It is evident that using a third of the computing power the estimated solution was resolved around 0.81 as opposed to $\alpha^* = 0.8$ for the known solution. In addition, the variation in least squares error when varying the number of integration time steps is negligible allowing for a smooth response in both the function value and derivative. Here, the function value is indicative of what is required when an accurate response is of importance for a design variable and of importance towards the end of a design optimization process. In turn, the derivative is indicative of the trend of a design variable and merely needs to point us in more or less the right direction which for the 1D case results in one of two options, left or right. A negative derivative is indicative of move right for improvement whereas a positive derivative is indicative of moving left for an improvement. For this example the two are equivalent and consistent pointing to the same solution.

However, by lowering the numerical fidelity of the computation to less than 10% of the known solution a clear distinction between the function value and derivatives becomes evident. Considering an even lower numerical fidelity model using a random number of time steps between 70 and 90 for each computed α. The least squares error is depicted in Figure 2(a), while the derivative of the least squares error w.r.t. the variable α is depicted in Figure 2(b). It is evident that using less than a tenth of the computing power the estimated solution from the function value is difficult to resolve. The variation between responses is significant as the number integration time steps between different values of α makes comparing the quality of solutions for different values of *salpha*. Hence, achieving an *accurate solution* is not achievable for this low fidelity computed solution. However, when we consider the trends of the solution as indicated by the derivative a unique solution around $\alpha = 0.83$ is evident as depicted in Figure 2(b). The estimated

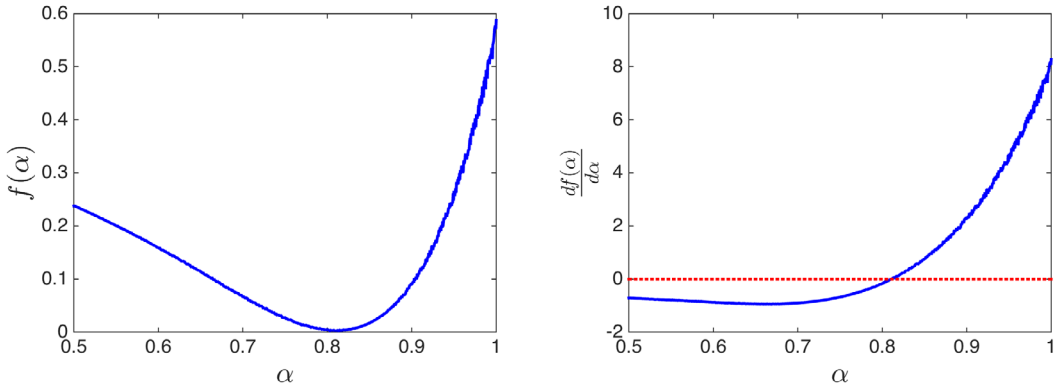

(a) (b)

Figure 1: Solution of (a) a cost function and (b) the derivative of the cost function w.r.t. the design variable α. For each α a differential equation was required to be solved. Every α was solved using a random number of integration time steps between 290 and 350.

solution here is remarkably close to the actual solution of $\alpha^* = 0.8$ given we expended less than 10% of the computing power. The implication of this observation for solving a design optimization problem in general is that by initially focussing more on the trends of a simulation and only the values towards convergence if required can have a significant computational saving.

To reiterate the discussion in Section 1, design optimization remains characterised by either the *analyse-wait-modify-analyse cycle* or more recently the *batch analyse-wait-modify-batch analyse cycle* utilizing mostly high fidelity numerical simulations as most design engineers or researchers do not distinguish between accurate solutions and accurate trends in the design process. Combining lower fidelity models with high performance solution strategies such as efficient GPU based DEM enables us to not only do simulations faster, but differently. This allows for the development of new and alternative paradigms of which ISD is an example.

3 OVERVIEW OF COMPUTING ARCHITECTURES

The two most common computing platforms that are readily available are the central processing unit (CPU) and the graphical processing unit (GPU), while field programmable gate arrays (FPGAs) allow for increased computing power they are costly. In modern computing the following three criteria dominate the selection computing architectures:

1. time to solution,
2. energy required to compute a solution,
3. capital cost for computing platform.

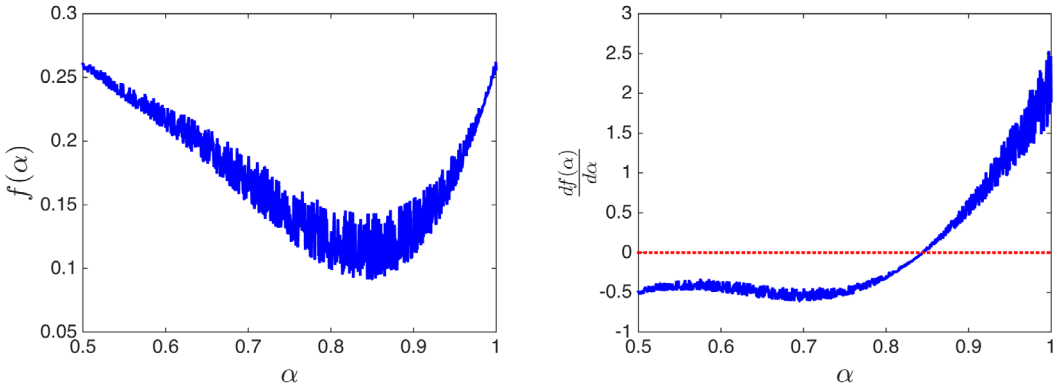

(a) (b)

Figure 2: Solution of (a) a cost function and (b) the derivative of the cost function w.r.t. the design variable α. For each α a differential equation was required to be solved. Every α was solved using a random number of integration time steps between 70 and 90.

The energy requirements to compute a solution are becoming increasingly more important to consider as the number of problems being solved daily is growing substantially with the potential for significant power savings. However, for a given architecture the time to solution and power requirements are two competing objectives as exemplified by the power characteristics of CMOS integrated circuits (ICs). Both CPUs and GPUs follow the CMOS IC power characteristics that are dominated by the two main contributors namely, static and dynamic power draw. The static power consumption is the power required when the transistors are not switching which is given by

$$P_S = V I_S, \tag{5}$$

with V the supply voltage to the circuit and I_S the static current flowing though the circuit. The dynamic power which consists of capacitive and transient power consumption and follows

$$P_D = aC \times V^2 \times f, \tag{6}$$

with a representing the fraction of transistors switching, C indicating the switched capacitance, V the supply voltage and f the clock frequency [11]. The higher the clock frequency the lower the latency but the more power the processing consumes.

However, the time to solution and energy required to compute a solution is not directly related to the clock frequency when we consider different computing architectures as the potential for parallelization of the problem at hand is an important point to consider. The CPU and GPU are two computing architectures designed for two very different problems.

The central processing unit (CPU) is a contemporary general-purpose processor that excels at computing multiple instructions to be executed sequentially on new or the same data. Parallelization of CPUs have extended to only a few multi-core processing units

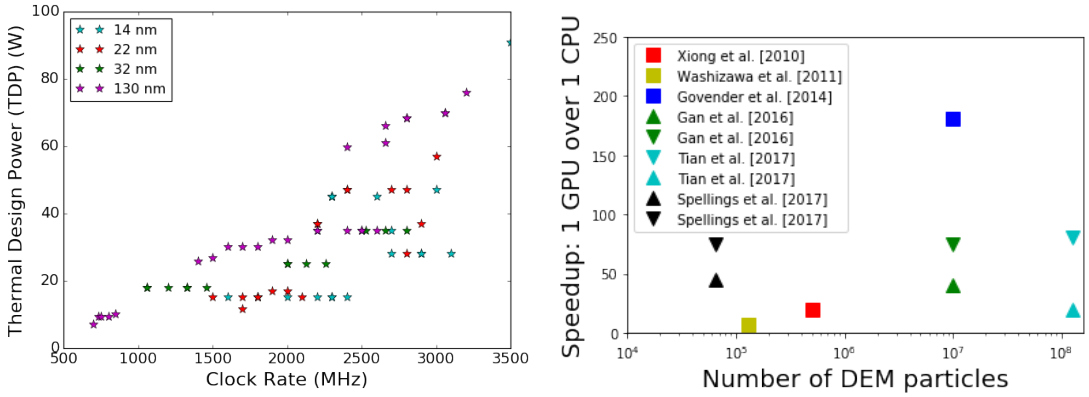

Figure 3: (a) Clock rate versus thermal design power for various transistor sizes of CPUs and (b) the speedup factor for 1 GPU over 1 CPU to compute the various number of particles.

(typically less than ≤ 32) with data being fed using limited memory bandwidth as a few cores can only compute so fast. These cores run at the highest clock cycles serving applications that require low latency at the cost of higher power demands. The relationship between clock rate as function of thermal design power (TDP) outlined by (6) is indicated in Figure 3(a) for various transistor sizes.

In turn, the graphical processing unit offers a vast number of simple, data-parallel and deeply multi-threaded cores that are fed data using high memory bandwidth. GPUs excel at problems that require the same operation to be performed on different data known as single instruction multiple data (SIMD) parallelization. The cores run at about one quarter ot third of the clock rate than the high-end CPUs reducing the power demand at the cost of sacrificing latency for throughput. The programming support for GPUs have improved significantly with CUDA supporting development for NVIDIA based GPUs while OpenCL renders support for AMDs manufactured GPUs. In addition, the GPU has significant speedup when conducting single precision floating point operations as opposed to double precision operations. Although, single precision DEM has only been explored by a limited number of researchers, the potential for additional computational performance and reduced memory requirements renders this an important consideration for future research. The reduced memory requirements allows for more particles to be solved using the same amount of memory which is important for memory limited computing platforms such as the GPU. In addition, the GPU is designed with a high bandwidth memory interface to allow large amounts of data to be moved in memory on the GPU for efficient large scale parallel processing.

DEM is ideally suited for GPU architectures as it is a throughput constrained computing problem, as a consequence it has resulted in significant speed-up over CPU based DEM simulations as depicted in Figure 3(b). The single precision performance by Govender et al. [12] indicates a significant improvement in computational performance of a

factor of 180 when considering the GPU above the CPU, the general GPU performance improvement is around a factor of 50 to 100. Figure 3(b) clearly demonstrates the benefit of utilizing the GPU to solve DEM problems, since DEM problems with large numbers of particles are ideally solved by architectures designed for high throughput problems.

4 PRELIMINARY INVESTIGATION TUMBLING MILL DESIGN LANDSCAPE

This study investigates the potential for adaptive particle refinement to speed-up design based discrete element simulations by conducting a pilot investigation with the set of preliminary results reported in [13]. This study investigates the effect of the lifter geometry on the distribution of the estimated power draw of the mill with the estimated normal and shear energies to be considered in a future study. The two variables for the lifter geometry are the width and height as depicted in Figure 4(b). The height is varied 1.2cm and 4.8cm, while the widths are varied between 2cm and 10cm.

For the purposes of our investigation we conduct three sets of analyses using three particle sizes. We consider the finest particle size to be the solution landscape. We therefore compare the response surface landscapes not only w.r.t. to the predicted values but also the distance each response surface's optimal design is from the known solution. Three particles sizes selected are $r_1 = 1$ in, $r_2 = 0.794$ in and $r_3 = 0.63$ in. As a first approach the selection of the sizes are based on the following criteria:

1. The radii being related by $0.5^{\frac{1}{3}} \approx 0.794$ should fill the same representative volume when number of particles are doubled.

2. The potential energy of the system stays the same when the effective masses m and heights h stay the same mgh, with g the gravitational acceleration.

3. The kinetic energy, $\frac{1}{2}mv^2$, stays the same when the mass stays the same and the velocity stays the same. The tumbling mill is modelled with prescribed rotations that enforces the same velocities as input the problem.

Selecting the particles following the relationship $r_2 = 0.794r_1$ ensure the masses to be the same, particle volume to be the same, as well as the potential energy as the particles are loaded to the same height when the particle number is doubled and particle volume halved for respectively 1000, 2000 and 4000 particles. The volumes being effectively the same for the three particle sizes are evident in Figures 5(a)-(c). The impulses to the problem will vary significantly due to the lumped nature of the particles.

We consider BlazeDEM-GPU [12], where the equations of motion are integrated using an explicit forward Euler scheme using a time step $\Delta t = 10^{-4}$. The particle-particle coefficient of restitution is 0.4 and the stiffness chosen to resolve the contact within at least 10 time steps. The static and dynamic coefficient of friction is chosen as 0.45 and the rolling resistance is selected as 0.001. The particle-cylinder and particle-lifter properties

coefficient of restitution is 0.4 and the stiffness chosen to resolve the contact within at least 10 time steps. The static and dynamic coefficient of friction between the particle-cylinder and particle-lifter is chosen as 0.5 and the rolling resistance is selected as 0.001. The particle density is assumed to be of Aluminum 2.7 cm/g^3.

After the 20 discrete element runs per particle diameter have been completed, as depicted in Figures 6(a)-(c), the radial basis function (RBF) response surfaces for each particle size was constructed as depicted in Figures 7(a)-(c). To construct the RBF surface the optimal ϵ was first determined by minimizing the leave-out-one-cross-validation error (LOOCVE) using a brute force strategy [13]. Once the optimal ϵ^* has been determined, it is used to construct the radial basis function (RBF) response surface.

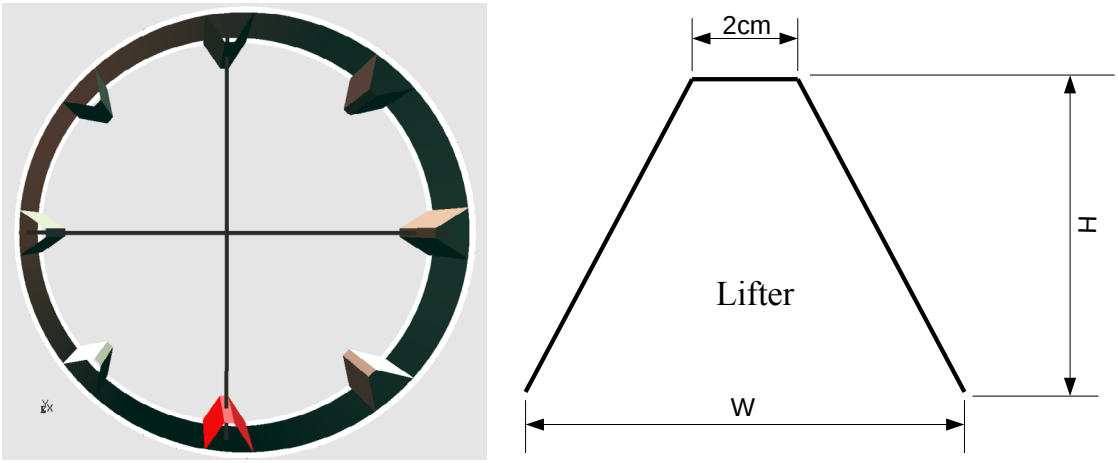

(a) (b)

Figure 4: (a) Modelled ball mill, with 90cm diameter, depth of 15cm and eight lifters, filled with spherical charge particles. (b) The geometry of the lifter parametrized using two variables [13].

The RBF predicted normalized power draw is depicted in Figures 7(a)-(c) by dividing by the configuration with the highest power demand. It is evident when considering the domains with the highest reported power demand all three simulations are within the same part of the design domain. This demonstrates promising results for utilizing such responses as objective function in design optimization problem, as the actual values are not so important as the design vector that coincides with the maximum power requirements or minimum.

In turn, when considering the actual values as exemplified by the contours that only show values limited between 0.8 and 0.9 as depicted in Figure 8(a)-(c) it is clear that the 1000 particles simulation seems to be inadequate, whilst the 2000 particle simulation demonstrates promising potential. This is an important consideration when considering constraint functions as constraints require accuracy as they usually define absolute re-

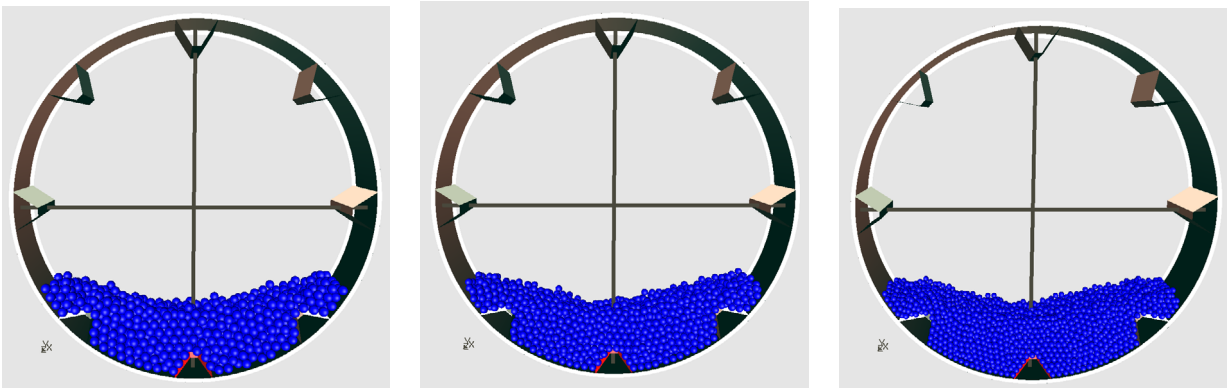

(a) 1000 particles of radius 1 in (b) 2000 particles of radius 0.794 in (c) 4000 particles of radius 0.63 in

Figure 5: Tumbling mill filled with three particle sizes namely (a) 1 in, (b) 0.794 in and (c) 0.63 in using respectively 1000, 2000 and 4000 particles.

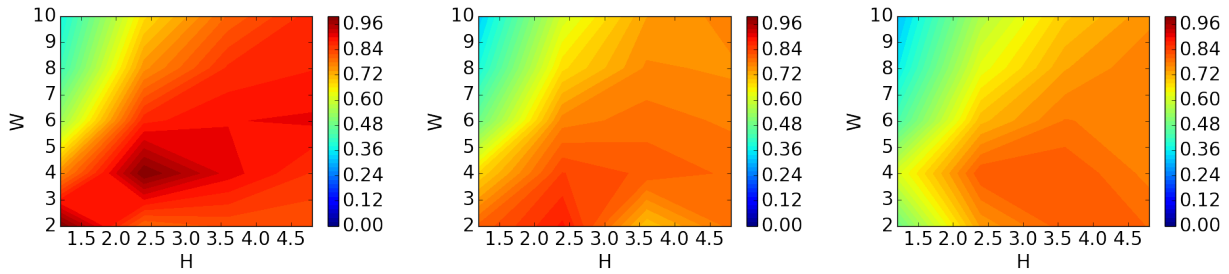

(a) 1000 particles of radius 1 in (b) 2000 particles of radius 0.794 in (c) 4000 particles of radius 0.63 in

Figure 6: Actual normalized power contours of the actual data, using the 20 full factorial design of experiment points, for the three particle sizes, namely (a) 1 in, (b) 0.794 in and (c) 0.63 in using respectively 1000, 2000 and 4000 particles.

strictions on the computed values. It is therefore important to note that starting with a too low numerical fidelity may be inadequate to save computational time when constraints are considered unless additional measures are taken which is part of our current investigation.

5 CONCLUSIONS

By combining lower fidelity models with high performance solution strategies such as efficient graphical processing unit (GPU) based discrete element modelling (DEM) enables us not to only do simulations faster but differently. This allows for the development of new and alternative paradigms of which interactive simulation and design was considered in this study, and essentially the paradigm for which the simulation environment BlazeDEM-

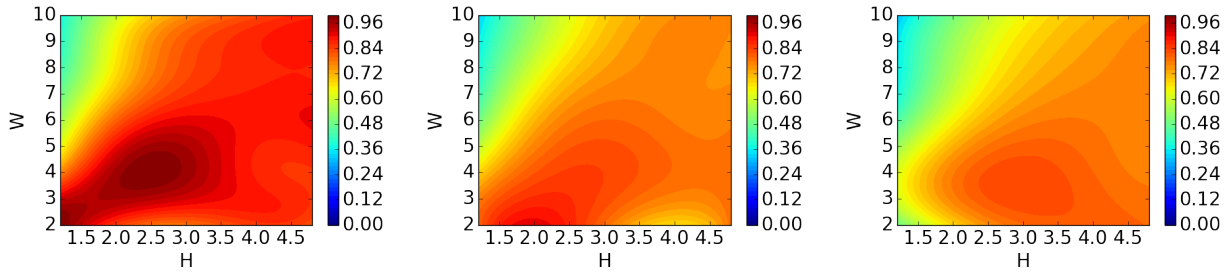

(a) 1000 particles of radius 1 in (b) 2000 particles of radius 0.794 in (c) 4000 particles of radius 0.63 in

Figure 7: RBF predicted normalized power contours of the actual data, using the 20 full factorial design of experiment points, for the three particle sizes, namely (a) 1 in, (b) 0.794 in and (c) 0.63 in using respectively 1000, 2000 and 4000 particles.

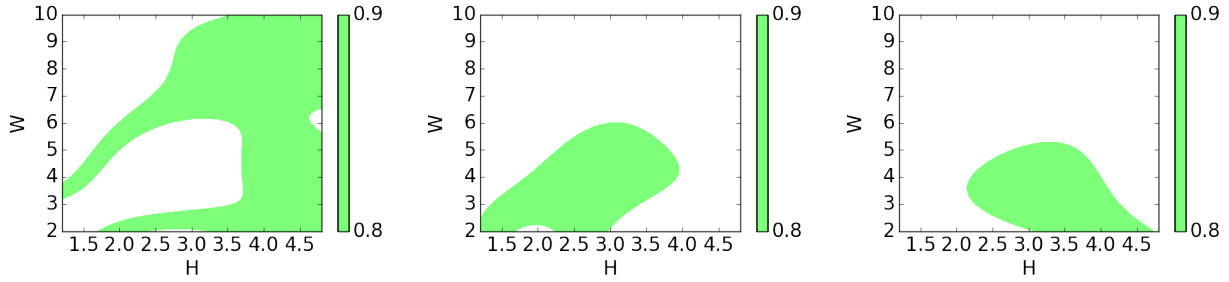

(a) 1000 particles of radius 1 in (b) 2000 particles of radius 0.794 in (c) 4000 particles of radius 0.63 in

Figure 8: All the designs that lies between the level sets 0.8 to 0.9 of the normalized power for the three particle sizes, namely (a) 1 in, (b) 0.794 in and (c) 0.63 in using respectively 1000, 2000 and 4000 particles.

GPU was developed. In addition to the design cycle, the role that this paradigm will play in education is invaluable as an in-house corporate training tool for young engineers to actively train and develop understanding for specific industrial processes. The initial results prove to be promising and warranting extensive research to be conducted in future.

Acknowledgements

We gratefully acknowledge the support of NVIDIA Corporation with the donation of the Titan X Pascal GPU used for this research.

REFERENCES

[1] Clearly P. and Sawley M. DEM modelling of industrial granular flows: 3D case studies and the effect of particle shape on hopper discharge. *App. Math. Mod.* (2002)**26**:89–111.

[2] Govender N., Wilke D.N. and Kok S., Collision detection of convex polyhedra on the NVIDIA GPU architecture for the discrete element method, *App. Math. Comp.*. (2015)**267**:810–829.

[3] Boukouvala F., Muzzio F., Ierapetritou M. G. and Y. Gao, Reduced-order discrete element method modeling, *Chem. Eng. Sci.* (2013)**95**:12–26.

[4] *Enhanced Intel SpeedStep Technology for the Intel Pentium M Processor (White Paper)*. Intel Corporation. (2004) Retrieved 2013-12-21.

[5] Wilke D.N., Govender N., Rajamani R.K. and Pizette P. *Geometric design of tumbling mill lifter bars utilizing the discrete element method*. 12th World Congress on Structural and Multidisciplinary Optimization 5th - 9th, June 2017, Braunschweig, Germany.

[6] Robinson T. D., Eldred M. S. Willcox K. E. and Haimes R. Surrogate-Based Optimization Using Multifidelity Models with Variable Parameterization and Corrected Space Mapping. *AIAA J.*. (2008)**46**:2814–2822.

[7] Leifsson L. and Koziel S. Multi-fidelity design optimization of transonic airfoils using physics-based surrogate modeling and shape-preserving response prediction, *J. of Comp. Sci.*. (2010)**1**:98–106.

[8] Wilke, D.N., Kok S. and Groenwold A.A. Relaxed error control in shape optimization that utilizes remeshing. *Int. J. of Num. Meth. in Eng.* (2013)**94**:273–289.

[9] Allaire D. and Wilcox K. A mathematical and computational framework for multifidelity design and analysis with computer models. *Int. J. Uncert. Quant.*(2014)**(4)**:1–20.

[10] Yorke J.A. and Anderson Jr W.N. Predator-Prey Patterns (Volterra-Lotka equations). *Proceedings of the National Academy of Sciences.*(1973)**70**.

[11] Wang Y. *Performance and Power Optimization of GPU Architectures for General-purpose Computing*. PhD University of South Florida (2014). Accessed by Graduate theses and Dissertations `http://scholarcommons.usf.edu/etd/5325`

[12] Govender N., Wilke D.N., Kok S. and Els R. Development of a convex polyhedral discrete element simulation framework for NVIDIA Kepler based GPUs, *Journal of Computational and Applied Mathematics*).(2014)**270**:386–400.

[13] Wilke, D.N., Govender N., Rajamani R.K. and Pizette P. Geometric design of tumbling mill lifter bars utilizing the discrete element method. *12th World Congress of Structural and Multidisciplinary Optimisation.*(2017).

V International Conference on Particle-based Methods – Fundamentals and Applications
PARTICLES 2017
P. Wriggers, M. Bischoff, E. Oñate, D.R.J. Owen, & T. Zohdi (Eds)

A FULLY EXPLICIT FLUID-STRUCTURE INTERACTION APPROACH BASED ON PFEM AND FEM

SIMONE MEDURI[1], MASSIMILIANO CREMONESI [1] AND UMBERTO PEREGO[1]

[1]Department of Civil and Environmental Engineering
Politecnico di Milano
Piazza Leonardo da Vinci, 32, 20133 Milano, Italy
simone.meduri@polimi.it; massimiliano.cremonesi@polimi.it; umberto.perego@polimi.it

Key words: Fluid-Structure Interaction; PFEM-FEM coupling; domain decomposition; explicit dynamics.

Abstract. Partitioned approaches for the solution of Fluid-Structure Interaction (FSI) problems are particularly interesting because, among other aspects, they allow for the reuse of existing software. In this work, we propose a partitioned scheme based on the weakly compressible PFEM for the fluid domain and SIMULIA Abaqus/Explicit for the solid domain. The coupling is treated with a domain decomposition approach based on the Gravouil-Combescure algorithm. This approach allows for the use of different time step size on the two phases (fluid and solid) and incompatible mesh at the interfaces. The main goal of the proposed fomrulation is to show the possibility of a strong fluid-structure interaction coupling within af fully explicit sframework. 2D test-cases will be presented to validate the proposed coupling technique. The explicit time integration scheme for both the fluid and solid subdomains, together with the explicit treatment of the coupling, makes this method appealing for large scale applications in a variety of engineering problems with fast dynamics and/or a high degree of non-linearity.

1 INTRODUCTION

The numerical simulation of fluid-structure interaction (FSI) problems involving free-surfaces is of great interest in many engineering applications. Particle-based methods, like PFEM, are particularly suited for the analysis of free-surface flows and fluid-structure interaction with large displacements of the interface. In the current work, a partitioned approach for the solution of the FSI problem is proposed. The fluid domain is discretized using the Particle Finite Element Method (PFEM). The weakly compressible formulation of fluid flow, originally proposed in [1] for the PFEM, allows for a fully explicit solution scheme. Thanks to the Lagrangian formulation, the free surface is directly defined by the current position of the particles, coinciding with the nodes of the fluid finite element

mesh, while the governing equations are imposed like in the standard FEM (see e.g. [2, 3, 4, 5, 6]). When the mesh becomes too distorted, a fast triangulation algorithm is used to redefine the connectivities. The structural domain is instead analysed with a standard commercial explicit FEM (SIMULIA Abaqus-Explicit). The coupling between the fluid and solid domains is treated with the GC Domain Decomposition approach [9]. On each subdomain the problem is solved independently and then the two solutions are linked at the interface using a Lagrange multiplier technique. The proposed method allows for different time-steps in the two subdomains and for non-conforming meshes at the interfaces between the solid and fluid domains. Moreover, this approach allows for an explicit coupling, without iterations, between the two subdomains. 2D test-cases will be presented to validate the proposed coupling technique. The explicit, high parallelizable, scheme for both the fluid and solid subdomains, together with the explicit treatment of the coupling, makes this method appealing for applications in a variety of large scale engineering problems with fast dynamics and/or a high degree of non-linearity.

2 GOVERNING EQUATIONS

The weakly compressible Navier-Stokes equations are used to model the fluid domain Ω_f^t. Introducing the coordinates in the current configuration $\mathbf{x}$, the fluid density ρ_f, the fluid velocity $\mathbf{v}_f$ and the external forces $\mathbf{b_f}$, mass and momentum conservations read:

$$\frac{d\rho_f}{dt} + \rho_f(\nabla_{\mathbf{x}} \cdot \mathbf{v}_f) = 0 \quad \text{in } \Omega_f^t \times [0,T] \tag{1}$$

$$\rho_f \frac{d\mathbf{v}_f}{dt} = \nabla_{\mathbf{x}} \cdot \boldsymbol{\sigma}_f + \rho_f \mathbf{b_f} \quad \text{in } \Omega_f^t \times [0,T] \tag{2}$$

where $\boldsymbol{\sigma}_f$ is the Cauchy stress tensor which can be decomposed into its deviatoric and isotropic parts: $\boldsymbol{\sigma}_f = -p_f\mathbf{I} + \boldsymbol{\tau}_f$. Under the hypothesis of weak compressibility, the pressure field p_f can be expressed as a function of the density ρ_f through the Tait equation:

$$p_f(\rho_f) = p_{0,f} + K_f \left[\left(\frac{\rho_f}{\rho_{0,f}} \right)^{\gamma} - 1 \right] \tag{3}$$

where $p_{0,f}$ is the reference pressure, $\rho_{0,f}$ the reference density, $\gamma = 7$ the specific heat ratio and K_f the bulk modulus.

Introducing now the solid density ρ_s, the solid velocity $\mathbf{v}_s$, the external forces on the solid domain $\mathbf{b_s}$ and the stress tensor $\boldsymbol{\sigma}_s$, the momentum conservation equation can be written in the solid domain Ω_s^t as:

$$\rho_s \frac{d\mathbf{v}_s}{dt} = \nabla_{\mathbf{x}} \cdot \boldsymbol{\sigma}_s + \rho_s \mathbf{b}_s \quad \text{in } \Omega_s^t \times [0,T] \tag{4}$$

Standard Dirichlet and Neumann boundary conditions are applied on both the domains.

3 NUMERICAL APPROACH

A standard Galerkin finite element approach is applied to obtain the semidiscretized form of momentum conservation equations for the fluid and solid domains:

$$\mathbf{M}_f \frac{d\mathbf{V}_f}{dt} = \mathbf{F}_{ext,f} - \mathbf{F}_{int,f} \quad \text{in } \Omega_f^t \times [0,T] \tag{5}$$

$$\mathbf{M}_s \frac{d\mathbf{V}_s}{dt} = \mathbf{F}_{ext,s} - \mathbf{F}_{int,s} \quad \text{in } \Omega_s^t \times [0,T] \tag{6}$$

where $\mathbf{M}$ are the mass matrices, $\mathbf{V}$ the vector of nodal velocities and $\mathbf{F}_{int}$ and $\mathbf{F}_{ext}$ the vectors of internal and external nodal forces, respectively.

Fluid mass conservation (1) is discretized starting from the Lagrangian strong form, leading to:

$$\mathbf{M}_\rho \mathbf{R}_f = \mathbf{R}_0 \tag{7}$$

where $\mathbf{R}_f$ contains the nodal values of the density field (details can be found in [1]).

A Central Difference Scheme [7] has been used to integrate equations (5-6) in time. It is important to recall that performing a mass lumping in the mass matrices, a fully decoupled system of equations can be obtained and fluid and solid velocities can be computed explicitly node by node. The proposed integration scheme is known to be conditionally stable, consequently an adaptive time step which guarantees the respect of the CFL condition has been used.

A partitioned approach is here proposed for the solution of the fluid-structure interaction problem. The fluid sub-problem is solved numerically through the weakly compressible PFEM (see [1]) while the solid sub-problem is analyzed using the commercial software Abaqus/Explicit [8].

4 THE COUPLING SCHEME

To couple the fluid and the solid subdomains, a partitioned approach, based on the so-called GC (Gravouil-Combescure) algorithm [9], has been used. This algorithm, originally conceived for non-overlapping structural domains, has been recently extended to FSI problems [10]. Applying the GC algorithm to FSI problems, the fluid and structural domain are solved independently, as if there was no interaction between them. The two separated analyses are then synchronized by considering a small system of constraint equations at the fluid-structure interface, ensuring the strong coupling of the partitioned approach. If explicit time integration is used for both the fluid and structural domain, as in the present case, the correction step consists in a small system of decoupled equations, resulting in a fully explicit coupled solver. The proposed algorithm allows for the use of incompatibles meshes at the fluid-solid interface and, moreover, guarantees the possibility of the use of different time steps in the two sub-domains. A complete description of the proposed approach can be found in [11].

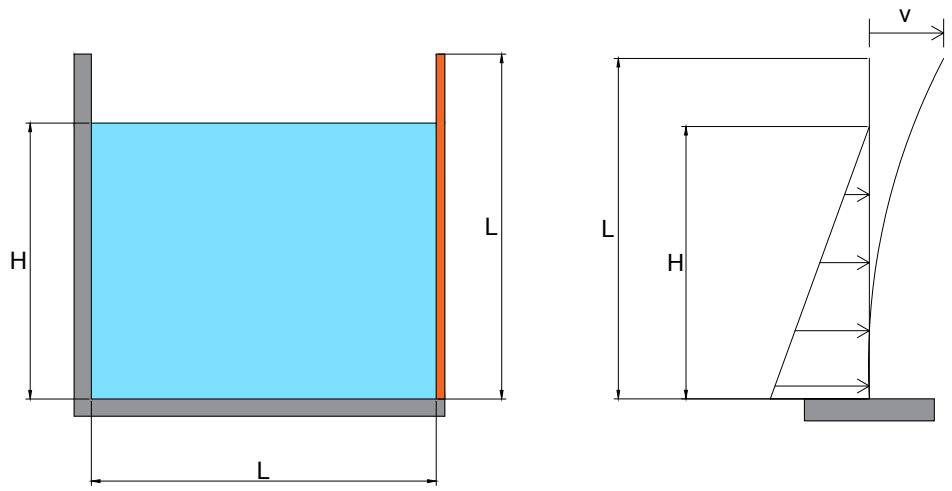

Figure 1: (a) Geometry of the numerical examples. (b) Equivalent Structural scheme.

5 NUMERICAL EXAMPLES

5.1 Beam under hydrostatic load

In the first validation case, the problem depicted in Fig. 1(a) and presented in [12] is considered. A tank full of water at rest has rigid walls on its left and bottom sides, while the wall on the right side is made of a deformable beam clamped at its bottom edge. This problem can be associated to a simple structural analysis scheme, i.e. a clamped beam subjected to hydrostatic load, as shown in Fig 1(b). The analytical solution in the framework of linear elasticity and small displacements provide a useful validation for the proposed method. The geometrical and mechanical parameters of the fluid and the structure are listed in Table 1. Conforming meshes of average size of 0.002 m are used, leading to 2400 linear triangles for the fluid and 50 two-node linear beam elements for the structure. The static analytical solution for the displacement of the upper edge of the beam represented in Fig 1(b) is given by:

$$v = \frac{p_{max} d}{E_s I_s} \left[\frac{H^4}{30} + (L - H) \frac{h^3}{24} \right]$$

where $p_{max} = \rho_f g H$ is the maximum value of the hydrostatic pressure at the bottom of the tank, g being the gravity acceleration, I is the moment of inertia of the beam cross-section and d is the out-of-plane thickness of the beam, which is assumed to be equal to the one of the fluid domain. Substituting the data of the problem at hand, one gets a horizontal displacement of $v = 0.09767\ mm$ and a maximum pressure at the bottom of the beam equal to $p_{max} = 784.8\ Pa$. These analytical values will be used for the validation of the numerical results obtained with the present approach.
Fig. 2(a) shows the time history of the horizontal displacement of the upper edge of the

Table 1: Beam under hydrostatic loading. Geometry and mechanical parameters.

Geometry	
L	$0.1\ m$
H	$0.08\ m$
d	$1\ m$
beam width	$0.012\ m$
Fluid	
Density	$\rho_f = 1000\ kg/m^3$
Viscosity	$\mu_f = 0.1\ Pa \cdot s$
Bulk Modulus	$K_f = 2.15 \cdot 10^9\ Pa$
Structure	
Density	$\rho_s = 2500\ kg/m^3$
Young Modulus	$E_s = 100 \cdot 10^6\ Pa$

beam, while Fig. 2(b) shows the time history of the pressure at the bottom edge. One can note that after the initial transient oscillations, the simulation reaches the steady state, which is in good agreement with the static analytical solution.

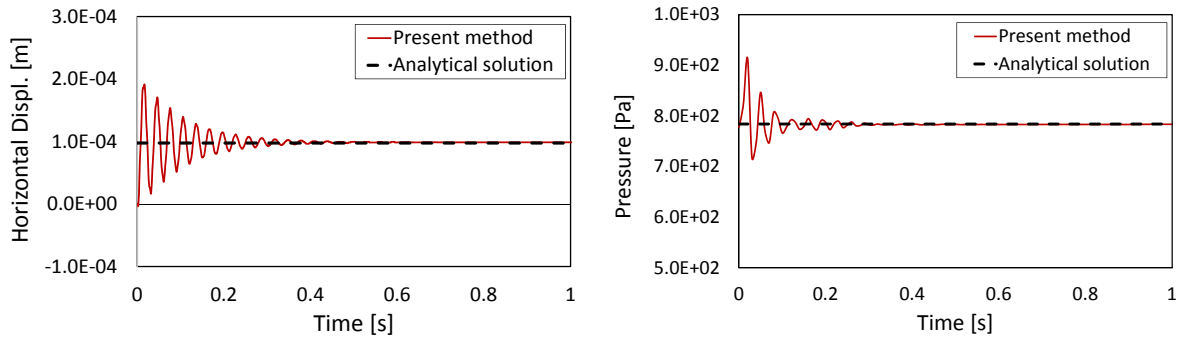

Figure 2: Beam under hydrostatic loading. (a) Time history of the horizontal displacement at the tip of the beam. (b) Time history of pressure at the bottom of the beam.

5.2 Tank interacting with a highly deformable beam

In this second example, a tank interacting with a highly deformable beam, originally proposed in [13], is considered. The geometry is the same of the previous case (Fig. 1(a)). The only different parameter is the beam Young's Modulus, which is $E_s = 1MPa$ in this case. Because of the lower beam stiffness, the analytical solution based on the hypothesis of small displacements and constant pressure is no longer valid. The beam deflection

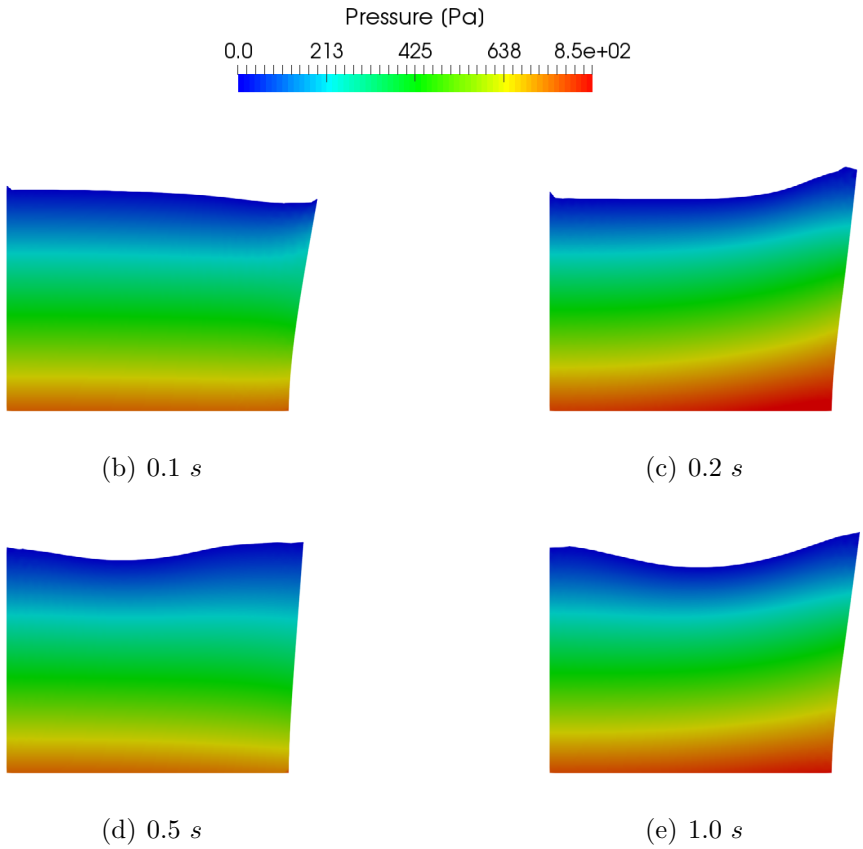

(b) 0.1 s (c) 0.2 s

(d) 0.5 s (e) 1.0 s

Figure 3: Tank interacting with a highly deformable beam. Snapshots of the simulation at different time instants.

generates a sloshing wave which interacts dynamically with the beam itself, leading to their oscillations. Fig. 3 shows some snapshots of the simulation that are qualitatively in good agreement with the numerical results presented in [13]. For a more quantitative validation, Fig. 4 shows the time histories comparison of the horizontal displacement at the tip of the beam. One can observe that the frequency of oscillations is the same and, despite a small overestimation of their peaks, the comparison between the two curves can be considered very satisfactory.

6 CONCLUSIONS

In the present work a fully explicit and fully Lagrangian PFEM-FEM coupling scheme has been proposed for the solution of fluid-structure interaction problems. The GC domain decomposition method has been used to couple the two subdomains. The GC algorithm ensures the strong coupling and the stability of the partitioned approach. A fully explicit approach with different time step sizes and incompatible meshes at the interface has been proposed and validated. The comparison of 2D-examples with analytical and numerical

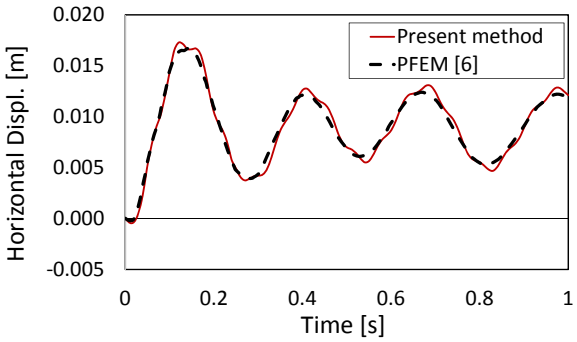

Figure 4: Tank interacting with a highly deformable beam. Time history of the horizontal displacement at the tip of the beam.

results presented in the literature shows the effectiveness and accuracy of the proposed coupling scheme. The resulting fully explicit solver is appealing for its possible application in a large variety of large scale engineering problems with fast dynamics and/or a high degree of non-linearity.

REFERENCES

[1] Cremonesi, M., Meduri, S., Perego, U. and Frangi, A. An explicit Lagrangian finite element method for free-surface weakly compressible flows. *Comp. Particle Mech.* (2017) DOI: 10.1007/s40571-016-0122-7

[2] Oñate, E., Idelsohn, S.R., del Pin, F. and Aubry,R. The Particle Finite Element Method. An Overview. *Int J Computational Method* (2004) **1**:267-307.

[3] Idelsohn, S. R., Oñate, E., Del Pin, F. and Calvo, N. Fluid-structure interaction using the Particle Finite Element Method. *Computer Meth. in Appl. Mech. and Engng.* (2006) **195**:2100-2123.

[4] Idelsohn, S. R., Mier-Torrecilla, M. and Oñate, E. Multi-fluid flows with the Particle Finite Element Method. *Computer Meth. in Appl. Mech. and Engng.* (2009) **198**:2750-2767.

[5] Idelsohn, S. R., Del Pin, F., Rossi, R. and Oñate, E. Fluid-structure interaction problems with strong added-mass effect. *Int. J. Numer. Meth. Engng.* (2009) **80**:1261-1294.

[6] Cremonesi, M., Ferri, F. and Perego U. A basal slip model for Lagrangian finite element simulations of 3D landslides. *Int J Numer Anal Met* (2017) **41**:30-53.

[7] Hughes, T. J. R. The Finite Element Method: Linear Static and Dynamic Finite Element Analysis. Dover Publications. (1987)

[8] Dassault Systèmes SIMULIA. *Abaqus Documentation.* Providence, RI, USA, (2016).

[9] Combescure, A. and Gravouil, A. A time-space multi-scale algorithm for transient structural nonlinear problems. *Mecanique et Industries* (2001) **2**:43-55.

[10] Nunez-Ramirez, J., Marongiu, J. C., Brun, M. and Combescure, A. A partitioned approach for the coupling of SPH and FE methods for transient non-linear FSI problems with incompatible time-steps. *Int. J. Numer. Meth. in Engng.*(2016) 1-46.

[11] Meduri, S., Cremonesi, M., Perego, U., Bettinotti, O., Kurkchubasche, A. and Oancea, V. A partitioned fully explicit Lagrangian Finite Element Method for highly nonlinear Fluid-Structure-Interaction problems. *International Journal for Numerical Methods in Engineering.* (2017) DOI:10.1002/nme.5602

[12] Zhu, M. and Scott, M. H. Direct differentiation of the Particle Finite-Element Method for fluid-structure interaction using the PFEM. *J Struct. Eng.* (2016) **142**(3).

[13] Zhu, M. and Scott, M. H. Direct differentiation of the quasi-incompressible fluid formulation of fluid-structure interaction using the PFEM. *Computer Particle Mech.* (2017) 1-13.

V International Conference on Particle-based Methods – Fundamentals and Applications
PARTICLES 2017
P. Wriggers, M. Bischoff, E. Oñate, D.R.J. Owen, & T. Zohdi (Eds)

LATTICE BOLTZMANN FLUX SOLVER FOR SIMULATION OF HYPERSONIC FLOWS

Z. X. MENG[1], C. SHU[2], L. M. YANG[3], W. H. ZHANG [4], F. HU[5] AND S. Z. LI[6]

[1] College of Aerospace Science and Engineering, National University of Defense Technology
Changsha, 410073, China
Corresponding author: mengzhuxuan1990@gmail.com
[2] Department of Mechanical Engineering, National University of Singapore
10 Kent Ridge Crescent, Singapore 119260, Singapore
mpeshuc@nus.edu.sg
[3] Department of Mechanical Engineering, National University of Singapore
10 Kent Ridge Crescent, Singapore 17576, Singapore
yangliming_2011@126.com
[4] College of Aerospace Science and Engineering, National University of Defense Technology
Changsha, 410073, China
zhangweihua@nudt.edu.cn
[5] College of Aerospace Science and Engineering, National University of Defense Technology
Changsha, 410073, China
hufan@163.com
[6] College of Aerospace Science and Engineering, National University of Defense Technology
Changsha, 410073, China
Lishengze12@gmail.com

Key words: Non-free parameter D1Q4 model, lattice Boltzmann flux solver, hypersonic flows, finite volume method

Abstract: In this paper, a stable Lattice Boltzmann Flux Solver (LBFS) is proposed for simulation of hypersonic flows. In LBFS, the finite volume method is applied to solve the Navier-Stokes equations. One-dimensional Lattice Boltzmann model is applied to reconstruct the inviscid flux across the cell interface, while the viscous flux is solved by conventional smooth approximation function. The present work extends the existing LBFS to calculate hypersonic flow field on the leeward, which is hard to get convergent results due to extremely low pressure effects in this area. Simulation of a biconics model is studied. It is discovered that the tail area of double cone is related to the maximum Mach number that could be convergent. The larger the diameter of tail area is, the smaller Mach number could be convergent. Hence, the low pressure area behind double cone tail will have large effects during the LBFS simulation of hypersonic flow. Two measurements are applied in this paper to overcome the low pressure problem. The first one is to apply a local block grid refinement method based on the flow conditions for improving the stability. The second is to add a constraint parameter to eliminate negative value and give out a proper one. Hence, LBFS is able to get convergent result of the hypersonic flow field on both windward and leeward. Several numerical examples are tested to compare the performance of method presented in this paper. Simulation results show that method present in this paper is able to calculate hypersonic flow field on the leeward with both fine accurate and efficient.

1 INTRODUCTION

The hypersonic flow field is a research focus with its special characteristics [1]: (1) strong shock effect will cause fierce compression after the shock wave, (2) viscosity greatly changed from wall surface to far field area, (3) for hypersonic vehicles flying in high altitude, continuous medium assumption is no longer appropriate because of low density effect. The computational fluid dynamics (CFD) is becoming more and more popular in simulating hypersonic flow field. The finite volume method (FVM) is widely used in existing numerical methods [2]. This largely attributes to its spatial discretization is carried out directly in the physical space. Hence, structural grid is suitable for discretization, which provides an effective way for solving complex geometry problems. In the process of solving N-S equations by FVM, flux solver is the key to evaluate viscous and invicid fluxes at cell interface. The viscous flux is evaluated by applying a smooth function approximation and inviscid flux is calculated by various upwind schemes such as Roe scheme [3], van Leer scheme [4] and AUSM (Advection Upstream Splitting Method) scheme [5].

Boltzmann equation-based method is an alternative approach for simulating compressible flow field, including DVBE [6][8] (discrete velocity Boltzmann equation) and gas-kinetic scheme [9]-[13]. Gas-kinetic scheme have better efficiency than DVBE method. However, both of them are less efficient and more complicated than conventional Navier- Stocks slovers.

Lattice Boltzmann Flux Solver (LBFS) is a more efficient method which is proposed by Ji et al. [14] and for simulating inviscid flows. LBFS is improved by Shu and Yang et al. [15]-[19] and has been proved catching strong shock wave and expansion wave very well. In LBFS, Euler equations are discretized by FVM and the inviscid flux at cell interface is reconstructed by local solution of 1-D compressible Lattice Boltzmann model. LBFS is more efficient and easy to apply than DVBE and gas-kinetic method due to only 1-D Lattice Boltzmann model is applied and macroscopic governing equations are solved. However, because of 1-D model is applied along normal direction at cell interface, the tangential effect cannot be properly considered. Viscous flux should be taken into account to solve viscous problems. From chapman-Enskog expansion analysis [19], the inviscid flux can be fully determined by equilibrium non-equilibrium distribution function at cell interface, and the non-equilibrium part can be treated as numerical dissipation. For compressible viscous flows, especially for hypersonic flows, the numerical dissipation should be controlled. A switch function is proposed by Yang et al. [20] to weight viscous numerical dissipation and has been proved performed well in viscous simulation. For hypersonic flow field, physical values such as pressure in leeward side can be extremely low. Hence it is very easy to get a negative value in calculating process, which make it very difficult to get a convergent result.

In this work, a stable LBFS is proposed for simulation of 2-D compressible hypersonic viscous flows. The inviscid flux is calculated by LBFS and viscous flux is computed by smooth function approximation. Multiblock grids and local grid refinement method are applied to improve calculation stability. Also a constraint parameter is added to eliminate negative value and give out a proper one in calculating process. Besides, the implicit LU-SGS method is used to speed up the convergence rate. In the end, a biconics model in Ma=9.86 flow field is simulated to validate the developed solver. The results of solver presented in this work is compared with van Leer and Roe scheme to evaluate the precision proposed in this article.

2 METHODOLOGY

In LBFS, Navier-Stockes equations are solved in macroscopic scale and local solution of Lattice Boltzmann equations are applied in to construct inviscid flux solver at the cell interface. It has been proved that particle potential energy is independent from lattice velocity [15]. Lattice velocity would be decided by higher momentum conservation relation in this work instead of by artificial selection in traditional method.

N-S equations of intergral form without source term can be written as following.

$$\frac{\partial}{\partial t}\int_{\Omega}\mathbf{W}d\Omega+\oint_{\Gamma}(\mathbf{F}_c-\mathbf{F}_v)ds=0 \tag{1}$$

In which the conservative variables $\mathbf{W}$, inviscid flux $\mathbf{F}_c$ and viscous flux $\mathbf{F}_v$ are given by Eq. (2) in 2-D flow field.

$$\mathbf{W}=\begin{bmatrix}\rho\\ \rho u\\ \rho v\\ \rho E\end{bmatrix},\ \mathbf{F}_c=\begin{bmatrix}\rho U_n\\ \rho u U_n+n_x p\\ \rho v U_n+n_y p\\ (\rho E+p)U_n\end{bmatrix},\ \mathbf{F}_v=\begin{bmatrix}0\\ n_x\tau_{xx}+n_y\tau_{xy}\\ n_x\tau_{yx}+n_y\tau_{yy}\\ n_x\Theta_x+n_y\Theta_y\end{bmatrix} \tag{2}$$

The expressions of normal velocity U_n and total energy E are shown as Eq. (3). Where $e=p/[(\gamma-1)\rho]$ is the potential energy of mean flow.

$$\begin{aligned}U_n&=n_x u+n_y v\\ E&=e+\frac{1}{2}(u^2+v^2)\end{aligned} \tag{3}$$

The integral of fluxes in Eq. (1) can be discretized by FVM and the approximated summation form can be written as

$$\frac{d\mathbf{W}_I}{dt}=-\frac{1}{\Omega_I}\sum_{i=1}^{N_f}(F_{ci}-F_{vi})S_i \tag{4}$$

In which I represents the control volume index, Ω_I is the volume and N_f is number of faces of control volume I. In this paper, the inviscid flux F_c in Eq. (4) will be solved by LBFS with non-free parameter D1Q4 model [18] and viscous flux F_v will be solved by central difference method.

2.1 Non-free parameter D1Q4 lattice Boltzmann model

The distribution of discrete lattice velocities for D1Q4 model is shown in Fig. 1. This model contains 4 equilibrium distribution functions f_1^{eq}, f_2^{eq}, f_3^{eq}, f_4^{eq} and 2 lattice velocities d_1, d_2 (shown as Eq. (5)). The derivation process details are shown in references [18] .

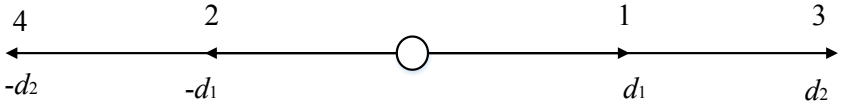

Figure 1: Distribution of discrete lattice velocities for D1Q4 model

$$
\begin{aligned}
f_1^{eq} &= \frac{\rho(-d_1 d_2^2 - d_2^2 u + d_1 u^2 + d_1 c^2 + u^3 + 3uc^2)}{2d_1(d_1^2 - d_2^2)} \\
f_2^{eq} &= \frac{\rho(-d_1 d_2^2 + d_2^2 u + d_1 u^2 + d_1 c^2 - u^3 - 3uc^2)}{2d_1(d_1^2 - d_2^2)} \\
f_3^{eq} &= \frac{\rho(d_1^2 d_2 + d_1^2 u - d_2 u^2 - d_1 c^2 - u^3 - 3uc^2)}{2d_2(d_1^2 - d_2^2)} \\
f_4^{eq} &= \frac{\rho(d_1^2 d_2 - d_1^2 u - d_2 u^2 - d_2 c^2 + u^3 + 3uc^2)}{2d_2(d_1^2 - d_2^2)} \\
d_1 &= \sqrt{u^2 + 3c^2 - \sqrt{4u^2 c^2 + 6c^4}} \\
d_2 &= \sqrt{u^2 + 3c^2 + \sqrt{4u^2 c^2 + 6c^4}}
\end{aligned}
\tag{5}
$$

In which $c = \sqrt{Dp/\rho}$ represents particular velocity of particles and D is space dimension. It has been proved by Yang [18] that physical conservation laws (Eq. (6)) can revivify the N-S equations by applying relations in Eq. (5). ξ_i means particle velocity in *i*-direction, for example $\xi_1 = d_1, \xi_2 = -d_1, \xi_3 = d_2$ and $\xi_4 = -d_2$. For higher dimensional problems, the D1Q4 model should be applied along the normal direction of cell interface [18] as is shown in Fig. 2 of the 2D case. The normal velocity U_n (Eq. (3)) and tangential velocity $U_\tau = (u_{\tau x}, u_{\tau y}) = \mathbf{u} - U_n \mathbf{n}$ in Fig. 2 will replace u in Eq. (6). Finally, we will get $u = U_n n_x + u_{\tau x}$.

$$
\begin{aligned}
\rho &= \sum_{i=1}^{4} f_i^{eq} \\
\rho u &= \sum_{i=1}^{4} f_i^{eq} \xi_i \\
\rho u^2 + \rho c^2 &= \sum_{i=1}^{4} f_i^{eq} \xi_i \xi_i \\
\rho u^3 + 3\rho u c^2 &= \sum_{i=1}^{4} f_i^{eq} \xi_i \xi_i \xi_i
\end{aligned}
\tag{6}
$$

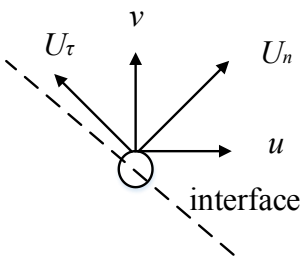

Figure 2: Application of 1D model to 2D case

By applying Eq. (6) to Eq. (2), we will get the conservation variable $\mathbf{W}$ and inviscid flux $\mathbf{F}_c$

of 2-D flow field as following.

$$\mathbf{W}=\begin{bmatrix}\rho\\ \rho(U_n n_x+u_{\tau x})\\ \rho(U_n n_y+u_{\tau y})\\ \rho(U_n^2/2+e)+\rho|U_\tau|^2/2\end{bmatrix},\ \mathbf{F}_c=\begin{bmatrix}\rho U_n\\ \rho(U_n^2+p)n_x+\rho U_n u_{\tau x}\\ \rho(U_n^2+p)n_y+\rho U_n u_{\tau y}\\ (\rho(U_n^2/2+e)+p)U_n+\rho|U_\tau|^2/2\end{bmatrix} \tag{7}$$

2.2 Inviscid flux model

Suppose that cell interface is located at $x_{c,j+1/2}=0$, then the inviscid flux at interface $\overline{\mathbf{F}}_c$ is decided by normal velocity and can be written as Eq. (8). In which the moments $\boldsymbol{\varphi}_a=\left[1,\xi_i,\xi_i^2/2+e_p\right]^T$ and $f_i(0,t)$ is the distribution function at cell interface. Generally speaking. $f_i(0,t)$ is summation of equilibrium part $f_i^{eq}(0,t)$ and non equilibrium part $f_i^{neq}(0,t)$.

$$\overline{\mathbf{F}_c}=\begin{bmatrix}\rho U_n\\ \rho U_n^2+p\\ (\rho(U_n^2/2+e)+p)U_n\end{bmatrix}=\sum_{i=1}^{4}\xi_i\boldsymbol{\varphi}_a f_i(0,t) \tag{8}$$

To recover N-S equations by Boltzmann equation from Chapman-Enskog analysis [19][21][22][23][24], the non-equilibrium part $f_i^{neq}(0,t)$ can be written as following.

$$f_i^{neq}(0,t)=-\tau\left(\frac{\partial f_i}{\partial t}+\xi_i\frac{\partial f_i}{\partial x}\right)\Big|_{(0,t)} \tag{9}$$

Then applying Taylor series expansion in tome and physics space, Eq. (9) can be simplified as following.

$$f_i^{neq}(0,t)=-\frac{\tau}{\delta t}\left[f_i(0,t)-f_i(-\xi_i\delta t,t-\delta t)\right]+o(\delta t) \tag{10}$$

At the cell interface the equillibrium distribution function is $f_i(0,t)=f_i^{eq}(0,t)$. $f_i(-\xi_i\delta t,t-\delta t)$ is equilibrium distribution function at surrouding point of the cell interface. Substituting Eq. (9) into Eq. (8) as following.

$$f_i(0,t)=f_i^{eq}(0,t)-\tau_0\left[f_i(0,t)-f_i(-\xi_i\delta t,t-\delta t)\right]+o(\delta t) \tag{11}$$

In which $\tau_0=\tau/\delta t$ is the dimensionless collision time and δt dt is the streaming time step and represents the physical viscous of N-S equations. The contribution of non-equlibrium part is always treated as numerical dissipation in LBFS. Therefore, τ_0 can be regarded as the weight of numerical dissipation. We have $\tau_0=\max\left\{\tau^L,\tau^R\right\}$ in this work. In which $\tau^L=\max_{j=1,N_{fL}}\left\{\tau_j\right\},\tau^R=\max_{j=1,N_{fR}}\left\{\tau_j\right\}$ and $,\tau_j=\tanh\left(C\frac{\left|p^L-p^R\right|}{p^L+p^R}\right)$. N_{fL} and N_{fR} are the number of control volume on left and right side of cell interface. The details can be found in [25].

Substituting Eq. (11) into Eq. (8) we will get inviscid flux $\overline{\mathbf{F}}_c$ which is decided by tangential velocity as following.

$$\begin{aligned}\overline{\mathbf{F}}_c &= \sum_{i=1}^{4}\xi_i\boldsymbol{\varphi}_a f_i(0,t)+\tau_0\left[\sum_{i=1}^{4}\xi_i\boldsymbol{\varphi}_a f_i(-\xi_i\delta t,t-\delta t)-\sum_{i=1}^{4}\xi_i\boldsymbol{\varphi}_a f_i(0,t)\right] \\ &= \overline{\mathbf{F}}_c^{\mathrm{I}}+\tau_0(\overline{\mathbf{F}}_c^{\mathrm{II}}-\overline{\mathbf{F}}_c^{\mathrm{I}})\end{aligned} \tag{12}$$

Total invisicid flux at cell interface considering tangential velocity contribution is shown as following.

$$\mathbf{F}_c = \mathbf{F}_c^{\mathrm{I}}+\tau_0(\mathbf{F}_c^{\mathrm{II}}-\mathbf{F}_c^{\mathrm{I}}) \tag{13}$$

$\mathbf{F}_c^{\mathrm{I}}$ represents contribution of equilibrium distribution function $f_i^{eq}(0,t)$ at cell interface and $\mathbf{F}_c^{\mathrm{II}}$ means equilibrium distribution function $f_i(-\xi_i\delta t,t-\delta t)$ at surrouding point of the cell interface.

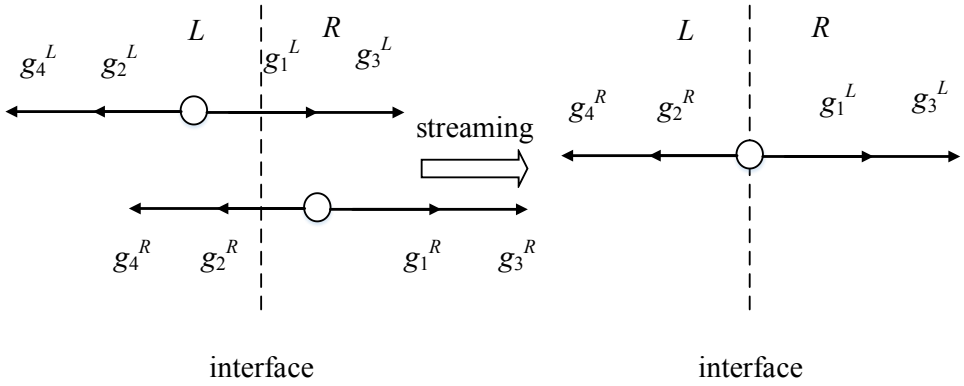

Figure 3: Streaming process based on D1Q4 model at cell interface

Supposing that a local Riemann problem is formed at cell interface, which is shown in Fig. 3. Hence, equilibrium distribution function $f_i(-\xi_i\delta t,t-\delta t)$ at surrouding point of cell interface can be decided by the location of $-\xi_i\delta t$, which is shown as Eq. (14).

$$f_i(-\xi_i\delta t,t-\delta t)=\begin{cases}f_i^L & -\xi_i\delta t\le 0\\ f_i^R & -\xi_i\delta t>0\end{cases} \tag{14}$$

More specifically, Eq. (14) can be written as following for D1Q4 model.

$$f_i(-\xi_i\delta t,t-\delta t)=\begin{cases}f_i^L & i=1,3\\ f_i^R & i=2,4\end{cases} \tag{15}$$

By applying the relationship of $f_i(0,t)=f_i^{eq}(0,t)-f_i^{neq}(0,t)$, the conservation flux which is decided by tangential velocity can be written as following.

$$\overline{\mathbf{W}}^M=\begin{bmatrix}\rho\\ \rho U_n\\ \rho(U_n^2/2+e)\end{bmatrix}=\sum_{i=1}^{4}\boldsymbol{\varphi}_a f_i^{eq}(0,t)+\sum_{i=1}^{4}\boldsymbol{\varphi}_a f_i^{neq}(0,t) \tag{16}$$

The subscript M means parameter on cell interface. The non-equilibrium part has no contribution to calculate conservation variables according to the compatibility condition [19], which is shown as following.

$$\sum_{i=1}^{4}\boldsymbol{\varphi}_a f_i^{neq}(0,t) = -\tau_0\sum_{i=1}^{4}\boldsymbol{\varphi}_a\left[f_i(0,t) - f_i(-\xi_i\delta t, t-\delta t)\right] = 0 \tag{17}$$

Substituting Eq.(17) into Eq. (16) we will get

$$\overline{\mathbf{W}}^M = \sum_{i=1}^{4}\boldsymbol{\varphi}_a f_i(0,t) = \sum_{i=1}^{4}\boldsymbol{\varphi}_a f_i(-\xi_i\delta t, t-\delta t) \tag{18}$$

By applying Eq. (15) into Eq. (18), the conservation flux which is decided by tangential velocity $\overline{\mathbf{W}}^M$ can be written as

$$\overline{\mathbf{W}}^M = \sum_{i=1,3}\boldsymbol{\varphi}_a f_i^L + \sum_{i=2,4}\boldsymbol{\varphi}_a f_i^R \tag{19}$$

Therefore, density, normal velocity and pressure at cell interface are obtained from Eq. (19). Then the tangential velocity at cell interface can be calculated by the following equation.

$$(\rho U_\tau)^M = \sum_{i=1,3} f_i^L U_\tau^L + \sum_{i=2,4} f_i^R U_\tau^R \tag{20}$$

In which U_τ^M, U_τ^L and U_τ^R are tangential velocity at cell interface, on the left and right side of cell interface respectively. Based on Eq. (19) and Eq. (20), all variables at cell interface such as ρ^M, p^M U_τ^M and U_n^M can be obtained. Substituting these variables to Eq. (5) and we can get the equlibrium distibution function $f_i(0,t)$ at cell interface.

The $\mathbf{F}_c^{\mathrm{I}}$ in Eq. (13) including two parts, which are $\overline{\mathbf{F}}_c^{\mathrm{I}}$ decided by normal velocity and the part decided by tangential velocity. Then $\mathbf{F}_c^{\mathrm{I}}$ can be written as following by applying variables at cell interface.

$$\mathbf{F}_c^{\mathrm{I}} = \begin{bmatrix} \rho U_n \\ (\rho U_n^2 + p)n_x + \rho U_n u_{\tau x} \\ (\rho U_n^2 + p)n_y + \rho U_n u_{\tau y} \\ (\rho({U_n}^2/2 + e) + p)U_n + \rho U_n \left|U_\tau\right|^2/2 \end{bmatrix} \tag{21}$$

Also $\mathbf{F}_c^{\mathrm{II}}$ is consists of $\overline{\mathbf{F}}_c^{\mathrm{II}}$ decided by normal velocity and the part decided by tangential velocity. Substituting equilibrium distribution function $f_i(-\xi_i\delta t, t-\delta t)$ at surrouding point of cell interface to Eq. (8) we will get $\overline{\mathbf{F}}_c^{\mathrm{II}}$ as following.

$$\overline{\mathbf{F}}_c^{\mathrm{II}} = \sum_{i=1,3}\xi_i\boldsymbol{\varphi}_\alpha f_i^L + \sum_{i=2,4}\xi_i\boldsymbol{\varphi}_\alpha f_i^R \tag{22}$$

Then the tangential velocity at cell interface can be calculated by the following equation.

$$
\begin{aligned}
(\rho U_n U_\tau)^M &= \sum_{i=1,3} \xi_i f_i^L U_\tau^L + \sum_{i=2,4} \xi_i f_i^R U_\tau^R \\
(\rho U_n |U_\tau|^2)^M &= \sum_{i=1,3} \xi_i f_i^L |U_\tau^L|^2 + \sum_{i=2,4} \xi_i f_i^R |U_\tau^R|^2
\end{aligned}
\tag{23}
$$

Now $\mathbf{F}_c^{\mathrm{II}}$ can be expressed as following. In which $f_i = f_i(-\xi_i \delta t, t - \delta t)$.

$$
\mathbf{F}_c^{\mathrm{II}} = \begin{bmatrix}
\sum_{i=1}^{4} \xi_i f_i \\
\sum_{i=1}^{4} \xi_i \xi_i f_i \bullet n_x + \sum_{i=1}^{4} \xi_i f_i \bullet U_{\tau x}^M \\
\sum_{i=1}^{4} \xi_i \xi_i f_i \bullet n_y + \sum_{i=1}^{4} \xi_i f_i \bullet U_{\tau y}^M \\
\sum_{i=1}^{4} \xi_i (\frac{1}{2} \xi_i \xi_i + e_p) f_i + \frac{1}{2} \sum_{i=1}^{4} \xi_i f_i \bullet |U_\tau^M|^2
\end{bmatrix}
\tag{24}
$$

By substituting Eq. (21) and Eq. (24) to Eq. (13) we get inviscid flux $\mathbf{F}_c$ on cell interface.

2.3 Viscous flux model

In this work, central difference scheme is applied to solve the visous flux $\mathbf{F}_v$. Stress tensor $\overline{\overline{\tau}}$ and flux vector Θ in Eq. (2) are given by

$$
\begin{aligned}
\overline{\overline{\tau}} &= \mu \left[\left(\nabla \mathbf{u} + (\nabla \mathbf{u})^T \right) - \frac{2}{3} (\nabla \bullet \mathbf{u}) \overline{\overline{\mathbf{I}}} \right] \\
\Theta &= \overline{\overline{\tau}} \bullet \mathbf{u} + k \nabla T
\end{aligned}
\tag{25}
$$

In which μ is dynamic viscosity and decided by Sutherland's law and turbulence model. k is thermal conductivity and $\overline{\overline{\mathbf{I}}}$ is unit matrix.

For physical variables on cell interface, such as u, v, w and k, can be calculated by arithmetic mean value on left and right side of cell interface, shown as following.

$$
\phi^M = \frac{1}{2} (\phi^L + \phi^R)
\tag{26}
$$

Where ϕ represents any physical variables. The derivatives in Eq. (25) are calculated by finite difference scheme and detils are shwon in reference [26].

2.4 Method to improve numerical stability

Multiblock grids are applied to refine local grid quality. Grids local refinement method is used near wall surface and block interface. Hence, scheme stablity has been improved by reducing spatial step, especially in the leeward side of flow field. Besides, a constraint judgement is added in our code to avoid negative value in calculating process. In this work, implicit LU-SGS method [27] is applied to speed up the convergence rate and keep calculation robust.

3 NUMERICAL SIMULATION

Biconics model is used to verify the present solver. The shape of biconics model is shown as Fig. 4. The head curvature radius is 3.84mm, semi-cone angle is 12.84 degree in front and 7 degree in back, while the length of front cone is 69.55mm and 122.24mm totally. The free stream has a pressure of $P_\infty = 59.92\text{Pa}$, temperature of $T_\infty = 48.88\text{K}$ and Mach number $Ma_\infty = 9.86$.

Fig. 5 shows mach number distribution obtained by present solver in this article. It can be seen clearly that LBFS can capture strong shock waves and flow inside the boundary layer exactly. The maximum Mach number is 16.93Ma.

Fig. 6 shows the pressure contours bibonics model without tail flow field, and Fig. 7 is the one has tail field. Fig. 8 and Fig. 9 show temperature distributions. One block grids are applied of flow field without tail simulation. It is easier for calculation convergent without low pressure effect in back tail flow.

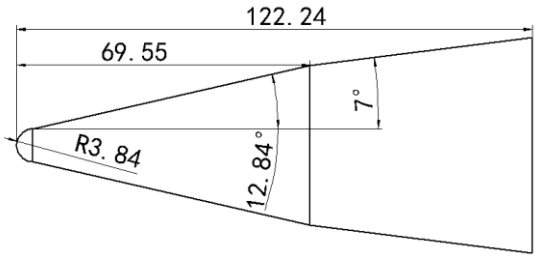

Figure 4: Measurements of biconics model

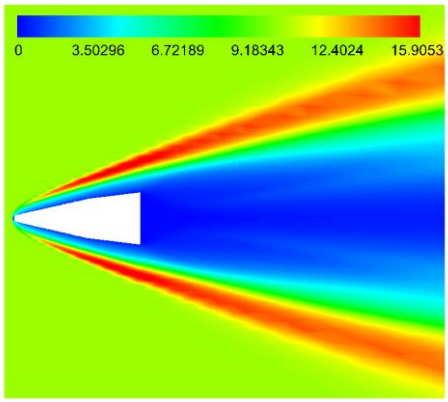

Figure 5: Mach number contours obtained by LBFS at Ma=9.86

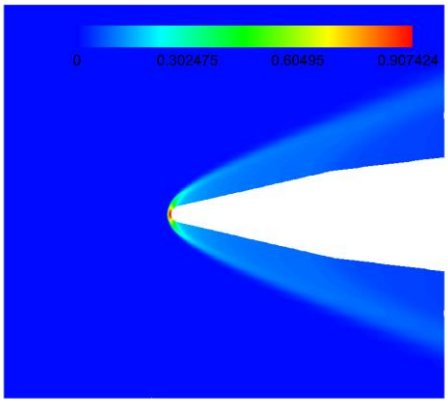

Figure 6: Pressure contours obtained by LBFS without back tail flow field

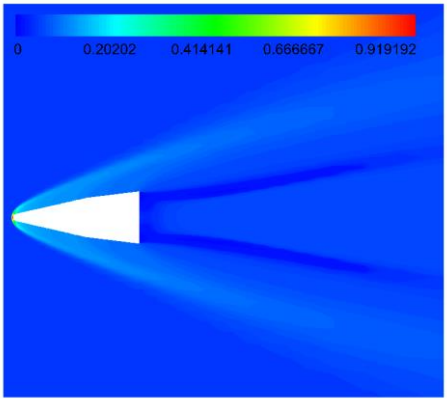

Figure 7: Pressure contours obtained by LBFS with back tail flow field

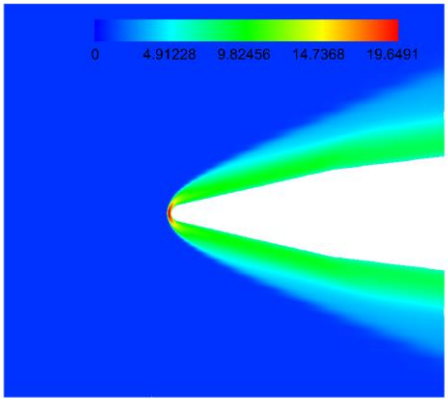

Figure 8: Temperature contours obtained by LBFS without back tail flow field

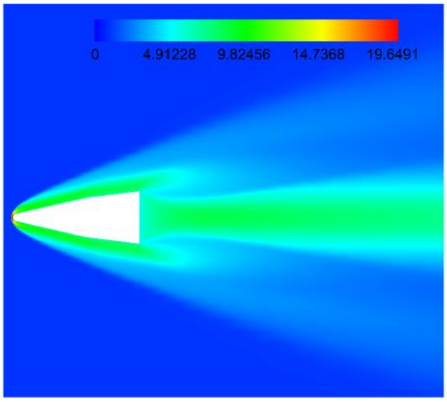

Figure 9: Temperature contours obtained by LBFS with back tail flow field

The hypersonic flow can only be affected by inflow in theory. To validate this we give out comparision of results in with and without back tail flow field which are shown as Fig. 10 and Fig. 11. Fig. 10 is comparison of pressure coefficient Cp. Results of with back tail flow field are shown by lines and without tail results are shown by symbols. Also to evaluate LBFS in this work, van Leer scheme and Roe scheme are applied and the results are shown below. Because high temperature is a focous problem in hypersonic flow research, we also discuss heat flux calculation here. Fig. 11 gives out comparison of heat flux. The experiment data is from reference [28].

Results in Fig. 10 and Fig. 11 show that LBFS in this work can offer both high computational accuracy and numerical stablity. Hence, it is demonstrated useful for aircraft research and design.

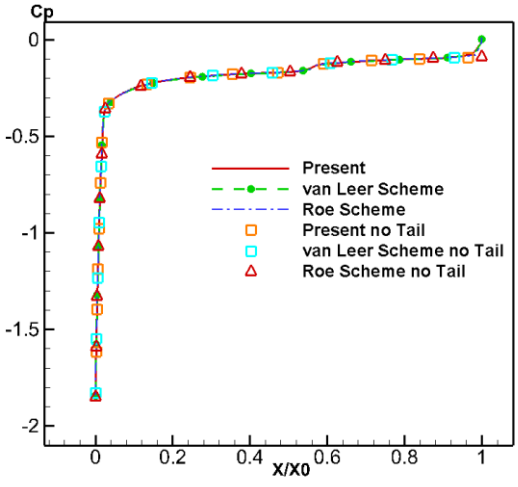

Figure 10: Cp comparison of biconics model between different methods

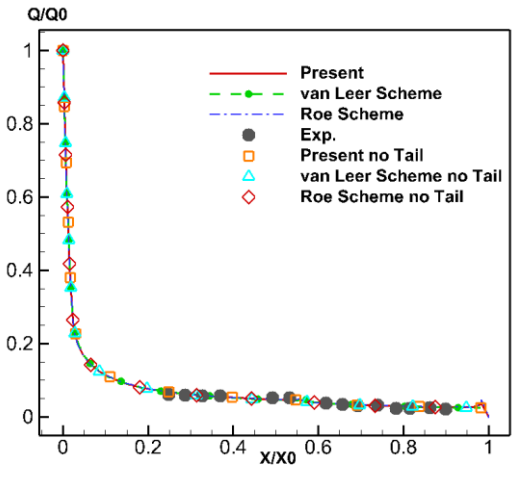

Figure 11: Heat flux ratio comparison of biconics model between different methods

4 CONCLUSIONS

This paper presents a stable lattice Boltzmann flux solver (LBFS) for simulation of 2-D compressible hypersonic viscous flows. The present work is a new application which make it possible for simulation in flow field of leeward wall surface. Physical values in leeward side can be extremely low in hypersonic flows due to strong shock effect. Negative values are easy exsting in calculating process. Hence, multiblock grids and local grid refinement method are applied to promise the calculation convergency. And we have added a constraint parameter to eliminate negative value in calculating process.

Numerical simulation of a biconics model in Ma=9.86 is used to validate the developed solver. The results comparison of solver presented in this work, van Leer and Roe scheme show that method presented in this work have high computational accuracy and stablity.

5 ACKONWLEDGMENT

The authors would like to appreciate Dr. Xinliang Li (Institute of Mechanics of Chinese Academy of Sciences) for his kindly help in programming our 2D Navier-Stokes code.

REFERENCES

[1] J. D. Anderson, Hypersonic and High Temperature Gas Dynamics. McGraw-Hill, 1989.
[2] J. Blazek, Principle and Application, Computation Fluid Dynamics, Elsevier, 2001.
[3] P. L. ROE, Approximate Riemann solvers, parameter vectors, and difference schemes, J. Comput.Phys., 43 (1981), pp. 357–372.
[4] B. VAN LEER, Flux vector splitting for the Euler equations, Lecture Notes in Physics, 170 (1982), pp. 507–512.
[5] M. S. LIOU AND C. J. STEFFEN, A new flux splitting scheme, J. Comput. Phys., 107 (1993), pp. 23–39.
[6] T. Kataoka, M. Tsutahara, Lattice Boltzmann method for the compressible Navier-Stokes equations with flexible specific-heat ratio, Phys. Rev. E, 69 (2004), R035701.
[7] K. Qu, C. Shu, Y.T. Chew, Alternative method to construct equilibrium distribution functions in lattice-Boltzmann method simulation of inviscid compressible flows at high Mach number, Phys. Rev. E, 75 (2007), 036706.
[8] Q. Li, Y.L. He, Y. Wang, W.Q. Tao, Coupled double-distribution-function lattice Boltzmann method for the compressible Navier-Stokes equations, Phys. Rev. E, 76 (2007), 056705.
[9] D. Chae, C. Kim, O.H. Rho, Development of an improved gas-kinetic BGK scheme for inviscid and viscous flows, J. Comput. Phys., 158 (2000), 1-27.
[10] K. Xu, A gas-kinetic BGK scheme for the Navier-Stocks equations and its connection with artificial dissipation and Godunov method, J. Comput. Phys., 171 (2001), 289-335.
[11] J. Jiang, Y.H. Qian, Implicit gas-kinetic BGK scheme with multigrid for 3D stationary transonic high-Reynolds number flows, Comput. Fluids, 66 (2012), 21-28.
[12] S.Z. Chen, K. Xu, C.B. Lee, Q.D. Cai, A unified gas kinetic scheme with moving mesh and velocity space adaptation, J. Comput. Phys., 231 (2012), 6643-6664.
[13] L.M. Yang, C. Shu, J. Wu, N. Zhao, Z.L. Lu, Circular function-based gas-kinetic scheme for simulation of inviscid compressible flows, J. Comput. Phys., 255 (2013), 540-557.
[14] C. Z. JI, C. SHU AND N. ZHAO, A lattice Boltzmann method-based flux solver and its

application to solve shock tube problem, Mod. Phys. Lett. B., 23 (2009), pp. 313–316.
[15] L. M. YANG, C. SHU AND J. WU, Development and comparative studies of three non-free parameter lattice Boltzmann models for simulation of compressible flows, Adv. Appl. Math. Mech., 4(2012), pp. 454–472.
[16] L. M. YANG, C. SHU AND J. WU, A moment conservation-based non-free parameter compressible lattice Boltzmann model and its application for flux evaluation at cell interface, Comput. Fluids, 79 (2013), pp. 190–199.
[17] C. SHU, Y. WANG, L. M. YANG AND J. WU, Lattice Boltzmann flux solver: an efficient approach for numerical simulation of fluid flows, Transactions of Nanjing University of Aeronautics and Astronautics, 31 (2014), pp. 1–15.
[18] L. M. YANG, Research on Compressible Lattice Boltzmann Model and Simplified Distribution Function-Based Flux Solver, Nanjing University of Aeronautics and Astronautics, 2016.
[19] Z.L. Guo and C. Shu, Lattice Boltzmann method and its applications in engineering, World Scientific Publishing, 2013.
[20] L.M. Yang, C. Shu, J. Wu., Extension of lattice Boltzmann flux solver for simulation of 3D viscous compressible flows, Computers and Mathematics with Application, 71 (2016): 2069-2081.
[21] R. BENZI, S. SUCCI AND M. VERGASSOLA, The lattice Boltzmann equation: theory and application,Physics Report, 1992.
[22] P. L. BHATNAGAR, E. P. GROSS AND M. KROOK, A model for collision processes in gases. I:small amplitude processes in charged and neutral one-component systems, Phys. Rev., 94 (1954),pp. 511–525.
[23] K. XU AND X. Y. HE, Lattice Boltzmann method and gas-kinetic BGK scheme in the low-Machnumber viscous flow simulations, J. Comput. Phys., 190 (2003), pp. 100–117.
[24] L.M. Yang, C. Shu, J. Wu. A hybrid lattice Boltzmann flux solver for simulation of viscous compressible flows. Adv. Appl. Math. Mech., 2016, 8(6): 887-910.
[25] L.M. Yang, C. Shu, J. Wu. A three-dimensional explicit sphere function-based gas-kinetic flux solver for simulation of inviscid compressible flows. Journal of Computational Physics, 295 (2015), 322-339.
[26] R.C. Swanson, R. Radespiel, Cell centered and cell vertex multigrid schemes for the Navier-Stokes equations, AIAA Journal, 29 (1991) 697-703.
[27] X. L. Li, D. X. Fu, Y. W. Ma, Direct numerical simulation of compressible turbulent flows, Acta Mech Sin, 26 (2010), 795-806.
[28] Miller C G. Experimental and predicted heating distributions for biconics at incidence in air at Mach 10[R].NASA-TP-2334, 1984.

V International Conference on Particle-based Methods – Fundamentals and Applications
PARTICLES 2017
P. Wriggers, M. Bischoff, E. Oñate, D.R.J. Owen, & T. Zohdi (Eds)

SEGREGATION IN SHEARED GRANULAR MEDIA – EFFECTS OF INTRINSIC PARTICLE PROPERTIES SUCH AS SIZE, DENSITY AND SHAPE

GERALD G. PEREIRA[1] AND PAUL W. CLEARY[2]

[1]Computational Modelling
Private Bag 10, Clayton South, AUSTRALIA
Gerald.Pereira@csiro.au and www.csiro.au

[2]Data61
Private Bag 10, Clayton South, AUSTRALIA
Paul.Cleary@csiro.au and www.csiro.au

Key words: Granular Materials, DEM, segregation, size, density, shape.
Abstract. When granular media which have different size, density, shape or even frictional properties flow they will tend to segregate. This is of fundamental scientific interest but also has significance in a variety of industries including mining, pharmaceuticals, food processing as well as for natural phenomena such as landslides. Here we consider segregation that occurs when a granular mixture is sheared, such as when it flows down along an inclined slope. A partially filled cylindrical drum is being slowly rotated about its axis (which is perpendicular to gravity) is a popular test-bed to examine sheared granular segregation. Here we consider simulation (Discrete Element Method, DEM), experiment and continuum theories in order to understand the segregation that occurs.

Using DEM simulations we can clearly determine the underlying causes of segregation which intimately depend on intrinsic particle properties such as their size, density and shape. We compare these DEM simulations with both experiments and continuum theories, for a number of these properties, and find very good agreement. It will be shown that segregation arising from differences in particle size is the strongest, with stable asymptotic states being reached after only one or two cylinder rotations. Density segregation is the next strongest followed by segregation due to particle shape. The underlying physical mechanism leading to segregation is different in each of these properties. We compare and contrast these mechanisms in detail.

1 INTRODUCTION

Mixing and segregation of granular mixtures is encountered in a variety of industries including minerals, polymer, food and pharmaceuticals processing. In some cases the sample is required to be as homogeneous as possible while any flow, vibrations or shear of the granular mixture will oppose this. On the other hand, in some circumstances separation of the mixture into its constituent parts is required so that one must understand how to harness the inherent segregation and maximise its rate and extent to attain the final goal. Experimentally it is known that any differences between the individual, constituent particles such as particle size, density, shape or frictional properties can lead to granular segregation when the mixture

is forced into motion [1]. Thus these intrinsic (particle-scale) properties control the macroscopic differences observed in the mixtures.

Although granular segregation is significant to a wide range of industries and applications and also is itself of scientific interest, it is still incompletely understood. For example, there is no set of continuum equations that can describe the segregation in detail, as there is for the Navier-Stokes equations for liquids (Meir et al, 2007). This is not surprising considering the individual particles themselves behave differently depending on their intrinsic properties (as mentioned above). How a cubical shaped particle moves down a sloped surface is quite different to how a spherical particle does.

In this work we focus on the effect of shear on granular mixtures. Shear occurs in a variety of scenarios such as Couette flow, Poiseuille flow or even flow of particles down an inclined surface. In this study we focus on sheared flow which occurs in a cylindrical tumbler roughly half-filled with a granular mixture. This particular set-up has been the focus of much experimental [2-8], theoretical [9-16] and simulations [17-21]. The cylinder is oriented with its axis perpendicular to the gravity vector and is rotated slowly (1-5 revs per minute) about this cylindrical axis. To focus on the particular physical mechanisms that underlie the granular segregation it is usual for the granular mixture to be made up of two distinct particle types, which is called a *binary mixture.* We consider in detail radial segregation of the mixture, i.e. segregation in a radial direction within a plane perpendicular to the cylinder axis.

A useful dimensionless number which is commonly used to characterize the flow regime for this particular set-up is the Froude number, defined as $Fr = \omega^2 R/g$, where ω is the rotational speed of the cylinder, R is the cylinder radius and g the magnitude of gravity. For the relatively slow cylinder rotations we consider here (mostly 1 rev/min), the flow is in the rolling regime. This means particles predominantly roll once the main flow in the cylinder has been established and the particle bed remains contiguous. Much faster rotational speeds lead to particles becoming separated spatially from the main bed.

In this paper we describe DEM simulations for this slowly rotating tumbler. One tracks individual granular particles, which are subject to a soft collision interaction model, and the entire granular segregation process that evolves is close to the true physical evolution. We shall show this is true by comparison with experiments. We shall also compare the DEM results with continuum models for granular segregation.

As the DEM procedure we use has been well documented previously (see [7,19-21]) we do not delve into it in any of this detail. However, we mention here a few important points about the variant used. Collisional forces are modelled with a soft contact model. Particles are allowed to overlap a certain amount, Δx and normal and tangential relative velocities (v_n and v_t respectively) determine the interaction forces via a linear spring and dashpot model. Since shape is one of the intrinsic properties considered we need to not only model spherical particles but also non-spherical ones which are given by the equi-axis super-quadric equation:

$$x^n + y^n + z^n = a^n \qquad (1)$$

For $n = 2$ this equation gives spheres of radius a, but as n increases the particles become more blocky in shape until as $n \to \infty$ the particle is a cube of side length $2a$.

2 DENSITY SEGREGATION

For granular mixtures composed of particles with different density (but same size and all are spherical) after around 2 rotations of the cylindrical tumbler a core of denser particles forms surrounded by a corona of less dense particles (see Fig. 1) form. As the cylinder rotates, particles are bought to the top of the upper flowing particle surface. The main segregation occurs in this upper region of the particle bed, where the denser particles sink into the core region, while the less dense ones flow down along the inclined free surface to the bottom of the inclined surface. This segregation mechanism is called *buoyancy*. Figure 1a shows the experimental results for this case (glass and lead particles) where the lead particles (dark grey) have migrated to the core of the particle bed and glass particles (light grey) migrate close to the cylinder walls. Figure 1b shows the corresponding DEM results also after 2 cylinder rotations. The small protruding rectangular ridges on the cylinder walls were included with the intention to mimic macroscopic surface roughness and prevent the rigid body slipping of the whole granular bed against the wall. This type of segregation state forms when (predominantly) all particles have a similar size. The similarity between experiments and DEM is apparent.

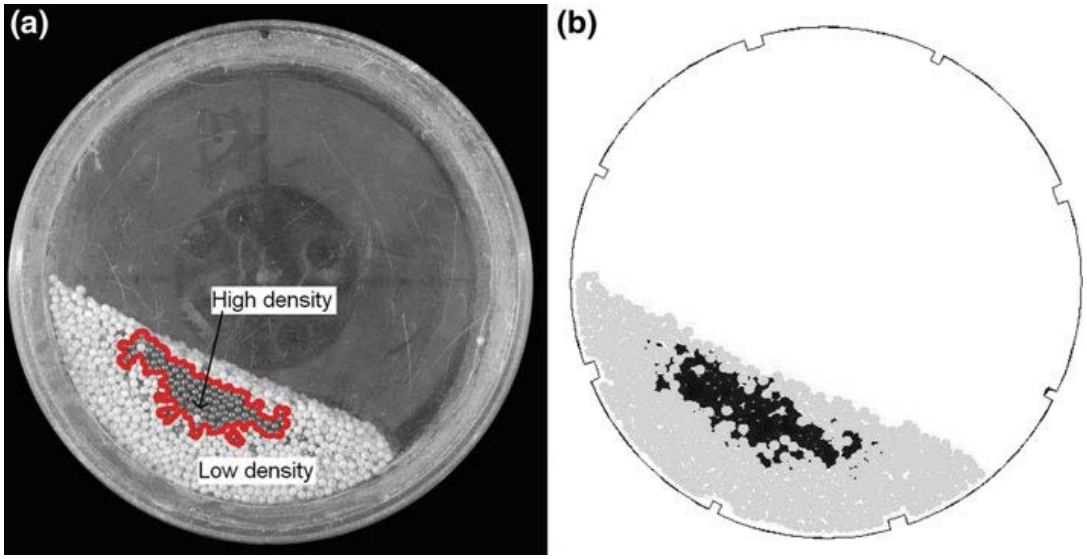

Figure 1. Particle distributions for density segregation for a cylinder fill fraction of 0.3 after 2 revolutions of the tumbler. a) Experimental result, and b) DEM result (Pereira et al, 2011). The red line in the experimental photo is used to calculate radial segregation fractions.

To make this comparison more quantitative, the normalized radial area is used. It is calculated as follows for both experiments and DEM. Snapshots of the particle distribution are taken at (small) regular time intervals (0.0625 revs). After two revolutions a boundary is defined around the main core of heavy particles (see red curve in Fig. 1a). This asymptotic boundary is subsequently superimposed on all earlier states, for both the experiment and the simulation, to determine the proportion of heavy particles currently enclosed within this boundary. The normalized radial area is defined as the number of heavy particles within the red boundary divided by the total number of particles.

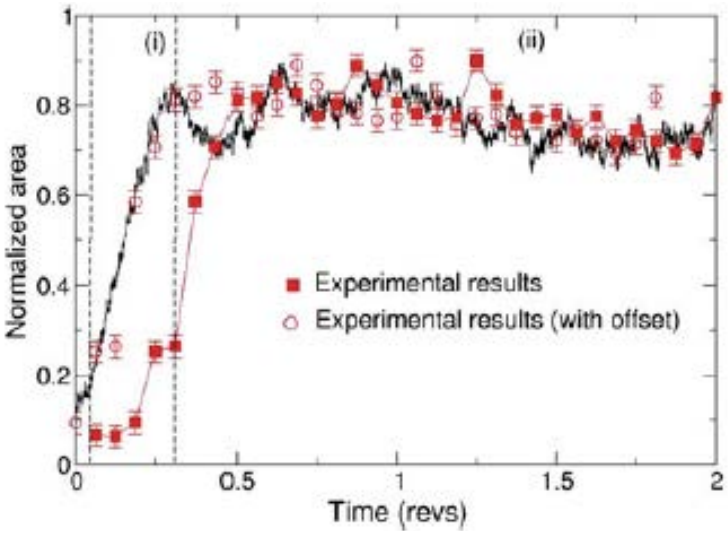

Figure 2. Radial segregation measure as a function of time (revolutions). The symbols are from experiment and the black line from DEM.

The evolution of the radial normalized area for both the simulation and experiment are shown in Fig. 2. The simulation exhibits a rapid increase (within 0.3 revs, region i) to around 0.8. After this (region ii) it tends to fluctuate about 0.75 and after two rotations has the value of 0.82. The comparison of the radial normalized area between simulation and experiments is excellent. Both show distinct temporal regimes in the segregation process. In the initial, rapid segregation regime, both simulations and experiments grow at the same rate and over the same period of time. Once they enter the equilibrium regime, they both show fluctuations of similar amplitude about their similar mean (plateau) values and have final values which are very similar. The main difference between simulation and experiments is when the initial slope failure occurs. For simulations this occurs earlier than for the experiments. In Fig. 2 we have also displayed the experimental results with a time offset of −0.1875 revs to account for the different time of flow initiation. With this offset accounted for the comparison is extremely good. The reason for this timing difference is that the DEM particle bed achieves it first failure much earlier than does the experiment. We postulate that this is due to particle shape – the DEM particles are exactly spherical while the experimental particles are fairly round but not exactly spherical. It is well known that spherical particle roll much more easily than even slightly non-round particles and a heap of such particles will form a stronger structure in contrast to spherical particles. Hence it is not surprising then that in DEM simulations, failure of the granular bed occurs earlier than in experiments. It is important to note though that the small shape differences do not affect the nature of the flow or segregation once initial slope failure has occurred.

Comparisons for other fill levels have also made, showing good overall agreement between DEM and experiments [7]. In these DEM simulations, the Froude number and the density ratio between the particle pairs was also systematically varied in order to study the functional dependence of the density segregation on these factors. A significant amount of density segregation is possible only for Froude number less than around 10^{-3}. Above this value, too much energy is supplied to the granular bed (from the cylinder rotation) which inhibits density segregation. The buoyancy mechanism is observed to become dominant over particle

diffusion for density ratios above 2 leading to strong segregation of the particle bed.

3 SIZE SEGREGATION

Consider next binary granular mixtures which differ only in their size (the particles densities are the same and their shapes are spherical). Segregation of the granular mixture occurs via a mechanism known as *percolation* whereby the smaller particles percolate down through the gaps between the larger particles. Although this effect has probably been known for many centuries it was first detailed for granular mixtures undergoing vibration and termed the Brazil nut effect [22]. Although vibration and shear flow differ somewhat in the details of their dynamics, the flowing top layer of the granular bed provides sufficient relative motion between particles to induce percolation of the smaller particles. For mixtures where particles differ in size only we obtain a core of small particles surrounded by a corona of large particles (see Fig. 3).

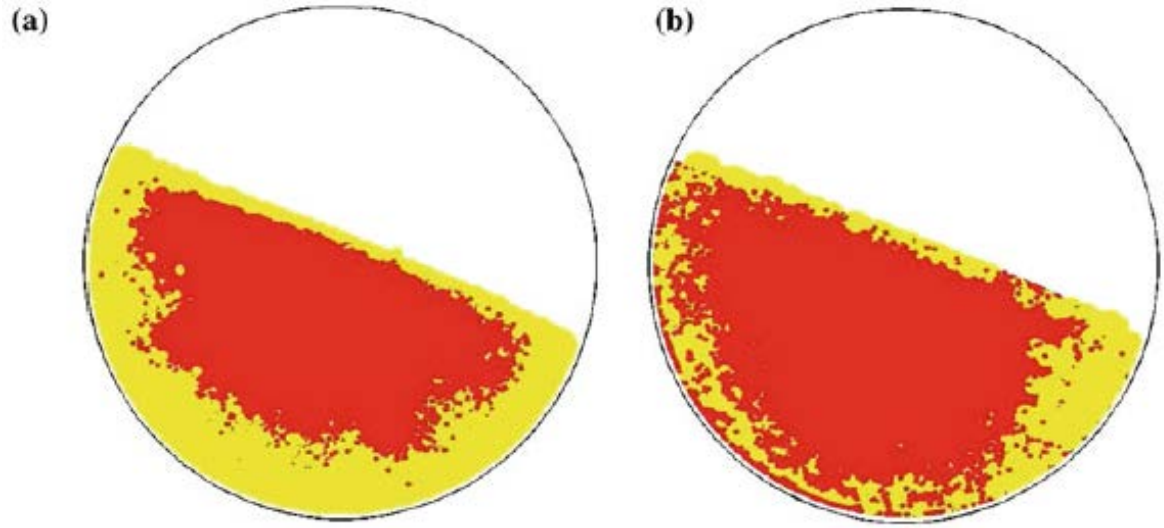

Figure 3. Equilibrium distribution of particles after 5 revolutions for different size (same density and spherical) binary granular mixture. Yellow represents large particles while red represents smaller particles. a) 1 mm and 2 mm diameter particles, and b) 1 mm and 4 mm diameter particles.

Figure 3a shows the segregation pattern after 5 rotations of the cylindrical tumbler for particles with a size ratio of 2 (ratio of radii). Here we see quite pure segregated states evolve with the small particles occupying a core region (which is almost pure red) and the large particle forming a corona region (almost pure yellow). However, note when the size ratio increases to 4 then the large particle region becomes less pure than occurs for a size ratio 2. This counter-intuitive result comes about from the fact that now the small particles are so small they have percolated to the bottom of the container, through the corona region. To understand the difference between the two cases, one should recognize that particles are packed together well in the coronal region. So for size ratio 2, this packing prevents “leakage” of smaller particles from the core into the corona, while for size ratio 4, even this close packing is not small enough to prevent small particles leaking through the pore network from the core to the corona.

Segregation of ternary granular mixtures (i.e. three different sets of particle sizes) was also modelled via DEM [19]. For example, Fig. 4 shows the segregated mixture after 5 cylinder rotations. Here we have used particle diameters 1 mm (blue), 2 mm (red) and 3 mm (yellow). As one might anticipate the smallest particles (blue) might migrate to the inner core, and the largest particles (yellow) migrate to the corona while the intermediate sized particles (red) are more or less found in between the other two. For different combinations of particle sizes, this segregation behaviour remains broadly similar for the smallest and largest particles, but the behaviour of the intermediate size particles is found to depend on their size ratios to the other two sizes and can accordingly be more dispersed through one or other of the two regions, see for example Fig. 4b for particle sizes 1, 2 and 4 mm.

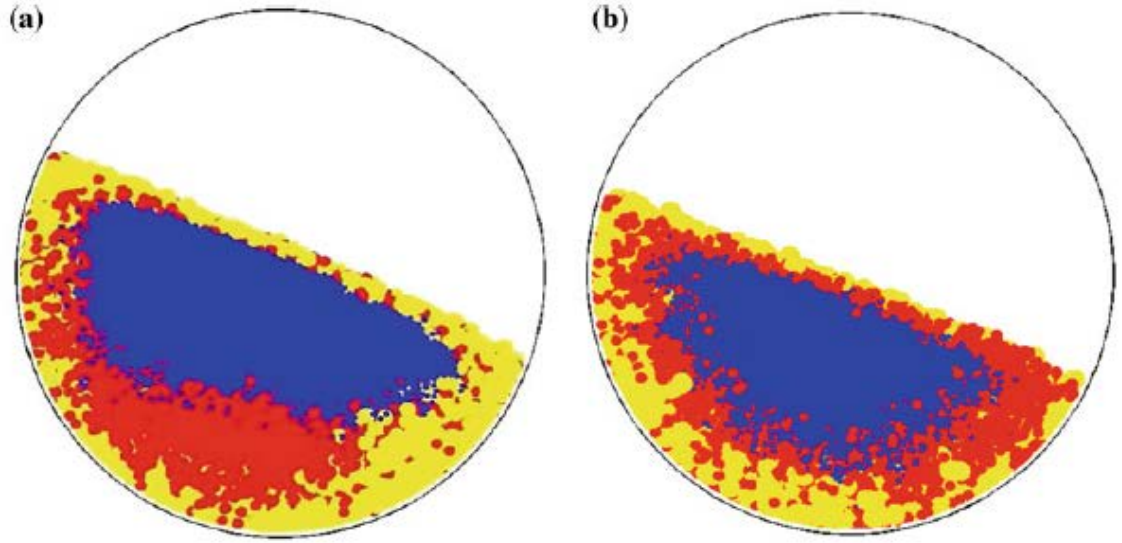

Figure 4. Equilibrium distribution of particles (after 5 revolutions) for a ternary granular mixture of different sizes (but with same density and spherical) particles. Yellow represents the largest particles, blue represents the smallest particles and red are intermediate sized ones. a) Particle diameters are 1 mm, 2 mm and 3mm, and b) particle diameters are 1 mm, 2 mm and 4 mm.

The amount of radial segregation was evaluated quantitatively by obtaining a (normalized) average of each particle type in 2 mm thick annuli from the cylinder centre, once equilibrium was established. This is shown in Fig. 5a, for a mixture with particle sizes 1, 2 and 3 mm. The smallest particle size has a peak close to the scaled radius of 0.2 (corresponding to the core) while the largest particles have a peak at scaled radius of around 0.95 (corresponding to the corona) with the intermediate size particles having a peak around scaled radius of 0.7 (which is in between the other two regions). To determine the strength of the competing mechanisms, one may compare this radial with the theoretical continuum model of Gray and Ancey [15]. While the details of the continuum model are too detailed to be given here, it focuses on the upper flowing (shear) layer and includes advection, diffusion (due to particle collisions) and segregation (due to particle size differences). The continuum model then involves four phenomenological parameters – a diffusion constant and three (binary) interaction terms which control segregation. These can be varied so that the segregation profile matches the DEM radial segregation profile (see Fig. 5b). The match between the two profiles is adequate which validates the dominant competing mechanisms (percolation and diffusion).

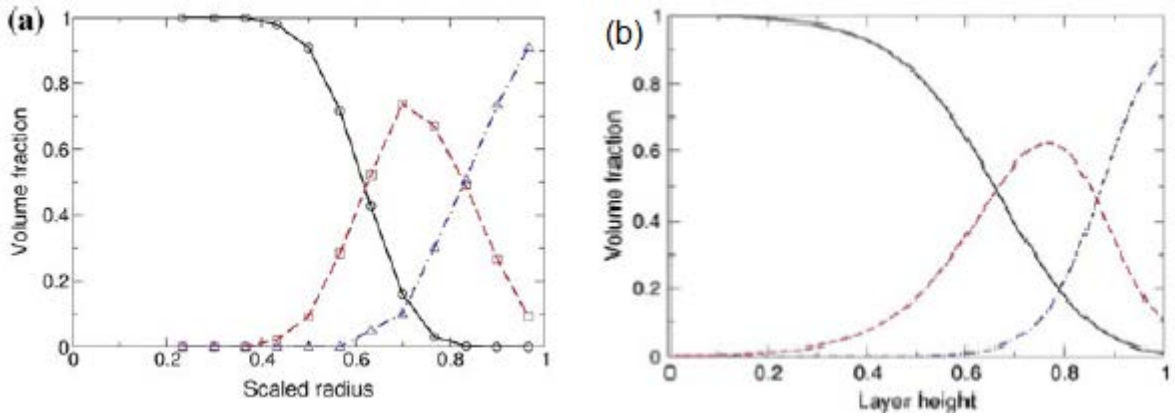

Figure 5. a) DEM volume fraction (of different sizes) as a function of distance from the cylinder centre (averaged over the axial direction) for the ternary mixture in Fig. 4a (1, 2 and 3 mm diameter particles). Circles – smallest particles, squares – intermediate particles, triangles – largest particles. Curves are guides for the eye. b) Results from Gray and Ancey's (2011) continuum model for different particle size mixtures. We have chosen he four coefficients so that the result is close to that shown in Fig. 5a. Black solid curve – largest particles, red dashed curve – intermediate particles and blue, dot-dashed curve – smallest particles.

4 SHAPE SEGREGATION

Now consider a binary granular mixture where particles differ only in their shape (their sizes and density being the same, with particles having the same *a* value in Eq. 1). Here we use particles which are either spherical or blocky (i.e. with an *n* value in Eq. 1 which is greater than 2). Figure 6 shows the segregation pattern for a binary granular mixture of particles of different shape after 9 rotations of the cylinder. In Fig. 6a we have a core of more blocky particles ($n = 4.55$, red) and a corona of spherical particles (blue). However, in contrast to size and density segregation we see that the boundary between the two particle types is quite diffuse, with red particles still distributed throughout the blue region and vice-versa. For a granular mixture with a higher ratio of *n* values (see Fig. 6b) it is now observed that the core and corona regions are more pure (here the red particles have an *n* value of 10.05, while the blue particles are spheres).

While the buoyancy mechanism underlies density segregation and percolation underlies size segregation, what gives rise to the segregation in the case of shape? We postulate that this relates to *flowability* of each particle shape [21]. As the cylinder rotates, the two types of particles are transported up to the top of the inclined free surface layer. At this point both sets of particles are at the same height, and so have the same amount of gravitational potential energy. As they begin their descent down along the flowing layer, the spherical particles travel faster than do the more blocky particles. The more blocky particles dissipate their available potential energy more quickly and so both travel more slowly and come to rest earlier within the flowing layer. At this point, other particles (mainly spherical ones) flow over them burying them at the bottom of the current shear layer. Over repeated passes through the shear layer the blocky particles move progressively towards the center to form a core region for the particle bed. Meanwhile the spherical particles which on average dissipate their potential energy more slowly have higher flow speeds in the surface shear layer and are typically able to reach the bottom of the slope and build up against the wall of the cylinder.

They are then transported around the cylinder, via rigid body rotation of the main bed. This shape segregation occurs within the top, flowing layer and provides a downward dynamic pressure in a continuum interpretative sense that causes them to migrate towards the core.

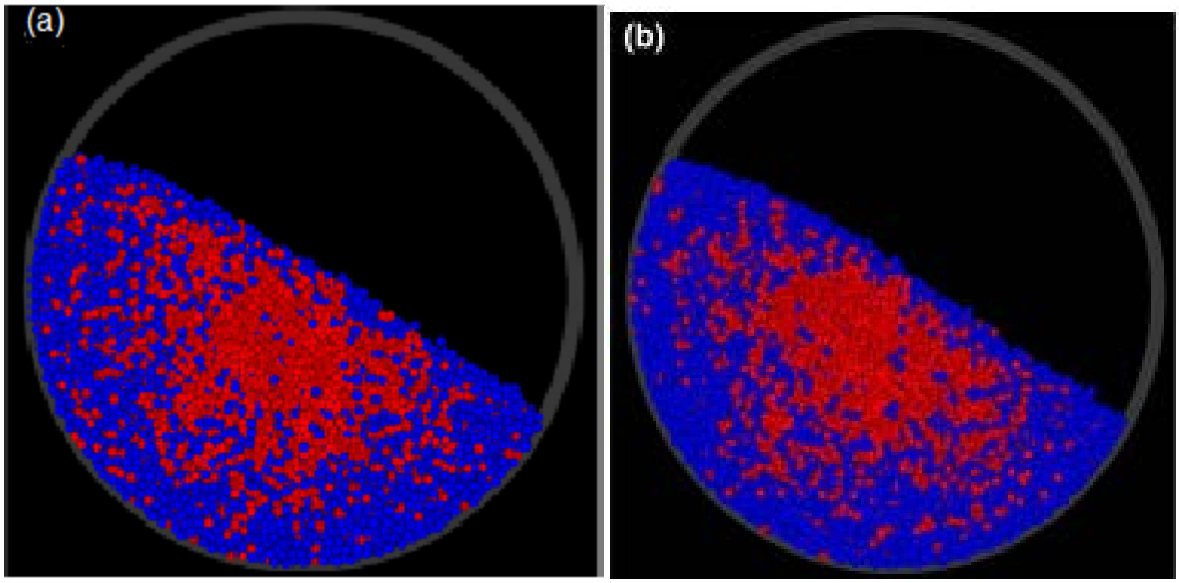

Figure 6. Particle distribution for binary mixture where particles only differ in their shape after 9 revolutions. a) spherical (n = 2) shown as blue and rounded cubical (n = 4.55) shown as red, and b) spherical (n = 2) shown as blue and sharp cubical (n = 10.05) (red).

The operation of this segregation mechanism was demonstrated by evaluating the surface layer speeds of the two particle types (spherical and blocky). At each time step during a DEM simulation, we evaluated (using only particles in the upper flowing layer): (i) the percentage of time that spherical particle had a speed greater than the blocky particle, (ii) the average differential in speed between the two particle types, and (iii) the average spread (standard deviation) in the average differential speed between the two particle types. The results are shown in Fig. 7 (with the left axis showing the percentage of time and the right axis showing the average differential speed) for four different shape ratios. For small shape ratio, the spherical particles 60% of the time have a larger speed than the blocky particles but at large shape ratio this increases to about 95% of the time. The speed differential (spherical particle speed – blocky particle speed) is 1.8 mm/s (with a spread of 6.6 mm/s) at the smallest shape ratio (of 1.25) but rises to 23.4 mm/s (with a spread of 13.6 mm/s) for the largest shape ratio (of 4.95) considered. These clearly indicate that for significantly blocky particle (i.e. large n) not only do the spherical particles *consistently* travel faster down the flowing layer than the blocky particles, they do so with a *significantly* larger surface speed. These differences then control the deposition location on the slope for each shape which drives the inward migration of the blockier particles.

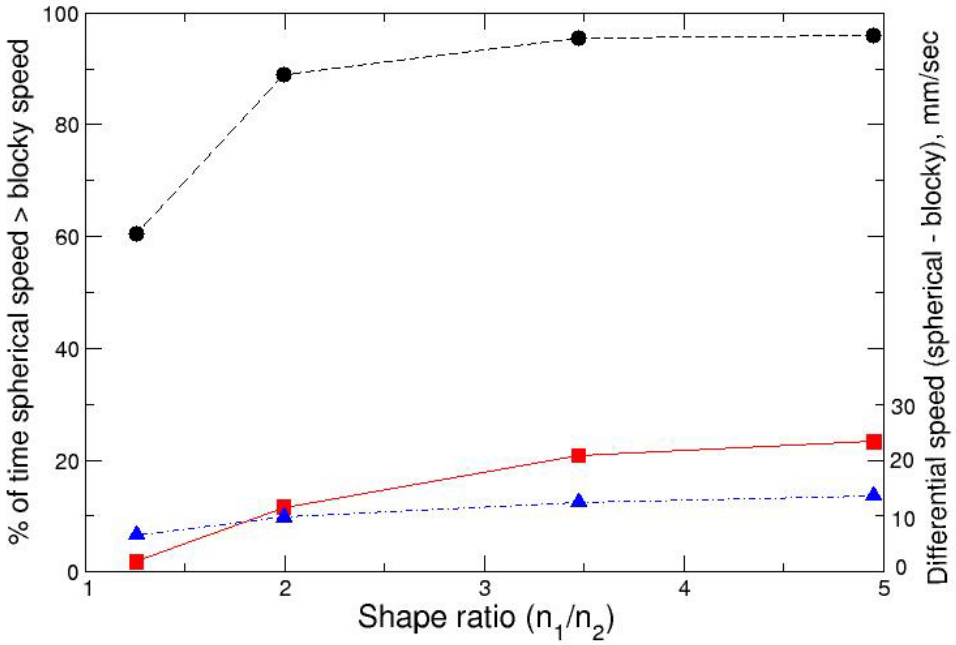

Figure 7. Difference in speeds between the two particle shapes (spherical and blocky) in the top, surface layer as a function of the shape ratio. The black circles are the percentage of time the spherical particles have a larger speed than the blocky particles (left axis). The red squares are the average differential speed in the surface layer between spherical and blocky particles and the blue triangles are the spread in average differential speed (right axis). Curves are drawn as guides for the eye.

5 COMPARISON BETWEEN DENSITY, SIZE AND SHAPE SEGREGATION

These DEM simulations have been not only able to determine the stable segregation patterns for granular mixtures which may differ either in particle density, size or shape but also other quantitative information. Here we can summarise the main outcomes as follows

- Size segregation appears to be the strongest of the three segregation mechanisms, closely followed by density segregation and both are much stronger than shape segregation. It was found that size segregation could lead to relatively pure core and corona regions, but only for a small range of particle size ratios – the ratio of radius of the big particles to small particles should be less than approximately 3. If the particle size ratio is greater than 3, leakage occurs which limits the segregation extent.
- Density segregation generally increases monotonically with particle density ratio. In shape induced segregation one never obtains pure regions of either particle type.
- The kinetics of segregation are equally fast for size and density segregation and slow for shape segregation. It takes of the order of 10 cylinder rotations before the (asymptotic) steady state is reached for shape segregation, while for the other two mechanisms it takes only 2-4 rotations. This correlates with the strength of segregation (above).
- For shape segregation the interface between regions is typically rather diffuse while it can be quite well defined for the other two.

- Segregation occurs *along* the top, flowing layer for shape segregation, while for size and density segregation it occurs *through* this top layer.

6 CONCLUSIONS

Intrinsic, micro-scale particle properties have been shown to play a vital role in the segregation of granular mixtures. Three specific properties have been studied in this work – those being particle density, size and shape. Each has a corresponding physical mechanism which underlies the granular segregation process that it drives. These are buoyancy for mixtures of different density, percolation for mixtures of different size and flowability for mixtures of different shape. In fact the last mechanism of flowability should also applies to particles with different surface roughness. Surface roughness has two contributions – macroscale roughness (which typically is described as being the shape of the particle) and microscale roughness (which is interpreted as the particle friction). So in a mixture of particles with different surface roughness, it would be expected that the rougher particles would segregate to the inner core.

The three segregation mechanisms have been compared and we have seen that size and density segregation are the strongest, with the segregation typically occurring within 2-3 cylinder rotations for this system. They also lead to fairly pure segregated regions (small or dense particles in the core and large or less dense particle in the corona). In contrast, shape segregation is much weaker, with a core of the more blocky particles and corona of the spherical particles forming after 5-10 cylinder rotations. Here the interface between segregated regions remains quite diffuse with many blocky particles dispersed in the corona and vice-versa. Whilst both density and size segregation evolve by particles moving through the upper surface, flowing layer shape segregation occurs when particles move with different speeds along this upper surface layer.

We have compared selected results with experiments and found excellent agreement. Some results were compared with continuum theory, so as to identify the strength of macro-scale mechanisms, and with appropriate choices of the phenomenological constants we have been able to achieve satisfactorily agreement between theory and simulations. The DEM technique has been shown to be ideal in understanding micso-scale details of granular segregation. For example calculation of the surface layer velocities for the different particle types can be readily done virtually, but with much more difficulty in experiments

REFERENCES

[1] Ottino, J.M. and Khakhar, D.V. Mixing and segregation of granular materials, *Ann. Rev. Fluid Mech.*, (2000) **32**, 55-91.

[2] Metcalfe, G., Shinbrot, T., McCarthy, J.J. and Ottino, J.M. Avalanche mixing of granular solids. *Nature* (1995) **374**, 39–41.

[3] Khakhar, D.V., McCarthy, J.J. and Ottino, J.M. Radial segregation of granular mixtures in rotating cylinders. *Phys. Fluids* (1997) **9**, 3600–3614.

[4] Cantelaube, F. and Bideau, D. Radial segregation in a 2d Drum: an experimental analysis. *Europhys. Lett*. (1995) **30**: 133–138.

[5] Taberlet, N., Losert, W. and Richard, P. Understanding the dynamics of segregation bands of simulated granular material in a rotating drum. *Europhys. Lett*. (2004) **68**, 522–528.
[6] Jain, N., Ottino, J.M. and Lueptow, R.M. Regimes of segregation and mixing in combined size and density granular systems: An experimental study. *Granul. Matter* (2005) **7**, 69–81.
[7] Pereira, G.G., Sinnott, M.D., Cleary, P.W. Liffmann, K., Metcalfe, G. and Sutalo, I. Insights from simulations into mechanisms for density segregation of granular mixtures in rotating cylinders, *Granular Matt.*, (2011) **13**, 53-74.
[8] Ahmed, S. John, S.E. Sutalo, I.D., Metcalfe, G. and Liffman, K. Exprimental study of density segregation at end walls in a horizontal rotating cylinder saturated with fluid: friction to lubrication transition. *Granul. Matter* (2012) **14**: 319–332.
[9] Drahun, J.A. and J.Bridgewater, J. The mechanisms of free surface segregation. *Powder Technol.* (1983) **36**: 39–53.
[10] Savage, S.B. and Lun, K.K. Particle size segregation in inclined chute flow of dry cohesionless granular solids. *J. Fluid Mech*. (1988) **180**, 311–335.
[11] Cantelaube, F. and Bideau, D. Radial segregation in a 2d Drum: an experimental analysis. *Europhys. Lett*. (1995) **30**: 133–138.
[12] Drahun, J.A. and J.Bridgewater, J. The mechanisms of free surface segregation. *Powder Technol.* (1983) **36**: 39–53.
[13] Makse, H.A.Stratification instability in granular flows, *Phys. Rev. E*, (1997), **56**, 7008-7016.
[14] Gray, J.M.N.T. and Thornton, A.R. A theory for particle size segregation in shallow granular free-surface flows. *Proc. R. Soc. Lond. Ser. A* (2005) **461**: 1447–1473.
[15] Gray, J.M.N.T. and Ancey, C. Multi-component particle segregation in shallow avalanches. *J. Fluid Mech*. (2011) **678**: 535–588.
[16] Gray, J.M.N.T. and Thornton, A.R. A theory for particle size segregation in shallow granular free-surface flows. *Proc. R. Soc. Lond. Ser. A* (2005) **461**: 1447–1473.
[17] Ristow, G.H. Particle mass segregation in a two-dimensional rotating drum. *Europhys. Lett*. (1994) **28**, 97–101.
[18] Taberlet, N., Newey, M., Richard, P. and Losert, W. On axial segregation in a tumbler; an experimental and numerical study, *J. Stat. Mech. Theor. Exp*. (2006) P07013.
[19] Pereira, G.G. and Cleary, P.W. Radial segregation of multi-component granular media in a rotating tumbler, *Granular Matt*., (2013) **15**, 705-724.
[20] Pereira, G.G. Tran, N. and Cleary, P.W. Segregation of combined size and density varying binary granular mixtures in a slowly rotating tumbler, *Granular Matt*., (2014) **16**, 711-732.
[21] Pereira, G.G. and Cleary, P.W. Segregation due to particle shape of a granular mixture in a slowly rotating tumbler", *Granular Matt*., (2017) **44**, 23.
[22] Rosato, A. Strandbourg, K.J., Prinz, F. and Swendsen, R.H. Why the Brazil nuts are on top—size segregation of particulate matter by shaking. *Phys. Rev. Lett*., (1987) **58**, 1038–1040.

V International Conference on Particle-based Methods – Fundamentals and Applications
PARTICLES 2017
P. Wriggers, M. Bischoff, E. Oñate, D.R.J. Owen, & T. Zohdi (Eds)

MODELLING OF THE THERMOCHEMICAL PROCESSES IN THE GASIFING REACTOR USING XDEM METHOD

IZABELA WARDACH ŚWIĘCICKA[1], DARIUSZ KARDAŚ[1] AND BERNHARD PETERS[2]

[1] Institute of Fluid-Flow Machinery Polish Academy of Sciences, Renewable Energy Department
PL-80231 Gdańsk, Fiszera 14 St., Poland
izabela.wardach@imp.gda.pl, dariusz.kardas@imp.gda.pl, http://www.imp.gda.pl

[2] University of Luxembourg, Faculty of Science, Technology and Communication
Maison du Nombre, 6 Avenue de la Fonte, L-4364 Esch-sur-Alzette, Luxembourg
bernhard.peters@uni.lu, http://www.uni.lu

Key words: XDEM, biomass pyrolysis, vaporization, single particle heating

Abstract. The goal of this work was to investigate the possibility of the XDEM (eXtended Discrete Element Method) program to simulate the behaviour of wood particles during the gasification process that was performed in the Institute of Fluid-Flow Machinery PASci (IMP PAN) INKA gasifier. The program is based on the Lagrangian approach for simulation of heat and mass transfer during thermal decomposition of the solid fuel particles.

1 INTRODUCTION

Typical thermochemical process of biomass in a fixed bed gasifier starts from drying, where moisture is released from fuel [1]. In the next step the volatiles are released and char is produced in the pyrolysis which occurs in the absence of oxygen. In the main gasification phase, gases are mixed with air and burned to CO_2 and H_2O. In the reduction zone charcoal combines with CO_2 and H_2O forming a combustible gas. The most important factors, which determine the composition and the quality of the syngas are the process temperature and the amount of supplied air/oxidation medium [1, 2]. Knowledge and understanding of each of these phenomena allows to get a better understanding of the whole process. This also provides to get better design and better operation parameters and, finally, better efficiency of energy conversion in the reactors.

The main goal of this work was to investigate the possibility of the XDEM program to simulate the behaviour of wood particles during the gasification process that was performed in the INKA gasifier [2].

2 XDEM METHOD

The XDEM method was developed by Peters and it aims at resolving the particulate phase with its various processes attached to the particles [3]. The main assumption of numerical modelling is that each particle undergoes a sequence of thermodynamic processes that are described by a set of one dimensional and transient conservation equations for mass, momentum and energy using Discrete Particle Method (DPM) [4, 5]. XDEM is a numerical technique that practically extends the dynamics of particles described by the classic DEM. This is graphically presented on Fig.1.

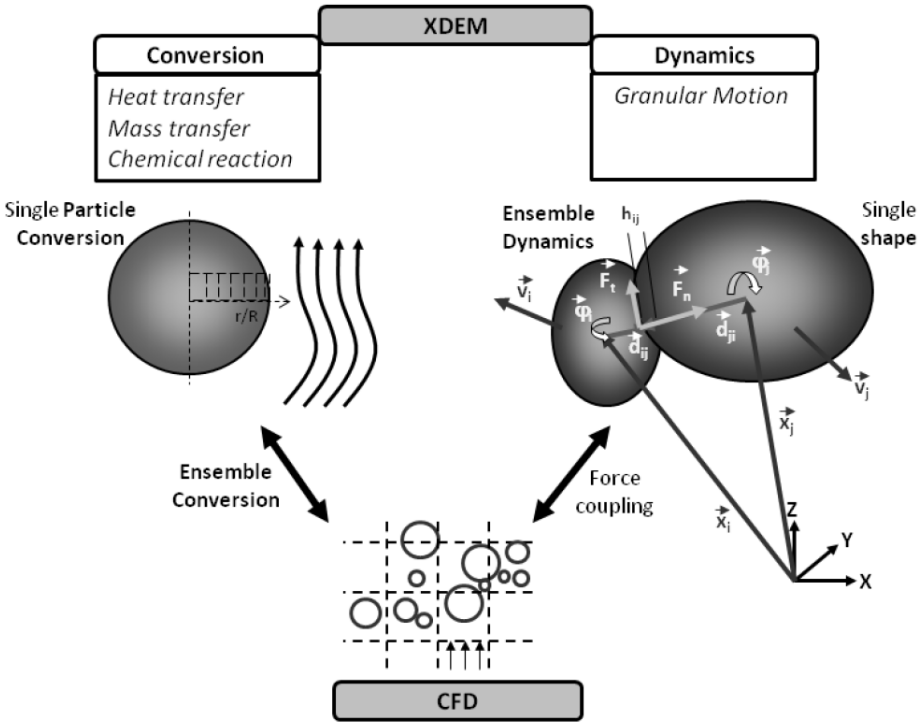

Figure 1: Scheme of the XDEM coupling with CFD [4]

While the DEM predicts position and orientation in space and time for each particle, the XDEM additionally estimates properties such as internal temperature and/or particle distribution, or mechanical impact with structures. The motion module of the DPM handles a sufficient number of geometric shapes that are believed to cover a large range of engineering applications. Relevant areas of application include furnaces for wood combustion, fluidized beds or predictions of emissions from combustion of coal or biomass. The thermodynamics module incorporates a physical-chemical approach that describes temperature and arbitrary reaction processes for each particle in an ensemble.

The coupling CFD (openFOAM solver for porous media [6]) with XDEM is realized

by the mass, momentum and heat transfer between fluid and particle part. The fluid flow is computed as a flow of gas in a porous zone, consisted of biomass particles and the gas phase filling empty spaces. The sum of all particle processes represents the overall behaviour, including heating, drying, pyrolysis and gasification.

Coupling XDEM and OpenFoam comes from the Lagrangian - Eulerian approach [4]. In Lagrangian modelling the motion and conversion of particles are computed basing on one-dimensional and transient conservation equations, which characterize energy and mass transport within each particle. It is also assumed that each particle consists of liquid, solid and gas phases, and gas is transported by diffusion and convection within the particle-pore space. All gaseous species are treated as an ideal gases and particles as an isotropic material, in which the properties may change only along the radial direction. Additionally, inside the particles there is a local thermal equilibrium between the solid and the gaseous species. Between neighbour particles heat transfer may occur through conduction and radiation. Heat and mass transfer from the fluid to the particles is computed through boundary conditions specified by the surrounding gas. Required convective heat transfer coefficients are estimated from Nusselt number semi-empirical correlation for mono-disperse and naturally arranged packed beds [7]. Appearing chemical reactions are modelled as equilibrium reactions for the available species. The motion module of DPM predicts particle positions, thus, the reactors/furnaces/boilers are naturally filled by gravity deposition.

Fluid flow is analysed based on the Eulerian approach, i.e. the fluid medium is treated as continuum. The analysed biomass/coal bed is characterized as a type of porous media in which fluid flow behaves like an external flow. Additionally, the fluid flow inside the free space is described by a three-dimensional Navier-Stokes and energy equations for incompressible flow. Moreover, Brinkmann or Forchheimer relations are used to appropriately model the drag shift from linear to non-linear behaviour. Heat and mass transfer from particle to fluid is done via source terms of the corresponding conservation equations.

3 "INKA" GASIFING REACTOR

The INKA reactor consists of one tube with three inlets at the top and one outlet at the bottom [2]. The height of the reactor is $H = 850$ mm and its diameter is $D = 206$ mm. The pipe inlets of 15 mm in diameter are located 300 mm from the top. The outlet is also a pipe with diameter of 65 mm and it is located 50 mm from the bottom. The schematic diagram of the reactor is presented on Fig.2.

In the real case, the gasifier is filled by the cuboid shape biomass particles of three different sizes, which are summarized in Tab.1. The upper level of the biomass bed is 300 mm above the air pipe inlets.

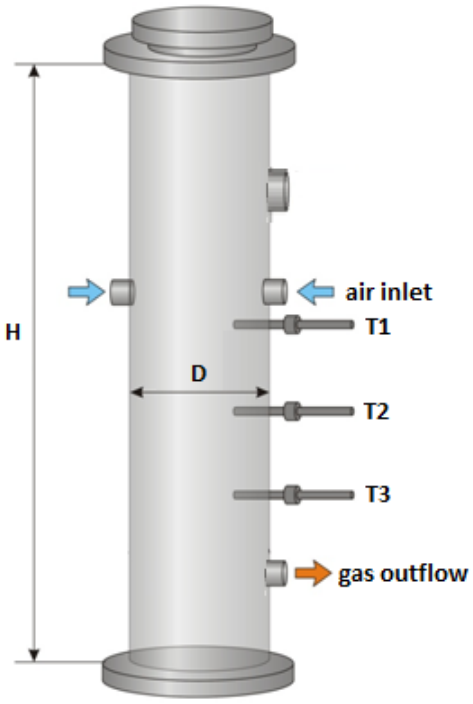

Figure 2: Scheme of the INKA gasifier INKA

Table 1: Shape parameters of the fuel wood chips

particles size	mean average size mm × mm × mm	mean volume mm^3	volume fraction %	mass fraction %
small	5 × 10 × 10	500	47	44
medium	20 × 7.5 × 6	900	29	28
large	34.5 × 18 × 15	9315	24	28

4 NUMERICAL SIMULATIONS - XDEM

Due to the fact that the real reactor is filled approximately by 35 000 particles, which is a very large number for testing case, the simplified geometry was used. It was decided to consider smaller reactor of 280 mm in height and 206 mm in diameter (Fig.3 - left picture). Because of the XDEM limitations it was assumed that the height of the CFD computational cell does not excess the value of 35 mm, which corresponds to the biggest length of the biomass block particle.

Such geometry was applied for calculation of test cases. In the first one only the flow of pure air in the small reactor was taken into account. For this purpose the *rhoPimpleFoam* solver was activated. For the second case the combustion of CH_4 in the air was considered

with only one step global reaction taken into account:

$$CH_4 + 0.5O_2 = CO_2 + 2H_2O. \quad (1)$$

For this test case the solver *reactingFoam* was used.

4.1 Filling the container

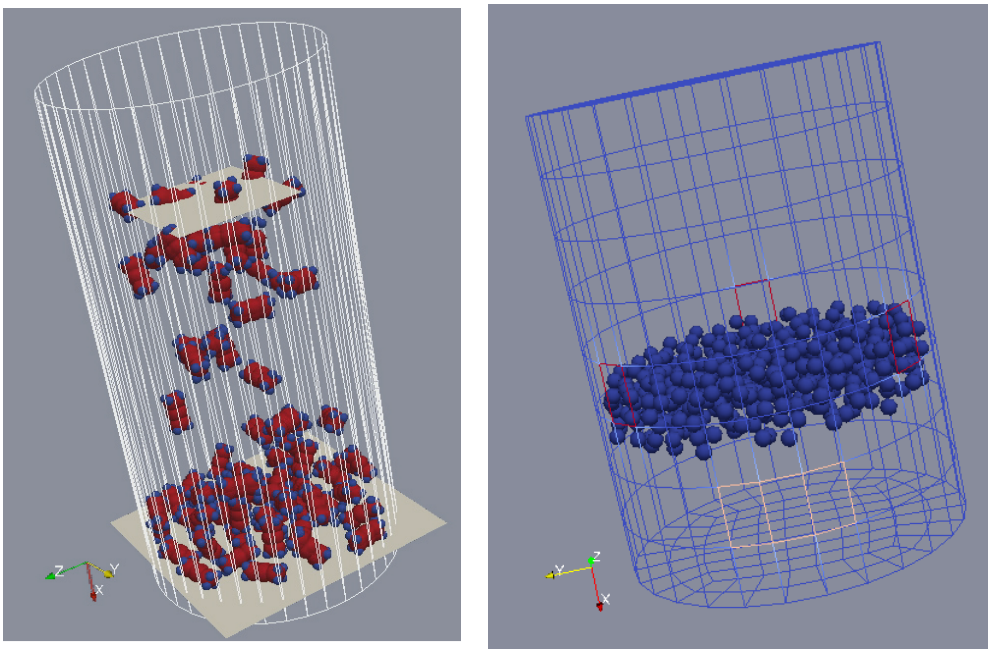

Figure 3: Filling the reactor with particles (left) and simplified geometry of the analysed geometry (right)

After CFD simulations the XDEM method (only its dynamic part) was adopted for filling the container with the particles. Two different cases were taken into account: at first step the container was filled with particles, which were of the same size (33mm x 15mm x 18mm), and with the particles of three different sizes. The calculations were stopped at certain time and the position of the particles were copied and put as an input file for coupled calculations with XDEM and OpenFOAM (Fig.3). This test case included only the drying process. After simulations the process of filling the container was repeated. Here the meshes for CFD simulations and for XDEM were ordered by choosing the same orientation direction, i.e. gravity in both cases was set according to OX direction. Now, the particles with the same and different sizes were injected into the gasifier with mass flow rate of 10 kg/s. Simulation filling time was set to 6 s and at the time of 1.8 s the injection was stopped. Following that the particles were still moved according to the process of gravitational settling on the bottom side of the reactor. The cylinder was filled approximately with 300 of biomass block particles.

After filling the container the position of the particles were copied and put as an input file to coupled calculation of XDEM and OpenFOAM. Due to the fact that the chosen shape of the particles was set as a block, the position (due to the orientation) of certain particles appeared to be unsuitable to the coupled calculation, i.e. the size of certain particles appeared to be larger than the size of the computational cell for CFD. It was decided then to change the size of mesh cells. The height of the cell was set to 45 mm, whereas the height of small reactor to 270 mm. Also the number of cells at the radial direction was reduced. To shorten the solution time the inlet and outlet boundary condition were set as a top and bottom walls of the cylinder. The simulation of drying process was repeated.

4.2 Vaporization model

Applying the reduced geometry, the coupled CFD and XDEM calculations were performed to simulate the drying process. For moisture vaporization from biomass particles the following approach was considered. It is based on balance between the energy available for evaporation and the amount of evaporated water. Thus, any heat above the evaporation temperature is available to evaporate water, which can be described as follows [8]:

$$\dot{S}_{\mathrm{H_2O}} = \begin{cases} \frac{(T-T_{evap})\rho c_p}{H_{evap}\delta t} & T \geq T_{evap} \\ 0 & T < T_{evap}, \end{cases} \tag{2}$$

where T, T_{evap}, H_{evap}, ρ, c_p, δt denote local particle temperature, evaporation temperature, evaporation enthalpy, particle density, specific heat of the particle and the time interval, respectively.

5 RESULTS

In Fig.4 and Fig.5 the XDEM/CFD numerical results are presented. In Fig.4 the propagation of the heating front in four different time steps can be observed. The fluid medium is air, which is composed from O_2 and N_2. As it can be seen the hot gas of the temperature 773 K flows into the cylinder from the top wall to the bottom wall. Gas velocity inlet v equals 2.3 m/s and operating pressure p equals 1 atm. Due to the heat transfer from hot air to cold biomass (with initial temperature of 293 K), the central temperature of each particle is increasing.

In Fig.4 the changes of the moisture content in each particle in four different time steps are presented. In this test case the initial moisture content in each particle is very small. Due to the heat propagation the particles are heated up, which leads to the water vaporization.

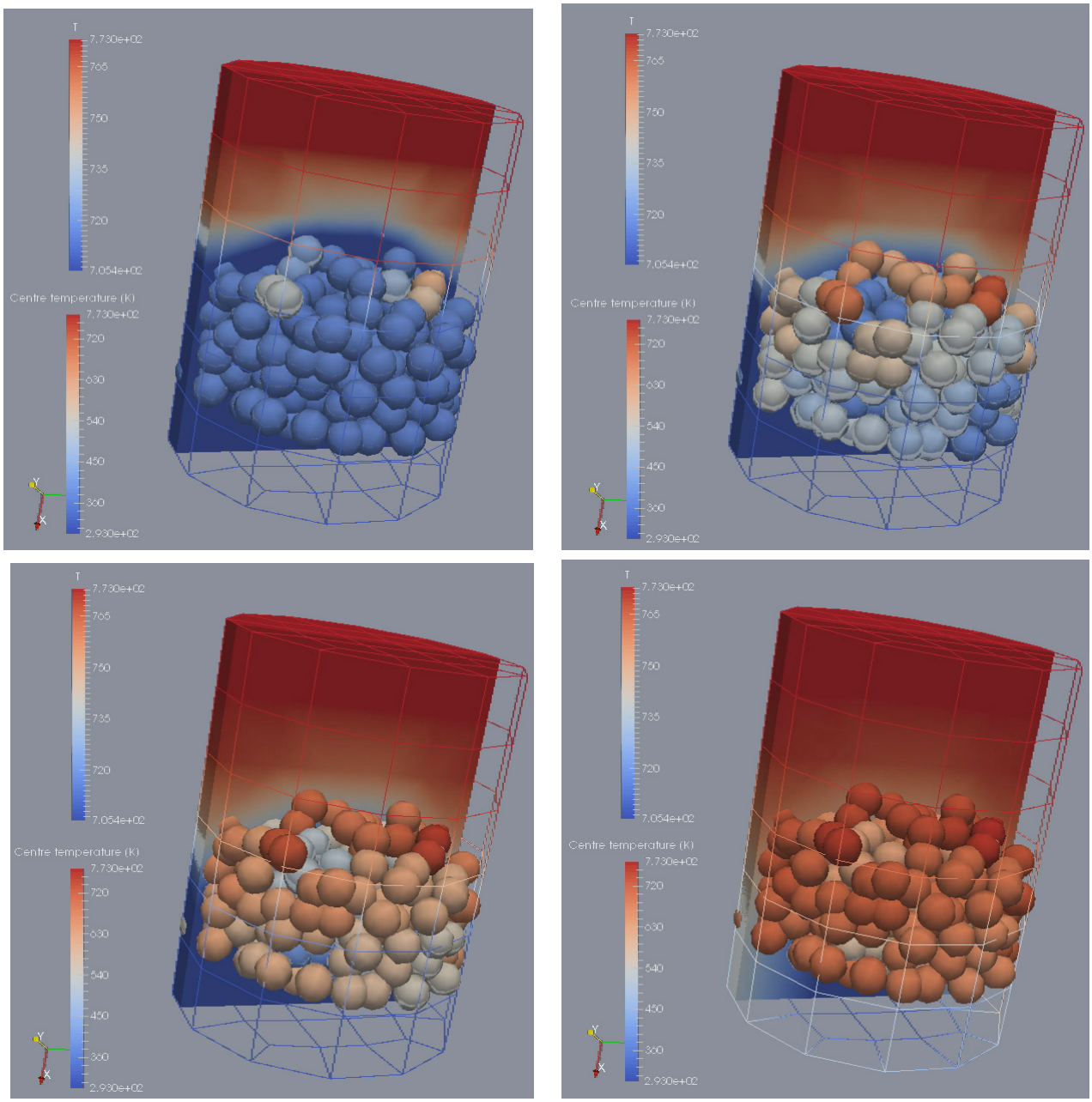

Figure 4: Temperature distribution in different time steps in the simplified analysed reactor

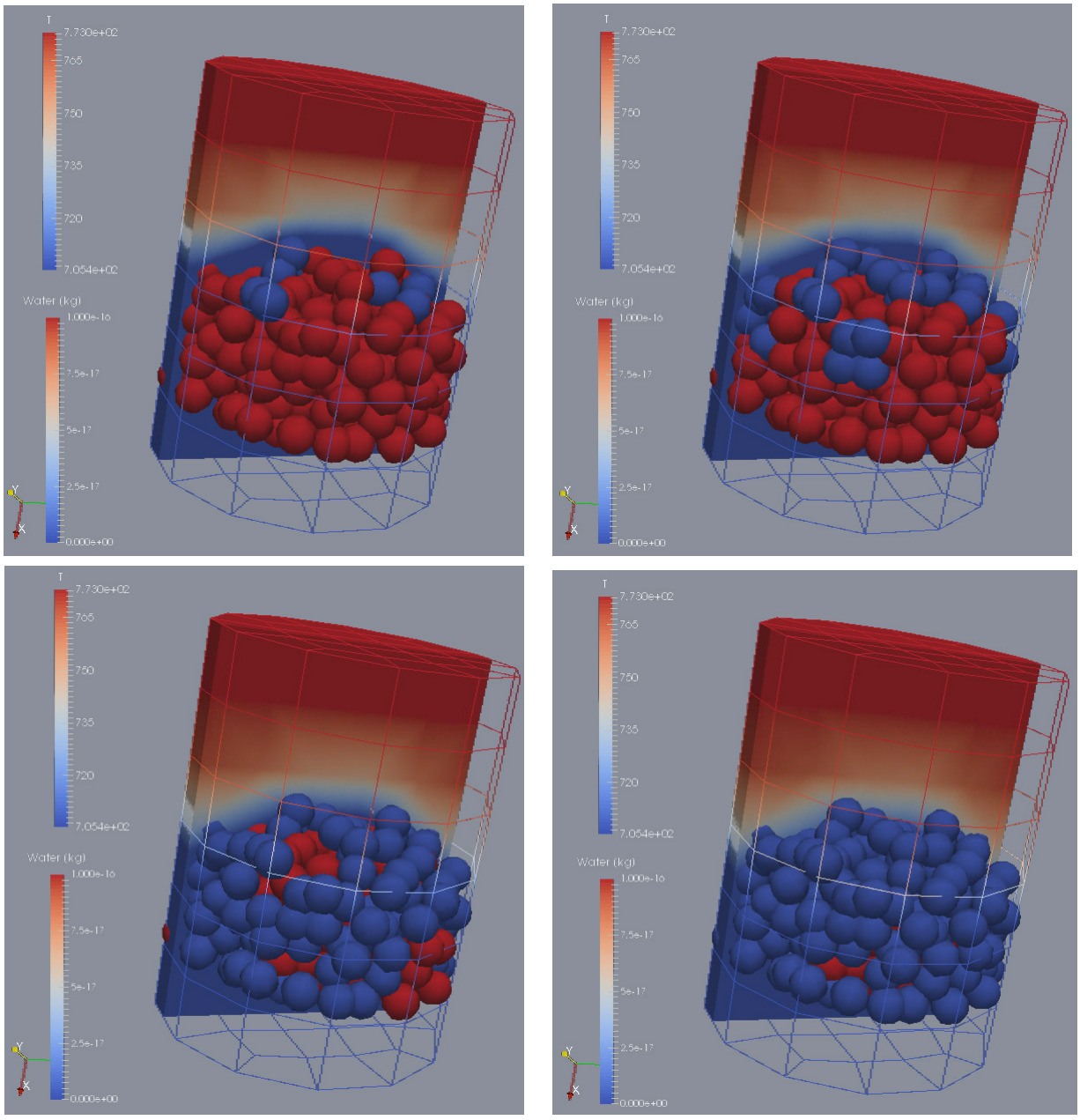

Figure 5: Water content in particles in different time steps in the simplified analysed reactor

6 NUMERICAL SIMULATIONS - ANSYS FLUENT

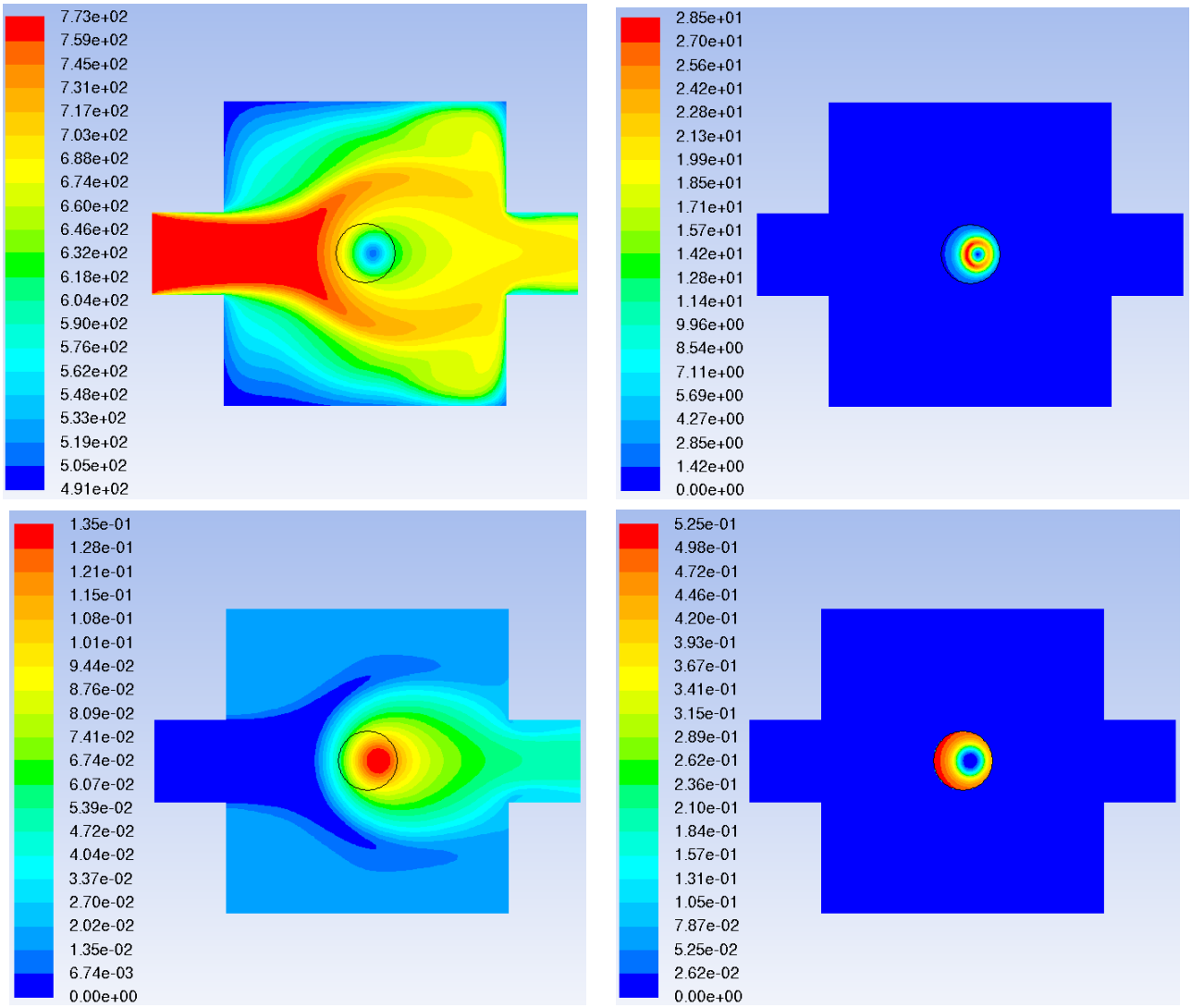

Figure 6: Particle parameters after 30 s of heating: temperature and gas mass source (top), volatiles mass fraction and porosity (bottom)

For comparison the numerical analysis of single wood particle heating obtained from ANSYS FLUENT is presented. The cold particle with diameter of 9 mm is heated by the stream of hot nitrogen. Temperatures of solid and gas are assumed to be at 298 K and 773 K, respectively. Gas inlet velocity was set to 2.3 m/s. Due to the heat transfer from the surrounding gases, the structure of particle is changing and the volatiles are released. The volatiles mass source term, the porosity and the wood density variation were implemented to the ANSYS FLUENT code by UDF function basing on the appropriate temperature

dependencies [9].

In Fig.6 the propagation of the heating front can be observed. The temperature of the particle is changing asymmetrically according to the hot gas flow direction. The average temperature of the particle at chosen time is ca. 620 K, which is the temperature the most intense pyrolysis for pine wood (data from TGA, [9]). Due to the increase of particle temperature the volatiles are released, what can be seen from the pictures showing the gas mass source (top right picture) and the mass fraction of released volatiles (bottom left picture). Gas mass source has a maximum value at the places corresponding to the particle temperature of 600 K. There is no gas release inside the particle, where its temperature is below 500 K. From the distribution of volatiles mass fraction, it can be observed that there is some kind of a gas-bag formed around the particle, which slows down the temperature propagation into the wood. Due to mass loss, also the porosity of wood is changing: from 0% in the colder parts to the 52.5% in the devolatilized parts of the analysed particle (right picture, at the bottom).

In the future this results can be compared with the single solid fuel particle analysis obtained from XDEM.

7 CONCLUSIONS

The main goal of this work was to investigate the possibility of the XDEM program to simulate the behaviour of wood particles during the gasification process that was performed in the real gasifier called INKA (IMP PAN). Basing on the test case calculations of the analysed gasifier, the following conclusions can be made:

- the XDEM method can be used to simulate heat and mass transfer processes in the biomass packed bed reactors, but it has some limitations concerning the number of the analysed particles,
- due to the computation time only the simplified geometries should be taken into account,
- the test case with the simplified geometry includes 300 particles, but the results with calculated temperature field and moisture content could be extended to large number of particles,
- the numerical results show propagation of the heating front and the change of the moisture content in each particle,
- to get better results at the first stage of the analysis using coupled XDEM/CFD, the behaviour of single particle during the gasification process should be considered,
- the single solid fuel particle XDEM analysis can be compared with other CFD simulations.

REFERENCES

[1] Basu, P. Biomass Gasification and Pyrolysis. Practical Design and Theory (2010), **1**, *Elsevier*, Oxford.

[2] Kluska, J. and Kazimierski, P. and Kardaś D. Effect of biomass settling in the fixed bed gasification reactor, CYSENI 2016, May 26-27, Kaunas, Lithuania, *Conference Materials*, (2016) ISSN 1822-7554.

[3] Peters, B. and Besseron, X. and Estupinan, A. and Hoffmann F. and Michael M. and Mahmoudi, A. Enhanced Thermal Process Engineering by the Extended Discrete Element Method (XDEM). *Univ. J. Eng. Sc.* (2013), **1(4)**: 139-145.

[4] Estupinan Donoso, A. A. and Peters, B. XDEM Used for Predicting Tungsten-Oxide Reduction. *CAPE Forum 2015, Computer Aided Process Engineering, University of Paderborn*, April 27-29 (2015), Paderborn, Germany.

[5] Mahmoudi, A. H. and Hoffmann, F. and Peters, B. Semi-resolved modeling of heat-up, drying and pyrolysis of biomass solid particles as a new feature in XDEM. *Appl. Therm. Eng.* (2016) McGraw Hill, **93**:1091–1104.

[6] OpenFoam, OpenFoam documentation, (2014). http://www.openfoam.com.

[7] Wakao, N. and Kaguei S. Heat and Mass Transfer in Packed Beds, McGraw-Hill, New York, (1982).

[8] XDEM Tutorials, LuXDEM Research Team, unpublished materials.

[9] Wardach-Święcicka, I. Modelling of physicochemical processes in a solid fuel particle in a stream of hot gases. *PhD Thesis - in Polish* (2016) IMP PAN, Gdańsk.

POWDER FLOW WITHIN A PHARMACEUTICAL TABLET PRESS – A DEM ANALYSIS

CLAUDIA HILDEBRANDT[1,*], SRIKANTH R. GOPIREDDY[2], REGINA SCHERLIESS[1] AND NORA A. URBANETZ[2]

[1] Department of Pharmaceutics and Biopharmaceutics
Christian-Albrechts-University Kiel, Grasweg 9a, 24118 Kiel, Germany
e-mail: childebrandt@pharmazie.uni-kiel.de, rscherliess@pharmazie.uni-kiel.de
web page: http://www.uni-kiel.de/Pharmazie/technologie/

[2] Daiichi-Sankyo Europe GmbH
Pharmaceutical Development, Luitpoldstr. 1, 85276 Pfaffenhofen, Germany
e-mail: Srikanth.Gopireddy@daiichi-sankyo.eu, Nora.Urbanetz@daiichi-sankyo.eu
web page: https://www.daiichi-sankyo.eu/

Key words: DEM analysis, pharmaceutical tableting, die filling, force feeder

Abstract. Numerical simulations in pharmaceutical industry are gaining importance as an advanced tool to elucidate the underlying physics in unit operations during tablet manufacturing. Out of different processing stages, powder flow within the tableting machine constitutes one critical step defining inter alia product safety in terms of content and content uniformity of the active pharmaceutical ingredient (API). By means of numerical simulations the Quality by Design (QbD) approach could be integrated to enhance product quality. However, the numerical simulations reported so far either evaluated the powder flow in a simplified system without considering the complex geometrical configuration within the rotary tablet press or used unrealistic micro-mechanical particle properties and sizes.

This work presents a numerical approach for studying the powder flow within a force feeder to die/cavity in a rotary tablet press with actual dimensions to evaluate the final product quality. The computations were carried out using an open source discrete element method (DEM) code. The investigated system consists of a hopper, a force feeder comprising three rotating paddle wheels, and a turret with 24 dies. A poly-disperse particle size distribution was used mimicking a low dose direct compression formulation with calibrated micro-mechanical material properties. First of all, a summary of the basic metrics such particle size distribution and mass hold up in the different parts of the feeder is provided. Subsequently emphasis is given to the powder flow patterns in the force feeder that are visualized by particles' coloring. Results reveal that (1) the powder feeding from the hopper into the feeder shows a gradient across the feeding hopper width causing an intriguing particle mixing, (2) particles are unequally refed from dosing wheel zone and (3) an intermixing between the reverse dosing and filling wheel zone can be identified. Those three visualized powder flow phenomena are supported by quantitative analysis and eventually their influence on the filled dies is being explained.

In conclusion, this study helps in visualizing powder flow in a pharmaceutical tablet press disclosing astonishing particle flow phenomena that have not been reported yet.

1 INTRODUCTION

Solid dosage formulations, in particular tablets, constitute the most important application route to deliver active pharmaceutical ingredients (API) to patients. Different quality attributes have to be met to ensure patient safety. Those requirements for tables are friability, resistance to crushing, disintegration, dissolution, and uniformity of dosage units [1]. "Quality is built into products by design" [2], cited from the ICH guideline Q8 and Quality by Design (QbD) paradigm, in other words, quality can be improved by implementation of science-based manufacturing of pharmaceutics. During tablet production on rotary tablet presses, three different steps are intertwined with each other and with the quality requirements. Those steps are the filling of powder through feeders into the dies, powder compaction, and finally tablet ejection. The first process step is achieved through material transfer by force feeders differing in terms of geometry, e.g. number and shape of paddle wheels.

QbD can be realized e.g. by numerical means of the discrete element method (DEM). This technique, in contrast to experiments, benefits of a high resolution on a particle level. However this already implies the inherent drawback of a high computational cost. Hence, most numerical studies reporting the die filling process focus on the effect of geometry design, process parameters, and micro-mechanical material properties [3, 4, 5]. Recent studies explain die filling into rotating dies by gravity [3,4] and force feeding containing different number of paddle wheels [5, 6]. Though the essential role of differently sized particles in pharmaceutical blends is only reported by few studies [4, 6].

In this work the die filling process in the context of a lab-scale rotary tablet press consisting of a filling system with three paddle wheels is investigated by DEM. Moreover a poly-disperse particle size distribution (PSD) is considered mimicking a direct compressible (DC) blend. The PSD reflects a mixture of excipients and API particles that is being compressed without prior granulation thereby emphasizing the importance of powder flowability as a whole [7]. The excipients in DC formulations are responsible for tablet dissolution in the gastrointestinal tract, flow aid, and bulk mass increase. With this given realistic system, light is shed on the die filling process and different means of process understanding are provided.

2 METHODOLOGY

The methodology used has already been reported in [8]. In brief, the methodology is as follows.

2.1 Discrete element method

After introduction of the DEM in 1979 it has evolved to a well-known approach in particle technology. This numerical model captures the trajectories of each and every particle in the system through Newton's equation of motion. Details about theory and algorithms are described in detail in [9, 10, 11]. All computations were performed using the open source DEM software LIGGGHTS [12], version 3.4.1. Same models to calculate normal, tangential, and non-contact forces as [3, 4] have been used.

2.1 Geometrical setup

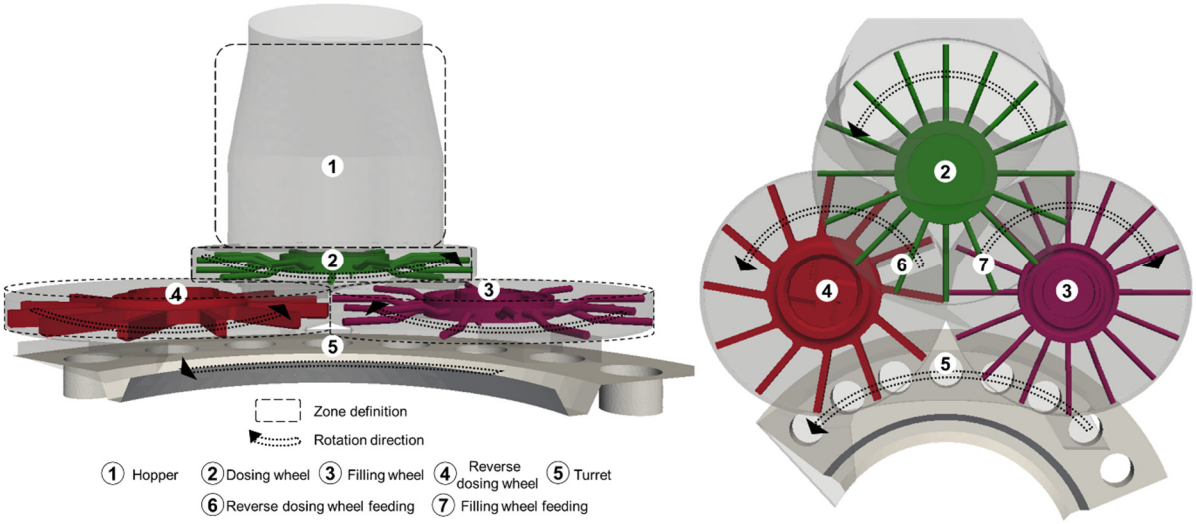

Figure 1: Illustration of the geometrical setup in front-(left) and top-(right) view.

The geometrical configuration and dimensions correspond to the "Fill-O-Matic" of a lab-scale FETTE 1200i rotary tablet press (Fette Compacting GmbH, Schwarzenbeck, Germany), and are illustrated in Fig. 1. It consists of a feeding hopper (① in Fig. 1) and a feeding plate consisting of three differently shaped paddle wheels. The dosing wheel (② in Fig. 1), reverse dosing wheel (④ in Fig. 1), and turret (⑤ in Fig. 1) are rotating in anti-clockwise, the filling wheel (③ in Fig. 1) in clockwise direction.

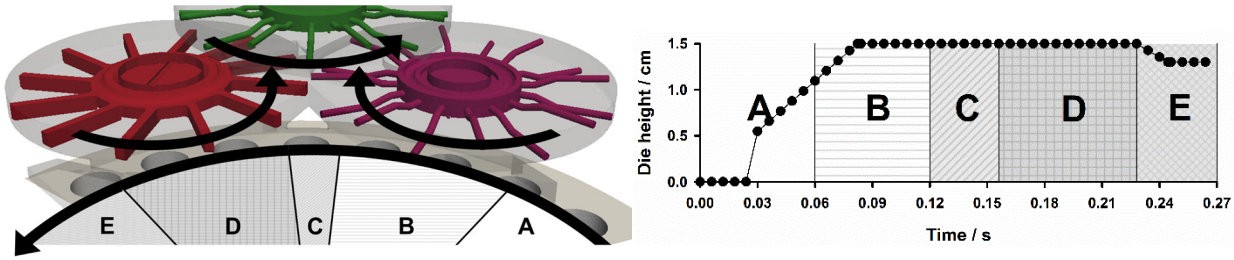

Figure 2: (Left) Illustration of die filling positions within Fill-O-Matic. Arrows indicate rotation direction of turret and paddle wheels. (Right) According die height at different die positions.

While the die diameter of 2.4 cm is constant, the die height is changing according to the die position during filling (Fig. 2). Initially, at the positioning of the filling wheel ("B" in Fig. 2), the lower punch is lowering during "fill cam" by 18.3 cm/s to create a maximal die height of 1.5 cm, and it remains constant (1.5 cm) during "C" and "D" in Fig. 2. At the end of filling, during "dosing cam", the lower punch is moving upwards by 0.2 cm at 12.2 cm/s to remove excess powder and to create a more confined powder bed ("E" in Fig. 2).

2.2 Material properties

As mentioned in the introduction, a PSD, shown in Fig. 3, reflecting a blend consisting of API and excipient particles was defined. For excipients, six different particle sizes ranging from 1000 – 2800 µm diameter at mean diameter of 2201 µm were selected. In DC formulations, API particles' flowability and compressive properties limit its maximal content [7]. A reasonable content of 5% and size ratio of 1:2 to excipients' mean diameter (API particle diameter of 1129 µm) [13] were chosen. Although absolute particle sizes used in simulations are much higher compared to true DC blends, the total number of simulated particles (~ 286,000) is already at the computational limit.

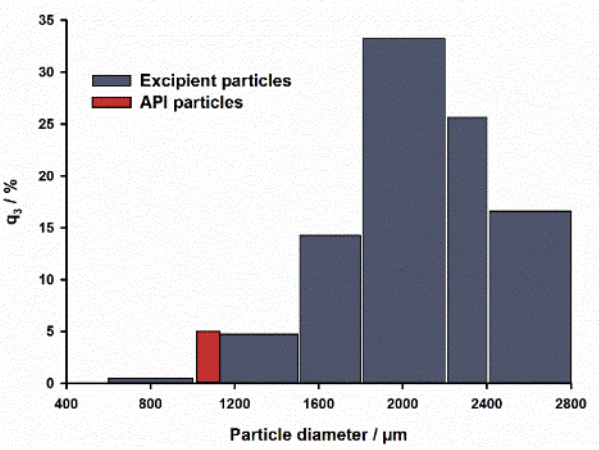

Figure 3: Particle size distribution consisting of 7 different sizes, out of which one particle size reflects API particles and the remaining are excipient particles of 2201 µm mean diameter.

Bulk density, angle of repose, and mass flow rate according to Ph. Eur. [1] of different pharmaceutical diluents (different grades of lactose, mannitol, and microcrystalline cellulose used in DC formulations) have been measured. Values obtained through experiments have been compared to numerical results, and micro-mechanical properties, especially non-contact force (represented by cohesion energy density (CED)) and friction between particles and geometry (coefficient of friction, particle-wall) have been adapted iteratively to obtain good results accordance. The adapted micro-mechanical properties used during filling and discharge are within the range of literature data [3-6], and are listed in Table 1.

Table 1: Material properties, the numbers in parenthesis correspond to steps in Table 2.

Parameter / Unit	Property of	Value during filling (❶-❸)	Value during discharge (❹)
Young's modulus / GPa	Particle	8.7	8.7
	Wall	210	210
Poisson's ratio / -	Particle	0.30	0.30
	Wall	0.35	0.35
Coefficient of restitution / -	Particle-particle	0.15	0.15
	Particle-wall	0.15	0.15
Coefficient of friction / -	Particle-particle	0.35	0.40
	Particle-wall	0.30	0.25
Cohesion energy density (CED) / MJ/m³	Particle	1.5	1.0

2.3 Initialization and die filling process

The system was filled with particles according to real experiments by a step-wise procedure, listed in Table 2. At the very beginning, powder was filled from the blending container into the feeding system hopper (step no. ❶, Table 2). Subsequently, powder was distributed evenly

within the Fill-O-Matic by slow paddle wheel rotations (❷, Table 2). Afterwards, the complete tableting machine was filled with powder by one turret rotation at low speed (❸, Table 2). Eventually after a physical time of 15.8 s, the completely filled system with particles is illustrated in Fig. 4.

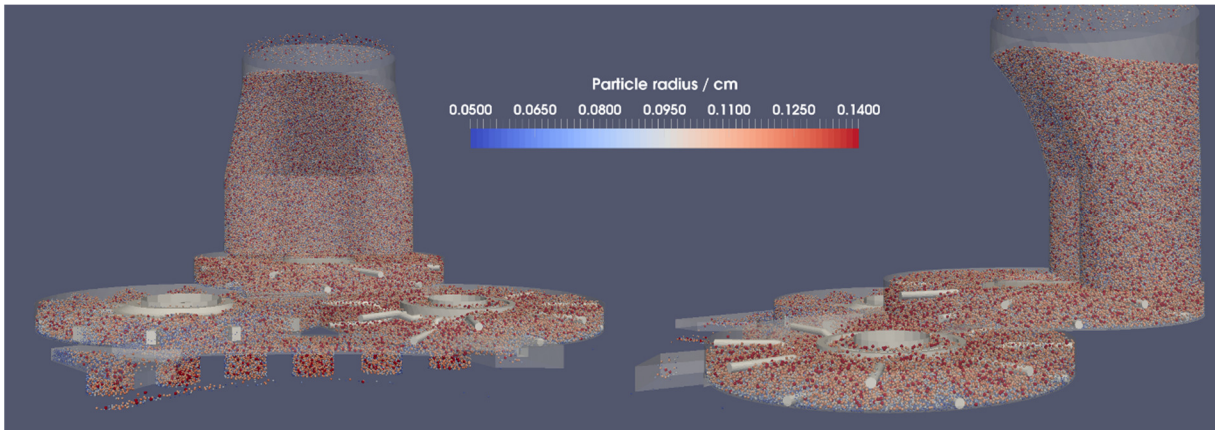

Figure 4: System at the end of filling (❸) and before discharge (❹) (Table 2) (left: front view, right: side view).

This filling procedure ensures constant filling level independent of subsequent process parameters and material properties (Table 1). Discharge or actual die filling process started by high speed tableting at increased paddle wheel speed (30 rpm) and turret speed (75 rpm) to generate a maximal output of 108,000 tablets/hour with 24 punch stations. To get an understanding of die filling during high speed tableting, ten turret revolutions to fill in total 240 dies have been performed. As particles filled in dies leave the simulation domain, continuous particles' refilling in the feeding hopper ensured constant mass in the system.

Table 2: Process parameters at different computation steps

No.	Description	Physical time / s	Turret speed / rpm	No. of turret rotations / -	Paddle wheel speed / rpm	No. of paddle wheel rotations / -
❶	Filling of hopper	0.8	0	0	0	0
❷	Filling of Fill-O-Matic	9	0	0	15	2.26
❸	Filling of turret	6	10	1	15	1.5
❹	Discharge	8	75	10	30	4

3 RESULTS AND DISCUSSION

The die filling process in an actual lab-scale pharmaceutical tablet press (FETTE 1200i) has been studied with a PSD typically found in DC formulations and with calibrated material properties. The filling of the Fill-O-Matic, following the standard procedure in experiments, and the die filling in high speed tableting at one selected combination of process parameters, namely paddle wheel and turret speed has been discussed extensively in [8]. The main focus of this manuscript will be laid on powder flow phenomena within the filling system.

3.1 Summary of basic die filling metrics

In [8] it has been shown, that not only during system filling but also during the die filling process, different mass hold up and particle size distributions as well as API contents, are generated at different locations of the Fill-O-Matic. The particles collected in the die originate from different positions within the Fill-O-Matic attributed to the turret rotation direction, mass flow rate from paddle wheel zones, and the die height (confer 2.1 and Fig. 2) which is only at its maximum height during rotation underneath the filling wheel zone ("B" in Fig. 2). As a result 50%, 14%, and 36% of the mass in the die stems from the filling wheel ("B"), the inter wheel ("C"), and the reverse dosing wheel ("D") zone, respectively. In totality, a constant API content and tablet mass over production time fluctuating within the range of mean ± one standard deviation are obtained [8].

In addition to the basic die filling metrics as described in [8], powder flow phenomena will be visualized qualitatively as well as quantitatively in the context of die filling process in the following.

3.2 Particle rearrangement in the system

Numerical simulations give the opportunity to look inside a given system, which is one of the major advantages compared to experiments. To visualize the powder flow within the Fill-O-Matic, the particles have been assigned different colors at the time point of discharge (t = 15.8 s, ❹ Table 2, Fig. 5), to see the temporal development of flow pattern within various zones of the whole system. Particles that are located in the dosing wheel zone (②, Fig. 1) are colored in green, in the filling wheel zone (③, Fig. 1) in pink, and the reverse dosing wheel zone in red (④, Fig. 1), respectively, as shown in Fig. 5. In addition to the paddle wheel zones, four additional horizontal zones in the feeding hopper (①, Fig. 1) have been created (Fig. 5A), to identify dead zones, if any exist. The rest of the particles are assigned blue color.

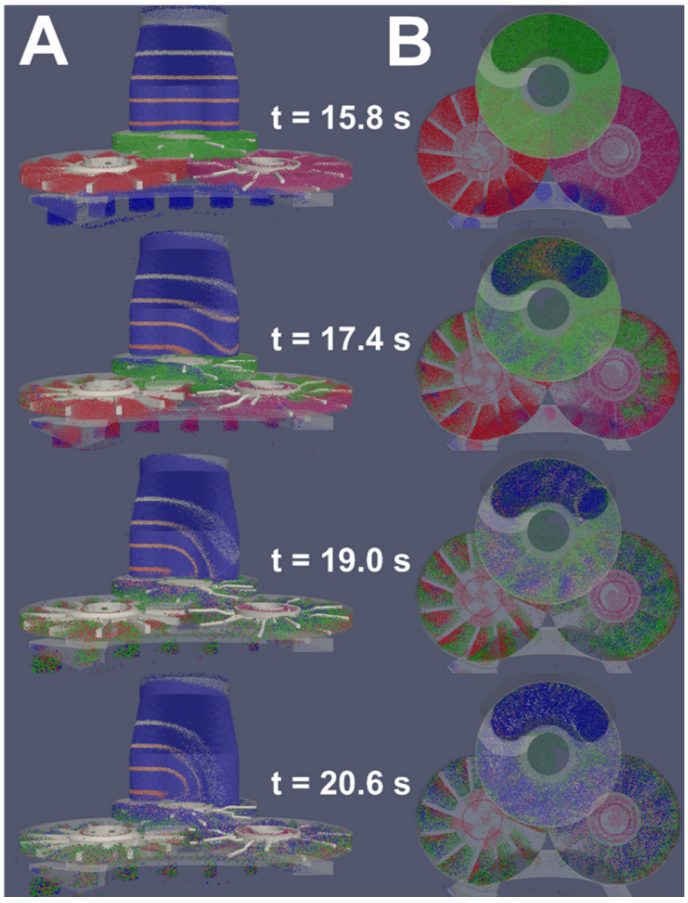

Figure 5: Coloring of the particles according to their initial position at time point of discharge (t = 15.8 s). Particles in the paddle wheel zones are assigned different colors in addition to four horizontal zones in the feeding hopper. Colored particles are tracked over time for the for the first 6 turret rotations at every 2nd rotation (t = 17.4 s for 2nd, t = 19.0 s for 4th, t = 20.6 s for 6th rotation, respectively). (A) Front-view, (B) top-view.

Three different main powder flow phenomena can be elucidated during die filling. (1) From Fig. 5A it becomes visible that the powder

feeding from the hopper into the Fill-O-Matic shows a gradient across the feeding hopper radius causing an intriguing particle mixing. Thereby particles that are located in the left half of the hopper tend to remain there (indicating a dead zone) throughout the complete discharge period since solely the particles from right hand side enter and refill the dosing wheel zone. The other two phenomena are visualized in Fig. 5B. (2) Less particles from the dosing wheel zone are refilling through the smaller feeding zone in ⑥ compared to ⑦ (refer Fig. 1), thereby less "green" colored particles are found in the reverse dosing wheel compared to the filling wheel zone (confer e.g. time point 17.4 s and 19.0 s in Fig. 5B). (3) Furthermore an intermixing between the two bottom paddle wheels can be identified. Underneath the dosing wheel zone, particles from the reverse dosing wheel zone ("red") and particles from the filling wheel zone ("pink") are interchanging from one zone into the other. This interchanging is found at the outer radial location. In the following, those three identified particle flow phenomena as illustrated in Fig. 5 are quantitatively evaluated.

3.3 Powder flow in the feeding hopper

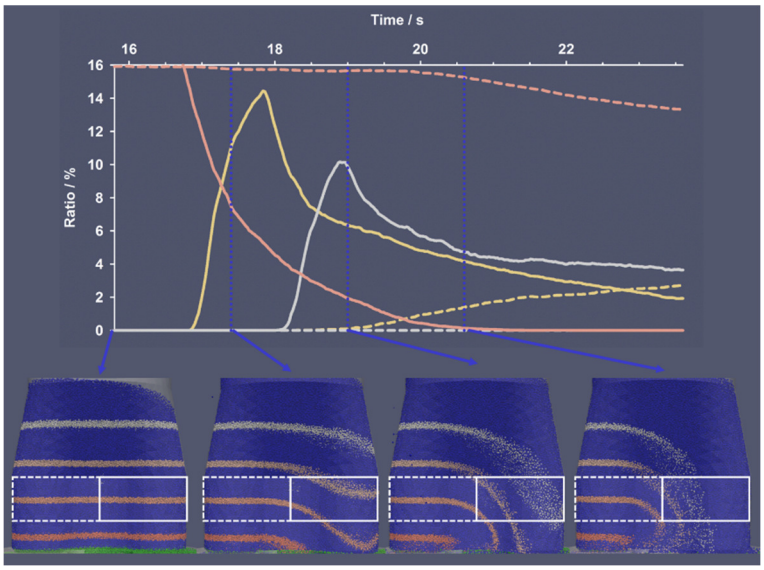

Figure 6: Qualitative distribution of colored particles in the middle part of the hopper, split into the left (dashed lines) and right (solid lines) half. Top: number frequency of colored particles; bottom: illustration of the system at 1.6 s intervals (15.8 s, 17.4 s, 19.0 s, and 20.6 s)

As already shown by particles coloring in Fig. 5A, particles are non-uniformly fed from the hopper into the dosing wheel zone. Four particle layers with a height of 0.5 cm were colored in grey, yellow, light orange, and dark orange, separated by zones of non-colored particles (dark blue, height of 2.5 cm). The colored particles zones as illustrated in Fig. 6 (bottom) are quantitatively analyzed over time for the middle part of the hopper (Fig 6, top) The hopper is split into a left (dashed lines), and right (solid lines) half and the number frequency of colored particles appearing in this zone are plotted over discharge time (Fig. 6, top). At the beginning (t = 15.8 s) 16% light orange colored particles are found both in left and right half of the hopper. Over time in the left half, the number frequency of light orange colored particles decreases only slightly ending with a minimum frequency of 13.8% (t = 23.7 s). As soon as light orange colored particles start to deplete, yellow colors from layers above appear at t = 18.2 s. In contrast to the left hopper half, completely different colored particles distribution is found in the right half. A very steep decrease of light orange colored particles with a parallel increase of yellow colored particles from layers above can be identified (t = 16.8 s). Moreover, as soon as those yellow colored particles start to disappear after their maximum at t = 17.8 s, the number frequency of grey colored particles increases.

At the end of discharge (t = 23.7 s), the left half of the hopper still contains initially located particles (light orange) indicating a dead zone. Particles in this zone may get consolidated over time as a result of the pressure exerted by the overlying powder bed in the feeding hopper and blending container. In contrast the right half has an increased mass throughput and particles over a hopper height of > 10 cm are fed into the dosing wheel zone. The reason being, as the dosing wheel is rotating in anti-clockwise direction (confer Fig. 1) underneath the hopper, main refeeding is achieved at the right half of the hopper. In follow up analysis the gradient and dead zone within the hopper have to be analyzed with respect to particle size segregation.

3.3 Particle refeeding

The second particle flow phenomenon as described in 3.2 and visualized in Fig. 5B, is the unevenly refeeding of particles from the dosing wheel (Fig. 1, ②) into the filling wheel (Fig. 1, ③) and reverse dosing wheel (Fig. 1, ④) zone. The number frequencies of green colored particles from the dosing wheel zone in the different paddle wheel zones over time are plotted in Fig. 7 (line colors according to paddle wheel zones, Fig. 1). Initially, all particles in the dosing wheel zone are colored in green (100% at t = 15.8 s). Over time they are depleting as result of refeeding into paddle wheel zones below (③ & ④ in Fig. 1) through refeeding holes (⑦ & ⑥) at the bottom of the dosing wheel zone. In parallel differently colored particles originating from hopper emerge (data not shown).

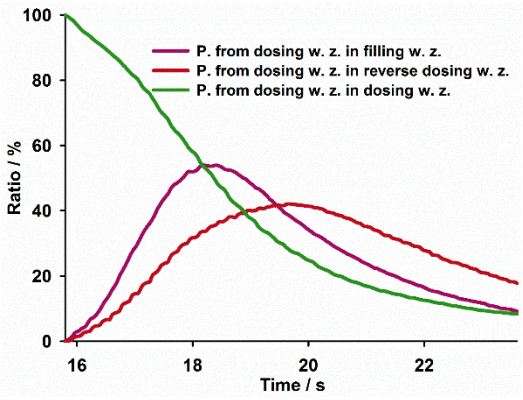

Figure 7: Number frequency of colored particles from dosing wheel zone (green in Fig. 5) in different locations of the Fill-O-Matic. Line colors: Green in dosing wheel, pink in filling wheel, and red in reverse dosing wheel zone.

Right at the beginning of die filling (t = 15.8 s), green colored particles start to show up in filling wheel and reverse dosing wheel zone. However, a steeper increase and a higher maximal value in the filling wheel zone can be identified (max. of 54% and 42% at t = 18.4 s and 19.6 s in filling wheel and reverse dosing wheel zone, respectively). The first explanation can be given by an increased mass flow rate that can be obtained through the larger refeeding hole into the filling wheel (⑦ in Fig. 1) compared to reverse dosing wheel zone (⑥ in Fig. 1). Second a higher mass throughput in the filling wheel zone requires a higher and faster refeeding. The increased mass throughput for the filling wheel zone is already shown in [8] by a 3-fold higher mass flow rate into the die and a 1.4-fold increased die mass contribution compared to the reverse dosing wheel zone (confer [8] and 3.1). The higher mass throughput in the filling wheel zone is also reflected by a steeper decrease of green colored particles after t = 18.4 s (Fig. 7).

3.4 Mixing between filling and reverse dosing wheel zone

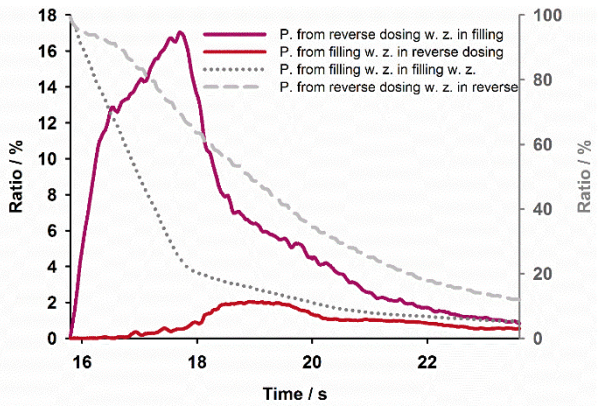

Figure 8: Grey lines: Number frequency of originally located particles and their depletion in filling (dotted) and reverse dosing (dashed) wheel zone. Colored lines: Number frequency of particles from reverse dosing in filling wheel zone (pink) and of particles from filling in reverse dosing wheel zone (red).

Not only a different refeeding rates of the two bottom paddle wheel zones could be shown (3.3) but also an intermixing between them is indicated by particles coloring in Fig. 5B. To quantitatively evaluate this observation, two different comparisons are described in the following.

First, the grey lines in Fig. 8 reflect the depletion of originally located particles in the filling (dotted) and reverse dosing (dashed) wheel zone. Within the first 2 s of discharge (t = 17.8 s) a very steep decrease of initially located particles in the filling wheel zone (pink in Fig. 5B, dotted grey line in Fig. 8) followed by a moderate decrease to a final frequency of 7.8% is found (confer below). In contrast, a sigmoidal decrease of particles from reverse dosing wheel zone within this zone is implied (grey dashed line in Fig. 8). In summary, particles tend to remain a significantly increased residence time within the reverse dosing wheel zone. Thereby more shear forces are exerted on particles which could bear the risk for particle attrition and over lubrication [5]. Those particles from reverse dosing wheel zone enter the die at last (confer Fig. 2) hence particles in the die and over the die height have experienced different shearing history which could potentially lead to tablet capping [4].

The second approach indicating the intermixing effect (3.2) is given by the solid colored lines in Fig. 8, showing the appearance of initially located particles from the filling in the reverse dosing wheel zone (red, Fig. 8) and from the reverse dosing in the filling wheel zone (pink, Fig. 8). At the level of the two bottom paddle wheel zones and underneath the dosing wheel zone, an unclosed intersection of 4.6 cm width is found that allows free particle motion across the filling and reverse dosing wheel zones (Fig. 1). A higher particle transfer from the reverse dosing into the filling wheel zone is found with a maximum contribution of 16.7% at t = 17.6 s (Fig. 8, pink). The reason being, the high mass throughput in the filling wheel zone (confer 3.3) requires a higher refeeding rate which cannot be caught up by refeeding from the dosing wheel zone. Thereby the reduced mass hold up is compensated by the mass exchange from reverse dosing wheel zone. Furthermore, the significantly reduced mass flow rate into the die from the reverse dosing wheel zone (confer [8] and 3.1) requires less refeeding hence only few particles originating from the filling wheel zone show up (2% at t = 18.9 s, Fig.8, red). It also gives explanation for the two differing curve slopes of particles from filling wheel zone in the same one (grey dotted line in Fig. 8, confer above). Particles that travel from the filling into the reverse dosing wheel zone can in parallel travel back into the former one. Hence they show up again in the filling wheel zone compensating the particle depletion by discharge into the die leading to a less steep curve of the slope (grey dotted line in Fig. 8 for t > 17.8 s).

3.5 Colored particles in dies

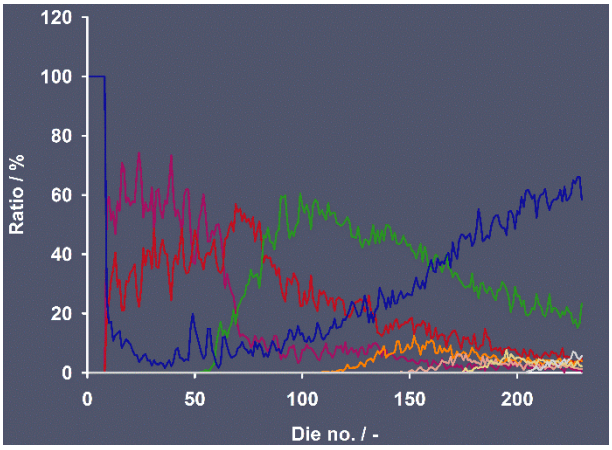

Figure 9: Number frequency of colored particles (confer Fig. 5 for initial position of colored particles) in the dies.

Last but not least, the appearance of colored particles in the filled dies is illustrated in Fig. 9 (confer Fig. 5 for initial position of colored particles). The first dies (1-8) have already been filled during turret filling stage (Table 2, ❸) being assigned to blue color. Die no. 9-13, the first filled dies at high turret speed, (Table 2, ❹) are mainly being filled by particles from filling (~ 60%, pink) and reverse dosing (~ 30%, red) wheel zone attributed to their different mass flow rates (confer 3.1). The low contribution of blue colored particles in those dies arises from particles that are initially located between Fill-O-Matic and turret (confer Fig. 5, t = 15.8 s).

The first particles from the dosing wheel zone appear in die no. 53 (t = 17.6 s), at the time point when almost maximum contribution of particles from dosing in filling wheel zone (confer Fig. 7, pink) is found. Red colored particles increase from the initial contribution of ~ 30% until a maximum of 57% in die no. 61 (t = 18.1 s) followed by a descent decrease until last filled die. Although the contribution of filled mass by reverse dosing wheel is only 36% (confer 3.1 and [8]) the observed maximum can be explained by the high particle exchange from the reverse dosing into filling wheel zone (confer 3.4 and Fig. 8). A constant increase of blue colored particles from the feeding hopper is found from die no. 50 (t = 17.7). Subsequently the horizontal colored zones from the feeding hopper (confer Fig. 5A and 6) with orange, light orange, yellow, and grey particles appear in die no. 108, 142, 168, and 197, respectively.

In summary, particles that are filled into the dies have travelled a different distance within the system and originate from different locations within the Fill-O-Matic. Thereby the first filled dies contain particles that have been exerted to less shear forces [5] which could result in different compressive properties thus tablet hardness and dissolution profiles. In other words, over production time unsteady tablet properties could be obtained which could bear the risk to fail in meeting the quality requirements [1]. With the help of numerical simulations, the QbD approach [2] could be integrated into the tablet production process by e.g. adapting the compression forces of upper and lower punch over production time to compensate the differing material properties.

4 SUMMARY AND CONCLUSION

This is the first study visualizing the die filling process by numerical means within an actual lab-scale rotary tablet press. Material properties, in particular particle size distribution, adapted to model a DC formulation of low API content and calibrated micro-mechanical properties were used.

Supported by basic metrics such as particle size distribution and mass hold up within the system (reported in [8]), powder flow phenomena could be elucidated by particles coloring analysis. Within the Fill-O-Matic three different main phenomena were demonstrated.

(1) Within the feeding hopper, a gradient across the radius of the hopper was found, showing a dead zone in the left half. Particles remain there almost stagnant over the complete discharge time bearing the risk of consolidation and solely particles from right half contribute to particles refeeding. (2) The different mass throughput of filling and reverse dosing wheel zone implicate a significantly altered refeeding rate from the dosing wheel zone. (3) The third phenomenon is provided by an intersection between filling and reverse dosing wheel zone enabling a free mass transfer from the reverse dosing into the filling wheel zone. In addition to this intermixing, particles tend to remain a longer residence time within the reverse dosing wheel zone bearing the risk of particle attrition and over lubrication. Eventually the analysis of colored particles filled into the dies shows that the first filled dies contain particles that have traveled a shorter distance within the system thereby could establish different compressive properties. Tablet quality might change over time constituting challenges to meet the tablet quality requirements of the authorities.

At this given parameter set, powder flow phenomena in different locations of the system were shown. However, in the next step additional setups will be performed according to a design of experiments. They will provide a clear picture on the influence of material properties in combination with process parameters on tablet quality. Eventually, a better understanding and an integrated QbD approach in pharmaceutical tableting can be generated by means of numerical simulation.

5 ACKNOWLEDGMENT

The authors would like to thank and acknowledge Mr. Thomas Heinrich (Fette Compacting GmbH, Schwarzenbeck, Germany) and his team for generously providing the FETTE 1200i Fill-O-Matic CAD files.

6 REFERENCES

[1] Ph. Eur. European Pharmacopoeia 9th edn, 2017.
[2] ICH, Guidance for Industry Q8 (R2) pharmaceutical development, 2009.
[3] Gopireddy, S.R. et al. Numerical simulation of powder flow in a pharmaceutical tablet press lab-scale gravity feeder. *Powder Technol.* (2016) **302**:309-327.
[4] Hildebrandt, C. et al. Towards the understanding of particle size segregation in a pharmaceutical tablet press lab-scale gravity feeder. Manuscript under preparation.
[5] Ketterhagen, W.R. Simulation of powder flow in a lab-scale tablet press feed frame: Effects of design and operating parameters on measures of tablet quality. *Powder Technol* (2015) **275**:361-374.
[6] Mateo-Ortiz, D. et al. Relationship between residence time distribution and forces applied by paddles on powder attrition during the die filling process. *Powder Technol.* (2015) **278**: 111-117.
[7] Jivray, M. et al. An overview of the different excipients useful for direct compression formulations. *Pharm Sci Technol To* (2007) **3**:58-63.

[8] Hildebrandt, C. et al. Numerical analysis of the die filling process within a pharmaceutical tableting machine, *8. Symposium "Produktgestaltung in der Partikeltechnologie"*, Karlsruhe, 2017.
[9] Zhu, H.P. et al., Discrete particle simulation of particulate systems: theoretical developments. *Chem Eng Sci* (2007) **62**:3378-3396.
[10] Herrmann, H.J. et al. Modeling of granular media on the computer. *Continuum Mech Therm* (1998) **10**:189-231.
[11] Ketterhagen, W.R. et al. Process modeling in the pharmaceutical industry using the discrete element method. *J Pharm Sci* (2009) **98**:442-470.
[12] Kloss, C. et al. Models, algorithms and validation of opensource DEM and CFD-DEM. *Progress in Computational Fluid Dynamics, An International Journal* (2012) **12**:140-152.
[13] Tang, P. et al. Methods for Minimizing Segregation: A review. *Particul Sci Technol* (2004) **22**:321-337.

V International Conference on Particle-based Methods – Fundamentals and Applications
PARTICLES 2017
P. Wriggers, M. Bischoff, E. Oñate, D.R.J. Owen, & T. Zohdi (Eds)

DEM ANALYSIS OF EFFECT OF INTERFACIAL TRANSITIONAL ZONES ON FRACTURE IN CONCRETE

MICHAŁ NITKA AND JACEK TEJCHMAN

Faculty of Civil and Environmental Engineering
Gdańsk University of Technology
Narutowicza 11/20, 80-233, Gdańsk, Poland
micnitka@pg.gda.pl, tejchmk@pg.gda.pl

Key words: DEM, concrete, 3D, ITZ, 3-point bending beam.

Abstract. The aim of this paper is to show 3D numerical results on progressive fracture of the concrete at aggregate level using discrete element method (DEM). The test were performed for three point bending beam. Concrete was modelled as heterogeneous material consisted four phases: aggregate, cement matrix, interfacial transitional zones (ITZs) and air voids. The microstructure of sample as position and shapes of aggregate and air voids were taken directly from laboratory test. The non-destructive method of X-ray microCT scans was used. The numerical results (both macro- and microscopic) were directly compared with own laboratory test and previous 2D calculations. The special attention was lied on the crack geometry evolution. The effect of different properties of ITZ was studied.

1 INTRODUCTION

Fracture of the concrete materials strongly depends upon a heterogeneous structure of materials over many different length scales. It is a fundamental and complex phenomenon in quasi brittle materials [1-3]. To better understand its behaviour the meso-scale level should be accurate described in numerical analysis. The concrete sample may be described as a four-phase material composed of aggregate, cement matrix, macro-voids and interfacial transitional zones. The presence of aggregate and ITZs is particularly important since the volume fraction of aggregate can be as high as 70-75% in concrete. The calculation outcomes in [4,5] evidently showed that considering real size and shape of aggregate was essential. Also the ITZ phase should be modelled since it is always the weakest regions in usual concretes wherein micro-cracking starts [6]. The highly heterogeneous ITZ are attractors for a crack propagation. ITZs are porous regions of the cement paste around aggregate particles which are perturbed by their presence. Its thickness is about 5-50 μm. Their origin lies in the packing of the cement grains against the much larger aggregate that leads to a local increase in porosity (micro-voids) and a presence of small cement particles. A paste with the lower *w/c* (higher packing density) or made of finer cement particles or smooth aggregates lead to ITZs of a smaller extent. (higher packing density) or made of finer cement particles or smooth aggregates lead to ITZs of a smaller extent. These layers are highly heterogeneous and damaged and thus critical for the concrete behaviour. The accurate understanding of the properties and behaviour of ITZ is one of the most important issues in meso-scale analyses because damage is initiated in the weakest region and ITZs are

just the weakest link in concrete.

The meso-modelling can be used to comprehensively study local phenomena at the micro-level such as the mechanism of the initiation, growth and formation of localized zones and cracks which affect the macroscopic concrete behaviour. In this paper the discrete element method was chosen as a good tool to describe fracture [2,4,5,7-16]. A non-linear response of concrete during bending under 3D conditions was analysed. The calculations were performed with the 3-dimensional open-source code YADE which was developed at Grenoble University [17,18]. A linear contact under compression was used. The normal and tangential contact forces satisfied the cohesive-frictional Mohr-Coulomb equation [12]. The internal structure of concrete (size, shape and location of aggregate and macro-voids, micro-porosity) was directly taken from 3D x-ray images using the micro-tomography SkyScan 117 [4,5]. The numerical results were compared with previous 2D calculations and with laboratory test [4]. The special attention was laid on the crack path and on influence of the ITZs properties.

2 OWN LABORATORY TEST ON CONCRETE BENDING BEAM

The notched concrete beam was used in experiments, with height H=80 mm, width B=40 mm and length L=320 mm. Notch was located in the middle and its height and width was equal 8 mm and 3 mm (Fig.1). The concrete mixture was composed of aggregate and sand grains ($d_{\max}$=16 mm, d_{50}=2 mm), Portland cement (CEM I 32.5 R) and water (the compressive strength was about 50 MPa). The total particle (aggregate and sand) volumetric content was V=75%. The total aggregate content with the diameter equal to or larger than 2 mm was V=37%. The initial porosity of concrete was about 5%. The concrete sample was subjected to quasi-static three-point bending test. The vertical force F_{max} was equal to 2.15 kN (the flexural tensile strength was $f_{t,flex}$=3.73 MPa). The more details about experiment can be found in [4,19].

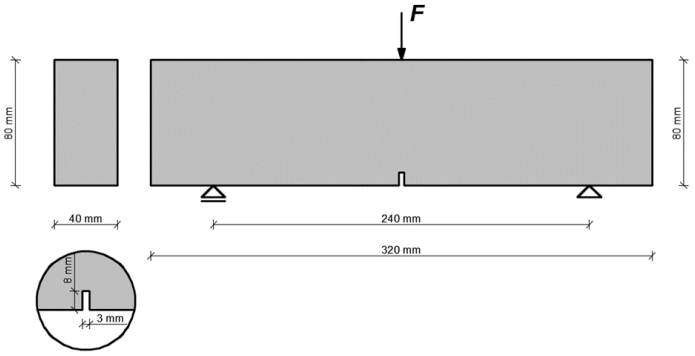

Fig.1: Geometry and boundary conditions of concrete beams subjected to three-point bending [4]

The distribution of aggregate and macro-voids in the concrete beams was determined based on microCT images of concrete cuboids (80×50×40 mm^3) cut from the middle part of beam after the tests [4]. Figure 2A shows 3D images of concrete internal structure obtained with the aid of SkyScan 1173 which represents a new generation in high-resolution desktop X-ray micro-computed tomography systems [19].

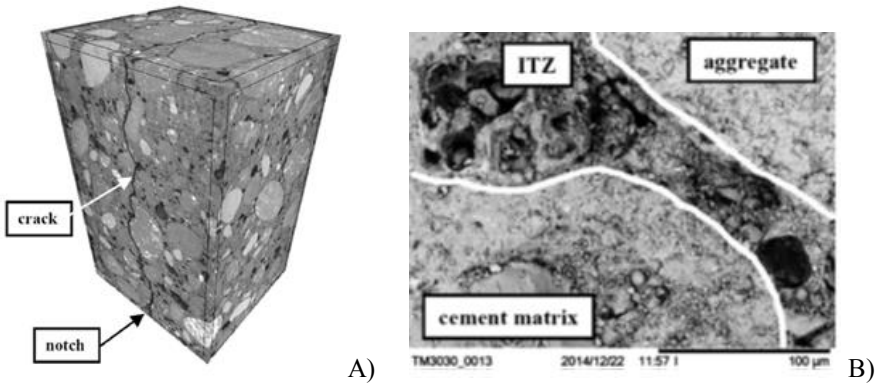

Fig.2: Experimental results: A) X-ray μCT images of cracked cuboidal specimens 80×50×40 mm^3 cut out from beam and B) scanning electron micrographs of ITZs around aggregate particles (magnification factor 1000) [4], [19]

The mine crack was strongly curved along beam height and width due to a random presence of aggregate grains and air voids (Fig.2A). It starts just above the notch and propagated upwards due to bending. The crack solely propagated through the weakest phase in concrete which were interfacial transitional zones (ITZs). Sometimes the crack can also propagate through a weak aggregate particle. Thus micro-cracking occurred first in ITZs and when two interfacial cracks occurred around adjacent aggregates, a crack inside the cement matrix initiated to bridge the interfacial cracks so that a connected crack path was formed. In order to observe porous structure of ITZs and measure its width, the scanning electron microscope (SEM) Hitachi TM3030 was used. The maximum magnification factor was 30'000. The width of ITZ varied between 30-50 μm and it did not depend on aggregate particle diameter (Fig. 2B) [4]. ITZs appeared around all aggregate grains (d_a≥2 mm) and usually covered about 80-90% of the aggregate circumference that was probably caused by a formation of water lenses beneath aggregate grains during mixing [23]. Other our experimental results showed that the width of ITZ reduced with decreasing aggregate roughness [5].

3 DISCRETE ELEMENT METHOD MODEL

The numerical analysis was performed by discrete element method (DEM). The open-source code YADE, developed at University of Grenoble, was used [17,18]. The code was successfully used for describing the behaviour of different engineering materials with a granular structure (mainly of granular materials by taking shear localization into account [20-23]). This model show also its capabilities in concrete fracture calculations under bending (2D analyses) [4] and uniaxial compression (2D and 3D simulations) [5,12]. Main advantage is ability to explicitly handle the discrete/heterogeneous nature of the material by modelling particle-scale properties including size and shape which play an important role in concrete fracture [4,5].

The algorithm used in the presented paper is based on the classical discrete element method formulation described by Cundall and Strack [24]. First, based on constitutive laws, interaction forces were calculated, when elements slightly interpenetrate each other. Next, the Newton's second law was used to compute acceleration of each particle, which was then time integrated to find the new position. This process was repeated until the simulation was finished.

The model takes advantage of the so-called soft-particle approach (i.e. the model allows for particle deformation which is modelled as an overlap of particles). During the simulations, particles may overlap that can be interpreted as a local contact deformation. A linear normal contact model under compression was used. The normal force was not restricted in compression. The interaction force vector representing the action between two spherical discrete elements in contact was decomposed into a normal and tangential vector, respectively. The normal forces acting on spheres were modelled by an elastic law with cohesion. The normal and tangential forces were linked to the displacements through the normal stiffness K_n and the tangential stiffness K_s (Fig.3) [17]

$$\vec{F}_n = K_n U \vec{N}, \tag{1}$$

$$\vec{F}_s = \vec{F}_{s,prev} + K_s \Delta \vec{X}_s . \tag{2}$$

where U is the overlap between spheres, $\vec{N}$ denotes the normal vector at the contact point, $\Delta\vec{X}$ is the increment of the relative tangential displacement and $\vec{F}_{s,prev}$ is the tangential force from the previous iteration. The stiffnesses were computed as the functions of the modulus of elasticity of the grain contact E_c and two neighbouring grain radii R_A and R_B (to determine the normal stiffness K_n) and the modulus of elasticity E_c and Poisson's ratio υ_c of the grain contact and two neighbouring grain radii R_A and R_B (to determine the tangential stiffness K_s), respectively [17]

$$K_n = E_c \frac{2R_A R_B}{R_A + R_B} \qquad \text{and} \qquad K_s = \nu_c E_c \frac{2R_A R_B}{R_A + R_B} . \tag{3}$$

If two grains in contact have the same size (R_A=R_B=R), the numerical stiffness parameters are equal to: K_n=E_cR and K_s=$\upsilon_c E_c$R, respectively (thus K_s/K_n=υ_c).

The contact forces $\vec{F}_s$ and $\vec{F}_n$ satisfied the cohesive-frictional Mohr-Coulomb equation (Fig.4d), used to capture the non-linear nature of concrete

$$\| \vec{F}_s \| - F^s_{\max} - \| \vec{F}_n \| \cdot \tan\mu \le 0 \quad \text{(before contact breakage)} \tag{4}$$

and

$$\| \vec{F}_s \| - \| \vec{F}_n \| \cdot \tan\mu \le 0 \quad \text{(after contact breakage)}, \tag{5}$$

where μ denotes the inter-particle friction angle and $\vec{F}^s_{\max}$ is the cohesive force between spheres. In tension, the maximum admissible normal force was $\vec{F}^n_{\min}$ if there was no a geometric contact between elements. If this normal force between spheres $\vec{F}^n_{\min}$ was reached, the contact was broken. Moreover, if any contacts between grains re-appeared, cohesion between them was not taken into account. A crack was considered as open if cohesive forces between grains (Eq.4) disappeared when a critical threshold was reached. The movement of fragments (mass-spring systems with cohesion) was similar to the rigid body movement.

A choice of a very simple constitutive law was intended to capture on average various contact possibilities in real concrete. Both the interparticle cohesive force and tensile force were

assumed as a function of the interparticle cohesive stress C (maximum shear stress at pressure equal to zero), interparticle tensile normal stress T and sphere radius R [17], [25]

$$F^{s}_{\max} = C \cdot R^2 \qquad \text{and} \qquad F^{n}_{\min} = T \cdot R^2 . \tag{6}$$

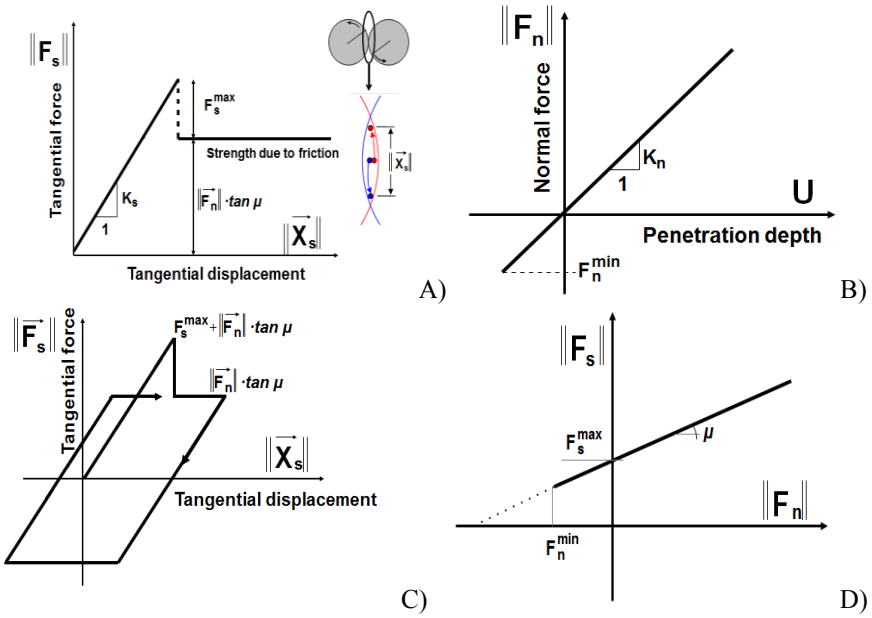

Fig.3: Mechanical response of DEM: A) tangential contact model, B) normal contact model, C) loading and unloading path in tangential contact model and D) modified Mohr-Coulomb model [12]

For two elements in contact, the smaller values of C, T and R were used. Because the proposed DEM is a fully dynamic formulation, a local non-viscous damping scheme was applied in order to dissipate excessive kinetic energy in a discrete system and facilitate convergence towards quasi-static equilibrium [26]. The damping parameter α_d was introduced to reduce contact forces acting on elements

$$\vec{F}^{k}_{damped} = \vec{F}^{k} - \alpha_d \cdot \mathrm{sgn}(\vec{v}^{k}) \,|\, \vec{F}^{k} \,|, \tag{7}$$

where $\vec{F}^{k}$ are the k[th]-components of the residual force and translational velocity, respectively. The positive damping coefficient α_d was smaller than 1 (sgn(•) returns the sign of the k[th] component of velocity). The equation could be separately applied to each k[th] component of the 3D vector x, y and z. The crack was not allowed to propagate through aggregate grains, i.e. the grain breakage has not been taken into account yet.

4 NUMERICAL ANALYSI

4.1 Input data

The concrete was modelled as four-phase material which consist aggregate cement matrix, ITZs and macro voids. The full 3D DEM analysis was performed on one concrete beam with exactly the same location and shapes of aggregate and macro voids as in experiment.

The specimen density (different phases) was determined with the aid of x-ray micro tomography. To describe the position of each voxel and its density (Figs.4Aa and 4Ba) the wave front *.obj file format was used. The high density shows aggregate (Fig.4Aa). The voxels with the density equal to the air density were assumed to be the macro-voids (Fig.4Ba). Next, the density volume was filled in with spheres (Figs.4Ab and 4Bb). The aggregate particles with the diameter higher than 2 mm were modelled only. The numerical volume of aggregate was 37% as in the experiment. All aggregate particles (2 mm$<d_a\leq$16 mm) were modelled as grain clusters with the diameter of d=2 mm (included from 2 up to 300 depending on its diameter) and all of them included ITZs around. ITZs were simply modelled as contacts between aggregate and cement matrix grains (thus they had no a physical width) in order to reduce calculations time. Note that simulation of the width of ITZs (0.03 mm - 0.05 mm) in the cement matrix would require very small spheres that would hugely increase the computational time. The spheres (0.5 mm$\leq d_{cm}<$2 mm) were solely assumed in the cement matrix; thus the smallest particle diameter in the specimen was 0.5 mm. The cement matrix grains filled the concrete specimen in about 97%. The macro-voids (with the diameter $d_{mv}\geq$1 mm) were modelled as empty regions.

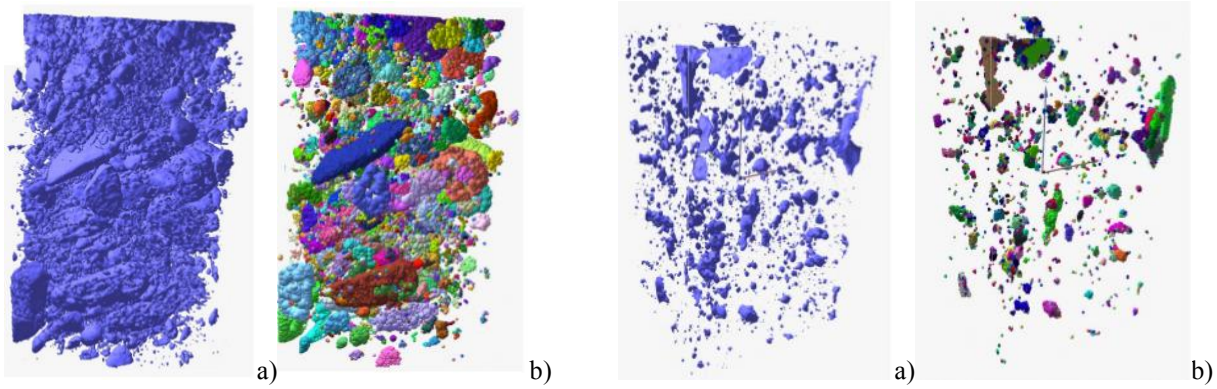

Fig.4: Three-dimensional view on aggregate (A) an macro-voids (B): a) based on density maps from x-ray micro tomographic images and b) replaced by elements (each colour corresponds to different diameter of aggregate cluster or macro-void)

The following five main local material parameters were needed for our discrete simulations: E, υ, μ, C and T. In addition, the particle radius R, particle mass density ρ and damping parameters α_d were required. Note that material softening was not assumed in the numerical model. The material parameters were calibrated in our previous 2D calculations [4]. The following parameters of the cohesion C and tensile strength T were used in all DEM analyses for the mid-region of the beam: cement matrix ($E_{c,cm}$=11.2 GPa, C_{cm}=140 MPa and T_{cm}=25 MPa) and ITZs ($E_{c,ITZ}$=7.8 GPa, C_{ITZ}=100 MPa and T_{ITZ}=17.5 MPa), which was 30% weaker than cement matrix. The choice of

reduction ratio was based on the experiments by nanoindentation [27]. With the assumed material properties and grain size distribution curve, the 2D and 3D DEM simulations provided the uniaxial compressive strength of about 50 MPa. similarly as in the experiments of Section 2 (f_c=51.81 MPa). In the remaining region outside the meso-region with large grains (Fig.5) was described by the same constants as form the cement matrix. The remaining parameters were constant for all phases and regions: υ_c=0.2 (Poisson's ratio of grain contact), μ=18^o (inter-particle friction angle), α_d=0.08 (damping parameter) and ρ=2.6 kG/m^3 (mass density). The prescribed damping parameter α_d and loading velocity v=2 mm/s did not affect the results (the inertial number I was <10^{-4} that always corresponded to a quasi-static regime) [12].

The beam with 3D particle clusters (Fig.5) included in total about 230'000 elements (220'000 elements in the meso-region 180'000 in the cement matrix and 40'000 in the aggregate) with d_{min}=0.5 mm. The calculations time was about 10-12 days using PC with CPU 3.30 GHz.

The detailed calibration procedure was described by [4,5,12] based on real laboratory tests on uniaxial compression or uniaxial tension of concrete specimens.

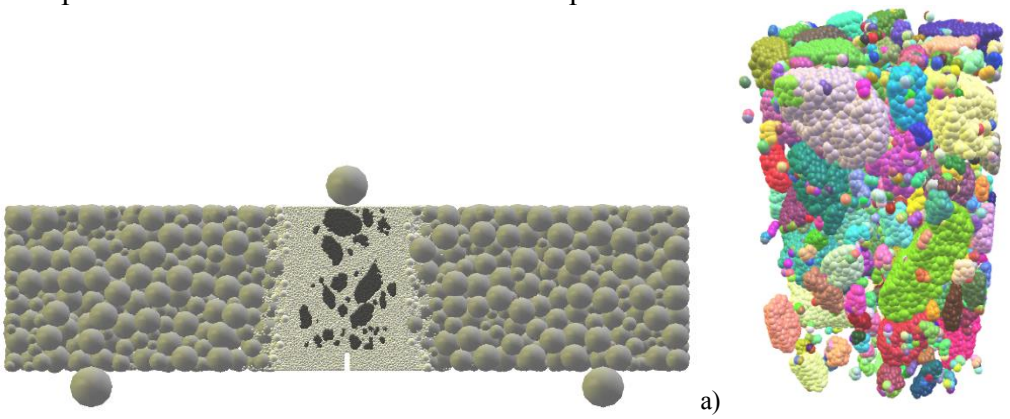

a) b)

Fig.5: Geometry of concrete beam model in DEM: a) front side of entire beam and c) 3D aggregate with ITZs in meso-region of 50×80×40 (each colour correspond different aggregate particles)

4.2 3D DEM results

The macroscopic numerical curves of vertical force versus CMOD were shown in Fig. 6. The 3D results were compared to previous 2D calculations and laboratory test. The obtained force peak (F=2.14 kN for CMOD=0.015 mm) was in good agreement with the experiment (F=2.18 kN for CMOD=0.017 mm). The residual force (CMOD=0.1 mm) was however higher by 100%. As compared to 2D results [4], the compressive strength was the same but the ductility was higher. Our earlier computations for uniaxial compression and tension [5,12] showed, the 3D calculations increase concrete ductility. The 3D curve was smoother than 2D curves due to a significantly larger number of particles in computations.

The crack path from 2D and 3D calculations and from laboratory test were presented in Fig. 7. The numerical crack shape in the vertical cross-section at the depth of 10 mm (Fig.7Ba) was like as in the experiment (Fig.7Aa). In the mid cross-section (Fig.7Bb) the shape was similar, however the aggregate just above notch was surround by crack from the other side than in the experiment (Fig.7Ab). Neverless both cracks ended at the same aggregate. In cross-section at the depth of 30 mm, the crack's onset had a different direction (Fig.7Ac) and furthermore the crack encircled next one aggregate grain along the opposite side, but finally ended at the same

position as the experimental macro-crack. As compared with 2D calculations [4], the calculated 3D crack path was similar (Figs.7Ca and 7Cc) or more realistic (see Fig.7Cb).

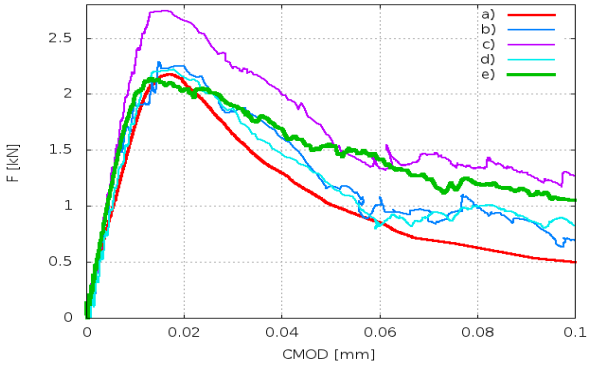

Fig.6: Evolution of vertical force *F* against CMOD in beam under 3-point bending: a) experimental curve (a), calculated curves in 3 different vertical cross-sections by 2D DEM (b-d) [4] and e) calculated curves by 3D DEM

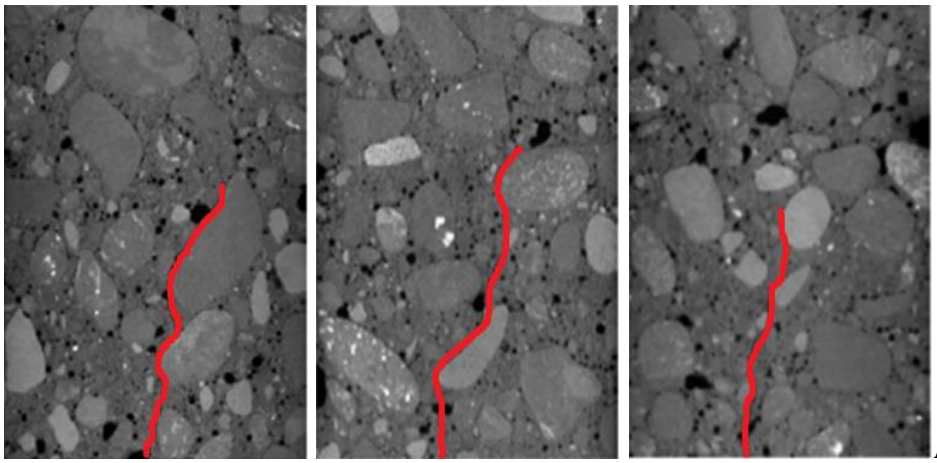
A)

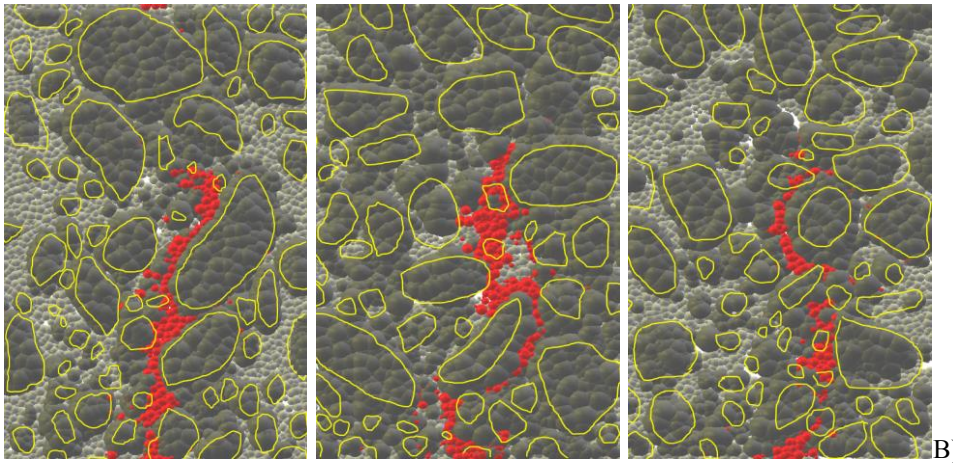
B)

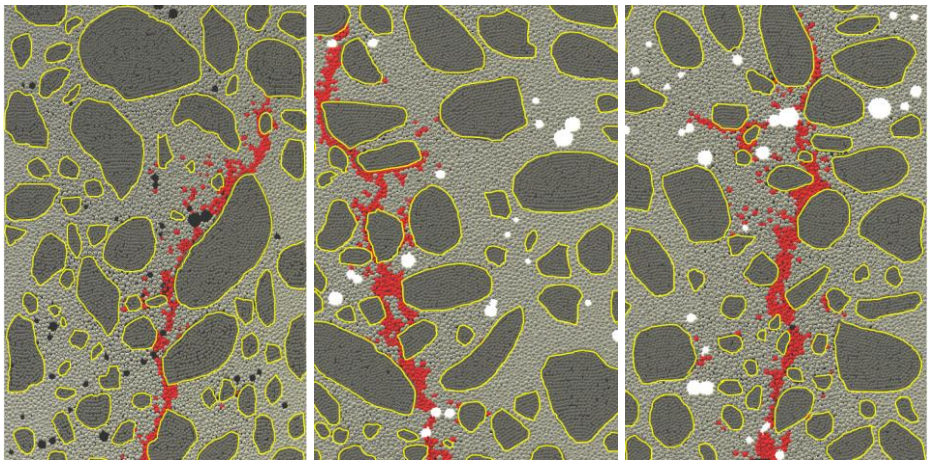
C)

Fig.7: Final crack trajectory in concrete beam above notch after test for CMOD=0.1 mm: A) based on micro-CT-image (red colour shows crack path), B) 3D DEM and C) 2D DEM [4] (red colour denotes elements with broken contacts, dark grey denotes aggregate, light grey denotes cement matrix) at depth of: a) 10 mm b) 20 mm and c) 30 mm from beam front side

4.3 Effect of ITZs properties

In Figure 8A the force – CMOD curves ware plotted for different strength of ITZs. The computations were performed for different ratios $E_{c,ITZ}/E_{c,cm}=C_{ITZ}/C_{cm}=T_{ITZ}/T_{cm}=r$ (with r=0.5, 0.7 and 0.9). The concrete beam stiffness and strength increase, since higher ratio was used (Fig. 8A). The material ductility increased with decreasing ratio r due to the growth of the macro-crack's propagation way through bridging interfacial micro-cracks. Thus, the macro-crack was more curved with the smaller ratio r (Fig.19B). For the ratio r=0.9, the macro-crack was almost straight. It propagated mostly through the cement matrix. For the ratio r=0.5, the macro-rack was more curved and propagated through the mortar and ITZs. The effect of r was similar in 3D and 2D analyses.

In Figure 9 the influence of the size of aggregates with ITZs was presented. Computations were done for ITZs phase around aggregate with diameter higher than 2mm (curve b) or higher than 3mm (curve c). The concrete strength, stiffness and brittleness became slightly higher with the smaller number of ITZ. The macro-crack's shape was not affected since the macro-crack was mostly attracted by ITZs located at large aggregate grains.

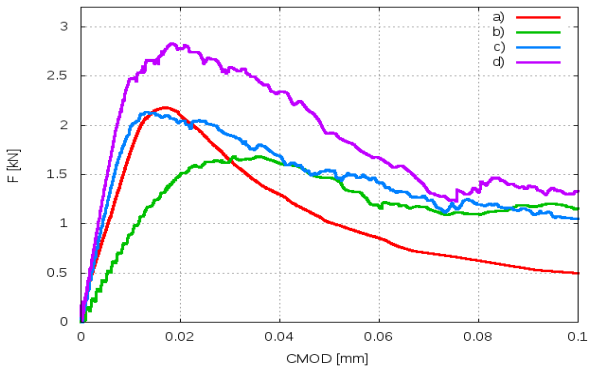

A)

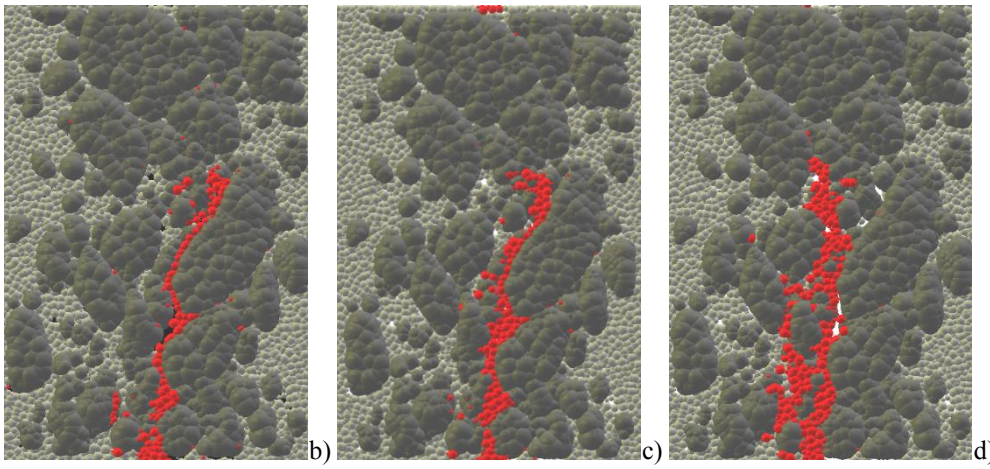

Fig.8: Effect of ITZs on evolution of vertical force F against CMOD (A) and crack shape (B) in beam under 3-point bending: a) experimental curve, b) $E_{c,ITZ}/E_{c,cm}$=0.5, C_{ITZ}/C_{cm}=0.5 and T_{ITZ}/T_{cm}=0.5, c) $E_{c,ITZ}/E_{c,cm}$=0.7, C_{ITZ}/C_{cm}=0.7 and T_{ITZ}/T_{cm}=0.7 and d) b) $E_{c,ITZ}/E_{c,cm}$=0.9, C_{ITZ}/C_{cm}=0.9 and T_{ITZ}/T_{cm}=0.9 (crack is shown in vertical cross-sectional slice at 10 mm from front specimen side for CMOD=0.1 mm)

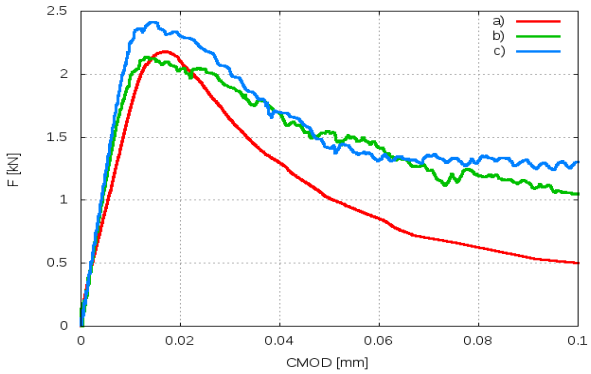

Fig.9: Effect of aggregate diameter with ITZs on evolution of vertical force F against CMOD in beam under 3-point bending: a) experimental curve, b) aggregate diameter d_a≥2 mm with ITZs and c) aggregate diameter d_a≥3 mm with ITZs

5 CONCLUSIONS

This paper shows capability of discrete element method (DEM) in fracture concrete calculations. The improvement between 2D and 3D calculations was presented. The 3D DEM model allow to understand micro-phenomena behaviour and predict the progressive nature of concrete fracture from the meso to macro level. Discrete models might progressively replace expensive experimental tests to study the influence of concrete meso-structure (aggregates size, aggregate shape, aggregate roughness, aggregate/mortar volume, micro- macro-porosity etc.) on the concrete behaviour. Thus the parametric studies within DEM might be used for the practical design of concrete with the improved desired performance. Directly from our numerical analysis, the following main conclusions may be pointed:

- The real shape of aggregate and the ITS around them have to be taken into calculations in order to realistic model micro fracture in concrete samples (i.e. bridging, branching).

- The influence of ITZs properties cannot be neglected in concrete modelling. With increasing stiffness and strength of this phase, the sample behave more brittle and its strength increase.
- The concrete strength, stiffness and brittleness became slightly higher with the smaller number of ITZs expressed by the larger diameter of aggregates d_a including ITZs.
- The shape and width of FPZ were more realistic since 3D calculations were performed. The macro response in force – CMOD curve was smoother, due to larger number of spheres in sample.

ACKNOWLEDGMENTS

The research work has been carried out within the project: ''*Innovative ways and effective methods of safety improvement and durability of buildings and transport infrastructure in the sustainable development*" financed partly by the European Union POIG.01.01.02-10-106/09-01) and the project ''*Experimental and numerical analysis of coupled deterministic-statistical size effect in brittle materials*" financed by the National Research Centre NCN (UMO-2013/09/B/ST8/03598).

REFERENCES

[1] Bažant, Z. and Planas, J. Fracture and size effect in concrete and other quasi-brittle materials. *CRC Press LLC*, Boca Raton (1997).
[2] Lilliu, G. and van Mier, J.G.M. 3D lattice type fracture model for concrete. *Engineering Fracture Mechanics* (2003) ***70***: 927-941.
[3] Tejchman, J. and Bobiński, J. Continuous and discontinuous modelling of fracture in concrete using FEM. *Springer, Berlin-Heidelberg (eds. W. Wu and R. I. Borja)* (2013).
[4] Skarżyński, Ł., Nitka, M. and Tejchman, J. Modelling of concrete fracture at aggregate level using FEM and DEM based on x-ray μCT images of internal structure, *Engineering Fracture Mechanics* (2015) **10** (147):13-35.
[5] Suchorzewski, J., Tejchman, J. and Nitka, M. Dicrete element method simulations of fracture in concrete under uniaxial compression based on its real internal structure, *International Journal of Damage Mechanics,* doi.: 10.1177/1056789517690915 (2017).
[6] Scrivener, K.L., Crumbie, A.K. and Laugesen, P. The interfacial transition zone (ITZ) between cement paste and aggregate in concrete. *Interface Science* (2004) **12**:411-421
[7] Du, C., Sun, L., Jiang, S. and Ying, Z. Numerical simulation of aggregate shapes of three-dimensional concrete and its applications. *Journal of Aerospace Engineer*ing (2013) 515-527.
[8] Hentz, S., Daudeville, L. and Donze, F. Identification and validation of a Discrete Element Model for concrete. *Journal of Engineering Mechanics ASCE* 130 (2004) **6**:709-719.
[9] Dupray, F., Malecot, Y., Daudeville, L. and Buzaud, E.A. Mesoscopic model for the behaviour of concrete under high confinement. *International Journal for Numerical and Analytical Methods in Geomechanics* (2009) **33:**1407-23.
[10] He, H., Guo, Z., Stroeven, P., Stroeven, M. and Sluys, L. J. Influence of particle packing on elastic properties of concrete. *Proc. First International Conference on Computational Technologies in Concrete Structures (CTCS'09),* Jeju, Korea, (2009), 1177-1197.
[11] Donzé, F.V., Magnier, S.A., Daudeville, L. and Mariotti, C. Numerical study of

compressive behaviour of concrete at high strain rates. *Journal for Engineering Mechanics,* 122(1999), **80:**1154-1163.
[12] Nitka, M. and J. Tejchman, J. Modelling of concrete behaviour in uniaxial compression and tension with DEM. *Granular Matter* (2015) **17,1**: 145-164.
[13] Groh, U., Konietzk, H., Walter, K. et al. Damage simulation of brittle heterogeneous materials at the grain size level, *Theoretical and Applied Fracture Mechanics* (2011) **55**:31-38.
[14] Carol, I., López, C.M., Roa, O. Micromechanical analysis of quasi-brittle materials using fracture-based interface elements. *International Journal for Numerical Methods in Engineering* (2001) **52**:193-215.
[15] Herrmann, H.J., Hansen, A. and Roux, S. Fracture of disordered, elastic lattices in two dimensions. *Physical Rev. B,* , (1989) **39**: 637-647.
[16] Kozicki, J. and Tejchman, J. Modelling of fracture processes in concrete using a novel lattice model. *Granular Matter* (2008) **10**, 377-388.
[17] Kozicki, J. and Donzé, F.V. A new open-source software developer for numerical simulations using discrete modeling methods. *Computer Methods in Applied Mechanics and Engineering* (2008) **197**:4429-4443.
[18] Šmilauer, V. and Chareyre, B. Yade DEM Formulation. Manual, (2011).
[19] Skarzynski, Ł. and Tejchman, J. Experimental investigations of fracture process in concrete by means of x-ray micro-computed tomography. *Strain* (2016) **52**:26-45.
[20] Widulinski, L., Tejchman, J., Kozicki, J. and Leśniewska, D. Discrete simulations of shear zone patterning in sand in earth pressure problems of a retaining wall. *Int. J. Solids and Structures* (2011) **48, 7-8**: 1191-1209.
[21] Kozicki, J., Niedostatkiewicz, M., Tejchman, J. and Mühlhaus, H.-B. Discrete modelling results of a direct shear test for granular materials versus FE results. *Granular Matter* (2013) **15, 5:** 607-627.
[22] Kozicki, J., Tejchman, J. and Műhlhaus, H.-B. Discrete simulations of a triaxial compression test for sand by DEM. *Int. J. Num. Anal. Methods Geom.* (2014) **38:** 1923-1952.
[23] Scrivener, K.L., Crumbie, A.K. and Laugesen, P. The interfacial transition zone (ITZ) between cement paste and aggregate in concrete. *Interface Science* (2004) **12:**411-421.
[24] Cundall, P.A. and Strack, O.D.L. A discrete numerical model for granular assemblies. *Geotechnique* (1979) **29**: 47-65.
[25] Ergenzinger, C., Seifried, R. and Eberhard, P.A. Discrete element model to describe failure of strong rock in uniaxial compression. *Granular Matter* (2011) **12(4):**341-364.
[26] Cundall, P.A. and Hart, R. Numerical modelling of discontinua. *Engineering Computations* (1992) **9:**101-113.
[27] Xiao, J., Li, W., Suc, Z., Lange, D.A. and Shah, S.P. Properties of interfacial transition zones in recycled aggregate concrete testes by nanoindentation, *Cement and Concrete Composites* (2013) **37:**276-292.

V International Conference on Particle-based Methods – Fundamentals and Applications
PARTICLES 2017
P. Wriggers, M. Bischoff, E. Oñate, D.R.J. Owen, & T. Zohdi (Eds)

DISCRETE ELEMENT MODELLING OF CONCRETE STRUCTURES UNDER HARD IMPACT

Andria Antoniou[1], Laurent Daudeville[2], Philippe Marin[3], Serguei Potapov[4]
[1]PhD candidate
Université Grenoble Alpes INP/CNRS, 3SR UMR 5521, 38000 Grenoble, France
email: andria.antoniou@3sr-grenoble.fr
URL: https://www.linkedin.com/in/andria-antoniou-713587b7/
[2]Professor
Université Grenoble Alpes INP/CNRS, 3SR UMR 5521, 38000 Grenoble, France
email: laurent.daudeville@univ-grenoble-alpes.fr
URL: http://people.3sr-grenoble.fr/users/ldaudeville/
[3]Associate professor,
Université Grenoble Alpes, CNRS, 3SR UMR 5521, 38000 Grenoble, France
e-mail: philippe_marin@yahoo.fr
URL: https://www.3sr-grenoble.fr/spip.php?article108&lang=fr
[4]Senior research scientist,
IMSIA EDF-CNRS-CEA-ENSTA UMR 9219, 91762 Palaiseau, France
e-mail: serguei.potapov@edf.fr
URL: http://www.imsia.cnrs.fr/spip.php?article105&lang=fr

Key words: DEM, Concrete, Impact, Numerical Modelling

Summary: *The increasing demand for infrastructure security requires accounting the risk of severe loading due to natural or manmade hazards, such as aircraft impacts. This paper presents a Discrete Element Method (DEM) approach implemented in EUROPLEXUS, fast dynamics software, able to predict damage of concrete structures under severe impacts. The proposed DEM model for concrete relies on the original developments of Cundall and Strack for granular materials that was extended to cohesive materials, such as concrete by introducing cohesive interactions in addition to contact ones. In order to validate the DEM approach, the simulation results of three hard impact tests are presented. The tests were performed by CEA Gramat on plain concrete targets with a passive confinement given by a steel jacket surrounding the cylindrical specimen and submitted to the impact of ogive-nosed steel projectiles.*

1 INTRODUCTION

Concrete structures are widely used as shielding barriers to protect sensitive infrastructures. Nowadays, Accidental conditions such as aircraft impacts on nuclear containments, even though, with low probability of occurrence during lifetime of a structure, demand for a designing under extreme loadings. Because of the extreme severity of such a loading, assessment of the protective structures must go far beyond verification of the

resistance to normal operating conditions: it is necessary to investigate the response of the structure until almost its complete failure to assess correctly its ultimate resistance capacity.

While continuous approaches such as the finite element method (FEM) are suitable for the nonlinear analysis of structures before failure, they reach their limits when trying to describe macro cracking and fragmentation mechanisms. The discrete element method (DEM) is a powerful alternative to FEM when advanced damage states and failure of concrete have to be studied. Indeed, DEM allows easily obtaining realistic macro-crack patterns and material fragments due to its discontinuous nature.

In previous paper, a coupled DEM-FEM approach was proposed with soft impact on RC structures [19]. This paper presents a DEM approach able to produce the experimental response of concrete structures under severe loading such as the hard impact due to the turbine of an aircraft engine. A geometric algorithm method based on a tetrahedral finite element mesh is employed for the discrete elements (DE) mesh generation, which uses a disordered assembly of rigid spherical elements of different sizes and masses although the elements do not represent the constituents of concrete. The spheres' interactions are modelled thanks to beam-like elements with a non-linear constitutive behaviour to model damage and compaction (closure of porosity). The strain rate effect is taken into account in tension. The proposed numerical method is validated with the simulation of three hard impact tests conducted by CEA Gramat [18] and the results of two penetration tests and one perforation tests are discussed. All the numerical developments were implemented in EUROPLEXUS [8] fast dynamics software.

2 DISCRETE ELEMENT MODEL

The DEM was originally developed to model granular materials such as sand by Cundall and Strack [4][5]. Afterwards, this method was extended by Hentz to cohesive materials such as concrete, by taking into account the cohesive interaction over the contact interaction [12]. A disordered polydisperse assembly of rigid spherical elements of different sizes and masses, which do not represent the concrete's constituents, is generated by a direct geometric algorithm proposed by Jerier et al. [14] *Figure 1*. The method is based on a special disordering technique of non-overlapping spheres that allows filling a given tetrahedral Finite Element mesh of the modelled specimen. This algorithm was implemented in SherePadder++ [23] free software, which was introduced into the open-source SALOME platform [21]. The DE model aims to reproduce the macroscopic experimental behaviour of concrete. Thus, DE mesh's assembly is required to be isotropic for undamaged concrete, which can be evaluated from the projection of the link's orientation. As has been shown by Potapov et al. [19] a FE mesh with 4 tetrahedra per edge and the ratios maximum over minimum radii $\frac{\text{Rmax}}{\text{Rmin}} = 3$, FE tetrahedron edge over the mean DE diameter $\frac{\text{FE}}{\text{DE}} = 4$ produces a satisfying distribution of interactions.

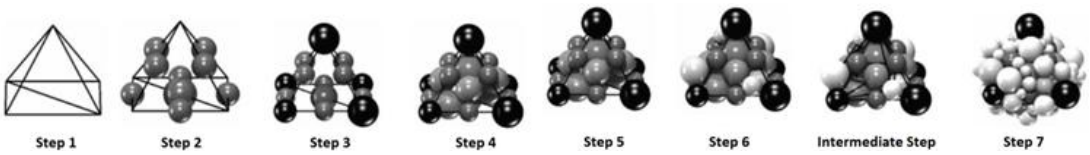

Figure 1 : DE mesh generator technique

2.1 Definition of interactions

An interaction is defined between two spheres a and b of radius R_a and R_b respectively inside an interaction range, which is determined by a interaction coefficient λ *Figure 2*.The two types of links are grouped and treated by the following equation (1), where $D_{a,b}$ is the distance between the centroids of the elements a and b and $\lambda \geq 1$.

$$\lambda\,(R_a + R_b) \geq D_{a,b} \tag{1}$$

A contact interaction is possible, when the distance between two particles is less than or equal to the sum of their radius, thus $\lambda=1$. In contrast, the cohesive interactions exist even when the elements are in certain distance where $\lambda>1$. A cohesive link receives also tensile forces and allows taking into account the effects of the cement matrix in concrete. The cohesive interactions are initialized at the beginning and they exist as long as are not broken whereas the new contact interactions are created throughout the procedure. Contrariwise, a contact link is acting only in compression. The number of links per element with its neighbours varies with the value of λ. The desired number of interactions can be set by adjusting the interaction coefficient. Then, the average number of interactions per discrete element is calculated as the number of links over the number of discrete elements equation (2). An average of 12 links per DE was selected by Rousseau [19].

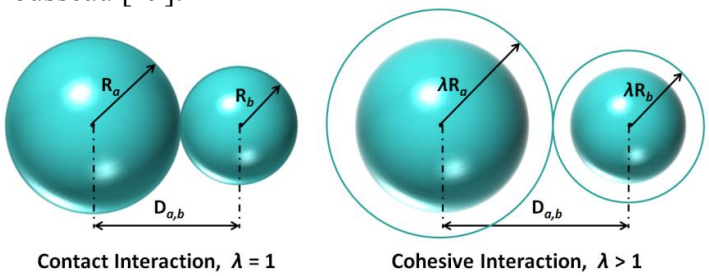

Figure 2: Contact Interaction and Cohesive Interaction

$$\text{average number of interactions per DE} = \frac{\text{number of links}}{\text{number of DE}} \tag{2}$$

2.2 Constitutive behaviour of discrete element concrete model

Unreinforced undamaged concrete is considered to be isotropic, homogeneous elastic and linear, whereas after cracking the behaviour becomes non-linear. Concrete's behaviour is modelled by means of two types of interactions. Contact links can create only contractive forces whereas cohesive links can receive also tensile forces. Two spheres not necessary in contact are related at an equivalent contact point with micro-macro phenomenological sping-like interactions, defined by local normal K_N and tangential K_S stiffnesses [11][19]. A third rolling spring-like interaction, K_R as rolling stiffness, has been implemented by Omar [16] in order to offer rolling resistance to the model and prevent from brittle failure. Moreover, the elastic behaviour of concrete is described by macro-micro relations proposed by Donzé [7], while a modified Mohr-Coulomb criterion is used for non-linear plastic behaviour [12][22].

2.3 Linear elastic constitutive behaviour

The relations for the elastic behaviour were created to describe the local microscopic parameters K_N and K_S from the global macroscopic elasticity coefficients, Young's modulus E, and Poisson's ration ν. The model of concrete in elasticity is originated from Voigt's hypothesis [3] and the best fit hypothesis [15] used for regular assemblies. Those approximations have been modified by Donzé [7] to take into account the disordered assemblies and the size of the interactive elements. Equation (3) shows the micro-macro relations between two elements a and b. $D_{init}^{a,b}$ represents the initial distance between two elements, with radius R_a and R_b and S_{int} is the interaction surface. Young's modulus E, and Poisson's ratio ν are considered the input values of the model whereas α, β and γ parameters need to be identified by mean of linear quasi-static compression and traction tests.

$$\begin{aligned} K_N &= \frac{E\, S_{int}}{D_{init}^{a,b}} \frac{1+\alpha}{\beta(1+\nu)+\gamma\,(1-\alpha\nu)} \quad (a) \\ K_S &= K_N \frac{1-\alpha\nu}{1+\nu} \qquad (b) \end{aligned} \tag{3}$$

Later, a study by Huang [13] has shown the dependence of the elastic macroscopic parameters on the ratio of shear stiffness over normal stiffness K_S/K_N. The expression of Young's Modulus given by Donzé's model [7][6] could be presented dimensionless eliminating its dependence on normal stiffness K_N, by adjusting a value E_0, which derives from the ratio $K_S/K_N = 1$, equation (4). The identification procedure of the linear elastic behaviour parameters α, β and γ is described by Hentz [11]. A compression test with the macroscopic parameters E = 25 GPa and ν = 0.16 performed by Gabet et al. [10] was simulated and the parameters were calibrated, $\alpha = 3.9$, $\beta = 3.75$ and $\gamma = 5$.

$$\frac{E}{E_0} = \frac{\frac{\beta}{\gamma} + \frac{K_S}{K_N}}{\frac{\beta}{\gamma} + 1} \frac{\alpha + 1}{\alpha + \frac{K_S}{K_N}} \tag{4}$$

2.4 Non-linear constitutive behaviour

The non-linear plastic behaviour of concrete, between two elements a and b, in tension is characterized by a local criterion of rupture which found in several studies [12][19][22]. A modified Mohr-Coulomb criterion with sliding function f_1 and a tensile rupture f_2 is used for cohesive links, equation (5). The modified Mohr-Coulomb criterion of cohesive interactions consists from a friction angle Φ_i, a cohesion stress C_0, a local tensile cut off stress T and a softening factor ξ. The softening factor ξ adjusts the tensile stiffness after damage in tension.

$$\begin{aligned} f_1(F_N, F_S) &= |F_S| - \tan(\Phi_i)\, F_N - S_{int} C_o \quad (a.\,\text{Sliding function}) \\ f_2(F_N, F_S) &= -S_{int} T - F_N \qquad\qquad (b.\,\text{Tensile damage}) \end{aligned} \tag{5}$$

The criterion of cohesive interactions equation (5) is separated in the cases below:

$f_2 \leq 0$ and $f_1 \leq 0$, the cohesive link is elastic

$f_2 \leq 0$ and $f_1 = 0$, the shear force follows the sliding function

When the second function, equation (5b) becomes greater than zero the damage of the cohesive link between two elements a and b is initialized because the component of the normal force F_N exceeds the maximum local tensile limit F_{tmax}. Hence, the link passes to the softening phase where the normal stiffness is defined as $\frac{K_N}{\xi}$. This regime is limited to a maximum distance of the two elements D_{el}^{max}. Once the cohesive link is broken and the two spheres come in contact, a new contact interaction is created, which follows a classical Mohr-Coulomb criterion with a contact angle Φ_c, equation (6).

$$f_1(F_N, F_S) = |F_S| - \tan(\Phi_C)\, F_N \quad (a.\,\text{Mohr} - \text{Coulomb}) \tag{6}$$

The criterion of contact interactions is divided in the next cases:

$f_1 \leq 0$, the contact link is opposed to interpenetration

$f_1 = 0$, the shear force follows the sliding function

The compressive non-linear plastic behaviour is governed by the compaction phenomenon, which occurs under high confinement. Once the elastic limit is excited $F_{cel} = \sigma_{cel} S_{int}$, the initialization of microcracks leads to a plastic regime until the plastic limit $F_{cpl} = \sigma_{cpl} S_{int}$, where consolidation take place, after the collapse of porosity and the closure of cracks, with a hardening branch. The stiffness of each branch is defined as the ratio of the initial stiffness of the link K_N over the parameters ξ_1 and ξ_2 respectively.

Figure 3 presents the two models, on the right is plotted the sliding functions, while on the left is illustrated the local link's behaviour. The microscopic parameters of the model need to be identified in order to result the macroscopic parameters, compressive σ_C and tensile σ_T strengths which are obtained from quasi-static tests in tension and compression. The compaction law parameters are defined by means of oedometric and hydrostatic tests obtained thanks to triaxial device that allows performing triaxial compression test on concrete with high confinement pressure. The non-linear behaviour parameters under low pressure were identified as C_0 = 3.5 MPa, T = 3 MPa, ξ = 3, φ_i = 30º and φ_c = 30º by modelling quasi-static tests with macroscopic σ_c = 34 MPa and σ_T = 3.4 MPa, *Figure 4*. For the parameters referred to high pressures σ_{cel} = 0.05GPa, σ_{cpl} = 0.3GPa, ξ_1 =1.5 and ξ_2 =0.3 were employed the Hydrostatic and Oedometric tests, *Figure 5* [10].

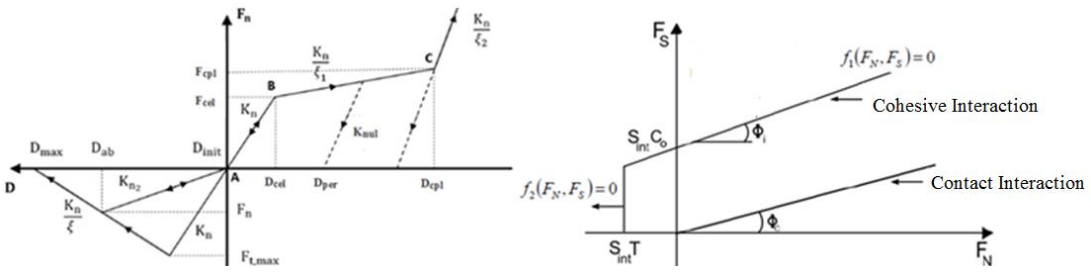

Figure 3: Local criterion of rupture

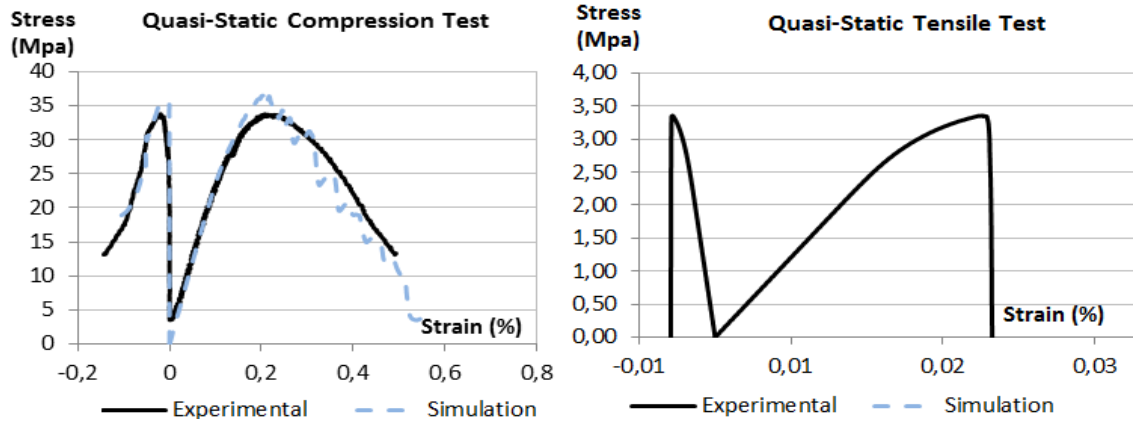

Figure 4: Simulation of quasi-static tests

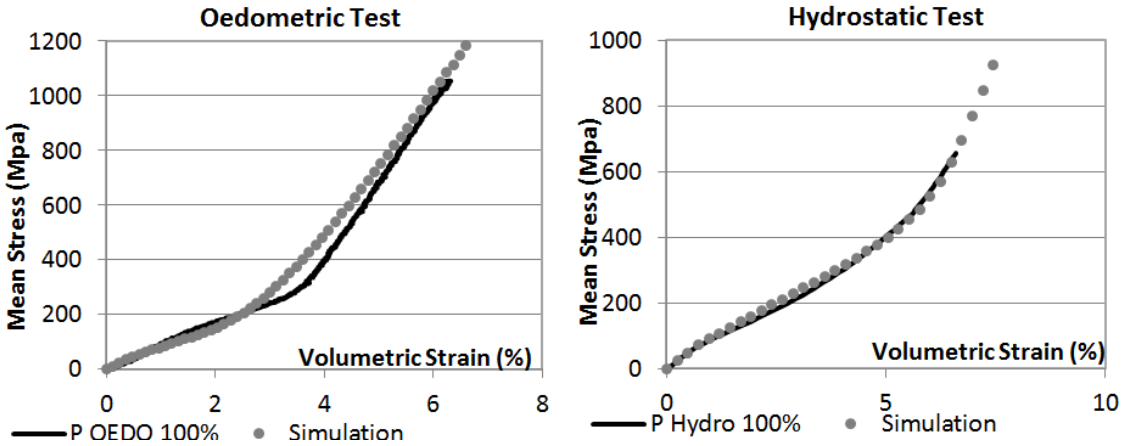

Figure 5: Calibration of under high pressure behaviour parameters, oedometric, hydrostatic tests

2.5 Strain rate dependency

The tensile strength of concrete increases under moderate and high loading rate, as has been observed experimentally. The model has implemented to account for the strain rate sensitivity with the dynamic increase factor (DIF) local equation (7). DIF is defined as the ratio of the dynamic tensile strength over the static tensile strength T_{dyn}/T_{st}. The increase is applied also on the maximum distance limit D_{max}, as can be seen on *Figure 6*. The local parameters $\dot{\varepsilon_{st}}$, $\delta 1$ and $\delta 2$ are calibrated with the help of a Hopkinson bar spalling test [1]. The experimental pullback velocity of the specimen's rear face, is reproduced with the parameters $\dot{\varepsilon_{st}} = 10^{-6}$, $\delta 1 = 0.052$ and $\delta 2 = 0.333$.

$$\mathrm{DIF} = \frac{T_{dyn}}{T_{st}} = \begin{cases} 1 & if\ \dot{\varepsilon} \le \dot{\varepsilon_{st}} \\ \left(\frac{\dot{\varepsilon}}{\dot{\varepsilon_{st}}}\right)^{\delta 1} & if\ \dot{\varepsilon_{st}} < \dot{\varepsilon} \le 1s^{-1} \\ \theta\left(\frac{\dot{\varepsilon}}{\dot{\varepsilon_{st}}}\right)^{\delta 2}, \theta = 10^{(6\delta 1 - 2)} & if\ \dot{\varepsilon} > 1s^{-1} \end{cases} \quad (7)$$

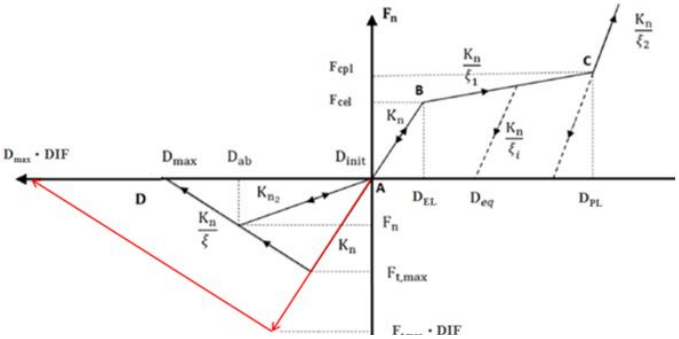

Figure 6: Constitutive model under dynamic loading

3 SIMULATION OF IMPACTS

The reliability of the proposed DEM numerical model is validated with the simulation of high velocity impacts on confined concrete. The numerical results are compared with the experimental data obtained by CEA Gramat.

3.1 Impact experiments

A series of impact tests have performed by CEA-Gramat. Ogive-nosed steel projectiles with a calibre-radius-head (nose radius to diameter ratio) 5.77, a shank diameter of 52.06 mm, a length of 299.43 mm and a mass 2.442 Kg, *Figure 7 (right)* were launched on fully saturated unreinforced cylindrical targets made of ordinary concrete R30A7 confined with a thin steel jacket. R30A7 concrete was widely investigated in previous studies [6]. The impacted specimen diameter is 800 mm, while the thickness is varying with 300 mm for perforation test and 800 mm for penetration test. The confined steel jacket has a thickness of 15 mm and it is anchorage on the concrete target. An accelerometer was embedded into the projectile *Figure 7 (right)* to record the axial deceleration during the experiment. In addition, after the test a topographic laser system was used to measure the crater dimension and the penetration depth. Three tests have been conducted with different striking velocities, one perforation test with 333m/s and two perforation test with higher velocity 347.4 m/s (HV) and lower velocity 227 m/s. "DEIMOS'' gas launcher *Figure 7 (left)* was employed to give the initial impulse on the strikers. *Figure 8* shows the perforation impact test at certain moments *(left)* and the damage mode of the penetration test (HV) *(right)*.

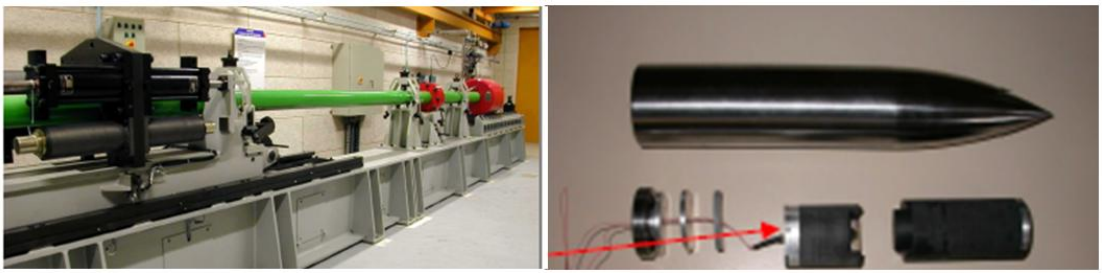

Figure 7: "DEIMOS" gas launcher (left), projectile with its accelerometer

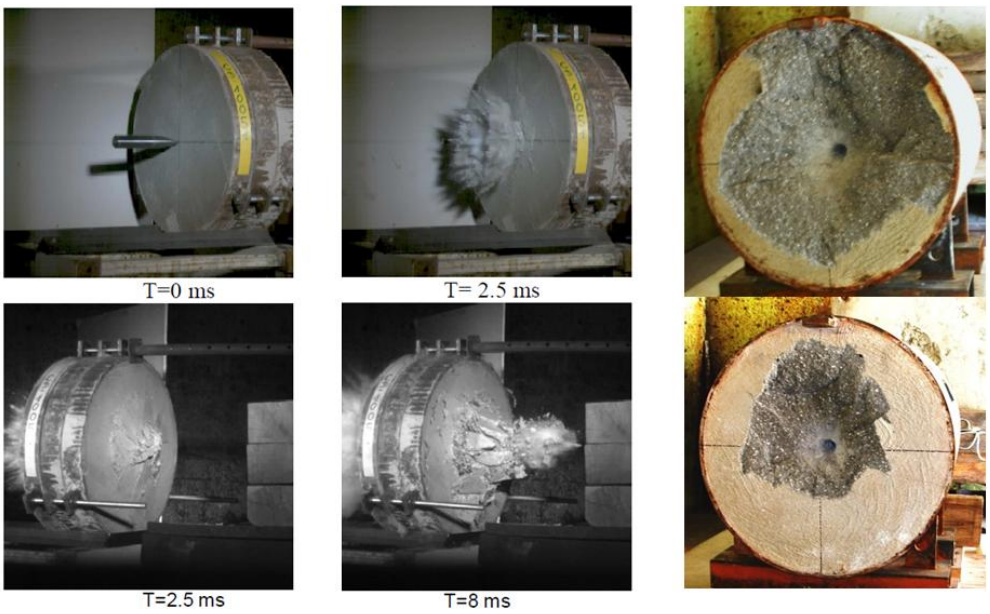

Figure 8: Perforation Impact (left), Penetration Impact (right)

3.2 Modelling of impact experiments

The cylindrical concrete specimen was modelled with DE, while for the steel projectile and the steel confining jacket were used tetrahedral FE, *Figure 9*. All meshes have been generated by using SALOME [21]. The DE concrete mesh was created from an eight tetrahedra FE mesh per short side (of the specimen's geometry) with SherePadder++ [23] direct geometrical algorithm. The eight tetrahedral FE mesh was selected in order to produce spheres with diameters similar to the FE size of the projectile and the steel jacket. The condition of similar sizes between FE and DE should be respected, for proper link creation. **Table 1** illustrates the DE properties of the perforation and penetration test. Furthermore, for the simulations of the three impact experiments 10% of damping was used.

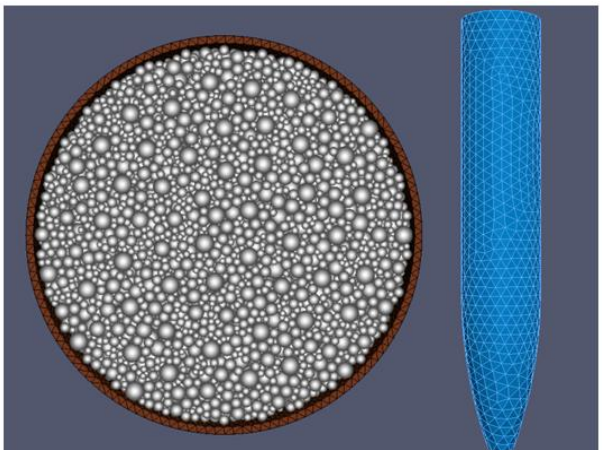

Figure 9: Model of impact test DE concrete with FE confined steel jacket (left), FE steel projectile (right)

Table 1: Properties of perforation and penetration DE meshes

Compactness	DE#	λ	Rmax (cm)	Rmin (cm)	Rmean (cm)
Perforation					
0.6086	141765	1.3986	0.9	0.3	0.471
Penetration					
0.6154	336467	1.402	0.9384	0.3128	0.491

Figure 10 shows the numerical and experimental results for the perforation impact test. On the left side is plotted the axial displacement of the projectile, while on the right side its velocity. Equivalently

Figure 12 presents the results for the penetration impact tests. The crack patter observed experimentally can be found on *Figure 11* for the perforation test and on *Figure 13* for the penetration (HV) test on the right side, whereas on the left side are given the damages obtained from the numerical simulations.

The numerical result has well predicted the experimental results. For the perforation test the results are thoroughly matched. However, a slight difference is observed on the curves of the penetration tests. The damage for both experiments seems to be quite similarly produced by the DE model, with more significant diagonal cracks at the bottom of the perforated specimen than the top. In addition, by comparing *Figure 8 (left)* with *Figure 11 (left)*, it is obvious that the phenomena observed experimentally, such as spalling on the front and scabbing on the rear face, have been successfully generated during the perforation test simulation. Furthermore, a cratering damage mode is following the penetration test, which it has also appeared at numerical results.

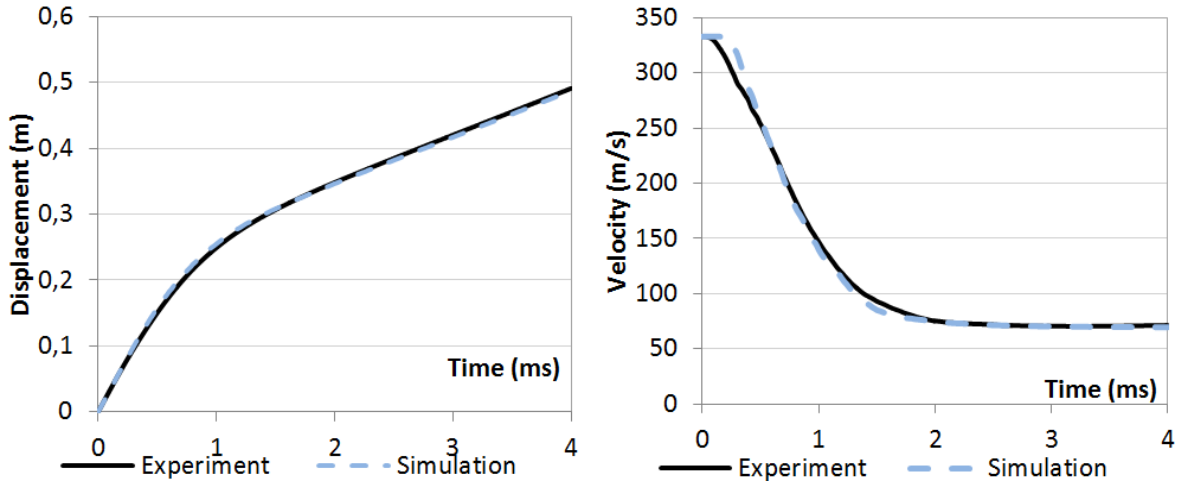

Figure 10: Perforation test, simulation and experiment, projectiles axial displacement (left), velocity (right)

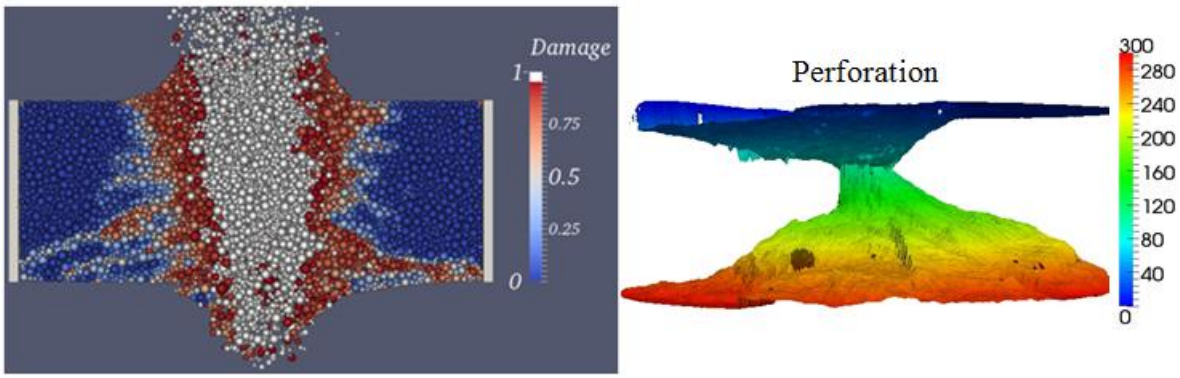

Figure 11: Perforation crack pattern, simulation (left) experiment (right)

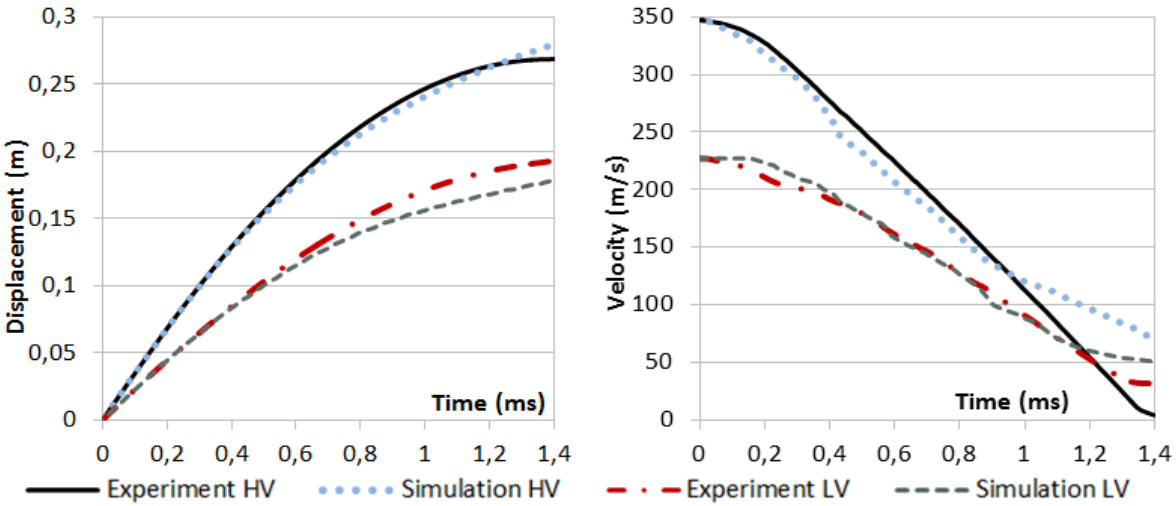

Figure 12: Penetration test, simulation and experiment, projectiles axial displacement (left), velocity (right)

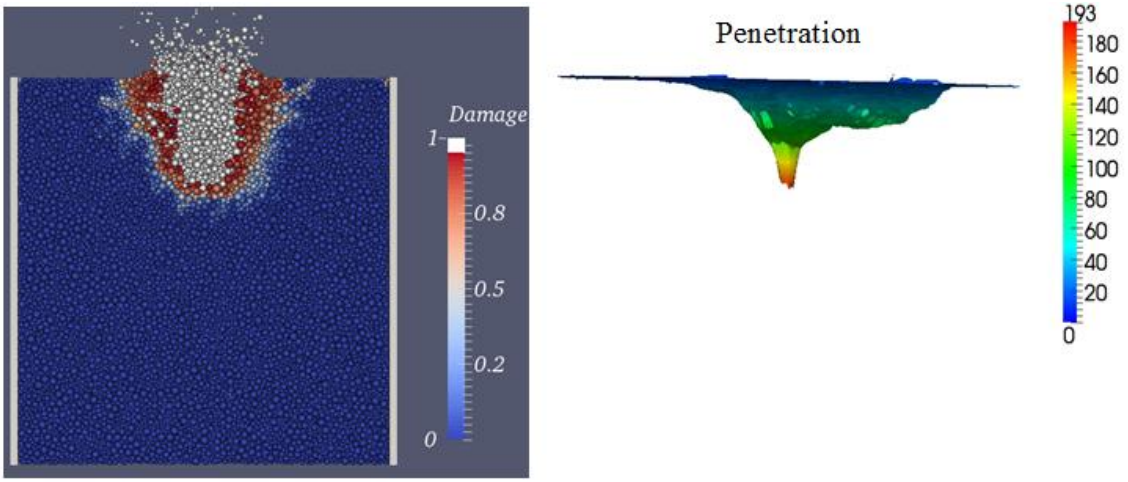

Figure 13: Penetration crack pattern, simulation (left) experiment (right)

4 CONCLUSION

In this paper a numerical method of DEM for concrete has proposed to model structure under severe loadings. The DEM approach has applied to simulate extreme impact experiments on thick confined concrete specimen, which can represent an aircraft strike on a nuclear shielding. Perforation and penetration tests were satisfying reproduce by the numerical results. The crack patterns appeared to be well accordance with the experimental ones. This study gives the motivation to proceed in simulating the response of industrial-size concrete structures.

REFERENCES

[1] Antoniou, A. Contribution to the experimental analysis and numerical modeling of spalling technique into concrete specimens under dynamic tension. Thesis master 2, Université Joseph Fourier, (2014).

[2] Bian, H., Jia, Y., Shao, J. and Pontiroli, C., Numerical study of a concrete target under the penetration of rigid projectile using an elastoplastic damage model, Engineering Structures, Journal Elsevier, p. 525-537 (2016)

[3] Cambou, B., Dubujet, P., Emeriault, F., and Sidoroff, F. (1995). Homogenization for granular materials. European journal of mechanics. A. Solids, 14(2), 255-276.

[4] Cundall, P.A. and Strack, ODL., "Discrete numerical-model for granular assemblies", Geotechnique, 29(1), 47-65 (1979).

[5] Cundall, P.A., Formulation of a three-dimensional distinct element model – Part I, A schele to detect and represent contacts in a system composed of many polyhedral blocks, International Journal of Rock Mechanics and Mining Sciences, Vol. 25, p. 107-116 (1988).

[6] Daudeville L., Malecot Y. 2011. Concrete structures under impact. European Journal of Environmental and Civil Engineering. 15(S1): 101-140.

[7] Donze, F.V., Richefeu, V., Magnier, S-A., Advances in Discrete Element Method Applied to Soil, Rock and Concrete Mechanics, EJGE

[8] EUROPLEXUS, A computer program for analysis of fast transient phenomena involving structures and fluids in interaction, available at http://www-epx.cea.fr

[9] Forquin, P., Sallier, L. and Pontiroli, C., A numerical study on the influence of free water content on the ballistic performance of plain concrete targets, Mechanics of Materials, Journal Elsevier, p. 176-189 (2015)

[10] Gabet, T., Vu, X.H., Malécot, Y. and Daudeville, L., A new experimental technique for the analysis of concrete under high triaxial loading, J.Phys IV. 134: 635-640 (2006).

[11]Hentz S., Daudeville L., Donzé F. “Identification and validation of a discrete element model for concrete, Journal of Engineering Mechanics", vol. 130, n°6, 2004b, p.709-719 (2004).

[12]Hentz, S., Daudeville, L. and Donze, F. V., Discrete element modelling of concrete submitted to dynamic loading at high strain rates. Computers and Structures. 82(29-30): 2509-2524 (2004)

[13]Huang, H., Lecampion, B. and Detournay, E., Discrete element modelling of tool-rock interaction I : rock cutting, International Journal for Numerical and Analytical Methods in Geomechanics 37: p. 1913-1929 (2013)

[14]Jerier J., Imbault D., Donze F. and Doremus P., “A geometric algorithm based on tetrahedral meshes to generate a dense polydisperse sphere packing”, Granular Matter, 11:43–52 (2009a)

[15]Liao, C.-L., Chang, T.-P., Young, D.-H. and Chang, C. S. (1997). Stress-strain relationship for granular materials based on the hypothesis of best fit. Int. j. Solids Structures, 34(31- 32):4087–4100

[16]Omar A., Marin P., Potapov S., Daudeville L. 3D discrete element modeling of concrete: Study of the rolling resistance effects on the macroscopic constitutive behavior., XII International conference on Computetional Plasticity-Fundamentals and Applications, COMPLAS XII Barcelona, p 575-586 (2013)

[17]Omar, A., Marin, P., Forquin, P. and Daudeville, L., Validation of a 3Ddiscrete element model in investigating dynamic tensile behaviour of concrete at high strain rates, 9th International Conference on Structural Dynamics, EURODYN, Porto 2014

[18]Pontiroli C., Erzar B. & Buzaud E. (2014). Concrete behaviour under ballistic impacts: Effects of materials parameters to penetration resistance and modeling with PRM model. Proceedings of Computational Modeling of Concrete and Concrete Structures (EURO-C 2014)

[19]Potapov, S., Masurel, A., Marin, P. and Daudeville, L., Mixed DEM/FEM modelling of advanced damage in reinforced concrete structures, ASCE Journal of Engineering Mechanics, ISSN 0733-9399 (2016)

[20]Rousseau J., Frangin, E., Marin, P., & Daudeville, L. (2008). Damage prediction in the vicinity of an impact on a concrete structure: a combined FEM/DEM approach. *Computers and Concrete*, *5*(4), 343-358.

[21]SALOME, Computer software, http://www.salome-platform.org

[22]Sazamoto, Y., Tsubota, H., Kasai, Y., Kishiba, N., Morikawa, H. (1998). Analytical studies on local damage to reinforced concrete structures under impact loading by discrete element method. Nuclear Engineering and Design, 179:157–177.

[23]SherePadder++, Computer software, https://subversion.assembla.com/svn/spherepadder/

[24]Vu, X. H., Malecot, Y., & Daudeville, L. (2009). Strain measurements on porous concrete samples for triaxial compression and extension tests under very high confinement. *The Journal of Strain Analysis for Engineering Design*, *44*(8), 633-657.

V International Conference on Particle-based Methods – Fundamentals and Applications
PARTICLES 2017
P. Wriggers, M. Bischoff, E. Oñate, D.R.J. Owen, & T. Zohdi (Eds)

LONG-TERM CYCLIC TRIAXIAL TESTS WITH DEM SIMULATIONS

GIANLUCA ZORZI*[1], FABIAN KIRSCH[1], FABIO GABRIELI[2] AND FRANK RACKWITZ[3]

[1] GuD Geotechnik und Dynamik Consult GmbH
Darwinstraße 13, 10589, Berlin
e-mail: zorzi@gudconsult.de, kirsch@gudconsult.de , web page: http://www.gudconsult.de

[2] Department of Civil Environmental and Architectural Engineering (ICEA)
University of Padova
Via Ognissanti 39, 35129 Padova, Italy
e-mail: fabio.gabrieli@unipd.it, web page: http://www.dicea.unipd.it

[3] Soil Mechanics and Geotechnical Engineering Division,
Technical University of Berlin
Gustav-Meyer-Allee 25, 13355 Berlin, Germany
e-mail: frank.rackwitz@tu-berlin.de,
web page: http://www.bau.tu-berlin.de/grundbau_und_bodenmechanik

Key words: DEM, cyclic loading, stress induced anisotropy

Abstract. Modeling the long-term performance of granular materials under cyclic loading conditions is still a challenge and a better understanding could provide a large benefit for the design of foundations. One typical application example are the foundations of wind turbines, for which the evolution of the soil mechanical behavior could lead to irreversible strain accumulation (with tilting and settlement) and dynamic resonance problems [1].

In this framework the Discrete Element Method [2] can provide useful information starting from a micromechanical point of view: it may allow engineers to increase their knowledge on the evolution of the mechanical behavior and to optimize the long-term design of these structures [3].

The present paper presents the capability of DEM to simulate a long-term cyclic drained triaxial test (up to 100,000 cycles). The results regard the progressive accumulation of plastic strain as function of the number of particles and the initial particles rearrangement. The influence of densification and contact orientation (anisotropy) in the evolution of the strength of the soil during the cyclic loading history is investigated.

1 INTRODUCTION

Repeated loadings are some of the main design driven factor for fatigue analysis of many civil structures like transportation facilities, industrial plant as well as wind turbine foundations. Considering the latter, which are subjected to millions of dynamic loadings during their lifetime, it is important to capture any change in soil properties which could have an impact on the behavior of the structure in terms of irreversible strain accumulation (settlement and tilting) and dynamic resonance problems [1].

Modeling accurately the evolution of soil properties under low amplitude cyclic stress loading is of great interest for geotechnical engineers, especially because there is a lack of accurate constitutive models focusing on these problems. During each loading cycle the soil experiences an accumulation of plastic deformations, with a partially open strain hysteresis loop. The smaller the loading amplitude is, the smaller the gap will be. These small vibrations and cyclic solicitations can be considered silent on the short term and the load-deformation behavior is quasi-elastic. However, in the long-term, they possibly result in a low but progressive degradation/damage of the structure and foundation, impacting the behavior of structures and their maintenance costs. Capturing this long-term behavior has been done applying different approaches in Finite Element Method (FEM). One is the application of the common engineering constitutive soil models (hysteretic approach), which is still a challenge and could possibly lead to inaccurate results due to the accumulation of numerical errors when hundred or thousand of cycles are applied [4]. Another strategy is to use the so-called explicit method such as the High Cycle Accumulation (HCA) model [4] or Cyclic Interaction Diagrams developed at NGI. The accumulation of plastic strains for a series of cyclic amplitude excitations are directly related to the number of cycles. These models are based on empirical macroscopic behavior of soil under cyclic loading obtained from experimental laboratory testing. However, the explicit models are either too much sophisticated or required extensive laboratory effort and are difficult to be used to analyze the soil behavior in other different loading conditions.

In the past decades Discrete Element Method (DEM, pioneered by Cundall et al. [2]) is becoming popular on simulating low amplitude cyclic triaxial tests, showing similarities to the overall macromechanical response of the laboratory tests and with the possibility to investigate the soil fabric evolution [6,7,8]. However, in those researches the application of rigid walls/membranes to simulate the real configuration required a large amount of particles and just few thousand of cycles were investigated. The DEM has proved to be a powerful method to study plasticity and non-linearity of granular materials which naturally arise from its intrinsic particle description without any particular mathematical hypothesis. Even though it is a good candidate for the comprehension and prediction of soil under cyclic loadings at a particles level point of view, its applicability in common geotechnical problems is still limited to the number of particles.

The present work shows the capability of DEM to simulate qualitatively a long-term cyclic drained triaxial test with low strain amplitude. The cyclic triaxial tests are simulated on a Representative Elementary Volume (REV) under stress-controlled conditions.

The trend of the accumulation of axial strains and strain amplitudes were analyzed in terms of reproducibility of the test results up to 10,000 cycles and with different number of particles (different REV sizes) up to 100,000 cycles. In the end, the analysis of the strength during different cyclic stages was linked to the evolution of the anisotropic soil fabric.

2 DISCRETE ELEMENT SIMULATIONS

2.1 Sample Generation

In the present analysis the DEM simulations were conducted using an open-source code YADE [9] based on a soft-particles approach. Spherical particles are considered to reduce the computational cost. The contact constitutive law is the classic elastic-plastic law with rolling

and twisting stiffness at the contact to take into account for grain roughness [9, 10]. The long-term cyclic drained triaxial tests are simulated with a cube-shaped cell called REV. A REV is characterized of Periodic Boundary (PB) conditions. Figure 1 is an example of a REV packing where the blank wire spheres are the exact copy from the opposite side.

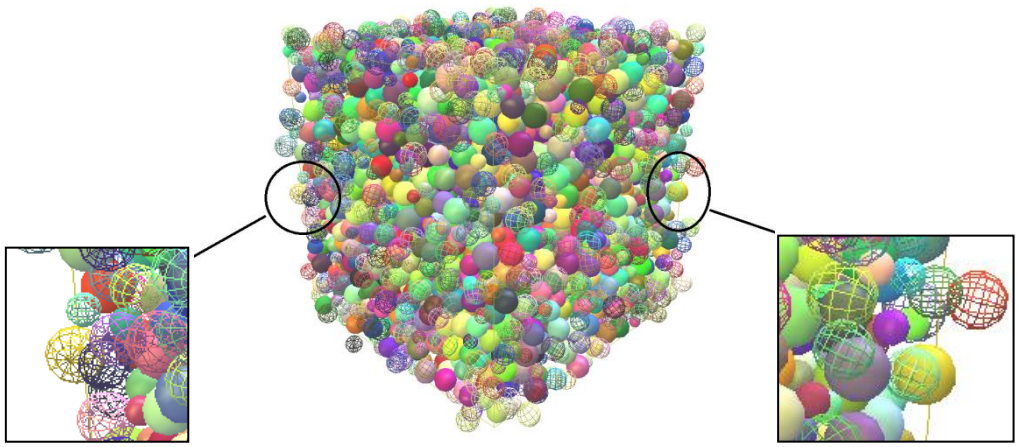

Figure 1: REV packing with periodic boundary conditions.

This configuration allows to use a smaller number of particles, which is important for computational reason and to avoid boundary effect problems arising when rigid-wall or membrane is used [11].

The aim of this paper is to show the capability of the DEM to simulate a long-term cyclic loading from a qualitative point of view and to study the initial departure of the grain assembly. Therefore, no contact law parameter calibration has been done but will be addressed in the future for a quantitative analysis of the cyclic behavior of soil. The contact parameters governing the macromechanical behavior are five and are listed in Table 1. These parameters represent an idealized cohesionless frictional material.

Table 1: Particles' contact parameters.

E_c [Pa]	4e8
v_c [-]	0.25
Phi_c [°]	32
Beta [-]	0.75
Eta [-]	0.75
Density [kg/m^3]	2535

The samples were generated in order to match two predefined global quantities: Particles Size Distribution (PSD) and target porosity. A procedure for sample preparation similar to that described in [5] was adopted. A very loose cloud of particles with random position, high porosity (non-overlapping particles) and predefined PSD was generated in an initially large cube-shaped cell. An isotropic compression was applied with a high value of contact friction angle until a stable sample was achieved. At this stage the porosity of the sample is higher than the target one. A decrease in contact friction angle was gradually applied until the

desired porosity was reached. The sample preparation was considered finished when the unbalanced force [9], which is the ratio between inertia and interaction forces, went below 10^{-3}. The contact friction angle was then set to the wanted value.

Regarding the PSD, the sample considered was a slightly uniform distribution with D_{min}=4 mm and D_{max} =8 mm. The target porosity for the sample preparation was set to be 0.50.

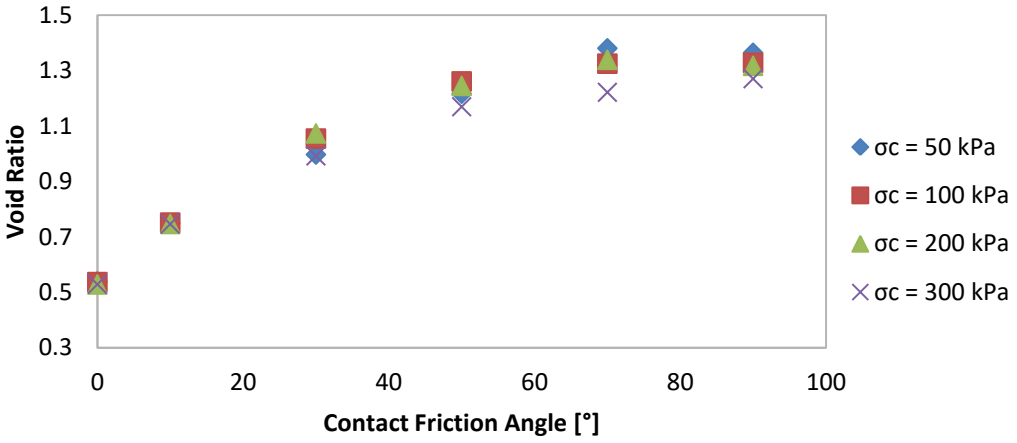

Figure 2: Void ratio of the REV for different friction angle and confining pressure.

The direct comparison in terms of porosity between laboratory and numerical samples, is not straighforward due to the difference in particles shape. Therefore, it would be more appropriate to compare relative densities and have different scales of minimum and maximum porosties between the laboratory and numerical samples. In order to have a complete overview of the relative state of density of the present sample, the minimum void ratio e_{min} and maximum void ratio e_{max} were calculated by imposing the contact friction angle to 0° and 90° respectively. The minimum and maximum void ration depend on the confining pressure being used, thus different samples were generated with different contact friction angles and 4 different confining pressures. For all the confining pressures a low strain rate was set. It is important to underline that, during the sample preparation, the velocity of the boundaries under the isotropic confining pressure has to be as low as possible to avoid the creation of an inhomogeneous contact force distribution. As figure 2 shows, the denser state is characterized by a small variation of the minimum void ratio with different isotropic confining pressures while the loosest state is more scattered: this depends on the initial grain arrangement and chain force formation. The minimum and maximum void ratios at 100 kPa of confining pressure was adopted. e_{min} and e_{max} were equal to 0.537 and 1.32, respectively.

2.2 Triaxial Compression Test

Monotonic triaxial tests were conducted to analyze the macroscopic behavior of the sample. The lateral stress was kept constant at the confining pressure of 100kPa while the vertical boundaries were moved vertically under strain-control conditions. Two stable samples with 3000 particles and having different initial porosities were generated. The first, referred as "dense", has an initial porosity of 0.358 (I_D=0.97). The second sample, named "loose ", is characterized by an initial porosity of 0.50 (I_D=0.408). The figures 3a and 3b

shows the deviatoric and volumetric behavior of the two samples.

The REV with 3,000 spheres mimics the classical drained triaxial compression test response of granular materials with different initial densities. Both samples reach the critical state with the same deviatoric shear stress and a quite constant volumetric strain. The loose state, which will be used for the cyclic loading triaxial test, shows the typical hardening behavior with shrinking.

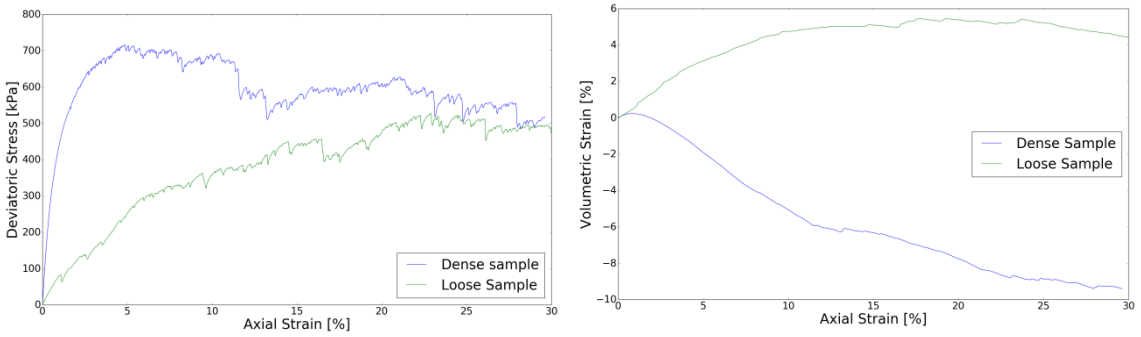

Figure 3: Triaxial test results of two DEM samples: (a) deviatoric and (b) volumetric behavior.

2.3 Cyclic Triaxial Test

Also in the simulation of the cyclic triaxial tests, the lateral confining pressure σ_c was kept constant at 100kPa while the vertical boundaries were cyclically moved under stress-control conditions. Figure 4 shows the cyclic stress path of the simulation in the *p'-q* plane, where *p* is the mean stress and *q* is the deviatoric stress. The first phase (horizontal red line) represents the isotropic confining phase up to a σ_c of 100kPa. Then the sample is sheared with a load σ_s of 40 kPa until the point (q_{av}, p_{av}) is reached. The cyclic loading stage was then performed with a stress amplitude σ_{amp} of 30 kPa. The values of the loading stresses can be found in table 2.

Table 2: Stress loading parameters

p_{iso}	100.00 kPa
p_{av}	113.33 kPa
q_{av}	40.00 kPa
q_{amp}	±30.00 kPa

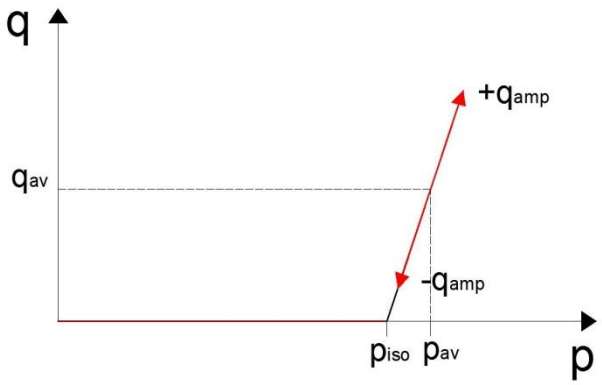

Figure 4: Cyclic Stress path

The mass of the PBs were adjusted in order to avoid inertial forces. The aim of the paper is to investigate the capability of the DEM to simulate the effect of a small strain amplitude on the long-term cyclic loading. Therefore, the cyclic stress was chosen in order to have a low cyclic strain amplitude of the order of 10^{-3} and the static load far from failure. For small

number of particles in the REV and long-term cyclic loading, the chance of having an inhomogeneous distribution of contact forces is high (again the initial sample preparation has a strong influence on the behavior of the assembly). During the cyclic test, the occurrence of a chain buckling leads to a sudden large increase of plastic strain [6].

The analyses of the results of the DEM cyclic triaxial tests were done by following the procedure and the remarks explained in [12], which are depicted in figure 5 [12] for a laboratory cyclic triaxial test.

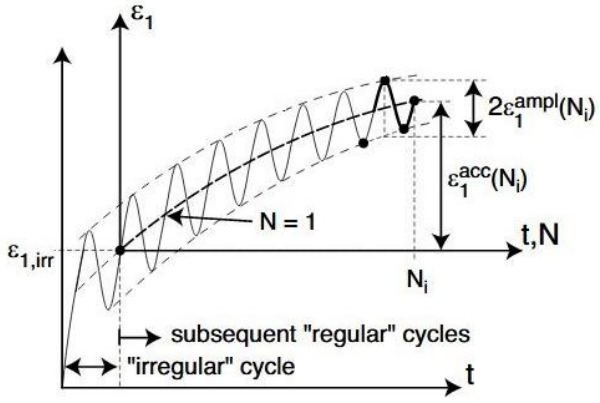

Figure 5: Cyclic Triaxial Test curve (modified from [12])

The cycles were divided in a first irregular cycle N_0 in which there is the largest deformation and in subsequent regular cycles $N_{i\ (i=1,..,n)}$.

The trend of the axial strain during the cyclic triaxial test was analyzed by calculating the axial strain accumulation (1) and the axial strain amplitude (2) from the first regular cycle N_1[12].

$$\varepsilon_{1,i}^{acc} = \frac{1}{2}[\varepsilon_1^{max}(N_{i+1}) + \varepsilon_1^{min}(N_i)] \qquad \textit{where i=1,...,n cycle} \tag{1}$$

$$\varepsilon_{1,i}^{amp} = \frac{1}{2}[\varepsilon_1^{max}(N_i) - \frac{1}{2}(\varepsilon_1^{min}(N_i) + \varepsilon_1^{min}(N_{i-1}))] \quad \textit{where i=1,...,n cycle} \tag{2}$$

The test was conducted using 3,000 spheres in a REV packing. The total number of cycles was 100,000. Figure 6 shows the trend of the axial strain accumulation plotted with the logarithm of the number of cycles. It is clearly visible that the rate of accumulation of axial strain decreases, reaching a constant value, which means that the soil reaches a stable configuration named shakedown state [13].

The shakedown state also emerges considering the trend of porosity as shown in figure 7. The first few thousand cycles are marked with the highest adaption period to the external cyclic solicitation, with the larger accumulation of permanent deformation. Subsequently to this adaption period, the material showed a resilient response to the increasing the number of cycle stresses, typical of the shakedown behavior [13].

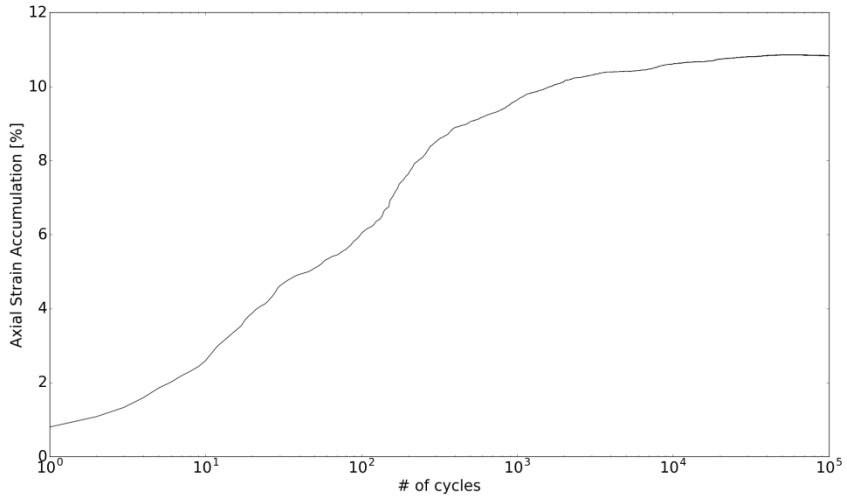

Figure 6: Axial Strain Accumulation of a REV with 3000 particles up to 100,000 cycles

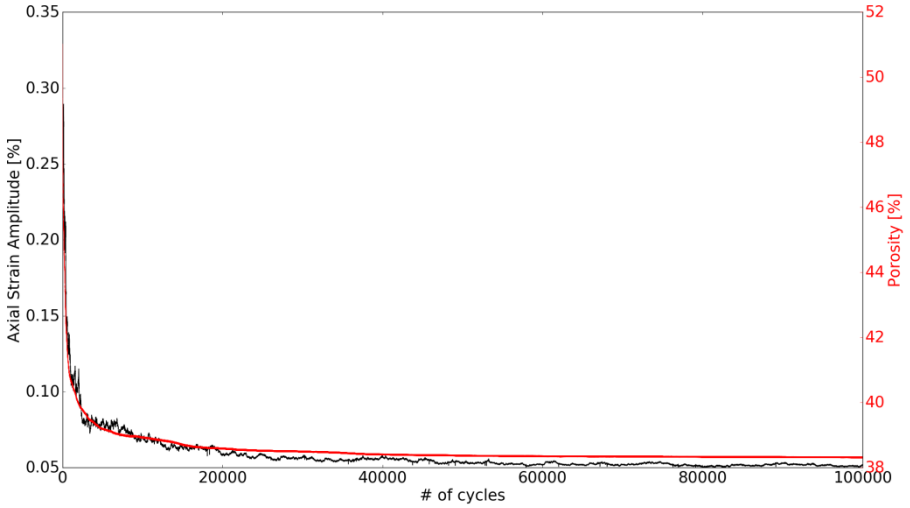

Figure 7: Trend of porosity (red line) and axial strain amplitude (black line) of a REV with 3000 particles up to 100,000 cycles

3. TEST REPEATABILITY OF CYCLIC TRIAXIAL TESTS

In the following, the degree of repeatability on the long-term cyclic behavior was investigated with different initial fabric and different number of particles. Different clouds of particles were prepared, with different initial random distributions and the procedure explained previously was used to create a stable packing.

Two different numbers of particles in a REV were considered: 2000 and 5000. For each number of particles, 10 samples were generated. The micromechanical parameters used in simulations are listed in table 1.

All the 20 samples were isotropically consolidated with a confining pressure of 100 kPa and cyclically loaded for 10,000 cycles. The target porosity during the sample preparation

was set 0.50 and from the inspection of the 20 samples the porosity differs of 0.03%.

Figures 8 shows the same cyclic behavior described earlier. The dispersion of the curves (i.e. repeatability) resulted lower with a large number of particles. This low variability is also depicted in figure 9, where the axial strain amplitude is plotted.

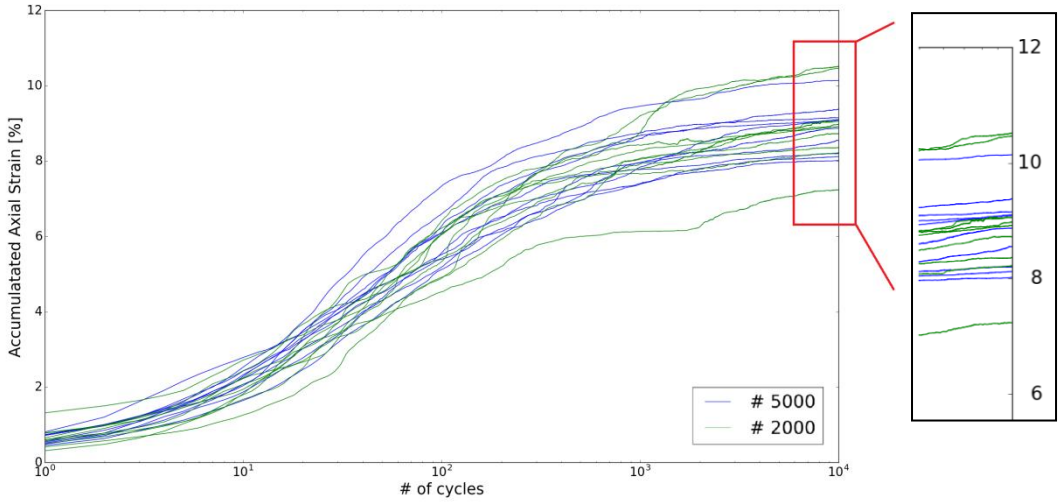

Figure 8: Axial Strain Accumulation for different initial packing.

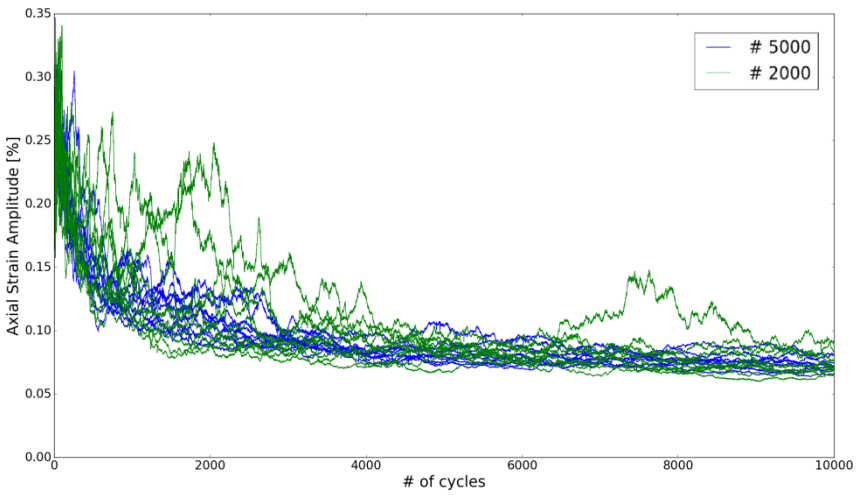

Figure 9: Axial Strain Amplitude for different initial packing.

4 INFLUENCE OF THE REV SIZE ON THE LONG-TERM CYCLIC BEHAVIOR

With regards to the cyclic tests, the choice of the number of particles to be used in the REV is of capital importance from a computational stand point: the larger the number of particles is, the longer the simulation will be; on the other hand a too small number of particles may lead to incorrect or unreliable results.

A minimum number of particles should be used to get reliable porosity, coordination number, stress and strain values [14]. The evaluation of the minimum amount of spherical particles for a REV can be done by looking at the orientation distribution of the contact

normal which should be close to a sphere shape-like under isotropic compression[5].

Figure 10 shows the axial strain accumulation up to 100,000 cycles for different REV. The rapid increase of deformation for a small sample (with 500 particles) is due to buckling effect of large chain forces [6]. Moreover, specimens with a low number of particles can have a poor normal contact force distribution which governs the cyclic behavior. By increasing the number of particles per sample there is an increase of the axial strain accumulation.

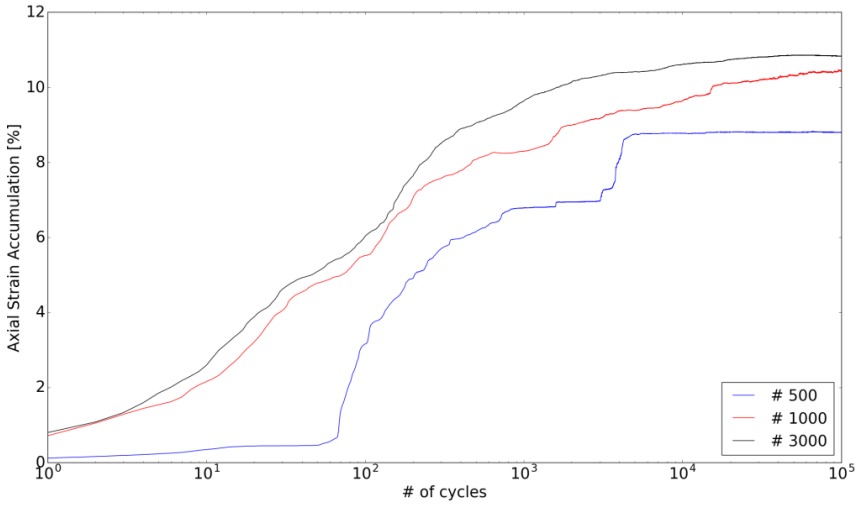

Figure 10: Axial Strain Accumulation as function of the # of particles for the sample.

5 STRENGTH AND STIFFNESS OF THE SAMPLE DURING CYCLIC STAGES

Cohesionless materials can benefit from low amplitude cyclic loading conditions, increasing their strength and stiffness after the cyclic loads. It is believed that this increment in stress is mainly due to the emergence of a densification process (decrease in porosity).

During the cyclic triaxial test for the REV with 3,000 spheres, the sample configuration was saved at 100/ 1,000/ 10,000/ 50,000/ 100,000 cycles, red points in figure 11. The samples were then unloaded until an isotropic confining pressure of 100kPa and the monotonic triaxial tests were conducted to analyze their strength and stiffness. The lateral stress was kept constant at the confining pressure of 100kPa while the vertical boundaries were moved vertically under strain-control conditions. In figure 12 and 13, it is clearly depicted that the sample is increasing its strength with the increasing of the number of cycles (solid lines), transforming from a typical hardening behavior with shirking (cycle 0) for loose material to a compaction-dilation behavior for dense materials.

At the same time, new samples were generated and monotonically sheared with the same exact porosity and isotropic confining pressure of 100kPa of the previously saved samples. Figure 12 and 13 show the difference between the monotonic triaxial tests of virgin samples (dashed lines) and cyclically loaded ones (solid lines) at the same porosity.

During a cyclic loading stress solicitation, the granular assembly decreases in density (behavior seen from a macroscopic point of view) but at the same time organizes its distribution of contact normal orientation in a favorable way to resist better against the external solicitation (stress induced anisotropy [6]). Figure 12 shows that the stress induced anisotropy (contact orientation) started to develop between 1,000 cycles (the red dashed and

solid lines are similar) and 10,000 cycles.

This effect could be studied with the DEM by analyzing the distribution of contact orientation. During the sample generation under an isotropic confining pressure and neglecting gravity, the contact orientation should reassemble a circular shape (isotropic fabric). After 100,000 cycles, the same distribution of contact orientation should evolve to adapt to the new stress conditions. Further investigation will be done to better characterized this phenomena.

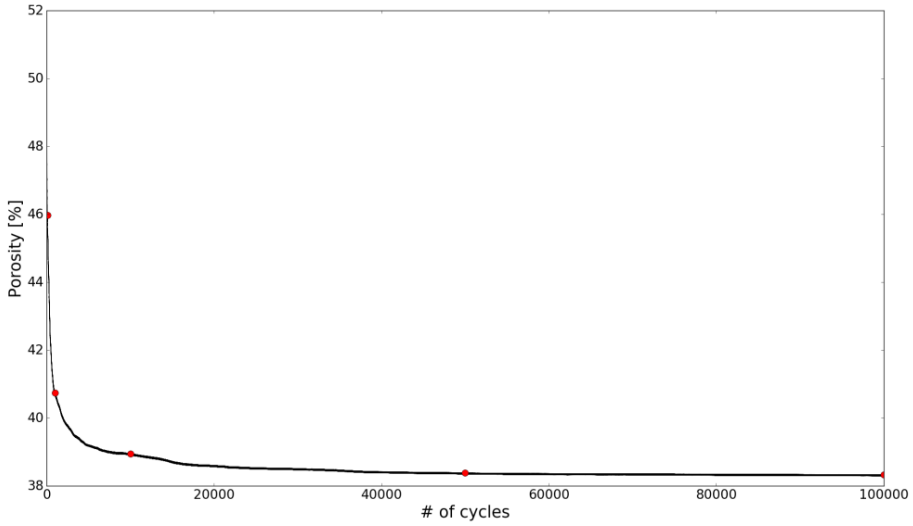

Figure 11: Porosity trend for 3,000 particles up to 100,000 cycles.

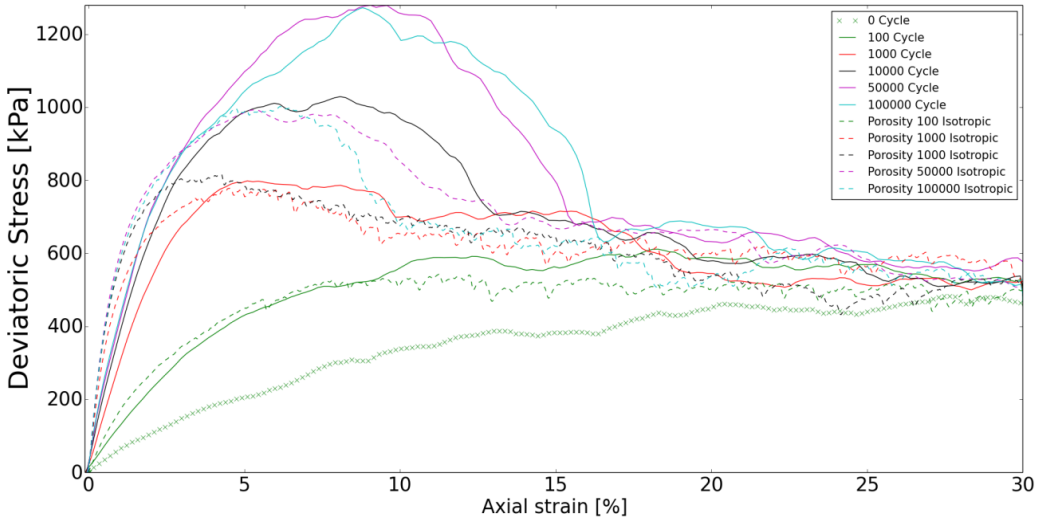

Figure 12: Triaxial tests results: deviatoric behavior. Solid line: anisotropic samples due to cyclic loading. Dashed line: isotropic samples.

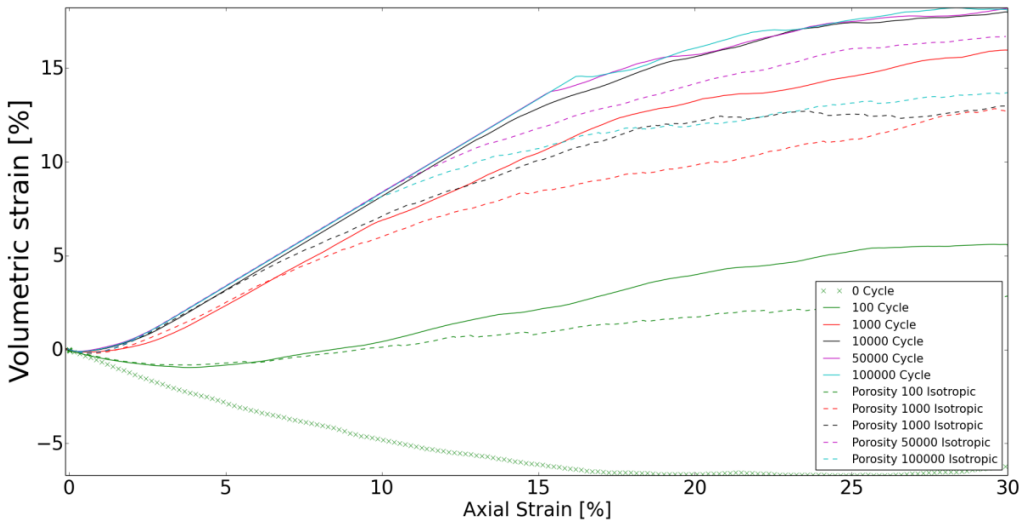

Figure 13: Triaxial tests results: volumetric behavior. Solid line: anisotropic samples due to cyclic loading. Dashed line: isotropic samples.

6 CONCLUSIONS

This paper shows the potentiality of DEM to simulate qualitatively a long-term cyclic triaxial test on a REV. The effect of different initial fabric and REV sizes have been investigated in relation to a large amount of cyclic loading. Future research will be to quantitative simulate cyclic triaxial test results of sand. It will allow a better understanding of the long-term behavior of granular materials from a micromechanical scale, possibly resulting as a base for an accurate formulation of constitutive models for cyclic loading.

AKNOLEDGEMENT

This research is part of the Innovation and Networking for Fatigue and Reliability Analysis of Structures - Training for Assessment of Risk (INFRASTAR) project. This project has received funding from the European Union's Horizon 2020 research and innovation programme under the Marie Skłodowska-Curie grant agreement No 676139. The computing facilities offered by CloudVeneto (CSIA Padova and INFN) are acknowledged.

REFERENCES

[1] Bhattacharya, S. (2014). Challenges in Design of Foundations for Offshore Wind Turbines. Engineering & Technology Reference. http://dx.doi.org/10.1049/etr.2014.0041

[2] Cundall, P. & Strack, O. (1979). A discrete numerical model for granular assemblies. Géotechnique, 29(1), 47-65. http://dx.doi.org/10.1680/geot.1979.29.1.47

[3] O'Sullivan, C. & Cui, L. (2009). Fabric Evolution in Granular Materials Subject to Drained, Strain Controlled Cyclic Loading. Powsers And Grains 2009: Proceedings Of The 6Th International Conference On Micromechanics Of Granular Media, 1145, 285-288. http://dx.doi.org/10.1063/1.3179914

[4] Niemunis, A., Wichtmann, T., & Triantafyllidis, T. (2005). A high-cycle accumulation model for sand. Computers And Geotechnics, 32(4), 245-263. http://dx.doi.org/10.1016/j.compgeo.2005.03.002

[5] Tong, A.-T., Catalano, E., Chareyre, B. (2012). Pore-scale flow simulations: model predictions compared with experiments on bi-dispersed granular assemblies, Oil & Gas Science and Technology - Rev. IFP , 67(35):743–752

[6] Hu, M., O'Sullivan, C., Jardine, R., & Jiang, M. (2010). Stress-induced anisotropy in sand under cyclic loading. *Granular Matter*, *12*(5), 469-476. http://dx.doi.org/10.1007/s10035-010-0206-7

[7] Nguyen, N., François, S., & Degrande, G. (2014). Discrete modeling of strain accumulation in granular soils under low amplitude cyclic loading. *Computers And Geotechnics*, *62*, 232-243. http://dx.doi.org/10.1016/j.compgeo.2014.07.015

[8] O'Sullivan, C., Cui, L., & O'Neill, S. (2008). Discrete Element Analysis of the response of granular materials during cyclic loading. Soils and Foundations, *48*(4), 511-530. http://dx.doi.org/10.3208/sandf.48.511

[9] Šmilauer, V. et al. (2015), Yade Documentation 2nd ed. The Yade Project. DOI 10.5281/zenodo.34073

[10] Widuliński, L., Kozicki, J., Tejchman, J. (2009). Numerical simulations of triaxial test with sand using DEM. *Archives of Hydroengineering and Environmental Mechanics*, 56 (3-4), 149-172.

[11] Radjai, F., Dubois T. (2011). *Discrete-element modeling of granular materials*, Wiley-Iste, 181-198, 978-1-84821-260-2.

[12] Wichtmann, T., Niemunis, A., & Triantafyllidis, T. (2009). On the determination of a set of material constants for a high-cycle accumulation model for non-cohesive soils. *International Journal For Numerical And Analytical Methods In Geomechanics*, n/a-n/a. http://dx.doi.org/10.1002/nag.821

[13] García-Rojo, R., & Herrmann, H. (2005). Shakedown of unbound granular material. *Granular Matter*, *7*(2-3), 109-118. http://dx.doi.org/10.1007/s10035-004-0186-6

[14] Kawano, K, Sullivan, CO, Shire, T. (2016). Using DEM to assess the influence of stress and fabric inhomogeneity and anisotropy on susceptibility to suffusion. "Proc. 8th Int. Conf. Scour and Erosion, Harris, Whitehouse & Moxon (Eds.)", 85-94.

V International Conference on Particle-based Methods – Fundamentals and Applications
PARTICLES 2017
P. Wriggers, M. Bischoff, E. Oñate, D.R.J. Owen, & T. Zohdi (Eds)

EXPERIMENTAL AND NUMERICAL INVESTIGATIONS OF CONCRETE BEHAVIOUR AT MESO-LEVEL DURING QUASI-STATIC SPLITTING TENSION

J. SUCHORZEWSKI[1] AND J. TEJCHMAN[1]

[1]Gdańsk University of Technology
Faculty of Civil and Environmental Engineering
80-233 Gdańsk-Wrzeszcz, Narutowicza 11/12

jan.suchorzewski@pg.gda.pl, tejchmk@pg.gda.pl

Key words: Concrete, Splitting Tensile Test, DEM, Fracture, Loading Strip, Meso-scale.

Abstract: The paper describes experimental and numerical results of quasi-static splitting tensile tests on concrete specimens at meso-scale level. The loading strip was made of plywood or steel. Fracture in concrete was detected at the aggregate level by means of three non-destructive methods: 3D x-ray micro-computed tomography, 2D scanning electron microscope and manual 2D digital microscope. The discrete element method was used to directly simulate experiments at the meso-scale. Concrete was modelled as a random heterogeneous 4-phase material composed of aggregate particles, cement matrix, interfacial transitional zones and macro-voids based on micro-tomographic images. Two-dimensional calculations with real concrete microstructure were carried out. A satisfactory agreement between numerical and experimental results was achieved. The evolution of contact normal forces, coordination number, broken contacts, grain rotations and crack displacements was also investigated. In addition, each energy component was calculated and analyzed at a different stress-displacement stage.

1 INTRODUCTION

The splitting tensile tests (also known as the Brazilian tests) are the most popular laboratory tests on concrete to determine its uniaxial tensile strength due to their loading and specimen shape simplicity. This test consists of applying a distributed compressive force along the length of a concrete cylinder, which induces a primarily tensile stress perpendicular to the loading plane of the specimen's cross-section with a sharp compressive stress near the points of load application. The tests are however sensitive to boundary conditions related to the width, shape and stiffness of a loading strip. The effect of boundary conditions on the initial global stiffness and post-peak behaviour of concrete specimens (strength-displacement curve, fracture) has not been investigated yet.

The fracture process in the splitting test with standard loading strips consists of two main stages: (1) a main macro-crack formation in the central vertical zone and (2) secondary cracks connecting the main vertical crack with edges of loading plates. In addition, the test outcomes

are subjected to a size effect, expressed by a decrease of both the nominal strength and ductility with increasing specimen diameter [1].

Our experimental and theoretical research works are aimed at understanding the concrete behaviour at the meso-scale during different failure modes in quasi-static splitting tension, depending upon the specimen diameter. Based on preliminary experiments, a quasi-brittle concrete behaviour took place with small specimen diameters (D=5 cm). For larger diameters (D=10 cm), a brittle concrete behaviour occurred. Finally, for large diameters ($D\geq$15 cm), a snap-back instability was observed (which is described by a positive slope in a stress-strain softening branch). In this paper concrete cylinders with the diameter of 0.15 m were experimentally and theoretically investigated. During laboratory tests, a snap-back instability occurred. The vertical load was transferred to concrete specimens through a steel cylinder (in the form of a line contact) or a plywood board (in the form of a surface contact). Fracture was monitored using a high resolution and non-destructive technique in the form of the 3D x-ray micro-computed tomography (using Skyscan 1173 [2]). In addition, the 2D scanning electron microscope (SEM) Hitachi TM3030 and manual 2D digital microscope 'Scalar' were used. The discrete element method (DEM) was applied to describe a non-linear global response of concrete during splitting tension. In this method concrete was considered at the meso-scale as 4-phase material (aggregate, cement matrix, macro-voids and interfacial transitional zones (ITZs)). The geometry of concrete micro-structure at the meso-level was incorporated into DEM from real concrete specimens by means of micro-tomography images. The model was successfully applied to concrete under bending and compression [3], [4]. These calculations showed that it was of importance to take into account the shape and position of aggregate particles and strength and number of ITZs for a realistic reproduction of concrete fracture. ITZs due to a porous structure acted as attractors for cracks and thus influenced the strength and brittleness of concrete. DEM was also used to the fracture description in concrete by other researchers. The splitting tensile tests for quasi-brittle materials were mainly simulated within continuum mechanics.

The main goal of the paper is threefold: 1) to check the capability of DEM for simulating quasi-static splitting tension in concrete specimens at the meso-level by taking a snap-back instability into account, 2) to check the effect of different boundary conditions on the strength and fracture (expressed by the different loading and support strip type) and 3) to investigate in detail the concrete behaviour during quasi-static splitting tension at the meso-scale level. The numerical outcomes were directly compared with the experimental results with respect to the measured stress-strain curves and observed crack patterns based on 3D μCT-images. The evolution of contact forces, broken contacts, internal energies and crack displacements at the aggregate level were also investigated by DEM. The innovative point is to the use of a 4-phase concrete mesoscopic model for fracture investigations based on the real internal concrete structure based on μCT. In the future the DEM calculations may replace laboratory tests to investigate the influence of the concrete meso-structure on its global behaviour.

2 EXPERIMENTS

2.1 Strength

The splitting tensile experiments were performed in the static loading machine ZWICK Roaller Z400 (Fig.1). The machine was equipped with a crack opening extensometer (Sandner EXR10-2x) within the measurement range of ±2 mm with the maximum error of 2%. The extensometer base was equal to 40 mm. The extensometer was located at the mid-height of the concrete specimen and glued to the specimen front side (Fig.1). The quasi-static tests were performed under the CMOD-control (CMOD - crack mouth opening displacement) with the displacement rate of 0.00001 (1×10^{-5}) mm/s. Two types of loading/supporting strips were used: deformable plywood boards with the thickness of t=3 mm and width of b=25 mm (Fig.1b) (as recommended by ASTM [5]) and rigid steel loading/supporting cylinders with the diameter of 20 mm (Fig.1a). Thus the vertical load was respectively transferred to specimen through a surface or line.

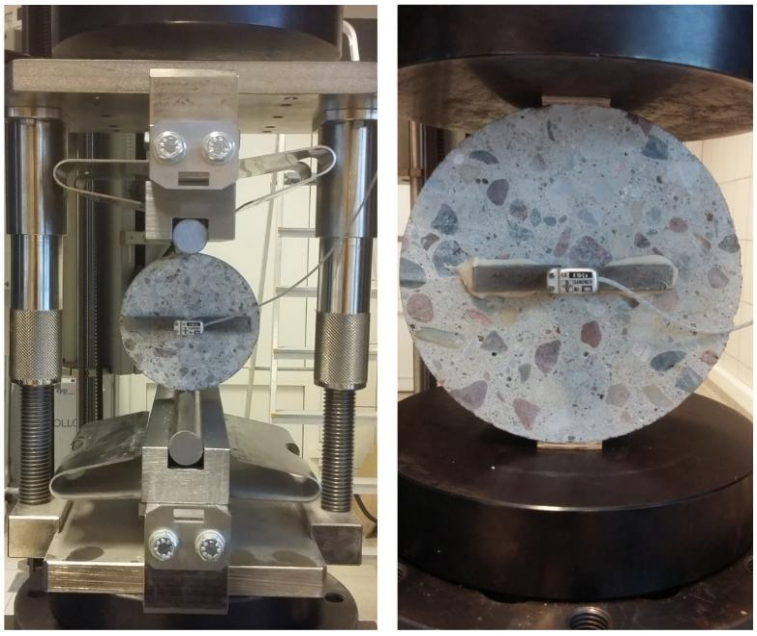

a) b)

Figure 1: View on loading machine Zwick Z400 with cylindrical concrete specimen of diameter D=150 mm and length L=60 mm for quasi-static splitting tensile tests: a) specimen loaded through steel cylinder and b) specimen loaded through plywood board

The minimum aggregate diameter was d_a^{min}=2 mm, maximum aggregate diameter was d_a^{max}=12 mm and mean aggregate diameter d^a_{50}=5 mm. The volumetric aggregate sieve content was 31.2% (diameter 2-8 mm), and 16.6% (diameter 8-12 mm). Thus, the aggregate volumetric content was 47.8%. The total particle volumetric content (sand and aggregate) in concrete was 75%. The concrete specimens with the diameter of D=150 mm were used. The minimum specimen length was assumed L=60 mm (=5×d_a^{max}). The mean standard compressive strength of

concrete tested on 3 cubic specimens 150×150×150 mm^3 was equal to $f_{c,cube}$=49.6 MPa and mean standard modulus of elasticity tested on 3 cylindrical specimens D=150 mm and length L=300 mm was E_c=33.1 GPa.

Several splitting tests on concrete were carried out. Figure 2A presents the representative experimental stress versus CMOD curves for concrete specimens using two types of the loading/supporting contact along the specimens (steel cylinder and plywood board). The CMOD evolution during loading was perfectly linear in time. The splitting tensile strength, calculated as $\sigma=2P_{max}/\pi DL$ (P_{max} - the maximum vertical piston force), varied between 3.26 MPa (P_{max}=47.2 kN, v=0.45 mm, CMOD=18 μm) and σ=3.64 MPa (P_{max}=51.2 kN, v=1.15 mm, CMOD=22 μm) for the steel loading/supporting cylinders (line contacts) and plywood loading/supporting boards (surface contacts), respectively. Thus, the splitting tensile strength was higher by about 10% for the plywood board. Looking at the curve of the stress σ versus CMOD (Fig.2A), initially concrete elastically behaved up to 70% of the maximum tensile stress σ and later slightly non-linearly up to the peak load. After pronounced material softening occurred up to the residual state to failure. The residual stress was reached for σ=2.3 MPa (plywood boards) and σ=1.9 MPa (steel cylinder) for CMOD=110 μm. When considering the experimental stress-vertical piston displacement diagram $\sigma=f(v)$ (Fig.2B), a clear snap-back instability occurred for v=1.15 mm (plywood loading board) and v=0.45 mm (steel loading cylinder), expressed by a simultaneous reduction of the stress and displacement. Shortly before the test end, the displacement v slightly increased due to the specimen defragmentation.

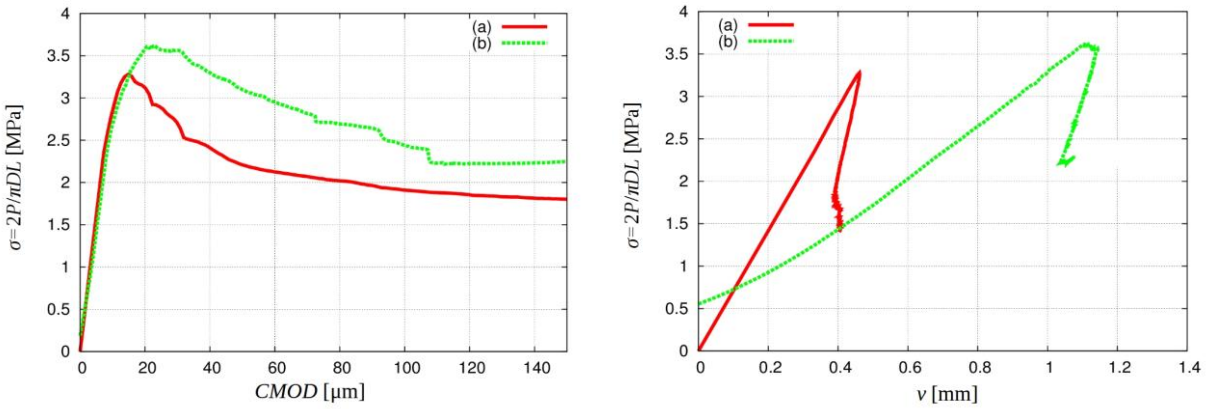

Figure 2: Experimental curves for concrete specimens with diameter D=0.15 m): A) splitting tensile stress $\sigma=2P/(\pi DL)$ versus CMOD and B) splitting tensile stress σ versus top vertical displacement v for 2 different loading systems a) steel cylinder and b) plywood board (P - vertical force, L - specimen length)

In all tests the main vertical macro-crack first occurred at the mid-height of the specimen in the central vertical zone (Fig.3). Then it propagated towards both the specimen top and bottom. Later depending upon the loading and support strip type it reached the top and the bottom of the specimen (Fig.3a) or branched to form a wedge directly under the plywood board (Fig.3b). Finally at failure, the concrete specimen was divided into two halves.

2.2 Concrete porosity

In order to measure more precisely the concrete porosity, a smaller concrete specimen (D=50 mm and L=60 mm) was cut out from the same concrete block and scanned by means of the 3D x-ray micro-tomograph Skyscan 1173. The x-ray micro-tomography (called micro-CT or μCT) is a 3D imaging technique which uses x-rays to create cross-sections of a physical object that is used to recreate a virtual model (3D model) without destroying the original object. Our x-ray micro-tomograph represents a new generation in high-resolution desktop X-ray micro-tomography systems [2]. The scans were completed to ten times faster with the same resolution and image quality as compared to previous micro-CT with a fixed source-detector design. The scanner was equipped with the newly developed 130 keV microfocus x-ray source with a very stable focal spot position and flat panel sensor of a large format (5 Mpx) with a special protection by a lead-glass fibre-optic window. As compared to usual X-ray micro-tomographs, this scanner has two basic advantages: a) large specimens up to 150 mm in diameter may be scanned and b) specimens are scanned with a higher precision (2-3 microns). Note that a continuous investigation of the entire fracture process under deformation with our X-ray micro-tomograph has not been possible for technical reasons yet. The measured total volume of voids was p=3.2% and the measured volume of voids with the equivalent diameter d_p<1 mm was p=1.6% .

2.3 Concrete fracture

The macro-crack images by means of the 3D x-ray micro-tomograph Skyscan 1173 are depicted in Fig.3 for the damaged specimen of Fig.3a after the test (D=0.15 m, L=0.06 m). In order to obtain a better accuracy in the X-ray micro-tomograph, the specimen width was diminished to 0.08 m after the test. The particular phases are shown in Fig.3A. The macro-crack was curved along the vertical and horizontal plane due to a random presence of aggregate grains (Figs.3B-3D). The micro-cracks always initiated in ITZs along aggregate particles since they were the weakest phase in concrete. When two interfacial cracks occurred around adjacent aggregates, a crack inside the cement matrix initiated to bridge the interfacial cracks so that a connected crack path was formed. Sometime it also crossed macro-voids and aggregate. On the specimen front side, the macro-crack crossed e.g. 3 aggregate particles. The crack branching also occurred.

In order to determine ITZs on the front surface of non-damaged specimens, the scanning electron microscope (SEM) HITACHI TM3030 with the maximum magnification factor 30'000 was used. The small specimen 40×40×1.5 mm^3 was used which was cut out from the initial concrete block. ITZs around particles were characterised by a porous structure as compared to the cement matrix (Fig.8). Their width varied between 10 μm and 25 μm. They appeared around all aggregate grains (d_a≥2 mm) and usually covered about 80-90% of the aggregate circumference that was probably caused by a formation of water lenses beneath aggregate grains during mixing. The width of ITZs was not connected with the aggregate diameter. Other experimental results showed that the width of ITZ reduced with decreasing aggregate roughness.

3 DISCRETE ELEMENT METHOD MODEL FOR CONCRETE

The 3D spherical discrete element model YADE takes advantage of the so-called soft-particle approach (i.e. the model allows for particle deformation which is modelled as an overlap of

particles) [6]. A linear normal contact model under compression was used. Aggregate grains were modelled as clusters composed of spheres. The interaction force vector representing the action between two spherical discrete elements in contact was decomposed into a normal and tangential vector, respectively. The normal forces acting on spheres were modelled by an elastic law with cohesion. The normal and tangential forces were linked to the displacements through the normal stiffness K_n and the tangential stiffness K_s. The stiffness parameters were computed with the aid of the modulus of elasticity of the grain contact E_c and two neighbouring grain radii R_A and R_B (to determine the normal stiffness K_n) and with the aid of the modulus of elasticity E_c and Poisson's ratio υ_c of the grain contact and two neighbouring grain radii R_A and R_B (to determine the tangential stiffness K_s), respectively [6].

The contact tangential forces F_s and normal forces F_n satisfied the cohesive-frictional Mohr-Coulomb equation using the inter-particle friction angle μ [6]. The normal force might be negative down to the minimum value of F_n min if there was no a geometrical contact between elements. If this minimum normal force between spheres F_n min was reached, the contact was broken. Moreover, if any contacts between grains re-appeared, cohesion between them was not taken into account. A crack was considered as open if cohesive forces between grains disappeared when a critical threshold was reached. A choice of a very simple linear elastic normal contact was intended to capture on average various contact possibilities in real concrete. One assumed that the cohesive force and tensile force were a function of the cohesive stress C (maximum shear stress at pressure equal to zero), tensile normal stress T and sphere radius R. To dissipate excessive kinetic energy in a discrete system, a simple local non-viscous damping scheme was adopted which assumed a change of forces by using the damping parameter.

Concrete was described in DEM computations as a four-phase material composed of aggregate, cement matrix interfacial transitional zones (ITZs) and macro-voids. The numerical analyses were performed on concrete specimens with the same aggregate location and shape as in experiment. In the first step, two-dimensional simulations were performed to significantly reduce the computation time. Thus the crack curvature along the specimen length was not taken into account. The 3D analyses significantly increase computation times but do not significantly affect the results except of a small reduction of material brittleness. The voids were modelled simply as empty regions with a real shape. In order to create the real aggregate shape in 2D calculations (2 mm$\leq d_a \leq$12 mm) based on images of the polished specimen surface and μCT scan, the clusters composed of spheres with the diameter of d=1.0 mm connected to each other as rigid bodies were used. One aggregate particle, depending upon its diameter, included 5-500 spheres. Based on experiments all aggregate grains with the diameter in the range of 2 mm $<d_a<$ 12 mm included ITZs. The cement matrix was modelled by spheres with the diameter 0.35 mm $\leq d_{cm}<$ 2 mm without ITZs. ITZs were simulated for the sake of simplicity as contacts between aggregate and cement matrix grains. Thus they had no a physical width in contrast to experiments. Note that simulation of the width of ITZs (0.010-0.025 mm) requires very small spheres. In 2D calculations, the specimen length L included one row of aggregate and cement matrix particles. The specimen preparation process consisted of 2 stages. Initially aggregate particles and clusters simulating voids were created. Later smaller particles were added until the final specimen was filled in 98.4% in order to realistically the experimental micro-porosity was measured with μCT as 1.6% (Section 2.2). After the cement matrix was created, the particles were removed at the place of voids. Next all contact forces due to the particle penetration were deleted. The following five main local material parameters were needed for our discrete

simulations: E, υ, μ, C and T. In addition, the particle radius R, particle mass density ρ and damping parameters α_d were required.

The following parameters of the cohesion and tensile strength were used in all DEM analyses: cement matrix ($E_{c,cm}$=15 GPa, C_{cm}=140 MPa and T_{cm}=25 MPa) and ITZs ($E_{c,ITZ}$=12 GPa, C_{ITZ}=112 MPa and T_{ITZ}=20 MPa) based on our earlier calculations [3,4,7]. ITZs were obviously the weakest phase. The ratio $E_{c,ITZ}/E_{c,cm}$=0.8 was chosen based on the experiments. The remaining ratios were also assumed as 0.8: C_{ITZ}/C_{cm}=0.8 and T_{ITZ}/T_{cm}=0.8 due to the lack of experimental results. Note that there were no contacts between aggregate grains (d_a≥2 mm). The remaining parameters were constant for all phases and regions: υ_c=0.2 (Poisson's ratio of grain contact), μ=18^o (inter-particle friction angle), α_d=0.08 (damping parameter) and ρ=2.6 kG/m^3 (mass density). The prescribed damping parameter α_d and velocity did not affect the results during bending [7]. In the case of α_d<0.08, the too excessive kinetic energy was always created during fracture (the tensile numerical test could not be performed without numerical damping due to excessively high velocities of particles (see also [7]). In turn, the effect of the α_d-value on global results for α_d≥0.08 became insignificant. The 2D concrete specimen under tensile splitting included in total about 20'000 spheres. The material constants were assumed based on the test on concrete not on the cement matrix (due to the lack of the detailed information on properties of ITZs). With the material constants assumed, the uniaxial compressive strength of the 2D four-phase concrete specimen (15×15 cm^2) was about 45 MPa and elastic modulus E=30 GPa (as in the experiments, Section 2.1).

4 DEM RESULTS

The 2D cylindrical concrete specimens of the diameter D=150 mm obtained using DEM with two different loading/supporting systems as compared to real specimens were modeled. The deformable strip of the plywood board at the top and bottom of the specimen was created from 240 spheres assembled together with the 50% lower stiffness than concrete (with this value the same global elastic stiffness was calculated as in the experiment). It had a full contact with the concrete specimen without wall friction. The rigid cylinder of steel at the top and bottom of the specimen was created by a single sphere of the diameter of 20 mm with the 10-times higher stiffness than concrete. The deformation was induced by prescribing the vertical top displacement in such way that the changes of CMOD were approximately linear in time (as in experiments). CMOD was calculated as a horizontal displacement at the specimen mid-height between mid-points of two regions with the area of A=5×15 mm^2 (based on preliminary calculations). The mid-points were at the distance of 40 mm as in the experiment (Fig.1). If the calculated CMOD was larger than the assigned CMOD growth (v_{CMOD}=1×10^{-5} mm/s), the difference was multiplied by the earlier calibrated proportional parameter n=1.5 since the inertia of the discrete system was different than this of the testing machine (u_{t+1}=n× u_t (CMOD$_{assigned}$-CMOD$_t$)). A too small averaging area A mainly contributed to excessive displacement oscillations. In addition in order to diminish the excessive kinetic energy after the contact breakage between the areas A, larger local damping was assumed in calculations (α_d^{local}=0.05) if the single grain velocity v_t was larger than 0.001 m/s. Next this velocity was reduced in the next step down to v_{t+1}=α_d•v_{t0}. In calculations, the time step dt was equal to dt=10^{-8} s.

Figure 3 presents the DEM results of the strength compared to the experiments. The strength's evolution σ versus CMOD and v was satisfactorily reproduced (Figs.3A and 3B). The

calculated maximum tensile stress was by 2% too low for the steel loading cylinder and by 10% too high for the plywood loading board than in experiments. The calculated residual tensile stress was the same for the steel loading cylinder and by 30% too high for the plywood board. The calculated rate of softening was similar for the steel cylinder and too small for the plywood board. The differences between numerical and experimental results are probably caused by the different stiffness of the plywood board than in experiments and some slight deviations between the calculated and theoretical CMOD evolution.

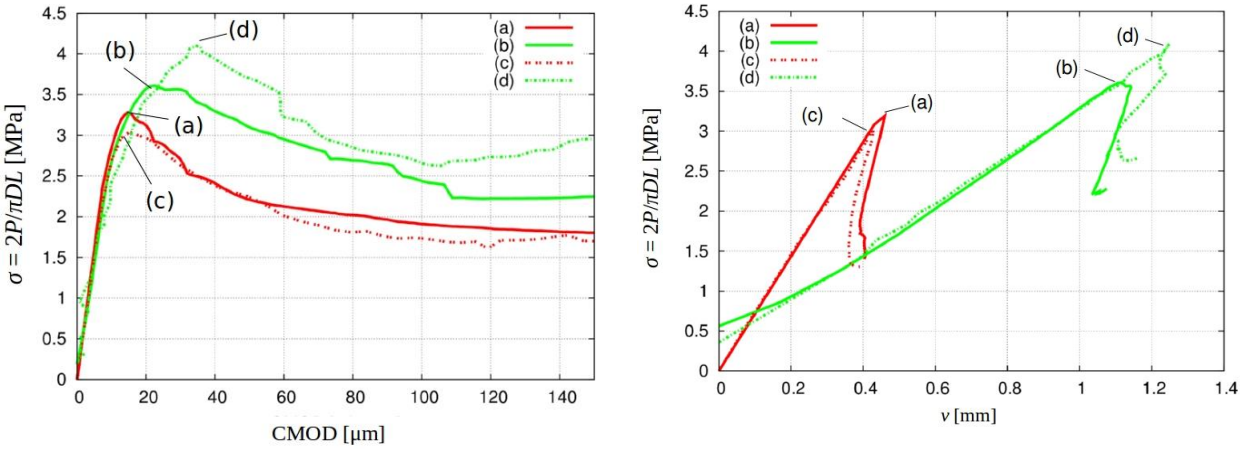

Figure 3: Calculated DEM results against experimental ones: A) strength σ against *CMOD*, B) strength σ against top vertical displacement v (B) (curves 'a' and 'b' - experiments, curves 'c' and 'd' - DEM, red lines - steel loading cylinder, green lines - plywood loading board)in experiment (a) and DEM (b) (continuous lines - experiments, dashed lines - DEM)

The calculated crack patterns were very similar to the experimental ones (Fig.4). In DEM calculations with the plywood strip (Fig.4Bb), the macro-crack followed exactly the same path as in experiments (Fig.4Ba). It also branched into rigid wedges at the same height (25% of D from the top and bottom). However, the crack shape in the wedge often followed the other side of the aggregate particle. In DEM calculations with the steel cylinder (Fig.4Ab), the macro-crack was more curved than in experiments (Fig.4Aa) and followed the opposite edges of aggregates in the lower specimen half. The large aggregate grain at the specimen bottom crushed in the experiment in contrast to DEM outcomes (our model has not included grain crushing yet). In DEM simulations, initially several single micro-cracks occurred in the entire specimen. The broken contacts first occurred always in ITZs at corners of aggregate particles wherein tensile forces were the largest (Fig.5Aa). Later micro-cracks started to concentrate in the vertical central zone at the specimen mid-height. Afterwards they connected with each other in the cement matrix by bridging and created a discrete macro crack in the vertical central zone (similarly as in the experiment) (Fig.5Ac). The crack propagated towards the top and bottom of the specimen for CMOD=30 μm. At the top and bottom, it branched by creating a clear wedge under the loading strip. At the test end (CMOD>150 μm), the specimen was symmetrically de-fragmented. The macro-cracks were always created by bridging interfacial micro-cracks (Fig.6).

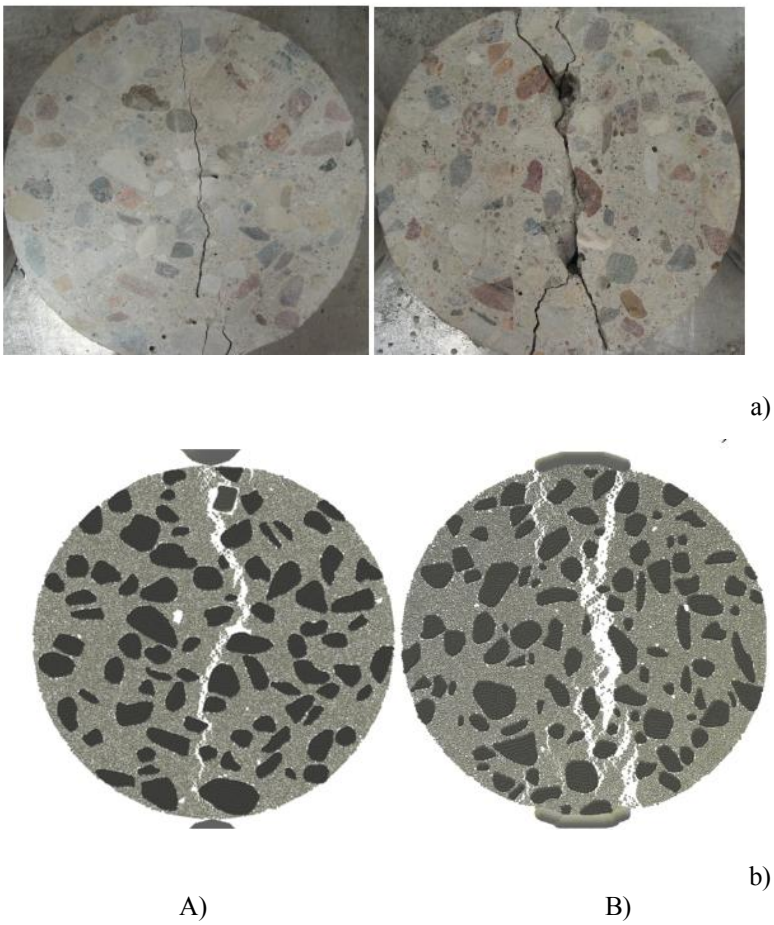

Figure 4: Experimental and calculated fractured specimens at residual state for CMOD>150 μm: a) experimental cracks and b) calculated cracks by DEM for A) steel loading cylinder and B) plywood loading board

Figure 5B presents the evolution of inter-particle normal contact forces. The blue lines indicate tensile and red lines compressive forces. The line thickness is proportional to the force magnitude. The external vertical splitting force was transmitted via a network of normal contact forces which formed force chains. They carried the majority of the loading and transmitted it on the entire system and were the predominant structure of internal forces at micro-scale. Initially large vertical compressive normal contact forces were created in the almost entire specimen (Fig.5Ba). Tensile normal forces occurred in a perpendicular (horizontal) direction. In the boundary regions compression obviously dominated over tension. Before the peak of the vertical force, the compression and tensile forces increased, however some single tensile forces started to break due to the contact damage (Fig.5Bb). After the load peak the horizontal tensile forces started to reduce (Fig.5Bc). When a vertical macro-crack occurred in the specimen, the compressive forces concentrated in the specimen mid-region whereas the tensile forces became

located mainly along the specimen circumference due to the compression of two separated specimen halves (Fig.5Bd).

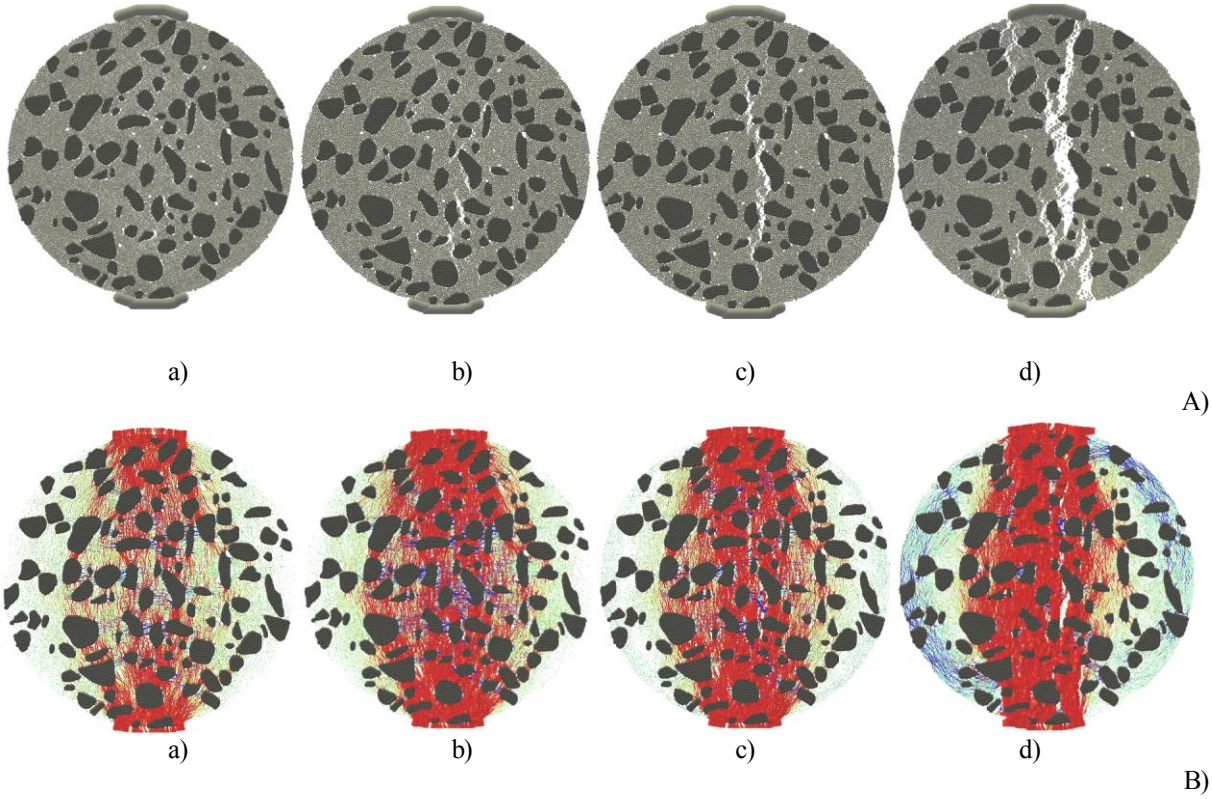

Figure 5: DEM results: A) evolution of cracking in concrete specimen and B) evolution of inter-particle tensile (blue lines) and compressive (red lines) normal contact forces for concrete specimen with plywood loading board versus CMOD: a) CMOD=10 μm, b) CMOD=20 μm, c) CMOD=30 μm and d) CMOD>150 μm (green colour denotes small values of internal forces)

The evolution of the total elastic energy was analysed during the continuing deformation process (test with the steel loading cylinder) (Fig.7) without a separation into recoverable and stored terms. For the vertical top displacement v corresponding to the peak load P_{max} (CMOD=20 μm, v=0.46 mm) (Fig.7A), the elastic internal energy was equal to 75% (normal energy - 52%, tangential energy - 23%), plastic dissipation was equal to 1%, energy of debonded contacts was equal to 2%, kinetic energy was equal to 0.5% and numerical damping was equal to 21.5% of the total energy. At the failure (v=0.43 mm, CMOD=150 μm), the elastic internal energy was 42%, plastic dissipation was 2.5%, contact breakage energy was equal to 5%, kinetic energy was 0.5% and numerical damping was 50% of the total energy. Due to the snap-back instability, the total internal energy reduced by 15%, the elastic normal internal energy reduced by 60% and the elastic tangential internal energy reduced by 20% (Fig.23B). In turn, the plastic dissipation, numerical damping and elastic energy from removed cohesive contacts increased by the factor 2.5, 2 and 2.5, respectively.

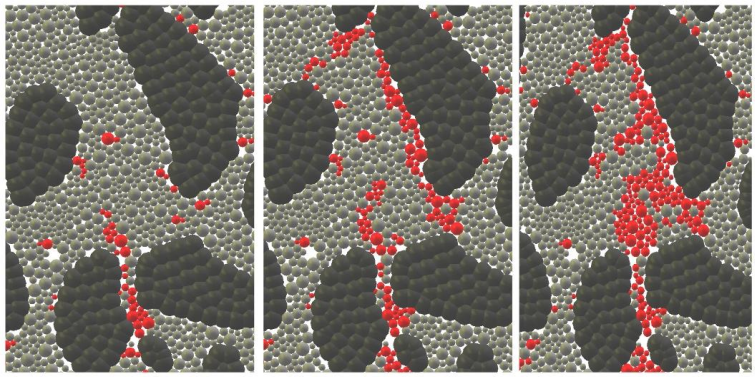

Figure 6: Mechanism of macro-crack creation in concrete specimen by bridging interfacial zones for plywood loading board: a) CMOD=10 μm, b) CMOD=15 μm and c) CMOD=20 μm (spheres in red indicate broken contacts and dark grey corresponds to aggregate)

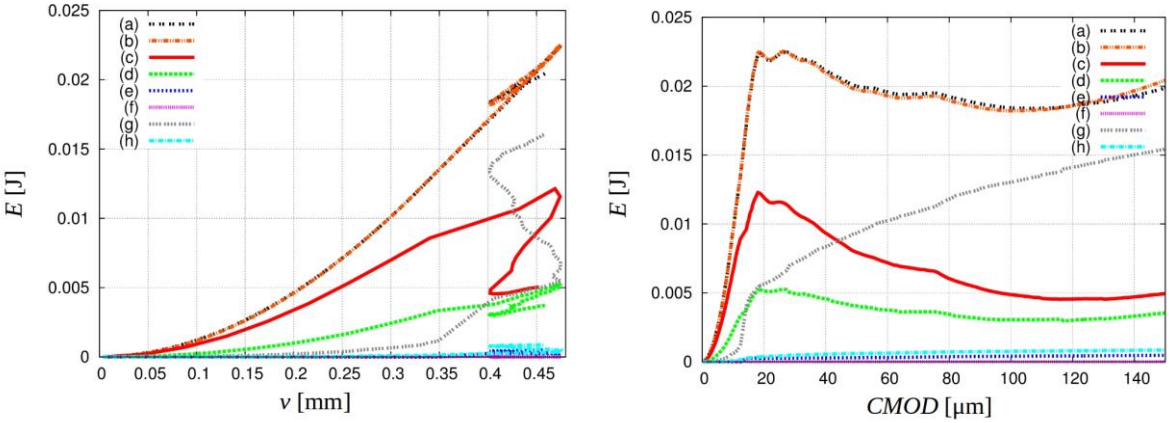

Figure 7: Energy evolution in 2D concrete specimen with steel loading cylinder versus vertical top displacement v (A) and CMOD (b) using DEM: a) external work, b) internal work, c) normal elastic energy, d) tangential elastic energy, e) plastic dissipation, f) kinetic energy, g) numerical damping and h) energy of debonded particles

In order to improve the numerical results with respect to the experiments, the DEM model will be enhanced by aggregate crushing, width of ITZs and 3D analyses. The experiments and DEM calculations will be continued for the different specimen diameters (D=5-30 cm).

5 ACKNOWLEDGEMENTS

The research work has been carried out within the project "*Experimental and numerical analysis of coupled deterministic-statistical size effect in brittle materials*" financed by the Polish National Science Centre NCN (UMO-2013/09/B/ST8/03598).

6 CONCLUSIONS

- The type of the loading strip significantly affected the concrete behaviour. The strength was smaller by 10%, CMOD corresponding to the strength was smaller by 20% and vertical displacement corresponding to the strength was smaller by 300% when a line loading contact was prescribed at the top. In experiments, a snap-back phenomenon occurred. A clear compressive wedge took place when plywood loading/supporting boards was used that caused the strength's increase.
- The macro-crack was curved along the specimen height and length due to a stochastic distribution of aggregates. It was initiated in the central region at the mid-height. Initially micro-cracks always occurred in ITZs and then propagated through a bridging mechanism. Several aggregates crushed during experiments. The width of ITZs was about 10-25 μm.
- DEM proved its capability to model concrete fracture in detail by taking the snap-back instability into account. The agreement of calculated stress-displacement results and crack shapes with experimental ones was satisfactory. A decrease of the strength of ITZs and minimum particle diameter in the mortar caused the reduction of both the splitting tensile strength and material brittleness.
- The external vertical splitting force was transmitted via a network of normal contact forces which formed clear force chains. Some compressive forces appeared also along the macro-crack edge due to aggregate inter-locking.
- Due to the snap-back instability, the total internal energy reduced by 15%, the elastic normal internal energy reduced by 60% and the elastic tangential internal energy reduced by 20%. The plastic dissipation, numerical damping and elastic energy from removed cohesive contacts increased by the factor 2.5, 2 and 2.5, respectively.

REFERENCES

[1] Tejchman, J. and Bobiński, J. Continuous and discontinuous modeling of fracture in concrete using FEM. Springer, Berlin-Heidelberg (eds. W. Wu and R. I. Borja), 2013.

[2] Skarżyński L. and Tejchman J. Experimental investigations of fracture process in concrete by means of x-ray micro-computed tomography. *Strain* (2016) **52**:26-45.

[3] Skarzynski, L. Nitka, M. and Tejchman, J. Modelling of concrete fracture at aggregate level using FEM and DEM based on X-ray CT images of internal structure. *Engineering Fracture Mechanics* (2015) **147**:13-35.

[4] Suchorzewski, J. Tejchman, J. and Nitka M. Discrete element method simulations of fracture in concrete under uniaxial compression based on its real internal structure. *International Journal of Damage Mechanics* (2017) **3**:. DOI: 10.1177/1056789517690915.

[5] ASTM, Standard Test Method for Splitting Tensile Strength of Cylindrical Concrete Specimens, C496M–04, 2004.

[6] Kozicki, J. and Donze, F.V. A new open-source software developer for numerical simulations using discrete modeling methods. *Computer Methods in Applied Mechanics and Engineering* (2008) **197**:4429-4443.

[7] Nitka, M. Tejchman. J. Modelling of concrete behaviour in uniaxial compression and tension with DEM. *Granular Matter* (2015) **17**(1): 145-164.

V International Conference on Particle-based Methods – Fundamentals and Applications
PARTICLES 2017
P. Wriggers, M. Bischoff, E. Oñate, D.R.J. Owen, & T. Zohdi (Eds)

A STABLE, IMPLICIT TIME INTEGRATION SCHEME FOR DISCRETE ELEMENT METHOD AND CONTACT PROBLEMS IN DYNAMICS

ROY LICHTENHELDT[1]

[1] German Aerospace Center (DLR) - Institute of System Dynamics and Control
Münchener Straße 20, 82234 Weßling, Germany
Roy.Lichtenheldt@dlr.de, www.dlr.de/sr

Key words: Granular Material, DEM, Integration, Solver, Contact Problems, Soil, Regolith

Abstract. The field of applications for Discrete Element Method is constantly growing, enabling the simulation of granular matter. However state of the art integration schemes are mostly adopted from other methods, which results in certain drawbacks in either performance and/or accuracy. The most common time integration schemes in Discrete Element Method are explicit algorithms which are conditionally stable, only. Attempts to use implicit schemes usually require evaluation of the right hand side of the equations of motion, i.e. a complete reevaluation of the neighborhood search and contact forces within predictor-corrector iterations. While both are most suitable for simulations of rapid flows, computational efficiency is sacrificed for simulations of dense granular matter. The algorithm presented in this paper is a predictor-corrector scheme using a prediction of the forces, without evaluating the right hand side, to get an implicit estimate for the next time step. This technique enables to speed up particle simulation while using considerably higher time steps. The usage of the algorithm and the correspondent time step control are shown in example problems and accuracy is verified.

1 INTRODUCTION

The rapid increase in computational performance enabled a rapid growth of Discrete Element Method (DEM) in a wide range of applications. As the method itself is still computational expensive, most research is focused on the applications themselves, leaving the method with several drawbacks [1]. One of these is the use of non-specialized time integration schemes. The most commonly used Verlet and Leapfrog integration schemes as well as their derivatives are explicit schemes, featuring conditional stability only. Hence their maximum time step is limited by a critical time step, calculated from the highest

eigen frequency of the system. According to [2], this yields:

$$\Delta t_{\max} = \min\left(r_{\mathrm{P}}\sqrt{\frac{\rho_{\mathrm{P}}}{E}}\right) \tag{1}$$

with $r_{\mathrm{P}}, \rho_{\mathrm{P}}, E$ being the radii, density and YOUNG's Modulus of the particles. These time steps easily reach regions of $[10^{-8}, 10^{-7}]$s for realistic parameter sets, like given in [1]. Implicit integration schemes, like the NEWMARK-β integrator implemented in Pasimodo [3, 4] are unconditionally stable for continuous forces [4], but only conditionally stable for the non-continuous nature of contact forces [5]. However their critical time step size for non-continuous forces is way bigger than the explicit one. Given that high-frequency oscillations are not important for the results accuracy in many applications like soil modeling, the critical time step evaluates to [5]:

$$\Delta t_{\max} \leq S_{\mathrm{f}} \cdot \frac{\delta_{\max}}{|\vec{v}_{\max}|} \tag{2}$$
$$\text{with } \delta_{\max} = |\vec{u}_{\mathrm{dyn}}| \cdot r_{\mathrm{P}}; \quad |\vec{u}_{\mathrm{dyn}}| \in [0.05; 0.1]$$

whereas $\vec{v}_{\max}$ is the maximum expected velocity of any particle in the simulation scenario, $\delta_{\max}$ is the maximum allowed overlap in soft sphere DEM and $\vec{u}_{\mathrm{dyn}}$ is the allowed relative overlap. This usually yields time step sizes in the range of $[10^{-6}, 10^{-4}]$s for realistic scenarios. As the step size in implicit schemes is allowed to be several orders of magnitude higher than in explicit schemes, the higher computational effort per step is easily justified. Implicit integration schemes are usually implemented as predictor corrector (PC) schemes, estimating and improving the value at time $t + \Delta t$. Due to the initially unknown acceleration or force value at time $t + \Delta t$, the predictor step is an explicit estimate. With this estimate the right hand side of the equations of motion can be evaluated by neighborhood search and contact evaluation in order to improve the estimate in the corrector. However these right hand side evaluations are especially expensive if several corrector steps are needed, or lower time steps are required due to demanded higher frequency result accuracy. Furthermore, the explicit predictor step potentially calls for more corrector steps, than an implicit predictor would.
Summarizing the state of the art, implicit integrators like the NEWMARK-β scheme [6] are superior to explicit schemes, at the cost of higher computational effort per step. Addressing the shortcomings of state of the implicit integrators this article will present an integration scheme, that approaches the per step performance of an explicit scheme while having the stability conditions and advantages of implicit schemes.

2 INTEGRATION SCHEME

In this section the integration scheme will be derived. Therefore the single steps yielding in an implicit scheme with implicit predictor but without the right hand side evaluations are explained. As a predictor corrector scheme is used to implement the algorithm, x_n denotes the value at iteration step n and index m denotes the converged value.

2.1 General Scheme

As a general basis of the novel integration scheme, the well known NEWMARK-β scheme [6] is enhanced. The NEWMARK scheme is given as follows:

$$\ddot{\vec{x}}(t+\Delta t) = \frac{\vec{F}_\mathrm{c}(t+\Delta t)}{m_\mathrm{p}} \tag{3}$$

$$\dot{\vec{x}}(t+\Delta t) = \dot{\vec{x}}(t) + \Delta t\Big((1-\gamma)\cdot\ddot{\vec{x}}(t) + \gamma\cdot\ddot{\vec{x}}(t+\Delta t)\Big) \tag{4}$$

$$\vec{x}(t+\Delta t) = x(t) + \Delta t\cdot\dot{\vec{x}}(t) + \Delta t^2\Big((\frac{1}{2}-\beta)\cdot\ddot{\vec{x}}(t) + \beta\cdot\ddot{\vec{x}}(t+\Delta t)\Big) \tag{5}$$

with $\vec{F}_\mathrm{c}(t+\Delta t), m_\mathrm{P}$ the contact forces and the particles mass, furthermore β and γ are the parameters of the NEWMARK scheme respectively. For the common choice of $\beta = 0.25$, $\gamma = 0.5$ the scheme is unconditionally stable in case of continuous forces and conditionally stable given Eq. 2 for non-continuous contact forces. This scheme can be implemented using an explicit predictor and thereafter improving the estimates by repeated right hand side evaluations at the estimated positions yielding new position estimates (see [4] for algorithm).

2.2 Predictor

In order to yield an implicit predictor step, the force or acceleration at time $(t+\Delta t)$ is needed. As the scheme especially targets the simulation of dense granular packages, the assumption of constant jolt $\frac{\mathrm{d}^3\vec{x}}{\mathrm{d}t^3}$:

$$\frac{\mathrm{d}^3\vec{x}}{\mathrm{d}t^3}(t) = \left.\frac{\mathrm{d}\ddot{\vec{x}}_m}{\mathrm{d}t}\right|_{(t-\Delta t)}^{t} \tag{6}$$

$$\frac{\mathrm{d}^3\vec{x}}{\mathrm{d}t^3}(t+\Delta t) = \frac{\mathrm{d}^3\vec{x}}{\mathrm{d}t^3}(t) \tag{7}$$

$$\frac{\mathrm{d}^3\vec{x}}{\mathrm{d}t^3}(0) = 0 \tag{8}$$

is made for the acceleration estimate, using the acceleration $\ddot{\vec{x}}_m$ at time t gathered by a single right hand side evaluation. As this estimate is calculated using the current step t and the previous step $t-\Delta t$, it is called left hand estimate and will have the upper index l throughout the paper. Thus the acceleration yields:

$$\ddot{\vec{x}}(t+\Delta t) = \ddot{\vec{x}}(t) + \int_t^{(t+\Delta t)} \left.\frac{\mathrm{d}^3\vec{x}}{\mathrm{d}t^3}\right|_{(t-\Delta t)}^{t} \mathrm{d}t \tag{9}$$

Using Eq. 4 and 9 a left hand velocity $\dot{\vec{x}}_0^l(t+\Delta t)$ estimate is calculated. In order to improve the estimate a right hand approximation is calculated using the assumption of

$$\frac{\mathrm{d}^3\vec{x}}{\mathrm{d}t^3}(t+2\Delta t) = \frac{\mathrm{d}^3\vec{x}}{\mathrm{d}t^3}(t+\Delta t) \tag{10}$$

as well as taking into account a possible change of sign in the velocity during the next step. The coverage of the change of sign is important, as for most force laws in DEM enlarging forces are emerging in approaching particle pairs, but forces are lowering during departure. If the change of sign is not regarded, the force in the consecutive step is overestimated, especially for larger step sizes, leading to non precise results of the corrector. Using $\dot{\vec{x}}_0^l(t+\Delta t)$ and the HADAMARD Product $\circ$ this yields:

$$\ddot{\vec{x}}_0^r(t+\Delta t) = \left(\ddot{\vec{x}}_0^l(t+\Delta t) + \gamma\Delta t \cdot \mathrm{sign}\Big(\dot{\vec{x}}_0^l(t+\Delta t) \circ \dot{\vec{x}}_m(t)\Big) \circ \int_{(t+\Delta t)}^{(t+2\Delta t)} \frac{\mathrm{d}\ddot{\vec{x}}_0}{\mathrm{d}t}\bigg|_t^{(t+\Delta t)} \mathrm{d}t \right) \tag{11}$$

As $\ddot{\vec{x}}_0^r(t+\Delta t)$ is a result of a velocity prediction at $(t+\Delta t)$ and $(t+2\Delta t)$, this yields in γ as a weight factor for the jolt. As the last step in the predictor operation, a centered estimate $\{\vec{x}_0^c(t+\Delta t), \dot{\vec{x}}_0^c(t+\Delta t), \ddot{\vec{x}}_0^c(t+\Delta t)\}$ is calculated:

$$\ddot{\vec{x}}_0^c(t+\Delta t) = (1-\alpha)\cdot\ddot{\vec{x}}_n^l(t+\Delta t) + \alpha\cdot\ddot{\vec{x}}_n^r(t+\Delta t) \tag{12}$$

$$\dot{\vec{x}}_0^c(t+\Delta t) = \dot{\vec{x}}_m(t) + \Delta t\Big((1-\gamma)\cdot\ddot{\vec{x}}_m(t) + \gamma\cdot\ddot{\vec{x}}_0^c(t+\Delta t)\Big) \tag{13}$$

$$\vec{x}_0^c(t+\Delta t) = \vec{x}_m(t) + \Delta t\cdot\dot{\vec{x}}_m(t) + \Delta t^2\left(\left(\frac{1}{2}-\beta\right)\cdot\ddot{\vec{x}}_m(t) + \beta\cdot\ddot{\vec{x}}_0^c(t+\Delta t)\right) \tag{14}$$

Thereby α is introduced in addition to the NEWMARK coefficients β and γ to allow for weighting towards left or right handed estimate. However the default recommendation of $\alpha = 0.5$ yields in the exactly centered acceleration. For the full PC-scheme, the choice of $\beta = 0.25$ and $\gamma = 0.5$ follows NEWMARK's suggestion. Yet, if the predictor is used without the corrector in order to save computational effort, the choice of $\gamma \approx 0.7$ is advised in order to introduce stability by moderate numerical damping. This use is only advisable if the force law itself cannot be covered by the corrector. Accordingly, if speed-up is crucial, it is better to use the left hand estimate predictor only, knowingly sacrificing the knowledge about possible change of sign in the velocity during the next step.

2.3 Force-law based Corrector

As the corrector is utilized to improve the estimates in the predictor to a valid forecast of the values at time $(t+\Delta t)$ it is iterated either till convergence or a maximum number of iterations m is reached. Thereby the acceleration estimate is improved using an assessment

of the force law used. In general this yields:

$$\ddot{\vec{x}}_n^c(t+\Delta t) = \ddot{\vec{x}}_m(t) + \int_t^{(t+\Delta t)} \left.\frac{\mathrm{d}^3\vec{x}}{\mathrm{d}t^3}\right|_t^{(t+\Delta t)} \mathrm{d}t \tag{15}$$

The future value of $\left.\frac{\mathrm{d}^3\vec{x}}{\mathrm{d}t^3}\right|_t^{(t+\Delta t)}$ is not assessable without rerunning neighborhood search and contact force evaluation. Thus it has to be calculated based on the previous iterations of the prediction, as well as the knowledge about the force law. In order to include the commonly used elastic normal forces in DEM an equivalent stiffness $\overline{c}(t)$ to estimate the next force can be defined as:

$$\overline{c}(t) = \nabla \circ \ddot{\vec{x}}\Big|_{\vec{x}_m(t-\Delta t)}^{\vec{x}_m(t)} \tag{16}$$

Evaluating $\ddot{\vec{x}}_n^c(t+\Delta t)$ using the elastic law and $\overline{c}(t)$ then yields:

$$\ddot{\vec{x}}_n^c(t+\Delta t) = \ddot{\vec{x}}_m(t) + \xi \int_{\vec{x}_m(t)}^{\vec{x}_{n-1}(t+\Delta t)} \left(\nabla \circ \ddot{\vec{x}}\Big|_{\vec{x}_m(t-\Delta t)}^{\vec{x}_m(t)}\right) \mathrm{d}\vec{x} \tag{17}$$

with $\xi \in [0,1]$ being a weighting factor dependent on the force law used, but usually chosen to be one. This forecast of acceleration is valid for both linear and non-linear force laws, including friction. As the contact itself needs to be covered by a sufficient number of time steps, changes in equivalent stiffness are sufficiently low even for non-linear force laws. After assessing the acceleration, the velocity and position are updated accordingly:

$$\dot{\vec{x}}_n(t+\Delta t) = \dot{\vec{x}}_m(t) + \Delta t\Big((1-\gamma)\cdot\ddot{\vec{x}}_m(t) + \gamma\cdot\ddot{\vec{x}}_n^c(t+\Delta t)\Big) \tag{18}$$

$$\vec{x}_n(t+\Delta t) = x_m(t) + \Delta t\cdot\dot{\vec{x}}_m(t) + \Delta t^2\left(\left(\frac{1}{2}-\beta\right)\cdot\ddot{\vec{x}}_m(t) + \beta\cdot\ddot{\vec{x}}_n^c(t+\Delta t)\right) \tag{19}$$

As the algorithm tends to converge within a few steps, using $m \in [2,5]$ is a good choice for fixed iterations without the need to control convergence saving computational effort.

Integration of the Rotations

Integration of the rotations of the six DOF particles is carried out analogous to the translation. The only difference is due to the use of quaternions at rotation-level.

2.4 Automatic Step Size Control

In order to allow the integrator to adapt its step size as well as number of iteration to the current behaviour of the solution, a time step size control is implemented.

Convergence of Corrector Loop

In order to allow the number of iteration to be controlled by convergence of the corrector, the maximum relative error of the acceleration $\varepsilon_{\mathrm{it}}(t+\Delta t, n)$ between two iterations is used. If $\varepsilon_{\mathrm{it}}(t+\Delta t, n) < \eta_{\mathrm{rel}}$ is true, the corrector iteration cycle is converged. $\varepsilon_{\mathrm{it}}(t+\Delta t, n)$ derives to:

$$\varepsilon_{\mathrm{it}}(t+\Delta t, n) = \sum_{i=1}^{k} \left(k\Delta t^2 \cdot \frac{\max\left(\left| {}^{i}\ddot{\vec{x}}_n^c(t+\Delta t) - {}^{i}\ddot{\vec{x}}_{n-1}^c(t+\Delta t) \right| \right)}{2 \cdot \left(\sum_{i=1}^{k} \left| {}^{i}\ddot{\vec{x}}_n^c(t+\Delta t) - {}^{i}\ddot{\vec{x}}_{n-1}^c(t+\Delta t) \right| + \eta_{\mathrm{abs}} \right)} \right) \tag{20}$$

with k the number of particles and η_{abs} an absolute tolerance value. This tolerance especially accounts for zero error in free falling particles.

Control of Time Step Size

The time step size is either controlled by the actual error $\varepsilon_r(t)$ of the acceleration estimation during the current step or by lowering the step if the corrector loop did not converge. The error is therefore derived to:

$$\varepsilon_r(t) = \sum_{i=1}^{k} \left(k\Delta t^2 \cdot \frac{\max\left(\left| {}^{i}\ddot{\vec{x}}_m^c(t) - {}^{i}\ddot{\vec{x}}^{\mathrm{cd}}(t) \right| \right)}{2 \cdot \left(\sum_{i=1}^{k} \left| {}^{i}\ddot{\vec{x}}_m^c(t) - {}^{i}\ddot{\vec{x}}^{\mathrm{cd}}(t) \right| + \eta_{\mathrm{abs}} \right)} \right) \tag{21}$$

with ${}^{i}\ddot{\vec{x}}_m^c(t)$ being the predicted acceleration of every particle i and ${}^{i}\ddot{\vec{x}}^{\mathrm{cd}}(t)$ the actual acceleration derived at the beginning of the next step using neighborhood search and contact force evaluation. $\varepsilon_r(t)$ itself actually describes the effect of the acceleration error on the accuracy of the calculated position at the end of the time step. The quotient $\mathfrak{z}(t)$ of the relative tolerance η_{rel} and $\varepsilon_r(t)$:

$$\mathfrak{z}(t) = \frac{\eta_{\mathrm{rel}}}{\varepsilon_r(t)} \tag{22}$$

is then used as input for the step size control law. This yields in adequate increase in time step in case of lower errors, i.e. lower number of changes in the contact neighbourhood.

3 APPLICATION & RESULTS

In order to verify the applicability of the integration scheme in DEM and contact dynamics, two example applications are evaluated in this section - a simple bouncing sphere and a piling experiment. Thereby the simple example will also be used in order to analyze energy conservation of the scheme. Prior to those applications the used force law is introduced. The integration scheme was also initially verified using the harmonic oscillator, which will not be shown in this paper, as the focus is on worst-case examples.

3.1 Contact Model

In order to show that the integrator does not only work for linear contact forces, but also non-linear laws including damping, the widely used HERTZian contact law is utilized instead of a linear law. Using the adaption for DEM shown in [5] the resultant force in case of overlap evaluates to

$$\vec{F}_{\mathrm{N}}^{nm} = \left(\frac{2E}{3(1-\nu^2)} \sqrt{r_{\mathrm{C}}^{nm} |\vec{\delta}^{nm}|^3} \right) \vec{n}_c^{\,n} + k_{\mathrm{Nmin}}^{nm} \dot{\vec{\delta}}^{nm} \tag{23}$$

with YOUNG's Modulus E, POISSON's Ratio ν, r_{C}^{nm} the mean particle radius of particles m and n and $\vec{\delta}^{nm}$ the overlap. $\vec{n}_c^{\,n}$ and $k_{\mathrm{Nmin}}^{nm} \leq 0$ are the contact normal for each particle and the damping coefficient respectively. In the first tests, only the normal force will be used. In the piling experiments shown later in the paper, frictional forces and rotational DOFs are added in order to check the applicability of the proposed integrator for general DEM problems. In order to model friction, the approach shown by LICHTENHELDT [1] is used:

$$\vec{F}_{c\mathrm{T}}^{nm} = c_{\mathrm{T}}^{nm} \cdot \vec{\delta}_{\mathrm{T}}^{nm} \cdot \mathrm{sign}\left(\vec{\delta}_{\mathrm{T}}^{nm} \cdot \dot{\vec{\delta}}_{\mathrm{T}}^{nm} \right) + k_{\mathrm{T}}^{nm} \cdot \dot{\vec{\delta}}_{\mathrm{T}}^{nm} \tag{24}$$

$$\vec{F}_{\mathrm{T}}^{nm} = \begin{cases} \vec{F}_{c\mathrm{T}}^{nm} & \forall\ |\vec{F}_{c\mathrm{T}}^{nm}| \leq |\vec{F}_{\mathrm{N}}^{nm}| \cdot \tan(\phi_{\mathrm{h}}) \ \wedge\ |\dot{\vec{\delta}}_{\mathrm{T}}^{nm}| \leq v_{\mathrm{Tmin}}^{nm} \\ \vec{F}_{\mathrm{N}}^{nm} \cdot \tan(\phi_{\mathrm{g}}) \cdot (\dot{\vec{\delta}}_{\mathrm{T}}^{nm})_0 & \forall\ |\vec{F}_{c\mathrm{T}}^{nm}| > |\vec{F}_{\mathrm{N}}^{nm}| \cdot \tan(\phi_{\mathrm{h}}) \ \vee\ |\dot{\vec{\delta}}_{\mathrm{T}}^{nm}| > v_{\mathrm{Tmin}}^{nm} \end{cases} \tag{25}$$

whereas $\phi_{\mathrm{g,h}}$ are the friction coefficients for sliding and sticking and c_{T}^{nm}, k_{T}^{nm} are the regularization stiffness and damping respectively. For rotations a commonly used rolling friction is added in order to provide proper rolling behaviour.

3.2 Bouncing Spheres

The first example models two spheres bouncing on each other perfectly centered. Therefore the lower sphere is fixed, while the upper sphere is free to fall until it contacts the second one. This example serves as benchmark in terms of energy conservation in cases with opening and closing contacts. These situations are worst-case for the scheme, as the impact and thus the sudden change in acceleration is not predicted beforehand, but only the step after the impact occurred. This makes this simple example more delicate in terms of verification compared to the harmonic oscillator. The example is fully conservative, thus no damping or friction is present.
The integration scheme has been tested for different time step sizes and automatic time stepping as shown in Fig. 1 (left). It can be seen, that even for large time steps in the sense of contact mechanics, stable solutions are found, i.e. no energy is generated. Only for a step size of $\Delta t = 10^{-3}$s there is a decrease in potential energy, as the integrator tends to damp the system numerically for arbitrarily high step sizes.

Furthermore it is worth mentioning, that the NEWMARK reference scheme showed an increase in energy for $\Delta t = 10^{-3}$s already.

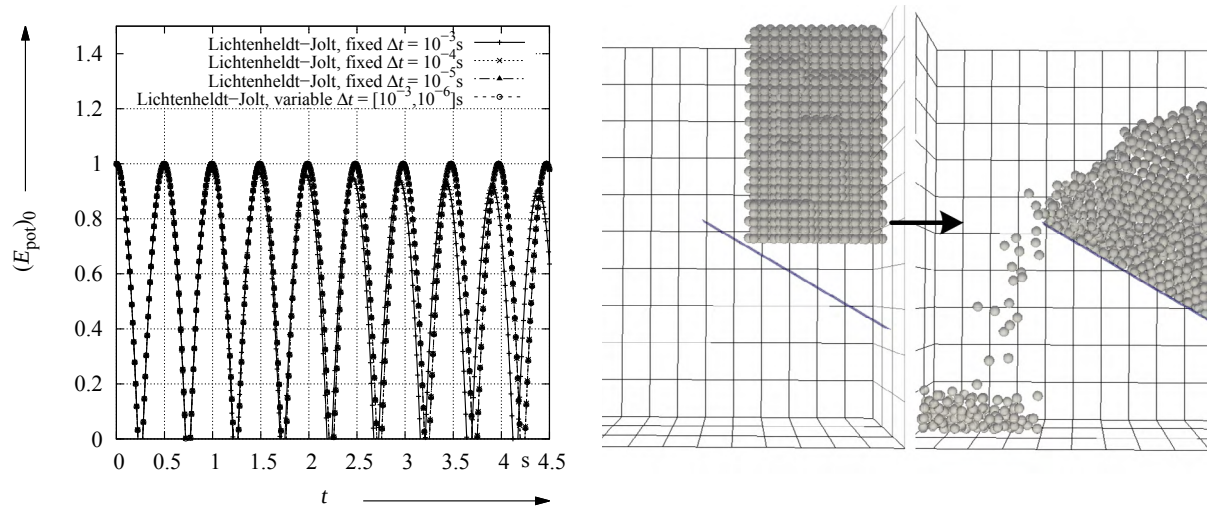

Figure 1: Normalized potential energy for the upper bouncing sphere for different time step sizes (left), Piling scenario with box and tilted plane visualized (right)

3.3 Piling Experiment

The piling scenario has been chosen as it features both, dense and flow states of granular matter making it an ideal test case for the proposed scheme. As shown in Fig. 1 (right), the scenario consists of a particle package dropping on an inclined plane creating a particle flow in the surrounding box until the pile is settled at the angle of repose. In the first test only normal forces are applied and the damping is set to 20% of critical damping. The same scenario is executed with the jolt-based and the reference integrator, whereas the NEWMARK scheme runs with $\Delta t = 10^{-5}$s and three iterations. For the jolt-based scheme both fixed step (three iterations) and variable step simulations are carried out dependent on the scenario. In the second test case frictional forces and rotational DOFs are added.

Accuracy

In Fig. 2 the jolt-based integrator is represented by gray particles, the NEWMARK integrator by green particles (note that the particles are scaled down for visibility) meshed via delaunay triangularization. Both results have been superimposed in Fig. 2 in order to allow for proper comparison. As it can be seen in the pictures, most of the gray particles are contained by the mesh, especially for the dense parts of the flow. Especially for the upper portion of particles situated in the pile there is almost no visible deviation. These qualitative findings are supported by the plotted total energy in Fig. 4 on the left. The jolt-based integrator shows slightly higher dissipation compared to the NEWMARK reference, but shows 2.11% of energy error, while increasing simulation speed.
In order to proof the applicability of the introduced scheme, it is tested with frictional contacts. Contact coefficients are chosen correspondent to [1]. Figure 3 shows the animated comparison as for the non-frictional case for fixed step simulations using $\Delta t = 10^{-5}$s. It

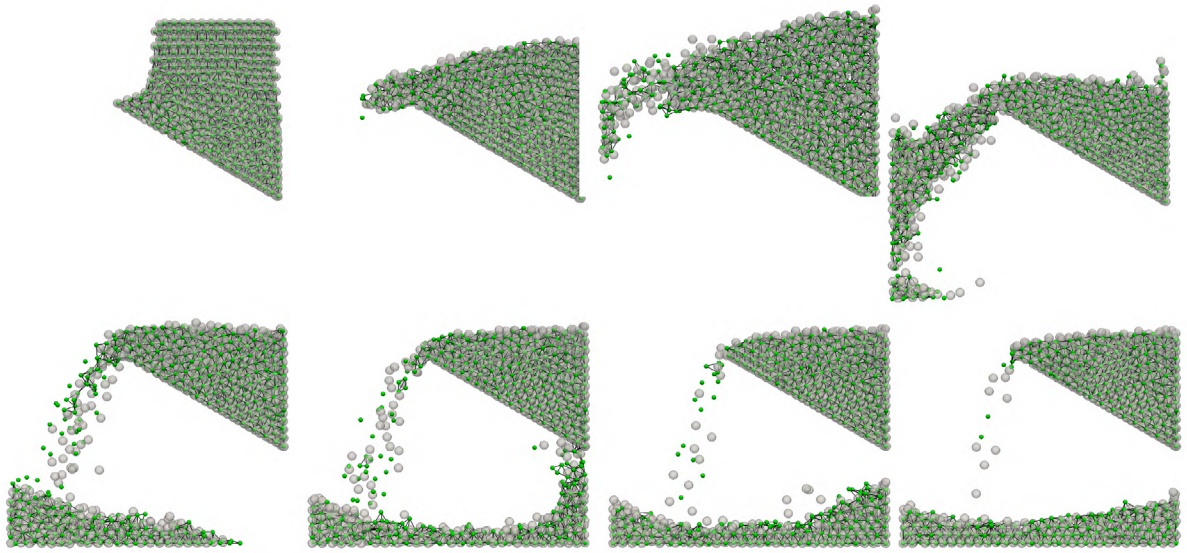

Figure 2: Piling for jolt-based (gray particles) and reference NEWMARK integrator (green meshed particles) for non-frictional contact

can be seen that the gray particles are again well contained in the mesh, however in the beginning the jolt-based integrator slightly lower volume in the upper pile and thus higher volume flow to the surrounding box. Given these slight variations it is still possible to capture the correct angle of the pile in every frame. The later frames with less particle movement are in even better agreement regarding the pile and the dense areas. Especially in the end of the simulation the same angle of repose is reached, i.e. the shear strength is covered correctly. Similar to the non-frictional piling, the frictional scenario also shows good agreement of the total energy compared to the reference integrator. Figure 4 shows the fixed step, as well as the variable step case. It can be seen, that the fixed step version is more precise, as the automatic time stepping tends to chose as high step sizes as possible in order to improve computational efficiency (see Figure 5 left). Regarding the relative error with respect to the reference scheme, both are well below 5% of error, whereas the fixed version is even below 2.2%. This result has been a surprise, as the corrector part of the scheme does not cover any kind of frictional or dissipative force but assumes a stiffness only. The fact that the forces are accurately assumed can also be seen in Fig. 5 right. The graph shows the maximum relative error between the converged prediction value $\ddot{\vec{x}}_m(t + \Delta t)$ of the last time step and the actual acceleration determined by contact detection in the current step. Most of the values are in the range of the desired value of 10^{-8}. All the values above have only minor influence on the results as they are in the same order of magnitude as the desired value and correspond to single particles changing their contact state. By activating back-stepping in the algorithm, these overshoots can be omitted while sacrificing some of the performance gain.

Performance

As in the previous section the new scheme showed sufficient accuracy, performance is compared to the reference solver accordingly. Therefore the same set of simulations as for the frictional piling case is used. Table 1 shows the results of the comparison. The

Table 1: Performance comparison of the integrators

Integrator	step size [s]	num. iterations	normalized time used []
NEWMARK	10^-5	3	1
LICHTENHELDT-Jolt	10^-5	3	0.5
LICHTENHELDT-Jolt	$[10^-6, 10^-2]$	$[1, 10]$	0.481
LICHTENHELDT-Jolt	$[10^-6, 10^-2]$	3	0.254

simulation time has been normalized to the NEWMARK result to allow easier comparison. The fixed step, fixed iteration jolt integrator is already two times faster than the reference. Sacrificing single percents of accuracy performance can be increased up to four times the speed of the reference integrator, by running step size controlled with fixed number

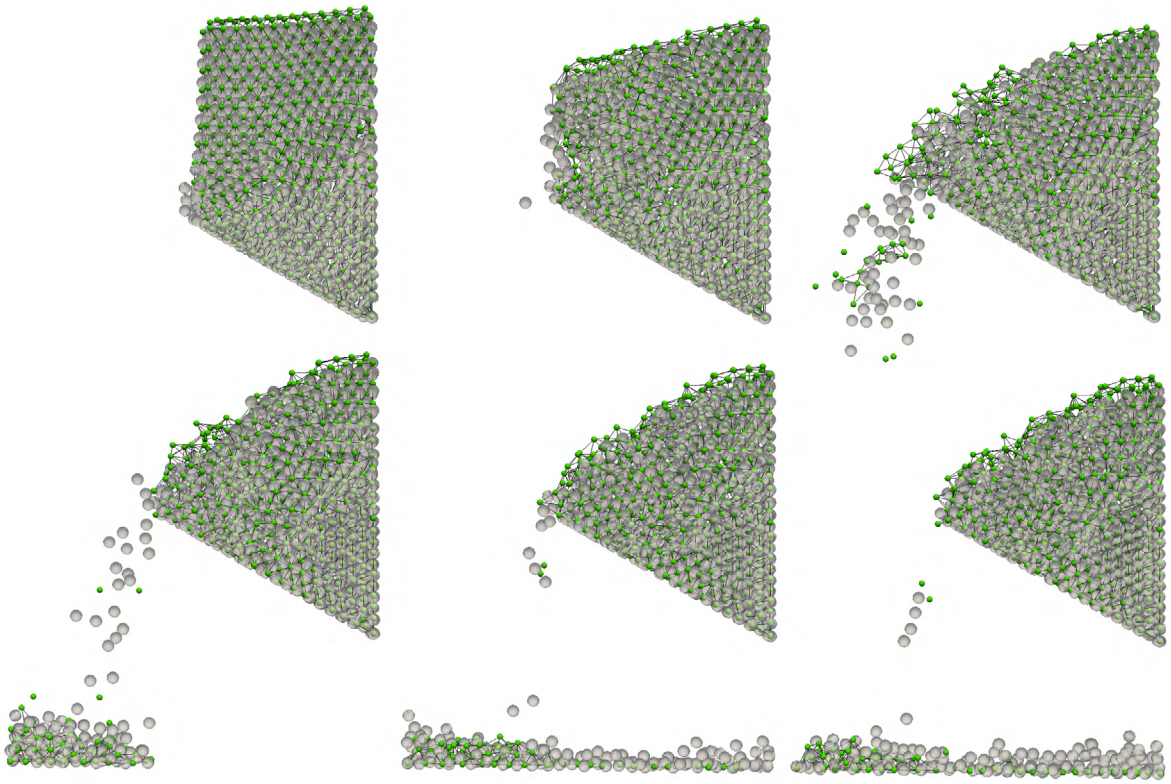

Figure 3: Piling for jolt-based (gray particles) and reference NEWMARK integrator (green meshed particles) for frictional contact

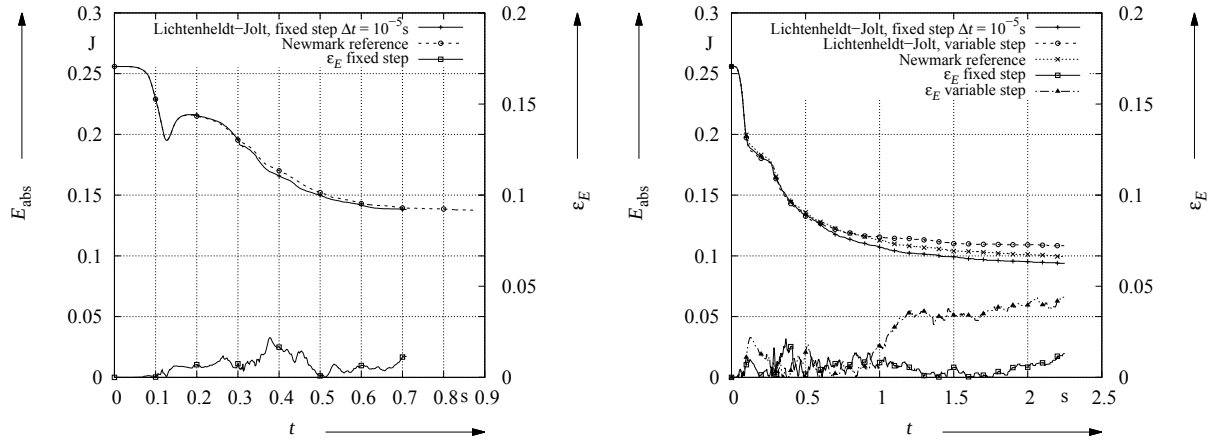

Figure 4: Total energy and relative energy error for the proposed and reference integrator for non frictional piling (left) and piling featuring friction (right)

of corrector iterations. Given the negligible loss in accuracy and the correctly covered shear strength of the material the integrator is a good alternative to the NEWMARK scheme whenever it comes to performance or software architecture. Compared to explicit integrators, both schemes showed great advantages as the time step could be chosen several orders of magnitudes higher.

4 CONCLUSION

In this article a novel implicit integration scheme has been proposed. On the basis of the NEWMARK integration scheme it uses a jolt-based approximation for the accelerations at the next time step. It specially targets particle simulations, as renewed contact detection and force evaluation at every corrector iteration are costly. Discarding these by using the

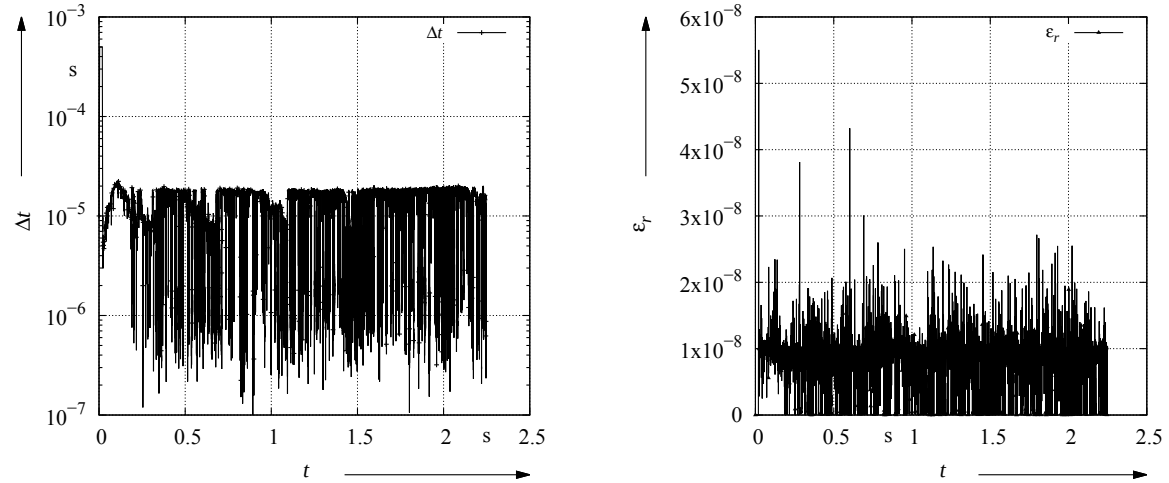

Figure 5: Time step size as chosen by the controller (left) and relative force error of the jolt-based prediction compared to the evaluated force (right)

approximation, the scheme also simplifies the architectural aspects of the code, making it easy to implement in any software featuring explicit integrators, which would not allow for renewed force calculation otherwise. Hence the scheme will also be used in DLR's GPU based simulation framework [7].
In the first sample applications it was shown, that the scheme is numerically stable for contact problems even up to arbitrarily high time steps and even for too large step sizes the integrator shows numerical damping instead of instability, making it most suitable for particle simulations. The scheme's accuracy has been verified using piling simulations and showed that for two times faster computation only 2.1% of error are arising. Tolerating negligibly low 4.4% of error results in an even higher speed up of a factor of four.
Given the advantages in performance, stability, implementation, architectural aspects and its direct applicability to GPU-computing paradigms, the LICHTENHELDT-Jolt integration scheme poses an interesting alternativ to both, common implicit and especially explicit schemes in Discrete Element Method.

ACKNOWLEDGEMENTS

Special thanks go to Simon Kerler, who's work required a simple efficient and implicit integration scheme and thus inspired this work.

REFERENCES

[1] R. Lichtenheldt. A novel systematic method to estimate the contact parameters of particles in discrete element simulations of soil. In *4th International Conference on Particle-based Methods - Particles 2015, pp 430-441, ISBN:978-84-944244-7-2, Barcelona*, 2015.

[2] V. Smilauer and B. Chareyre. Yade dem formulation. Technical report, Yade Documentation, The Yade Project, 1st ed., 2010. http://yade-dem.org/doc/formulation.html.

[3] F. Fleissner. Dokumentation, template-files und beispiele zum programmpaket "pasimodo". Template files, Inpartik & Universität Stuttgart, 2012.

[4] F. Fleissner. *Parallel Object Oriented Simulation with Lagrangian Particle Methods*. PhD thesis, Universität Stuttgart, 2010.

[5] R. Lichtenheldt. *Lokomotorische Interaktion Planetarer Explorationssysteme mit weichen Sandböden - Modellbildung und Simulation*. PhD thesis, Ilmenau University of Technology, ISBN 978-3-8439-2704-8, 2016.

[6] N.M. Newmark. A method of computation for structural dynamics. *Journal of the Engineering Mechanics Division*, pages 67–94, 1959.

[7] S. Kerler. Collision-based Particle Simulations on GPUs for Planetary Exploration Systems. Master's thesis, Augsburg University, 2017.

V International Conference on Particle-based Methods – Fundamentals and Applications
PARTICLES 2017
P. Wriggers, M. Bischoff, E. Oñate, D.R.J. Owen, & T. Zohdi (Eds)

DIRECT DETERMINATION OF GRANULAR PRESSURE IN LIQUID FLUIDIZED BEDS USING A DEM-BASED SIMULATION APPROACH

HAMED ABBASFARD[1], GEOFFREY EVANS[2] AND ROBERTO MORENO-ATANASIO[3]

[1] Chemical Engineering, The University of Newcastle
Callaghan 2308 NSW Australia
Hamed.Abbasfard@newcastle.edu.au

[2] Chemical Engineering, The University of Newcastle
Callaghan 2308 NSW Australia
Geoffrey.Evans@newcastle.edu.au

[3] Chemical Engineering, The University of Newcastle
Callaghan 2308 NSW Australia
Roberto.Moreno-Atanasio@newcastle.edu.au

Key words: Fluidized bed, DEM, Granular Pressure, Fluctuating Velocity

Abstract. In this paper, the fluidization of 8 mm glass particles in water has been simulated using a new methodology developed within the DEM framework. In this methodology, random liquid fluctuating velocities are used as direct input into the drag model. The specific aim of this study is to directly compute the granular pressure in a liquid fluidized bed. The granular pressure is defined using the particle-wall collision frequency and the corresponding particle momentum transport during the collision. Initially, we validated our model by comparing the relationship between superficial fluid velocity and bed expansion against the well-known Richardson-Zaki [1] equation. The results demonstrated a good agreement of our model. The granular pressure and temperature, as well as the particle-wall collision frequency, in the liquid fluidized bed were determined for superficial fluid velocities in the range between 0.08 and 0.32 m/s. The granular pressure exhibited a maximum (between 0.3-0.4 solid fraction) that matched the experimental measurements of Zenit et al. [2] for high inertia particles. The granular temperature also revealed a peak at a solid concentration of around 0.2 which is in line with the experimental measurements of Zivkovic et al. [3] and the model of Gervin et al. [4]. The set of the results presented in this study suggests that the approach used here is valid for obtaining the granular pressure and temperature for a wide range of volume fractions in liquid fluidized beds.

1 INTRODUCTION

The granular pressure is defined as the pressure exerted on the containing walls of the fluidized bed due to the collisions of particles with those walls. Batchelor [5] established the formulation of the mean motion of particles in a fluidized bed using a one-dimensional control volume stability analysis. All the parameters within Batchelor's model were correlated

with the local solid volume fraction ε_s as well as superficial liquid velocity u_{sf}. Hence, the expression of granular pressure is defined as [5]:

$$P_p = \varepsilon_s \rho_p F(\varepsilon_s) u_{sf}^2 \tag{1}$$

where $F(\varepsilon_s)$ is some function of the solid volume fraction for two limiting cases of 0 and packed bed solid volume fraction ($\varepsilon_{sp} \approx 0.62$). Batchelor [5] suggested the simplest form of $F(\varepsilon_s)$ as:

$$F(\varepsilon_s) = \frac{\varepsilon_s}{\varepsilon_{sp}}\left(1 - \frac{\varepsilon_s}{\varepsilon_{sp}}\right) \tag{2}$$

Ding and Gidaspow [6] proposed a relation for the granular pressure based on the Kinetic Theory of Granular Flow (KTGF) as [7]:

$$P_p = \varepsilon_s \rho_p \theta [1 + 2(1 + e_n) g_0 \varepsilon_s] \tag{3}$$

where θ and g_0 are the granular temperature and radial distribution function, respectively. The granular temperature based on KTGF [7] for a three-dimensional flowing granular material is defined as:

$$\theta = \frac{1}{3}\overline{v^2} \tag{4}$$

where $\overline{v^2}$ is the mean value of the squares of fluctuating velocities. The coefficient of restitution, e_n, is the ratio of the impact velocity to the rebound velocity. The square of the restitution coefficient is directly proportional to the loss of kinetic energy during inelastic collisions due to damping effect [8]. The concept of the radial distribution function, g_0, is like $F(\varepsilon_s)$ used by Batchelor [5] and some different representations of it are available in literature [9-11]. We determined the granular pressure using the form of the radial distribution function proposed by Bagnold [9] as:

$$g_0 = \left[1 - \left(\frac{\varepsilon_s}{\varepsilon_{sp}}\right)^{\frac{1}{3}}\right]^{-1} \tag{5}$$

Wang and Ge [12] presented a mathematical model based on energy balance analysis to predict the granular pressure in fluidized beds of high particle inertia which is defined as:

$$P_p = 2(1 + e_n)\varepsilon_s^2 \rho_p \theta g_0 \tag{6}$$

where all parameters are the same and determined similarly as per Eq. 3.

In this paper, we are aiming at the computation of the granular pressure in a liquid fluidized bed using DEM. We have developed a new methodology to simulate the random motion of the particles influenced by the random fluctuating liquid velocity field incorporated into the drag force. A methodology for directly defining of the granular pressure based on the momentum transport during the particle-wall collision and the corresponding frequency has been presented. The simulation results for the granular pressure has been compared to the

correlations available in the literature. The collision-wall frequency as well as the granular temperature in the liquid fluidized bed have also been reported here.

2 MODELING

Forces acting on the particle i are gravity, buoyancy, contact and drag, as:

$$\sum \overrightarrow{F_i} = \overrightarrow{F_{gb}} + \overrightarrow{F_c} + \overrightarrow{F_d} \tag{7}$$

The combined equation used for the gravity and buoyancy forces (in z direction) is:

$$F_{gb,z} = gV_p(\rho_L - \rho_p) \tag{8}$$

where V_p is the particle volume. In Eq. 1, $\overrightarrow{F_c}$ is the contact force. The soft sphere model was used to simulate particle-particle and particle-wall collisions [13]. The dominant fluid-particle interaction forces which are considered in this work are drag ($\overrightarrow{F_d}$) and buoyancy ($\overrightarrow{F_b}$). The drag model introduced by Di Felice [14] is used in Eq. 7 as it provides a smooth dependency of the drag force over the entire range of volume fractions [15].

A finite difference form of Newton's second law is used in DEM to determine particle's position, velocity and acceleration in each time step [8]. The new position of the particle centre after each time step can be found as:

$$\overrightarrow{S_i}(t + \Delta t) = \overrightarrow{S_i}(t) + \overrightarrow{v_i}(t)\Delta t + 0.5\frac{\sum \overrightarrow{F_i}(t)}{m_i}\Delta t^2 \tag{9}$$

where $\overrightarrow{v_i}(t)$ is the instantaneous particle velocity.

The fluid instantaneous fluctuating velocity used in the drag model is defined as:

$$\vec{u}(t) = \vec{\bar{u}} + \vec{u}'(t) \tag{10}$$

The local mean fluid velocity, $\vec{\bar{u}}$, in radial (x and y) direction is zero due to cylindrical symmetry. However, the mean value for the axial direction is equal to the interstitial fluid velocity (u_i) which is related to the local fluid volume fraction as:

$$\bar{u}_z = u_i = \frac{u_{sf}}{\varepsilon_{L,z}} \tag{11}$$

where u_{sf} is fluid superficial velocity and ε_L is the local liquid volume fraction.

Based on the Kinetic Theory of Granular Flow (KTGF), particle velocity can take random values in fluidized beds in both direction and magnitude [16, 17]. It is also believed that those random velocities follow a Gaussian-type Probability Distribution Function (PDF) in any direction [18-20]. As the particle constantly exchange momentum with the surrounding, liquid velocity values should also be random and fluctuating and following a Gaussian PDF with a

mean value and standard deviation in any direction. The standard deviation of the fluctuating liquid velocity is the root mean squared of the instantaneous fluctuating velocity, u_{rms}.

Based on turbulence theory [21], the influence of fluid turbulence on particle motion is described by [22]:

$$u_{rms}{}^2 = \left(1 + \frac{\tau_p}{T_L}\right)\overline{v^2} \tag{12}$$

where T_L and τ_p are the time scale of the fluid and particles, respectively. In an isotropic turbulence, the fluid time scale can be defined as $T_L = l/u_{rms}$ where l is the turbulence length scale [23]. Therefore, Eq. 12 can be written as:

$$u_{rms}{}^2 - \frac{\overline{v^2}\tau_p}{l} u_{rms} - \overline{v^2} = 0 \tag{13}$$

A relation for the particle time scale (relaxation time) was proposed by Bel F'dhila and Simonin [24] as:

$$\tau_p = \frac{\rho_p/\rho_L + C_A}{(3/4)\overline{C_d}/d_p\, u_t} \tag{14}$$

where C_A is the added mass coefficient and equal to 0.5 [25].

For the average particle speed Duris et al. [20] presented an empirical equation based on experimental measurements in a liquid fluidized bed:

$$\overline{v} = v_t \left[8.486 \left(Re_t \left(\frac{\mu}{\mu_w} \right)^{1.19} \right)^{-0.636} \left(\frac{u_{sf} - u_{mf}}{u} \right) \varepsilon_s^{0.5} \right]^{2/3} \tag{15}$$

and based on KTGF, we have [7]:

$$\overline{v^2} = (1.086\overline{v})^2 = 1.1794\overline{v}^2 \tag{16}$$

where v_t, Re_t, μ_w and u_{mf} are particle terminal velocity, particle Reynolds number based on terminal velocity, viscosity of water and fluid minimum fluidization velocity, respectively. The terminal and minimum fluidization velocities are determined from the correlations proposed by Loli et al. [26] and Wen and Yu [27], respectively.

As can be seen in Eq. 15, $\overline{v}$ is a function of the superficial fluid velocity, u_{sf}, and solid fraction, ε_s where the former is an input parameter and the latter can be defined using DEM. Therefore, the u_{rms}, which represents the level of liquid fluctuations, can be defined by solving the quadratic Eq. 13.

3 METHODOLOGY

3.1 Numerical simulation

Initially, particles were randomly positioned without overlapping in the simulation domain, which is a cylindrical column. The domain was divided into several cells (20-30 depending on bed height) along the axis of the column as shown in figure 1. Each cell height was always slightly larger than the smallest particle diameter in the system (1.5 times of particle diameter). The cells were used to determine the instantaneous and local volume fraction along the z direction. Initial values of the particle velocities were set to be zero.

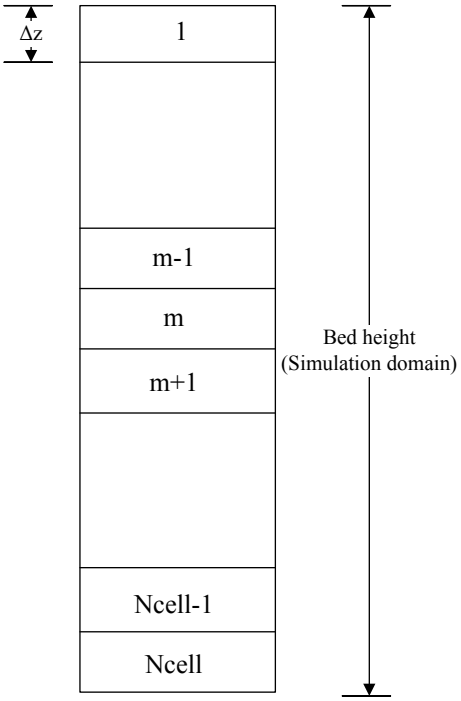

Figure 1: The simulation domain discretised into axial cells

A random fluid velocity drawn from the Gaussian PDF with the mean and standard deviation given by Eqs. 11-13 was associated to each particle at every updating interval which is defined following Crow et al. [28] approach and is about 0.01s. The standard deviation of the velocity distribution was a function of the fluid velocity and local volume fraction of the cell in which the particle centre was located. It is noted that based on PIV measurements, Reddy et al. [29] found that the axial fluid fluctuating velocity is 1.65 times that of the radial component and therefore we used that accordingly to find axial ${u^2}_{rms} = {u^2}_{rms,r} + {u^2}_{rms,z}$. This random fluid velocity was used to define the slip velocity and finally the drag force acting on each particle. Then, using a force balance (Eq. 7) along with the finite difference integration method (Eq. 9), the new position of the particle was defined. The flow chart of the simulation algorithm is schematically shown in figure 2.

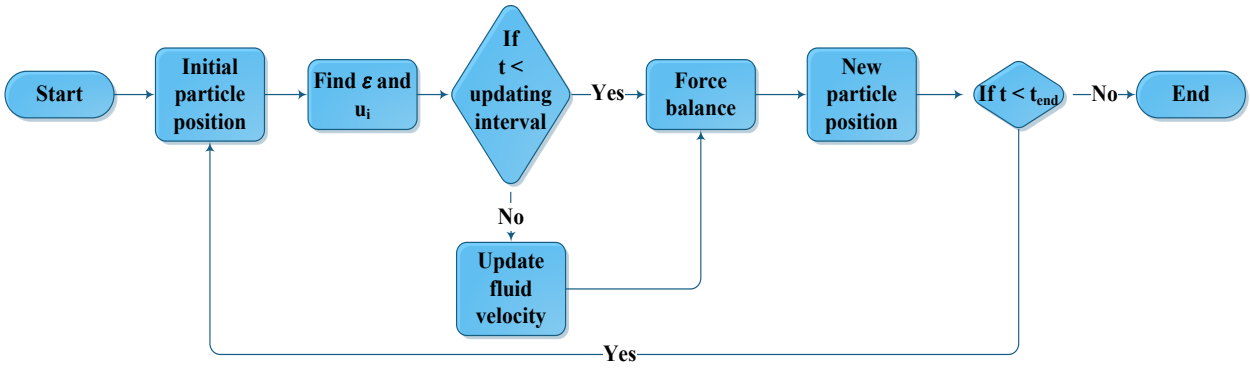

Figure 2: Schematic flow chart of simulation algorithm

The solid volume fraction of each cell is determined at any interval when the fluid fluctuating velocity and the drag coefficient are updated. Table 1 shows the required input parameters in the DEM simulations.

Table 1: Simulation input parameters

Properties	Value
Initial particle velocity (m/s)	0
Particle terminal velocity (m/s)	0.54
Minimum fluidization velocity (m/s)	0.06
No. of particles	201
Cell height (mm)	12
Liquid superficial velocity (m/s)	0.08-0.32
Stiffness (N/m)	100
Time step (s)	1×10^{-5}
Updating interval (s)	0.01
Coefficient of restitution	0.90
Richardson-Zaki index (n)	2.39

3.2 Granular pressure

In this paper, an attempt was made to numerically quantify the granular pressure in liquid solid fluidized beds using a method based on the KTGF definition of the granular pressure. In this method, the granular pressure was defined using the determination of particle-wall collision frequency and the corresponding particle momentum transport at the time of the collision. The momentum transport of the particles hitting the side wall of the cylindrical fluidized bed can be written as:

$$M_p = m\bar{v}(1+e) \tag{17}$$

The particle-wall collision frequency per unit area of the bed can also be defined as:

$$F_{p-w} = \frac{f_{p-w}}{A_s} = \frac{f_{p-w}}{\pi D_c h_e} \tag{18}$$

where h_e is the equilibrium bed height. Therefore, combining Eqs. 17 and 18, the granular pressure is defined as:

$$P_p = M_p F_{p-w} = \frac{m\bar{v}(1+e)f_{p-w}}{\pi D_c h_e} \tag{19}$$

4 RESULTS

4.1 Bed expansion

The well-known empirical correlation of Richardson and Zaki [1] was used to define the velocity-voidage relationship as:

$$u_{sf} = v_\infty \varepsilon_L^n \tag{20}$$

where n is the expansion index and v_∞ is the bed settling velocity at infinite dilution. Richardson and Zaki [1] suggested that the ratio of the bed settling velocity at infinite dilution to the single particle settling velocity in an infinite medium $\left(\frac{v_\infty}{v_t}\right)$ is a function of $\frac{d}{D_c}$ as:

$$v_\infty = v_t 10^{-\frac{d}{D_c}} \tag{21}$$

where v_t and D_c are the single particle settling velocity in an infinite medium and the column diameter, respectively. Figure 3 compares the simulation results of the liquid superficial velocity versus liquid volume fraction against the Richardson-Zaki [1] empirical equation. This figure illustrates that the simulation shows the same trend and in close agreement with the empirical correlation of Richardson and Zaki [1] for a wide range of liquid velocity and volume fraction. However, as can be seen, the behaviour of the fluidized bed in high voidage regions (approximately for ε_L > 0.85) is very complex [20, 30, 31]. As suggested by Eq. 21, $v_\infty < v_t$ and this makes the deviation of the simulation results at higher liquid volume fractions where the DEM results predict more realistically.

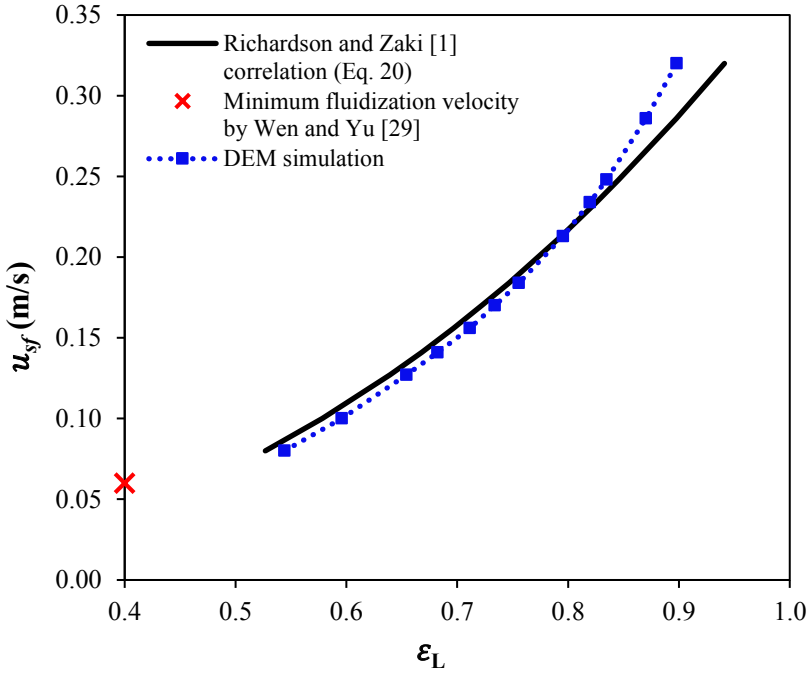

Figure 3: u_{sf} vs. ε_L; comparison of DEM simulation results to Richardson-Zaki [1] equation.

4.2 Granular temperature and pressure

Figure 4A and B shows the granular temperature and pressure versus solid volume fraction, respectively. Figure 4A exhibits a maximum at $\varepsilon_s \approx 0.1 - 0.2$. This also agrees with the experimental measurement of Zivkovic et al. [3] and simulation of Gervin et al. [4] that have reported the maximum granular temperature occurrence at $\varepsilon_s = 0.175$ and $\varepsilon_s \approx 0.1 - 0.2$, respectively.

Figure 4 B compares the DEM simulation results for the granular pressure using Eq. 19 to those obtained using the models proposed by Batchelor [5], Ding and Gidaspow [6] and Wang and Ge [12]. Our DEM results, Ding and Gidaspow [6] and Wang and Ge [12] models predict a maximum value in granular pressure for solid fractions of around 0.30-0.35, which is well in line with the reported experimental data by Zenit et al. [2] for high inertia particles. However, as can be seen, the maximum granular pressure calculated using Batchelor [5] model occurs at lower solid fraction of around 0.2 which also has been observed by experimental measurements of Zivkovic et al. [3] for high inertia particles.

Ghatage et al. [32] pointed out that this maximum value in the granular pressure might be a sign of a transition point from homogenous to heterogeneous regime. According to stability analysis, a fluidized bed can operate under either hydrodynamically stable or unstable condition depending upon the nature of dispersion [33].

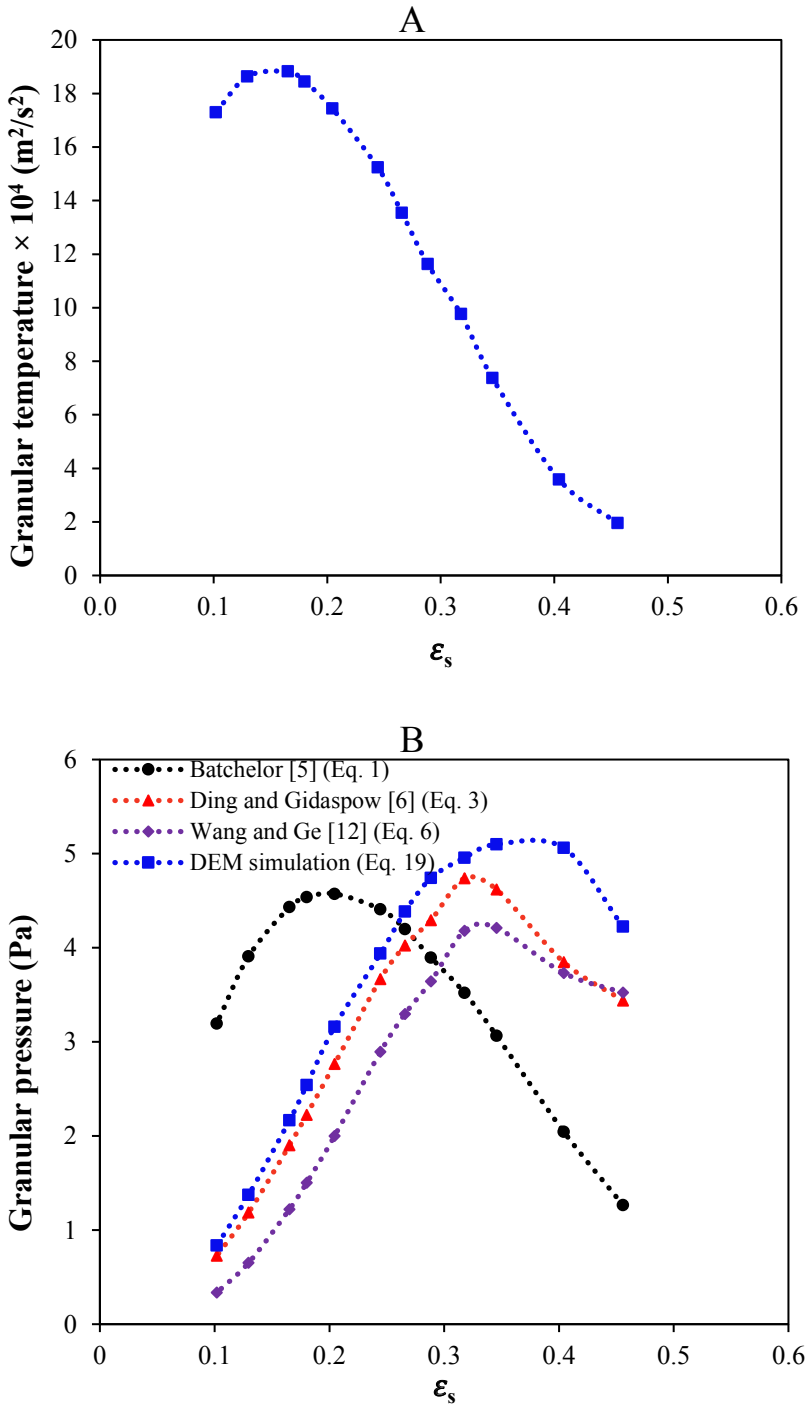

Figure 4: Granular temperature (A) and pressure (B) vs. solid volume fraction (ε_s).

Figure 5 shows the DEM simulation results for the collision to wall frequency versus solid volume fraction. Zenit et al. [2] claimed that at low concentrations, the value of the particle pressure is low as the particles are free to move and collision frequency is also smaller as

shown in figure 5. On the other hand, at high solid fractions collisions are more likely to occur. However, very short mean free path of the particles causes these collisions to occur at very small velocities producing low-impulse collisions, which result in a low value of the particle pressure [2, 4]. Therefore, a combined effect of the higher impact velocity as well as the collision frequency results in higher granular pressure at intermediate concentrations (ε_s = 0.30-0.35).

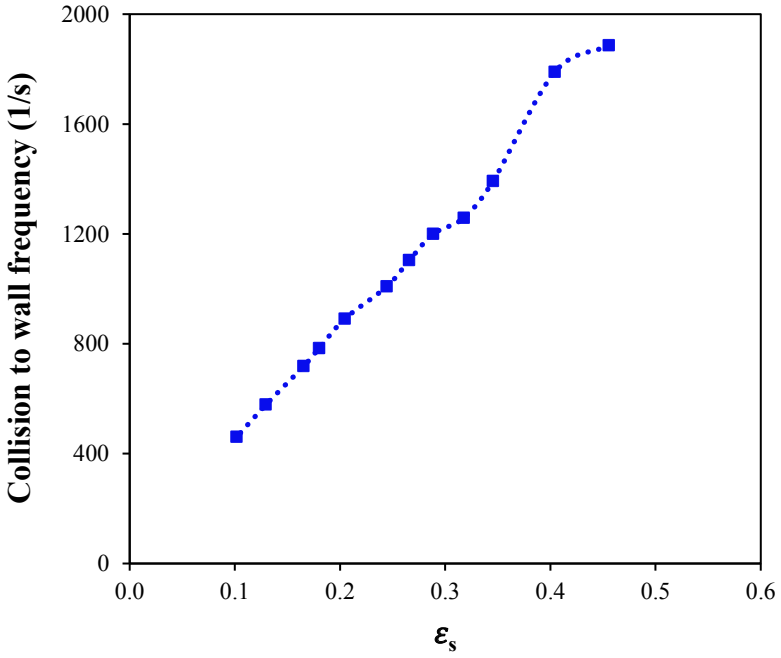

Figure 5: Collision to wall frequency (f_{p-w}) vs. solid volume fraction (ε_s).

7 CONCLUSION

In this study, a new DEM simulation approach has been used to simulate a liquid fluidized bed. A methodology based on the momentum transfer at the collision event was introduced to directly determine the granular pressure knowing the particle collision to wall frequency and speed.

In order to validate our DEM model, the bed expansion was compared to well-known Richardson-Zaki [1] equation where a good agreement was observed.

The granular pressure obtained by the DEM simulation then compared to some models available in literature. The quantity as well as the quality of the DEM results for the granular pressure agreed well with the majority of the current models. Similar peaks were observed in the intermediate concentration region (ε_s = 0.3-0.4) that is in line with the experimental

observation of Zenit et al. [2] for the granular pressure in liquid fluidized beds.

Further stability analysis needs to be carried out in order to come to a rational conclusion whether that peak observed in the granular pressure values is related to any possible transition from homogeneous to heterogeneous regime in liquid fluidized beds.

REFERENCES

[1] Richardson, J.F. and Zaki W.N. Sedimentation and fluidisation. Part I. *Trans. lnstn Chem. Engrs.* (1954) **32**:35-53.

[2] Zenit, R., Hunt, M.L. and Brennen, C.E. Collisional particle pressure measurements in solid-liquid flows. *J. Fluid. Mech.* (1997) **353**:261-283.

[3] Zivkovic, V., Biggs, M.J. and Glass, D. Granular Pressure in a Liquid-Fluidized Bed as Revealed by Diffusing Wave Spectroscopy. *AIChE J.* (2012) **58**:1069-1075.

[4] Gevrin, F., Masbernata, O. and Simonin, O. Granular pressure and particle velocity fluctuation prediction in liquid fluidized beds. *Chem. Eng. Sci.* (2008) **63**:2450-2464.

[5] Batchelor, G.K. A new theory of the instability of a uniform fluidized bed. *J. Fluid. Mech.* (1988) **193**:75-110.

[6] Ding, J., Gidaspow, D. A bubbling fluidization model using kinetic theory of granular flow. *AIChE J.* (1990) **36**(4):523-538.

[7] Gidaspow, D. *Multiphase flow and fluidization: continuum and kinetic theory descriptions*. Academic press, (1994).

[8] Abbasfard, H., Evans, G. and Moreno-Atanasio, R. Effect of van der Waals force cut-off distance on adhesive collision parameters in DEM simulation. *Powder Technol.* (2016) **299**:9-18.

[9] Bagnold, R.A. Experiments on a gravity-free dispersion of large solid spheres in a Newtonian fluid under shear. Proc R Soc London Ser A. (1954) **225**:49-63.

[10] Carnahan, N.F. and Starling, K.E. Equation of state for non-attracting rigid spheres. *J. Chem. Phys.* (1969) **51**:635-636.

[11] Lun, C. and Savage, S. The effects of an impact velocity dependent coefficient of restitution on stresses developed by sheared granular materials. *Acta Mech.* (1986) **63**:15-44.

[12] Wang, J. and Ge, W. Collisional particle–phase pressure in particle–fluid flows at high particle inertia. *Phys. Fluids*. (2005) **17**:128103.

[13] Cundall, P.A. and Strack, O.D. A discrete numerical model for granular assemblies. *Geotechnique.* (1979) **29** (1):47-65.

[14] Di Felice, R. The voidage function for fluid-particle interaction systems. *Int. J. Multiphase Flow*. (1994) **20**(1):153-159.

[15] Kafui, K., Thornton, C. and Adams, M. Discrete particle-continuum fluid modelling of gas–solid fluidised beds. *Chem. Eng. Sci.* (2002) **57**(13):2395-2410.

[16] Clift, R., Grace, J.R. and Weber, M.E. *Bubbles, drops, and particles*: Courier Corporation, (2005).

[17] Handley, D., A D, Butcher, K. and Franklin N. A study of fluid and particle mechanics in liquid-fluidised beds. *TRANSACTIONS OF THE INSTITUTION OF CHEMICAL ENGINEERS AND THE CHEMICAL ENGINEER.* (1966) **44**(7):T260.

[18] Carlos, C. and Richardson, J. Solids movement in liquid fluidised beds—I Particle

velocity distribution. *Chem. Eng. Sci.* (1968) **23**(8):813-824.
[19] Latif, B. and Richardson, J. Circulation patterns and velocity distributions for particles in a liquid fluidised bed. *Chem. Eng. Sci.* (1972) **27**(11):1933-1949.
[20] Đuriš, M., Radoičić, T.K., Garić-Grulović, R., Arsenijević, Z. and Grbavčić, Ž. Particle velocities in quasi two-dimensional water fluidized beds of spherical particles. *Powder Technol.* (2013) **246**:98-107.
[21] Hinze, J. *Turbulence*. McGraw-Hill. *New York.* (1975).
[22] Pozorski, J. and Minier, J-P. On the Lagrangian turbulent dispersion models based on the Langevin equation. *Int. J. Multiphase Flow.* (1998) **24**(6):913-945.
[23] Doroodchi, E., Evans, G., Schwarz, M., Lane, G., Shah, N. and Nguyen, A. Influence of turbulence intensity on particle drag coefficients. *Chem. Eng. J.* (2008) **135**(1):129-134.
[24] Bel Fdhila, R. and Simonin, O. Eulerian prediction of a turbulent bubbly flow downstream of a sudden pipe expansion. Paper presented at: Proceedings 5th Workshop on Two-Phase Flow Predictions (1992).
[25] Spelt, P. and Biesheuvel, A. On the motion of gas bubbles in homogeneous isotropic turbulence. *J. Fluid. Mech.* (1997) **336**:221-244.
[26] Lali, A., Khare, A., Joshi, J. and Nigam, K. Behaviour of solid particles in viscous non-Newtonian solutions: settling velocity, wall effects and bed expansion in solid-liquid fluidized beds. *Powder Technol.* (1989) **57**(1):39-50.
[27] Wen, C. and Yu, Y. A generalized method for predicting the minimum fluidization velocity. *AIChE J.* (1966) **12**(3):610-612.
[28] Crowe, C. An assessment of multiphase flow models for industrial applications. Paper presented at: Proceeding of FEDSM (1998).
[29] Reddy, R., Sathe, M., Joshi, J., Nandakumar, K. and Evans, G. Recent developments in experimental (PIV) and numerical (DNS) investigation of solid–liquid fluidized beds. *Chem. Eng. Sci.* (2013) **92**:1-12.
[30] Epstein, N. *Liquid Solids Fluidization*, in: W.C. Yang (Ed.), Handbook of fluidization and fluid-particle systems, Marcel Dekker, New York, (2003) 705-764.
[31] Di Felice, R. Liquid suspensions of single and binary component solid particles – an overview, *China Part.* (2007) **5**:312–320.
[32] Ghatage, S.V., Peng, Z., Sathe, M.J., et al. Stability analysis in solid–liquid fluidized beds: experimental and computational. *Chem. Eng. J.* (2014) **256**:169-186.
[33] Joshi, J.B., Deshpande, N.S., Dinkar, M. and Phanikumar, D.V. Hydrodynamic stability of multiphase reactors. *Adv. Chem. Eng.* (2001) **26**: 1-130.

V International Conference on Particle-based Methods – Fundamentals and Applications
PARTICLES 2017
P. Wriggers, M. Bischoff, E. Oñate, D.R.J. Owen, & T. Zohdi (Eds)

ENERGY BALANCE IN A PARTICLE SYSTEM

ARNO MAYRHOFER[1], ALICE HAGER[1] AND CHRISTOPH KLOSS[1]

[1]DCS Computing GmbH
Industriezeile 35, 4020 Linz
{arno.mayrhofer, alice.hager, christoph.kloss}@dcs-computing.com

Key words: DEM, Energy balance, Time integration.

Abstract. The energy distribution inside a particle system can be used to study the mechanical properties of such a system and its response to external perturbations. In the present article, the energy terms for typical discrete element models are derived. The derivation considers both Euler and Verlet integration schemes. Exemplary simulations are shown to demonstrate the validity of the derived formulation.

1 INTRODUCTION

The discrete element model (DEM) [1] is a widely used discrete model to simulate granular flows and has found its way from academia to industry. The DEM calculates the interaction of particles that are represented as volume elements (mostly spheres). To compute the interaction forces between two particles different variations of spring-damper systems are generally employed. As shown by [2] these models might cause artificial energy dissipation. However, [3] showed that explicit tracking of the dissipative energy is required and highlighted mistakes in earlier energy formulae, providing corrected formulations for Euler schemes. [4] also investigated energy in granular flows for comparably simple DEM models.

In the following the calculation of different energy terms in spring-damper systems is analysed using the standard Euler integration scheme. This is then followed by an extension to the velocity Verlet scheme, which is used in the LIGGGHTS® software. This will demonstrate the importance of the time integration scheme. Equipped with the general formulation several DEM models, from simple normal and lubrication models to a rather complicated bond model, will be reviewed.

The theoretical developments will be applied to four distinct test cases that show the validity of the present formulation and potential application areas. The first such area is model development and the second being the gaining of insight into the bulk. The latter can, for example, be used in engineering applications to determine energy usage of processes such as dredging.

2 DERIVATION

2.1 Euler scheme

Consider two particles that do not interact with each other at time t_0 and have no history of previous contacts. Then the total energy, assuming zero potential energy, of one particle is given by

$$\mathrm{E}_0 = \mathrm{E}_{\mathrm{kin},0} + \mathrm{E}_{\mathrm{pot},0} = \frac{\mathrm{m}\mathrm{v}_0^2}{2} \,. \tag{1}$$

The numeral subscripts denote the corresponding time step in the following and E_{kin} and E_{pot} are the kinetic and potential energy. v and m denote the velocity and mass of a particle, respectively. The Euler integration scheme reads

$$v_{i+1} = v_i + \frac{\Delta t}{m_i} F(x_i, v_i), \tag{2}$$

$$x_{i+1} = x_i + \Delta t \, v_i, \tag{3}$$

where x represents a particle position, Δt the time step size and $F(x_i, v_i)$ the forces computed based on the respective position and velocity.

Let the particles at time t_1 (with $\Delta t = t_1 - t_0$) interact with each other. The time integration of the velocity can also be written as

$$v_1 = v_0 + \frac{\Delta t\left(F_{e,0} + F_{d,0} + F_{ext,0}\right)}{m} \,, \tag{4}$$

where $F_{e,0}$, $F_{d,0}$ and $F_{ext,0}$ are the elastic, damping and external forces, respectively. The subscript 0 will be dropped for forces until the end of this section. The kinetic energy at t_1 can be written, using Eq. (4), as

$$E_{kin,1} = \frac{m v_1^2}{2} = \frac{m}{2}\left(v_0 + \frac{\Delta t}{m}\left(F_e + F_d + F_{ext}\right)\right)^2 . \tag{5}$$

Expansion of the right-hand side yields

$$E_{kin,1} = \frac{m}{2} v_0^2 + v_0 \Delta t F_e + v_0 \Delta t F_d + v_0 \Delta t F_{ext} + \frac{m}{2}\frac{\Delta t^2}{m^2} F_0^2 \,, \tag{6}$$

where F_0 is the sum of all forces acting on a particle. Shifting all terms from the left to the right, except for the kinetic energy one obtains

$$\frac{m}{2} v_1^2 - v_0 F_e \Delta t - v_0 F_d \Delta t - v_0 F_{ext} \Delta t - \frac{1}{2m} \Delta t^2 F_0^2 = \frac{m}{2} v_0^2 = E_{kin,0} = E_0. \tag{7}$$

Due to conservation of energy it is clear that the right-hand side is equal to E_1, i.e. the total energy of the system at time t_1. A DEM system is generally described using particles with a spring-damper interaction. Thus, the total energy can be split into four components:

$$E_1 = E_{kin,1} + E_{el,1} + E_{d,1} + \mathrm{E}_{\mathrm{pot},1}, \tag{8}$$

where $E_{el,1}$, $E_{d,1}$ and $E_{pot,1}$ are the elastic potential, dissipated and potential energy, respectively. The elastic potential energy E_{el} at time j is in general given by

$$E_{el,j} = -\sum_{i=0}^{j-1} v_{\alpha,i} F_{e,i} \Delta t \,, \tag{9}$$

where $v_{\alpha,i} = \alpha v_{\mathrm{i}+1} + (1-\alpha) v_{\mathrm{i}}$ and $\alpha \in [0,1]$. A similar argument holds for $E_{d,\mathrm{j}}$ and so

the energy budget can be written as

$$E_1 = \frac{m}{2} v_1^2 - v_\alpha F_{e,0} \Delta t - v_\beta F_{d,0} \Delta t - v_\gamma F_{ext} \Delta t. \tag{10}$$

Expanding the velocities yields

$$\begin{aligned} E_1 = \frac{m}{2} v_1^2 &- \alpha v_1 F_e \Delta t - (1-\alpha) v_0 F_e \Delta t \\ &- \beta v_1 F_d \Delta t - (1-\beta) v_0 F_d \Delta t \\ &- \gamma v_1 F_{ext} \Delta t - (1-\gamma) v_0 F_{ext} \Delta t \,, \end{aligned} \tag{11}$$

or

$$\begin{aligned} E_1 = \frac{m}{2} v_1^2 &- v_0 F_e \Delta t - v_0 F_d \Delta t - \mathrm{v}_0 F_{ext} \Delta t \\ &- \alpha (v_1 - v_0) F_e \Delta t - \beta (v_1 - v_0) F_d \Delta t - \gamma (v_1 - v_0) F_d \Delta t. \end{aligned} \tag{12}$$

The previously derived equation for $E_0 = E_1$ (Eq. (7)) can be recast slightly to read

$$\begin{aligned} E_1 = \frac{m}{2} v_1^2 &- v_0 F_e \Delta t - v_0 F_d \Delta t - v_0 F_{ext} \Delta t \\ &- \frac{1}{2m} \Delta t^2 \mathrm{F}_0 F_e - \frac{1}{2m} \Delta t^2 \mathrm{F}_0 F_\mathrm{d} - \frac{1}{2\mathrm{m}} \Delta \mathrm{t}^2 \mathrm{F}_0 \mathrm{F}_\mathrm{ext}. \end{aligned} \tag{13}$$

Equating these two expressions and removing the identical terms yields

$$\begin{aligned} -\frac{1}{2m} \Delta t^2 F_0 F_e - \frac{1}{2m} \Delta t^2 \mathrm{F}_0 F_d - \frac{1}{2m} \Delta t^2 \mathrm{F}_0 F_{ext} = &-\alpha (v_1 - v_0) F_e \Delta t \\ &-\beta (v_1 - v_0) F_d \Delta t \\ &-\gamma (v_1 - v_0) F_{ext} \Delta t. \end{aligned} \tag{14}$$

Since one of these terms scales with F_e and the other with F_d they can be equated separately, i.e.

$$-\frac{1}{2m} \Delta t^2 \mathrm{F}_0 F_e = -\alpha (v_1 - v_0) \mathrm{F}_\mathrm{e} \Delta t. \tag{15}$$

With the applied time integration (Eq. (4)), the left-hand side can be recast into

$$-\frac{1}{2} \Delta t (v_1 - v_0) F_e = -\alpha \Delta t (v_1 - v_0) F_e, \tag{16}$$

showing that

$$\alpha = \frac{1}{2}. \tag{17}$$

An identical argument can be made to demonstrate that

$$\beta = \frac{1}{2} \text{ and } \gamma = \frac{1}{2}. \tag{18}$$

It can now be concluded that the elastic potential energy of the system at time t_1 is given by

$$E_{el,1} = \left(v_0 + \frac{1}{2m} F_0 \Delta t\right) F_{e,0} \Delta t \,. \tag{19}$$

For an arbitrary time t_j the sum over all time steps needs to be taken, yielding, using identical arguments for the all energy types,

$$E_{el,\mathrm{j}} = \sum_{i=0}^{j-1} \left(v_\mathrm{i} + \frac{1}{2m} F_i \Delta t\right) F_{e,i} \Delta t \,,$$

$$E_{d,\mathrm{j}} = \sum_{i=0}^{j-1} \left(v_\mathrm{i} + \frac{1}{2m} F_i \Delta t\right) F_{d,i} \Delta t \,,$$

$$E_{pot,\mathrm{j}} = \sum_{i=0}^{j-1} \left(v_\mathrm{i} + \frac{1}{2m} F_i \Delta t\right) F_{ext,i} \Delta t + E_{pot,0} \,. \tag{20}$$

2.2 Verlet scheme

The most commonly used time integration scheme in LIGGGHTS® is the so-called velocity Verlet scheme, which changes the time integration to

$$v_{i+\frac{1}{2}} = v_i + \frac{\Delta t}{2\, m_i} F\left(x_i, v_{i-\frac{1}{2}}\right), \tag{21}$$

$$x_{i+1} = x_i + \Delta t\, v_{i+\frac{1}{2}}, \tag{22}$$

$$v_{i+1} = v_{i+\frac{1}{2}} + \frac{\Delta t}{2\, m_i} F\left(x_{i+1}, v_{i+\frac{1}{2}}\right). \tag{23}$$

The goal is to extract the energy information at the end of each time step. To achieve this, one time step will be viewed as two half steps for the velocity. This is possible because the energy formulation is independent of the position. As each of these half steps are Euler steps we can reuse the results of the previous section. Due to the similarity of the different energy components only E_{el} will be considered in the following. The change in elastic energy in a full Euler step is given by

$$\Delta E_{el,i-1,i} = E_{el,i} - E_{el,i-1} = \left(v_i + \frac{1}{2m} F_i \Delta t\right) F_{e,i} \Delta t \,, \tag{24}$$

as shown in Eq. (19). For the half Euler step that integrates v_i to $v_{i+1/2}$ the change in elastic energy is thus

$$\Delta E_{el,i,i+\frac{1}{2}} = \left(v_i + \frac{1}{2m} F_i \frac{\Delta t}{2}\right) F_{e,i} \frac{\Delta \mathrm{t}}{2} \,. \tag{25}$$

Similarly, integrating v from time $i + 1/2$ to $i + 1$ yields

$$\Delta E_{el,i+\frac{1}{2},i+1} = \left(v_{i+\frac{1}{2}} + \frac{1}{4m} F_{i+1} \Delta t\right) F_{e,i+1} \frac{\Delta \mathrm{t}}{2} \,. \tag{26}$$

Thus, the change of elastic energy over the full Verlet time step becomes

$$\Delta E_{el,i,i+1} = \left(v_i + \frac{1}{4m} F_i \Delta t\right) F_{e,i} \frac{\Delta t}{2} + \left(v_{i+\frac{1}{2}} + \frac{1}{4m} F_{i+1} \Delta t\right) F_{e,i+1} \frac{\Delta t}{2}. \tag{27}$$

Consequently, the energies at a time step j, for all different energy types considered, are given by

$$E_{el,\mathrm{j}} = \sum_{i=0}^{j-1} \left(v_i + \frac{1}{4m} F_i \Delta t\right) F_{e,i} \frac{\Delta t}{2} + \left(v_{i+1/2} + \frac{1}{4m} F_{i+1} \Delta t\right) F_{e,i+1} \frac{\Delta t}{2},$$

$$E_{d,\mathrm{j}} = \sum_{i=0}^{j-1} \left(v_i + \frac{1}{4m} F_i \Delta t\right) F_{d,i} \frac{\Delta t}{2} + \left(v_{i+1/2} + \frac{1}{4m} F_{i+1} \Delta t\right) F_{d,i+1} \frac{\Delta t}{2},$$

$$E_{pot,\mathrm{j}} = \sum_{i=0}^{j-1} \left(v_i + \frac{1}{4m} F_i \Delta t\right) F_{ext,i} \frac{\Delta t}{2} + \left(v_{i+1/2} + \frac{1}{4m} F_{i+1} \Delta t\right) F_{ext,i+1} \frac{\Delta t}{2} + E_{pot,0}\,. \tag{28}$$

3 DEM MODELS

In Section 4, several example simulations will be shown using the DEM models described in the following. The model responsible for the normal force is the standard Hertz-Mindlin [D04] model which is given as

$$F_e = \frac{4}{3} Y^* \sqrt{\|\delta_{ij}\| \, r_{ij}^*}\, \delta_{ij}\,, \tag{29}$$

$$F_d = -2 \sqrt{\frac{5}{6}} \beta \sqrt{S_n m^*}\, v_{ij,n} n_{ij}, \tag{30}$$

where Y^*, r_{ij}^* and m^* are the effective Young's modulus, radius and mass, δ_{ij} (> 0) and n_{ij} the distance and normal vector between the contact points, $v_{ij,n}$ the relative normal velocity and

$$\beta = \frac{\ln(e)}{\sqrt{\ln(e)^2 + \pi^2}}\,, \tag{31}$$

with e being the coefficient of restitution. Finally,

$$S_n = 2\, Y^* \sqrt{r_{ij}^* \|\delta_{ij}\|}\,. \tag{32}$$

The tangential model is the simplistic "no history" model [5], which assumes no spring in tangential direction, i.e. $F_e = 0$, giving only a contribution to the tangential dissipative force via

$$F_d = -2 \sqrt{\frac{5}{6}} \beta \sqrt{S_t m^*}\, \left(v_{ij} - v_{ij,n} n_{ij}\right), \tag{33}$$

where

$$S_t = 8\, G^* \sqrt{r_{ij}^* \|\delta_{ij}\|}\ , \tag{34}$$

and G^* is the effective shear modulus. Similarly, the lubrication model [6] also only defines a dissipative force given as

$$F_d = -\,6\,\pi\,\mu \frac{r_{ij}^2}{\|\delta_{ij}\|} v_{ij,n}\ , \tag{35}$$

where μ is the fluid viscosity and r_{ij} is the harmonic mean between the two particle radii. This force is active only if $\frac{2\,r_{ij}}{1000} < \|\delta_{ij}\| < 2\,r_{ij}$.

The bond model [7] is a combination of a normal and tangential spring-damper system that acts, even if overlaps are smaller than zero. The elastic force in normal direction is given as

$$F_e = k_n A \left(r_0 - x_{ij}\right), \tag{36}$$

where r_0 is the initial particle distance upon bond creation, x_{ij} is the distance between the particle centers, k_n the normal bond stiffness parameter and A the beam area, dependent on the beam radius which is a user defined multiple of the minimum particle radius. The elastic force in tangential direction is incrementally defined as

$$F_{e,i} = F_{e,i-1} + k_t\, A \left(v_{ij} - v_{ij,n} n_{ij}\right) \Delta t\ , \tag{37}$$

where k_t is the tangential bond stiffness parameter. Instead of using a traditional damping mechanism based on the velocity, a dissipative model is used. It reduces the elastic force in normal and tangential direction each time-step, i.e.

$$F_{e,i} = F_{e,i} \left(1 - \frac{\Delta t}{\Delta t_d}\right), \tag{38}$$

where Δt_d is the dissipation time scale and it should be noted that r_0 is adapted in normal direction, to reflect this dissipation. The dissipative force is then given as

$$F_d = F_{e,i} \frac{\Delta t}{\Delta t_d}\ . \tag{39}$$

Finally, care must be taken when contacts end, e.g. bonds are broken, as in that case the elastic potential is instantaneously converted into dissipated energy.

4 DEMONSTRATION

In the following a few basic test cases are shown, demonstrating the exactness of the developed formulae.

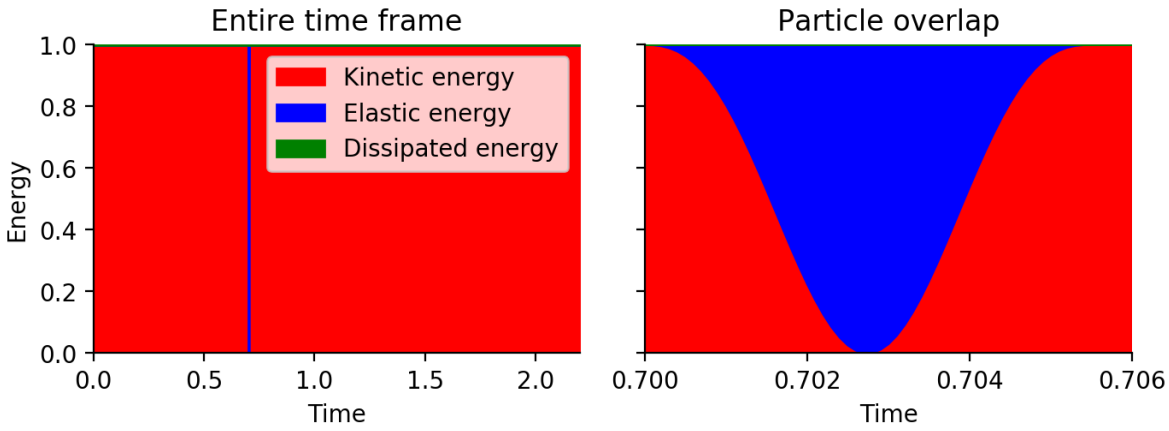

***Figure 1**: Energy balance for the normal contact of two particles*

4.1 Normal contact

In this case two particles of identical radius r and mass m are placed $2.2\,r$ apart. Their initial velocity is identical, except for the orientation. The coefficient of restitution is 1.0, i.e. no damping takes place and only the Hertz-Mindlin normal model will be active. In the following, all velocities and time scales are normalized with the initial particle velocity and radius. Figure 1 shows the kinetic, elastic and dissipated energy components over time. While the left pictures shows the whole time frame, the right shows the short period where the two particles overlap, i.e. when the normal model is active. It can be seen that the entire kinetic energy is converted to elastic energy until the point of maximum overlap. Afterwards, the the spring relaxes and the particles return to their original kinetic energy. Due to no damping, the dissipated is expected to remain zero. However, the elastic potential at the end of the contact is approximately 10^{-7}, showing that this model does not conserve energy perfectly. As this remaining elastic energy is dependent on the time step size it is clear that a numerical error is at the core of this mismatch. Similar behaviour was observed by [8]. Note that this does not

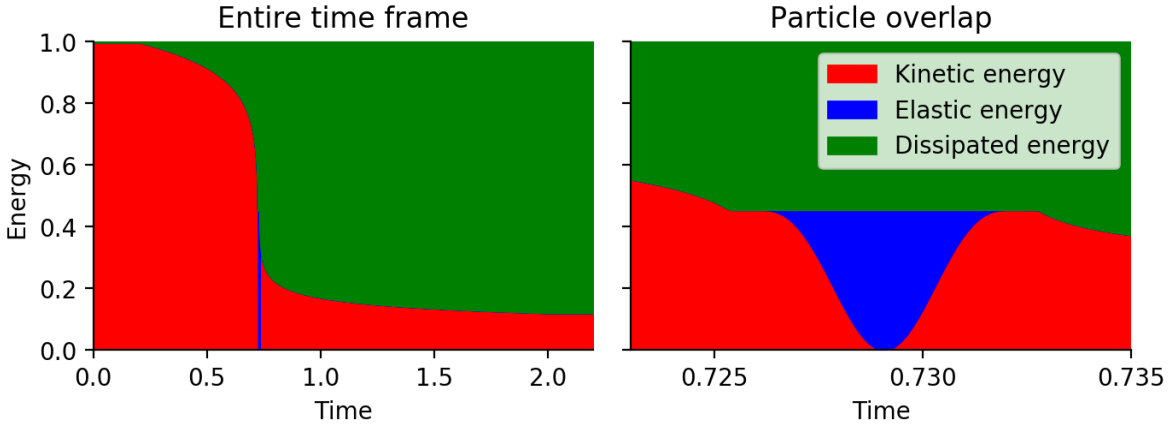

Figure 2: Energy balance of a particle contact using a lubrication model

change the present energy computation as this remaining elastic energy gets assigned to the dissipated energy value. Thus, it should be appreciated that the dissipated energy contains energy from both physical as well as numerical dissipation.

4.2 Normal contact with lubrication

The setup is identical to the previous case, except for the additional activation of the lubrication model. Compared to Figure 1, Figure 2 now shows the clear influence of the dissipation model, which significantly removes kinetic energy from the system. There is also a brief overlap of the particles, which is shown in detail in the right-hand-side figure. The brief constant areas of dissipation before the actual contact show the cut-off value of the lubrication model.

4.3 Bonded particles

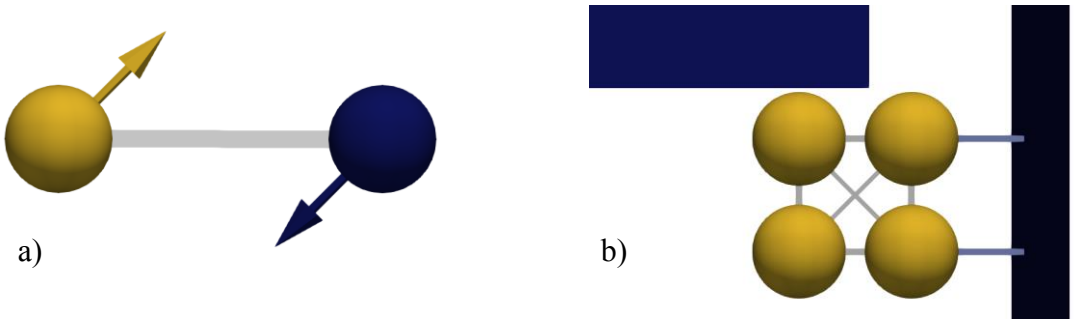

Figure 3: a) Setup of bonded particle case; b) Setup of case with bonded particles impacted by a wall

The setup for this case is similar to the one in Section 4.1. This time the bond model, including dissipative terms, is activated and the particles have a relative tangential velocity, which causes them to rotate. Figure 3a shows the initial state of the simulation with established bond. While rotations have not been treated in the derivation above, the extension is straightforward to include the angular kinetic energy and torques. The initial tangential

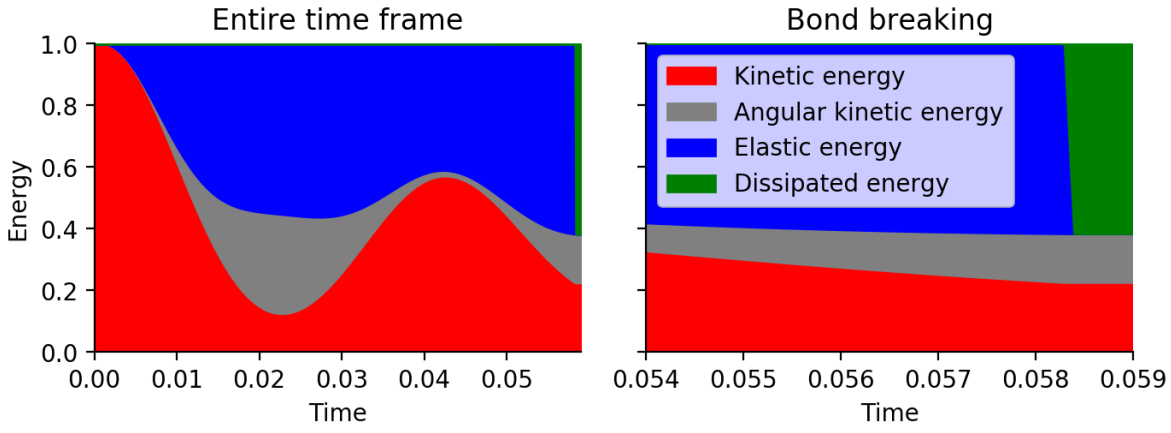

Figure 4: Energy balance of two bonded particles

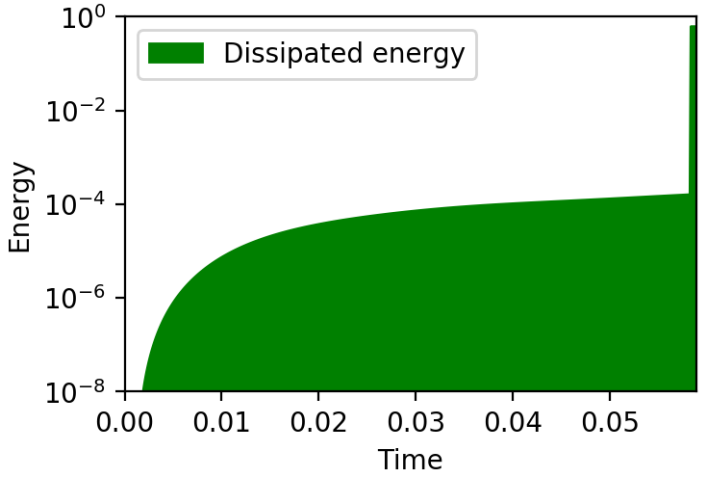

Figure 5: Dissipated energy during the interaction of two bonded particles

movement of the two particles causes the bond beam to rotate and induce an angular kinetic energy into the system as shown in Figure 4. The bond is designed such that the particles break when their distance is 1% larger than the initial distance. This is shown in detail on the right-hand-side of Figure 4, where the instantaneous conversion from elastic to dissipated energy takes place, followed by constant kinetic energies. Even though the dissipation model is active the effect during the time when the particles are bonded is rather low. Figure 5 shows the dissipated energy in a lin-log plot to demonstrate the effect of the model.

4.4 Bonded wall impact

The setup for this case can be seen in Figure 3b. Two particles are bonded with the right wall and the four particles are interconnected with bonds that can break if a stress magnitude is exceeded. The wall on the top left is a solid object with an initial velocity that has the freedom to accelerate in movement direction. Figure 6 shows the only 2 % of the total energy, as the kinetic energy of the wall fills the remainder. The light blue and green parts show the

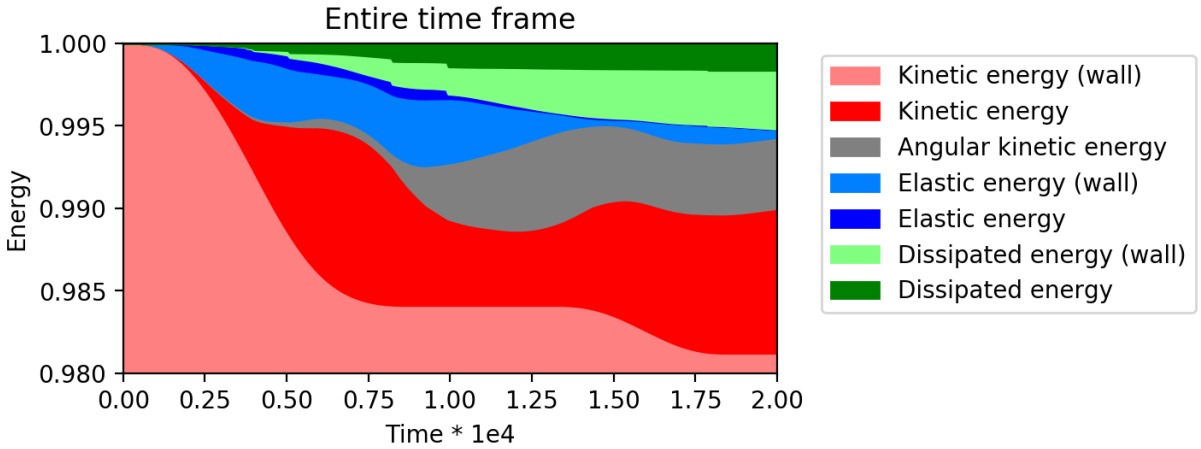

Figure 6: Energy balance during the impact of a wall onto bonded particles

elastic and dissipated energy between particle-wall contacts, whereas the dark ones show the associated energies for the particle-particle contacts. The jumps in elastic energy clearly show the breaking of the particle-particle bonds and the dissipated energy between wall and particles show the large damping occurring between the two. It should be noted that for all the calculations performed in Section 4 the total energy is preserved up to numerical epsilon.

5 CONCLUSION

The discrete element method mostly uses spring damper systems to represent different physical particle-particle and particle-wall interactions. In this paper, the equations for the energy balance of such systems was described for standard Euler integration and velocity Verlet schemes. It was shown that the use of the correct velocity needs to be used in order to guarantee energy conservation. The developed formulae were then applied to standard DEM models, showing their practical applicability. Finally, four different test cases were shown to demonstrate the validity of the developments. The last case exhibited 7 different energy types when a wall collided with four bonded particles.

The analysis of such a complex interplay in real-world applications will allow to gain further insight into the mechanics of particle systems. Examples are all types of particle-solid interactions, such as a stone impacting the seabed or the energy required to dredge the seabed. Additionally, the energies can be used as input into other models, e.g. the dissipated energy as source term for heat-conduction models. The test case with only a normal model has also shown that the present formulation allows to identify potential numerical energy losses in DEM models. This can allow model reformulations or development of correction terms.

REFERENCES

[1] P. A. Cundall and O. D. L. Strack, “A discrete numerical model for granular assemblies,” Géotechnique, vol. 29, no. 1, pp. 47–65, Mar. 1979.

[2] S. Luding, E. Clément, A. Blumen, J. Rajchenbach, and J. Duran, “Anomalous energy dissipation in molecular-dynamics simulations of grains: The ``detachment'' effect,” Phys. Rev. E, vol. 50, no. 5, pp. 4113–4122, Nov. 1994.

[3] B. N. Asmar, P. A. Langston, A. J. Matchett, and J. K. Walters, “Energy monitoring in distinct element models of particle systems,” Advanced Powder Technology, vol. 14, no. 1, pp. 43–69, Feb. 2003.

[4] S. Siiriä and J. Yliruusi, “Particle packing simulations based on Newtonian mechanics,” Powder Technology, vol. 174, no. 3, pp. 82–92, May 2007.A. Di Renzo and F. P. Di Maio, “Comparison of contact-force models for the simulation of collisions in DEM-based granular flow codes,” Chemical Engineering Science, vol. 59, no. 3, pp. 525–541, Feb. 2004.

[5] A. Di Renzo and F. P. Di Maio, “Comparison of contact-force models for the simulation of collisions in DEM-based granular flow codes,” Chemical Engineering Science, vol. 59, no. 3, pp. 525–541, Feb. 2004.

[6] W. Zhang, R. Noda, and M. Horio, “Evaluation of lubrication force on colliding particles for DEM simulation of fluidized beds,” Powder Technology, vol. 158, no. 1–3, pp. 92–101, Oct. 2005.

[7] D. O. Potyondy and P. A. Cundall, “A bonded-particle model for rock,” International

Journal of Rock Mechanics and Mining Sciences, vol. 41, no. 8, pp. 1329–1364, Dec. 2004.

[8] D. Zhang and W. J. Whiten, “An efficient calculation method for particle motion in discrete element simulations,” Powder Technology, vol. 98, no. 3, pp. 223–230, Aug. 1998.

Film Formations of Aggregates Due to Lateral Capillary Forces

Mark Doran[1]*, Paul Dastoor[2], Murray Sciffer[2] and Roberto Moreno-Atanasio[1]

[1] School of Engineering,
The University of Newcastle, Callaghan
New South Wales 2308, Australia
*e-mail: mark.doran@uon.edu.au

[2] School of Mathematics and Physical Sciences
The University of Newcastle, Callaghan
New South Wales 2308, Australia

Key words: DEM, lateral capillary forces, self-organisation, film formation binary dispersed.

Abstract. The lateral capillary force is of significant importance in liquid film coating processes [1]. This force, for particles much smaller than the capillary length, decays with the inverse of the separation distance between particles centres and is, thus, considered a long-range force [2]. In this paper, we study the role of this long-range force on the final structure of a film containing partially submerged nanoparticles.

We have used computer simulations based on Discrete Element Method (DEM) to investigate film formation of mono and binary disperse particle systems. The particle radii were 80 nm, 100 nm, and 120 nm with combinations of these particle sizes for the binary disperse system. To determine the nearest neighbours for the calculation of the lateral capillary force a Delaunay Triangulation method was used. The surface coverage of the partially submerged particles was 0.05, which coincides with a parallel experimental research. The forces included in the model are the lateral and vertical capillary forces, Brownian motion, contact forces, van der Waals attraction, fluid drag and hydrodynamic resistance. The structure of the aggregates formed was compared using three parameters, the isotropic ordering factor, non-dimensional boundary length and the pair (radial) correlation function.

The simulation results show that particles self-organise into isotropic aggregates due to lateral capillary forces. Particle size was shown to have little effect on final aggregate structures. Binary disperse systems were shown to have less ordered structures when compared to monodisperse systems as suggested by the decrease in peak sharpness of the pair correlation function. Increasing the particle size gap resulted in less ordering in the binary systems.

1 Introduction

Lateral capillary forces play an important role in the self-assembly of partially immersed particles. By being able to control the lateral capillary forces it is possible to form complex structures such as hexagonal packing [1,3]. Bowden et al [4] used lateral capillary forces between hexagonal particles floating on liquid surfaces to form a range of structures depending on the wetting of the hexagon faces. Similarly, the aim of this work is to harness the strength of lateral capillary forces that exist between organic nanoparticles to optimise the film structure of organic photovoltaic layers, which can affect the device efficiency [5–7].

Lateral capillary forces occur between particles partially immersed in a liquid. Lateral capillary forces are due to deformation of the liquid surface meniscus and has been studied both experimentally and theoretically [2,8–14]. Bragg and Nye [15] experimentally used capillary interaction forces to create two-dimensional arrays of bubbles floating on the surface of a soap solution. The crystal structures were used to compare the defects in the bubble arrays to defects in metallic lattices. The first attempt to quantitatively describe the capillary force

between bubbles floating on a liquid surface was by Nicholson [16], which was valid for bubbles less than 3 mm where a linearised solution to the Young-Laplace equation is valid.

The capillary force has been studied for many different geometries, such as floating horizontal cylinders [17], flat plates [18,19], vertical cylinders [19], spheres [19], particles and walls [8,14,19] and cubes [20]. The capillary force is different for each of these due to the solution of the Young-Laplace equation being geometry dependent. A detailed review of capillary forces can be found in Ref [21].

The Lattice Boltzmann numerical method has also been used to study lateral capillary forces [22,23], as well as several discrete element method (DEM) models [1,3,24,25]. Maenosono et al. [24] showed that over time particles, with diameters of 55 nm and 155 nm, form a cluster of hexagonal packing. They also found the presence of point defects, which occur is consistent their experimental research [26]. Nishikawa et al. [25] showed the formation of chain like structures at lower particle coverage, while at high coverage domains of hexagonal close packing were formed.

Fujita et al. [3] include other interparticle forces in their simulations. They showed that during evaporation the magnitude of the capillary, Brownian, electrostatic and van der Waals change and hence the concluded that all these forces played an important role on the self-ordering of particles. Depending on the magnitude of these forces three types of structures were formed; isotropic crystals, non-isotropic aggregates and isotropic arrangements. Due to the computational time required to determine the lateral capillary force Uzi, Ostrovski & Levy [1] developed a new model to calculate the capillary force which did not require the calculation of the liquid surface deformation directly. They found that particle size did not affect the final structures obtained.

This paper uses a DEM model to investigate the lateral capillary force on film formation. The previously mentioned DEM models [1,3,24] simulate similar systems with monodisperse particles. It is our intention to investigate the influence of particle size on the film formation due to lateral capillary forces. The simulations consists of binary dispersed particles systems and compare these to monodisperse systems. An important difference with previous studies in the literature is the use of binary particle distributions. These type of studies have never been carried out in the past.

2 Methodology

2.1 Discrete Element Method

DEM is a numerical computational technique that uses Newton's second law of motion to describe the motion of individual particles. This method was first developed by Cundall and Strack to study the motion of rocks [27]. The motion equation used in our computational model involves capillary forces, Brownian motion, contact forces, short range attractive forces, drag and hydrodynamic resistance. The motion equation is given by

$$m\frac{d\vec{r}^2}{dt^2} = \vec{F}_{cap} + \vec{F}_{brw} + \vec{F}_{cont} + \vec{F}_{vdw} + \vec{F}_{drag} + \vec{F}_{hyd} \quad (1)$$

where m is the mass, $\vec{r}$ is the displacement, t is time and $\vec{F}$ is the external force. The subscripts cap, brw, cont, vdw, drag and hyd refer to capillary forces, Brownian motion, contact forces, van der Waals interactions, fluid drag and hydrodynamic resistance respectively.

The capillary force is decomposed into vertical and lateral capillary directions. The vertical capillary force is given by Equation 2 [28].

$$\vec{F}_{vcap} = -2\pi\gamma R\sin(\theta)\sin(\theta+\varphi) \quad (2)$$

where γ is the surface tension, R is the particle radius, θ is the contact angle and ψ is the filling wetting angle.

The lateral capillary force is given by Equation 3 [29].

$$\vec{F}_{lcap} = 2\pi\gamma Q_i Q_j q K_1(qL) \quad (3)$$

where Q_i is the capillary charge $Q_i = r_i \sin(\varphi_i)$, q is the inverse of the capillary length $q=\sqrt{\frac{\rho g}{\gamma}}$, K_1 is the modified Bessel function of the second kind and L is the lateral distance between particle centres. An asymptotic solution valid when qL>>1 can be used to avoid computation of the modified Bessel function which reduces to Equation 3 to Equation 4 [14].

$$\vec{F}_{lcap} = \frac{2\pi\gamma Q_i Q_j q}{L} \quad (4)$$

The Brownian motion is given by a normal distribution with a mean of 0 and a standard deviation given by Equation 5 [30].

$$\sigma_{brw} = \sqrt{\frac{12\pi k_B T \mu R}{\Delta t}} \quad (5)$$

where k_B is the Boltzmann constant, T is temperature, μ is the liquid viscosity and Δt is the time step.

The contact is modelled by a linear spring dashpot, given by Equation 6 [27].

$$\vec{F}_{cont} = -k_p \delta_{n,} - 2\beta \vec{v}_n \sqrt{m_{ij}\, k_p} \quad (6)$$

where k_p is the spring coefficient, δ_n is the normal overlap, β is the damping coefficient and $\vec{v}_n$ is the normal velocity.

The van der Waals force is given by Equation 7 [31].

$$\vec{F}_{vdw} = \frac{AR_{ij}}{6d^2} \quad (7)$$

where A is the Hamaker constant, R_{ij} is the reduced radii and d is the separation distance between particle surfaces.

The drag force is modelled with stokes drag in Equation 8.

$$\vec{F}_{drag} = -6\pi\mu R\vec{v} \quad (8)$$

The hydrodynamic resistance is given by Equation 9 [32].

$$\vec{F}_{hyd} = -6\pi\mu \frac{R_{ij}^2}{d} \overrightarrow{v_n} \quad (9)$$

2.2 Screening of the lateral capillary force

The lateral capillary force decays with the inverse of the separation distance between particle centres as given by Equation 4 and can be dominant up to many particle radii as it is a long range force. This aspect makes the calculation of the force numerically expensive due to a large neighbour search range. Further complications occur due to the nature of the lateral capillary force. For other long range forces such as the electrical double layer, the total force on any given particle can be approximated using an Ewald summation [33].

The lateral capillary force occurs only between particles that are within the line of sight of each other and so techniques to scan and calculate other long range forces aren't able to be used. Several authors have studied different screening methods [1,3,24,25,34]. These screening methods attempt to scale the capillary force by a ratio, which is dependent on the fraction of neighbouring particles that are within direct line of sight. Then, the nearest neighbours are selected by a cut-off distance with a Vertlet list constructed.

To determine the nearest particles for the lateral capillary force a Delaunay triangulation of particles at the liquid surface was computed. The neighbours are formed from the Delaunay triangulation and the particles are screened using the screening methods in [1].

2.3 Characterisation of the particle aggregates

To quantify the structures that the particles form, three parameters have been used. The isotropic ordering factor (IOF), non-dimensional boundary length (NBL) and the pair (radial) correlation function. The IOF is the ratio of equilateral triangles to the total number of triangles from the constructed Delaunay triangulation. This parameter provides information about the isotropy of the system. The NBL is the ratio of the boundary length of the aggregate compared to the boundary length of a hexagonal packed structure and can be calculated by Equation 10 [3].

$$NBL = \frac{1}{6n}\sum_{k=0}^{6}(6-k)N(k) \tag{10}$$

where n is the number of particles, k is the coordinate number and N(k) is the number of particles with a coordinate number of k.

The IOF is close to 0 for a randomly distributed particle clusters and increases as the clusters become more hexagonally close packed (HCP), with a value of 1 for HCP. The NBL is equal to 1 when the system is randomly dispersed with no particle-particle contacts, and as the particles aggregate the value of the NBL drops reaching 0 when the system is HCP [3].

The pair correlation function g(r), is developed from creating a histogram with particle neighbours separation distance and normalised by Equation 11 [35].

$$g(r) = \frac{1}{N}\sum_{i=1}^{N}\frac{A_0 n_i(r)}{\pi(\delta r^2 + 2r\delta r)} \tag{11}$$

where N is the number of particles, A_0 is the average area per particle, $n_i(r)$ is the number of particles in the interval [r, r+δr]. The pair correlation function can be used to determine the degree of ordering for particle domains [35].

2.4 Simulation Parameters

The particles were initially randomly distributed with a surface coverage of 0.05 (2-D packing). The particle radii were 80 nm, 100 nm and 120 nm, with binary dispersed systems consisting of a combination of these particle sizes. Table 1 lists the simulation parameters.

Table 1: Simulation Parameters.

Parameter	Value	Unit
Number of particles	2000	
Temperature	25	°C
Particle density	1250	kg/m^3
Hamaker constant	1×10^{-20}	J
Spring coefficient	1.0	N/m
Restitution coefficient	0.5	
Time step	1×10^{-10}	s
Liquid density	1000	kg/m^3
Liquid viscosity	1.0	mPa s

3 Results

Figure 1 shows the time evolution of the IOF and NBL for the monodisperse systems with radii of 80 nm, 100 nm and 120 nm. The IOF and NBL start at 0 and 1, respectively, as the particles are randomly dispersed with no contacts. During the first micro second of simulations, the change in the IOF and NBL were very fast with the IOF decreasing and the NBL increasing as time progressed. This clearly suggests that the particles were self-organising due to the lateral capillary force. After this sharp initial change in the IOF and NBL, the rate slows until

the particles are self-organised into one or more large aggregates. The final structure was a crystalline lattice as the final IOF was high while the final NBL was low as suggested by [3]. The final values of IOF and NBL are similar for each particle size suggesting that the particle size has little influence on the self-organisation process, which was also shown by [1]. Further the final value of IOF for all three cases is close to 1, which indicates the crystal shows good isotropic ordering. The difference in time reaching an equilibrium state was due to a larger capillary force between larger particles.

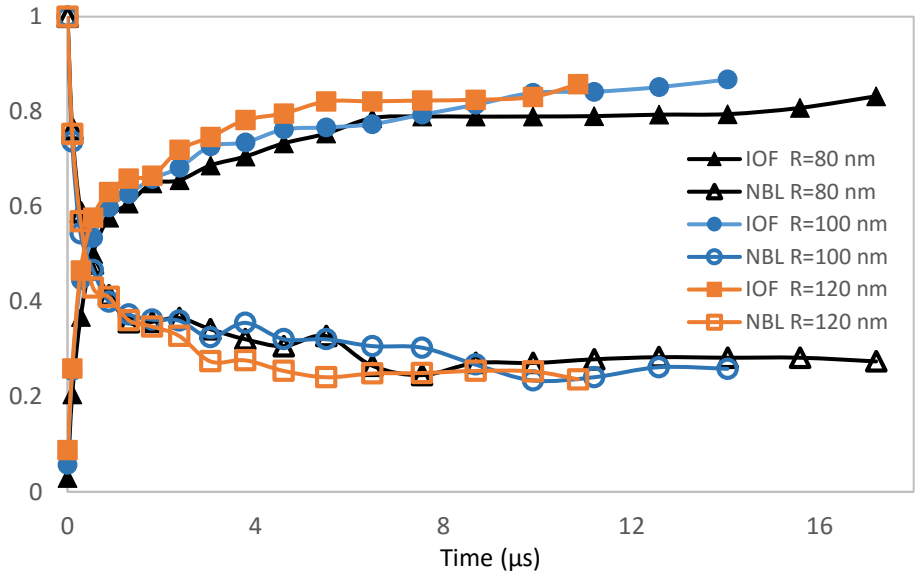

Figure 1: IOF and NBL for monodisperse systems with particle radii of 80, 100 and 120 nm.

The IOF and NBL for the binary particle distribution with particle radii of 80 nm and 100 nm is shown in Figure 2. The trends of the binary particle systems are consistent with the monodisperse systems (Figure 1). There was however little difference between the IOF and NBL of the three binary dispersed systems, despite a visually observable difference in crystalline structure. Therefore, the results for the other three cases have been omitted.

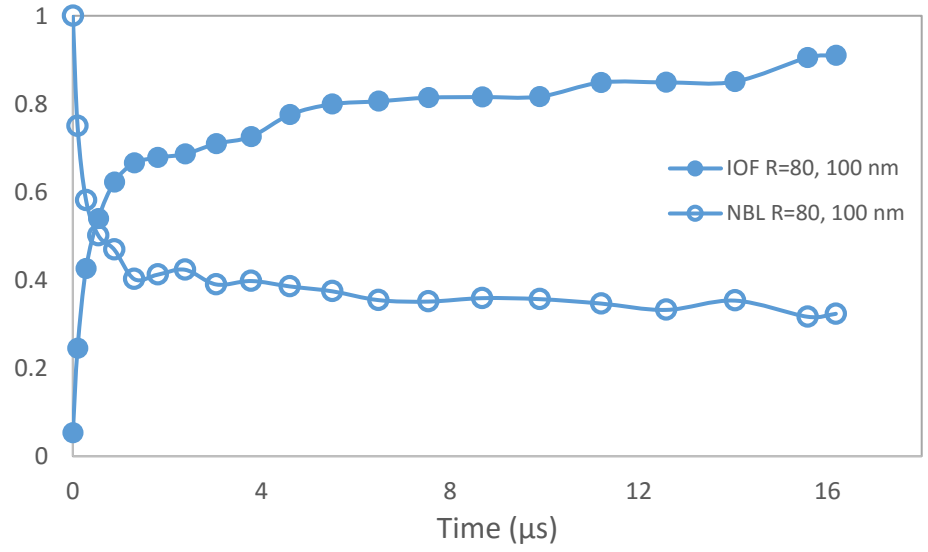

Figure 2: IOF and NBL for binary disperse system with particle radii of 80 and 100 nm.

In order to be able to compare the binary with the monodispersed systems the pair correlation function was used. The pair correlation function of the final structure for the 100 nm particle radii simulation is plotted in Figure 3. The distance is normalised by the particle diameter. The sharp peak at g(r) 1 signifies the particles nearest neighbours. The two peaks between 1.5 and 2 are consistent with a HCP structure, similar to the peaks between 2.5 and 3. The sharpness of these peaks show that the structure has some degree of ordering, consistent with a value of IOF close to 1. The pair correlation for the monodisperse systems with 80 nm and 100 nm particle radii were very similar and omitted due to no observable differences.

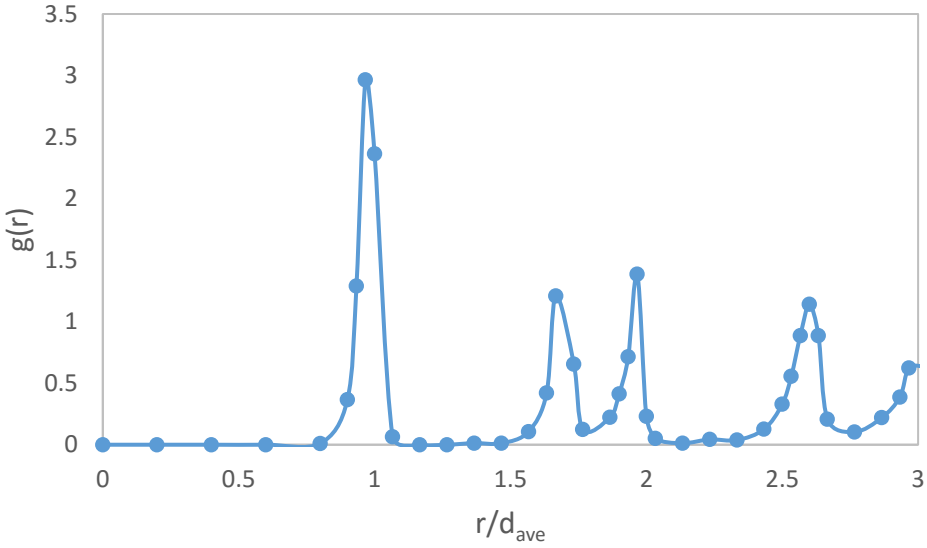

Figure 3: Pair correlation function for monodisperse system with particle radii of 100 nm.

The pair correlation functions plotted in Figure 4a-c are binary systems with particle radii 80-100 nm, 100-120 nm and 80-120 nm respectively, the particle separation distance was normalised by the average radius of particles. The systems with 80-100 nm and 100-120 nm particle radii have the same particle distribution gap of 20 nm. Their pair correlation functions were also similar, further showing that particle size had little effect on the final structures. For Figure 4a-c g(r) had 3 distinct peaks at around a dimensionless distance of 1. However, the monodisperse systems only shown 1 peak. The first of these peaks represent neighbours of the two smaller particle sizes, the middle between the small and large particle and the third between two of the larger particles.

The subsequence dual peaks observed in Figure 3 (monodisperse system) are not present in Figure 4a-c, which signifies a more ordered structure for the monodisperse systems. Figure 4c shows the results for the 80-120 nm binary system, which has a larger particle size distribution of 40 nm. The lack of peaks after the multiple peak around 1 when compared to Figure 4a-b indicates that the difference in particle sizes in binary systems impact the final ordering. Therefore, a narrower size distribution or monodisperse system produces a more ordered structure.

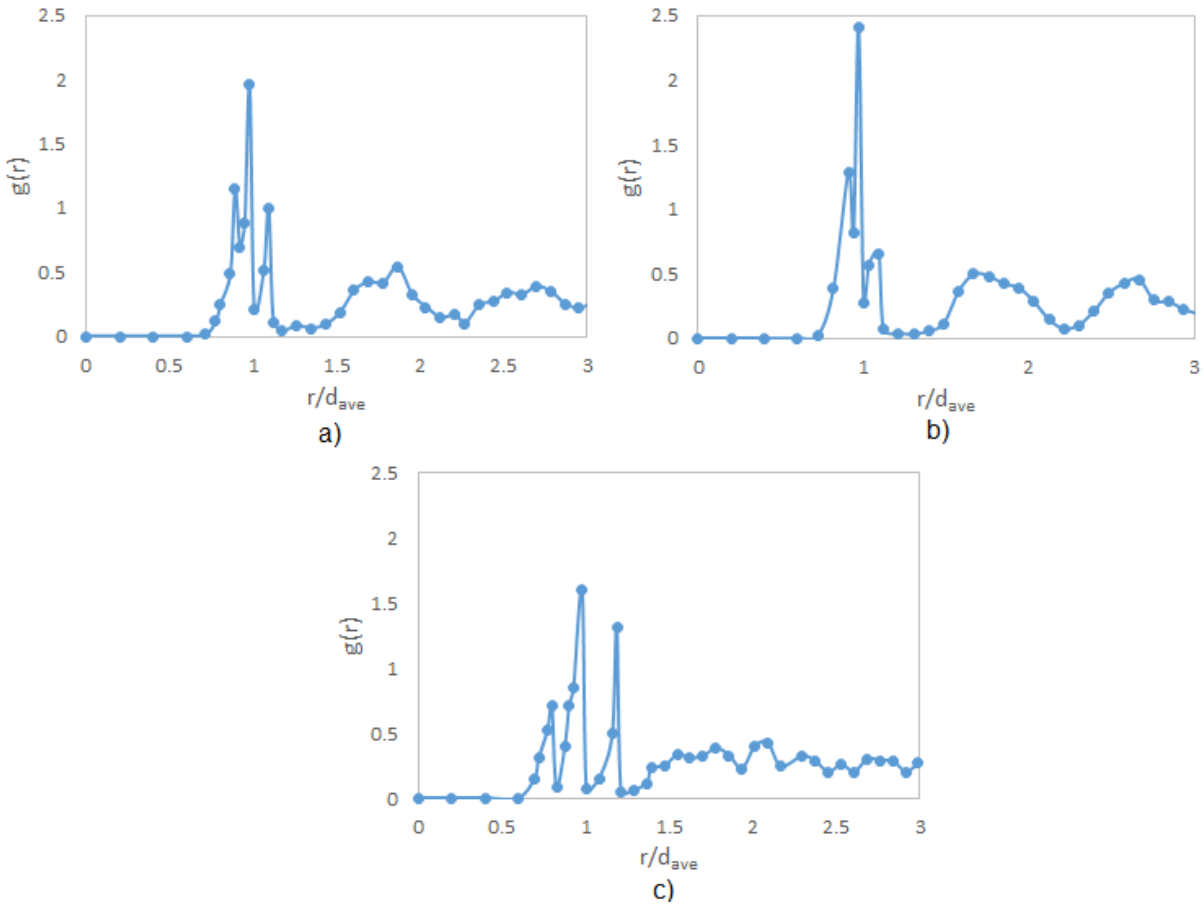

Figure 4: Pair correlation functions for the binary disperse system; a) particle radii of 80 and 100 nm, b) particle radii of 100 and 120 nm and c) particle radii of 80 and 120 nm.

4 Conclusion

The influence of particle size and particle distribution on the self-organisation of partially immersed nanoparticles in a thin liquid film due to lateral capillary forces was investigated using DEM simulations. The particles were found to form isotropic crystal aggregates, with domains of hexagonal packing. The size of particles in the mono and binary dispersed systems was shown to have little effect on the final crystal structure. The binary dispersed systems were found to have less ordered structures when compared to the monodisperse systems. Increasing the particle distribution gap in the binary dispersed system resulted in a less ordered crystalline structure.

5 References

[1] Uzi, A. Ostrovski, Y. and Levy, A. Modeling and simulation of particles in gas-liquid interface. *Adv. Powder Technol.* (2016) **27:** 112–123.

[2] Velev, O.D. Denkov, N.D. Paunov, V.N. Kralchevsky, P.A. and Nagayama, K. Direct Measurement of Lateral Capillary Forces. *Langmuir* (1993) **9:** 3702–3709.

[3] Fujita, M. Nishikawa, H. Okubo, T. and Yamaguchi, Y. Multiscale Simulation of Two-Dimensional Self-Organization of Nanoparticles in Liquid Film. *Jpn. J. Appl. Phys.* (2004) **43:** 4434–4443.

[4] Bowden, N. Choi, I. S. Grzybowski, B. A. Whitesides, G. M. and Street, O. Mesoscale Self-Assembly of Hexagonal Plates Using Lateral Capillary Forces : Synthesis Using the ‘ Capillary Bond ’. *J. Am. Chem. Soc.* (1999) 5373–5391.

[5] Harris, C. J. Belcher, W. J. and Dastoor, P. C. Effect of film thickness and morphology on the performance of photoelectrochemical cells based on poly(terthiophene). *Sol. Energy Mater. Sol. Cells* (2007) **91:** 1127–1136.
[6] Krebs, F. C. Fabrication and processing of polymer solar cells: A review of printing and coating techniques. *Sol. Energy Mater. Sol. Cells* (2009) **93:** 394–412.
[7] Ulum, S. *et al.* Determining the structural motif of P3HT:PCBM nanoparticulate organic photovoltaic devices. *Sol. Energy Mater. Sol. Cells* (2013) **110:** 43–48.
[8] Paunov, V.N. Kralchevsky, P.A. Denkov, N.D. Ivanova, L.B. and Nagayamab, K. Capillary meniscus interaction between a microparticle and a wall. *Colloids and Surfaces*. (1992) **67:** 119–138.
[9] Dushkin, C.D. Yoshimura, H. and Nagayama, K. Direct Measurement of Nanonewton Capillary Forces. *J. Colloid Interface Sci.* (1996) **181:** 657–660.
[10] Leonardo, R.Di Saglimbeni, F. and Ruocco, G. Very-Long-Range Nature of Capillary Interactions in Liquid Films. *Physical Review Letters.* (2008) **100:** 106103,1–4.
[11] Allain, C. and Cloitre, M. Intersection between Particles Trapped at Fluid Interfaces I. Free-Energy Analysis of the Interaction between Two Horizontal Cylinders. *J. Colloid Interface Sci.* (1993) **157:** 269–277.
[12] Allain, C. and Cloitre, M. Intersection between Particles Trapped at Fluid Interfaces II. Exact and Asymptotic Solutions for the Force between Two Horizontal Cylinders. *J. Colloid Interface Sci.* (1993) **157:** 261–268.
[13] Fortes, M. A. Attraction and repulsion of floating particles. *Can. J . Chem.* (1982)
[14] Kralchevsky, P. A. and Nagayama, K. Capillary Forces between Colloidal Particles. *Langmuir* (1994) **10:** 23–36.
[15] Bragg, L. and Nye, J.F.A. Dynamical Model of a Crystal Structure. *Proc. R. Soc. London. Ser. A. Math. Phys. Sci.* (1947) **190:** 474 LP-481.
[16] Nicolson, M. The interaction between floating particles. *Math. Proc. Cambridge Philos. Soc.* (1949) **45:** 288–295.
[17] Gifford, W.A. and Scriven, L.E. On the attraction of floating particles. *Chem. Eng. Sci.* (1971) **26:** 287–297.
[18] Saif, T.A. On the capillary interaction between solid plates forming menisci on the surface of a liquid. *J. Fluid Mech.* (2002) **473:** 321–347.
[19] Yuan, J. and Cho, S.K. Cheerios Effect and its Control by Contact Angle Modulation. in *Advances in Contact Angle, Wettability and Adhesion* (ed. Mittal, K. L.) Wiley, (2015).
[20] Gautam, A. and Jameson, G.J. The capillary force between a bubble and a cubical particle. *Miner. Eng.* (2012) **36–38:** 291–299.
[21] Kralchevsky, P.A. and Nagayama, K. Capillary interactions between particles bound to interfaces , liquid films and biomembranes. *Advances in Colloid and Interface Science.* (2000) **85:** 145–192.
[22] Shinto, H. Komiyama, D. and Higashitani, K. Lateral Capillary Forces between Solid Bodies on Liquid Surface: A Lattice Boltzmann Study. *Langmuir.* (2006) **22:** 2058–2064.
[23] Shinto, H. Komiyama, D. and Higashitani, K. Lattice Boltzmann study of capillary forces between. *Adv. Powder Technol.* (2007) **18:** 643–662.
[24] Maenosono, S. Dushkin, C. D. Yamaguchi, Y. Nagayama, K. &andTsuji, Y. Effect of growth conditions on the structure of two-dimensional latex crystals: modeling. *Colloid Polym. Sci.* (1999) **277:** 1152–1161.
[25] Nishikawa, H. Maenosono, S. Yamaguchi, Y. and Okubo, T. Self-assembling process of colloidal particles into two-dimensional arrays induced by capillary immersion force: A simulation study with discrete element method. *J. Nanoparticle Res.* (2003) **5:**

103–110.
[26] Dushkin, C.D. Lazarov, G.S. Kotsev, S.N. Yoshimura, H. and Nagayama, K. Effect of growth conditions on the structure of two-dimensional latex crystals: Experiment. *Colloid Polym. Sci.* (1999) **277:** 914–930.
[27] Cundall, P.A. and Strack, O.D.L. A discrete numerical model for granular assemblies. *Geotechnique* (1979) **29:** 47–65.
[28] Pitois, O. and Chateau, X. Small Particle at a Fluid Interface: Effect of Contact Angle Hysteresis on Force and Work of Detachment. *Langmuir* (2002) **18:** 9751–9756.
[29] Kralchevsky, P.A. Paunov, V.N. Denkov, N.D. Ivanova, I.B. and Nagayama, K. Energetical and force approaches to the capillary interactions betweeen particles attatched to a liquid fluid interface. *J. Colloid Interface Sci.* (1993) **155:** 420–437.
[30] Heyes, D.M. and Branka, A.C. Brownian dynamic simulations of self-diffusion and shear viscosity of near-hard-sphere colloids. *Physical Review E.* (1994) **50:** 2377–2380.
[31] Hamaker, H.C. The London—van der Waals attraction between spherical particles. *Physica* (1937) **4:** 1058–1072.
[32] Fan, T.H. and Vinogradova, O.I. Hydrodynamic resistance of close-approached slip surfaces with a nanoasperity or an entrapped nanobubble. *Phys. Rev. E* (2005) **72:** 66306.
[33] Belhadj, M. Alper, H.E. and Levy, R.M. Molecular dynamics simulations of water with Ewald summation for the long range electrostatic interactions. *Chem. Phys. Lett.* (1991) **179:** 13–20.
[34] Putkaradze, V. Screening in particle attraction by capillary forces : from centimeter to nanometer scales. in *International Symposium on Nonlinear Theory and its Applications (NOLTA2005)* (2005). 573–576.
[35] Hansen, P.H.F. Rodner, S. and Bergstro, L. Structural Characterization of Dense Colloidal Films Using a Modified Pair Distribution Function and Delaunay Triangulation. *Langmuir* (2001) **17:** 4867–4875.

V International Conference on Particle-based Methods – Fundamentals and Applications
PARTICLES 2017
P. Wriggers, M. Bischoff, E. Oñate, D.R.J. Owen, & T. Zohdi (Eds)

INCLINED CHUTE FLOW OF ROD-LIKE PARTICLES USING THE DISCRETE ELEMENT METHOD

MASATO SAEKI [1] AND RYOHEI ARAI [2]

[1] Dept. of Mechanical Engineering, Fuculty of Engineering,
Shibaura Institute of Technology
3-7-5 Toyosu, Koto-ku, Tokyo 135-8548, Japan
E-mail: saeki@sic. shibaura-it.ac.jp
URL: http://www.sic.shibaura-it.ac.jp/~saeki/index_E.html

[2] Graduate school Engineering and Science, Shibaura Institute of Technology,
3-7-5 Toyosu, Koto-ku, Tokyo 135-8548, Japan
E-mail: md14004@shibaura-it.ac.jp

Key words: Granular Materials, DEM, Rod-like particles, Contact Problems.

Abstract. An inclined chute flow of rod-like particles is investigated both experimentally and analytically. The behavior of the particles is solved by the discrete element method (DEM). The rod-like particle model consists of a cylinder, capped at both ends by hemispheres whose radii are the same as the radius of the cylinder. The rod-like particles have three translational degrees of freedom, their rotational motion being described through quaternions, and the interparticle contact is described by a force that accounts for the elastic and dissipative interactions. The contact patterns for the rod-like particles are classified into six types. In the experiment, brass and acrylic resin cylinders of uniform size were used. The validity of the theory was confirmed by comparing the experimental and analytical results. In addition, the effect of the particle material on the flow pattern was examined.

1 INTRODUCTION

The discrete element method (DEM) has become established as the primary numerical technique for simulating many industrial granular flows. The main advantage of the DEM is that it makes it possible to consider the effect of granularity, such as the particle size, number of particles, and friction between two particles. It is known that the dynamics of granular materials are strongly affected by their shape. When examining the effect of the particle shape on granularity, rod-like particles are often used. This is because rod-like particles are widely used in chemical, pharmaceutical, and other industries [1, 2]. There is considerable descriptive detail available on the dynamics of rod-like particles. However, most previous theoretical analyses have focused on the multi sphere method since it is possible to ensure computational efficiency for contact detection and force calculations [3-5]. As the contact between two spheres is different from that between two cylinders, the latter should be calculated in order to consider the real contact. The authors have proposed a contact model on the basis of each contact pattern for rod-like particles [6]. It was found that the numerical approach is effective for estimating the vibratory conveyance of acrylic resin cylinders. More studies are required in order to apply

the numerical approach to many engineering problems related to the motion of rod-like particles.

In this work, an inclined chute flow of rod-like particles is investigated both experimentally and analytically. The behavior of the particles is solved by the DEM. The rod-like particle model consists of a cylinder, capped at both ends by hemispheres whose radii are the same as the radius of the cylinder. The rod-like particles have three translational degrees of freedom, their rotational motion being described through quaternions, and the interparticle contact is described by a force that accounts for the elastic and dissipative interactions. The contact patterns for rod-like particles are divided into six types. In the experiment, brass and acrylic resin cylinders of uniform size were used. The validity of the theory was confirmed by comparing the experimental and analytical results. In addition, the effect of the particle material on the flow pattern was examined.

2 COMPUTATIONAL MODEL

Figure 1 shows the computational model. In this paper, the rod-like particle model consists of a cylinder with length L and two hemispheres with the same radius r. The translational motion of particle i is governed by Newton's second law of motion:

$$\sum_{j=1}^{N_c} \boldsymbol{F}_{ij} = m\ddot{\boldsymbol{r}}_i \,, \tag{1}$$

where N_c is the number of particles in contact with particle i, $\boldsymbol{F}_{ij}$ is the force exerted by particle j on particle i, and m is the particle mass.

Euler's rotational equations of motion for particle i become

$$\begin{aligned} I_X\dot{\omega}_i^X - (I_Y - I_Z)\omega_i^Y\omega_i^Z &= T_i^X \\ I_Y\dot{\omega}_i^Y - (I_Z - I_X)\omega_i^Z\omega_i^X &= T_i^Y \\ I_Z\dot{\omega}_i^Z - (I_X - I_Y)\omega_i^X\omega_i^Y &= T_i^Z \end{aligned} \,, \tag{2}$$

where I is the principal moment of inertia, ω is the angular velocity, and T is the torque acting on particle i.

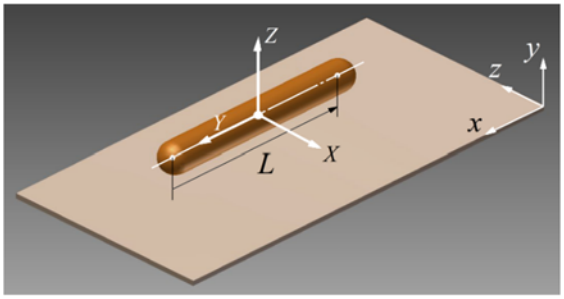

Figure 1: Rod-like particle model

3 PHYSICAL CONTACT MODEL

The contact patterns for rod-like particles are divided into six types. There are two patterns of contact between a rod-like particle and a wall, as shown in Figure 2. In the case of

interparticle contact, there are four contact patterns, as shown in Figure 3. The contact forces are determined by Hertzian contact theory.

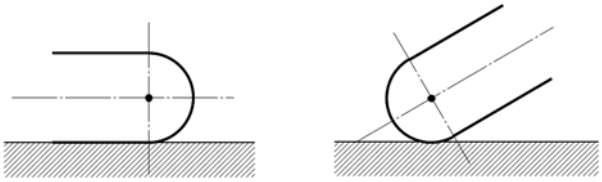

(a) Cylindrical contact (b) Hemispherical contact

Figure 2: A particle in contact with a wall

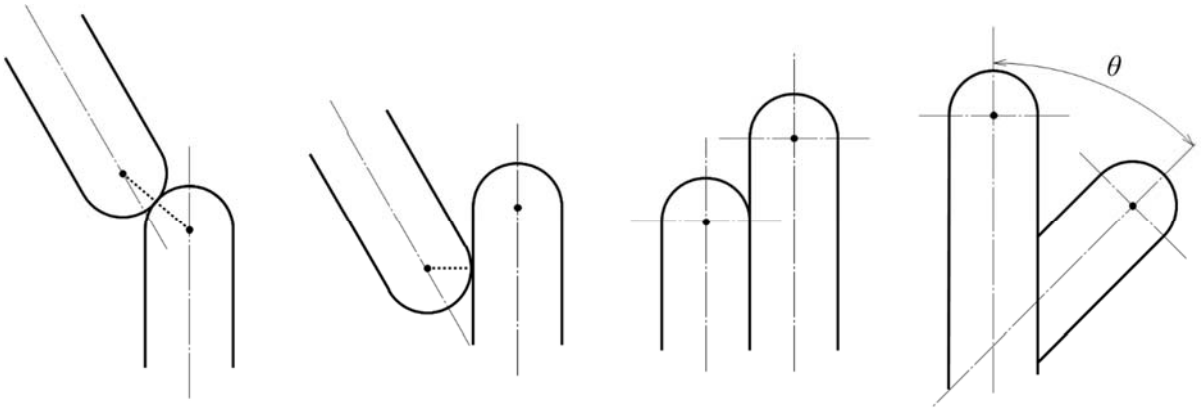

(a) Contact between two hemispheres (b) Contact between a hemisphere and a cylinder (c) Parallel Contact between two cylinders (d) Nonparallel contact between two cylinders

Figure 3: Interparticle contact

3.1 Cylinder in contact with wall

Figure 2(a) shows the contact between a cylindrical part and a wall. If a cylinder and a wall are pressed into contact with force P, then the half-width w of the contact area is expressed as

$$w = \sqrt{\frac{4rP}{\pi L}\left(\frac{1-{\nu_p}^2}{E_p}+\frac{1-{\nu_w}^2}{E_w}\right)}. \tag{3}$$

The deformation δ_n is given by

$$\delta_n = \frac{P}{\pi L}\left(\frac{1-{\nu_p}^2}{E_p}+\frac{1-{\nu_w}^2}{E_w}\right)\left(1.8864 + ln\frac{L}{2w}\right), \tag{4}$$

where E is the modulus of elasticity and ν is Poisson's ratio [7]. Subscripts p and w denote a particle and a wall, respectively.

Figure 4 shows the relationship between the deformation δ_n and P in the case of contact between a cylinder and a wall. The conditions used in the calculation are given in Table 1. The length L and radius r of the cylinder are 117.04mm and 1.98mm, respectively. In this figure, P

is proportional to δ_n and the coefficient of proportionality can then be determined from the slope k.

Table 1: Values of parameters

Modulus of elasticity E_p (GPa)	Acrylic resin	3.14
Modulus of elasticity E_p (GPa)	Brass	103
Modulus of elasticity E_w (GPa)	ABS	2.65
Poisson's ratio ν_p	Acrylic resin	0.35
Poisson's ratio ν_p	Brass	0.35
Poisson's ratio ν_w	ABS	0.35

Supposing that the normal component F_n of the contact force acting on the particles is given by the sum of the damping force and the elastic force, F_n is given by

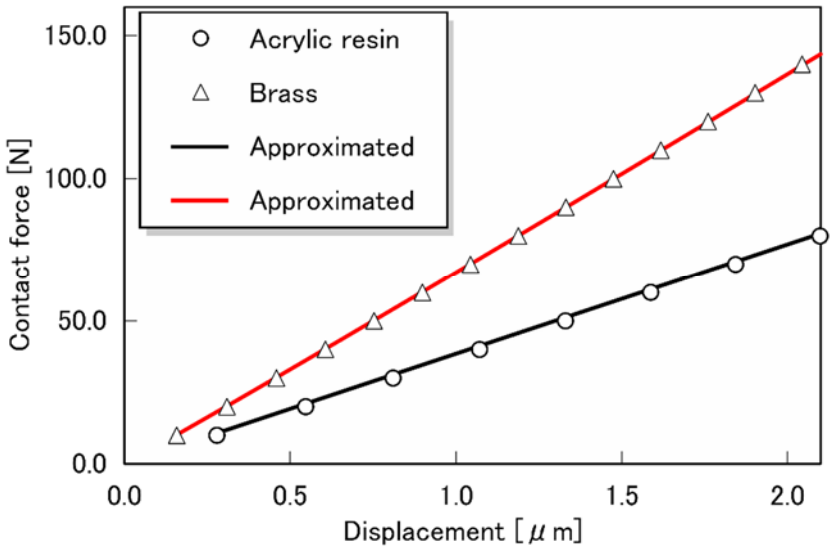

Figure 4: Contact force vs. deformation in the case of contact between a cylinder and a wall

$$F_n = k\delta_n + c\dot{\delta}_n \,, \tag{5}$$

where the damping coefficient c [7] is

$$c = \frac{2\sqrt{mk}}{\sqrt{1 + (-\pi/lne)^2}}. \tag{6}$$

The tangential force F_t is given by

$$F_t = -\frac{\mu F_n \dot{\delta}_t}{|\dot{\delta}_t|} \,, \tag{7}$$

where $\dot{\delta}_t$ is the tangential velocity and μ is the coefficient of friction between the particle and the wall.

3.2 Hemispherical part in contact with wall

Figure 2(b) shows the contact between a hemispherical part and a wall. Supposing that the contact is the same as that between a sphere and a wall, the normal component F_n of the contact force is given by

$$F_n = k{\delta_n}^{3/2} + \alpha\sqrt{mk}{\delta_n}^{1/4}\dot{\delta_n}\,. \tag{8}$$

The spring constant k is given by

$$k = \frac{4\sqrt{r}}{3}\cdot\frac{E_p E_w}{(1-{\nu_p}^2)E_w + (1-{\nu_w}^2)E_p}. \tag{9}$$

The damping constant α is determined from the coefficient of restitution [8].

3.3 Contact between hemispherical parts

Figure 3(a) shows the contact between two hemispherical parts. Supposing that the contact is the same as that between two spheres, the normal component F_n of the contact force is also given by Eq. (8). The spring constant k is given by

$$k = \frac{\sqrt{2r}E_p}{3(1-{\nu_p}^2)}. \tag{10}$$

3.4 Hemispherical part in contact with cylindrical part

Figure 3(b) shows the contact between a hemispherical part and a cylindrical part. In the case of contact, the normal component F_n of the contact force is also given by Eq. (8). The spring constant k [6] is given by

$$k = 0.974^{(-3/2)}\sqrt{\frac{8r}{27}}\cdot\frac{E_p}{1-{\nu_p}^2}. \tag{11}$$

3.5 Contact between two cylinders with parallel axes

Figure 3(c) shows the contact between two parallel cylindrical parts. If two cylinders are pressed together by force P, then the half-width w of the contact area is expressed as

$$w = \sqrt{\frac{4rP}{\pi L E_p}(1-{\nu_p}^2)}\,. \tag{12}$$

The deformation δ_n is given by

$$\delta_n = \frac{2P}{\pi L}\left(\frac{1-{\nu_p}^2}{E_p}\right)\left(1.8864 + ln\frac{L}{2w}\right). \tag{13}$$

Figure 5 shows the relationship between the deformation δ_n and the force P in the case of contact between two parallel cylinders. The conditions used in the calculation are given in Table 1. The length L and radius r of the cylinder are 117.04mm and 1.98mm, respectively. In this figure, $P$is exactly proportional to δ_n Therefore, in the case of contact, the normal component F_n of the contact force is also given by Eq. (5).

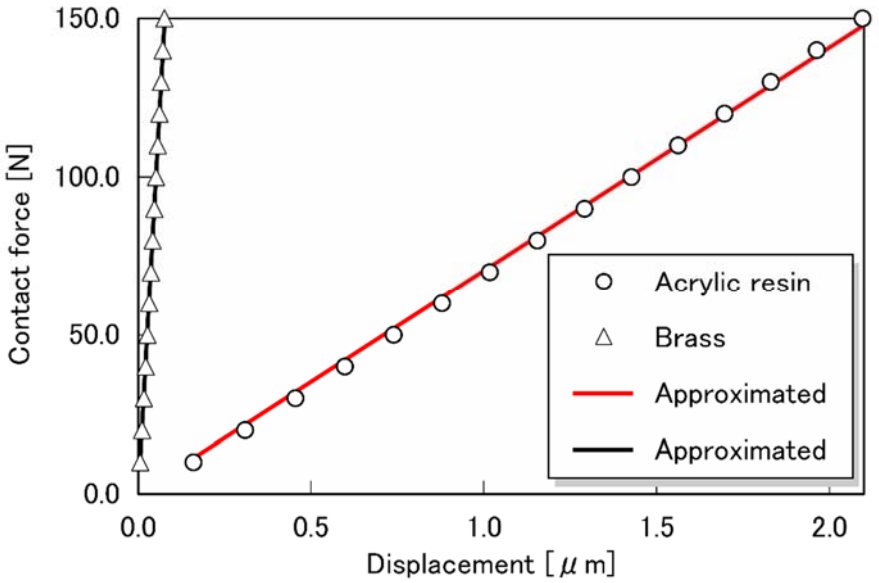

Figure 5: Contact force vs. deformation in the case of contact between two parallel cylinders

3.6 Contact between two cylinders with inclined axes

Figure 3(d) shows the contact between cylinders with inclined axes. In the case of contact, the normal component F_n of the contact force is also given by Eq. (8). The spring constant k [9] is given by

$$k = \frac{2}{3}\sqrt{r}\left(\frac{2K}{\pi\varepsilon}\right)^{(-3/2)} \cdot \frac{E_p}{1-{\nu_p}^2}, \tag{14}$$

where K and ε are

$$K = \int_0^{\pi/2} \frac{d\phi}{\sqrt{1-a^2 sin^2\phi}}, \tag{15}$$

$$\varepsilon = \sqrt[3]{\frac{1}{1-a^2} \cdot \frac{2S}{\pi}}. \tag{16}$$

In Eq. (16), S is given by

$$S = \int_0^{\pi/2} \sqrt{1-a^2 sin^2\phi}\, d\phi\,, \tag{17}$$

where a is the modulus of the elliptic integral. The contact angle θ is given by

$$\theta = cos^{-1}(2b^2 - 1)/2\,, \tag{18}$$

where b is given by

$$b = \frac{(2-a^2)S - 2(1-a^2)K}{a^2 S}. \tag{19}$$

Figure 6 shows the relationship between the spring constant k and the contact angle θ for the contact between cylinders with inclined axes.

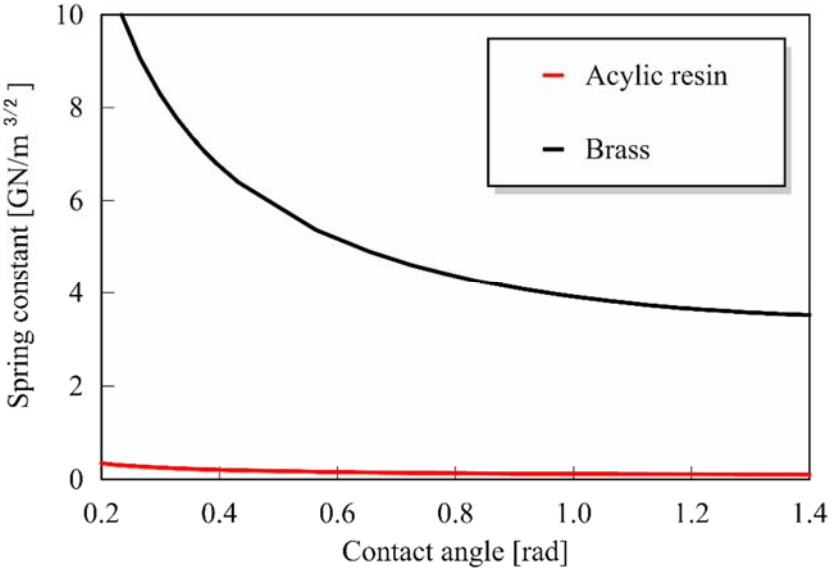

Figure 6: Spring contact vs. contact angle

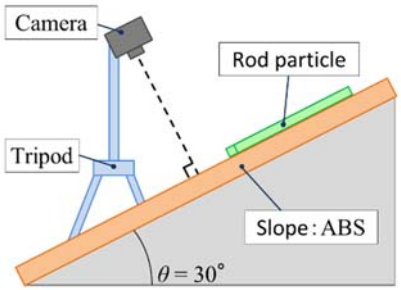

Figure 7: Experimental apparatus

4 EXPERIMENTS AND NUMERICAL APPROACH

Experiments were carried out to verify the validity of the numerical approach. In this study, the simulation code was developed using C++ language and OpenGL.

Figure 7 shows the experimental apparatus. The inclined chute was made of ABS and the inclination angle was 30°. The behavior of the particles was observed with a high speed camera (Casio Exlim EX-100) at 240fps and their movements were obtained with an image processing system. Brass and acrylic resin cylinders of uniform size were used.

Figure 8 shows the initial positions of six rod-like particles on the inclined chute. To examine the effect of interparticle contact, two particles were fixed firmly on the chute.

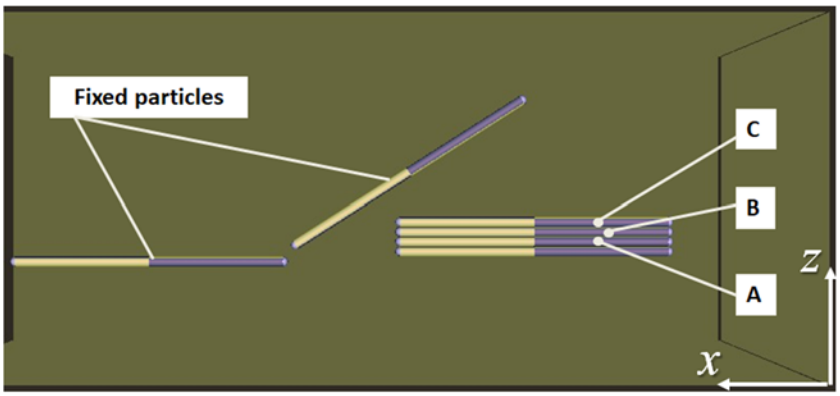

Figure 8: Initial positions of rod-like particles

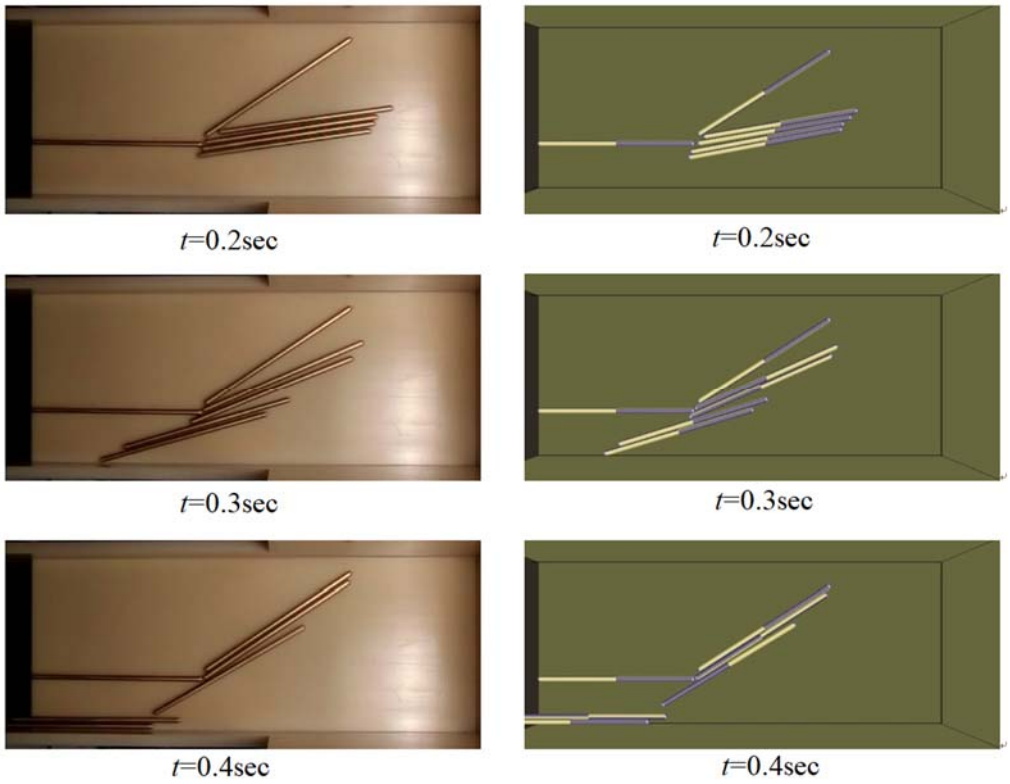

(a) Experimental results (b) Calculated results

Figure 9: Behavior of Brass particles

5 RESULTS AND DISCUSSION

Figures 9(a) and 9(b), respectively, show photographs of the experimental results and computer graphics created using the calculated results under the same conditions. It is found that the typical features of flow patterns of brass particles observed in the experimental results are well reproduced in the calculated results.

Figures 10(a) and 10(b) show the effects of the initial position of the brass particles and the

particle material on the time history of the movement of the particles along the *x*-axis, respectively. These figures also show the analytical and calculated results. This experiment was carried out three times. It was found that the effect of the initial position on the movement is greater than that of the particle material. It was also observed that the calculated results are in reasonably good agreement with the experimental results. Therefore, the numerical approach is effective for estimating the dynamical behavior of rod-like particles.

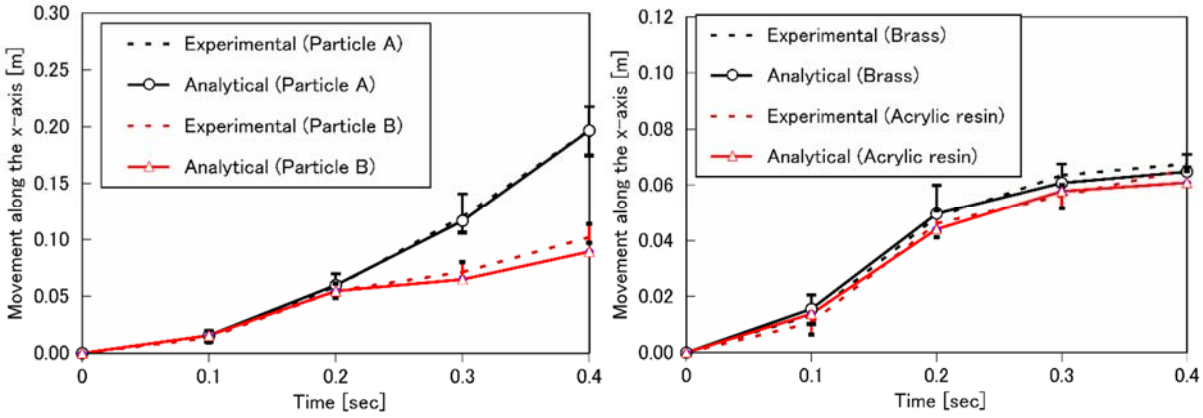

(a) Brass particles A and B (b) Brass and acrylic resin (particle C)

Figure 10: Time histories of the movement along the *x*-axis

6 CONCLUSIONS

An inclined chute flow has been modeled using the DEM for rod-like particles in order to understand the effect of the particle shape on such flows. The contact patterns for rod-like particles was classified into six types. The behavior of the rod-like particles was observed with a high speed camera and their movements were obtained with an image processing system. From the time histories of the movements for rod-like particles, it was found that the calculated results agree with the experimental results. Therefore, the numerical approach in this study is effective for addressing the engineering problems of rod-like particles.

REFERENCES

[1] Haeri, S., Wang, Y., Ghita, O. and Sun, J. Discrete element simulation and experimental study of powder spreading process in additive manufacturing, *Powder Technology*(2016) **306**: 45-54.

[2] Markauskas, D and Kacianauskas, R. Investigation of rice grain flow by multi-shpere particle model with rolling resistance, *Granular Matter* (2011)**13**: 143-148.

[3] Deng, X. L. and Dave, R. N. Dynamic simulation of particle packing influenced by size, aspect ratio and surface energy, *Granular Matter*(2013)**15**: 401-415.

[4] Marigo, M and Stitt, E. H. Discrete element method (DEM) for industrial applications: Comments on calibration and validation for the modelling of cylindrical pellets, *KONA Powder and Particle Journal* No.32 (2015): 236-252.

[5] Pournin, L., Weber, M., Tsukahara, M., Ferrez, J. A., Ramaioli, M. and Liebling, T. M. Three-dimensional distinct element simulation of spherocylinder crystallization, *Granular Matter* (2005) **7**: 119–126.
[6] Kidokoro, T., Arai, R. and Saeki, M. Investigation of dynamics simulation of granular particles using spherocylinder model, *Granular Matter* (2015) **17**: 743–751.
[7] Saeki, M., Minagawa, T. and Takano, E. Study on vibratory conveyance of granular materials JSME *International Journal C* (1998)**41**. No.4:704-709.
[8] Tsuji, Y., Tanaka, T. and Ishida, T. Lagrangian numerical simulation of plug flow of cohesionless particles in a horizontal pipe, *Powder Technology* (1992)**71**: 239-250.
[9] Okamoto, J., Nakayama, K., and Sato, M. *Introduction to tribology*, Saiwai Shobo (1990)

V International Conference on Particle-based Methods – Fundamentals and Applications
PARTICLES 2017
P. Wriggers, M. Bischoff, E. Oñate, D.R.J. Owen, & T. Zohdi (Eds)

INVESTIGATION OF MASS DISCHARGE RATE AND SEGREGATION FROM HOPPER BY DISCRETE ELEMENT METHOD

RAJ KUMAR[1], CHETAN M. PATEL[1], ARUN K. JANA[1]AND SRIKANTH R. GOPIREDDY[2]

[1]Department of Chemical Engineering, Sardar Vallabhbhai National Institute of Technology
Surat -395007, Gujarat, India
E-mail: cmp@ched.svnit.ac.in, webpage: http://www.svnit.ac.in

[2]Daiichi-Sankyo Europe GmbH, Pharmaceutical Development, Luitpoldstrasse 1, 85276 Pfaffenhofen, Germany
E-mail: srikanth.gopireddy@daiichi-sankyo.eu, https://www.daiichi-sankyo.eu/

Key words: Granular materials, hopper angle, discrete element Method, mass flow rate.

Abstract. Hoppers of different shape and angle are widely used in different industries particularly in handling of solids as storage units and in unit operations, e.g. mixing, tableting, etc. It is a challenge to choose a right hopper to achieve desired flow and insignificant segregation due to difference in material properties. General approach for the selection of optimum hopper for a given unit operation is based on the trial-and-error experimental approach. To address this optimum hopper selection, combined experimental and numerical approach is presented in this study. The objective of this study is to analyze the effect of mixture composition and hopper angle on the flow rate and segregation behavior. The numerical simulation of granular flow out of various conical hoppers was also performed using the discrete element method (DEM). The materials considered include different particle size glass bead particles in different proportions by mass. The experimental study is done to validate the DEM results, particularly, mass flow rate. The results analyzed include temporal development of mass fraction of a given particle size during discharge. In addition, the mass flow rate is also computed. The results indicate that fines percentage in the mixture, ratio of smallest particle size to largest in the mixture, and hopper angle plays significant role in determining the segregation and mass flow rate. The flow pattern found to be influenced by the hopper angle and mean particle size of mixture. The results of discharge rate from DEM are also compared with existing empirical correlations and finite element method based elastoplastic model. The DEM prediction shows a good agreement with the existing correlations for a wide range of hopper angles, and with the experimental data.

1 INTRODUCTION

The behavior of granular materials during discharge from hoppers or bins plays a crucial role in many industrial processes such as chemical, agricultural, food technology and pharmaceutical industries [1]. Granular flows can be extremely complex and in general are not well understood [2, 3]. The granular material cannot be considered as solid, liquid or gas to fully characterize their flow state. In fact they are characterized as the fourth state of matter

due to its puzzling nature and behaviour [3]. The gravity flow of bulk solids from bins and hoppers is a subject of considerable practical and theoretical interest. The key understanding towards the behavior of granular material in a hopper not only aids in obtaining the correct flow, but also to ensure that the hopper is properly designed to deliver quality product during processing time. The discharge dynamics from hopper depends upon several factors which include material properties, processing conditions and hopper geometry. The flow dynamics gets completely changed due to change in any one of these parameters, which may results in non-uniformity in product stream termed as segregation. The degree of segregation is greatly affected by factors such as particle size distribution width (span), mass fraction of individual components, mean particle diameter as well as the hopper angle. The different experimental and modeling studies were conducted in past owing to the importance of discharge dynamics of hopper. It includes flow mode identification i.e. funnel and mass flow as well as analysis of discharge rate and segregation behavior [4-8]. Apart from these, flows rate prediction from hopper attracted wide attention. The numbers of correlations have been proposed over many decades and are used to predict discharge rates of granular materials from hoppers of different angles. Some of them were based on the dimensional analysis and others on experimental results. From earlier investigations, a dimensional analysis suggests that flow rate is directly proportional to the bulk density of the system, gravitational acceleration, and outlet width of hopper. Beverloo et al. [4] performed experiments on mono-disperse particles. They presented the following empirical correlation for estimating the discharge rate out of a flat bottom hopper: $\dot{m} = C\rho\sqrt{g}(D - kd)^{2.5}$, where $\dot{m}$ is the mass flow rate, C is a constant (~ 0.58), D is the outlet diameter, k is shape factor (= 1.5 for spherical particles), and d is mean particle diameter [4]. Rose and Tanaka (RT) [5] introduced a multiplicative correction factor (F_{corr}) for the application of Beverloo correlation to the conical shape hoppers, and given as follow:

$$F_{corr} = \begin{cases} 1; & \tan\theta \tan\chi \geq 1 \\ (\tan\theta \tan\chi)^{-0.35}; & \tan\theta \tan\chi < 1 \end{cases}$$

where, θ is hopper angle from the vertical and χ is angle from the horizontal of the stagnant-flowing boundary. It is suggested that when no information about χ is available, it may assumed to be 45° [5]. Kurz and Munz investigated the flow properties of limestone and concluded that the mean particle size alone cannot be the used in order to determine granular flow behavior [6]. There have been several attempts to improve the Beverloo correlation to include the effects such as fill height [7], friction between granular material and hopper wall [9, 10,11], hopper outlet diameter [12], mean particle diameter [4], material density, and hopper angle [13]. The effect of hopper half angle, particle-wall friction and material properties on Beverloo constant C, while calculating the discharge rate has always been a matter of debate for many decades [4,14]. In the latest study, Zheng et al. [14] used elastoplastic model to predict the flow rate in conical hopper using finite element method (FEM). Their study introduced the dependency of internal friction angle (φ), hopper half angle (α), wall friction coefficient (μ) and dilatancy angle (ψ) to predict the mass flow rate constant C in Beverloo equation [14]. The equation takes the form by FEM results as follows:

$$C = 0.58\left(\frac{1-\cos^{m}\alpha}{\sin^{5/2}\alpha}\right)(1.08 - 0.0164\,\psi)$$

$$\text{where, } m = 4.25\, e^{-0.1\varphi} + 0.44e^{-8.5\mu} + 1.31$$

With increasing computacional resources, various simulation methods have been used to understand the flow dynamics inside hopper in addition to estimate the discharge rate. In this category, DEM [15] has become the widely adopted method for simulating particle behavior and seems to be an alternative method for use in the modeling the behaviour of bulk solids. DEM has been well established for simple flows for many years and was widely employed to study granular flow from hoppers [18, 19]. These investigations helped in the study of flow behavior, velocity distribution, segregation etc.during Hopper discharge.

2 MATERIALS AND METHODS

This section presents all the details about the materials and experimental setup. All the experiments are conducted at least in quintuple, unless otherwise mentioned, to provide mean and relative standard deviation (RSD). The details about numerical simulation are also given at the end of this section.

2.1 Experimental Setup

The experiments were performed using the spherical shaped glass beads. The glass beads particles with different sizes were grouped into three sets through sieving: (i) 0.71 mm < d_1< 0.85 mm (small size particles or fines), (ii) 1.0 < d_2< 1.7 mm (medium size particles), and (iii) 1.7 mm < d_3< 2 mm (large size particles), and the mean particle diameters of these sets were 0.78 mm, 1.35 mm, and 1.85 mm respectively. These sets were used to prepare binary and ternary mixture samples. The mixtures with different fines mass fraction were prepared by increasing fines amount by 10% successively, whereby coarse or medium size particles proportion was adjusted accordingly to achieve 100% mixture mass. Starting with binary mixture, which consists of coarse particles (mean diameter = 1.85 mm) and fines (mean diameter = 0.78 mm) as described above, was prepared by varying the fines amount by 10%, i.e. first binary mixture consisted of 10% fines and 90% coarse particles by mass (sample A, see Table 1). Similarly other samples were prepared as tabulated in the Table1.

Table 1: Detail of sample preparation for binary mixture.

Sample	Glass beads diameter (mm)		Mass percentage (%)	
	(d_1)	(d_3)	(d_1)	(d_2)
A	0.78	1.85	10	90
B	0.78	1.85	20	80
C	0.78	1.85	30	70
D	0.78	1.85	40	60

Similarly, the ternary mixtures were prepared by increasing fines mass percentage by 10% from one sample to other whereas remaining proportion is filled with equal mass percentage of coarse and medium size particles. For example, for ternary mixture 1, the fines mass percentage was 10 % whereas coarse and medium size particles mass % were adjusted to 45%

Table 2: Detail of sample preparation for ternary mixture

Sample	Glass beads diameter (mm)	Mass percentage (%)

	(d_1)	(d_2)	(d_3)	(d_1)	(d_2)	(d_3)
E	0.78	1.35	1.85	10	45	45
F	0.78	1.35	1.85	20	40	40
G	0.78	1.35	1.85	30	35	35
H	0.78	1.35	1.85	40	30	30

individually (sample E, see Table 2). The details about all the ternary mixture samples were presented in Table 2. The schematic of the experimental setups are given in Figure. 1. The setup consists of two conical shaped (at the bottom) hoppers which have hopper angle of 60° and 80°. These hoppers were custom built and made up of acrylic glass (see Figure. 1). The outlet diameter is same for both the hoppers and is equal to 10 mm. The outlet of these hoppers were designed in such manner that outlet can be closed while filling material, which can be easily opened during discharge rate measurement experiments without disturbing the hopper and filled material.

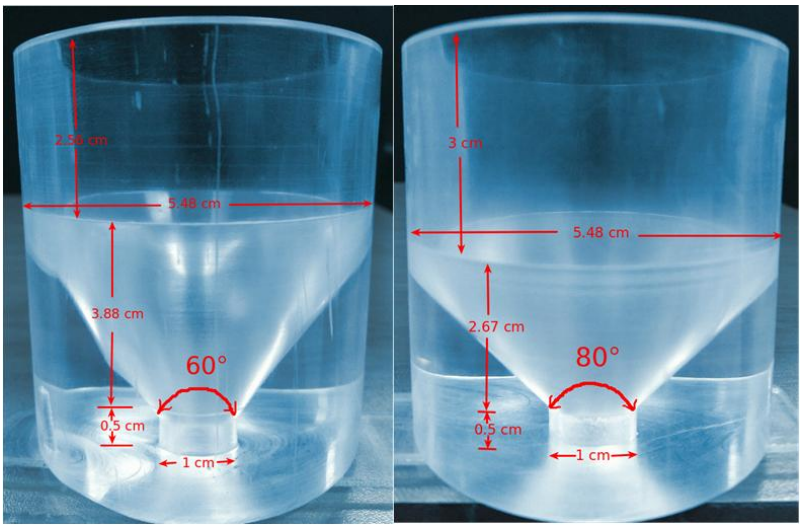

Figure 1: Schematic of the experimental hoppers having different internal angle.

A series of experiments using different mixture samples as shown in the Table 1 and 2, were carried out to study the mass discharge rate of the glass beads from the custom built hoppers. In all experiments, the same amount of sample (100 grams) was weighed and carefully filled into the hopper using consistent filling procedure to obtain the same degree of consolidation by closing the opening lid at the outlet. Once desired amount with consistency is filled into the selected hopper, the discharge rate measurement is performed by removing the outlet lid slowly and then recording the time for complete material discharge using a stopwatch. This procedure was repeated at least five times for selected hopper and selected material (Table 1 and 2), and a mean RSD of the discharge rate is calculated. To reduce electrostatic charge during filling and discharging, static energy discharge gun (Milty Zerostat 3 Anti-Static Gun, China) was used. This device emits positive and negative ions to effectively neutralize static charge that may be built up on surface.

2.2 Numerical simulations using DEM

The simulations are carried out using the three-dimensional DEM, which computes the trajectories of each and every particle using Newton's second law of motion. This is a well-established approach to study the granular material flow dynamics and the details about this method and theory can be found in [17]. Hertz and Mindlin & Deresiewicz theories are used to compute the normal and tangential forces, respectively. An open source DEM software known as LIGGGHTS (LAMMPS Improved for General Granular and Granular Heat Transfer Simulations) version 3.5.0 has been used to perform the simulations [16]. Refer to [16], to understand the implementation of different models in LIGGGHTS along with computational algorithms, and their validation. The material properties used in numerical simulations are given in Table 1, which corresponds to spherical glass-bead particles [18].

Table 3:Parameter considered in simulations.

Properties	Glass beads	Hopper wall (acrylic)	Glass beads – Hopper wall
Density (kg/cm^3)	2500	1800	-
Young'smodulus,Y (GPa)	70	3	-
Coefficient of restitution, e(−)	0.94	-	0.9
Poisson's ratio,v(−)	0.22	0.35	-
Coefficient of friction,μ (−)	0.2	-	0.5

3 RESULTS AND DISCUSSION

The results and discussion are separated into the following three sections. At first the discharge rate of single component or pure component material in both the hoppers (60° and 80°) were presented followed by the binary and ternary mixture's results. Next, a comparison of experimental discharge data with that of DEM numerical results was presented. Towards the end, the comparison of numerical simulations with that of empirical correlations such as Beverloo, Rose and Tanaka, FEM, etc. was established.

3.1 DISCHARGE RATE RESULTS

The main focus of this study to evaluate the discharge rate of pure component materials as well as the binary and ternary mixtures listed in Table 1 and 2, respectively. The experiments were performed as described in section 2.1 to capture the total time to discharge a constant amount of selected material in a given hopper. The results are presented in the following sub-sections.

3.1.1 Pure Component Material

The pure component material i.e., glass beads which were classified into three categories (refer section 2.1) were first analyzed to find the influence of particle size on the discharge rate for mono-sized particles (fines: 0.78 mm, medium-sized: 1.35 mm, coarse: 1.85 mm).The mass flow rate of each size glass beads having total mass of 100g was evaluated by recording the complete discharge time from hoppers. The mean mass discharge rate of these three mono-sized particles for both type of hoppers were depicted in Figure. 2.

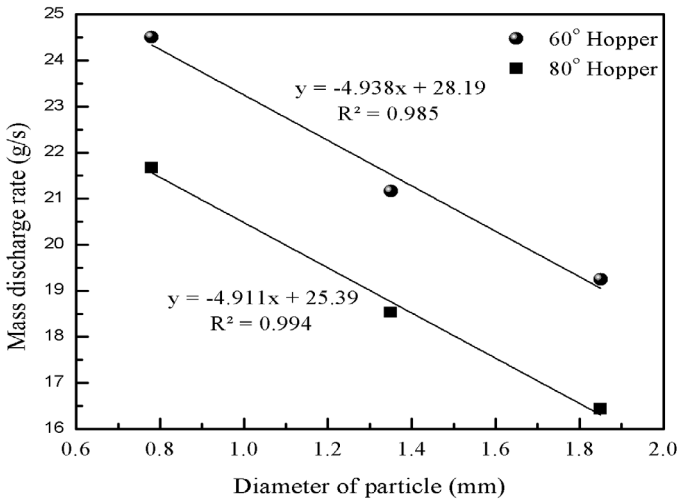

Figure 2: Mass flow rate as a function of particle diameter (mm) in different angle hopper.

The results are also tabulated along with RSD in Table 4 for these experiments. First of all, a low RSD (< 1%) indicates the reproducibility and reliability of these experiments. For both type of hoppers, the discharge rate decreases with increasing particle size as shown in the Figure 2 and Table 4, which is in agreement with the results reported in reference [6].

Table4: Mean discharge rate for single component in different angle hopper.

Particle diameter (mm)	Hopper angle (°)	Mean discharge rate (g/s)	Relative Standard Deviation (RSD) (%)
0.78	60	24.51	0.92
0.78	80	21.67	0.95
1.35	60	21.16	0.95
1.35	80	18.53	0.51
1.85	60	19.25	0.80
1.85	80	16.43	0.71

With 60° hopper, the discharge rate decreases from 24.51 g/s to 21.16 g/s, when the particle size was increased from 0.78 mm to 1.35 mm. The discharge rate further decreased to 19.25 g /s when the particle size was increased to 1.85 mm from 1.35 mm. Similar trend was observed for 80° hopper, where mass flow rate was decreased from 21.67 g/s to 18.53 g/s and further to 16.43 g/s with increase in diameter from 0.78 mm to 1.35 mm and from 1.35 mm to 1.85 mm respectively. Comparison of 60° with that of 80° revealed that the steeper the hopper (or in

other words the lower the hopper angle) higher the flow rate, which is independent of the particle size (see Figure 2 and Table 4), which is also in agreement with literature data [5]. The correlation between discharge rate and mean particle size used in these experiments were also shown in Figure 2 with very good correlation coefficient. Thus, for a fixed outlet diameter of hoppers, the flow rate exhibits a linear relationship with respect to particle diameter. Furthermore, the effect of hopper angle on flow rate was also observed in the Figure 2, showing decrease in mass flow rate by 10% as hopper angle was changed from 60° to 80°. These results indicate that small particle diameter (0.78 mm) granular material, particles exhibits very little resistance and behave more like a fluid, while large particle diameter experiences substantial amount of resistance and it becomes more difficult to get the particles to flow as the ratio between particle diameter to hopper outlet diameter increases.

3.1.2 Discharge Behaviour of Multicomponent Mixture Samples

The real particulate solids are composed of various sizes of particles and are more commonly encountered in industrial applications unlike single component granular materials. For this reason, binary (sample A to D, Table 1) and ternary (sample E to H, Table 2) mixtures were prepared, and the flow rates were measured as explained in section 2.1. The particle diameter of the mixtures was represented by the mean particle diameter. First, the mass flow rate of binary mixture having different percentage of fines (sample A to D, Table 1) was measured. The mass discharge rate of binary mixtures from both the 60° and 80° hoppers as a function of fine percentage was shown in the Figure. 3.

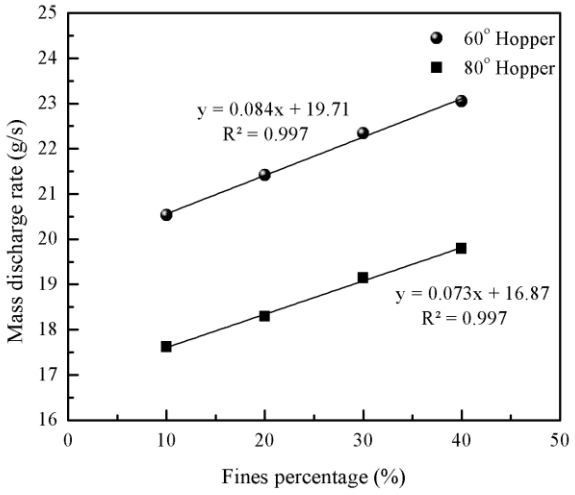

Figure 3: Mass flow rate as a function of fine percentage (binary mixture) in different angle hopper.

The flow rate of granular material increases linearly as the fines mass percentage increases for both types of hoppers as seen in the Figure 3. The good correlation between the flow rate and fines percentage with the correlation coefficient R^2 as high as 0.99 was observed. In addition to fine percentage, the effect of hopper angle on flow rate was also observed clearly. For

every 10% increase in fine particles amount, the flow rate was increased by a factor of 0.8 and 0.7 for 60° and 80° hopper respectively (Figure 3).The increase in flow rate in 80° hopper is less than that for 60° hopper, which could be due to steeper hopper walls in 60° hopper to ensure better particle movement compared to 80° hopper. Anand et al. [19] reported that with increasing mass fraction of fines in granular system mass discharge rate tend to increase. This increase in flow rate was attributed to the increase in flowing density during discharge [20]. It is evident that decrease in flow rate with increasing fines % was due to the particle distribution generated by changing fines mass %. A similar behavior was reported, wherein increase in mean diameter resulted in decrease in the flow rate [21]. Ternary mixtures were prepared by addition of a particles of intermediate size (as described in section 2.1) to study the effect of multicomponent mixture on the flow rate. Similar to the binary mixture the effect of mass % of fines on discharge rate was investigated by changing the fine % (samples E to H, Table 2). The effects of fines mass percentage on discharge rate is shown in the Figure 4.

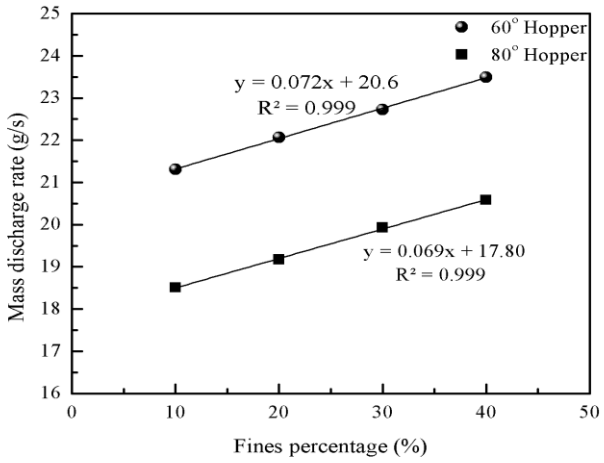

Figure 4: Mass flow rate as a function of fine percentage (ternary mixture) in different angle hopper.

In comparison to the binary mixture, the mass flow rate of the ternary mixture shows an improvement, which is attributed to the decrease of mean particle diameter due to addition of intermediate particles to binary mixture. Also, as the fine percentage was increased, the maximum mass flow rate corresponds to ternary mixture for same percentage of fines. This is explained based on the fact that better particles packing could be achieved when mixture was changed from binary to ternary results into increased flowing density during discharge. The effect of increase in fine content on discharge rate was reduced in ternary mixture compared to binary mixture, which can be clearly seen by comparing the slopes of Figure. 3 and Figure. 4. The mass flow rate increased by factor of about 0.07 with ternary mixtures whereas for binary mixtures the mass flow rate increases by a factor of about 0.08 for 60° hopper.

3.2 Mass Flow Rates Comparison with Different Correlations

The discharge flow rates obtained by experiments were validated using well-established correlations reported in literature as well as with DEM simulations. The basic equation to calculate the theoretical flow rate was published by Beverloo et al. [4]. This formula is for cylindrical orifices with flat bottom and thus does not consider the hopper angle. A correction factor based on the Rose and Tanaka [5] equation can be applied to improve Beverloo equation, which is a function of the hopper angle as described in section 1. In the latest study, Zheng et al. [14], developed an empirical correlation for predicting the mass discharge rate of conical hoppers based on FEM with elastoplastic model (refer to section 1). In this context, the measured data of flow rates for binary (samples A to D, Table 1) and ternary (samples E-F, Table 2) mixtures with both the hoppers (60°and 80°) were calculated using Rose and Tanaka (RT) correlation, DEM, and FEM based empirical correlation. The Figures 5(a) and 5(b) show the comparative prediction of these correlations along with DEM simulations and experimental data for binary mixture (samples A to D) in 60° and 80° hopper, respectively.

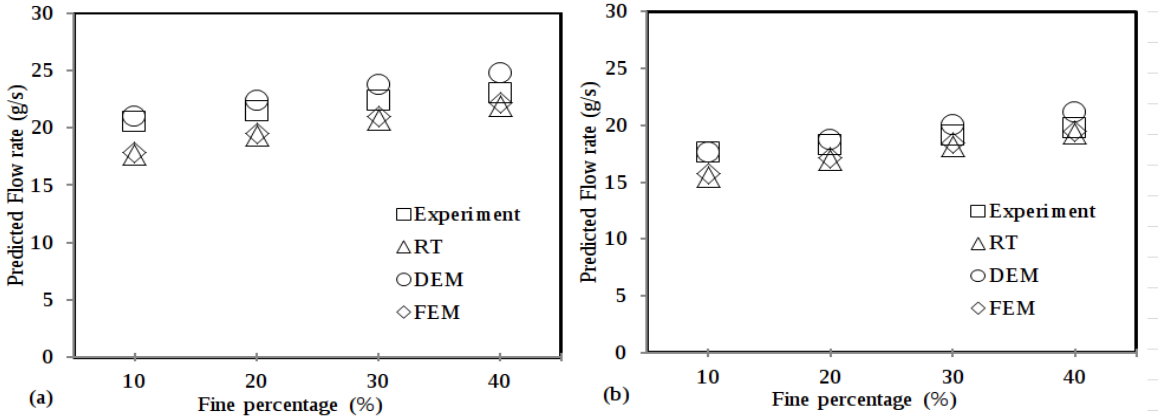

Figure 5: Comparison of mass flow rate between experiment, Rose and Tanaka, DEM and FEM based elastoplastic model for binary mixtures (samples A to D) in (a) 60° hopper (b) 80° hopper.

The results indicate that the flow rate increases with increasing fines content and this profile is very well captured by all the correlations and DEM results. The good agreement between the results obtained by DEM and experiments was observed for cases with lower fines content (< 30% by mass), whereas the empirical correlations (RT and FEM) underestimate the flow rates in these cases. One of the possible reasons for overprediction in DEM results for cases with fines content above 30 % may be due to the size difference between particles in simulations and experiments. Basically, simulations takes into account the exact sizes of particles whereas the actual glass beads used in experiments had a distribution in the sizes and hence were grouped into three sizes as described in Section 1. On the other hand, RT and FEM correlations underpredicts the experimental results by less than 10%. It was also found that the RT and FEM deviation with experimental flow rate were increase with decrease in fines content. Thus, it may be concluded that the fines fraction in mixture probably had a greater impact on predicting discharge rate. Furthermore, with the increase in internal angle of the hopper, the predicted discharge rates by FEM and those by RT correlations were improved with the experimental discharge rates.

3.3 Segregation Results

Figure.6 shows segregation results for 60° and 80° hoppers for sample D (x_f- 40%). The first 10% discharged material contain a lesser amount of fines due to filling process. Generally, larger particles roll down to the bottom of the Hopper during filling and this effect seems to be greater for 80° Hopper due to wide angle at bottom. For both 60° and 80° hoppers, almost equal proportion of fines were discharged until $M/M_{total} \approx 0.55$.

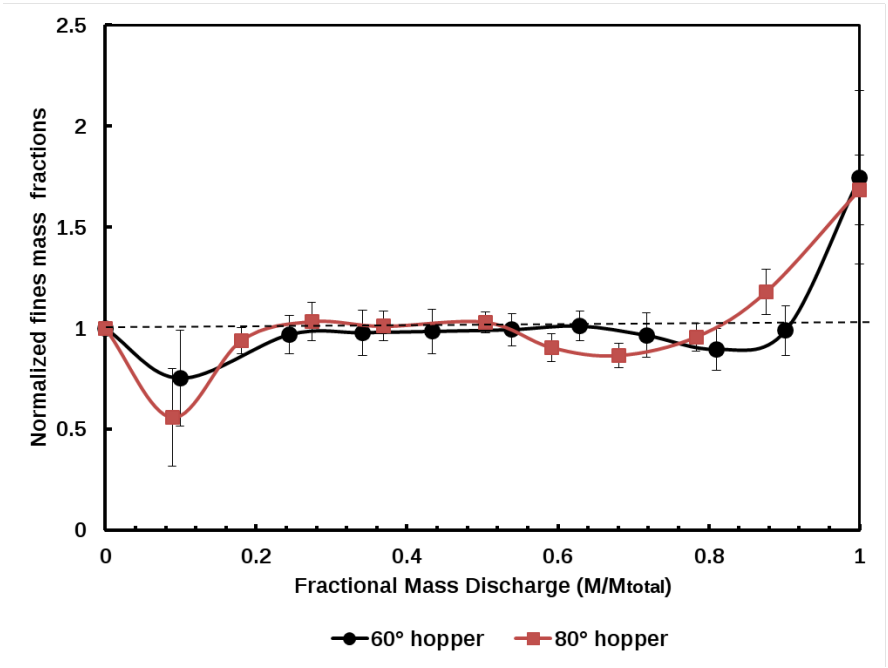

Figure 6: Experimental segregation results for sample D (x_f- 40%) in different angle hopper.

At approximately 60% mass discharged (M/M_{total} = 0.6), the behavior of granular material inside both hoppers vary significantly. For 80° hopper, the discharged mass was depleted in fines between 60 % to 80 % discharged mass. But after 80 %, discharge mass collected contain excess of fines due to segregation. Generally, after $M/M_{total} \approx 0.5$, coarse particles tend to occupy most of the centerline channel resulting in accumulation of fines at side walls of hopper and hence discharged material was depleted in fines approximately between $0.55 < M/M_{total} < 0.8$. During end discharge, the resulting accumulated fines were discharged. On the other hand, 60° Hopper attained fairly uniform fines mass fractions discharge as compared to 80° Hopper during initial discharge mass until $M/M_{total} \approx 0.7$. This might be due to increase in wall steepness as the Hopper wall angle was decreased to θ=60°. After $M/M_{total} \approx 0.7$, the discharge material was depleted in fines and during end discharge, material rich in fines was collected. Ketterhagen et al. [18] in their work also observed a similar behavior and concluded that as the internal angle of Hopper increases, the segregation of the granular material increases.

CONCLUSIONS

Firstly, the hopper angle is found to be significantly impacting the flow rate where it is shown that the steeper the hopper the better the flow rate out of the hopper. Next, with pure

component materials, it is reported that while keeping the outlet diameter constant, the larger the particle diameter the lesser the flow rate. The experimental data of these mixtures shows that presence fine particle in addition to coarse improves the overall flow rate where the fines particle imparts fluidity effect thereby increasing the flow rate. The observations made in this study are in agreement with the literature data. The comparison of experimental data with that of the well-known correlations and DEM results indicate that overall DEM results are better predicting the flow rates than the empirical correlations or FEM based correlations. However, it found that the DEM results are slightly over predicting especially in the higher fines content mixtures which attributed to the fact that there is slight difference between glass-bead particle sizes used in experiments and the ones used in DEM simulations. With this study it is possible to provide a first estimate of the discharge rates out of a given hopper without actually performing experiments. The focus of the future study is to investigate segregation behavior as mass is discharging which is currently ongoing. Some of these results will be presented at the Particles 2017 meeting.

REFERENCES

[1] Roberts, A. W. Particle technology - reflections and horizons: an engineering perspective. *Chem. Eng. Res. Des.* (1998) 76:775-796.

[2] Campbell, C. S. Rapid granular flows. *Ann. Rev. Fluid Mech*. (1990) 22:57-92.

[3] Jaeger, H. M., Nagel, S. R. Physics of the granular state. *Science*. (1992) 225:1523-1531.

[4] Beverloo, W. A., Leniger, H. A., Van de Velde, J. The flow of granular solids through orifices. *Chem. Eng. Sci*. (1961) 15:260-269.

[5] Rose, H., Tanaka, T. Rate of discharge of granular materials from bins and hoppers. *The Engineer.* (1959) 208:465-469.

[6] Kurz, H. P., Munz, G. The influence of particle size distribution on the flow properties of limestone powders. *Powder Technol*. (1975) 11:37-40.

[7] Brown, R. L., Richards, J. C. Profile of flow of granules through apertures. *Trans. Inst. Chem. Eng.* (1960) 38:243-250.

[8] Arteaga, P., Tüzün, U. Flow of binary mixtures of equal-density granules in hoppers-size segregation, flowing density and discharge rates. *Chem. Eng. Sci.* (1990) 45 (1): 205-223.

[9] Williams, J. C, The rate of discharge of course granular materials from conical mass flow hoppers. *Chem. Eng. Sci.* (1977) 32:247-255.

[10] Tüzün, U., Nedderman, R. M. Experimental evidence supporting kinematic modelling of the flow of granular media in the absence of air drag. *Powder Technol*. (1979) 24: 257-266.

[11] Tüzün, U., Nedderman, R. M. An investigation of the flow boundary during steady-state discharge from a funnel-flow bunker. *Powder Technol*. (1982) 31(1):27-43.

[12] Khanam, J., Nanda, A. Flow of granules through cylindrical hopper. *Powder Technol.* (2005)150:30-35.

[13] Nedderman, R. M., Tuzun, U. The flow of granular materials-I: discharge rates from hoppers. *Chem. Eng. Sci*. (1982) 37 (11):1597-1609.

[14] Zheng, Q. J., Xia, B. S., Pan, R. H., Yu, A. B. Prediction of mass discharge rate in conical hoppers using elastoplastic model. *Powder Technol*. (2017) 307:63–72.

[15] Cundall, P. A., Strack, O. D. L. A discrete numerical model for granular assemblies. *Geotechnique*. (1979) 29 (1):47-65.

[16] Kloss, C., Goniva, C., Hager, A., Amberger, S., Pirker, S. Models, algorithms and validation for opensource DEM and CFD-DEM. *Prog. Comput. Fluid Dy. An Int. J*. (2012) 12:140-152.

[17] Zhu, H. P., Zhou, Z. Y., Yang, R. Y. and Yu., A. B. Discrete particle simulation of particulate systems: Theoretical developments. *Chem. Eng. Sci*. (2007) 62 (13):3378-3396.

[18] Ketterhagen, W. R., Curtis, J.S., Wassgren, C.R., Hancock, B.C. Modeling granular segregation in flow from quasi-three-dimensional, wedge-shaped hoppers. *Powder Technol*. (2008) 179:126-143.

[19] Anand, A., Curtis, J. S., Wassgren, C.R., Hancock, B.C., Ketterhagen, W. R. Predicting discharge dynamics from a rectangular hopper using the discrete element method (DEM). *Chem. Eng. Sci*. (2008) 63:5821-5830.

[20] Dias, R. P., Teixeira, J. A., Mota, M.G., Yelshin, A. I. Particulate binary mixtures: dependence of packing porosity on particle size ratio. *Ind. Eng. Chem. Res*. (2004) 43:7912-7919.

[21] Humby, S., Tuzun, U., Yu, A. B. Prediction of hopper discharge rates of binary granular mixtures. *Chem. Eng. Sci*. (1998) 53:483-494.

V International Conference on Particle-based Methods – Fundamentals and Applications
PARTICLES 2017
P. Wriggers, M. Bischoff, E. Oñate, D.R.J. Owen, & T. Zohdi (Eds)

MECHANICAL BEHAVIOR OF BOUNDARY LAYER IN DISCRETE MODELS BASED ON VORONOI TESSELLATION

Jan Eliáš[1]

[1] Brno University of Technology
Faculty of Civil Engineering, Institute of Structural Mechanics
Veveří 331/95, Brno, 602 00, Czech Republic
jan.elias@vut.cz; http://www.fce.vutbr.cz/stm/elias.j/

Key words: discrete model, boundary layer, wall effect, concrete, elasticity, fracture

Abstract. The contribution introduces 2D and 3D discrete static model of concrete based on Voronoi tessellation. Attention is focused on the boundary region where, due to presence of boundaries, the orientation of contacts exhibits strong bias. The bias has consequences in mechanical behavior of the boundary region in both elastic and inelastic regimes. The boundary layer is typically weaker and more brittle compared to the interior and also stiffer or more compliant depending on macroscopic Poisson's ratio and straining direction.

1 INTRODUCTION

This contribution is a promotion of the recent journal paper [1], particular results and conclusions of the paper are shown in this contribution.

Solid matter occupies spatial domains defined by boundaries. It is known that there exists a layer in the vicinity of the boundary where the material properties might differ from the interior. The boundary layer might be result of several effects, for example actions of external environment. In concrete, the boundary layer typically differs also in grain size distribution having increased amount of small grains and mortar compared to the interior material [2]. The boundary layer of different material properties compared to interior affects mechanical behavior of concrete solids.

When simulating the concrete members, the boundary layer is typically not explicitly addressed (but exceptions exist, see e.g. [3]). However, it might be imposed by the nature of the model. This can be seen for example when using nonlocal models [4], which naturally create boundary layer of different behavior. The contribution shows that this is also the case of discrete models. Their mechanical behavior relies on discretization of a solid domain into particles with random irregular composition, but presence of the bound-

aries affects the irregularity and produces some boundary layer with different statistical distributions of geometrical variables.

However, the contact constitutive behavior of discrete models can also be developed to become completely independent on the geometry of the rigid bodies. It has been achieved both for elastic behavior [5, 6, 7] and inelastic behavior [8]. In such a case, the boundary layer has no mechanical consequences. In majority of the discrete models, the contact behavior take into account the geometry of the contact in both linear and nonlinear regimes and therefore the boundary layer is active.

Comparison of the boundary layer and interior tessellation geometry and stress is presented in the contribution. Due to unbiased behavior of the interior, analytical formulas can be developed for its macroscopic elastic behavior. The real mechanical behavior of the discrete system is compared with these analytical predictions. Most of the comparison is done via statistical characteristics called the mean value and standard deviation. Having some function $G = g(\gamma)$ dependent on random variable γ with probability density function $f(\gamma)$, the mean value, μ_G, and standard deviation, δ_G, is defined as

$$\mu_G = \int_{-\infty}^{\infty} g(\gamma) f_\gamma(\gamma) \mathrm{d}\gamma \qquad \delta_G = \sqrt{\int_{-\infty}^{\infty} (g(\gamma) - \mu_G)^2 f_\gamma(\gamma) \mathrm{d}\gamma} \tag{1}$$

2 GEOMETRY OF THE DISCRETE STRUCTURE

The studied model is a discrete system of rigid bodies connected at common facets by linear or nonlinear contacts. Both the 2D and 3D versions of the model are used here.

The algorithm for construction of the discrete model geometry is controlled by parameter $l_{\min}$. The domain of the simulated solid is filled with nuclei with random location in a sequential process. New nucleus is accepted only when its distance to all previously placed nuclei is lower than $l_{\min}$. The filling is terminated after a large number of subsequent rejections is detected, i.e. when the domain is saturated. Voronoi tessellation is performed to divide the domain into rigid bodies. According to [9], the nuclei are mirrored across the boundaries before performing the Voronoi tessellation. The tessellation then creates the boundaries of the rigid bodies exactly coinciding with the boundaries of the specimen (Fig. 1a).

In order to perform comparison with models without a boundary, periodic boundary conditions are used. During random placement of nuclei, every nucleus is periodically repeated twice in the y and z directions. The tessellation is then performed on a periodic structure that is $3\times$ larger in both the y and z directions. When solving the mechanical system, periodic images of nuclei have dependent DOFs and only one periodic image of each contact contributes to the strain energy and is therefore included in the stiffness matrix. This approach completely removes boundaries and creates ideal directionally unbiased geometry. The boundaries can be also inserted into the periodic structure., The nuclei in the central part of the prismatic specimen are mirrored across the xy and xz

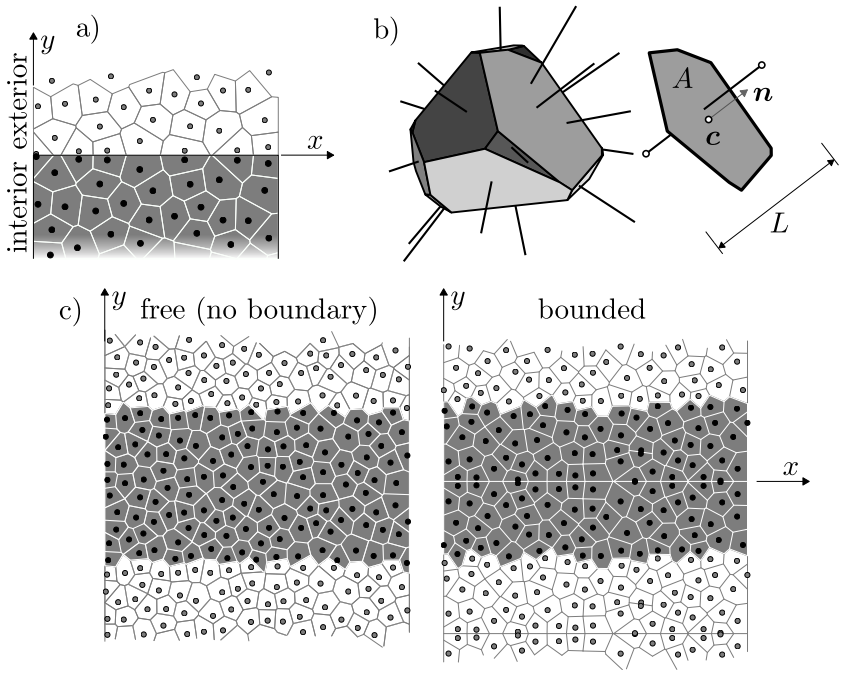

Figure 1: a) Boundary region and Voronoi tessellation on randomly placed nuclei in 2D; b) one 3D rigid body and one contact facet; c) periodic structure without and with the boundary in 2D.

plane. After tessellation, the planes xy and xz behave in the same way as the specimen boundary with directionally biased geometry in its vicinity. An example of the periodic boundary *free* and periodic *bounded* structures in 2D is shown in Fig. 1c.

Voronoi faces, here referred to as facets, represents the bonds between two bodies. The orientation of the contact facet is described by its *normal* direction, $\boldsymbol{n}$; the length of the contact is denoted $L = \|\boldsymbol{x}_a - \boldsymbol{x}_b\|$, its area is A and centroid is $\boldsymbol{c}$ (Fig. 1b).

3 CONTACT CONSTITUTIVE BEHAVIOR

The constitutive equations are taken from [10] and simplified. A full description of both linear and nonlinear constitutive equations and model kinematics is provided in [11].

Each body has three degrees of freedom in two dimensions (2×translation u, 1×rotation θ), and 6 in three dimensions (3×translation u, 3×rotation θ). Translations and rotations of the rigid bodies give rise to a displacement jump, $\boldsymbol{\Delta}$, measured at the centroid of the contact facets. The strain is measured by a scalar in the normal direction (N) and by a vector in the shear direction (T)

$$e_N = \frac{\boldsymbol{n} \cdot \boldsymbol{\Delta}}{L} \qquad \boldsymbol{e}_T = \frac{\boldsymbol{\Delta}}{L} - e_N \boldsymbol{n} \tag{2}$$

The shear strain is perpendicular to the normal direction $\boldsymbol{n}$. The stress is then calculated

based on the strain and two elastic parameters of the model, E_0 and α

$$s_N = (1-D)E_0 e_N \qquad \boldsymbol{s}_T = (1-D)E_0\alpha\boldsymbol{e}_T \tag{3}$$

Variable D is a measure of integrity loss of individual contacts called damage. When $D = 0$, the contact is intact and exhibits elastic behavior. Completely damaged element would have D equal to 1. The evolution of D is dependent on straining direction and is governed by additional model parameters, the tensile strength f_t and the fracture energy G_F. The more shear is involved, the higher the strength and energy dissipation at the facet, see [11] or directly the original model [10].

In elastic regime, one can derive simple formulas relating contact elastic parameters, E_0 and α, to the elastic parameters of isotropic homogeneous continuum, elastic modulus E and Poisson's ratio ν.

$$\begin{aligned}
&\nu = \frac{1-\alpha}{3+\alpha} && E = E_0\frac{2+2\alpha}{3+\alpha} && \text{2D, plane stress}\\
&\nu = \frac{1-\alpha}{4} && E = E_0\frac{(1+\alpha)(5-\alpha)}{8} && \text{2D, plane strain}\\
&\nu = \frac{1-\alpha}{4+\alpha} && E = E_0\frac{2+3\alpha}{4+\alpha} && \text{3D}
\end{aligned} \tag{4}$$

The derivation is based on a theory provided in [12] and its detail step-by-step explanation can be found in [1]. Three fundamental features of the tessellation are used in the derivation: (i) the normals are parallel to lines connecting two nodes in contact; (ii) there are no holes in the discrete structure, the solid is filled by the rigid bodies without any overlapping or gap; (iii) there is no directional bias in the geometry, i.e. all normal directions are equally probable and contact areas and lengths are independent on normal directions.

The first two features are automatically guaranteed by the Voronoi tessellation, while the third one depends on the process of placing the nuclei into the solid domain. It will be shown in the next section, that it is valid for the interior, but the boundary layer exhibits, due to mirroring of the nuclei in the boundary region, strong directional bias and deviation from the third assumption.

It is worth noting that equations (4) establish limitations in Poisson's ratio for discrete models. Using theoretical meaningful limits 0 and ∞ for parameter α, the maximum and minimum Poisson's ratio can be calculated as $\left(-1, \frac{1}{3}\right)$ for 2D plane stress, $\left(-\infty, \frac{1}{4}\right)$ for 2D plane strain and $\left(-1, \frac{1}{4}\right)$ for 3D model. Fortunately, representation of concrete with Poisson's ratio around 0.2 is possible in all cases.

4 DIRECTIONAL BIAS IN THE VICINITY OF BOUNDARIES

The elemental direction in the boundary layer is strongly biased towards normals aligned with the boundary. It is simply caused by the effort to create the boundary

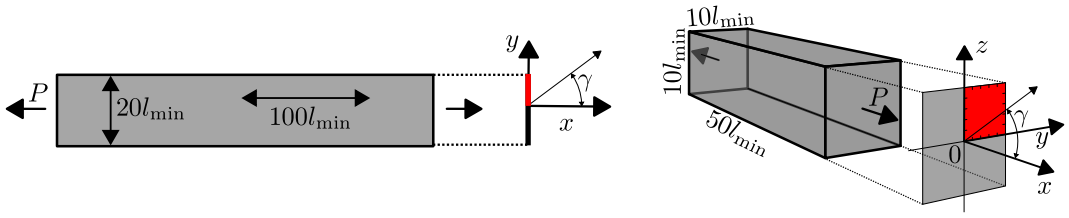

Figure 2: 2D and 3D specimens, dimensions, definition of the angular deviation γ and symmetric half or quarter of the cross-section in red.

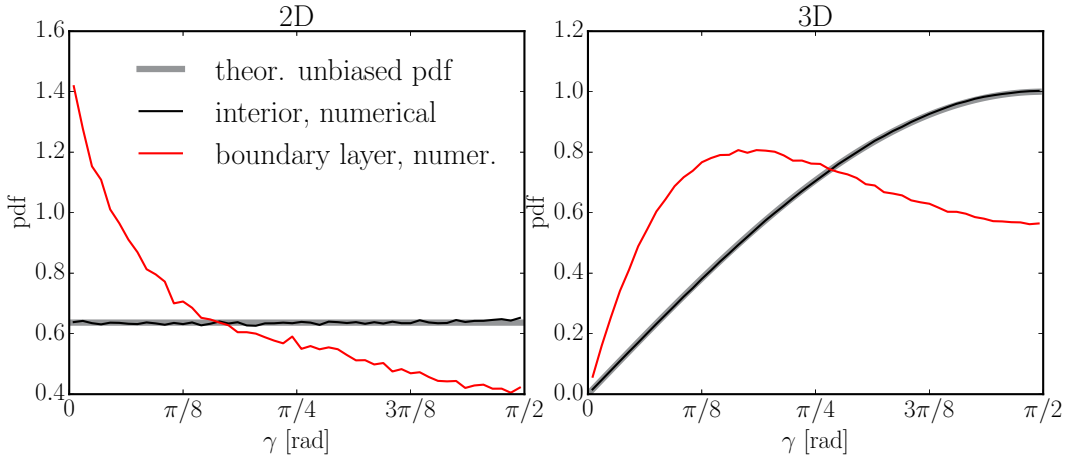

Figure 3: Probability distribution of the angular deviation from the x direction in 2D & 3D.

by the tessellation and there is no way known to the author how to reduce the effect or even get rid of it completely. The directional bias is demonstrated by variable γ, the angular deviation of the contact normal from the direction of the x axis, see Fig. 2.

The angular deviation, γ, is calculated in 2D and 3D model of prism shown in Fig. 2. In the ideal case where all the directions have the same probability, γ should have the following probability density

$$f_\gamma(\gamma) \quad \overset{\text{2D}}{=} \begin{cases} 2/\pi & \text{for } \gamma \in (0, \pi/2) \\ 0 & \text{otherwise} \end{cases} \quad \overset{\text{3D}}{=} \begin{cases} \sin(\gamma) & \text{for } \gamma \in (0, \pi/2) \\ 0 & \text{otherwise} \end{cases} \tag{5}$$

The specimens from the Fig. 2 were generated 500× in 2D and 3000× in 3D and angular deviation γ was extracted. Two regions were distinguished – the boundary layer where distance from the contact centroid to some boundary (parallel with the x axis) was lower than $l_{\min}$ and the interior containing all other contacts. The probability distributions of γ in these two groups are plotted in Fig. 3 together with the theoretical ideal distribution from Eq. (5). One can see that the interior has no directional bias while the boundary layer prefers elements aligned with the boundary.

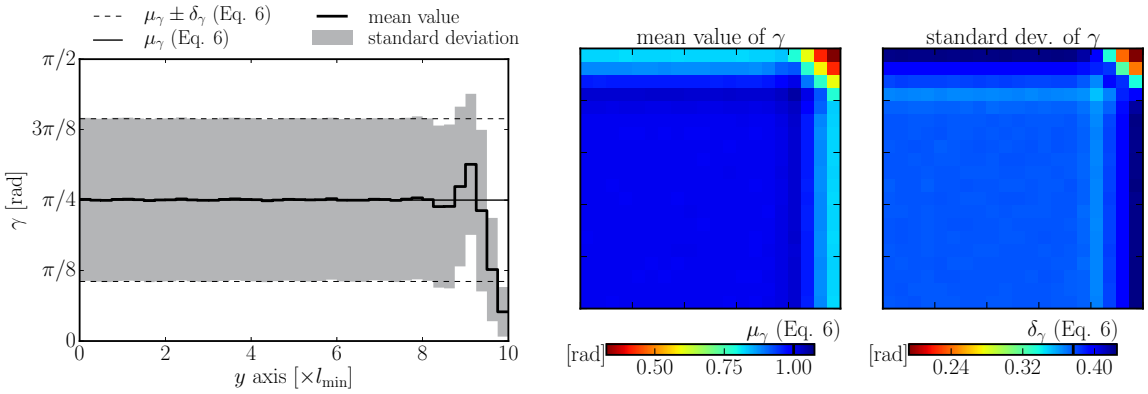

Figure 4: Statistical characteristics of the angular deviation from the x direction in 2D (left) & 3D (right) on symmetrical cross-section half or quarter, respectively.

To calculate the theoretical mean and standard deviation of γ, the distributions from Eq. (5) can be inserted into Eq. (1) and integrated for $g(\gamma) = \gamma$.

$$\mu_\gamma = \begin{cases} \dfrac{\pi}{4} & \text{2D} \\ 1 & \text{3D} \end{cases} \qquad \delta_\gamma = \begin{cases} \dfrac{\pi}{4\sqrt{3}} & \text{2D} \\ \sqrt{\pi - 3} & \text{3D} \end{cases} \tag{6}$$

These numbers are compared to an estimation of the mean and standard deviation calculated on the actual discrete systems in specimens from Fig. 2. Fig. 4 (left hand side) shows one symmetrical half of the cross section in the range $y = 0$ (center of the cross section) up to $y = 10 l_{\min}$ (boundary). The boundary layer exhibits a strong decrease in the mean indicating yet again that the elements are more aligned with the boundary. In 3D, Fig. 4 (right hand side) shows a symmetrical quarter of the cross section ranging from y, $z = 0$ (center of the cross section) up to y, $z = 5 l_{\min}$ (boundary). The bias in the boundary layer is similar to what was seen in 2D; it gets strongly emphasized in corners, where two perpendicular boundaries intersect.

5 ELASTIC BEHAVIOR

The prisms from the previous section were loaded by straining in the x direction (ε_{11}), while deformations in the y and z direction were unconstrained. Such loading results in a single tensorial stress component σ_{11} and the following strain components

$$\begin{array}{lll} \text{3D \& 2D plane stress} & \varepsilon_{11} = \dfrac{\sigma_{11}}{E} & \varepsilon_{22} = \varepsilon_{33} = -\dfrac{\nu \sigma_{11}}{E} = -\nu \varepsilon_{11} \\ \text{2D plane strain} & \varepsilon_{11} = \dfrac{\sigma_{11}(1-\nu^2)}{E} & \varepsilon_{22} = -\dfrac{\sigma_{11}(\nu+\nu^2)}{E} = \dfrac{\nu}{\nu-1}\varepsilon_{11} \end{array} \tag{7}$$

A simple assumption about the displacements and rotations of the bodies in the system when subjected to macroscopic uniform strain is now used. It is assumed that all the

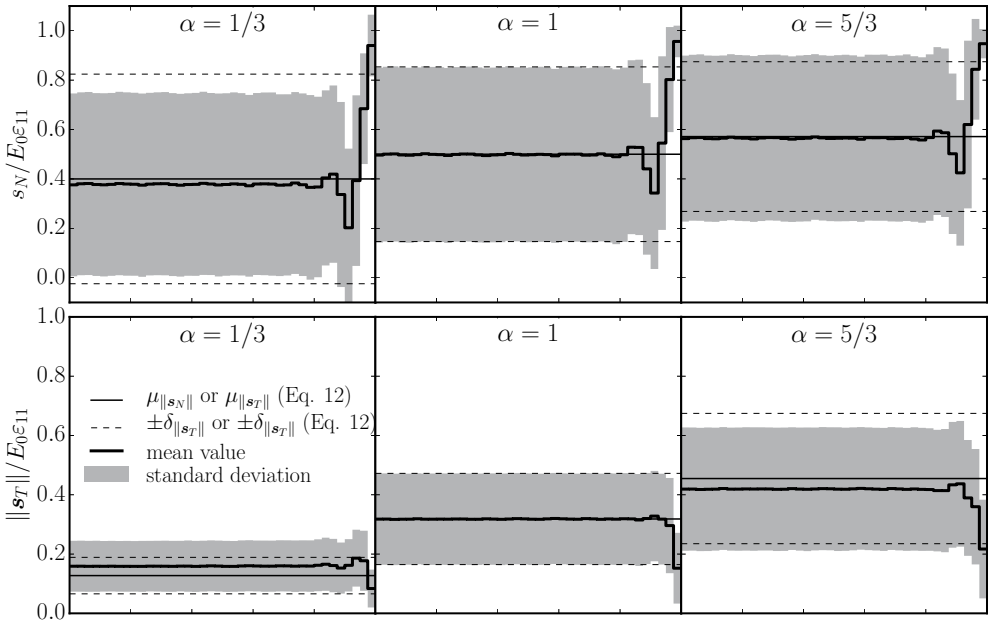

Figure 5: Average and standard deviation of normal stress (s_N, first row) and shear stress (s_T, second row) on a half cross section under tensile loading; 2D model, $\alpha = \{1/3,\ 1,\ 5/3\}$.

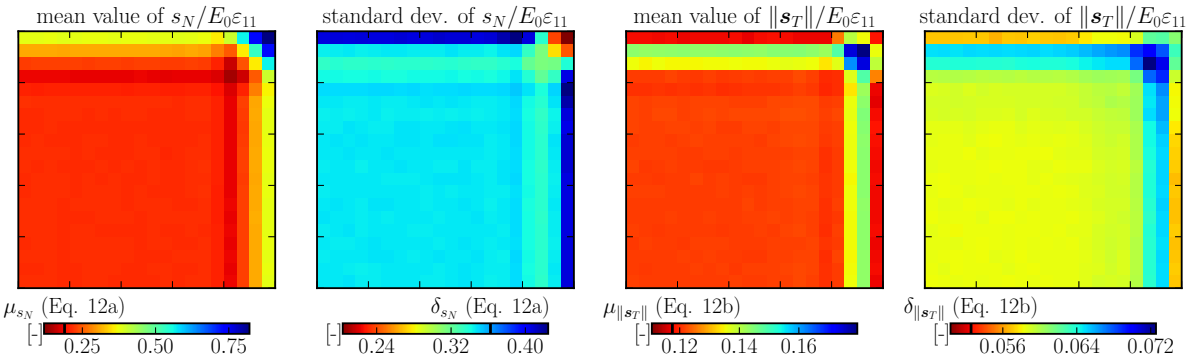

Figure 6: Average and standard deviation of the normal and shear stress on quarter cross-section; 3D model, $\alpha = 0.29$.

rotations are null ($\boldsymbol{\theta} = \boldsymbol{0}$) and the difference in displacements between any two nodes is

$$\boldsymbol{u}_b - \boldsymbol{u}_a = \boldsymbol{\varepsilon} \cdot (\boldsymbol{x}_b - \boldsymbol{x}_a) \tag{8}$$

Using assumption (8) and perpendicularity of the facet area to the element, the displacement jump is determined by the strain tensor

$$\boldsymbol{\Delta} = L\boldsymbol{\varepsilon} \cdot \boldsymbol{n} \tag{9}$$

Combining Eqs. (2)-(4), (7) and (9) the normal and tangential stress magnitude can be

evaluated

$$s_N = \varepsilon_{11} E_0 \left(\cos^2 \gamma - \frac{1-\alpha}{3+\alpha} \sin^2 \gamma \right) \tag{10}$$

$$\|\boldsymbol{s}_T\| = \varepsilon_{11} E_0 \alpha \sin \gamma \cos \gamma \frac{4}{3+\alpha} \tag{11}$$

The expression for the stress magnitudes is the same for both 2D simplifications and 3D. Now, the theoretical unbiased mean and standard deviation can be integrated with $g(\gamma) = s_N$ and $g(\gamma) = \|\boldsymbol{s}_T\|$ using Eq. 1

$$\mu_{s_N} = \begin{cases} \varepsilon_{11} E_0 \dfrac{1+\alpha}{3+\alpha} & \text{2D} \\ \varepsilon_{11} E_0 \dfrac{1+3\alpha}{3(3+\alpha)} & \text{3D} \end{cases} \qquad \delta_{s_N} = \begin{cases} \varepsilon_{11} E_0 \dfrac{\sqrt{2}}{3+\alpha} & \text{2D} \\ \varepsilon_{11} E_0 \dfrac{8}{3\sqrt{5}(3+\alpha)} & \text{3D} \end{cases} \tag{12a}$$

$$\mu_{\|\boldsymbol{s}_T\|} = \begin{cases} \varepsilon_{11} E_0 \alpha \dfrac{4}{\pi(3+\alpha)} & \text{2D} \\ \varepsilon_{11} E_0 \alpha \dfrac{4}{3(3+\alpha)} & \text{3D} \end{cases} \qquad \delta_{\|\boldsymbol{s}_T\|} = \begin{cases} \varepsilon_{11} E_0 \alpha \dfrac{\sqrt{2(\pi^2-8)}}{\pi(3+\alpha)} & \text{2D} \\ \varepsilon_{11} E_0 \alpha \dfrac{4}{3\sqrt{5}(3+\alpha)} & \text{3D} \end{cases} \tag{12b}$$

A comparison with a real discrete system behavior is shown for 2D and 3D in Figs. 5 and 6 for selected α parameters. The value $\alpha = 0.29$ has been chosen for 3D model because it is typical for concrete. The normal and shear stresses are normalized by $\varepsilon_{11} E_0$. One can see reasonable approximation of the stresses by analytical formulas (12a) and (12b) in the interior, the difference are caused by only approximate validity of the assumption (8). In the boundary layer, the normal stress increases while the shear stress decreases.

6 INELASTIC BEHAVIOR

A typical constitutive behavior, applied also here, is weaker and less ductile in tensile loading than in shear. Therefore, the boundary layer with a tendency of elements to be parallel to the boundary becomes weaker and more brittle under straining along its direction than the interior part.

The results are reported only for the 3D model with material parameters: $E_0 = 60\,\text{GPa}$, $\alpha = 0.29$, $f_\text{t} = 2.2\,\text{MPa}$ and $G_\text{t} = 35\,\text{J/m}^2$. These parameters were obtained in [11] by fitting a large experimental series [13] for $l_\text{min} = 10\,\text{mm}$. A periodic prisms of 200 mm in length (x axis) and square cross section of size 50 mm, 100 mm and 200 mm periodic in y and z directions are strained in uniaxial tension along the x direction.

The periodicity is used to remove the boundaries and the directional bias in its vicinity. To compare it with the bounded specimen, the boundaries are also introduced into the periodic structure by mirroring the nuclei across the xy and xz planes (Fig. 1c).

The nominal stress and elongation of the prisms are calculated 30 times with different geometry of the discrete structure and averaged. The averaged responses are shown in

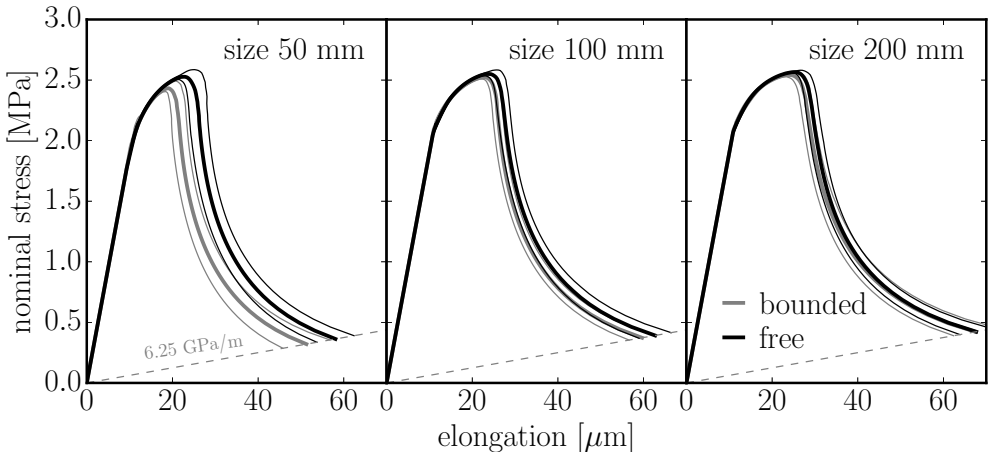

Figure 7: Averaged responses of periodic 3D model with (*bounded*) and without (*free*) boundaries loaded in pure tension

Fig. 7. The difference between the *bounded* and boundary *free* model decreases with size as the weak boundary layer occupies a lower portion of the specimen. In the worst case (the smallest specimen), the strength decreases by 4% and energy dissipation by 24% when boundaries are added.

7 CONCLUSIONS

The static discrete models with geometry of rigid bodies generated by Voronoi tessellation on randomly placed nuclei are studied. The standard elastic and inelastic contact behavior is applied.

- The contribution demonstrates the bias in the orientation of elements in the boundary layer. Contacts parallel to the boundary are represented with higher probability than what an unbiased model shall exhibit.
- Consequence of the orientation bias is that the elastic behavior of the boundary layer differ from the interior. When straining parallel to the boundary, the shear components are more relaxed while the normal components are loaded more compared to the elastic behavior of the interior. Therefore, for positive Poisson's ratios, the boundary layer becomes stiffer and vice versa.
- When the inelastic behavior has a typical form having both strength and fracture energy in the normal direction lower than in shear, the boundary layer becomes also weaker and less ductile.

Acknowledgement

The financial support provided by the Czech Science Foundation under project No. 15-19865Y is gratefully acknowledged.

REFERENCES

[1] Eliáš, J. Boundary layer effect on behavior of discrete models. *Materials* (2017) **10**:157.

[2] Bažant, Z.P. and Planas, J. *Fracture and size effect in concrete and other quasibrittle materials*. Boca Raton, Florida, USA: CRC Press (1997).

[3] Vořechovský, M. and Sadílek, V. Computational modeling of size effects in concrete specimens under uniaxial tension. *Int. J. Fracture* (2008) **154**:27–49.

[4] Havlásek, P., Grassl, P. and Jirásek, M. Analysis of size effect on strength of quasi-brittle materials using integral-type nonlocal models. *Eng. Fract. Mech.* (2016) **157**:72–85.

[5] Asahina, D., Ito, K., Houseworth, J.E., Birkholzer, J.T. and Bolander, J.E. Simulating the Poisson effect in lattice models of elastic continua. *Comput. Geotech.* (2015) **70**:60–67.

[6] Asahina, D., Aoyagi, K., Kim, K., Birkholzer, J.T. and Bolander, J.E. Elastically-homogeneous lattice models of damage in geomaterials. *Comput. Geotech.* (2017) **81**:195–206.

[7] Cusatis, G., Rezakhani, R. and Schauffert, E.A. Discontinuous Cell Method (DCM) for the simulation of cohesive fracture and fragmentation of continuous media. *Eng. Fract. Mech.* (2017) **170**:1–22.

[8] Berton, S. and Bolander, J.E. Crack band model of fracture in irregular lattices. *Comput. Method. Appl. M.* (2006) **195**:7172–7181.

[9] Bolander, J.E., Hong, G.S. and Yoshitake, K. Structural concrete analysis using rigid-body-spring networks. *Comput.-Aided Civ. Inf.* (2000) **15**:120–133.

[10] Cusatis, G. and Cedolin, L. Two-scale study of concrete fracturing behavior. *Eng. Fract. Mech.* (2007) **74**:3–17.

[11] Eliáš, J. Adaptive technique for discrete models of fracture. *Int. J. Solids Struct.* (2016) **100-101**:376–387.

[12] Kuhl, E., D'Addetta, G.A., Herrmann, H.J. and Ramm, E. A comparison of discrete granular material models with continuous microplane formulations. *Granul. Matter* (2000) **2**:113–121.

[13] Grégoire, D., Rojas-Solano, L.B. and Pijaudier-Cabot, G. Failure and size effect for notched and unnotched concrete beams. *Int. J. Numer. Anal. Met.* (2013) **37**:1434–1452.

V International Conference on Particle-based Methods – Fundamentals and Applications
PARTICLES 2017
P. Wriggers, M. Bischoff, E. Oñate, D.R.J. Owen, & T. Zohdi (Eds)

NUMERICAL MODELLING OF THE SEPARATION OF COMPLEX SHAPED PARTICLES IN AN OPTICAL BELT SORTER USING A DEM–CFD APPROACH AND COMPARISON WITH EXPERIMENTS

CHRISTOPH PIEPER[1], GEORG MAIER[2], FLORIAN PFAFF[3], HARALD KRUGGEL-EMDEN[4], ROBIN GRUNA[2], BENJAMIN NOACK[3], SIEGMAR WIRTZ[1], VIKTOR SCHERER[1], THOMAS LÄNGLE[2], UWE D. HANEBECK[3] AND JÜRGEN BEYERER[2]

[1]Department of Energy Plant Technology
Ruhr-University Bochum
Universitätsstraße 150, 44780 Bochum, Germany
e-mail: pieper@leat.rub.de, web page: https://www.leat.rub.de/

[2]Fraunhofer Institute of Optronics,
System Technologies and Image Exploration
Fraunhoferstraße 1, 76131 Karlsruhe, Germany

[3]Intelligent Sensor-Actuator-Systems Laboratory
Karlsruhe Institute of Technology
Adenauerring 2, 76131 Karlsruhe, Germany

[4]Mechanical Process Engineering and Solids Processing
Technical University Berlin
Ernst-Reuter-Platz 1, 10587 Berlin, Germany

Key words: Optical sorting, DEM, CFD, Complex shaped particles

Abstract. In the growing field of bulk solids handling, automated optical sorting systems are of increasing importance. However, the initial sorter calibration is still very time consuming and the precise optical sorting of many materials still remains challenging. In order to investigate the impact of different operating parameters on the sorting quality, a numerical model of an existing modular optical belt sorter is presented in this study. The sorter and particle interaction is described with the Discrete Element Method (DEM) while the air nozzles required for deflecting undesired material fractions are modelled with Computation Fluid Dynamics (CFD). The correct representation of the resulting particle–fluid interaction is realized through a one–way coupling of the DEM with CFD. Complex shaped particle clusters are employed to model peppercorns also used in experimental investigations. To test the correct implementation of the utilized models, the particle mass flow within the sorter is compared between experiment and simulation. The particle separation results of the developed numerical model of the optical sorting system are compared with matching experimental investigations. The findings show that the numerical model is able to predict the sorting quality of the optical sorting system with reasonable accuracy.

1 INTRODUCTION

The handling and sorting of bulk solids is of increasing importance due to continuously growing material streams [1]. Automated optical sorters can be used in addition to conventional separating processes like screens [2], which separate the material depending on physical properties like the size. Optical sorters are employed in a variety of industrial applications and are able to separate agricultural products or particulate chemical/pharmaceutical substances based on optical criteria [3]. The material stream is transported and isolated by chutes, slides or vibrating feeders and bypasses an optical sensor, before the bulk solids are separated into at least two fractions by pneumatic air nozzles. The nozzles are triggered based on the optical properties of the material.

Studies investigating the influence of optical sorter design and operation on sorting quality are still relatively scarce. De Jong and Harbeck [4] investigated the maximum throughput of an optical sorter based on different particle sizes in 2005, with the conclusion that the separation efficiency decreases if a minimum distance between adjacent particles is below a certain threshold. Pascoe et al. [5] developed a model for predicting the efficiency of their sorting system depending on the belt loading and the number of particles to be ejected. In a further study [6], the authors investigated the influence of special particle distribution on the sorting efficiency with the help of a Monte Carlo simulation. Particle ejection by compressed air has been investigated with a coupled DEM–CFD approach by Fitzpatrick et al. [7]. However, only the ejection stage with the resulting particle–fluid interaction was analyzed. In a previous study, we have shown that the DEM is able to correctly model the effect of different operating parameters on particle movement within an optical sorter [8].

In this study, a modular optical belt sorter consisting of a vibrating feeder, conveyor belt, compressed air nozzles for particle separation and a particle container is modelled with a coupled DEM–CFD approach. A sorting task is defined and an experiment on a fully operational modular sorting system is conducted. The particle separation results of the experiment are compared with those of the corresponding numerical setup.

2 METHODOLOGY

2.1 DEM-CFD approach

The Discrete Element Method (DEM) [9] is used to describe the modular optical belt sorter as well as the bulk solids investigated in this study. The DEM allows the detailed analysis of particle–particle and particle–wall interactions within the sorting system. Newton's and Euler's equations of motion are used to calculate the translational and rotational motion of every particle and can be written as

$$m_i \frac{d^2\vec{x}_i}{dt^2} = \vec{F}_i^c + \vec{F}_i^g + \vec{F}_i^{pf}, \tag{1}$$

$$\hat{I}_i \frac{d\vec{W}_i}{dt} + \vec{W}_i \times \left(\hat{I}_i \vec{W}_i\right) = \Lambda_i^{-1} \vec{M}_i, \tag{2}$$

where m_i is the particle mass, $d^2\vec{x}_i/dt^2$ the particle acceleration, $\vec{F}_i^c$ the contact force, $\vec{F}_i^g$ the gravitational force and $\vec{F}_i^{pf}$ is the particle–fluid force. The second equation gives the angular

acceleration $d\vec{W}_i/dt$ as a function of the angular velocity $\vec{W}_i$, the external moment resulting from the contact forces $\vec{M}_i$, the inertia tensor along the principal axis $\hat{I}_i$ and the rotation matrix converting a vector from the inertial into the body fixed frame Λ_i^{-1}. The utilized contact forces as well as the applied rolling friction model are presented in [8]. The non–spherical particles employed in this study are modelled with a multi–sphere approach. Here, spheres of different sizes are merged to form a cluster to accurately approximate complex particle shapes [10]. The general contact force laws remain equal to the ones used for spherical particles [11].

The compressed air nozzles used to separate undesired particles from the material stream are modelled with Computational Fluid Dynamics (CFD), solving the Navier Stokes equation based on a Finite Volume Method. This is achieved with the help of a detailed and locally refined hexagonal cell mesh. Both the fluid field as well as the enclosed nozzle are considered. The equation of continuity and the equation of momentum are solved

$$\frac{\partial \rho_f}{\partial t} + \nabla(\rho_f \vec{u}_f) = 0, \tag{3}$$

$$\frac{\partial(\rho_f \vec{u}_f)}{\partial t} + \nabla(\rho_f \vec{u}_f \vec{u}_f) = -\nabla p + \nabla(\bar{\bar{\tau}}) + \rho_f \vec{g}, \tag{4}$$

where $\vec{u}_f$ is the fluid velocity, ρ_f the fluid density, p the pressure and $\bar{\bar{\tau}}$ the fluid viscous stress tensor. The stress tensor can be written as

$$\bar{\bar{\tau}} = \mu_e \left[(\nabla \vec{u}_f) + (\nabla \vec{u}_f)^{-1}\right], \tag{5}$$

where μ_e is the effective viscosity determined from a k-ε model, which is widely used to model turbulent gas flows from nozzles [12-14].

To save computational time and due to the short activation duration of the nozzles a "one–way" coupling is performed between CFD and DEM to realize the particle–fluid interaction in the optical sorter. "One–way" coupling means that the fluid field is affecting the particle motion but not vice versa. The fluid velocity is averaged in every CFD cell and the resulting fluid velocity field is transferred to the DEM upon initialization. The particle–fluid force described in eq. (1) equals the sum of all individual particle–fluid forces. A popular model also suitable for complex shaped particles is the approach devised by Di Felice [15], where the respective force reads

$$\vec{F}_i^{pf} = \vec{F}_i^{d} + \vec{F}_i^{\nabla p} = \frac{1}{2}\rho_f |\vec{u}_f - \vec{u}_p| C_D A_\perp \varepsilon_f^{1-\chi}(\vec{u}_f - \vec{u}_p). \tag{6}$$

Here, $\vec{F}_i^{d}$ is the drag force, $\vec{F}_i^{\nabla p}$ the pressure gradient force, $\vec{u}_p$ the particle velocity, C_D the drag coefficient, $A_\perp$ the cross-sectional area perpendicular to the flow, ε_f the local fluid porosity and χ a correction factor. χ is a function of the particle Reynolds-number

$$Re = \varepsilon_f \rho_f d_p |\vec{u}_f - \vec{u}_p| / \mu_f \tag{7}$$

and is calculated as

$$\chi = 3.7 - 0.65 \exp\left(-\frac{(1.5 - \log(Re))^2}{2}\right), \tag{8}$$

where d_p is the particle diameter and μ_f the fluid viscosity. The drag coefficient is derived from a correlation proposed by Hölzer and Sommerfeld [16] and is written as

$$C_D = \frac{8}{Re}\frac{1}{\sqrt{\phi_\perp}} + \frac{16}{Re}\frac{1}{\sqrt{\phi}} + \frac{3}{\sqrt{Re}}\frac{1}{\phi^{3/4}} + 0.42 \times 10^{0.4(-\log(\phi))^{0.2}}\frac{1}{\phi_\perp}, \tag{9}$$

where $\phi_\perp$ is the crosswise sphericity, which is defined as the ratio between the cross-sectional area of a volume equivalent sphere and the projected cross–sectional area of the considered particle perpendicular to the flow. ϕ is the sphericity, namely the ratio between the surface area of a volume equivalent sphere and the surface area of the particle considered.

2.2 Experimental and numerical setup

A modular optical belt sorter is used to conduct the experiments presented and as a baseline for the numerical model and the simulations performed. The modular optical belt sorter combines all major components of a regular full size sorter with the advantage of being easy to adjust, handle and operate. The experimental and numerical setup is shown in Figure 1. Both setups consist of a vibrating feeder, a conveyor belt and the particle separation stage with compressed air nozzles, as well as a separation container. The vibrating feeder operates at a frequency of 50 Hz and at an angle of 25°. The amplitude of the feeder can be regulated. The conveyor belt runs at a constant velocity of 1.1 m/s and a total of sixteen air nozzles are employed for particle ejection.

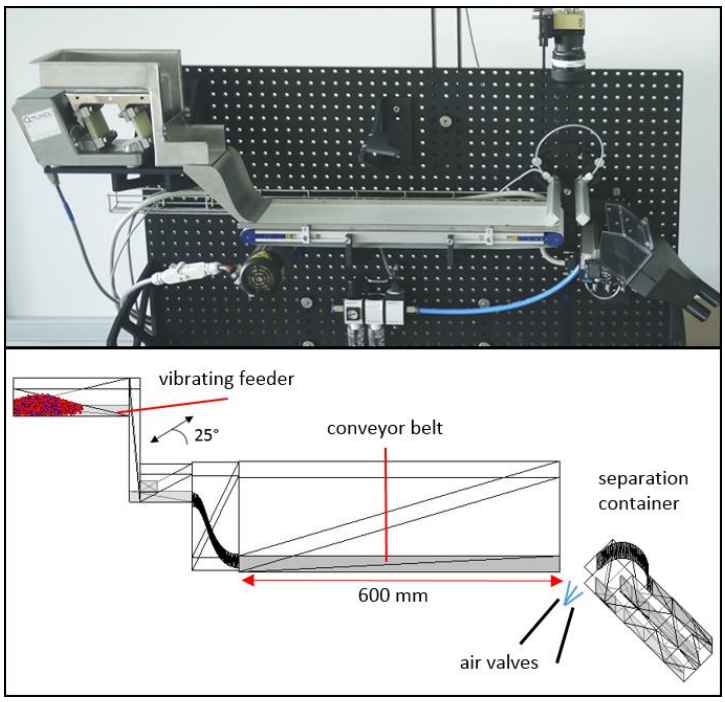

Figure 1: Experimental (top) and numerical (bottom) setup of the optical belt sorter

The sorting task in both the experiment and the simulation is to separate 10 g of colored peppercorns from 40 g of uncolored ones in batch operation. At the start of the process, the two particle fractions are mixed and a total of 50 g of peppercorns are randomly filled in a container, which is then placed on top of the already vibrating feeding system. The container is lifted and the particles are transported towards the conveyor belt by a slide. In the experimental investigation a line scan camera is located at the end of the belt. The color of passing particles is detected and depending on the y-location of the peppercorn, a specific nozzle is activated. The delay between particle detection and nozzle activation is calculated by assuming that the particle is moving with belt velocity. Particle movement orthogonal to the belt is neglected.

2.3 Investigated bulk solids and DEM operating parameters

The bulk solids chosen for the presented study are green peppercorns. They are selected due to their easy accessibility, importance in the optical sorting industry and irregular movement on the conveyor belt. The latter makes the sorting task especially difficult and allows a detailed analysis of the influence of different operational parameters.

In order to determine the particle properties and to model the peppercorns within the DEM a size, volume and density investigation is conducted. Based on a shadow projection of different peppercorns, five particle shape types are created using particle clusters. The approximation is performed with a MATLAB script by filling the depicted particle outline with 8–10 spheres, depending on the complexity of the shape. This can be seen in Figure 2. A volume–based size distribution with five different particle sizes is implemented to ensure a correct representation of the packing structure and local solid fraction distribution within a particle packing and therefore the overall approximation quality.

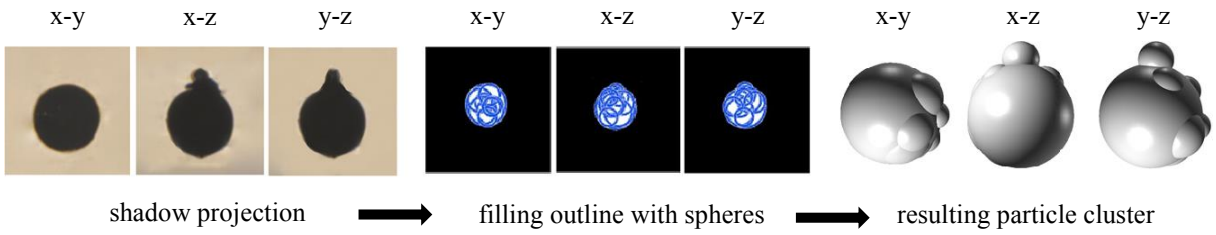

Figure 2: Peppercorn approximation for the DEM

Apart from the particle shape and size, important DEM parameters describing the particle–particle as well as particle–wall interaction have to be defined. The coefficients of normal restitution, Coulomb friction and rolling friction are initially determined experimentally on a single particle scale according to the procedures described by Höhner et al. [17] and Sudbrock et al. [18]. For the particle–wall contacts, the steel used for the vibrating feeder and slide of the sorter and the material of the conveyor belt are considered.

In order to optimize the resulting parameters, further tests are conducted and compared between experiments and simulation. To analyze the parameters in a dynamic scenario, a rotary drum with a steel/belt material outline is filled with peppercorns to account for one third of the drum volume. The drum is then rotated with a constant velocity and the resulting angle of repose is compared between simulation and experiment. A comparison can be seen in Figure 3.

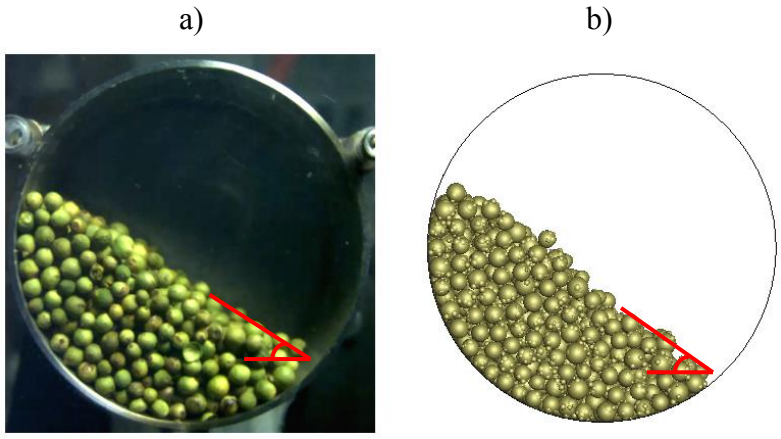

Figure 3: Angle of repose compared between a) experiment and b) simulation, dynamic scenario

In a second step, a static scenario is investigated, where a defined mass of peppercorns is filled into a stationary cylinder. The cylinder was previously placed on a steel/belt material base. Once the particles settle, the cylinder is lifted upwards with a defined velocity and the particles form a pile on the respective surface material. A second, wider ring prevents the almost spherical peppercorns from rolling off the test rig. Similar to the dynamic investigation the resulting angle of repose is compared between simulation and experiment, see Figure 4. Both sides of the pile are considered and the two angles are combined to calculate a total angle of repose.

Figure 4: Angle of repose compared between a) experiment and b) simulation, static scenario

After comparing the angles between the experiment and the simulation, the initial DEM particle parameters are slightly adjusted and another dynamic and static simulation is performed. The established angles are compared again and the process is repeated until the parameters employed result in matching angles of repose both for the static and dynamic scenario. The final particle parameters for the peppercorns are presented in Table 1. The rolling friction coefficient is considered to be equal for all contact forms.

Table 1: Particle properties of the peppercorns required for them DEM simulations

Particle property	Value
Average mass [g]	0.0271
Average density [kg/m²]	551.47
Restitution coefficient PP [-]	0.627
Restitution coefficient PW sorter [-]	0.721
Restitution coefficient PW belt [-]	0.701
Friction coefficient PP [-]	0.4
Friction coefficient PW sorter [-]	0.326
Friction coefficient PW belt [-]	0.336
Rolling friction coefficient [-]	0.00008

The DEM simulations are performed with a time step of $1 \cdot 10^{-5}$ s and a maximum particle overlap of 0.5 % of the particle diameter is ensured. The spring stiffness k^n and k^t as well as the damping coefficient γ^n are calculated from the chosen time step and the respective coefficient of restitution.

2.4 Air nozzle model and implementation within the numerical setup

To simulate the fluid flow within the air nozzle and in the resulting flow field forming at the nozzle outlet, a hexagonal mesh of the air nozzle interior and the adjacent airspace is created. A CAD model of the nozzle bar employed in the modular optical belt sorter (Figure 5 a) is used for generating the basic nozzle geometry, see Figure 5 b). Only one of the sixteen nozzles is utilized. The nozzle has one inlet and splits up into four nozzle outlets to cover the entire width of the conveyor belt.

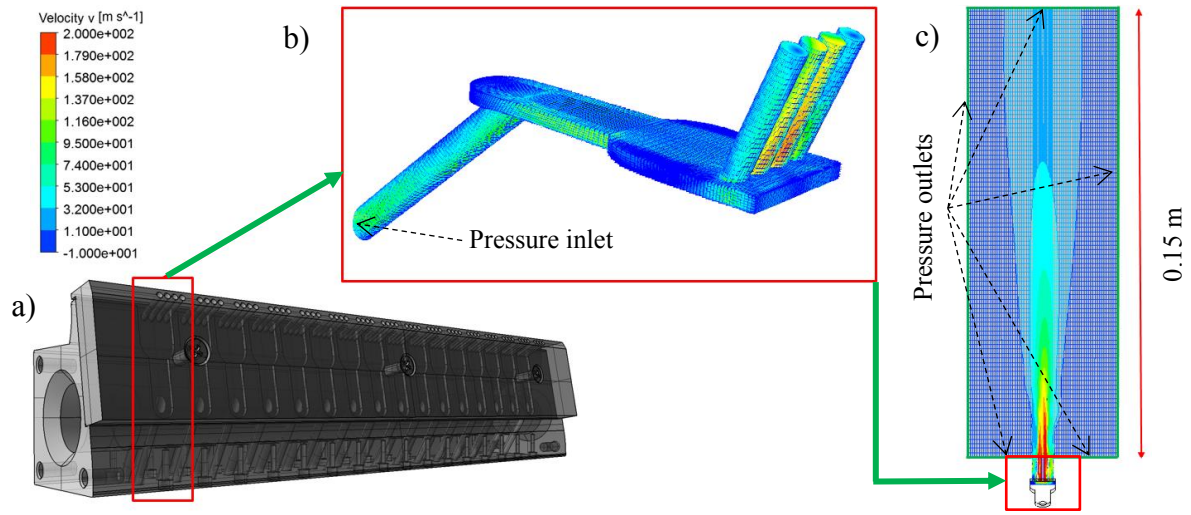

Figure 5: Air nozzle mesh b) derived from a CAD model of the sorting system nozzle bar a) and resulting fluid field c)

A pressure inlet is defined at the nozzle inlet and pressure outlets at the outer edges of the modelled airspace, see Figure 5 c). A gauge pressure of 1.25 bar is applied at the pressure inlet and the adjacent room is filled with quiescent air. The calculation is performed stationary and the fluid is assumed as incompressible. A standard k–ε turbulence model is employed. The air has a density of ρ_f = 1.225 kg/m², viscosity of μ_f = 1.7894 ·10^{-5} kg/(m·s) and a temperature of T_f = 293.15 K.

Once the CFD calculation has converged, the resulting fluid data is prepared for utilization within the DEM. As the resolution of the fluid grid is very fine with 1.86 million cells and would result in very long simulation durations when used in the DEM, the fluid properties are averaged to larger cells. In addition, the fluid field is trimmed to fit the air jet contours, which also reduces the amount of fluid cells and therefore the required calculation time. The new fluid cells have a dimension of 2 × 2 × 2 mm³ and cover a volume of 20 × 50 × 150 mm³. To model the entire nozzle bar, the fluid cell zone calculated for a single nozzle is duplicated sixteen times and joint together to form one large grid, now consisting of 159,375 cells.

When a particle enters the zone where the fluid cells are coupled with the DEM, the fluid properties of every fluid cell that lies within the particle boundary are averaged and used to calculate the particle–fluid force described in Section 2.1. If a particle enters a zone in which the fluid fields of two nozzles overlap, there are three different possibilities regarding which fluid properties are assigned to the fluid cells and used for calculation. Depending on the nozzles activated by the prediction algorithm at the particle detection stage, either nozzle 1, nozzle 2 or both nozzles are activated. In the first two cases, the fluid properties of the respective nozzle are considered. If both are activated, the fluid properties of the nozzle with the higher absolute velocity at the cell position are assigned to the fluid cell.

3 RESULTS AND DISCUSSION

3.1 Comparison of mass flow between experiment and simulation

To ensure that the particle approximation as well as the determined particle parameters are correct and suitable to model the particle behavior within the optical sorter, the mass flow of peppercorns is measured both experimentally and numerically. As the mass flow rate is highly dependent on the vibrating feeder amplitude, a high–speed camera is used to analyze the amplitude, angle and frequency of the induced vibration in detail. Results show that the frequency and vibration–angle are constant with values of 50 Hz and 25° respectively. The amplitude can be regulated with a transformer and three amplitudes of a_1 = 0.402 mm, a_2 = 0.278 and a_3 = 0.236 were measured and then used for the comparison.

To measure the exiting particle mass flow in the experimental setup, a scale with a collecting container is positioned at the end of the conveyor belt and connected to a computer. Both the air nozzles as well as the separation container are removed during the procedure. At the start of the experiment, the same procedure used for the separation investigation described in Section 2.2 is employed. 100 g of peppercorns are used in all iterations and the measurement is repeated three times for each investigated amplitude setting. The results are shown in Figure 6.

The figure shows that there is good agreement between the DEM simulations and the conducted experiments. Slight offsets can be seen at the end of the process, especially for small amplitudes. Here, the peppercorns in the simulation exit the system at a faster pace. Further

investigation showed that this is likely due to small irregularities and dents on the surface of the vibrating feeder of the experimental setup. These imperfections cause particle movement to slow down, especially when the peppercorns no longer move in bulk.

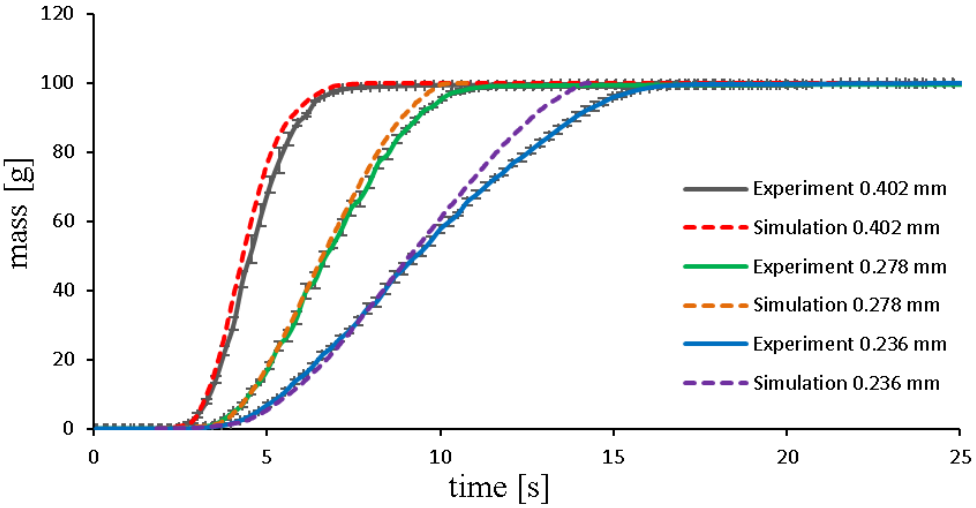

Figure 6: Exiting mass of peppercorns for different operating amplitudes compared between experiment and simulation

3.2 Comparison of separation results

For both the experimental and numerical investigation of particle separation, the operation procedure described in Section 2.2 is applied. The experiment is carried out first and important system parameters vital for efficient particle separation like valve activation duration, distance between particle detection and separation stage, applied nozzle gauge pressure and orientation of the separation container are defined and noted for the DEM–CFD Simulations. It is important to keep in mind that the goal of the conducted experiment is not to achieve a perfect separation quality, but to ensure that defined system parameters are used that can be transferred to the numerical setup. The system was deliberately run under difficult operating conditions and with a high particle feed rate in order to properly test the numerical accuracy. The experiment is conducted three times.

After the sorting process is complete, the peppercorns are extracted from the separation container and the separation quality is assessed by weighing the different particle fractions. This is of course not necessary for the simulation where the sorting result is directly written to a text file.

The findings of the conducted experimental and numerical sorting process and its comparison are presented in Figure 7. The error bars represent the standard deviation of the three conducted experiments. The results show that there is generally good agreement between the experiment and simulation. Figure 7 a) shows the percentage of the colored peppercorns ejected and not ejected from the material stream. The amount of particles ejected is only slightly higher for the simulation, which is most likely due to the fact that a small amount of particles is not correctly identified by the line scan camera. This is of course not the case in the

simulation. The separation results of the uncolored particles can be seen in Figure 7 b). Only a small amount of by–catch is produced and the simulation differs from the results obtained from the experiment only by a very small margin. The percentage of missing particles (particles that wrongly exit the sorting process, mostly at the separation stage) is shown in Figure 7 c). Here, the percentage of missing particles is significantly higher for the simulation compared to the experimental results. However, as already very few particles have a very high impact on this result and the standard deviation of the three experiments is fairly high, additional simulations and evaluation need to be performed.

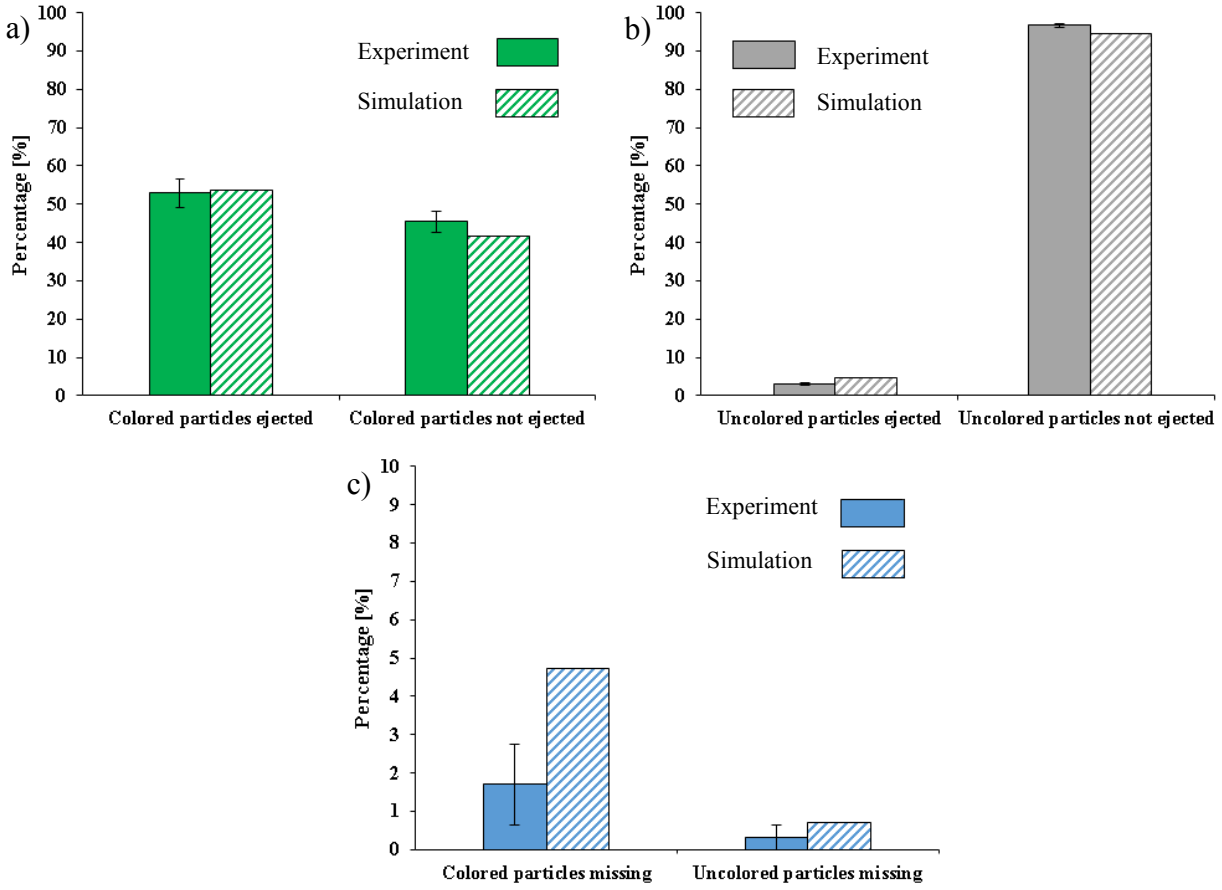

Figure 7: Comparison of particle separation results between experiment and simulation for a) ejected/not ejected colored particles, b) ejected/not ejected uncolored particles and c) colored/uncolored missing particles

4 CONCLUSION

A fully automated optical belt sorter was numerically modelled with a coupled DEM–CFD approach. Complex shaped particles were approximated with the help of particle clusters and DEM parameters were derived by experimental and numerical investigations. Particle mass flow through the optical sorter was analyzed for different vibrating feeder amplitudes in matching numerical and experimental setups. The compressed air nozzles of the sorter were modelled with CFD and the resulting fluid field coupled with the DEM upon initialization in a "one–way" coupling approach. An experiment with a defined sorting task was conducted on

the modular sorting system and separation results were compared to those of corresponding DEM–CFD simulations.

- The particle approximation of peppercorns by particle clusters and the DEM parameter definition shows good results when comparing the particle mass flow through the sorter between experiment and simulation. At low vibrating feeder amplitudes, the simulation shows a slightly higher mass flow rate compared to experimental findings, which is most likely explained by small imperfections on the surface of the vibrating feeder, causing the peppercorns' velocity to slow down.
- The comparison of the separation results shows good agreement between conducted DEM–CFD simulations and experiments. The presented modelling approach seems promising and suitable for further investigation.
- Additional research analyzing different operating parameters of the optical sorter is planned, where other particles like maize grains or coffee beans are employed. Altering other important system parameters like material composition, valve activation duration or conveyor belt velocity is also planned for future investigation.

Acknowledgement

The IGF project 18798 N of the research association Forschungs–Gesellschaft Verfahrens–Technik e.V. (GVT) was supported via the AiF in a program to promote the Industrial Community Research and Development (IGF) by the Federal Ministry for Economic Affairs and Energy on the basis of a resolution of the German Bundestag.

REFERENCES

[1] Duran, J. *Sands, Powders and Grains*. Springer New York, (2000).
[2] Stieß, M. *Mechanische Verfahrenstechnik 1*. Springer Berlin, (1995).
[3] McGlichey, D. *Characterisation of Bulk Solids.* Blackwell Publishing Ltd. Oxford, (2005).
[4] De Jong and Harbeck, T.P.R. Automated sorting of minerals: current status and future outlook. *Proc. 37th Can. Miner. Process. Conf.* (2005) 629-648.
[5] Pascoe, R.D., Udoudo, OB. and Glass H.J. Efficiency of automated sorter performance based on particle proximity information. *Miner. Eng.* (2015) **23**:806-812.
[6] Pascoe, R.D., Fitzpatrick, R. and Garratt, J.R. Prediction of automated sorter performance utilizing a Monte Carlo simulation of feed characteristics. *Miner. Eng.* (2015) **72**:101-107.
[7] Fitzpatrick, R.S., Glass H.J. and Pascoe R.D. CFD–DEM modelling of particle ejection by a sensor–based automated sorter. *Miner. Eng.* (2015) **79**:176-184.
[8] Pieper, C., Maier, G., Pfaff, F., et al. Numerical modeling of an automated optical belt sorter using the Discrete Element Method. *Powder Technol.* (2016) **301**:805-814.
[9] Cundall, P.A. and Strack, O.D.L. A discrete numerical model for granular assemblies. *Geotechnique* (1979) **29**:47-65.
[10] Kruggel-Emden, H., Rickelt, S., Wirtz, S. and Scherer, V. A study on the validity of the multi–sphere discrete element method. *Powder Technol.* (2008) **188**:153-165.
[11] Höhner, D., Wirtz, S., Kruggel-Emden, H. and Scherer, V. Comparison of the multi-sphere and polyhedral approach to simulate non-spherical particles within the discrete

element method: influence of temporal force evolution for multiple contacts. *Powder Technol.* (2011) **208**:643-656.

[12] Xue, K., Li, K., Chen, W., Chong, D. and Yan, J. Numerical investigation on the performance of different primary nozzle structures in the supersonic ejector. *Energy Procedia* (2017) **105**:4997-5004.

[13] Raj, A.R.G.S., Mallikarjuna, J.M. and Ganesan, V. Energy efficient piston configuration for effective air motion – A CFD study. *Applied Energy* (2013) **102**:347-354.

[14] Chu, H., Zhang, R., Qi, Y. and Kann, Z. Simulation and experimental test of waterless washing nozzles for fresh apricot. *Biosystems Engineering* (2017) **159**:97-108.

[15] Di Felice, R. The voidage function for fluid–particle interaction systems. *Int. J. Multiph. Flow* (1994) **20**:153-159.

[16] Hölzer, A. and Sommerfeld, M. New simple correlation formula for the drag coefficient of non-spherical particles. *Powder Technol.* (2008) **184**:361-365.

[17] Höhner, D., Wirtz, S. and Scherer, V. Experimental and numerical investigation on the influence of particle shape and shape approximation on hopper discharge using the discrete element method. *Powder Technol.* (2013) **235**:614-627.

[18] Sudbrock, F., Simsek, E., Rickelt, S., Wirtz, S. and Scherer, V. Discrete element analysis of experiments on mixing and stoking of monodisperse spheres on a grate. *Powder Technol.* (2011) **208**:111-120.

V International Conference on Particle-based Methods – Fundamentals and Applications
PARTICLES 2017
P. Wriggers, M. Bischoff, E. Oñate, D.R.J. Owen, & T. Zohdi (Eds)

TEXTURE AND STRESS TRANSMISSION IN BINARY GRANULAR COMPOSITES: COMPARISON BETWEEN SIMULATIONS AND EXISTING EXPERIMENTS

PAWARUT JONGCHANSITTO[1] AND ITTHICHAI PREECHAWUTTIPONG[1]

[1]Department of Mechanical Engineering, Faculty of Engineering, Chiang Mai University (CMU)
239 Huay Kaew Rd., Suthep, Muang district, Chiang Mai 50200, Thailand
e-mail: pawarut.j@cmu.ac.th and itthichai.p@cmu.ac.th

Key words: Molecular dynamics method, Granular media, Composites, Textures, Hydrostatic stresses.

Abstract. The morphology of two-dimensional cohesionless composite granular media obtained from thermoelastic stress analysis (TSA) experiments and molecular dynamics (MD) simulations is methodically compared by using the statistical analysis through the distributions of the hydrostatic stress in the particles and of the geometrical contact orientation between particles. Two different particles with a stiffness ratio of four between them are employed to prepare the numerical composite samples under study. Under a confined vertical compression in static conditions, experimental and numerical results are in good agreement in terms of the distributions of the hydrostatic stresses and of the contact directions.

1 INTRODUCTION

Sand, soil, and rock play a significant role in civil and geotechnical engineering to construct many infrastructures in our daily life, e.g. bridges, water dams, foundations, residential buildings, highways, etc. These are examples of granular materials, which are plentiful around us. In this context, a collection of solid particles, whose macroscopic mechanical behavior is governed by the inter-particle forces between contacts, is referred to as granular materials. They are composed from grains with a variety of sizes, shapes, and types of constitutive material. Due to a great diversity in grains, the behaviors of granular media are generally complex which cannot differentiate from those ordinary solids, liquids, and gases [1, 2]. Although this complexity remains far from well understood for researchers in many areas, there has been a significant effort for researchers describe and understand behaviors of granular materials during the past thirty years. Previous studies on granular mechanics mainly focus on mechanical behaviors of "non-composite" granular media, i.e. made of only one type of constitutive material, despite the fact that granular materials in engineering and industrial fields are prepared from various particles that their physical properties are different. That is why there is a lack of knowledge on mechanics of "composite" granular materials. Nonetheless, a few numerical and experimental studies pertaining to composite granular media can be found in the literature [3-6]. Recently, thermoelastic stress analysis (TSA) based on infrared (IR) thermography was experimentally performed to measure the hydrostatic stresses in the particles of two-dimensional composite

granular media [7]. This composite was prepared from two materials with different rigidity.

Since the first pioneering work performed more than the past four decades by Cundall ans Strack [8], the discrete or sometimes known as distinct element method (DEM) has proven to be a powerful and useful approach that provides a relationship between micromechanical data to macromechanical data by means of statistical mechanics [9]. The DEM was widely applied to investigate the mechanical behavior of non-composite granular media, e.g. the effects of the particle size and shape [10-12], the coefficient of friction [13], the surface energy [14] on contact force networks. From the authors' point of view, the DEM offers an effective way to investigate the mechanical behavior of composite granular materials. In this study, the molecular dynamics (MD) simulations which belong to the DEM are therefore applied to systematically model the two-dimensional non-cohesive composite granular system. Numerical results and experimental results obtained by thermoelastic stress analysis (TSA) experiments [7] are then statistically compared by using the granular texture in terms of distribution of the hydrostatic stress in the particles and contact orientation between particles. It must be noted that hydrostatic stresses provided by TSA experiments are used in this analysis instead of contact forces

The paper is organized as follows. Section 2 describes the theoretical aspects of MD simulations in terms of model for interaction forces, the details of numerical samples, and derivation of stress from contact forces. Section 3 is devoted to the statistical analysis and the comparison with experimental results.

2 THE MOLECULAR DYNAMICS MODELING

The molecular dynamics (MD) method relies on an explicit algorithm, which considers all particles of granular medium as rigid bodies with non-conforming surfaces [15]. The motions of each particle with respect to time are governed by Newton's equations of motion. These motion equations are numerically integrated using a predictor-corrector scheme with Gear's set of corrector coefficients [16].

2.1 Interaction force model

The interaction force model for contacting particles is an important part of the MD simulations. The interaction force is divided into a normal force and a tangential force. A variety of most commonly used force models in MD simulations was mentioned by Schäfer *et al.* [17]. In fact, local deformation in continuum mechanics occurs when two solid bodies are in contact [18]. Due to rigid bodies considered in the MD method, this deformation is easily modeled by using a virtual overlap δ at the contact point without change in the particle shape. The contact force is therefore calculated as a function of this virtual overlap (δ). In the case of circular disks, the virtual overlap between particles can be directly calculated from their vector position of the particle centers x_i and x_j and radii r_i and r_j:

$$\delta = \left(r_i - r_j\right) - \left|x_i - x_j\right| \tag{1}$$

In the case of $\delta > 0$, a simple model so-called the "linear spring-dashpot" [17-20] was employed to calculate the normal force between two particles in contact. The normal contact force can be separated into two components. The first component is an elastic repulsive force, which plays a role to withstand the deformation due to an external compression. It is simply

modeled as a linear spring. The second component is energy dissipation, which is relevant to an intrinsic characteristic of granular materials. It is represented through a viscous force. The expression of the normal force amplitude F_n can be written by

$$F_n = k_{eff}\delta + \alpha_n v_n \tag{2}$$

where k_{eff} is the effective contact stiffness, α_n is a normal damping coefficient, and v_n is the normal velocity (time derivative of the virtual overlap).

Due to the fact that the Coulomb's law of friction is a non-smooth function, we cannot directly apply this friction law to MD simulations. It can be additionally explained that the integration of Newton's equations of motion requires a smooth (mono-valued) friction law in such a way that the friction force can be mathematically expressed as a linear function of the sliding velocity v_s. As a consequence, the tangential force F_t in this study can be simply implemented by using a "regularized" form of the exact Coulomb's law [11, 17, 20], which can be computed by the following expression:

$$F_t = \min\left\{\left|\gamma_s v_s\right|, \mu F_n\right\} \cdot \mathrm{sign}\left(v_s\right) \tag{3}$$

where γ_s is the tangential viscosity coefficient and μ the coefficient of friction. It must be noted that the rotational motion due to the tangential force is allowed to be free in this study.

2.2 Preparation and simulation of numerical samples

Three similar composite configurations that used in the TSA experiments [7] were selected to prepare the two-dimensional numerical composite sample. This composite system was made of two constitutive materials with different rigidities as shown in Fig. 1a: polyoxymethylene (POM) appearing in black is termed a "stiff" particle, and high-density polyethylene (HDPE) appearing in white is a "soft" particle in the following. The stiff particle is approximately four times stiffer than the soft particle [7]. Table 1 gives the ratio of diameters D_{stiff}/D_{soft} and number of particles N_{stiff}/N_{soft} for each of the three configurations tested. Sample#1 is a monodisperse medium (D_{stiff}/D_{soft} = 1), whereas the others are bidisperse. It must be noted that in practice we aimed at analyzing only the effect of the D_{stiff}/D_{soft} ratio. This is a reason why the N_{stiff}/N_{soft} ratio for sample #1 and #2 are nearly close to 1, excluding sample #3. In addition, our analysis in the framework of 2D homogenization requires at least 300 particles to obtain relevant statistical values. This corresponds to the report in ref. [21] which mentioned that the linear scale of statistical homogeneity in a 2D assembly is a few tens of particle diameters. This criterion is reasonably satisfied for the three configurations under the study (see the last column in Table 1).

For each sample, the locations of particles were extracted from the optical image of real composite granular system from experiments (Fig. 1a). Such extracted positions were then employed to prepare the numerical samples inside a nearly square box consisting of four rigid plane walls. Fig. 1b presents an example of numerical preparation for sample #1. Under quasi-static conditions, a compressive vertical force of 60 kN was incrementally applied on the granular samples at the lower wall, while the other walls were still fixed during the test. The gravitational force was also considered during the simulations, even though it can be negligible compared to the magnitude of the external applied loading. It must be noted that all

contact types between particles consist of the contacts between stiff-stiff, soft-soft, and stiff-soft particles.

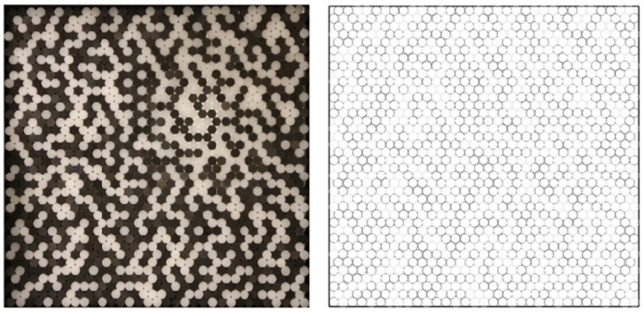

Figure 1: Experimental (a) and numerical (b) locations of the particles inside the composite sample #1.Note that for numerical sample, black color represents the stiff particle, while the soft one is indicated by grey color

Table 1: Three different samples used in this study

	Ratio of diameters D_{stiff} / D_{soft}	Number of cylinders N_{stiff} : N_{soft}	Ratio of cylinder numbers 1 : N_{stiff} : N_{soft}	Total number of cylinders
#1	1.0	638 : 597	1 : 0.94	1235
#2	1.6	334 : 371	1 : 1.11	705
#3	3.0	86 : 466	1 : 5.42	552

The normal and tangential forces between the inter-particle contacts are computed by using Eq. (2) and Eq. (3), respectively. The contact forces between wall and particles are also calculated by these expressions. Note that the effective contact stiffness k_{eff} is dependent of the types of contacting particles. The effective contact stiffness for the contact between stiff and soft particles is defined by $(k_{stiff} \times k_{soft})/(k_{stiff}+k_{soft})$. When the same types of material are in contact, k_{eff} is given by k_{stiff} for stiff and stiff contacting particles, by k_{soft} for soft and soft contacting particles. Furthermore, the contact stiffness in the case of the contact between wall and particles is simply considered by using the same value of k_{stiff}. The simulations were accomplished when the granular systems reached static equilibrium conditions. Next, the hydrostatic stress in each particle was determined from the list of normal and tangential forces obtained at the final stage of the simulations.

2.3 Determination of the hydrostatic stress in each particle

A definition of Cauchy stress tensor cannot be directly used in the meaning of granular (discrete) materials [22]. In addition, the simulations practically offer the forces between inter-particle contacts. In order to compare between the simulations and the experiments, it is necessary to derive the hydrostatic stress in each particle from the simulated interaction forces. In the past, several researches [23-25] proposed a stress tensor for discrete materials under equilibrium conditions, which relate the interaction forces in local scale to the stress tensor in macroscopic scale. The definition of the stress tensor at the macroscopic scale is

described by using a grain-by-grain approach based on the internal moment tensor $\mathbf{M}^{\mathbf{i}}$ of each particle p [25]. The symmetric second-order stress tensor σ_{ij} can be related to the interaction forces inside a granular assembly of volume V in the following way:

$$\sigma_{ij} = \frac{1}{V}\sum_{p\in V} M_{ij}^{p} = \frac{1}{V}\sum_{c\in V} f_i^c l_j^c \tag{4}$$

where the contact forces $f_1^c, f_2^c, \ldots, f_i^c$ act at the contact point c between the particles due to the external applied loading, and the vector l_j^c is the branch vector connecting the centroids of two particles in contact at point c. It is worth mentioning that the first summation in Eq. (4) is done over all particles, whereas the second summation is performed over the whole set of contacts within the volume V.

Next, the definition of the stress tensor at the macroscopic scale in Eq. (4) is developed at the particle scale to provide the stress tensor $\boldsymbol{\sigma}^{\mathbf{p}}$ in an individual particle. The stress tensor at the particle scale is calculated by the sum of the interaction forces and the radius vector of the particle at the contact point c along the particle perimeter over the particle volume V_p:

$$\sigma_{ij}^{p} = \frac{1}{V_p}\sum_{c\in V_p} f_i^c r_j^c \tag{5}$$

The list of normal and tangential forces obtained from the simulations is then employed to determine the stress tensor in each particle using Eq. (5). Under an assumption of plane stress satisfied in the present study, the eigenvalues of the stress tensor are used to compute the two in-plane principal stresses σ_1 and σ_2 of $\boldsymbol{\sigma}^{\mathbf{p}}$. The hydrostatic stress or average stress in each particle [24] is then determined by:

$$\sigma_{hyd} = \frac{(\sigma_1 + \sigma_2)}{2} \tag{6}$$

3 SIMULATION RESULTS AND COMPARISON WITH EXPERIMENTS

In this section, the numerical results obtained from MD simulations in this study and the experimental results obtained by thermoelastic stress analysis [7] are statistically analyzed by using the granular texture in terms of distribution of the hydrostatic stress in the particles and of the contact orientation between inter-particle contacts. Note that the results obtained by TSA experiments are fully described and discussed in a recent published paper (see ref. [7]).

3.1 Normalized hydrostatic stress networks

The simulations provide the network of normal contact forces for each sample as illustrated in Fig. 2a. The normal forces were represented by the red lines, whose thickness is proportional to the magnitude of the normal force. By comparing the three configurations, it is interesting to note that the larger particle size in granular system transmits the stronger force. Although the contact stiffnesses play a role in distribution of the force magnitude, the influence of polydispersity (in terms of particle size) on composite granular materials is still similar to what is observed in granular media made of only one type of constitutive

material [26]. Moreover, it is clearly observed that strong inhomogeneous interaction forces are exhibited in the composite system. This is a significant characteristic of non-composite granular medium. The normalized hydrostatic stress σ_{norm} networks for the simulations and experiments are shown in Figs. 2b and 2c, respectively. It must be noted that the definition of σ_{norm} is the ratio of the hydrostatic stress in the particle to the average hydrostatic stress value over the *whole* granular material. Similar to the contact force networks, heterogeneous stress fields are also observed in both monodisperse (sample #1) and bidisperse media (samples #2 and #3).

A triangular network, which mainly consists of straight lines inclined at ±60° with respect to the horizontal, is revealed in sample #1 for both the hydrostatic stress and contact force networks. This observation is not surprising due to the fact that the triangular network is a typical characteristic of monodisperse granular materials. It can be additionally seen that the highest stresses are found in the small particles for sample #2 and #3, although the strong force transmissions are provided by the larger particles as mentioned above. This can be explained by the fact that the division by V_p in Eq. (5) may cause high stress values when the particle size is small, even if this particle transmits low contact forces.

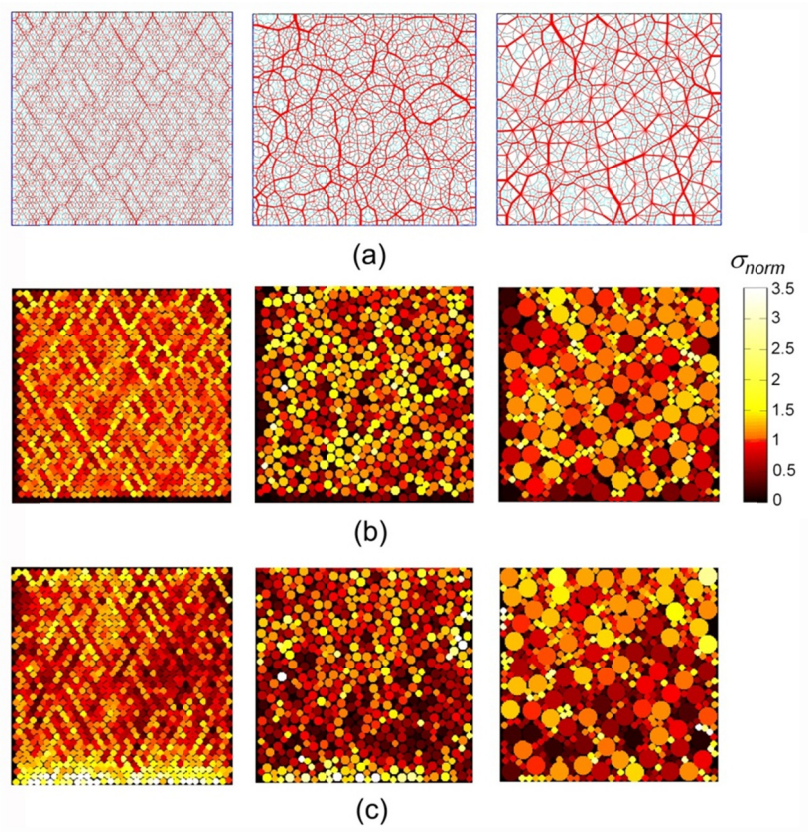

Figure 2: Results obtained for composite granular samples: (a) Normal contact force network obtained by MD simulation, (b) Field of normalized hydrostatic stress σ_{norm} determined from the simulated contact forces, and (c) Field of σ_{norm} obtained from the experiment

The differences between the hydrostatic stress networks obtained from simulations (Fig.

2b) and experiments (Fig. 2c) are anticipated. Indeed, it is not feasible to get precisely the same stress pattern between the experiment and the simulation at the particle scale. This may due to an inherent variation of parameters in any experiment: variation in terms of diameters, roundness, physical material properties, etc. A technical problem in the sense of particle locations may be also included. As a result, a micromechanical analysis of the experimental and numerical results is now performed through the granular texture.

3.2 Angular distribution of contact directions

In this section, the angular distribution of the contact directions is deduced from the experimental and numerical results. This is a useful statistical quantity to characterize the probability of contact orientation in each direction of the space. The angular distribution of the contact directions is relevant to the fabric tensor [27, 28], which enables us to understand the geometrical orientation of the particles and reveals a development of anisotropic structure of the granular system.

In the 2D representation, we characterize the angular distribution of contact directions by using the polar diagrams of the probability distribution $P(\theta)$ of the contact directions θ along the normal direction **n** as illustrated in Fig. 3. In this context, a definition of the function $P(\theta)$ is the ratio of the number of contacts in normal directions within an angular interval between θ - d$\theta/2$ and θ + d$\theta/2$ [28] to the total number of normal contacts in the system. There are 18 angular sectors lying between the angular range [0, 180°], which is plotted in the upper part of the diagram, while the bottom part corresponding to the range [0, -180°] is physically equivalent to the upper part. The contact between two particles in both the simulation and the experiment is detected when the distance between their centroids is lower than the sum of their radii. Four different types of contacts were analyzed by considering: all the contacts (Fig. 3a), only the stiff-stiff contacts (Fig. 3b), only the soft-soft contacts (Fig. 3c) and only the stiff-soft contacts (Fig. 3d). It must be noted that the term “all contacts” means all types of contact are considered: stiff-stiff, soft-soft, and stiff-soft. From Fig. 3, several comments can be made as follows:

- The contact directions in the monodisperse case (sample #1) are logically distributed along specific directions, i.e. 0°, 60°, and 120°, for whatever the type of contact considered: see the left column of Fig. 3. The polydisperse cases in samples #2 and #3 are taken into account. The contact directions are oriented in a quasi-homogeneous (isotropic) manner when the whole set of contacts are considered as shown in Fig. 3a. Considering the contact network between stiff-stiff particles in Fig. 3b, it can be clearly observed that the contacts are preferentially arranged along the axis of compression, i.e. the vertical axis, except for sample #3. In contrast, the other types of contact, i.e. soft-soft contacts in Fig. 3c and stiff-soft contacts in Fig. 3d, seem to be oriented along the specific directions as found in monodisperse case. These contact networks only play a role to maintain the granular system in equilibrium. In other words, the anisotropic structure of contacts between stiff-stiff particles is supported by such contact networks.
- The stiff-stiff contact network for sample #3 in Fig. 3b is considered. For both the experiment and the simulation, it is interesting to note that the distribution of the stiff-stiff contacts in sample #3 is inclined at about 45° from the vertical axis. This can be

explained by the fact relying on two reasons. First, a much difference between the cross-sections area of stiff particles and soft particles. Next, the effect of particle number on the contact orientations between soft and soft particles can be highlighted in sample #3 (Fig. 3c), which has a high number of soft particles compared to the number of stiff particles. The second reason leads to the contact directions between soft-soft particles tend to be arranged along particular directions as in the monodisperse case. Nevertheless, it can be noted that the contact network between stiff and stiff particles indeed makes an effort to arrange itself along the compression axis. As a consequence, the reason that is why the orientation of contacts between stiff-stiff particles in sample #3 is inclined at about 45° from the axis of compression is caused from a combination between the effect between stiff-stiff contact distributions and soft-soft contact distributions in this sample.

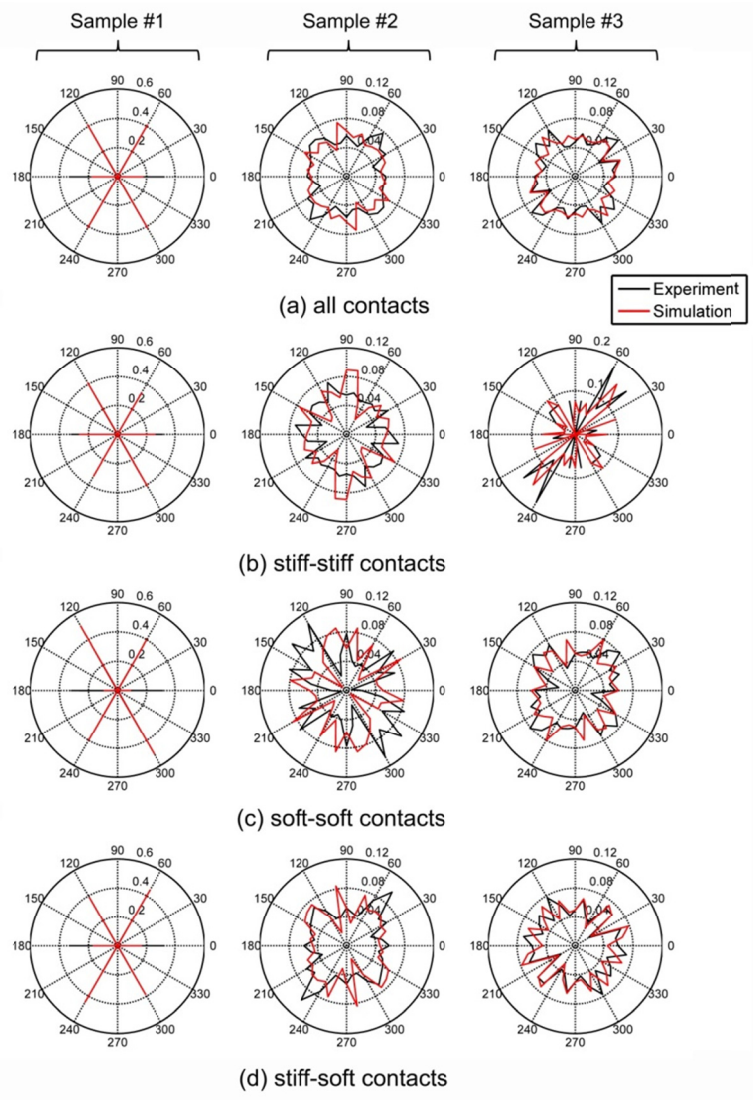

Figure 3: Polar diagram of the probability distribution of normal contact directions for each three composite samples: (a) all contacts, (b) only stiff-stiff contacts, (c) only soft-soft contacts, and (d) only stiff-soft contacts

From these several comments, it can be said that the results of the buildup of anisotropic structure owing to the mechanical loading obtained from the TSA experiments [7] and the MD simulations are good correlated from macroscopic point of view.

3.3 Statistical analysis of the hydrostatic stress distributions

In order to clearly characterize the distributions and correlations of the hydrostatic stresses in composite granular media, the probability distribution function P of the normalized hydrostatic stresses σ_{norm} for each sample is used in this section. As performed in the analysis of contact forces [29], we are able to separate the hydrostatic stress networks into two complementary networks by considering the average hydrostatic stress: the strong network and the weak network. The hydrostatic stresses which is greater than the average stress over the whole set of considered particles ($\sigma_{norm} \geq 1$) referred to as the "strong network", while the "weak network" consists of the particles carrying the hydrostatic stresses lower than the mean stress. The present work intends to analyze only the "strong network", because the high stresses are of great interest with regard to the breakage of granular materials in terms of particle crushing [30, 31]. The probability distribution functions of the normalized hydrostatic stresses in the strong network for each sample are plotted with normal scale (Fig. 4a) and with semi-logarithmic scale (Fig. 4b), respectively. Results provide three different analyses by considering only stiff particles, only soft particles, and then considering the whole set of the particles. It should be noticed that $P(\sigma_{norm})$ is determined by the ratio between the number of particles in the strong network and the total number of particles under the considered types of particle (stiff, soft, or both).

Let us now consider the whole set of the particles in Fig. 4, it is obvious that the functions $P(\sigma_{norm})$ are distributed as an exponential decay for both experiments and simulations. This distribution is characterized by the coefficient β, which can be written by the following expression:

$$P \propto e^{\beta(1-\sigma_{norm})} \tag{7}$$

This property corresponds to the well-known force distribution laws [20]. It is interesting to note that the exponential stress distribution law is also discovered in the strong network when only stiff particles and only soft particles are taken into account. In other words, the exponential distribution is a general characteristic of granular media in the strong network for both distributions of the contact force and the hydrostatic stress. This distribution shape is independent of the material types of the particle. Considering the value $P(\sigma_{norm} = 1)$ for all the particles in Fig. 4a, it is worth mentioning that the experimental and numerical percentages of particles in the strong network are mostly lower than 50%, i.e. $P(1) < 0.5$. This value is also observed for most of the experimental and numerical samples when only the stiff particles and only the soft particles are considered with respect to the total number of their own type. From these results in the sense of the stress distribution, it can be seen that both the experiments and the simulations are in good agreement.

Next, let us analyze the coefficient β in the semi-logarithmic plot as shown in Fig. 4b by means of the linear regression. This quantity can be used to compare the samples in terms of the probability to carry high stresses in the particles. There is high probability of a reaching significant hydrostatic stress in the granular media when the value of $|\beta|$ is low, while the

higher value of $|\beta|$ prevail to obstruct the particle crushing. For each of the three samples, the numerical values of $|\beta|$ are significantly lower than those of the experiments. It can be said that the probability to reach high stresses is overestimated by the simulations compared to the corresponding experiments. This situation is very useful if one uses simulations to design granular materials. However, the results follow the same trend between experiments and simulations: $|\beta_{\#1}| > |\beta_{\#2}| \approx |\beta_{\#3}|$. It can be observed that the two bidisperse composite samples exhibit a higher potentiality to carry high stresses than the monodisperse sample.

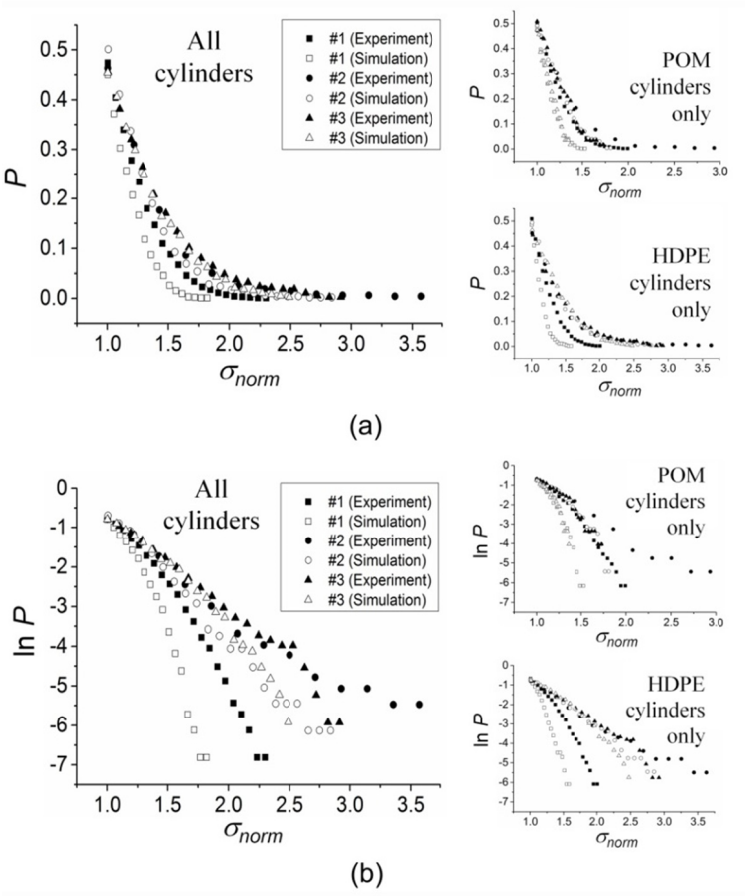

Figure 4: Probability distribution function P of the normalized hydrostatic stresses σ_{norm} in the strong network: plotting in (a) normal scale and (b) semi-logarithmic scale

4 CONCLUSION

The present study aimed at methodically analyzing the textural properties of 2D non-cohesive composite granular materials subjected to vertical confined compression. Molecular dynamics (MD) simulations were applied to model the three different composite configurations, which was completely tested by thermoelastic stress analysis (TSA) experiments [7]. The composite sample was constituted from two materials with different rigidities (stiff and soft particles). Both experimental and numerical results were compared in terms of hydrostatic stress distribution and contact direction distribution. It can be concluded that the experimental and numerical results follow the same trends in overview. In particular,

the distribution law of the hydrostatic stress in the strong network exhibits an exponential decay for all types of particle considered in the analysis (stiff, soft, or both), which is consistent with the well-known force distribution law [21]. In this network, there are less than 50% of particle numbers transmitting the stress greater than the average value. Considering in terms of geometrical orientation of the particles and their contacts in space, the anisotropic structure with an effort to arrange itself parallel to the direction of the external applied loading is evidently observed for the contact network between stiff and stiff particles. On the contrary, the equilibrium of the granular system is sustained by the other contact networks, i.e. soft-soft contacts and stiff-soft contacts.

Based on the global good agreement between experiments and simulations, it is important to notice that this study provides useful information obtained from the MD simulations in regard to composite granular materials. These numerical data are validated by the experimental data. In this manner, it can be said that the numerical simulations can be a supplementary tool to the experiments, in order to offer further information (difficult to obtain from the experiments) with regard to the mechanical behavior of composite granular media. Indeed, the optimum design of new composite granular systems could be done by using the simulations. Several parameters must be concerned in the design: constitutive material choice, proportion of particle number and size, and placement of particles in the system, for instance.

REFERENCES

[1] Jaeger, H.M. Sand, jams, and jets. *Phys. World* (2005) **18**(12):34-39.
[2] Jaeger, H.M. and Nagel, S.R. Granular solids, liquids, and gases. *Rev. Mod. Phys.* (1996) **68**(4):1259-1272.
[3] Budeshtskii, R.I. Mathematical model of granular composite materials. *Strength Mater+* (1971) **3**:912-916.
[4] Daraio, C., Nesterenko, V.F., Herbold, E.B., and Jin, S. Energy trapping and shock disintegration in a composite granular medium. *Phys. Rev. Lett.* (2006) **96**:058022.
[5] Wang, P.J., Xia, J.H., Li, Y.D., and Liu, C.S. Crossover in the power-law behavior of confined energy in a composite granular chain. *Phys. Rev. E* (2007) **76**:041305.
[6] Yang, Y., Wang, D., and Qin, Q. Quasi-static response of two-dimensional composite granular layers to a localized force. *Powder Technol.* (2014) **261**:272-278.
[7] Jongchansitto, P., Balandraud, X., Grédiac, M., Beitone, C., and Preechawuttipong, I. Using infrared thermography to study hydrostatic stress networks in granular materials. *Soft Matter* (2014) **10**(43):8603-8607.
[8] Cundall, P.A. and Strack, O.D.L. Discrete numerical-model for granular assemblies. *Géotechnique* (1979) **29**(1):47-65.
[9] Villard, P., Chavalier, B., Le Hello, B., and Combe, G. Coupling between finite and discrete element methods for the modeling of earth structures reinforced by geosynthetic. *Comput. Geotech*. (2009) **36**:709-717.
[10] Nguyen, D.H., Azéma, E., Radjai, F., and Sornay, P. Effect of size polydispersity versus particle shape in dense granular media. *Phys. Rev. E* (2014) **90**:012202.
[11] Peña, A.A., García-Rojo, R., and Herrmann, H.J. Influence of particle shape on sheared dense granular media. *Granul. Matter* (2007) **9**:279-291.
[12] Nouguier-Lehon, C., Cambou, B., and Vincens, E. Influence of particle shape and

angularity on the behaviour of granular materials: a numerical analysis. *Int. J. Numer. Anal. Meth. in Geomech.* (2003) **27**:1207-1226.
[13] Bardenhagen, S.G., Brackbill, J.U., and Sulsky, D. Numerical study of stress distribution in sheared granular material in two dimensions. *Phys. Rev. E* (2000) **62**(3):3882-3890.
[14] Preechawuttipong, I., Peyroux, R., Radjai, F., and Rangsri, W. Static states of cohesive granular media. *J. Mech. Sci. Technol.* (2007) **21**:1957-1963.
[15] Johnson, K.L. *Contact mechanics*. Cambridge University Press, (1985).
[16] Allen, M.P. and Tildesley, D.J. *Computer simulation of liquids*. Oxford Science Publications, (1987).
[17] Schäfer, J., Dippel, S., and Wolf, D.E. Force schemes in simulations of granular materials. *J. Phys. I* (1996) **6**:5-20.
[18] Matuttis, H.G., Luding, S., and Herrmann, H.J. Discrete element simulations of dense packings and heaps made of spherical and non-spherical particles. *Powder Technol.* (2000) **109**:278-292.
[19] Kruggel-Emden, H., Simsek, E., Rickelt, S., Wirtz, S., and Scherer, V. Review and extension of normal force models for the Discrete Element Method. *Powder Technol.* (2007) **171**:157-173.
[20] Jongchansitto, P., Preechawuttipong, I., Balandraud, X., and Grédiac, M. Numerical investigation of the influence of particle size and particle number ratios on texture and force transmission in binary granular composites. *Powder Technol.* (2017) **308**:324-333.
[21] Radjai, F., Jean, M., Moreau, J.J., and Roux, S. Force distributions in dense two-dimensional granular systems. *Phys. Rev. Lett.* (1996) **77**(2):274-277.
[22] Richefeu, V., Radjai, F., and El Youssoufi, M.S. Stress transmission in wet granular materials. *Eur. Phys. J. E* (2006) **21**:359-369.
[23] Kanatani, K. A theory of contact force distribution in granular materials. *Powder Technol.* (1981) **28**:167-172.
[24] Bagi, K. Stress and strain in granular assemblies. *Mech. Mater.* (1996) **22**:165-177.
[25] Cambou, B., Jean, M., and Radjai, F. *Micromechanics of granular materials*. John Wiley & Sons, (2009).
[26] Voivret, C., Radjai, F., Delenne, J.Y., and El Youssoufi, M.S. Multiscale force networks in highly polydisperse granular media. *Phys. Rev. Lett.* (2009) **102**:178001.
[27] Kruyt, N.P. Micromechanical study of fabric evolution in quasi-static deformation of granular materials. *Mech. Mater.* (2012) **44**:120-129.
[28] Rothenburg, L. and Bathurst, R.J. Analytical study of induced anisotropy in idealized granular materials. *Géotechnique* (1989) **39**:601-614.
[29] Radjai, F., Wolf, D.E., Jean, M., and Moreau, J.J., Bimodal character of stress transmission in granular packings. *Phys. Rev. Lett.* (1998) **80**(1):61-64.
[30] Russell, A.R., Wood, D.M., and Kikumoto, M. Crushing of particles in idealised granular assemblies. *J. Mech. Phys. Solids.* (2009) **57**:1293-1313.
[31] Arslan, H., Baykul, G., and Sture, S. Analysis of the influence of crushing on the behavior of granular materials under shear. *Granul. Matter* (2009) **11**:87-97.

V International Conference on Particle-based Methods – Fundamentals and Applications
PARTICLES 2017
P. Wriggers, M. Bischoff, E. Oñate, D.R.J. Owen, & T. Zohdi (Eds)

A CONVERGENCE ANALYSIS OF THE AFFINE PARTICLE-IN-CELL METHOD AND ITS APPLICATION IN THE SIMULATION OF EXTRUSION PROCESSES

J. LUIS SANDOVAL M.[1] AND GEORG C. GANZENMÜLLER[1,2]

[1] Fraunhofer Institute for High-Speed Dynamics,
Ernst-Mach-Institut (EMI)
Eckerstr. 4, D-79104 Freiburg i. Br., Germany
e-mail: jose.luis.sandoval.murillo@emi.fraunhofer.de, web page: http://www.emi.fraunhofer.de

[2] Institut für Nachhaltige Technische Systeme (INATECH),
University of Freiburg
Emmy-Noether Str. 2, D-79110 Freiburg i. Br., Germany
e-mail: georg.ganzenmueller@inatech.uni-freiburg.de, web page:
http://www.inatech.uni-freiburg.de

Key words: material point method, MPM, affine particle-in-cell method, APIC, mesh-free, convergence analysis, extrusion

Abstract. Simulation of extrusion processes represents a large challenge for commonly used numerical methods. In our application for example, a hot melt is extruded whilst being rapidly cooled. Under these conditions of quenching, spinodal phase separation occurs which causes the formation of a characteristic micro-structure of the extrudate, consisting of solid and liquid phases. We model this process using a variant of the Material Point Method (MPM) [4], namely the Affine Particle-In-Cell (APIC) method [13]. Its hybrid particle/grid character is advantageous for simulating both fluid and solid behavior: pure Eulerian particle methods, such as classic SPH, fail for simulating solids, particularly in tension, whereas pure Lagrangian methods generally cannot cope with large deformations caused by material flow. APIC improves upon the original MPM method by using a so-called locally affine velocity representation [13] which allows the conservation of linear and angular momentum without the need of potentially unstable Fluid-Implicit-Particle (FLIP) techniques [3]. We analyze the convergence behavior of APIC and compare its accuracy against a traditional MPM variant, the Generalized Interpolation Material Point Method (GIMP).

1 INTRODUCTION

Our case of study consists of an extrusion process, where a pressurized hot melt passes through a nozzle into a long channel, where the extrudate is gradually cooled. While

cooling, the melt starts separating into solid-like and fluid-like phases/structures. At the end of the process a product with solid-like characteristics is obtained. To numerically model this extrusion process we require a method able to describe material flow in form of plasticity and phase separation, both requiring of history variables that have to be advected along with the material flow.

While the liquid part of this process could be well simulated using established Eulerian mesh-based methods such as CFD [10], the solid mechanics would constitute a problem with such an approach. The same argument holds for traditional Eulerian Smooth Particle Hydrodynamics, which cannot accurately describe solid bodies. Lagrangian mesh-based methods on the other hand, are well suited for solid body mechanics, but cannot cope with the large deformations during liquid flow.

Material-Point methods however, incorporating both Eulerian mesh-based aspects and Lagrangian particle aspects, are known to be able to successfully simulate both liquid and solid behavior [9] . Broadly speaking, these methods interpolate the velocity and stress field from Lagrangian particles onto a rigid grid, and then solve the dynamic problem on the grid. At the end, the updated velocity field is transferred from the grid back to the particles. At the completion of a time step the entire grid is discarded, which underlines the meshfree character of these methods.

To avoid confusion, it is important to outline the family tree of particle/mesh methods. All of these methods derive from the original Particle-In-Cell (PIC) formulation [1], which uses a δ-distribution to interpolate values between grid and particles. The MPM method due to Sulsky [4] improved on this using linear interpolation. Today, GIMP methods [7] are commonly employed. GIMP uses higher-order polynomials, typically with a continuous first derivative of field values across neighboring cells on the grid. It is common in the literature to refer to all hybrid particle/mesh methods as MPM, regardless of the degree of smoothness of the interpolation function. We adopt the same approach here, but specify the details of the interpolation function where required.

A problem in MPM is the lack of conservation of angular momentum. Depending on how the equations of motion are integrated in time, this angular rotation is more or less severely dampened. The classic, PIC-style update uses interpolated grid velocities to advance the particles, while the more modern FLIP approach [3] interpolates only the grid accelerations back to the particles and performs the time integration in a Lagrangian manner. This approach is capable of conserving angular momentum, however, it is also severely unstable. To resolve this issue, linear combinations of FLIP and PIC updates are used in practice, which allow for a somewhat moderate dampening of rotational motion.

Recently, a promising evolution of the MPM, named APIC was published [13]. This method exhibits exact conservation of linear and angular momentum while employing true PIC-style updates. This is achieved by an enhanced interpolation scheme for the the velocity field whenever it is transferred to and from the grid. The enhancement considers gradients in the velocity field instead of assuming piecewise constant character. This greatly improves the MPM scheme, which does not conserve linear or angular momen-

tum by default. A number of visually compelling examples in the Computer Graphics community was already published using APIC [13, 14]. However, when it comes to engineering applications, a more detailed quantification of the accuracy has to be carried out. As to the author's knowledge, no formal study has been done regarding the convergence properties of APIC. In this work we study the convergence of APIC in terms of viscosity and velocity field by means of benchmark simulations of fluid flow: Couette flow and Hagen-Poiseuille flow.

In Sec. 2.2 we will give a brief description of the general aspects of MPM and APIC. We proceed by detailing our implementation of APIC. In Sec. 3 two convergence studies by means of fluid flow benchmark simulations are presented. There, the accuracy and convergence rate of APIC applied to Couette and Hagen-Poiseuille flows is analyzed and compared to MPM. In Sec. 4 we show how APIC can successfully simulate extrusion with a strong pressure drop, while classic MPM fails due to its unstable time integration approach. We draw conclusions in Sec. 5 and also indicate remaining challenges.

2 THEORY AND IMPLEMENTATION OF MPM AND APIC

MPM is a numerical method intended for solving the differential equations of continuum mechanics. The mass flow is discretized using particles, and a background grid serves as a scratch pad to compute the gradients. As in other numerical methods for the solution of continuum mechanics problems, a solution to the equation of motion is obtained by multiplication with a set of test functions, as shown below in its integral or so called *weak* form:

$$\int_\Omega \delta\boldsymbol{u} \cdot \rho\ddot{\boldsymbol{u}}\, d\Omega + \int_\Omega \nabla\delta\boldsymbol{u} : \boldsymbol{\sigma}\, d\Omega = \int_\Omega \delta\boldsymbol{u} \cdot \rho\boldsymbol{b}\, d\Omega \tag{1}$$

ρ is the density, $\ddot{\boldsymbol{u}}$ the acceleration vector, $\nabla\boldsymbol{u}$ the deformation gradient, $\boldsymbol{\sigma}$ is the Cauchy stress tensor, $\boldsymbol{b}$ is a field of body forces, and $\delta\boldsymbol{u}$ are the test functions (for simplicity, the boundary forces are ignored). The key idea of MPM is to solve the constitutive equations (strain-stress relationship) on the particles and the dynamics (forces and velocities) on the grid. For this purpose we need a set of test functions $w_{ip} = w(\boldsymbol{x}_p - \boldsymbol{x}_i)$, in MPM usually referred to as *kernel or weight functions*, where $\boldsymbol{x}_p$ and $\boldsymbol{x}_i$ are the positions of the particle p and the grid-node i respectively. These functions transfer information from particles to grid nodes and from nodes back to particles, The transfer from particles to grid nodes of a material property A and its gradient ∇A reads:

$$A_i = \sum_p A_p w_{ip} \tag{2}$$

$$\nabla A_i = \sum_p A_p \nabla w_{ip} \tag{3}$$

One way to define the kernel functions is to define first two sets of interpolation functions, the *particle characteristic functions* $\chi_p(\boldsymbol{x}) = \chi(\boldsymbol{x} - \boldsymbol{x}_p)$, and the *grid shape functions* $S_i(\boldsymbol{x}) = S(\boldsymbol{x} - \boldsymbol{x}_i)$. Such functions have to meet the condition

$$\sum_p \chi_p(\boldsymbol{x}) = \sum_i S_i(\boldsymbol{x}) = 1 \quad \forall \quad \boldsymbol{x} \tag{4}$$

so that any material property can be interpolated in space as $f(\boldsymbol{x}) = \sum_p f_p \chi_p(\boldsymbol{x}) = \sum_i f_i S_i(\boldsymbol{x})$, where $f_p = f(\boldsymbol{x}_p)$ and $f_i = f(\boldsymbol{x}_i)$ are the values of material property of particle p and node i respectively. The original MPM scheme is obtained when the characteristic function $\chi_p(\boldsymbol{x})$ is taken as the Dirac delta function:

$$\chi(\boldsymbol{x} - \boldsymbol{x}_p) = \delta(\boldsymbol{x} - \boldsymbol{x}_p) V_p \tag{5}$$

In contrast, for the GIMP method the characteristic functions can be arbitrarily chosen [7], which will determine the smoothness and accuracy of the solution. The kernel functions can then be derived as the convolution of both sets of functions in the form

$$w_{ip} = \frac{1}{V_p} \int_\Omega \chi(\boldsymbol{x} - \boldsymbol{x}_p) S(\boldsymbol{x} - \boldsymbol{x}_i) d\boldsymbol{x} \tag{6}$$

Substituting the *kernel functions* Eq. 6 into Eq. 1 we obtain:

$$\sum_p \rho_p \ddot{\boldsymbol{u}}_p w_{ip} + \sum_p V_p \boldsymbol{\sigma}_p \nabla w_{ip} = \sum_p m_p \boldsymbol{b} w_{ip} \tag{7}$$

The above line is rewritten using equations 2 and 3 to obtain a balance of forces on the grid as:

$$\dot{\boldsymbol{q}}_i = \boldsymbol{f}_i^{ext} - \boldsymbol{f}_i^{int}. \tag{8}$$

Here, $\boldsymbol{f}_i^{int} = \sum_p V_p \boldsymbol{\sigma}_p \nabla w_{ip}$ and $\boldsymbol{f}_i^{ext} = \sum_p m_p \boldsymbol{b} w_{ip}$ are the vectors of internal and external forces, respectively, and $\dot{\boldsymbol{q}}_i = \sum_p \rho_p \ddot{\boldsymbol{u}}_p w_{ip}$ is the rate of change of momentum. For a more detailed derivation, see [8, 7].

To complete the balance of forces, the state of stress is required. The Cauchy stress tensor $\boldsymbol{\sigma}_p^{t+\Delta t}$ can be determined from the constitutive relations as a function of the deformation gradient $\boldsymbol{F}_{\boldsymbol{p}}^{\boldsymbol{t+\Delta t}}$, which is obtained from integrating the velocity gradient $\boldsymbol{F}_p^{t+\Delta t} = e^{\Delta t \boldsymbol{L}_p^t} \boldsymbol{F}_p^t$. The velocity gradient itself, $\boldsymbol{L}^t$, is obtained using Eq. 3 as:

$$\boldsymbol{L}_p^t = \nabla \dot{\boldsymbol{u}}_p^t = \sum_i \dot{\boldsymbol{u}}_i^t \nabla w_{ip} \tag{9}$$

2.1 Implementation of MPM

At the beginning of every time step at time t the following information is located at each particle: mass m_p, volume V_p^t, position $\boldsymbol{x}_p^t$, velocity $\dot{\boldsymbol{u}}_p^t$, and stress $\boldsymbol{\sigma}_p^t$. Note that with the exception of mass all quantities have a superscript indicating the time step. This is because all but the particle mass are evolved in time throughout a series of steps, see Fig. 1.

First, the mass and current state of the velocity field is transferred to the grid. To conserve linear momentum, particle velocity is multiplied by the mass.

$$m_i^t = \sum_p m_p w_{ip}, \qquad \boldsymbol{q}_i^t = m_i^t \dot{\boldsymbol{u}}_i^t = \sum_p m_p \dot{\boldsymbol{u}}_{\boldsymbol{p}}^{\boldsymbol{t}} w_{ip} \tag{10}$$

Now the deformation gradient can be computed using Eq. 9. In the next step, the stresses are calculated using the constitutive model. Here is where the practical qualities of the MPM arise , since every particle can have different material model. Thus the interaction between different phases e.g. fluids and solids can be automatically handled.

With known particle stresses, Eq. 8 yields the rate of momentum on the grid nodes, which can be integrated in time to get the new grid momenta

$$\boldsymbol{q}_i^{t+\Delta t} = \boldsymbol{q}_i^t + \dot{\boldsymbol{q}}_i^{t+\Delta t} \Delta t \tag{11}$$

This completes the dynamic evolution of the grid. Updated particle velocities are obtained according to the PIC algorithm by transferring the grid velocity back to the particles:

$$\dot{\boldsymbol{u}}_p^{t+\Delta t} = \sum_i \dot{\boldsymbol{u}}_i^{t+\Delta t} w_{ip} = \sum_i \frac{\boldsymbol{q}_i^t + \dot{\boldsymbol{q}}_i^{t+\Delta t} \Delta t}{m_i} w_{ip} \tag{12}$$

The alternative FLIP update transfers only the change in velocity from grid to particles:

$$\dot{\boldsymbol{u}}_p^{t+\Delta t} = \dot{\boldsymbol{u}}_p^t + \Delta t \sum_i \frac{\dot{\boldsymbol{q}}_i^{t+\Delta t}}{m_i} w_{ip} \tag{13}$$

In standard MPM implementations, a typical combination of 99% FLIP and 1% PIC is used to achieve a compromise between dissipation and stability. Particle positions are updated by integrating the particle velocities:

$$\boldsymbol{x}_p^{t+\Delta t} = \boldsymbol{x}_p^t + \Delta t \sum_i \frac{\boldsymbol{q}_i^t + \dot{\boldsymbol{q}}_i^{t+\Delta t} \Delta t}{m_i} w_{ip} \tag{14}$$

The grid may subsequently be deleted, since a completely new grid can be created at the next time step and there is no need for storage of the old grid values.

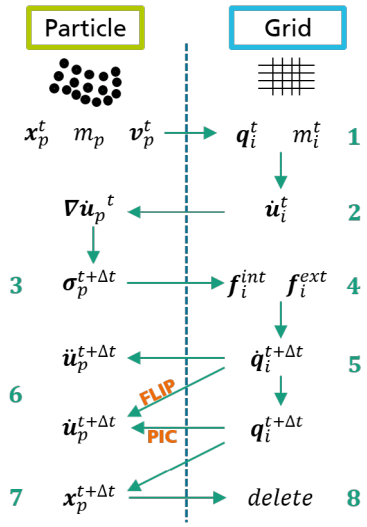

Figure 1: General algorithm of the MPM corresponding to the update-stress-first (USF) version.

2.2 APIC

MPM uses a piecewise constant interpolation in the particle/grid transfer of the velocity field. Particle mass m_p and momentum $\boldsymbol{q}_p^t = m_p \dot{\boldsymbol{u}}_p^t$ are transferred to grid nodes and then momentum is divided by mass at every node to obtain the velocity, see Eq. 10. Up to here, linear and angular momentum are conserved as long as the *kernel functions* meet the condition 4. However, particle velocity null modes (interpolated motions of particles which sum to zero on a grid node) can not be transferred to the grid due to lack of grid degrees of freedom. After the grid state of momentum is updated, velocities are transferred back to particles. In this process all velocity null modes which were not transferred to grid are lost, what causes loss of angular momentum. In a PIC transfer, old particle velocities are directly replaced with new interpolated velocities from grid, what can be seen as a filter of null modes, giving PIC its excessively dissipative characteristics. With FLIP, particle velocities are advanced, rather than overwritten, by interpolating only changes of grid velocities. This is what prevents complete loss of null modes on the particles. Thus FLIP avoids excessive dissipation but causes significant instabilities.

A solution to this problem was proposed in [13] which augments from the piecewise constant to a piecewise affine representation of particle velocity, while conserving the original PIC transfer from grid to points. The main concept of APIC is to store an additional matrix per particle which is used in the velocity transfer from particles to nodes in the form

$$\boldsymbol{q}_i^t = \sum_p m_p (\dot{\boldsymbol{u}}_p^t + \boldsymbol{C}_p^t (\boldsymbol{x}_i^t - \boldsymbol{x}_p^t)) w_{ip} \tag{15}$$

where $\boldsymbol{C}_p^t = \boldsymbol{B}_p^t (\boldsymbol{D}_p^t)^{-1}$. The matrices $\boldsymbol{D}_p^t$, which is similar to an inertia tensor, and $\boldsymbol{B}_p^t$ are defined as:

$$\boldsymbol{D}_p^t = \sum_i (\boldsymbol{x}_i^t - \boldsymbol{x}_p^t)(\boldsymbol{x}_i^t - \boldsymbol{x}_p^t)^T w_{ip} \tag{16}$$

$$\boldsymbol{B}_p^{t+\Delta t} = \sum_i \dot{\boldsymbol{u}}_i^{t+\Delta t} (\boldsymbol{x}_i^t - \boldsymbol{x}_p^t)^T w_{ip} \tag{17}$$

2.2.1 Aspects of our Implementation

Certain particularities of our implementation need to be addressed. First, we used a staggered rather than a collocated grid in order to avoid the even-odd instabilities of usual MPM implementations, which manifest themselves as checkerboarding of stress fields. [2]. Further, we calculate the velocity gradient directly on the grid using finite differences and transfer the grid velocity gradient back to particles using standard interpolation. We have observed that this approach yields a smoother velocity gradient, less prone to numerical instabilities due to noise in the velocity field. Apart from these aspects, our implementation follows the work flow illustrated in Fig. 1, incorporating the velocity representation and transfer scheme of APIC.

3 CONVERGENCE STUDY

In our case of study we want to describe the velocity field of a hot melt which is extruded and passed throughout a long channel where it is cooled. Here the velocity profile of the fluid along the channel is the great interest for us. To determine how accurate we can simulate/model that flow, we set up a numerical experiment in which we can compare our simulation results with the exact solution of a benchmark problem. Hagen-Poiseuille flow is a well known problem in fluid mechanics for which an exact solution has been already derived. Next, we describe the convergence study with respect to the space discretization we carried on of both, MPM and APIC using the above mention benchmark problem.

3.1 Hagen-Poiseuille Flow

Hagen-Poiseuille flow describes the behavior of a fluid flowing along a channel formed by two stationary, infinite parallel walls separated by a distance H. Due to the no-slip boundary conditions at the channel walls a characteristic velocity profile develops and evolves over time. An (almost exact) accurately approximated solution for this problem can be obtained by means of a series method. A set of APIC-simulations of this flow were carried out using different discretization varying the amount of particles which consequently changes the particle and grid-cell size. Afterwards, we determined the convergence of the method based on the error between the numerical results with a series solution from [5].

For the simulation a square lattice was used of N by N number of particles and one particle per grid cell maintaining a height channel $H = 5$ constant. At time $t = 0$ the

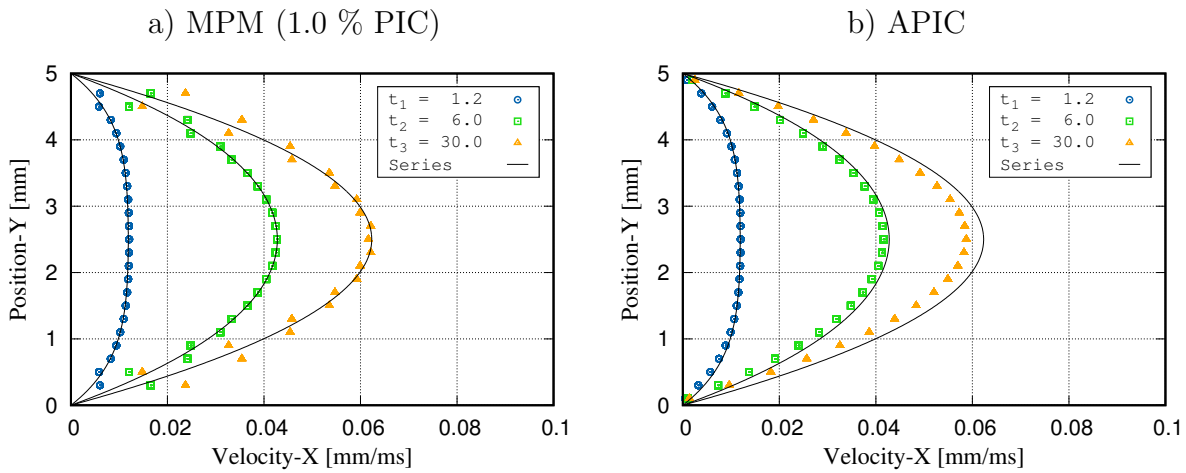

Figure 2: Velocity profile of a Hagen-Poiseuille flow at different time states. Continuous lines represent the exact solution obtained with a series method from [5]. Symbols represent the numerical results obtained with a) MPM with 1% PIC contribution (left) and b) APIC (right) using a cell size of 0.20 and particle radius of 0.10.

velocity is set to zero for all particles and for $t \geq 0$ a body force of 0.01 mm/ms^2 is set in x direction. No-slip boundary conditions with zero velocity are applied at the boundary grid nodes located at the bottom $y = 0$ and top $y = H$ of the channel. To emulate an infinitely long channel, periodic boundary conditions are applied at the left $x = 0$ and right $x = H$ sides of the lattice. The material properties used in this case were a density $\rho = 10^{-6}$ kg/mm^3, a bulk modulus $K = 1.4 \times 10^{-4}$ kN/mm^2 and a viscosity $\eta = 0.5 \times 10^{-6}$ GPa·ms.

In Fig. 2, the velocity profile at three different time plotted. The exact series solution is represented with continuous lines and numerical results using MPM with 1%PIC(left) as well as APIC (right) are represented with symbols. We observe that, although a good accuracy is obtained with MPM, significant numerical noise, or instabilities, deteriorate the velocity profile. The APIC solution, on the other hand, comes very close to the exact solution and without showing any instability.

To determine the convergence of both MPM and APIC, we measure the error of both methods obtained in a simulation of Hagen-Poiseuille flow with respect to an analytic series solution [5] using different discretization sizes. We defined the error as the velocity deviation of the numerical solution with respect to the series solution at the particle's position $e_p = v_p - v_s(x_p)$, where v_p is the is the particle position and $v_s(x_p)$ the series solution of the velocity evaluated at the particle position x_p. Then the total error of the whole simulation was computed as an L_2 norm defined as follows:

$$E = \frac{1}{N}\sqrt{\sum_{p=1}^{N} e_p^2} \tag{18}$$

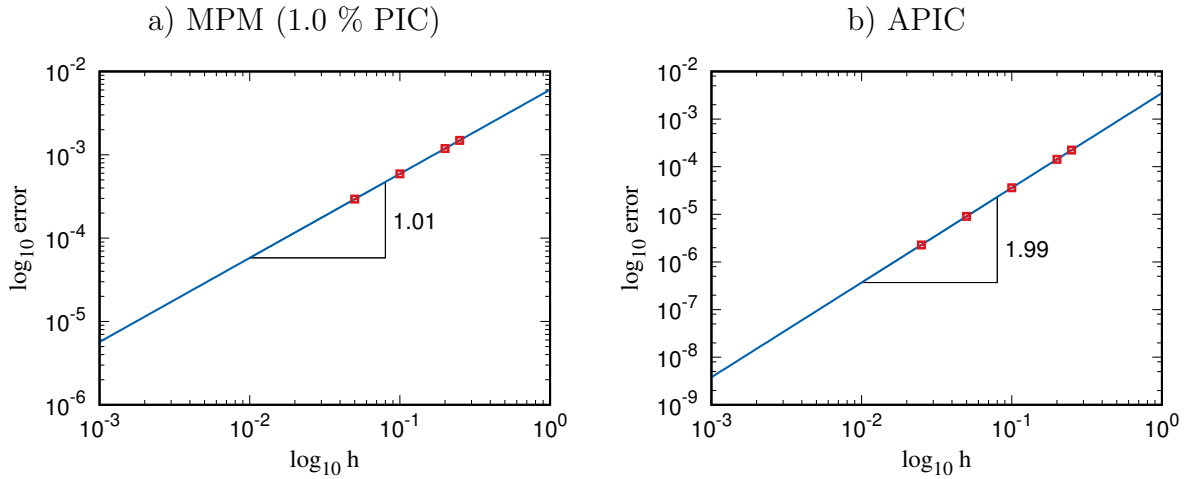

Figure 3: Convergence study for Hagen-Poiseuille flow using a) MPM with 1 % PIC contribution (left) and b) APIC (right). Simulations were performed with different cell sizes and the whole error was calculated as the L_2 norm of the difference between the series and the numerical solutions of velocities obtained at the particle positions. The logarithm of the L_2 norm of the error is plotted versus the logarithm of the cell size. The slope of the solid line which is a function fit of the error corresponds to the convergence order of the numerical method.

Fig. 3 shows a double-logarithmic plot of error versus discretization size obtained for the simulation of the Hagen-Poiseuille flow using MPM (left) and APIC (right). The solid line is the fit function of the error and its slope represents the order of convergence. The order of convergence close to unity obtained in the present study agrees well with previous studies such as [9]. Our new finding is, that APIC exhibits convergence of almost second order (1.99). This makes APIC a much better choice for studying viscous flows than conventional MPM methods.

4 EXAMPLE: EXTRUSION OF A HOT MELT

Having determined the accuracy and convergence of APIC against standard MPM, we now present a rather qualitative comparison of the simulation of an extrusion process of a highly viscous liquid. Modeling extrusion processes is a challenging task, as the strong pressure gradient of the converging flow tests the stability of the numerical code. A set of 2D simulations using APIC and MPM with different PIC-FLIP ratios were carried out to test the capabilities of both methods.

The simulation setup is based on the geometry of an extruder for meat surrogates based on vegetable proteins. It consists of a double screw extruder which moves material througho a nozzle into a long cooling channel, with a vertical flow height reduction from 25.4 mm up to 5.0 mm. The following material properties were used: Newtonian viscosity of 138.9 Pa·s, bulk modulus of 1.0 GPa and density of 1000 kg/m^3. An inflow boundary condition realizes a constant mass flow with a velocity of 2.7 mm/s. A cell size of 0.1 mm was used for the grid and a particle radius of 0.025 mm, which means 4 particles per grid

cell. The simulated time was 15 seconds. Mass scaling was used to achieve a practical time step of 0.6 ms.

Fig. 4 shows snapshots from the simulations using MPM with 1% and 20% PIC and APIC. At 1% PIC, the simulation becomes immediately unstable. With 20 % PIC, the solution already becomes severely damped, as can be inferred from the homogeneous flow profile immediately after the cross section reduction. In contrast, APIC shows a much more pronounced conical convergent flow after the nozzle. Thus, APIC improves the stability of the simulation whilst preserving characteristics of the flow.

5 CONCLUSIONS AND OUTLOOK

This work compares the recently published APIC [13] variant of MPM against the more commonly used GIMP variant. APIC's improves upon GIMP by employing a velocity field which conserves linear and angular momentum. APIC also maintains the stability associated with PIC-style updates of the velocity field, without being excessively dissipative as demonstrated in [13, 15]. Here, we study the Hagen-Poiseuille problem of viscous flow through a channel. We find that APIC exhibits an increased order of convergence in this case: while normal GIMP converges with 1st order, APIC converges with second order. This makes APIC an ideal candidate for our application, which considers an extrusion process of a pressurized highly viscous melt with simultaneous thermal quenching. The challenge here is that the material behavior changes from liquid to solid, which calls for special methods such as MPM to numerically describe this process.

APIC originates from the field of computer graphics, where aesthetically pleasing visual effects are obtained by simulating physical processes. For these applications, a trade-off between computational speed and convincing physical accuracy is optimal. We are confident, however, that APIC can also be used for simulations in engineering applications, where physical accuracy is a fundamental requirement. With the present work we start to investigate the applicability of APIC for the solution of engineering systems. Future work will address the accuracy and convergence behavior of this new method for solid body mechanics problems.

REFERENCES

[1] Evans, M.W. and Harlow, F.H. "The particle-in-cell method for hydrodynamic calculations", *Los Alamos Scientific Laboratory*, (1957).

[2] Harlow, F.H. and Welch, J.E. "Numerical Calculation of Time-Dependent Viscous Incompressible Flow of Fluid with Free Surface", *The Physics of Fluids*, Vol. 8, No. 12, (1965).

[3] Brackbill, J.U., Kothe D.B. and Ruppel H.M. "FLIP: a low-dissipation, particle-in-cell method for fluid flow", *Computer Physics Communications*, Tech Science Press, Vol. 48, pp. 25-38, (1988).

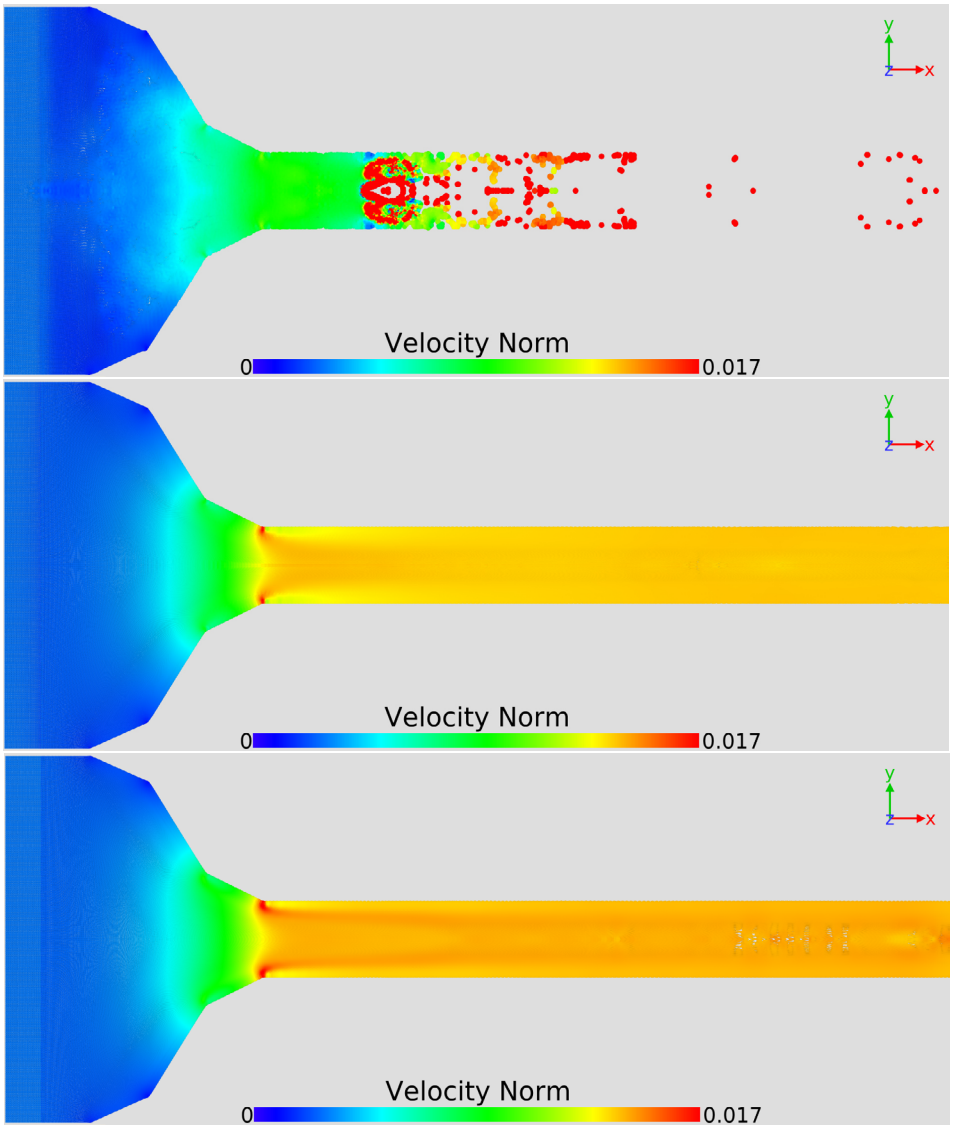

Figure 4: Snapshots of the 2D extrusion simulations using MPM with different PIC-FLIP ratios. Color scale shows the norm of the particle velocity. The snapshot for 20% PIC as well as APIC correspond to the end of the simulation at time $t = 15$ s. The snapshot of 1% PIC corresponds to the last time step simulated before the simulation broke due to instabilities.

[4] Sulsky, D., Chen,Z. and Schreyer, H.L. "A Particle Method for History-Dependent Materials", *Sandia Laboratories*, (1993).

[5] Morris, J.P., Fox, P.J. and Zhu, Y. "Modeling Low Reynolds Number Incompressible Flows Using SPH", *Journal of Computational Physics*, Vol. 136, No.1, pp. 214-226, (1997).

[6] Nairn, J.A. "Material Point Method Calculations with Explicit Cracks", *Computer Modeling in Engineering and Sciences*, Vol.4, No.6, pp. 649-664, (2003).

[7] Bardenhagen, S.G. and Kober, E.M. "The Generalized Interpolation Material Point Method", *Computer Modeling in Engineering and Sciences*, Tech Science Press, Vol. 5, No. 6, pp. 477-495, (2004).

[8] Buzzi, O., Pedroso, D.M. and Giacomini, A. "Caveats on the implementation of the Generalized Material Point Method", *Computer Modeling in Engineering and Sciences*, Tech Science Press, Vol. 31, No. 2, pp. 85-106, (2008).

[9] Wallstedt, P.C. and Guilkey, J.E. "An Evaluation of explicit time integration schemes for use with the generalized interpolation material point method", *Journal of Computational Physics*, Vol. 227, No. 22, pp. 9628-9642, (2008).

[10] Wendt, J.F. *Computational Fluid Dynamics An Introduction*, Springer, 3rd Edition, (2009).

[11] Wallstedt, P.C. and Guilkey, J.E. "A weighted least squares particle-in-cell method for solid mechanics", *International Journal for Numerical Methods in Engineering*, Vol. 85, No. 13, pp. 1687-1704, (2011).

[12] Edwards, E. and Bridson, R. "A high-order accurate particle-in-cell method", *International Journal for Numerical Methods in Engineering*, Vol. 90, No. 9, pp. 1073-1088, (2012).

[13] Jiang, C., Schroeder, C., Selle, A., Teran J. and Stomakhin, A. "The Affine Particle-In-Cell Method". *ACM Transactions on Graphics*, SIGGRAPH, (2015).

[14] Klár, G., Gast, T., Pradhana, A., Fu, C., Schroeder, C., Jiang, C. and Teran, J. "Drucker-Prager Elastoplasticity for Sand Animation", *ACM Transactions on Graphics*, SIGGRAPH, Vol. 35, No.4, (2016).

[15] Jiang, C., Schroeder, C. and Teran J., "An angular momentum conserving Affine-Particle-In-Cell method", *Journal of Computational Physics*, Vol. 338, pp. 137-164, (2017).

V International Conference on Particle-based Methods – Fundamentals and Applications
PARTICLES 2017
P. Wriggers, M. Bischoff, E. Oñate, D.R.J. Owen, & T. Zohdi (Eds)

ENHANCEMENT OF THE SPREADING PROCESS IN ADDITIVE MANUFACTURING THROUGH THE SPREADER OPTIMISATION.

S. Haeri[1]

[1] Department of Mechanical and Aerospace Engineering
75 Montrose St
University of Strathclyde
Glasgow
UK, G1 1XJ
E-mail: sina.haeri@strath.ac.uk

Key words: DEM, Powder Spreading, Additive Manufacturing, Particle Bed Fusion, Optimisation

Abstract. Powders used in Particle Bed Fusion (PBF) process are spread onto compact layers and then are sintered. This process is repeated layer by layer to form the final products. The author has recently characterised the process and it is found that spreading the particles with a counter-rotating roller produces a bed with higher qualities, i.e. lower void fractions and surface roughness [Powder Technology, 306 (2017) 45–54]. This is related to a particle dragging effect caused by the small contact area between powder grains and the blade. Therefore, here, it is postulated that changing the blade profile at the blade-bed contact point can significantly influence the contact dynamics and hence increase the blade's effectiveness as a spreading device for PBF. A set of computer simulations using Discrete Element Method (DEM) are performed at device scales to optimise the geometry of blade spreaders to yield the lowest void fraction and surface roughness. The blade profile is parametrised using a super-ellipse with three geometrical parameters. It is firstly demonstrated that geometric optimisation of a blade profile is an effective alternative to using more complex spreading devices. Secondly, for the proposed parametrisation, the optimum values are found using computer simulations which can generate very high quality powder beds with volume fractions close to the critical value.

1 INTRODUCTION

Powder Bed Fusion (PBS) is a promising Additive Manufacturing (AM) technology where polymeric or metallic particles, heated to just below their melting temperature are spread on a fabrication piston to form a thin powder bed (typically in the order of 0.1 mm) using a counter-rotating roller or a blade. Different technologies may then be used

to fuse the material powder. For example, in a Laser Sintering (LS) process, a laser beam is used to fuse the powder grains. After this stage, the fabrication piston lowers the part slightly and a new layer of powder is applied. The process is repeated until the product is fabricated [1].

Undoubtedly, the characteristics of individual particles have a significant effect on the success of PBF processes [2, 3, 4, 5]. In particular, Ziegelmeier [6] focused on understanding the bulk and flow behaviour of polymer powders in relation to the properties of produced parts in LS. They mainly concluded that the tensile strength and elongation at break are enhanced by increasing ϕ_s. Therefore, the discrete nature of particles cannot be ignored in any numerical technique used for design, prediction and understanding of PBF processes. The Discrete Element Method (DEM) is a particle based approach relying only on the first principles and is receiving significant attention recently for simulation of such systems. This is due to the capability of DEM to directly include the effects of grain characteristics such as material properties, size distribution and morphology. DEM was first proposed in late 1970s [7] and there is a large body of research on the method in geomechanics literature (see [8] for a modern introduction).

Application of DEM to PBF was pioneered by Zohdi [9, 10, 11] with regards to the development of laser heat sources and particle sintering models. Xiang et al. [12], simplified the process by considering an assembly of 4000 particles undergoing three processes in their DEM simulations: random packing, layering and compression. They showed that the solid volume fraction increases by increasing the layer thickness. Steuban et al. [13] also proposed a new framework for modelling the full process including a laser heat source and powder sintering. Lattice-Boltzmann models are also developed very recently to simulate the melting-solidification processes [14, 15]. However, they start from a random collection of spheres, rather that considering the full spreading process.

Haeri et al. [1] on the other hand provided DEM simulation of spreading process at *device scales* and used high ϕ_s and layer's surface roughness values as a measure of a successful powder spreading process (i.e. a high-quality bed). This is known to be directly correlated with the quality of final parts [6]. In their extensive parametric studies, Haeri et al. [1] investigated the effects of spreader type, its translational velocity, particle shape (and its distribution) and layer thickness on the bed quality. They parametrised elongated particles using their aspect ratios A_r and showed that the highest ϕ_s can be achieved at $\mathrm{A}_r = 1.5$. They also analysed the micro-structures of elongated particles to explain the relation between various process parameters and the bed quality. They investigated two different types of spreading devices: rollers and blades. The consensus in the community is that the rollers generally produce higher quality powder beds which was confirmed in this study. Haeri et al. [1] however, related this to a particle dragging phenomenon and a small contact area between a blade spreader and the bed.

In this paper, it is postulated that since a low-quality bed generated using a blade is essentially a result of its geometry – as was suggested in [1] – it can be rectified purely by geometric modification of the blade. Therefore, a new class of blades is proposed with

a modified head profile. The suggested profile is a supper-ellipse with three adjustable parameters. It is shown that simple geometrical modifications can significantly affect the bed quality and then using a series of computer simulations the best values for the these parameters are identified and reported.

2 Methodology

2.1 Discrete Element Method

The Large-scale atomic/molecular massively parallel simulator (LAMMPS) code [16] is used for all the DEM simulations. A linear Hookean spring-dashpot contact force model is applied to each pair of particles p and q whenever the two particles overlap, i.e. when $\delta_{pq} = R_p + R_q - r_{pq} > 0$, where $r_{pq} = \|\mathbf{r}_p - \mathbf{r}_q\|$, and $\|\cdot\|$ represents the Euclidean norm (magnitude) of any vector. In addition, R_k, $k \in \{p, q\}$, is the radius of the k^{th} spheroid and $\mathbf{r}_k$ is the position vector of its centre of mass (CoM). The normal and tangential components of spring-dashpot force are given by

$$\mathbf{F}^n = \kappa_n \delta_{pq} \mathbf{n}_{pq} - \gamma_n m^* \mathbf{v}^n_{pq} \tag{1}$$

$$\mathbf{F}^t = -\kappa_t \mathbf{u}^t_{pq} - \gamma_t m^* \mathbf{v}^t_{pq}, \tag{2}$$

where $\kappa_n, \gamma_n, \kappa_t$ and γ_t are spring elastic and damping constants in normal and tangential directions respectively. In addition, $\mathbf{v}^n_{pq}$ and $\mathbf{v}^t_{pq}$ are relative normal and tangential velocities. The effective mass is defined as $m^* = m_p m_q/(m_p + m_q)$ where m_k, $k \in \{p, q\}$, is the mass of k^{th} particle. The unit normal vector in the direction of the line connecting a pair of spheroid centres is presented by $\mathbf{n}_{pq}$ and elastic shear displacement by $\mathbf{u}^t_{pq}$. The tangential force is limited to $\|\mathbf{F}^t_{pq}\| \leq \mu_c \|\mathbf{F}^n_{pq}\|$ where μ_c is the Coulomb friction coefficient which is set to 0.5 in this study [1]. Similarly, a normal $\mathbf{F}^n_{pw}$ and a tangential force $\mathbf{F}^t_{pw}$ are defined between particle p and the bottom wall w.

Shape effects are considered in this paper and hence, a versatile multi-sphere technique is used [1]. In this paper, rod-shaped particles are considered which can be parametrised using an aspect ratio A_r. This is chosen since elongated particles with a similar aspect ratio distribution and round edges can be considered as approximations to a population of impact-milled PEEK particles [1]. In addition, rod-shaped particles with required aspect ratios of $\mathrm{A}_r = 1.5, 2.0, 2.5$ could be generated with 2, 3 and 4 spheroids, considerably reducing the costs of the computations. Therefore, these are used as approximations to the real particles for the optimisations stage where a large number of simulations are required.

The simulation set-up is depicted in Figure 1b. The bottom boundary is a rigid wall that exerts a normal and a tangential force on the particles (equivalent to assuming an infinity large sphere in Eqs. (1) and (2)). To prevent unbounded rotation of particles on the bottom wall, a rolling friction model is implemented [17, 18, 19]. The elastic spring constant κ_n, in Eq. (1) is set according to [20]. The coefficient of restitution is set to 0.5 and the values of Young's modulus, Poisson ratio and particle density are set to 3.7 GPa,

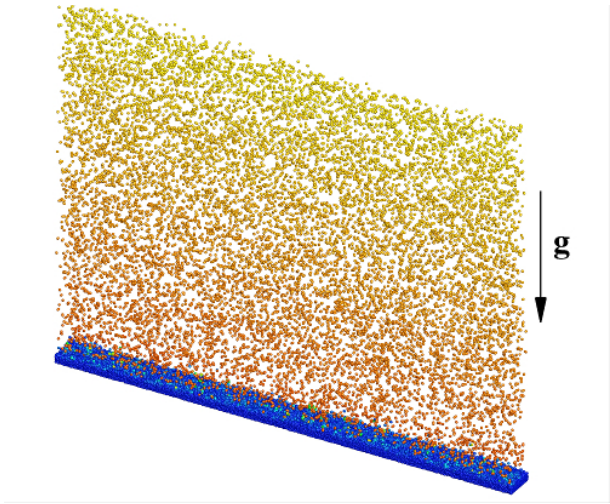

(a)

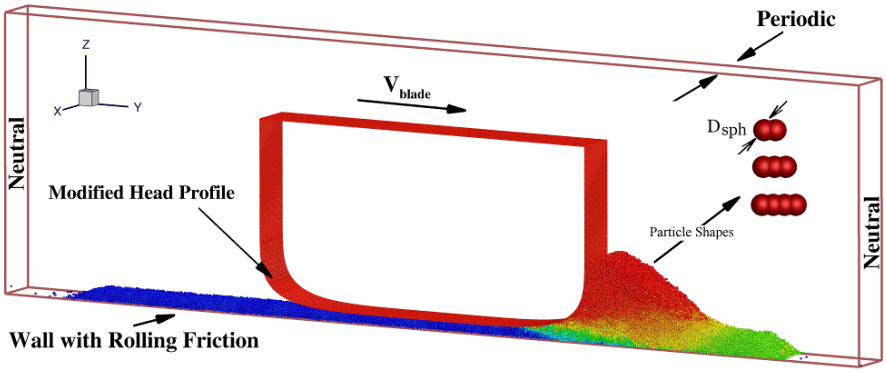

(b)

Figure 1: The device simulation set-up and initial preparations presented for a modified blade profile. (a) The initial bed preparation using a rain fall technique is presented; particles are coloured with their velocity magnitudes and diameters are not to scale for better presentation. (b) The rod-shaped particles with different aspect ratios A_r are presented using a multi-sphere approach. Also, the particles are coloured in a representative simulation with v_y (velocity in y-direction). Only a section of the spreader with a width L_x is simulated by choosing periodic boundary conditions in x-direction and in y-direction neutral walls are used (no interaction with particles).

0.4 and $\rho_{\text{rod}} = 1.3$ gr/cm^3 for all particles which are typical values for PEEK polymeric powders [21]. The spring constant κ_n is calculated from the Young's modulus and Poisson ratio using a characteristic velocity $V_c = V^T_{\text{blade}}$ [22, 1]. The tangential force constants κ_t and γ_t are respectively set to $2/7\kappa_n$ and $1/2\gamma_n$ respectively [22].

2.2 Simulation set-up and post-processing

The rods with various aspect ratios $A_r = 1.5,\ 2.0,\ 2.5$ are created by overlapping spheres with $\ell = 0.5$ (Figure 1b) and number densities of $N_{\text{A}_r} = 0.5,\ 0.3,\ 0.2$ respectively. The initial configuration (before the spreading starts) is prepared by pouring randomly generated particles on the bottom wall (see Figure 1a). This is done within a simulation box with dimensions $L_x = 2.46 \times 10^{-3}$, $L_y = 0.04$ and $L_z = 0.03$. The geometric parameters L_x, L_y and L_z are the width, length and height of the simulation box (red boundaries in Figure 1b). Note that all values are in SI units except otherwise stated. The preparation method is different from the delivery system in LS devices; nevertheless, since the powder is not compacted in the delivery piston and rests under its natural weight, this method of initiating the simulation, is adequate for the current purpose.

The box size in the flow-direction L_y changes to accommodate all the particles as they are spread and the corresponding walls exert no force on the particles (walls labelled neutral in Figure 1b). The number of particles in each simulation is adjusted to supply an initial thickness of $\delta_{init} \approx 10D_{\text{sph}}$ for all particle types, where D_{sph} is the diameter of spheres used to generate the rod-shaped particles. In addition, the blade displacement from the bottom wall, δ_{blade} is set to $5D_{\text{sph}}$ which is the profile's minimum distance to the bottom wall and essentially sets the powder bed thickness.

The solid volume fraction, ϕ_s, is calculated and its maximum value is used as the objective function – which means a more effective spreading process – to optimise the blade profile. The ϕ_s values are calculated using a Voronoi tessellation technique [23] and only a section of the bed away from the edges are considered to suppresses the end effects. This is, in fact, a reasonable assumption since the full extent of the bed in not normally used for fabrication; see [1] for further details.

3 The new blade design

Haeri et al. [1] argued that an "effective" bed-spreader contact, determines the quality of a prepared powder bed (a high ϕ_s and low ϵ), where ϵ is a measure of roughness. Based on visualisations of the bed-spreader contact dynamics they related this to a particle dragging phenomenon which distorts the bed if a spreader type did not provide an effective support for the particle heap that forms in front of the spreader (see Figure 1b). This suggests that a geometric modification of the spreader should in principle, significantly improve the bed's quality.

By modifying the spreader's head profile a new class of spreading devices is suggested.

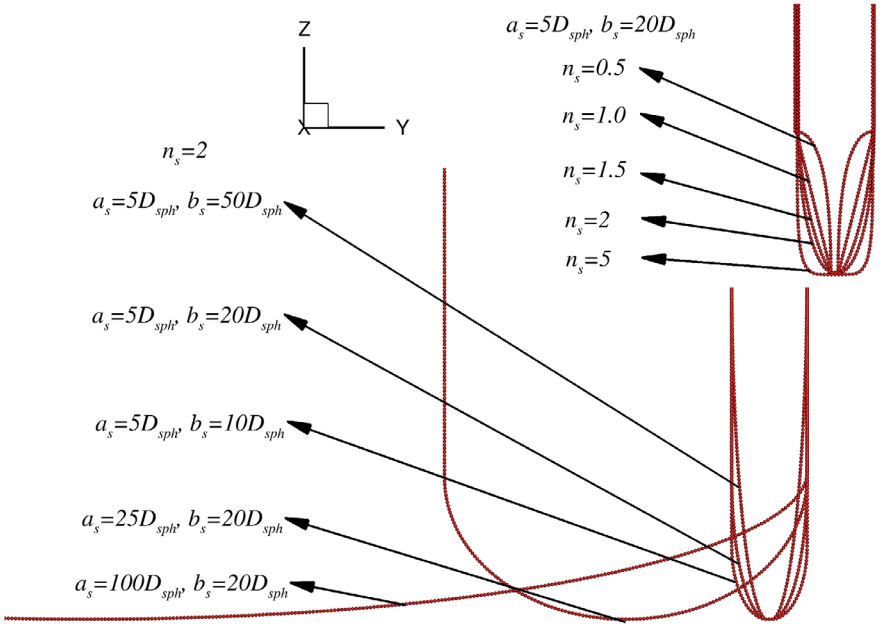

Figure 2: Different spreader profiles used for the optimisation. Only a subset of all designs are presented to show the effects of changing parameters a_s, b_s and n_s. Only half of the widest blade with $a_s = 100D_{\text{sph}}$ is presented.

A super-elliptic profile with three parameters n_s, a_s and b_s is proposed here:

$$\left|\frac{y}{a_s}\right|^{n_s} + \left|\frac{z}{b_s}\right|^{n_s} = 1. \tag{3}$$

The parameters n_s, a_s and b_s respectively, control the overall shape, width and height of the profile. The blade thickness is $w_s = 2a_s$ and its height is $h_s \gg b_s$. Note that the blade's height is longer than b_s and remains a straight line for $z > b_s + \delta_{\text{blade}}$, its value is chosen to be larger than the maximum height of the powder heap formed in front of the blade during the spreading process and has no effect on the optimisation results. In Figure 2 various profile shapes proposed for the optimisation are presented. Three values $(10, 25, 100)D_{\text{sph}}$ and $(10, 20, 50)D_{\text{sph}}$ are chosen for a_s and b_s respectively. The parameter n_s determines the overall shape of the profile. Initially, five different shapes $n_s \in \{0.5, 1.0, 1.5, 2.0, 5.0\}$ are considered (see Figure 2), however, after the initial optimisation a few more values are considered to show that the best identified n_s is in fact the optimum value.

3.1 Optimisation results and discussions

The results of 48 simulations with different optimisation parameters are presented in Figure 3. Before analysing the results any further, it is clear that the blade's geometry

is indeed a major parameter for controlling the bed quality. Figure 3 clearly shows the variation in ϕ_s from low values of $\phi_s \approx 0.4$ to values as high as $\phi_s \approx 0.58$. This proves the effectiveness of geometrical modification of the blade's head profile to maximise ϕ_s and indicates the validity of the initial hypothesis.

For comparison with a straight edge blade, the data from [1] are used. They performed simulations with mono-sized ($\mathrm{A}_r = 1.0 \cdots 2.5$) particles at similar operating conditions. However, they showed that the characteristics of poly-sized beds (with small variation in the aspect ratio) could be approximated by a number density weighted averaging. To find an approximate value for the poly-sized case considered here, a number density average of the mono-sized simulations of [1] is calculated. This can be written by $\phi_s = \sum N_i \phi_s(\mathrm{A}_{r,i})$ which yields a value of $\phi_s = 0.4$ for straight edge blade spreader of a mixture of particles with number densities considered in this paper.

The effects of overall profile shape are demonstrated in Figures 3a to 3e. In these figures, the value of the parameter n_s is changed which characterises the overall shape of the profile. A value of $n_s = 0.5$ generates a concave profile and the results are presented in Figure 3a. Evidently, this profile does not improve the compaction significantly, nevertheless, some improvement is observed especially for the lowest value of blade width of $5D_{\mathrm{sph}}$.

A linear profile can be generated by setting $n_s = 1$. The simulation results for this profile and different width and height parameters a_s and b_s are presented in Figure 3b. The bed quality – as expected – is a function of both profile height and also the spreader width. Generally, shorter (smaller b_s) and wider (larger a_s) profiles generate higher volume fractions ϕ_s. The sensitivity of the linear profile to height is higher for wider designs but almost no dependence on height is observed for narrow designs ($a_s = 5D_{\mathrm{sph}}$). It is also interesting to note that ϕ_s dependence on a_s for the concave profile ($n_s = 0.5$) is opposite to that of the linear profile and all the other convex profiles. It is believed that for a concave profile ($n_s = 0.5$) some particles may get clogged in the hollow region between the blade's head profile and the bottom surface (or the previous layers). Therefore, wider profiles generate smaller volume fraction for the $n_s = 0.5$ case whereas increasing a_s improves the quality for all other convex profiles (with $n_s \geq 1$).

Figures 3c to 3e show as the value of n_s increases from $n_s = 1.5$ to $n_s = 5.0$, for all the corresponding values of b_s and a_s the volume fraction increases indicating a better quality. In addition, the sensitivity to b_s also decreases such that for $n_s = 5.0$ the volume fraction is practically independent of b_s. This perhaps is not surprising since larger n_s values cause a condensation of curvature very close to the edges and the remaining sections of profile away from the edges are essentially straight lines. Therefore, changing b_s does not significantly change the profile characteristics. For all values of $n_s \geq 1$ wider profiles generate beds with larger ϕ_s. The current results show that optimisation of the profile is highly successful and ϕ_s for $n_s = 5.0$, $a_s = 100D_{\mathrm{sph}}$ and $b_s = 10D_{\mathrm{sph}}$ approaches a value of $\phi_s = 0.58$. This value is close to the critical volume fraction of spherical frictional particles (with $\mu_c = 0.5$) determined as $\phi_c = 0.587$ by Chialvo et al. [24]. Therefore, any

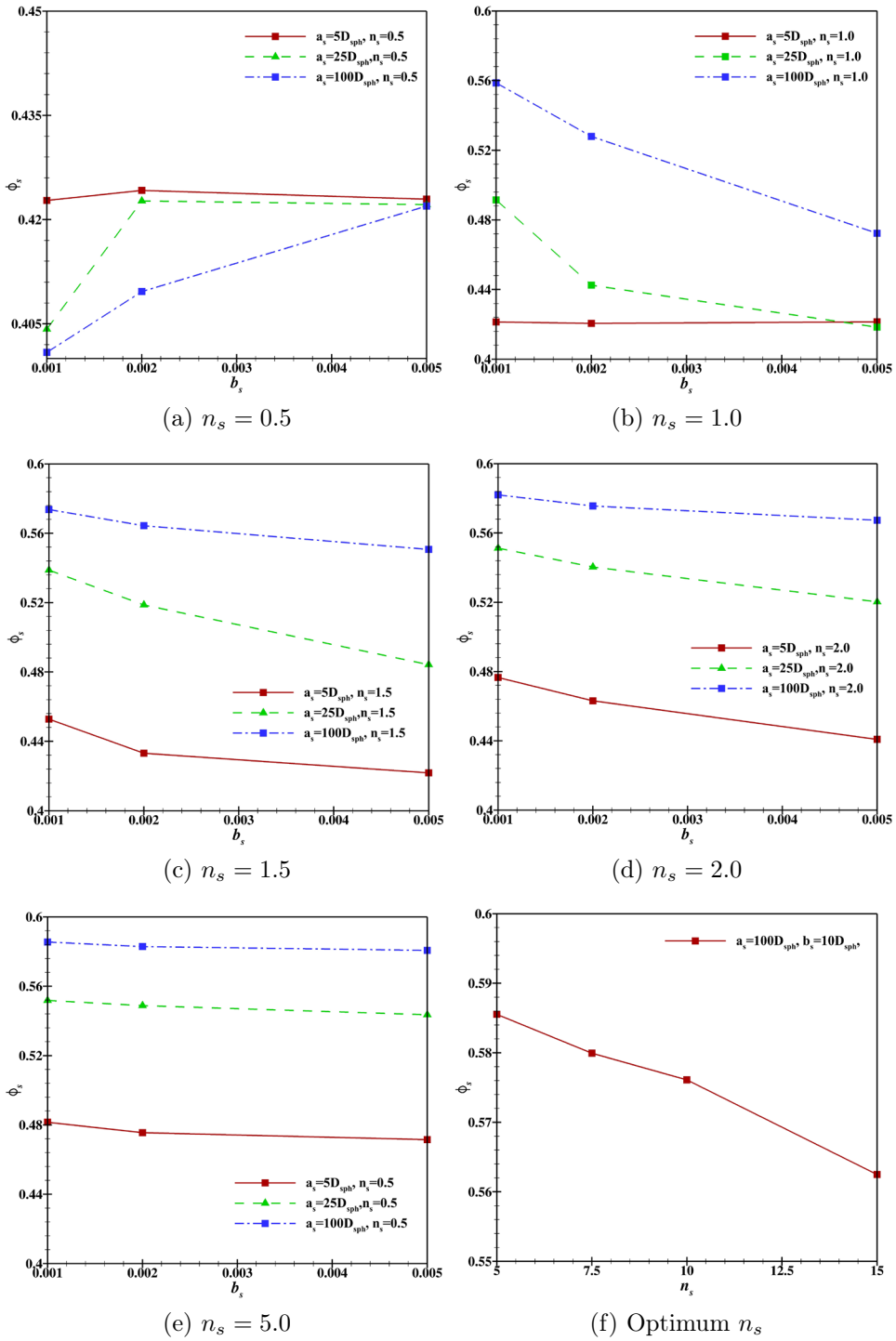

(a) $n_s = 0.5$ (b) $n_s = 1.0$

(c) $n_s = 1.5$ (d) $n_s = 2.0$

(e) $n_s = 5.0$ (f) Optimum n_s

Figure 3: Variations in solid volume fraction ϕ_s with different optimisation parameters. The values on b_s axis correspond to $(10, 20, 50) \times D_{\text{sph}}$.

further compaction without significant compression of the bed is not expected.

For the particular powder considered here (with the specified material and morphology characteristics) a larger ϕ_s is obviously not anticipated and hence further optimisation is redundant. Nevertheless, since the ϕ_s monotonically increased during the optimisation process (see Figure 3a to Figure 3e), a valid question is whether ϕ_s versus n_s curve has a plateau and one can choose an arbitrarily large n_s, or an optimum n_s value actually exists. It is important to note that as $n \to \infty$ the profile will approach a typical rectangular shape which as demonstrated in [1] significantly degrades the bed quality. Therefore, the existence of an optimum value for n_s is certain. To show that $n_s = 5.0$ is in fact that optimum value and generates the highest ϕ_s a series of the simulations with 3 other values of $n_s \in \{7.5, 10.0, 15.0\}$ are performed. The results are presented in Figure 3f which proves that $n_s = 5.0$ (noting the resolution of the current parametric study) must be the optimum profile shape.

In this section, the profile with parameters $n_s = 5.0$, $a_s = 100D_{\text{sph}}$ and $b_s = 10D_{\text{sph}}$ is identified as the optimum profile. A value of $b_s = 10D_{\text{sph}}$ $(= 1mm)$ may not be feasible to manufacture. However, noting the independence of ϕ_s from b_s in Figure 3e, one can choose a larger value of b_s to manufacture a spreader with more realistic physical dimensions.

4 Conclusion

In this paper it is first demonstrated that geometric optimisation of a blade type spreader can significantly improve the quality of a powder bed (a higher ϕ_s) that is generated by spreading for Particle Bed Fusion (PBF) processes. A new class of spreading devices is proposed by assuming a super-elliptic edge profile with three different parameters controlling width, height and the overall shape of the profile. A set of 48 device-scale DEM simulations are performed and the optimum values for these parameters are identified. It is shown that this optimisation is highly effective and packings close to the critical volume fraction is achievable. Therefore, the optimised blade is as effective as a roller. This could greatly reduce the production and maintenance costs of the PBF devices by obviating the need for significantly more expensive and complex spreading devices.

Acknowledgement

This work was supported by the Institution of Mechanical Engineers (IMechE) award EAC/KDF/OFFER/17/065. The author also gratefully acknowledges the use of ARCHER – The UK National Supercomputing Service (http://www.archer.ac.uk) – for conducting the simulations under the EPSRC's Resource Allocation Panel (RAP) Grant E504.

References

[1] S. Haeri, Y. Wang, O. Ghita, and J. Sun. Discrete element simulation and experimental study of powder spreading process in additive manufacturing. *Powder Technology*, 306:45–54, 2017. ISSN 0032-5910. doi: 10.1016/j.powtec.2016.11.002.

[2] I. Gibson and D. Shi. Material properties and fabrication parameters in selective laser sintering process. *RTejournal 3: Forum Rapid Technol.*, 1995.

[3] Y. Shi, Z. Li, H. Sun, S. Huang, and F. Zeng. Effect of the properties of the polymer materials on the quality of selective laser sintering parts. *IMechE Journal*, 218:247–253, 2004.

[4] R. D. Goodridge, K. W. Dalgarno, and D. J. Wood. Indirect selective laser sintering of an apatite-mullite glass-ceramic for potential use in bone replacement applications. *Proceedings of the Institution of Mechanical Engineers, Part H*, 220:57–68, 2006.

[5] L. Hao, M. M. Savalani, Y. Zhang, K. E. Tanner, and R. A. Harris. Effects of material morphology and processing conditions on the characteristics of hydroxyapatite and high-density polyethylene biocomposites by selective laser sintering. *Journal of Materials: Design and Applications*, 220:125–137, 2006.

[6] S. Ziegelmeier, P. Christou, F. Wöllecke, C. Tuck, R. Goodridge, R. Hague, E. Krampe, and E. Wintermantel. An experimental study into the effects of bulk and flow behaviour of laser sintering polymer powders on resulting part properties. *Journal of Materials Processing Technology*, 215:239–250, 2015.

[7] P. A. Cundall and O. D. L. Strack. A discrete numerical model for granular assemblies. *Geotechnique*, 29:47–65, 1979.

[8] E. Onate and D. R. J. Owen. *Particle-Based Methods: Fundamentals and Applications, Computational Methods in Applied*. Springer, 2011.

[9] T. I. Zohdi. Computation of the coupled thermo-optical scattering properties of random particulate systems. *Computer Methods in Applied Mechanics and Engineering*, 195:5813–5830, 2006.

[10] T. I. Zohdi. Rapid simulation of laser processing of discrete particulate materials. *Archives of Computational Methods in Engineering*, 20:309–325, 2013.

[11] T. I. Zohdi. Additive particle deposition and selective laser processing – a computational manufacturing framework. *Computational Mechanics*, 54:171–191, 2014.

[12] Z. Xiang, M. Yin, Z. Deng, X. Mei, and G. Yin. Simulation of forming process of powder bed for additive manufacturing. *Journal of Manufacturing Science and Engineering*, 138:081002, 2016.

[13] J. C. Steuben, A. P. Iliopoulos, and J. G. Michopoulos. Discrete element modeling of particle-based additive manufacturing processes. *Computer Methods in Applied Mechanics and Engineering*, 305:537–561, 2016.

[14] S. A. Khairallah, A. T. Anderson, A. Rubenchik, and W. E. King. Laser powder-bed fusion additive manufacturing: Physics of complex melt flow and formation mechanisms of pores, spatter and denudation zones. *Acta Materialia*, 108:36–45, 2016.

[15] A. Rai, H. Helmer, and C. Korner. Simulation of grain structure evolution during powder bed based additive manufacturing. *Additive Manufacturing*, 13:124–134, 2017.

[16] S. Plimpton. Fast parallel algorithms for short-range molecular dynamics. *Journal of Computational Physics*, 117:1–19, 1995.

[17] Y.C. Zhou, B.D. Wright, R.Y. Yang, B.H. Xu, and A.B. Yu. Rolling friction in the dynamic simulation of sandpile formation. *Physica A*, 269:536–553, 1999.

[18] J. Ai, J.-F. Chen, J.M. Rotter, and J.Y. Ooi. Assessment of rolling resistance models in discrete element simulations. *Powder Technology*, 206:269–282, 2011.

[19] C.M. Wensrich and A. Katterfeld. Rolling friction as a technique for modelling particle shape in dem. *Powder Technology*, 217:409–417, 2012.

[20] A. Di Renzo and F.P. Di Maio. Comparison of contact-force models for the simulation of collisions in dem-based granular flow codes. *Chemical Engineering Science*, 59: 525–541, 2004.

[21] ully. A comprehensive review of the materials properties of victrex® peek™ high performance polymer. enzo, VICTREX, 2016.

[22] J. Shäfer, S. Dippel, and D. Wolf. Force schemes in simulations of granular materials. *Journal de Physique I*, 6:5–20, 1996.

[23] C. H. Rycroft. Voro++: A three-dimensional voronoi cell library in c++. *Chaos: An Interdisciplinary Journal of Nonlinear Science*, 19:041111, 2009.

[24] S. Chialvo, J. Sun, and S. Sundaresan. Bridging the rheology of granular flows in three regimes. *Physical Review E*, 85:023305, 2012.

V International Conference on Particle-based Methods – Fundamentals and Applications
PARTICLES 2017
P. Wriggers, M. Bischoff, E. Oñate, D.R.J. Owen, & T. Zohdi (Eds)

3D MODELLING OF MATERIAL FLOW IN FRICTION STIR WELDING USING MOVABLE CELLULAR AUTOMATON METHOD

ALEXEY YU. SMOLIN[1], GALINA M. EREMINA[2] AND SERGEY G. PSAKHIE[3]

[1] National Research Tomsk State University (TSU)
pr. Lenina 36, 634050, Tomsk, Russia
E-mail: asmolin@ispms.tsc.ru , web page: http://www.tsu.ru

[2] Institute of Strength Physics and Materials Science (ISPMS)
Siberian Branch of Russian Academy of Sciences
pr. Akademicheskii 2/4, 634055, Tomsk, Russia
E-mail: rector@tsu.ru , web page: http://www. ispms.ru

[3] Institute of High Technology Physics, National Research Tomsk Polytechnic University
pr. Lenina 30, Tomsk, 634050, Russia
E-mail: sp@ispms.tsc.ru , web page: http://www.tpu.ru

Key words: Friction Stir Welding, Severe Plastic Deformation, Movable Cellular Automata, Particle-Based Modelling.

Abstract. The paper is devoted to the theoretical investigation of the peculiarities of material flow taking place in friction stir welding (FSW). The investigation was based on 3D computer simulation by the movable cellular automaton (MCA) method, which is a representative of the particle methods in mechanics of materials. Usually, material flow in FSW is simulated based on computational fluid mechanics, which assumes that the material is a continuum and does not take into account the material structure. MCA considers a material as an ensemble of bonded particles. Breaking of inter-particle bonds and formation of new bonds enables simulation of crack nucleation and healing, as well as mas mixing and microwelding. The simulation results showed that using pins of simple shape (cylinder, cone, pyramid) without shoulder results in small scattered displacements of the plasticised material in the workpiece thickness direction. Nevertheless, the optimal ratio of the longitudinal velocity to the rotational speed allows transporting of the welded material around the pin several times and producing the joint of good quality. Applying additional ultrasonic vibration to the pin may lead to better mixing of the plasticized material behind the pin.

1 INTRODUCTION

The structure of the modern materials may be very complex and have hierarchical nature starting from the nanoscale. The most of the modern materials are heterogeneous composites and may include so called soft components. One of the main properties of soft matter is its ability to change functional properties of the material which includes it. This primarily refers to heterogeneous contrast materials. The high mobility of soft matter and their low shear stiffness leads to intensive elastic energy dissipation in the system even at low applied stress.

The involvement of dissipation mechanisms induced by the redistribution of soft components results in a strong and nonlinear dependence of mechanical properties of the contrast material on the strain rate. The strain rate range where the change of the integral properties of the material occurs is determined by the time range of elastic energy dissipation and by the amplitudes of the contribution of dissipative constituents associated with the redistribution of soft components in the material volume.

The wide use of modern materials in technological and medical application causes new requirements for their joining. One of the hardest of them concerns keeping the material structure to be unchanged. A necessary requirement for the problem solving approach is the possibility to widely vary characteristic loading rates and time range of elastic energy dissipation in the material, mechanical properties of the components, and special features of the internal structure of contrast materials. These studies should be conducted in a wide range of spatial scales (from nanoscopic to macroscopic) and take into account the possibility of fracture of solid components accompanied by contact interaction of the crack surfaces and local stirring of fragments.

An important achievement of the last decades in the field of material joining is the development of friction stir welding (FSW) [1–4]. Recent studies have shown that FSW is an effective way to obtain high quality joints for structures of various dimensions and shapes. The main feature of the FSW is the ability to weld without melting of the joined materials, which allows avoiding changes in material properties due to hot temperatures and joining dissimilar alloys and materials including those that impossible to join by traditional welding technology [2, 3].

The main problem in the industrial application of FSW technology consists in finding the correct technological parameters of the process (such as the tool shape and size, rotation and travel speed, etc.) [2]. It is impossible to define the optimal technological parameters without full understanding the fundamental processes occurring in the material during FSW. The main fundamental problem here is to understand the mechanisms of severe plastic deformation that enable plastic flow, mass mixing and material coalescing behind the tool (i.e. plasticized material behaviour in FSW).

This paper is devoted to the theoretical investigation of the peculiarities of material flow taking place in FSW. The investigation was based on 3D computer simulation by the movable cellular automaton (MCA) method [5], which is a representative of the particle methods in mechanics of materials. Usually, material flow in FSW is simulated based on computational fluid mechanics, which assumes that the material is a continuum and does not take into account the material structure. MCA considers a material as an ensemble of bonded particles. Breaking of inter-particle bonds and formation of new bonds enables simulation of crack nucleation and healing, as well as mas mixing and microwelding.

2 METHOD OF MOVABLE CELLULAR AUTOMATA

MCA is a new efficient numerical method in particle mechanics that is different from methods in the traditional continuum mechanics. Within the frame of MCA, it is assumed that any material is composed of a certain amount of elementary objects (automata) which interact among each other and can move from one place to another, thereby simulating a real

deformation process. The automaton motion is governed by the Newton-Euler equations:

$$\begin{cases} m_i \dfrac{d^2 \mathbf{R}_i}{dt^2} = \sum\limits_{j=1}^{N_i} \mathbf{F}_{ij}^{\text{pair}} + \mathbf{F}_i^{\Omega}, \\ \hat{J}_i \dfrac{d\boldsymbol{\omega}_i}{dt^2} = \sum\limits_{j=1}^{N_i} \mathbf{M}_{ij} \end{cases} \tag{1}$$

where $\mathbf{R}_i$, $\boldsymbol{\omega}_i$, m_i and $\hat{J}_i$ are the location vector, rotation velocity vector, mass and moment of inertia of ith automaton respectively, $\mathbf{F}_{ij}^{\text{pair}}$ is the interaction force of the pair of ith and jth automata, $\mathbf{F}_i^{\Omega}$ is the volume-dependent force acting on ith automaton and depending on the interaction of its neighbours with the remaining automata. In the latter equation, $\mathbf{M}_{ij} = q_{ij}(\mathbf{n}_{ij} \times \mathbf{F}_{ij}^{\text{pair}}) + \mathbf{K}_{ij}$, here q_{ij} is the distance from the centre of ith automaton to the point of its interaction ("contact") with jth automaton, $\mathbf{n}_{ij} = (\mathbf{R}_j - \mathbf{R}_i)/r_{ij}$ is the unit vector directed from the centre of ith automaton to the jth one and r_{ij} is the distance between automata centres, $\mathbf{K}_{ij}$ is the torque caused by relative rotation of automata in the pair.

The forces acting on automata are calculated using deformation parameters, i.e. relative overlap, tangential displacement and rotation, and conventional elastic constants, i.e. shear and bulk moduli. A distinguishing feature of the MCA method is calculating of forces acting on the automata within the framework of multi-particle interaction [5], which provides for an isotropic behaviour of the simulated medium regarded as a consolidated body rather than a granular medium. Moreover, stress tensor components could be calculated for the automaton taking into account all the forces acting on the automaton [5], which enables the realization of various models of the plastic behaviour of materials developed in the frame of continuum mechanics.

A pair of elements might be considered as a virtual bistable cellular automaton, which permits simulation of fracture and cracks healing and microwelding by the MCA. In this work, a fracture criterion based on the threshold value of von Mises stress was used. A criterion based on the threshold value of plastic work was used for making a new bond between contacting automata. Switching of a pair of automata from bonded to non-bonded state and vice versa would result in a changeover in the forces acting on the elements; in particular, non-bonded automata would not resist moving away from one another.

Thus, the MCA makes a feasible simulation of solid body behaviour at different scale levels, including viscoelastic and plastic deformation, fragmentation and further interaction of fragments as a loose (granular) material [6–8].

3 DESCRIPTION OF THE MODEL

3.1 Material characterization

Here we model the process of FSW of two plates of aluminium-based alloy D16. The mechanical properties of the material were characterized by the following parameters: the shear modulus G = 27.27 GPa, the bulk modulus K = 66.67 GPa, the yield stress σ_y = 274 MPa. Plastic behaviour was simulated by linear hardening up to the strength limit σ_t =

800 MPa at the ultimate strain $\varepsilon_t = 0.15$. The automata in unbounded state switch to bounded state at the plastic work in the pair to be equal to $W_b = 50$ MJ/m^3.

3.2 Geometry of the model and scheme of loading

The geometry of the model is shown in Fig. 1. There were two plates of the dimensions 6.5×18.0 mm and the thickness 2.5 mm. Joining of the plates was performed by moving of the hard pin along axis *Y*. The pin also rotates with the velocity ω around its axis, which is always parallel to coordinate axis *Z*. Initially, the pin was placed at the distance of 6 mm from the left face.

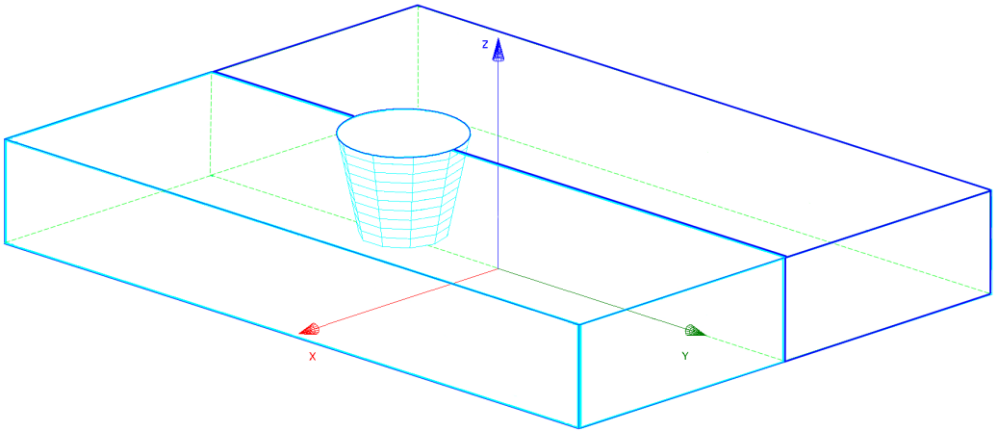

Figure 1: Initial geometry of the model

At the beginning of the joining process, the pin only rotates with the velocity $\omega = 800$ 1/s at the initial place, and its axis does not move. This preliminary stage is required for preparing plasticized zone around the pin and takes up to 5 full rotations. After that stage, the axis of the pin starts to move along axis *Y* with constant velocity V_t.

To simplify computations the following boundary conditions were set. To simulate the action from backing plate and pin shoulder the automata were not allowed to cross the lower and upper surface of the geometry. Unfortunately, this simplification did not account for the rotation of the pin shoulder and resulted in the size of plasticized zone smaller than one in the real process. At the other free surfaces of the plates, the automata were fixed.

3.3 A criterion for the weld quality

Behind the moving pin, the structure of the automata in the model weld region is not a periodic close packing as in the green material. The number of the bonded neighbours is not equal to the initial coordination number (12). It may be greater or less than 12. But the average number of the bonded neighbours is less than 12. The less is this number the weaker is the model weld material. To characterize the quality of the model weld we use the plot of the number of bonded automata N_l in the simulated system versus length of the pin path *S*. A typical picture for this plot is shown in Figure 2. A strong decrease of the bonded automata In the beginning of the pin path corresponds to the initial stage of the loading when the pin rotates and does not move. The main linear part of the plot corresponds to stable weld

formation and indicates a good quality of the weld.

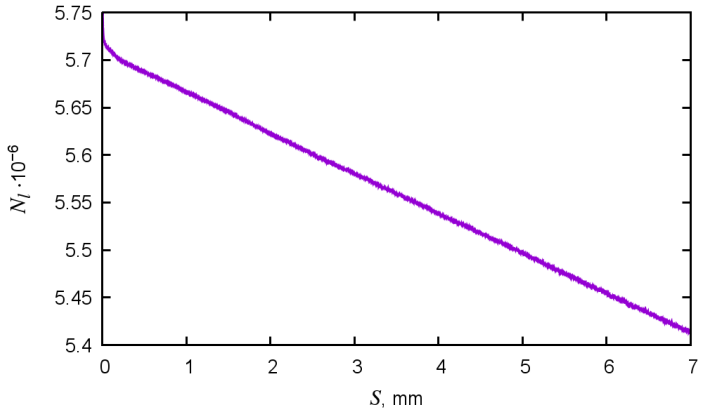

Figure 2: A plot for the number of bonded automata versus length of the pin path

4 SIMULATION RESULTS

First, let us consider the influence of the translation velocity V_t on the plot $N_l(S)$. For this purpose, the rotational velocity ω = 800 1/s was unchanged for all cases and the translation velocity was varied from 0.05 up to 0.50 m/s. The resulting plots $N_l(S)$ are shown in Figure 3. According to these results, the optimal value of V_t is equal to 0.10 m/s. The corresponding weld has the minimal number of unbounded automata and homogeneous distribution of them along the weld. The worst case corresponds to the velocity of 0.50 m/s. This simulation was aborted by the critical inhomogeneity of the weld. The results in Figure 3 also show that using of very slow translation of the pin results in the weld with the larger number of defects. These results are in very good agreements with the experimental evidence and the results of 2D simulations [2, 9].

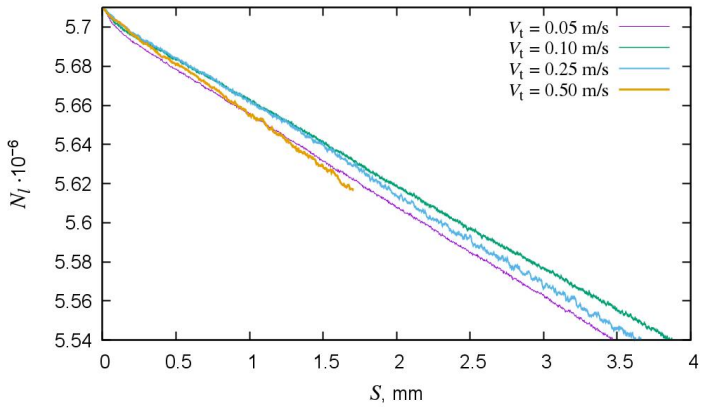

Figure 3: The plots $N_l(S)$ for different translation velocities V_t

For analysis of the influence of the pin shape on the FSW process within our model, several different pins were generated. Seven of them are shown in Figure 4. As one can see, these pins may be grouped by three basic geometrical bodies: cone, cylinder, and pyramid.

Cone and cylinder may have additional “wings” aimed to enforce material flow in the direction of the plate width (along axis *Z*).

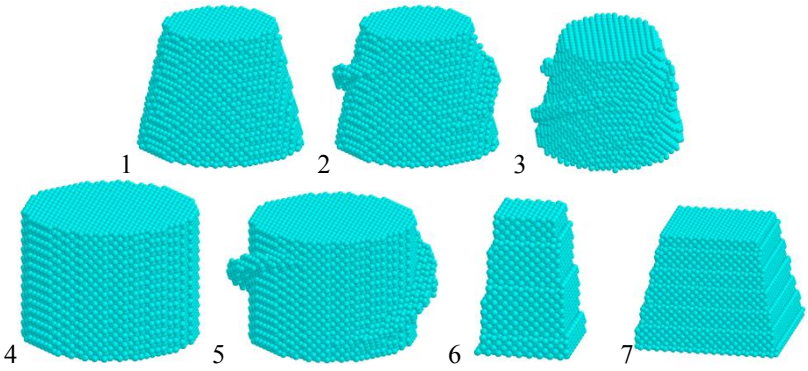

Figure 4: Seven different pin shapes used in simulations

The resulting plots $N_l(S)$ for different pin shapes are shown in Figure 5. First of all, one can see that maximal decay in the number of bonded automata occurring in the initial stage is proportional to the surface aria of the pin. However, the quality of the weld is determined by the inclination of the linear part of the curve $N_l(S)$. Therefore, the conclusion that may be drawn from the obtained results is that the best shapes for FSW pin are 2, 3, and 6 in Figure 4. From the other side, only shapes 1, 6, and 7 produce the homogeneous weld.

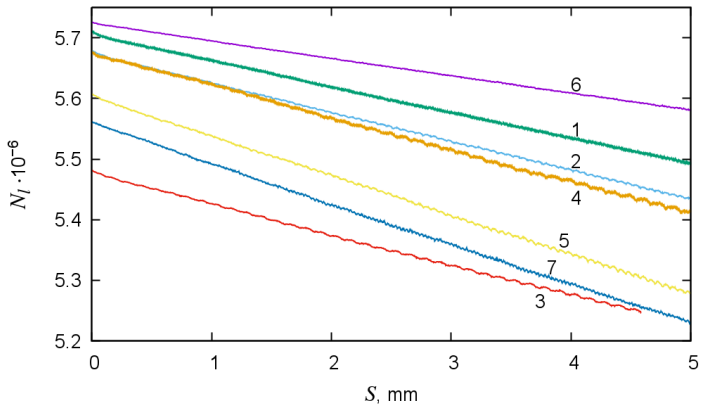

Figure 5: The plots $N_l(S)$ for different pins shown in Figure 4

The top view of the weld for the pin number 6 is shown in Figure 6. It has to be noted that the width of the weld for the pyramid is relatively wide comparing to the cone or cylinder because the width is determined by the diagonal of the square, which is the base of the pyramid, not by its side. The second important point is that this shape of the pin is not a body of revolution and hence provides better mixing of the plasticized material in the joint. But if compared with the wider pyramid (pin number 7) one may conclude that there an optimal ratio of the pyramid width and height should exist to produce the best weld.

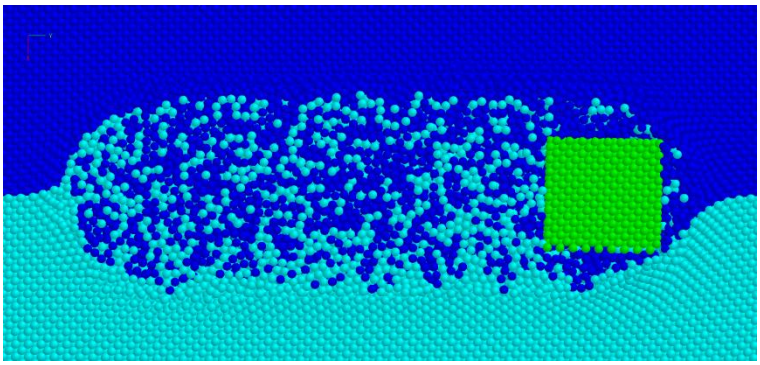

Figure 6: The top view of the weld produced by pin 4 in Figure 4

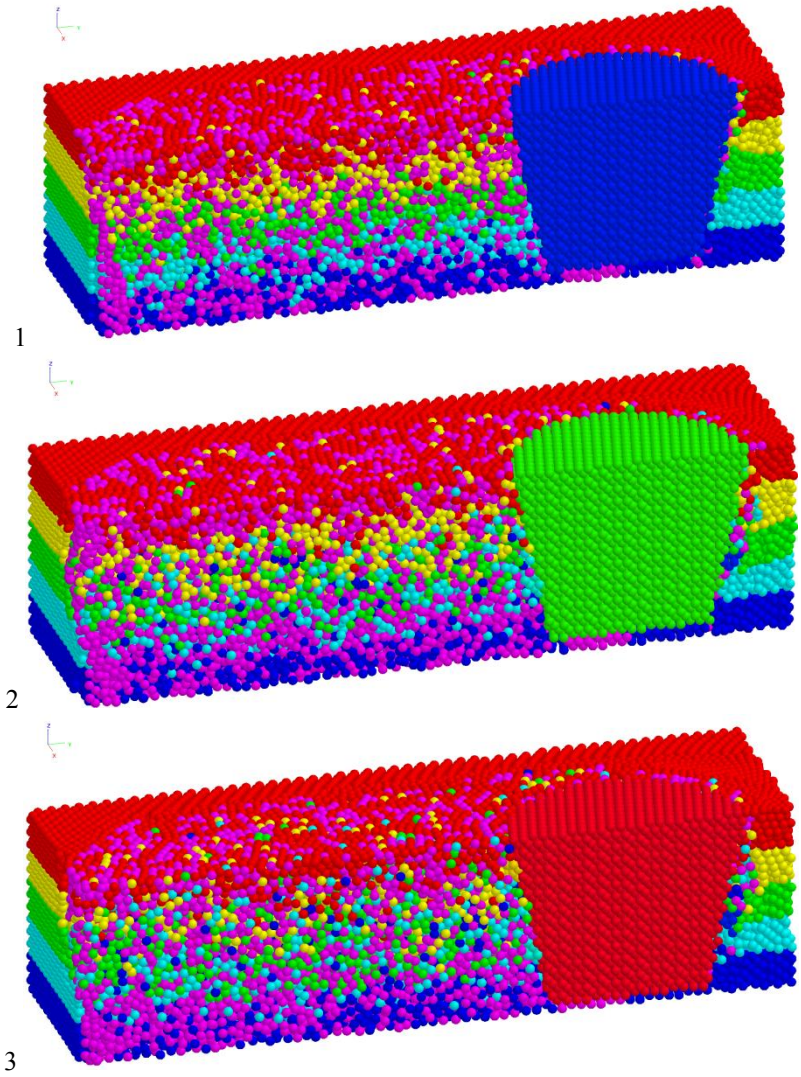

Figure 7: The top view of the weld produced by the pins 1–3 in Figure 4

To analyse the peculiarities of the material flow during friction stir welding executed by

pins 2, 3 with additional "wings" the initial automata in the plates were coloured by horizontal layers (along axis Z). The final distributions of the mixed automata in the welds produced by three conical pins are shown in Figure 7. The results demonstrate no significant role of the additional "wings" on the material flow in the direction of plate width. However, it is well known from the experimental evidence that there is a marked flow in this direction in the vicinity of the pin. To explain this difference in the experiments and our modelling results we assume that the main role in the flow in the plate width direction belongs to the pin shoulder that provides a wide area of rotating material in the top of the plate and substantial gradient of rotating mass along the plate width direction.

The next interesting point in the improvement of FSW is applying additional vibrations to the pin during the joining process. In our calculations, such an action was modelled by adding to the longitudinal velocity of the pin axis motion the following value

$$V_{us}=A_{us}\sin(2\pi\nu_{us}t), \tag{2}$$

where A_{us} is the amplitude and ν_{us} is the frequency of this vibrating action in ultrasound range. We varied the direction of the vibration (along axis X or Y), the values of its amplitude and frequency. Below we will characterize the power of this action by maximal displacement of the pin per one period of vibration D_{us}, not by the amplitude of the corresponding velocity A_{us}.

The simulation results showed that additional vibration applied perpendicularly to the direction of welding produces much less effect comparing to the longitudinal direction. That is why further we will discuss the results obtained with the vibration applied along axis Y.

The plots $N_l(S)$ for different vibration frequencies are shown in Figure 8. For comparison, this figure also contains the plot for the case of no vibration. The power of the vibrations was the same D_{us} = 15 μm.

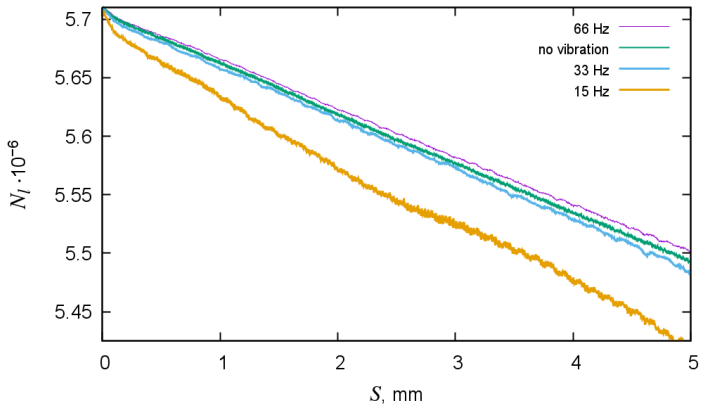

Figure 8: The plots $N_l(S)$ for different vibration frequencies ν_{us}

From the presented data one can conclude that the positive effect on the weld quality has vibrations of higher frequencies. For example, the vibration with ν_{us}= 15 Hz resulted in more defects in the weld and made the joining process to be unstable. From the other side, vibration with ν_{us}= 66 Hz allowed to enhance the weld quality. Varying of the vibration amplitude D_{us} in the range from 5 up to 100 μm showed that there was the optimal value of about 30 μm that allowed us to get the best weld characterized by the minimal inclination of the plot $N_l(S)$. The

conclusion that there are the optimal parameters of ultrasound vibration which allow producing the better weld quality is also in good qualitative agreement with the results of 2D simulations [9].

5 CONCLUSIONS

A 3D model of friction stir welding based on movable cellular automaton method is presented. The obtained simulation results allow us to draw the following conclusions.

- The optimal ratio of the longitudinal velocity to the rotational speed allows transporting of the welded material around the pin several times and producing the joint of good quality.
- Using the pins of simple shape (cylinder, cone, pyramid) without a shoulder results in small scattered displacements of the plasticised material in the workpiece thickness direction.
- Applying additional ultrasonic vibration to the pin may lead to better mixing of the plasticized material behind the pin.

6 ACKNOWLEDGMENTS

The investigation has been carried out at financial support of the grant No. 17-11-01232 of the Russian Science Foundation.

REFERENCES

[1] W.M. Thomas, E.D. Nicolas, J.C. Needham, M.G. Murch, P. Templesmith, C.J. Dawes, “Improvements to Friction Welding” GB Patent Application No.9125978.8, December (1991).

[2] V.A. Frolov, A.N. Ivanyukhin, A.N. Sabantsev, et al., “Friction stir welding – pluses and minuses”, *Welding International* **24**(5), 358–365 (2010).

[3] E.V. Sergeeva, “Friction stir welding in aerospace industry”, *The Paton Welding Journal* **5**, 56–60 (2013).

[4] W.M. Thomas and E.D. Nicholas, “Friction stir welding for the transportation industries”, *Materials & Design* 18(4–6), 269–273 (1997).

[5] E.V. Shilko, S.G. Psakhie, S. Schmauder, V.L. Popov, S.V. Astafurov, A.Yu. Smolin, “Overcoming the limitations of distinct element method for multiscale modeling of materials with multimodal internal structure”, *Computational Materials Science* **102**, 267–285 (2015).

[6] A.Yu. Smolin, Ig.S. Konovalenko, S.G. Psakhie “Identification of elastic waves generated in the contact zone of a friction couple”, *Technical Physics Letters* **33**(7), 600-603 (2007).

[7] A.Yu. Smolin, N.V. Roman, Ig.S. Konovalenko, G.M. Eremina, S.P. Buyakova, S.G. Psakhie, “3D Simulation of Dependence of Mechanical Properties of Porous ceramics On Porosity”, *Engineering Fracture Mechanics* **130**, 53–64 (2014).

[8] A.Yu. Smolin, E.V. Shilko, S.V. Astafurov, I.S. Konovalenko, S.P. Buyakova, S.G. Psakhie, “Modeling Mechanical Behaviors of Composites With Various Ratios of Matrix-Inclusion Properties Using Movable Cellular Automaton Method”, *Defence Techonlogy* **11**, 18–34 (2015).

[9] S. Astafurov, E. Shilko, E. Kolubaev, S. Psakhie, “A theoretical study of the influence of technological friction stir welding parameters on weld structures” *AIP Conference Proceedings* **1683**, 020012 (2015);

V International Conference on Particle-based Methods – Fundamentals and Applications
PARTICLES 2017
P. Wriggers, M. Bischoff, E. Oñate, D.R.J. Owen, & T. Zohdi (Eds)

NUMERICAL AND EXPERIMENTAL STUDY OF THE POWDER BED CHARACTERISTICS IN THE RECOATED BED OF THE ADDITIVE MANUFACTURING PROCESS

DANIEL S. NASATO[1], MARTIN HEINL[2], TINO HAUSOTTE[2] AND THORSTEN PÖSCHEL[1]

[1]Institute for Multiscale Simulation, Friedrich-Alexander University
Nägelsbachstrasse 49a, 91052 Erlangen, Germany
email: thorsten.poeschel@eam.uni-erlangen.de, web page: www.mss.cbi.fau.de

[2]Institute of Manufacturing Metrology, Friedrich-Alexander University
Nägelsbachstrasse 25, 91052 Erlangen, Germany
email: fmt@fau.de, web page: www.fmt.uni-erlangen.de

Key words: Granular Materials, DEM, Additive Manufacturing, Surface Roughness, Numerical simulation.

Abstract. Part of the optimization steps for additive manufacturing is related to the correct understanding of the mechanical behavior of the powder used in the process. Obtain this understanding based purely on experiments might be a difficult and sometimes prohibitive task. A particle-based numerical tool can provide critical information for correct understanding of powder deposition process. Numerical simulations through the Discrete Element Method (DEM) provide a useful mean to investigate the additive manufacturing process, given the possibility to study particle-scale information that are difficult to access experimentally.

The characteristics of the recoated powder bed are investigated in the packed bed region and onto the manufactured part using PA12 commercial powder. Particle size distribution, contact and non-contact cohesive forces are incorporated in the numerical model. Furthermore, the non-spherical shape of real particles is taken explicitly into account in numerical simulations. A blade-type recoating system is used to form the powder bed and its roughness is calculated.

Experimental measurements are performed by fringe projection. Several areas of the recoated powder layers can be scanned with this optical measurement method. Thus, the analyzed surface roughness can be compared with the simulated quantities to validate the numerical model.

The sintered part is modelled as a prescribed rigid static region in the simulated system. The powder recoated in the sintered region may have different characteristics (packing, roughness) compared to the powder bed region. Recoating process is modelled using two different shapes for the sintered region. The amount of material recoated and the surface roughness are then calculated for the powder bed as well as for the sintered region.

1 INTRODUCTION

Additive manufacturing (AM) is a technique where parts of nearly arbitrarily complex

geometries can be built directly from a three-dimensional (CAD) model by selectively melting layers of powder particles [1]. This has become more and more important for many industrial sectors in the last years and an increasing demand to widen the field of application is noticeable. However, there are still restrictions, e.g. processing speed and product quality, in beam-based additive manufacturing processes like selective laser sintering (SLS) [2].

In particular, understanding the mechanical behavior of the powder particles during the manufacturing process is essential for developing optimization routes towards improved part quality and shorter production time [3].

Discrete Element Method (DEM) describes the trajectory of each individual particle in the system along the time by means of integration of Newton's equation of motion. Useful information to improve part quality and reduce production time can be obtained through numerical simulations using DEM, as particle dynamics are modeled as a function of material properties and particle shape [1,4,5,6]. By choosing the correct collision parameters, particle size and particle shape, the real granular behavior is captured [8,10,11,12].

In this study, a recoating blade is used to spread a layer of particulate PA 12 material over the surface to be sintered. The quality of this layer of powder is investigated through numerical simulations by calculating the surface roughness of the deposited powder in the powder bed and in the sintered region for a recoating speed of 100 mm/s. Experimental measurements of roughness (Rq values) were carried through the fringe projection measuring method after recoating a layer of PA12 polymeric powder and the results were compared to numerical simulations.

The sintered region is of interest and investigated in a limited way. First few layers in the additive manufacturing process are specially affected by the irregular amount of material deposited due to the shrinking of the powder after the melting process. The sintering process is not explicitly simulated in DEM, but its geometry is prescribed using two different shapes. Roughness is calculated in these regions through numerical simulations.

2 METHODOLOGY

2.1. Particle model

Powder deposition process was simulated using the Discrete Element Method (DEM). Real shapes of commercially available PA12 [15] powder were approximated using a clump representation of the particles in the DEM simulations [3,16,17]. In addition, the DEM library LIGGGHTS® [18] was extended to consider bonded and nonbonded attractive particle interaction forces.

Images of commercially available PA12 [15] powder were used as a base to recreate an approximated real particle shape. Sphere are glued together forming a clump of spheres, spatially distributed to capture most of the real shape details. Center of mass and moment of inertia are calculated by means of a Monte Carlo integration, where many points (in the order of 10^6 points) are sampled on an equivalent sphere and points are located inside/outside the composing spheres (contained inside the equivalent sphere), making possible to detect overlapped regions and avoid including these regions twice in the calculations.

To represent the shapes of the sample, 10 different images or real particles [14,15] were used to obtain clumps used in the numerical simulations. Images of the particles and their corresponding DEM model are demonstrated in Figure 1. All templates were equally used

(10% in mass of each template).

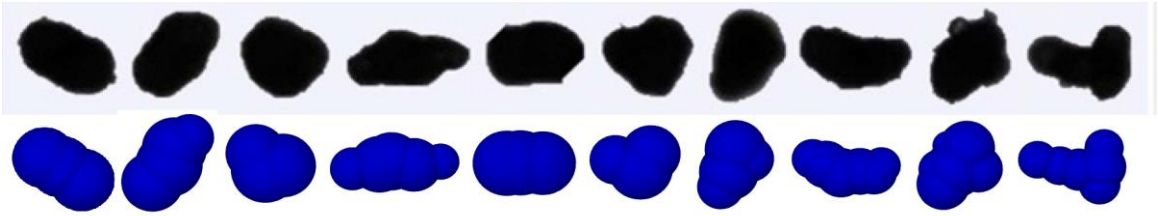

Figure 1 - Images of PA 12 particle templates used in numerical simulations. Top: Images of isolated PA 12 particles obtained through SEM [19]. Bottom: DEM representation of real particles by means of clumps.

Particle size distribution was experimentally measured for PA12 powder in [14]. Based on the experimental cumulative (Q3) distribution 5 different particles sizes were used in the numerical simulations as demonstrated in Figure 2. This size distribution was applied to each of the 10 particle templates shown in Figure 1.

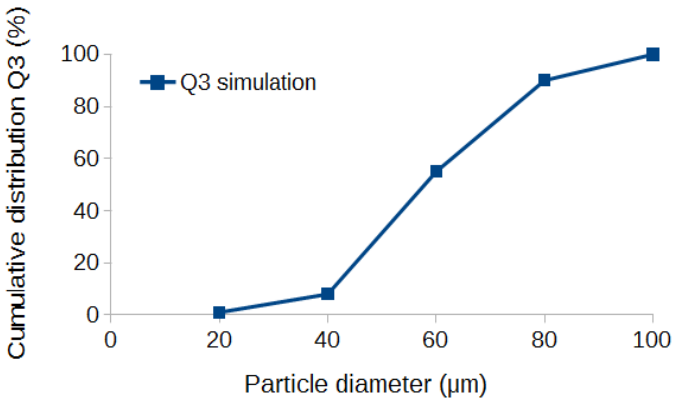

Figure 2- Cumulative distribution (Q3) of particle size adopted in the DEM simulations.

2.2. Inter particle force models

Normal and tangential forces during collision between particles are calculated. A viscoelastic interaction is assumed in the normal direction [20] and a modified Cundall-Strack [21] model is selected for computing the tangential component of the contact force [14]. The normal and tangential terms are given by:

$$\vec{F}_n = min\left(0, -\rho\xi^{\frac{3}{2}} - \frac{3}{2}A_n\rho\sqrt{\xi}\dot{\xi}\right)\vec{e}_n \tag{1}$$

$$\vec{F}_t = -min\left[\begin{array}{c}\mu|\vec{F}_n|, \\ \int_{path}\frac{4G}{2-\nu}\sqrt{R_{eff}\xi}d + A_t\sqrt{R_{eff}\xi}v_t\end{array}\right]\vec{e}_t \tag{2}$$

$$\xi = R_1 + R_2 - |\vec{r}_1 - \vec{r}_2| \tag{3}$$

ξ is the overlap of colliding particles, R_1 and R_2 are the radii of the particles, and $\vec{r}_1$ and $\vec{r}_2$ are their positions. $\vec{e}_n \equiv (\vec{r}_1 - \vec{r}_2)/|\vec{r}_1 - \vec{r}_2|$ is the normal unit vector. The elastic parameter ρ is a function of the effective radius $R_{eff} \equiv R_1 R_2/(R_1 + R_2)$, the Young's modulus Y, and the Poisson's ratio ν, in the form:

$$\rho \equiv \frac{2Y}{3(1-\nu^2)}\sqrt{R_{eff}} \tag{4}$$

The dissipative parameter A_n, depends on the material viscosity [20].

An additional term given by JKR equation is incorporated to the normal viscoelastic model to consider the attractive forces between particles in contact. This term adds an extra normal force in the opposite direction of the elastic force and is given by:

$$\vec{F}_{JKR} = 4\sqrt{\frac{\pi a^3 \gamma Y}{2(1-\nu^2)}}\vec{e}_n \tag{5}$$

where γ is the surface energy density and a is the contact radius related to the overlap in the form:

$$\xi = \frac{a^2}{R_{eff}} - \sqrt{\frac{8(1-\nu^2)\pi a \gamma}{Y}} \tag{6}$$

Due to the relatively small particle size non-contact van der Walls cohesive forces also have a significant influence in the flowability of the particulate material. These forces are incorporated in the DEM model in the following form:

$$\vec{F}_{vdW} = \begin{cases} [4\pi\gamma R_{eff}]\overrightarrow{e_n}, & if \quad \xi > 0 \\ \dfrac{[4\pi\gamma R_{eff}]D_{min}^2}{(\xi - D_{min})^2}\overrightarrow{e_n}, & if \quad -D_{max} \le \xi \le 0 \\ 0, & if \quad \xi < -D_{max} \end{cases} \tag{7}$$

where $Dmin = 1.65$ Å is a parameter introduced to avoid the singularity of the Hamaker equation, and $Dmax = 1$ μm is the maximal (cutoff) distance of the van-der-Waals interaction [14]. The intensity of this interaction is characterized by the Hamaker constant A_H, which is given by [14]:

$$A_H = 24\pi D_{min}^2 \gamma \tag{8}$$

The importance of JKR and van der Waals terms in the numerical model was addressed in previous studies when comparing experimental and numerical solid packing fraction [6]. Parameters used for the contact and non-contact force models for PA12 particles in the DEM simulations are depicted in Table 1. Sintered region is fixed - no motion is calculated, but collisions are computed normally.

To validate the inter-particle force model, Ref. [6] compared experimental results for the solid fraction of fine polydisperse powders covering a broad range of particle sizes applied in additive manufacturing. As presented in Ref. [6], predictions from simulations agreed quantitatively very well with the experiments.

Table 1 - Parameters used in contact and cohesion models in the numerical simulations.

Parameter	Symbol	Value
Particle material density	φ	1000 kg/m^3
Young's modulus	Y	2.3x10^7 Pa
Poisson's ratio	ν	0.40
Coulomb's friction coeff.	μ	0.50
Surface energy density	γ	0.1 mJ/m^2
Hamaker constant	A_H	0.2x10^{-21} J

2.3. Recoating process

The simulated system consists of a blade with length of 3 mm. The system has a width (y-direction) of 1mm and periodic boundary conditions are applied in this same direction. The length of the simulation domain is 10 mm (x-direction). The recoating blade was modelled based on the real geometrical characteristics. Only the region which is responsible for the recoating was used to reduce the computational time. Material is initially poured into a reservoir, which is then lifted and the blade spread the particles over the particle bed and the sintered region. The system is demonstrated in Figure 3.

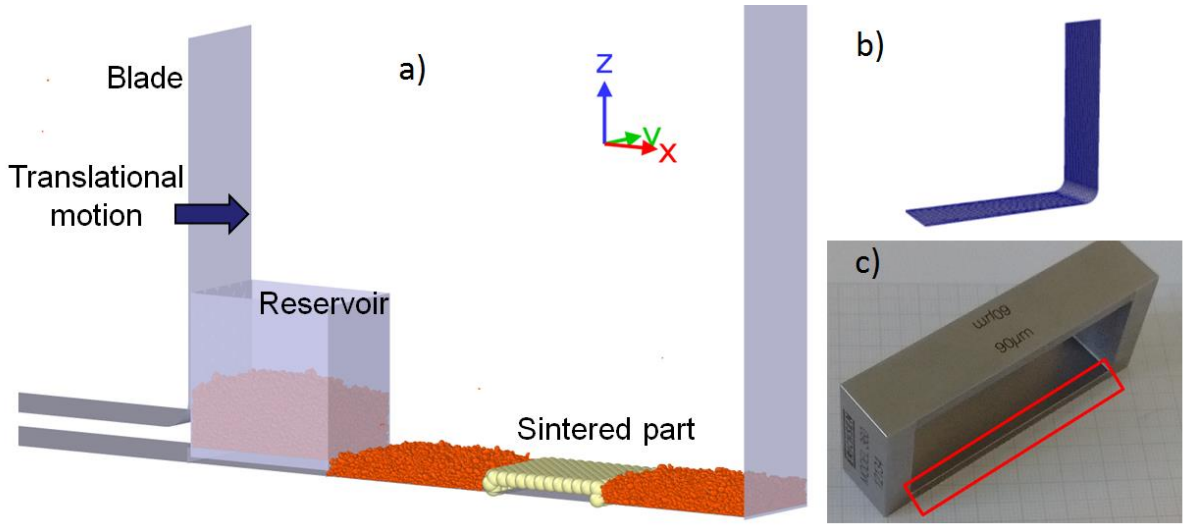

Figure 3 - Simulation domain with indications of the components. a) Translational motion of 100 mm/s is applied to the blade. Particles are recoated over the powder bed and sintered regions. b) details of the recoating blade used in simulations. c) recoating blade used in experiments. In red the region that effectively deposit the layer of material - region modelled in the numerical simulations.

Two different geometries for the sintered part were used, one consisting of a flat shape sintered region, as depicted in Figure 3, and another region of same size but with a concave shape, which can be seen in details in Figure 5.

Roughness was calculated for each of the simulated cases. The mean height of the particles was obtained in the powder bed and in the sintered region and the standard deviation from this mean is the roughness value (Rq) calculated from simulations. This procedure was repeated for three slices in the Y direction to obtain the mean roughness (Rq) and its standard

deviation.

2.4. Experimental procedure

The evaluation of the simulated roughness values has been proved by a surface measurement of several single layers of PA12 powder. The recoating blade dispenses the powder with a thickness of 120 µm and a recoating speed of 100 mm/s. As it is shown in Figure 4 the surface measurement is done by a projection of a planar, periodical and equidistant structured pattern on the recoated layer.

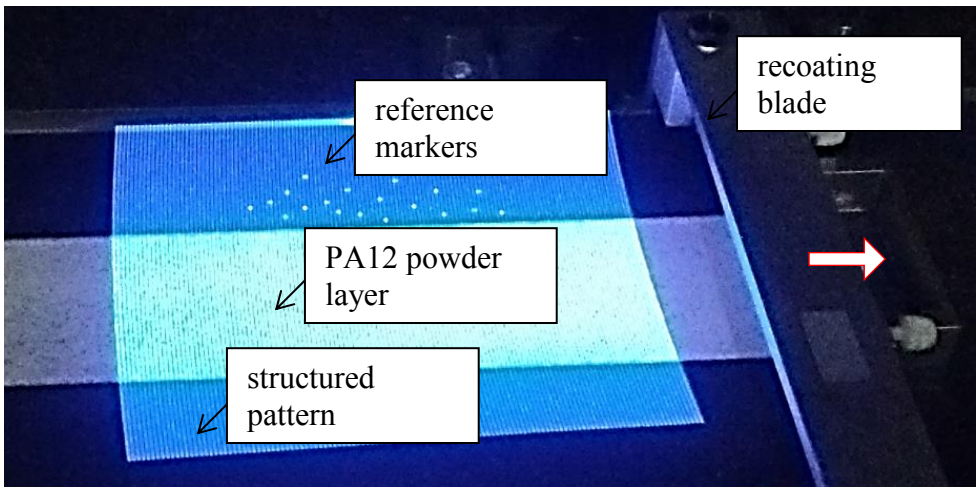

Figure 4 - Surface measurement of the recoated powder by fringe projection

The fringe projection measuring method is implemented by an optical ATOS Compact Scan 2M sensor, which is based on the principle of triangulation. At this point the powder layer is detected with two angled cameras from different observation directions to detect each surface point [22]. In addition, reference points are necessary for the optical observation to match the translational location of the powder in relation to the global coordinate system. The following surface studies are analyzed by TalyMap Platinum software to calculate the profile (2-D-) and the areal (3-D-)roughness parameters.

3 RESULTS

Experimental measurements were performed 3 times and the average values are shown with their respective standard deviation in Table 2. For validation purposes, roughness data calculated through numerical simulations are compared to Rq values. Details of the equations used to obtain the data points are shown in the Appendix.

Numerical results for both flat and concave sintered cases can be seen in Figure 5. A lateral snapshot of both cases is shown for comparison purposes. Differences mainly in the sintered region can be seen and will be quantified in more details. The powder bed region and sintered region considered for the roughness measurements are highlighted.

Table 2 – Experimental measurements of surface roughness and their respective standard deviation (σ). Values are in µm.

	Sa	Ra	Sq	Rq	Sz	Rz
Mean Value	16,00	8,10	20,10	10,20	267,70	45,60
Standard deviation (σ)	4,90	1,80	5,90	2,60	93,30	13,60

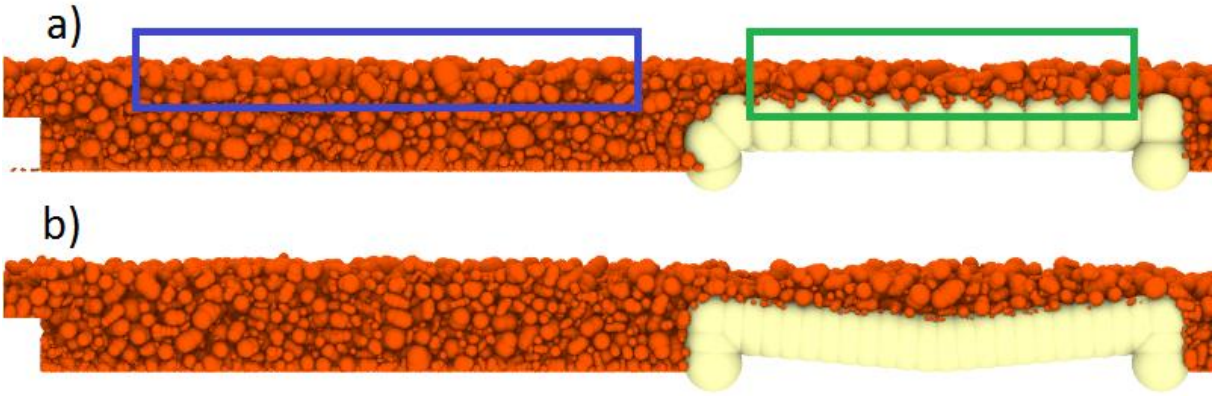

Figure 5 – Recoated powder layer for a) flat sintered region and b) concave sintered region. In blue is the region considered as powder bed region and in green the sintered region used for roughness measurements.

When comparing only the amount of material deposited over the sintered region, an increase of 34% in mass was found from the flat to the concave region (See Figure 6). Such differences in the amount of mass lead to density gradients of the final manufactured part.

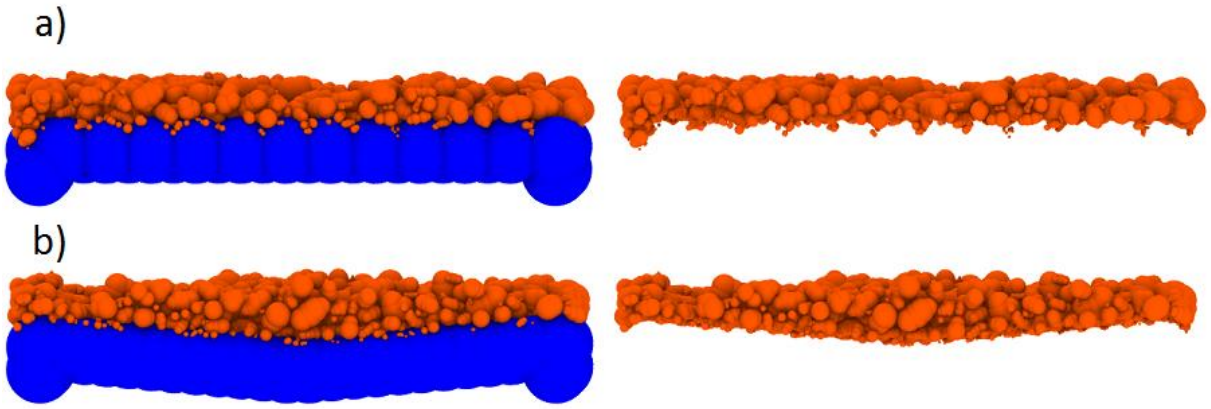

Figure 6 – Details of recoated powder layer for a) flat sintered region and b) concave sintered region. In the right-hand side one can visualize differences in the amount of material deposited for each case.

Surface roughness calculated for both (flat and concave) cases are shown in Table 3. A good agreement between numerical and experimental results was found when comparing the values of the powder bed – deviation of 8.1% for the flat sintered case and 2.7% for the concave sintered case, but still within the standard deviation of the experimental

measurements.

Roughness values for sintered region are relatively higher than those for the powder bed. An increase of 18.7% for the flat shape and 30.9% for the concave shape sintered region compared to their respective bed roughness. This can be attributed to the fact that in the powder bed region particles can penetrate the powder bed and re-accommodate. Also the way forces propagate in a granular or solid region are expected to be different [14]. We also noticed an increase of 16.8% when comparing the roughness of flat with the concave shape sintered.

Table 3 – Numerical results of roughness (Rq) for powder bed and sintered regions and their respective standard deviation (σ). Values are in μm. Results are for flat and concave cases.

Shape	Region	Rq	σ	Rq Experiment	σ
Flat shape sintered	Powder bed	9,37	0,39	10,2	2,6
	Sintered	11,12	1,8		
Concave shape sintered	Powder bed	9,92	0,65		
	Sintered	12,99	1,39		

4 CONCLUSION

A realistic model to simulate the additive manufacturing process using commercially available PA 12 polymeric powder was developed. Bonded and non-bonded cohesive forces were implemented for PA 12 powder, as well as realistic particle shape and particle size distribution. The sintered region was taken explicitly into account in our numerical simulations. Two different shapes for this region were used – one consisting of a flat shape and the other concave shape.

Experimental measurements using fringe projection technique could capture the surface roughness of recoated PA 12. A very good agreement was found from numerical and experimental results when comparing Rq values. Deviations of 8.1% for the flat sintered case and 2.7% for the concave sintered case were found, but still within the standard deviation of the experimental measurements.

The importance of considering the sintered region and its correct shape was also highlighted. Significant increase in roughness (up to 30.9% for concave shape case) was found when comparing to the roughness of the powder bed region. Furthermore, a significant increase (34%) in the mass deposited over the sintered region was also noticed comparing the flat to the concave sintered region. This consolidates the importance of the sintered region, which may lead to gradients in the density of the manufactured part affecting its quality. This is of importance in the initial layers of the manufacturing process, where the differences in the amount of mass recoated in each layer are larger. Sintered region should be explicitly resolved by melting the particles in the recoated layer to obtain a physically correct shape of the sintered region in a more detailed study.

APPENDIX

Table 4 - Definition of roughness parameters.

description	***2-D-roughness parameter (DIN EN ISO 4287)*[23]**	***3-D-roughness parameter (DIN EN ISO 25178-2)* [24]**
arithmetic average roughness	$R_a = \frac{1}{lc}\int \lvert z(x)\rvert dx$	$S_a = \frac{1}{A}\iint \lvert z(x,y)\rvert dxdy$
quadratic average roughness	$R_q = \sqrt{\frac{1}{lc}\int z^2(x)dx}$	$S_q = \sqrt{\frac{1}{A}\iint z^2(x,y)dxdy}$
maximum height roughness	$R_z = z_{max}(x) + z_{min}(x)$	$S_z = z_{max}(x,y) + z_{min}(x,y)$

l_c: measurement length A: measurement surface area $z(x,y)$: height profile

ACKOWLEDGMENTS

The authors want to thank the German Research Foundation (DFG) for funding the Collaborative Research Center 814 (CRC 814) – Additive Manufacturing, sub-projects B1, C4 and B6.

REFERENCES

[1] Campbell, R.I., Bourell, D. and Gibson, I. 2012, 'Additive manufacturing: rapid prototyping comes of age', Rapid Prototyping Journal, 18 (4), pp. 255 – 258.
[2] Schmidt, J., Sachs, M., Blümel, C., Winzer, B., Toni, F., Wirth, K.-E. and Peukert, W. 2014, 'A novel process route for the production of spherical LBM polymer powders with small size and good flowability', Powder Technology 261 pp. 78–86.
[3] Parteli, E.J.R. 2013, 'DEM simulation of particles of complex shapes using the multisphere method: Application for additive manufacturing'. AIP Conf. Proc. 1542, 185; doi: 10.1063/1.4811898.
[4] Zhang, H. P. and Makse, H. A. 2005, 'Jamming transition in emulsions and granular materials'. Phys. Rev. E 72, 011301.
[5] Pöschel, T. and Schwager, T. 2005, Computational Granular Dynamics, Springer, Heidelberg, 322 pp.
[6] Parteli, E.J.R., Schmidt, J., Blümel, C., Wirth, K.-E., Peukert, W. and Pöschel, T. 2014, 'Attractive particle interaction forces and packing density of fine glass powders', Scientific Reports 4: 6227; doi: 10.1038/srep06227.
[7] Zhu, H.P., Zhou, Z.Y., Yang, R.Y. and Yu, A.B. 2007, 'Discrete particle simulation of particulate systems: Theoretical developments', Chemical Enginnering Science 62, pp. 3378-3396.
[8] Paulick, M., Morgeneyer, M. and Kwade, A. 2015, 'Review on the influence of elastic properties on DEM simulation results', Powder Technology 283, pp. 66-76.
[9] Zhu, H.P., Zhou, Z.Y., Yang, R.Y. and Yu, A.B. 2008, 'Discrete particle simulation of particulate systems: A review of major applications and findings'. Chemical Engineering Science 63, pp. 5728-5770.
[10] Alenzi, A., Marinack, M., Higgs, C.F. and McCarthy, J.J. 2013, 'DEM validation using an annular shear cell', Powder Technology 248, pp. 131-142.
[11] Grima, A.P. and Wypych, P.W. 2011, 'Investigation into calibration of discrete element model parameters for scale-up and validation of particle-structure interactions under impact conditions', Powder Technology 212, pp. 198-209.
[12] Bierwisch, C., Kraft, T., Riedel, H. and Moseler, M. 2009, 'Three-simensional discrete element models for the granular statics and dynamics of powders in cavity filling', Journal of the Mechanics and Physics of Solids 57, pp.10-31.
[13] Goodridge, R.D., Tuck, C.J. and Hague, R.J.M. 2012, 'Laser sintering of polyamides and other polymers', Prog. Mater. Sci. 57 pp. 229–267.
[14] Parteli, E.J.R. and Pöschel, T. 2016, 'Particle-based simulation of powder application in additive manufacturing', Powder Technology 288 pp. 96–102.
[15] Rietzel, D., Kühnlein, D., Drummer, D. 2011, 'Selektives Lasersintern von teilkristallinen Thermoplasten', RTejournal Forum Rapid Technol. 6 (urn:nbn:de:0009–2–31138).
[16] Pei, C., Wu, C.-Y. and Adams, M. 2015, 'Numerical analysis of contact electrification of non-spherical particles in a rotating drum', Powder Technology 285 pp. 110-122.
[17] Taghavi, R. 2011, 'Automatic clump generation based on mid-surface', Proceedings of Continuum and Distinct Element Numerical Modeling in Geomechanics, Vol. 1, Melbourne, Australia.

[18] Kloss, C., Goniva, C., Hager, A., Amberger, S. and Pirker, S. 2012, 'Models, algorithms and validation for opensource DEM and CFD-DEM', Prog. Comput. Fluid Dy. 12, pp. 140–152.
[19] Rietzel D, Kühnlein F, Drummer D (2011). Selektives Lasersintern von teilkristallinen Thermoplasten. RTejournal Forum für Rapid Technologie, Vol. 6. (urn:nbn:de:0009231138)
[20] Brilliantov, N. V., Spahn, F., Hertzsch, J.-M. and Pöschel, T. 1996, 'A model for collision in granular gases', Phys. Rev. E 53 pp. 5382–5392.
[21] Cundall, P.A. and Strack, O.D.L. 1979, 'A discrete numerical model for granular assemblies', Geotechnique 29 pp. 47–65.
[22] DIN EN ISO 25178-6: 2010: Geometrical product specification (GPS) – Surface texture: Areal – Part 6: Classification of methods for measuring surface texture parameters. Beuth Verlag, 2010.
[23] CEN - European committee for standardization: DIN EN ISO 4287: 2009-11: 'Geometrical Product Specification (GPS) – Surface texture: Profile method – Terms, definitions and surface texture parameters'.
[24] CEN - European committee for standardization: DIN EN ISO 25178-2: 2012: 'Geometrical product specification (GPS) – Surface texture: Areal – Part 2: Terms, definitions and surface texture parameters'.

V International Conference on Particle-based Methods – Fundamentals and Applications
PARTICLES 2017
P. Wriggers, M. Bischoff, E. Oñate, D.R.J. Owen, & T. Zohdi (Eds)

NUMERICAL SIMULATION OF SOLIDIFICATION PHENOMENA OF MOLTEN DROPLET AT DIFFERENT IMPACT VELOCITY

S. KONDO[1], H. MAMORI[2], N. FUKUSHIMA[3], AND M. YAMAMOTO[2]

[1]Graduate School of Mechanical Engineering, Tokyo University of Science
6-3-1 Niijuku, Katsusika-ku, Tokyo, 125-8585, Japan
e-mail: 4516618@ed.tus.ac.jp

[2]Department of Mechanical Engineering, Tokyo University of Science
6-3-1 Niijuku, Katsusika-ku, Tokyo, 125-8585, Japan

[3]Department of Prime Mover Engineering, Tokai University
4-1-1 Kitakaname, Hiratsuka-shi, Kanagawa, 259-1292, Japan

Key words: Deposition phenomena, molten droplet, heat transfer, explicit-moving particle simulation

Abstract. Jet engines ingest sand and volcanic ash in the air and then the sand and ash reach a combustion chamber. Due to the high temperature of the chamber, sand and ash are melted and form the molten droplets. The molten droplets are rapidly cooled around the turbine blades and the end walls. The droplets are solidified and finally adhere on these surfaces. This deposition phenomenon causes many problems in the aircraft, e.g., deterioration of the turbine performance, disturbing the cooling flow of turbine blade, etc. To predict or prevent the deposition phenomenon, its mechanisms should be clarified. In the present study, we perform three-dimensional numerical simulations on deposition behavior of a single molten droplet on a cooled substrate. We compare the present numerical data and the experimental data in the previous study for validation and we observe effects of the drop velocity on the deposition phenomenon. As a numerical method, an explicit-moving particle simulation method is employed since the method is suitable for the large interface deformation system. The computational results show reasonable agreements with the experimental data, especially, at an early stage of the deposition. We confirm finger-like-structures which is a characteristic shape of the adhered droplet edge. As increasing of the initial droplet velocity, we found that the increase of the rebound particles.

1 INTRODUCTION

When jet engines are operated on volcanic ash clouds or sandy ground, sand or ash are ingested and melted in a high temperature combustion chamber. Because turbine components (e.g., blades, cooling flow orifices, end-walls, etc.) are colder than molten droplets, some droplets adhere and accrete on these surfaces. The deposition phenomenon does not only leads to deterioration of the turbine performance (e.g., blade performance and cooling effect [1]), but also increase the maintenance cost. Therefore, the prediction and understanding of the deposition phenomena are of importance from the engineering viewpoint. In previous studies,

for example, Webb et al. [2] made an experimental study for the coal ash deposition. They evaluated and quantified thickness sediments for four different ash types. They have shown that the chemical makeup of the ash also plays a crucial role in deposition formation and thickness. Although experiments in the research are conducted under some conditions, Computational Fluid Dynamics (CFD) makes it easier to apply various conditions.

Moreover, in the gas turbine, it is difficult to install some proves to measure the deposition phenomenon due to high temperature and pressure. Accordingly, we employ a numerical approach. As for a first step, in the present study, we focus on the deposition phenomenon of a single melted droplet on a flat surface. We can refer to a review about drop impact on a surface [3]. While engine components have a complex geometry and there are many melted droplets flowing in the gas turbine, the present simplified system (i.e., deposition of a single droplet on a flat surface) is expected to give us some physical insights of the deposition behavior.

The objectives of the present study are to simulate and investigate deposition behavior of a single melted droplet on a flat surface. Since a droplet has interfaces, which are largely deformed when it collides on the flat plate, we have employed an explicit moving particle method [4, 5] (referred to as the E-MPS method, hereafter). The E-MPS method is one of the Lagrangian methods. At first, we show comparisons between the present numerical results and the existing experimental data in the previous study [6] and discuss influences of the initial drop velocity on the deposition behavior.

2 CALCULATION METHOD

2.1 E-MPS METHOD

In the E-MPS method, the fluid motion is reproduced by computational particles. The fluid motion is governed by the continuity and Navier-Stokes equations, as

$$\frac{\partial \rho}{\partial t} = 0, \tag{1}$$

$$\frac{Du}{Dt} = -\frac{1}{\rho}\nabla P + \nu \nabla^2 u + g + \frac{1}{\rho}\sigma\kappa\delta n, \tag{2}$$

respectively. Here, u is velocity vector, ρ is density, P is pressure, ν is kinematic viscosity, g is acceleration of the gravity, σ is surface tension coefficient, κ is curvature, δ is the delta function, and n is the normal vector. For the spatial discretization of the governing equations, the following gradient and Laplacian models are employed as,

$$\nabla \phi = \frac{d}{n^0} \sum_{j \neq i} \frac{\phi_j - \phi_i}{\left|\mathbf{r}_{ij}\right|^2} \mathbf{r}_{ij} w_{ij}, \tag{3}$$

$$\nabla^2 \phi = \frac{2d}{\lambda n^0} \sum_{j \neq i} \left(\phi_j - \phi_i\right) w_{ij} . \tag{4}$$

Here, ϕ is physical quantity such as velocity, d is dimensional number of calculation, n^0 is the number of density of the particles, and w_{ij} is a weight function. The subscripts of i and j are indices of computational particles and $\mathbf{r}_{ij}$ is a distance vector between particles, indices of which are i and j. The coefficient λ is defined by Eq. (5).

$$\lambda = \frac{\sum_{j \neq i} \left| r_j - r_i \right|^2 w\left(\left| r_j - r_i \right| \right)}{\sum_{j \neq i} w\left(\left| r_j - r_i \right| \right)}, \tag{5}$$

where r_i is a coordinate vector of i th particle and w is a weight function for average. Since the droplet is solidified on a surface due to heat transfer, the energy equation, Eq. (6), is also solved in this simulation.

$$\frac{DT}{Dt} = \frac{k}{\rho C_P} \nabla^2 T + \frac{1}{\rho C_P} Q. \tag{6}$$

Here, T is temperature, C_p is specific heat, k is thermal conductivity, and Q is amount of heat generation. The Laplacian model (as shown in Eq. (4)) is also applied to Eq. (6) and the discretized energy equation is written by the following equation,

$$T_i^{n+1} = T_i^n + \frac{k_i}{\rho_i C p_i} \Delta t \frac{2d}{n\lambda} \sum_j (T_j^n - T_i^n), \tag{7}$$

when a target computational particle, index of which is i, is affected by surrounding either coagulated particles or melted particles, indices of which are j. Here, Δt is a size of time step and the superscript of n is time step. When a target computational particle, index of which is i, is affected by both surrounding coagulated particles and melted particles, indices of which are j, we apply the following discretized equations,

$$T_i^{n+1} = T_i^n + \frac{k_i}{\rho_i C_i} \Delta t \frac{2d}{n\lambda} \sum_j \frac{1}{2} (T_s^n - T_i^n), \tag{8}$$

$$T_s = \frac{\sqrt{\rho_i C_i k_i} T_i^n + \sqrt{\rho_j C_j k_j} T_j^n}{\sqrt{\rho_i C_i k_i} + \sqrt{\rho_j C_j k_j}}. \tag{9}$$

Here, T_s denotes the mean temperature between a target particle and a surrounding particle in the solid or liquid phase. The physical properties, ρ, C_p and k with the subscripts of i and j denotes the properties on i th and j th particles, respectively.

2.2 SOLIDIFICATION MODEL

The latent heat h_{ls} play an important role in a deposition phenomenon. Figure 1 explains our solidification model including the latent heat effects. The initial condition of a droplet is in a liquid phase. When the droplet temperature, T, reaches the melting temperature, $T_{melting}$, the liquid-computational particles are in a transient state with the constant temperature at $T_{melting}$. When the computational particles lose the latent heat, h_{ls}, the computational particles are treated as solid-phase particles. We define the liquid fraction, γ_m: γ_m=0 in a solid phase; $0<\gamma_m<1$ in a transient phase; $\gamma_m = 1$ in a liquid phase, as shown in Eq. (10).

$$\begin{array}{lll} Solid & when & \left(\quad T < T_{liquidus} \quad , \quad \gamma_m = 0 \quad \right) \\ Transient & when & \left(\quad T = T_{liquidus} \quad , \quad 0 < \gamma_m < 1 \quad \right) \\ Liquid & when & \left(\quad T > T_{liquidus} \quad , \quad \gamma_m = 1 \quad \right) \end{array} \tag{10}$$

$$\gamma_m^{n+1} = \gamma_m^n + \frac{\Delta h}{h_{ls}} \tag{11}$$

The time advancement of the liquid fraction, γ_m, is described in Eq. (11). Here, Δh denotes the enthalpy change between particles in a transient phase. Δh is calculated by the following heat conduction equation, Eq. (12) or Eq. (13)

$$\Delta h = \frac{\Delta t}{\rho_i} \frac{2d}{\lambda n_i} \sum_{j \neq i} \left\{ k_{ij} \left(T_j - T_i \right) w_{ij} \right\} \tag{12}$$

Equation (12) is applied when both particles i and j are not in the transient phase. The enthalpy change, Δh, between particles in different phases is computed by Eq. (13) using T_s defined in Eq. (9).

$$\Delta h = \frac{\Delta t}{\rho_i} \frac{2d}{\lambda n_i} \sum_{j \neq i} \frac{1}{2} \left\{ k_{ij} \left(T_s - T_i \right) w_{ij} \right\} \tag{13}$$

Mean thermal conductivity, k_{ij}, in Eqs. (12) and (13) is calculated from thermal conductivity of particles i and j in the following equations [7], Eq. (14) or Eq. (15).

$$k_{ij} = 2k_i k_j / \left(k_i + k_j \right) \tag{14}$$

$$k_{ij} = \begin{cases} k_j & when \quad \left(i : Transient \right) \\ k_i & when \quad \left(j : Transient \right) \end{cases} \tag{15}$$

When both particles i and j are not in the transient phase, we use Eq. (14) to calculate the mean thermal conductivity. Equation (15) indicates that, when particle i is in a transient phase, we use the thermal conductivity of particle j; when particle j is in a transient phase, we use the thermal conductivity of the particle i as k_{ij}.

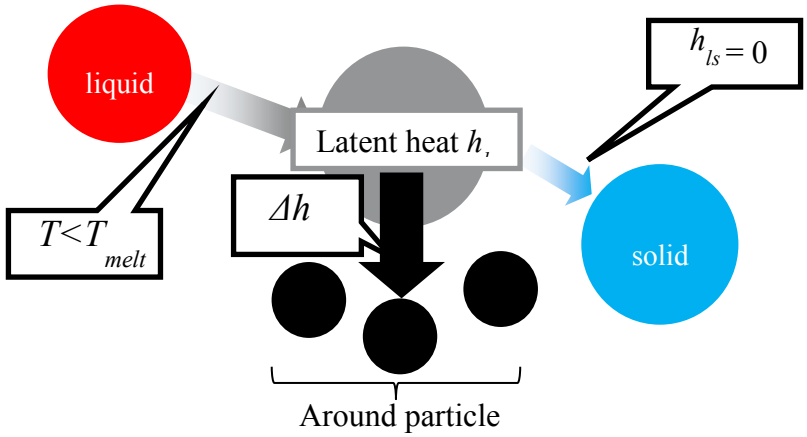

Figure 1 Schematics of a solidification model.

3 COMPUTATIONAL CONDITION

Figure 2 shows the initial condition of a droplet. A single molten droplet collides and adheres on a cooled flat plate. The numerical condition in the present study is set to be similar to the experiments conducted by Shakeri and Chandra [6]: the droplet consists of Sn; the collision angle of 90 degree; the initial diameter of the droplet D_0 is set to be 2.2 [mm]; the initial temperature of the droplet is 519 [K]; the substrate is made by stainless steel; the substrate temperature is kept constant at T_{wall} = 298 [K]. The simulations are conducted at three different collision velocities, v_0 = 10, 20 and 30 [m/s] to clarify effects of collision velocity. In addition, the simulation in the case of the collision velocity of 4.0 [m/s] is also performed to validate our simulation by comparison with the experimental data [6]. In Table 1, the physical properties of Sn are summarized. The droplet is represented by aggregation of computational particles. The number of computational particles is about 195,000. Initial state of all the computational particles is liquid. In the coagulation model, the latent heat is considered as described in section 2.2.

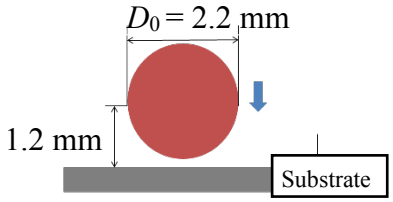

Figure 2 Initial condition of a single molten droplet.

Table 1 Physical properties of Sn.

Properties	Symbol		
Thermal conductivity	k_{liquid}	[W/mK]	33.6
	k_{solid}	[W/mK]	62.2
Specific heat	$C_{p\ liquid}$	[J/kgK]	244
	$C_{p\ solid}$	[J/kgK]	226
Density	ρ_{liquid}	[kg/m^3]	6,980
	ρ_{solid}	[kg/m^3]	7,200
Melting temperature of Sn	$T_{melting}$	[K]	505

4 RESULTS AND DISCUSSION

Figure 3 shows a time series of snapshots of a colliding and adhering molten Sn droplet when the collision angle is 90 degree. The time t begins when the droplet starts falling. The collision velocity is 4 m/s. The liquid, transient (i.e. liquid to solid), and solid particles are colored by red, white, and blue, respectively. We observed that the droplet collides, spreads, and coagulates on the surface of the substrate. The behavior reasonably agrees with the experimental results [6]. Furthermore, finger-like-structures, which are typical structures in the deposition, are observed at the circumference of the adhered droplet as shown in Fig. 3(l) (pointed out by the red circle).

Figure 4 shows a time series of snapshots of the droplet from the side view. We found the clearance between the edge of the droplet and the substrate. These characteristics are also observed in the experiment conducted by Tabbara et al. (2012) [8].

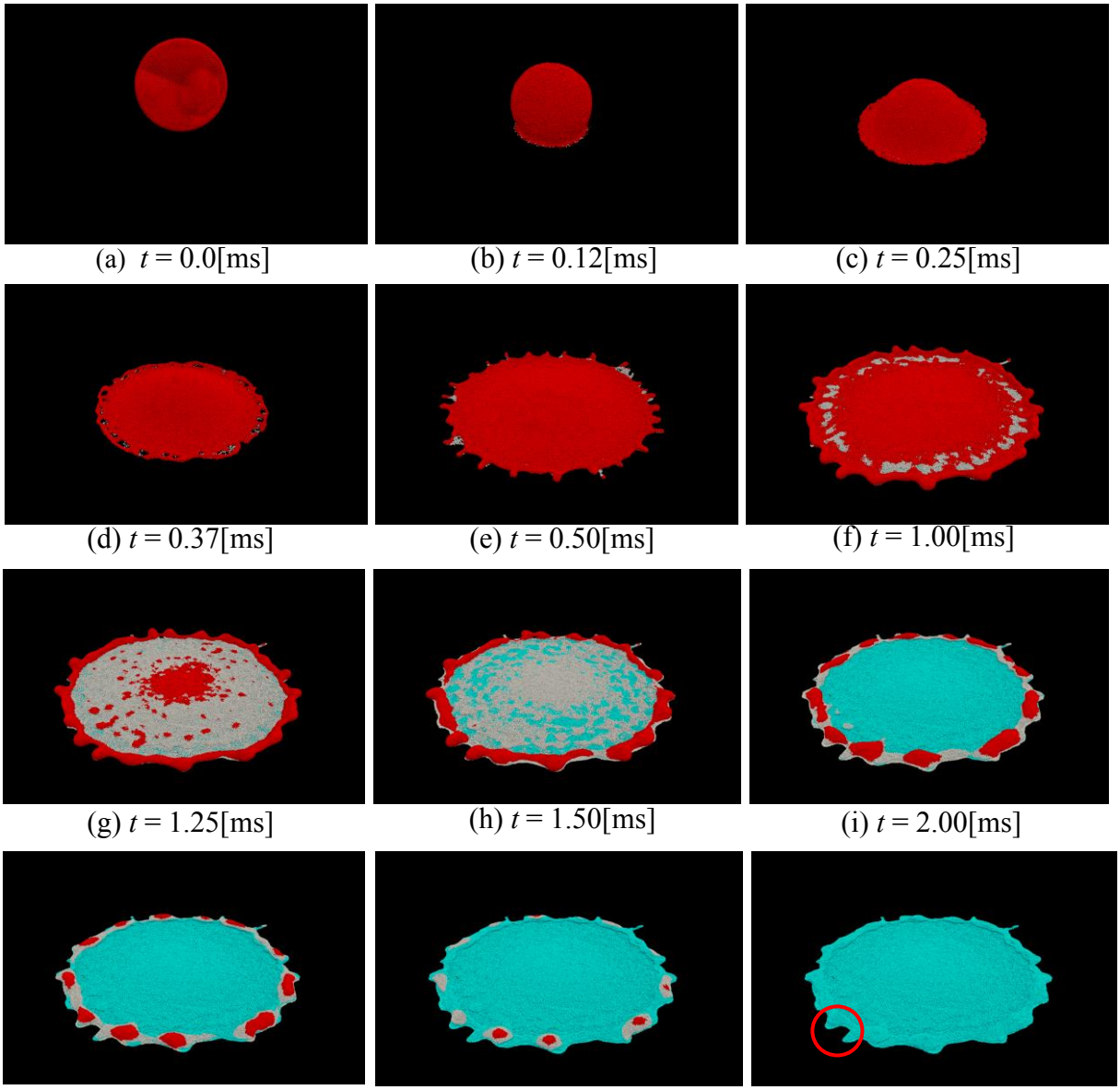

(a) t = 0.0[ms] (b) t = 0.12[ms] (c) t = 0.25[ms]

(d) t = 0.37[ms] (e) t = 0.50[ms] (f) t = 1.00[ms]

(g) t = 1.25[ms] (h) t = 1.50[ms] (i) t = 2.00[ms]

(j) t = 2.50[ms] (k) t = 3.50[ms] (l) t = 4.00[ms]

Figure 3 Time series of snapshots of the deposition of the Sn droplet in the case of the collision angle of 90 degree at the collision velocity of 4 m/s (bird's eye view).

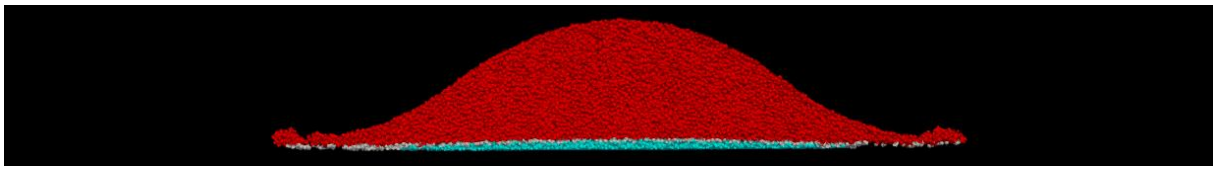

(a) t = 0.37[ms]

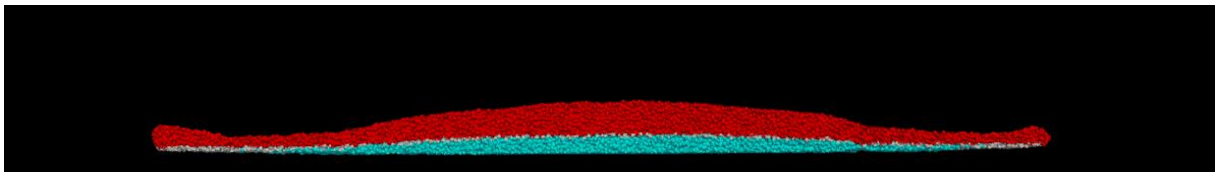

(b) t = 0.75[ms]

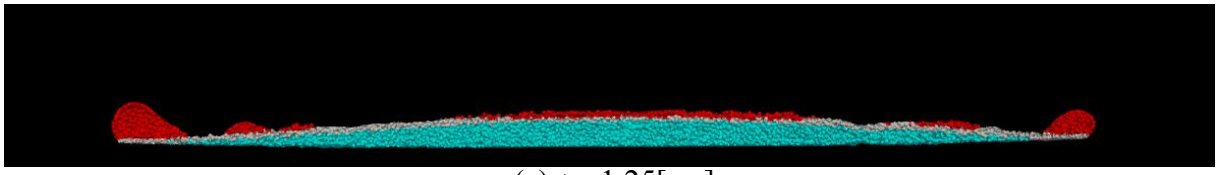

(c) t = 1.25[ms]

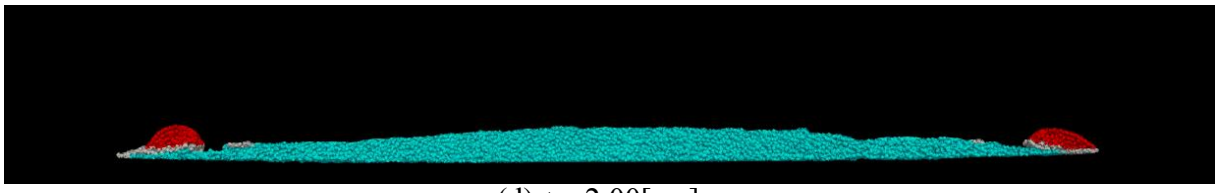

(d) t = 2.00[ms]

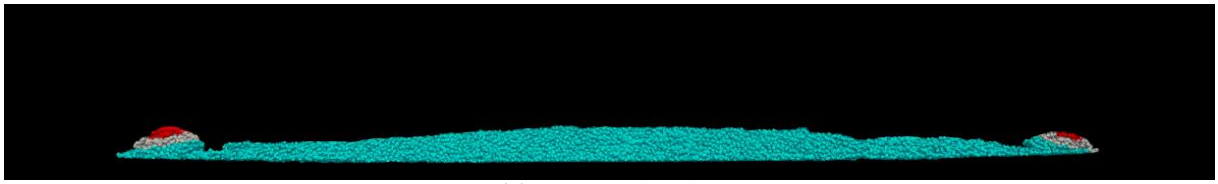

(e) t = 3.00[ms]

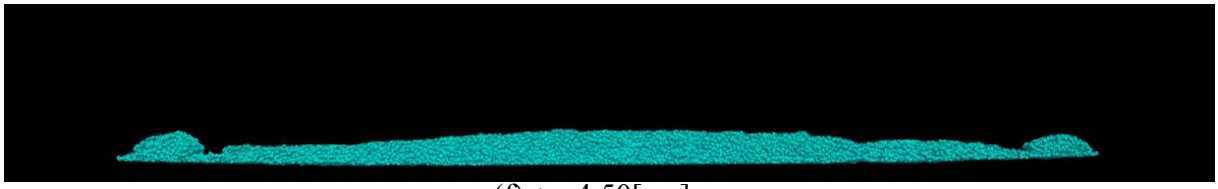

(f) t = 4.50[ms]

Figure 4 Time series of snapshots of the deposition of the Sn droplet in the case of the collision angle of 90 degree at the collision velocity of 4 m/s (side view).

Here, we evaluate a time variation of the droplet diameter spreading on the surface, quantitatively. Since the droplet has many fingers, there are some possible definitions of the diameter. Figure 5 describes the definition of the diameter D in the present study. We extract the finger which is closest to the x-axis and measure the x position of the top of the finger. The x-position is refereed to as the diameter of D. Although the strict maximum diameter of the droplet is the distance between the origin and the top of the nearest finger, the difference between D and the strict diameter is less than 2 % due to very small angle θ.

Figure 6 shows the time variation of the non-dimensional droplet diameter, D/D_0. D_0 is the initial diameter of the droplet, which is described in section 3. The dimensional time t begins when the droplet starts falling. At $t < 0.5$ [ms], the non-dimensional droplet diameter agrees with the experimental data [6]. In time advance, the non-dimensional diameter continues to increase at $t < 1.5$ [ms], then decreases slightly at 1.5 [ms] $< t < 2.5$ [ms], and reaches a steady state in both numerical and experimental results. The decrease of the diameter at 1.5 [ms] $< t < 2.5$ [ms] is due to the surface tension of the liquid phase of the droplet: the liquid runs off the finger, the surface tension suppresses to expand the diameter, and then the liquid comes back. Subsequently, the non-dimensional diameter reaches a steady state. We note that the resultant diameter is smaller than that of the experimental data [6]. Because the constant temperature is imposed as the boundary condition on the surface of the substrate in the present study, the solidification speed is faster and then the diameter in the transient and solid phase is smaller than the experimental results.

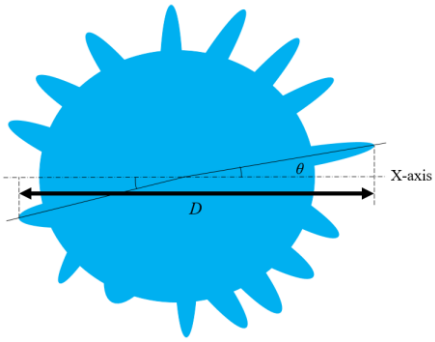

Figure 5 Definition of a diameter of an adhered droplet in the present study.

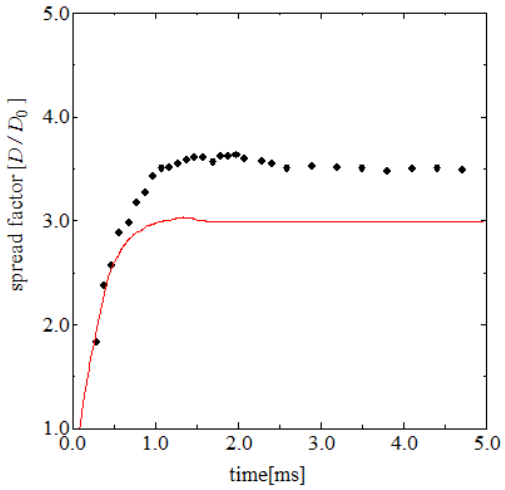

Figure 6 Time variation of non-dimensional droplet diameter: black line, the result in the present simulation at the collision velocity of 4 m/s; dot, the experimental data obtained by Shakeri et al. (2002) [6].

Figure 7 shows a times series of snapshots of coagulation behaviors of the Sn droplet in the cases of three different collision velocities, v_0 = 10, 20 and 30 [m/s]. The liquid, transient (i.e. liquid to solid), and solid particles are colored by red, white, and blue, respectively. As increase of the initial drop velocity, the number of splashing particles increases and finger-structures are not generated since many particles tend to rebound in the wall-normal direction.

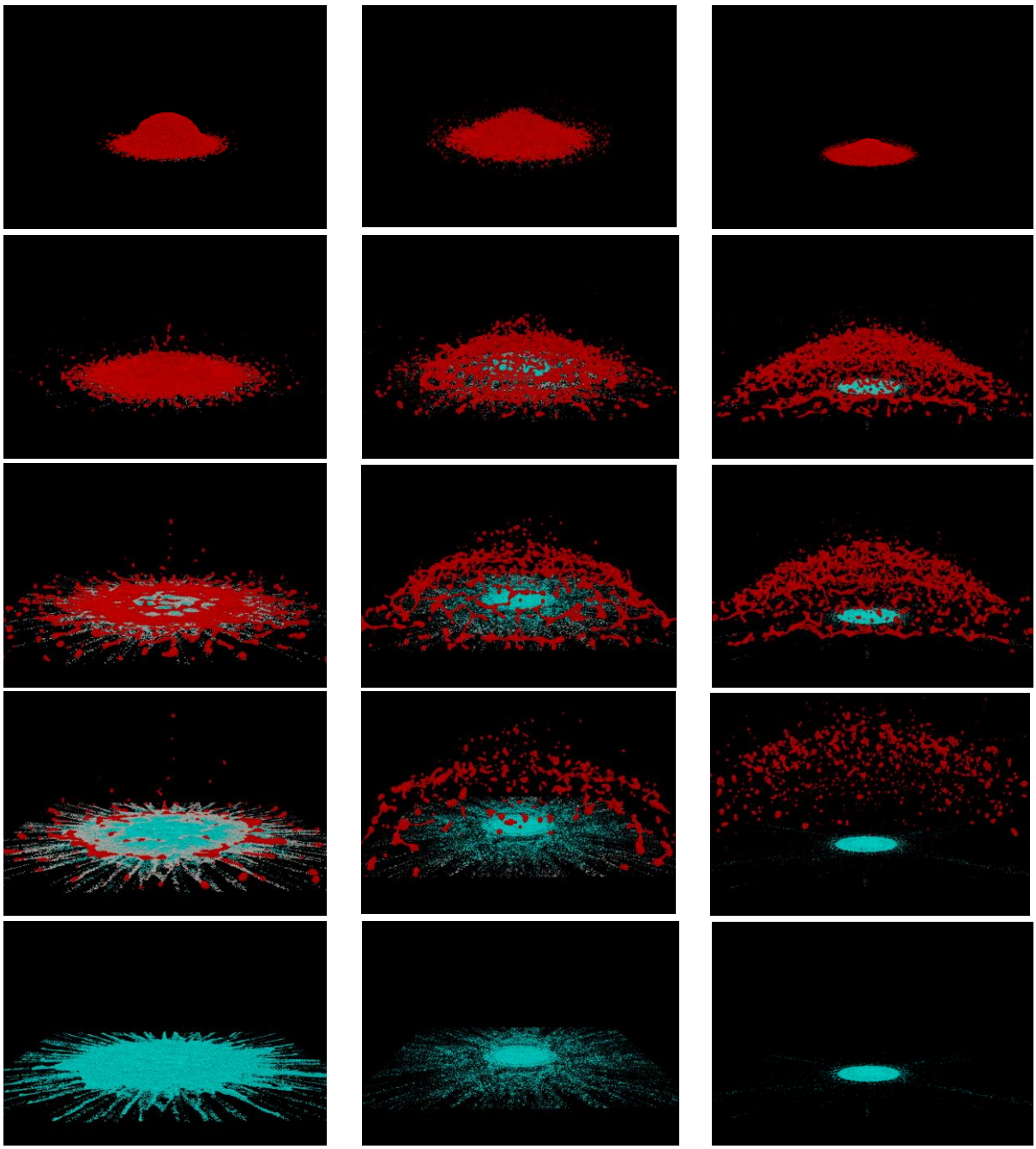

Figure 7 Time series of snapshots of deposition behavior of the Sn droplet for different initial velocities: left column, v_0=10 m/s; middle column, v_0=20 m/s; right column, v_0=30 m/s.

5 CONCLUSIONS

We perform numerical simulations on deposition phenomena of a single molten Sn droplet on a flat surface of the substrate in the cases of four different collision velocities by means of the E-MPS method. The latent heat is considered to reproduce the coagulation behaviors of the droplet. The results show that the simulation reproduces that the droplet collides, spreads, and coagulates on the substrate. The time variation of non-dimensional diameter obtained by the simulation shows the similar tendency to the existing experimental results. The quantitative difference between the numerical and experimental results is attributed to the difference of thermal boundary condition on the substrate surface. We also investigate effects of the impact velocity on behaviors of a colliding droplet. Finger-like-structures, which are a typical structure in the deposition, are observed at the circumference of the adhered droplet in cases of lower collision velocity, while finger-structures are not generated since many particles tend to rebound in cases of higher collision velocity.

REFERENCES

[1] S. Singh and D. K. Tafti, “Prediction of Sand Transport and Deposition in a Two-Pass Internal Cooling Duct”, ASME J. Engineer. Gas Turbines Power, 138, (2016), pp.1-12.

[2] J. Webb et al., “Coal Ash Deposition on Nozzle Guide Vanes - Part I: Experimental Characteristics of Four Coal Ash Types”, J. Turbomach., 135 (2013), 021033, pp.1-9.

[3] C. Josserand et al., “Drop Impact on a Solid Surface” Annu. Rev. Fluid Mech., 48 (2016), pp. 365-391.

[4] M. Oochi et al., “Explicit MPS Algorithm for Free Surface Flow Analysis”, Trans. Jpn. Soc. Comput. Eng. Sci., 20100013, (2010), 8 pp.

[5] R. Takahashi et al., “Development and Elaboration of Numerical Method for Simulating Gas-Liquid-Solid Three Phase Flows based on Particle Based Method.” Int. J. Comput. Fluid. Dyn., 30 (2016), pp. 120-128.

[6] S. Shakeri and S. Chandra, “Splashing of Molten Tin Droplets on a Rough Steel Surface”, Int. J. Heat Mass Transfer, 45, (2002), pp. 4561-4575.

[7] H. Ikeda, “Numerical Analysis of Fragmentation Processes in Vapor Explosions using Particle Method”, Doctoral Dissertation of the Tokyo University, (1999), pp. 63-69.

[8] H. Tabbara et al., “Modelling of Impingement Phenomena for Molten Metallic Droplets with Low to High Velocities”, Int. J. Heat Mass Transfer, 55 (2012), pp. 2081-2086.

V International Conference on Particle-based Methods – Fundamentals and Applications
PARTICLES 2017
P. Wriggers, M. Bischoff, E. Oñate, D.R.J. Owen & T. Zohdi (Eds)

PROCESS SIMULATION OF DEEP PENETRATION LASER WELDING BY COUPLING A SMOOTHED PARTICLE HYDRODYNAMICS MODEL WITH A RAY-TRACING SCHEME

Haoyue Hu[1], Florian Fetzer[2], Peter Berger[2] and Peter Eberhard[1]

[1]Institute of Engineering and Computational Mechanics, University of Stuttgart,
Pfaffenwaldring 9, 70569 Stuttgart, Germany
[haoyue.hu, peter.eberhard]@itm.uni-stuttgart.de
http://www.itm.uni-stuttgart.de/

[2]Institut für Strahlwerkzeuge, University of Stuttgart,
Pfaffenwaldring 43, 70569 Stuttgart, Germany
[florian.fetzer, peter.berger]@ifsw.uni-stuttgart.de
http://www.ifsw.uni-stuttgart.de/

Key words: Smoothed Particle Hydrodynamics (SPH), Deep Penetration Laser Welding, Heat Transfer, Phase Transition, Ray Tracing, Co-Simulation.

Abstract. Deep penetration laser welding is a preferred joining technique in industry due to high welding speeds and flexibility regarding material and geometry. In deep penetration laser welding, the high intensity of the laser irradiation causes a part of the material to evaporate instantaneously such that a vapor-filled capillary is formed within a few milliseconds. To simulate this laser welding process, the meshless Lagrangian Smoothed Particle Hydrodynamics (SPH) method is applied. For accurate modeling of the laser-material interaction, the SPH simulation is coupled with a ray-tracing scheme. Using this co-simulation technique, the geometry of the capillary is tracked throughout the welding simulation to gain additional insights.

The developed model is able to capture the characteristics of the welding process independently from material and process parameters. An advantage of the simulations compared to experiments is that further values like the absorbed power or intensity distribution at the surface of the material can be continuously obtained. Moreover, the SPH model provides a good estimation for the dimensions of the weld pool. This is demonstrated by means of welding examples with an oscillating laser beam. Therefore, SPH in combination with a ray-tracing scheme is a suitable method for the process simulation of deep penetration laser welding and a valuable tool for finding optimal process parameters, e.g. optimal trajectories for the laser beam to affect the resulting weld to a desired shape.

1 INTRODUCTION

Nowadays laser welding is universally applied for joining tasks in industry. The popularity of laser welding results from its flexibility regarding geometry and material properties, high degree of automation, high welding speeds and narrow heat-affected zones. Weld defects such as pores, spatter, and humping may, however, still occur. Improving the weld quality by reducing weld defects and increasing the process efficiency remain two crucial tasks subject to current research. Experimental data and simulation results complement one another in understanding all physical phenomena occurring during laser welding and in achieving welds with high quality in a more efficient manner.

During deep penetration laser welding, the high intensity of the laser beam leads to instantaneous evaporation of the material at the surface of the workpiece. A vapor-filled capillary is formed that moves with the laser beam through the workpiece. Due to multiple reflections of the laser beam at the capillary walls, the absorption behavior becomes very complex depending on the precise surface geometry.

An overview of different models for deep penetration laser welding is found in [1]. The models use different numerical methods to include main physical aspects during laser welding to a various level of complexity. The main aspects to be modeled are the interaction between laser beam and workpiece, the free-surface melt flow, the heat transfer including all occurring phase transitions, and the fluid-structure interaction between the different phases.

We tackle the modeling process by using a co-simulation approach. The workpiece is modeled based on the meshless Lagrangian Smoothed Particle Hydrodynamics (SPH) [2, 3] method. Being first introduced for astrophysics problems, the applications now range from large deformations in solid structures to free-surface and multi-phase fluid flow problems. The SPH method is applied here for modeling both the solid and liquid phases and the heat transfer including phase transitions. In addition, a ray-tracing scheme is applied that approximates the laser beam through a large number of rays and tracks each ray according to geometrical optics. The co-simulation approach has been presented in [4, 5]. Some numerical examples by applying this method are shown in [6].

In this work, the developed SPH model coupled with a ray tracer in a co-simulation is applied to simulate a laser welding scenario with an oscillating laser beam. In Section 2, the main features of the SPH model for laser welding are outlined. In Section 3, the coupling of the SPH simulation with a ray-tracing scheme and the workflow during the co-simulation is presented. Examples using this co-simulation approach are illustrated in Section 4 for laser welding with beam oscillations. Conclusions and an outlook are given in Section 5.

2 MODELING WITH SPH

In a mathematical sense, the SPH method is a general discretization technique that transforms a system of partial differential equations into decoupled ordinary differential

equations. During time integration, the integrals are further simplified into sums of the individual contributions of surrounding discretization points (so-called 'particles') within a specified area given by the smoothing length.

The weakly compressible SPH formulation of Monaghan summarized in [7] is applied for modeling both solid and liquid phases. Heat conduction and heat sources are considered in the model according to [8]. The governing equations for conservation of mass, linear momentum, and energy are extended to a thermomechanically coupled formulation by combining mechanical and thermal deformations and stresses into the same framework [9]. For the liquid phase, temperature-dependent surface tension is taken into account using a model from [10]. Different heat conductivities and heat capacities are specified for the solid and liquid phases to account for the varying material properties. Fluid-structure interaction is modeled at a physical level by unifying the stress tensors for both solid and liquid phases.

The phase changes currently considered in the model are melting, evaporation, and resolidification. The specific enthalpy is used as an equivalent variable of the thermal energy stored in the system. When only small pressure changes are assumed, the increase in enthalpy is approximately equal to the amount of heat added to the system. Therefore, a change in enthalpy may be converted to a change in temperature with the heat capacity as proportionality factor. The latent heat of fusion and evaporation are released or absorbed by the material in a transition range between two phases. During the SPH simulation, when a particle melts or resolidifies, this particle type is dynamically changed from a solid to a fluid particle or vice versa.

The gas phase motion is currently not simulated, and the effects of evaporation are only considered through the recoil pressure acting on the surface of the weld pool. The particles that evaporate are deleted during the simulation after the evaporation has completed. The recoil pressure acting on the surface of an evaporating material due to high-intensity laser radiation is calculated according to [11].

The SPH model is implemented into the software package Pasimodo [12], which is used for the welding simulations.

3 CO-SIMULATION WITH A RAY-TRACING SCHEME

The co-simulation between the SPH simulation in Pasimodo and the ray-tracing scheme as implemented in [13] is based on a server-client architecture, in which Pasimodo acts as the server, and the ray tracer as a client. All required data are exchanged via a TCP/IP network protocol.

The workflow of the co-simulation is briefly described in the following. A more detailed version may be found in [4]. An ellipsoidal plane is used as the initial surface geometry for the ray tracer. The calculated absorbed intensities for each surface triangle are transferred to Pasimodo as initial energy input through the laser beam. In Pasimodo heat source particles are added at the center of gravity positions of each triangle. The transformation of intensities to heat source particles is described in detail in [5].

In Pasimodo the welding simulation is performed with these dynamically added heat source particles. After a user-defined coupling time interval, the current surface geometry is detected and reconstructed. The detection of surface particles follows the method depicted in [14]. Based on the detected surface particles and their approximated normal vectors, the surface of the capillary and weld pool is reconstructed and a triangle mesh is generated.

The updated geometry and the temperature of the surface particles are then sent to the ray tracer in PLY format [15]. Using the updated input data, the ray tracer again delivers the absorbed intensity distribution and sends it to Pasimodo. This co-simulation loop is repeatedly executed until the welding simulation has finished.

4 EXAMPLES

Intentional oscillations of the laser beam are subject to current research in order to influence the resulting weld seam to a desired shape, e.g. a perfect rectangular cross section that is able to withstand higher loads. A further motivation for laser beam oscillations is to stabilize the welding process and to reduce weld defects [16, 17, 18]. Optical systems with increased precision regarding focus position have been developed in the past years such that the laser beam can follow almost arbitrarily given trajectories.

In this section, the first example is the seam welding process of an iron sheet. Afterwards, the laser beam is subjected to an oscillating motion to investigate the impact of these oscillations on the capillary and weld.

4.1 Welding of an iron sheet

In the following example, a seam welding process of an iron sheet is simulated. The discretized workpiece with the dimensions 4 x 2.5 x 2 mm^3 consists of approximately 163000 particles arranged in a rectangular grid at the beginning. A laser with a Gaussian beam profile, a focal diameter of 200 μm, and a power of 5000 W is applied. The focus position is the upper surface of the workpiece. The feed rate is specified as 6 m/min. The coupling time interval for the co-simulation loop is set to 50 μs.

During the simulation, a capillary with a depth of 1.11 mm and a width of 0.52 mm is formed through the welding process. Three geometries of the reconstructed capillary with their absorbed intensities are depicted in Fig. 1 which shows the evolution of the capillary over time.

The temperature distribution after 25 ms and the different phases are visualized in Fig. 2. The dark grey particles remained solid during the whole welding process, the blue particles form the liquid weld pool, and the light grey particles shape the resolidified weld seam with a depth of 1.15 mm and a width of 0.87 mm. Since the evaporated particles are deleted during the simulation, these are not shown in the figure.

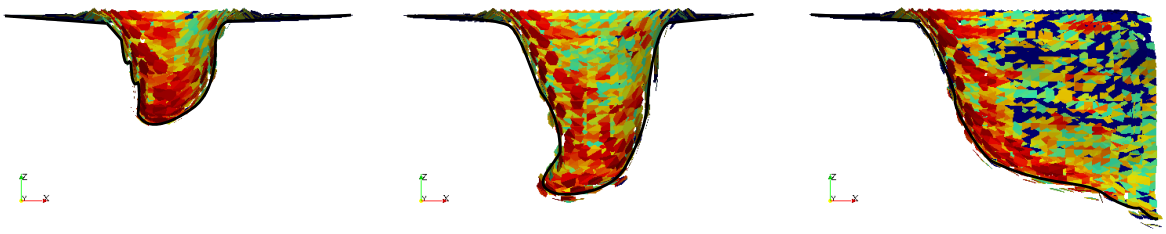

(a) $t = 2.5\,\mathrm{ms}$ (b) $t = 5\,\mathrm{ms}$ (c) $t = 15\,\mathrm{ms}$

Figure 1: Capillary cross section with intensity distribution (red: high intensity, blue: low intensity) in the xz-plane during welding of iron.

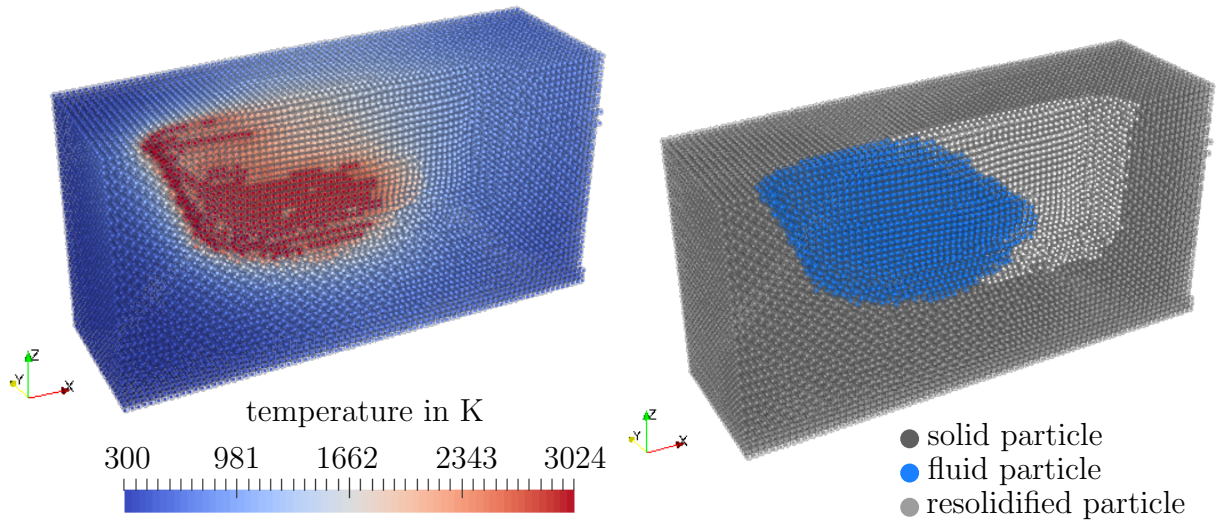

Figure 2: Temperature distribution (left) and different phases (right) during welding of iron at $t = 25\,\mathrm{ms}$ (view of surface and mid cross section).

4.2 Influence of laser beam oscillations on the weld

During the simulations, all process parameters are read at each coupling time step in the general co-simulation approach. Therefore, a complex trajectory of the laser beam is easily specified to keep the simulated welding process as flexible as possible.

Oscillations in y-direction

To demonstrate the model capabilities, in the following example the laser beam is oscillating in y-direction due to a sinusoidal excitation

$$y(t) = A \sin(2\pi f t) \tag{1}$$

in addition to feed in x-direction. The superposed motion of the laser beam is shown in Fig. 3.

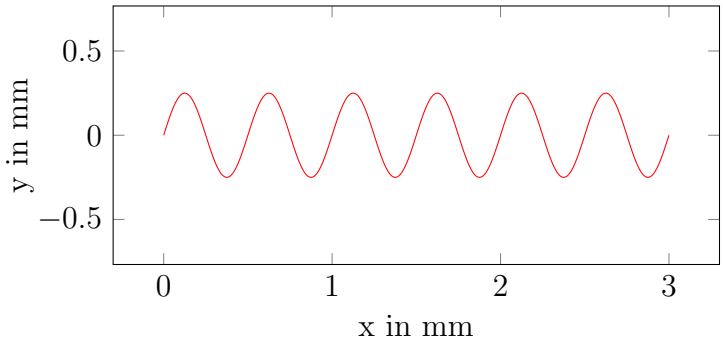

Figure 3: Resulting trajectory of laser beam with a feed rate $v = 6\,\mathrm{m/min}$, an amplitude $A = 250\,\mu\mathrm{m}$, and an oscillation frequency $f = 200\,\mathrm{Hz}$.

With multi-physics simulations, the influence of amplitude A and frequency f of the sinusoidal excitation on the resulting weld may be investigated. The chosen process parameters are $P = 5000\,\mathrm{W}$, $d_f = 200\,\mu\mathrm{m}$, and $v = 6\,\mathrm{m/min}$ as stated in the previous subsection. The simulated process duration is 30 ms, which corresponds to six to fifteen oscillation cycles of the laser beam in the range from 200 to 500 Hz.

In Fig. 4 three different cross sections of the capillaries and weld seams at $t = 20\,\mathrm{ms}$ are depicted, where the amplitude is varied from $0\,\mu\mathrm{m}$ to $500\,\mu\mathrm{m}$, and the oscillation frequency from 0 Hz to 500 Hz. It can be seen that a change in amplitude and frequency while keeping other process parameters constant influences the capillary and weld cross sections to a high extent.

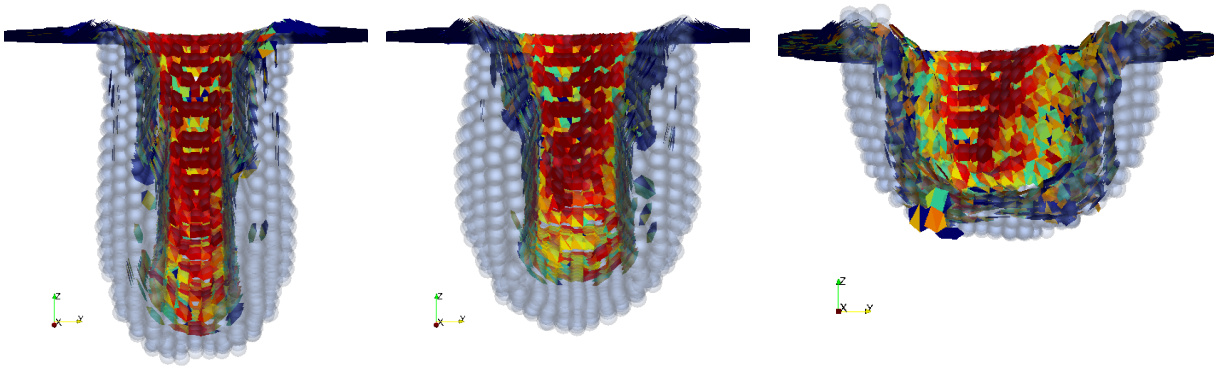

(a) $A = 0$, $f = 0$ (b) $A = 250\,\mu\mathrm{m}$, $f = 500\,\mathrm{Hz}$ (c) $A = 500\,\mu\mathrm{m}$, $f = 200\,\mathrm{Hz}$

Figure 4: Capillary cross section with intensity distribution (red: high intensity, blue: low intensity) and weld cross section in the xy-plane during welding of iron at $t = 20\,\mathrm{ms}$.

The consequences of the variation of amplitude and frequency on the capillary and weld seam dimensions are plotted in Fig. 5. With increasing amplitude the weld seam becomes wider and less deep. The same tendency is observed for an increasing oscillation frequency for this example. However, the influence of the frequency is less pronounced than the influence of the amplitude. These findings agree well with experimental observations obtained for welding aluminum to copper [19]. Furthermore, a higher frequency results in a smoother seam profile along the y-axis without distinct maximum and minimum values. In contrast, the simulation with $A = 500\,\mu\text{m}$ and $f = 200\,\text{Hz}$ shows a fissured capillary geometry that gets deeper close to the point of maximum deflections in y-direction.

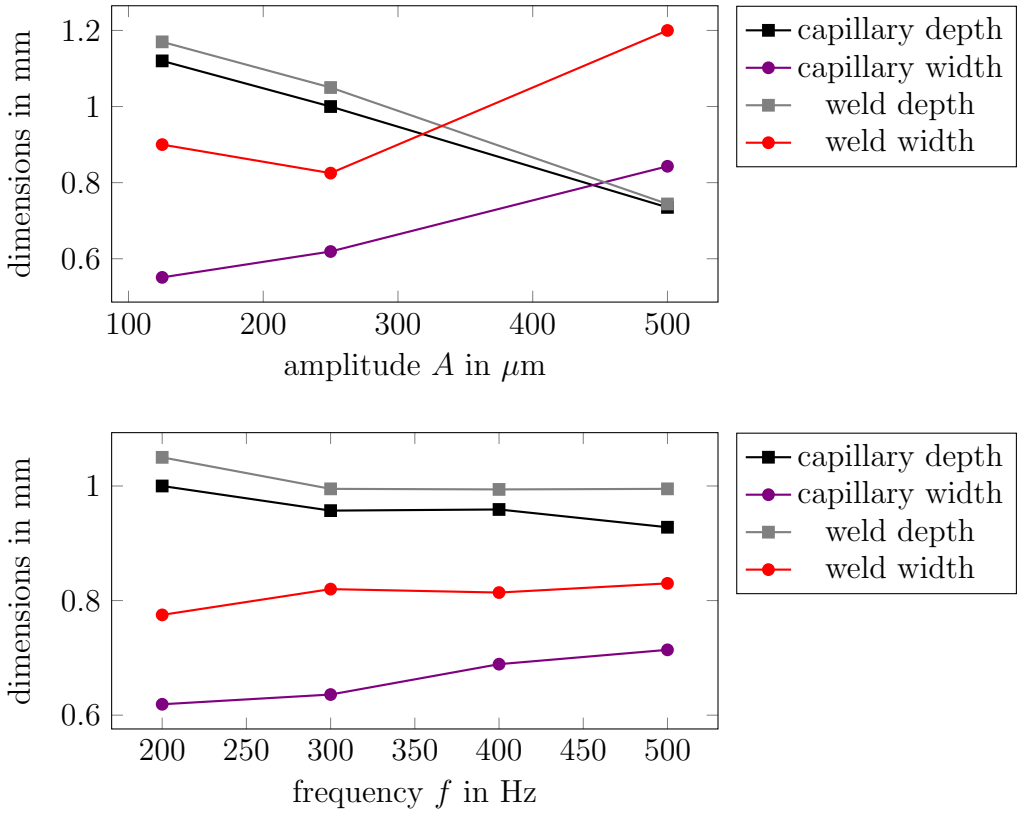

Figure 5: Resulting capillary and weld dimensions depending on the amplitude A in y-direction at a constant frequency of 200 Hz (top) and the frequency f at a constant amplitude of 250 μm (bottom) during welding of iron at a laser power of 5000 W.

Oscillations in both x- and y-direction

In a further example the laser beam is oscillating in x- and y-direction due to a sinusoidal excitation with same amplitude A and frequency f, but with a phase shift $\varphi = \pi/2$

such that the beam follows the trajectory

$$\begin{aligned} x(t) &= vt + A\sin(2\pi ft)\ , \\ y(t) &= A\sin(2\pi ft - \varphi)\ , \end{aligned} \tag{2}$$

close to a circular motion as shown in Fig. 6. According to [16], this trajectory is most frequently applied in industrial practice. As an example, such a rotating laser beam is used to suppress spatter and surface voids during welding of copper in [17].

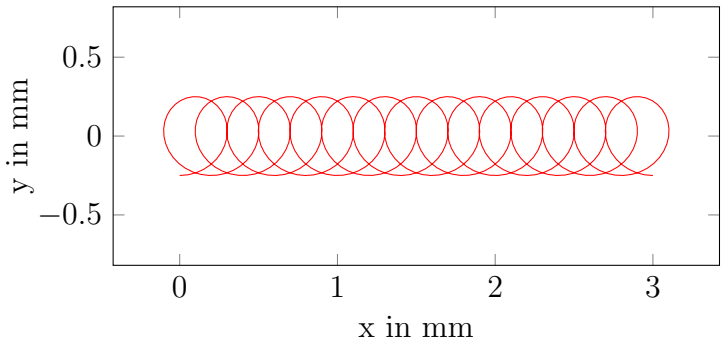

Figure 6: Resulting trajectory of laser beam with a feed rate $v = 6\,\mathrm{m/min}$, an amplitude $A = 250\,\mu\mathrm{m}$, an oscillation frequency $f = 500\,\mathrm{Hz}$, and a phase shift $\varphi = \pi/2$.

The resulting cross sections of the capillary and weld seam at $t = 20\,\mathrm{ms}$ are depicted in Fig. 7a. Compared to the beam oscillation with same amplitude and frequency only in y-direction as shown in Fig. 7b, the weld seam is much wider at the expense of a smaller depth.

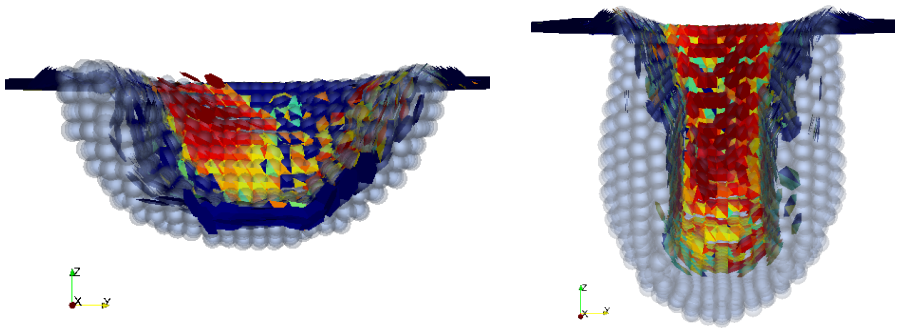

(a) $A = 250\,\mu\mathrm{m}$, $f = 500\,\mathrm{Hz}$, oscillations in x- and y-direction

(b) $A = 250\,\mu\mathrm{m}$, $f = 500\,\mathrm{Hz}$, oscillations in y-direction

Figure 7: Capillary cross section with intensity distribution (red: high intensity, blue: low intensity) and weld cross section in the xy-plane during welding of iron at $t = 20\,\mathrm{ms}$.

5 CONCLUSIONS

The process of laser welding is simulated using the SPH method, where both the solid and liquid phase are modeled in detail. The model accounts for significant physical effects such as surface tension, heat conduction, and free-surface melt flow. The phase transitions between melting, solidification, and evaporation are considered together with the absorption or release of the latent heat of fusion and evaporation. The evaporated material is currently not modeled, but the recoil pressure that affects the melt is implemented based on a physical model in [11].

A co-simulation approach is presented by coupling an SPH code with a ray tracer to simulate the laser-material interaction in deep penetration welding. Data is exchanged through a TCP/IP protocol. Additional procedures in the co-simulation are the transformation of intensities into heat source particles interacting with other SPH particles at the surface of the melt, the detection of surface particles, and the subsequent surface reconstruction.

The proposed simulation approach is flexible regarding the specification of process parameters and can be applied for a variety of welding scenarios. This is exemplarily shown for welding with different laser beam trajectories, where the feed is superposed with an oscillating motion in y-direction, and also in both x- and y-direction, resulting in a helical trajectory. The simulations can capture main characteristics of the welding process and predict the weld dimensions and cross section shapes. It is shown that beam oscillations affect the resulting weld seam shape to a high degree. The variation of amplitude has a major influence on capillary depth and width, whereas the influence of frequency on the shape is minor. However, a higher frequency might be preferred to achieve smoother welds.

Even though the simulations deliver valuable estimations on weld dimensions and geometry, the quantitative results still need to be validated. All material parameters are in reality highly dependent on temperature. Therefore, more temperature-dependent material parameters should be used to model the welding process more precisely. One way would be to provide lookup tables and interpolating the values. Another method is to use empirical models that can cover the trends in the changing parameters for a certain type of material or a temperature region. This is an important, but not much investigated topic that needs further research.

In order to make further predictions on the weld quality such as surface roughness, number of pores, and extent of spatter, further extensions in the model are required, especially the inclusion of the gas phase motion and condensation. Both the spatial and temporal resolution for the co-simulation need to be refined to make more qualified statements. In this regard, a reasonable model extension is to use an adaptive SPH discretization scheme that refines the resolution of the workpiece in regions of interest around the capillary, while coarsening the resolution in regions that are far away from the laser beam.

ACKNOWLEDGMENT

The research leading to the presented results has received funding from the German Research Foundation (DFG) in the joint project EB 195/13-1 and GR 3172/18-1 'Modeling of the capillary in laser beam penetration welding with the Smoothed Particle Hydrodynamics Method'. This support is highly appreciated.

REFERENCES

[1] Svenungsson, J.; Choquet, I.; Kaplan, A.F.H.: Laser Welding Process – a Review of Keyhole Welding Modelling. In Proceedings of the 15th Nordic Laser Materials Processing Conference (NOLAMP15), Lappeenranta, Finland, 2015.

[2] Gingold, R.A.; Monaghan, J.J.: Smoothed Particle Hydrodynamics: Theory and Application to Non-Spherical Stars. Monthly Notices of the Royal Astronomic Society, Vol. 181, pp. 375–389, 1977.

[3] Lucy, L.B.: A Numerical Approach to the Testing of the Fission Hypothesis. The Astronomical Journal, Vol. 82(12), pp. 1013–1024, 1977.

[4] Hu, H.; Fetzer, F.; Berger, P.; Eberhard, P.: Simulation of Laser Welding Using Advanced Particle Methods. GAMM-Mitteilungen, Vol. 39, pp. 149–169, 2016.

[5] Hu, H.; Eberhard, P.; Fetzer, F.; Berger, P.: Towards Multiphysics Simulation of Deep Penetration Laser Welding Using Smoothed Particle Hydrodynamics. In Proceedings of the VII European Congress on Computational Methods in Applied Sciences and Engineering (ECCOMAS Congress 2016), Hersonissos, Crete, Greece, 2016.

[6] Hu, H.; Eberhard, P.; Fetzer, F.; Berger, P.: Simulation of Laser Welding with SPH and a Ray-Tracing Scheme. In Proceedings of the 12th International Smoothed Particle Hydrodynamics European Research Interest Community Workshop (SPHERIC 2017), Ourense, Spain, 2017.

[7] Monaghan, J.J.: Smoothed Particle Hydrodynamics and Its Diverse Applications. Annual Review of Fluid Mechanics, Vol. 44, pp. 323–346, 2012.

[8] Cleary, P.W.; Monaghan, J.J.: Conduction Modelling Using Smoothed Particle Hydrodynamics. Journal of Computational Physics, Vol. 148, pp. 227–264, 1999.

[9] Hu, H.; Eberhard, P.: Thermomechanically Coupled Conduction Mode Laser Welding Simulations Using Smoothed Particle Hydrodynamics. Computational Particle Mechanics, 2016. doi:10.1007/s40571-016-0140-5

[10] Tong, M.; Browne, D.J.: An Incompressible Multi-Phase Smoothed Particle Hydrodynamics (SPH) Method for Modelling Thermocapillary Flow. International Journal of Heat and Mass Transfer, Vol. 73, pp. 284–292, 2014.

[11] Chen, X.; Wang, H.-X.: A Calculation Model for the Evaporation Recoil Pressure in Laser Material Processing. Journal of Physics D: Applied Physics, Vol. 34, pp. 2637–2642, 2001.

[12] Pasimodo, http://www.itm.uni-stuttgart.de/research/pasimodo. Accessed June 7, 2017.

[13] Michalowski, A.: Untersuchungen zur Mikrobearbeitung von Stahl mit ultrakurzen Laserpulsen (in German). Doctoral thesis, Institut für Strahlwerkzeuge (IFSW), University of Stuttgart. Munich: Herbert Utz Verlag, 2014.

[14] Barecasco, A.; Terissa, H.; Naa, C.F.: Simple Free-Surface Detection in Two and Three-Dimensional SPH Solver. Selected Paper from the International Symposium on Computational Science 2013, Kanazawa, Japan, 2013.

[15] PLY – Polygon File Format, http://paulbourke.net/dataformats/ply/. Accessed June 7, 2017.

[16] Schweier, M.; Heins, J.F.; Haubold, M.W.; Zaeh, M.F.: Spatter Formation in Laser Welding with Beam Oscillation. Physics Procedia, Vol. 41, pp. 20–30, 2013.

[17] Miyagi, M.; Zhang, X.; Kawahito, Y.; Katayama, S.: Surface Void Suppression for Pure Copper by High-Speed Laser Scanner Welding. Journal of Materials Processing Technology, Vol. 240, pp. 52–59, 2017.

[18] Sommer, M.; Weberpals, J.-P.; Müller, S.; Berger, P.; Graf, T.: Advantages of Laser Beam Oscillation for Remote Welding of Aluminum Closely above the Deep-Penetration Welding Threshold. Journal of Laser Applications, Vol. 29(1), pp. 012001, 2017.

[19] Fetzer, F.; Jarwitz, M.; Stritt, P.; Weber, R.; Graf, T.: Fine-Tuned Remote Laser Welding of Aluminum to Copper with Local Beam Oscillation. Physics Procedia, Vol. 83, pp. 455–462, 2016.

V International Conference on Particle-based Methods – Fundamentals and Applications
PARTICLES 2017
P. Wriggers, M. Bischoff, E. Oñate, D.R.J. Owen, & T. Zohdi (Eds)

DEVELOPMENT OF SURFACE TENSION MODEL WITH MANY-BODY POTENTIAL FORCE

MASAHIRO KONDO [1]

[1]Nuclear Professional School, School of Engineering, University of Tokyo
7-3-1, Hongo, Bunkyo-ku, Tokyo, Japan, 113-8656
e-mail: kondo@vis.t.u-tokyo.ac.jp

Key words: Surface tension, MPS, SPH, many-body potential, free surface flows

Abstract. A new approach to calculate surface tension in a particle method is proposed. In particle methods, one way to calculate surface tension is introducing pairwise potential force, which is long-range attractive and short-range repulsive. However, the potential force acts not only on the surface but also inside the fluid bulk, which causes unrealistic pressure increase in the droplet or shrinkage of the droplet. In this study, a many-body potential is introduced for surface tension calculation instead of the pairwise potential. The new approach is tested in the droplet oscillation calculation, capillary pressure calculation and capillary rise calculation. The surface tension could be estimated consistently in these calculations.

1 INTRODUCTION

One of the advantage of particle methods is to capture the complex motion of the dynamic free-surface flows. It is important to take surface tension into consideration to calculate the free surface flows, especially in analysing fluid motion in microstructures or droplet break up behaviours. There are mainly two ways to calculate surface tensions in particle methods [1,2]. One is to introducing surface tension force by discretising the continuum surface force (CSF) model [3]. However, the first approach does not conserve linear momentum of the particle system, and it might cause strange motion of droplet. Another way is to introduce pairwise potential force, which is long-range attractive and short range repulsive [4-6]. This approach can conserve linear momentum and the formulation is much simpler than the CSF approach. Since the mechanical energy conservation is good with the potential force, its numerical stability is also good. However the pairwise potential force acts not only on the surface of the fluid but also acts inside the fluid bulk. Because of this force inside, unrealistic pressure increase in the droplet or the droplet shrinkage occurred [5]. The pairwise force tends to be large, and the time step width has to be small enough, which is not favourable for numerical efficiency.

In this study, a new model for surface tension calculation is developed. A many-body potential force is introduced instead of the pairwise potential force in the context of Moving Particle Full-implicit (MPF) [7] method, and the new model is tested in the calculations of droplet oscillation, capillary pressure and capillary rise, and the surface tensions are estimated through these calculations.

2 NUMERICAL METHOD

2.1 Incompressible calculation [7]

To simulate incompressible free surface flows, Moving Particle Full-implicit method [7] was used in this study. In the method, the following governing equation was adopted.

$$\rho \frac{du_i}{dt} = \frac{\partial}{\partial x_j} \mu \dot{\varepsilon}_{ij} + \frac{\partial}{\partial x_i} (\lambda \dot{\varepsilon}_{kk} + \kappa \varepsilon_{kk}) + \rho g_i \tag{1}$$

Since this equation approaches to the usual incompressible Navie-Stokes (NS) equation when we set the parameters λ and κ large enough, it can be used instead of the incompressible NS equation. The first term on the right hand side is the viscosity term and the second term is equivalent to the pressure term in the general NS equation for incompressible flow. Here, the pressure is expressed as

$$P = -(\lambda \dot{\varepsilon}_{kk} + \kappa \varepsilon_{kk}) . \tag{2}$$

In particle methods, the governing equations are replaced by particle interaction forces. The interaction is limited in a finite range using an effective radius r_e and a weight function w^{ij} as

$$\begin{aligned} w^{ij} &= \frac{W^{ij}}{N_0} \\ W^{ij} &= \begin{cases} (r_e - d^{ij})^2 & (d^{ij} < r_e) \\ 0 & (d^{ij} > r_e) \end{cases} \\ N_0 &= \sum_{init} W^{ij} \end{aligned} \tag{3}$$

In this study, the particle interaction models for gradient, divergence and Laplacian operators are formulated as

$$\begin{aligned} \nabla \phi &\approx \sum_j (\phi^j + \phi^i) \mathbf{r}^{ij} \frac{w'^{ij}}{d^{ij}} \\ \nabla \cdot \mathbf{A} &\approx \sum_j (\mathbf{A}^j - \mathbf{A}^i) \mathbf{r}^{ij} \frac{w'^{ij}}{d^{ij}} \\ \nabla^2 \phi &\approx \sum_j (\phi^j - \phi^i) \frac{w'^{ij}}{d^{ij}} \end{aligned} \tag{4}$$

where w^{ij}' is the differential of the weight function shown in Eq. (3). The particle interaction models are formulated in a similar manner compared to the Smoothed Particle Hydrodynamics (SPH) [1] formulation, however, the weight function (Eq. (3)) instead of the SPH kernel function is used in this study. The differential of this weight function is non-zero at d^{ij}=0 so as to keep the particle arrangement uniform.

When we discretize the governing equation (Eq.(1)) with the particle interaction models, the force acting on the particles are formulated as

$$\rho_0 \frac{d\mathbf{u}^i}{dt} = \mu \sum_j (\mathbf{u}^j - \mathbf{u}^i) \frac{w'^{ij}}{d^{ij}} - \sum_j (P^j + P^i) \mathbf{r}^{ij} \frac{w'^{ij}}{d^{ij}} + \rho_0 \mathbf{g} \ , \tag{5}$$

where

$$P^i = -\lambda \sum_j (\mathbf{u}^j - \mathbf{u}^i) \cdot \mathbf{r}^{ij} \frac{w'^{ij}}{d^{ij}} + \kappa (1 - \sum_j w^{ij}) \tag{6}$$

Since the potential energy and dissipative function for the discretized equation can be written, thermodynamic consistency of the particle system after discretization is assured. It implies that the mechanical energy of the system monotonically decrease, and this property is important for stable calculation.

The equations (5) and (6) will be a linear matrix equation whose unknowns are the velocity **u** and the pressure *P*. Since the coefficient matrix is symmetric, it can be solved by conjugated residual (CR) method.

2.2 Surface tension model using many body potential

The surface tension is calculated in the similar manner to the SPH pressure calculation, where another normalized weight function

$$\begin{aligned} w_s^{ij} &= \frac{W_s^{ij}}{N_{s0}} \\ W_s^{ij} &= \begin{cases} \left(1 - \left(\frac{d^{ij}}{r_{es}}\right)^2\right)^2 & (d^{ij} < r_{es}) \\ 0 & (d^{ij} > r_{es}) \end{cases} \\ N_{s0} &= \sum_{init} W_s^{ij} \end{aligned} \tag{7}$$

is used. The parameters like density and pressure are calculated as

$$\begin{aligned} \rho_s^i &= \sum_j m w_s^{ij} \\ P_s^i &= -a(\rho_0 - \rho_s^i) \end{aligned} \tag{8}$$

where ρ_0 is the bulk density at the initial state, and a is a coefficient to control the magnitude of surface tension. The interaction force with respect to surface tension is formulated as

$$\mathbf{F}_s^{ij} = \frac{m}{\rho_0} \sum_j (P_s^j + P_s^i) \mathbf{r}^{ij} \frac{w_s^{ij'}}{d^{ij}} \tag{9}$$

Because of the low particle number density close to the surface, the pressure P_s will be negative, and it yields the long-range attractive force, which can simulate surface tension.

Since the force can be derived from the potential formulated as

$$E_s = \frac{a}{2\rho_0} \sum_i (\rho_0 - \rho_s^i)^2 \tag{10}$$

$$F_s^i = -\frac{\partial E_s}{\partial \mathbf{x}_i}, \tag{11}$$

it conserves mechanical energy and also the linear momentum of the system.

3 CALCULATIONS

Using the same set of the parameters shown in Table 1, droplet oscillation, capillary pressure and capillary rise will be calculated, and surface tension σ were estimated through each calculation. For the uniform arrangement of the particles during the calculation, the effective radius for the surface tension term r_{es} should be larger than the effective radius for the pressure term r_e. It is because the range of the attractive force due to the surface tension term is to be larger than the range of the repulsive force due to the pressure term.

Table 1: Parameters used in the calculations

Parameters	Values
Time step Δt	0.001
Particle spacing l_0	0.01
Mass m	0.0001
Viscosity μ	1.0×10^{-10}
Effective radius for pressure and viscosity terms r_e	0.015
Bulk viscosity κ	100
Bulk modulus λ	10000
Effective radius r_{es}	0.032
Coefficient in the surface tension calculation a	0.01

3.1 Droplet oscillation calculation

Figure 1 shows the initial state of the droplet oscillation calculation. The radius of the droplet is R=0.3 and the shear rate of 1.0 is given at the initial state. The snapshots of the calculation is shown in Figure 2, where the oscillating droplet can be seen. The time history of the x radius of the oscillating droplet is shown in Figure 3. Even when the viscosity is set very small value, the oscillation decay occurred. It is because the particle method has its intrinsic viscosity. The surface tension σ can be estimated using the theoretical period of oscillation [4]

$$\tau = 2\pi\sqrt{\frac{R^3\rho}{6\sigma}} \tag{12}$$

Since the theory is applicable for the oscillation in a small fluctuation, the oscillation period after decay was used to calculate the surface tension coefficient σ. With this calculation, it was estimated that σ=0.044.

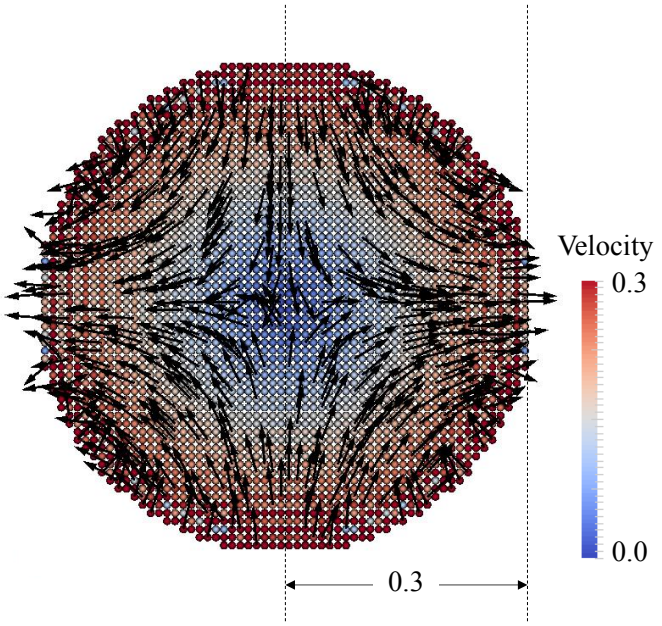

Figure 1: Initial velocity in the droplet oscillation calculation

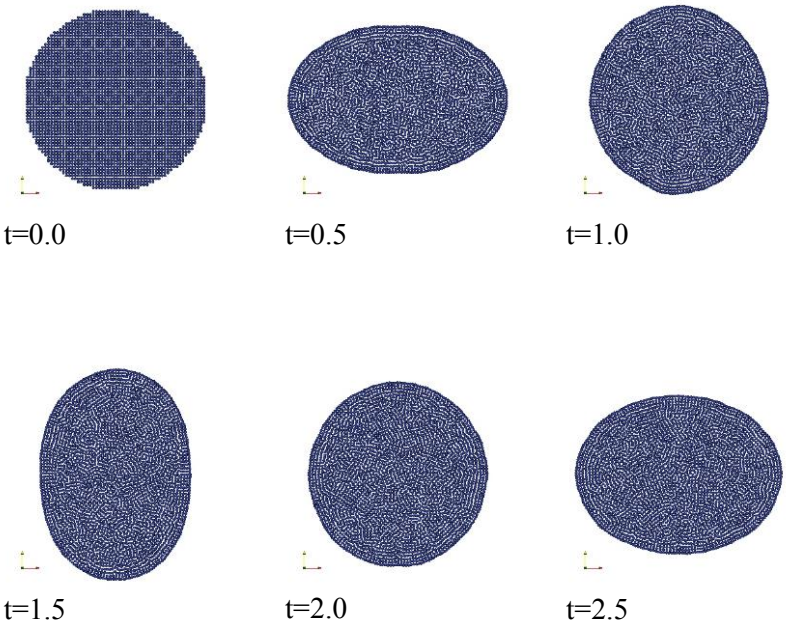

Figure 2: Droplet oscillation calculation

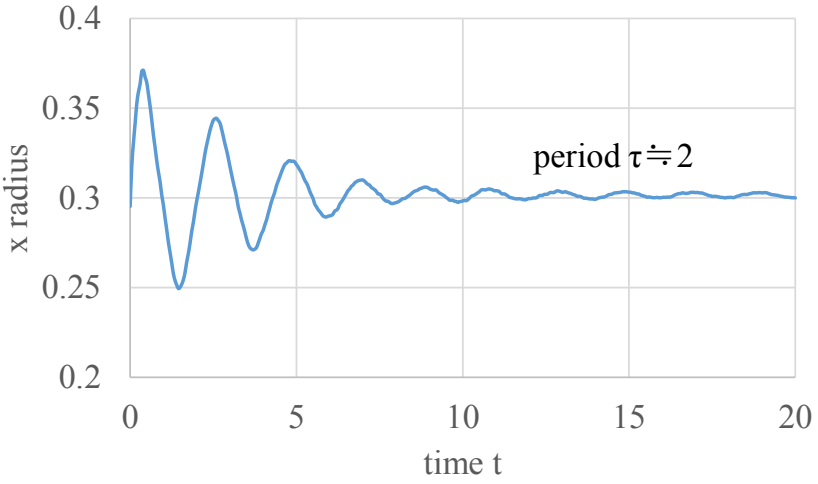

Figure 3: History of x radius of the oscillating droplet

3.2 Capillary pressure

According to the Young-Laplace equation [4], the relation between the radius of the equilibrium droplet and the pressure inside the droplet is given as

$$P_{in} = \frac{\sigma}{R} \tag{13}$$

To estimate the surface tension from this equation, the equilibrium droplets having various radiuses R=0.1, 0.2, 0.3, 0.4, 0.5 are calculated. Since the raw pressure value suffered from the numerical fluctuation, the spatial-averaging and time-averaging were conducted to know the inner pressure of the droplets. In the spatial-averaging, the pressure calculated by Eq. (6) is averaged after extracting the particles near the surface. In the time-averaging, the spatial-averaged pressure was averaged in the time range of 1.0 after equilibrium is reached. The relation between $1/R$ and the averaged pressure P_{in} is shown in Figure 4. From the figure and Eq. (13), an approximate surface tension σ=0.037 was obtained.

Figure 5 shows the potential energy with respect to the surface tension term. The potential only located on the surface while almost no potential was observed in the fluid bulk. It implies that the force acts only on the surface and does not cause the unrealistic pressure rise which was observed in the surface tension calculation using pairwise potential [5].

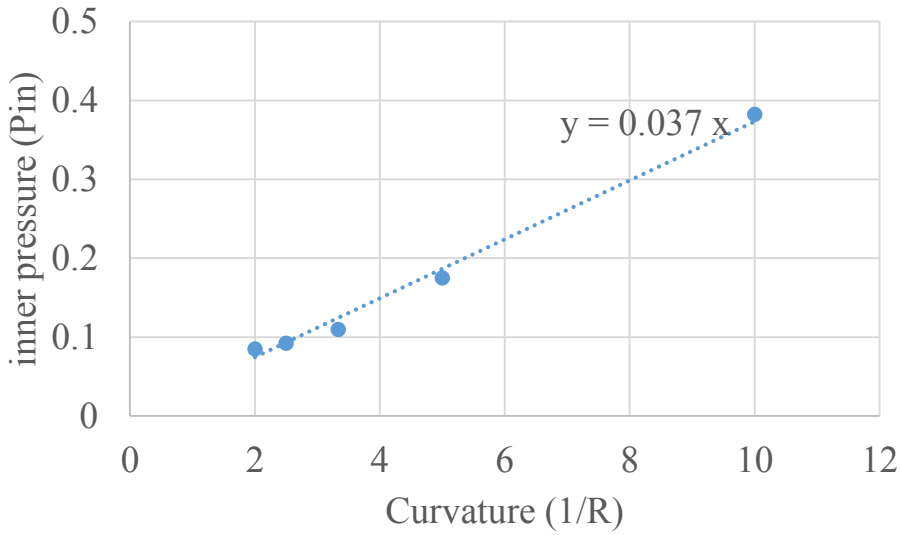

Figure 4: Relation between $1/R$ and inner pressure P_{in}

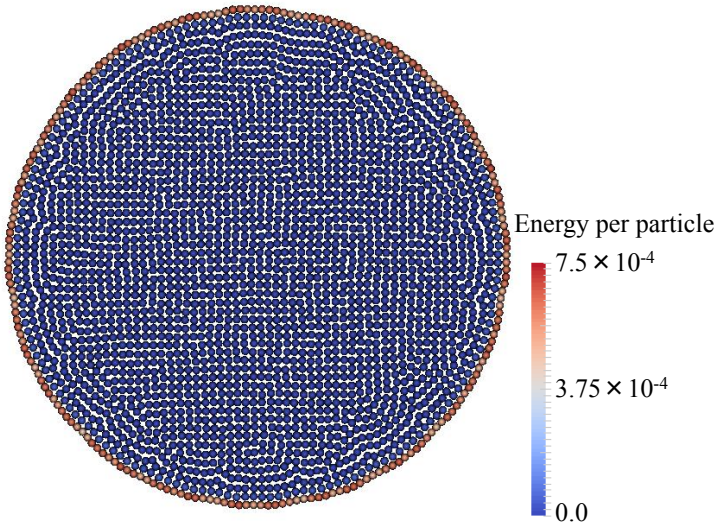

Figure 5: Potential energy with respect to the surface tension calculation

3.3 Capillary rise

The initial state of the capillary rise calculation is shown in Figure 6. The sideward boundaries are set as periodic boundaries. The walls are expressed by the red fixed particles, at which the calculations are conducted in the same manner as at the blue moving particles except for the position update. The gravity g=1.0 is given. The snapshots of the calculation

are shown in Figure 7. After the liquid rose in between walls, it reached the equilibrium state at around t=3.0. Since the relation among the elevation difference h_1-h_2, the curvatures of the surfaces $1/R_1$, $1/R_2$ and surface tension σ are given as

$$\rho g(h_1 - h_2) = \sigma\left(\frac{1}{R_1} - \frac{1}{R_1}\right) \tag{14}$$

in the equilibrium state [4], the surface tension can be estimated as σ=0.041, where h_1-h_2=0.54, R_1=0.06 and R_2=0.30 (Figure 8) were used.

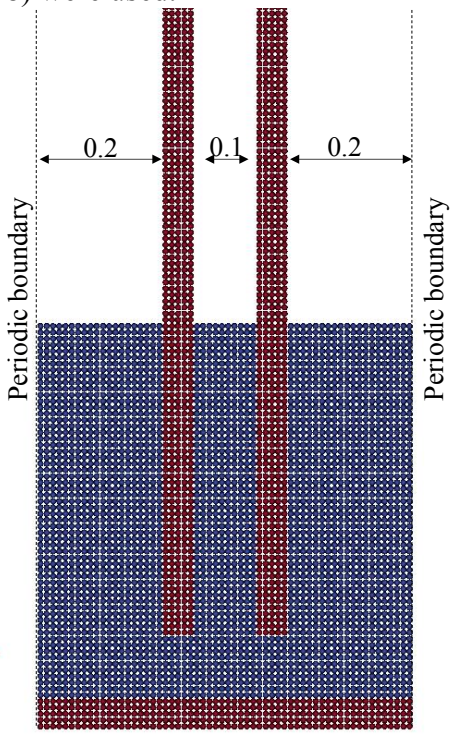

Figure 6: Initial state of the capillary rise calculation

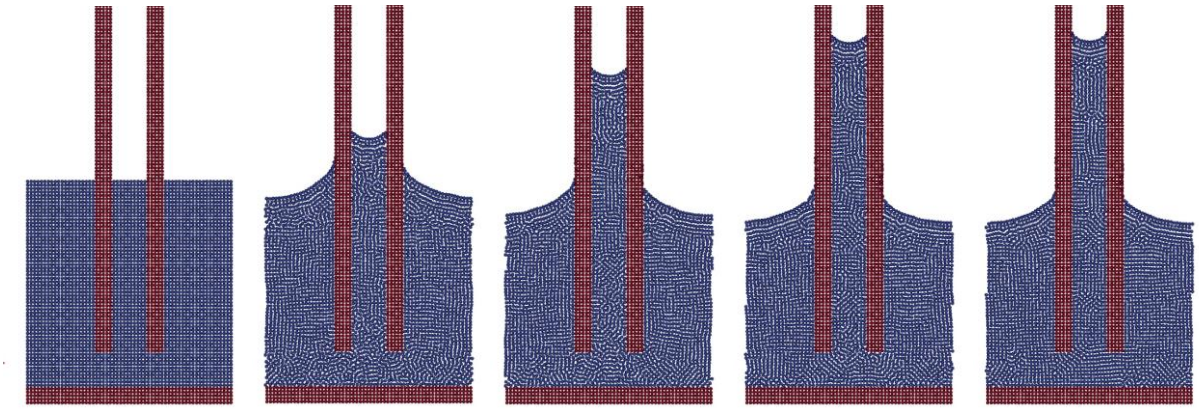

Figure 7: Capillary rise calculation

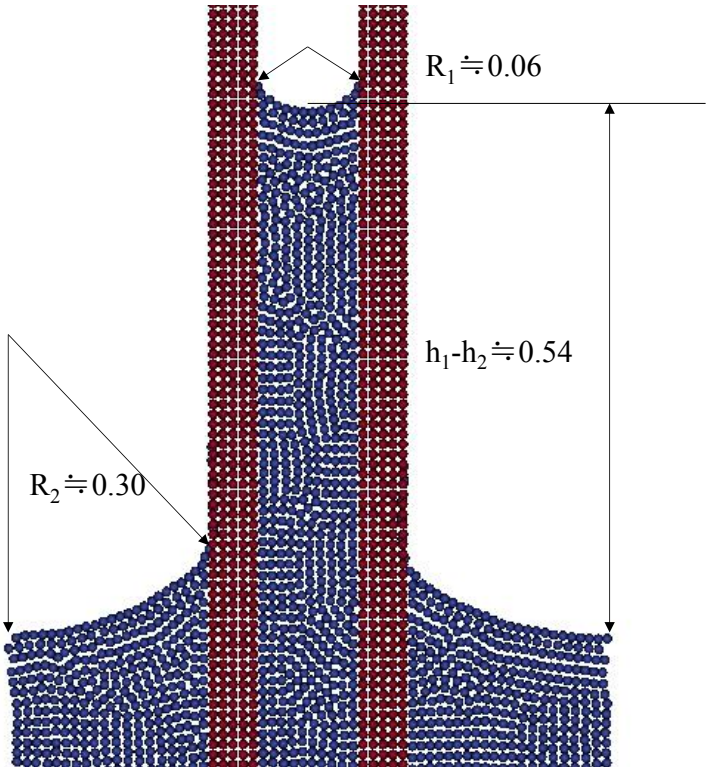

Figure 8: Length at the equilibrium state

Though the droplet oscillation calculation, the capillary pressure calculation and the capillary rise calculation, the surface tensions σ were estimated. The values obtained were not contradictory. It implies the applicability of the new surface tension calculation model using many-body potential.

4 CONCLUSIONS

A new model for surface tension calculation is developed. A many-body potential force is introduced in the context of Moving Particle Full-implicit method [7]. The new surface tension model is tested in the calculations of droplet oscillation, capillary pressure and capillary rise. Since the surface tensions estimated through each calculation are not contradictory, it is confirmed that the new model can well express surface tension in the particle method.

REFERENCES

[1] J.J. Monaghan, Simulating free surface flows with SPH, Journal of Computational Physics **110**, 399-406 (1994)

[2] S. Koshizuka and Y. Oka, Moving-Particle Semi-Implicit methods for fragmentation of incompressible fluid, Nuclear Science and Engineering **123**, 421-434 (1996)

[3] J.P. Morris, Simulating surface tension with smoothed particle hydrodynamics, Int. J. Numer. Meth. Fluids **33**, 333–353 (2000)

[4] A. Tartakovsky and P. Meakin, Modeling of surface tension and contact angles with smoothed particle hydrodynamics, Physical Review E **72**, 026301 (2005)

[5] M. Kondo, S. Koshizuka and M. Takimoto, Surface tension model using inter-particle force in particle method, 5th Joint ASME/JSME fluid engineering conference, San Diego, July 30-August 2, 2007, FEDSM-37215.
[6] M. Kondo, S. Koshizuka and M. Takimoto, Surface tension model using inter-particle potential force, Transactions of JSCES, Paper No. 20070021 (2007) (in Japanese)
[7] M. Kondo, A particle method for incompressible flow analysis using coupled implicit solver for pressure and velocity, Proceedings of 21st JSCES annual conference, A-3-2 (2016)

FUSIONAL METHOD OF MPS AND FEM THROUGH TETRAHEDRAL MESH GENERATION

JUNYA IMAMURA[1]

[1]*imi* Computational Engineering Laboratory
Wako-shi, Honcho 31-9-803, 351-0114 Saitama, Japan
E-mail: jimamura@ra2.so-net.ne.jp

Key words: Improved Helmholtz-decomposition, MPS, FEM, Non-equidistant FDM

Abstract. The moving-particle semi-implicit (MPS) method is used as a density method for moving surfaces. The main disadvantage of previous density methods was that mass conservation was difficult to achieve because the mean density varied due to elemental diffusion; in contrast, MPS satisfies mass conservation. The density method is also very suitable as a finite element method (FEM), thus leading to the concept of an MPS-FEM fusion method. The MPS method especially incorporates a weight function for calculating the particle number density. Because the weight function is a Kernel function, the MPS-FEM fusion method includes a novel Kernel function similar to the weight function of MPS. The masses (particles) occupy positions on the vertex nodes of the tetrahedral elements, and the mesh must be recomposed for the time step advance by using a mesh generation technique. The masses are distributed in the control volume (CV) according to the Karnel function, and mass conservation must be satisfied by mesh regeneration using the apparent new density ρ. The method is composed of FEM and a conceptual Helmholtz decomposition (*H-d*) using $\boldsymbol{u}^L$- and $\boldsymbol{u}^T$-elements for displacement $\boldsymbol{u} = \boldsymbol{u}^L + \boldsymbol{u}^T$ (where *L*: *Lateral* and *T*: *Transverse*). Nevertheless, an improved Helmholtz decomposition method (*iH-d*) is applied here to satisfy the conservation laws.

1 INTRODUCTION

I present a numerical calculation model of an incompressible flow field with free surfaces. The model is based primarily on the moving-particle semi-implicit (MPS) method, but calculation is performed by the finite element method (FEM) to include not only scalar potential flow but also vorticity flow. Thus, I apply Helmholtz decomposition (*H-d*) to represent the velocities.

Moreover, I consider the scalar potential term of *H-d* inappropriate to represent dilatational components. For this reason, I propose an improved Helmholtz decomposition (*iH-d*). The objective of the present study is to build a route for applying *iH-d* to free surface flow problems.

MPS is the best method for such free surface problems, because it conserves mass perfectly and is the only method disregarding surfaces. In addition, MPS allows nonlinear mechanisms, and it can therefore be used to solve contact problems. In the flow problem, the free surface implies mechanism nonlinearity, i.e., changes from the Dirichlet boundaries to the Neumann boundaries or the reverse.

In the free-surface MPS problem, the compressible flow plays an important role because this is apparently a compressible flow problem. Therefore, FEM is required for the compressible

flow calcuation.

The *iH-d* method allows compressibility by representing the velocity vector separately, i.e., with the dilatational term and the rotational term.

The *iH-d* rotational term is incompressible at any time (automatically solenoidal). However, not only vorticity but also the shear strains in the fluid must be incompressible.

Normal strains induce volume changes, whereas shear strains induce shape changes but no volume changes. This is the basic assumption for applying *iH-d* to free-surface problems.

In reverse, MPS causes high discretization (example discretization model shown in Fig. 1).

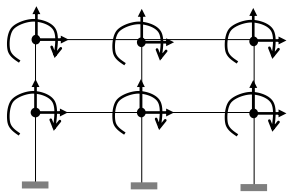

Figure 1: Nodal model (continua → Frame work)

This problem can be explained by Kondo's indication [3] that the original MPS formulation lacks angular momentum terms. For the equilibrium equations of the above framework model, $\Sigma M_i=0$ is required in addition to $\Sigma N_i=0$ on the nodes. This problem is automatically resolved when we use FEM, in which distributed rigidity and re-reduced particle density is assumed.

2 REDUCING AND RE-REDUCING: FINITE ELEMENTS ←→ PARTICLES

2.1 Initial setting

The numerical scheme is constructed by FEM, generating tetrahedral elements by joining two particles with a straight line. This process is called grid generation in initial setting.

The particles include inner mass particles and boundary particles, and the boundary particles include zero-mass particles on the Dirichlet boundary and nonzero–mass particles on the Neumann boundary; nonequal masses are allowed.

At the time of the initial setting, the system is divided into sub-domains, and all particles are set on the centre of gravity, with the exception of the particles on the Neumann boundary. Overall, the following steps are executed:

(1) Setting the nodes on the Dirichlet boundaries → without mass (zero-mass)
(2) Setting the nodes on the Neumann boundaries → with mass
(3) Dividing the system to sub-domains for particles with mass → infinite number and mass
(4) Constructing the tetrahedral elements (by any existent scheme) → nonequally masses are allowed
(5) Adaptive element generation for isolated (flying) particles (in future work)

The above steps are illustrated in Fig. 2.

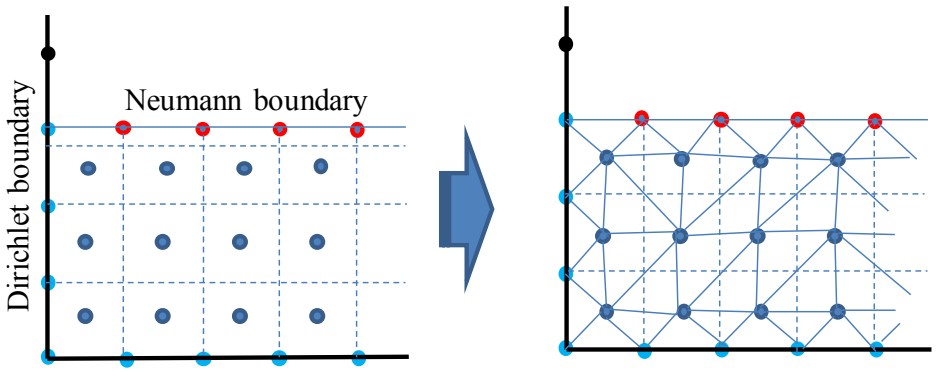

Figure 2: Initial setting procedure

2.2 Re-reducing particle mass to density

To apply FEM, density is indispensable. m_i is the mass of the concerned particle i, $V_{j,i}$ is the control volume (CV) of the j-th element that shares a node with i, and the mass m_i is distributed to the individual CV in the inverse ratio following Eq. (1).

$$\frac{1}{V_{i,1}} : \frac{1}{V_{i,2}} : \frac{1}{V_{i,3}} : \cdots : \frac{1}{V_{i,n}} \tag{1}$$

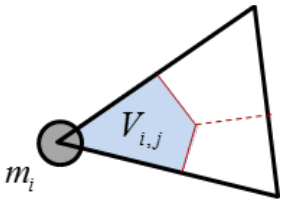

Figure 3: Re-reducing of particle mass to ρ

ρ has a positive physical value, so it is represented by the exponent of the r-variable, i.e., $\rho = exp(r)$. ρ is constant in CV, but discontinuous in the element; consequently, mass conservation is shown in (2) without advection terms.

$$\frac{D\rho}{Dt} + \rho div\boldsymbol{U} = 0 \;\rightarrow\; \frac{\partial r}{\partial t} + div\boldsymbol{U} = 0 \tag{2}$$

3 IMPROVED HELMHOLTZ DECOMPOSITION

3.1 Helmholtz decomposition

According to the Helmholtz theorem, an arbitrary vector field $\boldsymbol{u}$ can be represented in Eq. (3) using a scalar potential $\nabla\phi$ and a vector potential $\boldsymbol{\psi}$ under the restriction of the Coulomb gauge.

$$\boldsymbol{u} = \nabla\phi + curl\boldsymbol{\psi} \quad (div\boldsymbol{\psi} = 0) \tag{3}$$

Let us think about the displacement vector $\boldsymbol{u}$ in a solid. The simplest example is the cantilever, which is statically deterministic and can neglect the shearing strain, i.e., $\boldsymbol{u}=\nabla\phi$.

However, we cannot obtain the numerical result expected by FEM using $\nabla\phi$.

3.2 Improved Helmholtz decomposition

Therefore, I proposed the improved Helmholtz decomposition represented in Eq. (4).

$$\left.\begin{array}{l} \text{fluid} : \boldsymbol{u} = (\nabla_{diag}\boldsymbol{\psi} + \nabla\phi) + \nabla_{curl}\boldsymbol{\psi} \\ \text{solid} : \boldsymbol{u} = (\nabla_{diag}\boldsymbol{\psi} + \nabla\phi) + \nabla_{shr}\boldsymbol{\psi} \end{array}\right\} \quad (\nabla\phi \Rightarrow \boldsymbol{0}, div\nabla_{shr}\boldsymbol{\psi} = 0) \quad (\Rightarrow 0 \quad \text{means minimize}) \tag{4}$$

The novel operator used in Eq. (4) is defined as follows:

$$\text{Def. of novel operator}: \begin{Bmatrix} \nabla_{diag} \\ \nabla_{shr} \\ \nabla_{curl} \end{Bmatrix} \boldsymbol{u} \equiv \begin{Bmatrix} \boldsymbol{\varepsilon} \\ \boldsymbol{\gamma} \\ \boldsymbol{\omega} \end{Bmatrix}, \qquad where \quad 2\nabla\boldsymbol{u} = \begin{bmatrix} \varepsilon_1, & \gamma_3, & \gamma_2 \\ \gamma_3, & \varepsilon_2, & \gamma_1 \\ \gamma_2, & \gamma_1, & \varepsilon_3 \end{bmatrix} + \begin{bmatrix} \varepsilon_1, -\omega_3, & \omega_2 \\ \omega_3, & \varepsilon_2, -\omega_1 \\ -\omega_2, & \omega_1, & \varepsilon_3 \end{bmatrix}, \quad \gamma_i \equiv \gamma_{i-1,i+1}$$

$$(i = 1,2,3)(i+1 = 2,3,1)(i-1 = 3,1,2)$$

$$(\therefore i+2 = i-1, \; i-2 = i+1)$$

$$\begin{Bmatrix} \nabla^2_{diag} \\ \nabla^2_{shr} \\ \nabla^2_{curl} \end{Bmatrix} \equiv \begin{Bmatrix} \nabla_{diag}\nabla_{diag} \\ \nabla_{shr}\nabla_{shr} \\ \nabla_{curl}\nabla_{curl} \end{Bmatrix}$$

The expression for the fluid in the definition assumes that the Navier–Stokes (N.S.) equation is represented in rotational form. When the N.S. equation is represented in shearing form, the expression in the second row (using $\nabla_{shr}\boldsymbol{\psi}$) is the same as for the solid.

The dilatational component in *iH-d* is represented by the orthogonal component of the rotational components and modified with $\nabla\phi$, which is constrained by the gauge.

3.3 Strain potential and chain low

According to the Helmholtz theorem, the arbitrary vector field should be decomposed. By analogy to the numerical formula, *iH-d* can be applied to the strain vector shown in Eq. (5).

$$\text{"}strain\ \ potential\text{"}: \left.\begin{array}{l} \boldsymbol{\omega} = (\nabla_{diag}\boldsymbol{\Psi} + \nabla\Phi) + \nabla_{curl}\boldsymbol{\Psi} \\ \boldsymbol{\gamma} = (\nabla_{diag}\boldsymbol{\Psi} + \nabla\Phi) + \nabla_{shr}\boldsymbol{\Psi} \end{array}\right\} \quad (\nabla\Phi \Rightarrow \boldsymbol{0}, div\nabla_{shr}\boldsymbol{\Psi} = 0) \tag{5}$$

$$where \quad \begin{cases} \boldsymbol{\omega} \equiv \{\varepsilon_i\} + \{\omega_i\} \\ \boldsymbol{\gamma} \equiv \{\varepsilon_i\} + \{\gamma_i\} \end{cases}$$

iH-d decomposes also the vector potential $\boldsymbol{\psi}$ shown in Eq. (6).

$$\boldsymbol{\psi} = (\nabla_{diag}\boldsymbol{\psi} + \nabla\vartheta) + \nabla_{curl}\boldsymbol{\psi} \quad (\nabla\vartheta \Rightarrow 0, \; div\nabla_{curl}\boldsymbol{\psi} = 0) \tag{6}$$

I call the above the “low chain of the Helmholtz decomposition”. The low chain can be endlessly developed, and, therefore, *iH-d* can only be represented numerically.

3.4 Scoop up residuals of an equation to $\nabla\phi$

The scalar potential ϕ and the pressure P function have the same spatial effects. The dilatational component modified by $\nabla\phi$, $\nabla_{diag}\boldsymbol{\psi}$, represents the volumetric ratio $div\boldsymbol{u}^L = div\nabla_{diag}\boldsymbol{\psi}$. The conceptual function of $\nabla\phi$ is illustrated in Fig. 4. The numerical scheme for minimizing ($\nabla\phi \Rightarrow \boldsymbol{0}$) consists of two steps. First, $\nabla\phi$ scoops up the residual of an equation represented by $\boldsymbol{u}$, e.g., $A+div\boldsymbol{u}^L \rightarrow \nabla\phi$ (Eq. (7)), and then $\nabla\phi$ gives the offset values of $\boldsymbol{u}$ which are explained later (in the section 4.7).

$$\int_{\Omega} \{(A + divu) + \nabla\phi\} \cdot \delta\nabla\phi d\Omega = 0 \tag{7}$$

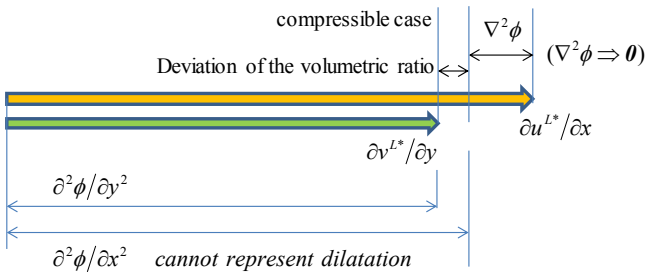

Figure 4: Conceptual function of $\nabla\phi$

3.5 *iH-d* elements

I propose the *iH-d* elements in Fig. 5, in which shows an example of $\nabla\phi$. This element shape is applied for $\nabla\psi_i$, $\nabla\Phi$, nd ∇P. ({ }$_k$: on vertex, { }$_{COG}$: on the center of gravity)

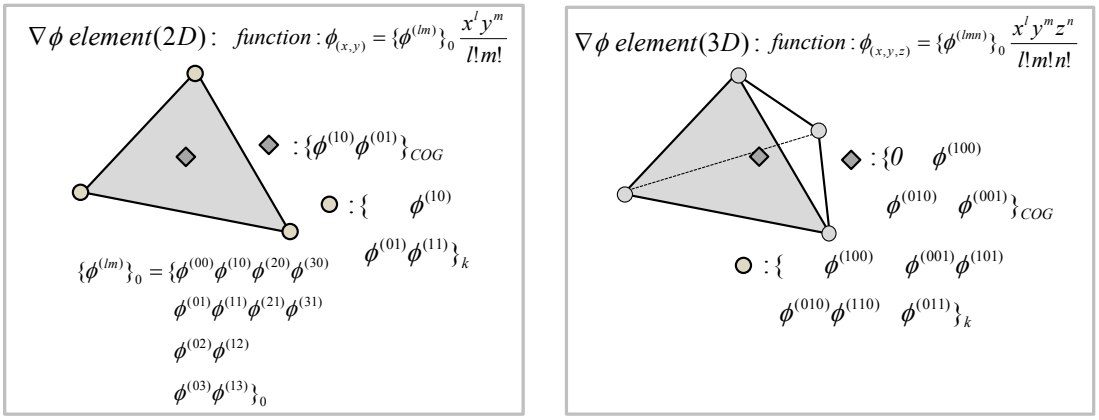

Figure 5: *iH-d* elements $\nabla\phi$ for 2D and 3D

The element function is expressed in the finite Taylor series, and the adopted terms are represented in Fig. 5 with the coefficient terms for 2D in the left part of the figure (no notice for 3D). The functions for 2D and 3D are incomplete 3rd order functions. Both functions have a zero interceptor $\{\phi^{(00)}\}_0 = 0$.

4 NUMERICAL SCHEME

4.1 Navier–Stokes equation

The mass conservation equation is shown in Eq. (2). The Navier–Stokes equation used in this paper is shown in Eq. (8) in the rotational form, where $\boldsymbol{U}$ is the velocity vector, ρ is the density, $\boldsymbol{g}$ is the gravity, P is the pressure, and μ is the viscosity.

$$\rho(\frac{D\boldsymbol{U}}{Dt} + \boldsymbol{U} \cdot div\boldsymbol{U} - \boldsymbol{g}) + \nabla P - \mu(\frac{4}{3}\nabla div\boldsymbol{U} - \nabla^2_{curl}\boldsymbol{U}) = 0 \tag{8}$$

4.2 Time axially central FDM

I apply the central difference method to the time axis shown in Eq. (9), where $\boldsymbol{u}$ is the displacement vector, Δt is the time pitch, and n is the time step ($n=0,1,2,3,\cdots$).

$$U_i^n = \frac{u_i^{n+1} - u_i^{n-1}}{2\Delta t}, \quad \{\frac{\partial U_i}{\partial t}\}^n = \frac{u_i^{n+1} - 2u_i^n + u_i^{n-1}}{\Delta t^2} \tag{9}$$

The states are known for n-1 and n , and unknown for n-1, and the displacements $\boldsymbol{u}^{L,n+1}$ and $\boldsymbol{u}^{T,n+1}$ are used as variables, i.e., unknown parameters $\{\nabla \boldsymbol{\psi}\}_k^{n+1}$, $\{\nabla \boldsymbol{\psi}\}_{COG}^{n+1}$

ρ, $\nabla \phi$, $\nabla \Phi$, and ∇P are the elements used here.

For n-1 and n+1, I use the grid generated at n, but using the corresponding data for each spatial position shown in Fig. 6

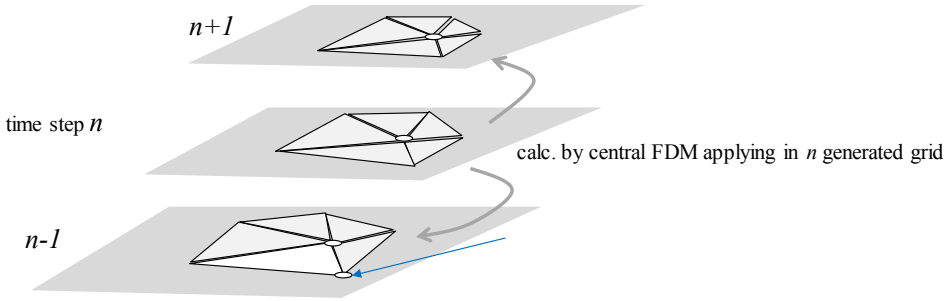

Figure 6 Grid usage

4.3 Initial setting of ∇P element

The gravity acceleration g_z and the density ρ_0 are known, and so the node parameter $\{P^{(001)}\}_k$ can be determined algebraically, using Eq. (10).

$$\{P^{(001)}\}_k = \rho_0 g_z \tag{10}$$

By this initial setting, the system is maintained stable, and ∇P triggers the dam breaking problem, as is shown for example in Fig. 7.

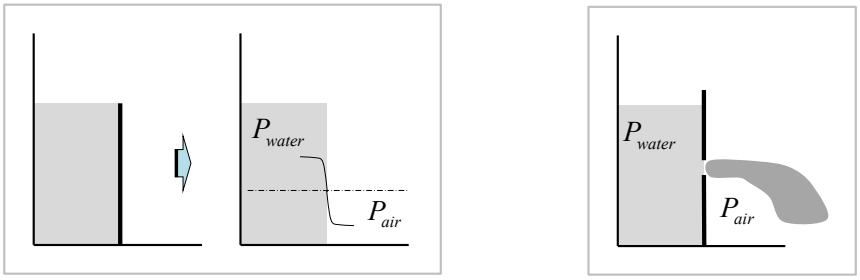

Figure 7 Dam breaking and discharge

4.4 Momentum conservation excluding source and charge

The Navier–Stokes equation is resolved on the time step *n*-section by iteration, through the weighted residual method.

The scheme can be explained better by dividing it into step groups. In the first step group, elements $\nabla\phi$, ρ, ∇P, $\nabla \boldsymbol{\Phi}$ are calculated, and in the second step group, element $\nabla \boldsymbol{\psi}$ is calculated.

The concept of the proposed scheme is explained by Eq. (11) and Eq. (12), where $\boldsymbol{1} \equiv \{1,1,1\}$.

$$\frac{\partial \rho}{\partial t} + \boldsymbol{U} \cdot \nabla \rho + \rho(div \boldsymbol{U}^L + \nabla^2 \phi) = 0 \tag{11}$$

$$\{\rho(\frac{\partial \boldsymbol{U}}{\partial t} + \boldsymbol{U} \cdot \nabla \boldsymbol{U} - \boldsymbol{g}) + \rho_0 \boldsymbol{g} + \nabla P\} - \mu\{\frac{4}{3}\nabla(div \boldsymbol{U}^L + \boldsymbol{1} \cdot \nabla \boldsymbol{\Phi}) - \nabla^2_{curl} \boldsymbol{U}^T\} = 0 \tag{12}$$

Both equations mean to conserve the momentum excluding sourcing and charging into the system.

Eq. (11) excludes sourcing through a continuity equation using $\nabla\phi$.

Eq. (12) excludes external force sourcing using ∇P and internal force sourcing using $\nabla \boldsymbol{\Phi}$. The solenoidal term is unrelated to sourcing.

4.5 Boundary value problems for *iH-d* elements

The *iH-d* element satisfies C^1-continuity. However, the boundary value problem is incompatible with C^1-continuity, because up to 2nd derivative must be determined with other conditions explained in Eq. (13), or by the hybridization method shown in Eq. (14).

$$\beta u + \alpha \frac{\partial u}{\partial n} \quad \vdots \quad \frac{\partial^2 u}{\partial n^2}, \frac{\partial^2 u}{\partial s \partial n}, \cdots \Rightarrow to\ be\ solved\ by\ other\ condition \tag{13}$$

$$\left.\begin{aligned} \beta\theta + \alpha \frac{\partial \theta}{\partial n} = \varphi \quad on\Gamma \quad (\nabla\phi - \theta \Rightarrow 0 \quad in\Omega) \\ \beta\Lambda + \alpha \frac{\partial \Lambda}{\partial n} = \vartheta \quad on\Gamma \quad (\nabla\theta - \Lambda \Rightarrow 0 \quad in\Omega) \end{aligned}\right\} \tag{14}$$

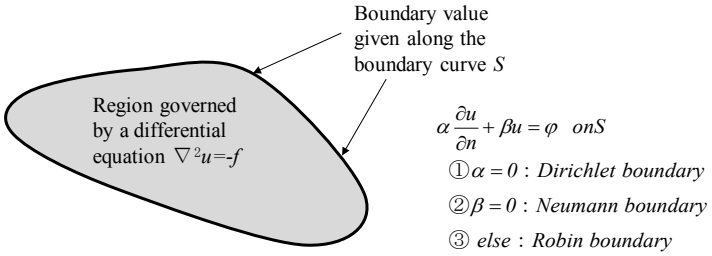

Figure 8 The boundary value problem

Thus (according to the former), the twist parameter is varied on the vertex in order to minimize the twist value in the element shown in Eq. (15) ($\{\phi^{(11)}\}_k$: free on the boundary).

$$\int_{\Omega} \phi^{(11)} \cdot \frac{\partial \phi^{(11)}}{\partial \{\phi^{(11)}\}_k} d\Omega = 0 \tag{15}$$

Eq. (15) is represented in the 2D case. Up to the 2nd derivative can be varied, but the constraint condition is represented as ($\phi^{(11)} \Rightarrow 0$) for simplicity.

4.6 The first group step

The node parameters $\{\nabla \phi\}_k$, ρ, $\{\nabla P\}_k$ and $\{\nabla \Phi\}_k$ are obtained from Eq. (16).

$$\left.\begin{aligned}
&① \ \nabla\phi \leftarrow \int_{\Omega} \{(\frac{\partial r}{\partial t} + div\boldsymbol{U}^L)\cdot \boldsymbol{I}^T + \nabla^2_{diag}\phi\}\cdot\delta\nabla^2_{diag}\phi\}d\Omega = 0 \quad (\phi^{(11)} \Rightarrow 0)\\
&② \ \rho : r \leftarrow \int_{CV} \{\frac{\partial r}{\partial t} + div(\boldsymbol{U}^L + \nabla\phi)\}\cdot\delta r\}d\Omega = 0 \quad inCV\\
&③ \ \nabla P \leftarrow \int_{\Omega} \{\rho(\frac{D\boldsymbol{U}^L}{Dt} - \boldsymbol{g}) + \rho_0\boldsymbol{g} + \nabla P\}\cdot\delta\nabla P\}d\Omega = 0 \quad (P^{(11)} \Rightarrow 0)\\
&④ \ \nabla\Phi \leftarrow \int_{\Omega} \{(div\boldsymbol{u}^L\cdot\boldsymbol{I}^T + \nabla\Phi)\}\cdot\delta\nabla\Phi\}d\Omega = 0 \quad (\Phi^{(11)} \Rightarrow 0)
\end{aligned}\right\} \tag{16}$$

4.7 The second step

The node parameters $\{\nabla \boldsymbol{\psi}\}_k$ are obtained from Eq. (17) and the accompanying constraint condition is shown in the 2nd row.

The incremental $\{\nabla \Delta\boldsymbol{\psi}\}_k$: $\Delta\boldsymbol{U}$ are unknown parameters in the simultaneous equation.

$$\begin{aligned}
⑤ \ \nabla\boldsymbol{\psi} \leftarrow & \int_{\Omega} \{\rho(\frac{D\boldsymbol{U}}{Dt} - \boldsymbol{g}) + \rho_0\boldsymbol{g} + \nabla P - \mu(\frac{4}{3}\nabla div\boldsymbol{U}^L - \nabla^2_{curl}\boldsymbol{U}^T)\}\cdot\delta\nabla\boldsymbol{\psi}\ d\Omega\\
& + \int_{\Omega} \{\frac{1}{\Delta t}(\Delta\boldsymbol{U}^L - \nabla\phi) + \nu\frac{4}{3}(\nabla_{diag}\Delta\boldsymbol{U}^L - \nabla\Phi)\}\cdot\delta\nabla\boldsymbol{\psi}\ d\Omega = 0 \quad (\psi_i^{(11)} \Rightarrow 0)
\end{aligned} \tag{17}$$

$$where\ \boldsymbol{U}^m = \boldsymbol{U}^{m-1} + \Delta\boldsymbol{U} \quad (m = 0,1,2,3,\cdots)$$

①～⑤ are iterated until converged.

4.8 Gauge for *iH-d* scheme

$\nabla \boldsymbol{\psi}$ have ninedegrees of freedom. Therefore, nine equations are needed to obtain *iH-d* parameters. (Notice; Using the cubic interpolation procedure (CIP), ∇(N.S. eq.) = *0* is solved to obtain $\nabla \boldsymbol{u}$.)

I call the relationship between $\nabla_{curl}\boldsymbol{\psi}$ and $\nabla_{shr}\boldsymbol{\psi}$ "conjugate". $\nabla_{curl}\boldsymbol{\psi}$ is a conjugate variable of $\nabla_{shr}\boldsymbol{\psi}$ and vice versa.

The Eq. (9) supplement constraint condition ($\nabla_{shr}\boldsymbol{\psi} \Rightarrow \boldsymbol{0}$) stabilizes the numerical calculation. I call this conditions also "gauge".

To calculate $div\boldsymbol{u}$, a gauge ($\nabla_{imi}\boldsymbol{u} \Rightarrow \boldsymbol{0}$) is necessary, as seen in Eq. (18) and Eq. (19); a novel operator ∇_{imi} is defined in Eq. (19).

$$2div\boldsymbol{u} = 2(\frac{\partial u}{\partial x}+\frac{\partial v}{\partial y}+\frac{\partial w}{\partial z}) = (\frac{\partial u}{\partial x}+\frac{\partial v}{\partial y})+(\frac{\partial v}{\partial y}+\frac{\partial w}{\partial z})+(\frac{\partial w}{\partial z}+\frac{\partial u}{\partial x}) \tag{18}$$

$$\boldsymbol{1}\cdot\nabla_{imi}\boldsymbol{u} \equiv (\frac{\partial u}{\partial x}-\frac{\partial v}{\partial y})+(\frac{\partial v}{\partial y}-\frac{\partial w}{\partial z})+(\frac{\partial w}{\partial z}-\frac{\partial u}{\partial x}) \tag{19}$$

5 PARTICULARITY OF 2D MODEL

To ensure the above 2D scheme is necessary condition to ensure the 3D calculations.

The Helmholtz decomposition (Eq. (3)) for < x−y > 2D can be represented in Eq. (20) using the suffices (*i = 1, 2, 3*), (*i + 1 = 2, 3, 4*), and (*i−1 = 3, 1, 2*); also, for < y−z > 2D it is shown in Eq. (21).

$$<x-y>2D\begin{cases} u=\dfrac{\partial\phi}{\partial x}+\dfrac{\partial\psi_3}{\partial y} \\ v=\dfrac{\partial\phi}{\partial y}-\dfrac{\partial\psi_3}{\partial x} \end{cases} \Rightarrow \begin{cases} u_i = \dfrac{\partial\phi}{\partial x_i}+\dfrac{\partial\psi_{i-1}}{\partial x_{i+1}} \\ u_{i+1}=\dfrac{\partial\phi}{\partial x_{i+1}}-\dfrac{\partial\psi_{i-1}}{\partial x_i} \end{cases} \tag{20}$$

$$\Downarrow$$

$$<y-z>2D\begin{cases} v=\dfrac{\partial\phi}{\partial y}+\dfrac{\partial\psi_1}{\partial y} \\ w=\dfrac{\partial\phi}{\partial z}-\dfrac{\partial\psi_1}{\partial y} \end{cases} \Leftarrow \begin{cases} u_{i+1} = \dfrac{\partial\phi}{\partial x_{i+1}}+\dfrac{\partial\psi_i}{\partial x_{i+2}} \\ u_{i+2}=\dfrac{\partial\phi}{\partial x_{i+2}}-\dfrac{\partial\psi_i}{\partial x_{i+1}} \end{cases} \tag{21}$$

We can express it in the same way also for < z−x > 2D. 3D can be expressed by summation of these equations. Thus, it is sufficient by the explanation for 2D.

However, in 2D, $\nabla_{diag}\boldsymbol{\psi}$ cannot be applied, because ψ_1 and ψ_2 are lacking in $\nabla_{curl}\boldsymbol{\psi}$.

It must be remembered that the 2D model calculates 3D, and the axisymmetric 1D model do also 3D.

Accordingly, the 2D model can be used to represent 3D by introducing the *z*-axis shown in Eq. (22).

$$\left.\begin{aligned}\psi_1 &= g_{1,(x,y)} + z \cdot g_{2,(x,y)} \\ \psi_2 &= h_{1,(x,y)} + z \cdot h_{2,(x,y)}\end{aligned}\right\} \tag{22}$$

Nevertheless, it must also be remembered that the integrals of the odd functions $z \cdot g_2$' are zeros.

The vertex stretching terms also appear by introducing the z-axis; theoretically, these stretching terms are zeros in 2D. This means that the *iH-d* scheme using Eq. (22) satisfies [stretching terms=***0***], numerically.

6 CONCLUSIONS AND FUTURE WORKS

- The biggest merits of MPS are that it conserves mass perfectly, and is not affected by the existence of surfaces. Conversely, these are the week points of FEM.
- One of the characteristics of FEM is that it can be used for calculations without angular momentum terms.
- I proposed in this paper an MPS-FEM fusion method that incorporates the advantages of both models.
- I interpret MPS as a sort of density method for a moving surface.
- Accordingly, the fusion method may be used for compressible flow calculations.
- I apply here the *iH-d* elements and scheme.
- Going further, in my future work, I am going to finish developing an adoptive scheme for maintaining a tetrahedral element by sub-division of a particle.
- The numerical verifications are also going to be conducted in the near future.
- The forced cavity must be chosen as a benchmark test problem to verify the results of this paper.

REFERENCES

[1] K. Sugihara and J. Imamura, *Stress analysis by non-equidistant finite difference method (4th paper)*, Transaction of AIJ, vol.178, pp. 17-24, (1970).
[2] J. Imamura and T. Tanahashi, *Improved HSMAC method: An improvement based on Helmholtz-Hodge theorem*, Transaction of JSCES, Paper No. 20100010, (2010).
[3] M. Kondo, *Angular momentum conserving particle method for high viscos fluid calculation*, Proceedings of the conference on computational engineering and science, vol. 22, JSCES, 2017
[4] J. Imamura, *Proposal of improved Helmholtz-decomposition and the finite element, and application to fluid and solid*, vol. 22, JSCES, 2017
[5] J. Imamura, *Helmholtz-decomposition of solid, and study on Eulerian solution*, vol. 22, JSCES, 2017
[6] J. Imamura, *Concept of fusional method of MPS and FEM through non-equidistant finite difference method*, vol. 22, JSCES, 2017
[7] A.E.H. Love, *A treatise on the mathematical theory of elasticity*, Dover Publications, 1926
[8] Y.C. Fung, *Foundation of solid mechanics*, Prentice-Hall, 1965

V International Conference on Particle-based Methods – Fundamentals and Applications
PARTICLES 2017
P. Wriggers, M. Bischoff, E. Oñate, D.R.J. Owen, & T. Zohdi (Eds)

A STUDY OF PRINCIPLE STRESS ROTATION ON GRANULAR SOILS USING DEM SIMULATION OF HOLLOW CYLINDER TEST

B. FARHANG[1], A. A. MIRGHASEMI[2]

[1] Benyamin Farhang, Ph.D. Candidate of Soil Mechanics and Foundation Engineering
School of Civil Engineering, College of Engineering, University of Tehran, Tehran, Iran
E-mail: b.farhang@ut.ac.ir

[2(✉)] Ali Asghar Mirghasemi, Professor of Soil Mechanics and Foundation Engineering
School of Civil Engineering, College of Engineering, University of Tehran, Tehran, Iran
E-mail: aghasemi@ut.ac.ir

Key words: Discrete element method, Granular soils, Hollow cylinder apparatus, principal stress rotation.

Abstract. This study presents a numerical modelling of HCT (Hollow Cylinder Test) using DEM (Discrete Element Method) by developing of TRUBAL code on granular soils. Due to high expenditures of HCT, a verified numerical modelling of this test was developed. In addition, this numerical model can be used to address the gap in understanding the relationship between the particle-scale interactions and the overall material response. In the introduced numerical model (HCTBALL), plane and cylindrical walls were defined to apply the boundary forces and stresses. Also, an efficient method was presented to apply the torque. The displacements of inner and outer walls were interdependent while applying the torsion to control the intermediate principal stress parameter (b). To verify the model, the results of experimental hollow cylinder tests on Firoozkooh sand under monotonic loading and drained condition were employed. Therefore, the simulations were compared qualitatively with experiments to verify the presented model. It is observed that the deviatoric stress at failure, increased with a decreasing rate by increasing the confining pressure. By increasing the rotation angle of principal stress direction, the difference between deviatoric stresses in specific confining pressures was decreased.

1 INTRODUCTION

This paper presents a numerical modelling of HCT using DEM by developing of TRUBAL code (Cundall, 1989 – Aston Version) on granular soils under monotonic loading and drained condition.

Soils, usually show anisotropic behavior that depends on their structure (inherent and induced formation history) and environmental factors. These environmental factors (seismic loads, traffic, sea waves and etc.) cause principal stress rotation which plays an important role in soils behaviour and ignoring this factor may cause an insecure design of geotechnical structures. The hollow cylinder apparatus is a versatile testing device widely employed to investigate the constitutive behavior of soils under generalized stress conditions, including principal stress rotation, anisotropy and non-coaxiality [1, 2]. Saada et al. [3, 4] pioneered the

use of HCA for investigating the effects of principal stress rotation in sands and clays. Several theoretical and experimental research have been carried out on the rotation of principal stress directions and its importance in soil response by researchers [1, 2, 5-7]. The HCA is able to apply a torsion and therefore a shear stress in the soil sample which results in the principal stress axis rotations.

Regarding all the capabilities, with HCT and all the other experimental tests, the micromechanical parameters of soils cannot be investigated and there could be some limitations to change the testing conditions quickly and effortlessly. DEM can solve this problems and could be used as a virtual laboratory to fill the gap in understanding the relationship between the particle-scale interactions and the overall material response. It is a numerical tool that can be used to address this gap, because the particle-scale interactions which cannot be measured in laboratory tests, can easily be monitored in "virtual" tests [8]. This method firstly used by Cundall [9] to simulate progressive large-scale movements in blocky rock systems. BALL was extended to an early version of TRUBAL by Cundall and Strack that used linear spring contact laws. Cundall extended the above early version of TRUBAL [10]. In this version, nonlinear contact laws are used.

Thereafter, various research were carried out to develop the TRUBAL code for different studies. Dorostkar and Mirghasemi [11] extended the TRUBAL code to calculate the anisotropy parameters of particles in micro scale. Recently, numerical simulations of hollow cylinder test have been carried out using PFC3D software by Li, et al. to investigate the propagation of shear band in granular soils [12, 13]. In the current study, the three-dimensional simulation of the HCT was done by developing TRUBAL code to investigate the shear strength parameters of granular soils with the ability to control the intermediate principle stress parameter b. This parameter plays an important role in the behavior of soils. Numerical simulations were carried out with drained and monotonic loading conditions. To verify the presented numerical simulation, the results of experimental drained hollow cylinder tests on Firoozkooh sand under monotonic loading conditions [14] were used.

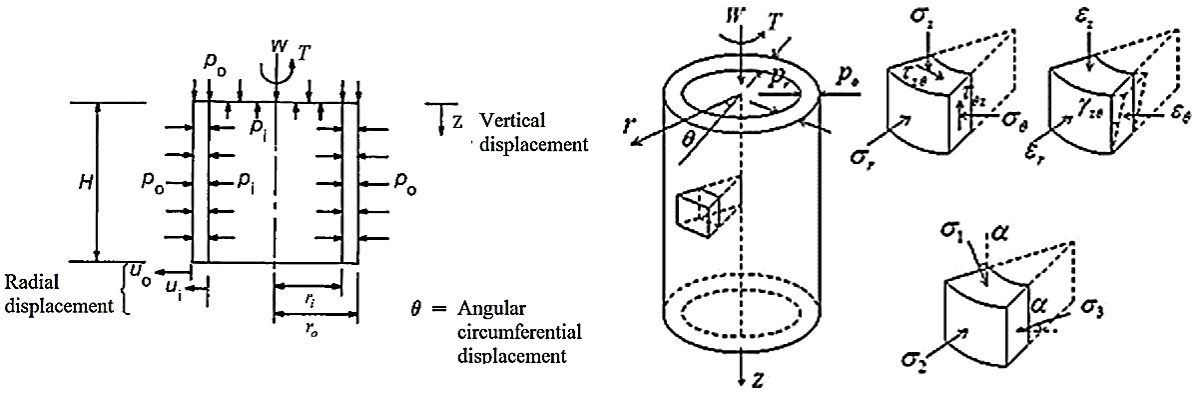

Figure 1: Forces acting on the hollow cylinder specimen [7, 12]

2 HOLLOW CYLINDER TEST

The HCA, allows independent control of the magnitudes of principal stresses and their directions (α). Figure 1 shows the idealized stress condition in a hollow cylindrical element subjected to the axial load (W), torque (T), internal pressure (P_i) and external cell pressure (P_o).

During shearing, the torque (T) applies shear stresses ($\tau_{\theta z} = \tau_{z\theta}$) in the horizontal plane of the sample. The axial load (W), applies the vertical stress (σz), and Pi and Po control the radial and circumferential stresses (σ_r and σ_θ). Hight et al. [7] proposed equations for the average stress and strain calculations for the HCA. These are the same as those in Yang et al. [15].

3 SIMULATION USING DEM

In this study, the three-dimensional simulation of the HCT was done by developing the ASTON version of TRUBAL code named GRANULAR (Derived from Cundall's DEM Code Trubal Version 1.51: 9 May 1989) to investigate the mechanical behavior of granular soils with the ability to control the intermediate principle stress parameter b. Numerical simulations were carried out with drained and monotonic loading conditions.

To calculate the particle-particle and particle-wall normal contact forces, Hertzian model and for the tangential contact forces, Mindlin and Deresiewicz model [16] were used. The details and algorithms of contact forces, torsional force calculations and the procedure of intermediate principal stress parameter control are beyond the scope of this paper.

In this study, 4500 particles were generated randomly with five different diameters of 4, 5, 6, 7 and 8 mm. The specimen geometry was chosen in a way [7, 17] to minimize the effect of non-uniformity. Dimensions of test specimens used for simulations were 200 mm length hollow cylinders having a 20 mm thickness, 60 mm inside and 100 mm outside diameters. Also, these dimensions were the same as the experimental dimensions [14] used to verify the DEM results. At this study, rigid walls were defined to apply the boundary forces. These walls were defined in plane and cylindrical shapes. The coefficient of friction for both inner and outer cylindrical walls were set to zero to allow the boundary particles freely move in contact with boundaries.

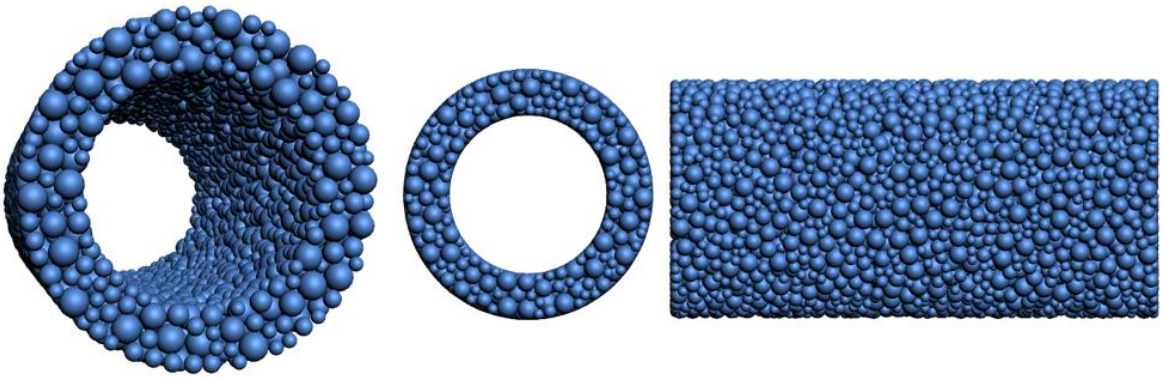

Figure 2: Final model after the isotropic compaction phase and before the deviatoric loading phase

Gravity was set to zero during the entire simulation procedure. Axial force was applied using the upper plane-wall and radial forces were applied using the inner and outer cylindrical walls. Walls can be operated independently from each other and have the ability to move strain-controlled or stress-controlled (servo-control). Also, as previously described, to control the intermediate principal stress parameter (b) while applying the torsion, the inner and outer stresses were dependent to each other. It should be noticed that periodic boundaries cannot be used when using the walls. Figure 2 shows the final model after the isotropic compaction phase and before the deviatoric loading phase. All samples in this stage had an initial void ratio “e” of 0.7 and simulations were carried out as shown in Table 1.

Table 1: Data table of simulation tests

Parameters	Value
Confining Pressure P'_0 (KPa)	200 400 600 800 1000
α (°)	0.0 15.0 30.0 45.0

To apply the torque (T), particles which were adjacent to the upper plane wall, were used. The upper plane wall applies the vertical force as well. In deviatoric stress application phase, all walls with the stress servo control mode and a limited velocity, were commenced to move. This limited velocity value is determined by the unbalanced force ratio of particles in the system. A small magnitude of ξ =10-3 was shown to be adequate.

4 VERIFICATION

To verify the model, the results of experimental hollow cylinder tests on Firoozkooh sand [14] under monotonic loading and drained condition were employed. There are still some limitations in this study such as spherical particles were used for simplicity which could not consider the effects of particle shape. Also the gradation of granular soil and its material properties which is employed in the numerical model, is not the same as used in experiments. Therefore, the results presented here, are compared qualitatively.

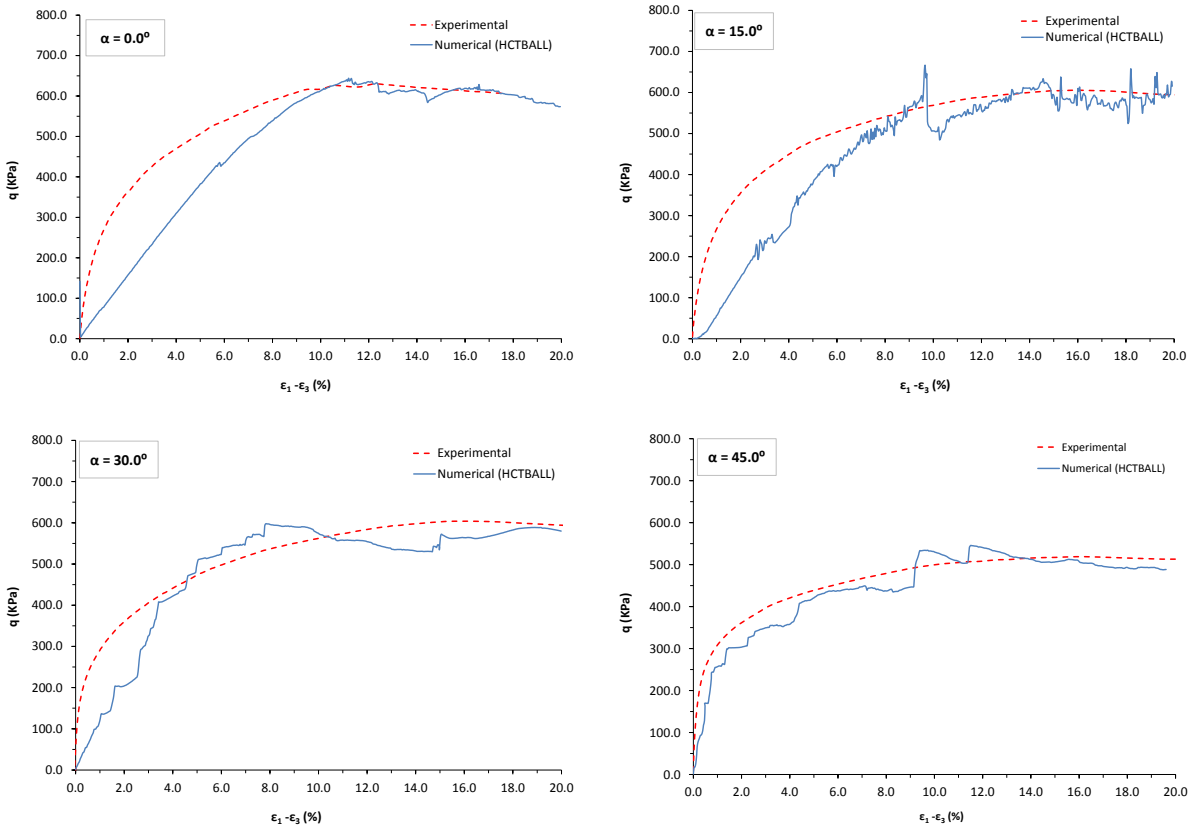

Figure 3: Comparing the experimental and numerical results of deviatoric stress-strain response in a hollow cylinder specimen with P'_0 = 200 KPa, b = 0.0 and different α angles

Comparing the presented model and experimental results according to Figure 3, it is shown that there was a close association between this model and the experiments. Also, α value was controlled during each test as shown in Figure 4. It is shown that there is a good control of α value in the numerical simulations.

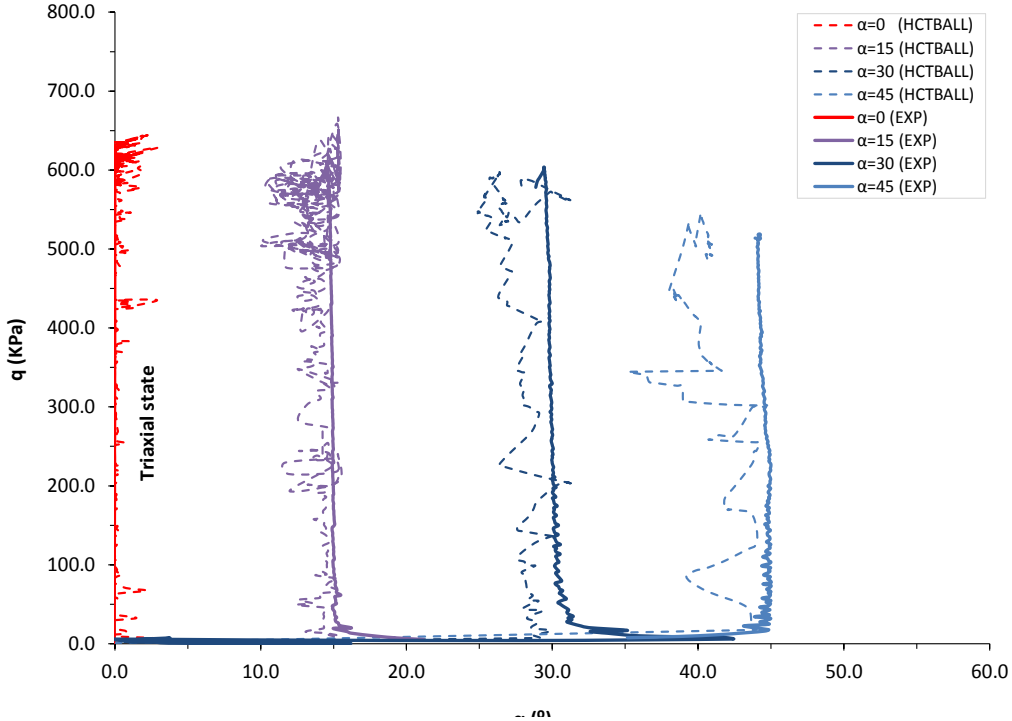

Figure 4: Comparing the experimental and numerical results of deviatoric stresses in a hollow cylinder specimen with different α angles and P0 = 200 KPa

5 RESULTS

Numerical results of deviatoric stresses in a hollow cylinder specimen with different confining pressures for different α angles are shown in Figure 5. It is observed that the deviatoric stress increased with a decreasing rate by increasing the confining pressure in different α values. As α was increased, the difference between deviatoric stresses with different confining pressures was decreased. The results of deviatoric stress values are summarized in Table . It is observed that by increasing P'0, the difference between deviatoric stresses, were increased as shown in Figure 6.

Table 2: Deviatoric stress values (q) for numerical simulations

	α = 0.0°	α = 15.0°	α = 30.0°	α = 45.0°
P'₀ = 200 KPa	574	615	575	488
P'₀ = 400 KPa	1153	1092	836	702
P'₀ = 600 KPa	1612	1492	1200	898
P'₀ = 800 KPa	2113	1928	1251	1182
P'₀ = 1000 KPa	2599	2122	1554	1427

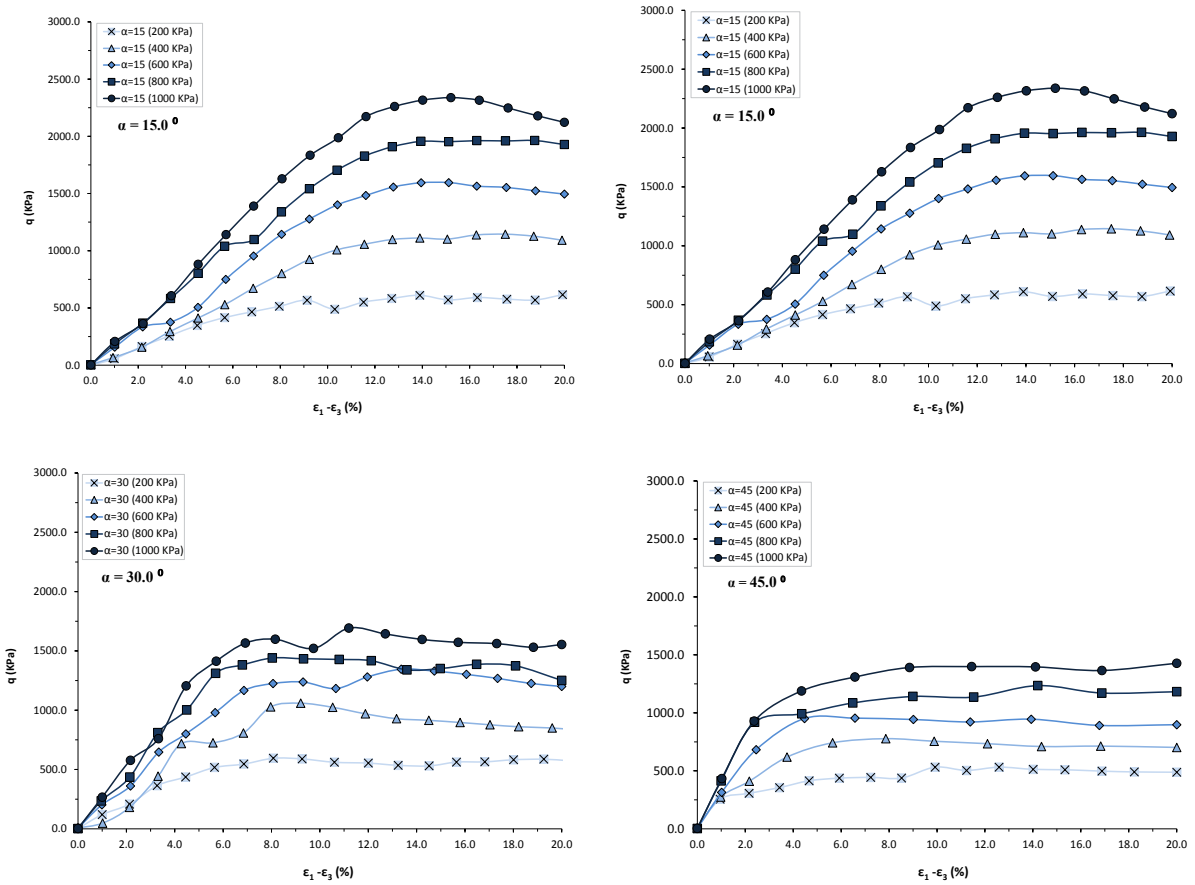

Figure 5: Numerical results of deviatoric stress versus axial strain in a hollow cylinder specimen with different P_0 for b = 0.0 and α angles of 0.0, 15.0, 30.0 and 45.0 degrees

6 CONCLUSION

The results reported in this paper, illustrated that the presented numerical model is a proper tool to study the effects of principal stress rotation on granular soils and the stress-strain behavior of granular media was presented.

It was observed that the deviatoric stress at failure, increased with a decreasing rate by increasing the confining pressure. By increasing the rotation angle of principal stress direction, the difference between deviatoric stresses in specific confining pressures was decreased. Moreover by increasing the confining pressure, the difference between deviatoric stresses in specific α values, were increased.

In this paper it was shown that it is possible to obtain the essential features of the mechanical behavior of granular materials under complex stress state by using DEM.

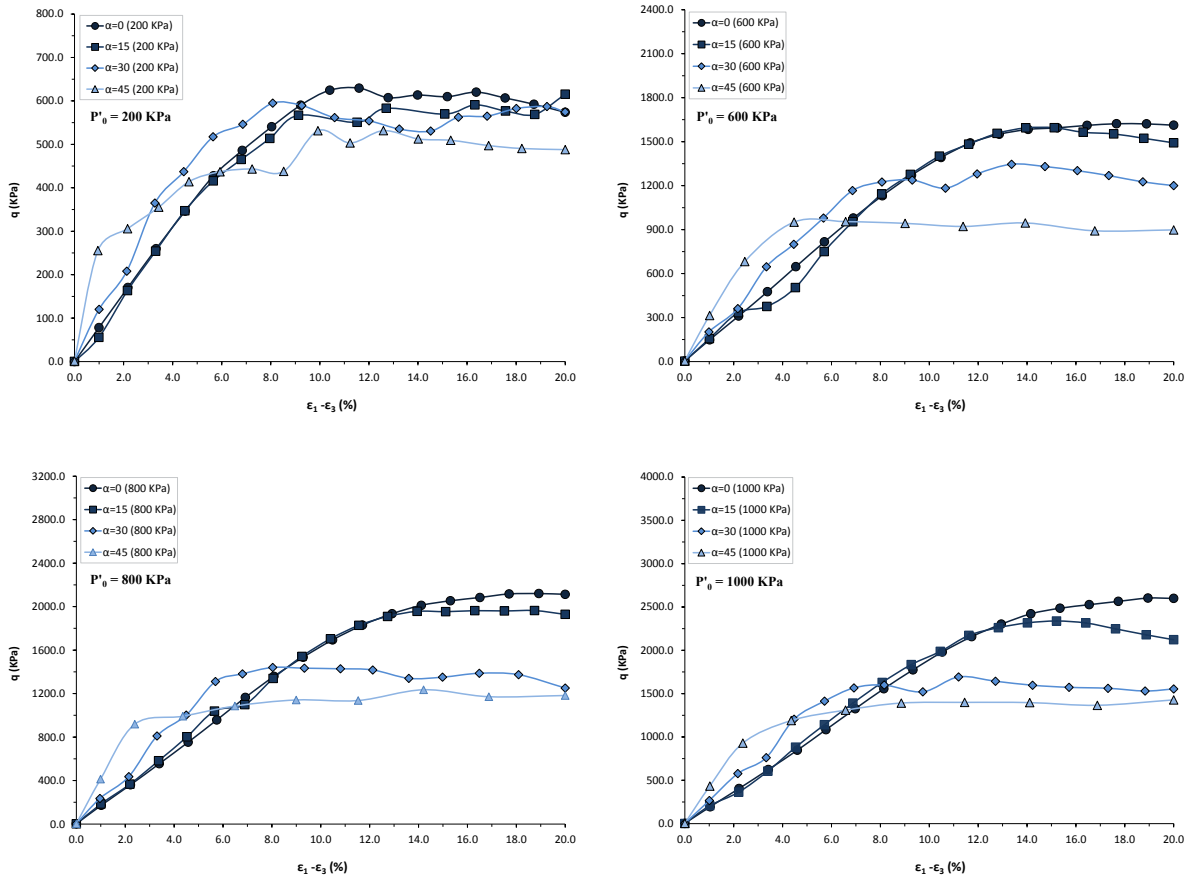

Figure 6: Numerical results of deviatoric stress versus axial strain in a hollow cylinder specimen with different α angles for P_0 of 200, 600, 800 and 1000 KPa

REFERENCES

[1] Symes MJPR, Gens A, Hight DW. Undrained anisotropy and principal stress rotation in saturated sand. Géotechnique. 1984;34(1):11-27.

[2] Gutierrez M, Ishihara K, Towhata I. FLOW THEORY FOR SAND DURING ROTATION OF PRINCIPAL STRESS DIRECTION. Soils and Foundations. 1991;31(4):121-32.

[3] Saada A, Townsend F. State of the art: laboratory strength testing of soils. Laboratory shear strength of soil, ASTM STP. 1981;740:7-77.

[4] SAADA AS. Hollow cylinder torsional devices: their advantages and limitations. ASTM special technical publication. 1988977):766-95.

[5] Symes M, Gens A, Hight D. Drained principal stress rotation in saturated sand. Geotechnique. 1988;38(1):59-81.

[6] Naughton PJ, O'Kelly BC. Stress non-uniformity in a hollow cylinder torsional sand specimen. Geomechanics and Geoengineering. 2007;2(2):117-22.

[7] Hight DW, Gens A, Symes MJ. The development of a new hollow cylinder apparatus for investigating the effects of principal stress rotation in soils. Géotechnique. 1983;33(4):355-83.

[8] O'Sullivan C. Particle-based discrete element modeling: geomechanics perspective. International Journal of Geomechanics. 2011;11(6):449–64.
[9] Cundall PA. The measurement and analysis of accelerations in rock slopes: Imperial College London (University of London), 1971.
[10] Cundall P. Computer simulations of dense sphere assemblies. Micromechanics of granular materials. 1988;4:113-23.
[11] Dorostkar O, Mirghasemi AA. Micro-mechanical study of stress path and initial conditions in granular materials using DEM. Computational Particle Mechanics. 2015:1-13.
[12] Li B, Zhang F, Gutierrez M. A numerical examination of the hollow cylindrical torsional shear test using DEM. Acta Geotechnica. 2015;10(4):449-67.
[13] Li B, Guo L, Zhang F-s. Macro-micro investigation of granular materials in torsional shear test. Journal of Central South University. 2014;21(7):2950-61.
[14] Romiani HM. Evaluation of Inherent and Induced Anisotropy of Sandy Soils Using Hollow Torsion Apparatus. Tehran - Iran: IUST (Iran University of Science and Technology), 2014.
[15] Yang Z, Li X, Yang J. Undrained anisotropy and rotational shear in granular soil. Geotechnique. 2007;57(4):371-84.
[16] Mindlin RD, Deresiewicz H. Elastic spheres in contact under varying oblique forces. ASME J Appl Mech. 1953;20:327-44.
[17] Sayao A, Vaid Y. A critical assessment of stress nonuniformities in hollow cylinder test specimens. Soils Found. 1991;31(1):60-72.

V International Conference on Particle-based Methods – Fundamentals and Applications
PARTICLES 2017
P. Wriggers, M. Bischoff, E. Oñate, D.R.J. Owen, & T. Zohdi (Eds)

COMPARISON OF TWO DEM STRATEGIES FOR MODELLING CORTICAL MESHES

F. GABRIELI[1], A. POL[1] AND K. THOENI[2]

[1]ICEA department
University of Padova
via Ognissanti 39
35129 Padova (Italy)
fabio.gabrieli@unipd.it

[2]Centre for Geotechnical Science and Engineering
University of Newcastle
Callaghan, NSW 2308, Australia

Key words: DEM, YADE, Remote Interaction, Cylinder, Grid.

Abstract. This work deals with the particle-based modelling of cortical wire meshes. Such meshes are being used in many engineering applications but their modelling is particularly complex because of the common large displacement serviceability conditions, the chance of localized failures, and the intrinsic geometrical and mechanical anisotropies. The discrete element method has proved to be an excellent numerical tool for the investigation of such structures. Here, two modelling strategies are compared using a wire-node description and a wire-cylinder description: in the first the wire mesh is described by a collection of spheres at nodes linked by long-range interaction forces, in the second the wires are represented by means of interconnected cylinders. The force-displacement constitutive model of the interactions is calibrated based on specific tensile tests. The comparison is performed on results of tensile tests and punch tests on a reference mesh panel.

1 INTRODUCTION

Metallic cortical wire meshes are currently being used in many engineering applications, especially for the mitigation of the rockfall hazard along slopes and for protection of people and infrastructures. They wrap rock cliffs or steep soil slopes supporting the horizontal and tangential stresses which arise from the weathering of the shallow layers. The evaluation of the contact and the stress distribution between these structures and the backfill material as well as the knowledge of the strain behaviour of these meshes is relevant for their correct design.

These structures are constituted by ordered intersections of steel wires and cables generally having a ductile mechanical behaviour. The complex geometries and pattern of the wires, their different material properties, and the existence of non-trivial boundary conditions make these structures difficult to be modelled as simple continuum membranes. Moreover, their high deformability and the chance of local ruptures in the mesh make the numerical modelling of such structures very challenging. One of the approaches for efficiently simulating these structures is the discrete element method (DEM) which is particularly well suited to treat high

deformable problems including discontinuities and complex failure modes [1]. The DEM approach also allows to efficiently handle the mechanical behaviour at the contact between these meshes and other elements.

This work shows a comparison of two different discrete element modelling strategies for the simulation of a double-twisted hexagonal wire mesh. The first one represents the wire mesh as a collection of remote interactions. The second strategy, describes each wire of the mesh in a more realistic way as a collection of interconnected cylindrical elements. The two modelling strategies are applied to a tensile test and a punch test and the results are compared.

2 THE WIRE-NODE APPROACH

In the first model, each node of the mesh is represented by a fictitious spherical particle that concentrates the mass of the related wires, while the wires are substituted by long-range tensile interaction forces having zero mass and no shape (Figure 1a). This representation permits to efficiently decrease the computational effort in terms of contact detection and rigid body dynamic [2,3]. The approach has been successfully applied to the modelling of large scale drapery systems [4].

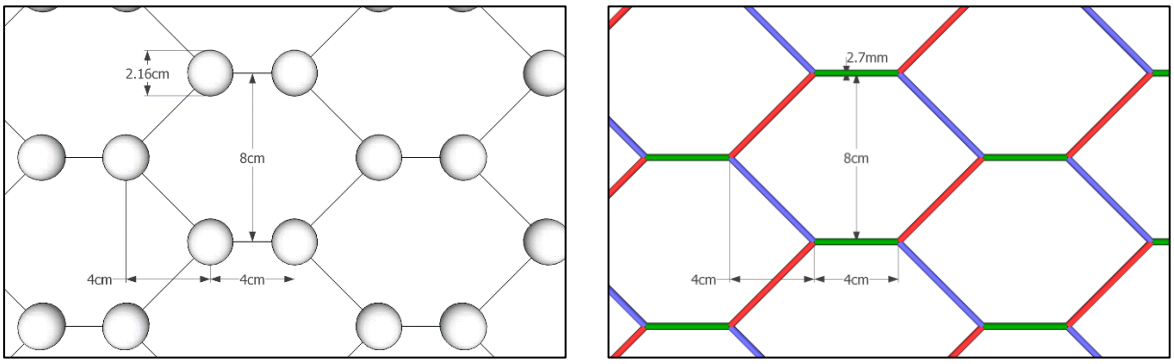

(a) (b)

Figure 1: Sketch of the (a) wire-node approach and (b) wire-cylinder approach.

The density of these nodal particles is calibrated to match the total mass of the mesh panel while, for arbitrary convention, their radius is fixed equal to 4 times the single wire diameter. In this way the inertial properties of the mesh are correctly conserved also for analyzing dynamic problems like impacts. These nodal particles generally cannot touch one each other (this probability is very low in well-posed boundary problems like the one presented here), while contacts between the particles and other external elements are permitted to study the interaction of the mesh with other bodies and surfaces.

The long-range contact forces between nodal particles have been implemented in the model on the basis of laboratory results of single wire and double-twist tensile tests [2]. These stress-strain curves were implemented in the long-range constitutive interaction model by using a piecewise linear approximation. Only tensile forces are allowed as the wires would generally buckle under compression.

In Figure 2, the tensile constitutive models for single wire and double-twisted wire are depicted.

It can be seen that the single wire interaction law has a higher initial stiffness compared to the one of the double-twisted wire as well as a higher maximum tensile elongation.

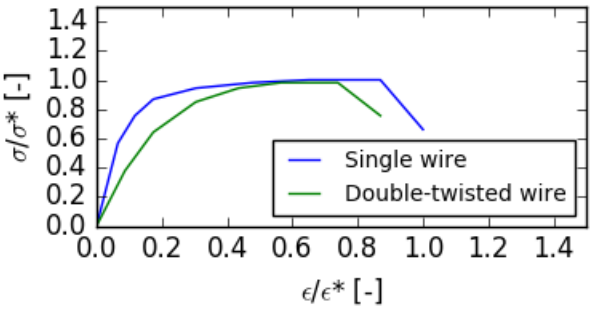

Figure 2: Normalized stress-strain tensile curves for the wires of the double-twisted wire mesh.

Two methods have been used to assign the constitutive model at each wire type [2]: a deterministic model and a stochastic one. The deterministic model uses the same two interaction laws previously described for the two wire types. In the second approach, instead, the two piecewise curves are corrected with a stochastically distorted wire model which is used to model the variability of mechanical and geometrical properties in the wire mesh. The two parameters controlling this second model are λ_u, which defines an initial horizontal shift for the force-displacement curve, and λ_F, which modifies the stiffness of the wire in the shifted part. These parameters mostly act on the mechanical behavior of the first phase of the tests, during the initial tensile deformations, when the hexagons are geometrically distorted. Indeed, during this phase, single and double-twisted wires are stretched from completely unloaded conditions showing an initial softer tensile response which leads to a horizontally shift of the force-displacement curves.

2 THE WIRE-CYLINDER APPROACH

In the second approach, interconnected rigid cylinders [5] with a diameter of the single wire are used to represent single and double-twisted wires (Figure 1b). The connections between these cylindrical elements are represented by perfect hinges. As in the previous model, the mechanical response of the wire-cylinder is calibrated only on the basis of tensile laboratory tests performed on samples of single wires and double-twisted wires. Differently from the previous model, these solid bodies have a physical shape, similar to the real one, and they may experience contact with other bodies along the cylindrical wire lateral surface. The contact between a single wire-cylinder and other elements (spheres, cylinders, pfacets) is treated with a hierarchical strategy that finally reduces to only two types of contact: sphere-sphere or sphere-plane. In our case, only normal forces between these bodies are considered while frictional tangential forces have been set equal to zero (i.e. mimicking a frictionless mesh). In Figure 3, the contact between a hypothetic wire and two facets (or pfacets) of an idealized body is depicted comparing the two approaches. With regards to the mesh, it is clear that the contact with angular bodies as well as the interception of small particles may be better described with the wire-cylinder approach but the price to be paid for the improved realistic representation is the higher computational effort. This particular aspect will be further discussed in Section 5.

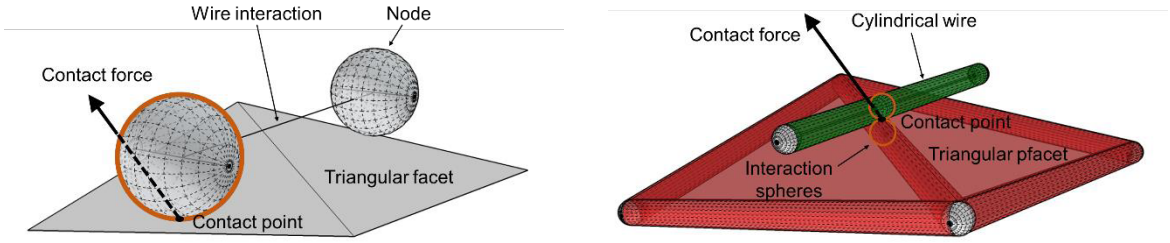

(a) (b)

Figure 3: Sketch of the contact between two facets and one wire using the (a) wire-node approach and (b) wire-cylinder approach.

Wire-cylinder elements could potentially handle bending and twisting moments at nodes like elastic perfectly plastic beams [6] but this option was not considered to allow a clear comparison with the first model.

3 TENSILE TEST

The two approaches are tested with reference to a tensile test on a rectangular mesh panel of size 36x92cm. Details about the setup and the procedure of this experiment can be found in [2]. In Figure 4, the mesh panel used is depicted, while boundary conditions applied at the nodes are marked with red triangles and blue dots.

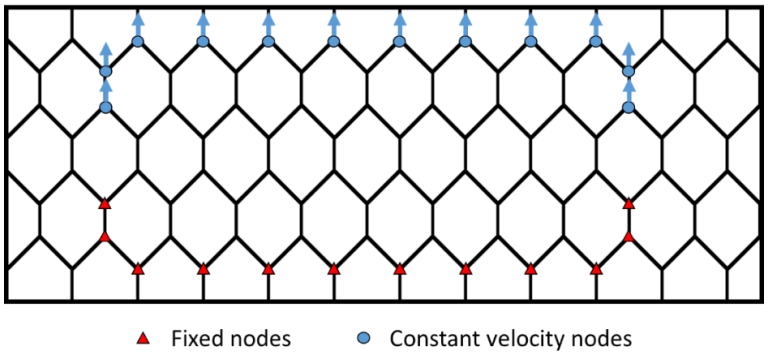

Figure 4: Sketch of the mesh sheet used in the tensile test with the imposed nodal boundary conditions.

The results of the deterministic and stochastic model using the two approaches are depicted in Figure 5 and compared with the experimental result. It is clear that the deterministic model of the wire is not able to reproduce the response of the mesh panel, while the stochastic one, after calibration, is in agreement with the laboratory result. The deterministic model, in this case, gives a stiffer response that is not realistic. This is mainly due to the regular geometry of the numerical mesh and to the perfect rigidity of the boundary conditions (constraints) in the numerical model as well. Instead, the introduction of some geometrical irregularities leads to a less rigid behavior of the mesh panel in the initial part of the test which is not reproducible with the deterministic model.

Regarding the comparison of the two approaches, they appear very similar with a little

discrepancy for the stochastic model which is compatible with the intrinsic randomness of the initial geometrical and mechanical conditions.

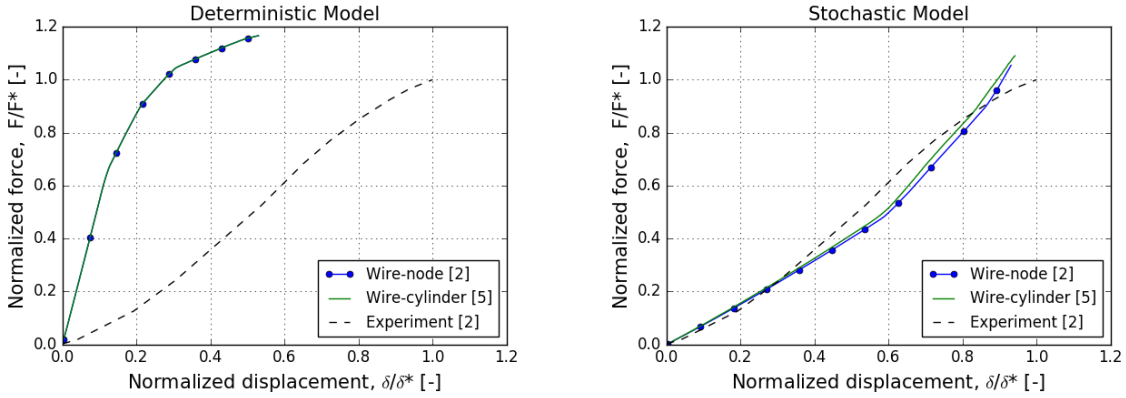

Figure 5: Comparison of wire-node approach and wire-cylinder approach with reference to a tensile test using (a) a deterministic model (b) a stochastically distorted model after calibration.

4 PUNCH TEST

In order to assess the differences of the two approaches with regards to the contact of the wire mesh with other bodies we also considered the results of punch tests where the wires come in contact with the external punching element [3].

The two models have been tested with reference to a 3 x 3 m mesh panel. The punching element is represented by a frictionless spherical cup with a curvature radius equal to $R = 1.2$ m, diameter equal to 1 m and smoothed edges having a curvature radius of $r = 0.05$ m.

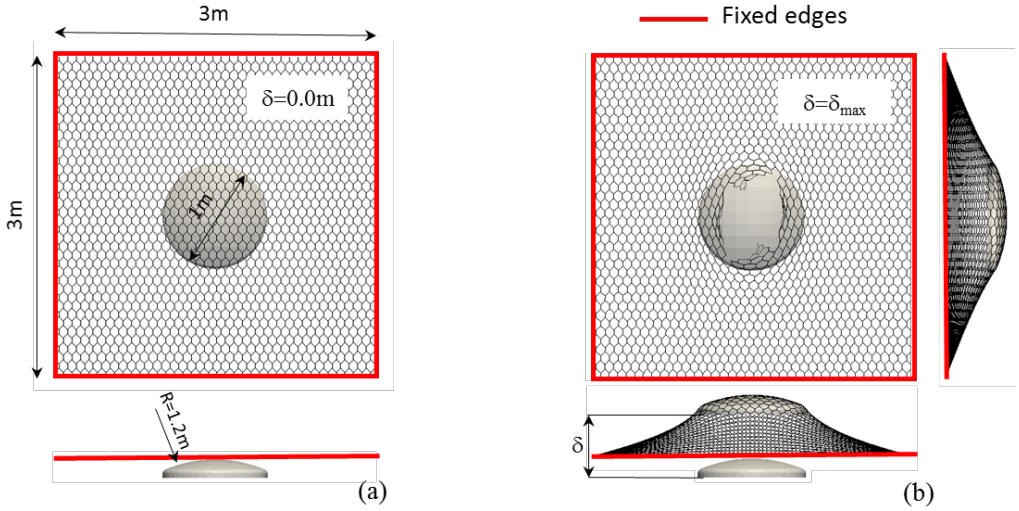

Figure 6: Snapshots of punch test geometry (a) at the beginning of the test and (b) at failure.

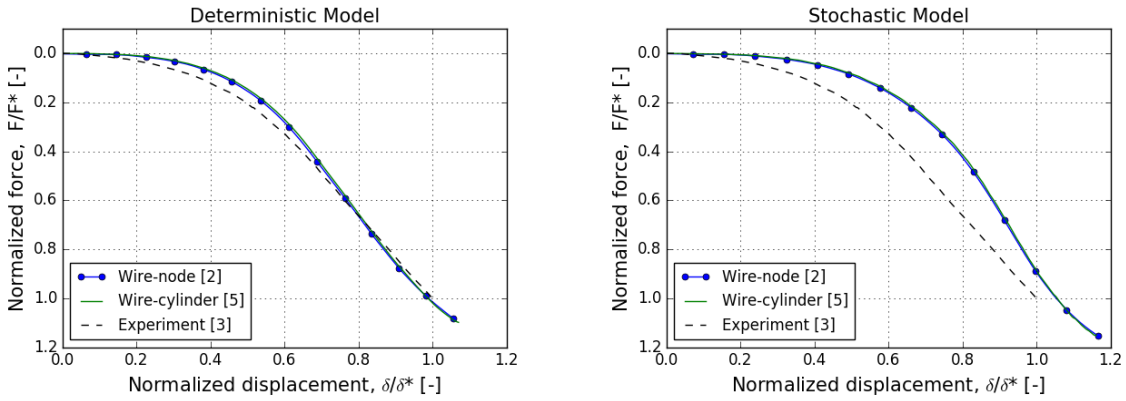

(a) (b)

Figure 7: Comparison of wire-node approach and wire-cylinder approach with reference to the punch test using (a) a deterministic model and (b) a stochastically distorted model after calibration.

Differently from the tensile test, the deterministic and the stochastic models provide approximately the same results: this is also confirmed by the low values of the stochastic parameter λ_u after calibration ($\lambda_u = 0.02$). Moreover, as in the previous test the two approaches resulted approximately equal with small differences which are probably due to the intrinsic randomness linked with the stochastic model and also to the emergence of slightly shifted contact positions and directions.

5 TIMING PERFORMANCE

With regards to the computational performance of the two approaches we compared the computational time of a representative time window of the punch test in the same conditions: same velocity of the punching element, fixed time step $dt = 1.3\text{x}10^{-6}$ s and equal number of time steps.

Figure 8 reports the results of these tests underlining the computational cost of each phase of the DEM algorithm. From the figure we note that the importance, in terms of relative computational time, of the different phases of the DEM algorithm is roughly the same for the two considered approaches. Only a slightly higher influence of the contact detection phase is notable in the wire-cylinder approach than in the other case. Besides that, the total time requests for the computation with the wire-cylinder approach is approximatively equal to 4.5 times the one for the wire-node approach (respectively 1223 s and 266 s).

It is interesting now to focus on the ratio of total time to the total number of bodies. The upper histogram in Figure 8 shows that the computational cost, with reference to the number of bodies, for the wire-cylinder approach (#bodies = 9197) is approximatively equal to 2 times the one required using the wire-node approach (#bodies = 3584). Therefore, the computational time required using the wire-cylinder approach is controlled by the greater number of bodies, as well as by the higher computational complexity of the contact detection ('SortCollider') and forces calculation phases ('InteractionLoop').

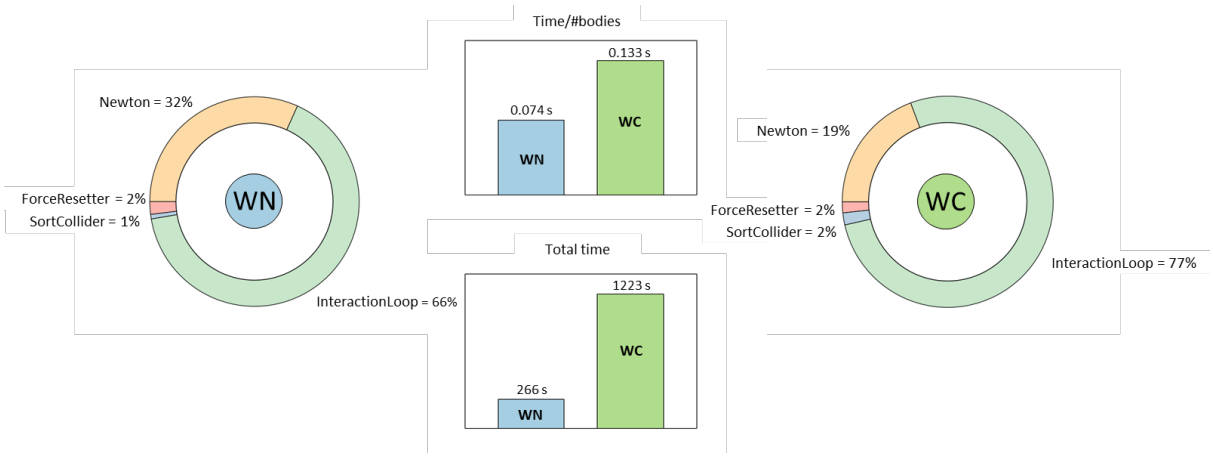

Figure 8: Comparison of (a) wire-node approach (WN) and (b) wire-cylinder approach (WC) with reference to a punch test in terms of computational time. The different phases of the DEM algorithm are split.

6 CONCLUSIONS

In this work the discrete element method has been proved to be an excellent tool to describe the mechanical behavior of wire meshes in quasi-static loading conditions. The good agreement of numerical and experimental results also confirms the potentials of this method for the characterization of the behavior of the mesh in contact with large bodies.

Both the wire-cylinder approach and the wire-node approach applied to the wire mesh representations are proved to be broadly equivalent in terms of the overall mechanical response for what concern tensile and punch tests, with small discrepancies due to the different contact position and direction using the two methods and also to the intrinsic randomness connected with the stochastic model.

The differences in terms of number of bodies to be stored as well as the treatment of contact detection and contact dynamics lead to a higher computational cost of the wire-cylinder approach. The latter appears more suitable to handle the details of realistic contacts with small elements or angular particles especially in mesh-soil embedded conditions, whereas to study problems where the wire mesh interacts with large bodies or without external bodies (as in the tensile test) the wire-node approach allows to obtain a good approximation of the real response with much lower computational costs.

Further investigations are required to study the effect of other parameters like contact friction, and twisting and bending stiffness of the wires with the wire-cylinder approach.

REFERENCES

[1] D. Bertrand, F. Nicot, P. Gotteland and S. Lambert, “Modelling a geo-composite cell using discrete analysis”, *Computers and Geotechnics* 32(8), 564-577 (2005).

[2] K. Thoeni, C. Lambert, A. Giacomini, S.W. Sloan, “Discrete modelling of hexagonal wire meshes with a stochastically distorted contact model”, *Computers and Geotechnics* 49, 158-169, (2013).

[3] A. Pol, F. Gabrieli, K. Thoeni and N. Mazzon, “Discrete element modelling of punch tests with a double-twist hexagonal wire mesh”, J. Corominas, J. Moya, M. Janeras, editors, RocExs 2017 *6th Interdisciplinary Workshop on Rockfall Protection*, 145-148, (2017).

[4] K. Thoeni, A. Giacomini, C. Lambert, S.W. Sloan, J.P. Carter, "A 3D discrete element modelling approach for rockfall analysis with drapery systems", *International Journal of Rock Mechanics and Mining Sciences* 68, 107-119 (2014).
[5] A. Effeindzourou, B. Chareyre, K. Thoeni, A. Giacomini and F. Kneib. "Modelling of deformable structures in the general framework of the discrete element method". *Geotextiles and Geomembranes* 44(2): 143-156 (2016).
[6] F. Bourrier, F. Kneib, B. Chareyre, T. Fourcaud, "Discrete modeling of granular soils reinforcement by plant roots", *Ecol. Eng.*, 61: 646–657 (2013).

V International Conference on Particle-based Methods – Fundamentals and Applications
PARTICLES 2017
P. Wriggers, M. Bischoff, E. Oñate, D.R.J. Owen, & T. Zohdi (Eds)

COUPLED DISTINCT ELEMENT METHOD COMPUTATIONAL FLUID DYNAMICS ANALYSES FOR RESERVOIR LANDSLIDE MODELLING

S. UTILI[1], T. ZHAO[2], GB CROSTA[3],

[1] School of Civil Engineering and Geosciences, Newcastle University,
Drummond Building, Newcastle upon Tyne, United Kingdom
stefano.utili@newcastle.ac.uk

[2]College of Water Resource and Hydropower, Sichuan University,
Chengdu, China
tzhaoslide@outlook.com

[3] Department of Earth and Environmental Sciences, Universita degli studi Milano Bicocca,
Piazza della Scienza 4, 20126 Milano, Italy
giovannibattista.crosta@unimib.it

Key words: Vajont landslide, impulse wave, rapid rockslide, coupled DEM-CFD.

Abstract. The Vajont landslide involved a large mass of rock splashing at high speed into the reservoir which in turn generated a high impulse water that overtopped the dam and swept away the downstream village. In several cases of reservoir landslide, albeit the flood defence structures may remain intact, a catastrophe still occur due to the generation of a ‚tsunami' wave. Since the features of the tsunami wave strongly depend on the physics of the rock splashing and the subsequent rock – water interaction, a numerical tool accounting for such physics is required for predictions to be reliable.

Here, the formulation of a coupled 3D Distinct Element Method (DEM) – Computational Fluid Dynamics (CFD) code used to simulate the rock slide from onset to impact with the reservoir and the subsequent generation of the impulse wave, is presented. To run realistic simulations in an affordable runtime, coarse graining is employed. The main results of quasi 3D analyses in plane strain along two cross-sections representative of the eastern and western slope sectors are presented. The results show to be in broad agreement with the available recorded observations.

1 INTRODUCTION

Landslide generated waves can be major hazards for developed areas on reservoirs, fjords, and lakes because the large mass and kinetic energy of landslides can generate waves that release tremendous forces on surrounding coastal areas and hillslopes. Damage caused by landslide tsunami runup can extend to areas well-above the shoreline, endanger human life, and cause major economic impacts, as indicated by large events that have occurred in recent history. A recent example is the 3 million m3 rockslide impacted Chehalis Lake in British Columbia, Canada, in 2007, generating a wave that stripped vegetation to elevations over 38 m above the shoreline [1,2]. The tsunami left a deposit of woody debris that formed a dam at the lake outlet,

exposing a downstream community to outburst flood hazards and requiring a lengthy and costly debris removal program [2]. [3] have presented a new set of experiments run in the laboratory at reduced scale that together with the theoretical study of [4] provide a first theoretical conceptual framework to study tsunamis generated by granular landslides. From their valuable dimensional analysis, it emerges that several physical parameters affect the generation of the tsunami and behaviours ranging from a wave whose amplitude quickly attenuates completely to a wave that propagates unabated are possible.

Among all the landslide induced tsunamis the most investigated event is indeed the Vajont rockslide [5] which is the object of this paper. The landslide involved approximately 270 million m^3 of rock and generated water waves probably averaging 90 m above the dam crest. 100 and 200 metres high water wave traces were observed along the left and right valley flanks, respectively [6]. The displaced water initially raised along the opposite valley flank and then overtopped the dam flooding successively the downstream village of Longarone, along the Piave river valley, causing more than 2,000 casualties.

Even though parallel computation techniques have been developed, the number of particles which can be simulated on PCs or PC clusters is still far smaller than that typical of real slopes (*e.g.* thousands of billions of grains). To overcome this problem, coarse graining (Sakai et al. 2012) is employed. In this technique, a coarse particle represents a collection of real fine particles. As a result, a large-scale DEM simulation of granular flow can be performed using a relatively small number of calculated particles [7].

The theory and methodology of the DEM-CFD coupling model are introduced in the next section together with the governing equations for particle motion, particle-fluid interaction and fluid flow. In the following section, the coarse graining technique is described. Finally, the main results of the simulations of the Vajont event are summarised.

2 THEORY AND METHODOLOGY

The DEM code ESyS-Particle [8] and the CFD code OpenFOAM [9] were employed for the simulations presented here. The coupling algorithm originally written in YADE [10] was implemented in ESyS-Particle by the authors [11]. The mechanical contact law between solid particles is based on linear springs and frictional tangential sliders plus rolling resistance [12].

The fluid–particle interaction force consists of two parts: hydrostatic and hydrodynamic forces. The hydrostatic force acting on a single particle, *i*, accounts for the influence of fluid pressure gradient around the particle, i.e. buoyancy [13]. The hydrodynamic forces acting on a particle are the drag, lift and virtual mass forces; the latter two forces being neglected. The drag force acting on an individual solid particle is here calculated using the empirical correlation proposed by [14]. The drag force coefficient is defined according to the correlation proposed by [15].

The governing equations of fluid flow in a fluid–solid mixture system can be derived from the theory of multi-phase flow [16], in which the free surface condition is resolved by the Volume of Fluid method [17]. In our numerical simulations, the fluid domain is initially discretized into a series of mesh cells, in which the solid particles may be dispersed. In each fluid mesh cell, the volume fraction of the summation of fluid phases is n (i.e. porosity), for

which, the volume fraction occupied by the fluid phase 1 (e.g. water) is β ($0 \leq \beta \leq 1$), while it is 1 - β for the other phase.

3 COARSE GRAINING TECHNIQUE

We assume that: (1) one large particle represents a clump of real sized sand grains (see Fig. 1); (2) the fine grains are bonded together, so that they can move as a whole; (3) the translational and rotational motion of the coarse grain and the clump of fines grains are the same; (4) the contact forces acting on the coarse grains are the summation of contact forces acting on this clump of real grains by the neighbouring grains. The fluid viscous drag force acting on the coarse particle is calculated by balancing the coarse particle and a clump of real particles. This particle scale up method is called e ‘‘coarse grain model’’ in the literature [7].

Denoting the sizes of the coarse grain particle and original real sand particle as D and d respectively, the number of particles (N) in the clump can be approximated as: $N = D^3/d^3$. The drag force acting on the clump is the summation of the drag forces acting on all the grains. Thus, the drag force on a scaled particle in the CFD-DEM code should be scaled up by a factor α with $\alpha = F_d/F'_d$, F_d the drag force acting on the clump and the drag force acting on the scaled particle. By setting the Reynolds numbers the same, the values of the drag force coefficient are the same for both the real fluid flow and the numerical models, so $\alpha = D/d$. Simulations were run for different values of α. As shown in Table 1, α was set to 1, 5 and 10, so that one large particle in the DEM can represent a clump of fine grains ranging in number from 1 to 10^3. The hydrostatic forces acting on a coarse particle and a clump of fine grains are the same, because it is determined only by the volume of solid materials. It is also noted that other parameters for the coarse and real particles are the same, so that realistic soil properties can be modelled in numerical simulations.

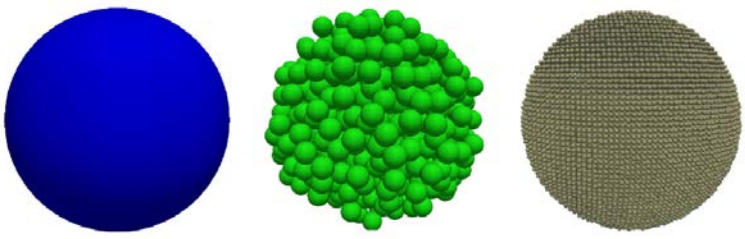

Fig. 1 Schematic view of the scaling law used in the DEM, α is the scaling factor.

4 RESULTS OF THE NUMERICAL SIMULATIONS

A plan view of the Vajont rockslide is shown in Fig. 2a, together with the traces of the two cross sections A–A and B–B, representative of the eastern and western sectors of the slide, and herein analysed. The profiles along these cross sections are illustrated in Fig. 2b and 2c. Details of the generation procedure of the slope mass are given in [18].

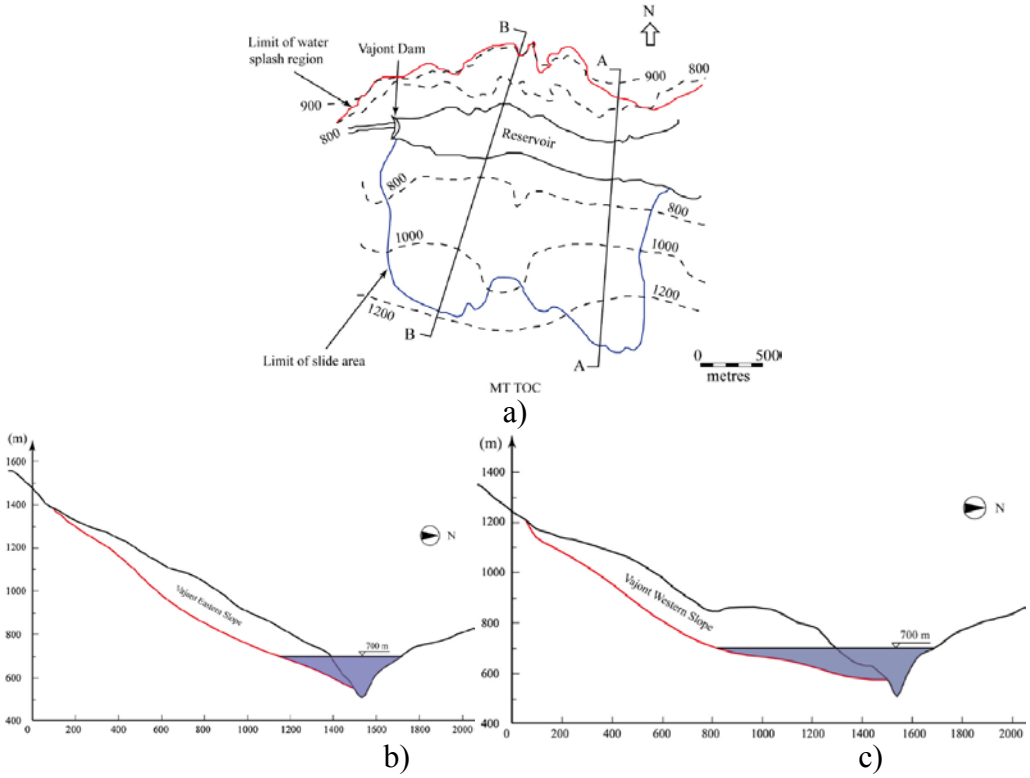

Fig. 2 a) Plan view of the Vajont rockslide with the straight lines indicating the cross sections A-A and B-B corresponding to the easter and western slopes of the Vajont valley respectively; b) profile of the eastern slope; c) profile of the western slope. The water reservoir is in blue.

The input parameters adopted for both the DEM and CFD models are listed in Table 1 and have been chosen ac- cording to available data and some simplified assumptions concerning the failure surface, the material strength and the physical mechanical properties. No numerical damping is employed. This is because although several damping models exist in the literature, few of them are underpinned by experimental evidence. Secondly, when modelling rockslides, and especially rapid ones, any damping would alter the mechanical behaviour exhibited by the system significantly.

Parameters	Value	Parameters	Value
DEM Parameters			
Number of grains, N	21,600–24,550	Shear stiffness, K_s (N/m)	2.7×10^9
Particle diameter, D (m)	[1.8, 3.8]	Rolling stiffness, K_r (N/m)	0
Density, ρ_s (kg/m^3)	2650	Inter-particle friction angle, θ (°)	30
Sample porosity, n	0.37–0.45	Basal friction angle, θ_b (°)	10
Normal stiffness, K_n (N/m)	3×10^9	Damping coefficient, β	0
CFD Parameters			
Water density, ρ_w (kg/m^3)	1000	Air density, ρ_a (kg/m^3)	1.225
Water viscosity, μ_w (Pa s)	0.001	Air viscosity, μ_a (Pa s)	1.8×10^{-5}
Simulation parameters			
Gravity, g (m/s^2)	9.81	CFD time step, Δt_2 (s)	1.0×10^{-3}
DEM time step, Δt_1 (s)	1.0×10^{-5}	Coupling frequency[a]	100

Table 1. Input parameters of the DEM-CFD model.

Figure 3 illustrates the evolution of slope deformation and the motion of water wave during the sliding of Vajont eastern slope (section A–A in Fig. 2b). The slope mass is initially coloured grey and green at different parallel layers, so that its deformation can be clearly identified during the rocksliding. It can be observed that at the beginning of the slide, the slope mass moves as a whole on the failure surface and quickly slides into the reservoir with a slight rotational component of motion, generating water waves. The water wave moves in the sliding direction and splashes onto the northern bank of the Vajont valley. Near the flow front, the CFD mesh cells are filled with both water and air, thus, the colour representing the water phase is less intense.

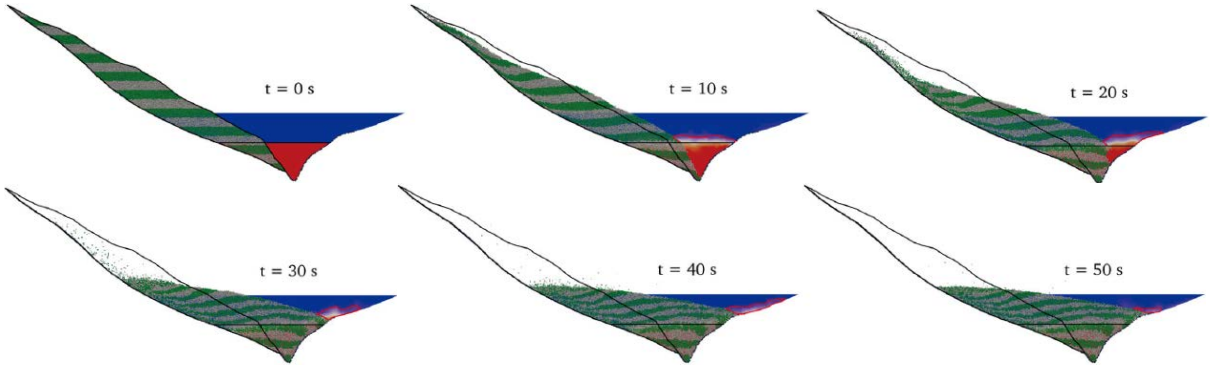

Fig. 3 Evolution of slope section A-A. The granular mass is initially coloured in horizontal stripes to follow the internal deformation. For the fluid domain, red and blue represent water and air respectively with the smear colour representing the air-water mixture. The splashed water wave is represented by regions enclosed by red curves.

The velocity of the water wave and its height time are illustrated in Figs. 4 and 5 respectively for the simulation of both sections considered, Easter and Western. It can be observed that the water waves move initially slowly towards as the slope mass slides into the reservoir. After 15 seconds and 8 seconds respectively from initiation, the wave velocities increase to their peaks value of 20 m/s and 18 m/s respectively. Then they decrease gradually to zero. After that (see the vertical dashed lines in the figures), the splashed water wave flows back into the reservoir, and above the slide mass as represented by the gradual increase of water wave velocity.

According to Fig. 10, it can be observed that the elevation of water wave increases gradually from zero to the peak value of 130 m. After reaching the maximum height at 43 s since the onset of the slope failure, it de- creases slowly due to the back flow of water into the reservoir. The final elevation of water in the reservoir is about 35 m above the initial reservoir water level.

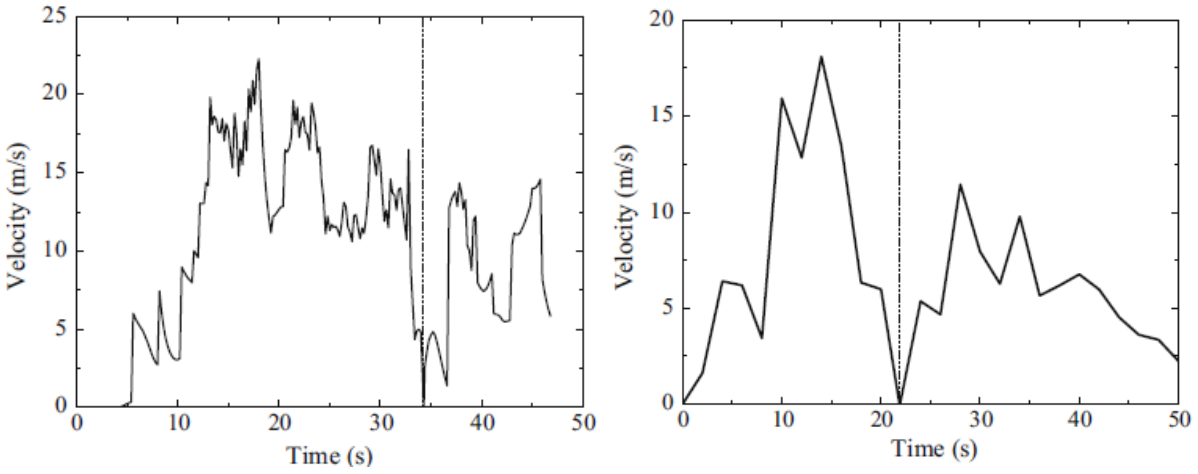

Fig. 4 Speed of the overtopping wave above the reservoir level: a) eastern section; b) western section.

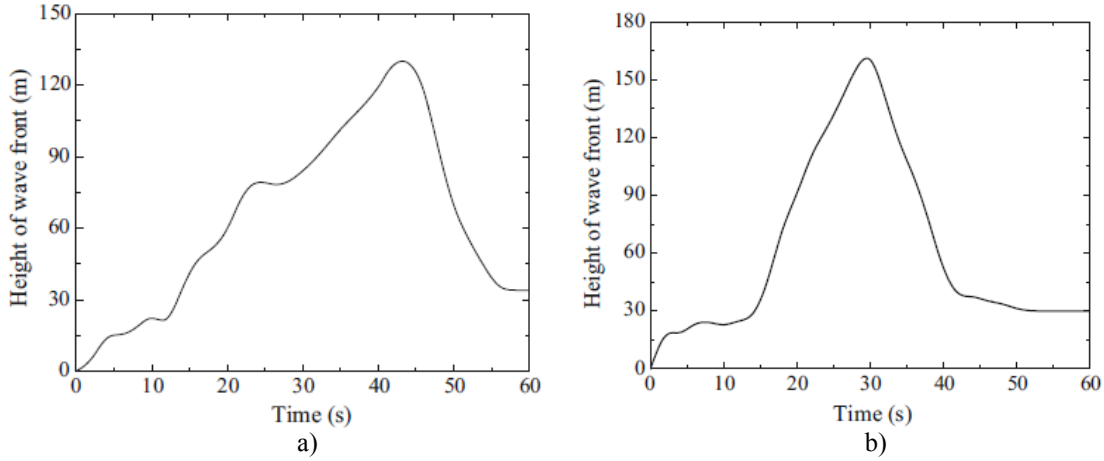

Fig. 5 Height of the overtopping wave above the reservoir level: a) eastern section; b) western section.

5 CONCLUSIONS

The current 3D plane strain DEM simulations have captured the general features (e.g. slope and wave motions) of the Vajont rockslide at the eastern and western sectors. The use of high fluid viscosity and coarse grain model has shown the possibility to model realistically both the slope and wave motions.

The average slope velocity for the slopes and the corresponding water wave velocities together with the maximum height of the wave runup on the opposite valley flank for both slopes turn out to be in very close to the field observations at the same spots.

ACKNOWLEDGMENTS

This project has received funding from the European Union's Horizon 2020 research and innovation programme under the Marie Skłodowska-Curie grant agreement No 645665.

REFERENCES

[1] Brideau, MA., Sturzenegger, M, Stead, D., Jaboyedoff, M., Lawrence, M., Roberts, NJ. and Clague JJ. (2012), Stability analysis of the 2007 Chehalis lake landslide based on long-range terrestrial photogrammetry and airborne LiDAR data, Landslides, 9(1), 75–91.

[2] Roberts, NJ., McKillop, RJ., Lawrence, MS., Psutka, JF., Clague, JJ., Brideau, MA. and Ward BC. (2013), Impacts of the 2007 landslide generated tsunami in Chehalis Lake, Canada, in Landslide Science and Practice, edited by C. Margottini , P. Canuti, and K. Sassa, pp. 133–140, Springer, Berlin.

[3] Miller, GS., Take, AW., Mulligan RP. and McDougall, S. (2017), Tsunamis generated by long and thin granular landslides in a large flume, J. Geophys. Res. Oceans, 122, doi:10.1002/2016JC012177.

[4] Mulligan, RP., Take, WA. (2017). On the transfer of momentum from a granular landslide to a water wave. Coastal Engineering, 125: 16-22.

[5] Semenza, E., Ghirotti, M. (2000) History of the 1963 Vaiont slide: the importance of geological factors. Bull Eng. Geol Env, 59: 87-97.

[6] Chowdhury, R. (1978) Analysis of the Vajont slide—new approach. Rock Mechanics 11(1): 29–38.

[7] Sakai, M., Takahashi, H., Pain, CC., Latham, J-P., Xiang, J. (2012) Study on a large-scale discrete element model for fine particles in a fluidized bed. Adv Powder Technol 23(5): 673–681

[8] Abe, S., Place, D., Mora, P. (2004) A parallel implementation of the lattice solid model for the simulation of rock mechanics and earthquake dynamics. Pure appl Geophys 161(11–12):2265–2277.

[9] OpenCFD (2004) OpenFOAM—The open source CFD toolbox, http://www.openfoam.com/

[10] Chen, F., Drumm, EC., Guiochon, G. (2011) Coupled discrete element and finite volume solution of two classical soil mechanics problems. Comput Geotech 38(5): 638–647.

[11] Zhao, T., Houlsby, GT., Utili, S. (2014). Investigation of granular batch sedimentation via DEM-CFD coupling. Granular matter, 16(6): 921-932.

[12] Jiang, MJ., Yu, HS., Harris, D. (2005) A novel discrete model for granular material incorporating rolling resistance. Comput Geotech 32(5): 340–357.

[13] Kafui, KD., Thornton, C., Adams, MJ. (2002) Discrete particle- continuum fluid modelling of gas–solid fluidised beds. Chem Eng Sci., 57(13):2395–2410

[14] Di Felice, R. (1994) The voidage function for fluid–particle interaction systems. Int J Mult. Flow 20(1): 153–159.

[15] Brown, P., Lawler, D. (2003) Sphere drag and settling velocity revisited. J Environ Eng 129(3): 222–231.

[16] Brennen, CE. (2005) Fundamentals of multiphase flow. Cambridge University Press, Cambridge.

[17] Hirt, CW., Nichols, BD. (1981) Volume of fluid (Vof) method for the dynamics of free boundaries. J Comput Phys, 39(1): 201–225.

[18] Zhao, T., Utili, S., Crosta, GB. (2016) Rockslide and impulse wave modelling in the Vajont reservoir by DEM-CFD analyses. Rock Mech Rock Eng 49: 2437-2456.

V International Conference on Particle-based Methods – Fundamentals and Applications
PARTICLES 2017
P. Wriggers, M. Bischoff, E. Oñate, D.R.J. Owen, & T. Zohdi (Eds)

GRAIN SCALE PARAMETERS IN DISSIPATIVE DRIVEN CONSTITUTIVE MODELS

RECTOR A. MUKWIRI[1], WILLIAM M. COOMBS[1], YOUSEF GHAFFARI MOTLAGH[2] AND CHARLES E. AUGARDE[1]

[1] School of Engineering and Computing Sciences
Durham University
Durham, DH1 3LE, UK
E-mail: r.a.mukwiri@durham.ac.uk, w.m.coombs@durham.ac.uk,
charles.augarde@durham.ac.uk
URL: https://www.dur.ac.uk/ecs/

[2] School of Chemical and Process Engineering
University of Leeds
Leeds LS2 9JT, UK
E-mail: Y.GhaffariMotlagh@leeds.ac.uk
URL: https://engineering.leeds.ac.uk/staff/859/Dr_Joseph_Ghaffari_Motlagh

Key words: DEM, energy dissipation, compression, sands, hyperplasticity

Abstract. Soil has generally been treated as a continuum from as early as the eighteenth century. Since then the analysis of soil behaviour in practical engineering analyses and development of constitutive models has depended on a continuum assumption. However, in order to gain a deeper understanding of the behaviour of soils and their particulate nature, there is a need to move from continuum mechanics to discrete models. Such modelling is possible using the Discrete Element Method (DEM). In this paper an open source DEM particle simulation software, LIGGGHTS is used to study the relationships between grain scale parameters and energy dissipation in granular media in one-dimensional compression. The influence of particle size distribution, void ratio, and inter-particle friction coefficient on energy dissipation are studied and discussed. In order to measure the dissipated energy, changes in energy terms are traced at every time step and the principle of energy conservation applied. It is hoped that the knowledge gained of the relationship between grain scale parameters and energy dissipation will help in the formulation of constitutive relationships within the hyperplasticity framework. It is envisioned that relating grain scale parameters to constitutive models will allow the formulation of models that are purely based on the micro-mechanics of granular media.

1 INTRODUCTION

Soil has generally been treated as a continuum from as early as the eighteenth century [2]. This assumption has since then been used in engineering design for practical purposes. Indeed many constitutive models are built on this assumption. However, in order to understand soils better, we need to move from continuum mechanics to a discrete method of study. Such a method is the Discrete Element Method (DEM) originally introduced by Cundall and Strack [1]. The DEM allows us to study soil at a particle level and gain a better understanding of its behaviour. Studying soil at grain scale will hopefully minimise the need to make assumptions when defining constitutive models. The DEM is here used to investigate grain scale parameters in relation to energy dissipation, a core component of the hyperplasticity approach to constitutive modelling [6].

The hyperplasticity approach allows the constitutive behaviour of a material to be derived from a free-energy function and a dissipation rate function [6]. This approach stems from the works of Ziegler[12] and Houlsby [5]. Once these scalar functions have been specified, the yield function, flow rule and the stress and strain relationships can be derived without need of any additional assumptions. The first scalar function is derived from the First law of Thermodynamics and the dissipation function is a consequence of the Second law of Thermodynamics.

By understanding the fundamental causes of energy dissipation in a DEM simulation, a dissipation function could potentially be formulated leading to a constitutive relationship formulation directly informed by physical measurements at a particle level. In this paper, relationships between energy dissipation and grain scale parameters for one-dimension compression problems are discussed. The grain scale parameters explored are: the inter-particle friction coefficient, particle size distribution and the initial void ratio. The relationship between these parameters and energy dissipation is discussed.

The rest of the paper is laid out as follows. Section 2 will describe the simulation procedure followed for the DEM simulations. In Section 3 the energy calculations are detailed. Section 4 describes parameters varied in this paper. The results from the simulations are reported and described in Section 5. The paper will finally provide some conclusions in Section 6.

2 SIMULATION PROCEDURE

One-dimensional compression simulations were carried out using DEM. An open source DEM particle simulation software, LIGGGHTS, developed by Kloss et al. [7] was used for this study. Unlike commercial DEM software, LIGGGHTS has no user interface. A simulation is driven using a text-based input script containing a series of commands to conduct the simulation. This input script is read sequentially making the ordering of statements important. Before the execution commands, the input script should have the initialisation settings specified and the simulation set up.

The initialisation settings and parameters are those that need to be specified before

the particles can be generated. These settings and parameters include the boundary style, units, region size, neighbour sorting, time step size, and atom style. In this study the boundary was specified to be of a moving style to allow vertical movements during loading and unloading.

To ensure a stable simulation, a time step, Δt of 1×10^{-7}s was used. When a very large time step is used, some of the contacts are not detected since the acceleration values that used to update the particle positions are not current. This value was arrived at based on the method for calculating the DEM critical time step proposed by O'Sullivan and Bray [11] for different particle arrangements. For non uniform contacts arrangement, the critical time step is given as $0.221\sqrt{m/K}$ where m is the particle mass and K is the contact stiffness was taken to be the greater of either the normal or tangential contact stiffness values. For a stable simulation, a value equal to or less than the critical value needs to be used.

The simulated particles where spheres of Poisson's ratio of 0.25, Young's modulus of 70MPa, and density of 2650kg/m^3 per particle. The density value was chosen based on the fact the dominant mineral in sands is quartz, which has a density of 2650kg/m^3. This value is also typically adopted in the DEM simulation of sands (for example in [3] and [9]).The particle-wall coefficient of friction was kept at zero.

After all the specific settings and parameters were specified, a model of a cylinder with a covered base extending to the simulation bounds, and a top circular mesh to cover the sample were input to the simulation as STereoLithography (STL) files to provide an enclosure of 30mm diameter by 10mm height. These meshes were made of triangular elements. Particles were then packed in the enclosed space and then allowed to settle.

The particles were then densified to different initial void ratio values in the range 0.43 - 0.7 by moving the top platen downwards at constant velocity, following which the particles were allowed to settle. The void ratio is calculated as

$$e = \frac{V_v}{V_s}, \tag{1}$$

where V_v and V_s are volumes of void and solids respectively. The top platen vertical velocity was calculated from

$$v_{mesh} = \frac{V_s(e_{tar} - e_{cv})}{t_{steps}\pi R^2 \Delta t}, \tag{2}$$

where e_{tar} and e_{cv} are the target and current void ratios, t_{steps} is the number of time steps to run, and R is the sample radius. After being densified, the particles were then compressed to $e_{tar} = 0.2$ on the loading cycle then unloaded to their initial void ratio value. Figure1 shows a sketch of the simulations before (a) and at the end of loading (b), and at the end of unloading (c). At the end of unloading, the samples had undergone some permanent deformation compared to the start of the simulation due to the rearrangement of particles.

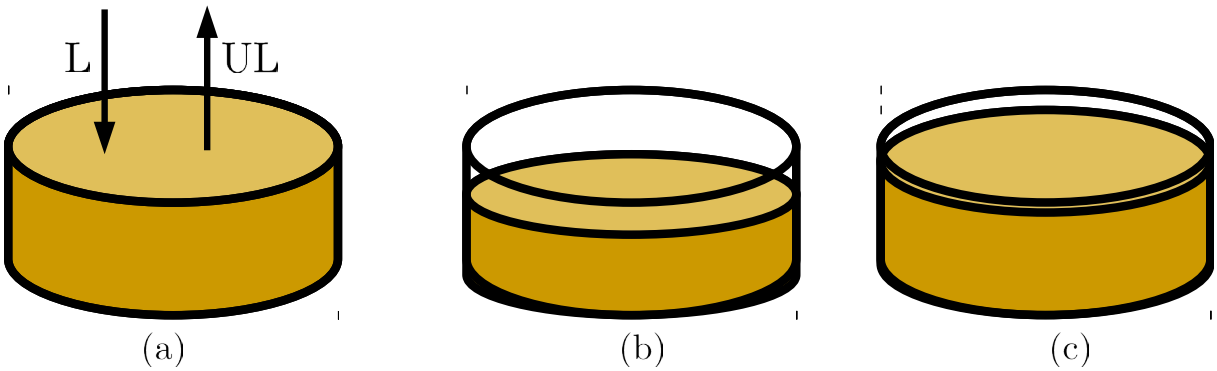

Figure 1: Loading (L) and unloading (UL): (a) before loading samples; (b) end of loading; (c) end of unloading

Results files were output throughout the simulation for later post processing for energy calculations. The particle data output included: position vectors, velocity values, total forces, particle radii and IDs, normal and tangential contact forces, and particle-particle overlap distances. These data were output every 25000 time steps, which was found to be sufficient data to understand the various behaviours during simulations. The stress data on the meshes was also output at the same intervals in separate files and later post processed to give the compression force.

3 ENERGY MONITORING

To facilitate the study of energy dissipation for the tests conducted, energy monitoring was done by post processing the files output during the simulations using Matlab. The energy equation used was

$$dE_p + dW = dE_k + dE_\mu + dE_\zeta + dU, \tag{3}$$

where dE_p is the change in potential energy, dW the change in boundary work, dE_k the change in kinetic energy, dE_μ the dissipated frictional energy, dE_ζ the change in dissipated energy through damping, and dU the change in stored work.

The total change in dissipated energy, dE_η during the simulations comes from the dE_μ and dE_ζ terms of (3). Since the simulations are pseudo-static, it was found that the potential and kinetic energies were usually each $\approx 10^6$ times smaller than either of the boundary work or the stored elastic energy. We can therefore re-write (3) as

$$dE_\eta \approxeq dW - dU \tag{4}$$

The change in boundary work is calculated as:

$$dW = \left(\sum_{j=1}^{m} \sigma_v^j A_S^j \right) \delta x, \tag{5}$$

where σ_v^j is the normal stress on mesh j, m is the total number of mesh elements on the boundary mesh considered, and δx is the change in displacement of the boundary mesh. A_S^j is the surface area of triangular mesh element j considered and is obtained by

$$A_S^j = \frac{1}{2}|\mathbf{AB} \times \mathbf{AC}|, \tag{6}$$

where the area of each triangular element with vertices A, B and C is calculated from the cross product between vectors **AB** and **AC**.

Changes in the stored energy are due to the evolution of normal and tangential contact forces. The summation of strain energy for all the contacts is equal to the stored energy, dU and is calculated as

$$dU = dU^n + dU^t, \tag{7}$$

where dU^n and dU^t are the contributions from normal and tangential contact forces and are equal to

$$dU^n = \int_0^{\delta_n} \underbrace{\overbrace{\frac{4}{3}E^*\sqrt{R^*\delta_n}}^{K_n}\,\delta_n \mathbf{n}}_{F^n}\, d_n \tag{8}$$

and

$$dU^t = \int_0^{\xi_t} \underbrace{\overbrace{8G^*\sqrt{R^*\delta_n}}^{K_t}\,\boldsymbol{\xi_t}}_{F^t}\, d\xi_t, \tag{9}$$

respectively. F^n and F^t are in turn the normal and tangential contact forces and K_n and K_t are the corresponding stiffness parameters from the Hertzian contact model, which governed how the spherical particles interacted at contact. Two particles 1 and 2 have an effective radius, $R^* = R_1R_2/(R_1 + R_2)$, which is the geometric mean of radii R_1 and R_2. $\delta_n = R_1 + R_2 - d_{12}$ and is the overlap at contact between the two particles in the normal direction where d_{12} is the distance between their centres. The effective Young's modulus, $E^* = 0.5E/(1 - \nu^2)$, is derived from the particles' material Young's modulus, E and Poisson's ratio, ν. In Equation (8), $\mathbf{n}$ is the normal vector for the particles in contact. The term $\boldsymbol{\xi_t}$ in Equation (9) is the tangential displacement and is calculated by integrating the tangential relative velocity over the contact time [4].

4 SIMULATION PARAMETERS VARIED

Sands are typically made up of different grain sizes which give rise to Particle Size Distributions (PSDs). These can be defined using the coefficient of uniformity (C_u), which is a shape parameter given as

$$C_u = \frac{d_{60}}{d_{10}}. \tag{10}$$

d_{60} and d_{10} respectively are particle diameters for which 60% and 10% of the material by mass is finer. PSDs affect the soil responses. For example, McDowell and Bolton [8] studied the effect of particle size distribution on pile end resistance using two PSDs. It was found that the peak pile resistance during penetration was a function of the PSD. Smaller particles increased the level of resistance in the soil. PSD also affects the compressibility of grains [9].

Friction between particles, μ is means by which most energy is dissipated in granular media. The friction coefficient between particles was therefore varied along with PSD and the initial void ratio, e_{ini} in the present study with no particle crushing involved. Table 1 shows the varied parameters for each simulation. Results from these simulations are discussed next.

Table 1: Simulation test parameters

Simulation	C_u	e_{ini}	μ
1	1	0.7	0.5
2	1.3	0.7	0.5
3	2	0.7	0.5
4	2	0.7	0.2
5	2	0.7	0.25
6	2	0.7	0.3
7	2	0.7	0.35
8	2	0.7	0.4
9	2	0.7	0.45
10	2	0.7	0.5
11	2	0.67	0.5
12	2	0.64	0.5
13	2	0.61	0.5
14	2	0.58	0.5
15	2	0.55	0.5
16	2	0.52	0.5
17	2	0.49	0.5
18	2	0.46	0.5
19	2	0.43	0.5

5 RESULTS AND DISCUSSION

Minh and Cheng [10] observed that the compression of sands is due to the rearrangement of particles and elastic compression. During unloading of the sand sample, particles would be unstressed but would not have the same level of rearrangement as in the loading, and would have experienced unrecoverable deformation. These observations should be reflected in the energy dissipation curves for simulations.

The results from the current study show that a higher C_u results in less energy dissipation for $1 < C_u \leq 2$ as shown in Figure 3 for simulations 1-3 in Table 1. This observation may be explained as follows. As smaller particles are introduced, the particle contacts network becomes more resistant to sliding. More of the input energy is as a result stored. This suggests that the rate of energy dissipation for these simulations is negatively correlated to the coefficient of uniformity.

Figure 2 shows a plot of the void ratio against the vertical stress for simulations 1-3 in Table 1. The circled part highlights an area where the pressure drops. There is a sudden rearrangement within the specimen of $C_u = 1$ and $C_u = 1.3$ due to pockets of voids being filled rapidly. This change in pressure results in an increase of dissipated energy corresponding to the rearrangement of particles.

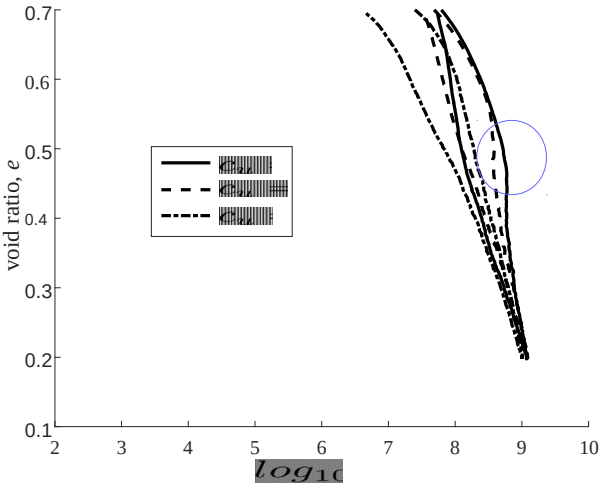

Figure 2: e-logσ_v

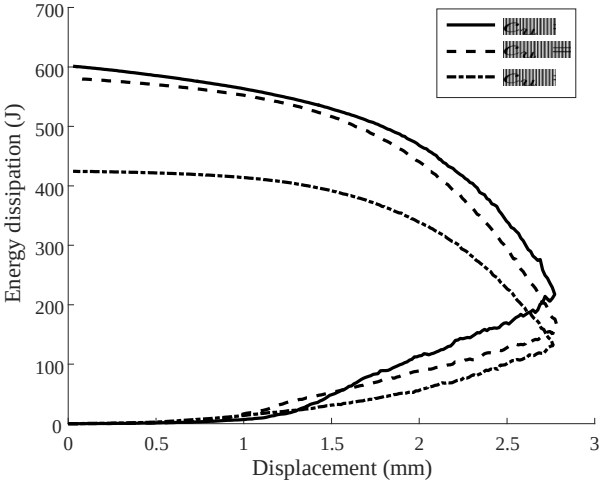

Figure 3: Dissipated energy against displacement

The inter-particle friction coefficient (μ) was varied between 0.5 and 0.2. The friction coefficient affects how fast the particles can be packed, a feature observed during the insertion of particles. A lower friction coefficient makes it easier to pack particles. Though not utilised in this paper, this fact is generally exploited to speed up the particle packing stage of the simulation by using a low μ value during the particle insertion stage and changing it to the desired value later.

Figure 4 shows a plot of void ratio against the log of vertical stress graphs for the different μ values. The variation between different μ values is not significant. This is mainly due to the fact that changes in void ratio are largely due to the compression of the particles which is mainly governed by the movement of the top platen.

A higher friction coefficient results in more energy dissipation during loading as observed in Figure 5 for Simulations 4-9 (Table 1). This is consistent with the fact that energy is largely lost through friction. Less energy is dissipated on the unloading curves because of some permanent settlement of particles during compression, however the trend of energy dissipation is still directly proportional to the friction coefficient. The rate of energy dissipation based on this result would therefore be expected to be positively correlated with the inter-particle coefficient of friction.

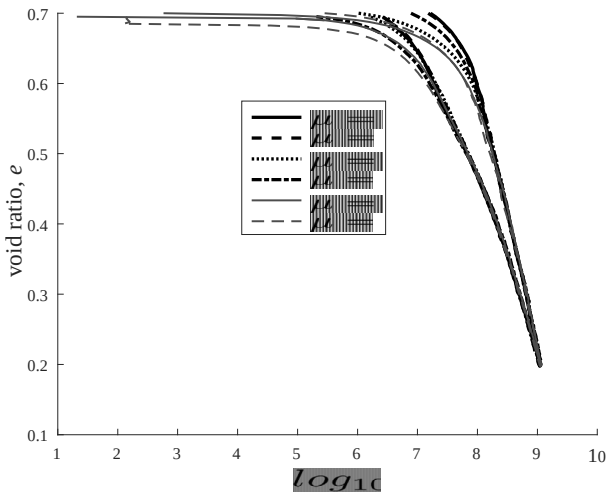

Figure 4: e-logσ_v

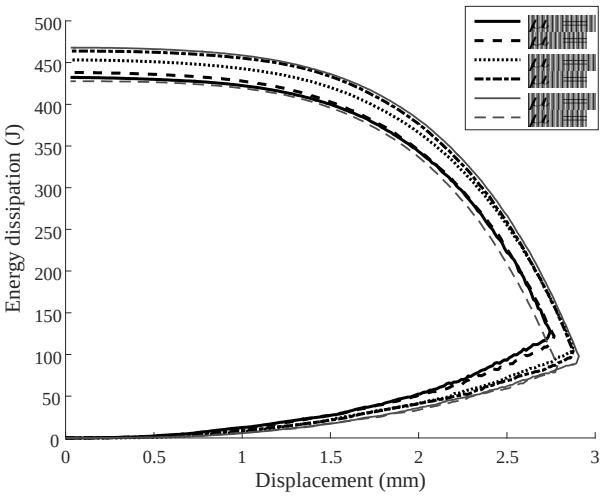

Figure 5: Dissipated energy against displacement

Loading and unloading cycles were simulated for ten different initial void ratios (e_{ini}) from $0.7-0.43$ (see Table 1: simulations 10-19). Results from these simulations are shown in Figure 6. It can be seen from this graph that towards the end of simulations a similar compression path was followed as would be expected. The differences correspond to the oscillations of particles during the simulations.

The energy dissipation curves shown in Figure 7 become steeper with a decreasing e_{ini} during compression. This is because more input work is required to move particles through the same displacement and since most of this work is not stored energy, then it is dissipated largely through friction. It can also be seen that there is a similar steepness achieved at a greater displacement for samples with a higher e_{ini}. On unloading, more energy is dissipated as the e_{ini} decreases. These results suggest that the rate of energy dissipation is negatively correlated with the initial void ratio.

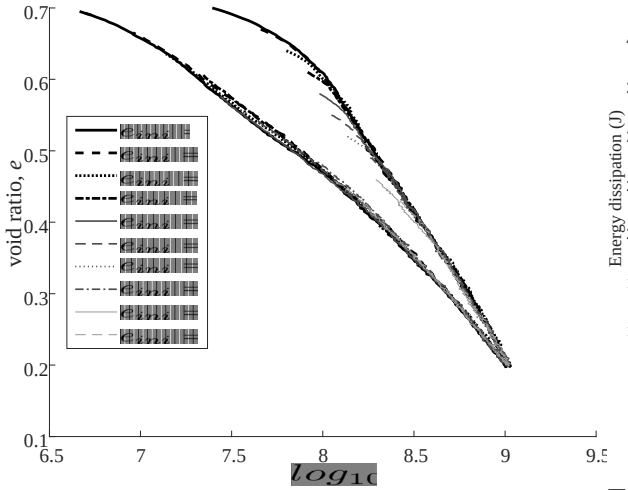

Figure 6: e-logσ_v

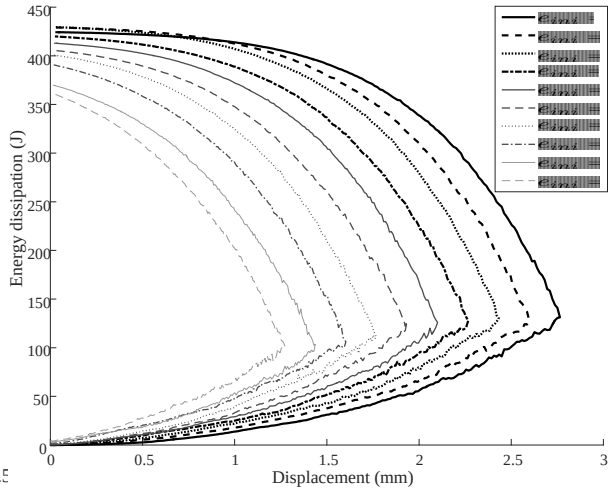

Figure 7: Dissipated energy against displacement

6 CONCLUSIONS

One-dimensional compression tests using the DEM have been conducted including loading and unloading cycles using spherical particles whose properties were set to those of sands. Throughout these simulations, data was output and then post processed in Matlab for energy dissipation. PSD, initial void ratio, and the coefficient of friction were the three parameters varied in the present study. Increasing the coefficient of uniformity was found to decrease the energy dissipated. It was proposed that this observation is due to the fact that as smaller particles are introduced, which reduce on the sliding of particles while increasing the amount of stored energy. A lower initial void ratio resulted in steeper curves for energy dissipation and is due to the fact that more input energy is required to move the particles through the same displacement at lower e_{ini} values most of which is dissipated. A higher friction coefficient between particles resulted in more energy dissipation during loading and unloading of the samples. This is due to the fact that energy is mainly lost through friction, which is directly proportional to its coefficient. A negative correlation between energy dissipation rates for the simulations conducted with either e_{ini} or C_u is envisioned. On the other hand, a positive correlation between the inter-particle coefficient of friction with the energy dissipation rate is expected. It is hoped that studies of the relationship between grain scale parameters and energy dissipation will lead to the formulation of the constitutive models directly informed by grain scale parameters.

REFERENCES

[1] P. A. Cundall and O. D. L. Strack. A discrete numerical model for granular assemblies. *Géotechnique*, 29:47–65, 1979.

[2] R. Davis and A. Selvadurai. *Plasticity and Geomechanics*. Cambridge University Press, 2002.

[3] J. P. De Bono and G. R. McDowell. Discrete element modelling of one-dimensional compression of cemented sand. *Granular Matter*, 16:79–90, 2014.

[4] X. Dou, Y. Mao, and Y. Zhang. Effects of contact force model and size distribution on microsized granular packing. *J. Manuf. Sci. Eng*, 136(2):021003, 2014.

[5] G. Houlsby. *A Study of Plasticity Theories and Their Applicability to Soils*. PhD thesis, University of Cambridge, 1981.

[6] G. Houlsby and A. Puzrin. *Principles of Hyperplasticity*. Springer, 2006.

[7] C. Kloss, C. Goniva, A. Hager, S. Amberger, and S. Pirker. Models, algorithms and validation for opensource DEM and CFD-DEM. *Progress in Computational Fluid Dynamics, An Int. J.*, 12:140–152, 2012.

[8] G. McDowell and M. Bolton. Effect of particle size distribution on pile tip resistance in calcareous sand in the geotechnical centrifuge. *Granular Matter*, 2:179–187, 2000.

[9] G. McDowell and J. de Bono. On the micro mechanics of one-dimensional normal compression. *Géotechnique*, 3:166–172, 2013.

[10] N. H. Minh and Y. P. Cheng. A dem investigation of the effect of particle-size distribution on one-dimensional compression. *Géotechnique*, 63:44–53, 2013.

[11] C. O'Sullivan and J. Bray. Selecting a suitable time-step for discrete element simulations that use the central difference time integration approach. *Engineering Computations*, 21(2-4):278–303, 2003.

[12] H. Ziegler. *An introduction to thermomechanics*. North Holland Pub. Co, Amsterdam, 2nd edition, 1983.

V International Conference on Particle-based Methods – Fundamentals and Applications
PARTICLES 2017
P. Wriggers, M. Bischoff, E. Oñate, D.R.J. Owen, & T. Zohdi (Eds)

INVESTIGATIONS OF QUASI-STATIC VORTEX-STRUCTURES IN 3D SAND SPECIMENS BASED ON DEM AND HELMHOLTZ-HODGE VECTOR FIELD DECOMPOSITION

J. KOZICKI[1] AND J. TEJCHMAN[2]

[1]Gdansk University of Technology
80-233 Gdansk, Narutowicza 11/12
jkozicki@pg.gda.pl

[2]Gdansk University of Technology
80-233 Gdansk, Narutowicza 11/12
tejchmk@pg.gda.pl

Key words: Granular Materials, Plane strain compression, DEM, Helmholtz-Hodge decomposition, Vortex-structures.

Abstract. The paper presents some three-dimensional simulation results of granular vortex-structures in cohesionless initially dense sand during quasi-static plane strain compression. The sand behaviour was simulated using the discrete element method (DEM). Sand grains were modelled by spheres with contact moments to approximately capture the irregular grain shape. The Helmholtz-Hodge decomposition (HHD) of the displacement vector field from DEM calculations was used. The variational discrete multiscale vector field decomposition allowed for separating a vector field into the sum of three uniquely defined components: curl free, divergence free and harmonic. Vortex-structures were strongly connected to shear localization. They slightly changed along the specimen depth. They localized in locations where shear zones ultimately developed.

1 INTRODUCTION

Granular vortex-structures defined as the roughly swirling (rotating) motion of several grains around a common central point were frequently observed in experiments on granular materials [1]-[3] and in calculations using the discrete element method (DEM) [4]-[9]. They became apparent in experiments and calculations when the motion associated with uniform (affine) strain was subtracted from the actual granular deformation. They are reminiscent of turbulence in fluid dynamics, however the amount of the grain rotation is several ranges of magnitude smaller (~0.01^o-0.1^o) than the fluid vortex rotation, their life time is also short than of eddies in turbulent fluid flow and granular flow is too slow to induce inertial forces characteristic for turbulences in fluid. The vortices have been mainly observed in shear zones that are the fundamental phenomenon in granular bodies. A dominant mechanism responsible for the vortex formation was the breakage of force chains [4], [7]. The collapse of main force chains lead to a formation of larger voids and their build-up to a formation of smaller voids [7]. Kozicki and Tejchman [8], [9] and Tordesillas et al. [4] showed that shear localization may be predicted very early through vortex-structures that means new perspectives for a

detection of impending failure in granular bodies (inherently connected with shear localization) within continuum mechanics. In continuous and discontinuous numerical calculations and laboratory experiments, shear localization is usually identified in granular bodies by grain rotations or micro-polar rotations or by an increase of void ratio.

The aim of the present paper is to present the results of 3D vortex-structures in sand during quasi-static plane strain compression by using the Helmholtz-Hodge decomposition (HHD) of a vector field [10], [11] calculated by the discrete element method (DEM) [8]. Attention was paid to the relationship between vortex-structures and shear localization with respect to the location and formation moment. The analyses were carried out with spheres with contact moments to approximately capture the irregular grain shape. In order to accelerate the computation time, some simplifications were assumed in analyses: large spheres with contact moments, linear sphere distribution, linear normal contact model and no particle breakage. A three-dimensional discrete model YADE developed at University of Grenoble by Donze and his co-workers was applied [12], [13]. The discrete calculations were solely carried out with initially dense sand. The innovative point of our calculations are 3D granular vortex-structures which have not been calculated in granular materials yet.

In our previous paper we calculated 2D vortex-structures during a quasi-static passive wall translation based on the Helmholtz-Hodge decomposition (HHD) of a vector field calculated by the discrete element method (DEM) [9]. The discrete vector field decomposition proved to be an objective, universal and effective technique for identifying all 2D vortex-structures during granular flow which was directly based on single grain displacement increments (but not on displacement fluctuations). The method did not use any additional non-objective parameters. However the method did not determine the size of vortex-structures. A strong connection between the location of vortex-structures and progressive shear localization was found out. The vortex-structures were the precursor of shear localization since they clearly concentrated in the area where shear zones ultimately later formed. Thus the ultimate shear zone pattern was detected in early loading stages. The vortex-structures allowed to identify shear localization significantly earlier than e.g. based on single grain rotations which were always a reliable indicator of shear localization. They developed from the deformation process beginning. They solely emerged in main shear zones. They had a tendency to move along shear zones. Their number varied and was larger on average at the residual state. The right-handed vortices were dominant in the curved shear zone and left-handed ones were dominant in the radial shear zone. In the curved shear zone, the predominant period of right-handed vortices was 4% of u/h during the entire wall movement. In the radial shear zone, the predominant period of left-handed vortices was also 4% of u/h. In the residual state, local regions of dilatacy and contractancy alternately happened along globally dilatant shear zones with a dominance of local dilatancy.

2 THREE-DIMENSIONAL DEM MODEL

In order to simulate the behaviour of real sand, the 3D explicit spherical discrete element model YADE, developed at University of Grenoble [12]-[13]. DEM includes the simple mathematical treatment of engineering problems (complex global constitutive relationships are replaced by simple local contact laws) and has the natural predisposition to account for material heterogeneity. The outstanding advantages of DEM include its ability to explicitly

handle the discrete/heterogeneous nature of the material by modelling particle-scale properties including size and shape which play an important role in shear localization. The disadvantages is an enormous computational cost and an extensive calibration based on experimentally measured macro-scale properties. The algorithm used in the present DEM which is based on a description of particle interactions in terms of force laws involves in general main steps [14]. First, based on constitutive laws, interaction forces between discrete elements are computed. Second, the Newton's second law is applied to determine for each element the resulting acceleration, which is then time integrated to find the new position. This process is repeated until the simulation is finished. The method takes advantage of the so-called soft-particle approach, i.e. the model allows for particle deformation which is modelled as an overlap of particles. During the simulations, particles may overlap that can be interpreted as a local contact deformation. A linear elastic normal contact model was used only. In compression, the normal force was not restricted and could increase indefinitely. The interaction forces acting on each element in the form of normal and tangential forces were linked to the displacements through the normal stiffness K_n and tangential stiffness K_s

$$\vec{F}_n = K_n U \vec{N}, \tag{1}$$

$$\vec{F}_s = \vec{F}_s + \Delta\vec{F}_s \qquad \text{with} \qquad \Delta\vec{F}_s = K_s \Delta\vec{X}_s, \tag{2}$$

where U is the penetration depth between discrete elements, $\vec{N}$ denotes the unit normal vector at the contact point and $\Delta\vec{X}_s$ is the incremental tangential displacement vector. The unloading was assumed to be purely elastic. The stiffness parameters were calculated in terms of the modulus of elasticity of the grain contact E_c and two contacting grain radii R_A and R_B (to determine the normal stiffness K_n) and in terms of the modulus of elasticity E_c and Poisson's ratio υ_c of the grain contact, and grain radii R_A and R_B (to determine the tangential stiffness K_s) of two contacting spheres, respectively [12]

$$K_n = E_c \frac{2R_A R_B}{R_A + R_B} \qquad \text{and} \qquad K_s = \nu_c E_c \frac{2R_A R_B}{R_A + R_B}. \qquad , \tag{3}$$

If the grain radius $R_A=R_B=R$, the stiffness parameters are equal to: $K_n=E_c\ R$ and $K_s=\upsilon_c\ E_c\ R$ (thus $K_s/K_n=\upsilon_c$), respectively. The frictional sliding starts at the contact point when the contact forces $\vec{F}_s$ and $\vec{F}_n$ satisfy the limit Coulomb condition

$$\left\|\vec{F}_s\right\| - \left\|\vec{F}_n\right\| \times \tan\mu \le 0 \tag{4}$$

with μ as the inter-particle friction angle (tension was not allowed). No forces are transmitted when grains are separated. The elastic contact constants were specified from the experimental data of a triaxial compression sand test and could be related to the modulus of elasticity of grain material E and its Poisson ratio ν [15], [16].

In order to increase the rolling resistance of pure spheres, clusters of spheres or contact moments were introduced. The normal force was assumed to contribute to the rolling

resistance. The contact moment increments were calculated by means of the rolling stiffness K_r multiplied by the angular rotational increment vectors $\Delta\vec{\omega}$

$$\Delta M = K_r \Delta\vec{\omega}\,. \tag{5}$$

The rolling stiffness K_r [kNm] in Eq.5 was related to the tangential stiffness K_s [kN/m] in Eq.2 by the following formula

$$K_r = \beta \times K_s \times R^2 = \beta \times K_s \times R_A R_B\,, \tag{6}$$

where β is the dimensionless rolling stiffness coefficient and R is the equivalent grain radius (at small displacements $dX_r \approx dX_s$). The dimensionless rolling coefficient η specifies the limit friction moment of the rolling motion [12]

$$|\vec{M}| - \eta \frac{R_A + R_B}{2} |\vec{F}_n| \le 0\,. \tag{7}$$

Because the proposed DEM is a fully dynamic formulation, a local non-viscous damping scheme was applied [14] in order to dissipate excessive kinetic energy in a discrete system and facilitate convergence towards quasi-static equilibrium. The damping parameter α was introduced to reduce contact forces and moments acting on elements

$$\vec{F}^k_{damped} = \vec{F}^k - \alpha \cdot \mathrm{sgn}(\vec{v}^k)\,|\vec{F}^k| \quad \text{and} \quad \vec{M}^k_{damped} = \vec{M}^k - \alpha \cdot \mathrm{sgn}(\vec{\omega}^k)\,|\vec{M}^k|\,, \tag{8}$$

where $\vec{F}^k$ and $\vec{M}^k$ are the k^{th} components of the residual force and moment vector and $\vec{v}^k$ and $\vec{\omega}^k$ are the k^{th} components of the translational and rotational velocity. A positive damping coefficient α is smaller than 1 (sgn(•) returns the sign of the k^{th} component of velocity). The equations are separately applied to each k-th component of a 3D vector x, y and z. The effect of damping is insignificant in quasi-static calculations [15], [16].

The five main local material parameters are necessary in our DEM simulations: E_c (modulus of elasticity of the grain contact), ν_c (Poisson's ratio of the grain contact), μ (inter-particle friction angle), β (rolling stiffness coefficient) and η (limit rolling coefficient). In addition, a particle radius R, particle mass density ρ and numerical damping parameter α are required. The DEM material parameters: E_c, ν_c, μ, β, η and α were calibrated using the corresponding homogeneous axisymmetric triaxial laboratory test results on Karlsruhe sand with the different initial void ratio and lateral pressure by Wu [17]. The procedure for determining the material parameters in DEM was described in detail by Kozicki et al. [15], [16]. The index properties of Karlsruhe sand are: mean grain diameter d_{50}=0.50 mm, grain size between 0.08 mm and 1.8 mm, uniformity coefficient U_c=2, maximum specific weight γ_d^{max}=17.4 kN/m^3, minimum void ratio e_{min}=0.53, minimum specific weight γ_d^{min}=14.6 kN/m^3

and maximum void ratio e_{max}=0.84. The sand grains are classified as sub-rounded/sub-angular. The following material constants were found in DEM by fitting numerical outcomes with experimental ones during homogeneous triaxial compression: E_c=0.3 GPa, ν_c=0.3, μ=18^o, β=0.7, η=0.4 ρ=2.55 g/cm^3 and a=0.08.

3 DEM RESULTS OF PLANE STRAIN COMPRESSION

Our numerical outcomes with respect to 3D vortex-structures were related quasi-static plane strain compression. The results of 3D DEM calculations were described in detail in [8]. The granular specimen used in DEM had the same size as in the experiments by Vardoulakis [18], namely: the width b=4 cm, height h=14 cm and depth l=8 cm (out-of-plane direction) (Fig.2). The linear grain distribution curve was assumed; the grain diameter range was between 1.25 mm and 3.75 mm with d_{50}=2.5 mm. About 56'000 spheres were used with the same material constants. The initial void ratio was e_o=0.53. The flexible vertical walls were assumed to model the membrane surrounding the specimen in experiments (Figs.2a and 2b). Both the front and rear specimen sides 4×14 cm^2 were blocked in a perpendicular direction to the specimen to enforce plane strain conditions. The bottom surface 4×8 cm^2 was fixed in a vertical direction and the top surface 4×8 cm^2 was subjected to the constant vertical displacement u_1. Along the top, bottom and membrane granular surfaces, the inter-particle friction angle was μ=0. During the loading process, the constant confining pressure of σ_c=200 kPa was applied through the flexible membrane.

Figure 2 demonstrates the typical evolution of the mobilized internal friction angle (calculated with principal stresses from the Mohr's equation) versus the vertical normal strain $\varepsilon_1=u_1/h$ and volumetric strain ε_v versus ε_1 for two specimens. Figure 3 shows the distribution of sphere rotations ω and void ratio e in the vertical mid-section slice with the area of 4×14 cm^2 and thickness of 5×d_{50} (1.25 cm, d_{50}=2.5 mm) cut out from the granular specimen 4×14×8 cm^3. The both quantities were calculated from the volumetric cell V_c=5d_{50}×5d_{50}×5d_{50} moved by d_{50} in two directions within the slice to create a 2D grid of the averaged values from the cell. The cell size, which was smaller than the shear zone thickness t_s, was chosen with preliminary calculations. The averaging cell larger than V_c caused the results too diffusive and with the smaller cell volume V_c, the results started too strongly fluctuate.

Similarly as in real experiments [18], the initially dense specimen showed an asymptotic behaviour; it exhibited initially small elasticity, hardening (connected first to contractancy and then dilatancy), reached a peak of ϕ_{max}=46^o at about of ε_1=5%, gradually softened and dilated reaching a residual state of ϕ_{max}=30^o at the large vertical strain of 25-30% (Fig.3). The coordination number was initially about 5 and decreased down next to 3.8 during shearing due to dilatancy. During deformation a distinct internal inclined shear zone occurred inside the sand specimen which was marked by shear strain, larger grain rotation and volume increase (Fig.3). The thickness of the inclined interior shear zone t_s was on average in the residual state for ε_1=30% about t_s=25 mm (10×d_{50}) based on strain deformation in the specimen. The calculated shear zone inclination to the bottom was 60^o at ε_1=10% and 67^o at ε_1=30%.. In the calculated shear zone, the mean void ratio and grain rotation were: e>0.65 and ω>25^o. The specimen globally dilated in the shear zone. At the critical state, the maximum average void ratio was 0.70-0.80 in the shear zone and 0.53-0.60 outside. The maximum resultant rotation in the shear zone at the peak (ε_1=5%) was about ω=5^o and at the residual

state for ε_1=30% between ω=50°-55°. Based on both the cumulative rotation and void ratio (Fig.3), the internal inclined shear zone may be noticed for $\varepsilon_1 \geq 5\%$.

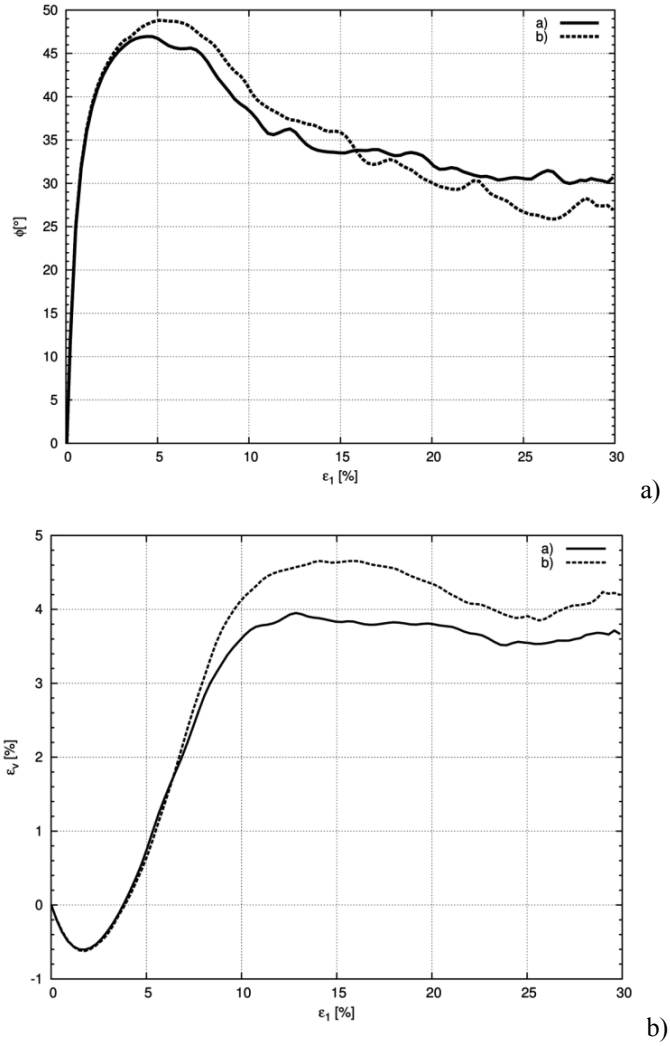

Figure 2: DEM results for plane strain compression with initially dense sand (e_o=0.53, σ_c=200 kPa, d_{50}=2.5 mm, E_c=0.3 GPa, ν_c=0.3, μ=18°, β=0.7, η=0.4) for two simulations: a) mobilized internal friction angle ϕ versus normalized vertical displacement of specimen top $\varepsilon_1=u_1/h$ and b) volumetric strain ε_v versus ε_1 (h - initial specimen height) [8]

4 HELMHOLTZ-HODGE DECOMPOSITION (HHD)

4.1 Calculation's method

The Helmholtz-Hodge decomposition (HHD) of vector fields is one of the fundamental theorems in fluid dynamics [10], [11], [19]. It describes a vector displacement increment field in terms of its curl-free and divergence-free components based on potential functions. The unique Helmholz-Hodge decomposition of the smooth 3D vector field $\vec{\xi}$ provides the following formula

$$\vec{\xi} = \vec{\nabla} u + \vec{\nabla} \times \vec{v} + \vec{h}, \tag{10}$$

where $\nabla = \left(\frac{\partial}{\partial x}, \frac{\partial}{\partial y}, \frac{\partial}{\partial z}\right)^T$ is the gradient, $\nabla \cdot = \left(\frac{\partial}{\partial x} + \frac{\partial}{\partial y} + \frac{\partial}{\partial z}\right)$ denotes the divergence operator, $\nabla \times$ is the curl operator, u denotes the scalar potential field, $\vec{v}$ is the vector potential field and $\vec{h}$ denotes the harmonic vector field. The gradient of the scalar potential function $\vec{\nabla} u$ is called the curl-free component and is related to expansion/contraction (because is irrotational) while the curl of the vector potential function $\vec{\nabla} \times \vec{v}$ is called the divergence-free component and is related to vorticity and pure shear (because is incompressible). The harmonic component which contains the non-integrable component of the field, is related to pure translation.

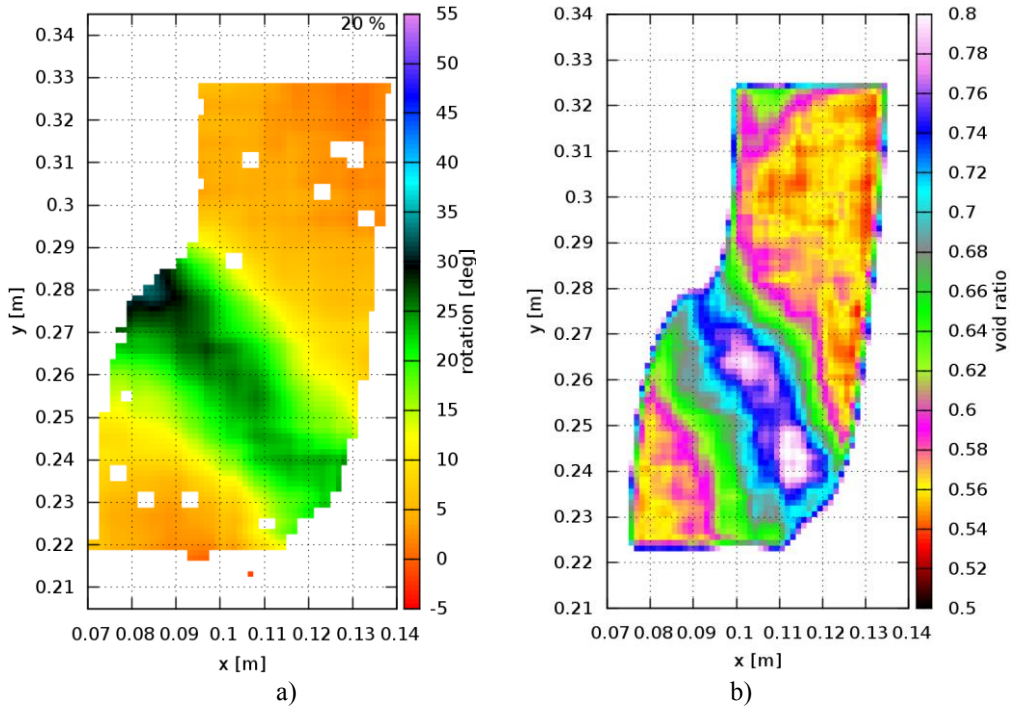

Figure 3: DEM results for plane strain compression test with initially dense sand (e_o=0.53, σ_c=200 kPa, d_{50}=2.5 mm): average cumulative grain rotation distribution and average cumulative void ratio distribution in degrees in granular specimen for vertical normal strain ε_l=20% [8]

A variational calculus approach was used [20] which allowed for finding the vector fields $\vec{\nabla} u$ and $\vec{\nabla} \times \vec{v}$ by examining the difference between the unknown vector field and provided field $\vec{\xi}$. By requesting that this difference is minimum (the minimum was found by assuming that the derivatives of the functionals were equal to zero, the vector fields $\vec{\nabla} u$ and $\vec{\nabla} \times \vec{v}$ were explicitly determined. The explicit calculation for $\vec{\nabla} u$ and $\vec{\nabla} \times \vec{v}$ was given in [9].

The accurate discrete multiscale Helmholz-Hodge decomposition of vector fields on arbitrary tetrahedral grids was proposed in [19]. In order to create a grid, the centre of each sphere was a node in the Delaunay triangulation and the i-th node had the coordinate $\vec{r}_i$. Then

the discrete piecewise-constant vector field $\vec{\xi}(\vec{r_i}) = \sum_k \psi_k(\vec{r})\,\overrightarrow{\xi_k}$ was created by assigning the constant vector value $\overrightarrow{\xi_k}$ to each k-th tetrahedron (ψ_k is the piecewise-constant basis function equal to 1 inside the k-th tetrahedron and 0 otherwise). This value was calculated as the average of sphere displacement increments $\overrightarrow{d_n}$ which constituted each tetrahedron $\overrightarrow{\xi_k} = 1/4\sum_{n=1}^{n=4}\overrightarrow{d_n}$ in the 3D case or each triangle $\overrightarrow{\xi_k} = 1/3\sum_{n=1}^{n=3}\overrightarrow{d_n}$ in the 2D case. Since u and $\vec{v}$ are the piecewise linear functions described using a piecewise-linear basis shape function $\phi_i(\vec{r})$, their derivatives ∇ will be piecewise-constant, hence the solution for the piecewise-constant $\vec{\xi}(\vec{r})$ discrete vector field is exact [19].

4.2 Boundary conditions

In order to obtain a unique solution, appropriate boundary conditions have to be assumed [11], [21]. The system of linear equations in HHD was solved using the following general boundary conditions: $\vec{\nabla}\times\vec{v}$ (divergence-free component - incompressible component) was tangential to the domain boundary $\vec{v}|_{\partial T}$=0 and $\vec{\nabla}u$ (curl-free component - irrotational component) was orthogonal to the boundary domain $u|_{\partial T}$=0. The proof of uniqueness and orthogonality for these boundary conditions, called N-P (normal-parallel) boundary conditions, which should be always maintained for flow problems can be found in [22]. Note that a change of these boundary conditions suggested in [23] may create an invalid or ill-posed problem [24]. The so-called Hodge-Morrey-Friedrichs boundary conditions may be also used [11]. The boundary conditions obviously influence vector fields close to specimen boundaries. In particular when the spheres' number is low; vortex-structures may be solely detected in the specimen centre since the vector field $\vec{\nabla}\times\vec{v}$ is forced by boundary conditions to be parallel to boundaries. In our previous calculations [9] the number of spheres along the height and length of the granular specimen was high enough (200-400) and the effect of boundaries proved to be insignificant on the distribution of vortices based on preliminary calculations. Due to a rather small number of particles along the specimen width during plane strain compression (≈16=b/d_{50}=40/2.5), the effect of boundary conditions during calculations of vortex-structures was weakened by introducing virtual particles outside boundaries [22]. Artificial nodes were added in the Delaunay's triangular mesh at the distance of up to 50 mm around the specimen (with the grid inter-node distance of 1 mm).The vector $\vec{\xi}$ in these artificial nodes was calculated using the Gaussian averaging for true specimen nodes with the averaging radius of 80 mm (2×b).

5 NUMERICAL RESULTS

Figures 4 and 5 show the calculated 3D vortex-structures in the granular specimens. The spatial view on the net of vortex-structures is shown in Fig.4 (the vortex-structures are shown in the form of cylinders which linked all local maxima). Figure 5 presents the vortex-structures at 3 different vertical cross-sections (specimen front side, specimen mid-depth and specimen rear side) for 5 different vertical normal strains ε_1: ε_1=1.5%, ε_1=3%, ε_1=5%, ε_1=10% and ε_1=20%. The circles denote the spots where the vertical cross-sections intersected the 3D vortex lines of Fig.4.

The vortex-structures appeared from the begin of the specimen deformation. They were immediately concentrated in the region of the shear zone occurrence. Thus the ultimate shear zone turned out to be encoded in the grain kinematics from the deformation onset. This outcome is in accordance with our earlier calculation results for plane strain compression based on displacement fluctuations [8] and calculation results based on bottlenecks in force transmission through the contact network [24]. The right-handed vortices (green circles) were created during progressive deformation. The distribution of vortex-structures was not uniform in the specimen and their number was different in vertical cross-sections up to the residual state. The number of vortex-structure was smaller in 3D simulations than in 2D ones.

6 CONCLUSIONS

- The vortex-structures were the precursor of shear localization since they clearly concentrated in the area where a shear zone ultimately later formed. Thus the ultimate shear zone was detected in early loading stages. The vortex-structures allowed to identify shear localization significantly earlier than e.g. based on single grain rotations or an increase of void ratio which were always a reliable indicator of shear localization. They developed from the deformation process beginning.
- An early prediction possibility of shear localization through vortex-structures may open new perspectives for a detection of impending failure in granular bodies (inherently connected with shear localization) within continuum mechanics.

ACKNOWLEDGMENT

The authors would like to acknowledge the support by the grant 2011/03/B/ST8/05865 "*Experimental and theoretical investigations of micro-structural phenomena inside of shear localization in granular materials*" financed by the Polish National Science Centre.

REFERENCES

[1] Utter, B. and Behringer, RP. Self-diffusion in dense granular shear flows. *Phys. Rev. E*. (2004) **69** (3), 031308-1–031308-12.
[2] Abedi, S., Rechenmacher A.L. and Orlando A.D. Vortex formation and dissolution in sheared sands. *Granular Matter* (2012) **14**: 695-705.
[3] Richefeu, V., Combe, G. and Viggiani G. An experimental assessment of displacement fluctuations in a 2D granular material subjected to shear. *Geotechnique Letters* (2012) **2**:113-118.
[4] Tordesillas, A., Pucilowski, S., Lin, Q., Peters, J.F. and Behringer, RP. Granular vortices: identification, characterization and conditions for the localization of deformation. *Journal of Mechanics and Physics of Solids* (2016) **90**: 215-241.
[5] Peters, J.F. and Walizer, L.E. Patterned non-affine motion in granular media**.** *Journal of Engineering Mechanics* (2013) **139** (10): 1479-1490.
[6] Nitka M, Tejchman J. Modelling of concrete behaviour in uniaxial compression and tension with DEM. *Granular Matter* 2014, 17 (1), 145-164.
[7] Nitka M, Tejchman J, Kozicki J, Leśniewska D. DEM analysis of micro-structural events within granular shear zones under passive earth pressure conditions. *Granular Matter* 2015, 3, 325-343.

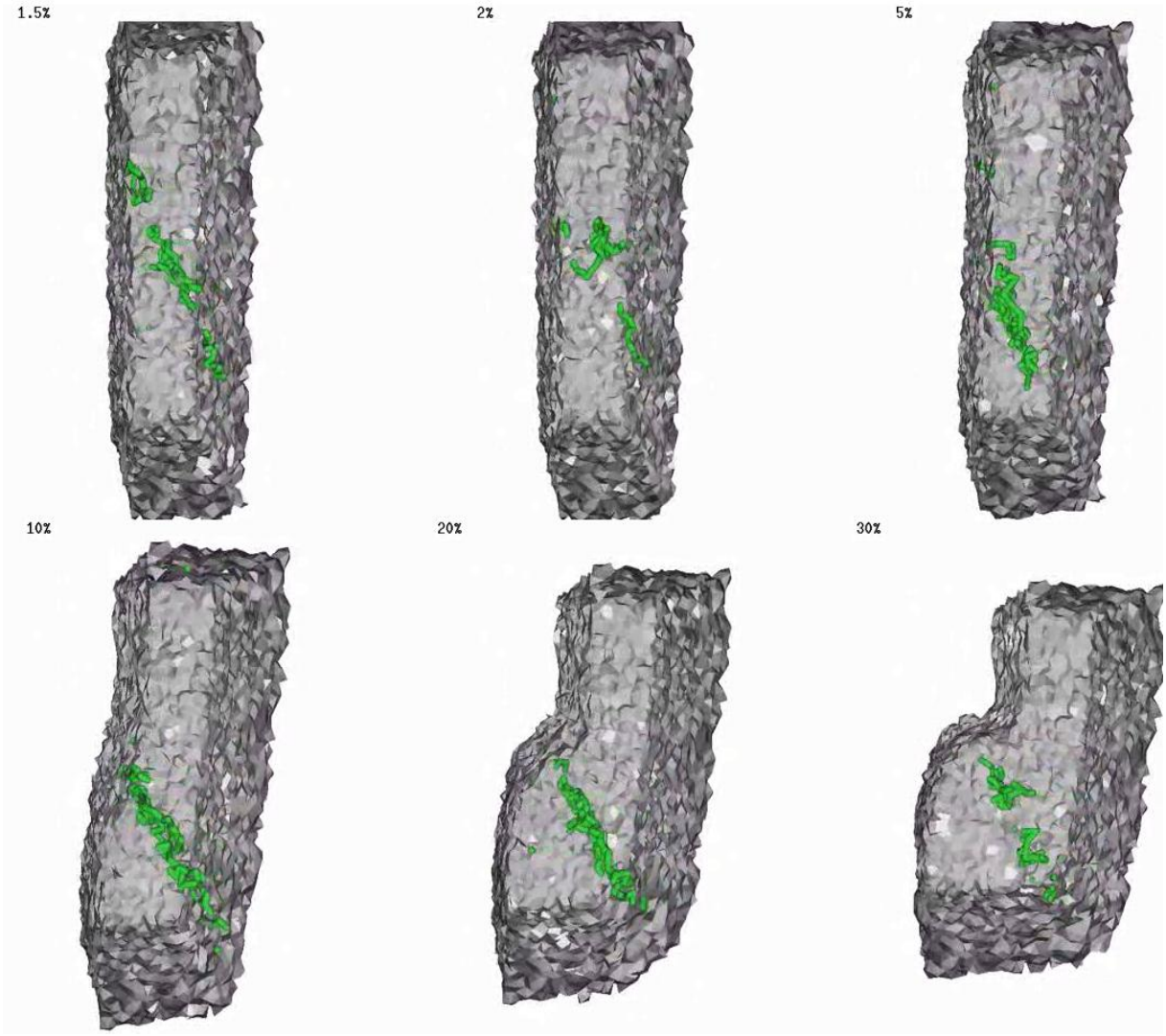

Figure 4: 3D vortex-structures in 3 for different vertical normal strain ε_l=1.5%-30% (green lines link local minima (right-handed vortices)

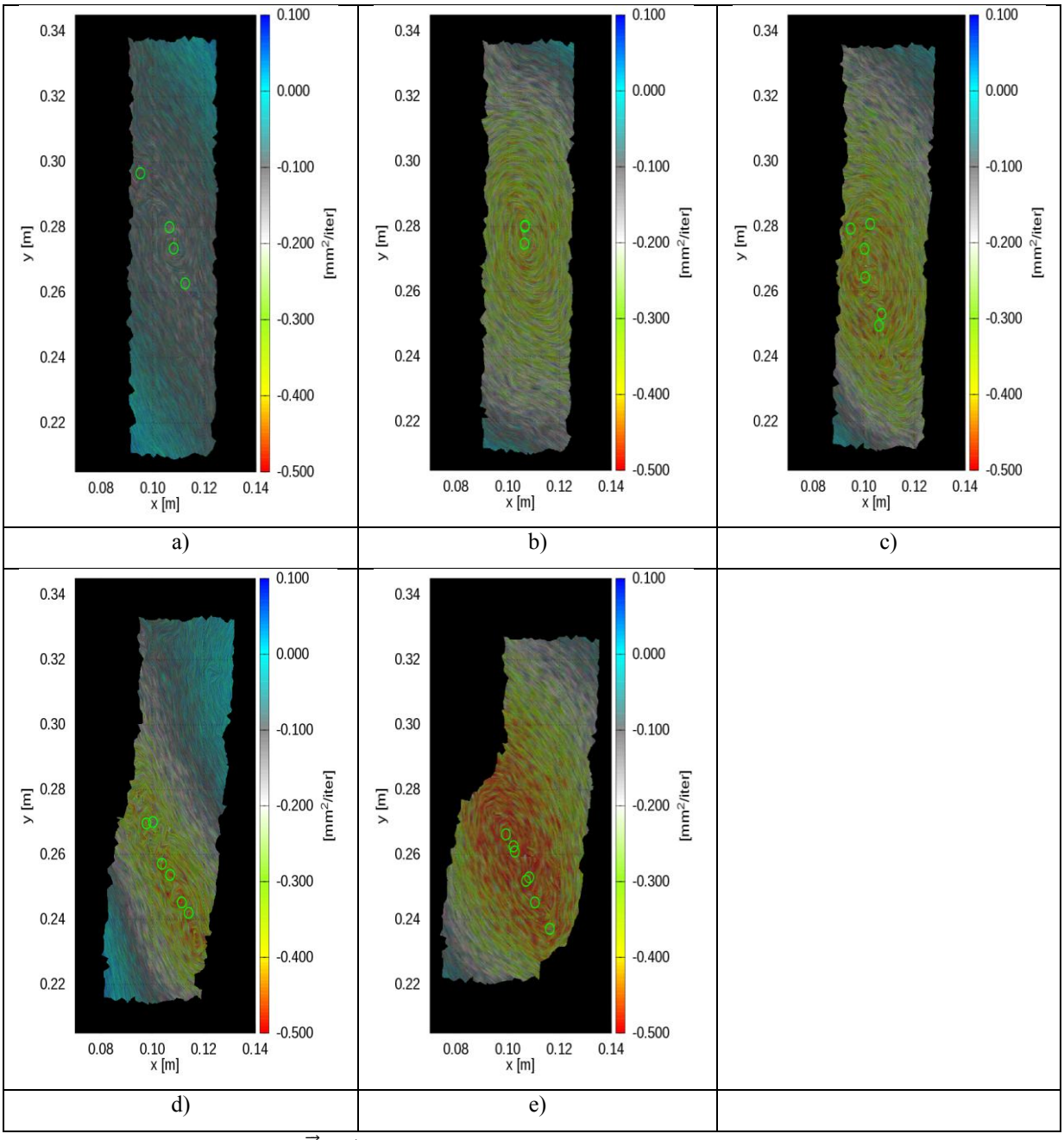

Figure 5: 3D vector field curl $\vec{\nabla} \times \vec{v}$ (divergence-free component related to vorticity) in granular specimen area $x \times y$ in vertical cross-section at specimen mid-depth for different vertical normal strain ε_1: a) ε_1=1.5%, b) ε_1=3%, c) ε_1=5%, d) ε_1=10% and e) ε_1=20%, (scale denotes component of vector potential $\vec{v}$ perpendicular to specimen in [mm^2/iteration]), green circles describe local minima (right-handed vortices))

[8] Kozicki, J. and Tejchman, J. DEM investigations of two-dimensional granular vortex- and anti-vortex- structures during plane strain compression. *Granular Matter* (2016) **2**, 20: 1-28.
[9] Kozicki J, Tejchman J. Investigations of quasi-static vortex structures in 2D sand specimen under passive earth pressure conditions based on DEM and Helmholtz-Hodge vector field decomposition. *Granular Matter* (2017) **19** (2), 19-31.
[10] Helmholtz H. Über Integrale der Hydrodynamischen Gleichungen, Welche den Wirbelbewegungen Entsprechen. (German) *J. für die Reine und Angewandte Mathematik* (1858) **55**: 25-55.
[11] Bhatia, H. and Pascucci, V. The Helmholtz-Hodge decomposition - a survey. *IEEE Transactions on Visualization and Computer Graphics* (2013), **19** (8): 1386-1404.
[12] Kozicki, J. and Donze, F.V. A new open-source software developed for numerical simulations using discrete modelling methods. *Computer Methods in Applied Mechanics and Engineering* (2008) **197**: 4429-4443.
[13] Šmilauer, V. and Chareyre, B. *Yade DEM Formulation*. Manual (2011).
[14] Cundall, P.A. and Strack, O.D.L. A discrete numerical model for granular assemblies. *Geotechnique* (1979) **29**: 47-65.
[15] Kozicki, J., Tejchman, J. and Mróz, Z. Effect of grain roughness on strength, volume changes, elastic and dissipated energies during quasi-static homogeneous triaxial compression using DEM. *Granular Matter* (2012) **14**(4):457-468.
[16] Kozicki, J., Tejchman J. and Műhlhaus, H.B. Discrete simulations of a triaxial compression test for sand by DEM. *Int. J. Num. Anal. Methods in Geomech.* (2014) **38**: 1923-1952.
[17] Wu, W. Hypoplastizität als mathematisches Modell zum mechanischen Verhalten granularer Stoffe. *Heft 129, Institute for Soil- and Rock-Mechanics, University of Karlsruhe*, 1992.
[18] Vardoulakis, I. Shear band inclination and shear modulus in biaxial tests. *Int. J. Numer. Anal. Methods Geomech*. (1980) **4**: 103-119.
[19] Tong, Y, Lombeyda, S, Hirani, A.N. and Desbrun, M. Discrete multiscale vector field decomposition. *ACM Transactions on Graphics* (TOG) (2003) 22 (3): 445-452.
[20] Gelfand, I.M. and Fomin, S.V. Calculus of variations. Dover Publications INC, Mineola, New York, 1963 (re-published in 2001), ISBN 9780486414485.
[21] Denaro, F.M. On the application of the helmholtz-hodge decomposition in projection methods for incompressible flows with general boundary conditions. *Int. J. Numerical Methods in Fluid*s (2003) **43**: 43-69.
[22] Petroneto, F., Paiva, A., Lage, M., Tavares, G., Lopes, H. and Lewiner, T. Meshless Helmholz-Hodge decomposition. *IEEE Transactions on Visualization and Computer Graphics* 2010, **16**: 338-349.
[23] Bhatia, H., Norgard, G., Pascucci, V. and Bremer, P.T. Comments on the meshless helmholtz-hodge decomposition. IEEE Transactions on Visualization and Computer Graphics (2013) **19** (3): 527-529.
[24] Tordesillas A, Pucilowski S, Tobin S, Kuhn M, Ando E, Viggiani G, Druckrey A. and Alshibli K. Shear bands as bottlenecks in force transmission. *EPL* (2015) **110**: 58005.

3 TITLE, AUTHORS, AFFILIATION, KEY WORDS

The first page must contain the Title, Author(s), Affiliation(s), Key words and the Summary. The Introduction must begin immediately below, following the format of this template.

3.1 Title

The title should be written centered, in 14pt, boldface Roman, all capital letters. It should be single spaced if the title is more than one line long.

3.2 Author

The author's name should include first name, middle initial and surname. It should be written centered, in 12pt boldface Roman, 12pt below the title.

3.3 Affiliation

Author's affiliation should be written centered, in 11pt Roman, 12pt below the list of authors. A 12pt space should separate two different affiliations.

3.4 Key words

Please, write no more than six key words. They should be written left aligned, in 12pt Roman, and the line must begin with the words **Key words:** boldfaced. A 12pt space should separate the key words from the affiliations.

3.5 Summary (optional)

Use 12pt Italic Roman for the summary. The word **Summary** must be set in boldface, not italicized, at the beginning of the first line. The text should be justified and separated 12pt from the key words, as shown in the first page of these instructions.

4 HEADINGS

4.1 Main headings

The main headings should be written left aligned, in 12pt, boldface and all capital Roman letters. There should be a 12pt space before and 6pt after the main headings.

4.2 Secondary headings

Secondary headings should be written left aligned, 12 pt, boldface Roman, with an initial capital for first word only. There should be a 12pt space before and 6pt after the secondary headings.

5 EDITORIAL HEADING

The first page has to include the Editorial Heading, as shown in the first page of these instructions. Successive pages will include the name of the authors.

6 TEXT

The normal text should be written single-spaced, justified, using 12pt (Times New) Roman in one column. The first line of each paragraph must be indented 0.5cm. There is not inter-paragraph spacing.

7 PAGE NUMBERS

In order to organize the Full Paper, it is better to number the pages. Page numbers are not included in the printing box.

8 FIGURES

All figures should be numbered consecutively and captioned. The caption title should be written centered, in 10pt Roman, with upper and lower case letters.

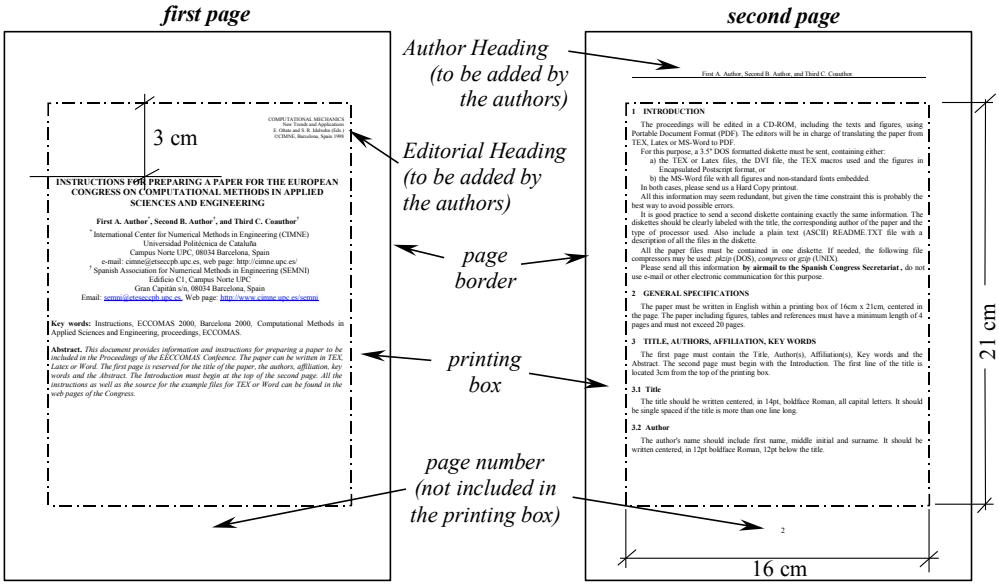

Figure 1: Page layout

A 6pt space should separate the figure from the caption, and a 12pt space should separate the upper part of the figure and the bottom of the caption from the surrounding text.

Figures may be included in the text or added at the bottom of the Full Paper.

9 EQUATIONS

A displayed equation is numbered, using Arabic numbers in parentheses. It should be centered, leaving a 6pt space above and below to separate it from the surrounding text.

The following example is a single line equation:

$$Ax = b \tag{1}$$

The next example is a multi-line equation:

$$Ax = b \tag{2}$$

10 TABLES

All tables should be numbered consecutively and captioned, the caption should be 10pt Roman, upper and lower case letters.

Table 1: Example of the construction of one table

C11	C12	C13
C21	C22	C23
C31	C32	C33
C41	C42	C43
C51	C52	C53

A 6pt space should separate the table from the caption, and a 12pt space should separate

the table from the surrounding text.

11 FORMAT OF REFERENCES

References should be quoted in the text by superscript numbers [1,2] and grouped together at the end of the Full Paper in numerical order as shown in these instructions.

12 CONCLUSIONS

- Full Papers in format for publication should be submitted electronically via the web page of the Conference, before May 26, 2017. The file must be converted to Portable Document Format (PDF) before submission. The maximum size of the file is 4 Mb.
- The speaker (corresponding author) is expected to pay his registration fee during the advance period (before May 26, 2017) for the presentation to be included in the final program of the Conference.

REFERENCES

[1] Zienkiewicz, O.C. and Taylor, R.L. *The finite element method*. McGraw Hill, Vol. I., (1989), Vol. II, (1991).

[2] Idelsohn, S.R. and Oñate, E. Finite element and finite volumes. Two good friends. *Int. J. Num. Meth. Engng* (1994) **37**:3323-3341.

V International Conference on Particle-based Methods – Fundamentals and Applications
PARTICLES 2017
P. Wriggers, M. Bischoff, E. Oñate, D.R.J. Owen, & T. Zohdi (Eds)

DISCRETE ELEMENT MODELLING OF GRANULAR COLUMN COLLAPSE TESTS WITH INDUSTRIAL APPLICATIONS

JOEL TORRES-SERRA[1], DEEPAK R. TUNUGUNTLA[2], IRANA F.C. DENISSEN[2], ANTONIO RODRÍGUEZ-FERRAN[3] AND ENRIQUE ROMERO[3]

[1] Técnicas Mecánicas Ilerdenses, S.L.
Polígono industrial Camí dels Frares, c. Alcarràs, parc. 66, 25190 Lleida, Spain
e-mail: j.torres@tmipal.com

[2] Multi-Scale Mechanics, Engineering Technology/MESA+
University of Twente, P.O. Box 217, 7500 AE Enschede, The Netherlands

[3] Universitat Politècnica de Catalunya – BarcelonaTech
Campus Nord, c. Jordi Girona, 1-3, 08034 Barcelona, Spain

Key words: DEM, granular column collapse, particle size distribution, coarse-graining.

Abstract. The effect of particle size distribution on dry granular flows of spherical particles has been numerically investigated. A quasi-two-dimensional granular column collapse set-up has been modelled using the Discrete Element Method (DEM). Systems formed by monodisperse particles of radius $R = 0.01$ m and polydisperse particles of the same average radius and coefficient of uniformity $C_u = 1.9$ have been studied for initial granular columns aspect ratios of 1.1 and 2.2. The results using monodisperse and narrow particle size distributions show similar evolution of the run-out profiles, the final run-out distance being reached in less than one second in every configuration. Averaged velocity fields have been obtained, from which peak values of longitudinal and vertical components of velocity have been found.

1 INTRODUCTION

Describing the behaviour of granular materials is a challenging issue for the packaging industry where bulk handling equipment is designed to handle a wide range of powders and bulk solids varying in both physical and mechanical properties. As a result, not only performance of packaging equipment is negatively affected but also are packaging quality and the whole process itself. Furthermore, environmental conditions such as relative humidity also have serious consequences on the efficiency of material conveying techniques.

Thereby even a small improvement in the efficiency of equipment can lead to both significant financial and environmental benefits.

For this purpose, the granular column collapse set-up is used, as it is known to provide deep insights into the dynamics of granular flow regimes both at particle and bulk level [1]. However, as an alternative to experiments, in this paper the discrete element method (DEM) is utilised because of its ability to effectively control and quantify the micro-scale parameters, what is often very difficult to do in an experiment. Several particle properties, including size [2], shape [3] and density [4], are known to affect the bulk macroscopic behaviour. However, as a stepping stone, this study focusses on numerically investigating the effects of varying particle size distribution by utilising the open-source particle simulation package MercuryDPM [5]. Eventually, the goal is to systematically model the effects of varying particle properties, which in turn would help us define and improve decision-making strategies for the design of packaging equipment.

The following sections present the simulation methodology and the findings of our investigation.

2 METHODOLOGY

2.1 DEM model

In the implemented simulations, a linear normal contact model is used to describe particle motion of the translational degrees of freedom, where the inter-particle contact parameters comprise normal stiffness, k_n, and viscous dissipation, γ_n, as well as the tangential counterparts k_t, γ_t. Additionally, the tangential or sliding friction coefficient, μ_t, is used to define a Coulomb-type coupling between the tangential and normal components of the force acting on particle i, $\mathbf{f}_i$, due to contact with neighbour particles j:

$$\mathbf{f}_i = \sum_j \left(f_n \mathbf{n} + f_t \mathbf{t}\right) \tag{1a}$$

$$f_n = \begin{cases} 0 & \delta_n \leq 0 \\ k_n \delta_n + \gamma_n v_n & \delta_n > 0 \end{cases} \tag{1b}$$

$$f_t = \min\left\{\mu_t f_n; k_t \delta_t + \gamma_t v_t\right\} \tag{1c}$$

where δ_n is overlap between particles, δ_t is tangential spring of active contacts and v_n, v_t are the normal and tangential components of relative velocity, respectively. Regarding rotational degrees of freedom, the contribution to torque of inter-particle rolling resistance is accounted for using stiffness, dissipation and friction coefficients, k_r, γ_r, μ_r, and torsional resistance is described using parameters k_o, γ_o, μ_o, which, along with tangential coefficients, define total torque on particle i, $\mathbf{q}_i$, as discussed by Luding [6]:

$$\mathbf{q}_i = \sum_j \left[\left(\mathbf{l}_i \times \mathbf{f}_i\right) + \mathbf{q}_i^t + \mathbf{q}_i^r + \mathbf{q}_i^o\right] \tag{2}$$

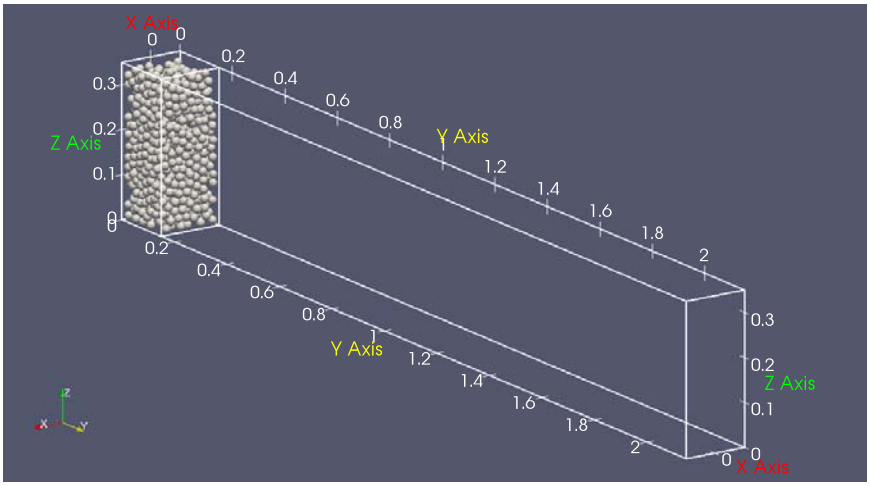

Figure 1: Simulation set-up of the granular column collapse channel. Dimensions in [m]

where $\mathbf{l}_i$ is the branch vector and $\mathbf{q}_i^t$, $\mathbf{q}_i^t$, $\mathbf{q}_i^t$ are respectively the tangential, rolling and torsional components of total torque.

2.2 Granular column collapse set-up

A quasi-two-dimensional granular column collapse simulation set-up has been studied to assess the influence of particle size polydispersity on the run-out process. The considered domain consists in a prismatic horizontal channel of total length 2150 mm, height 350 mm and width 150 mm, along which run-out takes place. An auxiliary vertical wall is initially placed at length 150 mm, which forms a reservoir of square section where the granular columns are generated, as shown in Figure 1. Granular piles are allowed to settle in the reservoir under gravity, until stationary initial packing conditions are reached. The arrangement of particles is then instantaneously released onto the channel, by removing the auxiliary vertical wall from the simulation domain.

Spherical particles have been simulated, with particle density $\rho_p = 2000\ \mathrm{kg\,m^{-3}}$. Two different particle size distributions (PSD) of the granular material have been studied:

- Monodisperse PSD with particle radius $R = 0.01$ m;
- Polydisperse PSD with average particle radius $R = 0.01$ m. Randomly generated radii are obtained by linear interpolation between input values from $R = 5.0 \times 10^{-3}$ m to $R = 1.5 \times 10^{-2}$ m, as shown in Figure 2. The coefficient of uniformity of the polydisperse particle system is $C_u := D_{60}/D_{10} = 1.9$.

Moreover, simulations with two different number of particles of the system have been carried out, being $N = \{500, 1000\}$ for assemblies of monodisperse spheres and respectively adjusted to $N = \{405, 809\}$ in the polydisperse case, by enforcing the total mass of the system to be preserved.

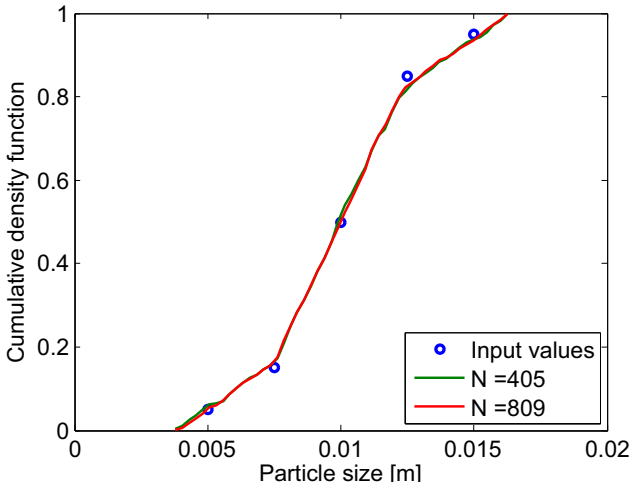

Figure 2: Cumulative distribution function for the polydisperse PSD

Table 1: Inter-particle contact parameters of granular column collapse simulations

		Stiffness $[\mathrm{N\,m^{-1}}]$ $k_\square$	Dissipation $[\mathrm{N\,s\,m^{-1}}]$ $\gamma_\square$	Friction coefficient $\mu_\square$
Normal	$\square_n$	2.0×10^4	0.5	—
Tangential	$\square_t$	2.0×10^3	0.1	0.5
Rolling	$\square_r$	2.0×10^3	0.1	0.05
Torsional	$\square_o$	2.0×10^3	0.1	0.05

Mechanical properties of the contacts are shown in Table 1. Since a linear spring–dashpot contact model has been used, overdamping of the system is prevented by controlling the value of contact eigenfrequencies. The values of normal stiffness and viscous dissipation of the particles fulfil the following relation:

$$\gamma_n = \sqrt{2 k_n m_{\min}} \tag{3}$$

where $m_{\min}$ corresponds to the minimum particle mass of the system. Mechanical parameters governing particle–wall interactions have not been modified with respect to inter-particle contact properties.

3 RESULTS AND DISCUSSION

Total mass of the system is $m = 4.189$ kg and $m = 4.245$ kg respectively for the case with $N = 500$ monodisperse particles and $N = 405$ polydisperse particles. Analogously, total mass is $m = 8.378$ kg and $m = 8.4806$ kg respectively for the case with $N = 1000$ monodisperse particles and $N = 809$ polydisperse particles. Therefore, the considered particle system configurations are approximately equivalent with respect to the total mass of the system.

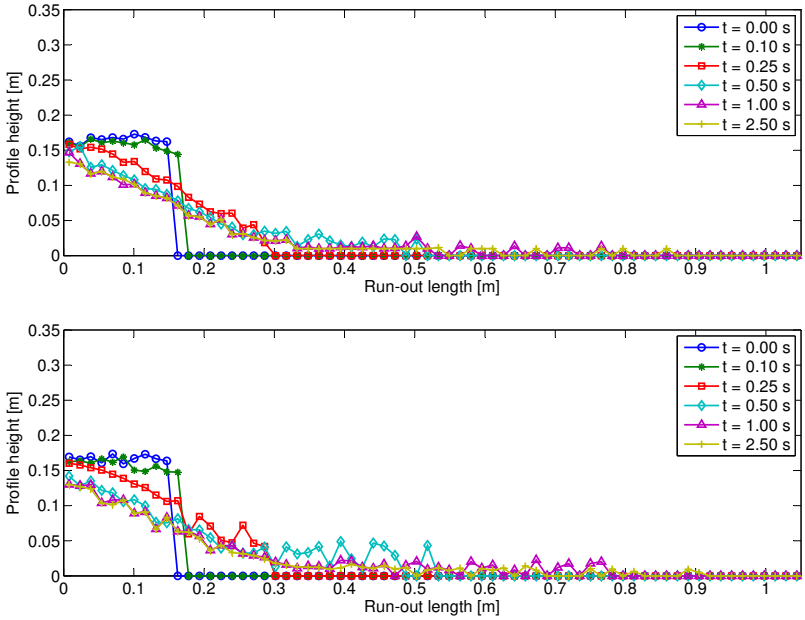

Figure 3: Lateral profile tracking from $t = 0$ s to $t = 2.5$ s: $N = 500$ monodisperse particles (upper); and $N = 405$ polydisperse particles (lower)

System stability is controlled by adjusting the normal contact parameters, which results in a critical contact time, t_c, and coefficient of restitution, r, that are $t_c = 1.438 \times 10^{-3}$ and $r = 0.918$ for the monodisperse case, and $t_c = 3.325 \times 10^{-4}$ and $r = 0.686$ for the case with size polydispersity. Introducing size polydispersity while preserving average particle size by mass leads to smaller stable time increments in the numerical scheme. Additionally, the critical restitution coefficient is decreased, although to a lesser extent, in the polydisperse case.

Evolution of flow profiles has been tracked in the YZ plane, time being measured from the onset of flow, in order to identify final run-out distance at the end of the simulation. Initial column heights are $H = 0.165$ m and $H = 0.167$ m respectively for the case with $N = 500$ monodisperse particles and $N = 405$ polydisperse particles, resulting in a column aspect ratio $a = 1.1$, with respect to the reservoir base length (0.150 m). At the same time, column heights are $H = 0.336$ m and $H = 0.326$ m respectively for the case with $N = 1000$ monodisperse particles and $N = 809$ polydisperse particles, the initial column aspect ratio being $a = 2.2$. Particle positions are averaged over the channel width, along which granular flow is mainly homogeneous, thus providing the lateral observation of the run-out, as shown in Figure 3 and Figure 4. It is observed that the whole collapse to run-out process lasts for about a second in every configuration. Thereafter, the system is found to remain in a stable configuration with a constant morphology of the free surface and a few moving particles located near the flow front. Final run-out distance is therefore defined as the channel length comprising 95% of the mass of the system, considering 5% ot the

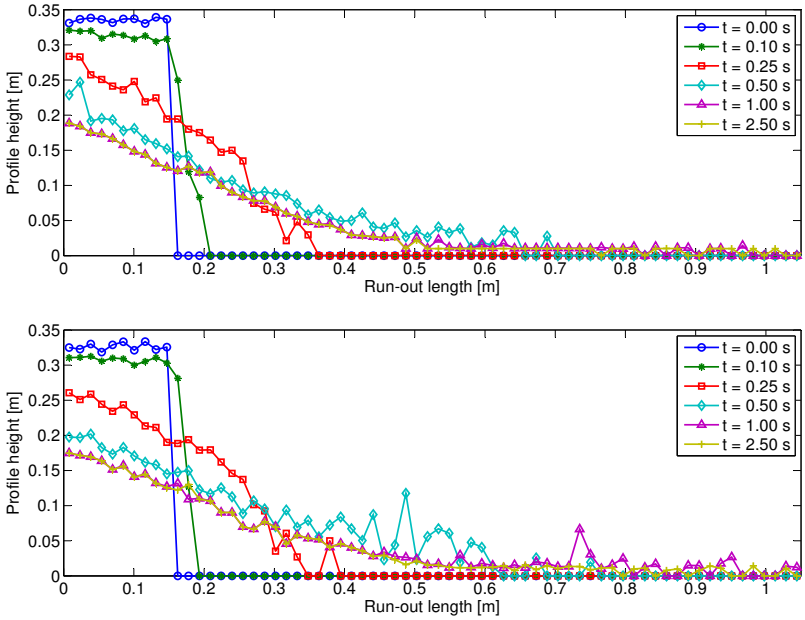

Figure 4: Lateral profile tracking from $t = 0$ s to $t = 2.5$ s: $N = 1000$ monodisperse particles (upper); and $N = 809$ polydisperse particles (lower)

total mass corresponds to particles ahead of the flow front. After run-out, at $t = 1$ s, final run-out distance for the configurations with $N = 500$ monodisperse particles and $N = 405$ polydisperse particles are $L = 0.387$ m and $L = 0.418$ m, respectively. In addition, for the computations with $N = 1000$ monodisperse particles and $N = 809$ polydisperse particles, final run-out distances are respectively $L = 0.572$ m and $L = 0.603$ m.

In order to map the particle data onto a continuum field, an accurate micro-macro mapping technique called coarse graining is used [7, 8]. Coarse-grained velocity field, fully averaged over the channel width (X Axis), $\langle \mathbf{v}(\mathbf{x},t)\rangle_x$, is obtained by:

$$\langle \mathbf{v}(\mathbf{x},t)\rangle_x = \frac{\left\langle \sum_{i=1}^{N} m_i \mathbf{v}_i(t)\phi(\mathbf{x}-\mathbf{x}_i(t))\right\rangle_x}{\left\langle \sum_{i=1}^{N} m_i \phi(\mathbf{x}-\mathbf{x}_i(t))\right\rangle_x} \tag{4}$$

where m_i is the particle mass, $\mathbf{v}_i(t)$ is the time-dependent particle velocity and $\phi(\mathbf{x}-\mathbf{x}_i(t))$ is a coarse-graining function. In this study, a gaussian function has been used, with scale equal to the maximum particle radius of the particle assembly, $w = \max_i\{R_i\}$. Table 2 summarizes peak values for longitudinal, v_y, and vertical, v_z —negative downwards, components of velocity during run-out.

As far as the simulations with $N = 500$ and $N = 405$ particles are concerned, peak v_y is larger for the case with polydisperse spheres. Maximum values attained are in agreement in the case of $N = 1000$ and $N = 809$ particles, althoguh peak v_z is observed at a later time during run-out for the case of size polydisperse particles. Figure 5 shows maps of

Table 2: Peak values of v_y and v_z at respective time instants, t

	v_y $[\mathrm{m\,s^{-1}}]$	t [s]	v_z $[\mathrm{m\,s^{-1}}]$	t [s]
Monodisperse $N = 500$	0.855	0.25	−0.769	0.20
Polydisperse $N = 405$	1.078	0.30	−0.757	0.25
Monodisperse $N = 1000$	1.517	0.35	−1.413	0.30
Polydisperse $N = 809$	1.588	0.55	−1.154	0.30

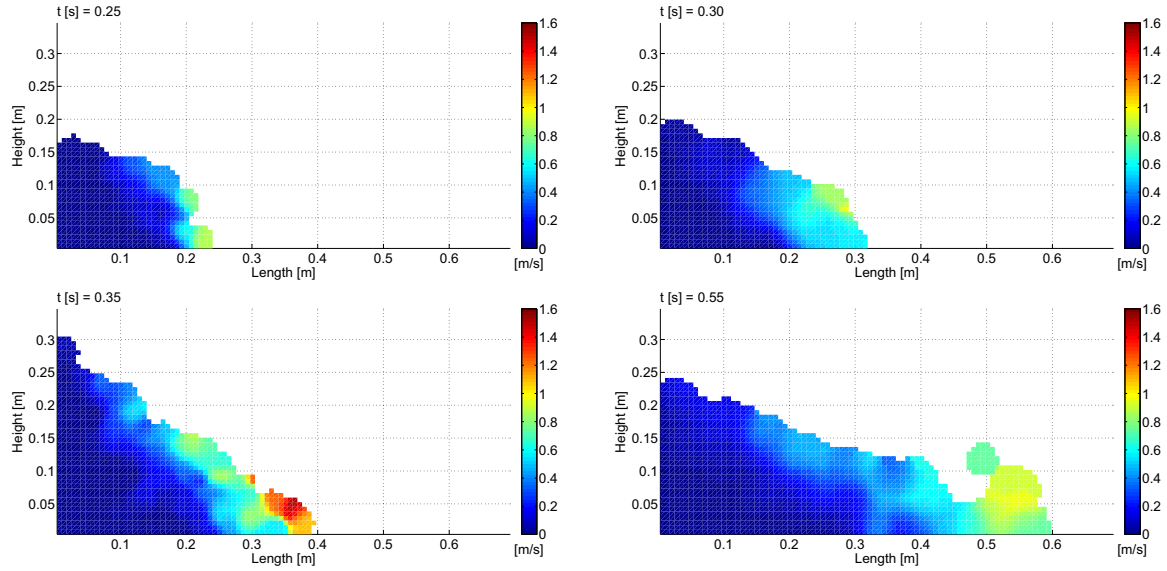

Figure 5: Peak v_y velocity maps: $N = 500$ monodisperse particles (upper-left); $N = 405$ polydisperse particles (upper-right); $N = 1000$ monodisperse particles (lower-left); $N = 809$ polydisperse particles (lower-right)

v_y along the channel (Y Axis) at the respective times when peak velocity is reached. Vertical component of velocity (Z Axis), at respective time instants of peak values of v_z, is shown in Figure 6.

In light of the results, notable differences in flow behaviour have not been identified when comparing granular collapse of spheres of radius $R = 0.01$ with another sphere assembly of the same average particle size and corresponding to a narrow-graded material. Evolution of laterial profiles during run-out is analogous, resulting in final deposits in the form of shallow slopes. The velocity fields established during flow propagation also show similar trends, as for all simulations a flow front is rapidly developed, dominated by the longitudinal component of velocity.

4 CONCLUDING REMARKS

The effect of particle size on run-out profiles, final run-out distances and averaged peak velocities has been analysed for two granular column collapse set-ups using two

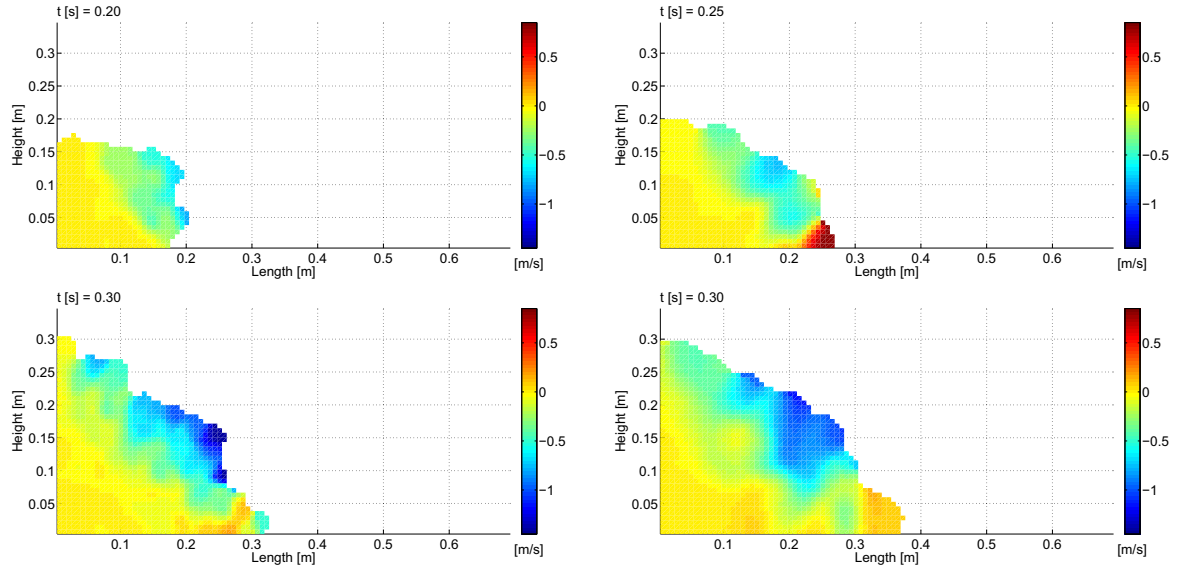

Figure 6: Peak v_z velocity maps: $N = 500$ monodisperse particles (upper-left); $N = 405$ polydisperse particles (upper-right); $N = 1000$ monodisperse particles (lower-left); $N = 809$ polydisperse particles (lower-right)

monodisperse and polydisperse spherical particles. In future investigations, the influence of other particle properties and environmental effects are to be studied, including:

- Average partice size reduction, leading to an increase of the number of particles and different flow behaviours,
- Polydispersity in particle shape, comparing the use of spherical and non-spherical particles, namely ellipsoids, and
- Hygroscopicity effect, adding water content to particle assemblies to observe capillary behaviour in the pendular state.

ACKNOWLEDGEMENTS

The first author would like to acknowledge the financial support provided by Project 2014 DI 075, "Optimization of dosing systems for bulk solids using experimental and numerical techniques", funded by the Industrial Doctorates Plan of the Government of Catalonia.

REFERENCES

[1] Torres-Serra, J., Romero, E., Rodríguez-Ferran, A., Caba, J., Arderiu, X., Padullés, J.-M. and González, J. Flowability of granular materials with industrial applications. An experimental approach. In: *Powders and Grains 2017: 8th International Con-*

ference on Micromechanics of Granular Media EPJ Web of Conferences, Vol. 140, (2017).

[2] Lu, H., Guo, X., Liu, Y. and Gong, X. Effect of Particle Size on Flow Mode and Flow Characteristics of Pulverized Coal. *KONA Powder Part. J.* (2015) **32**:143–153.

[3] Fu, X., Huck, D., Makein, L., Armstrong, B., Willen, U. and Freeman, T. Effect of particle shape and size on flow properties of lactose powders. *Particuology* (2012) **10**(2):203–208.

[4] Tunuguntla, D., Bokhove, O. and Thornton, A. A mixture theory for size and density segregation in shallow granular free-surface flows. *J. Fluid Mech.* (2014) **749**:99–112.

[5] Weinhart, T., Tunuguntla, D.R., van Schrojenstein-Lantman, M.P., van der Horn, A.J., Denissen, I.F.C., Windows-Yule, C.R., de Jong, A.C. and Thornton, A.R. *MercuryDPM*: A Fast and Flexible Particle Solver Part A: Technical Advances. In: Li X., Feng Y., Mustoe G. (eds) *Proceedings of the 7th International Conference on Discrete Element Methods. DEM 2016.* Springer Proceedings in Physics, Springer, Singapore, Vol. 188, (2017).

[6] Luding, S. Introduction to discrete element methods. *European Journal of Environmental and Civil Engineering* (2008) **12**(7–8):785–826.

[7] Weinhart, T., Thornton, A. R., Luding, S. and Bokhove, O. From discrete particles to continuum fields near a boundary. *Granul. Matter* (2012) **14**(2):289–294.

[8] Tunuguntla, D.R., Thornton, A.R. and Weinhart, T. From discrete elements to continuum fields: Extension to bidisperse systems. *Comp. Part. Mech.* (2016) **3**:349–365.

V International Conference on Particle-based Methods – Fundamentals and Applications
PARTICLES 2017
P. Wriggers, M. Bischoff, E. Oñate, D.R.J. Owen, & T. Zohdi (Eds)

MPM SIMULATIONS OF GRANULAR COLUMN COLLAPSE WITH A NEW CONSTITUTIVE MODEL FOR THE SOLID-FLUID TRANSITION

IRENE REDAELLI[1], FRANCESCA CECCATO[2], CLAUDIO G. DI PRISCO[3] AND PAOLO SIMONINI[4]

[1] Politecnico di Milano (DICA),
Piazza Leonardo da Vinci 32, Milano 20133, Italy
irene.redaelli@polimi.it

[2] Università degli Studi di Padova (DICEA),
Via Ognissanti 39, Padova 23129
francesca.ceccato@dicea.unipd.it

[3] Politecnico di Milano (DICA),
Piazza Leonardo da Vinci 32, Milano 20133, Italy
claudio.diprisco@polimi.it

[4] Università degli Studi di Padova (DICEA),
Via Ognissanti 39, Padova 23129
paolo.simonini@unipd.it

Key words: dense granular flows, MPM, column collapse, constitutive modelling.

Abstract. Dry granular flows are very common both in many natural phenomena (flow-like landslides) as well as in industrial processes. To model granular flows in the framework of continuum mechanics, a key issue is the formulation of a suitable constitutive model, capable of capturing the complex rheological behaviour of the granular material in a wide range of strain rates. In this contribution, a physically based model capable of reproducing the behaviour of granular materials in different flow regimes is briefly summarized. Both the stress tensor and the dissipated energy are calculated as the sum of a quasi-static and a collisional contribution: the former one is modelled by employing an elasto-plastic model incorporating the critical state concept, whereas the latter stems from the kinetic theory of granular gases. The constitutive model has been implemented in the MPM research code Anura3D and applied to the simulation of the collapse of a dry granular column. The results show that the model can deal with the phase transition between the solid- and the fluid-like behaviour. The evolution of the state variables, the state of stress and the energy contributions is investigated in details.

1 INTRODUCTION

Flows of dry granular materials characterizes many natural and industrial processes. An important feature of granular materials is that, depending on the strain rates and the grain packing, they may behave like a solid, a liquid or a gas. Two different particle interaction mechanisms can be identified in granular materials: (i) enduring frictional contacts among grains involved in force chains and (ii) inelastic collisions. At high particle concentrations and slow strain rates (quasi-static regime), the first mechanism prevails and the material behaves like a solid, where force chains span the entire domain. At low concentrations and very high strain rates (collisional regime), the second mechanism prevails and the material behaves like a granular gas. In between these two conditions, both mechanisms are relevant, the material is in the "transition regime" and behaves like a granular liquid.

The Discrete Element Methods (DEM) is commonly employed to study the flow of granular materials because it is capable of automatically take into account large displacements as well as the granular nature of the material: however, this approach becomes inefficient for high numbers of grains. Large-scale phenomena are more often studied with continuum methods that apply a macroscopic approach. A key issue in this problem is the definition of a constitutive relationship suitable for reproducing the transition form a solid- to fluid-like behaviour of the material.

In the literature, quasi-static and collisional conditions are often tackled by employing different approaches. The constitutive models proposed within the soil mechanics community, consider only the quasi-static regime disregarding the effect of collisions among grains. The collisional regime has been largely studied in the context of kinetic theories of granular gases, where the granular temperature is introduced as a state variable measuring the degree of agitation of the system. To reproduce the intermediate regime, several constitutive models have been proposed in the literature [2,1]; however many of them considers only steady state conditions.

This paper investigates the potentialities of a recently proposed constitutive model [3] in the simulation of dry granular column collapse with the Material Point Method (MPM). The constitutive model, summarized in Section 2, is based on kinetic theory and critical state elasto-plasticity; it can capture the mechanical response of a granular material under a wide range of strain rates. The unique state variables of this constitutive model are the granular temperature T and the void ratio e, which govern the solid-to-fluid phase transition.

MPM is a point-based method specifically developed for large deformations of history dependent materials. It simulates large displacements by means of Lagrangian points moving through an Eulerian grid [4]. A brief introduction of the method is provided in Section 3, followed by a description of the numerical model used for the presented simulations.

Section 4 discusses the results of the column collapse problem; in particular, we focus on the energy dissipation mechanisms and the phase transitions.

2 THE CONTINUUM APPROACH FOR GRANULAR FLOWS

The constitutive model considers an assembly of identical spherical particles of diameter d and density ρ_p. For the sake of simplicity, inherent and/or induced evolving anisotropy are disregarded. This discontinuous medium can be described, in the framework of continuum mechanics, by writing the field equations, derived from the conservation laws of mass,

momentum and energy as it follows:

Mass balance: $$\frac{1}{1+e}\frac{De}{Dt} - \nabla \cdot \mathbf{u} = 0 \quad (1)$$

Momentum balance: $$\frac{\rho_s}{1+e}\frac{D\mathbf{u}}{Dt} = \frac{\rho_s}{1+e}\mathbf{f} - \nabla \cdot \boldsymbol{\sigma} \quad (2)$$

Energy balance: $$\frac{1}{1+e}\frac{DE}{Dt} = -\boldsymbol{\sigma} : \dot{\boldsymbol{\varepsilon}} - \nabla \cdot \mathbf{q} - \Gamma \quad (3)$$

where D/Dt denotes the material time derivative, e = void ratio, $\mathbf{u}$ = vector of the macroscopic mean velocity, $\mathbf{f}$ = vector of the external forces per unit volume, $\boldsymbol{\sigma}$ = stress tensor, E = specific internal stored energy, $\mathbf{q}$ = vector of the energy flux per unit area and unit time, $\dot{\boldsymbol{\epsilon}}$ = strain rate tensor and Γ = dissipated energy. In this paper, for the sake of simplicity, the energy flux $\mathbf{q}$ is disregarded.

A parallel scheme is assumed, which implies that E is calculated as the sum of the specific elastic stored energy E_q and the kinetic fluctuating energy E_c

$$E = E_q + E_c \quad (4)$$

Γ results by the sum of the energy dissipated by force chains Γ_q and the energy dissipated by inelastic collisions Γ_c

$$\Gamma = \Gamma_q + \Gamma_c \quad (5)$$

$\boldsymbol{\sigma}$ is given by the sum of a quasi-static contribution $\boldsymbol{\sigma}_c$, associated with long elapsing frictional contacts among grains involved in force chains, and a collisional contribution $\boldsymbol{\sigma}_q$, associated with inelastic collisions among grains.

$$\boldsymbol{\sigma} = \boldsymbol{\sigma}_q + \boldsymbol{\sigma}_c \quad (6)$$

2.1 Quasi static contribution

In this paragraph the quasi-static contributions, E_q, Γ_q and $\boldsymbol{\sigma}_q$ are derived on the basis of standard perfect elasto-plasticity incorporating the critical state concept

The main ingredients are

- Strain rate additivity: $\dot{\boldsymbol{\epsilon}} = \dot{\boldsymbol{\epsilon}}^e + \dot{\boldsymbol{\epsilon}}^p$,where e and p stand for the elastic reversible and the plastic irreversible contribution, respectively
- The specific hyperelastic stored energy (Gibbs energy function) [5]:

$$E_q = \frac{p_0^{2-n}}{p_a^{1-n}k(1-n)(2-n)} - \frac{p_q}{3k(1-n)} \quad (7)$$

where

$$p_0 = \left(\frac{p_q^2}{9} + \frac{k(1-n)\mathbf{s}_q : \mathbf{s}_q}{2g} \right)^{0.5} \quad (8)$$

p_q = mean quasi-static stress, $\mathbf{s}_q$ = deviatoric stress tensor, k and g are two macroscopic material dimensionless constitutive parameters associated with the bulk and shear stiffness respectively, n = non-dimensional constant and p_a =

atmospheric pressure.

- A yield locus $f(\boldsymbol{\sigma}_q)=0$, of the Lade and Duncan type, together with the consistency rule $\dot{f}=0$. f has been defined on the basis of DEM simulations [6–8] and its size depends on the triaxial compression stress ratio M_c.
- The critical state locus equation $G_1(p_q,e)=0$, function p_q and e, defined on the basis of DEM simulations [9]. G_1 is affected by the particle Young modulus E_p, by the critical void ratio e_c (representing the critical state void ratio for $p_q=0$) and by the material parameter a_L.
- The plastic potential $g(\boldsymbol{\sigma}_q,e)=0$, evolving with e and $\boldsymbol{\sigma}_q$, in order to incorporate the critical state into the model [10,11]. g is affected by E_p and by δ, which is a macro-parameter influencing the rapidity in achieving the critical state locus [3]. As a consequence, the flow rule, necessary to compute the plastic strain rate $\dot{\boldsymbol{\varepsilon}}^p$, is non-associated.
- An extended consistency rule, $\dot{G}_1=0$, which imposes that the critical state locus cannot be abandoned once is reached (critical regime)[3]. In fact, the basic idea of the model is that $f=G_1=0$ represents an attractor locus for the material. Therefore, condition $\dot{G}_1=0$, implies that under the critical regime, the void ratio evolution is governed by the mean quasi static stress via the critical state locus definition. In this regime, the plastic volumetric strain rate does not obey the flow rule but is computed by depurating the total volumetric strain rate of the elastic component.

For the sake of brevity, the analytical expression of f, g and G_1 are here omitted, but can be found in [3,16].

According to the previous assumptions it is now possible calculate the plastic dissipated energy as

$$E_q = \boldsymbol{\sigma}_q : \dot{\boldsymbol{\varepsilon}}^p \tag{9}$$

and the quasi static stress tensor

$$\boldsymbol{\sigma}_q = \mathbf{D}_q \dot{\boldsymbol{\varepsilon}}^p \tag{10}$$

where $\mathbf{D}_q(\boldsymbol{\sigma}_q,e)$ is the quasi-static stiffness fourth order tensor, depending on the quasi static stress tensor $\boldsymbol{\sigma}_q$ and the void ratio e. The details of the derivation of $\mathbf{D}_q$ are reported in [3,16].

2.2 Collisional contribution

The collisional contributions E_c, Γ_c and $\boldsymbol{\sigma}_c$ are function of both the void ratio e and the granular temperature T. In particular, according to kinetic theories of granular gases [12], the fluctuating kinetic energy is

$$E_c = \frac{3}{2}\rho_s \frac{1}{1+e} T \tag{11}$$

The expression of the energy dissipated by inelastic collisions Γ_c is based on the extended

kinetic theory [13], modified by Berzi and Jenkins [14], to take into account the role of particle stiffness on collisions. Its expression is reported in [14] and it is affected by ρ_p, d, the normal and effective coefficient of restitution [15] ε_n and ε_{eff}, respectively.

The collisional stress tensor is modelled according to the kinetic theory described in [12], taking also into account the modification introduced by Berzi and Jenkins [14]. The analytical expression of $\boldsymbol{\sigma}_c$ is given by

$$\boldsymbol{\sigma}_c = \boldsymbol{\Phi}^v : \dot{\boldsymbol{\varepsilon}} + \mathbf{h}^v \tag{12}$$

In Equation 12 $\boldsymbol{\Phi}^v(e,T)$ and $\mathbf{h}^v(e,T)$ are a fourth-order and a second-order tensor, respectively. They are affected by ρ_s, d, E_s, ε_n and a material constant e_m and their analytical form can be found in [16].

2.3 The visco-perfect-elasto-plastic constitutive relationship

According to Equation 6, the stress tensor is the sum of the quasi static and collisional contributions. To this purpose, the quasi-static contribution is expressed in finite form by integrating in time Equation 10

$$\boldsymbol{\sigma}_q = \mathbf{D}_q : \dot{\boldsymbol{\varepsilon}}\Delta t + \hat{\boldsymbol{\sigma}}_q \tag{13}$$

where Δt is the integration time step and $\hat{\boldsymbol{\sigma}}_q$ is the quasi-static stress tensor calculated at the previous time step.

From Equation 12 and Equation 13, the total stress tensor reads

$$\boldsymbol{\sigma} = \mathbf{D}^{vep} : \dot{\boldsymbol{\varepsilon}} + \mathbf{c} \tag{14}$$

where $\mathbf{D}^{vep}$ $(\boldsymbol{\sigma}_q, e, T)$ is the visco-elasto-plastic fourth-order tensor

$$\mathbf{D}^{vep} \equiv \mathbf{D}^q \Delta t + \boldsymbol{\Phi}^v \tag{15}$$

and $\mathbf{c}(\hat{\boldsymbol{\sigma}}_q, e, T)$ is a second-order tensor given by

$$\mathbf{c} = \hat{\boldsymbol{\sigma}}_q + \mathbf{h}^v \tag{16}$$

According to this model, different flow regimes can be defined.

1. The visco-elastic regime, when $f<0$ or $f=0$ and $\dot{f}=0$
2. The visco-ealsto-plastic regime, when $f=\dot{f}=0 \cap G_1 \neq 0$
3. The critical regime: when $f=\dot{f} = G_1=0 \cap e < e_c$
4. The collisional regime: when $f=\dot{f} = G_1=0 \cap e \geq e_c$

The description of these regimes and the analytical expression of $\mathbf{D}^{vep}$ and $\mathbf{c}$ for each regime is reported in [3].

3 THE NUMERICAL MODEL

MPM has been developed to overcome the difficulties arising when simulating large deformation problems with Lagrangian FEM. In the last 10 years the number of applications, ranging from solid to fluid mechanics, has been significantly increasing. In the field of geomechanics it has been used to study a number of problems such as slope stability [18,17],

granular flow propagation [19,20], soil penetration problems [22,23,21], soil erosion and sedimentation [24,25].

MPM uses two level of discretization. On one hand, the continuum body is discretized by means of a set of material points (MP) that carry all the information of the continuum (density, velocity, stresses, state parameters etc.). On the other hand, the spatial region where the body move through is discretized by a finite element mesh that allows to solve the discretized governing equation of motion. Large deformations are simulated by MP moving through a fix mesh as shortly summarized in Figure 1.

The constitutive model is implemented as a user defined model in the MPM dynamic explicit research code Anura3D (www.anura3d.eu)[26]. The constitutive equations are integrated explicitly; in particular, a Dormand-Prince method with substepping and correction for yield surface drift is applied for the quasi-static stresses [27].

The specific collisional dissipated energy and the plastic dissipated energy are integrated by means of the mid-point rule. The kinetic fluctuation energy and the elastic stored energy are computed with equations (11) and (7), respectively, at the end of the time step as function of the updated stress state and granular temperature.

The simulated 2D column collapse problem considers a 0.1m-high, 0.1m-long column (aspect ratio $a=l/h=1$). The model is 0.005m-wide.

The mesh is structured and counts 5610 tetrahedral elements (Figure 2). The bottom of the mesh is fully fixed, while roller boundary conditions are applied on the other surfaces. 10 MP are initially placed inside each active element for a total number of 14400 MP.

Stresses are initialized with horizontal coefficient at rest K_0=0.5. The material parameters are summarized in Table 1.

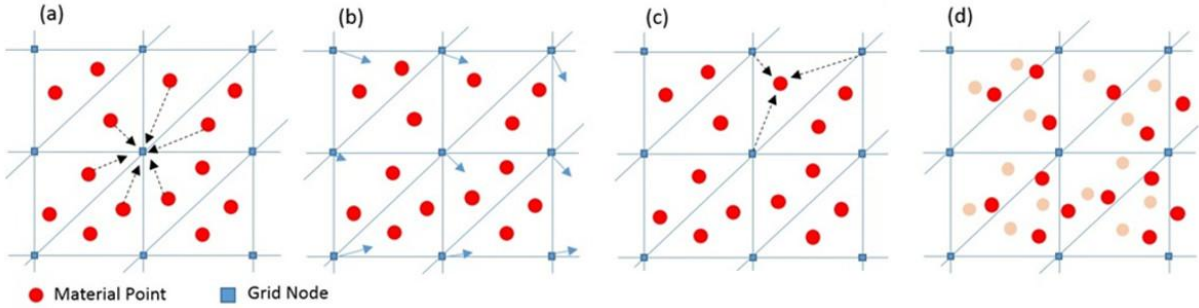

Figure 1 Computation scheme of MPM: a) interpolate state variables to the grid nodes, (b) solve the governing equations of motions at the nodes, (c) update MP velocity, strain, stress etc., (d) update MP housekeeping.

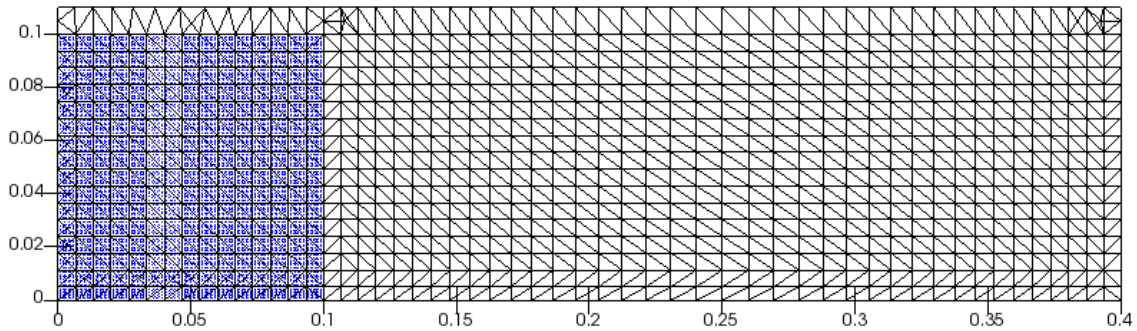

Figure 2 Geometry and discretization of the numerical model

Table 1 Material properties and initial state variables

Grain diameter	d [m]	0.002
Grain density	ρ_s [kg/m^3]	2532
Grain Young modulus	E_p [Pa]	3e+08
Normal restitution coefficient	ε_n	0.879
Parameter of collisional functions	e_m	1.5
Critical void ratio	e_c	0.709
Parameter of CSL	a_L	0.56
elastic constant related to bulk modulus	K	380
elastic constant related to shear modulus	G	48
Parameter of plastic potential	δ	0.35
Stress ratio under triaxial compression	Mc	0.9
Effective restitution coefficient	ε_{eff}	0.59
Initial void ratio	e_0	0.71
Initial granular temperature	T_0 [m^2/s^2]	1e-15

4 RESULTS

The collapse of a granular column is a well-established experiment that consists in releasing a column of granular material by removing its lateral support on to a flat surface. The column then fails and some of its mass flows on to the flat surface before it is deposited.

Figure 3 shows the deviatoric strains at the material points (MP) at different time instants, from which the development of the failure surface can be noted. The failure surface defines the boundary between a static cone with small strains (bottom left, blue MP) and a mobilised mass (top right, red MP). During the collapse, the mobilised mass slides along the failure surface and crumbles upon the base. The friction between the mobilised mass and the static region or the boundary, as well as the collisions between grains, dissipate energy and slows down the mobilised mass until static conditions are reached.

Figure 4 and Figure 5 show the specific collisional dissipated energy and the specific plastic dissipated energy, respectively. It can be noted that dissipation due to inelastic collisions among particles mainly occurs inside the mobilized mass, while the plastic dissipation mainly occurs at the sliding surface.

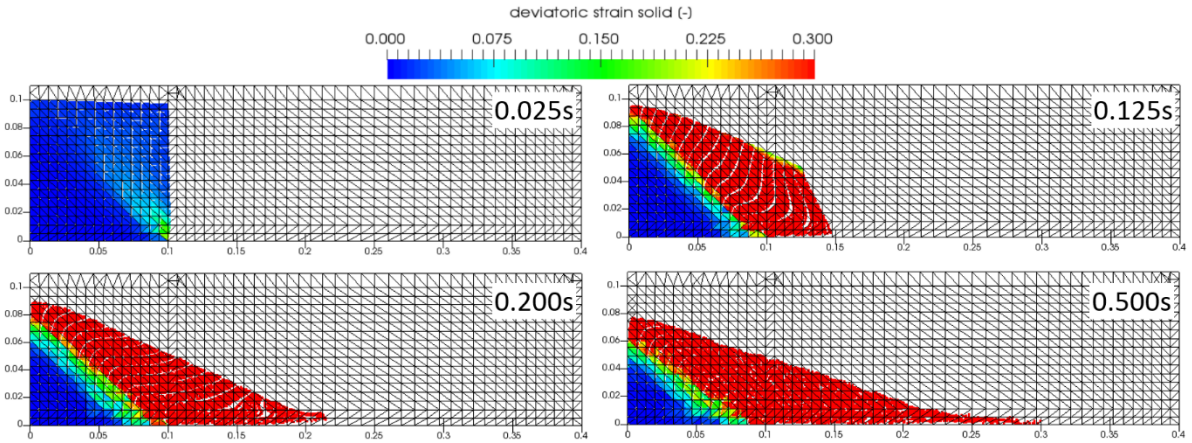

Figure 3 Deviatoric strain at the MP in different time instants

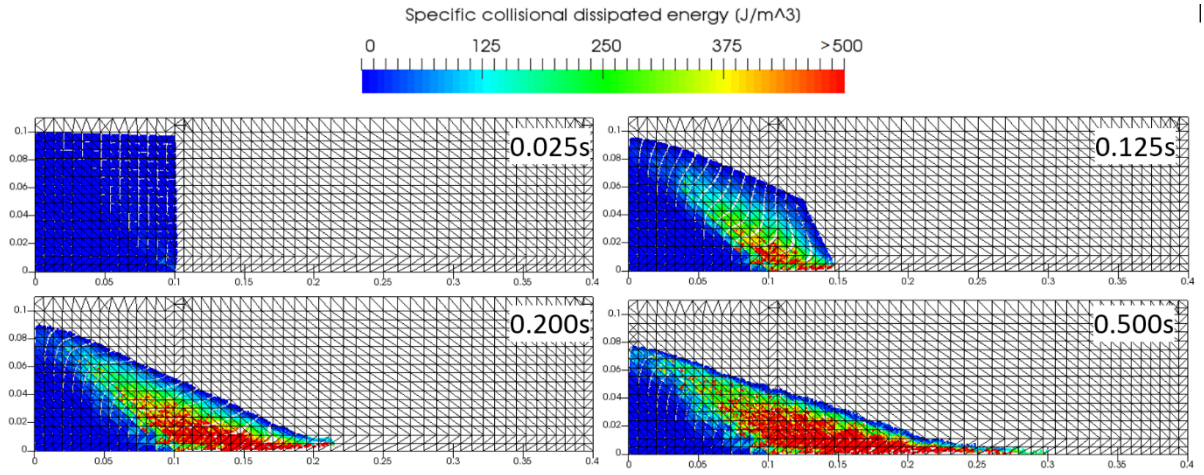

Figure 4 Specific collisional dissipated energy at the MP in different time instants

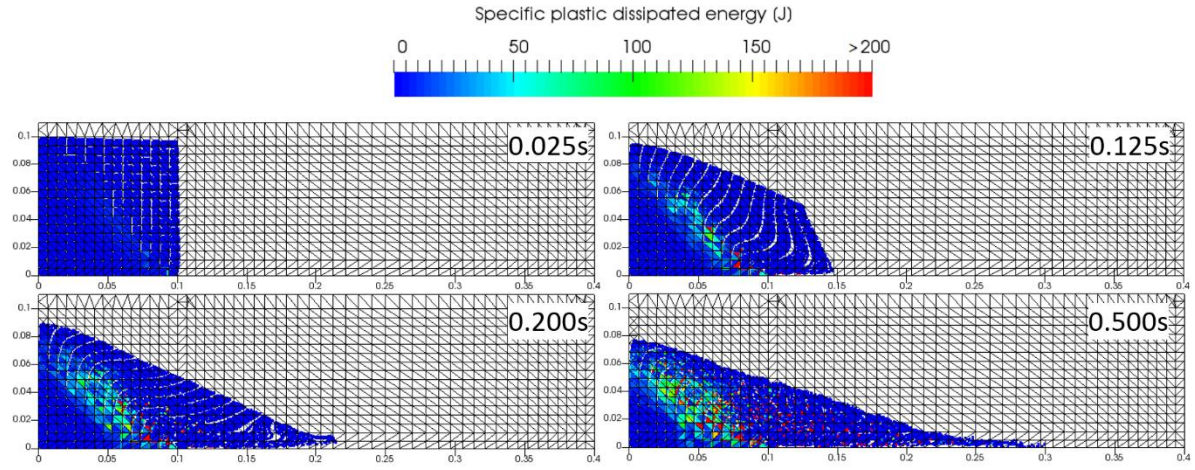

Figure 5 Specific plastic dissipated energy at the MP in different time instants

Integrating the specific energies at the MP, it is possible to obtain the time evolution of the collisional dissipated energy, the plastic dissipated energy, the kinetic fluctuation energy and the elastic stored energy (Fig. 6). Collisional dissipated energy is significantly higher than the plastic dissipated energy, meaning that collisions between grains is a key phenomenon in this problem. The kinetic fluctuation energy and the elastic stored energy are very small compared to the plastic and collisional dissipation. The kinetic fluctuation energy increases up to a peak and then tends to zero under static conditions.

In addition to the form of internal energy shown in Figure 6, it is also interesting to monitor the evolution of the potential energy (*EP*) and the kinetic energy (*EK*) of the system. There are computed by summing up the potential energy and the kinetic energy of each MP according to Equations 17 and 18 respectively:

$$EP = \sum_{p=1}^{N} m_p g\, y_p \tag{17}$$

$$EK = \sum_{p=1}^{N} \frac{1}{2} m_p\, \boldsymbol{v_p} \cdot \boldsymbol{v_p} \tag{18}$$

where m_p=mass of the MP, $\boldsymbol{v_p}$=velocity, y_p=elevation, N=total number of MP, g=gravity acceleration.

The potential energy of the system decreases with time (Fig. 7). This decrement of potential energy (ΔEP) obviously coincide with the work of the external forces. The potential energy transforms in kinetic energy and internal energy of the system, the latter is partially stored and partially dissipate as previously discussed. In contrast, the kinetic energy of the system increases up to a peak and then tends to zero. The peak of kinetic energy occurs approximately at time $= 1.1\sqrt{H/g}$, where $\sqrt{H/g}$ corresponds to the time taken by a single particle in free fall to travel from the centre of the column to the base (Fig. 7).

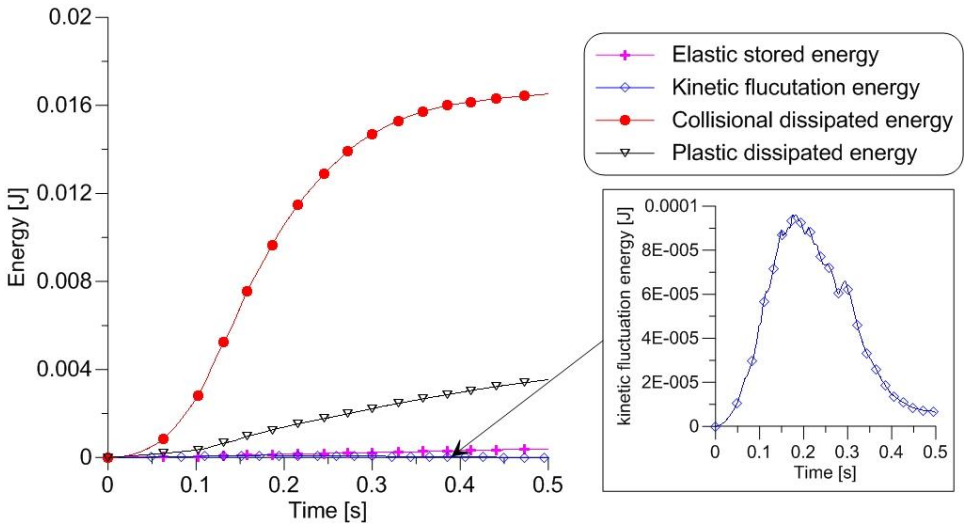

Figure 6 Evolution of internal energy types.

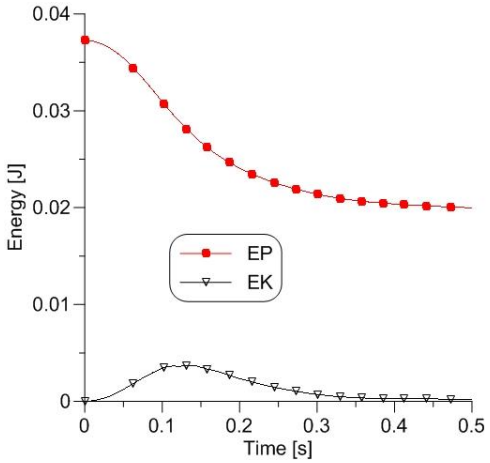

Figure 7 Evolution of kinetic energy and potential energy of the system

Figure 8

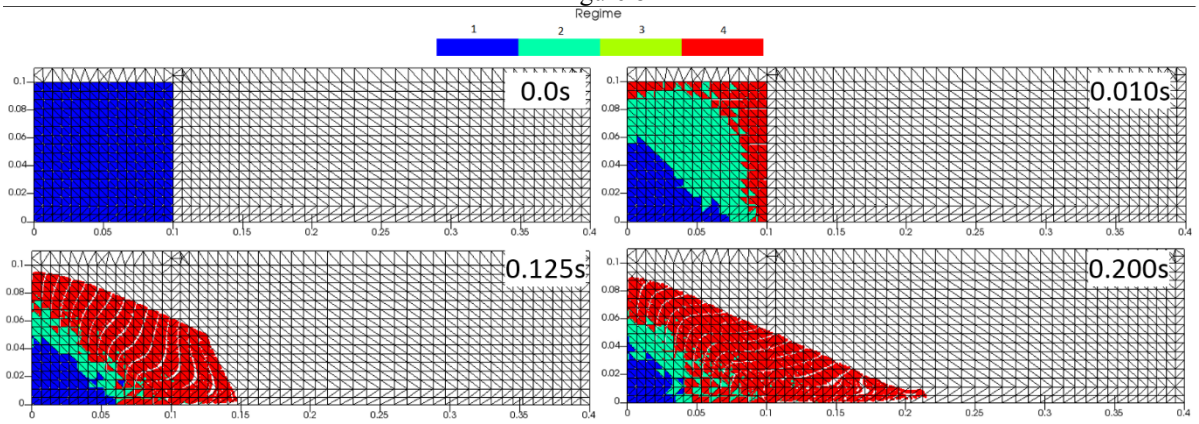

Figure 8 shows the transition between different regimes observed during the column collapse. Initially all the MP discretizing the column are in visco-elastic regime (#1), then gravity forces and the lack of fixities on the right side induce an increase of the deviatoric stress and a volumetric expansion, thus the MP move to the visco-elasto-plastic (#2), the critical (#3) and the collisional regimes (#4). This phenomenon interests the most superficial MP first, characterized by a lower state of stress, then propagates to the deeper MP. In other words, with the increasing of the deviatoric strain rate, a phase transition is observed. This phase transition occurs more rapidly in the areas characterized by al lower state of stress.

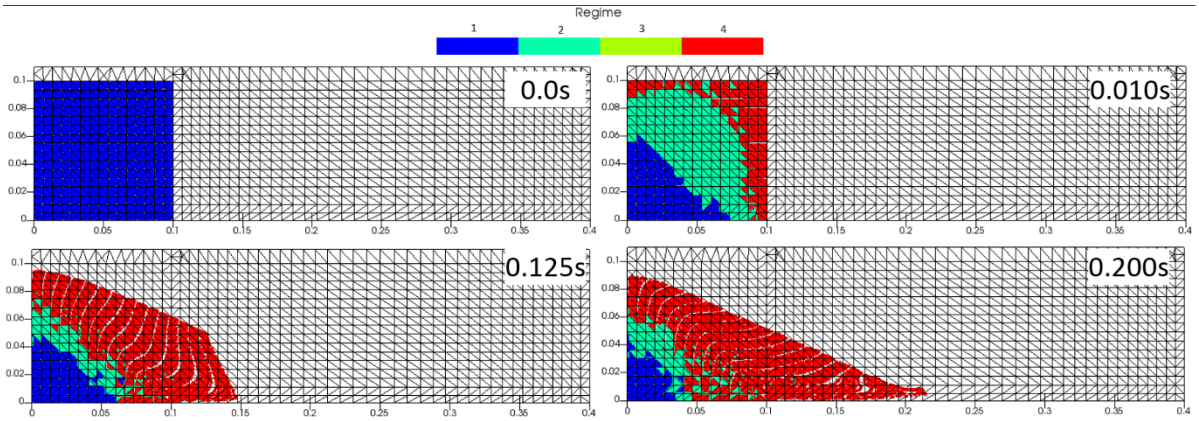

Figure 8 transitions over different regimes

5 CONCLUSIONS

This paper explores the potentialities of a recently proposed constitutive approach for the simulation of dense granular flows considering a column collapse problem. A parallel scheme is assumed, in which the stresses, the dissipated energy and the energy flux are assumed to be obtained by linearly adding a collisional and a quasi-static contribution. The first contribution stems from the kinetic theory of granular gases. For the latter contribution, an elasto-plastic model based on critical state theory has been adopted. In the solid-to-fluid phase transition, a key role is played by the void ratio and the granular temperature, the unique state variables of the model. This innovative constitutive approach is implemented in the MPM code Anura3D.

The energy dissipation mechanisms are a key issue in predicting the collapse behaviour and the run-out distance; and they are primarily controlled by the constitutive model. The results showed that significant amount of energy is dissipated by inelastic grain collisions, especially within the mobilized mass. This contribute is fundamental in the description of the phenomenon and should not be neglected. Plastic dissipation mainly occurs at the sliding surface and at the bottom of the mesh. This contribute is controlled by the elastoplastic law applied for the computation of quasi-static stress.

This paper has investigated in details the column collapse (flow inception) in which, according to the introduced constitutive model, the MP experience a transition between different regimes: visco-elastic, visco-elastoplastic, critical and collisional. In other words, the transition from a soild to a fluid state is well captured by the model.

For the sake of brevity, the deposition phase has not been investigated and it will the subject of future research. Future developments must also include the role of granular temperature diffusion within the granular mass.

REFERENCES

[1] Forterre, Y., and Pouliquen, O., Flows of Dense Granular Media, *Annu. Rev. Fluid Mech.* (2008) **40** 1–24.

[2] Berzi, D., Di Prisco, C. G., and Vescovi, D., Constitutive relations for steady, dense granular flows, *Phys. Rev. E - Stat. Nonlinear, Soft Matter Phys.* (2011) **84** 1–6.

[3] Redaelli, I., di Prisco, C., and Vescovi, D., A visco-elasto-plastic model for granular materials under simple shear conditions, *Int. J. Numer. Anal. Methods Geomech.* (2015) n/a-n/a.
[4] Sulsky, D., Zhou, S.-J., and Schreyer, H. L., Application of a particle-in-cell method to solid mechanics, *Comput. Phys. Commun.* (1995) **87** 236–252.
[5] Amorosi, A., Houlsby, G. T., and Rojas, E., Elastic moduli of soils dependent on pressure: a hyperelastic formulation, *Géotechnique* (2005) **55** 383–392.
[6] Barreto, D., and O'Sullivan, C., The influence of inter-particle friction and the intermediate stress ratio on soil response under generalised stress conditions, *Granul. Matter* (2012) **14** 505–521.
[7] Thornton, C., Numerical simulations of deviatoric shear deformation of granular media, *G´eotechnique* (2000) **50** 43–53.
[8] Zhao, J., and Guo, N., Unique critical state characteristics in granular media considering fabric anisotropy, *Geotechnique* (2013) **36** 695–704.
[9] Sun, J., and Sundaresan, S., A constitutive model with microstructure evolution for flow of rate-independent granular materials, *J. Fluid Mech.* (2011) **682** 590–616.
[10] Roscoe, K. H., and Burland, J. B., On the generalised stress-strain behaviour of wet clay, in *Eng. Plast.*, eds. Heyman, J., and Leckie, F. A., (Cambridge Univesrity Press, Cambridge, (1968), pp. 535–609.
[11] ZHAO, J., and GUO, N., Unique critical state characteristics in granular media considering fabric anisotropy, *Géotechnique* (2013) **63** 695–704.
[12] Garzó, V., and Dufty, J. W., Dense fluid transport for inelastic hard spheres., *Phys. Rev. E* (1999) **59** 5895–5911.
[13] Lun, C. K. K., Savage, S. B., Jeffrey, D. J., and Chepurniy, N., Kinetic theories for granular flow: inelastic particles in Couette flow and slightly inelastic particles in a general flowfield, *J. Fluid Mech.* (1984) **140**.
[14] Berzi, D., and Jenkins, J. T., Steady shearing flows of deformable, inelastic spheres, *Soft Matter* (2015) **11** 4799–4808.
[15] Jenkins, J. T., and Zhang, C., Kinetic theory for identical, frictional, nearly elastic disks, *Phys. Fluids* (2002) **14** 1228–1235.
[16] Redaelli, I., Constitutive modelling of the solid-to-fluid transition in granular matters, Ph.D. thesis, Politecnico di Milano, Italy, (2015).
[17] Soga, K., Alonso, E., Yerro, A., Kumar, K., and Bandara, S., Trends in large-deformation analysis of landslide mass movements with particular emphasis on the material point method, *Géotechnique* (2016) **66** 248–273.
[18] Andersen, S., and Andersen, L., Modelling of landslides with the material-point method, *Comput. Geosci.* (2010) **14** 137–147.
[19] Ceccato, F., Study of flow landslide impact forces on protection structures with the Material Point Method, in *Landslides Eng. Slopes. Exp. Theory Pract. Proc. 12th Int. Symp. Landslides*, (2016), pp. 615–620.
[20] Fern, E. J., and Soga, K., The Role of Constitutive Models in MPM Simulations of Granular Column Collapses, *Acta Geotech.* (2016) **11** 659–678.
[21] Phuong, N. T. V., van Tol, A. F., Elkadi, A. S. K., and Rohe, A., Numerical investigation of pile installation effects in sand using material point method, *Comput. Geotech.* (2016) **73** 58–71.

[22] Ceccato, F., Beuth, L., and Simonini, P., Analysis of Piezocone Penetration under Different Drainage Conditions with the Two-Phase Material Point Method, *J. Geotech. Geoenvironmental Eng.* (2016) **142** 4016066.
[23] Ceccato, F., and Simonini, P., Numerical study of partially drained penetration and pore pressure dissipation in piezocone test, *Acta Geotech.* (2016) **12** 195–209.
[24] Martinelli, M., and Rohe, A., Modelling fluidisation and sedimentation using material point method, in *1st Pan-American Congr. Comput. Mech.*, (2015).
[25] Martinelli, M., Rohe, A., and Soga, K., Modeling dike failure using the material point method, (2017) **0** 1–8.
[26] Redaelli, I., Ceccato, F., and Simonini, P., Solid-fluid transition in granular flows : MPM simulations with a new constitutive approach, in *1st Int. Conf. Mater. Point Method*, (2017), pp. 1–6.
[27] Sloan, S. W., Abbo, A. J., and Sheng, D., Refined explicit integration of elastoplastic models with automatic error control, *Eng. Comput.* (2001) **18** 121–194.

V International Conference on Particle-based Methods – Fundamentals and Applications
PARTICLES 2017
P. Wriggers, M. Bischoff, E. Oñate, D.R.J. Owen, & T. Zohdi (Eds)

A MODEL OF GRANULAR MATERIALS PARTIALLY CEMENTED BY BACTERIAL CALCITE

ELAHEH KASHIZADEH [1], ABHIJIT MUKHERJEE [2] AND ANTOINETTE TORDESILLAS [3]

[1]Department of Civil Engineering, Curtin University
Bentley WA 6102, Australia
E-mail address: Elaheh.kashizadeh1@postgrad.curtin.edu.au, URL: http://www.curtin.edu.au/

[2]Department of Civil Engineering, Curtin University
Bentley WA 6102, Australia
E-mail address: Abhijit.mukherjee@curtin.edu.au, URL: http://www.curtin.edu.au/

[3]School of Mathematics and Statistics, University of Melbourne
Victoria 3010, Australia
E-mail address: atordesi@unimelb.edu.au, URL: http://www.unimelb.edu.au/

Key words: MICP, Loose, Dense, Soil, Mechanical properties, DEM

Abstract. Nature aggregates granular materials such as sand, silt and clay into form beach rocks, anthills and other forms of microbialites. A common bio-geo-chemical cementation occurs due to the mineralization of calcium through bacterial enzymatic action, often called Microbial Induced Calcium Carbonate Precipitation (MICP). Unlike engineered cement, which consumes very high amounts of energy and emits large quantities of CO2, this natural cementation occurs in ambient conditions, with negligible energy consumption. Hence, it is a sustainable construction method. Natural cementation is a gradual process, where grains are initially bonded to form clumps. The clumps grow in size to form aggregates, finally creating free standing columns. Numerical models of the mechanical behaviors of cemented grains at the various stages of aggregation offer a way to explore and understand this process. In this paper, we propose a discrete element method (DEM) of aggregated granular materials formed due to MICP. The model is applied to study different levels of aggregation of sand, from sand heaps involving unbonded and bonded grains to free standing columns. The results are compared against experiments and the most important parameters are discussed.

1 INTRODUCTION

Granular materials such as sand, silt and clay are basic resources for construction. They are used in their natural unbonded forms such as earth embankments, and in bonded forms as in concrete. A binder, typically cement, is used to bond the grains together. The mechanism of resistance for loading in the loose and the bonded forms is fundamentally different. The loose material depends on the inter-granular friction for resistance against an applied force while the bonded material that behaves as a solid block has considerable inter-granular cohesion. A

numerical model that is able to capture all the stages of sand aggregation is challenging.

Presently, 3.6 billion tonnes per annum of Portland Cement is produced, contributing approximately 6% of all anthropogenic greenhouse gases [1]. Technologies that dramatically reduce or possibly eliminate Portland cement must be explored in order to improve the sustainability quotient of civil infrastructure. Recently, a new natural cementation, MICP, has been introduced as an alternative to cement binder [2]. In this process, bacterial enzymes are utilized to nucleate calcium carbonate as the cementing material [3]. Several important applications of the process is reported [4-6]. To optimize the process it is important to complement the experiments with a reliable numerical model. The model should be able to capture all phases of aggregation: from an assembly of loose grains to a free-standing assembly of fully aggregated (bonded) grains. In this paper, we propose a model of aggregated granular materials formed due to MICP using the discrete element method (DEM).

MICP is a bio-geo-chemical process that is performed to synthesise granular materials for a designed mechanical performance. Different aspects of the process, such as mass transport, bio-chemical reactions and consequent alternation in the mechanical response of the material have been modelled. Reactive transport models have been introduced to model biogrouting of soil [7, 8]. There have been attempts to simulate the bio-chemical process involved in MICP by solving transport and thermodynamic equations [9]. However, combining it with mechanical models is not reported hitherto. The mechanical property of sand columns resulting from MICP has been predicted using DEM [10, 11]. In these models MICP has been simulated as a homogenised cohesive system. However, the process can be highly localised, at least in the early stages. Moreover, a model of the mechanical response of a granular material from MICP at all levels of aggregation has not been reported.

The use of DEM for modelling granular materials dates back to Cundall & Strack [12]. The effect of non-idealized particle shapes on strength and deformation has extensively studied and one approach is by clustering idealized shape grains (e.g., circular disks and spheres)[13]. With the significant increase of computing power, discrete element models have been used to study the deformation of granular materials under a wide range of conditions in various fields including: geomechanics, pharmaceuticals, petroleum engineering, to name a few examples[14]. The present work is a first step towards the development of a DEM framework for modelling the mechanical behaviour of granular materials under MICP at all stages of aggregation. The model is applied to study the different levels of aggregation of sand, from sand heaps involving unbonded and bonded grains to free-standing columns. The results are compared against simulations and experiments and the most important parameters are discussed.

2 DEM MODELLING

In this study, a large complex granular system is considered as n-body structure of interconnected spheres. The center of each sphere is connected to the center of nearest contacted sphere(s). The connected lines create a complex network (Figure 1). Material constitutive properties are assigned to each connection.

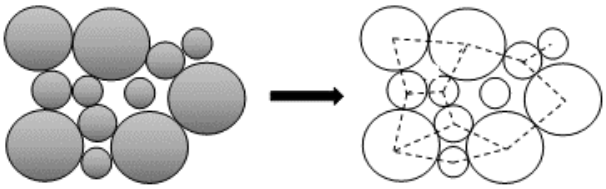

Figure 1: Relation between a granular material and a highly complex structural frame[15]

A spring–dashpot system is used for assigning the constitutive properties [11]. To simulate the contact forces between connected spheres; the spring, the divider and the dashpot model the contact force, the separation and damping . Figure 2 illustrates different spring-dashpot systems that are designed in numerical model to address normal, shear and rolling contacts.

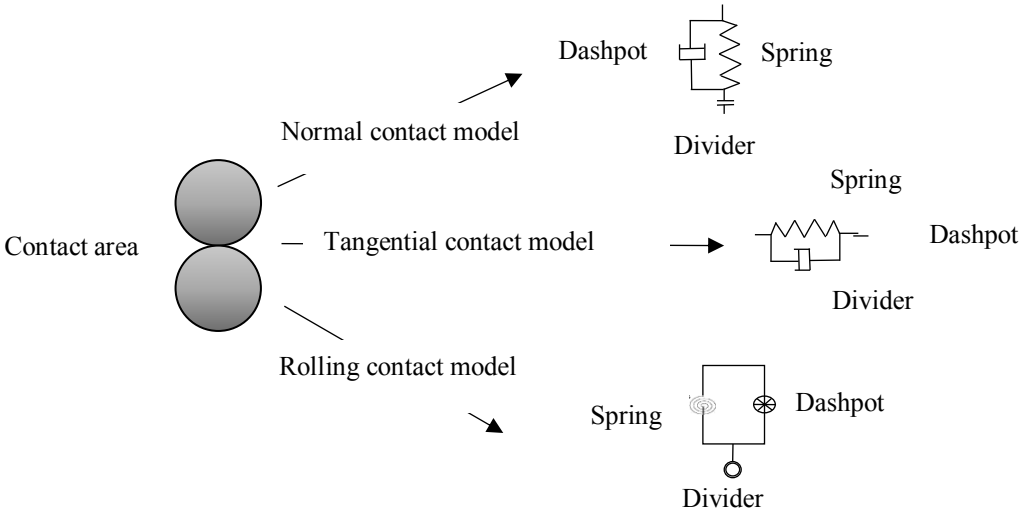

Figure 2: The contact models for grains with rolling resistance by Cundall [11]

A constitutive model with a combination of Hooke's and Coulomb's laws defines the interaction between the contacting particles:

$$f^n = k^n \Delta u^n + b^n \Delta \dot{u}^n \tag{1}$$

$$f^t = k^t \Delta u^t + b^t \Delta \dot{u}^t, for \left|\Delta u^t\right| < \mu \left|f^n\right| / k^t \tag{2}$$

Where:

f_n	Normal force component
f_t	Tangential force component
k^n & k^t	Spring stiffness coefficients
b^t & b^n	Viscous damping coefficients
μ	Coulomb friction coefficient
Δu^t & Δu^n	Relative normal and tangential displacement
$\Delta \dot{u}^t$ & $\Delta \dot{u}^n$	Relative normal and tangential translational velocities

The normal stiffness, k^n, shear stiffness, k^s and rolling stiffness, k^r parameters were calculated, as follows (Figure 2)

$$k^n = E_c \frac{2R_1R_2}{R_1 + R_2} \tag{3}$$

$$k^s = E_c v_c \frac{2R_1R_2}{R_1 + R_2} \tag{4}$$

$$k^r = \beta K^s R_1 R_2 \tag{5}$$

Where Ec is the Young modulus, vc is the Poisson ratio, R1 and R2 are the radii of the two connected spheres and β is the rolling stiffness coefficient. In the DEM model, by modelling the rolling resistance, I^c, the moments are introduced. The rolling resistance or contact moment—defined in an analogous fashion to Coulomb's law—is expressed as:

$$\begin{aligned} I^c &= k^r \Delta\alpha + b^r \Delta\dot{\alpha}, for \left|\Delta\alpha\right| < \mu^r R_{\min} \left|f^n\right| / k^r \\ I^c &= \mu^r R_{\min} \left|f^n\right|, for \left|\Delta\alpha\right| \geq \mu^r R_{\min} \left|f^n\right| / k^r \end{aligned} \tag{6}$$

Where:

R_{min} Minimum radii of the two interacting particles

k^r Rolling stiffness coefficients

μ^r Friction coefficient

$\Delta\alpha$ Relative rotation

$\Delta\dot{\alpha}$ Relative rotational velocities

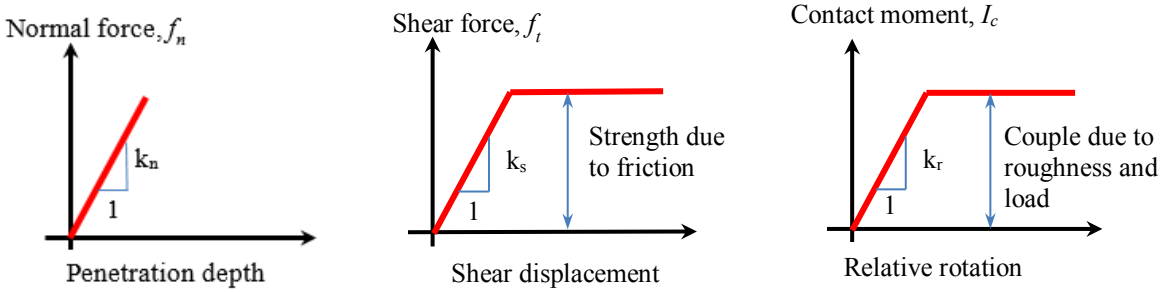

Figure 3: Mechanical stiffness of normal, tangential and rolling contact models[16]

Based on Mohr-Coulomb equation Figure 3 represents the mechanical response of normal, tangential and rolling contact model [17].

To solve the complex granular mechanism a numerical approach should be adopted [15]. In this paper an explicit finite difference, time-stepping algorithm, based on a Newton integration

equation, has been developed. The present numerical model is validated with experimental studies.

3 METHODOLOGY

To understand the mechanical behavior of granular materials a discrete element model (DEM) has been developed by using open-source discreet element software (YADE).To illustrate the capability of our numerical approach for modelling loose, semi- aggregated and fully aggregated samples, a series of investigations are carried out.

Numbers of spheres are created with specific grain size distribution in defined cubic format. Then property of material is assigned to spheres by defining the micro parameters. By controlling the number of grains and size of cube are the desired porosity is defined. The DEM models are closely calibrated to the initial configurations and packing densities of the experimental, as well as the contact and size distributions of the constituent particles.

3.1 Loose and Semi-aggregated Grains

In a loose or semi-aggregated state, the grains do not form a solid mass. Thus, they deform under the action of gravity and form a heap. When they are packed in a container and then the walls are removed, the grains move to form a heap. In the loose state, the grains are free to slide or roll over other grains once the intergranular friction is overcome. There is no cohesion between the grains. Partial aggregation is considered to be a state when some grains have bonded together due to MICP and formed a clump. Although the movement of the grains is prevented somewhat due to the formation of clumps, but the bonding is not wide spread so that the formation of heap under the action of gravity is prevented. The shape of the heap is dependent on the degree of aggregation. The semi aggregated state is modelled by rigidly connecting three grains together to create triads. The fraction of triads is proportional to the degree of aggregation. The shape of the heap is altered due to the formation of triads.

To illustrate the capability of our numerical approach to model this effect, a model has been developed in YADE. A cubic granular sample surrounded by walls is developed. All walls are removed simultaneously and the grains fall under the action of gravity. The released grains roll and slip on each other until their motion is below a set threshold. The threshold is set on the mean force magnitude of inter-particle interactions. Initially, there are a lot of movements, and the time progresses the particles stabilize into a shape resulting in negligible interaction forces. The tolerance value for this study for mean forces is 1e-2 Pa. In other words, the heap obtained when the mean interaction force drops below this threshold, all grains are considered static and the heap is considered to be the final configuration. A common assumption is that the shape of the heap will be conical and it can be represented by just the angle of repose. However, for semi-aggregated grains the shape of the heap is more complex and more parameters may be necessary to define the shape.

3.2 Aggregated Grains

In case of aggregated samples, the specimen retains its shape under the action of gravity. In addition to the frictional resistance against the relative motion between the grains, there is inter-granular cohesion due to the deposition of calcium carbonate at the grain intersections. The cohesive strength is dependent on the degree of MICP. As the samples are able to retain their shapes under the action of gravity, it is not necessary to contain them with the walls. Cylindrical samples have been developed with the specified grain size distribution. The samples have been

subjected to uniaxial compression at a constant rate until they collapse. In contrast to the previous case, in case of aggregated samples, the grains are tightly connected in the beginning. As a result, there is very little inter-granular movement, but as the load increases the inter-granular stress exceed the cohesive strength of MICP at a few locations resulting in cracking. As the cracking in the sample increases, the inter-granular movement also becomes more pronounced. As a result, the mean force magnitude of inter-particle interactions rises exponentially at the end of the numerical process indicating large inter-granular motions leading to collapse.

4 RESULTS

Results of simulation of grains aggregated in varying degrees by MICP using YADE is presented here. The aim is to validate the numerical observations with experimental results. The DEM simulation is controlled by the parameters described in (eqns. 1-6) that determine the inter-granular interaction (micro-parameters). It is not possible to have all these parameters measured experimentally. Thus, some of the parameters are adjusted to obtain the desired macro-parameters such as the angle of repose or the compressive strength.

4.1 Loose spherical glass bids

Zhou et al. [18] studied the angle of repose for mono-sized coarse spheres with 2mm diameter glass beads constrained by two glass walls separated by 40mm. The numerical model was developed by developing a container consisting of four glass walls with 80×8mm in pan and 40mm in height. The contained was filled with 2mm diameter glass bids. Then two smaller walls have been removed to allow flow of bids under the action of gravity. Flow through the shorter sides was allowed while the longer sides were rigidly constrained. The micro-parameters for the simulation are presented in Table 1 and the shape of the heap after 10000000 time steps is illustrated in Fig. 4. The angle of repose measured from the simulation and the experimentally observed angle are around 37°. Clearly, the present DEM model was able to model the stable configuration of the heap of glass beads.

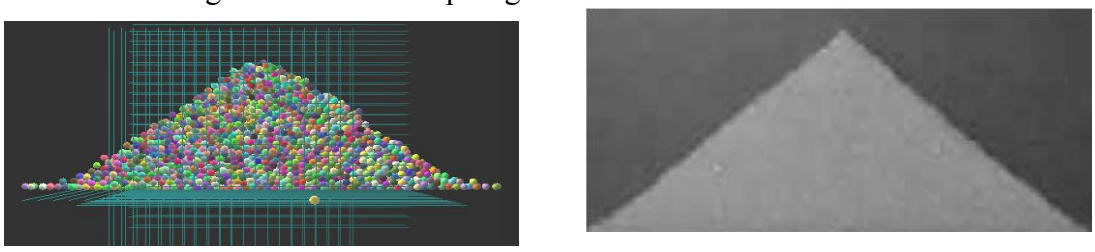

(a) (b)

Figure 4: (a) The proposed numerical model in this study, (b) The experimental study by Zhou *et al*. [18], the angle of repose in both study is 37 degree

Table 1: The variables which have been considered for validation

Name of variable	Base value	Name of variable	Base value
Number of particles	2000	Density	2500 kNs2/m
Time step	10000000	Poisson ratio	0.3
Particle size	2 mm	Young's Modulus	2.16e6 Pa
Rolling friction coefficient	0.05	Damping	0.4
Sliding friction coefficient	0.5	Friction angle	22◦
Container thickness	40 mm		

4.2 Semi-aggregated granules

To assess the intermediate situation, when a few grains have aggregated, but it is not enough to prevent the flow under the action of gravity, an experiment with a box of popcorns was conducted. The popcorns can approximate the shape of a triad where three spheres are clumped together signifying partial aggregation. A plastic container was filled with popcorns. The box was placed faced down on a firm table (Fig. 5a). Then the container was lifted suddenly. The popcorn takes the shape of a heap (Fig. 5b). The shape of the heap is noted by fitting a smooth curve to the contour of the heap.

(a) (b)

Figure 5: Angle of repose study with pop-corn (a) pop-cons in container (b) accumulated shape of pop-corns after removing the container

The experiment has been simulated in a numerical model where the popcorn has been approximated as three spheres joined as a triad. The shape of the heap after 1e7 time steps is illustrated in (Fig. 6a) where the number of grains are 5000. A confined space of the same shape and size of the container is created by introducing four rigid walls. The confined space has been filled with the triads. Then the walls have been removed and the triads have been allowed to move until a stable configuration is reached (Fig. 6a). The shapes obtained from the experiment and the numerical model have been found to agree very well.

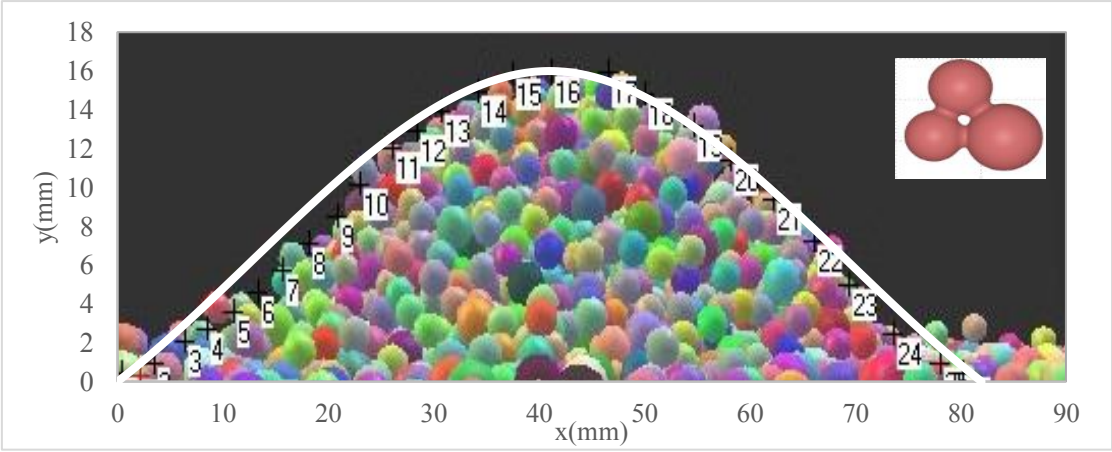

(a)

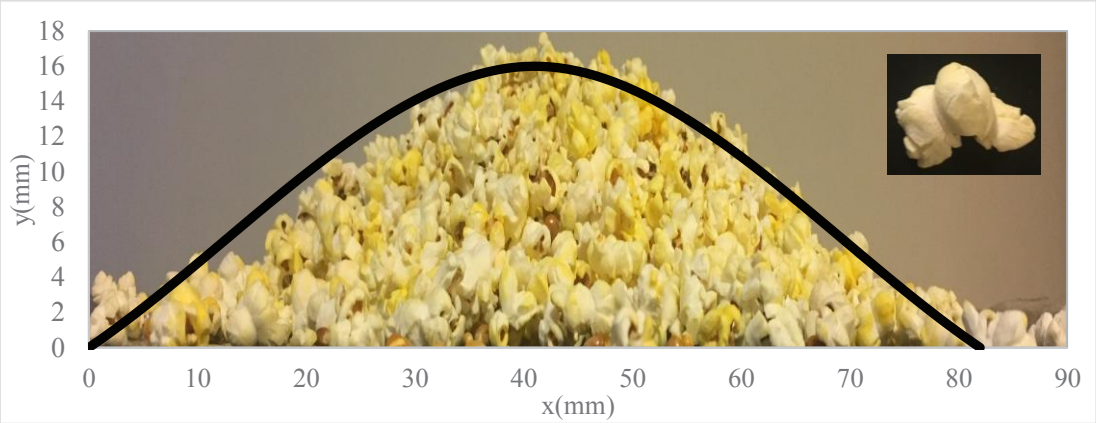

(b)

Figure 6: Comparison of Numerical model – the coloured grains have been used to make clumps distinguishable (a) and Experimental study (b) for semi-aggregated heaps, where the pop-cone grains shape is simulated as 3 spheres clumped

4.3Aggregated cylinders

Simulations of aggregated particles are validated with two experimental results at different extents of aggregation and particle size distribution. Jawad et al. [19] reported the results of unconfined compression tests of sand of single particle size (Fig. 7a) aggregated with MICP. While Porter et al. [20] reported MICP in well graded sand samples(Fig. 7b). Both samples were simulated in DEM and subjected to a displacement controlled unconfined compression test and the stress-strain curve for the sample has been plotted. It is important to set the micro-parameters for DEM to obtain a close fit with the experiments. The initial part of the curve is closely related to the elastic modulus of the grains. When the inter-granular stress exceed the strength of the cementation the grains start separating, sliding and rolling. Under these conditions the cohesion parameters play the most important role. Post-peak part of the stress-strain curve is dominated by the rolling stiffness and plastic moment limit strain.

Table 2 shows the values of parameters that are studied in the numerical approach to model the experimental of Jawad et al. [19]. Figure 8 illustrates the stress-strain curves from the numerical and experimental results. It can be seen that the two curves agreed overall. However, there are local differences between them. The initial slope of the numerical curve was considerably higher than that of the experiment. However, the slope reduced considerably between 2 and 4% strain and there was a good agreement at the peak stress and the strain at that instant. It is known that the samples created through MICP often have unevenness at their end surfaces, As a result, the initial slope is lower than expected as during the initial loading the uneven areas get gradually flattened resulting in more uniform distribution of stresses within the sample. The post-peak behavior of the samples was similar.

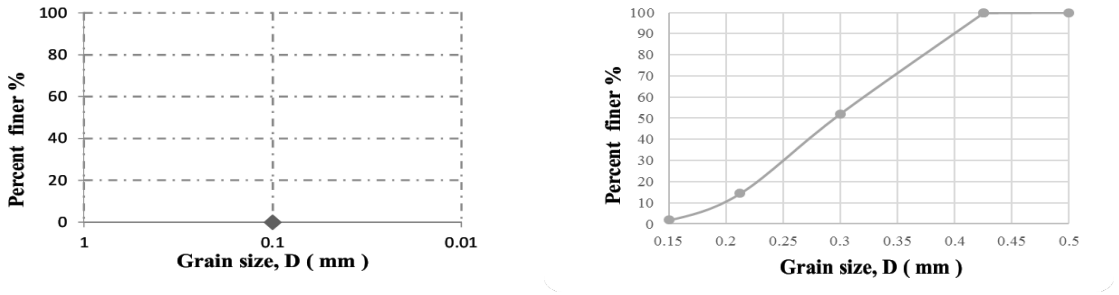

(a) (b)

Figure 7: Sand grain distribution to study Jawad *et al.* [19] , Porter *et al.* [20]

Table 2 Optimum values of micro parameters to model Jawad [19] experimental results

Name of variable	Base value	Name of variable	Base value
Number of particles	10000	Height of sample	80mm
Time step	1e7	Diameter of sample	37mm
Particle size	0.1 mm	Porosity	37.67%
Friction angle	36.5◦	Young modulus	17e6 Pa
Sliding friction coefficient	0.4	Normal cohesion	30e4 Pa
Density	2500 Kg/m3	Shear cohesion	9e6 Pa
Poisson ratio	0.4	Rolling stiffness coefficient	0.5
Damping	0.4	Plastic moment limit coefficient	0.15

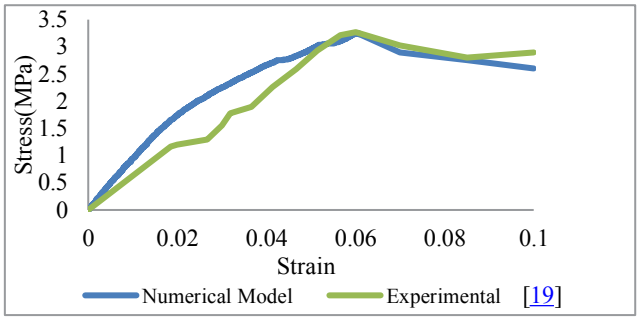

Figure 8: The stress–strain of the proposed numerical and experimental study [19]

The experiment reported by Porter et al. [20] has well graded grains. The samples have been given a lower level of MICP treatment resulting in intermediate level of aggregation, enough to have a cylinder but of lower strength than the previous example. The sphere packing technique is used to model the experimental samples to reach the porosity of sample around 36%. The parameters set in the DEM for this example are presented in Table 3. The stress-strain plots of the experimental and the numerical results are presented in Fig. 9. In this case too there was a good overall match between the experiment and numerical simulation. The initial apparent softness in the sample due to the unevenness of the loading surfaces is discernible in this experiment as well. The peak stress in the simulation occurred slightly later than that observed in the experiment. The post-peak behavior was captured well by the DEM. These examples demonstrate the capability of DEM in capturing the stress-strain behavior of

granular samples aggregated by MICP for a range of grain size distribution and extent of aggregation.

Table 3: Optimum values of micro parameters to model Porter *et al*. [20] experimental results

Name of variable	Base value	Name of variable	Base value
Number of particles	10000	Height of sample	60mm
Time step	1e7	Diameter of sample	30mm
Particle size	0.45 mm and 0.07 mm	Porosity	37.67%
Friction angle	36.5◦	Young modulus	17e6 Pa
Sliding friction coefficient	0.4	Normal cohesion	25e6 Pa
Density	2500 Kg/m3	Shear cohesion	6e3 Pa
Poisson ratio	0.4	Rolling stiffness coefficient	0.15
Damping	0.4	Plastic moment limit coefficient	0.15

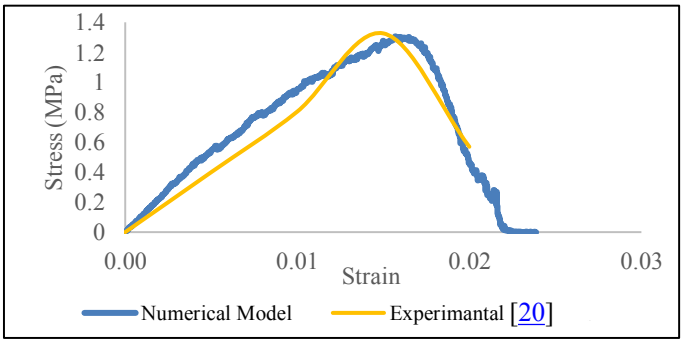

Figure 9: The stress–strain of the proposed numerical in current study and experimental study by Porter *et al*. [20]

We further explore the ability of DEM to identify cracks as they develop in the sample with the increasing load. Figure 10 shows the network of inter-granular distance for the grains on the surface of the cylinder. As cracks appear the grains that were initially cemented together separate when the stress in the cementation exceeds the cohesive strength. It can be noted that DEM predicts a developing vertical crack as the loading progresses. The red areas can be considered as separation as in those areas the distance between the grains has exceeded the average inter-grain distance at the beginning of the experiment. DEM predicts a vertical split failure of the sample. Fig. 11 presents the failure predicted by the DEM and that obtained in the experiment. There is a striking similarity between the two. Thus, it can be concluded that DEM is able to predict the failure mode of the Aggregated MICP samples.

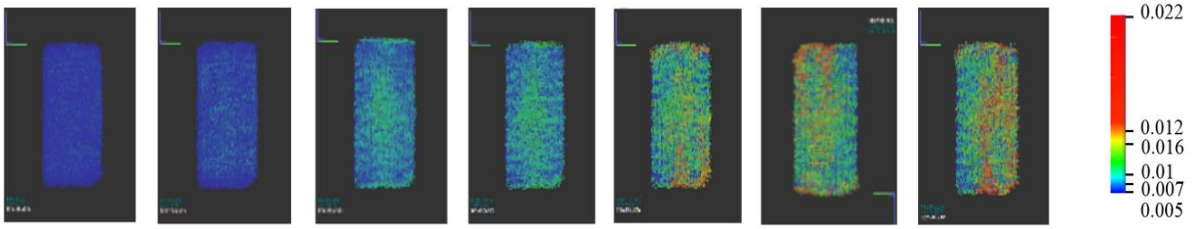

Figure 10: Inter-grain distances at different stages of the compression test on a highly complex structural frame where different colours are representing distance between grains, the blue is the smallest and red is largest distance– unit is mm

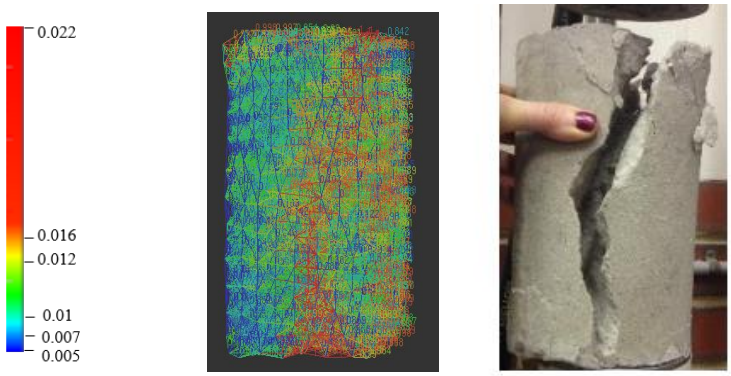

Figure 11: Comparison of failure modes obtained through the experiment and DEM simulation –unit is mm

6 CONCLUSIONS

This investigation explore the capability of DEM simulation for aggregation of grains by MICP to different extents. Comparing the series of simulation results with experiments the following conclusions can be made:

- Dem is able to model the aggregation of sand due to MICP at all the stages. The overall stress-strain graphs match well. However, the parameters of DEM must be set properly to get the best results.
- The shape of semi-aggregated heap can be modelled by clumping of grains to form triads.
- The stress-strain graphs of aggregated cylinders as obtained in the experiments can be emulated through DEM. However, the limit strength parameters such as cohesion and plastic moment limit have to be set properly.
- The inter-grain distance is a good measure for tracking cracks in aggregated cylinders. The failure mode predicted by the DEM was very close to that obtained in the experiment.
- The results of this investigation encourage us to explore the DEM modelling further for capturing MICP for a wide range of applications. A reliable numerical model would certainly expand the understanding of this exciting new technology for a wide range of applications.

7 REFERENCES

[1] Imbabi, M.S., C. Carrigan, and S. McKenna, Trends and developments in green cement and concrete technology. International Journal of Sustainable Built Environment, 2012. 1(2): p. 194-216.
[2] Achal, V., et al., Biomineralization for sustainable construction - A review of processes and applications. Earth-Science Reviews, 2015. 148: p. 1-17.
[3] Achal, V. and A. Mukherjee, A review of microbial precipitation for sustainable construction. Construction and Building Materials, 2015. 93: p. 1224-1235.
[4] Achal, V., A. Mukherjee, and M.S. Reddy, Microbial Concrete: Way to Enhance the Durability of Building Structures. Journal of Materials in Civil Engineering, 2011. 23(6):

p. 730-734.
[5] Achal, V., et al., Corrosion Prevention of Reinforced Concrete with Microbial Calcite Precipitation. Aci Materials Journal, 2012. 109(2): p. 157-163.
[6] Achal, V., A. Mukherjee, and M.S. Reddy, ORIGINAL RESEARCH: Biocalcification by Sporosarcina pasteurii using corn steep liquor as the nutrient source. Industrial Biotechnology, 2010. 6(3): p. 170-174.
[7] Laloui, L. and S. Fauriel, Birout propagation in soils.pdf. Multiscale and Multiphysics Processes in Geomechanics, 2011(SSGG): p. 77–80.
[8] Van Wijngaarden, W., et al., Modelling Biogrout: a new ground improvement method based on microbial-induced carbonate precipitation. Transport in Porous Media, 2011. 87(2): p. 397-420.
[9] Bouchelaghem, F. and L. Vulliet, Mathematical and numerical filtration-advection-dispersion model of miscible grout propagation in saturated porous media. International Journal for Numerical and Analytical Methods in Geomechanics, 2001. 25(12): p. 1195-1227.
[10] Yang, P., et al., 3D DEM Simulations of Drained Triaxial Compression of Sand Strengthened Using Microbially Induced Carbonate Precipitation. International Journal of Geomechanics, 2016: p. 04016143.
[11] Cundall, P.A., The measurement and analysis of accelerations in rock slopes. 1971, University of London.
[12] Cundall, P.A. and O.D. Strack, A discrete numerical model for granular assemblies. Géotechnique, 1979. 29(1): p. 47-65.
[13] Steefel, C.I., D.J. DePaolo, and P.C. Lichtner, Reactive transport modeling: An essential tool and a new research approach for the Earth sciences. Earth and Planetary Science Letters, 2005. 240(3): p. 539-558.
[14] Yeh, G.-T. and V.S. Tripathi, A critical evaluation of recent developments in hydrogeochemical transport models of reactive multichemical components. Water Resources Research, 1989. 25(1): p. 93-108.
[15] O'Sullivan, C., Particulate discrete element modelling. 2011: Taylor & Francis.
[16] Kozicki, J. and J. Tejchman. Numerical simulations of sand behaviour using DEM with two different descriptions of grain roughness. in II International Conference on Particle-based Methods–Fundamentals and Applications. Particles. 2011.
[17] Kozicki, J. and F. Donzé, A new open-source software developed for numerical simulations using discrete modeling methods. Computer Methods in Applied Mechanics and Engineering, 2008. 197(49): p. 4429-4443.
[18] Zhou, Y., et al., An experimental and numerical study of the angle of repose of coarse spheres. Powder Technology, 2002. 125(1): p. 45-54.
[19] Jawad, F. and J.-J. Zheng, Improving Poorly Graded Fine Sand with Microbial Induced Calcite Precipitation. 2016.
[20] Hannah Porter, N.K.D., Abhijit Mukherjee, Sustainable Road Bases with Microbial Carbonate Precipitation. SCMT4, Las Vegas, USA, August 7-11, 2016, 2016.

V International Conference on Particle-based Methods – Fundamentals and Applications
PARTICLES 2017
P. Wriggers, M. Bischoff, E. Oñate, D.R.J. Owen, & T. Zohdi (Eds)

A LANGUAGE AND DEVELOPMENT ENVIRONMENT FOR PARALLEL PARTICLE METHODS

Sven Karol[1,4], Tobias Nett[1], Pietro Incardona[2,3], Nesrine Khouzami[1], Jeronimo Castrillon[1], Ivo F. Sbalzarini[2,3]

[1] Chair for Compiler Construction
Center for Advancing Electronics Dresden, TU Dresden, Dresden, Germany
[tobias.nett|sven.karol|nesrine.khouzami|jeronimo.castrillon]@tu-dresden.de

[2] Chair of Scientific Computing for Systems Biology, Faculty of Computer Science, TU Dresden, Dresden, Germany

[3] MOSAIC Group, Center for Systems Biology Dresden,
Max Planck Institute of Molecular Cell Biology and Genetics, Dresden, Germany
[incardon@mpi-cbg.de|ivos]@mpi-cbg.de

[4] Baselabs GmbH, Ebertstr. 10, 09126 Chemnitz, Germany

Key words: Particles Method, discrete element method, Gray-Scott, Lennard-Jones, PPME, PPML, DSL

Abstract. We present the Parallel Particle-Mesh Environment (PPME), a domain-specific language (DSL) and development environment for numerical simulations using particles and hybrid particle-mesh methods. PPME is the successor of the Parallel Particle-Mesh Language (PPML), a Fortran-based DSL that provides high-level abstractions for the development of distributed-memory particle-mesh simulations. On top of PPML, PPME provides a complete development environment for particle-based simulations usin state-of-the-art language engineering and compiler construction techniques. Relying on a novel domain metamodel and formal type system for particle methods, it enables advanced static code correctness checks at the level of particle abstractions, complementing the low-level analysis of the compiler. Furthermore, PPME adopts Herbie for improving the accuracy of floating-point expressions and supports a convenient high-level mathematical notation for equations and differential operators. For demonstration purposes, we discuss an example from Discrete Element Methods (DEM) using the classic Silbert model to simulate granular flows.

1 INTRODUCTION

Developing applications for scientific high-performance computing (HPC) requires in-depth knowledge of the underlying, potentially heterogeneous hardware and programming

models, as well as the corresponding numerical simulation methods and parallel programming patterns. This leads to a low level of achievable abstraction, which is known to cause the "knowledge gap" in scientific programming [22]. To address this gap, scientific libraries and domain-specific languages (DSLs) have evolved into an important toolset in scientific HPC. In the domain of particle methods, this notably includes the Parallel Particle Mesh library (PPM) [23, 22, 4] and the Parallel Particle Mesh Language (PPML) [3, 5] as a library and a DSL for large-scale scientific HPC. The abstractions in PPM and PPML allow scientific programmers to write more concise and declarative code in comparison to hand-coded implementations. Essentially, it frees developers from the burden of writing boilerplate code that manages parallelism, synchronization, and data distribution. However, PPML has downsides, which we address in PPME [17]: The lightweight embedding of PPML into Fortran, based on language macros, and the lack of a fully integrated language model prevent advanced code analysis and complex compile-time computations. This makes debugging PPML programs hard and prohibits domain-specific static code optimization [11]. In contrast, PPME closely follows the paradigm of language-oriented programming [28], where extensible DSLs are created to describe and solve software problems instead of writing programs in general-purpose languages. This serves to increase maintainability and productivity through domain abstractions. PPME is integrated into the meta programming system (MPS) [8, 16], a model-driven language workbench [9]. We developed a language model that enables us to implement analysis and optimization algorithms that are well-suited for particle methods. The model is the basis of a formal type system for particle simulations, including optional verification of physical dimensions. This enables advanced domain-specific correctness checks at compile time, such as checking for dimensional correctness. PPME further supports numerical accuracy optimization capabilities of floating-point expressions by leveraging domain knowledge and adopting the Herbie accuracy checker [19]. Due to MPS' projectional editing capabilities, convenient high-level mathematical notation for equations and differential operators is supported. In this paper, we present PPME and show its use in Discrete Element Methods (DEM). In particular, we use PPME to implement a simulation of granular flows on distributed-memory parallel computers using a classical Herzian contact force model.

The remainder of this paper is structured as follows: Section 2 discusses related work. Section 3 presents the architecture of PPME and its integration with the PPM Library. Section 4 introduces our case study from the domain of discrete element methods while its implementation in PPME and results are discussed in Section 5. Section 6 concludes the paper and gives an outlook of future work.

2 RELATED WORK

In scientific computing, several DSL-like approaches have successfully been proposed in the past: Blitz++ [25] is a template-based library and DSL for generating stencils from high-level mathematical specifications of mesh-based computations. Freefem++ [10] is a software toolset and DSL for finite-element methods. This DSL allows users to

define analytic or finite-element functions using domain abstractions such as meshes and differential operators. Liszt [7] extends Scala with domain-specific statements for defining solvers for partial differential equations on unstructured meshes with support for several parallel programming models including message passing. The FEniCS project [13] created a finite element library, the unified form language (UFL) [1], and several optimizing compilers for generating code that can be used with the library. Firedrake [20] adds composing abstractions such as parallel loop operations.

Domain-specific optimizations carry great potential since scientific codes often induce specific boundaries on data access and numeric algorithms. This has been particularly studied for representation code of element tensors in the finite-element method [18]. The representation code is written in UFL variational forms. The proposed optimization strategies yield significant runtime speedups and leverage domain knowledge to automate nontrivial optimizations. Loop-level optimizations for finite-element solvers in the COmpiler For Fast Expression Evaluation (COFFEE) [15] are discussed in Ref. [14]. Therein, heuristics are used to predict operation counts at runtime, using well-known transformations such as code motion, expansion, and factorizations. Domain-specific optimizations are superior to general-purpose ones that are used by standard compilers to reduce the operation count in nested loops.

This includes checking and optimizing variables based on their physical dimensions. For this, an analysis technique based on unit annotations has been proposed [6] that does not require extending or changing the base language. Furthermore, unit annotations for linear-algebra and finite-element calculations are available [2], which is comparable to what we have realized for particle methods with dimensional annotations in PPME.

3 THE PARALLEL PARTICLE-MESH ENVIRONMENT (PPME)

PPME is part of the PPM stack and provides several abstractions and analysis algorithms for parallel particle-mesh methods. The PPM library supports simulations of both discrete and continuous models using either particles, meshes, or a combination thereof. In discrete models, particles directly interact by pairwise kernels. In continuous models, differential operators are discretized on particles using, e.g., the SPH or DC-PSE methods [24]. In DC-PSE, the discretized kernels are automatically computed at runtime. As PPM is a Fortran library, clients are required to write plain Fortran code in order to use the library. PPML partially frees the developer from this burden by providing a collection of macros and code transformations that can be used as high-level abstractions. However, using PPML can be problematic as it does not provide error checking and debugging capabilities so that errors are only detected by the compiler in the generated Fortran code and are not related to the PPML program. PPME addresses this problem by analyzing the user code and providing an extensible infrastructure for incorporating domain-specific optimizations.

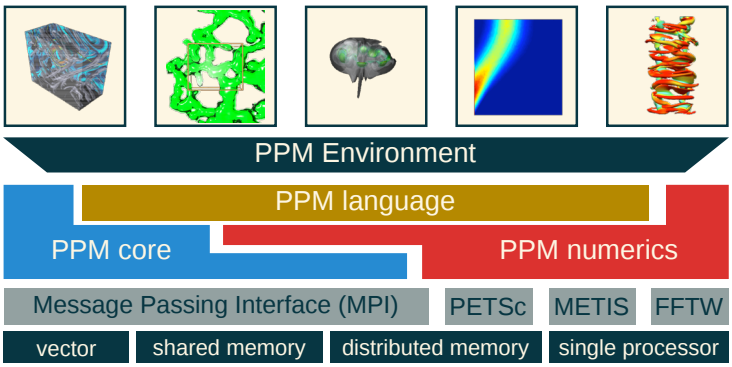

Figure 1: Layered architecture of the PPM/PPME stack.

3.1 Architecture of PPME

Figure 1 provides an overview of the current PPM/PPME stack. The architectural details of the computer hardware are located on the lowest layer and are accessed through common low-level libraries such as MPI for message passing, PETSc for direct and iterative solvers, METIS [12] for graph partitioning, and FFTW for Fourier transforms. In the layer above, the PPM library provides its major subcomponents: *PPM core* contains the distributed Fortran data structures and methods for describing particle simulations, while *PPM numerics* provides frequently used numerical algorithms such as multi-grid solvers, spectral solvers, boundary element methods, and fast multipole methods [21]. These are partly implemented using the objects provided by the PPM core, and partly based on wrapping external libraries. PPML sits on top of PPM. Based on its abstractions, mixed with plain Fortran for direct library access, PPML provides a high-level domain-specific language that is translated to plain Fortran code code that links against the PPM Library, as well as the underlying libraries [3, 5]. Offering a consistent DSL layer, PPME resides in the top-most layer and does not require any adaptation of the underlying framework. Thus, it uses PPML as an intermediate representation, preserving its concepts and abstractions so that the original tool chain remains intact. However, PPME allows scientists to bypass the details of the PPML programming languages and the problem associated with debugging or optimizing PPML programs. PPME is generic to all types of particle and particle-mesh methods, such that different "client applications", symbolized by the square boxes on top, can be implemented.

3.2 Internal Structure of PPME

Internally, PPME is organized in language packages as illustrated in Figure 2. These packages correspond to *solutions* in MPS, constituting the domain language model. We briefly describe the packages here. For a more detailed discussion on the model and type system we refer to Ref. [17].

The package `ppme.expressions` provides a domain-independent set of notations for

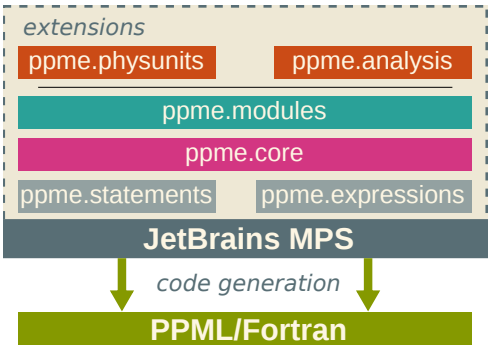

Figure 2: Internal structure of PPME and integration into the MPS language workbench.

mathematical and logical expressions, and literals for integer and floating-point numbers. Moreover, the base types available in PPME and parts of the type system (static analysis) are defined in this package. The package `ppme.statements` contains universal imperatives, such as expression statements, if-else clauses, and loops. The type system is enriched with variable support where necessary. The core package `ppme.core` contains elements that are tailored to particle methods, domain-specific types, expressions, and statements, e.g., a *timeloop* construct. The package `ppme.modules` provides the top-level structure for client programs written in PPME. Modules contain the simulation code and optional control parameters. A module translates to a PPML client that then translates to Fortran code.

A major concept of PPME, and of language-oriented programming in general, is to flexibly add language extensions as needed. So far, we have incorporated two optional extensions: The package `ppme.physunits` enables annotating further meta information to variables and constants. This includes specifications of physical units and dimension which are then accessible to the type system. The package `ppme.analysis` provides an exemplary binding of *Herbie* as an external analysis tool for improving floating-point expressions [19]. This integration is based on a general framework enabling the access of custom tools into the environment. For details on both extensions and application examples, we refer to Ref. [17].

3.3 Code Generation

We illustrate PPME by comparing the input and output of the PPME code generator in a simple example: a Gray-Scott reaction-diffusion simulation. The two versions of the code, PPML and PPME, are juxtaposed in Figure 3. For both, we show the part that integrates the governing equations discretized over the particle set c using the 4th-order Runge-Kutta method ("rk4"). In PPME, the equations are conveniently defined over particle attributes, here the two scalar fields U and V. Static analysis extracts the required information from the code, for example identifying two applications of differential operators, $\nabla^2 c \to U$ and $\nabla^2 c \to U$, and automatically deriving and adding local variables

PPME

```
deqn method "rk4" on c
∂c→U/∂t = constDu * ∇² c→U - c→U * c→V² + F * (1.0 - c→U)
∂c→V/∂t = constDv * ∇² c→V + c→U * c→V² + (F + kRate) * c→V
end deqn
```

PPML

```
rhs grayscott_rhs_0(U=>c, V)
  get_fields(dU, dV)

  dU = apply_op(L, U)
  dV = apply_op(L, V)

  foreach p in particles(c) with positions(x) sca_fields(U, V, dU, dV)
    dU_p = constDu * dU_p - U_p * (V_p**2) + F * (1.0 - U_p)
    dV_p = constDv * dV_p + U_p * (V_p**2) - (F + kRate) * V_p
  end foreach
end rhs
```

Figure 3: Equations of a Gray-Scott reaction-diffusion system in PPME (input) and PPML (output).

dU and dV for them. In the generated PPML code, this information is then contained explicitly, demonstrating some key benefits of a holistic code representation and analysis: since all required information is extracted by the PPME compiler, redundant statements encoding this information are explicitly avoided, which leads to less code, less compile-time errors, and improved readability. Also note PPME's support of basic mathematical notation, such as the Nabla operator ∇ and the partial derivative ∂. From the initial 4 lines of PPME code, 11 lines of PPML code, and more than 100 lines of Fortran code are generated, which corresponds to factor of 25 in code-size reduction (cf. [17]).

4 CASE STUDY: DISCRETE ELEMENT METHODS (DEM)

Discrete element methods are a fundamental tool for the study of granular materials. It has been shown that DEM methods allow determining material properties [32] and effective macroscopic dynamics for which closed-form theory lacks. Therefore, DEM simulations have become invaluable in the search for continuum theoretic descriptions of granular matter [36, 33, 34, 35]. In the processing industry, granular materials are center stage, and DEM simulations are widely used to engineer and optimize production and transport processes. DEM simulations, for example, have been used to understand packing in a cylindrical container [39] for better silo engineering, and to study concrete structures under load in order to predict failure points and weaknesses [29, 30, 31].

Granular materials can be modeled by interacting particles, where each particle is a physical granule or a volume of material [38]. The modeled interaction between the particles defines the microscopic behavior of the material.

A classical model for DEM simulations of spherical granular flows is the Silbert model [37]. It includes a Herzian contact force, as well as elastic deformation of the grains. Each particle is represented by the location of its center of mass $\vec{r}_i$ and is characterized by its radius R, mass m, and polar moment of inertia I. Whenever two particles i and j collide or are in contact with each other, the radial elastic contact deformation is given by:

$$\delta_{ij} = 2R - r_{ij}\,, \tag{1}$$

with $\vec{r}_{ij} = \vec{r}_i - \vec{r}_j$ the vector connecting the two particle centers and $r_{ij} = \|\vec{r}_{ij}\|_2$ its length. The normal (radial) and tangential components of the relative velocity at the point of contact are given by:

$$\vec{v}_{n_{ij}} = (\vec{v}_{ij} \cdot \vec{n}_{ij})\, \vec{n}_{ij}\,, \tag{2}$$

$$\vec{v}_{t_{ij}} = \vec{v}_{ij} - \vec{v}_{n_{ij}} - R\,(\vec{\omega}_i + \vec{\omega}_j) \times \vec{n}_{ij}\,, \tag{3}$$

where $\vec{n}_{ij} = \vec{r}_{ij}/r_{ij}$ is the unit normal vector connecting the two particle centers, $\vec{\omega}_i$ is the angular velocity of particle i, and $\vec{v}_{ij} = \vec{v}_i - \vec{v}_j$ the relative velocity of the two particles. The tangential elastic displacement $\vec{u}_{t_{ij}}$ is integrated over time for the duration of contact, using an explicit Euler time-stepping scheme:

$$\vec{u}_{t_{ij}} \leftarrow \vec{u}_{t_{ij}} + \vec{v}_{t_{ij}} \delta t \tag{4}$$

with time-step stize δt. This deformation is stored for each particle and for each contact point. For a new contact, the tangential elastic displacement is initialized to zero. Thus for each unique pair of interacting (colliding) particles, the normal and tangential contact forces become:

$$\vec{F}_{n_{ij}} = \sqrt{\frac{\delta_{ij}}{2R}}\ \left(k_n \delta_{ij} \vec{n}_{ij} - \gamma_n m_{\text{eff}} \vec{v}_{n_{ij}}\right)\,, \tag{5}$$

$$\vec{F}_{t_{ij}} = \sqrt{\frac{\delta_{ij}}{2R}}\ \left(-k_t \vec{u}_{t_{ij}} - \gamma_t m_{\text{eff}} \vec{v}_{t_{ij}}\right)\,, \tag{6}$$

where $k_{n,t}$ are the elastic constants in the normal and tangential direction, respectively, and $\gamma_{n,t}$ the corresponding viscoelastic constants. The effective collision mass is given by $m_{\text{eff}} = \frac{m_i m_j}{m_i + m_j}$. In order to enforce Coulomb's law $\|\vec{F}_{t_{ij}}\|_2 < \|\mu \vec{F}_{n_{ij}}\|_2$, the tangential force of each contact point is bounded by the normal force. This is achieved by scaling the tangential force with

$$\vec{F}_{t_{ij}} \leftarrow \vec{F}_{t_{ij}} \frac{\|\mu \vec{F}_{n_{ij}}\|_2}{\|\vec{F}_{t_{ij}}\|_2}. \tag{7}$$

This implies a truncation of the elastic displacement, since the Coulomb limit is reached when two spheres slip against each other without inducing additional deformations. Thus, the deformation is truncated as:

$$\vec{u}_{t_{ij}} = -\frac{1}{k_t}\left(\vec{F}_{t_{ij}} \sqrt{\frac{2R}{\delta_{ij}}} + \gamma_t m_{\text{eff}} \vec{v}_{t_{ij}}\right). \tag{8}$$

Considering that each particle i interacts with all particles j it is in contact with, the total resultant force on particle i is computed by summing the contributions of all contact pairs (i, j). Including also gravity, we obtain the total force on grain i:

$$\vec{F}_i^{\text{tot}} = m\vec{g} + \sum_j \left(\vec{F}_{n_{ij}} + \vec{F}_{t_{ij}}\right), \tag{9}$$

```
1
create topology topo with
  boundry condition:      "ppm_param_bcdef_periodic"
  decomposition:          <no decomposition>
  processor assignment:   <no processor_assignment>
  ghost size:             cutoff + skin

2
{! fields and properties
  property <real, ppm_dim, "velocity", <no prec>, true> v
  property <real, ppm_dim, "force", <no prec>, true> F
  property <real, ppm_dim, "omega", <no prec>, true> omega
  property <real, ppm_dim, "tau", <no prec>, true> tau
  property <real, max_contacts_def, "contacts_def", <no prec>, true> cpd
  property <real, max_contacts, "contacts_ids", <no prec>, true> cpi
  property <real, 1, "n_cp", <no prec>, true> ncp
  property <real, 1, "type", <no prec>, true> tt
  property <real, 1, "gid", <no prec>, true> gid
}

3
v_nij = (v_rel[1] * n_ij[1] + v_rel[2] * n_ij[2] + v_rel[3] * n_ij[3]) * n_ij;

4
v_tij = v_rel - v_nij - v_cross;

5
[F_nij = SQRT(delta_ij/2/R) * (k_n*delta_ij*n_ij(:) - gamma_t*m_eff*v_nij(:))]

6
F_tij = F_tij * (F_nij_sq / F_tij_sq);
```

Figure 4: Excerpts of the PPME code for parallel DEM simulations.

where $\vec{g}$ is the acceleration due to gravity. In the Silbert model, particles also have a rotational degree of freedom. Therefore, the total torque on particle i is calculated as:

$$\vec{T}_i^{\text{tot}} = -R \sum_j \vec{n}_{ij} \times \vec{F}_{t_{ij}} \,. \tag{10}$$

We integrate the equations of motion using the second-order accurate leap frog scheme

$$\vec{v}_i^{n+1} = \vec{v}_i^n + \frac{\delta t}{m} \vec{F}_i^{\text{tot}} \,, \qquad \vec{r}_i^{n+1} = \vec{r}_i^n + \delta t \vec{v}_i^{n+1} \tag{11}$$

$$\vec{\omega}_i^{n+1} = \vec{\omega}_i^n + \frac{\delta t}{I_i} \vec{T}_i^{\text{tot}} \,, \tag{12}$$

where $\vec{r}_i^n$, $\vec{v}_i^n$, $\vec{\omega}_i^n$ denote respectively the position, velocity, and angular velocity of particle i at time step n, and δt is the time-step size.

5 RESULTS

We describe how the above DEM model is implemented in PPME and present the results of a simulation using 82,300 particles. Figure 4 shows excerpts of the PPME code for the model described in Section 4. The code for setting up the parallel simulation is in section (1). It defines the external boundary conditions on the computational domain, decomposes the problem onto the available processors, and adds ghost (halo) layers around each processor. The particle properties and their datatypes are defined and initialized by the code section (2). Each particle property has a datatype, a dimension, a human-readable name, a numerical precision, a flag stating whether this property is required, and

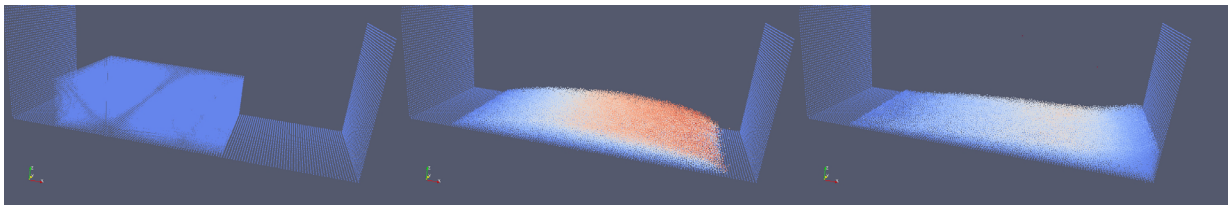

(a) t = 0 s (b) t = 2.0 s (c) t = 4.0 s

Figure 5: Visualization of PPME simulation results of an avalanche down and inclined plane. The panels show the particles at the indicated times. Color from blue to red indicates the x-component of the velocity of the particles.

a variable name. The remaining code (3-6) shows the implementations of Equations 2, 3, 5 and 7, respectively. Equation 2 is an example of native PPME code, using particle properties. Equation 5 is an example of inline Fortran code, enabling access to functions not supported in PPME.

We illustrate the PPME implementation using a classical test case for granular flow simulations: an avalanche down an inclined plane. The same test case has also previously been implemented in PPM [26, 27], enabling direct comparison of the codes and results. We set up the simulation as described [27] and run it using 82,300 particles with $k_n = 7.849$, $k_t = 2.243$, $\gamma_n = 3.401$, $\mu = 1$, $R = 0.06$. All particle masses are set to $m = 0.001$ and the gravitational acceleration to $g = 9.81$. The size of the box-shaped domain is fixed to $8.4 \times 3.0 \times 3.18$. Initially, the particles are placed on a regular Cartesian grid inside a box of size $4.26 \times 3.06 \times 1.26$. The simulation box is inclined by 30 degrees in the xz plane by appropriately rotating the gravity vector. The y-direction of the domain is periodic. Figure 5 visualizes the simulation results at different time points, showing the avalanche down the inclined plane. Color indicates the x-component of the particle velocity from low (blue) to high (red). The fixed walls on the bottom, left, and right of the domain are modeled by immobile particles of the same kind. The visualizations are done using ParaView, directly reading the VTK files produced by a single PPME "print" statement, illustrating the parallel file I/O amenities of PPME.

6 CONCLUSIONS

We presented PPME, an integrated development environment for parallel particle-mesh simulations. PPME is based on a complete language model for particle methods. Based on the core model, PPME provides an extensible static type system, including physical dimensions. For demonstration purposes, we exemplarily implemented a classical DEM model in PPME and used it to generate executable Fortran code that links against the PPM library and can be executed on distributed-memory computers using message passing. In the future, we will extend PPME to support additional abstractions from the particle-mesh domain. We will improve the internal architecture of PPME by adding

an additional target-language abstraction layer in order to be able to support output languages other than Fortran. This will provide a versatile and standard platform for parallel particle methods across a wide range of applications from discrete to continuum simulations.

ACKNOWLEDGEMENTS

This work was partly supported by the German Research Foundation (DFG) within the Cluster of Excellence "Center for Advancing Electronics Dresden".

REFERENCES

[1] Martin S. Alnæs, Anders Logg, Kristian B. Ølgaard, Marie E. Rognes, and Garth N. Wells. Unified form language: A domain-specific language for weak formulations of partial differential equations. *ACM Trans. Math. Softw.*, 40(2):9:1–9:37, 2014.

[2] Mark A. Austin. Matrix and finite element stack machines for structural engineering computations with units. *Adv. Eng. Softw.*, 37(8):544–559, 2006.

[3] Omar Awile. *A Domain-Specific Language and Scalable Middleware for Particle-Mesh Simulations on Heterogeneous Parallel Computers*. PhD thesis, Diss. ETH No. 20959, ETH Zürich, 2013.

[4] Omar Awile, Ömer Demirel, and Ivo F. Sbalzarini. Toward an object-oriented core of the PPM library. In *Proc. ICNAAM, Numerical Analysis and Applied Mathematics, International Conference*, pages 1313–1316. AIP, 2010.

[5] Omar Awile, Milan Mitrović, Sylvain Reboux, and Ivo F. Sbalzarini. A domain-specific programming language for particle simulations on distributed-memory parallel computers. In *Proc. III Intl. Conf. Particle-based Methods (PARTICLES)*, Particles 2013, pages 436–447, Stuttgart, 2013.

[6] Phil Cook, Colin Fidge, and David Hemer. Well-Measuring Programs. In *Proc. of ASWEC'06*, volume 54, pages 253–261, Sydney, 2006. IEEE.

[7] Zachary DeVito, Niels Joubert, Francisco Palacios, Stephen Oakley, Montserrat Medina, Mike Barrientos, Erich Elsen, Frank Ham, Alex Aiken, Karthik Duraisamy, et al. Liszt: a domain specific language for building portable mesh-based PDE solvers. In *Proc. of SC '11*, page 9. ACM, 2011.

[8] Sergey Dmitriev. Language Oriented Programming: The Next Programming Paradigm. *JetBrains onBoard*, (November), 2004.

[9] Martin Fowler. Language workbenches: The killer-app for domain specific languages?, 2005.

[10] Frederic Hecht. New development in freefem++. *J. of Num. Math.*, 20(3-4):251–266, 2012.

[11] Sven Karol, Pietro Incardona, Yaser Afshar, Ivo F. Sbalzarini, and Jeronimo Castrillon. Towards a Next-Generation Parallel Particle-Mesh Language. In *Proc. of DSLDI'15*, pages 15–18, 2015.

[12] George Karypis and Vipin Kumar. Multilevel k-way partitioning scheme for irregular graphs. 48:96–129, 1998.

[13] Anders Logg, Kent-Andre Mardal, and Garth Wells, editors. *Automated Solution of Differential Equations by the Finite Element Method*. Number 84 in LNCSE. Springer, 1 edition, 2012.

[14] Fabio Luporini, David A. Ham, and Paul H. J. Kelly. An algorithm for the optimization of finite element integration loops. Technical Report, arXiv.org, 2016.

[15] Fabio Luporini, Ana Lucia Varbanescu, Florian Rathgeber, Gheorghe-Teodor Bercea, J. Ramanujam, David A. Ham, and Paul H. J. Kelly. Cross-loop optimization of arithmetic intensity for finite element local assembly. *ACM Trans. Archit. Code Optim.*, 11(4):57:1–57:25, 2015.

[16] MPS - 3.2 - Documentation. User's Guide, 2015.

[17] Tobias Nett, Sven Karol, Jeronimo Castrillon, and Ivo F Sbalzarini. A domain-specific language and editor for parallel particle methods. *arXiv preprint arXiv:1704.00032*, 2017.

[18] Kristian B. Ølgaard and Garth N. Wells. Optimizations for quadrature representations of finite element tensors through automated code generation. *ACM Trans. Math. Softw.*, 37(1):8:1–8:23, 2010.

[19] Pavel Panchekha, Alex Sachez-Stern, James R. Wilcox, and Zachary Tatlock. Automatically Improving Accuracy for Floating Point Expressions. In *PLDI'15*, volume 50, pages 1–11. ACM, jun 2015.

[20] Florian Rathgeber, David A. Ham, Lawrence Mitchell, Michael Lange, Fabio Luporini, Andrew TT McRae, Gheorghe-Teodor Bercea, Graham R. Markall, and Paul HJ Kelly. Firedrake: automating the finite element method by composing abstractions. *arXiv preprint arXiv:1501.01809*, 2015.

[21] I. F. Sbalzarini, J. H. Walther, B. Polasek, P. Chatelain, M. Bergdorf, S. E. Hieber, E. M. Kotsalis, and P. Koumoutsakos. A software framework for the portable parallelization of particle-mesh simulations. *Lect. Notes Comput. Sc.*, 4128:730–739, 2006.

[22] Ivo F. Sbalzarini. Abstractions and middleware for petascale computing and beyond. *Intl. J. Distr. Systems & Technol.*, 1(2):40–56, 2010.

[23] Ivo F. Sbalzarini, J. H. Walther, M. Bergdorf, S. E. Hieber, E. M. Kotsalis, and P. Koumoutsakos. PPM - A highly efficient parallel particle-mesh library for the simulation of continuum systems. *Journal of Computational Physics*, 215(2):566–588, 2006.

[24] Birte Schrader, Sylvain Reboux, and Ivo F. Sbalzarini. Discretization correction of general integral PSE operators in particle methods. *J. Comput. Phys.*, 229:4159–4182, 2010.

[25] Todd L. Veldhuizen. Blitz++: The library that thinks it is a compiler. In *Advances in Software Tools for Scientific Computing*, number 10 in LNCSE, pages 57–87. Springer, 2000.

[26] Jens H. Walther and Ivo F. Sbalzarini. Large-scale parallel discrete element simulations of granular flow. In *Proceedings of the International Conference on Discrete Element Modelling (DEM07)*, Brisbane, Australia, 2007.

[27] Jens H. Walther and Ivo F. Sbalzarini. Large-scale parallel discrete element simulations of granular flow. *Engineering Computations*, 26(6):688–697, 2009.

[28] Martin P. Ward. Language Oriented Programming. *Software Concepts and Tools*, 15(4):147–161, 1994.

[29] F. Camborde and C. Mariotti and F.V. Donzé *Numerical study of rock and concrete behaviour by discrete element modelling*. Computers and Geotechnics, Vol. 27., (2000).

[30] Sébastien Hentz, Laurent Daudeville, and Frédéric V. Donzé *Numerical study of rock and concrete behaviour by discrete element modelling*. Computers and Geotechnics, 130(6):709–719, (2004).

[31] W. J. Shiu, F. V. Donzé, and L. Daudeville *Compaction process in concrete during missile impact: a dem analysis*. Computers and Concrete, 5(4):329–342, (2008).

[32] Hunt, M.L. *Discrete element simulations for graular material flows: effective thermal conductivity and self-diffusivity*. International Journal of Heat and Mass Transfer, Vol. 40 No. 13, pp. 3059-68, (1997).

[33] Daerr, A. and Douady, S. *Two types of avalanche behaviour in granular media*. Nature, Vol. 399, pp. 241-3, (1999).

[34] Douady, S., Andreotti, B., Daerr, A. and Cladé *From a grain to avalanches: on the physics of granular surface flows*. Comptes Rendus Physique, Vol. 3, pp. 177-87, (2002).

[35] Dutt, M., Hancock, B., Bentham, C. and Elliot, J. *An implementation of granular dynamics for simulating frictional elastic particles based on the DL_POLY code*. Computer Physics Communications, Vol. 166, pp. 26-44, (2005).

[36] de Gennes, P.G. *Granular matter: a tentative view*. Reviews of Modern Physics, Vol. 71 No. 2, pp. 374-82, (1999).

[37] Silbert, L.E., Grest, G.S. and Plimpton, S.J. *Boundary effects and self-organization in dense granular flows*. Physics of Fluids, Vol. 14 No. 8, pp. 2637-46, (2002).

[38] Stefan Luding *Introduction to discrete element methods* . European Journal of Environmental and Civil Engineering (2008).

[39] Landry, J.W., Grest, G.S., Silbert, L.E. and Plimpton, S.J. *Confined granular packings structure, stress, and forces*. Physical Review E, Vol. 67, p. 041303, (2003).

V International Conference on Particle-based Methods – Fundamentals and Applications
PARTICLES 2017
P. Wriggers, M. Bischoff, E. Oñate, D.R.J. Owen, & T. Zohdi (Eds)

APPLICATION OF CONTINUUM FORMS FOR PREDICTING ELASTIC WAVE PROPERTIES OF BRICK MORTAR SYSTEM

SUMET SUPPRASERT[1], LALITH WIJERATHNE[2], MUNEO HORI[3] AND JIAN CHEN[4]

[1] Earthquake Research Institute
University of Tokyo, Bunkyo, Tokyo 113-0032, Japan
[1]sumet.res@gmail.com, [2]lalith@eri.u-tokyo.ac.jp, [3]hori@eri.u-tokyo.ac.jp

[4] Advanced Institute for Computational Science
RIKEN, Minatoshima-Minami, Kobe 650-0047, Japan
jchen@riken.jp

Key words: continuum forms, regularly packed bricks, predicting elastic wave characteristics, continuumnization

Abstract. We developed three continuum forms for brick structures, predicted the elastic wave characteristics and investigated the range of validity of the predictions. One of the continuum form is based on *continuumnization* by Hori et al. and the other two are based on Taylor series expansion. Both continuumnization and second order Taylor expansion based continuum forms can predict p- and s-wave characteristics accurately for wavelengths larger than 7 times the brick dimensions. The second order Taylor expansion can also predict the r-wave characteristics accurately in the same range of wavelengths. It is demonstrated that the full Taylor series based continuum form can predict the elastic wave properties to a remarkable accuracy for the whole range of frequencies and wave numbers. These predictions will be useful in verification of simulation codes, utilizing FEM for analyzing brick structures and engineering applications like non-destructive testing, vibration control, etc.

1 INTRODUCTION

We propose three equivalent continuum forms for identifying the elastic wave properties of regularly packed brick-mortar systems and apply those to analytically predict the characteristics of elastic waves properties. These analytical predictions can be used in wide range of applications like verification of numerical codes, non-destructive identification of material properties, vibration control, design, etc.

Two approaches are used in deriving continuum forms; *Continuumnization* proposed by Hori et al.[1] and Taylor series expansion. A regularly packed brick mortar system is

idealized as a discrete block spring system. Three continuum forms of governing equations are obtained assuming the existence of smooth and continuous vector fields which can approximate the field variables of the idealized discrete system. Continuumnization utilizes the limiting process to approximate difference operations in the discrete form of the governing equations, while the other two continuum forms approximate the field variables of idealized discrete system using Taylor series expansion. One of the Taylor series based continuum form uses second order Taylor expansion while the other uses the whole Taylor series. The continuum from obtained with the whole Taylor series can predict the elastic wave characteristics up to the smallest meaningful wavelength, while the predictions of the other two are accurate within the wavelengths of engineering applications.

The rest of the paper is organized as follows. The section two presents the derivations of the three continuum forms of equation of motion, and corresponding characteristic equations for predicting wave properties for regularly packed brick mortar systems. The third section investigates the range of applicability of each continuum form. Some concluding remarks are given in the last section.

2 CONTINUUM FORMS FOR REGULARLY PACKED BRICK SYSTEM

As the starting point to derive the three equivalent continuum forms, first the discrete equations of motion for a regularly packed brick mortar system is obtained. The rest of this section presents the derivation of the three continuum forms and the analytical predictions of the elastic wave properties.

2.1 Regularly packed bricks as a discrete system

We idealize a single layer brick wall as a network of rigid rectangular blocks connected with infinitesimally short linear elastic springs, as shown in Fig.1(a). The springs represent elasticity of both the bricks and mortar layers while the domain of each rigid block includes a portion of cement layers so that the domain occupied by the brick mortar system is perfectly tessellated.

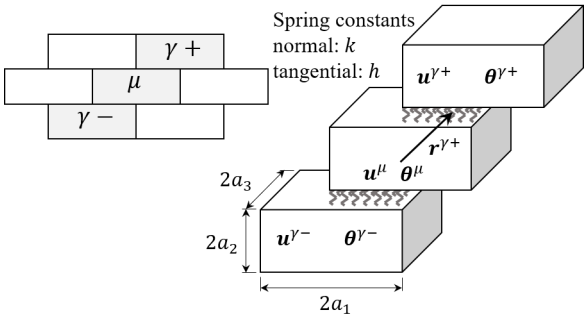

(a) Neighboring blocks of regularly packed bricks

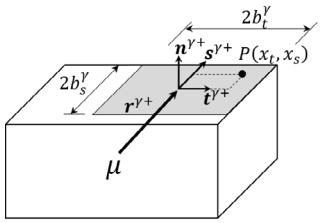

(b) Contact area of two neighboring blocks

Figure 1: Idealized block-spring model.

Consider an arbitrary block μ of a regularly packed brick mortar system (see Fig. 1(a)) and let its centroid be $\boldsymbol{x}^{\mu}$. The pair of neighbors located in the γ^{th} direction, $\boldsymbol{r}^{\gamma\pm}$, are denoted as $\gamma\pm$, and let their centroids be $\boldsymbol{x}^{\mu}+2\boldsymbol{r}^{\gamma\pm}$. Note that $\boldsymbol{r}^{\gamma\pm}$ denote the relative position vectors of the centroid of the contact areas with the neighbors $\gamma\pm$. Let $\boldsymbol{n}^{\gamma}$, $\boldsymbol{t}^{\gamma}$ and $\boldsymbol{s}^{\gamma}$ be an orthonormal coordinate system on contact area with the neighboring block in $\boldsymbol{r}^{\gamma+}$ direction (see Fig. 1(b)). Let the dimension of this rectangular contact area be $2b_t^{\gamma}\times 2b_s^{\gamma}$. Let (x_t,x_s) be an arbitrary point on this contact area, with respect to this local coordinate system.

Assume that the bricks are rigid and undergo infinitesimally small translations and rotations. Let the translation and rotation of μ^{th} block be $\boldsymbol{u}^{\mu}$ and $\boldsymbol{\theta}^{\mu}$, while those of neighbors are $\boldsymbol{u}^{\gamma\pm}$ and $\boldsymbol{\theta}^{\gamma\pm}$. The corresponding relative displacement at the point (x_t,x_s) is

$$\boldsymbol{L}^{\mu\gamma+} = \left(\boldsymbol{u}^{\gamma+}-\boldsymbol{u}^{\mu}\right)-\left(\boldsymbol{\theta}^{\gamma+}+\boldsymbol{\theta}^{\mu}\right)\times\boldsymbol{r}^{\gamma+}+\left(\boldsymbol{\theta}^{\gamma+}-\boldsymbol{\theta}^{\mu}\right)\times\left(x_t\boldsymbol{t}^{\gamma+}+x_s\boldsymbol{s}^{\gamma+}\right).$$

If k and h are the normal and tangential spring constants, respectively, the elastic energy stored in the spring due to the relative deformation $\boldsymbol{L}^{\gamma+}$ is

$$V^{\mu\gamma+} = \frac{1}{2}\int_{-b_s^{\gamma}}^{b_s^{\gamma}}\int_{-b_t^{\gamma}}^{b_t^{\gamma}} k\left(\boldsymbol{n}^{\gamma+}\cdot\boldsymbol{L}^{\mu\gamma+}\right)^2+h\left\{\left(\boldsymbol{t}^{\gamma+}\cdot\boldsymbol{L}^{\mu\gamma+}\right)^2+\left(\boldsymbol{s}^{\gamma+}\cdot\boldsymbol{L}^{\mu\gamma+}\right)^2\right\}\mathrm{d}x_t\mathrm{d}x_s,$$

and the Lagrangian for the whole discrete system is

$$\mathcal{L} = \sum_{\mu}\left(\frac{1}{2}m\dot{\boldsymbol{u}}^{\mu}\cdot\dot{\boldsymbol{u}}^{\mu}+\frac{1}{2}\dot{\boldsymbol{\theta}}^{\mu}\cdot\boldsymbol{I}\cdot\dot{\boldsymbol{\theta}}^{\mu}-V^{\mu}\right), \tag{1}$$

where $V^{\mu}=\frac{1}{2}\sum_{\gamma}(V^{\mu\gamma+}+V^{\mu\gamma-})$. m and $\boldsymbol{I}$ are the mass and inertia tensor of each block.

Applying the Hamilton's principal of stationary action, $\delta\int\mathcal{L}\mathrm{d}t=0$, we can obtain the following governing equations of motion for the discrete system

$$\begin{aligned} m\ddot{\boldsymbol{u}}^{\mu} &= \sum_{\gamma}\boldsymbol{K}^{\mu\gamma}\cdot\left(\boldsymbol{u}^{\gamma+}-2\boldsymbol{u}^{\mu}+\boldsymbol{u}^{\gamma-}\right)-\hat{\boldsymbol{K}}^{\mu\gamma}\cdot\left(\boldsymbol{\theta}^{\gamma+}-\boldsymbol{\theta}^{\gamma-}\right) \\ \boldsymbol{I}\cdot\ddot{\boldsymbol{\theta}}^{\mu} &= \sum_{\gamma}\left(\hat{\boldsymbol{K}}^{\mu\gamma}\right)^{\mathrm{T}}\cdot\left(\boldsymbol{u}^{\gamma+}-\boldsymbol{u}^{\gamma-}\right)-\overline{\boldsymbol{K}}^{\mu\gamma}\cdot\left(\boldsymbol{\theta}^{\gamma+}+2\boldsymbol{\theta}^{\mu}+\boldsymbol{\theta}^{\gamma-}\right)+\overline{\overline{\boldsymbol{K}}}^{\mu\gamma}\cdot\left(\boldsymbol{\theta}^{\gamma+}-2\boldsymbol{\theta}^{\mu}+\boldsymbol{\theta}^{\gamma-}\right), \end{aligned} \tag{2}$$

where

$$
\begin{aligned}
\boldsymbol{K}^{\mu\gamma} &= 4b_t^\gamma b_s^\gamma (k\boldsymbol{n}^\gamma\otimes\boldsymbol{n}^\gamma + h\boldsymbol{t}^\gamma\otimes\boldsymbol{t}^\gamma + h\boldsymbol{s}^\gamma\otimes\boldsymbol{s}^\gamma) \\
\hat{\boldsymbol{K}}^{\mu\gamma} &= 4b_t^\gamma b_s^\gamma \{k\boldsymbol{n}^\gamma\otimes(\boldsymbol{r}^\gamma\times\boldsymbol{n}^\gamma) + h\boldsymbol{t}^\gamma\otimes(\boldsymbol{r}^\gamma\times\boldsymbol{t}^\gamma) + h\boldsymbol{s}^\gamma\otimes(\boldsymbol{r}^\gamma\times\boldsymbol{s}^\gamma)\} \\
\overline{\boldsymbol{K}}^{\mu\gamma} &= 4b_t^\gamma b_s^\gamma \{k(\boldsymbol{r}^\gamma\times\boldsymbol{n}^\gamma)\otimes(\boldsymbol{r}^\gamma\times\boldsymbol{n}^\gamma) + h(\boldsymbol{r}^\gamma\times\boldsymbol{t}^\gamma)\otimes(\boldsymbol{r}^\gamma\times\boldsymbol{t}^\gamma) + h(\boldsymbol{r}^\gamma\times\boldsymbol{s}^\gamma)\otimes(\boldsymbol{r}^\gamma\times\boldsymbol{s}^\gamma)\} \\
\overline{\overline{\boldsymbol{K}}}^{\mu\gamma} &= \frac{4}{3}\left\{h\left(b_t^\gamma b_s^{\gamma 3} + b_t^{\gamma 3} b_s^\gamma\right)\boldsymbol{n}^\gamma\otimes\boldsymbol{n}^\gamma + kb_t^\gamma b_s^{\gamma 3}\boldsymbol{t}^\gamma\otimes\boldsymbol{t}^\gamma + kb_t^{\gamma 3} b_s^\gamma \boldsymbol{s}^\gamma\otimes\boldsymbol{s}^\gamma\right\}
\end{aligned}
$$

For the sake of brevity, γ denotes $\gamma+$ in the above set of equations. It is straight forward to obtain expressions for $\gamma-$ using the following relations: $\boldsymbol{K}^{\mu\gamma+}=\boldsymbol{K}^{\mu\gamma-}$; $\hat{\boldsymbol{K}}^{\mu\gamma+}=-\hat{\boldsymbol{K}}^{\mu\gamma-}$; $\overline{\boldsymbol{K}}^{\mu\gamma+}=\overline{\boldsymbol{K}}^{\mu\gamma-}$; and $\overline{\overline{\boldsymbol{K}}}^{\mu\gamma+}=\overline{\overline{\boldsymbol{K}}}^{\mu\gamma-}$. The set of equations for discrete system given in Eq. (2) can be used to simulate a brick structure as a mass spring system. Though the elastic wave characteristics for given brick mortar properties can be obtained by analyzing the results of such simulations, what is desired for design and verification purposes is the predictability of wave characteristics for arbitrary material properties.

2.2 Equivalent continuum forms

The derivations of the different continuum forms presented in this paper are motivated by Hori et al.'s work on Continuumnization. Hence we first briefly present the outline of their formulation of continuum form, followed by the newly proposed Taylor series approach. Both the approaches assume the presence of smooth vector fields $\boldsymbol{u}$ and $\boldsymbol{\theta}$ which satisfy $\boldsymbol{u}(\boldsymbol{x}^\mu)=\boldsymbol{u}^\mu$ and $\boldsymbol{\theta}(\boldsymbol{x}^\mu)=\boldsymbol{\theta}^\mu$, and make different approximations to the discrete terms $\boldsymbol{u}^{\gamma\pm}-\boldsymbol{u}^\mu$ and $\boldsymbol{\theta}^{\gamma\pm}\pm\boldsymbol{\theta}^\mu$ of Eq. 2.

2.2.1 Continuumnization

In their original work on continuumnization, Hori et al. expressed the discrete terms $\boldsymbol{u}^{\gamma\pm}-\boldsymbol{u}^\mu$ and $\boldsymbol{\theta}^{\gamma\pm}-\boldsymbol{\theta}^\mu$ with differential operators considering the limits $\lim_{\|\boldsymbol{r}^\gamma\|\to 0}\frac{\boldsymbol{u}^{\gamma\pm}-\boldsymbol{u}^\mu}{\|\boldsymbol{r}^\gamma\|}\approx \pm\boldsymbol{r}^\gamma\cdot\nabla\boldsymbol{u}$ and $\lim_{\|\boldsymbol{r}^\gamma\|\to 0}\frac{\boldsymbol{\theta}^{\gamma\pm}-\boldsymbol{\theta}^\mu}{\|\boldsymbol{r}^\gamma\|}\approx\pm\boldsymbol{r}^\gamma\cdot\nabla\boldsymbol{\theta}$. As it will be shown in section 2.2.3, an equivalent continuum form can be obtained by substituting these approximations to Eq. 2.

2.2.2 Taylor series

Instead of using the limiting process, here we use Taylor series expansion to obtain continuous approximations for discrete terms $\boldsymbol{u}^{\gamma\pm}-\boldsymbol{u}^\mu$ and $\boldsymbol{\theta}^{\gamma\pm}-\boldsymbol{\theta}^\mu$. As an example, $\boldsymbol{u}^{\gamma\pm}$ can be approximated as

$$
\boldsymbol{u}^{\gamma\pm} \approx \boldsymbol{u}^\mu \pm 2r_i\left[\frac{\partial\boldsymbol{u}}{\partial x_i}\right]_{\boldsymbol{x}^\mu} + 2r_ir_j\left[\frac{\partial^2\boldsymbol{u}}{\partial x_i\partial x_j}\right]_{\boldsymbol{x}^\mu} \pm \frac{2^3 r_ir_jr_k}{3!}\left[\frac{\partial^3\boldsymbol{u}(\boldsymbol{x})}{\partial x_i\partial x_j\partial x_k}\right]_{\boldsymbol{x}^\mu} + \ldots \qquad (3)
$$

Based on the above expression, we can approximate $(\boldsymbol{u}^{\gamma+}\pm\boldsymbol{u}^{\gamma-})$ and $(\boldsymbol{u}^{\gamma+}-\boldsymbol{u}^{\gamma-})$ as

$$\begin{aligned}
\boldsymbol{u}^{\gamma+}+\boldsymbol{u}^{\gamma-} &\approx 2\boldsymbol{u}^{\mu}+\frac{2^3 r_i r_j}{2!}\left[\frac{\partial^2 \boldsymbol{u}(\boldsymbol{x})}{\partial x_i \partial x_j}\right]_{\boldsymbol{x}^\mu}+\frac{2^5 r_i r_j r_k r_l}{4!}\left[\frac{\partial^4 \boldsymbol{u}(\boldsymbol{x})}{\partial x_i \partial x_j \partial x_k \partial x_l}\right]_{\boldsymbol{x}^\mu}+\ldots \\
\boldsymbol{u}^{\gamma+}-\boldsymbol{u}^{\gamma-} &\approx \left[\frac{\partial \boldsymbol{u}(\boldsymbol{x})}{\partial x_i}\right]_{\boldsymbol{x}^\mu} 2^2 r_i+\frac{2^4 r_i r_j r_k}{3!}\left[\frac{\partial^3 \boldsymbol{u}(\boldsymbol{x})}{\partial x_i \partial x_j \partial x_k}\right]_{\boldsymbol{x}^\mu}+\ldots
\end{aligned} \tag{4}$$

Similarly, it is straight forward to express $(\boldsymbol{\theta}^{\gamma+}\pm\boldsymbol{\theta}^{\gamma-})$. The Taylor series approach uses the above expressions for approximating the discrete terms $(\boldsymbol{u}^{\gamma+}\pm\boldsymbol{u}^{\gamma-})$ and $(\boldsymbol{\theta}^{\gamma+}\pm\boldsymbol{\theta}^{\gamma-})$ in terms of continuous vector fields $\boldsymbol{u}(\boldsymbol{x})$ and $\boldsymbol{\theta}(\boldsymbol{x})$.

2.2.3 Equivalent continuum forms of discrete governing equations

Neglecting all the third or higher order derivatives terms of Eq. 4 and substituting to Eq. 2, we can obtain the following second order accurate continuum form for the idealized discrete brick mortar system.

$$\begin{aligned}
\frac{m}{V_b}\ddot{\boldsymbol{u}} &= \nabla\cdot(\boldsymbol{c}:\nabla\boldsymbol{u})-\boldsymbol{q}:\nabla\boldsymbol{\theta} \\
\frac{1}{V_b}\boldsymbol{I}\cdot\ddot{\boldsymbol{\theta}} &= \boldsymbol{q}^{\mathrm{T}}:\nabla\boldsymbol{u}-\boldsymbol{d}\cdot\boldsymbol{\theta}+\nabla\cdot(\boldsymbol{v}:\nabla\boldsymbol{\theta}),
\end{aligned} \tag{5}$$

where V_b is the volume of a block. $\boldsymbol{c}$, $\boldsymbol{q}$, $\boldsymbol{d}$, and $\boldsymbol{v}$ are 4^{th}, 3^{rd}, 2^{nd}, and 4^{th}-order tensors composed of material and geometric (i.e. block geometry and packing) properties. Explicit expressions for these tensors for the second order Taylor series based continuum form are

$$\begin{aligned}
\boldsymbol{c} &= \frac{16}{V_b}\sum_{\gamma} b_t^{\gamma} b_s^{\gamma}\left(k\boldsymbol{r}^{\gamma}\otimes\boldsymbol{n}^{\gamma}\otimes\boldsymbol{r}^{\gamma}\otimes\boldsymbol{n}^{\gamma}+h\boldsymbol{r}^{\gamma}\otimes\boldsymbol{t}^{\gamma}\otimes\boldsymbol{r}^{\gamma}\otimes\boldsymbol{t}^{\gamma}+h\boldsymbol{r}^{\gamma}\otimes\boldsymbol{s}^{\gamma}\otimes\boldsymbol{r}^{\gamma}\otimes\boldsymbol{s}^{\gamma}\right) \\
\boldsymbol{q} &= \frac{16}{V_b}\sum_{\gamma} b_t^{\gamma} b_s^{\gamma}\left\{k\boldsymbol{n}^{\gamma}\otimes\boldsymbol{r}^{\gamma}\otimes(\boldsymbol{r}^{\gamma}\times\boldsymbol{n}^{\gamma})+h\boldsymbol{t}^{\gamma}\otimes\boldsymbol{r}^{\gamma}\otimes(\boldsymbol{r}^{\gamma}\times\boldsymbol{t}^{\gamma})+h\boldsymbol{s}^{\gamma}\otimes\boldsymbol{r}^{\gamma}\otimes(\boldsymbol{r}^{\gamma}\times\boldsymbol{s}^{\gamma})\right\} \\
\boldsymbol{d} &= \frac{16}{V_b}\sum_{\gamma} b_t^{\gamma} b_s^{\gamma}\left\{k(\boldsymbol{r}^{\gamma}\times\boldsymbol{n}^{\gamma})\otimes(\boldsymbol{r}^{\gamma}\times\boldsymbol{n}^{\gamma})+h(\boldsymbol{r}^{\gamma}\times\boldsymbol{t}^{\gamma})\otimes(\boldsymbol{r}^{\gamma}\times\boldsymbol{t}^{\gamma})+h(\boldsymbol{r}^{\gamma}\times\boldsymbol{s}^{\gamma})\otimes(\boldsymbol{r}^{\gamma}\times\boldsymbol{s}^{\gamma})\right\} \\
\boldsymbol{v} &= \frac{16}{3V_b}\sum_{\gamma} b_t^{\gamma} b_s^{\gamma}\boldsymbol{r}^{\gamma}\otimes\Big\{\Big\{h\left(b_s^{\gamma 2}+b_t^{\gamma 2}\right)\boldsymbol{n}^{\gamma}\otimes\boldsymbol{r}^{\gamma}\otimes\boldsymbol{n}^{\gamma}+kb_s^{\gamma 2}\boldsymbol{t}^{\gamma}\otimes\boldsymbol{r}^{\gamma}\otimes\boldsymbol{t}^{\gamma}+kb_t^{\gamma 2}\boldsymbol{s}^{\gamma}\otimes\boldsymbol{r}^{\gamma}\otimes\boldsymbol{s}^{\gamma}\Big\} \\
&\quad -3\left\{k(\boldsymbol{r}^{\gamma}\times\boldsymbol{n}^{\gamma})\otimes\boldsymbol{r}^{\gamma}\otimes(\boldsymbol{r}^{\gamma}\times\boldsymbol{n}^{\gamma})+h((\boldsymbol{r}^{\gamma}\times\boldsymbol{t}^{\gamma})\otimes\boldsymbol{r}^{\gamma}\otimes(\boldsymbol{r}^{\gamma}\times\boldsymbol{t}^{\gamma})+(\boldsymbol{r}^{\gamma}\times\boldsymbol{s}^{\gamma})\otimes\boldsymbol{r}^{\gamma}\otimes(\boldsymbol{r}^{\gamma}\times\boldsymbol{s}^{\gamma}))\right\}\Big\}
\end{aligned}$$

In the original work by Hori et al.[1], a first order approximation is made for the term $(\boldsymbol{\theta}^{\gamma+}+2\boldsymbol{\theta}^{\mu}+\boldsymbol{\theta}^{\gamma-})\approx 4\boldsymbol{\theta}(\boldsymbol{x}^{\mu})$, instead of $4\boldsymbol{\theta}+4r_i r_j\left[\frac{\partial^2\boldsymbol{\theta}(\boldsymbol{x})}{\partial x_i\partial x_j}\right]_{\boldsymbol{x}^\mu}$ used in the above second order Taylor series approximation. Consequently, the term $\nabla\cdot(\boldsymbol{v}:\nabla\boldsymbol{\theta})$ of Eq. 5 is not present in the continuum form of governing equations from continuumnization.

Table 1: Wave velocities and corresponding modes $\{u_1,u_2,\theta_3\}$ for θ_ξ=90° and θ_ξ=0°. $\zeta=a_2/a_1$ and $\eta=h/k$

wave type	θ_ξ=90°		θ_ξ=0°	
	phase velocity	mode shape	phase velocity	mode shape
p	$\sqrt{\frac{2ka_2}{\rho}}$	$\{0,1,0\}$	$\sqrt{\frac{ka_2(\eta+4\zeta)}{2\rho\zeta^2}}$	$\{1,0,0\}$
s	$\sqrt{\frac{2ka_2\eta(1+4\eta\zeta)}{\rho(1+4\eta\zeta+4\eta\zeta^2)}}$	$\left\{1,0,-\frac{4\eta\zeta^2\xi\mathrm{i}}{1+4\eta\zeta+4\eta\zeta^2}\right\}$	$\sqrt{\frac{2ka_2\eta(1+4\eta\zeta)}{\rho(1+4\eta\zeta+4\eta\zeta^2)}}$	$\left\{0,1,-\frac{(1+4\eta\zeta)\xi\mathrm{i}}{1+4\eta\zeta+4\eta\zeta^2}\right\}$
r	-	$\{0,0,1\}$	-	$\{0,0,1\}$

While the above second order Taylor expansion based continuum form was independently developed by the authors, Stefanou et al.[2] also have proposed similar idea of obtaining equivalent continuum form of regularly arranged brick structures based on second order Taylor expansion.

2.2.4 Prediction of elastic wave characteristics

A major advantage of Eq.(5) is that it makes it possible to analytically study the dynamic characteristics of the approximated discrete system. As an example, consider the two dimensional single layered brick wall shown in Fig.2. For this given packing, we can evaluate the four tensors, $\boldsymbol{c}$, $\boldsymbol{q}$, $\boldsymbol{d}$, and $\boldsymbol{v}$, and obtain the equivalent continuum form of equations of motion (i.e. Eq.(5)). Taking the Fourier transform of the resulting equations, with the kernel of $e^{\imath(\boldsymbol{\xi}\cdot\boldsymbol{x}-\omega t)}$, where $\boldsymbol{\xi}=\xi\{\cos\theta_\xi,\sin\theta_\xi\}$, and solving the resulting characteristic equations, the relations between the wave frequencies and wave numbers for in-plane deformations can be obtained. Since the system is anisotropic, the wave velocities depend on the direction of the propagating wave. Table 1 shows the p-, s- and r- wave charateristics based on the continuum form with the second order Taylor expansion.

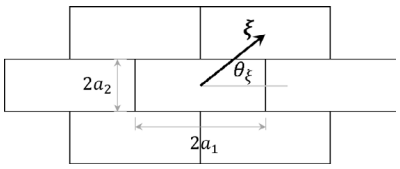

Figure 2: A single layered 2 dimensional brick arrangement.

Though r-wave speed is undefined, we can obtain following expression for frequency of rotational mode

$$\omega_{\mathrm{spin}}=\sqrt{\frac{3ka_1^2+12ha_1a_2+12ha_2^2}{2\rho a_1^2a_2+2\rho a_2^3}}. \tag{6}$$

2.2.5 Prediction of elastic wave characteristics based on an arbitrary order approximation

In the section 2.2.3, we used only the terms up to the second order derivatives in Eq.(4). It surely is odd to consider all the infinite terms of the Taylor expansion in approximating variables. However lets consider all the terms of Taylor series expansion and obtain a continuum form, which is obviously too complicated for any practical use. The presence of some series solutions make it is possible to obtain a quite compact characteristic equation when all the infinite terms of Eq.(4) are used.

With a little bit of mathematical manipulations, the following two relations for the Fourier transform of Eq.(4) can be established; note that all the infinite terms in the Taylor series are included.

$$\begin{aligned}\int \left(\boldsymbol{u}^{\gamma+}+\boldsymbol{u}^{\gamma-}\right) e^{\imath(\boldsymbol{\xi}\cdot\boldsymbol{x}-\omega t)}\mathrm{d}\boldsymbol{x}\mathrm{d}t &\approx 2\left(1-2\sin^2(\boldsymbol{\xi}\cdot\boldsymbol{r}^{\gamma})\right)\hat{\boldsymbol{u}}\\ \int (\boldsymbol{u}^{\gamma+}-\boldsymbol{u}^{\gamma-}) e^{\imath(\boldsymbol{\xi}\cdot\boldsymbol{x}-\omega t)}\mathrm{d}\boldsymbol{x}\mathrm{d}t &\approx 2\imath\{\sin(2\boldsymbol{\xi}\cdot\boldsymbol{r}^{\gamma})\}\hat{\boldsymbol{u}}\end{aligned} \tag{7}$$

$\hat{\boldsymbol{u}}$ and $\hat{\boldsymbol{\theta}}$ are the Fourier transform of $\boldsymbol{u}$ and $\boldsymbol{\theta}$ with respect to the kernel $e^{\imath(\boldsymbol{\xi}\cdot\boldsymbol{x}-\omega t)}$. Now, approximating the discrete terms $(\boldsymbol{u}^{\gamma+}\pm\boldsymbol{u}^{\gamma-})$ and $(\boldsymbol{\theta}^{\gamma+}\pm\boldsymbol{\theta}^{\gamma-})$ of Eq.(4) with the full Taylor series and taking the Fourier transform, we can obtain the following set of equations.

$$0 = \det\begin{bmatrix} -\omega^2\boldsymbol{M}+\sum_{\gamma}4\sin^2(\boldsymbol{\xi}\cdot\boldsymbol{r}^{\gamma})\boldsymbol{K}^{\mu\gamma} & 2\imath\sum_{\gamma}\sin(2\boldsymbol{\xi}\cdot\boldsymbol{r})\hat{\boldsymbol{K}}^{\mu\gamma} \\ -2\imath\sum_{\gamma}\sin(2\boldsymbol{\xi}\cdot\boldsymbol{r}^{\gamma})\left(\hat{\boldsymbol{K}}^{\mu\gamma}\right)^{\mathrm{T}} & -\omega^2\boldsymbol{I}+4\sum_{\gamma}\left(\cos^2(\boldsymbol{\xi}\cdot\boldsymbol{r}^{\gamma})\overline{\boldsymbol{K}}^{\mu\gamma}+\sin^2(\boldsymbol{\xi}\cdot\boldsymbol{r}^{\gamma})\overline{\overline{\boldsymbol{K}}}^{\mu\gamma}\right)\end{bmatrix}$$

$\boldsymbol{M}=m\mathbf{1}$ is the mass matrix and $\boldsymbol{I}$ is the inertia tensor of a brick; $\mathbf{1}$ is the identity matrix.

Though the above is too complicated to solve for analytical relations between frequencies and wave numbers, ω and $\boldsymbol{\xi}$, we can numerically solve it to find relation between ω and $\boldsymbol{\xi}$. As it will be shown in the next section, the wave properties predicted with this characteristic function is valid for much wider range of wave numbers, compared to above obtained predictions from continuumnization and second order Taylor series approximation.

3 VERIFICATION OF THE PREDICTED WAVE PROPERTIES

To verify the elastic wave characteristics predicted in sections 2.2.4 and 2.2.5 and identify the applicable range of these predictions, we compared the predicted properties with the results obtained from a Rigid Body Spring Model (RBSM) simulation. The details of this comparison is presented in this section.

3.1 Basic problem settings

A brick wall of width 20.3m and height 13.0m shown in Fig.3 was used for the RBSM simulations. The bricks are 60mm in width, 30mm in height, and 40mm in thickness. The density of each block is assumed to be 1850kg/m^3. k and h, are determined as 5.12×10^{11}N/m^3 and 2.22×10^{11}N/m^3, respectively.

For the sake of simplicity, 2D settings was assumed and the domain was excited with an in-plane wave at center of the domain. We considered 3 cases with different inputs. First and second cases were with transnational waves of vertical and horizontal excitation. The third case was with a rotational wave input. In all the cases, the wave form shown in Fig. 3b was used.

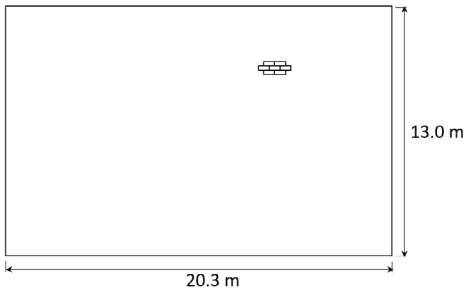

(a) Domain

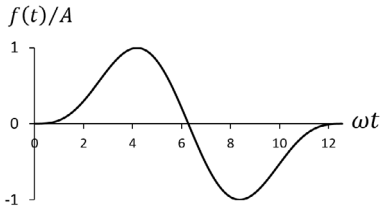

(b) Input wave $f(t)=\frac{4}{3\sqrt{3}}A\left(\sin\frac{\omega t}{2}-\frac{1}{2}\sin\omega t\right)$

Figure 3: Domain and the wave form used in the numerical experiments.

A and ω are the amplitude and circular frequency of the input. For vertical and horizontal inputs A=2mm while A=0.035 radians for the rotational input. To obtain narrow wave fronts, so that peaks and valleys of waves are clearly visible, input circular frequency ω is set 1.57×10^4radian/s for vertical and horizontal input, and 2.11×10^5radian/s for rotational input.

In order to obtain accurate results, we used a second order velocity Verlet algorithm with $1\mu s$ time step for time integration. As an indirect check of accuracy of the simulation, energy and momentum of the whole system were monitored. Near perfect preservation of energy and momentum was observed, indicating that the simulations were accurate.

3.2 Comparison of translational waves

The color contours of Fig. 4(a) and (b) show the distribution of translational wave amplitudes at time 2ms. The two black color curves indicate the analytically predicted wave fronts based on the continuum form from the second order Taylor expansion presented in the section 2.2.3.

3.2.1 P-wave

As is seen, the analytically predicted p-wave fronts are in good agreement with numerical results in the regions indicated with letter A. The wave profiles along section P-P, shown in the left side pair of Fig.5 clearly indicate that the analytical predictions are in good agreement with the numerical results. In Fig.4(a), since the input wave is oriented in vertical direction, the p-wave amplitude is highest in up and down directions, while it is extremely low in other directions. This is why no p-wave fronts are visible in the numerical results except in up and down directions in Fig.4(a), and left and right directions in Fig.4(b).

3.2.2 S-wave

Also, the Fig. 4(a) and (b) show that the theoretically predicated s-wave fronts are also in good agreement with that of numerical results in the regions marked with letter B. The right hand side pair in Fig.5 provides clear evidences to support this claim. Amplitude of the main s-wave is weak in most directions, except orthogonal to the direction of excitation. This is why there seems to be a significant mismatch between numerical and analytical wave fronts in regions except B.

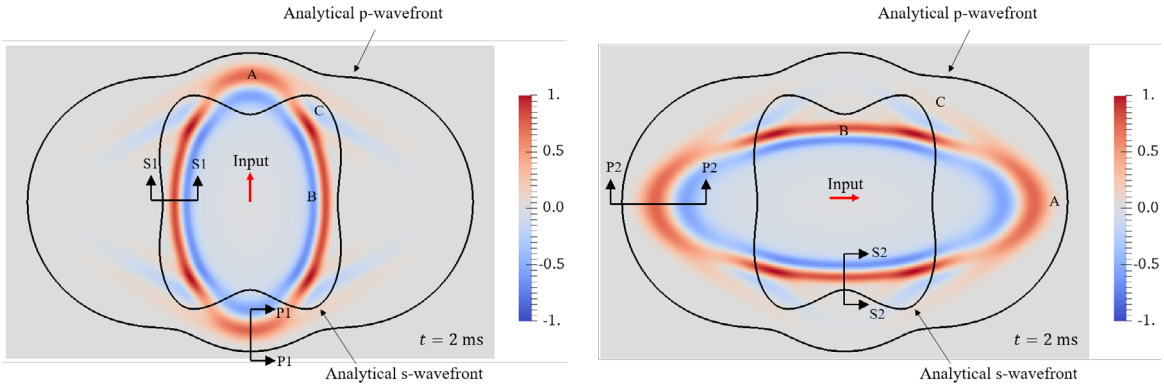

(a) with vertical input (b) with horizontal input

Figure 4: Comparison of predicted p- and s-wave fronts with those of numerical results, at 2 ms. The colors indicate the amplitude of translational waves.

3.3 Comparison of rotational waves

Fig. 6 shows the distribution of the amplitudes of rotational waves (r-wave) generated by the rotational wave input, at 2 ms. Unlike the translational wave inputs, dispersion of the rotational wave occurs. In order to check the accuracy of predictions, we compared the circular frequency ω versus the normalized wave number ξa_i where a_1 and a_2 are the

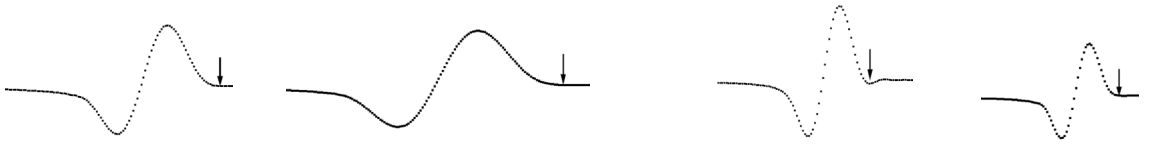

(c) along sections P-P (f) along sections S-S

Figure 5: P-wave profiles along sections P-P (left pair) and s-wave profiles along sections S-S (right pair), at 2 ms. Arrows indicates the analytically predicted wave front.

half of the dimensions of a brick (see Fig.2). The ω versus ξa_i relations of the numerical results are obtained by Fast Fourier Transform (FFT) with respect to space and time. FFT was conducted for two narrow vertical and horizontal spatial domains shown with yellow lines in Fig.6.

The results of the double FFTs are shown in Fig.7. As seen, in addition to the r-wave, small amplitude p- and s-waves are also present. This gives us a good opportunity to make a further check the accuracy of predicted p- and s- wave characteristics.

Figure 7 (a) and (b) compare the predictions with continuumnization by Hori et al.[1]. The analytical prediction of rotational frequency is in agreement only in a small neighborhood of $|\xi a_1|=|\xi a_2|=0$, and it rapidly diverges when move away from this small neighborhood. This is not surprising since continnumnization uses only the 0^{th}-order approximation $(\boldsymbol{\theta}^{\gamma+}+2\boldsymbol{\theta}^{\mu}+\boldsymbol{\theta}^{\gamma-})\approx 4\boldsymbol{\theta}^{\mu}$.

As show in Fig. 7 (c) and (d), the predictions with the second order Taylor expansion (see section 2.2.3) are in good agreement with the numerical solution within the range $|\xi a_i|<0.5$. P-, s- and r-wave predictions based on this continuum form are valid for the wavelengths grater than 7 times the size of bricks.

The advantage of the continuum form obtained with the full Taylor series is clearly seen in Fig. 7 (e) and (f). Analytical predictions for s- p- and r-waves are in near perfect agreement with the numerical results for a whole range of wave numbers considered. Note that we limited our analysis to the range $\xi a_i \leq 1.5$ since it corresponds to the shortest meaningful wavelength for the considered problem; $\xi a_i \leq 1.5$ includes wavelengths two times larger than the respective dimensions of a brick.

4 CONCLUDING REMARKS

Three equivalent continuum forms are developed for regularly packed brick structures and utilized to predict the elastic wave characteristics. The predicted p- and s-waves characteristics based on continnumnization and second order Taylor expansion are accurate for wavelengths greater than 7 times the size of bricks. In case of r-wave, while the predictions of second order Taylor expansion approach is accurate in the same wavelength range, that of continnumnization is limited to narrow range of wavelengths. The full Taylor series based continuum form can predict the elastic wave properties to a remarkable accuracy

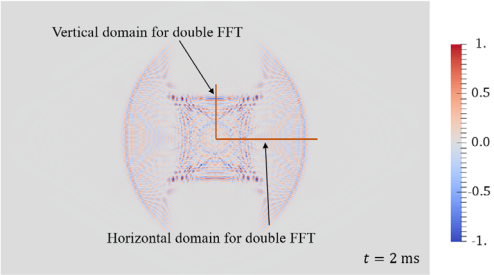

Figure 6: Magnitude of the rotational waves at 2 ms, generated by rotational wave input. Two lines indicate the domains used for double FFT.

for the whole range of wave numbers. These predictions will be useful in verification of numerical simulations and engineering applications like non-destructive testing, vibration control, structural design, etc. For the ordinary design purposes the predictions based on continnumnization or second order Taylor expansion is sufficient, while the full Taylor series model will be useful in physics applications involving high frequencies. Further, it is straight forward to develop Finite Element extensions based on these continuum forms for analyzing brick structures.

REFERENCES

[1] Hori, M., Wijerathne, L., Chen, J. and Ichimura, T.: Continuumnization of regularly arranged rigid bodies, *Journal of JSCE*,Vol. 4, pp. 38-45, 2016.

[2] Stefanou, I., Sulem, J. and Vardoulakis, I.:Three-dimensional cosserat homogenization of masonry structures: elasticity, *Acta Geotechnica*, *Springer Verlag*, Vol. 3(1), pp.71-83, 2008.

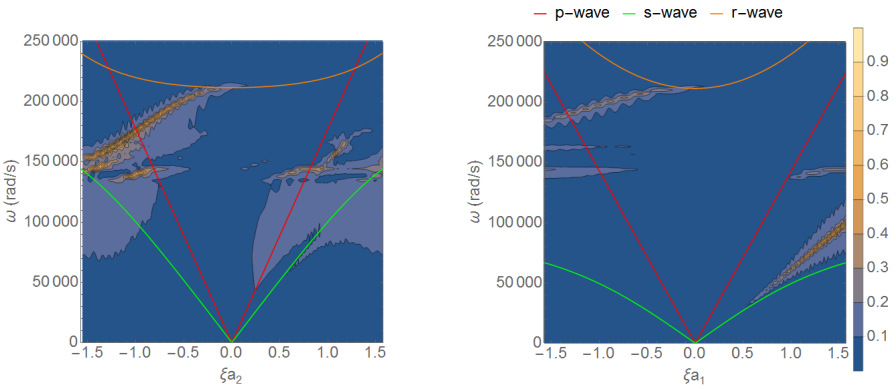

(a) Along the vertical domain (b) Along the horizontal domain

Continnumnization

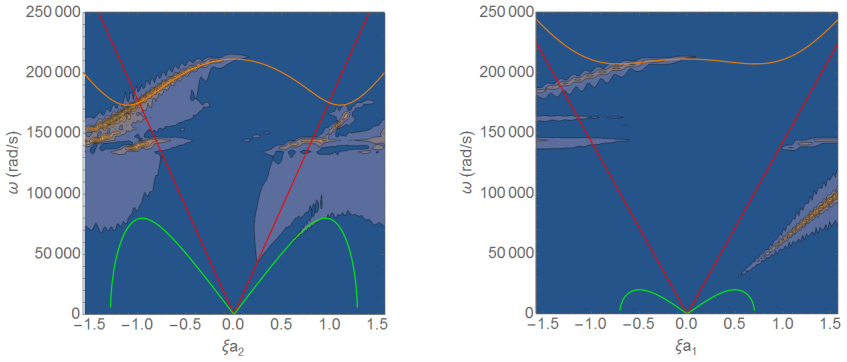

(c) Along the vertical domain (d) Along the horizontal domain

Second order Taylor series

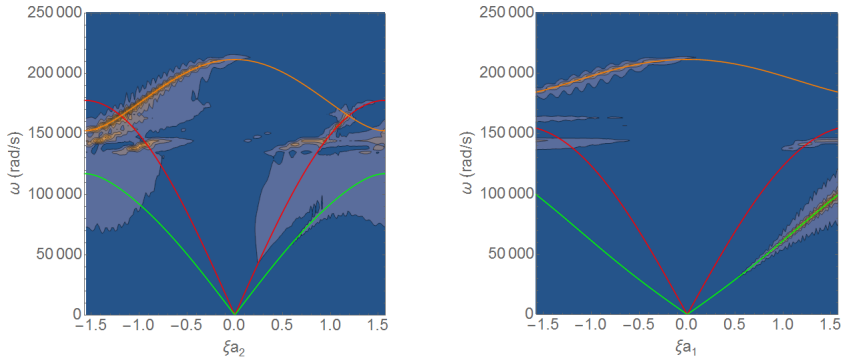

(e) Along the vertical domain (f) Along the horizontal domain

Full Taylor series

Figure 7: Comparison of numerical results and the analytical predictions based on different continuum forms. Contour plots show the numerically obtained amplitude of ω vs. ξa_i relation. The curves shows the analytical prediction for p-, s- and rotational waves.

V International Conference on Particle-based Methods – Fundamentals and Applications
PARTICLES 2017
P. Wriggers, M. Bischoff, E. Oñate, D.R.J. Owen, & T. Zohdi (Eds)

INVESTIGATION OF PARTICLE PROPERTIES ON THE HOLDING FORCE IN A GRANULAR GRIPPER

Steven Meuleman[1,*], Vincent Balt[1,*], Ahmed Jarray[1,2] and Vanessa Magnanimo[1]

[1] Multi Scale Mechanics (MSM)
University of Twente, NL-7500 AE Enschede, The Netherlands.
s.meuleman@student.utwente.nl
v.a.balt@student.utwente.nl

[2] Research Center Pharmaceutical Engineering GmbH
Graz, Austria

[*] These authors contributed equally

Key words: DEM, granular gripper, surface roughness, dry friction

Abstract. The granular gripper is an innovative device designed to grasp objects using the jamming properties of granular materials. However, these properties that influence its performance is still poorly understood. Moreover, to date, there is no numerical model for the granular gripper. In this paper, we combine numerical and experimental approaches to examine the effects of the mechanical properties of the grains on the grip force, with the goal to gain better insight on the influence of these properties and to improve the performance of the granular gripper.
On the numerical side, a model based on Discrete Elements Method (DEM) is developed to predict the effect of the granular properties, such as the roughness, on the holding force. Two different ways of modelling the gripper system are presented and compared. The DEM model is tested for different pressures around the jamming pressure. On the experiment side, a granular gripper apparatus is mounted and used to find the relationship between the grains properties and the holding force. The experimental apparatus is also used to validate the DEM model.
We found that grains with higher surface roughness result in a higher holding force on a cubical aluminium object. We also found agreements between the results of the experiments and the DEM models. Lastly, advice is given about approximating the holding force for a given gripper system and about further optimizing this system in terms of holding force, pressure and particle roughness.

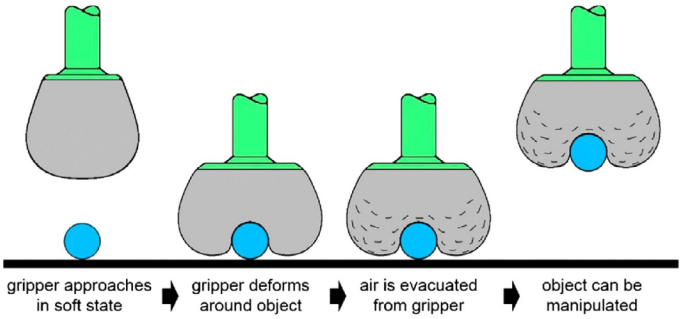

Figure 1: Functioning of the granular gripper [1].

1 Introduction

Gripping, holding and moving parts in industrial applications are tasks done by robotic grippers. Often these tasks are done by complex robotic hands which require a lot of processing power and optimization [1, 2]. However, a new and more universal way of gripping objects has come to light. A lot of complexity and therefore costs can be avoided by gripping objects using a granular gripper [1, 2, 3]. The functioning of the granular gripper consists of four phases which are shown in figure 1. The holding force that is exerted on the object has three contributions, static friction from surface contact, geometrical interlocking and vacuum suction from an airtight seal [2]. This research will mainly focus on the static friction contribution. The holding force at jamming pressure can be used to determine the performance of a granular gripper. The jamming point, the jamming transition from a fluid-like state of the granular material to a solid-like state occurs at this jamming pressure [4]. Optimization of the granular gripper will help improving its performance and therefore its usability. Discrete element method modelling is a useful tool for this optimization problem. In DEM modelling deformations of particles are simplified to the overlap, δ, of two particles which corresponds to an interaction force [5].

So far ground coffee is found to have the best properties for a high strength-to-weight ratio. A property that is used to measure the performance of systems containing granular material [3], like the gripper. A hypothesis for this is the influence of the surface roughness and irregularities [3], because ground coffee is relatively rough and non-spherical compared to other granular media such as glass beads for example. In order to explore the influence of roughness on the gripper performance, the problem is studied by combining gripper experiments, microscope image analysis on single particles roughness and numerical simulations. A roughness experiment is first conducted to identify the roughness of different batches of particles by taking samples. Also from the other batches of particles containers are filled and tested in the granular gripper set-up. Then, the roughness is examined against the holding force in the granular gripper and an implementation of the roughness in the simulation is established.

2 Roughness experiment

2.1 Method

Samples of Silibeads® Type M Borosilicate glass beads with a diameter of $2.5 \pm 0.2\ mm$ are tested. Both a matte as well as a polished type is used in the experiments. The experiment is conducted using the Keyence VK-9700 series Color 3D Laser Scanning Confocal Microscope. The microscope is used with the laser shutter as well as the aperture shutter opened. The lens with 100x magnification was used for making surface measurements of the centre of the particle surface. Afterwards the results are processed by the VK Analyser software that comes with the microscope. In this software, the scanned surface is flattened using the "sec curved surf.(auto)" correction method. The value for RMS_f is then found by taking the root mean squared roughness of the whole measured surface which is about 105 μm x 140 μm. After each experiment, it is made sure that the same bead is not used again in any later experiment. By linear fitting measurement data from [6] the following approximation is found for the mean RMS_f value in micrometers and the static coefficient of friction μ_s:

$$\mu_s = 2.012 \cdot RMS_f - 0.0026 \tag{1}$$

2.2 Results

Type	Mean RMS_f $[\mu m]$	St. dev. $[\mu m]$
polished 2.5 mm	0.060	0.016
polished 4 mm	0.152	0.028
matte 2.5 mm	0.458	0.018
matte 4 mm	1.063	0.122

Table 1: Surface roughness results for the flattened plane RMS roughness, RMS_f for a surface of 105 μm x 140 μm.

Type	Mean coefficient
polished 2.5 mm	0.12
polished 4 mm	0.3
matte 2.5 mm	0.92
matte 4 mm	2.14

Table 2: Mean static friction coefficient, μ_s, approximation using equation (1).

In table 1 the average flattened RMS surface roughness values can be found. For each type 6 experiments are conducted. The standard deviation from the mean is also shown as a measure of accuracy. In figure 2 examples of typical tested surfaces for the respective

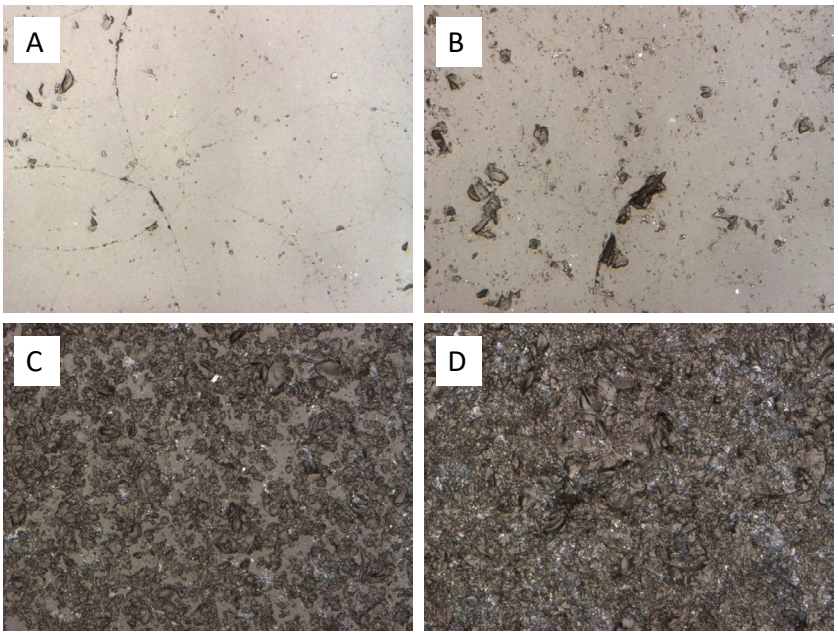

Figure 2: Microscopical view of the surface of the samples. A: polished 2.5 mm, B: polished 4 mm, C: matte 2.5 mm, D: matte 4 mm.

types are shown which consists of two layers. The first layer is the coloured view from the microscope and the second view is the laser view. The flattened RMS surface roughness values are filled into equation (1) to approximate the static friction, μ_s. The result can be found in table 2. Since the friction values in [6] did deviate much at the same roughness, this friction value is only an indication.

2.3 Conclusions & discussion

In table 1 it can be seen that the matte Silibeads® Type M Borosilicate glass beads have a higher RMS_f value than the polished ones. This difference is also expected for the static friction, μ_s, values. A bigger diameter results in a higher RMS_f value and therefore also a higher static friction, μ is expected.

3 Model validation

3.1 Method

A model of the granular gripper set-up is made to simulate the holding force. Firstly, some experiments are conducted using the experimental set-up. Then in the simulation the same experiment is conducted. Afterwards the results are compared. The DEM software that is used for doing the simulations is LIGGGHTS®-PUBLIC version 3.5 [7]. The contact model that is used for all contacts is the Hertz model combined with the tangential history model. For the contact between the aluminium cube and the particles,

a function "limitForce" was used to prevent attractive forces which is unwanted behaviour [8]. Both models and the function are included in the software. In both the experiment and the simulation, the holding force is determined by taking the highest force value that occurred while being in the upward motion. The residuary settings of both the set-up and the model will now be discussed.

The polished & matte Type M borosilicate 2.5 mm particle types from section 2 are used for model verification. For every particle type one or two containers are utilized in the experimental set-up. The weight for every container filled with particles is tested not to differ more than 10 $grams$ from the measured average of 310 $grams$. It is chosen to do this for a more accurate performance comparison between the types. In the simulation, the friction coefficient values from table 2 are used for the holding force comparison.

3.1.1 Experimental set-up

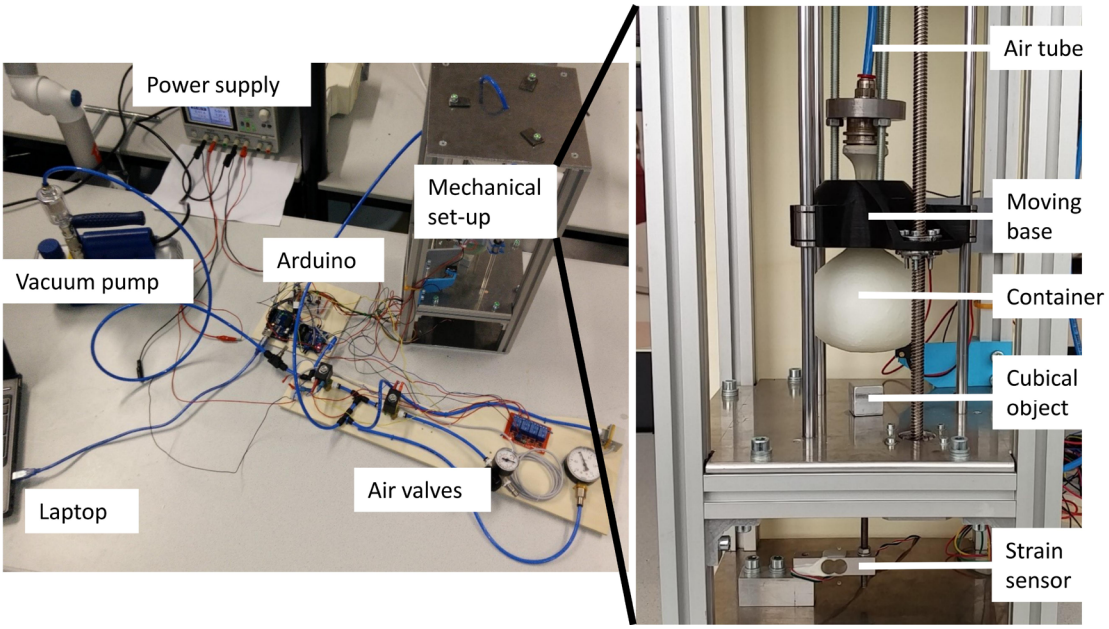

Figure 3: On the left: total set-up, on the right: mechanical part of the set-up.

Property	Value	Unit
Particle diameter	0.0025	m
Bellow radius	0.025	m
Total mass particles	0.310 ± 0.010	kg

Table 3: Properties used in the experiment.

The experimental set-up consists of a latex container with an empty weight of 3 *grams* containing the granular material. The latex container is connected to a vacuum pump which can generate a compressive pressure on the container, see figure 3. When doing experiments the vacuum pump was put on another table to reduce vibrations. Additionally, the mechanical part of the set-up was placed on a piece of foam to damp vibrations.

The latex container is connected to a frame which can be seen on the right side of figure 3 by means of a stepper motor and bearings, so the upward and downward movement can be controlled. Below the latex container, an aluminium cube is located which is connected to a force sensor. The stepper motor and air valves are controlled by an Arduino board and the sensor output is sent to a computer where the data can be analysed. The properties of the particles used are shown in table 3.

The Arduino script consists of six separate phases. In the first phase, the container moves to the reference position at the top of the set-up. In the second phase, the offset for the sensor values are calculated and implemented in the script. In the third phase, a negative pressure of $40kPa$ is applied, which is then released back to $0kPa$. This is repeated once to obtain a better packing and make the packing independent of previous cycles. In the fourth phase, the container moves down onto the object which is connected to a micro load cell. Then in the fifth phase, a negative pressure is applied to get the particles into the jammed state. When the target pressure is reached, the particles get some time to settle and then a negative pressure is applied twice again. This is to ensure the container has the right pressure and the particles had enough time to settle. Then in phase six, the container moves up and the holding force is measured. This movement is slower compared to the upward movement to allow for more precise measurements. This cycle is repeated 9 times. The maximum operating pressure that can be reached using this set-up is $85kPa$.

3.1.2 Simulation properties

First, the results of the granular gripper simulation are matched to the results of the experiment. Afterwards the influence of a variety of properties on the holding force is tested in the simulation. The simulation consists of the same phases as the Arduino script used in the experiment, described in section 3.1.1, except for reapplying the pressure and resetting the pressure.

The material specific properties that are used in this simulation are shown in table 4. Since the width/length ratio of the particles is between 0.96 and 1 according to [9] and because in the simulation there is no effective way of modelling different width/length ratios, a perfectly round sphere with a width/length ratio of 1 is modelled. The static friction value, μ_s, for the latex container - particle contact is about 2 (although it depends on the applied normal force) according to the sliding test in [10]. However, friction values can be different for different surfaces of the same material and it can also behave differently in simulation, therefore it is decided to use a value for the friction that is at maximum 5

Property	Value	Unit	Src
E-modulus	$6.40 \cdot 10^{10}$	N/m^2	[9]
Specific weight	2230	kg/m^3	[9]
Width/length ratio	1	–	[9]*
Container - particle μ_s	0.40	–	[10]*
Glass Poisson's ratio	0.2	–	[11]
Glass - glass COR	0.95	–	[12]
Glass - glass μ_s	0.94	–	[13]*

Table 4: Material specific properties used in simulation.

Property	Value	Unit
Cube edge length	0.02	m
Particle diameter	0.0025	m
Container edge length	0.04	m
Neighbor distance	0.0015	m
Time-step	$1.2 \cdot 10^{-7}$	s
Insertion and settle time	0.0240	s
Move up time	0.0312	s
Settling time	0.0432	s
Move down time	0.382	s

Table 5: Time and distance properties used in simulation.

times smaller or bigger than the values found in literature. To match the results of the experiments it is chosen to lower the container - particle friction value to 0.4, since the holding forces experienced in the experiments are much smaller than the holding forces in the simulation. Information about measurements of the static friction, μ_s, between aluminium and latex surfaces, which is the contact between the cube and the container could not be found. For the container - cube contact no accurate μ_s value could be found. Therefore, the particle - container - cube contact μ_s value will be determined by the container - particle friction used to match the simulation to the experiment.

The time and distance properties used in the simulation are shown in table 5. The phases of the simulation are inserting the particles, settling, moving up the cube, applying the pressure, settling and finally moving the cube down. These six phases are similar to the phases of the experiment, except the simulations are not consecutive and therefore no positive pressure is applied and the negative pressure is only applied once. The time-step is checked to be smaller than 15% of the Rayleigh- and Hertz time to ensure an accurate simulation. The four factors that influence the simulation time most are found to be the total number of particles, the amount of neighbours per particle (particles within neighbour distance), the total time and the time-step. Therefore, the minimum possible values of these properties for accurate simulation will be used to save computation time.

3.1.3 Modelling the latex container for different pressures

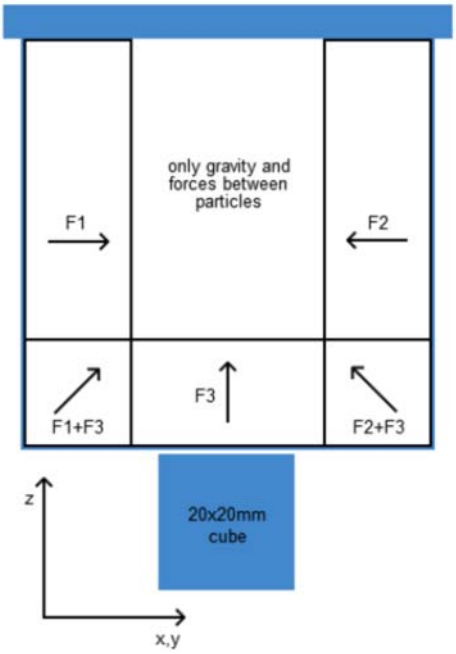

Figure 4: The "wallforces" approach.

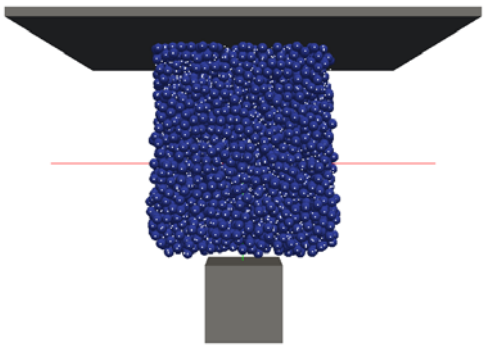

Figure 5: The model of the granular gripper

When the pressure is applied to the container, the container shrinks, exerts force on the particles that are in touch with it and deforms around them. LIGGGHTS® makes use of fixed walls and does not have the option to make a container that deforms under load. So, to model the container at different air pressure differences between the inside and the outside of the container, another approach is needed. The sides of the container are modelled with forces on particles in certain regions. These "wallforce"-regions are located at the sides of a cubical container. The "wallforces" that act on the particles in these regions have a direction towards the centre of the cube see figure 4. Because they have overlap in the lower corners of the cube the wallforces will be summed. All shown "wallforces" in figure 4 have the same magnitude. The magnitude of the "wallforces" is determined by multiplying the desired pressure with the surface area of the container and dividing it by the number of particles that experience a "wallforce". The "wallforces" approach is more like the deformation of the latex container compared to a fixed wall approach. Because with the "wallforces", the total shape of the latex container can change but it will result in stresses which is also the case for a latex container experiment. A cubical container is chosen in the simulation because only one direction for the force per "wallforce" can be chosen. The upper wall is the only wall where no "wallforce" is acting. Instead a plate that moves downward progressively based on the force that is applied on it is put there to keep the pressure inside the container constant, see figure 5.

When the container is moving to the upper reference position in the experiment (phase six of the Arduino script and of the simulation), the particles do not completely fill up the space where the cube used to be since the particles are in jammed state. To model this effect of the container between the aluminium cube and the particles when the cube is moving down, the "wallforces" approach is also applied here but with the forces directing outwards.

3.2 Results

3.2.1 Experiment

In figure 6 and figure 7 the holding force is shown for 2.5mm smooth and 2.5mm matte particles respectively at different operating pressures. At each pressure 9 experiments, shown in dark grey, are conducted consecutively. Furthermore, at each pressure 5 simulations with different insertion patterns are conducted. The small lines show the standard deviation. For both experiments and simulations, the median value is used for plotting the bars. A typical result for an experiment run is shown in figure 9. This graph shows a steady increase in the holding force as the container moves upwards. Then when the limit of the holding force is reached, the container suddenly dispatches from the cube.

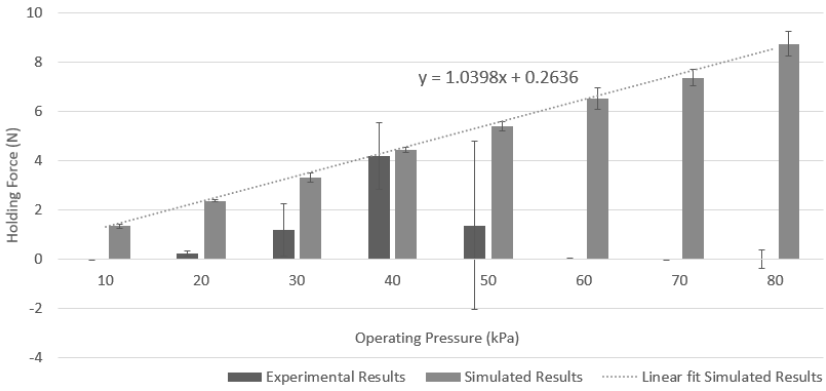

Figure 6: The holding force as a function of the operating pressure. The container is filled with 2.5mm smooth particles in both the experiments and the simulations.

.

The force values shown in figures figure 6 and figure 7 seem to be rising steadily from 0 to 40kPa and then suddenly disappears.

3.2.2 Simulation

In figure 8 a typical result for a simulation is shown. Compared to figure 9, there is a difference in the time scale because of the computation time reduction. The line is plotted at the moment the cube starts moving down (phase 4 of the Arduino script). In

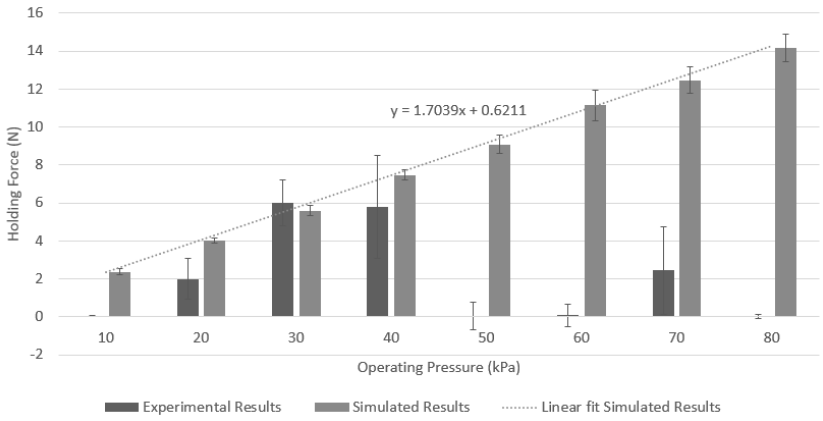

Figure 7: The holding force as a function of the operating pressure. The container is filled with 2.5mm matte particles in both the experiments and the simulations.

.

the simulation, the container does not suddenly dispatch from the cube due to the way the movement is modelled. In the simulation, the cube moves down following a cosine like path whereas in the experiment, the container only starts moving when the maximum holding force is reached and it then suddenly dispatches. In figure 6 and figure 7 the peak holding forces of the simulation for different pressures are shown. A linear fit is made of the data of which the equation can also be found in figures 6 and 7.

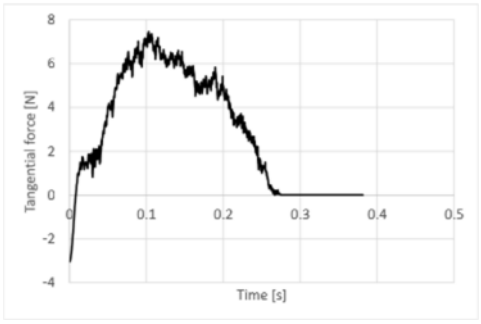

Figure 8: Holding force simulation at 40 kPa

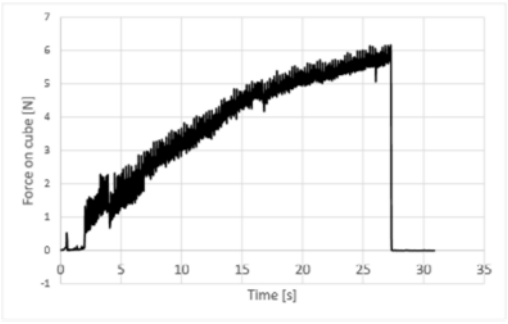

Figure 9: Holding force experiment at 40 kPa

3.3 Conclusions

Although 9 experiments are conducted for each pressure in the experimental set-up and the median is taken to exclude outliers, shown in figure 6 and figure 7, a jamming pressure could not be found since the data does not seem to follow a trend. The simulation data, however, follows a linear trend. When looking at the holding forces around 40kPa, the forces of the simulation appear to be in the same order of magnitude as the experiments.

Although the holding force of the simulation does not correspond over the entire range of operating pressures to the holding force in the experiments, the increase in holding force from matte compared to polished particles as seen in the experiments is also visible in the simulation results.

Furthermore, the matte particles result in a higher holding force compared to the smooth particles in both the simulations, as well as in the experiments.

3.4 Discussion

A possible explanation for the reduction in holding force at higher pressures shown in figures 6 and 7, is that due to the larger pressure, the container is stretched more and therefore the friction of the container is reduced. However, this does not explain why the holding force drops to 0 at higher pressures. Since there is no clear trend that can be determined from the experiments, these results are assumed to be not reliable by the authors.

Figures 6 and 7 show that the holding force as function of the operating pressure in the simulations follows a clear linear trend, which seems plausible.

4 Outlook

Even though a large amount of time is spent on examining the cause of the large deviations and the absence of a clear trend in the holding force, no cause is found. Advised is to look at alternatives for the container, for example thicker ones.

REFERENCES

[1] E. Brown, N. Rodenberg, J. Amend, A. Mozeika, E. Steltz, M. R. Zakin, H. Lipson, and H. M. Jaeger, Universal robotic gripper based on the jamming of granular material, *Proceedings of the National Academy of Sciences*, (2010), 107(44):18809–18814.

[2] John R. Amend, Eric Brown, Nicholas Rodenberg, Heinrich M. Jaeger, and Hod Lipson, A positive pressure universal gripper based on the jamming of granular material, *IEEE Transactions on Robotics*, apr 2012, 28(2):341–350.

[3] Nadia G. Cheng, Maxim B. Lobovsky, Steven J. Keating, Adam M. Setapen, Katy I. Gero, Anette E. Hosoi, and Karl D. Iagnemma, Design and analysis of a robust, low-cost, highly articulated manipulator enabled by jamming of granular media, *Proceedings - IEEE International Conference on Robotics and Automation*, (2012), 4328–4333.

[4] Stefan Luding, Granular matter: So much for the jamming point, *Nature Physics*, (2016), 1–2.

[5] Stefan Luding, Introduction to discrete element methods: basic of contact force models and how to perform the micro-macro transition to continuum theory, *European Journal of Environmental and Civil Engineering*, (2008), 12(7-8):785–826.

[6] C. O'Sullivan, M. Coop, and I. Cavarretta, The influence of particle characteristics on the behaviour of coarse grained soils, *Géotechnique*, (2010), 60(6):413–423.

[7] Christoph Kloss, Christoph Goniva, Alice Hager, Stefan Amberger, and Stefan Pirker, Models, algorithms and validation for opensource dem and cfd–dem, *Progress in Computational Fluid Dynamics, an International Journal*, (2012), 12(2-3):140–152.

[8] JKU Linz DCS Computing GmbH and Sandia Corporation, Gran model hertz model, (2016).

[9] Sigmund Lindner GmbH, SiLibeads Glass beads Type M Borosilicate, Microglass beads Product Data Sheet, (2016).

[10] Ari J. Tuononen, Onset of frictional sliding of rubber-glass contact under dry and lubricated conditions, *Scientific Reports*, (2016), 6(April):27951.

[11] G N Greaves, A L Greer, R S Lakes, and T Rouxel, Poisson's ratio and modern materials, *Nature Materials*, (2011), 10(11):823–837.

[12] Martin C Marinack Jr., Richard E Musgrave, and C Fred Higgs, Experimental investigations on the coefficient of restitution of single particles, *Tribology Transactions*, (2013), 56(4):572–580.

[13] Raymond A. Serway, *Physics for Scientists and Engineers*, Harcourt College Pub, 4 edition, (1999).

V International Conference on Particle-based Methods – Fundamentals and Applications
PARTICLES 2017
P. Wriggers, M. Bischoff, E. Oñate, D.R.J. Owen, & T. Zohdi (Eds)

USING NON-SMOOTH MULTI-DOMAIN DYNAMICS TO IMPROVE THE SAFETY ON HAUL ROADS IN SURFACE MINING

K. Thoeni[1], M. Servin[2] and A. Giacomini[1]

[1] Centre for Geotechnical Science and Engineering
The University of Newcastle
Callaghan, NSW 2308, Australia
http://www.newcastle.edu.au

[2] UMIT Research Lab
Umeå University
Umeå, SE-90187, Sweden
http://www.umu.se

Key words: NDEM, MBD, Haul Truck, Granular Material, Collision

Abstract. The paper presents a preliminary numerical study aimed to improve the safety on haul roads in surface mining. The interaction and collision between granular berms and ultra-class haul trucks are investigated by using non-smooth multi-domain dynamics. The haul truck is modelled as a rigid multibody system and the granular berm as a distribution of rigid particles using the discrete element method. A non-smooth dynamics approach is applied to enable stable and time-efficient simulation of the full system with strong coupling. The numerical model is first calibrated using full-scale data from experimental tests and then applied to investigate the collision between the haul truck and granular berms of different geometry under various approach conditions.

1 INTRODUCTION

Berms of granular materials are commonly used along haul roads of surface mines to protect haul trucks from rolling over an edge and to avoid collisions. Their current design is based on rules of thumb [1]. However, their behaviour is still poorly understood and accidents, where haul trucks collide with a berm and run over the edge and down the front slope, are still happening on a regular basis [2]. In addition, there is common sense that the current rules of thumb do not apply to the new generation of ultra-class haul trucks but it is unclear how berms need to be designed in order to be efficient for stopping a runaway haul truck. Hence, the need for a more rigorous design approach is emerging within the mining industry and accurate specific numerical modelling could represent a valid tool for this purpose. The main aim of the current research is to understand, how

efficient granular berms are in stopping a runaway haul truck. Therefore, it is crucial to understand the behaviour of a granular berm upon collision with a haul truck travelling at various velocities. This problem is very complex and has to take into account large displacements of the granular material the berm is built of and the interaction of such material with large-scale mobile equipment. In addition, the variability of the available material on site used to build the berms, mostly waste rock material of various origins and grade, should also be considered [1]. Generally this material has a huge variation in terms of particle size, particle shape and hardness and cannot be easily characterised.

The *discrete element method* (DEM) is widely used to study the dynamic behaviour of granular materials including waste rock material. More recently, the DEM has also been coupled to *multibody dynamics* (MBD) for the investigation of soil–structure interaction problems and the simulation of the working process of construction machines [3, 4]. MBD allows studying the dynamic behaviour of interconnected rigid or flexible bodies, each of which can undergo large translational and rotational displacements. It is therefore the ideal method to model mobile equipment such as the haul truck. Coupled with the DEM it will allow to capture the dynamic behaviour of the machine and its interaction with granular material in an efficient way. Simulation coupling is, however, associated with a number of challenges that affect the computational performance, stability or interface forces between the coupled systems [5].

The following work presents an attempt to provide a deeper understanding of the problem using non-smooth multi-domain dynamics. The haul truck and the granular berm are modelled by means of a non-smooth approach to multibody dynamics and discrete elements that automatically support strong coupling without co-simulation. The general numerical framework is presented in Section 2 followed by a discussion on the calibration and validation (Section 3). Finally, preliminary results of simulations of collisions between a haul truck and granular berms of different berm geometry under various approach conditions are presented in Section 4.

2 NUMERICAL FRAMEWORK

The haul truck and the granular berm are modelled within the non-smooth multi-domain dynamics framework of the commercial software package AGX Dynamics [6]. In *non-smooth multi-domain dynamics*, the simulated system is composed by multiple heterogeneous subsystems with stiff dynamics and unanticipated events where the connectivity and number of variables suddenly change. The dynamics that occur on short time scales, compared to the time-step, are best treated as non-smooth [7, 8, 9]. This means that velocities may change discontinuously in accordance with some impact law, expressed in terms of inequality and complementarity conditions, in addition to the equations of motion and the differential algebraic equations used to describe the sub-systems. This is necessary for implicit time-stepping of dynamic systems with impacts, dry friction, joint limits, electric and hydraulic circuit switching that cause instantaneous impulse propagation throughout the system. The *non-smooth discrete element method* (NDEM)

implemented in AGX Dynamics can be seen as a time-implicit version of the classical smooth DEM [10]. The contact forces are modelled using impact laws and kinematic constraints for unilateral contacts and friction. Hence it allows strong dynamic coupling with other multibody systems such as the haul truck.

The equations of motion for modelling granular materials strongly coupled with rigid multibody systems are [11]:

$$\begin{aligned}
\mathbf{M}\dot{\mathbf{v}} + \dot{\mathbf{M}}\mathbf{v} &= \mathbf{f}_{\text{ext}} + \mathbf{G}_{\text{n}}^{\text{T}}\boldsymbol{\lambda}_{\text{n}} + \mathbf{G}_{\text{t}}^{\text{T}}\boldsymbol{\lambda}_{\text{t}} + \mathbf{G}_{\text{r}}^{\text{T}}\boldsymbol{\lambda}_{\text{r}} + \mathbf{G}_{\text{j}}^{\text{T}}\boldsymbol{\lambda}_{\text{j}}, && (1)\\
0 \leq \varepsilon_{\text{n}}\boldsymbol{\lambda}_{\text{n}} + \mathbf{g}_{\text{n}} + \tau_{\text{n}}\mathbf{G}_{\text{n}}\mathbf{v} &\perp \boldsymbol{\lambda}_{\text{n}} \geq 0, && (2)\\
\gamma_{\text{t}}\boldsymbol{\lambda}_{\text{t}} + \mathbf{G}_{\text{t}}\mathbf{v} &= 0, \quad |\boldsymbol{\lambda}_{\text{t}}^{(\alpha)}| \leq \mu_{\text{t}}|\mathbf{G}_{\text{n}}^{(\alpha)\text{T}}\lambda_{\text{n}}^{(\alpha)}|, && (3)\\
\gamma_{\text{r}}\boldsymbol{\lambda}_{\text{r}} + \mathbf{G}_{\text{r}}\mathbf{v} &= 0, \quad |\boldsymbol{\lambda}_{\text{r}}^{(\alpha)}| \leq \mu_{\text{r}} r|\mathbf{G}_{\text{n}}^{(\alpha)\text{T}}\lambda_{\text{n}}^{(\alpha)}|, && (4)\\
\varepsilon_{\text{j}}\boldsymbol{\lambda}_{\text{j}} + \eta_{\text{j}}\mathbf{g}_{\text{j}} + \tau_{\text{j}}\mathbf{G}_{\text{j}}\mathbf{v} &= 0. && (5)
\end{aligned}$$

Eq. (1) is the Newton-Euler equation of motion for rigid bodies with external (smooth) forces $\mathbf{f}_{\text{ext}}$ and constraint force $\mathbf{G}^{\text{T}}\boldsymbol{\lambda}$ with Lagrange multiplier $\boldsymbol{\lambda}$ and Jacobian $\mathbf{G}$, divided into normal (n), tangential (t), rolling (r) and articulated and possibly motorised joints (j). $\mathbf{M}$ is the generalised mass matrix and $\mathbf{v}$ is the generalised velocity vector. Eqs. (2)-(3) are the Signorini-Coulomb conditions with constraint regularisation and stabilisation terms ε_{n}, τ_{n} and γ_{t}. With $\varepsilon_{\text{n}} = \tau_{\text{n}} = 0$, Eq. (2) states that bodies should be separated or have zero overlap, $\mathbf{g}_{\text{n}}(\mathbf{x}) \geq 0$, and if so the normal force should be non-cohesive, $\boldsymbol{\lambda}_{\text{n}} \geq 0$. With $\gamma_{\text{t}} = 0$, Eq. (3) states that contacts should have zero relative slide velocity, $\mathbf{G}_{\text{t}}\mathbf{v} = 0$, provided that the friction force remains bounded by the Coulomb friction law with friction coefficient μ_{t}. Eq. (4) similarly constrains relative rotation of contacting bodies provided the constraint torque do not exceed the rolling resistance law with rolling resistance coefficient μ_{r} and radius r. The constraint force, $\mathbf{G}_{\text{j}}^{\text{T}}\boldsymbol{\lambda}_{\text{j}}$, arise for articulated rigid bodies jointed with kinematic links and motors represented with the generic constraint of Eq. (5). With $\varepsilon_{\text{j}}, \tau_{\text{j}} = 0$ and $\eta_{\text{j}} = 1$, it becomes an ideal holonomic constraint $\mathbf{g}(\mathbf{x}) = 0$. For $\varepsilon, \eta = 0$ and $\tau = 1$, it becomes an ideal Pfaffian constraint $\mathbf{G}\dot{\mathbf{x}} = 0$. With $\varepsilon, \eta, \tau \neq 0$ it can represent a generic constraint with compliance and damping.

The Lagrange multiplier $\boldsymbol{\lambda}$ become an auxiliary variable to solve for in addition to position and velocity. The regularisation and stabilisation terms, ε and γ, introduce compliance and dissipation in motion orthogonal to the constraint manifold. The numerical time integration scheme is based on the SPOOK stepper [12] derived from discrete variational principle for the augmented system $(\mathbf{x}, \mathbf{v}, \boldsymbol{\lambda}, \dot{\boldsymbol{\lambda}})$ by applying a semi-implicit discretisation. Stepping the system position and velocity, $(\mathbf{x}_i, \mathbf{v}_i) \rightarrow (\mathbf{x}_{i+1}, \mathbf{v}_{i+1})$, from time t_i to $t_{i+1} = t_i + h$ involves solving a mixed complementarity problem [13]. This is solved using a hybrid solver where a projected Gauss-Seidel solver [10] is applied for the NDEM subsystem and a direct solver for the articulated rigid multibodies.

3 CALIBRATION AND VALIDATION

The experimental full-scale tests presented in [1] are used for calibration of the main input parameters and validation of the coupled model. In the experiments, a haul truck reversed into a trapezoidal granular berm and the motion of the truck was monitored using high-speed cameras. The granular material is modelled by spherical particles with a diameter in the range of 60 to 700 mm. The granular berm is initialised in a mould and friction is set to zero initially in order to get a dense granular assembly. The shape effect of the particles is taken into account using a rolling friction model. The haul truck considered in the following study is a CAT 797F. This is an ultra-class haul truck with a gross vehicle weight of 624 t (fully loaded). The load is not modelled explicitly, instead the mass of the empty body is adapted to reflect the gross vehicle weight. The centre of mass of the vehicle is positioned to reflect the manufacturer's specifications (i.e., mass distribution front 34% and rear 66%). The key dimensions of the truck are summarised in Tab. 1. The MBD model of the truck is built from a simplified CAD model and comprises 19 rigid bodies. The suspension is explicitly modelled and the tyres are represented by a two-body tyre model [14].

Table 1: Key dimensions of the CAT 797F.

Description	Dimension
Overall rear tyre width	6.23 m
Overall length	15.08 m
Height (empty)	7.00 m
Wheelbase	7.19 m
Tyre diameter	4.02 m
Tyre width	1.47 m

A sensitivity analysis is performed to identify the most critical parameters. The analysis showed that the contact parameters (e.g., elasticity, friction, rolling) have a secondary influence on the results. The two main parameters influencing the results are the centre of mass of the vehicle and the geometry of the berm. The former is not known exactly and it is assumed according to the manufacturer's specifications. The latter is crucial especially in the area where the truck first contacts the berm. In fact, the numerical model of the berm introduces a sharp kink between terrain and berm. In the experimental tests, the transition from terrain to berm is much smoother and the shape of the berm in the experiment is not a perfect trapezoid.

Fig. 1 shows a comparison between the measured results of one test presented in [1] and the numerical predictions using the final set of calibrated parameters. The numerical model is able to predict the general trend of the experimental test reasonably well, however, it can be noted that the predicted wheel climb and horizontal wheel displacement

are slightly lower. The numerical model gives almost identical results for both left hand side (LHS) and right hand side (RHS) whereas the experimental values vary considerably between the two wheels. This is justified by the ideal trapezoidal shape of the numerical berm compared to the rather irregular berm shape used in the experiment. Fig. 2 shows a comparison of a screenshot of the numerical simulation and an image from the experimental tests where this difference can clearly be seen.

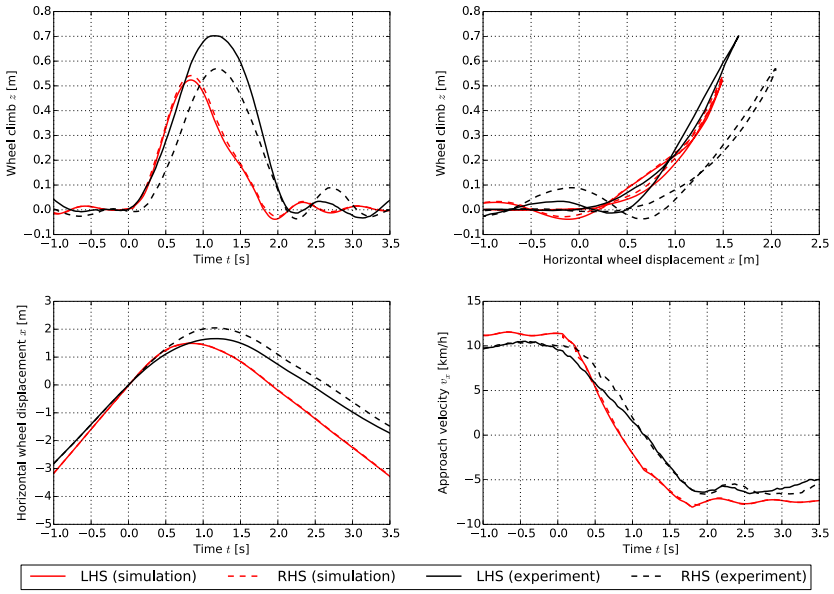

Figure 1: Measured vs. predicted results for final set of calibrated parameters.

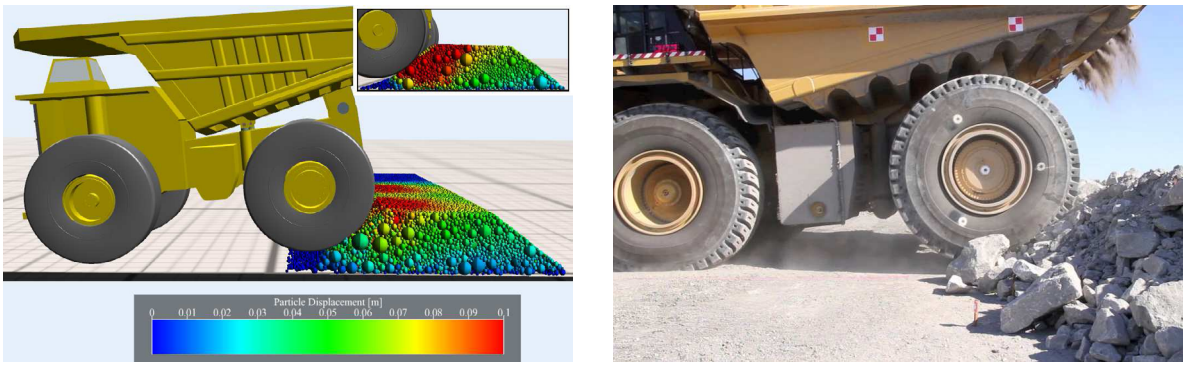

Figure 2: Screenshot of the numerical simulation (left) and corresponding picture from the experimental full-scale testing (right) at maximum wheel climb.

4 NUMERICAL INVESTIGATIONS

In the following, the numerical model is applied to investigate if the haul truck can be safely stopped by the granular berm. In particular, the study considers the collision between the haul truck and granular berms of different geometry under various approach conditions. Two main scenarios are considered. In the first scenario, the ultra-class haul truck is reversing into a triangular berm at relatively low velocity. This represents a dump-point scenario similar to the one investigated in [1]. The second scenario represents a runaway haul truck that is colliding head-on with a granular berm at higher velocities. Such a scenario is relevant for trapezoidal roadside berms and ramps where truck drivers could potentially lose control. In both cases, the length of the granular berm is 12 m and the truck is initialised with a specific velocity in the centre in front of the berm. The batter angle of the berms is 40°. The particle size distribution is the same as in Section 3.

Figs. 3–4 and Figs. 5–6 summarise the results for the first scenario where the haul truck is reversing with a velocity of $v = 15\,\mathrm{km/h}$ and colliding with a triangular berm of height $H = 2\,\mathrm{m}$ and $H = 3\,\mathrm{m}$ respectively. From the horizontal wheel position in Fig. 3 it can clearly be seen that the rear axle passes the centreline of the berm with $H = 2\,\mathrm{m}$. Fig. 5 shows the same results for a berm with $H = 3\,\mathrm{m}$. In this case, the numerical model predicts that the rear axle of the truck is not passing the centreline. Hence, increasing the berm height from $H = 2\,\mathrm{m}$ to $H = 3\,\mathrm{m}$ provides safe stopping conditions and at the same time it keeps the truck back from the edge of a dump. It should be noted, that the maximum reversing speed of a CAT 797F ultra-class haul truck is $v = 11.9\,\mathrm{km/h}$. The considered reversing velocity is slightly higher in order to be on the safe side.

Figs. 7–8 and Figs. 9–10 summarise the results for the second scenario where the haul truck is colliding head-on with a trapezoidal granular berm with $H = 4\,\mathrm{m}$ and a top width of $B = 1\,\mathrm{m}$ and $B = 4\,\mathrm{m}$ respectively. The truck is initialised with a velocity of $v = 40\,\mathrm{km/h}$ (the actual top speed of a CAT 797F is $v = 67.6\,\mathrm{km/h}$). For the berm with $B = 1\,\mathrm{m}$ the numerical model predicts that the front axle passes the end of the berm (Fig. 7). This could have fatal consequences considering that in most cases there would be a slope at the other side of the berm. Increasing the berm width from $B = 1\,\mathrm{m}$ to $B = 4\,\mathrm{m}$ provides safe stopping conditions (Fig. 9). This can also be seen when comparing the screenshots in Fig. 8 and Fig. 10.

5 CONCLUSIONS

In this paper, non-smooth multi-domain dynamics is used to investigate the collision between an ultra-class haul truck and granular berms used in surface mining. The haul truck is represented by rigid bodies interconnected with ideal joints and the granular material is modelled using rigid spherical particles. First, the numerical model is calibrated and validated using full scale experimental tests. Then the model is used to investigate two typical scenarios. In the first scenario the truck is reversing into a triangular berm. The effect of the berm height is shown. In the second scenario the truck is colliding

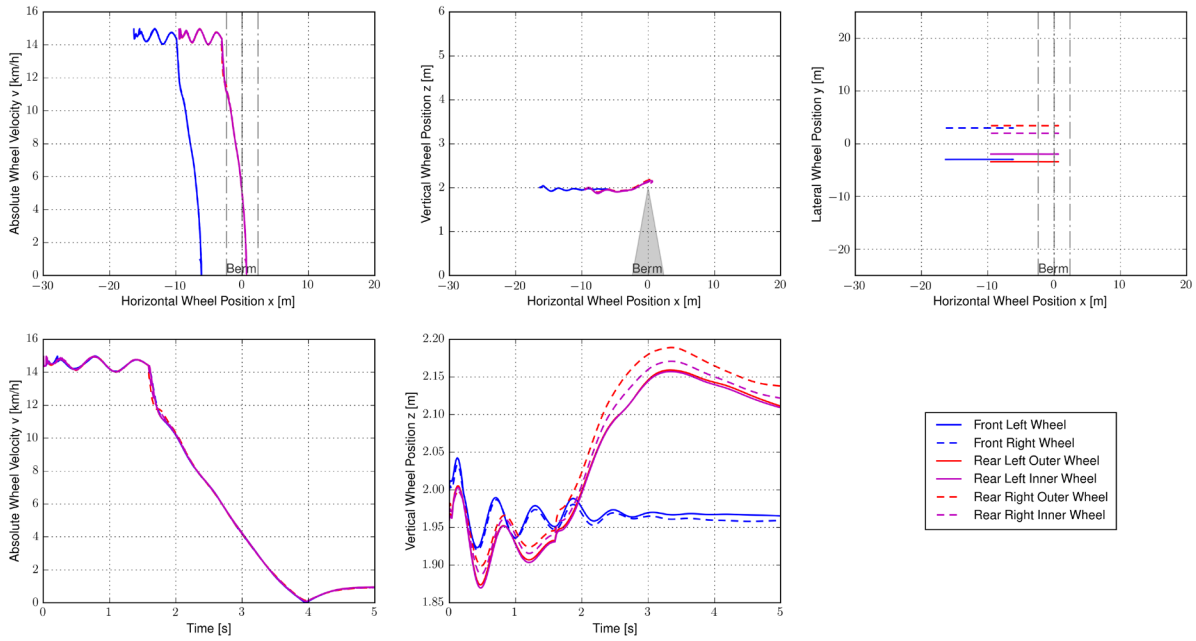

Figure 3: Summary of results for reversing scenario with $v = 15\,\mathrm{km/h}$ and triangular berm with $H = 2\,\mathrm{m}$.

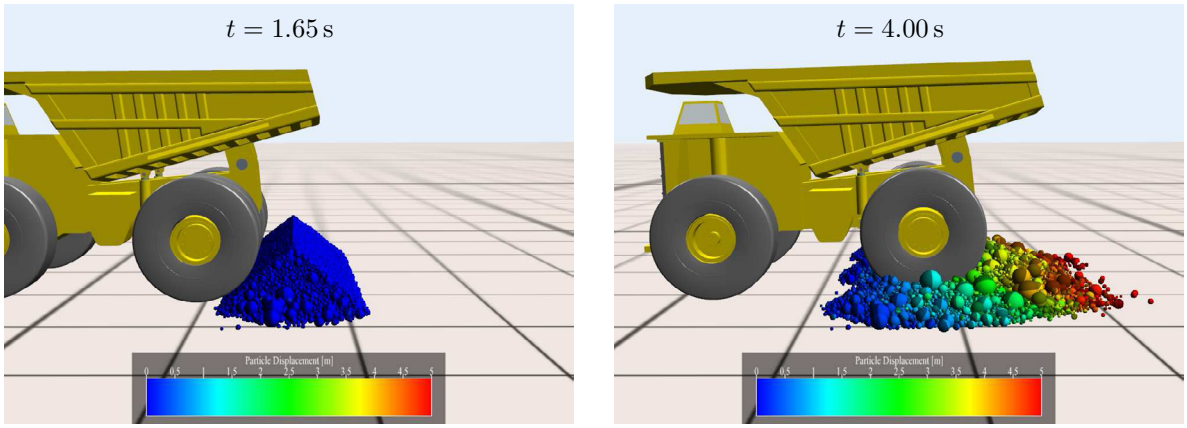

Figure 4: Screenshots of the collision at different time steps t for reversing scenario with $v = 15\,\mathrm{km/h}$ and triangular berm with $H = 2\,\mathrm{m}$.

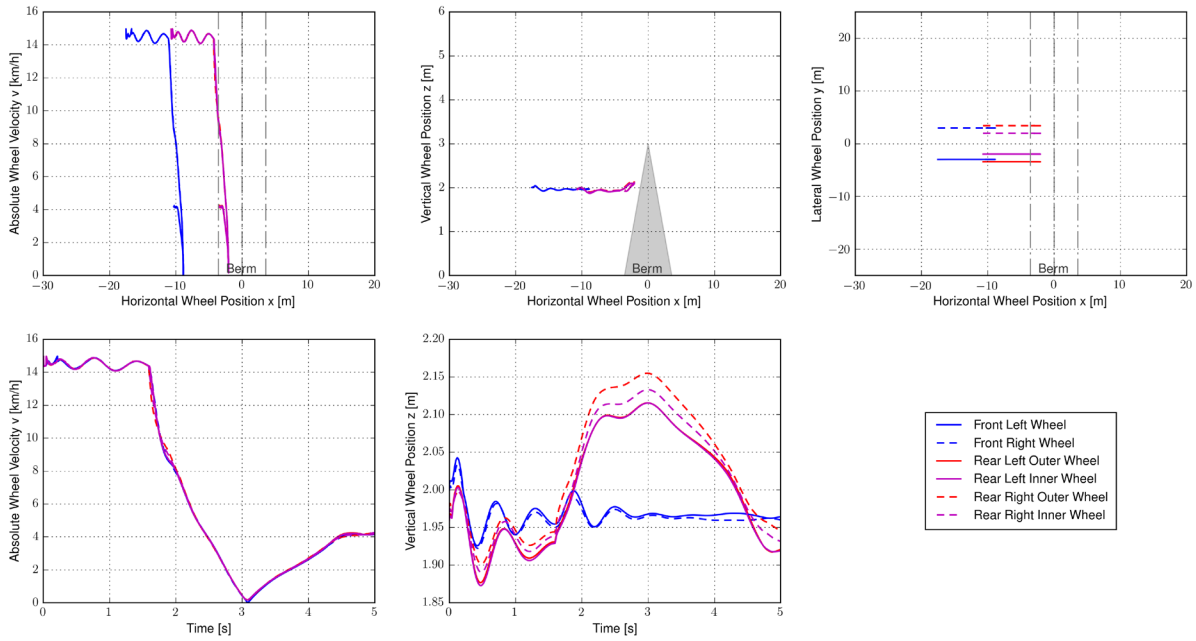

Figure 5: Summary of results for reversing scenario with $v = 15\,\mathrm{km/h}$ and triangular berm with $H = 3\,\mathrm{m}$.

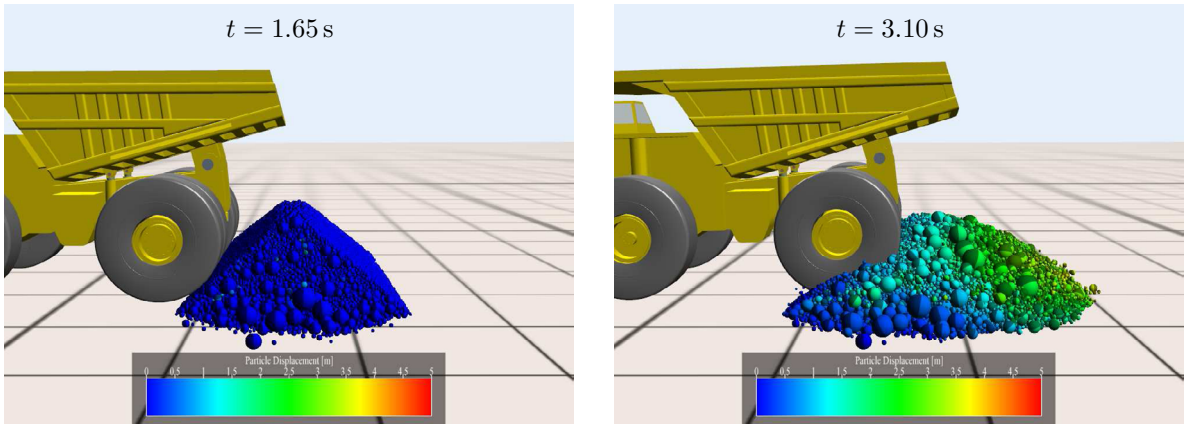

Figure 6: Screenshots of the collision at different time steps t for reversing scenario with $v = 15\,\mathrm{km/h}$ and triangular berm with $H = 3\,\mathrm{m}$.

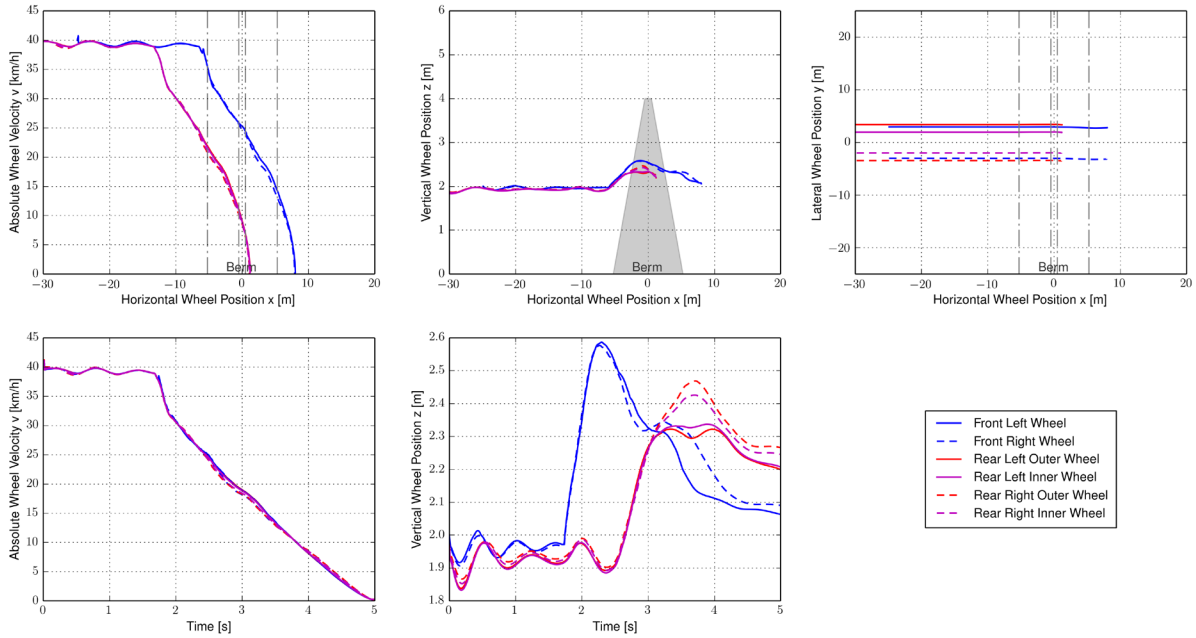

Figure 7: Summary of results for head-on collision with $v = 40\,\text{km/h}$ and trapezoidal berm with $H = 4\,\text{m}$ and $B = 1\,\text{m}$.

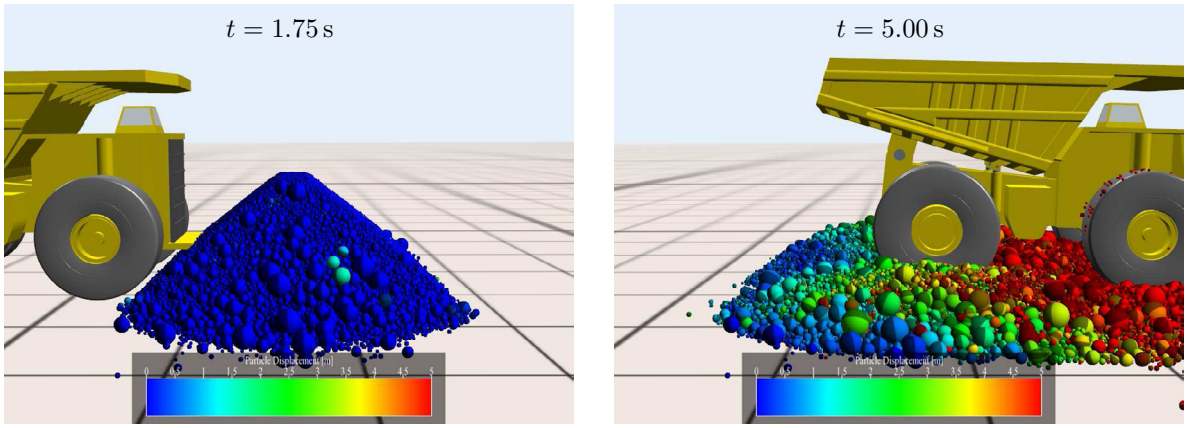

Figure 8: Screenshots of the collision at different time steps t for head-on collision with $v = 40\,\text{km/h}$ and trapezoidal berm with $H = 4\,\text{m}$ and $B = 1\,\text{m}$.

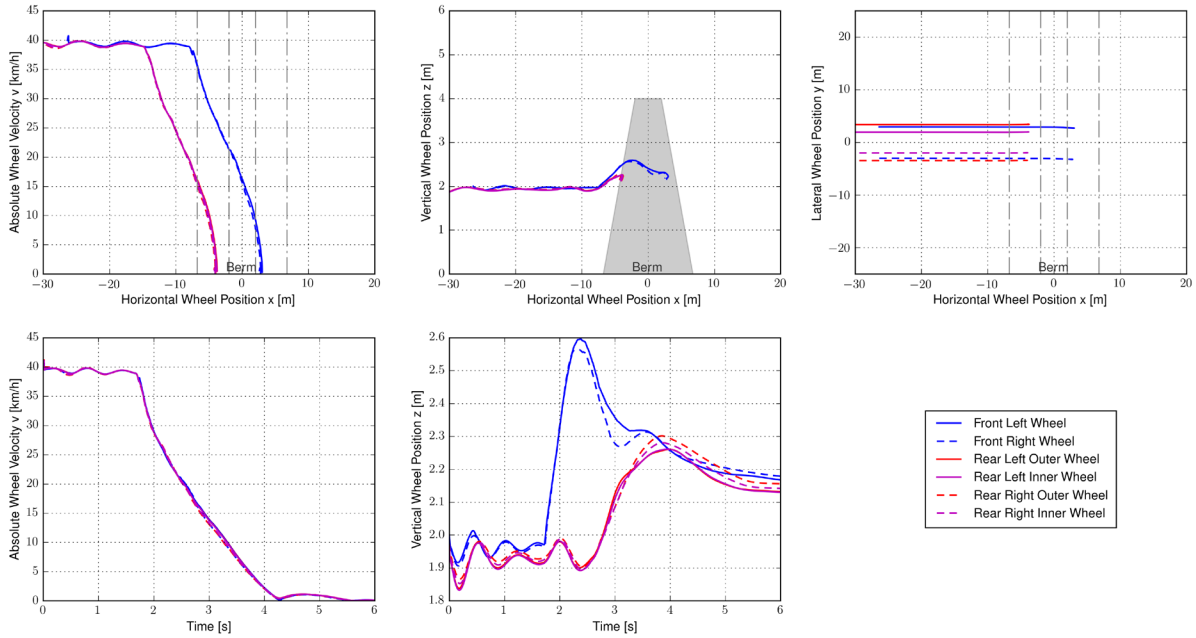

Figure 9: Summary of results for head-on collision with $v = 40\,\text{km/h}$ and trapezoidal berm with $H = 4\,\text{m}$ and $B = 4\,\text{m}$.

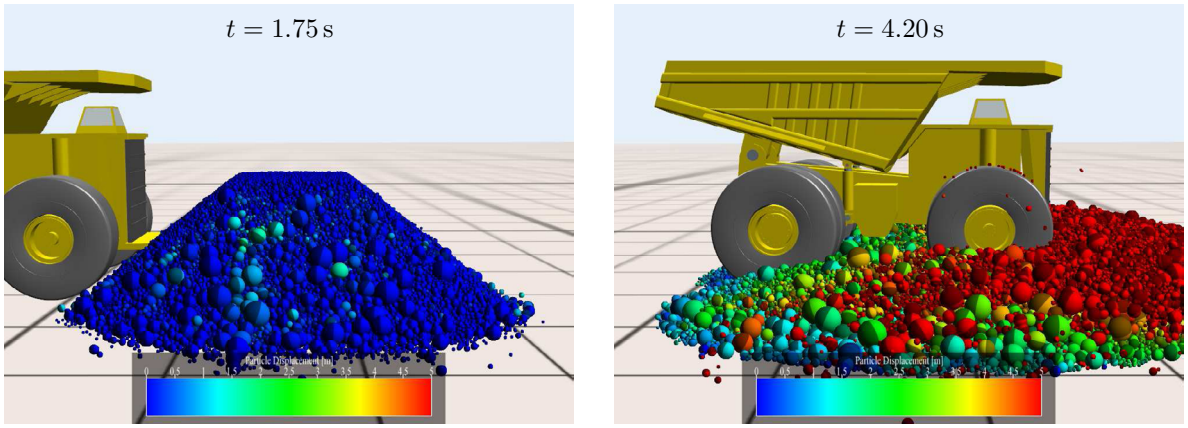

Figure 10: Screenshots of the collision at different time steps t for head-on collision with $v = 40\,\text{km/h}$ and trapezoidal berm with $H = 4\,\text{m}$ and $B = 4\,\text{m}$.

head-on with a trapezoidal berm. In this case the height is kept constant and the effect of the width of the berm is shown. A more detailed analysis is currently on the way to provide surface mining operators with more rigorous guidelines.

REFERENCES

[1] Giacomini, A., Thoeni, K.. Full-scale experimental testing of dump-point safety berms in surface mining. *Canadian Geotechnical Journal* (2015) **52**(11):1791–1810.

[2] Giacomini, A., Thoeni, K.. Energy Adsorption Capacity of Muck Piles and Their Status as Engineered Hard Barriers. Tech. Rep. ACARP C21032, Australian Coal Association Research Program, (2014).

[3] Alsaleh, M.. Soil – Machine Interaction: Simulation and Testing. In: Bonelli, S., Dascalu, C., Nicot, F., (editors). *Advances in Bifurcation and Degradation in Geomaterials*, Springer Series in Geomechanics and Geoengineering 11. Springer, (2011), p. 165–176.

[4] Gruening, T., Kunze, G., Katterfeld, A.. Simulating the working process of construction machines. In: Bonelli, S., Dascalu, C., Nicot, F., (editors). *Proceedings of Bulk Solids Europe 2010*. (2010), p. 1–10.

[5] Kübler, K., Schiehlen, W.. Two methods of simulator coupling. *Mathematical and Computer Modelling of Dynamical Systems* (2000) **6**(2):93–113.

[6] Algoryx Simulation, . AGX Dynamics. http://algoryx.se. (2017).

[7] Acary, V., Brogliato, B.. *Numerical Methods for Nonsmooth Dynamical Systems: Applications in Mechanics and Electronics*. Springer Verlag, (2008).

[8] Moreau, J.. Numerical aspects of the sweeping process. *Computer Methods in Applied Mechanics and Engineering* (1999) **177**:329–349.

[9] Jean, M.. The non-smooth contact dynamics method. *Computer Methods in Applied Mechanics and Engineering* (1999) **177**(3–4):235–257.

[10] Servin, M., Wang, D., Lacoursière, C., Bodin, K.. Examining the smooth and nonsmooth discrete element approach to granular matter. *International Journal for Numerical Methods in Engineering* (2014) **97**:878–902.

[11] Servin, M., Wang, D.. Adaptive model reduction for nonsmooth discrete element simulation. *Computational Particle Mechanics* (2016) **3**(1):107–121.

[12] Lacoursière, C.. Regularized, stabilized, variational methods for multibodies. In: P. Bunus, D.F., Führer, C., (editors). *The 48th Scandinavian Conference on Simulation and Modeling (SIMS 2007), 30-31 October, 2007, Göteborg (Särö), Sweden*,

Linköping Electronic Conference Proceedings. Linköping University Electronic Press, (2007), p. 40–48.

[13] Murty, K.. *Linear Complementarity, Linear and Nonlinear Programming*. Helderman-Verlag, Heidelberg, (1988).

[14] Brandl, M.. Agx dynamics two-body tire model - for real-time vehicle simulation. Internal documentation at Algoryx Simulation, (2015).

V International Conference on Particle-based Methods – Fundamentals and Applications
PARTICLES 2017
P. Wriggers, M. Bischoff, E. Oñate, D.R.J. Owen, & T. Zohdi (Eds)

GRAY-SCALE LATTICE BOLTZMANN – AN ATTEMPT TO BRIDGE MULTIPLE LENGTH SCALES

GERALD G. PEREIRA[1] AND M. BEN CLENNELL[2]

[1]Computational Modelling, CSIRO
Private Bag 10, Clayton South, 3169, AUSTRALIA
Gerald.Pereira@csiro.au and www.csiro.au

[2]Energy, CSIRO
Bentley, 6098, AUSTRALIA
Ben.Clennell@csiro,au and www.csiro.au

Key words: Lattice Boltzmann, porous media, heterogeneous, multiphase, convection.
Abstract. Understanding and controlling the flow of fluids through porous media such as rocks, fibres, granular media and paper is of fundamental significance to a variety of industries such as oil and gas, chemical production, health and sanitary products. Numerical modelling of this physical process can be difficult not only because of the complex, three-dimensional topology of the porous medium but also because of computational limitations. For example, shale rocks which is now being intensively investigated for its oil and gas resources have porosity over a wide range of length scales from nano-metres up to millimetres. It has been shown that the micro-porosity is fundamental to the fluid movement through the rock. However, current numerical models, which work off computed tomographical (CT) scans of the rock will be excessively large if they are to fully model all length scales which may span six or more orders of magnitude.

Here we consider the development of a lattice Boltzmann (LB) technique which may be able to solve the fluid flow over a wide range of length scales. In the past LB techniques have proven to be ideal to model fluid flow in complex porous media since it can readily import and process digital data from CT scans. Hence the fluid flow field is quickly determined and permeabilities can be predicted. However, when the CT data contains micro-porosity, the conventional LB method is not applicable and a modified LB method needs to be developed. Here we consider a gray-scale LB method which works on voxels which are not fully void or solid but something in between, i.e. each voxel is partially resistant to fluid flow. We firstly outline the model, then validate it on test cases and then demonstrate its applicability on real porous media.

We develop models not only for single phase fluid flow, but also multiphase fluid flow (i.e. a gas and a liquid) as well as a temperature model, where the temperature field is advected by the fluid flow. For all these cases the models are developed and validated and then demonstrated on realistic media. It is shown that the gray-scale LB model may be able to solve for fluid flow through multiple length scales – a difficult computational problem which is of increasing significance in many real-world applications.

1 INTRODUCTION

The lattice Boltzmann (LB) method is a fluid particle based numerical method which considers the Boltzmann transport equation as the basis for fluid motion. The lattice Boltzmann solution is restricted to discrete lattice sites (nodes) but has proven to be a powerful alternative to solving the Navier-Stokes equations, especially for problems with complex boundaries [1, 2] such as those found in porous media.

In the past the LB method has been successfully to solve for fluid flow through rocks, such as sandstone, carbonates and shales or fibrous materials such as paper products. In these cases if a digital image of the sample (i.e. a computed tomo-graphical or CT scan) is available, the LB method may be applied to this image to obtain the fluid flow through the sample. Conventionally, each voxel of the digital image corresponds to a region of solid material (i.e. not available for fluid flow) or pore space (i.e. void region which is available for fluid flow) and the LB method solves then on all the void voxels, with appropriate boundary conditions at the interface between solid and void. The fluid flow through the porous sample may be then determined. In this paper we refer to such a model as a black-white model as each voxel (lattice node) corresponds to either solid or fluid. Through a Chapman-Enskog expansion, the LB scheme has been shown to be equivalent to solving the Navier-Stokes equations for fluid flow [1, 2].

The gray-scale LB method attempts to lift the restriction that each lattice node is either fluid or solid. In this case, nodes can be anything between solid or void, i.e. a gray-scale value. Fluid can then flow through these gray lattice nodes, but there is an increased fluid resistance associated with this flow. The magnitude of this fluid resistance at a particular voxel will be related to the degree of gray shading of that voxel. Such a model should be useful in situations where the corresponding CT scan has a lower resolution than the fine-scale structure of the sample (i.e. the CT scan resolution may be of the order of microns, but the pore structure might be of the order of 10-100nm). Thus a specific voxel will contain both solid and void regions and would appear as a shade of gray in the CT image.

To develop a suitable gray-scale LB model it is useful to first outline the main steps for the conventional (black-white) LB solution. LB is a class of cellular automata, which is solved on a regular lattice (usually simple-cubic in three dimensions). On each lattice vertex or node, where the location of each node is the centre of a voxel from the CT scan, a set of fluid particle distribution functions is defined. There are Q distribution functions defined on each node. LB method then consists of three main steps. The first step is called streaming, in which all fluid packets (distributions) are moved to adjacent sites. This streaming can be correlated to the normal advection of fluid. The second step is called bounce back, which accounts for fluid-solid boundary conditions. Here fluid packets at boundary nodes are reversed in direction (or more complicated half-way bounce back or interpolation boundary conditions may be implemented). The final step in LB is a collision step where fluid packets converging on a given node are redistributed according to the Maxwell distribution. The LB method then consists of iterating these three steps (in a pseudo time-stepping manner) to give a solution. In the gray-scale model there are no fluid-solid boundaries, as such. All voxels are allowed a certain degree of flow. This can be related to the solid fraction in that voxel, but other effects such as tortuosity, topology, mineral content etc can be included into the model to contribute

to the voxel's resistance to flow. To account for this, a partial bounce-back rule is imposed on each voxel [3,4].

This means at each voxel a certain fraction of fluid packets (which were streamed into a node) will be bounced back. We denote the fraction of fluid packets, which are bounced back at a node by n_s ($0 \leq n_s \leq 1$) and each node can have a different n_s value.

At important question in the implementation of a suitable gray-scale LB model is how does one estimate the bounce-back fractions n_s from a gray-scale CT sample? As a first-step towards doing this, we estimate this by using the partial volume fractions of materials and pores which are generated through a data-constrained modelling (DCM) approach [5]. In this method each voxel is represented by partial volumes of various different materials rather than the binary value of only one material present in the traditional image segmentation. The DCM methodology has been applied to a number of other systems successfully. It is important to emphasize that n_s may have a number of other contributions, rather than just partial volume fractions of different materials, e.g. fine-scale topology, tortuosity and anisotropy.

In this paper we present a gray-scale model for single phase fluid flow through a digital image of porous media where each voxel (which makes up the digital image) imparts a certain resistivity to fluid flow. We only use a single-relaxation time (SRT) in this paper, although the gray-scale can be readily applied to multiple relaxation time schemes. After validating the model, we apply it to real-world rock samples. We then show how the gray-scale LB model can be extended to multiphase, immiscible flow and again validate the model against test cases, before applying it to some more realistic samples. Finally we couple the gray-scale fluid flow model to heat transfer, where the heat may be convected via the fluid or heat may naturally diffuse through the fluid. The heat transfer model is once again validated against test cases before application to an actual rock sample.

2 GRAY-SCALE LB

The LB model is a mesoscopic numerical method used to study incompressible fluid dynamics. Its main advantages over more conventional CFD techniques (which directly solve the Navier-Stokes equations) are its programming simplicity, computational efficiency and inherent parallelism due to a large amount of local computations. In addition, as mentioned in the Introduction, it naturally deals with complex porous media if suitable digital information is provided. Details of this method, applied to single phase flow, are available [1,2] and thus we shall only focus here on the LB method applied to gray-scale models.

As explained in the Introduction, LB consists of streaming, collision and bounce-back at boundaries. More complex and accurate boundary conditions such as half-way bounce-back or linear interpolation boundary conditions are also possible. In the collision step particle distributions relax towards a given equilibrium distribution - a Maxwellian distribution. Then macroscopic properties such as fluid density, fluid velocity and the stress tensor can be derived from the particle distributions. If we are dealing with only a single fluid, one set of particle distributions is defined, i.e. $f(\boldsymbol{r}, \boldsymbol{u}, t)$ which denotes the distribution of particles travelling with a particular velocity $\boldsymbol{u}$ at time t at lattice node $\boldsymbol{r}$. We will only consider a three dimensional (3D) model in this paper so that we implement the common D3Q19 model which indicates that there are 18 possible vectors, $\boldsymbol{e}_i$, in which particles may move in addition to the

null vector. These 18 possibilities are the vectors (±1, 0, 0), (0,±1,0), (0,0,±1), (±1,±1,0), (±1,0,±1), (0,±1,±1).

We solve the following LB equation at every node for the distribution function with velocity e_i:

$$f_i(\boldsymbol{r}+\boldsymbol{e}_i\Delta t, t+\Delta t)-f_i(\boldsymbol{r},t)=-\frac{1}{\tau}\left[f_i(\boldsymbol{r},t)-f_i^{eq}(\boldsymbol{r},t)\right]. \quad (1)$$

The term f_i^{eq} is the equilibrium Maxwell distribution given by

$$f_i = w_i\rho\left[1+\frac{\boldsymbol{e}_i\bullet\boldsymbol{u}^{eq}}{c_s^2}+\frac{(\boldsymbol{e}_i\bullet\boldsymbol{u}^{eq})^2}{2c_s^4}-\frac{\boldsymbol{u}^{eq}\bullet\boldsymbol{u}^{eq}}{2c_s^2}\right], \quad (2)$$

where w_i are weights which are defined for the given D3Q19 model. In Eq.(1), τ represents a relaxation time and it can be shown to be related to kinematic viscosity via $\nu = c_s^2(\tau - 1/2)$ where c_s is the sound speed and c_s^2 equals 1/3. The pressure, P, in this model is given by the equation of state $P = c_s^2\rho$. The LB equation (1) is known in the literature as single relaxation time (SRT) scheme, because only one relaxation time is involved.

The relationship to macroscopic parameters such as density and velocity are given by

$$\rho = \sum_i f_i \quad and \quad \rho\boldsymbol{u} = \sum_i f_i\boldsymbol{e}_i. \quad (3)$$

To model forces (such as body forces to mimic gravity or even surface forces between different phases when we model two or more phases) we add an explicit forcing term to the LB equation (1). This forcing term is defined by

$$\Im_i = \frac{F\bullet(\boldsymbol{e}_i-\boldsymbol{u}^{eq})}{\rho c_s^2}f_i^{eq}, \quad (4)$$

where $\boldsymbol{F}$ is the force. The macroscopic velocities are modified in this case to $\rho\boldsymbol{u} = \sum_i f_i\boldsymbol{e}_i + \boldsymbol{F}/2$ and $\boldsymbol{u}^{eq} = \boldsymbol{u}$. This implementation of an applied force is not only accurate, but also exhibits correct time evolution of the flow.

Typically LB methods solve on (100%) void nodes and don't solve on solid nodes. To simulate no-slip boundary conditions, at boundaries between void and solid nodes, a bounce-back step is performed which simply reverses the direction of the streamed distribution function. In the gray LB methods, one solves at *all* nodes. Since there are no solid nodes, as such, a full bounce back is not performed. Rather, on any given node a certain fraction of the fluid packets that are streamed into that node are bounced back. This fraction of fluid packets which are bounced back at any given node is given by n_s and so equation (1) is replaced by

$$f_i(\boldsymbol{r}+\boldsymbol{e}_i\Delta t, t+\Delta t) = (1-n_s)f_i(\boldsymbol{r},t)-\frac{1}{\tau}(1-n_s)\left[f_i(\boldsymbol{r},t)-f_i^{eq}(\boldsymbol{r},t)\right]+(1-n_s)\Im_i + n_s\,\hat{f}_i(\boldsymbol{r},t). \quad (5)$$

The last term with the circumflex on the distribution function indicates the distribution function to be added is in the opposite direction to i. The parameter n_s is between 0 and 1, and can be related to voxel compositional and/or topological properties (among other things). The macroscopic velocity is now

$$\rho\boldsymbol{u} = (1-n_s)\left(\sum_i f_i\boldsymbol{e}_i + \boldsymbol{F}/2\right). \quad (6)$$

Equation 5 represents the gray-scale LB model of Walsh et al [3]. This gray-scale LB model was validated against the Brinkman extended Darcy model with the flow field equation

given by

$$\nabla^2 u - \left(\frac{\phi}{\nu}\right) u = \frac{1}{\rho\nu} G \qquad (7)$$

where G is a driving force or pressure gradient, u is the velocity field, ν is the kinematic viscosity, ρ fluid density and ϕ is a damping coefficient. Equation 7 is the Brinkman extended Darcy equation where ϕ is related to n_s via $\phi = 2n_s$ [3]. When $\phi \to 0$, the solution to (7) returns to the standard Poiseuille equation. It can be solved analytically with solution expressed as

$$u(y) = -\frac{G}{\phi\rho}\left[1 - \frac{\cosh[r(y - L/2)]}{\cosh(r \cdot L/2)}\right] \quad , \qquad (8)$$

where ϕ and r are related via $r = (\phi/\nu)^{1/2}$.

Solutions for various n_s values are shown in Fig, 1 and we also show the corresponding permeability as a function of n_s. Excellent agreement is found between the analytic and LB gray-scale method. Further comparisons for layered channels (i.e. variable n_s) between the LB gray-scale model and analytic solution also show excellent agreement [4].

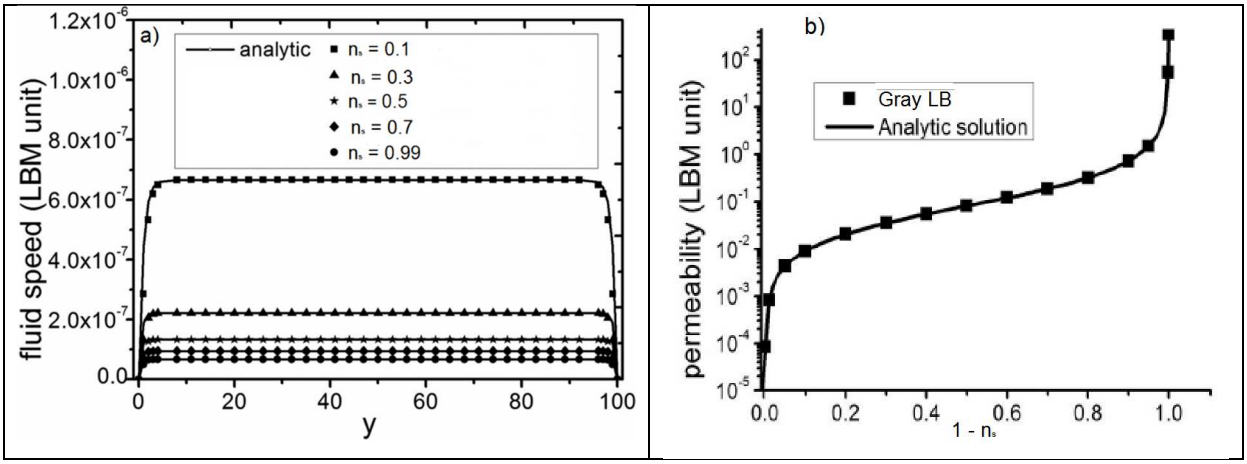

Figure 1a) Comparison between analytic solution (black curves) and LB gray-scale model for various n_s values for a) velocity field and b) effective permeability for Brinkman flow in a 3D channel .

3 MULTIPHASE FLOW

Figure 1 gives us some confidence in the single phase gray-scale LB model so that we now proceed to applying an extension of it to two (or more) immiscible phases. In principle there can be n phases. To model this with our LB method we now define n sets of distributions functions, which represent each immiscible phase - $f^1(\mathbf{r},\mathbf{u},t)$ ... $f^n(\mathbf{r},\mathbf{u},t)$. For each phase we solve the LB equation at node i. So for the k^{th} phase (where $k \in 1,...n$) we need to solve the LB equation (1), with k (possibly different) relaxation times. Values for various macroscopic variables in this model then follow almost analogously to the single phase equations for density, viscosity and momentum flux for each phase.

To model immiscibility between phases we implement the *pseudo-potential* model [6] which employs nearest neighbour inter-particle potentials to model the interactions between

components. In a sense this follows physical reality at the microscopic level where molecules interact via short-range Lennard-Jones type potentials. In the original Shan-Chen [7] model lattice nodes which have a separation of less than or equal to $2^{1/2}$ units are coupled together. The interaction potential between components is accommodated via a force, F^k which is introduced through the added force term (Eq. (4)). The equilibrium velocity is re-defined to accommodate multiple phases, i.e., $\boldsymbol{u}_k^{eq} = \boldsymbol{u}'$. Here $\boldsymbol{u}'$ is a combined velocity and to satisfy momentum conservation must be

$$\boldsymbol{u}' = \frac{\sum_k \tau_k^{-1} \rho_k \boldsymbol{u}_k}{\sum_k \tau_k^{-1} \rho_k} \quad . \qquad (9)$$

The fluid-fluid interaction for phase k at lattice node $\boldsymbol{r}$ is then given by

$$\boldsymbol{F}^k(\boldsymbol{r}) = \rho_k(\boldsymbol{r}) \sum_{k \neq k'} g_{kk'} \sum_i w(|\boldsymbol{e}_i|^2) \rho_{k'}(\boldsymbol{r} + \boldsymbol{e}_i) \boldsymbol{e}_i \ , \qquad (10)$$

where $g_{kk'}$ is the interaction potential (or coupling parameter) between dissimilar components. The weights w depend on the separation between interacting nodes with $w(1)=1/6$ and $w(2)=1/12$. Note, we assume the coupling is zero for similar components. The pressure in this model is given by the equation of state

$$P = c_s^2 \sum_k \rho_k + \frac{1}{2} \sum_{kk'} g_{kk'} \rho_k \rho_{k'} \ . \qquad (11)$$

One of the issues with this nearest neighbour implementation is that it leads to large spurious currents which are a numerical artefact. These numerical artefacts, if not reduced to a minimum, will lead to large numerical instabilities. Thus we shall attempt to reduce these numerical instabilities. It has been found extending the range of the pseudo-potential leads to a significant reduction (up to 1000 times) of these spurious currents. The range of pseudo-potential can in principal go to infinity but this of course comes at a computational cost. We have implemented here both 6th order (including all neighbours less than or equal to 2 units away) and 8th order (including all neighbours less than or equal to $8^{1/2}$ units away) pseudo-potentials. This increases the number of neighbours to be sampled from 18 (Shan-Chen) to 32 (6^{th} order) to 64 (8^{th} order), but greatly enhances the numerical stability of the method. Weights, which are required in Eq. (9), for the additional neighbour pairs have been given previously.

The final step in the gray-scale, multiphase LB model is to incorporate the effect of voxel resistivity to flow. We assume the resistivity of a particular voxel can be different for different phases. Physically this may be the case if there are different materials in a voxel which have different slip conditions with different fluids. So equation (5) becomes:

$$f_i^k(\boldsymbol{r} + \boldsymbol{e}_i \Delta t, t + \Delta t) = (1 - n_s^k) f_i^k(\boldsymbol{r}, t) - \frac{1}{\tau_k}(1 - n_s^k)\left[f_i^k(\boldsymbol{r}, t) - f_i^{k,eq}(\boldsymbol{r}, t)\right] + (1 - n_s^k)\Im_i^k + n_s^k \hat{f}_i^k(\boldsymbol{r}, t). \qquad (12)$$

The macroscopic velocity for each phase is defined similarly to equation (6) with suitable n_s^k, f^k and $\boldsymbol{F}^k$ values used for each component.

For the simulations presented here we use $\tau_A = 1$, $\tau_B = 2.0$, which implies $\nu_A = 1/6$, $\nu_B = 1/2$, the mass of phase A is 1.0 while mass of phase B is 2.0. The surface tension g_{AB} between phases is 1.33. Note, that unless we use the numerically stable multiphase model described above, we would not be able to have a disparity in these values (between the phases) and such a large g_{AB} value.

We initially look at two-phase channel flow, i.e. phase 1 displacing phase 2 in a narrow channel (width 42 units, depth 22 units and length 152 units). We tried a range of n_s values to see how the flow changed. Figure 2 (which is a slice taken at the middle of the smallest dimension) shows the flow for n_s = 0.1 with a given body force of 6.8 x 10^{-3}. Note that we impose periodic boundary conditions in the direction parallel to the body force, i.e. any fluid exiting the domain through a face perpendicular to the body force vector re-enters on the opposite face. Other cases of n_s = 0.0, 0.05, 0.3, 0.5 and 0.7 were also simulated with the gray-scale LB method.

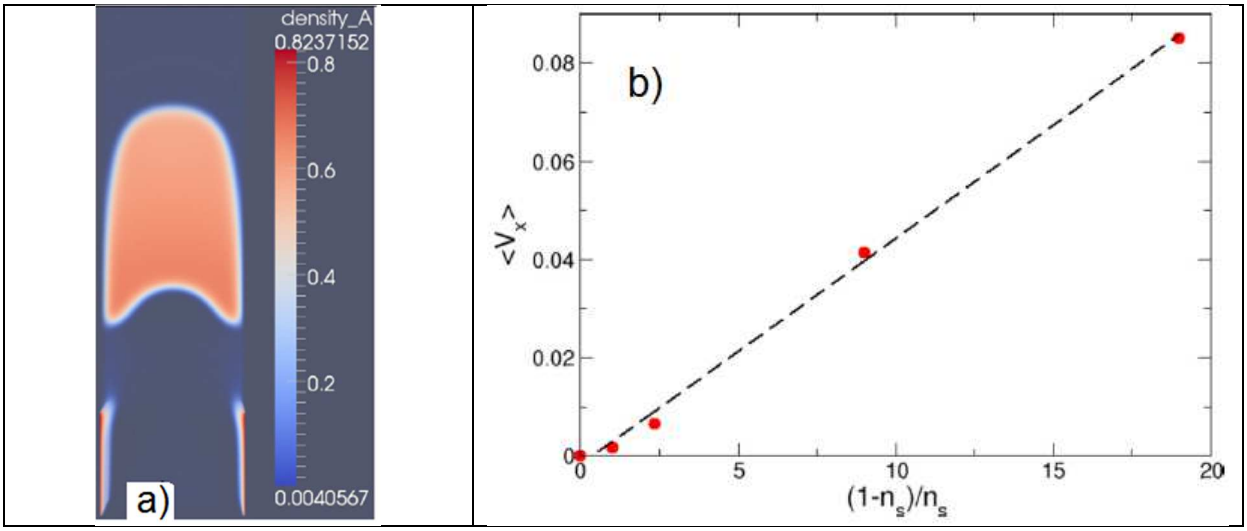

Figure 2. a) Two phase flow in a channel of width 41 units and depth 21 units for n_s = 0.1 after 2100 LB time-steps. The A-phase begins at the bottom of the channel. b) Plot of the average channel velocity of phase A versus $(1-n_s)/n_s$. Red circles come from gray-LB method while the dashed line is a best fit to these results with a gradient of 4.6×10^{-3}.This dashed line should be compared to Eq. 14.

The shape of the interfaces in Fig. 2 result from a combination of the surface tension, applied body force and applied n_s value. In Fig. 2a although the n_s value is 0.1, the comparatively large body force results in a large fluid velocity, which yields a curved (parabolic) interface profile. As the n_s value is increased, the interface becomes less curved and more flattened. A larger body force needs to be applied as the n_s value is increased because n_s is directly related to fluid drag.

According to Darcy's Law the average velocity in a porous medium is given by

$$\langle V_x \rangle = \frac{Gk}{\nu\rho} \quad . \qquad (13)$$

So the average velocity is proportional to the permeability, k. In the gray-scale models the permeability is related to n_s via $k = (1-n_s)\nu/2n_s$ [3], so that the average velocity along the channel is given by

$$\langle V_x \rangle = \frac{G(1-n_s)}{2n_s\rho} \quad . \qquad (14)$$

We can determine the average velocity quite easily in these simulations by tracking the location of the advancing interface (fluid front). Doing this for the four different simulations (at the same G value) and plotting the average velocity as a function of n_s gives Fig. 2b. Note, we have also added the $n_s = 1$ value which gives zero channel speed (see equation (6)). We obtain a linear relationship between the average channel velocity and $(1-n_s)/n_s$, as predicted by equation (14). Furthermore, from the gradient of the graph and assuming an average A-phase density of 0.75, we predict the body force is 6.9×10^{-3}, which agrees well with the body force we have applied in these cases.

Further test were also carried out to validate the model [4] and demonstrated the model was accurate. One important note here is that to increase the numerical stability of this model it is desirable to use multiple relaxation time (MRT) scheme,

4 GRAY-SCALE LB WITH TEMPERATURE COUPLED TO FLOW

The temperature field is assumed to be only advected by the fluid flow. Viscous fluid heating is assumed to be insignificant and hence is neglected in this model. The model used for the temperature field calculation is the *passive-scalar* model and has been implemented before with a single-relaxation time LB model for binary (black-white) nodes [8]. The temperature field obeys the equation

$$\frac{\partial T}{\partial t} + (u \cdot \nabla)T = \nabla \cdot (\alpha \nabla T) + \psi \qquad (15)$$

where T is the temperature, u is the velocity field, α is the thermal diffusivity and ψ accounts for all (heat) source terms. This equation has a similar form to the momentum (Navier-Stokes) equation and so the same equilibrium distribution function (i.e. Eq. 2) that has already been used for the fluid density and velocity fields may be also used for the temperature. However a different relaxation time (in the collision operation, i.e. Eq. 5) is used. This relaxation time, which we denote as τ_α is related to the thermal diffusivity by $\alpha = c_s^2(\tau_\alpha - 1/2)$. The temperature is then given by the summation of probability distribution functions, with τ_α used in the collision process. Appropriate boundary conditions are used on the temperature field (at boundaries between solid and liquid) such as constant temperature and at inlets or outlets [9] .

To validate the gray-scale LB temperature model we again consider Brinkman flow solution for the fluid (Eq. 8) and couple this with temperature evolution equation (15). We consider the steady-state solution so that the time dependent term is zero. The solution depends on the Peclet number, Pe, which is defined ratio of advective transport to diffusive transport. We solve this partial differential equation in a channel with a uniform n_s value. The n_s value determines the magnitude of the fluid velocity which in turn determine the Peclet number. The partial differential equation is solved with a finite difference method and the solution is then compared to the corresponding gray-scale LB solution. Figure 3 shows comparison of the longitudinal (in the direction of the pressure gradient) and orthogonal

temperature profiles for a Peclet number of 0.194. The black circles correspond to the LB simulation solution while the red curve corresponds to the finite difference solution of the continuum partial differential equation. Excellent agreement is obtained between the two methods. Further validations have also been carried out for other Peclet values [9] which show a similar level agreement between LB and finite difference solution. This indicates the LB gray-scale method has good accuracy.

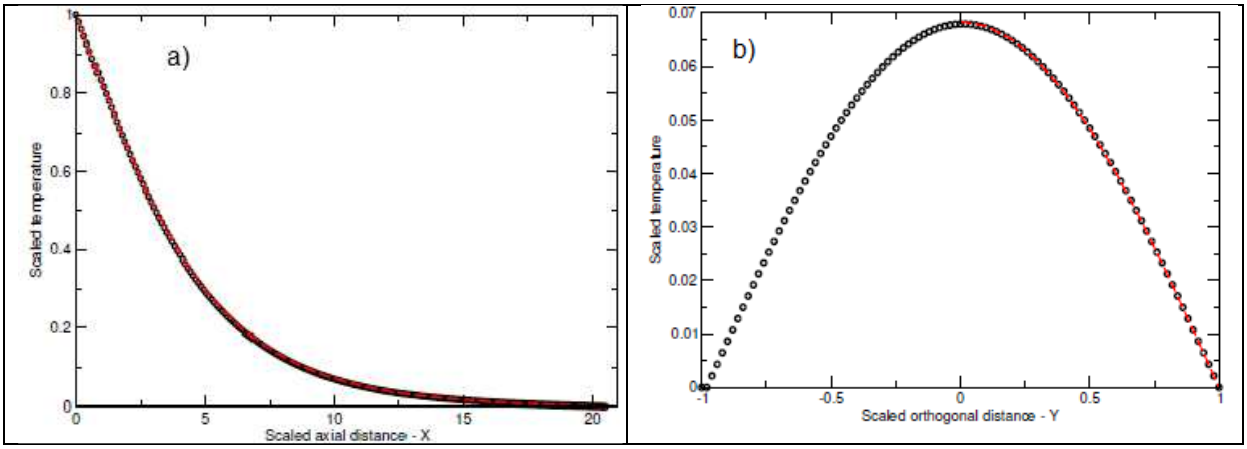

Figure 3: Temperature profile in a 2D Brinkman channel for Peclet number of 0.194 (n_s = 0.4). a) Along the centre-line, parallel to the pressure gradient direction. b) Orthogonal to the centre-line at X = 0.35. Black circles are gray-scale LB result while red-dashed lines are results from finite-difference solution.

5 APPLICATION TO REAL SAMPLES

We have so far validated the gray-scale LB model for single phase flow, multiphase immiscible flow and a coupled fluid flow and temperature model. We would now like to demonstrate the developed models on real world, physical samples. To do this we apply the gray-scale model we have just outlined to digital sample of tight sandstones which consists of quartz, albite, calcite and pyrite obtained from the Yaodian area of Yan'an in Erdors Basin, China. The 3D microscopic distribution of mineral phases in the sample is generated with the DCM software [5]. Each voxel represents a size of 3.7 × 3.7 × 3.7 μm^3 and the total size of the domain we apply the LB method to is 100 × 100 × 120 voxels.

In the sample pyrite, quartz and albite are not permeable. Fluid can flow through the void and the partially permeable calcite. The resistivity to fluid flow of the calcite is not known precisely and so we assume it is proportional to the solid calcite fraction in a voxel. The proportionality constant is denoted n_s^c and can vary from zero (no resistivity) up to one (complete resistivity to fluid flow). Then the bounce-back fraction for a given voxel is given by $n_s = 1 - v_o - n_s^c v_c$, where v_o and v_c denote the volume fractions of void and calcite in a particular voxel respectively.

5.1 Single phase flow

Figure 4 shows the voids (dark blue) and semi-permeable calcite (lighter blue to white) regions in the sample. The solid regions (quartz, albite, pyrite) have been made transparent so as to make the void and calcite regions more easily visible. For this case we use

a n_s^c value of 0.2 which leads to a porosity in the sample of 0.11. To drive the fluid flow a body force of 6.8×10^{-7} in the positive z direction of the sample.

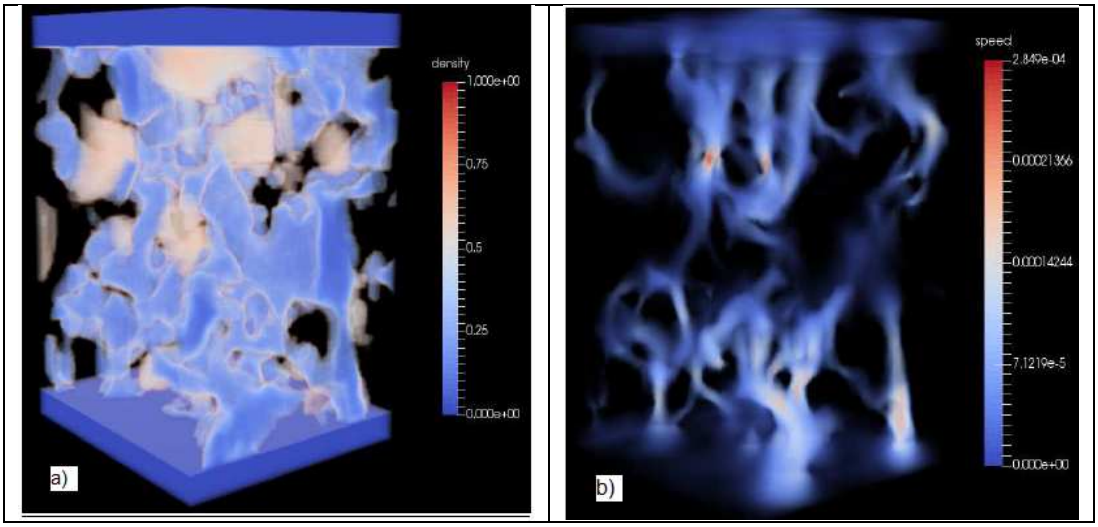

Figure 4: Tight sandstone sample on which we performed the gray-scale LB calculation. a) Distribution of voids (blue) in gray-scale sample. b) Velocity field.

The steady state flow field for the sample is shown in Fig. 4b. One can clearly see lighter coloured flow-paths which align generally with the long (z-axis) of the sample which is primarily due to the body-force in the z direction, but also may indicate a degree of anisotropy in the underlying rock micro-structure. The maximum speed in the sample is approximately 2.8×10^{-4} and is achieved in a few regions (e.g. in the middle of the sample). Overall the speed of the fluid is quite small and reflects the fact that the medium has very low porosity and thus should be quite impermeable. To calculate the sample's permeability, k, we can use the following equation

$$k = \frac{\nu}{G}\langle u \rangle \quad , \qquad (16)$$

where u is the superficial velocity (i.e in the direction of the body force, G) and the angular brackets represent a statistical average over the whole sample. Using this equation we estimate the permeability of the sample is 5.703×10^{-14} m^2 or 57.03 mD. This relatively low permeability reflects a low convective fluid flow.

5.2 Multi-phase immiscible flow

To demonstrate multiphase flow on the rock sample of Fig, 4a we initially placed a reservoir of the invading phase at the inlet (bottom end) and the rock sample is filled with the defending phase (with periodic boundary conditions on all faces). The immiscible fluids are driven through the sample with the same body force (as for single phase flow). In this case there is no (wetting or non-wetting type) interaction of the fluids with the solid matrix, although this can be readily incorporated into the model [6].

Figure 5a shows the flow pattern at breakthrough of the invading phase. In this

complex three-dimensional media, it is difficult to get a full idea of the flow a two-dimensional snap-shot. However, they do show preferential fingering of the invading phase, following paths of least (fluid) resistance. We also calculate the permeability at various times (invading fluid volume fraction) during the flood and this is given in Fig. 5b. For three dimensional flow, both phases can simultaneously have non-zero relative permeability, while in two-dimensions this is generally not possible, i.e. as soon as the invading phase breaks through the defending phase gets cut-off.

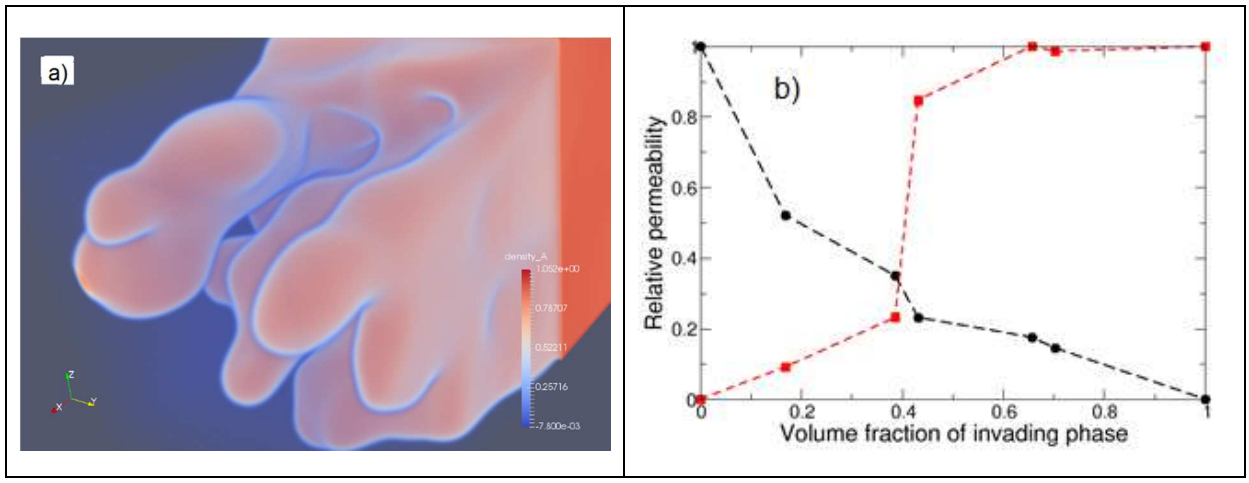

Figure 5 Two phase immiscible flow through the gray-scale tight sandstone sample of Fig. 4a. a) Invading phase (redish-orange colour) at breakthrough. b) Relative permeability curves for invading phase (red) and defending phase (black). The symbols correspond to the LB simulation, while the dashed-lines are only for the eye.

5.3 Coupled temperature and fluid flow

The temperature field for the same rock sample was simulated with two different thermal diffusivities of 1/6 and 1/30. The first diffusivity of 1/6 coupled with the low velocity field magnitude results in a low Peclet number flow. As a result the calculated temperature (Fig. 6a) is quite uniform with a creamy/white shading. As soon as one moves away from the inlet (where the temperature is 1.75) the temperature diminishes rapidly to one. As the solid regions in the sample have an imposed (boundary) temperature of one, the temperature in the adjacent semi-permeable regions is also close to one and the flow field has little effect on the temperature. Thus we are in the diffusion dominated regime for this flow.

For the smaller diffusivity of 1/30 the temperature field shows much more variability with orange/redish colours dispersed throughout the sample. These regions correspond to the higher fluid flow regions (and also the void regions) of the sample. Hence fluid convection now transports the temperature field through the sample.

6 CONCLUSION

We have presented a LB model to treat digital samples where voxels can have a continuum of values between zero and one, which we call a gray-scale model. The model has been developed for single phase flow, multiphase flow and coupled temperature and fluid flow. Each model was firstly validated quantitatively with independent methods and excellent

agreement was obtained. Then each method was applied to a real-world rock sample. The flow fields, fluid displacements and temperature fields were all realistic, which gives us confidence in future applications of this technique.

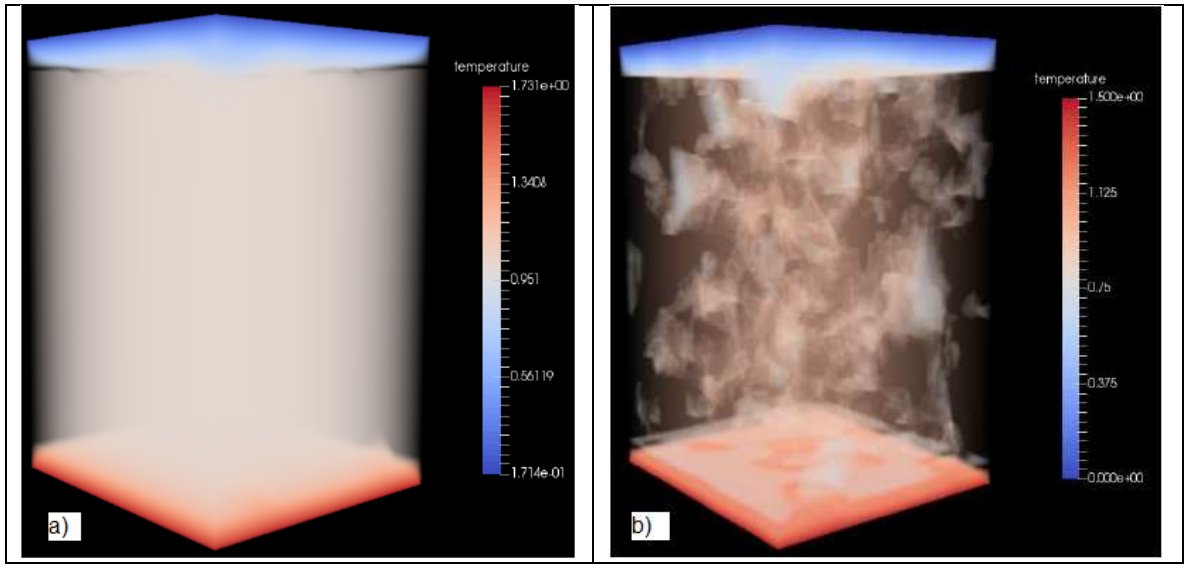

Figure 6: Temperature field for the tight sandstone sample shown in Fig. 4a. a) For a thermal diffusivity of 1/6 which gives a diffusive dominated temperature distribution and b) for a thermal diffusivity of 1/30 which gives a convective dominated temperature distribution.

REFERENCES

[1] Succi, S. *The lattice Boltzmann equation for fluid mechanics and beyond*. Oxford Science, (2001).

[2] Chen, S. and Doolen, G.D. Lattice Boltzmann method for fluid flows. *Annu. Rev. Fluid Mech.* (1998) **30**:329-364.

[3] Walsh, S.D.C., Burwinkle, H. and Saar, M.O. A new partial bounce-back LB method for fluid flow through heterogeneous porous media, *Comp. Geosci*., (2009) **35**: 1186-1193.

[4] Liu, R.R., Yang, Y.S., Pereira, G.G., Clennell, M.B., Taylor, J.A. and Pan, K. Lattice Boltzmann modelling of permeability of porous materials with partially percolating voxels, *Phys. Rev. E*, (2014) **90**: 03301(1-10).

[5] Li, R.R. Chu, C. Yang, Y.S. and Pereira, G.G. CSIRO Data Access Portal (2014). doi: 10.4225/08/53F6E72A0D35E.

[6] Pereira, G.G. A multiphase single relaxation lattice Boltzmann model for heterogeneous porous media, *Appl. Math. Modell.*, (2017) **44**: 160-174.

[7] Shan, X. and Chen, H. Lattice Boltzmann model for simulating multiple phases and components, *Phys. Rev. E*, (1993) **47**:1815–1819.

[8] Shan, X. Simulation of Rayleigh-Bernard convection using a lattice Boltzmann method, *Phys. Rev. E*, (1997) **55**: 2780-2788.

[9] Pereira, G.G., Wu, B. and Ahmed, S. Gray-scale temperature and flow lattice Boltzmann model, submitted to *Comp. Geosci.*, (2017).

V International Conference on Particle-based Methods – Fundamentals and Applications
PARTICLES 2017
P. Wriggers, M. Bischoff, E. Oñate, D.R.J. Owen, & T. Zohdi (Eds)

THERMAL LATTICE BOLTZMANN SIMULATION OF DIFFUSION/ FORCED CONVECTION USING A DOUBLE MRT MODEL

BOGDAN KRAVETS, HARALD KRUGGEL-EMDEN

Mechanical Process Engineering and Solids Processing (MVTA)
Technical University Berlin (TU Berlin)
Ernst-Reuter-Platz 1, 10587 Berlin, Germany
e-mail: kravets@tu-berlin.de, kruggel-emden@tu-berlin.de, web page: http://www.mvta.tu-berlin.de

Key words: Particle, Heat Diffusion, Forced Convection, Thermal LBM, Double MRT approach.

Abstract. The Lattice-Boltzmann method (LBM) is an alternative and flexible approach for computational fluid dynamics (CFD). Unlike many other direct numerical simulation (DNS) techniques, LBM is not solving the Navier-Stokes equations but is based on the kinetic theory and the discrete Boltzmann equation. LBM utilizes a Cartesian mesh and hence does not require a complex mesh derivation or a re-meshing in case of moving boundaries. Thermal LBM (TLBM) which is capable of solving thermal convection/diffusion problems relies on a set of two distribution functions, the so called double distribution function (DDF) approach; one for the fluid density and one for the internal energy. For the carried out numerical investigations a 3D TLBM framework is derived involving a multiple-relaxation-time (MRT) collision operator for both, the fluid and the temperature field which is yet not applied widely. Hydrodynamic and thermal boundary conditions are represented by interpolated bounce back schemes. The derived TLBM framework is applied to diffusion and convection-diffusion problems (e.g. forced convection) for plane and curved boundaries and is validated against analytical solutions, when available or compared to established correlations. The thermal MRT operator is further compared against an existing LBM model based on a thermal Bhatnagar-Gross-Krook (BGK) operator regarding accuracy and numerical stability. Averaged and local heat transfer coefficients are presented. The findings indicate that the double MRT framework with interpolated boundary conditions offers a highly accurate and efficient approach for the analysis of heat transfer problems especially for particle/fluid systems under detailed resolved flow.

1 INTRODUCTION

CFD simulations of particle/fluid systems – like packed beds, fluidized beds and pneumatic conveying – which resolve the flow around particles, have become increasingly important in the past [1–8]. Resolved flow approaches provide the most detailed level of insight and can e.g. be applied for creating closure correlations for momentum [2–4] and heat transfer [5–8] for single particles and particle packings. Derived closures can be used for large particle/fluid systems where the flow conditions are prescribed by a non-resolved CFD approach as it is often the case in the DEM/CFD.

Established DNS methods rely mostly on solving the discretized Navier-Stokes equations

using particle surface-adapted meshes. A less frequently used technique to perform CFD simulations of particle/fluid systems is the so called lattice Boltzmann method (LBM). In contrast to other established DNS simulations, LBM relies on the discrete Boltzmann equation and is primary used in combination with an equidistant Cartesian grid. Thermal (LBM) relies on a double distribution function approach [9], where the hydrodynamic part is represented by density distributions f_i and the thermal part by energy distributions g_i. Here the hydrodynamic side can be prescribed by the Bhatnagar–Gross–Krook [10] or by multiple-relaxation-time collision models [11] and the thermal side was solely represented by the Bhatnagar–Gross–Krook model in the past [9]. MRT/MRT or double MRT models, meaning hydrodynamic and thermal part are solved by a MRT operator, were introduced most recently [12,13]. It should be noted, that the MRT collision operator is more advanced and is reported to be more accurate and stable than the BGK operator.

Boundary conditions have also a great influence on the simulations results regarding accuracy and stability. The most common boundary condition is the so called half way bounce back rule. Based on that very native method interpolated bounce back routines were presented for hydrodynamic [14] and thermal side [1]. Besides interpolated bounce back methods boundary conditions using energy balancing of a node under the usage of summation and target/actual-value comparison were introduced by Liu et al. [15]. The present study deals with the evaluation of the thermal MRT collision operators and the influence of thermal boundary conditions. A double MRT framework is compared against a MRT/BGK model using different boundary conditions with regard to numerical accuracy. Local and global heat transfer is addressed and compared to analytical solutions or to results obtained from scientific literature.

2 NUMERICAL METHOD

2.1 Lattice Boltzmann Method

The underlying numerical method of this investigation is a three dimensional double distribution function Lattice Boltzmann model. The fluid flow is represented by a multiple-relaxation-time collision operator (MRT) with 19 discrete velocity directions (D3Q19) as proposed by d'Humiéres et al. [11] which is described by the following expression:

$$f_i(\vec{x} + \vec{e_i}\Delta t, t + \Delta t) = f_i(\vec{x}, t) - \langle M^{-1} \cdot \hat{S} \cdot [m_i(\vec{x}, t) - {m_i}^{eq}(\vec{x}, t)]\rangle_i + F_i, \quad (1)$$

where f_i is the density distribution function, with $\vec{e}_i$ being the discrete velocity of each distribution function. In eq. (1) F_i is an external force which can be applied along the $i - th$ lattice direction if desired. M is a $n \times n$ transformation matrix and $\hat{S}$ a $n \times n$ diagonal collision matrix, with n being the number of discrete directions e.g. $n = 19$ for D3Q19. For a detailed description e.g. of the choice of relaxation rates or equilibrium momenta ${m_i}^{eq}$ the reader is referred to [11].

For the thermal side three collision operators are investigated here: a D3Q19 Bhatnagar-Gross-Krook operator (BGK) proposed by Peng et al. [16], which is given by:

$$g_i(\vec{x} + \vec{e}_i\Delta t, t + \Delta t) = g_i(\vec{x}, t) - \frac{1}{\tau_g}[g_i(\vec{x}, t) - {g_i}^{eq}(\vec{x}, t)], \quad (2)$$

a D3Q7 MRT and a D3Q19 MRT model proposed by Li et al. [12] which are based on the

model proposed by Yoshida and Nagaoka [13] and are represented by the following expression:

$$g_i(\vec{x} + \vec{e_i}\Delta t, t + \Delta t) = g_i(\vec{x}, t) - \langle M^{-1} \cdot \hat{S}_g \cdot \left[m_{i_g}(\vec{x}, t) - m_{i_g}^{eq}(\vec{x}, t) \right] \rangle_i . \quad (3)$$

In eqs. (2) and (3) g_i is the energy distribution function and M and $\hat{S}_g$ are transformation and collision matrix respectively. M is given in [11] for a D3Q19 and in [13] for a D3Q7 model. Li et al. [12] propose equilibrium momenta m^{eq} for both D3Q7 and D3Q19 schemes. The underlying discrete velocities for the D3Q7 and the D3Q19 model are shown in Figure 1.

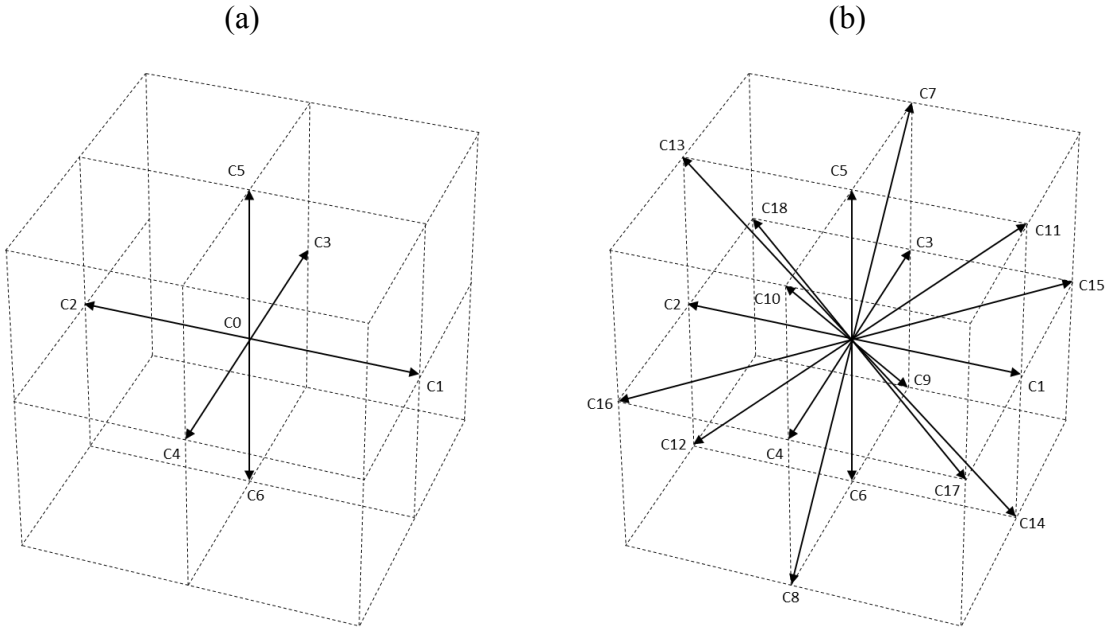

Figure 1: Discrete velocity vectors in (a) D3Q7 and (b) D3Q19 model.

2.2 Hydrodynamic Boundary Conditions

The most common hydrodynamic boundary condition in LBM is the so called bounce back rule, where the distribution function pointing outside the numerical domain is reflected in the reversed direction:

$$f_{\bar{i}}(\vec{r}_i, t + \Delta t) = f_i^*(\vec{r}_i, t), \quad (5)$$

where $f_{\bar{i}}$ denotes the unknown incoming density distribution and f_i^* denotes the post collision distribution function which points outwards towards the fluid boundary. Here it is assumed that the wall is located in the middle between two lattice nodes. In case the wall is not located at $\Delta x/2$ the interpolated bounce back rule proposed by Bouzidi et al. [14] can provide more accurate results. The unknown distribution functions can be prescribed by linear or by quadratic interpolation. In the present study only quadratic interpolation is used for the hydrodynamic boundary conditions. Figure 2 schematically shows the interpolated bounce back routine with dependence on the wall position q. For further details see [14].

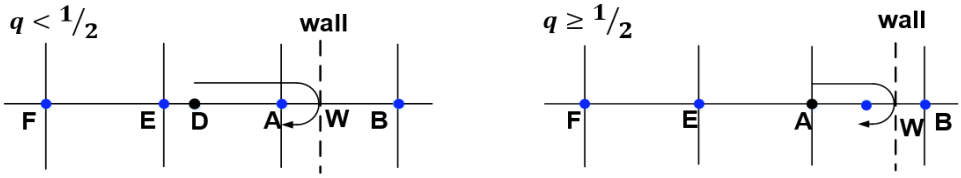

Figure 2: Schematic representation of the interpolated boundary condition [14].

2.3 Thermal Boundary Conditions

Based on the idea of the simple bounce back, Yoshida and Nagaoka [13] proposed the following thermal Dirichlet boundary condition:

$$g_{\bar{i}}(\vec{r}_i, t + \Delta t) = -g_i{}^*(\vec{r}_i, t) + \varepsilon_D \phi_D \tag{4}$$

Similar to the hydrodynamic boundary conditions $g_{\bar{i}}$ denotes the unknown energy distribution and $g_i{}^*$denotes the known post collision energy distribution which points outwards of the fluid domain towards the fluid boundary. With ϕ_D being the Dirichlet source term representing the internal energy at the regarded node and ε_D the Dirichlet coefficient which depends on the weighting factor of the LBM model [3,4]. Li et al. [1] extended this model to an interpolated thermal bounce back (similar to the hydrodynamic boundary condition proposed by Bouzidi et al. [14]) and proposed three different interpolation schemes of which scheme 1

$$g_{\bar{i}}(\vec{r}_i, t + \Delta t) = (-2q) g_i^*(\vec{r}_i, t) + (2q - 1) g_i^*(\vec{r}_i - \vec{e}_i, t) + \varepsilon_D \Phi_D \quad \text{for } q < \frac{1}{2}, \tag{5}$$

$$g_{\bar{i}}(\vec{r}_i, t + \Delta t) = -\frac{1}{2q} g_i^*(\vec{r}_i, t) + \frac{(2q - 1)}{2q} g_i^*(\vec{r}_i, t) + \frac{1}{2q} \varepsilon_D \Phi_D \quad \text{for } q \geq \frac{1}{2} \tag{6}$$

and scheme 3

$$g_{\bar{i}}(\vec{r_i}, t + \Delta t) = -\, g_i^*(\vec{r_i}, t) + \frac{(2q - 1)}{(2q + 1)} g_i^*(\vec{r_i} - \vec{e_i}, t) + \frac{(2q - 1)}{(2q + 1)} g_{\bar{i}}^*(\vec{r_i} - \vec{e_i}, t) + \frac{2\, \varepsilon_D \Phi_D}{(2q + 1)} \tag{7}$$

are considered in the present study. Scheme 1 and scheme 3 reduce to the simple thermal bounce back in eq. (4) for $q = 1/2$.

Apart from the interpolated thermal bounce back other thermal boundary conditions were proposed in the near past. Liu et al. [15] proposed the following thermal boundary rule:

$$g_{\bar{i}}(\vec{r}_i, t + \Delta t) = g_i{}^*(\vec{r}_i, t) + w_i G_c, \tag{8}$$

where $g_{\bar{i}}$ and $g_i{}^*$ are the unknown and known distributions respectively, w_i the weighting factor of the LBM model and G_c is the corrector which is enforcing the internal energy and is given as:

$$G_c = \frac{\rho_0 e - \rho_0 e^*}{\sum_{i=0}^{n} \omega_i}. \tag{9}$$

Here e^* is the target value for internal energy, and e is the actual internal energy and which can be determined by linear

$$\rho_0 e_A = \rho_0\big(e_W + (e_E - e_W)\big)\frac{\overline{AW}}{\overline{EW}}\,, \tag{10}$$

or by quadratic interpolation

$$\rho_0 e_A = \rho_0\left(e_W + (e_E - e_W)\frac{\overline{AW}}{\overline{EW}} + \Big(\frac{e_E - e_W}{\overline{EW}} - \frac{e_F - e_E}{\overline{EF}}\Big)\frac{\overline{AE}\cdot\overline{AW}}{\overline{FW}}\right). \tag{11}$$

The internal energy for a lattice can be obtained by the summation of all energy distributions $e = \sum_{i=0}^{n} g_i$. If the regarded point (e.g. E, F) doesn't coincide with the LBM mesh (curved boundary), trilinear interpolation is used to determine the value in this point. For details on the geometric properties / location of E, F see [17].

3 RESULTS

3.1 Heat diffusion cases

As an initial case a 1D diffusion problem is regarded. A simulation domain of the length L with constant boundary temperature $T_s = 10$ and the initial Temperature $T_{init} = 0$ was selected. To study the performance of the collision operators and boundary conditions the simulation domain was refined as follows: $L = 20, L = 40, L = 80, L = 160$ and $L = 320$. The boundary wall was located between two nodes (simple half way bounce back rule). Thermal MRT collision operators for D3Q7 and D3Q19 [13] as well as the thermal BGK operator for D3Q19 proposed by Peng et al. [16] were studied. Furthermore, two different boundary conditions [1,15] were investigated. Thermal relaxation time was set to $\tau_g = 0.53$ for all simulations. The obtained temperature profile was compared to an analytical solution.

This analytical solution for a 1D diffusion problem with constant boundary conditions is given by the following expression:

$$T(x,t) = T_s + (T_{init} - T_s)\sum_{n=0}^{\infty} a_n \exp\left(-\frac{n^2\pi^2\alpha t}{L^2}\right) sin\left(\frac{n\pi x}{L}\right), \tag{12}$$

where $a_n = 4/\pi n$ for odd n and zero for even n, α is the thermal conductivity and t the simulation time. The analytical expression can be used with physical or non-dimensional LBM quantities.

Figure 3 shows the averaged relative error for each simulation. As can be seen from the obtained results all investigated collision operators and boundary conditions are second order accurate in space. For 1D diffusion problems MRT D3Q7 provides the greatest accuracy which is in good agreement with results presented by Li et al. [1]. It can be noted, that the investigated thermal MRT models proposed by Yoshida and Nagaoka [13] are superior in terms of accuracy compared to thermal BGK proposed by Peng et al. [16]. Boundary conditions proposed by Yoshida and Nagaoka [13] are three to five times more accurate compared to boundary conditions proposed by Liu et al. [15]. It should be stressed out in conclusion, that the boundary conditions have a major influence on the numerical accuracy.

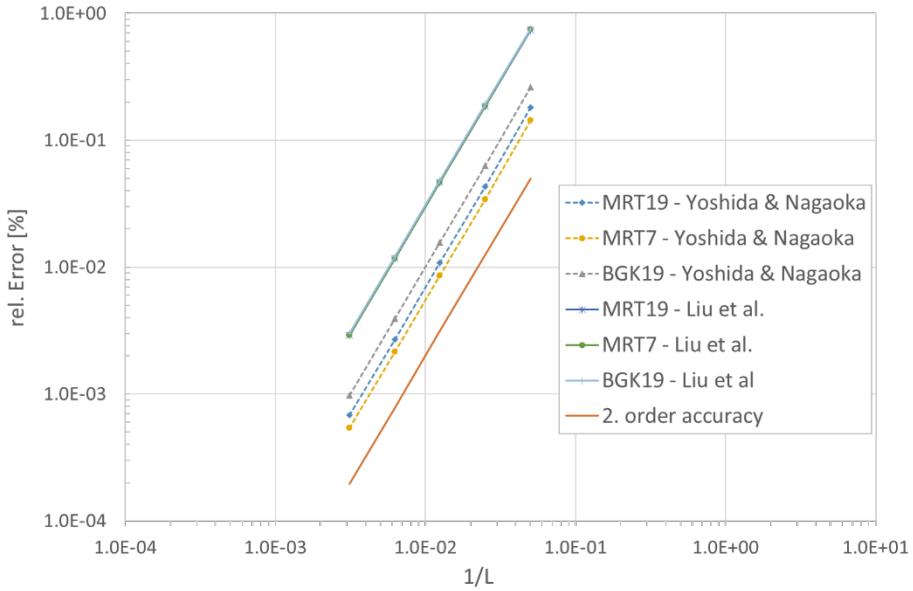

Figure 3: Relative error over grid resolution $1/L$ for the 1D thermal diffusion problem.

As second case a 3D diffusion problem is considered. The cubic domain of size $8 \cdot d_p$ has periodic boundaries. The particle diameter is varied as follows: $d_p = 5$, $d_p = 10$, $d_p = 20$ and $d_p = 40$. The thermal relaxation time was chosen as $\tau_g = 0.53$. The analytical solution to the described problem is given by

$$T(x,t) = T_s + (T_S - T_\infty)\frac{R}{x}\left(1 - erf\left(\frac{x-R}{\sqrt{4t\alpha}}\right)\right) \qquad for\ x > R, \tag{13}$$

where erf is the error function, x is the distance from the sphere center and R the particle radius. T_∞ is the temperature of the undisturbed fluid and can be considered as the initial temperature for a sufficient small simulation time t. Figure 4 shows the temperature distribution of the described case.

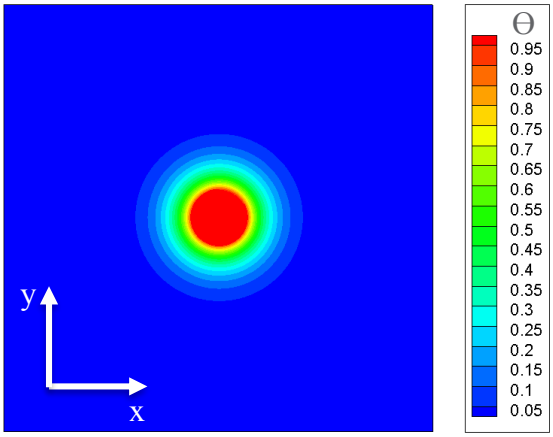

Figure 4: Distribution of dimensionless temperature $\theta = (T - T_i)/(T_s - T_i)$ around a fixed sphere.

In contrast to 1D diffusion problems – where the distance from wall to fluid node is constant for each node – curved boundaries have a different wall-node distance for every discrete node. This influences the numerical error as was shown by Li et al. [1]. It can be concluded from the presented results in Figure 5 that all investigated collision operators and boundary conditions provide second order accuracy for curved boundaries regarding the grid resolution. Thermal MRT collision operators [12,13] are more accurate compared to the investigated thermal BGK operator [16]. However, boundary conditions have a major influence on the numerical accuracy. It should be noted that boundary conditions proposed by Li et al. [1] have a greater numerical accuracy in the regarded case than the conditions proposed by Liu et al. [15].

In particular scheme 1 (eqs. (5)-(6)) provides the best accuracy. Linear and quadratic interpolated boundary conditions proposed by Liu et al. [15] rely on 3D interpolation routines to determine the exact node temperature which causes a greater numerical error and an irregular course. quadratic interpolated boundary conditions are superior to linear interpolated. Scheme 1 provides the greatest accuracy among all investigated boundary conditions.

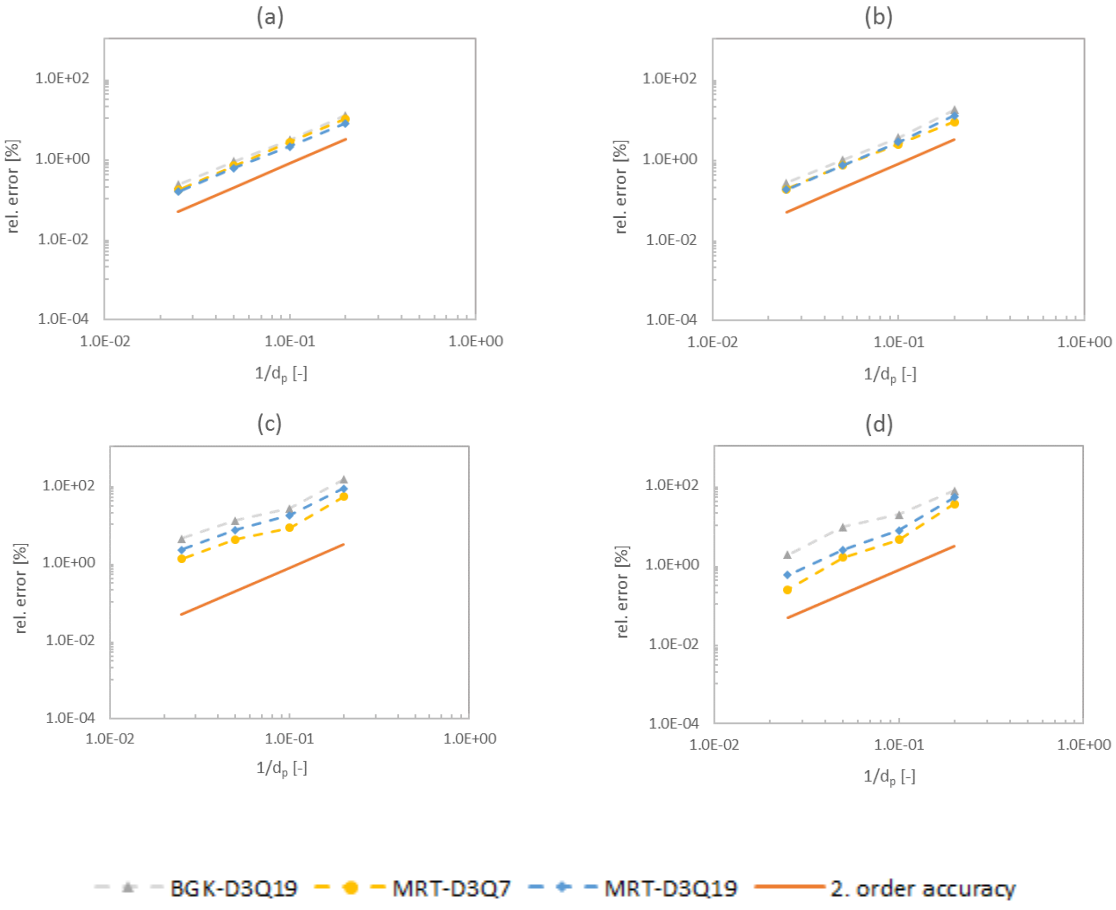

Figure 5: Relative error over grid resolution $1/d_p$ for diffusive heat transfer of an isothermal sphere: (a) thermal bounce back scheme 1, (b) thermal bounce back scheme 3, (c) linear interpolation and (d) quadratic interpolation.

3.2 Forced convection case

Numerical investigations of an isothermal sphere passed by a fluid were performed in order to study the influence of the convective part of the thermal LBM model. The Reynolds number was stepwise increase up to $Re = 800$ and the Prandtl number was set to $Pr = \nu/\alpha = 1$ for all simulations. To eliminate wall effects the simulation domain was chosen to be $30 \cdot d_p \times 15 \cdot d_p \times 15 \cdot d_p$ with $d_p = 40$ with adiabatic and free slip boundary conditions at walls parallel to the flow. The flow is initiated at $-x\ wall$ with a constant fluid velocity and temperature. To verify the correctness of the flow conditions and the accuracy of the implemented LBM framework the obtained drag coefficients C_D were compared against established scientific closure correlations [18–24] and experimental data [25]. Obtained drag coefficients are presented in Figure 6.

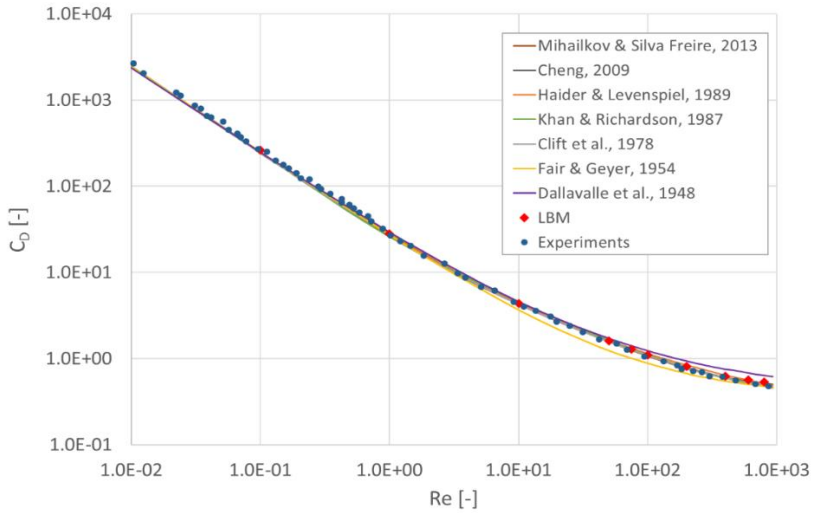

Figure 6: Drag coefficient over Reynolds number for a static sphere.

It can be concluded that the LBM reflects the flow conditions very accurately and in very good agreement with published results. If we regard the most recent correlation proposed by Mikhailov and Silva Freire [18] we obtain an average error of 3.72% for the present study.

For convection diffusion problems scheme 1 (eqs. (5)-(6)) proposed by Li et al. [1] with all introduced thermal collision operators were regarded. Particle averaged (or global) Nusselt numbers were evaluated and are presented in Figure 7 (a). Regarding the heat fluxes of the used set up, where the only heat sources are the domain inflow and the particle surface, and the heat sink is the domain outflow, the following relationship for the particle averaged Nusselt number can be derived:

$$Nu = \frac{U_0 A_{inlet}}{\pi d_p \alpha} \frac{(\bar{T}_{outlet} - \bar{T}_{inlet})}{(T_S - \bar{T}_{inlet})}, \tag{14}$$

where A_{inlet} is the surface area of the inlet, U_0 the fluid velocity (or superficial velocity) at the inlet, $\bar{T}_{outlet}$ and $\bar{T}_{inlet}$ are the velocity averaged fluid temperatures at the inlet and outlet of the domain and T_S is the particle surface temperature.

It can be concluded from the obtained results, that thermal BGK and MRT models prove high accurate results for convection-diffusion problems. However, the BGK operator remains stable only up to $Re = 240$ for $d_p = 40$. Thermal MRT models are up to three times more numerically stable than the thermal BGK model. Please note that the thermal BGK referred in this work is the collision operator proposed by Peng et al. [16]. It should be noted that BGK operators with a different g^{eq} may behave differently.

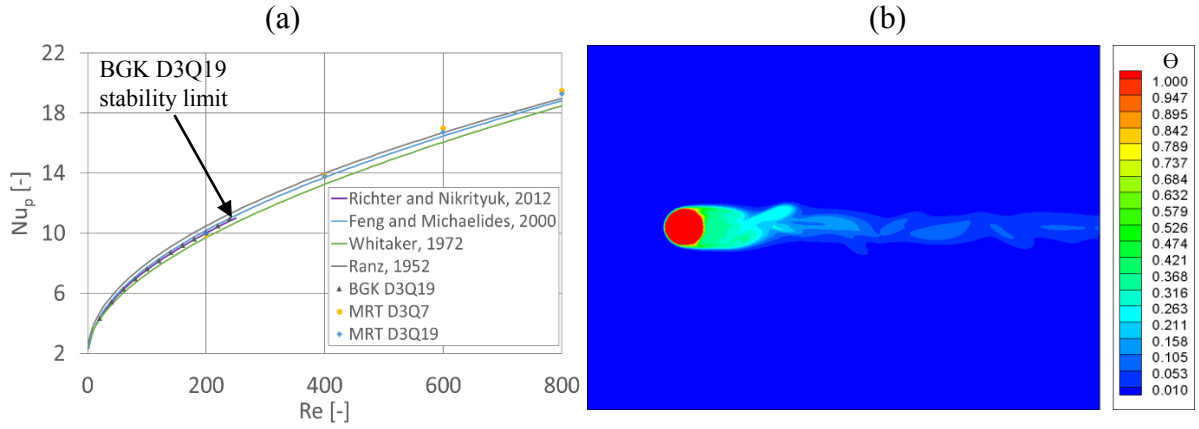

Figure 7: (a) Nusselt numbers over Reynolds numbers for a sphere attributed to forced convection at $Pr = 1$ (b) Distribution of dimensionless temperature $\theta = (T - T_{inlelt})/(T_s - T_{inlet})$ for $Re = 800$ and $Pr = 1$ prescribed with a double MRT D3Q19 model and scheme 1 (eq. (5)-(6)) at the sphere surface.

To evaluate local heat transfer coefficients, the temperature gradient at the boundaries is regarded:

$$Nu_i = h_f \cdot \frac{d_p}{k_f} = \frac{\partial T_i}{\partial x_i} \frac{d_p}{\left(T_S - T_{ref}\right)}, \tag{15}$$

where Index i represents the $i-th$ boundary node in which the local Nusselt number is evaluated. The particle diameter d_p is the reference length, T_S is the particle surface temperature and T_{ref} is the particle reference temperature which is here the temperature of the undisturbed fluid ($\overline{T}_{inlet}$). Apart from eq. (14) particle averaged Nusselt numbers can also be obtained by surface integration:

$$Nu = \frac{1}{\pi d_p^2} \int Nu_i dA \tag{16}$$

If the treatment is discrete, we can simplify this equation to $\mathrm{Nu} = \sum Nu_i / n_{nodes}$. Nu_i is the local Nusselt number (see eq. (15)) and n_{nodes} the number of considered discrete nodes. For more details on calculation of local heat transfer coefficients see [26].

Figure 8 (a) shows the obtained Nusselt numbers plotted over the corresponding polar angle ϕ for $\mathrm{Re} = 200$ and $\mathrm{Pr} = 1$.The maximum of the Nusselt number is located at the front stagnation point ($\phi = 0°$) while the minimum can be found at $\phi \approx 130°$ for the presented Reynolds number. The obtained results are compared to numerical studies by Dhole et al. [27].

It can be concluded, that the thermal MRT and the BGK models in combination with scheme 1 provide not only very accurate particle averaged Nusselt numbers but also accurately reflect their local distribution. The deviations to Dhole et al. [27] can be explained by the advantage of surface adapted meshes used in the introduced study. Especially the evaluation in a Cartesian mesh is regarded as a limiting factor. As can be seen in Figure 8 (a) and (b) D3Q7 suffers from notable over- and underestimation in the area of the curved boundary ($\phi \approx 20 - 70°$). This can be explained by the lack of some of the discrete velocities in the D3Q7 model which are however provided in the D3Q19 model.

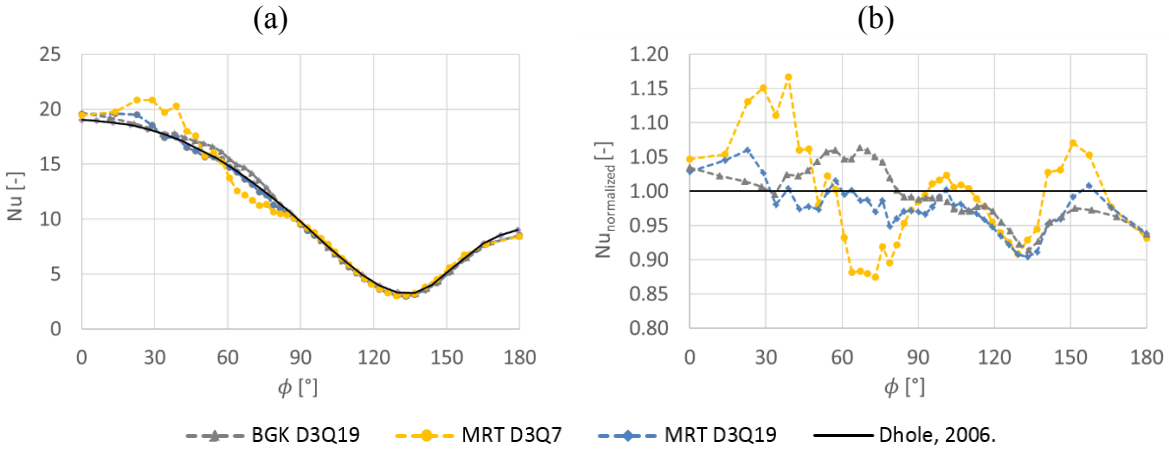

Figure 8: (a) Local Nusselt numbers of a sphere over polar angle ϕ for $Re = 200$ and $Pr = 1$ (b) Local Nusselt numbers normalized with results by Dhole et al. [27].

4 CONCLUSIONS

- A thermal LBM framework based on a double MRT model has been derived and its performance has been evaluated. Diffusion and convection-diffusion problems for plane and curved boundaries have been studied. It was shown that the presented LBM models provide highly accurate results for particle averaged and local heat transfer coefficients. Second order accuracy in space for all cases was achieved.
- MRT/MRT models [12] are superior to MRT/BGK [16] models in terms of numerical stability and accuracy. Double MRT models are up to three times more stable than the investigated thermal BGK operator.
- For curved boundaries the D3Q19 model provides more accurate results than the D3Q7 model, especially when the local heat transfer distribution is regarded. D3Q7 suffers from notable over- and underestimation in the area of the curved boundary ($\phi \approx 20 - 70°$) due to possibly the lack of some discrete velocities in the D3Q7 model.
- Thermal boundary conditions based on the thermal bounce back idea [1], are more accurate compared to boundary conditions based on energy balance and the usage of target/actual-value comparison [15]. Furthermore, methods based on the bounce back idea are far more efficient, since no 3D interpolation is required.

REFERENCES

[1] Li, L., Mei, R. and Klausner, J.F. Boundary conditions for thermal lattice Boltzmann equation method. *J. Comput. Phys.* (2013) **237**:366–395.

[2] Hill, R.J., Koch, D.L. and Ladd, A.J.C. The first effects of fluid inertia on flows in ordered and random arrays of spheres. *J. Fluid Mech.* (2001) **448**:213–241.

[3] Hill, R.J., Koch, D.L. and Ladd, A.J.C. Moderate-Reynolds-number flows in ordered and random arrays of spheres. *J. Fluid Mech.* (2001) **448**:243–278.

[4] Beetstra, R., Van Der Hoef, M.A. and Kuipers, J.A.M. Drag force of intermediate reynolds number flow past mono- and bidisperse arrays of spheres. *AIChE J.* (2007) **53**:489–501.

[5] Gunn, D.J. Transfer of heat or mass to particles in fixed and fluidised beds. *Int. J. Heat Mass Transf.* (1978) **21**:467–476.

[6] Gnielinski, V. Wärme- und Stoffübertragung in Festbetten. *Chemie Ing. Tech.* (1980) **52**:228–236.

[7] Tavassoli, H., Peters, E.A.J.F. and Kuipers, J.A.M. Direct numerical simulation of fluid-particle heat transfer in fixed random arrays of non-spherical particles. *Chem. Eng. Sci.* (2015) **129**:42–48.

[8] Wakao, N., Kaguei, S. and Funazkri, T. Effect of fluid dispersion coefficients on particle-to-fluid heat transfer coefficients in packed beds. Correlation of nusselt numbers, *Chem. Eng. Sci.* (1979) **34**:325–336.

[9] He, X., Chen, S. and Doolen, G.D. A Novel Thermal Model for the Lattice Boltzmann Method in Incompressible Limit. *J. Comput. Phys.* (1998) **146**:282–300.

[10] Bhatnagar, P.L., Gross, E.P. and Krook, M. A Model for Collision Processes in Gases. I. Small Amplitude Processes in Charged and Neutral One-Component Systems. *Phys. Rev.* (1954) **94**:511–525.

[11] D'Humières, D., Ginzburg, I., Krafczyk, M., Lallemand, P. and Luo, L.-S. Multiple-relaxation-time lattice Boltzmann models in three dimensions. *Philos. Trans. A. Math. Phys. Eng. Sci.* (2002) **360**:437–451.

[12] Li, L., Mei, R. and Klausner, J.F. Lattice Boltzmann models for the convection-diffusion equation: D2Q5 vs D2Q9. *Int. J. Heat Mass Transf.* (2017) **108**:41–62.

[13] Yoshida, H. and Nagaoka, M. Multiple-relaxation-time lattice Boltzmann model for the convection and anisotropic diffusion equation. *J. Comput. Phys.* (2010) **2297**:774–7795.

[14] Bouzidi, M., Firdaouss, M. and Lallemand, P. Momentum transfer of a Boltzmann-lattice fluid with boundaries, *Phys. Fluids.* (2001) 13:3452–3459.

[15] Liu, C.-H., Lin, K.-H., Mai, H.-C. and Lin, C.-A. Thermal boundary conditions for thermal lattice Boltzmann simulations, *Comput. Math. with Appl.* (2010) **59**:2178–2193.

[16] Peng, Y., Shu, C. and Chew, Y.T. Simplified thermal lattice Boltzmann model for incompressible thermal flows, *Phys. Rev. E.* (2003) **68**:26701.

[17] Kruggel-Emden, H., Kravets, B., Suryanarayana, M.K. and Jasevicius, R. Direct numerical simulation of coupled fluid flow and heat transfer for single particles and particle packings by a LBM-approach. *Powder Technol.* (2016) **294**:236–251.

[18] Mikhailov, M.D. and Freire, A.P.S. The drag coefficient of a sphere: An approximation using Shanks transform. *Powder Technol.* (2013) **237**:432–435.
[19] Cheng, N.S., Comparison of formulas for drag coefficient and settling velocity of spherical particles. Powder Technol. (2009) **189**:395–398.
[20] Haider, A. and Levenspiel, O. Drag coefficient and terminal velocity of spherical and nonspherical particles. *Powder Technol.* (1989) **58**:63–70.
[21] Khan, A.R. and Richardson, J.F. The Resistance To Motion of a Solid Sphere in a Fluid, Chem. Eng. Commun. (1987) **62**:135–150.
[22] Clift, M.E., Grace, R. and Weber, J.R. Bubbles, Drops and Particles. (1978).
[23] Fair, G.M. and Geyer, J.C. Water Supply and Waste-water Disposal, Wiley, (1954).
[24] DallaValle, J.M. and Klemin, A., Micromeritics: the technology of fine particles. (1943) 428 .
[25] Schlichting, H. and Gersten, K. Boundary-Layer Theory, Vol. IX (2017).
[26] Kravets, B. and Kruggel-Emden, H. Investigation of local heat transfer in random particle packings by a fully resolved LBM-approach. *Powder Technol.* (2017) **318**:293–305.
[27] Dhole, S.D., Chhabra, R.P. and Eswaran, V. A numerical study on the forced convection heat transfer from an isothermal and isoflux sphere in the steady symmetric flow regime. *Int. J. Heat Mass Transf.* (2006) **49**:984–994.

V International Conference on Particle-based Methods – Fundamentals and Applications
PARTICLES 2017
P. Wriggers, M. Bischoff, E. Oñate, D.R.J. Owen, & T. Zohdi (Eds)

AN APPROACH TO DEM MATERIAL CHARACTERIZATION IN COHEISVE GRANULAR BULK SOLID MATERIALS

LIZ I. DEL CID[1] AND AJITH SUBRAMANIAN[2]

[1,2]Overland Conveyor Company, Inc.
ThyssenKrupp Industrial Solutions, USA
1536 Cold Blvd, Bldg. 4 Suite 150
Lakewood, Colorado, USA 80401
[1]LDelCid@overlandconveyor.com, [2]AjithSub@overlandconveyor.com
http://www.overlandconveyor.com/

Key words: Granular Materials, DEM, Angle of Repose, Cohesion, Contact Problems.

Abstract. In bulk handling applications, such as conveying and storage, understanding the DEM particle characteristics to best simulate the flow of particulate systems at the macroscopic scale addresses an uncertainty in the DEM simulation of operational unit design and handling scenarios. This research provides a better understanding of the role adequate DEM material properties have on the flow-ability of bulk solid materials through the development, implementation and application of a generic material model procedure used in developing DEM input properties from physical testing data. This investigation proposes coupling physical material testing procedures with a DEM history dependent particle-particle macroscopic elasto-plastic adhesive contact model that accounts for both elastic and plastic contact deformations and cohesive attractions [1, 2]. The research application tasks are focused on three major areas: 1) measure a bulk solid's cohesive and frictional properties under mass flow and pressure, 2) simulate each material sample through a series of test controlled standards, 3) verify the suitable predicted material properties in the test applications simulate and are comparable to experimental results. As part of physical testing, such simulations can be used as part of the optimization for bulk handling design and operation.

1 INTRODUCTION

The interactions between granular bulk material and machinery plays an important role in our mining industry. A promising model of these interaction comes from the discrete element method. The difficulty with DEM however, is determining the behavioral flow of the macro material from the material micro-properties. In DEM, each particle has material parameters that influence the particle and its bulk behavior (e.g. spring stiffness, friction coefficients, damping values, bonding strength). Laboratory experiments and in-situ tests are necessary to determine these properties before any useful modelling can be performed. Developing methods to accurately calibrate and numerically quantify the bulk mechanical behavior of granular materials from measured properties is a formidable task [3-5]. Even then, the resulting simulations and the validity of the measured parameters is not without uncertainty.

The objective of this study is to develop a calibration process in which the DEM material parameters can be determined. For this purpose, experimental and DEM results from shear tests and industry field tests are used.

2 NUMERICAL MODELING USING A MACRO ELASTO-PLASTIC ADHESIVE (MEPA) MODEL

The contact model used in this study follows the MEPA cohesive model implementation for stress history dependency. The MEPA model is a three branched non-linear contact model that simulates the elastic and plastic regimes of particulate solids. It is capable of modeling material yielding through hysteresis and steady-state flow. This section describes the approach to the contact duration with cohesive attraction for each particle contact.

2.1 The MEPA Cohesive Model

The MEPA model uses a maximum force-based failure criterion. It determines the maximum displacement of the contact with a material stiffness described by the material's tensile strength, elastic modulus and Poisson's ratio. This model is used to simulate the mechanical behavior of material physical data in a shear test rather than the micro and molecular mechanics laws. It simulates the results from the physical testing used to determine the parameters of the Mohr-Coulomb shear failure criterion and complements studies in cohesive, frictional bulk solids for micro- and macro-models of different materials [6-12].

2.2 Particle Contact Constitutive Model

The relationship between the interaction force and the normal overlap of two rigid DEM particles is shown in Figure 1. The loading, unloading/re-loading and cohesive branches in the MEPA model are represented by four parameters: the virgin loading stiffness parameterk_1, the unloading and reloading stiffness parameter k_2, the cohesive stiffness parameter k_{adh} and the index parameter n, controlling the nonlinear force-displacement response of the system [9-11]. In the initial loading of the contact, the force increases with stiffness k_1. A linear viscous damping dash-pot is used to dissipate energy during contact. Cohesion between the contacts is represented by cohesive stiffness k_{adh}, which allows for attraction forces controlled by a limiting force f_{min}. Note, when n = 1, the model becomes linear and is represented by the branched model of Figure 1a. If k_1 is set equal to k_2, the model is reduced to the linear or Hertzian contact model previously discussed. Each branch can be expressed by the following sets of bounding equations:

$$f_1(\delta) = k_1\delta^n \tag{1}$$

$$f_2(\delta) = k_2\left(\delta^n - \delta_p^n\right) \tag{2}$$

$$f_3(\delta) = -k_{adh}\delta^n \tag{3}$$

where $f_1(\delta)$ represents the virgin loading branch, $f_2(\delta)$ the re/unloading branch, and $f_3(\delta)$ the cohesive branch. The branched relationship as a whole can be expressed as:

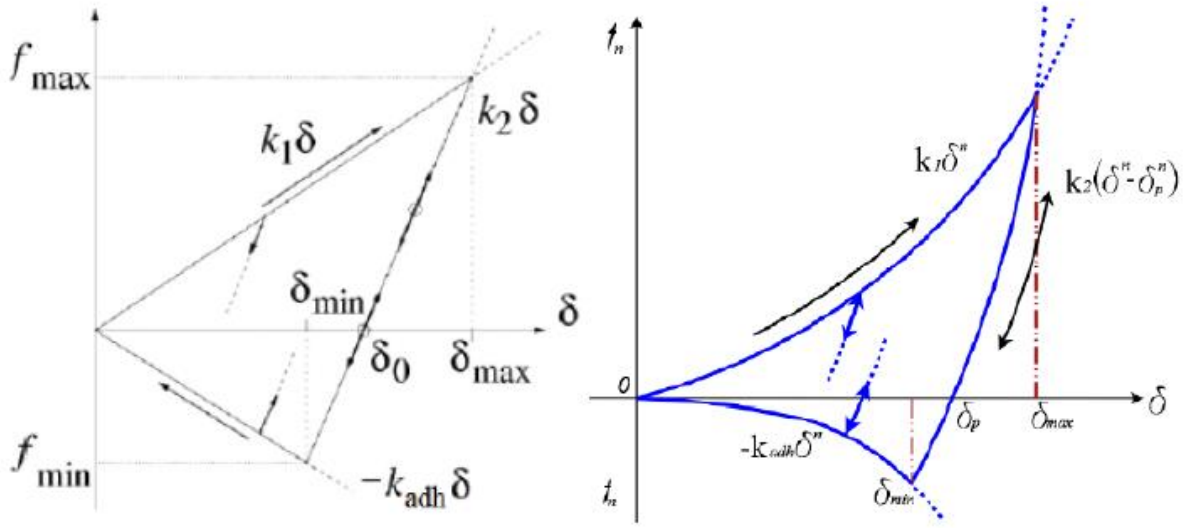

(a) Linear MEPA cohesive contact law. (b) Non-linear MEPA cohesive contact law.

Figure 1: Different MEPA contact models from [13].

$$f_{hys} = \begin{cases} f_1(\delta) & if \quad f_2(\delta) \geq f_1(\delta) \\ f_2(\delta) & if \quad f_1(\delta) > f_2(\delta) > f_3(\delta) \\ f_3(\delta) & if \quad f_3(\delta) \geq f_2(\delta) \end{cases} \tag{4}$$

The normal force on particle i is described by:

$$\boldsymbol{f}_0^n = -\gamma_n \boldsymbol{v}_n + f_{hys}\boldsymbol{n} \tag{5}$$

with the normal direction unit vector $\hat{n}$ directed from the center of particle j to particle i. The variable $\boldsymbol{v}_n$ describes the normal relative velocity of the particle and γ_n the viscous dissipation coefficient. The tangential force includes dissipation due to Coulomb friction and tangential elasticity that allows for stick-slip behavior at the contact level [6, 11-12]. The tangential force is related to the normal force via Coulomb's law in equation 6.

$$f^t \leq \mu_s f_{hys} \tag{6}$$

The maximum adhesion is determined by the stiffness parameters and the maximum normal overlap f_{max}. The tangential stiffness is calculated based on the contact stiffness k_t, which is set to the value of k_1. The tangential force is calculated from the product of the tangential stiffness and the tangential displacement, subject to the frictional limit according to Coulomb's law. At the maximum contact overlap, f_{max}, the contact stiffness increases instantaneously to the value k_2. Further loading and unloading is defined by the force-displacement relation $f = f_2(\delta)$. Elastic unloading to a zero contact force leads to a non-zero contact overlap equal to the maximum plastic contact indentation, $\delta = \delta_p$, which is recorded and updated over the contact lifetime. When the contact overlap is further decreased as the

particles separate, the contact force enters the tensile regime. The maximum tensile contact force $f = -k_{adh}\delta_{min}^{n}$ that the contact can experience corresponds to a contact displacement $\delta = \delta_{min}$. Further unloading in the tensile regime generates a tensile contact force that decreases in accordance with $f = -k_{adh}\delta$. In addition to the loading and unloading branches shown in Figure 1a and b, loading and unloading may also occur within the bounding branches. Any loading stage within the bounding branches loads or unloads elastically in accordance with $f = f_2(\delta)$ [14].

3 SETUP OF CALIBRATION PROCEDURE

To provide the experimental shearing data of the material under various conditions, the laboratories of Jenike & Johanson are used. To assist in the calibration of numerical parameters required for DEM simulations a set of in situ materials tests are also performed. The material properties should represent a range of possible operating conditions, as used in the design process. These standards will be inferred to be applicable by choice of and referenced by the test laboratory. A secondary purpose of the testing is for the DEM analyst to understand unique properties of the materials outside of the tests described that might impact the behavior of the bulk material.

3.1 Material Preparation

Proper collection of data for DEM simulations starts with a representative collection of the sample material. Figure 2 shows an example of material pulled from a transfer line and has been dried before proceeding. The bulk material is further sieved for size distribution and conditioned for uniformity of testing. All material smaller than ~1.5mm is set aside and not included in further testing.

Figure 2: Images of received material (Waste Rock and Clay Ore)

3.2 Density Testing

The density of the test samples is evaluated using containers having a minimum minor dimension of 10x the median particle for each sample. The container is filled through a sieve

approximately 2x the median size and weighed after filling without vibration or jostling. The container with material is weighed and the internal dimensions of the container measured to calculate the volume. The average density is defined as the total material mass divided by the volume filled by the material [15].

In the simulation, the assembly of particles is given an initial density and the system allowed to reach static equilibrium. The density is calculated in the same manner as the physical test. Using an iterative approach, the DEM particle density is modified until the average density is representative of the measured value.

3.3 Wall Friction

The preferred method of measuring the wall friction is with a modified shear cell with a minimum dimension of 5x the median particle. A bed depth of at least 3x the median particle is used to limit rotation. If a shear cell is used, tests will be made with pressures up to the equivalent hydrostatic pressure of approximately 50x the median particle deep.

In situ test cases where a layer of a single particle deep slides on an inclined plane without rolling, the wall friction is determined as the tangent of the wall angle determined from an inclined plane test procedure as shown in figure 3.

(a) Image of netting for wet bulk sliding.

(b) DEM vector simulation for the sliding friction analysis of wet clay ore.

Figure 3: Lab image of wall friction lab and DEM simulation setup.

In the simulation, the particles are initially at rest as the plane increases in angle from the horizontal. The velocity vector of the particles are tracked and the wall friction angle calculated as the angle upon which the velocity vector of the particles is no longer moving with the plane and the angular velocity is still zero indicating slip condition only.

3.4 Rotational Resistance

Rotational resistance is tested on an inclined plane test stand. If the particles roll before sliding on an inclined chute material, the sliding will have to be determined with a shear cell test and the rolling resistance is determined with an inclined test on the wall material sample. If it is necessary to prevent particle sliding on an inclined plane the rolling resistance is tested with an otherwise smooth surface equipped with lateral rows of wire of diameter ~20% of the

median particle size spaced at 2x the particle median size. Alternatively, a machined saw tooth surface of the same dimensions oriented to resist sliding is used.

In the simulation, the particles are initially at rest as the plane increases in angle from the horizontal. The angular velocity of the particles are tracked and the rotational resistance coefficient calculated as the angle upon which the angular velocity of the particles is non-zero.

3.5 Angle of Repose

A conical angle of repose test as described in the CEMA 550 with a rough base is used to characterize the bulk material flow potential. For the DEM simulation, the geometry is scaled to the selected particle size accordingly. Figure 4 displays pile formations obtained following the testing standard.

(a) Dry waste rock pile formation (b) Wet clay ore file formation

Figure 4: Lab image of angle of repose pile formation for dry and wet waste rock and clay.

Figure 5 demonstrates the DEM simulation iterations of the same simulated procedure as the sliding inter particle friction coefficient increases. The number of iterations required depends on the accuracy desired and the initial friction coefficient range. Typically 6 iterations are performed with dry loose material under a one degree tolerance of the measured angle of repose. Figure 6 displays the measurement made by the DEM simulation when the system has reached static equilibrium.

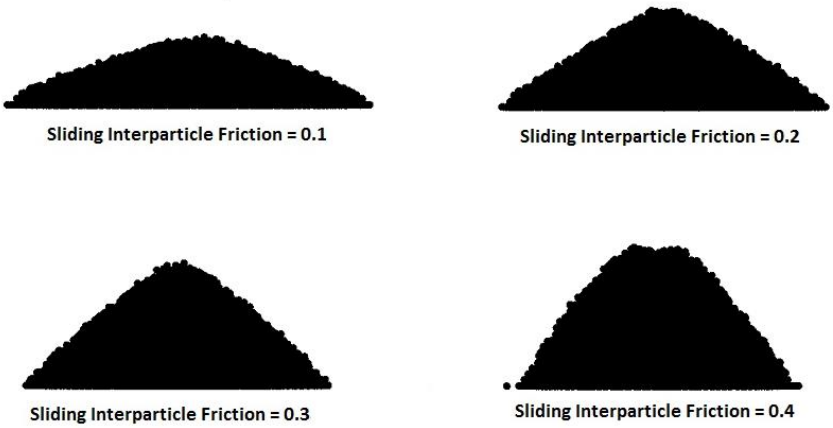

Figure 5: Angle of repose iterations of simulated material.

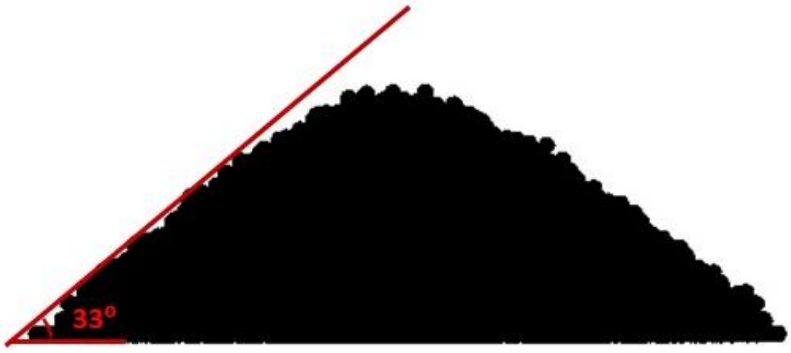

Figure 6: Angle of repose of final material simulation.

3.5 Physical Translational Shear Tester

The physical shearing test performed uses the Jenike Shear Tester, a translational shear tester. The shear cell is composed of a base located on the frame of the shearing machine. A ring rests on top of the base with a cover or lid. The surface conditions of the bottom of the cover and the inside of the base are rough to increase adhesion of the tested solid. The material is loaded into the base and ring and then covered. A normal force, F_N is applied centrally on the cover and held. The upper part of the shear cell is displaced horizontally against the fixed bottom base by a stem. The measured value is the shearing force exerted by the stem [16]. The normal stress, σ, and the shear stress, τ, acting in the horizontal plane between the top and bottom rings are determined by dividing the normal force, F_N; and shear force, F_S, by the cross-sectional area of the shear cell, A. The standard shear cell is 95.25 mm in diameter with a shearing rate of 4:487 x 10^{-5} $\frac{m}{sec}$ [16, 17]. A schematic of the physical tester with the dimensions defined in millimeters is shown in figure 7.

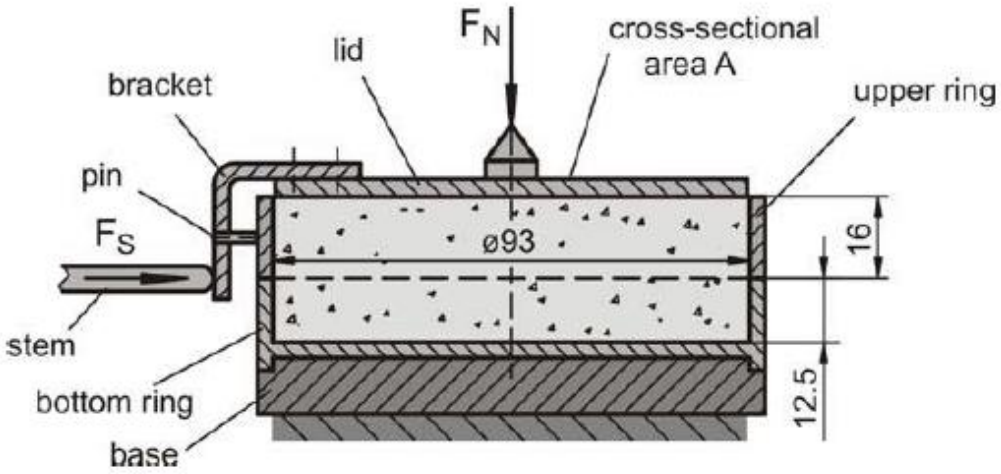

Figure 7: Jenike and Johanson direct shear test schematic from [16].

In the simulation, the experimental data sets are obtained with the ring cell shear tester developed by Dietmar Schulze [18, 19] are used to minimize localized stresses. Figure 8

shows a schematic of a ring shear tester series RST-01 [16, 18-20]. The ring-shaped bottom ring of the shear cell contains the material sample, while the lid is placed on top of the material and fixed at a crossbeam. A normal force is exerted to the crossbeam in the rotational axis of the shear cell and transmitted through the lid to the material sample. The counterbalance force, F_A, acts in the center of the crossbeam and counteracts the gravity forces of the lid, the hanger, and the crossbeam [16]. To shear the sample, the lid and the bottom ring of the shear cell rotate relative to each other. This is achieved by rotating the bottom ring while the lid and the crossbeam are prevented from rotating by the connecting tie-rods. Each of the tie-rods are fixed at a load-beam from which the forces acting on cell can be measured. The test procedure is comparable to the one performed by the Jenike shear tester. The yield locus from the measured shear points as per the physical test procedure. Modeling the consolidation of material with time history is the advantage of using the MEPA model as the particle contact model.

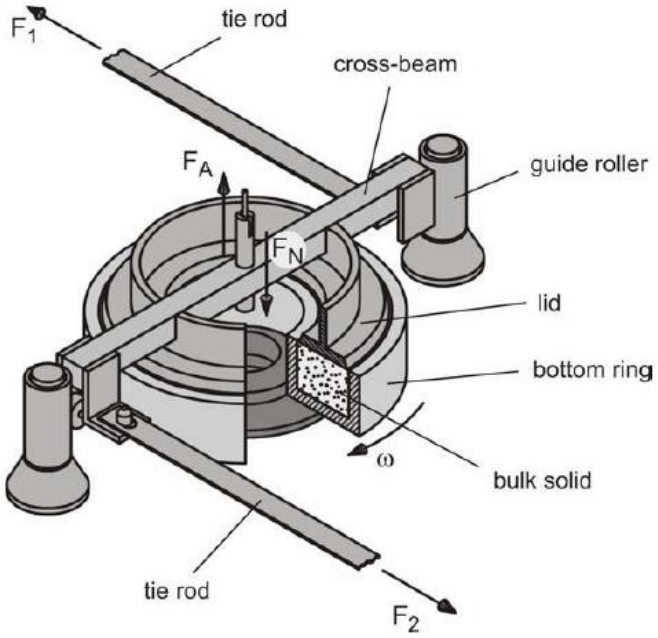

Figure 8: Shear Cell of a ring shear tester type RST-01 from [16, 18-20].

4 BULK MATERIAL PROPERTIES DETERMINATION

This procedure to DEM material characterization has been used for dry material over a number of industry projects. Cohesive materials provide the greatest uncertainly in material flow behavior. For this investigation various tests were conducted on wet copper ore with a top size of 7 mm. The simulation involved evaluating the particle size distribution seen in figure 9. Some of the experimental parameters are listed on Table 1. The boundary material for static wall friction testing #2B finish stainless steel sheet. An image of the copper ore material is shown in figure 10.

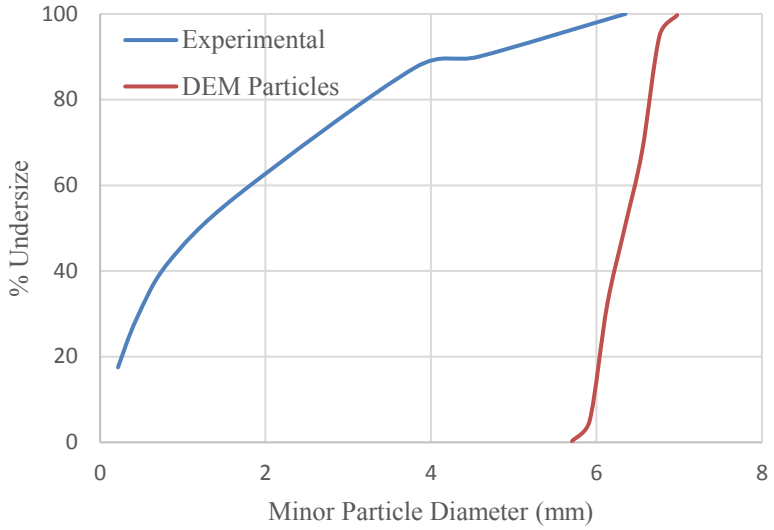

Figure 9: Particle size distribution of copper ore.

(a) Physical copper ore material at 8% mc (b) Virtual DEM copper ore material at 8% mc.

Figure 10: Lab and DEM simulation image of the sample material copper ore at 8% moisture content.

Table 1: Measured properties of iron ore

Parameter	value
Particle Density, ρ_s $(kg\ m^{-3})$	2481.3
Bulk Density, ρ_{bl} $(kg\ m^{-3})$	1042.8-1752.4 (5% wb moisture content)
Bulk Density, ρ_{bl} $(kg\ m^{-3})$	1350.4-1797.3 (8% wb moisture content)
Internal Frictional Angle, φ (degrees)	47.3 (5% wb moisture content)
Internal Frictional Angle, φ (degrees)	46.7 (8% wb moisture content)
Wall Friction Angle, φ (degrees)	30.0 (5% wb moisture content)

5 RESULTS AND DISCUSSION OF DEM MATERIAL CHARACTERIZATION

The approach to characterizing cohesive copper ore started with lab tests, which provided the parameters values of Table 1 and the failure envelopes for a range of conditions. To begin, the young's modulus was set to known values for copper ore, approx. 113-119 GPa with a

Poisson's ratio of 0.34. These parameters governed the stiffness, k_1 and k_2, values of the elasto-plastic model. The inter-particle friction and cohesive stiffness were adjusted to simulate the experimental measured profile of the Mohr Coulomb failure criteria. For copper ore with 5% moisture content, figure 11 displays the data the DEM simulation was to closely match. The inter particle friction and cohesive stiffness used came to 0.35 and $k_{adh} = 3.56x10^8 \frac{N}{m}$ respectively. Figure 12 displays the resulting DEM profile of this condition.

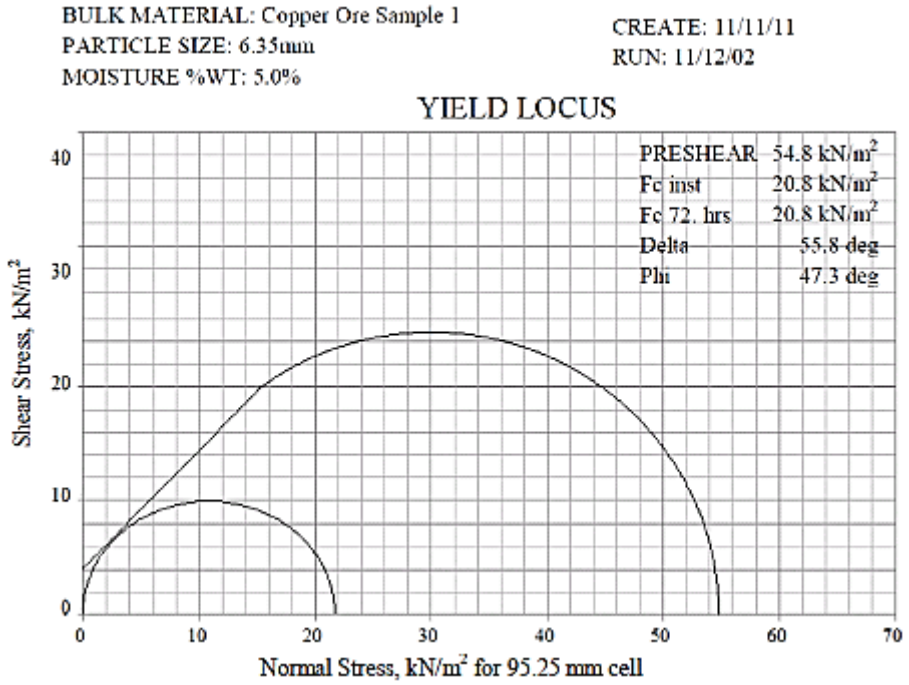

Figure 10: Physical testing results of the loading for Copper Ore Sample 1 at 5% mc.

The angle of repose simulation was not performed as this test has a greater uncertainty with highly cohesive materials. However, the wall friction test using the inclined plane simulation was performed and a frictional coefficient value of 0.7 was observed resulting in a wall frictional angle of 35 degrees ± 3 degrees. The number of iterations performed was not sufficient to more closely simulate the laboratory findings. Table 2 summaries the DEM parameters determined through the simulation of the laboratory tests. Utilizing the parameters determined for copper ore, the agglomeration of the physical material can be observed in the virtual DEM simulated material as seen in figure 10. To perform a through calibration requires computation time and human resources. For this material set, a loose tolerance was acceptable to minimize project cost.

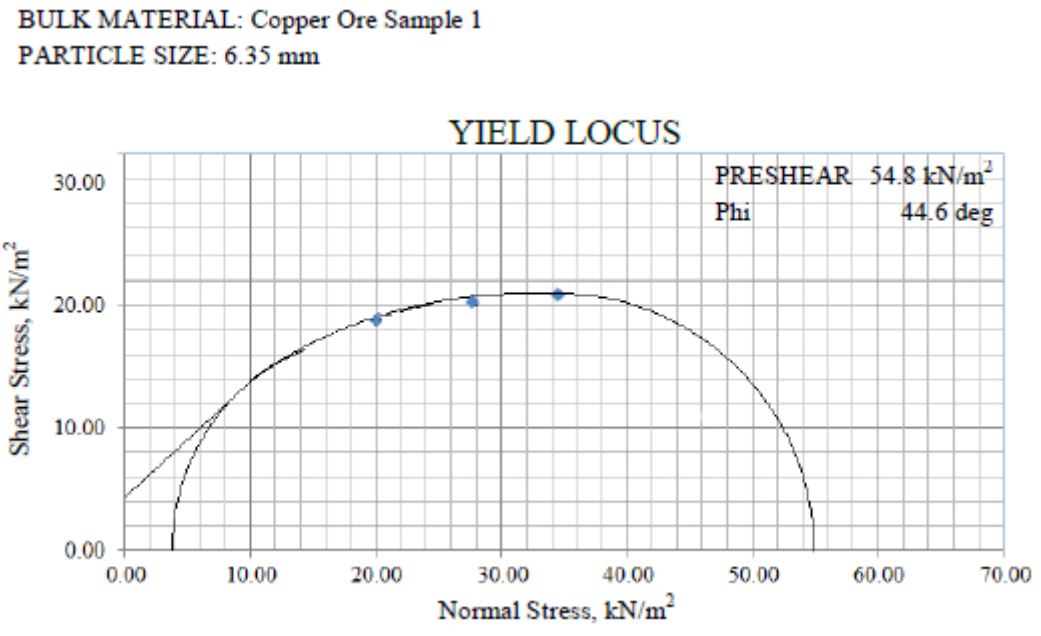

Figure 11: Simulated testing results of the loading for Copper Ore Sample 1 at 5% mc.

Table 2: Simulated properties of iron ore

Parameter	Simulation value
Internal Frictional Angle, φ (degrees)	47 ± 3 (5% wb moisture content)
Internal Frictional Angle, φ (degrees)	45 ± 3 (8% wb moisture content)
Cohesive Stiffness, $k_{adh}\left(\frac{N}{m}\right)$	$3.56\ x\ 10^8$ (5% wb moisture content)
Cohesive Stiffness, $k_{adh}\left(\frac{N}{m}\right)$	$5.93\ x\ 10^8$ (8% wb moisture content)
Wall Friction Angle, φ (degrees)	35 ± 3 (5% wb moisture content)

6 CONCLUSION

Numerous methods for material testing were presented to assist in the calibration process of the material parameters needed in DEM simulations. In this study, numerical results for cohesive granular material was compared to experimental data of copper ore at varying moisture content levels. The DEM parameters such as frictional coefficients and cohesive stiffness were varied until acceptable material conditions were met. The developed technique has proven to be successful in our projects involving the transfer of dry granular materials and has shown promising results in the calibration of cohesive materials. For full implementation of this method, optimizing simulation time would aid the computational cost. Further investigation is being conducted to access the validity and accuracy of our approach to DEM material characterization for cohesive granular materials.

8 REFERENCES

[1] L. Del Cid and G. Mustoe, “A Discrete Element Analysis of Cohesive Granular Bulk Solids Materials”, Proceedings of the IV Int. Conf. on Particle-Based Methods –

Fundamentals and Applications, 237-247 (2015).
[2] L. Del Cid (2015). A Discrete Element Methodology for the Analysis of Cohesive Granular Bulk Solid Materials (Doctoral dissertation). Colorado School of Mines.
[3] C.J. Coetzee, and D.N.J Els, "Calibration of Granular Material parameters for DEM Modelling and Numerical Verification by Blade-Granular Material Interaction", Journal of Terramechanics, 46 (2009) 15-26.
[4] C.J. Coetzee, and D.N.J. Els, "Calibration of Discrete Element Parameters and the Modelling of Silo Discharge and Bucket Filling", Computer and Electronics in Agriculture 65 (2009) 198-212.
[5] C.J. Coetzee, D.N.J Els, and G.F. Dymond, "Discrete Element Parameter Calibration and the Modelling of Dragline Bucket Filling", Journal of Terramechanics, 47 (2009) 33-44.
[6] Antony S. J., W. Hoyle, and Y. Ding. Granular materials: fundamentals and applications. Royal Society of Chemistry, 2004.
[7] Brown R. L. and J. C. Richards. Principles of powder mechanics. 1970.
[8] Radjaï F., F. Dubois, et al. Discrete-element modeling of granular materials. Wiley, 2011.
[9] Johnson K.L., K. Kendall, and A. D. Roberts. Surface energy and the contact of elastic solids. Proceedings of the Royal Society of London. A. mathematical and physical sciences, 324(1558):301-313, 1971.
[10] Lian G., C. Thornton, and M. J. Adams. A theoretical study of the liquid bridge forces between two rigid spherical bodies. Journal of Colloid and Interface Science, 161(1): 138{147, 1993.
[11] Gröger T., U. Tüzün, and D. M. Heyes. Modelling and measuring of cohesion in wet granular materials. Powder Technology, 133(1):203-215, 2003.
[12] Thakur S., J. P. Morrissey, J. Sun, J. F. Chen, and J. Y. Ooi. Particle scale modelling of cohesive powders for bulk handling applications. In EDEM Conference, 2011.
[13] da Cruz F., S. Emam, M. l. Prochnow, J. N. Roux, and F. Chevoir. Rheophysics of dense granular materials: Discrete simulation of plane shear flows. Physical Review E, 72(2):021309, 2005.
[14] Savage S. B. The mechanics of rapid granular flows. Advances in applied mechanics, 24:289-366, 1984.
[15] A. Grima and P. Wypych, "Development and Validation of Calibration Methods for Discrete Element Modelling", Granular Matter 13 (2011) 127-132.
[16] Schulze D. Flow properties of powders and bulk solids. Braunschweig/Wolfenbu ttel, Germany: University of Applied Sciences, 2006.
[17] Jenike A. W. Storage and ow of solids, bulletin no. 123. Bulletin of the University of Utah, 53(26), 1964.
[18] Schulze D. Development and application of a novel ring shear tester. Aufbereitungs-technik, 35(10):524-535, 1994.
[19] Schulze D. A new ring shear tester for flowability and time consolidation measurements. In Proc. 1st International Particle Technology Forum, pages 11-16, 1994
[20] Standard ASTM. D6773-02: Standard shear test method for bulk solids using the Schulze ring shear tester, ASTM international.

V International Conference on Particle-based Methods – Fundamentals and Applications
PARTICLES 2017
P. Wriggers, M. Bischoff, E. Oñate, D.R.J. Owen, & T. Zohdi (Eds)

ESTIMATION OF GRANULAR FLOW IMPACT FORCE ON RIGID WALL USING MATERIAL POINT METHOD

S. SEYEDAN [1], W.T. SOŁOWSKI [2]

[1] Department of Civil Engineering, Aalto University
Rakentajanaukio 4 A, 02150 Espoo, Finland
seyedmohammadjavad.seyedan@aalto.fi

[2] Department of Civil Engineering, Aalto University
Rakentajanaukio 4 A, 02150 Espoo, Finland
wojciech.solowski@aalto.fi

Key words: Granular Materials, Sand Flow, Generalized Interpolation Material Point.

Abstract. Landslides and avalanches cause loss of lives, as well as generate significant economic cost. Protection barriers help reduce the impact of such events. However, the design of the barriers requires the prediction of the landslide flow trajectory and the estimation of impact force. Material Point Method appears to have great potential for estimating those, since it can account for large displacement nature of sediment flows and their nonlinear behaviour. Therefore, it may be able to capture the complex interaction of landslides or avalanches with the ground and structures.

This study focuses on simulating granular flows with Generalized Interpolation Material Point Method. The calculations use a constitutive model inspired by the Bagnold theory of granular flow [1] to model sand landslide / avalanche experiment [2] with sand treated as a linear elasto-plastic material. Shown simulations aim was to replicate the experiment. In particular, the paper focuses on estimation of the impact force of sand flow on a fixed rigid wall. Such force estimation is a first step to validate the Generalized Interpolation Material Point Method for use as a tool for the design of barriers defending against landslides and avalanches.

1 INTRODUCTION

Natural or manmade phenomena may cause instabilities in slopes resulting in landslides and sediment flows. These flows may contain soil, debris and rock mixed together. The avalanches can reach high speed quickly after formation and carry significant amount of energy. Therefore, they can ravage areas and impose destructive forces onto anything on their way. The sediment flows and avalanches results in significant damages to infrastructures and economic losses every year while being also a threat to people living in the landslide prone areas. In order to reduce the threat of debris flows, protective actions are necessary. For example, protective barriers placed on the path of debris flows can stop the flows or at least decrease their speed and energy. Economical design of those protective barriers requires estimation of debris flow / avalanche impact force.

Researchers have used different approaches for estimating the impact force of debris flows. Empirical models were used alongside statistical analysis to identify problematic slopes [3]–[5]. Such an approach is certainly useful for general risk estimation. However, it is of limited help in design of the protection structures, as it cannot take details of each case into consideration. On the other hand, there are experimental data and tests which investigate the impact force of flows, e.g. [2], [6]–[8]. These tests are the most accurate and reliable approach, however, they can be very expensive, require significant time and, in many cases, simply not feasible as they cannot replicate full scale landslide. Therefore, numerical simulations may be the method, which could offer affordable assessment of the impact force of sediment flows. For example, Moriguchi et al. [2] performed numerical simulations within computational fluid dynamic framework, confined interpolation profile and Bingham constitutive model to simulate granular flow and estimated impact force of it on rigid obstacles [2]. On the other hand, Ceccato and Simonini [9] used Material Point Method (MPM) for modelling granular flows experiment in [2]. They used two different constitutive models (elastic-perfectly plastic and viscoplastic models) to describe granular materials.

This paper uses Generalized Interpolation Material Point to estimate normal impact force of sand flow on rigid barriers. The investigation focuses on replicating the dry Toyoura sand flow experiments [2].

2 GENERAL SPECIFICATIONS

2.1 Description of Laboratory Experiments

This paper presents modelling of small scale experiments on sand flow performed by Moriguchi et al. [2]. The described experiment involved placing 50 kg of dry Toyoura sand in a box on top of a flume with variable slope angles. After quick opening of the box, the sand flew on the flume surface, which was coated with the same sand used for the experiment. A load cell at the bottom of the flume measured the normal impact force on the obstacle. The opening mechanism is believed to be such that the sand box opening has no effect on the initial flow behaviour of the sand. Figure 1 shows a schematic illustration of the tests.

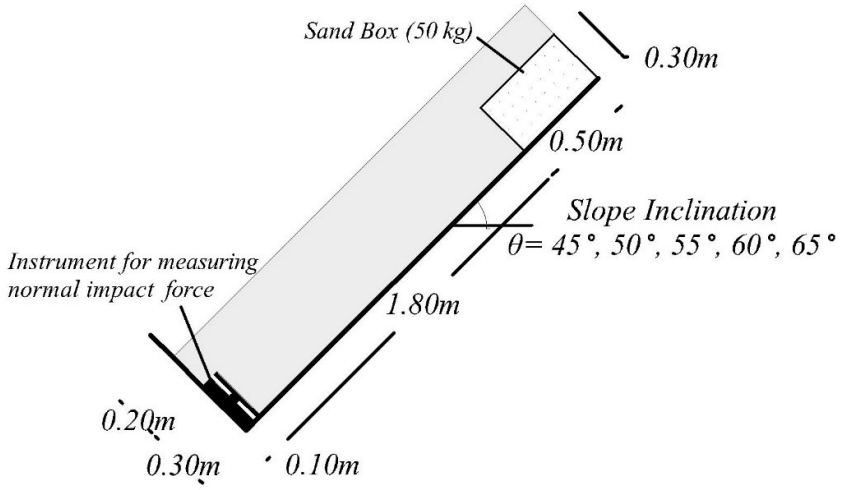

Figure 1- schematic illustration of the experiment tests (after [2])

2.2 Description of Numerical Models

The simulations shown used Generalized Interpolation Material Point (GIMP) method and investigated flow of Toyoura sand. Bardenhagen and Kober introduced GIMP in 2004 as an advancement to Material Point Method [10]. MPM is itself a development in particle cell method (PIC) tailored for solid mechanic by Sulsky et al. [11], [12]. Material Point Method simulations have the advantage of being free from mesh tangling common e.g. in the Finite Element Method and have no problem in modelling fluid-structure interaction [13] while using the continuum mechanics framework. In this research, GIMP method encoded in the software suite Uintah (http://uintah.utah.edu) was used.

The calculations approximated the laboratory experiments as plane strain problems with the flume in all models aligned to the horizontal axis and gravity varying instead of changing the flume inclination. In all the simulations, rigid wall was 0.3m high and 0.1m thick. The initial distance between the rigid wall and sand was 1.8m. Furthermore, a layer of the same sand, but fixed, approximated the surface coating. All the numerical model included an extra 0.3m domain in the left side of the rigid wall similar to simulations performed in [2]. This extra domain allowed for simulation of sand overtopping the wall. Figure 2 shows the schematics of numerical models used in this research. This figure also shows the temporary walls in the models. These walls blocked sand in the first 0.5s of simulation to replicate the initial stress in the soil and modelled the box in the experiments. The total simulation time was 2.5s, with the temporary walls deleted from all the models after the first 0.5s.

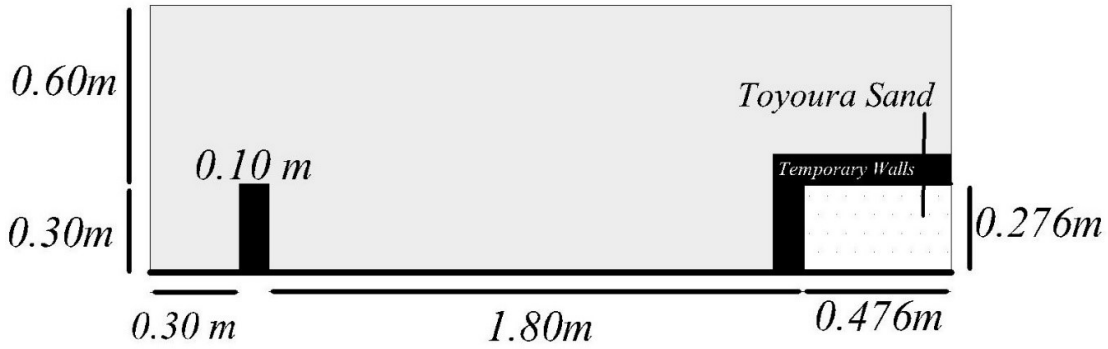

Figure 2- schematics illustration of numerical models

2.3 Constitutive Model

Numerical simulations used an elasto-plastic constitutive model based on the Mohr-Coulomb model enhanced with Bagnold scaling [1]. The sand was assumed to be a linear elastic material for stress states not on the yield surface. Equation 1 shows the formulation for 2 dimensional Coulomb friction criterion where τ is shear stress, σ is normal stress, $\tan\varphi$ is friction angle and c is cohesion [14]. Granular materials are cohesionless and c value is 0 in them.

$$\tau - \tan\varphi\,\sigma - c = 0 \tag{1}$$

Experiments have shown that flow of granular material happens in parallel layers [1]. Bagnold used this observation to express a dependency between shear stress and rate of shearing. Internal stress also effects shear stress along each layer. Those led to Bagnold scaling relation shown in equation 2 where τ is the shear stress, σ is the normal stress, $\tan\varphi$ is the internal friction parameter and $\dot{\gamma}$ is the rate of simple shear.

$$\tau - \tan\varphi\,\sigma \propto \dot{\gamma}^2 \tag{2}$$

The equation above can be generalised and used to enhance the Mohr-Coulomb model. Comparison of equations 1 and 2 shows that during the flow of granular material non-zero strain rate leads to some shear resistance, which is mathematically same to the Mohr-Coulomb cohesion. Therefore, one can use a factor of shear rate squared ($\eta\,\dot{\gamma}^2$) instead of cohesion in the Mohr-Coulomb yield surface equation. Such model should be suitable for granular flow that is flow for materials in which cohesion for small strain rates would be zero. Equation 3 shows the obtained formulation of the modified Mohr-Coulomb yield surface,

$$F = (\sigma_1 - \sigma_3) - (\sigma_1 + \sigma_3)\sin\varphi - 2\,(\eta\,\dot{\gamma}^2)\cos\varphi = 0 \tag{3}$$

where σ_1 the maximum is principal stress, σ_3 is the minimum principal stress, φ is the friction angle, $\dot{\gamma}$ is the rate of simple shear and η is the calibration parameter. The difference between this formulation and the Mohr-Coulomb model is just the replacement of cohesion with the factor related to the shear strain rate squared.

The implemented yield surface and its rate dependent mechanism of flow has provided good predictions when solid fraction of granular flow is constant (i.e. uniform flow). On the other hand, this constitutive law does not have any way to account for the non-uniformity [14] in the flow. Therefore possible non-uniformity of the flow should be addressed differently.

3 NUMERICAL MODEL

3.1 Choosing Parameters of Constitutive Model

The model requires calibration of 2 elastic parameters and 3 parameters related to the yield surface and flow behaviour of the material. The elastic parameters used were the shear modulus and the Poisson ratio. The shear modulus of sand is high at very small strain and decreases when strains become larger [15]. In the calculations, as the sand is in the state of flow and very large shear strains are applied to it, a very low value of 20 kPa was used. Even though the chosen value of shear modulus is very low, the extensive set of data provided in [15] on shearing of sand suggests that it is not unrealistic. Elastic modulus in this range has been used in other researches investigating granular flows [9], [16].

Investigations on heap flows and rough inclined planes [14], [17], [18] revealed the existence of two regions in the granular flows. One region in lower parts where the ground surface prevents the grains from flowing freely and deform volumetrically. Another region is near the surface of the flow where nothing blocks the motion of grains. The constitutive model implemented in the simulations cannot address that difference. Therefore, the simulations approximated that constrain with soil layers which have different Poison ratio to account for the non-uniformity of the material during the flow. In all the models, 5 layers of sands with different Poisson ratio were considered at the initial state. Figure 3 shows Poisson ratio of each

layer and their height in the beginning of simulations. Poisson ratio of the lowest layer was 0.495 (non-compressible) while the top layer had a Poisson ratio of 0.3 (a standard value for the Poisson ration for Toyoura sand).

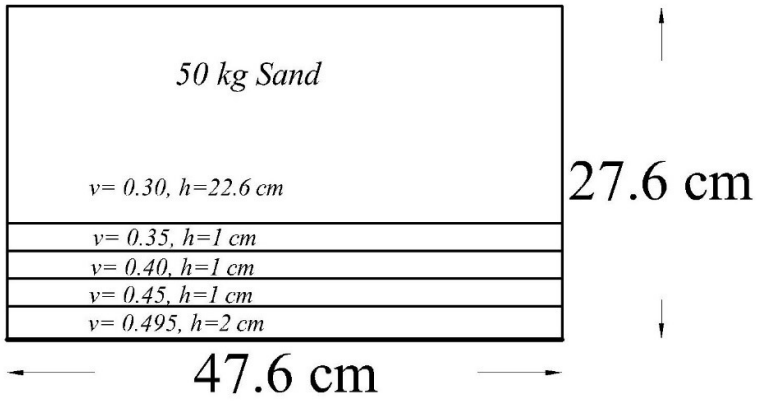

Figure 3- Poisson ratio of layers and their height (Not scaled)

The friction and dilation angles control the plastic behaviour of sand in the Mohr-Coulomb model. Laboratory tests on granular materials, including Toyoura sand, have shown that the friction angle at the critical state is independent from the initial void ratio and stress path. Furthermore, variations in the volumetric strain becomes zero when the critical state is reached [19]. The implemented constitutive model in this research is unable to model hardening / softening behaviour of soils. In addition, the initial void ratio of Toyoura sand in the experiment (0.917) is very close to the critical void ratios of Toyoura sand considering the possible range of pressure in the experiment. Therefore, we assumed that reaching the yield surface and the critical state happened simultaneously in the models. Consequently critical friction angle of Toyoura sand, which is 31° [20], and 0° dilation angle were used in all the simulations. Table 1 summarizes the parameters used in the simulations of the sand flow experiments.

Table 1- parameters in the numerical simulations

$\gamma\ (\frac{kg}{m^3})$	$G\ (kPa)$	υ	$\varphi\ (°)$	$\psi\ (°)$
1379	20	0.3 0.35 0.4 0.45 0.495	31	0

3.2 Calibration of Constitutive Model

Data available from the experiment on 45° inclination test was used in calibration of the extra parameter (η) in the constitutive model. That calibration parameter (η) was chosen such that the simulation gives very good estimation of the normal force as well as a similar flow profile to the one in the experiment. Figure 4 shows the calculated and experimental normal

force on the wall in time. It is clear that the numerical model estimated the normal force very well with the parameter η chosen equal to $0.15\ (Pa.s)^2$. It also shows that the model with $\eta = 0.15\ (Pa.s)^2$ estimated arrival time of the flow to the end of flume quite well.

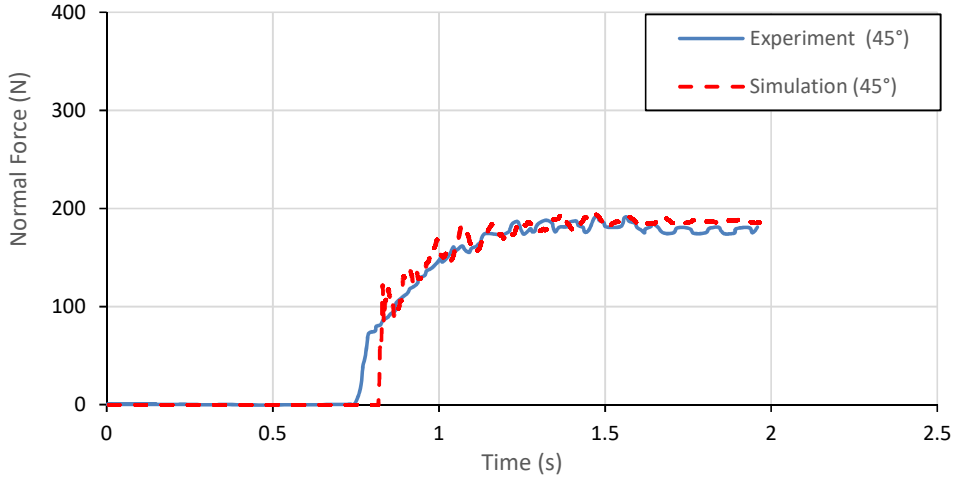

Figure 4- result of calibration

Furthermore, Figure 5 shows the simulated flow profile for the test with 45° and compares it with the experimental free surface of flowing sand (indicated by the black line). The simulated flow profile match the experiment free surface well especially in the later stages of the experiment.

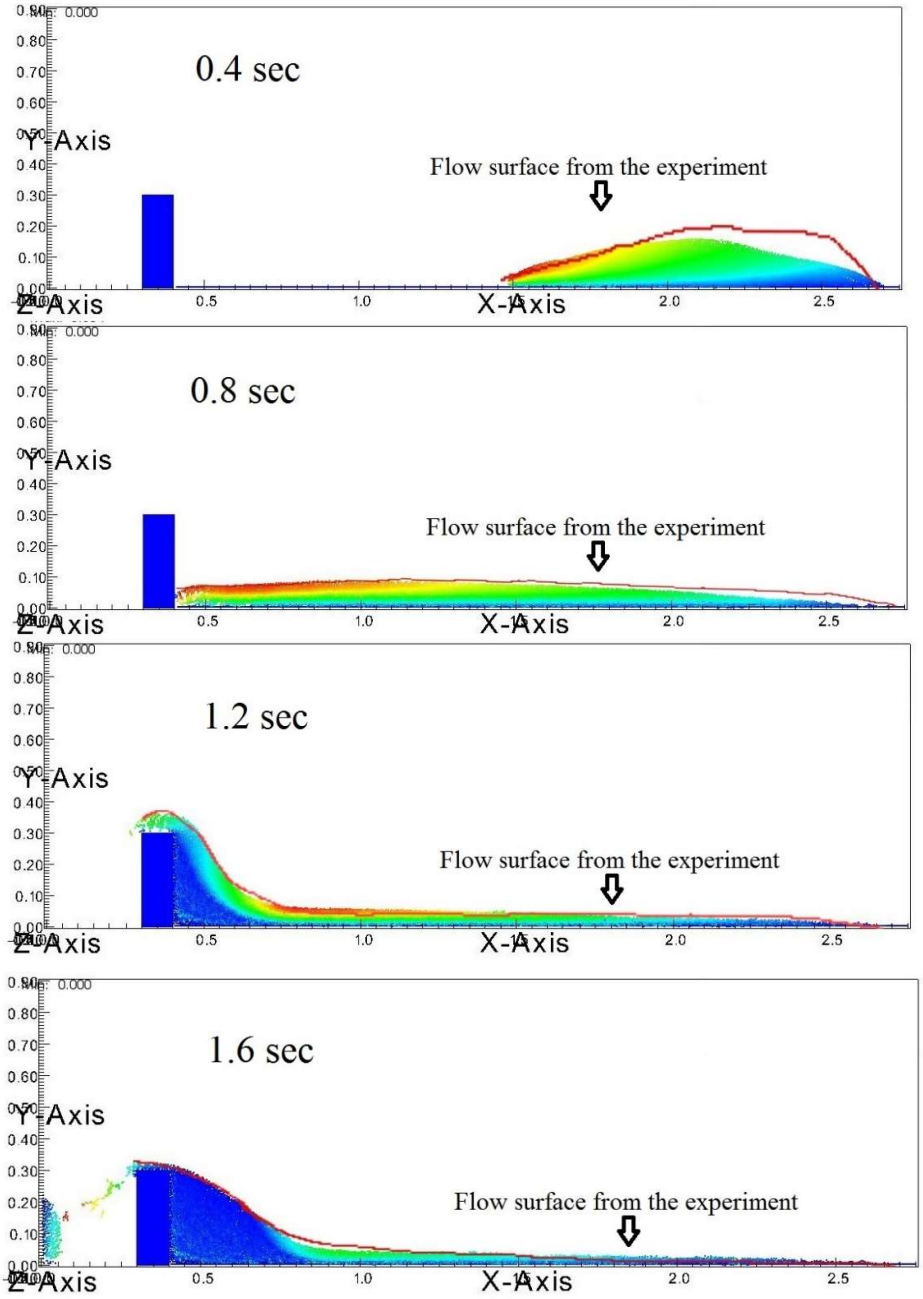

Figure 5- flow profile of numerical model with 45° inclination and 5 $(Pa.s)^2$

4 VALIDATION OF THE NUMERICAL MODEL

After calibration of the constitutive model, simulations modelled the experiments with 50°, 55°, 60° and 65° inclinations. All the simulations used 35064 particles, square computational grid of 5mm, same parameters of constitutive model as shown in Table 1 with the only variation

being the inclination of slope. The numerical parameters were the same as in the simulation used for calibration, described in section 3.

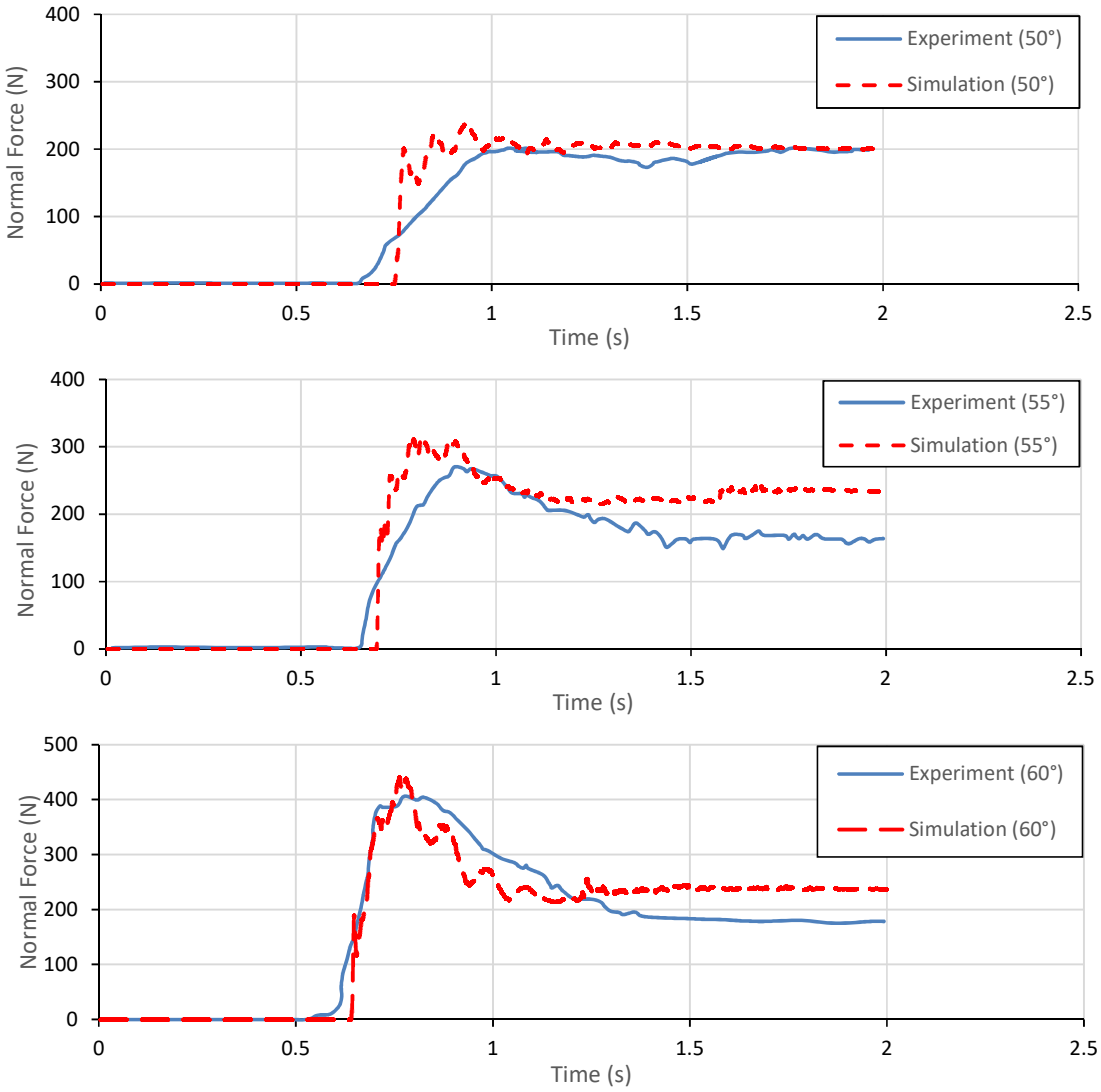

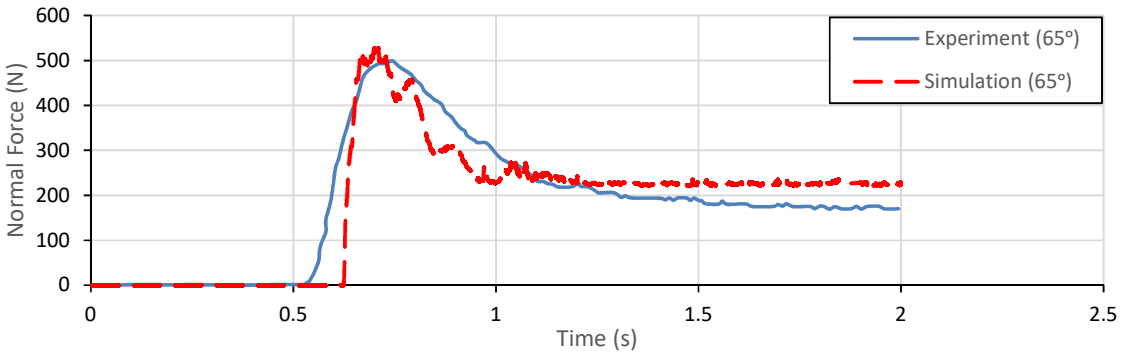

Figure 6- results of force estimations in experiments with 50°, 55°, 60° and 65° inclinations

Figure 6 shows that the numerical results replicate the soil flow experiments well. The arrival time of sand to the end of flume and the overall variations of normal force were predicted quite well especially for the 60° and 65° inclination experiments. Nevertheless, the simulations failed to estimate exactly the increase of normal force at the beginning of impact. That could be a result of the linear elasticity assumption or the constitutive model incapability of considering the softening / hardening behaviour. Also, the estimated normal force for all the experiments showed some oscillations which is one of the common problem in MPM based modelling. Nonetheless, the peak values of the force from the experiments have been recovered well. That is important, as the peak value is usually the critical one for the design of the impact barriers.

5 CONCLUSION

Granular landslides and avalanches are a consequence of slope instabilities and cause loss of lives and significant economic costs. This study used Generalized Interpolation Material Point method with a Mohr-Coulomb based constitutive model, extended with Bagnold scaling, to simulate experiments on sand flows. Results of the calculations are in a good agreement with those from the experiments. Simulations estimated arrival time of sand flows maximum impact and residual normal forces very well. The results of the study indicate capability and competence of GIMP for simulating sand flows and granular avalanches. They also show considerable improvement when compared to previous attempts for modelling these investigations ([2], [9]). However, the used constitutive model needs to be perfected, taking into account non-linearity in shear modulus with strain and more accurate modelling of volume change of the soil.

ACKNOWLEDGEMENT

The work has been partially funded by the Academy of Finland under the project ‘Progressive failure and post-failure modelling of slopes with Generalized Interpolation Material Point Method (GIMP)’, decision number is 286628.

REFERENCES

[1] J. Duran, *Sands, Powders, and Grains*, vol. 54, no. 4. New York, NY: Springer New

York, 2000.

[2] S. Moriguchi, R. I. Borja, A. Yashima, and K. Sawada, “Estimating the impact force generated by granular flow on a rigid obstruction,” *Acta Geotech.*, vol. 4, no. 1, pp. 57–71, Mar. 2009.

[3] T. KUSUMOTO, Y. NAKASE, M. FUJIMOTO, and S. NAKAI, “A study of landslide reaching distance in case analysis by statistical method,” *J. Japan Landslide Soc.*, vol. 43, no. 1, pp. 1–8, 2006.

[4] H. MORIWAKI, “A Prediction of the Runout Distance of a Debris,” *Landslides*, vol. 24, no. 2, p. 10–16_1, 1987.

[5] A. E. Scheidegger, “On the prediction of the reach and velocity of catastrophic landslides,” *Rock Mech. Felsmechanik Mec. des Roches*, vol. 5, no. 4, pp. 231–236, Dec. 1973.

[6] Y.-J. Jiang and Y. Zhao, “Experimental investigation of dry granular flow impact via both normal and tangential force measurements,” *Géotechnique Lett.*, vol. 5, no. 1, pp. 33–38, Jan. 2015.

[7] Y.-J. Jiang and I. Towhata, “Experimental Study of Dry Granular Flow and Impact Behavior Against a Rigid Retaining Wall,” *Rock Mech. Rock Eng.*, vol. 46, no. 4, pp. 713–729, Jul. 2013.

[8] C. W. W. Ng, D. Song, C. E. Choi, L. H. D. Liu, J. S. H. Kwan, R. C. H. Koo, and W. K. Pun, “Impact mechanisms of granular and viscous flows on rigid and flexible barriers,” *Can. Geotech. J.*, vol. 54, no. 2, pp. 188–206, Feb. 2017.

[9] F. Ceccato and P. Simonini, “Granular Flow Impact Forces on Protection Structures: MPM Numerical Simulations with Different Constitutive Models,” *Procedia Eng.*, vol. 158, pp. 164–169, 2016.

[10] S. G. Bardenhagen and E. M. Kober, “The generalized interpolation material point method,” *C. - Comput. Model. Eng. Sci.*, vol. 5, no. 6, pp. 477–495, 2004.

[11] D. Sulsky, Z. Chen, and H. L. Schreyer, “Particle method for history-dependent materials,” *Comput. Methods Appl. Mech. Eng.*, vol. 118, no. 1–2, pp. 179–196, Sep. 1994.

[12] D. Sulsky and H. L. Schreyer, “Axisymmetric form of the material point method with applications to upsetting and Taylor impact problems,” *Comput. Methods Appl. Mech. Eng.*, vol. 139, no. 1–4, pp. 409–429, Dec. 1996.

[13] V. P. Nguyen, *Material point method: basics and applications*, no. May. 2014.

[14] K. Kamrin and M. Z. Bazant, “Stochastic flow rule for granular materials,” *Phys. Rev. E*, vol. 75, no. 4, p. 41301, Apr. 2007.

[15] S. OZTOPRAK and M. D. BOLTON, “Stiffness of sands through a laboratory test database,” *Géotechnique*, vol. 63, no. 1, pp. 54–70, Jan. 2013.

[16] F. Ceccato, “Study of large deformation geomechanical problems with the Material Point Method,” University of Padua, 2014.

[17] G. D. . MiDi, “On dense granular flows,” *Eur. Phys. J. E*, vol. 14, no. 4, pp. 341–365, Aug. 2004.

[18] T. S. Komatsu, S. Inagaki, N. Nakagawa, and S. Nasuno, “Creep Motion in a Granular Pile Exhibiting Steady Surface Flow,” *Phys. Rev. Lett.*, vol. 86, no. 9, pp. 1757–1760, Feb. 2001.

[19] D. M. Wood, *Soil Behaviour and Critical State Soil Mechanics*. Cambridge: Cambridge University Press, 1991.

[20] R. VERDUGO and K. ISHIHARA, “The Steady State of Sandy Soils.,” *SOILS Found.*, vol. 36, no. 2, pp. 81–91, 1996.

V International Conference on Particle-based Methods – Fundamentals and Applications
PARTICLES 2017
P. Wriggers, M. Bischoff, E. Oñate, D.R.J. Owen, & T. Zohdi (Eds)

HYDRO-MECHANICAL COUPLED DUAL DOMAIN MATERIAL POINT METHOD STABILIZED WITH A NULL-SPACE FILTER

Q. A. TRAN[1], W.T. SOŁOWSKI[2] AND E. CUMMINGS[3]

[1] Department of Civil Engineering, Aalto University
Rakentajanaukio 4 A, 02150 Espoo, Finland
tran.quocanh@aalto.fi

[2] Department of Civil Engineering, Aalto University
Rakentajanaukio 4 A, 02150 Espoo, Finland
wojciech.solowski@aalto.fi

[3] Department of Civil Engineering, Aalto University
Rakentajanaukio 4 A, 02150 Espoo, Finland
evan.cummings@aalto.fi

Key words: Large strain modelling, hydro-mechanical coupling, Material Point Method, Dual Domain Material Point Method, null-space filter.

Abstract. The Material Point Method (MPM) is a continuum-based numerical method especially suitable for solving large deformation problems. In this paper, we investigate the null-space errors present in MPM solutions. The paper establishes a null-space stability condition which is used to examine the null-space errors in different versions of the MPM. This analysis shows that a B-splines MPM satisfies the null-space stability condition and therefore reduces greatly the errors associated with the null-space. In contrast, the MPM, the Generalized Interpolation Material Point Method (GIMP) and the Dual Domain Material Point Method (DDMP) show non-trivial null-spaces in the mapping. To remove the null-space errors, this paper utilizes QR factorization method, which is similar to the Single Value Decomposition (SVD) method, but requires fewer computations. This paper simulates several problems with hydro-mechanical coupled Dual Domain Material Point Method (DDMP) formulation both with and without null-space error reduction. The simulations indicate that the null-space filter can improve significantly the accuracy of the pore water pressure for both gravity loading and consolidation in large strain simulation.

1. INTRODUCTION

Ringing instability problems have been defined by Brackbill [1] as a source of errors in the Particle-in-cell (PIC) method. The instability induced a large amplitude fluctuation of the

particle density in PIC caused by the mismatch of degree of freedoms between particles and grid. Edwards and Bridson [2] showed that this noise is unavoidable in PIC because of the greater number of particles than grid points. Subsequently, Gritton and Berzin [3] showed that there is a link between the ringing instability and the null-space mapping in the particle methods and adopted a Single Value Decomposition (SVD) to remove the null-space errors. Similarly, Hammerquist and Nairn [4] also proposed XPIC(m) to reduce the null-space errors from the mapping matrix.

The Material Point Method (MPM) has been based on the Particle-in-cell method [5]. Unfortunately, the Material Point Method due to similar characteristic to PIC has similar issues related to the null-space errors. This paper investigates the null-space errors in the MPM framework. It also explains why the null-space errors can be reduced when a high order of interpolation is used or there is no null-space error for the case of 1 material point per cell.

Shown results match convergence analyses of Bardenhagen and Kober [6] who proposed the Generalized Interpolation Material Point Method (GIMP). They also suggested that one material point per cell may be the optimal discretization scheme for the GIMP to minimize the errors although they could not decouple the cell-crossing errors and the ringing instability errors in the analyses. However, Tran et al. [7] showed that too few material points per cell may generate errors in the MPM when applied to gas dynamic. Therefore, reducing the number of material points per cell is not always feasible and removing the null-space errors in other way is critical. To achieve this goal, this paper develops the QR factorization method to remove the null-space to achieve the higher accuracy in the MPM formulations.

To demonstrate the capability of the QR factorization method to remove the null-space filter, this work applies the method to the hydro-mechanical coupled Dual Domain Material Point Method (DDMP) formulation [8]. While the previous versions of hydro-coupled MPM are validated successfully in the small strain benchmarks, the large strain benchmarks have not been too successful as the null space errors accumulate in-line with strains. The paper shows that by using a null-space filter, the pore water pressure can achieve a desirable accuracy for the large strain benchmark simulations. Shown benchmarks include gravity loading and large strain consolidation problems.

2. PROBLEM DEFINITION

The MPM formulations [5] has been enhanced leading, among others, to GIMP [6], [9], B-splines MPM [10] and DDMP [11]. This study utilises the stress mapping scheme in the MPM formulations as shown in Figure 1. The stress states associated with the material points and the current time step "k" ($\sigma_{\boldsymbol{p}}^{\boldsymbol{k}}$) are interpolated to the nodes, leading to the nodal internal forces ($\boldsymbol{f}_{\boldsymbol{n}}^{\boldsymbol{int,k}}$). This interpolation uses the gradient of the shape function ($\nabla\mathbf{N}$). At the nodes, the balance equations are solved to obtain the nodal velocities at the end of the time step, denoted by "L" ($\mathbf{v}_{\boldsymbol{n}}^{\boldsymbol{L}}$). Subsequently, the nodal velocity is mapped back to the gradient velocity of the material points ($\nabla\mathbf{v}_{\boldsymbol{p}}^{\boldsymbol{k+1}}$) and the compatibility and constitutive equations are used to determine the stress of material points in the next time step "k+1" ($\sigma_{\boldsymbol{p}}^{\boldsymbol{k+1}}$).

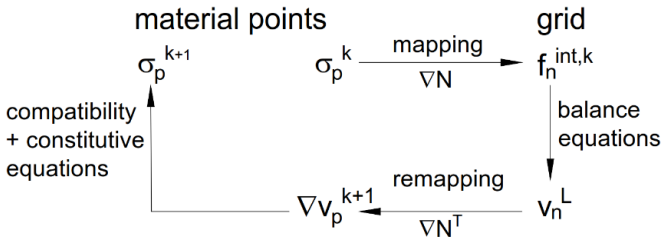

Figure 1. Schematic of stress mapping scheme in MPM

Consider a domain Ω discretised into N_p material points on a background grid with N_n nodes. The linear mapping of stress can be written in the matrix form as follows:

$$\mathbf{f}^{\mathbf{int}}_{\boldsymbol{n},\mathrm{N_n\ x\ 1}} = \nabla\mathbf{N}_{\mathrm{N_n\ x\ N_p}} \cdot \boldsymbol{\sigma}_{\boldsymbol{p},\mathrm{N_p\ x\ 1}} \tag{1}$$

where $\mathbf{f}^{\mathrm{int}}_{\boldsymbol{n},\mathrm{N_n\ x\ 1}}$ is the global nodal internal forces vector, $\boldsymbol{\sigma}_{\boldsymbol{p},\mathrm{N_p\ x\ 1}}$ is the global vector containing stress in the material points and $\nabla\mathbf{N}_{\mathrm{N_n\ x\ N_p}}$ is the linear mapping matrix, denoted as $\nabla\mathbf{N}$. Similarly, the mapping of the velocity can be written as:

$$\nabla\mathbf{v}_{\mathbf{p},\mathrm{N_p\ x\ 1}} = \nabla\mathbf{N}_{\mathrm{N_p\ x\ N_n}} \cdot \mathbf{v}^{\mathrm{L}}_{\mathbf{n},\mathrm{N_n\ x\ 1}} \tag{2}$$

where $\nabla\mathbf{v}_{\mathbf{p},\mathrm{N_p\ x\ 1}}$ is the global gradient velocity vector for all material points, $\mathbf{v}^{\mathrm{L}}_{\mathbf{n},\mathrm{N_n\ x\ 1}}$ is the global nodal velocity vector at the end of time step and $\nabla\mathbf{N}_{\mathrm{N_p\ x\ N_n}} = \nabla\mathbf{N}^{\boldsymbol{T}}_{\mathrm{N}_n\ \mathrm{x\ N}_p}$ is the linear transformation matrix, denoted $\nabla\mathbf{N}^{\mathbf{T}}$.

In the linear algebra, the rank of the linear mapping, rank($\nabla\mathbf{N}$), is defined as the number of independent vector spaces (dimensions) generated by the columns of the matrix. The null-space between two vector spaces $\mathbf{f}^{\mathrm{int}}_{\boldsymbol{n}}$ and $\boldsymbol{\sigma}_{\boldsymbol{p}}$ is the set of all elements $\boldsymbol{\sigma}^{\mathbf{null}}_{\boldsymbol{p}}$ such that $\nabla\mathbf{N}.\boldsymbol{\sigma}^{\mathbf{null}}_{\boldsymbol{p}} = 0$. The nullity of the matrix, denoted null($\nabla\mathbf{N}$) is the number of independent null-spaces generated by the columns of the matrix. According to the dimension theorem, the sum of rank and nullity is equal to either the number of columns or the number of nodes as:

$$\mathrm{rank}(\nabla\mathbf{N}) + \mathrm{null}(\nabla\mathbf{N}) = N_p \tag{3}$$

$$\mathrm{rank}(\nabla\mathbf{N}) + \mathrm{null}(\nabla\mathbf{N}^{\mathbf{T}}) = N_n \tag{4}$$

The presence of the null-space in the linear transformation leads to the instability of the solutions because the null-space can result in either no solution or infinite solutions for the eq.(1) and eq.(2). To derive an unique solution, it is necessary to produce a MPM formulation which the nullity of the transformation in eq.(3) and eq.(4) is zero. In other words, the MPM formulation can be more stable if the linear mapping ∇N is full rank (the linear mapping achieves maximum rank with $\mathrm{rank}(\nabla\mathbf{N}) = \min(N_p, N_n)$). In contrast, if ∇N is rank deficient ($\mathrm{rank}(\nabla\mathbf{N}) < \min(N_p, N_n)$), the MPM formulation may become unstable due to null-space errors. Therefore, the null-space stability condition for the MPM formulation is:

$$\begin{cases} \text{stable formulation} & \text{if } \mathrm{null}(\nabla\mathbf{N}) \text{ or } \mathrm{null}(\nabla\mathbf{N}^{\mathbf{T}}) = 0 \\ \text{unstable formulation} & \text{if } \mathrm{null}(\nabla\mathbf{N}) \text{ and } \mathrm{null}(\nabla\mathbf{N}^{\mathbf{T}}) > 0 \end{cases} \tag{5}$$

In the classical MPM, there is a non-trivial null-space in the linear mapping $\nabla\mathbf{N}$. The null-

space may induce errors in stress. However, the material point discretization affects the null-space errors. For example, one material point per cell can remove the null-space error because, in MPM, rank($\nabla\mathbf{N}$) is equal to the number of the cell. Therefore, the null-space stability condition is satisfied (rank($\nabla\mathbf{N}$) $= N_{cell} = N_p$ therefore null($\nabla\mathbf{N}$) $= 0$ in eq.(3)). However, in general, the number of material points are greater than the number of nodes ($N_p > N_n$). In these cases, the MPM formulation is susceptible to the null-space errors. Therefore, it is necessary to enhance the method with some algorithms which would lead to satisfying the null-space stability condition (5) or removing the null space errors. In the next sections, three such algorithms are presented in detail including:

- algorithm 1 –improvements in the gradient of the shape function
- algorithm 2 – employing a null-space filter
- algorithm 3 – includes additional full rank mapping

3. ALGORITHMS REMOVING THE NULL-SPACE INSTABILITY

3.1. Algorithms 1 – improving the gradient of the shape function

In case $N_p \gg N_n$, the rank of the matrix $\nabla\mathbf{N}$ is restricted by the number of nodes (rank($\nabla\mathbf{N}$) $\leq N_n$). Therefore, null($\nabla\mathbf{N}$) > 0 and the null-space stability condition can only be satisfied if null($\nabla\mathbf{N}^{\mathbf{T}}$) $= 0$. The rank(∇N) depends on both the material point discretization and the choice of the gradient of the shape function. Therefore, to satisfy the null-space stability condition, we can select higher order shape function, leading to higher order gradient of the shape function ∇N such that rank(∇N) $= N_n$. Then it satisfies the null-space stability condition as null($\nabla\mathbf{N}^{\mathbf{T}}$) $= 0$.

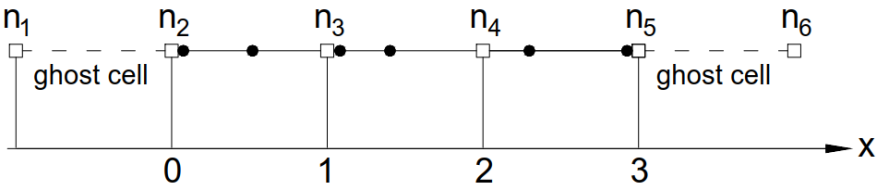

Figure 2. Irregular material point generation

To further examine the influence of the gradient of the shape function in the null-space stability condition, we compute the null-space for different types of gradient of the shape function (MPM, GIMP, DDMP and cubic B-splines) in a one-dimensional example. The domain consists of 6 material points generated irregularly, with 2 material points per cell. The grid has four main nodes ($N_n^{main} = 4$). Figure 2 presents the geometry, where the material points position is indicated by the black dots and nodes are shown as empty squares. The Generalised Interpolation Material Point Method requires additional ghost cells for the mapping (extra nodes). Consequently, the linear mapping extends its dimensions thanks to the ghost nodes. In this example, the number of ghost nodes is equal to two ($N_n^{ghost} = 2$). Therefore, the

total nodes for the GIMP are: $N_n = N_n^{main} + N_n^{ghost} = 4 + 2 = 6$

Table 1. Null-space computations for different computations

Choice of $\nabla\mathbf{N}$	N_p	N_n	rank($\nabla\mathbf{N}$)	null($\nabla\mathbf{N}$)	null($\nabla\mathbf{N}^{\mathbf{T}}$)
MPM	6	4	3	3	1
GIMP	6	6	5	1	1
DDMP	6	4	3	3	1
Cubic B-splines	6	4	4	2	0

Table 1 shows results of the null-space computation of the problem in Figure 2, based on equation (5). The results shown are for the linear mapping $\nabla\mathbf{N}^{\mathbf{T}}$ as in the four different formulations of the material point method. Based on the null-space stability condition, the linear mappings of the MPM, GIMP and DDMP were considered as unstable because they can generate the null-space leading to errors. In contrast, B-splines MPM in the shown example is a stable formulation because it satisfies the null-space stability condition.

To additionally demonstrate the null-space errors, we simulate a one-dimensional propagation of a compression wave. A compression wave is generated in the middle of an elastic bar with Young's modulus E = 0.04Pa and a length L = 4m. The initial strain is:

$$\varepsilon^o(x, t = 0) = -0.12e^{-60(x-L/2)^2} \tag{6}$$

The analytical solution for that problem at time t is:

$$\varepsilon^t(x, t) = 0.0005\left(e^{-60\left((x-L/2)-0.01t\right)^2} + e^{-60\left((x-L/2)+0.01t\right)^2}\right) \tag{7}$$

In the numerical model, the bar is discretized regularly with 2 material points per cell on a grid made from 400 cells. The problem aim is to investigate only the null-space noise. Therefore, the solution employs small amplitude of strain which means that no single material point crosses to a new cell. The gradient of the shape function for node "i" and the corresponding numerical simulations for the MPM, GIMP, DDMP and B-splines, compared with the analytical results are shown in Figure 3 - Figure 10. These results show that the MPM, GIMP and DDMP produce unstable solutions after 500 time steps corresponding to the final time t = 5s. In contrast, the solution obtained using B-splines is stable replicating closely the analytical one. These numerical observations confirm the analyses based on the null-space stability condition. It is interesting to note that both DDMP and B-splines provide a second-order gradient of the shape function but the DDMP shows a significant null-space errors while the B-splines MPM does not. The null-space errors in the DDMP is inherited from the classical MPM because DDMP uses a weight function to averaging the value in MPM ($\nabla\mathbf{N}$(MPM)) and node-based function ($\nabla\tilde{\mathbf{N}}$).

In summary, the analysis shows that the null-space errors affect simulation results significantly. Removing the null-space errors – as shown with the B-splines MPM, leads to much better match of the simulation results with the analytical solution.

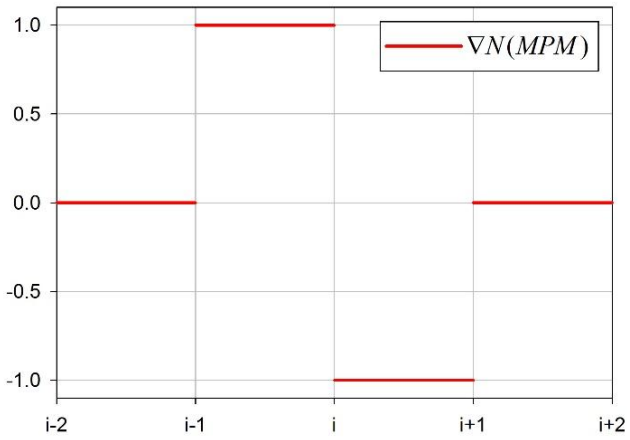

Figure 3. linear-basis gradient of the shape function

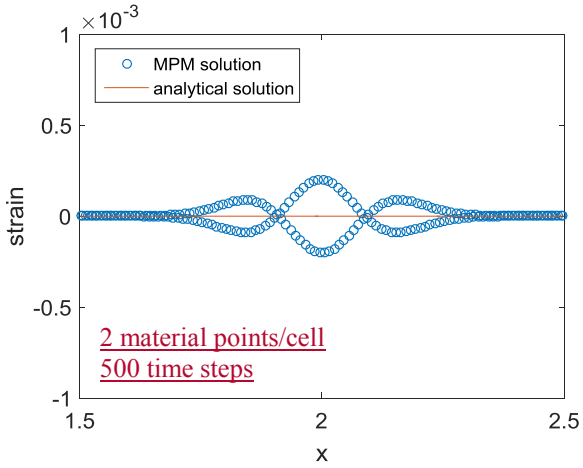

Figure 4. MPM numerical solution

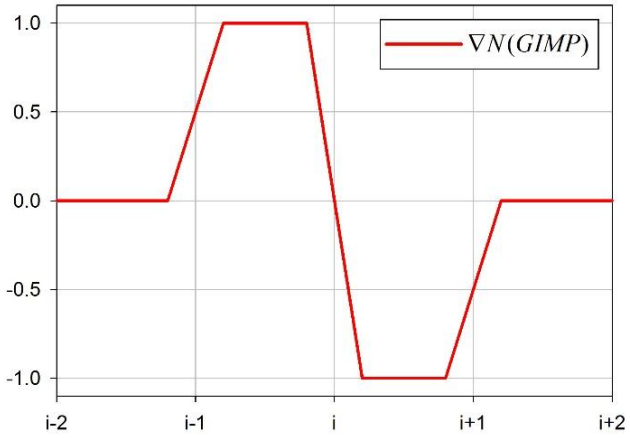

Figure 5. GIMP gradient of the shape function

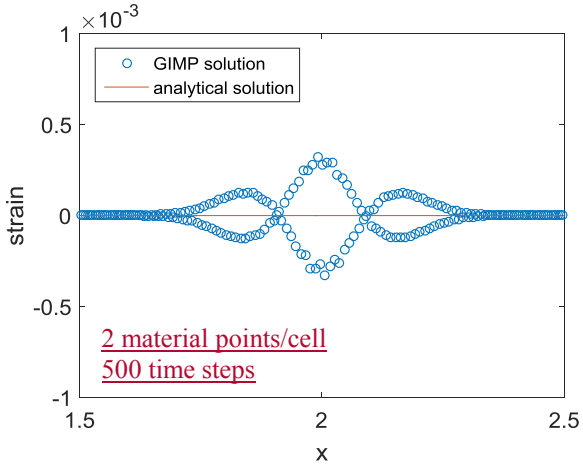

Figure 6. GIMP numerical solution

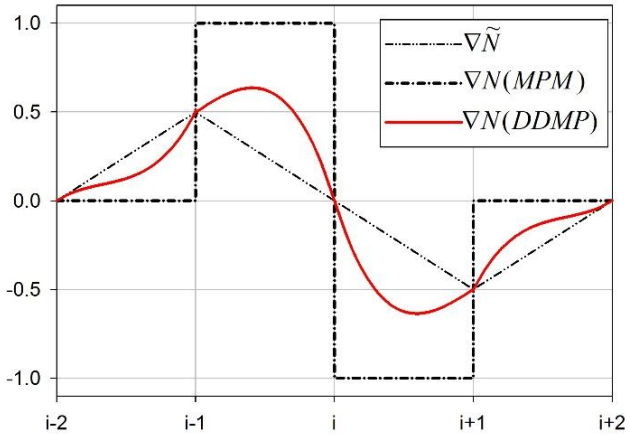

Figure 7. DDMP gradient of the shape function

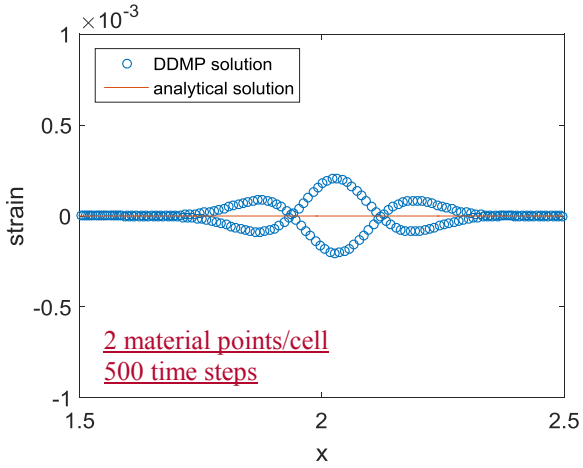

Figure 8. DDMP numerical solution

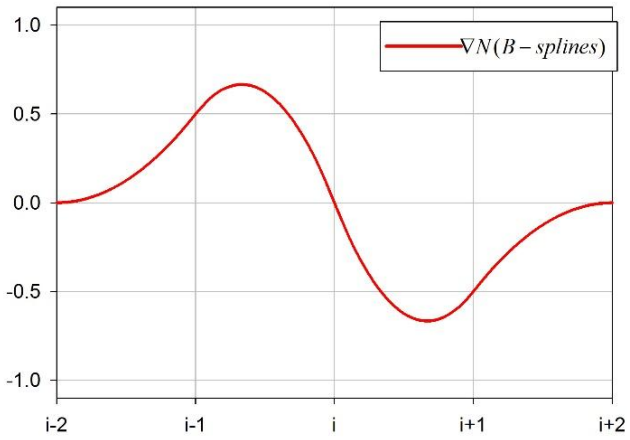

Figure 9. Cubic B-splines gradient of the shape function

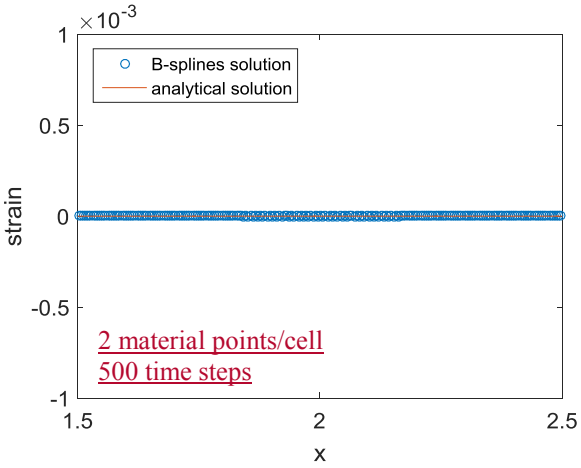

Figure 10. Cubic B-splines numerical solution

3.2. Algorithm 2 – null-space filter

When the MPM solution does not satisfy the null-space stability condition, the algorithm can be enhanced so it would remove the null-space errors in other way, i.e. $\nabla \mathbf{v_p^{null}}$. In this case, instead of satisfying the null-space stability condition as in the case above, we remove the null-space components (errors) in the solutions at every time step (see Figure 11). Therefore, the non-null-space solution at the next time step "k+1" could be calculated as:

$$\nabla \mathbf{v_p^*} = \nabla \mathbf{v_p} - \nabla \mathbf{v_p^{null}} \tag{8}$$

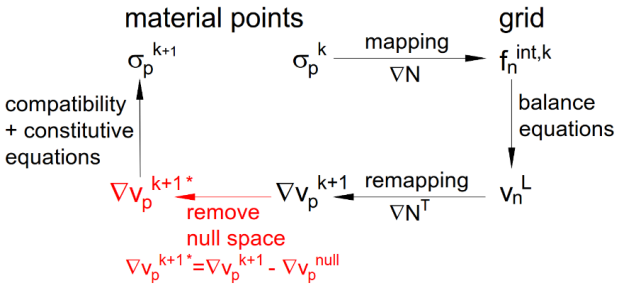

Figure 11. Schematic of solution 2 – null-space filter

In the classical MPM, the matrix $\nabla \mathbf{N}$ has a non-trivial null-space. Gritton and Berzin [12] proposed a SVD method to remove the null-space. Similarly, this paper adopts the QR method using Householder Triangularization algorithm [13] which is less numerically expensive than the SVD computation for both global and local filter. In the MPM formulation, the matrix $\nabla \mathbf{N}^{\mathrm{T}}$ can be written in the reduced QR factorization form as follows:

$$\nabla \mathbf{N}^{\mathrm{T}}{}_{\mathrm{N_p\ x\ N_n}} = \mathbf{Q}_{\mathrm{N_p\ x\ N_n}} \cdot \mathbf{R}_{\mathrm{N_n\ x\ N_n}} \tag{9}$$

where $\mathbf{Q}$ is the unitary matrix which the columns $\boldsymbol{q}_i$ $(i = [1\ N_n])$ are orthonormal and span in the space $\mathbb{R}^{N_n}$. Considering an arbitrary vector $\nabla \mathbf{v_p}$, the null-space component ($\nabla \mathbf{v_p^{null}}$) of the

vector $\nabla \mathbf{v_p}$ is orthogonal to the orthonormal set $\{\boldsymbol{q}_1, \boldsymbol{q}_2, \dots, \boldsymbol{q}_r\}$ with $r = rank(\nabla \mathbf{N}) = rank(\mathbf{R})$. Therefore, the non-null-space solutions ($\nabla \mathbf{v_p^*}$) are the projections of the vector $\nabla \mathbf{v_p}$ in the subspace $\mathrm{Q} = \mathrm{span}(\mathbf{q}_i)$ with $\{\boldsymbol{q}_1, \boldsymbol{q}_2, \dots, \boldsymbol{q}_r\}$.

$$\nabla \mathbf{v_p^*} = \mathrm{Proj_Q}(\nabla \mathbf{v_p}) = \sum_{i=1}^{r} (\boldsymbol{q}_i^T \nabla \mathbf{v_p}) \boldsymbol{q}_i \tag{10}$$

In MPM, $r = rank(\nabla \mathbf{N}) = N_c$ with N_c is the number of cells. Although equation (9) is written in a global form, in practice, we apply the null space filter locally, for each grid cell. Therefore, the size of the matrix $\nabla \mathbf{N}_{local}$ is $N_{pc}\ x\ N_{nc}$ with $rank(\nabla \mathbf{N}_{local}) = 1$ (N_{nc} is the number of nodes of the cell and N_{pc} is the number of material points inside the cell). Application of the local filter is significantly less expensive numerically than the global filter. Figure 12 shows the numerical solutions for the DDMP with null-space filter, using QR method. The results show that the local QR method can remove the null-space errors in the solutions at lower computational cost than the local SVD method. Figure 13 compares the computation costs for the given example in the section 3.1. The difference of computation costs between the SVD method and QR method will be larger when bigger, multi-dimensional problems are considered. The difference will also increase in line with the number of calculated time steps.

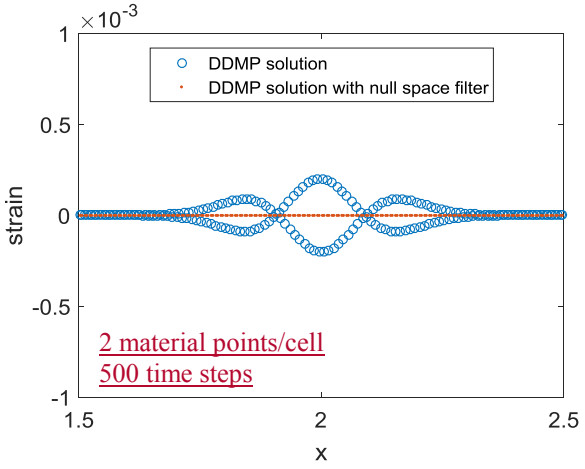

Figure 12. Numerical solution in DDMP with and without null-space filter

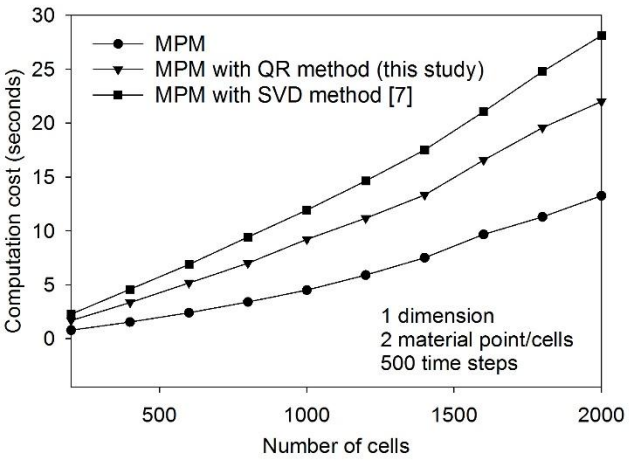

Figure 13. Computation costs of the null-space filter

3.3. Algorithm 3 – additional full rank mapping

Finally, if the mapping in the MPM does not satisfy the null-space stability condition, at the end of each time step, we can apply an additional full-rank mapping to remove the null-space. For example, in MPM, the shape function mapping ($\mathbf{N}$) can be used because the shape function mapping is full rank ($\mathrm{rank}(\mathbf{N}) = \min(N_p, N_n)$). Similar solutions are applied in the literature to improve stress visualization [14] or local null-space filter [12] (see Figure 14). However, an additional mapping can cumulate additional errors through the mapping. Therefore, we do not present this solution in greater detail.

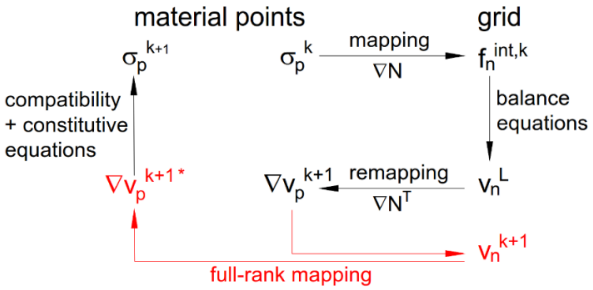

Figure 14. Schematic of solution 3

4. APPLICATION TO THE HYDRO-MECHANICAL PROBLEMS

In this section, we show the application of null-space filter to the hydro-mechanically coupled problem. The hydro-mechanically coupled balance equations base on the velocity-velocity formulation [15] The momentum balance equations for the liquid and solid phase are:

$$n\rho_w \boldsymbol{a_w} = -n\nabla p_w + n\rho_w \boldsymbol{b_w} - \boldsymbol{f_d} \tag{11}$$

$$(1-n)\rho_s \boldsymbol{a_s} = \nabla.\sigma' - (1-n)\nabla p_w + (1-n)\rho_s \boldsymbol{b_s} + \boldsymbol{f_d} \tag{12}$$

where n is the porosity, ρ_w is the liquid density, $\boldsymbol{a_w}$ is the liquid accelerations, $\boldsymbol{b_w}$ is the liquid body force, $\boldsymbol{f_d}$ is the dragging momentum determined from the Darcy law. For the solid phase, $\mathbf{a_s}$ is the solid accelerations, ρ_s is the solid density, $\mathbf{b_s}$ is the solid body force. The hydro-mechanical formulation was first implemented in MPM [16]. Later, it was extended to GIMP [17] and to DDMP [8] as those methods mitigate the cell-crossing errors. These formulations were validated for the small strain problems. In the small strain regime, usually the null-space errors in the pore water pressure profile are small in the hydro-coupled simulations. However, the null-space errors are cumulated significantly quicker in large deformation problems. In this paper, the algorithm 2 – additional null space filter with QR method was used to remove the null-space component of volumetric liquid strain in the solution. That led to a stable pore water pressure also in the large strain regime.

To demonstrate the null-space filter in the hydro-mechanically coupled DDMP formulation, we simulate two examples including gravity loading and consolidation. The problem is one dimensional, where 1m high elastic column of fully saturated porous material is discretized in 100 soil material points and 100 water material points. The grid cell size is l_p = 0.02m leading to 50 cells with 2 material points per cell. Young's modulus of the soil is 10 MPa, the density

$\rho_s = 2143$ kg/m^3, the initial porosity $n_o = 0.3$ and the initial permeability $k_o = 10^{-3}$ m/s. The bulk modulus of the water is 2200 MPa with the water density $\rho_w = 1000$ kg/m^3. The time step is 10^{-6} which satisfies the Courant condition. To generate the null-space errors, we select in case (i) high value of gravity (alternatively the solution could be obtained with a low Young's modulus) and in case (ii) high consolidating pressure. The obtained solutions of hydro-mechanically coupled DDMP with and without null-space filter are compared.

Figure 15 presents the large strain gravity loading simulations with the gravitational acceleration g = 1500 m/s. The saturated soil column reached equilibrium condition after 2 seconds, corresponding to 2 million time steps. Upon examination of Figure 15, it is evident that the accuracy of the pore water pressure using the null-space QR filter in the equilibrium condition is greatly improved and only minimal deviation from the analytical solution can be seen. For the large strain consolidation simulations, the consolidating pressure was equal to 2 MPa. The numerical solution was compared with the large strain consolidation analytical solution [18] at the degree of consolidation (U_s) of 0.05 and 0.5 respectively (see Figure 16 and Figure 17). The mismatch at the beginning of consolidation (U_s =0.05) is due to the reflection from the boundary. Nevertheless, the consolidation simulations show a significant null-space errors accumulating with time while those errors were removed by using the QR method leading to accurate long-term solution.

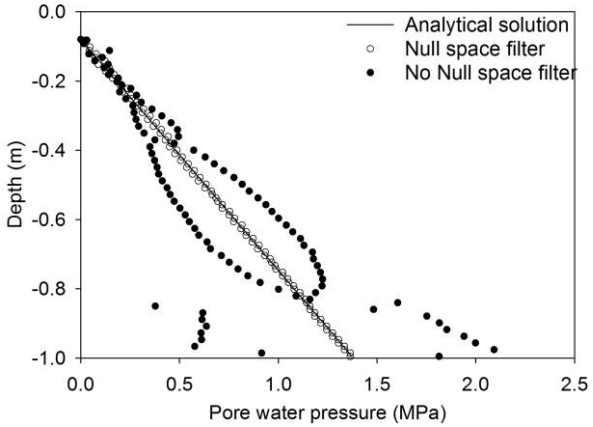

Figure 15. Large strain gravity loading using DDMP with null-space filter

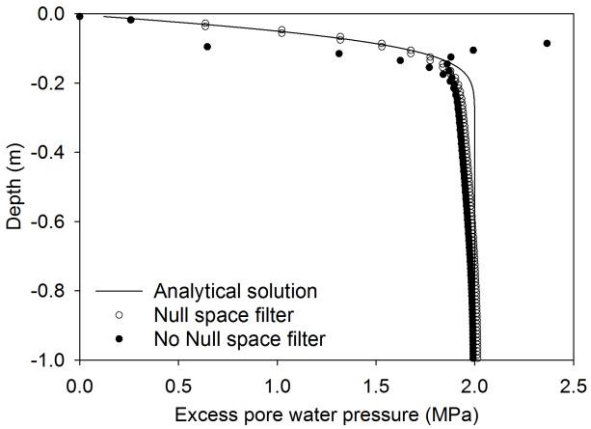

Figure 16. Large strain consolidation using DDMP with null-space filter, $U_s = 0.05$

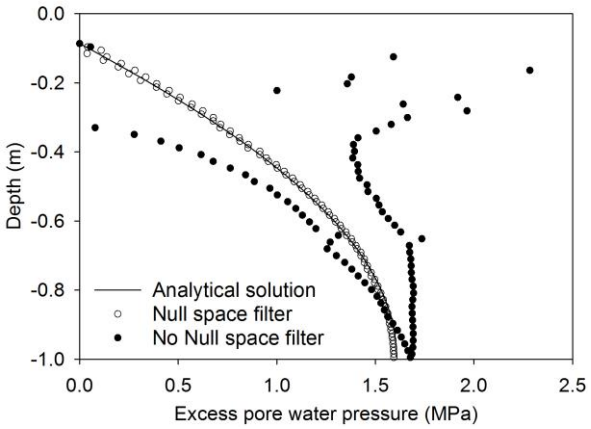

Figure 17. Large strain consolidation using DDMP with null-space filter, $U_s = 0.5$

5. CONCLUSION

This paper investigates null-space errors in the MPM formulations. First, a null-space stability condition is established to examine the null-space errors. If the mapping in the MPM is full rank, the formulation becomes stable. In contrast, the formulation is unstable if the mapping is rank deficient. Furthermore, the null-space stability condition was used to analyse different MPM formulations. The results show that while the classical MPM, GIMP and DDMP contain a rank deficient mapping, the cubic B-splines MPM have a full rank mapping and therefore, B-splines MPM formulation can reduce the null-space errors.

Alternative solutions are introduced such as a null-space filter formulation. As a novelty, we propose QR method to remove entirely null-space errors. The proposed method is similar to the SVD method [12] but requires significantly less computations. Finally, the QR method is used to the hydro-mechanical large strain simulations. The results show that the QR method can reduce greatly the noise due to null-space errors. Currently, we are working to scale up the method for multi-dimensional models and investigate the computational cost more closely.

Acknowledgement: This research was funded by the Academy of Finland under the project 'Progressive failure and post-failure modelling of slopes with Generalized Interpolation Material Point Method (GIMP)' under decision number 286628.

REFERENCES

[1] J. U. Brackbill. The Ringing Instability in Particle-in-cell calculations of low-speed flow. *Journal of computational physics* (1988) **75**:469-492.

[2] E. Edwards y R. Bridson. A high-order accurate particle-in-cell method. *International Journal for numerical methods in engineering* (2012) **90**(9):1073-1088.

[3] C. Gritton, M. Berzins and R. Kirby. Improving accuracy in particle methods using null spaces and filters. *In: Onate E, Bischoff M, Owen DRJ, Wriggers P, Zohdi T (eds) Proceedings of the IV International Conference on Particle-based Methods*, Barcelona, Spain, 2015.

[4] C. C. Hammerquist and J. A. Nairn. A new method for material point method particle updates that reduces noise and enhances stability. *Computer methods in applied mechanics and engineering* (2017) **318**:724-738.

[5] D. Sulsky, S. J. Zhou and H. L. Schreyer. Application of a particle-in-cell method to solid mechanics. *Computer Physics Communications* (1995) **87**:236-252.

[6] S. Badenhagen and E. Kober. The generalized interpolation material point method. *Computer Modeling in Engineering & Science* (2004) **5**:477-495.

[7] L. T. Tran, J. Kim and M. Berzin. Solving time-dependent PDEs using the material point method. *International journal for numerical methods in fluids* (2010) **62**:709-732.

[8] Q. A. Tran and W. Solowski. Large strain consolidation modelling using Dual Domain Material Point Method. *The 15th International Conference of the International Association for Computer Methods and Advances in Geomechanics*, Wuhan, China, 2017.

[9] W. Solowski and S. Sloan. Evaluation of material point method for use in geotechnics. *International Journal for Numerical and Analytical methods in Geomechanics* (2015) **39**:685-701.

[10] M. Steffen, R. M. Kirby and M. Berzins. Analysis and reduction of quadrature errors in the material point method. *International Journal for numerical methods in engineering* (2008) **76**:922-948.

[11] D. Zhang, X. Ma and P. Giguere. Material Point Method enhanced by modified gradienet of shape function. *Journal of Computational Physics* (2011) **230**:6379-6398.

[12] C. Gritton and M. Berzins. Improving accuracy in the MPM method using a null space filter. *Computational Particle Mechanics* (2016) **3**:1-12.

[13] L. N. Trefethen y L. David Bau. *Numerical Linear Algebra*. SIAM, 1997.

[14] S. M. Andersen and L. V. Andersen. Analysis of Stress Updates in the Material Point Method. *In L. Damkilde, L. Andersen, A. S. Kristensen, & E. Lund (Eds.), The Nordic Seminar on Computational Mechanics* (2009):129-134.

[15] O. C. Zienkiewicz and T. Shiomi. Dynamic behaviour of saturated porous media: the generalized Biot formulation and its numerical solution. *International Journal of Numerical and Analytical Methods in Geomechanics* (1984) **8**(1):71-96.

[16] S. Bandara and K. Soga. Coupling of soil deformation and pore fluid flow using material point method. *Computers and Geotechnics* (2015) 63:199-214.

[17] C. Liu, Q. Sun, F. Jin and G. G. D. Zhou. A fully coupled hydro-mechanical material point method for saturated dense granular materials. *Powder Technology,* in Press, 2017.

[18] K. H. Xie and C. J. Leo. Analytical solutions of one-dimensional large strain consolidation of saturated and homogeneous clays. *Computers and Geotechnics* (2004) **31**:301-314.

[19] D. Sulsky and M. Gong. Improving the Material Point Method. *Innovative Numerical Approaches for Multi-Field and Multi-Scale Problems. Lecture notes in Applied and Computational Mechanics* (2016) **81**:217-240.

V International Conference on Particle-based Methods – Fundamentals and Applications
PARTICLES 2017
P. Wriggers, M. Bischoff, E. Oñate, D.R.J. Owen, & T. Zohdi (Eds)

NONLINEAR STABILITY OF THE MPM METHOD

Martin Berzins[1]

[1] SCI Institute, University of Utah, Salt Lake City, USA
mb@sci.utah.edu www.sci.utah.edu

Key words: MPM Nonlinear Stability

Abstract. The Material Point Method (MPM) has been very successful in providing solutions to many challenging problems involving large deformations. The nonlinear nature of MPM makes it necessary to use a full nonlinear stability analysis to determine a stable timestep. The stability analysis of Spigler and Vianello is adapted to MPM and used to derive a stable timestep bound for a model problem. This bound is contrasted against a traditional CFL bound.

1 Introduction

The Material Point Method (MPM) may be viewed as being a solid mechanics method that is derived from the fluid implicit particle, FLIP and PIC methods and which has had considerable success on large deformation problems. Despite this success many theoretical issues to do with MPM remain unresolved. One such issue is the stability of the method, given its nonlinear nature. Currently either a fourier-based analysis e.g. [3, 10] or energy-conservation approach e.g. [1] is taken. However Wallstedt and Guilkey [14] rightly point out that the nonlinear nature of the MPM scheme makes classic linear stability analysis inappropriate. Similarly while energy conservation is of great importance it does not necessarily imply stability [11]. One way to start to address this is to note that the standard time integration methods used in MPM corresponds to the use of the semi-implicit Euler method, or symplectic Euler-A [9]. There is convergence and stability analysis of this method in [12] and this analysis is sufficiently general to be applied to the MPM, providing that care is taken with the nonlinear nature of MPM. The intention here is to use this approach to shed some light on the nonlinear stability of MPM by considering a one dimensional model problem as an ordinary differential equations system in the values at particles and nodes. While this does not address the well-known issues to do with ringing that we have previously considered [7, 3], the aim is to consider how to bound the timestep when nonlinearity is taken into account. Consequently Section 2 described the MPM method and the model problem used, while Section 3 provides the theoretical framework for the stability analysis in Section 4 which is summarized in Section 5.

2 A Simplified Form of MPM Method for Analysis

The description of MPM used here follows [7] in that the model problem used here is a pair of equations connecting velocity v, displacement u and density ρ (here assumed constant):

$$\frac{Du}{Dt} = v, \tag{1}$$

$$\rho \frac{Dv}{Dt} = \frac{\partial \sigma}{\partial x} + b, \tag{2}$$

with a linear stress model $\sigma = E\frac{\partial u}{\partial x}$ for which Young's modulus, E, is constant, a body force b and with appropriate boundary and initial conditions. For convenience a mesh of equally spaced $N+1$ fixed nodes X_i with intervals $I_i = [X_i, X_{i+1}]$, on on the interval $[a,b]$ is used where

$$a = X_0 < X_1 < ... < X_N = b, \tag{3}$$

$$h = X_i - X_{i-1}. \tag{4}$$

Further it is assumed that there are m particles between each pair of nodes, situated at x_p^n points where at each time step, $t^n = \delta t * n$, where n is the nth time step, and the computed solution at the pth particles will be written as $u_p^n = u(x_p^n, t^n)$. Suppose that the particles in interval i lie between X_i and X_{i+1} and have positions $x_{im+j}, j = 1, .., m$. The calculation of the internal forces in MPM at the nodes requires the calculation of the volume integral of the divergence of the stress, [14], which is written as

$$f_i^{int} = -\frac{1}{h}\sum_p D_{ip}^* \sigma_p V_p. \tag{5}$$

The coefficients DS_{ip}^* may be chosen to reproduce derivatives of constant and linear functions exactly, [7], in a similar way to that used in other particle methods e.g. [4]. A further simplification is to assume uniform particle masses and that the initial volume of the particles is uniform for the m particles in an interval. The particle volumes are defined using the absolute value of the deformation gradient, $|F_p^n|$, and the initial particle volume,

$$V_p^n = |F_p^n|\frac{h}{m}, \; where \; F_p^0 = 1. \tag{6}$$

From (5) the acceleration equation in MPM method after cancelling h and using constant density is:

$$a_i^{n+1} = \frac{-1}{m}\left(\sum_{x_p \in I_{i-1}} D_{ip}^{n*}\sigma_p^n |F_p^n| + \sum_{x_p \in I_i} D_{ip}^{n*}\sigma_p^n |F_p^n|\right) \tag{7}$$

In the case of GIMP, [2], two extra terms involving particles $X_p \in I_{i-1}$ and $x_p \in I_{i+2}$ are also needed. The equation to update velocity at the nodes, as denoted by v_i^n is then given by

$$v_i^{n+1} = v_i^n + dt a_i^{n+1}. \tag{8}$$

Using linear interpolation gives the equation for the update of the particle velocity:

$$v_p^{n+1} = v_p^n + dt[\lambda_{ip} a_i^{n+1} + (1-\lambda_{ip}) a_{i+1}^{n+1}], x_p \in I_i \tag{9}$$

where $\lambda_{ip} = \frac{x_p - X_i}{h}, x_p \in I_i$. The use of GIMP basis functions would give rise to an extended stencil involving a_{i-1}^{n+1} and a_{i+2}^{n+1}. The equation for the particle position update is

$$x_p^{n+1} = x_p^n + v_p^{n+1} dt. \tag{10}$$

The immediate use of the updated velocity v_p^{n+1} in this and subsequent equations is the Symplectic Euler Method. The update of the deformation gradients and stresses is given using their linear spatial derivative defined by :

$$\frac{\partial v^{n+1}}{\partial x}(x_p) = \frac{(v_{i+1}^{n+1} - v_i^{n+1})}{h}, x_p \in I_i. \tag{11}$$

The displacement is updated using

$$F_p^{n+1} = F_p^n + \frac{\partial v^{n+1}}{\partial x}(x_p) F_p^n dt, x_p \in I_i. \tag{12}$$

While stress is updated using the appropriate constitutive model and Young's Modulus, E,

$$\sigma_p^{n+1} = \sigma_p^n + dt E \frac{\partial v^{n+1}}{\partial x}(x_p), x_p \in I_i. \tag{13}$$

In the case of GIMP the derivative $\frac{(v_{i+1}^{n+1} - v_i^{n+1})}{h}$ is replaced by a four point stencil.

$$\frac{\partial v^{n+1}}{\partial x}(x_p) = \sum_{j=i-1}^{i+2} \gamma_{j,i} v_j^{n+1}, x_p \in I_i. \; where \; \frac{-1}{h} \leq \gamma_{j,i} \leq \frac{1}{h}. \tag{14}$$

3 Stability of Time Integration Using the Spigler and Vianello Approach

Spigler and Vianello [12] consider ordinary and partial differential equations of the form

$$\dot{u} = f(t,u,u), 0 < t \leq T, u(0) = u_0 \tag{15}$$

and apply the semi-implicit Euler method used by MPM to this as given by:

$$u^{n+1} = u^n + dt \; f(t_n, u^{n+1}, u^n). \tag{16}$$

It is assumed that the exact solution $\bar{u}$ to the PDE satisfies the perturbed equations given by

$$\bar{u}^{n+1} = \bar{u}^n + dt \; f(t_n, \bar{u}^{n+1}, \bar{u}^n) + \delta^{n+1}, \tag{17}$$

where δ^{n+1} is the local truncation error. Spigler and Vianello introduce a perturbed scheme given by

$$\bar{v}^{n+1} = \tilde{u}^n + dt\ f(t_{n+1}, \bar{v}^{n+1}, \tilde{u}^n) + \delta^{n+1}, \tag{18}$$

$$\tilde{u}^{n+1} = \bar{v}^{n+1} + \tilde{\sigma}^{n+1} \tag{19}$$

where $\tilde{\sigma}^{n+1}$ is a local error on the current timestep. Subtracting equation (17) from (18) and adding and subtracting a term then gives

$$\bar{v}^{n+1} - u^{n+1} = \bar{u}^n - u^n + dt\ f(t_{n+1}, \bar{v}^{n+1}, \tilde{u}^n) - dt\ f(t_{n+1}, \bar{v}^{n+1}, u^n) \tag{20}$$

$$+ dt\ f(t_{n+1}, \bar{v}^{n+1}, u^n) - dt\ f(t_{n+1}, u^{n+1}, u^n) + \delta^{n+1}. \tag{21}$$

Defining the error as

$$\varepsilon^n = \bar{v}^n - u^n. \tag{22}$$

taking the inner product of equation (21) with ε^n ,using Cauchy-Schwartz on the right hand side of this equation, and taking norms and using a Lipshitz condition gives the error inequality [12]

$$||\varepsilon^{n+1}|| \leq (1 + dtK_2)||\tilde{u}^n - u^n|| + dtK_1||\varepsilon^{n+1}|| + ||\delta^{n+1}||. \tag{23}$$

While the quantity K_1 is defined by [12] via a one-sided Lipshitz condition constant, here the stronger, but equivalent, condition [8] is used

$$||f(t_n, \bar{v}^{n+1}, u^n) - f(t_n, u^{n+1}, u^n)|| \leq K_3||\bar{v}^{n+1} - u^{n+1}|| \tag{24}$$

that ensures that the one-sided condition also holds if K_1 is replaced by K_3. K_2 is defined by [12] as being a Lipshitz constant that satisfies the equation

$$||f(t_n, \bar{v}^{n+1}, u^n) - f(t_n, \bar{v}^{n+1}, \tilde{u}^n)|| \leq K_2||\tilde{u}^n - u^n||. \tag{25}$$

Regardless of which approach is used we arrive at the equation (20) in [12]:

$$||\tilde{u}^{n+1} - u^{n+1}|| \leq \frac{1 + dtK_2}{(1 - dtK_3)}||\tilde{u}^n - u^n|| + \frac{||\delta^{n+1}||}{(1 - dtK_3)} + ||\tilde{\sigma}^{n+1}||. \tag{26}$$

The stability condition stated by [12] is then given by

$$dt(K_2 + K_3) \leq 1. \tag{27}$$

In showing how to apply such stability results to nonlinear problems Fekete and Farago [5, 6] reference extensive earlier work, that uses locally Lipshitz continuous functions, In this case it is necessary to find a constant R such that a function, say, $f(x)$ satisfies a Lipshitz condition on an open ball of center z and radius L denoted by B_R which may depend on the timestep where

$$B_L(z) := \{y \in \mathbb{R}^m : ||y - z|| \leq L\} \tag{28}$$

and the Lipshitz condition is then given on this ball by

$$||f(x)-f(y)|| \leq K||x-y||, \forall x,y \in B_L. \tag{29}$$

In order to use the [12] theory, we now define vector quantities over the number of particles. Let the total number of particles be npt. Then vectors of particle velocities $\mathbf{v}_p^n$, and nodal velocities $\mathbf{v}_N^n$ are defined as:

$$\mathbf{v}_p^n = \left[v_1^n, ..., v_{npt}^n\right]^T, \tag{30}$$

$$\mathbf{v}_N^n = \left[v_1^n, ..., v_N^n\right]^T. \tag{31}$$

The vectors of particle positions $\mathbf{x}_p^n$, stresses σ_p^n and deformation gradients $\mathbf{f}_p^n$ are given by

$$\mathbf{x}_p^n = \left[x_1^n, ..., x_{npt}^n\right]^T, \tag{32}$$

$$\sigma_p^n = \left[\sigma_1^n, ..., \sigma_{npt}^n\right]^T, \tag{33}$$

$$\mathbf{f}_p^n = \left[F_1^n, ..., F_{npt}^n\right]^T. \tag{34}$$

The MPM vectors that correspond to those used by [12] are now defined by:

$$u^n = \begin{bmatrix} \mathbf{v}_N^n \\ \mathbf{v}_p^n \\ \sigma_p^n \\ \mathbf{f}_p^n \\ \mathbf{x}_p^n \end{bmatrix}, \bar{v}^n = \begin{bmatrix} \bar{\mathbf{v}}_N^n \\ \bar{\mathbf{v}}_p^n \\ \bar{\sigma}_p^n \\ \bar{\mathbf{f}}_p^n \\ \bar{\mathbf{x}}_p^n \end{bmatrix} \text{ and } \tilde{u}^n = \begin{bmatrix} \tilde{\mathbf{v}}_N^n \\ \tilde{\mathbf{v}}_p^n \\ \tilde{\sigma}_p^n \\ \tilde{\mathbf{f}}_p^n \\ \tilde{\mathbf{x}}_p^n \end{bmatrix}. \tag{35}$$

The vector norm used is given by the 2 norm given by

$$||\mathbf{y}_p^n||_2 = \sqrt{\sum_{i=1}^{N_{tot}} (y_i^n)^2}, \text{ where } N_{tot} = N + 4Nm. \tag{36}$$

It is useful to have the elementary result

$$\left[\sum_{j=1}^{m} b_i\right]^2 \leq m \sum_{j=1}^{m} b_i^2, for\ b_i \geq 0. \tag{37}$$

4 MPM with Symplectic Euler A Integration (Stress Last)

The approach of [12] is now applied to the stress-last case as described by Bardenhagen [1] which uses the Euler-A symplectic scheme discussed by [9]. The vector form of the equations for the update of velocities, stresses and deformation gradients and then positions are given by the following equations. The vector form of equations (7, 8) and (7, 9) are:

$$\mathbf{v}_N^{n+1} = \mathbf{v}_N^n + dt\mathbf{H_N}(\mathbf{x}_p^n, \sigma_p^n, \mathbf{f}_p^n), \tag{38}$$

$$\mathbf{v}_p^{n+1} = \mathbf{v}_p^n + dt\mathbf{H_p}(\mathbf{x}_p^n, \sigma_p^n, \mathbf{f}_p^n). \tag{39}$$

The vector form of equations (13), (12) and (10) are written as:

$$\sigma_p^{n+1} = \sigma_p^n + dt\mathbf{S}(\mathbf{v}_N^{n+1}), \tag{40}$$
$$\mathbf{f}_p^{n+1} = \mathbf{f}_p^n + dt\mathbf{G}(\mathbf{f}_p^n, \mathbf{v}_N^{n+1}), \tag{41}$$
$$\mathbf{x}_p^{n+1} = \mathbf{x}_p^n + dt\mathbf{v}_p^{n+1}. \tag{42}$$

Using this notation and that used to define the vectors (35) the MPM method may be written as

$$\begin{bmatrix} \bar{\mathbf{v}}_N^{n+1} \\ \bar{\mathbf{v}}_p^{n+1} \\ \bar{\sigma}_p^{n+1} \\ \bar{\mathbf{f}}_p^{n+1} \\ \bar{\mathbf{x}}_p^{n+1} \end{bmatrix} - \begin{bmatrix} \mathbf{v}_N^{n+1} \\ \mathbf{v}_p^{n+1} \\ \sigma_p^{n+1} \\ \mathbf{f}_p^{n+1} \\ \mathbf{x}_p^{n+1} \end{bmatrix} = \begin{bmatrix} \bar{\mathbf{v}}_N^{p+1} \\ \bar{\mathbf{v}}_p^n \\ \bar{\sigma}_p^n \\ \bar{\mathbf{f}}_p^n \\ \bar{\mathbf{x}}_p^n \end{bmatrix} - \begin{bmatrix} \mathbf{v}_N^{n+1} \\ \mathbf{v}_p^{n+1} \\ \sigma_p^n \\ \mathbf{f}_p^n \\ \mathbf{x}_p^n \end{bmatrix} + dt \begin{bmatrix} \mathbf{H}_N(\tilde{\mathbf{x}}_p^n, \tilde{\sigma}_p^n, \tilde{\mathbf{f}}_p^n) - \mathbf{H}_N(\mathbf{x}_p^n, \sigma_p^n, \mathbf{f}_p^n) \\ \mathbf{H}_p(\tilde{\mathbf{x}}_p^n, \tilde{\sigma}_p^n, \tilde{\mathbf{f}}_p^n) - \mathbf{H}_p(\mathbf{x}_p^n, \sigma_p^n, \mathbf{f}_p^n) \\ \mathbf{0} \\ \mathbf{G}(\tilde{\mathbf{f}}_p^n, \mathbf{v}_N^{n+1}) - \mathbf{G}(\mathbf{f}_p^n, \mathbf{v}_N^{n+1}) \\ \mathbf{0} \end{bmatrix}$$

$$+dt \begin{bmatrix} \mathbf{0} \\ \mathbf{0} \\ \mathbf{S}(\bar{\mathbf{v}}_N^{n+1}) - \mathbf{S}(\mathbf{v}_N^{n+1}) \\ \mathbf{G}(\mathbf{f}_p^n, \bar{\mathbf{v}}_N^{n+1}) - \mathbf{G}(\mathbf{f}_p^n, \mathbf{v}_N^{n+1}) \\ \bar{\mathbf{v}}_p^{n+1} - \mathbf{v}_p^{n+1} \end{bmatrix}. \tag{43}$$

4.1 Lipshitz constants

The results of [12] require the determination of the Lipshitz constants K_2 and K_3 where:

$$\left\| \begin{bmatrix} \mathbf{H}_N(\tilde{\mathbf{x}}_p^n, \tilde{\sigma}_p^n, \tilde{\mathbf{f}}_p^n) - \mathbf{H}_N(\mathbf{x}_p^n, \sigma_p^n, \mathbf{f}_p^n) \\ \mathbf{H}_p(\tilde{\mathbf{x}}_p^n, \tilde{\sigma}_p^n, \tilde{\mathbf{f}}_p^n) - \mathbf{H}_p(\mathbf{x}_p^n, \sigma_p^n, \mathbf{f}_p^n) \\ \mathbf{0} \\ \mathbf{G}(\tilde{\mathbf{f}}_p^n, \mathbf{v}_N^{n+1}) - \mathbf{G}(\mathbf{f}_p^n, \mathbf{v}_N^{n+1}) \\ \mathbf{0} \end{bmatrix} \right\| \leq K_2 \left\| \begin{bmatrix} \bar{\mathbf{v}}_N^n - \mathbf{v}_N^n \\ \bar{\mathbf{v}}_p^n - \mathbf{v}_p^n \\ \bar{\sigma}_p^n - \sigma_p^n \\ \bar{\mathbf{f}}_p^n - \mathbf{f}_p^n \\ \bar{\mathbf{x}}_p^n - \mathbf{x}_p^n \end{bmatrix} \right\| \tag{44}$$

$$\left\| \begin{bmatrix} \mathbf{0} \\ \mathbf{0} \\ \mathbf{S}(\bar{\mathbf{v}}_N^{n+1}) - \mathbf{S}(\mathbf{v}_N^{n+1}) \\ \mathbf{G}(\mathbf{f}_p^n, \bar{\mathbf{v}}_N^{n+1}) - \mathbf{G}(\mathbf{f}_p^n, \mathbf{v}_N^{n+1}) \\ \bar{\mathbf{v}}_p^{n+1} - \mathbf{v}_p^{n+1} \end{bmatrix} \right\| \leq K_3 \left\| \begin{bmatrix} \bar{\mathbf{v}}_N^{n+1} - \mathbf{v}_N^{n+1} \\ \bar{\mathbf{v}}_p^{n+1} - \mathbf{v}_p^{n+1} \\ \bar{\sigma}_p^{n+1} - \sigma_p^{n+1} \\ \bar{\mathbf{f}}_p^{n+1} - \mathbf{f}_p^{n+1} \\ \bar{\mathbf{x}}_p^{n+1} - \mathbf{x}_p^{n+1} \end{bmatrix} \right\|. \tag{45}$$

4.2 Bounding the Lipshitz Conditions K_2

At particle position $x_p \in I_i$, the local part of the equation for L_2 is

$$\left[\mathbf{G}(\mathbf{f}_p^n, \bar{\mathbf{v}}_N^{n+1}) - \mathbf{G}(\mathbf{f}_p^n, \mathbf{v}_N^{n+1})\right]_p = F_p \frac{(\Delta v_i - \Delta v_{i-1})}{h} \tag{46}$$

where $\Delta v_i = \left[\bar{\mathbf{v}}_N^{n+1} - \mathbf{v}_N^{n+1}\right]_i$. Writing this as a vector equation and taking norms gives:

$$||\mathbf{G}(\mathbf{f}_p^n, \bar{\mathbf{v}}_N^{n+1}) - \mathbf{G}(\mathbf{f}_p^n, \mathbf{v}_N^{n+1})|| = (\sum_{p=1}^{npt} (F_p \frac{(\Delta v_i - \Delta v_{i-1})}{h})^2)^{1/2},$$

$$||\mathbf{G}(\mathbf{f}_p^n, \bar{\mathbf{v}}_N^{n+1}) - \mathbf{G}(\mathbf{f}_p^n, \mathbf{v}_N^{n+1})|| \leq \frac{F_{maxp}}{h}\sqrt{m}\sum_{i=1}^{N}(\Delta v_i - \Delta v_{i-1})^2)^{1/2},$$

$$\leq \frac{F_{maxp}}{h} 2\sqrt{m}||\Delta \mathbf{v}||, \tag{47}$$

where $F_{maxp} = max_p|F_p|$ and where the factor of $\sqrt{m}$ appears as the same gradient is used at each of m particles in an interval. Similarly at the same particle position

$$\left[\mathbf{S}(\bar{\mathbf{v}}_N^{n+1}) - \mathbf{S}(\mathbf{v}_N^{n+1})\right]_p = E\frac{(\Delta v_i - \Delta v_{i-1})}{h} \tag{48}$$

and so

$$||\mathbf{S}(\bar{\mathbf{v}}_N^{n+1}) - \mathbf{S}(\mathbf{v}_N^{n+1})|| \leq |E|\frac{2\sqrt{m}}{h}||\Delta \mathbf{v}||. \tag{49}$$

The final equation of (45) is satisfies by a Lipshitz constant with value one. Combining these results, after noting that they apply to different parts of the right side of (45), gives

$$K_3 \leq max(1, \frac{2\sqrt{m}}{h}(|E| + F_{maxp})). \tag{50}$$

4.3 Defining the Lipshitz Conditions for the Function $G(...)$ in Equation (44)

From equation (46) at particle position $x_p \in I_i$

$$\left[\mathbf{G}(\bar{\mathbf{f}}_p^n, \mathbf{v}_N^{n+1}) - \mathbf{G}(\mathbf{f}_p^n, \mathbf{v}_N^{n+1})\right]_p = (\bar{F}_p^n - F_p^n)\frac{(v_i^{n+1} - v_{i-1}^{n+1})}{h}. \tag{51}$$

Squaring both sides gives

$$|\left[\mathbf{G}(\bar{\mathbf{f}}_p^n, \mathbf{v}_N^{n+1}) - \mathbf{G}(\mathbf{f}_p^n, \mathbf{v}_N^{n+1})\right]_p|^2 \leq |(\bar{F}_p^n - F_p^n)^2(\frac{(v_i^{n+1} - v_{i-1}^{n+1})}{h})^2, p = 1, ...Nm, \tag{52}$$

where i is defined by which $x_p \in I_i$. Summing over the number of particles p and using a similar argument as in Section 4.2 gives

$$||\left[\mathbf{G}(\bar{\mathbf{f}}_p^n, \mathbf{v}_N^{n+1}) - \mathbf{G}(\mathbf{f}_p^n, \mathbf{v}_N^{n+1})\right]|| \leq K_2^*||(\bar{\mathbf{f}}_p -, \mathbf{f}_p)|| \tag{53}$$

where

$$K_2^* = Max_i|\frac{(v_i^{n+1} - v_{i-1}^{n+1})}{h}|. \tag{54}$$

4.4 Defining the Lipshitz Conditions for the Function $H_N(...)$ in Equation (44)

Applying the triangle inequality to the first equation in the equations defined by (44) gives:

$$||\mathbf{H_N}(\tilde{\mathbf{x}}_p^n, \tilde{\sigma}_p^n, \tilde{\mathbf{f}}_p^n) - \mathbf{H_N}(\mathbf{x}_p^n, \sigma_p^n, \mathbf{f}_p^n)|| \leq ||\mathbf{H_N}(\tilde{\mathbf{x}}_p^n, \sigma_p^n, \mathbf{f}_p^n) - \mathbf{H_N}(\mathbf{x}_p^n, \sigma_p^n, \mathbf{f}_p^n)||+$$
$$||\mathbf{H_N}(\tilde{\mathbf{x}}_p^n, \tilde{\sigma}_p^n, \mathbf{f}_p^n) - \mathbf{H_N}(\tilde{\mathbf{x}}_p^n, \sigma_p^n, \mathbf{f}_p^n)|| + ||\mathbf{H_N}(\tilde{\mathbf{x}}_p^n, \tilde{\sigma}_p^n, \tilde{\mathbf{f}}_p^n) - \mathbf{H_N}(\tilde{\mathbf{x}}_p^n, \tilde{\sigma}_p^n, \mathbf{f}_p^n)||. \quad (55)$$

This condition may be broken down into three parts

$$||\mathbf{H_N}(\tilde{\mathbf{x}}_p^n, \sigma_p^n, \mathbf{f}_p^n) - \mathbf{H_N}(\mathbf{x}_p^n, \sigma_p^n, \mathbf{f}_p^n)||+ \leq K_{2,2}^N||\tilde{\mathbf{x}}_p^n - \mathbf{x}_p^n||, \quad (56)$$

$$||\mathbf{H_N}(\tilde{\mathbf{x}}_p^n, \tilde{\sigma}_p^n, \mathbf{f}_p^n) - \mathbf{H_N}(\tilde{\mathbf{x}}_p^n, \sigma_p^n, \mathbf{f}_p^n)|| \leq K_{2,0}^N||\tilde{\sigma}_p^n - \sigma_p^n||, \quad (57)$$

$$||\mathbf{H_N}(\tilde{\mathbf{x}}_p^n, \tilde{\sigma}_p^n, \tilde{\mathbf{f}}_p^n) - \mathbf{H_N}(\tilde{\mathbf{x}}_p^n, \tilde{\sigma}_p^n, \mathbf{f}_p^n)|| \leq K_{2,1}^N||\tilde{\mathbf{f}}_p^n - \mathbf{f}_p^n||. \quad (58)$$

For which by using the properties of vector norms if follows that

$$K_2 \leq K_{2,0}^N + K_{2,1}^N + K_{2,2}^N. \quad (59)$$

The *i*th component of the left side of equation (57) may be written as

$$\left[\mathbf{H}_N(\tilde{\mathbf{x}}_p^n, \tilde{\sigma}_p^n, \mathbf{f}_p^n) - \mathbf{H}_N(\tilde{\mathbf{x}}_p^n, \sigma_p^n, \mathbf{f}_p^n)\right]_i = \tilde{a}_i^{n+1} \quad (60)$$

where

$$\tilde{a}_i^{n+1} = \frac{1}{m}\left(\sum_{p\in I_i} D_{ip}^{n*}\delta\sigma_p^n|F_p^n| + \sum_{p\in I_{i-1}} D_{ip}^{n*}\delta\sigma_p^n|F_p^n|\right) \quad (61)$$

and

$$\delta\sigma_p^n = \tilde{\sigma}_p^n - \sigma_p^n. \quad (62)$$

Upon defining

$$DF^n = max_p|D_{ip}^{n*}F_p^n| \quad (63)$$

allows equation (60) to be written as

$$|\left[\mathbf{H}_N(\tilde{\mathbf{x}}_p^n, \tilde{\sigma}_p^n, \mathbf{f}_p^n) - \mathbf{H}_N(\tilde{\mathbf{x}}_p^n, \sigma_p^n, \mathbf{f}_p^n)\right]_i| \leq \frac{1}{m}DF^n \sum_{x_p\in I_i\cup I_{i-1}} |\delta\sigma_p^n|. \quad (64)$$

Squaring both sides, summing over *i* nodes and using (37) gives

$$||\mathbf{H}_N(\tilde{\mathbf{x}}_p^n, \tilde{\sigma}_p^n, \mathbf{f}_p^n) - \mathbf{H}_N(\tilde{\mathbf{x}}_p^n, \sigma_p^n, \mathbf{f}_p^n)||^2 \leq (\frac{1}{m}DF^n)^2 2m\sum_p(\delta\sigma_p^n)^2 \quad (65)$$

which after taking the square root gives

$$||\mathbf{H}_N(\tilde{\mathbf{x}}_p^n, \tilde{\sigma}_p^n, \mathbf{f}_p^n) - \mathbf{H}_N(\tilde{\mathbf{x}}_p^n, \sigma_p^n, \mathbf{f}_p^n)|| \leq (\frac{1}{m}DF^n)\sqrt{2m}||\delta\sigma|| \quad (66)$$

and so

$$K_{2,0}^N \leq (\sqrt{\frac{2}{m}} DF^n. \tag{67}$$

For equation (58) the pth component of the vector $\delta\mathbf{f}$ is defined by

$$\delta f_p^n = \tilde{f}_p^n - f_p^n. \tag{68}$$

After defining

$$D\sigma^n = max_p |D_{ip}^{n*} \sigma_p^n|, \tag{69}$$

and a similar argument as above leads to

$$|\left[\mathbf{H}_N(\tilde{\mathbf{x}}_p^n, \tilde{\sigma}_p^n, \tilde{\mathbf{f}}_p^n) - \mathbf{H}_N(\tilde{\mathbf{x}}_p^n, \tilde{\sigma}_p^n, \mathbf{f}_p^n)\right]_i| \leq \frac{1}{m} D\sigma^n \sum_{x_p \in I_i \cup I_{i-1}} |\delta F_p^n|. \tag{70}$$

A similar argument as in equations (65, 66,67) then gives

$$K_{2,1}^N \leq \sqrt{\frac{2}{m}} D\sigma^n. \tag{71}$$

In the case of equation (56) the original MPM method does not satisfy a Lipshitz condition. This is seen from the dependence of the mapping constants D_{ip}^{n*} on the particles $\mathbf{x}_p^n$. Let

$$\delta D_{ip}^{n*} = D_{ip}^{n*}(\tilde{\mathbf{x}}_p^n) - D_{ip}^{n*}(\mathbf{x}_p^n), \tag{72}$$

then in the case of the original MPM method (see equation (5)),

$$\begin{aligned} D_{ip}^{n*}(x_p^n) &= -1, x_p \in I_{i-1} \\ D_{ip}^{n*}(x_p^n) &= 1, x_p \in I_i \\ D_{ip}^{n*}(x_p^n) &= 0 x_p \notin I_{i-1} \text{ and } x_p \notin I_i \end{aligned}$$

and so the values of δD_{ip}^{n*} are either 0 if the perturbed particle does not leave the interval of the unperturbed particle or $\pm 2/h$ or $\pm 1/h$ if the perturbed particle does, regardless of the gap between the particles. Given this jump discontinuity no Lipshitz constant is possible. In contrast for the GIMP method, see (29) and Figure 4b in [13], it follows that

$$|D_{ip}^{n*}(\tilde{x}_p^n) - D_{ip}^{n*}(x_p^n)| \leq \frac{2}{l} |\tilde{x}_p^n - x_p^n| \tag{73}$$

where l is the nominal width associated with the particle. Let

$$\sigma F^n = max_p |F_p^n \sigma_p^n|, \tag{74}$$

then the change in acceleration in the left side of equation (56) as denoted by δa_i^{n+1} is given by

$$\delta a_i^{n+1} = \frac{1}{m} \left(\sum_{p \in I_i} \delta D_{ip}^{n*} \sigma_p^n |F_p^n| + \sum_{p \in I_{i-1}} \delta D_{ip}^{n*} \sigma_p^n |F_p^n| \right). \tag{75}$$

and satisfies the inequality

$$|\delta a_i^{n+1}| \leq \frac{2}{lm}\sigma F^n \sum_{p\in I_i\cup I_{i-1}} |\delta x_p^n| \tag{76}$$

where

$$\delta x_p^n = \tilde{x}_p^n - x_p^n. \tag{77}$$

Similar arguments as in the previous section give the result

$$K_{2,2}^N \leq \frac{2}{l}\sqrt{\frac{2}{m}}\sigma F^n. \tag{78}$$

4.5 Defining the Lipshitz Conditions for the Function $H_p(...)$ in Equation (44)

Again this equation can be broken down into three parts

$$\begin{aligned}||\mathbf{H}_p(\tilde{\mathbf{x}}_p^n,\tilde{\sigma}_p^n,\tilde{\mathbf{f}}_p^n)-\mathbf{H}_p(\mathbf{x}_p^n,\sigma_p^n,\mathbf{f}_p^n)|| \leq ||\mathbf{H}_p(\tilde{\mathbf{x}}_p^n,\sigma_p^n,\mathbf{f}_p^n)-\mathbf{H_p}(\mathbf{x}_p^n,\sigma_p^n,\mathbf{f}_p^n)||+\\ ||\mathbf{H}_p(\tilde{\mathbf{x}}_p^n,\tilde{\sigma}_p^n,\mathbf{f}_p^n)-\mathbf{H}_p(\tilde{\mathbf{x}}_p^n,\sigma_p^n,\mathbf{f}_p^n)||+||\mathbf{H}_p(\tilde{\mathbf{x}}_p^n,\tilde{\sigma}_p^n,\tilde{\mathbf{f}}_p^n)-\mathbf{H}_p(\tilde{\mathbf{x}}_p^n,\tilde{\sigma}_p^n,\mathbf{f}_p^n)||\end{aligned} \tag{79}$$

and three Lipstitz constants used to bound the terms on the right side of this equation:

$$||\mathbf{H}_p(\tilde{\mathbf{x}}_p^n,\sigma_p^n,\mathbf{f}_p^n)-\mathbf{H}_p(\mathbf{x}_p^n,\sigma_p^n,\mathbf{f}_p^n)|| \leq K_{2,2}^p||\tilde{\mathbf{x}}_p^n-\mathbf{x}_p^n|| \tag{80}$$

$$||\mathbf{H}_p(\tilde{\mathbf{x}}_p^n,\tilde{\sigma}_p^n,\mathbf{f}_p^n)-\mathbf{H}_p(\tilde{\mathbf{x}}_p^n,\sigma_p^n,\mathbf{f}_p^n)|| \leq K_{2,0}^p||\tilde{\sigma}_p^n-\sigma_p^n|| \tag{81}$$

$$||\mathbf{H}_p(\tilde{\mathbf{x}}_p^n,\tilde{\sigma}_p^n,\tilde{\mathbf{f}}_p^n)-\mathbf{H}_p(\tilde{\mathbf{x}}_p^n,\tilde{\sigma}_p^n,\mathbf{f}_p^n)|| \leq K_{2,1}^p||\tilde{\mathbf{f}}_p^n-\mathbf{f}_p^n|| \tag{82}$$

Equation (81) is considered first using the definition in (62). Let

$$\tilde{a}_i^{n+1} = \frac{1}{m}\left(\sum_{p\in I_i} D_{ip}^{n*}\delta\sigma_p^n|F_p^n| + \sum_{p\in I_{i-1}} D_{ip}^{n*}\delta\sigma_p^n|F_p^n|\right). \tag{83}$$

$$\tilde{a}_{i+1}^{n+1} = \frac{1}{m}\left(\sum_{p\in I_{i+1}} D_{i+1p}^{n*}\delta\sigma_p^n|F_p^n| + \sum_{p\in I_i} D_{i+1p}^{n*}\delta\sigma_p^n|F_p^n|\right). \tag{84}$$

and note that from equations (7,9) the pth component of equation (81 is

$$\left[\mathbf{H}_p(\tilde{\mathbf{x}}_p^n,\tilde{\sigma}_p^n,\mathbf{f}_p^n)-\mathbf{H}_p(\tilde{\mathbf{x}}_p^n,\sigma_p^n,\mathbf{f}_p^n)\right]_p = \left[\lambda_{ip}\tilde{a}_i^{n+1}+(1-\lambda_{ip})\tilde{a}_{i+1}^{n+1}\right]. \tag{85}$$

Using the same approach as in equations (64) to (66) gives the inequality

$$|\left[\mathbf{H}_p(\tilde{\mathbf{x}}_p^n,\tilde{\sigma}_p^n,\mathbf{f}_p^n)-\mathbf{H}_p(\tilde{\mathbf{x}}_p^n,\sigma_p^n,\mathbf{f}_p^n)\right]_p| \leq= \frac{1}{m}DF^n \sum_{x_p\in I_{i-1}\cup I_i\cup I_{i+1}} |\delta\sigma_p^n| \tag{86}$$

and, as above, summing over 3 intervals and 3m particles gives

$$K_{2,0}^p = \sqrt{\frac{3}{m}}DF^n. \tag{87}$$

For equation (82) a similar argument as above again leads to

$$|\left[\mathbf{H}_p(\tilde{\mathbf{x}}_p^n,\tilde{\sigma}_p^n,\tilde{\mathbf{f}}_p^n)-\mathbf{H}_p(\tilde{\mathbf{x}}_p^n,\tilde{\sigma}_p^n,\mathbf{f}_p^n)\right]_i| \leq \frac{1}{m}D\sigma^n \sum_{x_p\in I_{i-1}\cup I_i\cup I_{I+1}} |\delta F_p^n| \tag{88}$$

and then

$$K_{2,1}^p = \sqrt{\frac{3}{m}}D\sigma^n. \tag{89}$$

The final case gives

$$|\left[\mathbf{H}_p(\tilde{\mathbf{x}}_p^n,\sigma_p^n,\mathbf{f}_p^n)-\mathbf{H}_p(\mathbf{x}_p^n,\sigma_p^n,\mathbf{f}_p^n)\right]_p| \leq \frac{1}{lm}\sigma F^n \sum_{p\in I_{i-1}\ \cup I_i\cup I_{i+1}} |\delta x_p^n| \tag{90}$$

resulting in

$$K_{2,2}^p = \sqrt{\frac{3}{ml}}\sigma F^n. \tag{91}$$

5 Summary

It is now possible to define the constants in the stability condition (27). The constant K_3 is defined by equation (54). Collecting together the different local Lipshitz conditions with respect to the vectors multiplied by those constants from equations (56,57,58,80,81,82) gives

$$K_2 \leq K_{2,0}^N + K_{2,0}^P + K_{2,1}^N + K_{2,1}^P + K_2^* + K_{2,2}^N + K_{2,2}^P) \tag{92}$$

Bringing together (67,71,78,87,89,91), then gives

$$K_2 \leq K_2^* + \alpha(DF_n + D\sigma_n + \frac{2}{l}\sigma F_n) \tag{93}$$

where $\alpha = \frac{\sqrt{2}+\sqrt{3}}{\sqrt{m}}$. The only part of this that is a conventional CFL type condition is the coefficient K_2^*, however even this term depends on the velocity gradients. This expression gives additional weight to the comments in [10] about how more than a conventional CFL condition is needed. As this approach uses a quite general ODE form and only general information about stencils. It is thus possible to extend the idea to GIMP,simply be redefining the stencil widths and associated coefficient values. An extension to multi-dimensions is also possible.

Acknowledgements

This research was partially sponsored by the Army Research Laboratory under Cooperative Agreement Number W911NF-12-2-0023. The views and conclusions contained in this document are those of the authors and should not be interpreted as representing the official policies, either expressed or implied, of the Army Research Laboratory or the U.S. Government.

REFERENCES

[1] S. Bardenhagen, Energy conservation error in the material point method for solid mechanics, Journal of Computational Physics, 180, 2002, 383-403.

[2] S. Bardenhagen and E. Kober, The generalized interpolation material point method, Computer Modeling in Engineering and Science, 5 (2004), 477-495.

[3] J. Brackbill, The ringing instability in particle-in-cell calculations of low-speed flow, Journal of Computational Physics, 75, 1988, 469-492.

[4] G. A. Dilts, Moving-least-squares-particle hydrodynamics consistency and stability, International Journal for Numerical Methods in Engineering, 44, 1999, 1115-1155.

[5] I. Fekete and I. Farago, Stability concepts and their applications. Computers & Mathematics with Applications, 67,12, pp. 2158 - 2170, 2014.

[6] I. Farago, M.E. Mincsovics and I. Fekete, Notes on the basic notions in nonlinear numerical analysis, EJQTDE, Proc. 9th Coll. QTDE (2012), (6), pp. 122.

[7] C.E. Gritton and M. Berzins, Improving Accuracy In the MPM Methods by Using a Null Spaces Filter, Comp. Part. Mech. 2017, 4 131-142.

[8] W. Hundsdorfer and J.G Verwer, Numerical Solution of Time Dependent Advection-Diffusion-Reaction Equations. Springer Series in Computational Mathematics 33, 2003.

[9] B. Leimkuhler and S. Reich, Simulating Hamiltoniam dynamics. Canbridge Monographs on Applied and Computational Science. Cambridge University Press 2004.

[10] M. Gong, Improving the Material Point Method, Ph.D. thesis, The University of New Mexico (2015). http://hdl.handle.net/1928/30386

[11] M. Ortiz, A note on energy conservation and stability of nonlinear time-stepping algorithms. Computers and Structures 24, 1, 1986, 167-168.

[12] R. Spigler and M, Vianello, Convergence analysis of the semi-implicit Euler method for abstract evolution equations. Numer. Func. Anal. and Opt.16, 1995, 5-6, 785-803.

[13] M. Steffen, P.C. Wallstedt, J.E. Guilkey, R.M. Kirby and M. Berzins, Examination and Analysis of Implementation Choices within the Material Point Method (MPM), Computer Modeling in Engineering & Sciences, 2008, 31, 2, 107-127.

[14] P. C. Wallstedt and J. E. Guilkey, An evaluation of explicit time integration schemes for use with the generalized interpolation material point method. J. Comput. Phys. 2008, 227, 22, 9628-9642.

V International Conference on Particle-based Methods – Fundamentals and Applications
PARTICLES 2017
P. Wriggers, M. Bischoff, E. Oñate, D.R.J. Owen, & T. Zohdi (Eds)

SMOOTH PLASTICITY AND DAMAGE MODEL FOR THE MATERIAL POINT METHOD

CHRISTOS D. SOFIANOS[1], VLASIS K. KOUMOUSIS[2]

[1]National Technical University of Athens
Institute of Structural Analysis & Aseismic Research
Zografou Campus, 15780 Athens, Greece
e-mail: sofianoschristos@yahoo.gr

[2] National Technical University of Athens
Institute of Structural Analysis & Aseismic Research
Zografou Campus, 15780 Athens, Greece
e-mail: vkoum@central.ntua.gr

Key words: MPM, Damage, Plasticity.

Abstract. In the Material Point Method (MPM) the structure is discretized into a set of material points that hold all the state variables of the system [1] such as stress, strain, velocities etc. A background grid is employed and the variables are mapped to the nodes of the grid. The conservation of momentum equations with energy and mass conservation considerations are solved at the grid nodes and the updated state variables are again mapped back to the material points updating their positions and velocities. The background grid is used only to solve the governing equations at the end of each computational step and then it is reset back to its original undeformed configuration. It is used only as a scratchpad for calculations and thus mesh distortion that constitutes a problem in Finite Element simulations is avoided. In this work the explicit formulation of the MPM is employed. According to the strain decomposition rule the strains are uncoupled into an elastic and an inelastic part. The constitutive law follows a Bouc-Wen [2] type formulation for smooth transition from the elastic to the inelastic regime. In the same manner the constitutive equations for elastoplasticity coupled with damage are smoothed according to Lemaitre's elastoplastic damage theory [3,4]. The above formulation is expressed and incorporated in the tangent modulus of elasticity as Heaviside type functions that control the inelastic behavior and damage. Results are presented that validate and verify the proposed formulation in the context of the Material Point Method.

1 INTRODUCTION

The Material Point Method is an extension of the Particle in Cell (PIC) method. It is a hybrid method in a sense that it is based both on a Lagrangian and a Eulerian description. In Lagrangian methods the computational grid is embedded and deformed with the material. On the contrary in Eulerian methods the computational grid is fixed and the material moves through the grid. Eulerian methods are more appropriate in problems in which the material

becomes heavily distorted.

The MPM tracks the deformation history of the material points and drastically reduces the numerical dissipation that can be found in Eulerian methods. In MPM since the grid is fixed and the particles track the deformation, problems related to mesh distortion and element entanglement are alleviated. It has been used successfully in slope stability problems, sea ice dynamics [11], multiphase flows [9], hypervelocity problems [10] etc.

The method is considered a hybrid method since it takes advantage of both the Eulerian and Lagrangian description. At the beginning of each time step a Eulerian background grid is employed. The material is discretized into a number of material points that hold the properties and the state of the material (such as position, velocity, density, mass, stresses, strains etc.). The properties are then transferred to the background grid nodes where the governing equations are solved. The material points are then updated and the background grid is reset to its original form. Although the background grid nodes can be moved it is not necessary and in practice is often avoided. This happens mainly because in a structured grid the identification of the element that each material point lies in is straightforward and computationally inexpensive. This is in contrast with mesh-free methods like the Smoothed Particle Hydrodynamics where the nearest neighbor search takes a significant percentage of the computational time.

2 THE MATERIAL POINT METHOD

The material points hold all the properties: position, velocity, mass, stress, strain. The governing equations consist of conservation equations, the constitutive equation, kinematic condition as well as boundary conditions and initial values. These equations, in their general form, are presented below:

$$\begin{aligned}
&\text{Mass conservation:} && pJ = p_0 \\
&\text{Momentum conservation:} && \sigma \cdot \nabla + pb = p\dot{v} \\
&\text{Energy conservation:} && p\dot{e} = D : \sigma + ps + \nabla \cdot \left(k \nabla T \right) \\
&\text{Constitutive equation:} && \sigma = \sigma \left(D, \sigma, \text{etc} \right) \\
&\text{Rate of deformation:} && D = \frac{1}{2} \left(L + L^T \right)
\end{aligned} \tag{1}$$

where σ denotes the Cauchy stress, p the current density, b the body force per unit mass and $\dot{v}$ is the acceleration. As in the Finite Element Method the MPM also uses the weak form formulation. In the Material Point Method each particle represents a sub-domain of the whole domain Ω. Using the Dirac delta function the mass density can be expressed as a function of the material point positions and the material point masses as:

$$p = \sum_{i=1}^{N_p} m_p \delta \left(x - x_p \right) \tag{2}$$

The material gradients are calculated on a background computational grid in a similar manner to Finite Elements. The solution is approximated with the use of shape functions. This way

the velocities and accelerations of the material points are expressed by the following relations, in terms of the grid nodal accelerations:

$$v\left(x_p\right)=\sum_{i=1}^{N} v_i N_i \quad , \quad \alpha\left(x_p\right)=\sum_{i=1}^{N} \frac{dv_i}{dt} N_i \tag{3}$$

In both relations the summation is over element nodes of the background grid that the material point resides in. In this work the shape functions used are cubic B-Splines [5]. They have been shown to reduce the quadrature errors and the grid crossing errors associated with discontinuous shape functions [6]. Applying the Galerkin method and using the previous relations in the momentum equation, integrals are replaced by sums and the momentum equation is stated as:

$$\sum_{i=1}^{N} m_i \frac{dv_i}{dt} = F_i^{\text{int}} + F_i^{ext} \tag{4}$$

where the internal and the external forces are defined as:

$$F_i^{\text{int}} = -\sum_{i=1}^{N_p} \frac{m_{p,i}}{p} \sigma_{p,i} \nabla N_i \quad , \quad F_i^{ext} = \tau_i + b_i \tag{5}$$

Subscript p,i denotes the material point i.

The main algorithm of the MPM is the following: firstly, the mass momentum and internal forces are mapped from the particles to the background grid nodes. The nodal force vector is computed and the nodal momenta are updated. Then information is transferred back to the material points by updating their velocities and positions. The last step based on the Modified Update Stress Last scheme of MPM is to recalculate the grid nodal momenta based on the new particle velocities and calculate the new stress based on the strain increments. In this last step for an elastic material the plane stress elasticity matrix is used. Based on the theory of plasticity and damage, the stress increments will be calculated from the strain increments times the tangent elasticity matrix.

$$\{\dot{\sigma}\} = [E_t]\{\dot{\varepsilon}\} \tag{6}$$

3 SMOOTH PLASTICITY AND DAMAGE

The elastoplastic model coupled with damage that is used in this work is Lemaitre's model [3-4]. It can simulate the evolution of internal damage as well as isotropic or kinematic hardening. The additive decomposition of the strain rates tensor is:

$$\{\dot{\varepsilon}\} = \{\dot{\varepsilon}^e\} + \{\dot{\varepsilon}^{pl}\} \tag{7}$$

while the yield function has the following form:

.

$$\Phi = \frac{\sqrt{3J_2\left(s-\eta\right)}}{\left(1-D\right)} - \sigma_y \quad , \quad \sigma_y = {\sigma_y}^0 + H'\varepsilon_{ps} \tag{8}$$

where η is the back stress tensor and D is the damage parameter, which can take values from zero to one, $\sigma_y^{\,0}$ is the initial yield strength and H' is the hardening modulus. The coupled elastoplastic damage constitutive law is stated as:

$$\{\sigma\} = (1-D)[C]\{\varepsilon - \varepsilon_{pl}\} \tag{9}$$

Differentiating equation (9) and using the expression for the plastic strains based on the flow rule the following relation is derived:

$$\{\dot{\sigma}\} = (1-D)[C]\left\{\{\dot{\varepsilon}\} - \dot{\lambda}\left\{\frac{\partial \Phi}{\partial \{\sigma\}}\right\}\right\} - \dot{D}[C]\{\varepsilon - \varepsilon_{pl}\} \tag{10}$$

The evolution equation for the damage variable is given by [4]:

$$\dot{D} = \dot{\lambda}\frac{H_3}{1-D}\left(-\frac{Y}{r}\right)^s \tag{11}$$

where H_3 is a Heaviside function that holds a critical value (damage threshold) such as damage growth can start only at this critical value. Parameters r and s are material constants and are identified from experimental procedures, while Y is the thermodynamical force conjugate to the damage internal variable and is given by:

$$Y = -\frac{1}{2}\{\varepsilon^e\}^T[C]\{\varepsilon^e\} \tag{12}$$

Using equations (10) and (11) the following relation is obtained:

$$\{\dot{\sigma}\} = (1-D)[C]\{\dot{\varepsilon}\} - \dot{\lambda}\left\{(1-D)[C]\left\{\frac{\partial \Phi}{\partial \{\sigma\}}\right\} + \frac{H_3}{1-D}\left(-\frac{Y}{r}\right)^s[C]\{\varepsilon - \varepsilon_{pl}\}\right\} \tag{13}$$

The consistency condition states that:

$$\dot{\Phi} = 0 \tag{14}$$

which leads to:

$$\begin{aligned} &\left\{\frac{\partial \Phi}{\partial \{\sigma\}}\right\}^{\mathrm{T}}\{\dot{\sigma}\} + \frac{\partial \Phi}{\partial D}\dot{D} - H'\dot{\lambda} = 0 \Rightarrow \\ &\left\{\frac{\partial \Phi}{\partial \{\sigma\}}\right\}^{\mathrm{T}}\{\dot{\sigma}\} + \frac{\partial \Phi}{\partial D}\left(\dot{\lambda}\frac{H_3}{1-D}\left(-\frac{Y}{r}\right)^s\right) - H'\dot{\lambda} = 0 \end{aligned} \tag{15}$$

Substituting relation (13) into (15) and solving for the plastic multiplier the following relation is derived:

$$\dot{\lambda} = \lambda_1^D(1-D)\left\{\frac{\partial \Phi}{\partial \{\sigma\}}\right\}^{\mathrm{T}}[C]\{\dot{\varepsilon}\} \tag{16}$$

where λ_1^D is given by the following formula:

$$\lambda_1^D = \left\{ H' + (1-D) \left\{ \frac{\partial \Phi}{\partial \{\sigma\}} \right\}^{\mathrm{T}} [C] \left\{ \frac{\partial \Phi}{\partial \{\sigma\}} \right\} + \frac{H_3}{1-D} \left(-\frac{Y}{r} \right)^s \left(\left\{ \frac{\partial \Phi}{\partial \{\sigma\}} \right\}^{\mathrm{T}} [C] \{ \varepsilon - \varepsilon_{pl} \} - \frac{\partial \Phi}{\partial D} \right) \right\}^{-1} \tag{17}$$

The previous equations hold when yielding has occurred. In order to generalize the plastic multiplier in the whole domain [7-8] and smooth the transition from the elastic to the inelastic regime two Heaviside type functions are used [2,12], thus making redundant the need for a piece wise approach for the domains of the Kunh-Tucker conditions:

$$H_1 = \left| \frac{\Phi}{\Phi_0} \right|^n \quad , \qquad H_2 = 0.5 + 0.5 sign\left(\{\varepsilon\}^T \{\dot{\sigma}\} \right) \tag{18}$$

This way the final expression for the plastic multiplier becomes:

$$\dot{\lambda} = H_1 H_2 \lambda_1^D (1-D) \left\{ \frac{\partial \Phi}{\partial \{\sigma\}} \right\}^{\mathrm{T}} [C] \{\dot{\varepsilon}\} \tag{19}$$

Plugging the plastic multiplier back to the strain rate equation (13) and after some algebraic manipulation the following relation is derived:

$$\{\dot{\sigma}\} = (1-D)[C] \left\{ [I] - H_1 H_2 \lambda_1^D (1-D) \left[\left\{ \frac{\partial \Phi}{\partial \{\sigma\}} \right\} \left\{ \frac{\partial \Phi}{\partial \{\sigma\}} \right\}^{\mathrm{T}} + \frac{H_3}{(1-D)^2} \left(-\frac{Y}{r} \right)^s \{\varepsilon_{el}\} \left\{ \frac{\partial \Phi}{\partial \{\sigma\}} \right\}^{\mathrm{T}} \right] [C] \right\} \{\dot{\varepsilon}\} \tag{20}$$

This way the tangent constitutive matrix can be directly calculated for each material point by replacing the classic elasticity matrix in (6) thus facilitating the solution and neglecting the need for a demanding bookkeeping mechanism.

4 NUMERICAL EXAMPLES

4.1 Cantilever beam considering plasticity only

This example is about a cantilever beam subjected to a tip point load. Material is steel with *E=210GPa*, and yield strength of s_y*=240MPa*. The dimensions of the beam are *1m* by *0.1m*. In this analysis the beam was discretized with 360 material points and 1440 points. The force is applied gradually over time until its maximum value. The force-displacement diagram at the tip of the beam is presented in Figure 1 and is compared with results from Finite Element code. In addition, the Von Mises stresses are presented in Figure 2. Results are in good agreement and the hysteretic MPM model can accurately predict both the displacement history of the beam as well as its stress state.

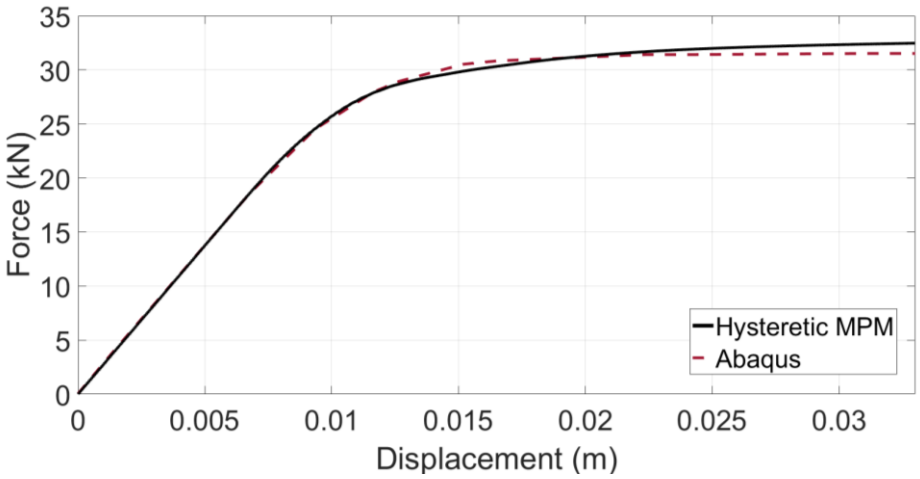

Figure 1: Beam force – displacement diagram.

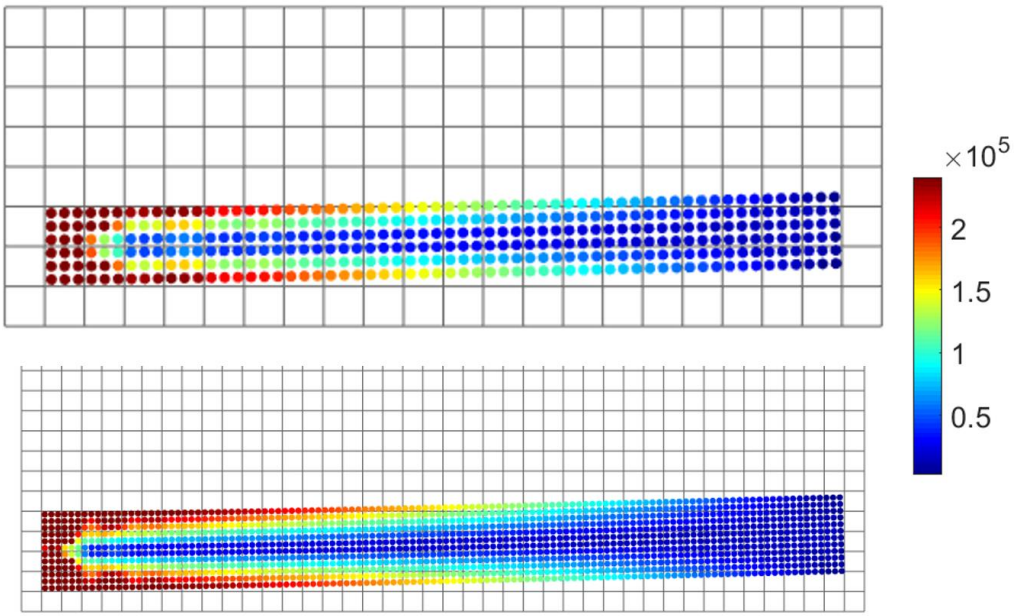

Figure 2: Von Mises stresses.

4.2 Cantilever beam considering plasticity and damage

For this example, the same cantilever beam is analyzed but this time damage is also considered. The beam is again discretized using 360 and 1440 material points. In both cases 9 points per element are used. In the first case the element size (of the background grid) is taken as 0.05m while for the second case 0.025m. Parameters regarding plasticity are kept the same. In Figure 3 the stress – strain diagram for the material point that lies on the left corner of the beam is presented. In Figure 4 the value of the damage index D across the whole beam is plotted for both discretizations. The maximum value of D is 1 and represents a failed material

while when it is close to 0 the material is considered undamaged. As expected the damaged region is focused around the fixed end of the beam.

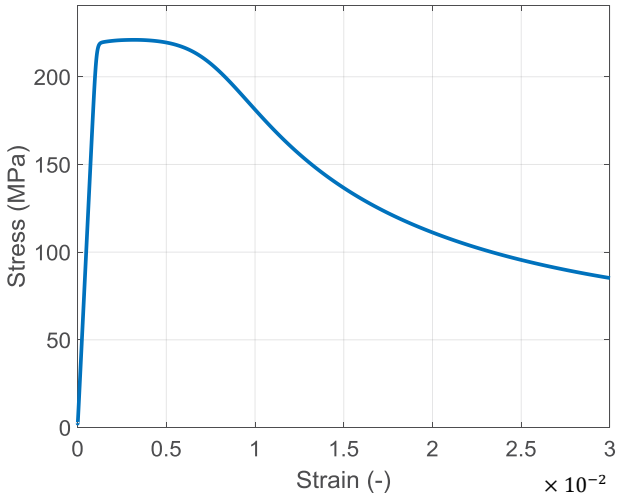

Figure 3: Von Mises Stress – Strain diagram.

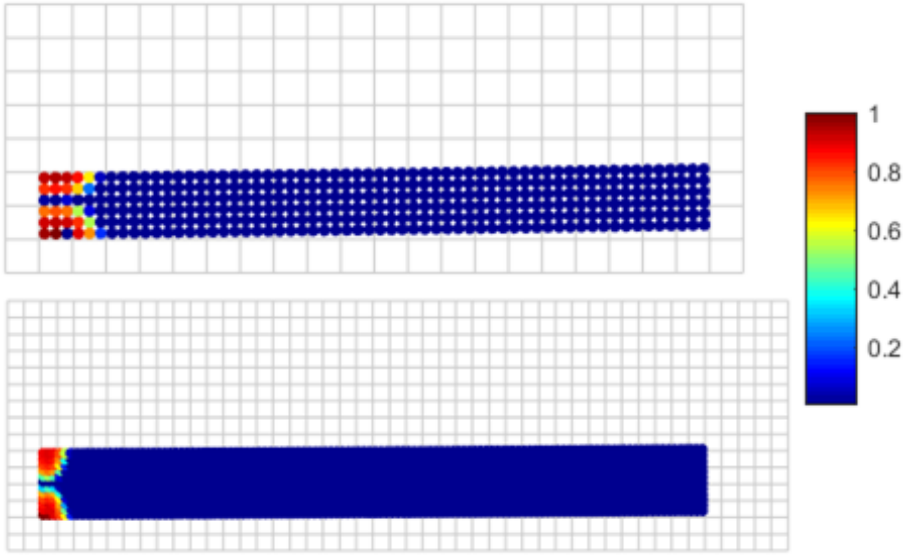

Figure 4: Damaged regions and damaged index.

5 CONCLUSIONS

- The Material Point Method is used in an explicit formulation scheme to model plasticity and damage under dynamic loading.
- The hysteretic - plasticity model for nonlinear analysis accounts for smooth transition from the elastic to the inelastic regime.

- The damage model is also smoothed.
- The plasticity and damage model have been incorporated into the MPM framework by modifying the tangent modulus of elasticity.
- Use of higher order cubic B-Splines effectively minimizes the grid crossing errors and improves the accuracy of the MPM method.
- Numerical examples are presented that verify the proposed model ability to simulate plastic and damage phenomena.

6 ACKNOWLEDGMENTS

The authors would like to acknowledge the support from the "RESEARCH PROJECTS FOR EXCELLENCE IKY/SIEMENS".

REFERENCES

[1] Sulsky, D., Chen Z. and Schreyer H.L., *A particle method for history-dependent materials*. Comput. Methods, Appl. Mech. Eng. 118,179 (1994).

[2] Bouc R. *Forced vibration of mechanical system with hysteresis*. Proc. 4th Conf. on Nonlinear Oscillation, Prague

[3] Lemaitre, J.. *A Continuous Damage Mechanics Model for Ductile.* Fracture. J. Engng. Mat. Tech., 107, 83–89, (1985a)

[4] Lemaitre, J. *Coupled Elasto-plasticity and Damage Constitutive Equations*. Comp. Meth. Appl. Mech. Engng, 51, 31–49, (1985b)

[5] Andersen S., Andersen L., *Analysis of spatial interpolation in the material-point method*. Computers and Structures 88 (2010), 506-518.

[6] Steffen M, Kirby RM, Berzins M. *Analysis and reduction of quadrature errors in the material point method (MPM)*. International Journal for Numerical Methods in Engineering;76:(2008), 922–48

[7] Triantafyllou S., Koumousis V., *Bouc-Wen Hysteretic Plane Stress Element*, Journal of Engineering Mechanics, 138 (2012), 235-246

[8] Casciati F. *Stochastic dynamics of hysteretic media*. In: Krée P., Wedig W. (eds) Probabilistic Methods in Applied Physics. Lecture Notes in Physics, vol 451. Springer, Berlin, Heidelberg, (1995)

[9] Zhang D. Z., Zou Q., VanderHeyden W. B., and Ma X.. *Material point method applied to multiphase flows*. Journal of Computational Physics, 227(6):3159–3173, (2008)

[10] Zhang X., Sze K.Y., and Ma S., *An explicit material point finite element method for hypervelocity impact*. International Journal for Numerical Methods in Engineering, 66(4):689– 706, (2006)

[11] Sulsky D., Schreyer H.L., Peterson K., Kwok R., and Coon M., *Using the material-pointmethod to model sea ice dynamics*. Journal of Geophysical Research, 112(C2):C02S90, (2007)

[12] Sofianos, C. and Koumousis, V., Hysteretic model for the explicit material point method. 6th ECCOMAS Thematic Conference on Computational Methods in Structural Dynamics and Earthquake Engineering, COMPDYN 2017, Rhodes Island, Greece, (2017)

V International Conference on Particle-based Methods – Fundamentals and Applications
PARTICLES 2017
P. Wriggers, M. Bischoff, E. Oñate, D.R.J. Owen, & T. Zohdi (Eds)

ACCURACY COMPARISON OF DIFFERENT APPROACHES FOR VORTEX SHEET DISCRETIZATION ON THE AIRFOIL IN VORTEX PARTICLES METHOD

KSENIIA S. KUZMINA[1], ILIA K. MARCHEVSKY[1], DARIO MILANI[2] AND EVGENIYA P. RYATINA[1]

[1] Bauman Moscow State Technical University (BMSTU), Applied mathematics department
2-nd Baumanskaya st., 5/1, 105005, Moscow, Russia
E-mail: kuz-ksen-serg@yandex.ru, iliamarchevsky@mail.ru, evgeniya.ryatina@yandex.ru

[2] Bauhaus Universität Weimar, Civil Engineering faculty
Marienstrasse 13a, 99423 Weimar
E-mail: dariomilani89@hotmail.it

Key words: Vortex Particles Method, Boundary Integral Equation, Galerkin Approach, Finite Element Method, Discontinuity Extraction

Abstract. The hierarchy of numerical schemes is developed for the solution of the boundary integral equation which arises in the vortex particles method. Two different approaches are considered and numerical schemes are presented, which provide 1-st and 2-nd order of accuracy with respect to two different norms. The developed finite element-type schemes have nearly the same computational cost as the simplest scheme with piecewise-constant solution. The necessary formulae are presented for linear system coefficients for the considered schemes.

1 Introduction

One of the key questions which arise in implementations of meshless Lagrangian vortex particle methods for viscous incompressible flow simulation around the airfoil, is the choice of numerical approach for no-slip (or no-through in case of inviscid flow simulation) boundary condition satisfaction on the surface line of the airfoil.

The airfoil in the flow in the most general case can be replaced with vortex sheets (attached and free) and attached source sheet. In coupled hydroelastic problems intensities of all these sheets are unknown; if law of motion for the airfoil is known, or it is rigid and immovable, only free vortex sheet intensity is unknown.

The boundary condition according to one of two possible approaches (which will be described later) to its satisfaction can be written down in form of integral equation of the first or the second kind [1]. The kernels of such equations have very different properties.

In the present paper the surface line of the airfoil is assumed to be approximated by polygon, which consists of rectilinear segments (usually called "panels"). The unknown vortex sheet intensity is approximated by piecewise-constant or piecewise-linear distribution. In the last case, it can be continuous or discontinuous, or continuous everywhere except some specified points that correspond to sharp edges and angle points of the airfoil. Some numerical schemes are considered and estimations for their accuracy and computational cost are obtained.

2 Brief description of vortex methods

Vortex particles methods of flow simulation around airfoils are based on considering the vorticity as a primary computed variable and on the fundamental principle, which was discovered by prof. N.E. Zhukovsky in 1906: an immovable airfoil influences the inviscid incompressible flow just as attached vortex sheet placed on its surface line [2]. So it is possible to replace airfoil with vortex sheet and the main problem is how to determine the intensity of this vortex sheet. For some airfoil shapes (elliptical and Zhukovsky wing airfoils) it can be found by using conformal mappings technique [3], we use such solutions as benchmarks for verification of the numerical schemes being developed.

When solving the Navier-Stokes equations the classical Zhukovsky approach remains correct in principle. However, it is required to account for the transfer of vorticity from the body surface to the flow which lead the vortex sheet to be free instead of being attached, Therefore, according to Lighthill's approach [4] the phenomena can be modelled as a result of vorticity generation on the surface line K due to vorticity flux action within the small time period. Then the vorticity, which is concentrated in this vortex sheet with intensity $\gamma(\boldsymbol{r})$, $\boldsymbol{r} \in K$, becomes part of the vortex wake and moves in the flow according to the governing equations.

When we consider a hydroelastic problems, — where either the law of motion is known *a priori* or coupled hydroelastic problem is being solved — in addition to free vortex sheet also attached vortex sheet (γ^{att}) and attached source sheet (q^{att}) should be introduced [5, 6]. In the simplest case, when velocity of the surface line points $\boldsymbol{V}_K(\boldsymbol{r})$ can be expressed explicitly as the function that depends on point position and time, the intensities of the attached sheets can be found explicitly:

$$\gamma^{att}(\boldsymbol{r}) = \boldsymbol{V}_K(\boldsymbol{r}) \cdot \boldsymbol{\tau}(\boldsymbol{r}), \qquad q^{att}(\boldsymbol{r}) = \boldsymbol{V}_K(\boldsymbol{r}) \cdot \boldsymbol{n}(\boldsymbol{r}), \qquad \boldsymbol{r} \in K,$$

where $\boldsymbol{\tau}(\boldsymbol{r})$ and $\boldsymbol{n}(\boldsymbol{r})$ are tangent and normal unit vectors to the airfoil surface line, respectively, $\boldsymbol{n}(\boldsymbol{r}) \times \boldsymbol{\tau}(\boldsymbol{r}) = \boldsymbol{k}$ ($\boldsymbol{k}$ is unit vector orthogonal to the flow plane).

Attached and free vortex sheet intensity vectors defined as

$$\boldsymbol{\gamma}^{att}(\boldsymbol{\xi}) = \gamma^{att}(\boldsymbol{\xi})\,\boldsymbol{k}, \qquad \boldsymbol{\gamma}(\boldsymbol{\xi}) = \gamma(\boldsymbol{\xi})\,\boldsymbol{k},$$

are then introduced to reconstruct the velocity field in flow domain S, by employing the generalized Biot — Savart law [7]:

$$\boldsymbol{V}(\boldsymbol{r}) = \boldsymbol{V}_\infty + \frac{1}{2\pi}\int_S \frac{\boldsymbol{\Omega}(\boldsymbol{\xi})\times(\boldsymbol{r}-\boldsymbol{\xi})}{|\boldsymbol{r}-\boldsymbol{\xi}|^2}dS_\xi + \frac{1}{2\pi}\oint_K \frac{\boldsymbol{\gamma}(\boldsymbol{\xi})\times(\boldsymbol{r}-\boldsymbol{\xi})}{|\boldsymbol{r}-\boldsymbol{\xi}|^2}dl_\xi + \\ + \frac{1}{2\pi}\oint_K \frac{\boldsymbol{\gamma}^{att}(\boldsymbol{\xi})\times(\boldsymbol{r}-\boldsymbol{\xi})}{|\boldsymbol{r}-\boldsymbol{\xi}|^2}dl_\xi + \frac{1}{2\pi}\oint_K \frac{q^{att}(\boldsymbol{\xi})(\boldsymbol{r}-\boldsymbol{\xi})}{|\boldsymbol{r}-\boldsymbol{\xi}|^2}dl_\xi, \quad (1)$$

where $\boldsymbol{\Omega}(\boldsymbol{\xi}) = \Omega(\boldsymbol{\xi})\boldsymbol{k} = \operatorname{curl}\boldsymbol{V}$ is vorticity distribution in the flow domain.

The crucial point is that the computation of the limit value of flow velocity on the surface line of the airfoil directly by using (1) is impossible. In fact, velocity field $\boldsymbol{V}(\boldsymbol{r})$ has jump discontinuity there [8]: vortex and source sheets from mathematical point of view are the curves at which tangent and normal components of velocity have jumps, respectively. In order to take them into account, the corresponding non-integral terms should be considered as elaboration of expression (1):

$$\boldsymbol{V}_-(\boldsymbol{r}) = \boldsymbol{V}(\boldsymbol{r}) - \frac{\gamma(\boldsymbol{r}) - \gamma^{att}(\boldsymbol{r})}{2}\boldsymbol{\tau}(\boldsymbol{r}) + \frac{q^{att}(\boldsymbol{r})}{2}\boldsymbol{n}(\boldsymbol{r}), \qquad \boldsymbol{r}\in K. \quad (2)$$

3 Integral equation for vortex sheet intensity distribution

Attached vortex sheet intensity distribution can be found from boundary integral equation which follows from boundary condition satisfaction on the surface line:

$$\boldsymbol{V}_-(\boldsymbol{r}) = \boldsymbol{V}_K(\boldsymbol{r}), \qquad \boldsymbol{r}\in K. \quad (3)$$

It can be shown [1], that there are two equivalent sufficient conditions for equality (3) satisfaction:

- equality between normal components of velocities (N-scheme):

$$\boldsymbol{V}_-(\boldsymbol{r})\cdot\boldsymbol{n}(\boldsymbol{r}) = \boldsymbol{V}_K(\boldsymbol{r})\cdot\boldsymbol{n}(\boldsymbol{r}), \qquad \boldsymbol{r}\in K, \quad (4)$$

- equality between tangent components of velocities (T-scheme):

$$\boldsymbol{V}_-(\boldsymbol{r})\cdot\boldsymbol{\tau}(\boldsymbol{r}) = \boldsymbol{V}_K(\boldsymbol{r})\cdot\boldsymbol{\tau}(\boldsymbol{r}), \qquad \boldsymbol{r}\in K. \quad (5)$$

It is required to notice at this point that the resulting integral equations with respect to unknown $\gamma(\boldsymbol{r})$, which can be derived from (4) and (5) after substituting there (2), have quite different properties.

Usually in vortex methods boundary condition is being written down in form (4) and it leads to the 1-st kind singular integral equation:

$$\frac{1}{2\pi}\oint_K Q_n(\boldsymbol{r},\boldsymbol{\xi})\gamma(\boldsymbol{\xi})\,dl_\xi = f_n(\boldsymbol{r}), \qquad \boldsymbol{r}\in K, \quad (6)$$

where the kernel $Q_n(\boldsymbol{r},\boldsymbol{\xi})$ is unbounded (singular) of Hilbert-type

$$Q_n(\boldsymbol{r},\boldsymbol{\xi}) = \frac{\boldsymbol{k}\times(\boldsymbol{r}-\boldsymbol{\xi})}{|\boldsymbol{r}-\boldsymbol{\xi}|^2}\cdot\boldsymbol{n}(\boldsymbol{r}) = -\frac{\boldsymbol{\tau}(\boldsymbol{r})\cdot(\boldsymbol{r}-\boldsymbol{\xi})}{|\boldsymbol{r}-\boldsymbol{\xi}|^2}.$$

The right-hand side $f_n(\boldsymbol{r})$ depends on the airfoil shape, incident flow velocity, airfoil surface line velocity and vorticity distribution in the flow domain:

$$f_n(\boldsymbol{r}) = -\frac{1}{2}q^{att}(\boldsymbol{r}) - \boldsymbol{n}(\boldsymbol{r}) \cdot \left(\boldsymbol{V}_\infty - \boldsymbol{V}_K(\boldsymbol{r}) + \frac{1}{2\pi}\int_S \frac{\boldsymbol{\Omega}(\boldsymbol{\xi}) \times (\boldsymbol{r}-\boldsymbol{\xi})}{|\boldsymbol{r}-\boldsymbol{\xi}|^2} dS_\xi + \right.$$
$$\left. + \frac{1}{2\pi}\oint_K \frac{\boldsymbol{\gamma}^{att}(\boldsymbol{\xi}) \times (\boldsymbol{r}-\boldsymbol{\xi})}{|\boldsymbol{r}-\boldsymbol{\xi}|^2} dl_\xi + \frac{1}{2\pi}\oint_K \frac{q^{att}(\boldsymbol{\xi})(\boldsymbol{r}-\boldsymbol{\xi})}{|\boldsymbol{r}-\boldsymbol{\xi}|^2} dl_\xi \right). \quad (7)$$

For approximate numerical solution of equation (6) specific quadrature formulae are required, it can be discrete vortices-type quadrature formulae [8], which permits to pick out the principal value in Cauchy sense of the corresponding singular integral.

When the numerical scheme of vortex method is being constructed on the basis of "tangent" approach (5), the resulting integral equation is the 2-nd kind Fredholm-type:

$$\frac{1}{2\pi}\oint_K Q_\tau(\boldsymbol{r}, \boldsymbol{\xi})\gamma(\boldsymbol{\xi})\, dl_\xi - \frac{1}{2}\gamma(\boldsymbol{r}) = f_\tau(\boldsymbol{r}), \qquad \boldsymbol{r} \in K, \quad (8)$$

where the kernel

$$Q_\tau(\boldsymbol{r}, \boldsymbol{\xi}) = \frac{\boldsymbol{k} \times (\boldsymbol{r}-\boldsymbol{\xi})}{|\boldsymbol{r}-\boldsymbol{\xi}|^2} \cdot \boldsymbol{\tau}(\boldsymbol{r}) = \frac{\boldsymbol{n}(\boldsymbol{r}) \cdot (\boldsymbol{r}-\boldsymbol{\xi})}{|\boldsymbol{r}-\boldsymbol{\xi}|^2}$$

is uniformly bounded function when K is smooth curve and unbounded only in proximity to angle points or sharp edges of non-smooth airfoil surface line K, and right-hand side has the following form:

$$f_\tau(\boldsymbol{r}) = -\frac{1}{2}\gamma^{att}(\boldsymbol{r}) - \boldsymbol{\tau}(\boldsymbol{r}) \cdot \left(\boldsymbol{V}_\infty - \boldsymbol{V}_K(\boldsymbol{r}) + \frac{1}{2\pi}\int_S \frac{\boldsymbol{\Omega}(\boldsymbol{\xi}) \times (\boldsymbol{r}-\boldsymbol{\xi})}{|\boldsymbol{r}-\boldsymbol{\xi}|^2} dS_\xi + \right.$$
$$\left. + \frac{1}{2\pi}\oint_K \frac{\boldsymbol{\gamma}^{att}(\boldsymbol{\xi}) \times (\boldsymbol{r}-\boldsymbol{\xi})}{|\boldsymbol{r}-\boldsymbol{\xi}|^2} dl_\xi + \frac{1}{2\pi}\oint_K \frac{q^{att}(\boldsymbol{\xi})(\boldsymbol{r}-\boldsymbol{\xi})}{|\boldsymbol{r}-\boldsymbol{\xi}|^2} dl_\xi \right). \quad (9)$$

It should be noted, that both equations (6) and (8) have infinite set of solutions. In order to select the unique solution, the additional equation should be added, which usually is being written down in the following form:

$$\oint_K \gamma(\boldsymbol{\xi}) dl_\xi = \Gamma. \quad (10)$$

The assignment of the value of the integral from solution over the surface line is the most common type for the additional condition for unsteady problems.

4 Problem discretization

When solving problem using vortex methods, vortex wake (vorticity distribution in the flow) is normally being simulated by discrete vortex-type singularities — vortex elements:

$$\Omega(\boldsymbol{r},\, t) = \sum_{w=1}^{n} \Gamma_w \tilde{\delta}(\boldsymbol{r} - \boldsymbol{r}_w). \tag{11}$$

Here n is number or vortex elements; Γ_w and $\boldsymbol{r}_w$ are intensities and positions of vortex elements, respectively; $\tilde{\delta}$ is two-dimensional Dirac delta function. Taking into account (11), we obtain for the integral term, which corresponds to the integral over the flow domain in right-hand side functions (7) and (9)

$$\frac{1}{2\pi}\int_S \frac{\boldsymbol{\Omega}(\boldsymbol{\xi}) \times (\boldsymbol{r} - \boldsymbol{\xi})}{|\boldsymbol{r} - \boldsymbol{\xi}|^2} dS_\xi = \sum_{w=1}^{n} \frac{\Gamma_w}{2\pi} \frac{\boldsymbol{k} \times (\boldsymbol{r} - \boldsymbol{r}_w)}{|\boldsymbol{r} - \boldsymbol{r}_w|^2}.$$

The simplest way to discretize the surface line K of the airfoil is to approximate it by polygon consisting of N rectilinear legs K_i, which we call hereinafter "panels". Let's denote lengthes of the panels as L_i, their normal and tangent unit vectors as $\boldsymbol{n}_i$ and $\boldsymbol{\tau}_i$, respectively, $i = 1, \ldots, N$. Now all the integrals over the surface line in the previous formulae can be written down as sums of integrals over the panels.

5 Numerical schemes for vortex sheet intensity computation

For numerical solution of the integral equations (6) or (8) with additional condition (10) the ideas of the Galerkin method are used. According to this approach vortex sheet intensity distribution can be expressed as linear combination of some basis functions $\phi_k(\boldsymbol{r})$ with unknown coefficients, which can be found from the orthogonality condition of the residual $p(\boldsymbol{r})$ of the corresponding integral equation to projection functions $\psi_k(\boldsymbol{r})$:

$$\oint_K p(\boldsymbol{r})\psi_k(\boldsymbol{r}) dl_r = 0. \tag{12}$$

Number of projection functions should be equal to number of unknown coefficients.

For simplicity in this paper we suppose that there is no vorticity in the flow and the airfoil is immovable and non-deformable, so the intensities of the attached vortex and source sheets are equal to zero. These assumptions do not however limit the generality of the following considerations. The discretization procedure of the corresponding terms of the right-hand side (7) or (9) should be constructed similarly to free vortex sheet discretization.

In this section we describe several numerical schemes, which follow from the different ways of the basis and projection functions choice. Four of them are based on T-scheme and one scheme corresponds to N-scheme.

In order to estimate the accuracy of the numerical schemes the measures used are

- a measure $\|\Delta\gamma\|_{C^h}$, which allows the average values $\bar{\gamma}_i$ of computed vortex sheet intensity over the panels to be compared with average values of exact solution $\bar{\gamma}_i^*$:

$$\|\Delta\gamma\|_{C^h} = \max_i |\bar{\gamma}_i - \bar{\gamma}_i^*|;$$

- the traditional L_1 norm of the error:

$$\|\Delta\gamma\|_{L_1} = \oint\limits_K |\gamma(s) - \gamma^*(s)|J(s)ds \approx \sum_{k=1}^{N} \int\limits_{s_k}^{s_{k+1}} |\gamma(s) - \gamma^*(s)|J_k\, ds,$$

  where $\gamma(s)$ is approximate solution, parameterized by arbitrary variable s whose change corresponds to motion along the panels; $J(s)$ is the Jakobian of such parametrization and J_k is its average value over the k-th panel; $\gamma^*(s)$ means the projection of the exact solution to the corresponding point of the panel; s_j is parameter value which corresponds to the beginning of the j-th panel.

In all schemes the resulting system of linear algebraic equations is dense and non-symmetric, so the most suitable way to solve it is Gaussian elimination method.

5.1 Scheme with piecewise-constant solution

Introducing piecewise-constant basis functions $\phi_0^i(\boldsymbol{r})$, $i = 1, \ldots, N$:

$$\phi_0^i(\boldsymbol{r}) = \begin{cases} 1, & \boldsymbol{r} \in K_i, \\ 0, & \boldsymbol{r} \notin K_i, \end{cases}$$

we construct solution as piecewise-constant function $\gamma(\boldsymbol{r}) = \sum\limits_{i=1}^{N} \gamma_i \phi_0^i(\boldsymbol{r})$.

In this case the residual of integral equation (8) has the following form:

$$p(\boldsymbol{r}) = \frac{1}{2\pi} \sum_{j=1}^{N} \left(\gamma_j \int\limits_{K_j} Q_\tau(\boldsymbol{r}, \boldsymbol{\xi}) dl_\xi \right) - \frac{1}{2} \sum_{i=1}^{N} \gamma_i \phi_0^i(\boldsymbol{r}) - f_\tau(\boldsymbol{r}).$$

Choosing projection functions equal to the basis functions: $\psi_i(\boldsymbol{r}) = \phi_0^i(\boldsymbol{r})$, we obtain the following system of linear algebraic equations from condition (12):

$$\frac{1}{2\pi} \int\limits_{K_i} \left(\sum_{j=1}^{N} \gamma_j \int\limits_{K_j} Q_\tau(\boldsymbol{r}, \boldsymbol{\xi}) dl_\xi \right) dl_r - \frac{1}{2} \gamma_i L_i = \int\limits_{K_i} f_\tau(\boldsymbol{r}) dl_r, \quad i = 1, \ldots, N, \tag{13}$$

with additional equation which follows from approximation of (10):

$$\sum_{i=1}^{N} \gamma_i L_i = \Gamma. \tag{14}$$

The linear system (13), (14) is overdetermined; in order to regularize it the approach suggested by I.K. Lifanov [8] is used. The resulting system has the following matrix form:

$$\begin{pmatrix} A & I_N \\ L & 0 \end{pmatrix} \begin{pmatrix} \gamma \\ R \end{pmatrix} = \begin{pmatrix} b \\ \Gamma \end{pmatrix}, \tag{15}$$

where A is square matrix block of size $N \times N$;

$$A_{ij} = \frac{1}{2\pi} \int\limits_{K_i} \Big(\int\limits_{K_j} Q_\tau(\boldsymbol{r}, \boldsymbol{\xi}\,) dl_\xi \Big) dl_r - \frac{L_i}{2} \tilde{\delta}_{ij}, \quad i,\, j = 1,\, \ldots,\, N;$$

$\tilde{\delta}_{ij}$ is Kronecker delta; I_N is column consists of ones; $L = (L_1,\, \ldots,\, L_N)$ is row consists of panel lengthes; b is right-hand side vector with components

$$b_i = \int\limits_{K_i} f_\tau(\boldsymbol{r}\,) dl_r, \quad i = 1,\, \ldots,\, N.$$

$\gamma = (\gamma_1,\, \ldots,\, \gamma_N)^T$ is vector of unknown coefficients; R is regularization variable.

Matrix of this system has size $(N+1) \times (N+1)$, so Gaussian elimination procedure has computational cost $(N+1)^3/3 \approx N^3/3$.

Piecewise-constant approximation provides the 2-nd order of accuracy for average values of vortex sheet intensity over the panels and only the 1-st order of accuracy in L_1 norm:

$$\|\Delta\gamma\|_{C^h} \sim N^{-2}, \quad \|\Delta\gamma\|_{L_1} \sim N^{-1}.$$

5.2 Scheme with discontinuous piecewise-linear solution

The simplest way to improve accuracy is by piecewise-linear solution representation over the panels as to substitute the piecewise-constant one.

In addition to the earlier mentioned piecewise-constant basis functions $\phi_0^i(\boldsymbol{r})$, piecewise-linear basis functions $\phi_1^i(\boldsymbol{r})$ can be introduced, that vary from the value $-\frac{1}{2}$ to $\frac{1}{2}$ over the i-th panel and are equal to 0 over the other panels:

$$\phi_1^i(\boldsymbol{r}) = \begin{cases} \dfrac{(\boldsymbol{r} - \boldsymbol{c}_i) \cdot \boldsymbol{\tau}_i}{L_i}, & \boldsymbol{r} \in K_i, \\ 0, & \boldsymbol{r} \notin K_i, \end{cases}$$

where $\boldsymbol{c}_i$ is center of the i-th panel.

Thus, the numerical solution is piecewise-linear discontinuous function which has the following form: $\gamma(\boldsymbol{r}) = \sum\limits_{i=1}^{N} \big(\gamma_i \phi_0^i(\boldsymbol{r}) + \delta_i \phi_1^i(\boldsymbol{r})\big)$, where γ_i and δ_i are unknown coefficients.

Residual of the integral equation (8)

$$p(\boldsymbol{r}) = \frac{1}{2\pi} \sum_{j=1}^{N} \left(\gamma_j \int\limits_{K_j} Q_\tau(\boldsymbol{r}, \boldsymbol{\xi}) dl_\xi + \delta_j \int\limits_{K_j} Q_\tau(\boldsymbol{r}, \boldsymbol{\xi}) \phi_1^j(\boldsymbol{\xi}) dl_\xi \right) - \frac{1}{2}\gamma(\boldsymbol{r}) - f_\tau(\boldsymbol{r})$$

should be orthogonal to projection functions, which again are chosen equal to basis functions: $\psi_k(\boldsymbol{r}) = \left\{\phi_0^i(\boldsymbol{r}),\, \phi_1^i(\boldsymbol{r})\right\}_{i=1}^N$.

Total vorticity over the i-th panel doesn't depend on δ_i coefficient, because the average value of ϕ_1^i basis function is equal to zero, so the approximation of the additional condition (10) has the same form (14).

After regularization procedure, which is carried out similarly to the previous case, the resulting linear system has size $(2N+1)\times(2N+1)$ and can be written down in form

$$\begin{pmatrix} A^{00} & A^{01} & I_N \\ A^{10} & A^{11} & O_N \\ L & O_N & 0 \end{pmatrix} \begin{pmatrix} \gamma \\ \delta \\ R \end{pmatrix} = \begin{pmatrix} b^0 \\ b^1 \\ \Gamma \end{pmatrix}, \tag{16}$$

where A^{pq}, $p,\, q = 0,\, 1$ are square matrix blocks of size $N \times N$

$$A_{ij}^{pq} = \frac{1}{2\pi} \int\limits_{K_i} \left(\int\limits_{K_j} Q_\tau(\boldsymbol{r}, \boldsymbol{\xi})\phi_q^j(\xi)dl_\xi \right) \phi_p^i(r)dl_r - D^p L_i \tilde{\delta}_{ij}\tilde{\delta}_{pq}, \quad p,\, q = 0,\, 1, \quad i,\, j = 1,\, \ldots,\, N;$$

$\tilde{\delta}_{ij}$ and $\tilde{\delta}_{pq}$ are Kronecker deltas; $D^0 = -\frac{1}{2}$, $D^1 = -\frac{1}{24}$; $\gamma = (\gamma_1,\, \ldots,\, \gamma_N)^T$ and $\delta = (\delta_1,\, \ldots,\, \delta_N)^T$ are vectors of unknown coefficients; I_N is column consists of ones; O_N is row/column consists of zeros; $L = (L_1,\, \ldots,\, L_N)$ is row consists of panel lengthes; b^0 and b^1 are vectors which form together the right-hand side:

$$b_i^p = \int\limits_{K_i} f_\tau(\boldsymbol{r})\phi_p^i(r)dl_r, \quad i = 1,\, \ldots,\, N.$$

This numerical scheme provides the 2-nd order of accuracy both for $\|\Delta\gamma\|_{C^h}$ and $\|\Delta\gamma\|_{L_1}$ errors, but the computational cost of this scheme is $(2N+1)^3/3 \approx 8N^3/3$ and it is 8 times higher than the previously considered piecewise-constant scheme.

5.3 Finite element type numerical scheme (tangent)

Note that in the framework of the piecewise-linear scheme numerical solution was considered to be discontinuous at the every node of the surface line discretization. However, for smooth airfoils the exact solution for vortex sheet intensity is continuous. This fact makes it possible to implement principles of the finite element method (FEM) and consider linear shape functions $\hat{\phi}^i$ of the 1-st order (fig. 1) as basis and projection functions (the governing equation is being solved in the framework of tangent approach (8)).

Functions $\hat{\phi}^i$ can be expressed through the previously introduced functions ϕ_0^i and ϕ_1^i:

$$\hat{\phi}^i(\boldsymbol{r}) = \begin{cases} \dfrac{1}{2}\phi_0^{i-1}(\boldsymbol{r}) + \phi_1^{i-1}(\boldsymbol{r}), & \boldsymbol{r} \in K_{i-1}, \\ \dfrac{1}{2}\phi_0^i(\boldsymbol{r}) - \phi_1^i(\boldsymbol{r}), & \boldsymbol{r} \in K_i. \end{cases} \tag{17}$$

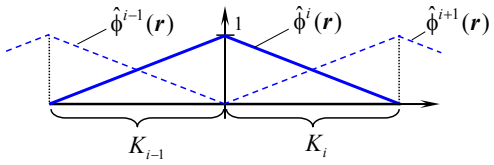

Figure 1: Linear shape functions

The resulting regularized linear algebraic system has the form

$$\begin{pmatrix} \hat{A} & I_N \\ \hat{L} & 0 \end{pmatrix} \begin{pmatrix} \hat{\gamma} \\ R \end{pmatrix} = \begin{pmatrix} \hat{b} \\ \Gamma \end{pmatrix}, \tag{18}$$

where $\hat{\gamma} = (\hat{\gamma}_1, \ldots, \hat{\gamma}_N)^T$ is vector of unknown variables; $\hat{\gamma}_i$ is the value of vortex sheet intensity at the i-th node (which coincides with the beginning of the i-th panel).

Coefficients of matrix block $\hat{A}$ (which size is $N \times N$) can be expressed through the previously introduced coefficients of matrices A^{pq}, $(p,\, q = 0,\, 1)$:

$$\hat{A}_{ij} = \frac{1}{4}\left(A^{00}_{ij} + A^{00}_{i-1,j} + A^{00}_{i,j-1} + A^{00}_{i-1,j-1}\right) + \frac{1}{2}\left(-A^{01}_{ij} - A^{01}_{i-1,j} + A^{01}_{i,j-1} + A^{01}_{i-1,j-1}\right) +$$
$$+ \frac{1}{2}\left(-A^{10}_{ij} + A^{10}_{i-1,j} - A^{10}_{i,j-1} + A^{10}_{i-1,j-1}\right) + \left(A^{11}_{ij} - A^{11}_{i-1,j} - A^{11}_{i,j-1} + A^{11}_{i-1,j-1}\right).$$

Components of vector $\hat{L}$ and right-hand side vector $\hat{b}$ also can be expressed through the coefficients introduced in section 5.2:

$$\hat{L}_i = \frac{1}{2}\left(L_i + L_{i-1}\right), \quad \hat{b}_i = \frac{1}{2}\left(b^0_i + b^0_{i-1}\right) - \left(b^1_i - b^1_{i-1}\right).$$

The matrix size now is $(N+1) \times (N+1)$, so the computational cost of the solution procedure remains the same as for piecewise-constant scheme ($N^3/3$), but it provides the 2-nd order of accuracy for both errors $\|\Delta\gamma\|_{C^h}$ and $\|\Delta\gamma\|_{L_1}$ in case of flow simulation around smooth airfoils. If the surface line of the airfoil has sharp edges or angle points, the exact solution is discontinuous and can be unbounded in proximity to these points, so the developed approach can't be applied.

5.4 Finite element type numerical scheme (normal)

This section presents a common approach widely employed in bluff body aerodynamics e.g. in bridge aerodynamics [9], which is the counterpart of the scheme devised in section 5.3. The present scheme considers the "normal" approach framework to enforce the boundary conditions. In order to solve numerically the integral equation (6), basis functions are chosen the same (linear shape functions (17)), but the projection functions now are Dirac delta functions:

$$\psi_i(\boldsymbol{r}) = \tilde{\delta}(\boldsymbol{r} - \boldsymbol{c}_i),$$

where $\boldsymbol{c}_i$ is center of the i-th panel.

The resulting linear system has the form

$$\begin{pmatrix} A^* \\ L^* \end{pmatrix} \gamma^* = \begin{pmatrix} b^* \\ \Gamma \end{pmatrix}, \tag{19}$$

where matrix coefficients A^*_{ij} and right hand-side coefficients b^*_i are expressed as the following:

$$A^*_{ij} = \frac{1}{2\pi} \int\limits_{K_j} Q_n(\boldsymbol{c}_i, \boldsymbol{\xi}\,)\hat{\phi}^j(\xi\,)dl_\xi, \qquad b^*_i = f_n(\boldsymbol{c}_i), \qquad i,\, j = 1,\, \ldots,\, N;$$

row L^* consists of the same coefficients as earlier, $L^*_i = \hat{L}_i = \frac{1}{2}(L_i + L_{i-1})$; $\gamma^* = (\gamma^*_1, \ldots, \gamma^*_N)^T$ is vector of unknown variables; γ^*_i is the value of vortex sheet intensity at the i-th node (which coincides with the beginning of the i-th panel)

The main difference with the previous numerical scheme (18) is that here no regularization parameter is employed. The matrix size now is $(N+1) \times N$, and linear system (19) is being solved by using least squares technique. Thus, the computational cost of the solution procedure proportional to $2N^3/3$, and this method provides the 2-nd order of accuracy for both errors $\|\Delta\gamma\|_{C^h}$ and $\|\Delta\gamma\|_{L_1}$ in case of flow simulation around smooth airfoils.

5.5 FEM-type approach with discontinuities extraction

In order to simulate correctly the flow around non-smooth airfoils, the numerical scheme (5.3) can be improved: the solution has discontinuities at angle points and sharp edges, their positions are known, and at the corresponding nodes two discontinuous basis functions $\tilde{\phi}_+$ and $\tilde{\phi}_-$ can be introduced instead of function $\hat{\phi}$ (17).

Let's consider that angle point corresponds to the node with index i, than $\tilde{\phi}^i_+$ and $\tilde{\phi}^i_-$ over the panels K_{i-1} and K_i adjoined the i-th node are shown in fig. 2

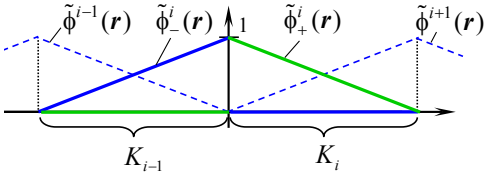

Figure 2: Discontinuous basis functions in neighborhood of angle point

The numerical solution in this case has the form $\gamma(\boldsymbol{r}) = \sum\limits_{i \notin D} \tilde{\gamma}_i \tilde{\phi}^i + \sum\limits_{i \in D} \left(\tilde{\gamma}^-_i \tilde{\phi}^i_- + \tilde{\gamma}^+_i \tilde{\phi}^i_+\right)$, where D is the set of d nodes where vortex sheet intensity is discontinuous. Coefficients $\tilde{\gamma}^-_i$ and $\tilde{\gamma}^+_i$ mean limit values of the solution on both sides of such points.

The "modified" basis functions also can be expressed through the functions ϕ_0^i and ϕ_1^i:

$$\tilde{\phi}_-^i(\boldsymbol{r}) = \frac{1}{2}\phi_0^{i-1}(\boldsymbol{r}) + \phi_1^{i-1}(\boldsymbol{r}), \quad \boldsymbol{r} \in K_{i-1},$$
$$\tilde{\phi}_+^i(\boldsymbol{r}) = \frac{1}{2}\phi_0^{i}(\boldsymbol{r}) - \phi_1^{i}(\boldsymbol{r}), \quad \boldsymbol{r} \in K_{i},$$

The other basis functions remain the same as in (17): $\tilde{\phi}^i(\boldsymbol{r}) = \hat{\phi}^i(\boldsymbol{r})$, $i \notin D$.

Projection functions are chosen to be equal to basis functions; for simplicity we assume that there is only one angle point, and it coincides with node $i = 1$, which is placed between the panels K_1 and K_N. So resulting linear system

$$\begin{pmatrix} \tilde{A} & I_{N+1} \\ \tilde{L} & 0 \end{pmatrix} \begin{pmatrix} \tilde{\gamma} \\ R \end{pmatrix} = \begin{pmatrix} \tilde{b} \\ \Gamma \end{pmatrix}$$

has size $(N+2) \times (N+2)$, its coefficients are expressed through A_{ij}^{pq} from section 5.2:

$$\tilde{A}_{11} = \frac{1}{4}A_{11}^{00} - \frac{1}{2}A_{11}^{01} - \frac{1}{2}A_{11}^{10} + A_{11}^{11};$$
$$\tilde{A}_{1j} = \frac{1}{4}\big(A_{1j}^{00} + A_{1,j-1}^{00}\big) - \frac{1}{2}\big(A_{1j}^{01} + A_{1,j-1}^{01}\big) - \frac{1}{2}\big(A_{1j}^{10} + A_{1,j-1}^{10}\big) + \big(A_{1j}^{11} + A_{1,j-1}^{11}\big);$$
$$\tilde{A}_{1,N+1} = \frac{1}{4}A_{1N}^{00} + \frac{1}{2}A_{1N}^{01} - \frac{1}{2}A_{1N}^{10} - A_{1N}^{11};$$
$$\tilde{A}_{i1} = \frac{1}{4}\big(A_{i1}^{00} + A_{i-1,1}^{00}\big) - \frac{1}{2}\big(A_{i1}^{01} + A_{i-1,1}^{01}\big) - \frac{1}{2}\big(A_{i1}^{10} + A_{i-1,1}^{10}\big) + \big(A_{i1}^{11} + A_{i-1,1}^{11}\big);$$
$$\tilde{A}_{i,N+1} = \frac{1}{4}\big(A_{iN}^{00} + A_{i-1,N}^{00}\big) + \frac{1}{2}\big(A_{iN}^{01} + A_{i-1,N}^{01}\big) - \frac{1}{2}\big(A_{iN}^{10} + A_{i-1,N}^{10}\big) - \big(A_{iN}^{11} + A_{i-1,N}^{11}\big);$$
$$\tilde{A}_{N+1,1} = \frac{1}{4}A_{N1}^{00} - \frac{1}{2}A_{N1}^{01} + \frac{1}{2}A_{N1}^{10} - A_{N1}^{11};$$
$$\tilde{A}_{N+1,j} = \frac{1}{4}\big(A_{Nj}^{00} + A_{N,j-1}^{00}\big) - \frac{1}{2}\big(A_{Nj}^{01} + A_{N,j-1}^{01}\big) + \frac{1}{2}\big(A_{Nj}^{10} + A_{N,j-1}^{10}\big) - \big(A_{Nj}^{11} + A_{N,j-1}^{11}\big);$$
$$\tilde{A}_{N+1,N+1} = \frac{1}{4}A_{NN}^{00} + \frac{1}{2}A_{NN}^{01} + \frac{1}{2}A_{NN}^{10} + A_{NN}^{11}; \quad i,\, j = 1,\, \ldots,\, N.$$

The first and last components of vectors L^* and b^* are

$$\tilde{L}_1 = \frac{L_1}{2}, \quad \tilde{L}_{N+1} = \frac{L_N}{2}, \quad \tilde{b}_1 = \frac{b_1^0}{2} - b_1^1, \quad \tilde{b}_{N+1} = \frac{b_N^0}{2} + b_N^1.$$

The other coefficients of matrix $\tilde{A}$ and vectors $\tilde{b}$ and $\tilde{L}$ remain the same as in section 5.3:

$$\tilde{A}_{ij} = \hat{A}_{ij}, \quad \tilde{b}_i = \hat{b}_i, \quad \tilde{L}_i = \hat{L}_i, \qquad i,\, j = 2,\, \ldots,\, N.$$

So, every discontinuity extraction adds one extra unknown variable and in general case matrix size is $(N+d+1) \times (N+d+1)$, where $d \ll N$, and computational cost of solution procedure remains nearly the same as earlier: $(N+d+1)^3/3 \approx N^3/3$.

This scheme provides the 2-nd order of accuracy for both errors $\|\Delta\gamma\|_{C^h}$ and $\|\Delta\gamma\|_{L_1}$ in case of flow simulation around arbitrary airfoils.

Conclusions

The developed numerical schemes for boundary integral equation solution in vortex particles method provide 1-st and 2-nd order of accuracy with respect to average value of vortex sheet intensity over the panels and in L_1 norm. Expressions for the corresponding linear system coefficients are presented. In order to compute the integrals the exact analytical formulae [10] can be used.

Acknowledgement

The research is supported by Russian Science Foundation (proj. 17-79-20445).

REFERENCES

[1] Kempka, S.N., Glass, M.W., Peery, J.S. and Strickland, J.H. Accuracy considerations for implementing velocity boundary conditions in vorticity formulations. *SANDIA REPORT* (1996) SAND96-0583 UC-700. 52 p.

[2] Tokaty, G. *A History and Philosophy of Fluid Mechanics*. Courier Corporation (1994).

[3] Chanson, H. *Applied Hydrodynamics: An Introduction to Ideal and Real Fluid Flows*. CRC Press (2009).

[4] Lighthill, M. *Boundary Layer Theory*. Ed. J. Rosenhead. OUP (1963): 54–61.

[5] Anronov, P.R., Guvernuk, S.V. and Dynnikova, G.Ya. *Vortex Methods for Computation of Unsteady Hydrodynamic Loads*. Moscow State University Press (2006).

[6] Kuzmina, K.S. and Marchevsky, I.K. The modified numerical scheme for 2D flow-structure interaction simulation using meshless vortex element method. *Proceedings of the 4th International Conference on Particle-Based Methods — Fundamentals and Applications, PARTICLES 2015* (2015): 680–691.

[7] Saffman, P.G. *Vortex Dynamics*. CUP (1993).

[8] Lifanov, I.K. *Singular Integral Equations and Discrete Vortices*. Utrecht: VSP (1996).

[9] Milani, D. and Morgenthal, G. Adaptive Methods for the simulation of Multiscale Fluid Dynamic Phenomena using Vortex Particle Methods with applications to Civil Structures. *Proceedings of the 4th International Conference on Particle-Based Methods — Fundamentals and Applications, PARTICLES 2015* (2015): 379–390.

[10] Kuzmina, K.S., Marchevsky, I.K. and Ryatina, E.P. Exact analytical formulae for linearly distributed vortex and source sheets influence computation in 2D vortex methods. *Journal of Physics: Conference Series* (2017). In press.

V International Conference on Particle-based Methods – Fundamentals and Applications
PARTICLES 2017
P. Wriggers, M. Bischoff, E. Oñate, D.R.J. Owen, & T. Zohdi (Eds)

EFFICIENT SEMI-ANALYTICAL INTEGRATION OF VORTEX SHEET INFLUENCE IN 3D VORTEX METHOD

ILIA K. MARCHEVSKY AND GEORGY A. SHCHEGLOV

Bauman Moscow State Technical University (BMSTU)
Applied mathematics department, Aerospace systems department
2-nd Baumanskaya st., 5/1, 105005, Moscow, Russia
E-mail: iliamarchevsky@mail.ru, shcheglov_ga@bmstu.ru

Key words: 3D incompressible flow, vortex method, tangential velocity, boundary condition, singularity exclusion

Abstract. The original numerical scheme is developed for vortex sheet intensity computation for 3D incompressible flow simulation using meshless Lagrangian vortex methods. It is based on tangential components of the velocity boundary condition satisfaction on the body surface instead of widespread condition for normal components. For the body triangulated surface the corresponding integral equation is approximated by the system of linear algebraic equations, which dimension is doubled number of triangular panels. Vortex layer intensity on the panels assumed to be piecewise-constant.

The coefficients of the matrix are expressed through double integrals over the influence and control panels. When these panels have common edge or common vertex these integrals become improper. In order to compute them it is necessary to exclude the singularities, i.e., to split the integrals into regular and singular parts. Regular parts are expressed by smooth functions, so they can be integrated numerically with high precision by using Gaussian quadrature formulae. For singular parts exact analytical integration formulae are derived.

The developed approach allows to raise significantly the accuracy of vortex layer intensity computation in vortex method for flow simulation around arbitrary 3D bodies.

The test problem of flow simulation around the sphere is considered. The exact analytical solution is known for it, and the developed numerical scheme provides more accurate results in comparison with 'classical' 3D vortex method, especially when non-uniform unstructured triangular meshes are used for bodies surface representation. It allows to use arbitrary triangular mesh on body surface and to refine mesh near sharp edges, what is especially important for flow simulation around bodies with complicated geometry.

1 Introduction and problem statement

The problem of 3D incompressible flow simulation around immovable body is considered. The governing equations are Navier — Stokes equations

$$\nabla \cdot \vec{V} = 0, \quad \frac{\partial \vec{V}}{\partial t} + (\vec{V} \cdot \nabla)\vec{V} = \nu \nabla^2 \vec{V} - \frac{\nabla p}{\rho_\infty},$$

with boundary conditions

$$\lim_{r \to \infty} \vec{V} = \vec{V}_\infty, \quad \lim_{r \to \infty} p = p_\infty, \quad \vec{V}(\vec{r},\, t)\Big|_{\vec{r} \in K} = \vec{0},$$

where $\vec{V}$ is flow velocity; p — pressure; $\rho_\infty = \text{const}$ — density; ν — kinematic viscosity coefficient; $\vec{V}_\infty$ and p_∞ are parameters of the incident flow; K is body surface.

The viscosity assumed to be small, so according to L. Prandtl's theory it is possible to take its influence into account only as a cause of vorticity generation on body surface. So, the flow can be considered inviscid, with vorticity flux from the surface.

The immovable body is simulated by the influence of vortex sheet with unknown intensity $\vec{\gamma}(\vec{r},\, t)$, which is placed on the body surface, $\vec{r} \in K$. The vorticity flux can be simulated if this vortex sheet is free; it means that at every time step this sheet is split into separate vortex elements which form vortex wake around the body.

Vortex wake evolution can be simulated by using one of Lagrangian vortex element methods [1, 2].

Vorticity flux simulation is one of the most important problems is vortex sheet intensity computation. There are two fundamental approaches, which are based on elimination of the limit values of normal or tangential velocity components on the body surface [3]. These approaches can be called "N-scheme" and "T-scheme", respectively.

The accuracy of N-scheme, especially in FSI-applications, when the bodies are movable and deformable, sometimes is not enough for practice. In 2D-case T-scheme allows to obtain much more accurate results, but it requires the usage of more precise integration schemes [3]. Such schemes are constructed and investigated by authors for 2D-case [4].

The aim of the present research is development of the numerical algorithm for T-scheme in 3D case.

2 Integral equation for vortex sheet intensity

Due to the presence of vortex sheet on the body surface, velocity field, which can be expressed by using generalized Biot — Savart law, has jump discontinuity, and its limit

value from body side is

$$\vec{V}_-(\vec{r},\,t) = \vec{V}_\infty + \frac{1}{4\pi}\int\limits_{S(t)} \frac{\vec{\Omega}(\vec{\xi},\,t)\times(\vec{r}-\vec{\xi}\,)}{\left|\vec{r}-\vec{\xi}\,\right|^3} dS_\xi + \\ + \frac{1}{4\pi}\int\limits_{K} \frac{\vec{\gamma}(\vec{\xi},\,t)\times(\vec{r}-\vec{\xi}\,)}{\left|\vec{r}-\vec{\xi}\,\right|^3} dS_\xi - \frac{\vec{\gamma}(\vec{r},\,t)\times\vec{n}(\vec{r}\,)}{2}, \quad \vec{r}\in K.$$

Here $S(t)$ is vortex wake region; $\vec{\Omega}(\vec{\xi},\,t) = \operatorname{curl}\vec{V}(\vec{\xi},\,t)$ is vorticity distribution in $S(t)$, which assumed to be known; $\vec{n}(\vec{r}\,)$ is unit outer normal vector to body surface K.

In order to satisfy the boundary condition on the body surface, vortex sheet intensity should satisfy the integral equation $\vec{V}_-(\vec{r},\,t) = \vec{0}$, $\vec{r}\in K$.

As it proved in [3], it is enough to satisfy this equation only for tangent component of the limit value of velocity field:

$$\vec{n}(\vec{r}\,)\times\Big(\vec{V}_-(\vec{r},\,t)\times\vec{n}(\vec{r}\,)\Big) = \vec{0}.$$

It leads to the integral equation of the 2-nd kind

$$\frac{\vec{n}(\vec{r}\,)}{4\pi}\times\left(\int\limits_K \frac{\vec{\gamma}(\vec{\xi},\,t)\times(\vec{r}-\vec{\xi}\,)}{\left|\vec{r}-\vec{\xi}\,\right|^3}\times\vec{n}(\vec{r}\,)dS_\xi\right) - \frac{\vec{\gamma}(\vec{r},\,t)\times\vec{n}(\vec{r}\,)}{2} = \vec{f}(\vec{r},\,t), \quad \vec{r}\in K, \qquad (1)$$

where

$$\vec{f}(\vec{r},\,t) = -\vec{n}(\vec{r}\,)\times\left(\vec{V}_\infty + \frac{1}{4\pi}\int\limits_{S(t)} \frac{\vec{\Omega}(\vec{\xi},\,t)\times(\vec{r}-\vec{\xi}\,)}{\left|\vec{r}-\vec{\xi}\,\right|^3}\,dS_\xi\right)\times\vec{n}(\vec{r}\,)$$

is known vector function.

3 Integral equation discretization

In order to find approximate solution of integral equation (1), which kernel is unbounded when $|\vec{r}-\vec{\xi}\,|\to 0$, the following assumptions can be made:

1. Body surface is triangulated into N flat cells K_i with areas A_i and normal vectors $\vec{n}_i$, $i = 1,\ldots,N$.

2. The unknown vortex sheet intensity on the i-th cell is constant vector $\vec{\gamma}_i$, $i = 1,\ldots,N$, which lies in the plane of the i-th cell, i.e. $\vec{\gamma}_i\cdot\vec{n}_i = 0$.

3. The integral equation (1) is satisfied on average over the cells.

According to these assumptions the discrete analogue of equation (1) can be derived:

$$\frac{1}{4\pi A_i}\sum_{j=1}^{N}\int\limits_{K_i}\left(\int\limits_{K_j}\vec{n}_i\times\left(\frac{\vec{\gamma}_j\times(\vec{r}-\vec{\xi})}{\left|\vec{r}-\vec{\xi}\right|^3}\times\vec{n}_i\right)dS_\xi\right)dS_r-\frac{\vec{\gamma}_i\times\vec{n}_i}{2}=$$

$$=\frac{1}{A_i}\int\limits_{K_i}\vec{f}(\vec{r},\,t)dS_r,\quad i=1,\ldots,N. \quad (2)$$

To write down (2) in form of linear algebraic system we should choose local orthonormal basis on every cell $(\vec{\tau}_i^{\,(1)},\,\vec{\tau}_i^{\,(2)},\,\vec{n}_i)$, where tangent vectors $\vec{\tau}_i^{\,(1)}$, $\vec{\tau}_i^{\,(2)}$ can be chosen arbitrary and $\vec{\tau}_i^{\,(1)}\times\vec{\tau}_i^{\,(2)}=\vec{n}_i$. So $\vec{\gamma}_i=\gamma_i^{(1)}\vec{\tau}_i^{\,(1)}+\gamma_i^{(2)}\vec{\tau}_i^{\,(2)}$ and we can project (2) for every i-th panel on directions $\vec{\tau}_i^{\,(1)}$ and $\vec{\tau}_i^{\,(2)}$:

$$\begin{aligned}
&\frac{1}{4\pi A_i}\vec{\tau}_i^{\,(1)}\cdot\left(\sum_{j=1}^{N}\gamma_j^{(1)}\vec{\nu}_{ij}^{\,(1)}+\sum_{j=1}^{N}\gamma_j^{(2)}\vec{\nu}_{ij}^{\,(2)}\right)-\frac{\gamma_i^{(2)}}{2}=\frac{b_i^{(1)}}{A_i},\\
&\frac{1}{4\pi A_i}\vec{\tau}_i^{\,(2)}\cdot\left(\sum_{j=1}^{N}\gamma_j^{(1)}\vec{\nu}_{ij}^{\,(1)}+\sum_{j=1}^{N}\gamma_j^{(2)}\vec{\nu}_{ij}^{\,(2)}\right)+\frac{\gamma_i^{(1)}}{2}=\frac{b_i^{(2)}}{A_i}.
\end{aligned} \quad (3)$$

Here

$$\vec{\nu}_{ij}^{\,(k)}=\int\limits_{K_i}\left(\int\limits_{K_j}\frac{\vec{\tau}_j^{\,(k)}\times(\vec{r}-\vec{\xi})}{\left|\vec{r}-\vec{\xi}\right|^3}dS_\xi\right)dS_r,\quad b_i^{(k)}=\int\limits_{K_i}\vec{\tau}_i^{\,(k)}\cdot\vec{f}(\vec{r},\,t)\,dS_r,\quad k=1,\,2;\;i,j=1,\,\ldots,\,N.$$

Algebraic system (3) has infinite set of solutions; in order to select the unique solution we should satisfy additional condition for total vorticity (integral from the vorticity over the body surface)

$$\int\limits_{K}\vec{\gamma}(\vec{r},\,t)dS_r=\vec{0},$$

which can be written down in the following form:

$$\sum_{i=1}^{N}A_i\left(\gamma_i^{(1)}\vec{\tau}_i^{\,(1)}+\gamma_i^{(2)}\vec{\tau}_i^{\,(2)}\right)=\vec{0}. \quad (4)$$

System (3)-(4) is overdetermined, it should be regularized, for example, by introducing the 'regularization vector' $\vec{R}=\left(R_1,\,R_2,\,R_3\right)^T$:

$$\begin{aligned}
&\frac{1}{4\pi A_i}\vec{\tau}_i^{(1)}\cdot\left(\sum_{j=1}^{N}\gamma_j^{(1)}\vec{\nu}_{ij}^{(1)}+\sum_{j=1}^{N}\gamma_j^{(2)}\vec{\nu}_{ij}^{(2)}\right)-\frac{\gamma_i^{(2)}}{2}+\vec{R}\cdot\vec{\tau}_i^{(2)}=\frac{b_i^{(1)}}{A_i},\\
&\frac{1}{4\pi A_i}\vec{\tau}_i^{(2)}\cdot\left(\sum_{j=1}^{N}\gamma_j^{(1)}\vec{\nu}_{ij}^{(1)}+\sum_{j=1}^{N}\gamma_j^{(2)}\vec{\nu}_{ij}^{(2)}\right)+\frac{\gamma_i^{(1)}}{2}+\vec{R}\cdot\vec{\tau}_i^{(1)}=\frac{b_i^{(2)}}{A_i},\\
&\sum_{j=1}^{N}A_j\left(\gamma_j^{(1)}\vec{\tau}_j^{(1)}+\gamma_j^{(2)}\vec{\tau}_j^{(2)}\right)=0,\qquad i=1,\,\ldots,\,N.
\end{aligned}\tag{5}$$

Numerical computations show that system (5) is well-conditioned; its dimension is $2N+3$.

4 Matrix coefficients calculation

The main problem for practical usage of the suggested approach is coefficients $\vec{\nu}_{ij}^{(k)}$ calculation for system (5):

$$\vec{\nu}_{ij}^{(k)}=\vec{\tau}_j^{(k)}\times\int\limits_{K_i}\left(\int\limits_{K_j}\frac{\vec{r}-\vec{\xi}}{\left|\vec{r}-\vec{\xi}\right|^3}dS_\xi\right)dS_r=\vec{\tau}_j^{(k)}\times\vec{I}_{ij},\quad k=1,\,2,\quad i,\,j=1,\,\ldots,\,N\tag{6}$$

Integral $\vec{I}_{ij}$ is calculated over triangular cells K_i and K_j, where i-th cell we call 'control', j-th cell — 'influence' cell.

4.1 The general approach

The inner integral in (6) over the influence cell K_j

$$\vec{J}_j(\vec{r})=\int\limits_{K_j}\frac{\vec{r}-\vec{\xi}}{\left|\vec{r}-\vec{\xi}\right|^3}dS_\xi\tag{7}$$

can be calculated exactly. There is well-known way for analytical calculation of integral (7) via considering of the integral from $\left|\vec{r}-\vec{\xi}\right|^{-1}$ with respect to $\vec{\xi}$ over the triangle K_j:

$$\vec{J}_j(\vec{r})=\int\limits_{K_j}\frac{\vec{r}-\vec{\xi}}{\left|\vec{r}-\vec{\xi}\right|^3}dS_\xi=\int\limits_{K_j}\nabla_\xi\frac{1}{\left|\vec{r}-\vec{\xi}\right|}dS_\xi=-\int\limits_{K_j}\nabla_r\frac{1}{\left|\vec{r}-\vec{\xi}\right|}dS_\xi=-\nabla_r\left(\int\limits_{K_j}\frac{1}{\left|\vec{r}-\vec{\xi}\right|}dS_\xi\right).$$

The last integral is very usual in potential theory, analytical expression for it can be found, for example, in [5]. However, that expression is cumbersome and it also should be differentiated with respect to components of vector $\vec{r}$.

Using computational software of symbolic mathematics *Wolfram Mathematica* and Handbook of integrals [6] it is possible to integrate (7) straightforwardly if vectors

$\vec{s}_k = \vec{r}_k^{\,(j)} - \vec{r}$, $k = 1, 2, 3$, are only known, where $\vec{r}$ is point for which integral (7) is calculated, $\vec{r}_k^{\,(j)}$ are vertices of K_j triangular cell. Denoting

$$\vec{e}_k^{\,(j)} = \frac{\vec{s}_{k+1} - \vec{s}_k}{\left|\vec{s}_{k+1} - \vec{s}_k\right|} = \frac{\vec{r}_{k+1}^{\,(j)} - \vec{r}_k^{\,(j)}}{\left|\vec{r}_{k+1}^{\,(j)} - \vec{r}_k^{\,(j)}\right|}, \qquad \vec{\sigma}_k = \frac{\vec{s}_k}{\left|\vec{s}_k\right|}, \quad k = 1, 2, 3,$$

and assuming all the indices to be calculated using a modulus of 3, we obtain

$$\vec{J}_j(\vec{r}) = \Theta_j \vec{n}_j + \vec{\Psi}_j \times \vec{n}_j, \quad j = 1, \ldots, N,$$

where

$$\vec{\Psi}_j = \sum_{k=1}^{3} \ln\left(\frac{\left|\vec{s}_k\right|}{\left|\vec{s}_{k+1}\right|} \frac{1 + \vec{e}_k^{\,(j)} \cdot \vec{\sigma}_k}{1 + \vec{e}_k^{\,(j)} \cdot \vec{\sigma}_{k+1}} \right) \vec{e}_k,$$

and Θ_j is solid angle subtended by triangular cell K_j which can be calculated, for example, by using the formula [7]

$$\Theta_j = 2 \arctan\left(\frac{\vec{s}_1 \vec{s}_2 \vec{s}_3}{\left|\vec{s}_1\right| \cdot \left|\vec{s}_2\right| \cdot \left|\vec{s}_3\right| + \left(\vec{s}_1 \cdot \vec{s}_2\right)\left|\vec{s}_3\right| + \left(\vec{s}_2 \cdot \vec{s}_3\right)\left|\vec{s}_1\right| + \left(\vec{s}_3 \cdot \vec{s}_1\right)\left|\vec{s}_2\right|} \right),$$

here $\vec{s}_1 \vec{s}_2 \vec{s}_3$ denotes the scalar triple product of the vectors.

The outer integral in (6)

$$\vec{I}_{ij} = \int\limits_{K_i} \vec{J}_j(\vec{r})\, dS_r \tag{8}$$

can't be simply expressed analytically in elementary functions, so the suitable way for its computation is Gaussian quadrature formula usage:

$$\vec{I}_{ij} = \int\limits_{K_i} \vec{J}_j(\vec{r})\, dS_r \approx A_i \sum_{p=1}^{N_{GP}} \omega_p \vec{J}_j(\vec{\eta}_p),$$

where N_{GP} is number of Gaussian points; ω_p are weight coefficients; $\vec{\eta}_p$ are positions of Gaussian points. Values of ω_p and $\vec{\eta}_p$ for different values of N_{GP} can be found, for example, in [8].

It works perfectly if influence and control cells are far one from the other; numerical experiments show that it is enough to use the corresponding quadratures with small number of points ($N_{GP} = 1 \ldots 4$).

However, for cells which have common edge or common vertex (such cells we call 'neighboring cells') the corresponding integral is improper, so Gaussian quadratures become unsuitable. Direct numerical computation of improper integral is non-trivial problem, so for such cases semi-analytical approach is developed.

If the cells have common edge or common vertex, we need to exclude the singularity from the $\vec{J}_j(\vec{r})$ and write it down as sum of two terms:

$$\vec{J}_j(\vec{r}) = \vec{J}_j^{\,\mathrm{reg}}(\vec{r}) + \vec{J}_j^{\,\mathrm{sing}}(\vec{r}).$$

where $\vec{J}_j^{\,\mathrm{reg}}(\vec{r})$, which has the form

$$\vec{J}_j^{\,\mathrm{reg}}(\vec{r}) = \big(\Theta_j(\vec{r}) - \Theta_j^{\,\mathrm{sing}}(\vec{r})\big)\vec{n}_j + \big(\vec{\Psi}_j(\vec{r}) - \vec{\Psi}_j^{\,\mathrm{sing}}(\vec{r})\big) \times \vec{n}_j,$$

has no singularities and can be easily integrated numerically with high accuracy by using Gaussian quadrature formulae

$$\int\limits_{K_i} \vec{J}_j^{\mathrm{reg}}(\vec{r})\, dS_r \approx A_i \sum_{p=1}^{N_{GP}} \omega_p \vec{J}_j^{\mathrm{reg}}(\vec{\eta}_p).$$

For the improper (singular) integral

$$\int\limits_{K_i} \vec{J}_j^{\,\mathrm{sing}}(\vec{r})\, dS_r = \left(\int\limits_{K_i} \Theta_j^{\,\mathrm{sing}}(\vec{r})\, dS_r\right)\vec{n}_j + \left(\int\limits_{K_i} \vec{\Psi}_j^{\,\mathrm{sing}}(\vec{r}) dS_r\right) \times \vec{n}_j$$

exact analytical formulae are derived, which are shown below.

4.2 Neighboring cells with common edge

If cells K_i and K_j have common edge with directing unit vector $\vec{e}_3$, as it is shown in fig. 1, singular terms have the following form (hereinafter upper index (j) in unit vectors $\vec{e}_1^{\,(j)}$, $\vec{e}_2^{\,(j)}$ and $\vec{e}_3^{\,(j)}$ is omitted):

$$\Theta_j^{\,\mathrm{sing}}(\vec{r}) = 2\Big(\arctan\frac{\vec{b}\,\vec{e}_2\,\vec{e}_3}{|\vec{b}\,|(1-\vec{e}_2\cdot\vec{e}_3) - \vec{b}\cdot(\vec{e}_2-\vec{e}_3)} - \arctan\frac{\vec{a}\,\vec{e}_1\,\vec{e}_3}{|\vec{a}\,|(1-\vec{e}_1\cdot\vec{e}_3) + \vec{a}\cdot(\vec{e}_1-\vec{e}_3)}\Big),$$

$$\vec{\Psi}_j^{\,\mathrm{sing}}(\vec{r}) = \vec{e}_3 \ln\frac{|\vec{a}\,|\cdot|\vec{c}\,| - \vec{a}\cdot\vec{c}}{|\vec{b}\,|\cdot|\vec{c}\,| - \vec{b}\cdot\vec{c}} + \vec{e}_1 \ln\frac{|\vec{a}\,| + \vec{a}\cdot\vec{e}_1}{|\vec{c}\,|} + \vec{e}_2 \ln\frac{|\vec{b}\,| - \vec{b}\cdot\vec{e}_2}{|\vec{c}\,|},$$

where

$$\vec{c} = \vec{r}_1^{\,(j)} - \vec{r}_3^{\,(j)}, \quad \vec{a} = \vec{r}_1^{\,(j)} - \vec{r}, \quad \vec{b} = \vec{r}_3^{\,(j)} - \vec{r},$$

Expression for $\Theta_j^{\,\mathrm{sing}}$, as well as all scalar multipliers of $\vec{\Psi}_j^{\,\mathrm{sing}}$ can be integrated analytically over the cell K_i, an finally we obtain:

$$\int\limits_{K_i} \Theta_j^{\,\mathrm{sing}}(\vec{r})\, dS_r = -2A_i\big(q_0(\xi,\alpha,\beta,\mu,\gamma,\lambda) + q_0(\xi,\beta,\alpha,\sigma,\delta,\theta)\big),$$

$$\int\limits_{K_i} \vec{\Psi}_j^{\,\mathrm{sing}}(\vec{r})\, dS_r = A_i\big(q_{12}(\xi,\alpha,\beta,\mu,\gamma,\lambda)\vec{e}_1 + q_{12}(\xi,\beta,\alpha,\sigma,\delta,\theta)\vec{e}_2 + q_3(\alpha,\beta)\vec{e}_3\big).$$

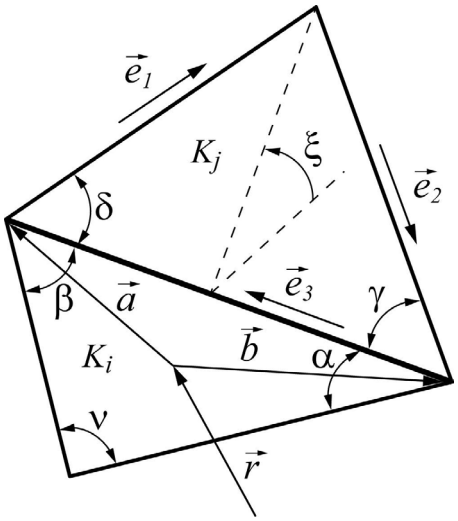

Figure 1: Cells K_i and K_j in case of having common edge

Here auxiliary functions q_0, q_{12} and q_3 have the form

$$q_0(\xi,\alpha,\beta,\mu,\gamma,\lambda) = \arctan\frac{\sin\xi\sin\alpha\sin\gamma}{1-\cos\alpha+\cos\gamma+\cos\lambda} + \\ + \frac{\sin\gamma\sin\nu}{\sin^2\mu\sin\alpha}\Bigg(\big(\cos\beta\sin\gamma-\sin\beta\cos\gamma\cos\xi\big)\arctan\frac{\sin\xi\sin\alpha\sin\gamma}{1+\cos\alpha-\cos\gamma+\cos\lambda} + \\ + \sin\xi\sin\beta\Big(\cos^2\frac{\mu}{2}\ln\frac{\cos\beta/2}{\sin\nu/2}+\sin^2\frac{\mu}{2}\ln\frac{\sin\beta/2}{\cos\nu/2}+\ln\frac{\cos\lambda/2}{\sin\gamma/2}\Big)\Bigg),$$

$$q_{12}(\xi,\alpha,\beta,\mu,\gamma,\lambda) = \\ = -\frac{3}{2}+\frac{1}{\sin\alpha\sin^2\mu}\Bigg(\ln(1+\cos\lambda)\sin\beta(\cos\nu+\cos\mu\cos\lambda) + \\ + \ln(1-\cos\gamma)\sin\nu(\cos\beta+\cos\gamma\cos\mu) + \\ + \ln\frac{\sin\beta}{\sin\nu}\sin\beta(1-\cos\mu)(\cos\nu-\cos\lambda) - \\ - \sin\nu\sin\beta\Big(-2\sin\xi\sin\gamma\arctan\frac{\sin\xi\sin\gamma\sin\alpha}{1+\cos\lambda-\cos\gamma+\cos\alpha} + \\ + (\sin\gamma\cos\beta\cos\xi-\sin\beta\cos\gamma)\ln\frac{1-\cos\nu}{1+\cos\beta}\Big)\Bigg),$$

$$q_3(\alpha,\beta) = \frac{\sin\nu}{\sin\beta}\ln\Big(\tan\frac{\alpha}{2}\tan\frac{\nu}{2}\Big)+\frac{\sin\nu}{\sin\alpha}\ln\Big(\tan\frac{\beta}{2}\tan\frac{\nu}{2}\Big)+\ln\Big(\tan\frac{\alpha}{2}\tan\frac{\beta}{2}\Big).$$

Here α and β are the angles of the triangle K_i, which adjoin the common edge of the cells K_i and K_j, $\nu=\pi-\alpha-\beta$; γ and δ are the angles of the triangle K_j, which adjoin the

common edge; ξ is the angle between the planes of the cells K_i and K_j; angles σ, μ, λ and θ can be calculated by using formulae

$$\sigma = \pi - \arccos(\cos\alpha\cos\delta + \cos\xi\sin\alpha\sin\delta),$$
$$\mu = \pi - \arccos(\cos\beta\cos\gamma + \cos\xi\sin\beta\sin\gamma),$$
$$\lambda = \pi - \arccos(\cos\alpha\cos\gamma - \cos\xi\sin\alpha\sin\gamma),$$
$$\theta = \pi - \arccos(\cos\beta\cos\delta - \cos\xi\sin\beta\sin\delta).$$

4.3 Neighboring cells with common vertex

If cells K_i and K_j have common vertex, for example as it is shown in fig. 2, the regular part $\vec{J}_j^{\,\mathrm{reg}}(\vec{r})$ has the following form (the previous denotation is used):

$$\Theta_j^{\,\mathrm{sing}}(\vec{r}) = -2\Big(\arctan\frac{\vec{b}\,\vec{e}_{**}\,\vec{e}_0}{|\vec{b}\,|(1+\vec{e}_{**}\cdot\vec{e}_0)+\vec{b}\cdot(\vec{e}_{**}+\vec{e}_0)} - \arctan\frac{\vec{b}\,\vec{e}_{*}\,\vec{e}_0}{|\vec{b}\,|(1+\vec{e}_{*}\cdot\vec{e}_0)+\vec{b}\cdot(\vec{e}_{*}+\vec{e}_0)}\Big),$$
$$\vec{\Psi}_j^{\,\mathrm{sing}}(\vec{r}) = -\Big(\vec{e}_{**}\ln\frac{|\vec{b}\,|+\vec{b}\cdot\vec{e}_{**}}{\sqrt{A_j}} - \vec{e}_{*}\ln\frac{|\vec{b}\,|+\vec{b}\cdot\vec{e}_{*}}{\sqrt{A_j}}\Big),$$

where $\vec{b} = \vec{r}_c^{\,(j)} - \vec{r}$; $\vec{e}_0$ is unit vector of intersection line of the planes of the cells K_i and K_j; $\vec{e}_*$ and $\vec{e}_{**}$ are unit vectors of sides of cell K_j, as it is shown in fig. 2.

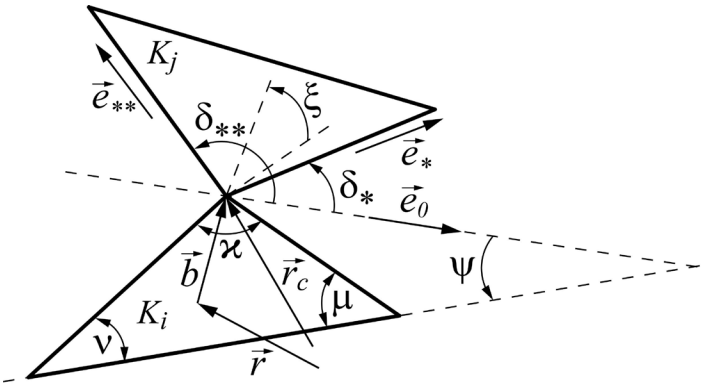

Figure 2: Cells K_i and K_j in case of having common vertex

These expressions also can be integrated analytically over the cell K_i:

$$\int\limits_{K_i} \Theta_j^{\,\mathrm{sing}}(\vec{r})\,dS_r = -2A_i\big(q_4(\delta_{**}) - q_4(\delta_*)\big),$$
$$\int\limits_{K_i} \vec{\Psi}_j^{\,\mathrm{sing}}(\vec{r})\,dS_r = -A_i\big(q_5(\delta_{**})\vec{e}_{**} - q_5(\delta_*)\vec{e}_*\big).$$

The auxiliary functions q_4 and q_5 are the following:

$$q_4(\delta) = \frac{1}{\sin\psi\sin\varkappa}\Bigg(\sin\mu\sin(\nu+\psi)\arctan\frac{\sin\xi\sin\delta/2}{\cos\xi\sin\delta/2+\cos\delta/2\cot(\nu+\psi)/2} - \\ - \sin\nu\sin(\mu-\psi)\arctan\frac{\sin\xi\sin\delta/2}{\cos\xi\sin\delta/2+\cos\delta/2\tan(\mu-\psi)/2} - \\ - \frac{\sin\mu\sin\nu\sin\psi\sin\delta}{D}\Bigg(2(\cos\xi\cos\delta-\cot\psi\sin\delta)\omega + \\ + \sin\xi\Big(\ln\Big(\frac{1+\cos\lambda}{1-\cos\theta}\frac{\sin\nu}{\sin\mu}\Big)+\cos\sigma\ln\Big(\tan\frac{\nu}{2}\tan\frac{\mu}{2}\Big)\Big)\Bigg)\Bigg),$$

$$q_5(\delta) = -\frac{3-\ln 2}{2} + \frac{\sin\mu\sin(\nu+\psi)\ln(1-\cos\theta)-\sin\nu\sin(\mu-\psi)\ln(1+\cos\lambda)}{\sin\varkappa\sin\psi} + \\ + \frac{1}{2}\ln\frac{\sin\nu\sin\mu}{\sin\varkappa} - \frac{\cos\nu\sin\mu}{\sin\varkappa}\ln\sin\nu - \frac{\cos\mu\sin\nu}{\sin\varkappa}\ln\sin\mu - \\ - \frac{2\sin\nu\sin\mu}{D\sin\varkappa\sin\psi}\Bigg(\sin\delta\big(\sin\psi\cos\delta\cos\xi-\cos\psi\sin\delta\big)\ln\frac{1-\cos\theta}{1+\cos\lambda} - \\ - \sin\psi\big(\sin\delta\cos\psi\cos\xi-\cos\delta\sin\psi\big)\ln\Big(\tan\frac{\nu}{2}\tan\frac{\mu}{2}\Big) + \\ + \sin\psi\Big(2\omega\sin\delta\sin\xi-\frac{1}{2}\Big(\big(1-\sin^2\delta(1+\cos^2\xi)\big)\sin 2\psi-\sin 2\delta\cos 2\psi\cos\xi\Big)\ln\frac{\sin\nu}{\sin\mu}\Big)\Bigg).$$

Here we denotes for simplicity

$$D = 2\sin^2\psi+\sin^2\delta\big(\sin^2\xi+(1+\cos^2\xi)\cos 2\psi\big)-\sin 2\delta\sin 2\psi\cos\xi, \\ \omega = \arctan\frac{\sin\xi\sin\delta\sin\varkappa/2}{\cos\xi\sin\delta\sin(\nu+\psi+\varkappa/2)+\cos\varkappa/2-\cos\delta\cos(\mu-\psi+\varkappa/2)}.$$

Here $\varkappa$ is the angles of the triangle K_i, which adjoins the common vertex of the cells K_i and K_j; μ and ν are the other angles of cell K_i; ξ is the angle between the planes of the cells K_i and K_j; ψ is the angle between $\vec{e}_0$ and the side of triangle K_i, which is opposite to common vertex; δ_* and δ_{**} are the angles between $\vec{e}_0$ and vectors $\vec{e}_*$ and $\vec{e}_{**}$, respectively; angles σ, λ and θ can be calculated by using formulae

$$\sigma = \pi - \arccos\big(\cos\psi\cos\delta+\cos\xi\sin\psi\sin\delta\big), \\ \lambda = \pi - \arccos\big(\cos\delta\cos(\mu-\psi)-\cos\xi\sin\delta\sin(\mu-\psi)\big), \\ \theta = \pi - \arccos\big(\cos\delta\cos(\nu+\psi)+\cos\xi\sin\delta\sin(\nu+\psi)\big).$$

5 Numerical experiment

The developed semi-analytical numerical scheme makes it possible to use arbitrary triangular surface mesh even of very low quality. The corresponding linear system is being solved by using Gaussian elimination procedure. In the numerical examples shown below `Eigen` library, developed for C++, has been used [9]. In fig. 3 the results are shown for some test cases: flow around the sphere (with close to uniform mesh), flow around a weight (with mesh cells of very different size) and flow around a fish model (some mesh cells are very long and narrow). Red lines in the centers of cells shows the direction of vorticity in vortex sheet.

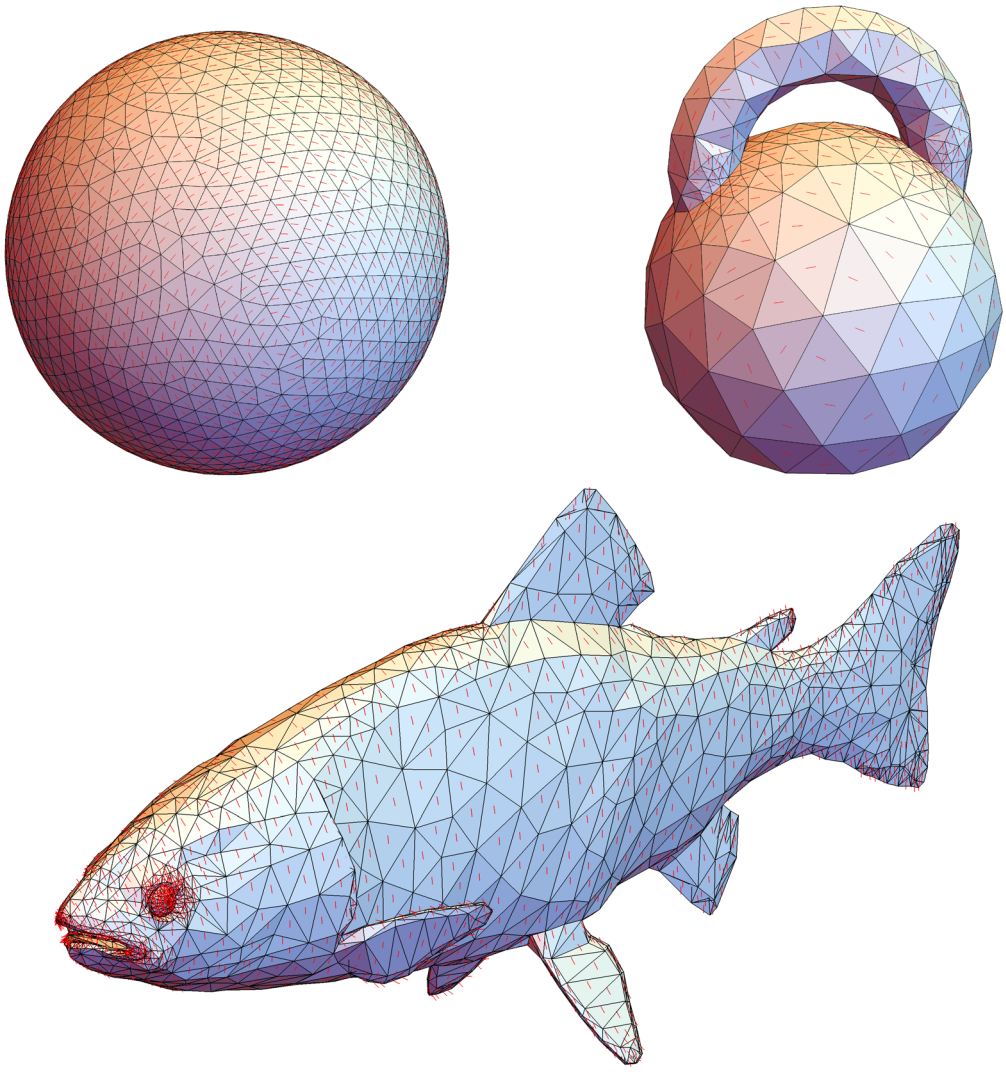

Figure 3: Vortex sheet on the sphere (number of panels $N = 2814$); on the weight ($N = 636$) and on the fish ($N = 3194$)

6 Conclusions

The derived formulae for $\vec{I}_{ij}$ makes it possible to construct numerical procedure for solving of the discrete analogue of the integral equation for vortex sheet intensity calculation in the framework of 'tangent' approach. It allows to use arbitrary triangular mesh on body surface and to refine mesh near sharp edges, that is especially important for flow around 3D wings simulation. Despite the fact that the dimension of the linear system in the developed numerical scheme is twice as large then in traditional implementations of vortex methods, its accuracy is much higher.

Acknowledgement

The research is supported by Russian Science Foundation (proj. 17-79-20445).

REFERENCES

[1] Cottet, G.-H. and Koumoutsakos, P.D. *Vortex Methods: Theory and Practice*. CUP (2000).

[2] Marchevsky, I.K. and Shcheglov, G.A. 3D vortex structures dynamics simulation using vortex fragmentons, *ECCOMAS 2012 — European Congress on Computational Methods in Applied Sciences and Engineering, e-Book Full Papers*, Vienna (2012), 5716–5735.

[3] Kempka S.N., Glass M.W., Peery J.S. and Strickland J.H. Accuracy considerations for implementing velocity boundary conditions in vorticity formulations, *SANDIA REPORT SAND96-0583*, UC-700 (1996).

[4] Kuzmina, K.S. and Marchevsky, I.K. The modified numerical scheme for 2D flow-structure interaction simulation using meshless vortex element method. *Proc. of the 4th International Conference on Particle-Based Methods — Fundamentals and Applications, PARTICLES 2015*, Barcelona (2015), 680–691.

[5] Antonov, V.A., Nikiforov, I.I. and Kholshevnikov, K.V. *Elements of the theory of the gravitational potential, and some instances of its explicit expression*. St.-Petersburg University Press (2008) (in Russian).

[6] Gradshteyn, I.S., Ryzhik, I.M., Jeffrey, A. (Ed.) and Zwillinger, D. (Ed.) *Gradshteyn and Ryzhik's Table of Integrals, Series, and Products*. Elsevier (2007).

[7] Van Oosterom, A. and Strackee, J. The Solid Angle of a Plane Triangle. *IEEE Trans. Biom. Eng. BME-30* (1983) **2**:125–126.

[8] Zienkiewicz, O.C., Taylor, R.L. and Zhu, J.Z. *The Finite Element Method: Its Basis and Fundamentals*. Elsevier (2013).

[9] Eigen library for linear algebra. http://eigen.tuxfamily.org.

V International Conference on Particle-based Methods – Fundamentals and Applications
PARTICLES 2017
P. Wriggers, M. Bischoff, E. Oñate, D.R.J. Owen, & T. Zohdi (Eds)

HIGH-ORDER NUMERICAL SCHEME FOR VORTEX SHEET APPROXIMATION IN VORTEX METHODS FOR 2D FLOW SIMULATION

KSENIIA S. KUZMINA AND ILIA K. MARCHEVSKY

Bauman Moscow State Technical University (BMSTU)
Applied mathematics department
2-nd Baumanskaya st., 5, 105005, Moscow, Russia
E-mail: kuz-ksen-serg@yandex.ru, iliamarchevsky@mail.ru

Key words: vortex method, boundary integral equation, curvilinear panels, Galerkin method

Abstract. The problem of high-order numerical schemes developing is considered for solving of boundary integral equation for vortex sheet intensity, which arises in 2D meshless vortex particle methods. Curvilinearity of the airfoil surface line is taken into account: its shape is approximated by Hermite cubic spline interpolation instead of rectilinear panels which are usually used in vortex methods. Coefficients of system of linear algebraic equations are represented by define integrals of known functions. For some coefficients (which can not be calculated numerically) approximate analytic formulae are obtained, the other coefficients can be computed using 4 point Gaussian integration. The developed numerical scheme provides 4-th order of accuracy for average values of vortex sheet intensities over the panels.

1 INTRODUCTION

Vortex method [1, 2, 3, 4] is well-known meshless lagrangian particle method, which allows to solve efficiently number of actual engineering problems. The main idea of vortex method is that vorticity is considered as a primary computed variable. The airfoil influence is replaced by a vortex sheet placed on the airfoil surface line. Its intensity can be found from boundary condition on the airfoil surface line. The modification of vortex method is used which corresponds to the integral equation of the 2-nd kind with bounded kernel (for smooth airfoils) [5, 6]. When solving this equation in vortex methods airfoil is usually approximated with a polygon consisting of N rectilinear segments (panels) and solution of boundary integral equation is assumed to be piecewise-constant or piecewise-linear function. Numerical experiments show that in some cases such approach doesn't allow to obtain high order of accuracy, this fact has a negative effect on the whole problem solution, especially for significantly nonuniform mashes of the airfoil surface line. This

problem can be solved by improving of airfoil surface line discretization, i.e. by taking into account its curvilinearity.

The aim of this paper is to develop new numerical scheme for boundary integral equation approximation, which provides high order of accuracy.

2 The governing equations

The problem of two-dimensional incompressible flow simulation around rigid immovable airfoil is considered. In vortex method at every time step two sub-problems should be solved:

- vortex sheet intensity computation on the surface line of the airfoil;
- vorticity motion simulation in the flow.

The airfoil in the flow can be replaced with vortex sheet on its surface line, because the vortex sheet with appropriate intensity distribution influences the flow exactly in the same way as the airfoil itself [8, 9].

So the unknown intensity distribution $\gamma(\boldsymbol{r})$ can be found from the solution of some boundary integral equation which corresponds to no-slip (for viscous flow) or no-through (for inviscid media) boundary condition.

Two different approaches can be distinguished to derivation of such boundary integral equation [5], and that one which is based on the equality to zero of the tangent component of velocity limit value on the surface line seems to be most efficient. It leads to the Fredholm-type boundary integral equation of the second kind:

$$\frac{1}{2\pi}\oint_K Q_\tau(\boldsymbol{r},\boldsymbol{\xi})\gamma(\boldsymbol{\xi})dl_\xi - \frac{\gamma(\boldsymbol{r})}{2} = f_\tau(\boldsymbol{r}), \quad \boldsymbol{r}\in K. \tag{1}$$

Its kernel is uniformly bounded function for C^2-smooth curves (*i.e.*, when parametric equations of the surface line belong to C^2 class with respect to arc length) and it has the following form:

$$Q_\tau(\boldsymbol{r},\boldsymbol{\xi}) = \frac{\boldsymbol{k}\times(\boldsymbol{r}-\boldsymbol{\xi})}{|\boldsymbol{r}-\boldsymbol{\xi}|^2}\cdot\boldsymbol{\tau}(\boldsymbol{r}),$$

where $\boldsymbol{\tau}(\boldsymbol{r})$ is tangent unit vector.

It should be noted, that the alternative approach which is based on zero value of the normal components of flow velocity on the surface line [5], leads to singular integral equation of the 1-st kind with Hilbert-type kernel, so special numerical procedures should be applied in order to compute the principle value of the corresponding integral [7].

Right-hand side $f_\tau(\boldsymbol{r})$ of the equation (1) in the considered case is known function, which depends on the shape of the airfoil, incident flow velocity and vorticity distribution in the flow. In the most general case it also depends on the surface line velocity, which is unknown function in coupled hydroelastic problems, when the surface line of the airfoil

moves under hydrodynamic loads. If the motion and/or deformation low of the airfoil is known, the right-hand side $f_\tau(\boldsymbol{r})$ again becomes known function.

In order to take into account non-zero velocity of the airfoil surface line, the attached source sheet and attached vortex sheets should be introduced [2, 10]. All the approaches and formulae being discussed hereinafter can be easily generalized for such case. The arbitrary vortity distribution in the flow domain also can be considered, but for simplicity we assume that the is no vorticity in the flow domain at all, in this case the right-hand side $f_\tau(\boldsymbol{r})$ has the simplest form:

$$f_\tau(\boldsymbol{r}) = -\boldsymbol{V}_\infty \cdot \boldsymbol{\tau}(\boldsymbol{r}), \tag{2}$$

where $\boldsymbol{V}_\infty$ is incident flow velocity.

The equation (1) has infinite set of solutions, which follows from the fact that the corresponding integral operator has the eigenvalue $\lambda = 0$. In particular, for circular airfoil $\lambda = 0$ corresponds to the eigenfunction which is equal to constant.

In order to select the unique solution, which is physically plausible, the most convenient way is to add an extra equation for the total value of vorticity, which the vortex sheet contains, *i.e.*, the integral of the solution should be equal to the given value:

$$\oint_K \gamma(\boldsymbol{\xi}) dl_\xi = \Gamma, \tag{3}$$

The value Γ is usually known from the physical sense of the considered problem, in particular, for unsteady flow simulation its value follows from the Helmholtz theorems and their analogues for viscous flows.

3 Numerical schemes on the surface line of the airfoil

3.1 Airfoil discretization by using rectilinear panels

The simplest way to approximate the shape of the airfoil is to replace it with polygon. The legs of the polygon are usually called "panels". Vortex sheet intensity distribution over the panels is normally assumed to be piecewise-constant or piecewise-linear.

The most accurate schemes with piecewise-constant vorticity distribution provide the 2-nd order of accuracy for average values of solution (vortex sheet intensity) over the panels, and the 1-st order of accuracy in L_1 norm. The schemes with piecewise-linear vorticity distribution just a little more accurate with respect to average values of solution over the panels, but they provide the 2-nd order of accuracy in L_1 norm.

It should be noted, that the accuracy becomes much lower when the lengthes of neighboring panels differ significantly. From the mathematical point of view it can be explained by the following way: instead of smooth part of the curve in numerical simulation we simulate, in fact, flow around the airfoil with angle points (fig. 1). In proximity to such point the kernel of the integral equation (1) becomes unbounded, and the exact solution for such airfoil shape can has "unphysical" weak singularity in angle points.

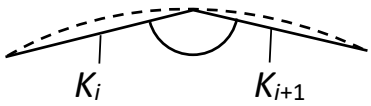

Figure 1: The part of airfoil surface and two rectilinear panels

In case of uniform splitting of the surface line of the airfoil into panels the mentioned singularities of the kernel, which arise at the endings of the panels, compensate each other. However, if neighboring panels lengthes differ appreciably, these singularities influences are significant and it leads to the errors of the coefficients computation of the resulting system of linear algebraic equations.

So, when the discretization of the surface line of the airfoil is uniform or close to uniform, the most accurate results for equations (1), (3) numerical solution, as the rule, can be obtained when the following approach is being used, which is similar to Discontinuous Galerkin (DG) [11] method. The approximate numerical solution is assumed to be linear combination of basis functions (constant and linear ones; it is useful to provide zero average value for linear basis function, which means that is orthogonal to the constant basis function). The unknown coefficients are found from solution of the linear system which corresponds to the residual orthogonality to basis functions. Naturally, when the described approach is being implemented, the numerical solution has discontinuities (jumps) between the panels.

3.2 Airfoil discretization taking into account curvilinearity of the panels

In [12] numerical scheme is developed which permits to take into account explicitly the curvilinearity of the surface line of the airfoil approximate it by smooth curve of spline-type or Hermite spline type. It provides the 4-th order of accuracy for the solution average values over the curvilinear panels, but its computational cost is extremely high, so it hardly can be implemented in practical applications.

In the present paper simplified numerical scheme is considered which provides the same (4-th) order of accuracy for approximate solution of boundary integral equation.

Let's denote the vertices of the airfoil as $\boldsymbol{C}_i$, $i = 1, \ldots, N$, rectilinear lines C_iC_{i+1} we call "chords" of the airfoil. As in [12], the surface line of the airfoil over the i-th chord is being approximated by smooth curve, that has the following parametric equation:

$$\boldsymbol{r}_i(t) = \boldsymbol{C}_i + L_i^0 \left(t\, \boldsymbol{\tau}_i^0 + p_i(t)\, \boldsymbol{n}_i^0 \right), \quad t \in [0;\, 1]. \tag{4}$$

Parameter values $t = 0$ and $t = 1$ correspond to the beginning and ending of the panel; L_i^0 is length of the i-th chord; $\boldsymbol{\tau}_i^0$ and $\boldsymbol{n}_i^0$ are tangent and normal unit vectors for the i-th chord. Function $p_i(t)$ is cubic polynomial:

$$p_i(t) = \alpha_i\, t(t-1) + \beta_i\, t(t-1/2)(t-1), \tag{5}$$

where the coefficients α_i and β_i can be found from the following condition: the directions of tangent vector should be the same for exact shape of the airfoil and its approximate representation (fig. 2). They can be written down in explicit form.

$$\alpha_i = -\frac{1}{2}(\tan\varphi_i + \tan\psi_i), \quad \beta_i = (\tan\varphi_i - \tan\psi_i).$$

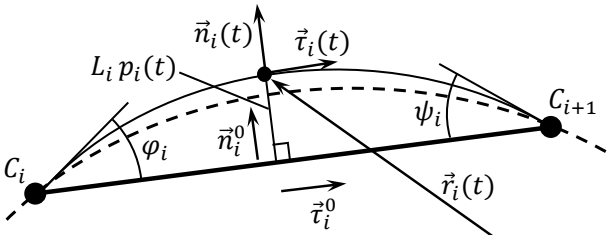

Figure 2: Curvilinear panel and the i-th chord of the airfoil

It should be noted, that if the curvilinear part of the airfoil surface line is represented over the i-th panel as smooth curve, that belongs to C^4 class, the error of the airfoil shape approximation with Hermite spline has order of $O(L_i^4)$.

3.3 Integral equation approximation

In order to construct numerical scheme for equations (1), (3), the principal ideas of Discontinuous Galerkin (DG) method seems to be useful. We introduce constant and linear basis functions $\varphi_0^i(t)$ and $\varphi_1^i(t)$, $i = 1, \ldots, N$, each of these functions differs from zero only on the i-th panel:

$$\varphi_0^i(t) \equiv 1, \qquad \varphi_1^i(t) = t - \frac{1}{2}, \qquad t \in [0;\, 1].$$

The solution over the every panel of the airfoil is considered to be linear distribution with respect to parameter t:

$$\gamma\big(\boldsymbol{r}_i(t)\big) = \gamma_i\varphi_0^i(t) + \delta_i\varphi_1^i(t), \qquad t \in [0;\, 1], \qquad i = 1, \ldots, N.$$

The unknown coefficients γ_i and δ_i can be found from orthogonality condition. The residual of the equation (1) on the i-th panel, which has the following form:

$$z_i(t) = \sum_{j=1}^{N} \left(\gamma_j \int_0^1 Q_\tau\big(\boldsymbol{r}_i(t),\, \boldsymbol{r}_j(\xi)\big)\, \varphi_0^j(\xi)\, J_j(\xi) d\xi + \right.$$
$$\left. + \delta_j \int_0^1 Q_\tau\big(\boldsymbol{r}_i(t),\, \boldsymbol{r}_j(\xi)\big) \varphi_1^j(\xi)\, J_j(\xi)\, d\xi \right) -$$
$$- \frac{\gamma_i\varphi_0^j(t) + \delta_i\varphi_1^j(t)}{2} - f_\tau\big(\boldsymbol{r}_i(t)\big), \quad i = 1, \ldots, N,$$

should be orthogonal to projection functions, which are chosen to be equal to basis functions $\varphi_0^i(t)$ and $\varphi_1^i(t)$.

Here

$$J_j(\xi) = \left\| \frac{d\boldsymbol{r}_j(\xi)}{d\xi} \right\| = L_j^0 \sqrt{1 + \left(\alpha_j(2\xi - 1) + \beta_j \left(3\xi^2 - 3\xi + \frac{1}{2} \right) \right)^2}$$

is the Jacobian, which is calculated according to the approximation (4), (5).

Discrete analogue of the equation (3) has the following form:

$$\sum_{j=1}^{N} \left(\gamma_j \underbrace{\int_0^1 \varphi_0^j(\xi)\, J_j(\xi) d\xi}_{L_j} + \delta_j \underbrace{\int_0^1 \varphi_1^j(\xi)\, J_j(\xi) d\xi}_{L_j^*} \right) = \Gamma.$$

As the result, we obtain linear system of algebraic equations, which is overdetermined. In order to regularize it, an additional variable R is introduced nearly in the same way as in [7]. The resulting system, being split into blocks, has the form

$$\underbrace{\begin{pmatrix} A^{00} + D^{00} & A^{01} + D^{01} & I_N \\ A^{10} + D^{10} & A^{11} + D^{11} & O_N \\ L & L^* & 0 \end{pmatrix}}_{M} \begin{pmatrix} \gamma \\ \delta \\ R \end{pmatrix} = \begin{pmatrix} b^0 \\ b^1 \\ \Gamma \end{pmatrix}.$$

Here blocks A^{pq} are $N \times N$ square matrices; D^{pq} are diagonal matrices, $p, q = 0, 1$; L and L^* are rows consist of panel lengthes L_i and coefficients L_i^*, respectively; I_N is column consists of ones; O_N is column consists of zeros; γ and δ are columns of unknown coefficients; b^0 and b^1 are the columns which form the right-hand side of the system.

The coefficients of the matrices A^{pq} and D^{pq} should be computed by using the following formulae:

$$A_{ij}^{pq} = \frac{1}{2\pi} \int_0^1 \left(\int_0^1 Q_\tau(\boldsymbol{r}_i(t), \boldsymbol{r}_j(\xi)) \varphi_q^j(\xi) J_j(\xi) d\xi \right) \varphi_p^i(t) J_i(t) dt,$$

$$D^{pq} = \operatorname{diag} \left\{ -\frac{1}{2\pi} \int_0^1 J_i(t) \left(\varphi_1^i(t) \right)^{p+q} dt \right\}, \quad p, q = 0, 1, \quad i, j = 1, \ldots, N.$$

The easiest way for non-diagonal coefficients computation for matrices A^{pq}, which provides the necessary accuracy, is numerical integration using Gaussian quadrature formulae with 4 integration points.

Note, that the computational complexity of the procedure of the integrals numerical calculation can be reduced significantly. In order to take into account the mutual influence of the panels which are sufficiently far one from the other, number of Gaussian points can be reduced. However, the investigation of this case in detail requires special research.

At the same time the accuracy of the suggested method can be not enough for the airfoils with sharp edges, when the neighboring panels (in proximity to sharp edge) are very close one to the other. In such cases much higher accuracy of numerical integration is required; this problem is not considered in the framework of this paper either.

For diagonal elements of the matrices A^{pq} the error of numerical integration is also unacceptably high, but for them the following approximate analytical formulae are derived:

$$A_{ii}^{00} \approx \left(\frac{\alpha_i}{2\pi} - \frac{\alpha_i^3}{12\pi}\right) L_i, \qquad A_{ii}^{01} \approx \left(\frac{\beta_i}{24\pi} - \frac{\alpha_i^2 \beta_i}{144\pi}\right) L_i,$$
$$A_{ii}^{10} \approx \left(\frac{\beta_i}{12\pi} - \frac{23\alpha_i^2 \beta_i}{720\pi}\right) L_i, \quad A_{ii}^{11} \approx -\frac{\alpha_i^3}{144\pi} L_i.$$

The coefficients of the matrices D^{pq} also can be computed approximately by using the following formulae:

$$D_{ii}^{00} \approx -\left(\frac{1}{2} - \frac{\beta_i^2}{80}\right) L_i, \quad D_{ii}^{01} = D_{ii}^{10} \approx -\frac{\alpha_i \beta_i}{60} L_i, \quad D_{ii}^{11} \approx -\left(\frac{1}{24} + \frac{\alpha_i^2}{180}\right) L_i.$$

Lengthes of the panels L_i and coefficients L_i^* can be computed analytically with high precision as

$$L_i \approx L_i^0 \left(1 + \frac{\alpha_i^2}{6} + \frac{\beta_i^2}{40}\right), \qquad L_i^* \approx L_i^0 \alpha_i \beta_i \left(\frac{1}{30} - \frac{\alpha_i^2}{70}\right).$$

Right-hand side vector coefficients are computed by using formulae

$$b_i^p = \frac{1}{L_i} \int_0^1 f_\tau\big(r_i(t)\big)\, \varphi_p^i(t) J_i(t)\, dt, \quad p = 0,\, 1, \;\; i = 1,\, \ldots,\, N.$$

3.4 Accuracy estimation

For some simple particular cases, for example, for the problem of flow simulation around elliptical airfoil [13], it is possible to derive exact analytical solution $\gamma^*(s)$ for vortex sheet intensity by using conformal mappings theory (here s is a parameter which parameterizes the exact shape of the surface line of the airfoil).

If the linear algebraic system is solved and values of the variables γ_i and δ_i, $i = 1, \ldots, N$, are found, approximate vortex sheet intensity distribution is known. Introducing for it the same parametrization as for exact solution and comparing them in L_1 norm,

$$\|\Delta\gamma\|_{L_1} = \oint_K |\gamma(s) - \gamma^*(s)|\, dl_s,$$

one can found that the error is proportional to panel length in square, *i.e.*, the developed numerical scheme provides the second order of accuracy.

However, in vortex methods sometimes it is much more important to provide high accuracy for average values of vortex sheet intensity over the panels:

$$\tilde{\gamma}_i = \frac{\Gamma_i}{L_i} = \frac{1}{L_i} \int_0^1 \left(\gamma_i \varphi_0^i(t) + \delta_i \varphi_1^i(t)\right) J_i(t) dt, \quad i = 1, \ldots, N.$$

So the error for such values is calculated as the following:

$$\|\Delta\gamma\|_{C^h} = \max_{i=1,\ldots,N} |\tilde{\gamma}_i - \tilde{\gamma}_i^*|,$$

where

$$\tilde{\gamma}_i^* = \frac{1}{L_i} \int_0^1 \gamma^*(s) dl_s, \quad i = 1, \ldots, N.$$

is the exact average values of vortex sheet intensity over the panels.

4 Numerical experiment

In the fig. 3 the dependencies of errors $\|\Delta\gamma\|_{C^h}$ on number of panels are shown for flow simulation around elliptical airfoils with different ratios of semiaxes with equal panel lengthes. It is seen that the developed numerical scheme provides 4-th order of accuracy.

The error for total quantities of vorticity over the panels, consequently, has the 5-th order of accuracy.

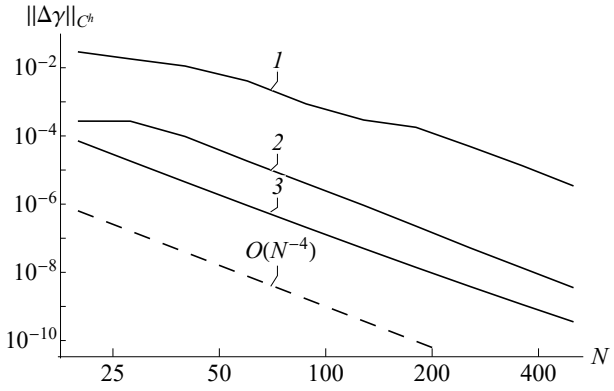

Figure 3: Dependencies of errors of average values of vortex sheet intensity computation over the panels on number of panels for elliptical airfoils with different ratios of semiaxes: *1* — 1 : 5; *2* — 1 : 2; *3* — 1 : 1; dashed line corresponds to the 4-th order of accuracy (in logarithmical scale)

5 Conclusions

New numerical scheme is developed for solving of boundary integral equation, which arises in flow simulation around airfoils using vortex methods. This scheme makes it possible to take into account the curvilinearity of the airfoil surface explicitly by using

Hermite spline interpolation. For numerical solution of integral equation the approach based on the ideas of discontinuous Galerkin method is used. The numerical solution is represented by piecewise-linear function. Such approach provides 2-nd order of accuracy in norm L_1 and 4-th order — for average values for vortex sheet intensities over the panels.

Acknowledgements

The research is supported by President's grant for young Russian PhD scientists (proj. MK-7431.2016.8), Russian Ministry of Education and Science (proj. 9.2422.2017) and Russian Foundation for Basic Research (proj. 17-08-01468).

REFERENCES

[1] Dynnikova, G. Ya. The Lagrangian approach to solving the time-dependent Navier-Stokes equations. *Dokl. Phys* (2004) **11**:648–652.

[2] Anronov, P.R., Guvernuk, S.V. and Dynnikova, G.Ya. *Vortex Methods for Computation of Unsteady Hydrodynamic Loads*. Moscow State University Press (2006, In Russian).

[3] Cottet, G.-H. and Koumoutsakos, P. D. *Vortex methods. Theory and practice.* Cambridge University Press, (2008).

[4] Lewis, R. I. *Vortex element methods for fluid dynamic analysis of engineering systems.* Cambridge University Press, (2005).

[5] Kempka, S. N., Glass, M. W., Peery, J. S. and Strickland, J. H. Accuracy considerations for implementing velocity boundary conditions in vorticity formulations. *SANDIA REPORT SAND96-0583 UC-700* (1996).

[6] Marchevsky, I. K. and Moreva, V. S. Vortex element method for 2D flow simulation with tangent velocity components on airfoil surface. *ECCOMAS 2012 — European Congress on Computational Methods in Applied Sciences and Engineering, e-Book Full Papers*, Vienna (2012), 5952–5965.

[7] Lifanov, I. K. and Belotserkovskii, S. M. *Methods of Discrete Vortices*. CRC Press, (1993).

[8] Prager, W. Die druckverteilung an Körpern in ebener Potentialströmung. *Phys. Z.* (1928) **29**:865–869.

[9] Rosenhead, L. The formation of vortices from a surface of discontinuity. *Proc. R. Soc. London Ser. A* (1931) **134**:170–192.

[10] Kuzmina, K.S. and Marchevsky, I.K. The modified numerical scheme for 2D flow-structure interaction simulation using meshless vortex element method. *Proceedings of the 4th International Conference on Particle-Based Methods — Fundamentals and Applications, PARTICLES 2015* (2015): 680–691.

[11] Cockburn, B. and Shu, C.-W. Runge-Kutta Discontinuous Galerkin methods for convection-dominated problems *J. of Scientific Computing* (2001) **16, 3**:173–261.

[12] Kuzmina, K. S. and Marchevsky, I. K. High-order numerical scheme for vortex layer intensity computation in two-dimensional aerohydrodynamics problems solved by vortex element method. *Herald of the Bauman Moscow State Technical University, Series Natural Sciences* (2016) **6**:93–109.

[13] Chanson, H. *Applied Hydrodynamics: An Introduction to Ideal and Real Fluid Flows.* CRC Press (2009).

V International Conference on Particle-based Methods – Fundamentals and Applications
PARTICLES 2017
P. Wriggers, M. Bischoff, E. Oñate, D.R.J. Owen, & T. Zohdi (Eds)

HYDRODYNAMIC LOADS SIMULATION FOR 3D BLUFF BODIES BY USING THE VORTEX LOOPS BASED MODIFICATION OF THE VORTEX PARTICLE METHOD

GEORGY A. SHCHEGLOV AND SERGEY A. DERGACHEV

Bauman Moscow State Technical University (BMSTU)
2-nd Baumanskaya st., 5, 105173 Moscow, Russia
E-mail: shcheglov_ga@bmstu.ru

Key words: 3D incompressible flow, vortex method, closed vortex loop, bluff body, pressure distribution.

Summary. *The modification of vortex method is developed which is based on closed vortex loops usage for calculation of unsteady aerodynamic loads acting on bluff bodies. It is shown that such approach has number of advantages for vortex wakes evolution simulation after bluff bodies. Each vortex loop can be considered as the separate vortex "superelement", which doesn't generate any additional vorticity. The loops generation algorithm permits to simulate the separation zone due to the self-organization of the loops. The obtained results are in satisfactory agreement with known experimental data.*

1 INTRODUCTION

For calculation of unsteady aerodynamic loads acting on aircraft moving at low subsonic speed vortex methods are highly efficient, as they require significantly less computational resources in comparison with grid-based methods. There are number of models of vortex elements known for flow simulation around spatial bodies: closed vortex framework, vortex filament, vorton, vortex dipole, vortex fragmenton, etc. Each of them has some advantages and restrictions.

In 'classical' vortex element methods, for example, in the discrete vortex method [1], vorticity is concentrated in vortex framework segments and it is absent outside the filaments segments in the flow. However, this method requires number of empirical models to determine the location of the vortex sheet separation lines. In case of vortex methods with separated vortex particles flow separation regions are being formed 'naturally' due to vorticity flux approach – vortex elements generation on the whole streamlined surface and further self-organization of the vortons in the flow [2, 3]. The main part of the vorticity is concentrated close to vortex elements (vortons) at points or at line segments. However, in the flow domain, according to the Helmholtz theorems, there will be distributed non-zero 'additional' vorticity. Its intensity vanishes on infinity [4]. This additional vorticity may cause significant errors when computing aerodynamic loads acting the body. Recently, there have been proposed an approach according to which the vorticity flux is being simulated by vortex filament loops generation on the body surface for 3D smoke dynamics simulation [5].

The aim of this paper is validation of vortex element method modification based on closed vortex loops usage for calculation of unsteady aerodynamic loads acting on bluff bodies.

2 PROBLEM STATEMENT AND NUMERICAL METHOD DESCRIPTION

The incompressible 3D flow around fixed rigid body is considered. The flow of the media, which has small viscosity and constant density ρ_∞ is described by the continuity equation and momentum equation with no-slip boundary condition on the body surface and perturbation decay boundary condition on infinity. Initial conditions correspond to the circulation-free flow. It is necessary to find the unknown pressure distribution on the body surface.

The assumption about incompressibility of the flow allows to find the velocity field $\vec{V}(\vec{r},t)$ by using the Biot – Savart law from vorticity distribution $\vec{\Omega} = \nabla \times \vec{V}$ with automatic satisfaction of boundary conditions on infinity. The pressure field also can be found from vorticity distribution by using analog of the Cauchy – Lagrange integral [6]. The assumption about viscosity smallness allows to take its influence into account only for simulation of two processes: the vorticity flux near body surface and vortex filaments reconnection in the flow.

For the lagrangian description of vorticity evolution the momentum equation has the following form:

$$\frac{D\vec{r}}{Dt} = \vec{V}, \qquad \frac{D\vec{\Omega}}{Dt} = (\vec{\Omega}\cdot\nabla)\vec{V}\ , \tag{1}$$

where $\vec{r}$ is vorticity markers positions. No-slip boundary condition is satisfied by implementing of vorticity flux approach [7, 8]. Boundary vortex sheet intensity can be found from no-through condition on body surface $\vec{r}_K$ with unit normal vector $\vec{n}_K$

$$\vec{V}_K \cdot \vec{n}_K = 0\,. \tag{2}$$

Then vortex sheet is being transformed into vorticity $\vec{\Omega}_K$, which is added to the vortex wake in the flow.

The developed vortex element method modification is based on the closed vortex loops usage for numeric solution of system (1) with condition (2) on time interval $0 \le t \le T$. Vortex wake consists of the K closed vortex filaments – vortex loops of the same circulation Γ. Loop with number $k \in [1,K]$ is simulated by the polygonal vortex line with number of vertices N_k. Vertices of a polyline with number $i \in [1,N_k]$ are considered as the Lagrangian markers $\vec{r}_{ki}$. The markers motion is described by ODE:

$$\frac{d\vec{r}_{ki}}{dt} = \vec{V}_{ki}, \quad \vec{r}_{ki}(0) = \vec{r}^{\,o}_{ki}, \quad i = 1,...,N_k, \quad k = 1,...,K\,. \tag{3}$$

We assume the loop legs between two vertices to be rectilinear segments $\Delta\vec{r}_{ki} = \vec{r}_{ki+1} - \vec{r}_{ki}$ and they induce the velocity $\vec{v}_{ki}(\vec{r})$ in the flow as vortex fragmentons, regularized by introducing of small smoothing radius ε [5].

For boundary condition (2) satisfaction linear system

$$[\sigma]\{\gamma\} = \{V_n\}, \tag{4}$$

should be solved for unknown circulations γ_j ($j \in [1,N_p]$) of vortex fragmenton frameworks,

placed on N_p body surface panels. For solving of (4) the regularization variable and additional condition is used: algebraic sum of vortex frameworks circulations should be equal to zero.

Finally, the velocity of the *i*-th marker of the *k*-th loop has the form

$$\vec{V}_{k\,i} = \vec{V}_\infty + \Gamma \sum_{l=1}^{K} \sum_{m=1}^{N_k} \vec{v}_{lm}\left(\vec{r}_{k\,i}\right) + \sum_{j=1}^{N_p} \gamma_j \sum_{s=1}^{N_j} \vec{v}_{sj}\left(\vec{r}_{k\,i}\right), \tag{5}$$

where $\vec{V}_\infty$ - constant incident flow velocity; N_j - number of vortex fragmentons in *j*-th vortex framework.

Numerical integration of system (3) is carried out by using numerical method of the first order of accuracy (explicit Euler method) with constant step Δt. Initial conditions for markers positions in (3) are parameters of the loops at the time of their generation on surface of the streamlined body. At every time step several procedures for smoothing of loops geometry, loop segments length alignment and loops reconnection are used [9]. Vortex loops generation algorithm is described below.

Pressure field at every time step is being calculated from the positions of loops by using the analog of the Cauchy – Lagrange integral. Aerodynamic loads are determined by integration of the pressure distribution over the surface of the body. In this research stationary loads are computed by averaging over the period of simulation. To implement the numerical method, the C++ program was developed, which uses MPI technology for parallel computations.

3 VORTEX LOOPS GENERATION ALGORITHM

Vortex loops generation algorithm consists of three main operations:

1. *Vortex sheet generation.* By solving of (4) circulations of vortex frameworks on the body panels can be found.

2. *Vortex loops construction.* Firstly, maximal and minimal intensities $M = \max(\gamma_j)$ and $m = \min(\gamma_j)$ should be found. Then each *j*-th panel should be split into N_j triangles (Fig.1). The potential scalar function is being introduced on the body surface, and its values at the control points of the panels are equal to the circulations of the corresponding vortex frameworks: $G_j = \gamma_j$. Its values at the corners of the framework are defined by circulations averaging for the frameworks which are adjacent to this point. For example, for the quadrangular panel shown in fig. 1:

$$\Phi_2 = (\gamma_1 + \gamma_2 + \gamma_3 + \gamma_4)/4 \tag{6}$$

The potential distribution over the triangle with known values at vertices is determined by linear interpolation. Potential level lines determine the initial shape of the vortex loops. For each value of the potential there can one or more closed level lines, each of them corresponds to one vortex loop. The number of level lines is determined as the integer part of expression

$$N_q = [(M - m)/\Gamma] - 1 \tag{7}$$

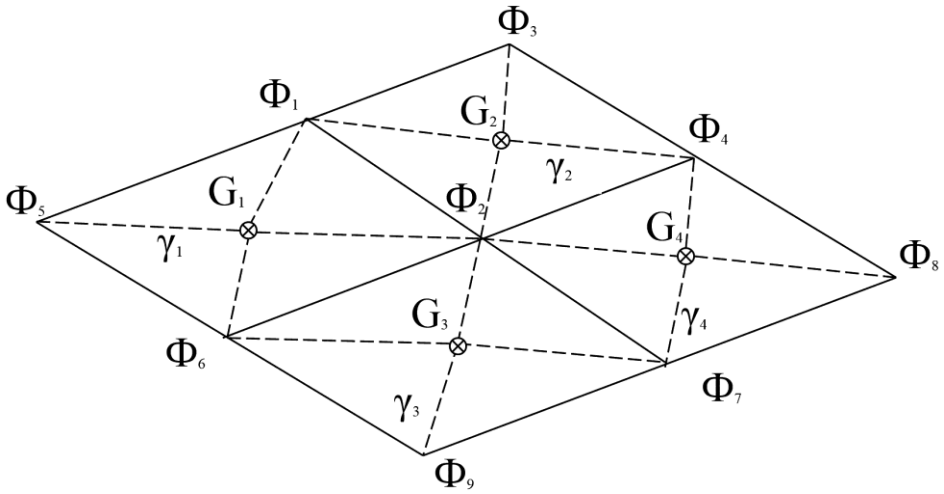

Figure 1: Example of splitting of a vortex framework into triangles

3. *Vortex loops dropping.* The constructed vortex loops should be shifted from the surface in the direction of a normal on small constant distance Δ. These new loops are being added to vortex wake loops database. On the current step, after generation of a loop, its contribution to the velocity field (5) is not considered, and for velocity field influence of the corresponding framework on body surface is taken into account.

When vortex elements move in the flow, marker positions of some of them can appear inside the body due to numerical errors. In such cases, the loop's leg, which intersects the body surface, is replaced with the other loop legs, which lay on the body surface and provide the shortest way by means of Dijkstra's algorithm [10].

4 MODEL PROBLEMS DESCRIPTION

For validation of the developed algorithm, several model problems are considered. The first problem is flow simulation around a sphere of unit radius. On the surface of the corresponding geometric model a mesh consists of $N_p = 1917$ triangular frameworks ($N_j = 3$) was built. The smoothing radius of the vortex element was chosen equal to $\varepsilon = 0.004$, time integration step $\Delta t = 0.01$, the length of the segment with which the loop was constructed $\alpha = 0.01$; the constant circulation of the vortex loop $\Gamma = 0.03$. The parameters of the algorithm [9] for simulation of the evolution of vortex loops are the following: nominal length of loop segment $h = 0.01$, loop smoothing angle threshold $\varphi = 160°$, loops reconnection distance $\mu = 0.015$, length decreasing coefficient $\lambda = 1.3$, number of segments in reconnection zone $\Omega = 7$. The number of loops in the wake at the end of simulation was equal to $K = 104$. The total number of segments in the wake was around 77 700. The shape of a vortex loops in the wake at the end of the simulation is shown in Fig.2.

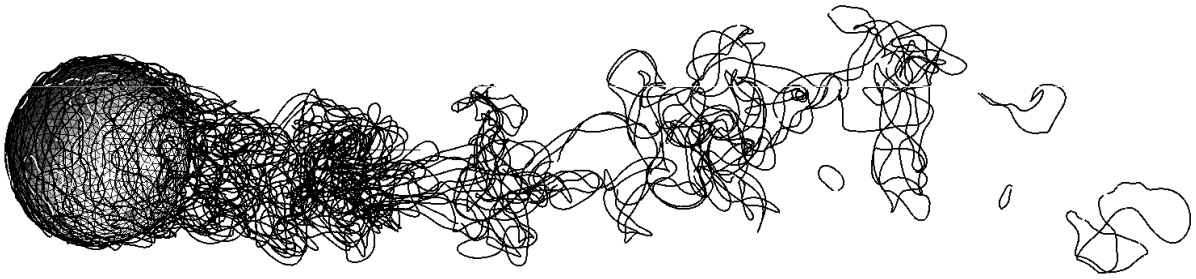

Figure 2: Vortex wake consists of closed vortex loops past the sphere

On Fig.3 the comparison of calculated results with the experiment [11] is shown: solid line – the dependence of the pressure coefficient C_p on the angular coordinate ϕ (in radians). Zero value of the x-axis of this diagram corresponds to the flow stagnation point. Dotted line denotes the experimental results for the Reynolds number $\mathrm{Re} = 10^6$ and dashed line denotes the experimental results for $\mathrm{Re} = 10^4$. The calculation time of 500 steps on 6 computers with Quad core Intel I7 3.0 GHz was about 4 hours, which yields a speedup of 3.5 times compared to the program used in [5].

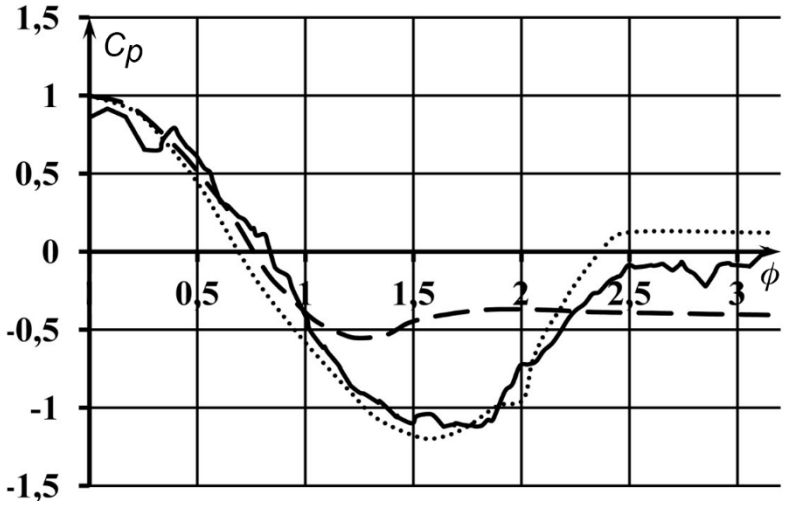

Figure 3: Dependence of the pressure coefficient for the sphere in comparison with experiment [11]

The second model problem is flow simulation around a circular cylinder with dimensions $D = 0.2$, $L = 2.55$. On the surface of the corresponding geometric model a mesh consists of $N_p = 4570$ triangular frameworks ($N_j = 3$) was built. The model parameters are the following: $\varepsilon = 0.001$, $\Delta t = 0.0044$, $\alpha = 0.01$; $\Gamma = 0.005$, $h = 0.01$, $\varphi = 160°$, $\mu = 0.015$, $\lambda = 1.4$, $\Omega = 7$. The number of loops in the wake at the end of simulation was equal to $K = 35$. The total number of segments in the wake was around 70 000. The shape of a vortex loops in the wake at the end of the simulation is shown in Fig.4.

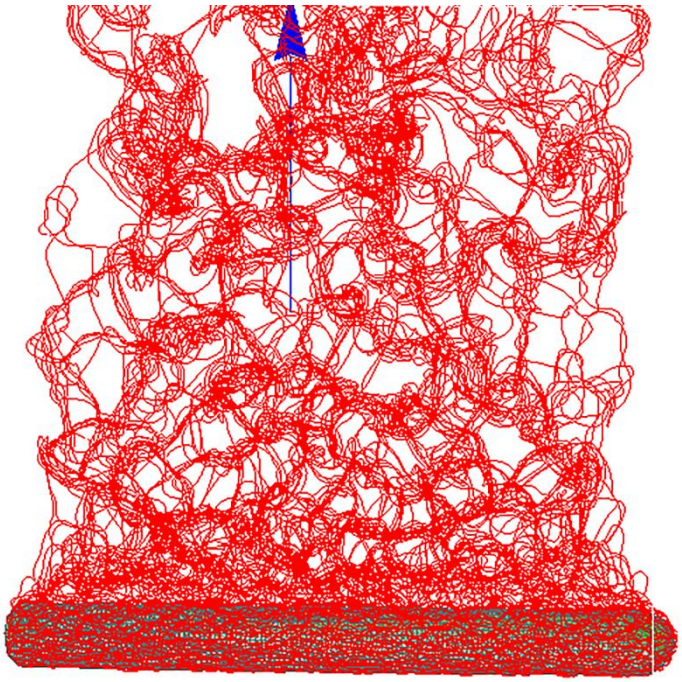

Figure 4: Vortex wake consists of closed vortex loops past the cylinder

On Fig.5 the comparison of calculated results with the experiment [12] is shown: solid green line is the dependence of the pressure coefficient C_p on the angular coordinate ϕ (in radians). Zero value of the x-axis of this diagram corresponds to the flow stagnation point. Blue line denotes the experimental results for the Reynolds number $\mathrm{Re} = 10^4$, violet line denotes the experimental results for $\mathrm{Re} = 10^5$ and red line denotes the experimental results for $\mathrm{Re} = 10^6$.

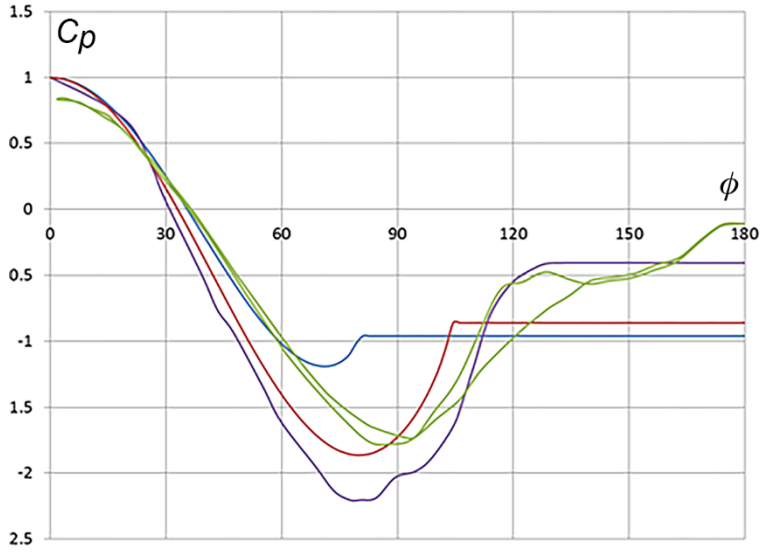

Figure 5: Dependence of the pressure coefficient for the sphere in comparison with experiment [12]

5 CONCLUSIONS

The validation of the developed modification of vortex element method with closed vortex loops showed that it has number of advantages for simulation of the evolution of vortex wakes behind bluff bodies:

- Each vortex loop can be considered as the separate vortex "superelement", which does not generate any additional vorticity.
- The loops generation algorithm allows to simulate the separation zone due to the self-organization of loops.

The obtained results are in satisfactory agreement with known experimental data. Further research will be devoted to the analysis of the influence of model parameters on the accuracy of the results and improvement of software code.

REFERENCES

[1] Belotserkovsky, S.M. et al. *3D detached flows around bodies of arbitrary shape*. Moscow, TSAGI, (2000). (In Russian: *Trekhmernoe otrihvnoe obtekanie tel proizvoljnoyj formi*).

[2] Kamemoto, K. On Contribution of Advanced Vortex Element Methods Toward Virtual Reality of Unsteady Vortical Flows in the New Generation of CFD. *J. of the Brazilian Society of Mechanical Sciences and Engineering.* (2004) V. 26, No 4.: 368-378.

[3] Alkemade, A.J.Q. *On Vortex Atoms and Vortons*: PhD Thesis. Delft, (The Netherlands), (1994).

[4] Marchevsky, I.K. and Shcheglov, G.A. 3D vortex structures dynamics simulation using vortex fragmentons. *ECCOMAS 2012, e-Book Full Papers, Vienna*, (2012): 5716–5735.

[5] Weißmann, S. and Pinkall, U. Filament-based smoke with vortex shedding and variational reconnection. *ACM Trans. Graph*. (2010) Vol. 29, No 4, article 115. 12 p.

[6] Dynnikova, G.Ya. An analog of the Bernoulli and Cauchy-Lagrange integrals for a time-dependent vortex flow of an ideal incompressible fluid. *Fluid Dynamics.* (2000) Vol. 35, No 1: 24-32.

[7] Lighthill, M.J. Introduction. *Boundary Layer Theory Laminar Boundary Layers Ed. by J. Rosenhead*. New-York: Oxford University Press, (1963): 54-61.

[8] Kempka, S.N., Strickland, J.H., Glass, M.W. and Peery, J.S. *Accuracy Considerations for Implementing Velocity Boundary Conditions in Vorticity Formulations* Sandia Report. SAND96-0583 UC-700. (1996)

[9] Dergachev, S.A. and Shcheglov, G.A. Flow around 3D bodies simulation by using vortex element method with closed vortex loops. *Heralds of MGTU GA.* (2016) No 223 (1): 19-25. (in Russian)

[10] Dijkstra, E.W. A note on two problems in connexion with graphs. *Numerische Mathematik.* (1959) Vol.1: 269-271.

[11] Flachsbart, O. Der Widerstand von Kugeln in der Umgebung der kritischen Reynoldschen Zahl. *Ergebnisse der Aerodynamischen Versuchsanstalt zu Göttingen.* IV. Lieferung, (1932): 106-108.

[12] Parkinson, G.V. and Jandali, T. A wake source model for bluff body potential flow *J. of Fluid Mechanics* (1970), Vol. 40, No. 3: 577-594

Investigation of Enhanced Polygon Wall Boundary Model in PNU-MPS Method

Soh-Myung, Chung*, Seong-Jun, Ji*, Hee-Sung, Shin*, Jong-Chun, Park*

Se-Min, Jeong†, and Kyung-Sung, Kim††

* Department of Naval Architecture and Ocean Engineering
Pusan National University
2 Busandaehak-ro 63beon-gil, Geumjeong-gu, Busan 46241, Korea
e-mail: jcpark@pnu.edu, web page: http://sil.pusan.ac.kr

† Department of Naval Architecture and Ocean Engineering
Chosun University
309 Pilmon-daero, Dong-gu, Gwangju 61452, Korea
e-mail: smjeong@chosun.ac.kr

†† School of Naval Architecture and Ocean Engineering
Tongmyong University
428 Sinseon-ro, Nam-gu, Busan 48520, Korea
e-mail: keiuskim@tu.ac.kr

ABSTRACT

With regard to demonstration of fluid flow, there are two descriptions which are Eulerian description and Lagrangian description. In the field of CFD (Computational Fluid Dynamics), a number of studies relevant to grid method based on Eulerian description have been conducted generally. However, when the grid method is employed to simulate flow field, it is inevitable to give consideration to convection term which generates severe numerical diffusion and fluctuation. To obtain the accuracy of solution, a different type of method based on Lagrangian description is come to the fore. Numerical approaches following Lagrangian description have been called meshfree or particle method. Even though particle method does not accompany convection term and fully satisfies conservation of mass, its studies have not been carried out extensively because it is difficult to implement the boundary conditions correctly due to insufficient number of particles in the vicinity of boundary. It affects directly the stability of flow field and accuracy in computation.

In MPS (Moving Particle Semi-implicit) method [1], fixed-type of dummy particles are placed inside wall boundary. By placing extra particles as the wall, it seems to be not easy to satisfy the boundary condition for sharp-edged or extremely thin body configuration.

In this study, the enhanced polygon wall boundary model, which was suggested originally by Mitsume et al. [2], is employed to the PNU-MPS (Pusan-National-University-modified MPS) method [3] to improve and stabilize the analysis of fluid flow with arbitrary-shaped body including sharp-edged body configuration without any additional particles. The developed simulation method, called as PNU-MPS-POLY, is adopted to the Couette flow and the lid-driven cavity flow with various corner angles. The present simulation results are validated through comparison with the analytic solutions, the experiments [4], and other simulation results [5,6].

ACKNOWLEDGEMENTS

This research was supported by the Basic Science Research Program through the National Research Foundation of Korea (NRF) funded by the Ministry of education (No. 2015R1D1A1A01) and the IT R&D program of MOTIE/KEIT [10060329, Development of numerical simulator for environmental load on ship and offshore in polar region].

REFERENCES

[1] Koshizuka, S, and Oka, Y, "Moving-Particle Semi-Implicit Method for Fragmentation of Incompressible Fluid", *Journal of Nuclear Science and Engineering*, **123**, 421-434 (1996).

[2] Mitsume, N., Yoshimura, S., Murotani, K. and Yamada, T., "Explicitly represented polygon wall boundary model for the explicit MPS method", *Computational Partcile Mechanics*, **2**, 73-89 (2015).

[3] Lee, BH, Park, JC, Kim, MH, and Hwang, SC, "Step-by-step improvement of MPS method in simulating violent free-surface motions and impact-loads", *Computer Methods in Applied Mechanics and Engineering*, **200**, 1113-1125 (2011).

[4] Ghia, U., Ghia, K.N., and Shin, C.T., "High-Re Solutions for Incompressible Flow Using the Navier-Stokes Equations and a Multigrid Method", *Journal of Computational Physics*, **48**, 387-411 (1982).

[5] Demirdzic, I., Lilek, Z. and Peric, M., "Fluid Flow and Heat Transfer Test Problems for Non-Orthogonal Grids: Bench-Mark Solution", *International Journal for Numerical Methods in Fluids*, **15**, 329-354 (1992).

[6] Moon, JK, Park, JC, Chun, HH, and Suh, SB, "Numerical Simulation on Laminar Flow Past a Rotary Oscillating Circular Cylinder", *Journal of the Society of Naval Architects of Korea*, **42(4)**, 368-378 (2005).

V International Conference on Particle-based Methods – Fundamentals and Applications
PARTICLES 2017
P. Wriggers, M. Bischoff, E. Oñate, D.R.J. Owen, & T. Zohdi (Eds)

MOVING PARTICLE SIMULATION WITH SOLID-SOLID CONTACT

RUBENS A. AMARO JUNIOR, PEDRO H. S. OSELLO AND LIANG-YEE CHENG

Department of Construction Engineering (PCC)
Polytechnic School of University of São Paulo (EPUSP)
Cidade Universitária, 05508-070 São Paulo, Brazil
rubens.amaro@usp.br, http://www.pcc.usp.br/home/

Key words: Solid-solid contact, rigid body dynamics, MPS, Moving particle simulation.

Abstract. Problems of fluid-structure interaction with free surface flow and multi-body interactions are highly nonlinear and complex phenomena, which is challenging for computational modeling and simulation. In the presence of contact or collision between solids, numerical modeling to detect collision and prevent penetration between bodies is required. The objective of this work is to study a numerical model for solid-solid contact and/or collision, based on contact mechanics theories, to reproduce the macroscopic properties of the multi-body interactions in Moving Particle Simulation (MPS) method. MPS is a fully Lagrangian meshfree particle-based approach that is suitable for the modeling complex geometries with large displacements and deformation, including free surface flow with fragmentation and merging and interaction of fluid with multi-bodies. Analytical results are used to perform the calibration of the numerical friction coefficient. The model is applied to a case of free solid transport in free surface flow, modeled as a 3D experimental dam breaking event, in which free solids interact each other and fixed walls. The numerical results from MPS are compared with numerical and experimental results.

1 INTRODUCTION

Fluid-structure interaction with free surface flow and multi-body interactions, are highly nonlinear and complex hydrodynamic phenomena, which is challenging problems for computational modeling and simulation. Among the effective numerical methods used to simulate these phenomena an important approach is the particle-based method, in which the physical domain is represented by a set of points (particles). However, despite the easier implementation and flexibility of these methods, one of the relevant topics is concerning the numerical treatment of contacts between bodies when contact or collision between solids occurs. To date, different techniques have been proposed for particle methods to deal with the contact between solids, such as impulse-based repulsion models [1,2] and linear [3,4,5] or nonlinear [6] springs and dashpots. Based on contact mechanics theories, the objective of this work is to study a nonlinear spring and dashpot model of solid-solid contact and/or collision for Moving Particle Simulation (MPS) method [7]. MPS is a fully Lagrangian meshfree particle-based approach suitable for the modeling of complex geometries with large displacements and deformation, including free surface flow with fragmentation and coalescence and interaction of fluid with multi-bodies. The relationship between the numerical and analytical friction coefficient is investigated by a case of block's sliding along

a slope, subjected to gravity acceleration. For the validation, a 3D experimental dam breaking event, in which free cubic solids interact each other and fixed walls [6], is simulated. Numerical results of solid position obtained by the proposed model are compared with available numerical and experimental results.

2 NUMERICAL METHOD

In MPS method, the differential operators of the governing equations of continuum are replaced by operators based on a weight function. For a given particle i, the influence of a neighbor particle j is defined by weight function ω_{ij}

$$\omega_{ij} = \begin{cases} \frac{r_e}{\|\vec{r}_{ij}\|} - 1 & \|\vec{r}_{ij}\| \leq r_e \\ 0 & \|\vec{r}_{ij}\| > r_e \end{cases}, \tag{1}$$

where r_e is the effective radius that limits the range of influence and $\|\vec{r}_{ij}\|$ is the distance between i and j. In the present work, is used the effective radius $r_e = 2.1 l_0$, where l_0 is the initial distance between two adjacent particles.

The summation of the weight of all the particles in the neighborhood of the particle i is defined as its particle number density n_i, which is proportional to the fluid density

$$n_i = \sum_{j \neq i} \omega_{ij}. \tag{2}$$

For a scalar function ϕ, the gradient and Laplacian operators are defined in Eq. 3 and Eq. 4, respectively

$$\nabla \phi = \frac{d}{n^0} \sum_{j \neq i} \frac{\phi_j - \phi_i}{\|\vec{r}_{ij}\|^2} \vec{r}_{ij} \omega_{ij}, \tag{3}$$

$$\nabla^2 \phi = \frac{2d}{\lambda_i n^0} \sum_{j \neq i} (\phi_j - \phi_i) \omega_{ij}, \tag{4}$$

where d is the number of spatial dimensions and n^0 is the initial value of n_i. Finally, λ_i is a correction parameter so that the variance increase is equal to that of the analytical solution, and is calculated by

$$\lambda_i = \frac{\sum_{j \neq i} \omega_{ij} \|\vec{r}_{ij}\|^2}{\sum_{j \neq i} \omega_{ij}}. \tag{5}$$

2.1 Fluid dynamics

The governing equations of incompressible viscous flow are expressed by the conservation laws of mass and momentum:

$$\frac{D\rho}{Dt} = \rho \nabla \cdot \vec{u} = 0, \tag{6}$$

$$\frac{D\vec{u}}{Dt} = -\frac{\nabla P}{\rho} + \nu\nabla^2\vec{u} + \vec{f}, \tag{7}$$

where ρ is the fluid density, $\vec{u}$ is the velocity vector, P is the pressure, ν is the kinematic viscosity and $\vec{f}$ is the external force vector.

To solve the incompressible viscous flow, a semi-implicit algorithm is used in the MPS method. At first, predictions of the particle's velocity and position are carried out explicitly by using viscosity and external forces terms of the momentum conservation. Then the pressure of all particles is calculated by the Poisson equation for the pressure as follows

$$\nabla^2 P_i^{t+\Delta t} - \frac{\rho}{\Delta t^2}\alpha P_i^{t+\Delta t} = -\gamma\frac{\rho}{\Delta t^2}\frac{n_i^* - n^0}{n^0}, \tag{8}$$

where Δt is the time step, n_i^* is the particle number density calculated based on the displacement of particles obtained in the prediction step, α is the coefficient of artificial compressibility and γ is the relaxation coefficient. Both α and γ are used to improve the stability of a computation method. Also, to provide the stabilization of MPS, the pressure gradient is modified as [7]

$$\nabla P = \frac{d}{n^0}\sum_{j\neq i}\frac{P_j - \hat{P}_i}{\|\vec{r}_{ij}\|^2}\vec{r}_{ij}\omega_{ij}, \tag{9}$$

where $\hat{P}_i$ is the minimum pressure between the neighborhood of the particle i.

Finally, the velocity of the particles is updated by using the pressure gradient term of the momentum conservation and the new positions of the particles are obtained. Validations of the present numerical method (MPS) can be found in previous works. To mention few, we have: The pressure variations inside a tank structure caused by sloshing [8]. Computed pressures on the block and free surface elevation of three-dimensional dam break problem [9]. Displacement of the elastic plate interacting with dam breaking and sloshing [10].

2.2 Boundary conditions

In order to identify the free-surface boundary, the present work used the particle number density condition [7] and the neighborhood particles weighted geometric center deviation condition [11]. A particle is defined as free-surface particle and its pressure is set to zero when its particle number density particle number density n_i is smaller than $\beta_1 n^0$, and the magnitude of the weighted average deviation σ_i is greater than $\delta_1 l_0$.

Solid wall boundary condition is imposed by using three layers of fixed particles. The particles that form the layer in contact to the fluid are denominated wall particles, of which the pressure is computed by solving Poisson equation for the pressure (Eq. 8), together with the fluid particles. The particles that form two other layers are denominated dummy particles. Dummy particles are used to assure the correct calculation of the particle number density of the wall particles. Pressure is not calculated in the dummy particles.

2.3 Rigid body dynamics

For the rigid body dynamics, the governing equations of motion are those of translational motion and rotational motion expressed as

$$m\vec{a} = \sum \vec{f}_{ext}, \tag{10}$$

$$\vec{I} \cdot \dot{\vec{\omega}} + \vec{\omega} \times (\vec{I} \cdot \vec{\omega}) = \sum \vec{M}_{ext}, \tag{11}$$

where m is the total mass of the rigid body, $\vec{a}$ is the acceleration vector at the center of the rigid body, $\vec{f}_{ext}$ is external forces, $\vec{I}$ is the inertia matrix, $\vec{\omega}$ is the angular velocity about the principal axes of the rigid body and $\vec{M}_{ext}$ is the external moment. The rigid body is discretized by a finite number of particles whose relative positions remain unchanged during the simulation. The external forces are calculated considering the effect of gravity $\vec{f}_g$, hydrodynamic forces on the rigid surface $\vec{f}_h$ and contact forces between the rigid bodies $\vec{f}_c$. The contribution of hydrodynamic added to gravity force and moment $\vec{M}$ acting on the rigid body are calculated as

$$\vec{f}_h + \vec{f}_g = -\iint_S P d\vec{s} + m\vec{g}, \tag{12}$$

$$\vec{M} = -\iint_S \vec{r} \times P d\vec{s}, \tag{13}$$

where the vector $\vec{r}$ denotes the position vector from the center of the rigid body and $d\vec{s}$ is the area multiplied by the normal vector on the rigid body surface. Focusing the impulsive hydrodynamic loads on the rigid solid, shear forces were neglected in Eq. 12 and only the normal force due pressure was considered.

The contact/collision force between the rigid bodies $\vec{f}_c$ is decomposed into normal $\vec{f}_n$ and tangential $\vec{f}_s$ components. Both forces are modeled by using a penalty-based spring dashpot model inspired by the Discrete Element Modelling (DEM) formulation [12]. They are decomposed into a repulsion force $\vec{f}^r$, proportional to the penetration between particles, and a damping force $\vec{f}^d$, representing the energy dissipation during the deformation.

The normal forces between a pair of particles ij are described following a non-linear Hertz's elastic contact theory [13]:

$$\vec{f}_{n,ij} = \vec{f}^r_{n,ij} + \vec{f}^d_{n,ij} = k_{n,ij}\delta_{ij}^{3/2}\vec{n}_c - c_{n,ij}\delta_{ij}^{1/4}\dot{\delta}_{ij}\vec{n}_c, \tag{14}$$

where $k_{n,ij}$ is the stiffness constant of pair ij, $\delta_{ij} = l_0 - \|\vec{r}_{ij}\|$ is the particle overlap (penetration), $\dot{\delta}_{ij} = (\vec{u}_j - \vec{u}_i) \cdot \vec{n}_c$ is the rate of penetration, $c_{n,ij}$ is the damping constant and $\vec{n}_c$ is the contact/collision normal vector.

The stiffness constant and damping constant are given by

$$k_{n,ij} = \frac{4}{3}E_{ij}\sqrt{l_{0,ij}}, \quad c_{n,ij} = C_n\sqrt{6m_{ij}E_{ij}\sqrt{l_{0,ij}}}, \tag{15}$$

where C_n is the ratio of the collision (which must be specified) and E_{ij}, m_{ij} and $l_{0,ij}$ are obtained as

$$E_{ij} = \frac{E_i E_j}{(1-\nu_j)E_i + (1-\nu_i)E_j}, \quad m_{ij} = \frac{m_i m_j}{m_i + m_j}, \quad l_{0,ij} = \frac{l_{0,i} l_{0,j}}{l_{0,i} + l_{0,j}}, \tag{16}$$

with E_i, E_j; and ν_i, ν_j as the Young's modulus and the Poisson's ratio of particles i and j, respectively. In the present work, only one resolution l_0 is used for all domain, thus leading to $l_{0,ij} = l_0/2$. In case j is a particle belonging to a fixed rigid wall, $m_j \to \infty$, implying that $m_{ij} = m_i$.

Tangential forces are given by a linear dash-pot following by the Coulomb friction law or repulsive and damped forces by assuming a linear model. The Coulomb law is modified with a sigmoidal function in order to make it continuous at the origin regarding the tangential velocity [14]:

$$\vec{f}_{t,ij} = \min\left(\mu_j \left\|\vec{f}_n\right\| \tanh\left(8\dot{\delta}_{ij}^t\right)\vec{t}_c, k_{t,ij}\delta_{ij}^t\vec{t}_c - c_{t,ij}\dot{\delta}_{ij}^t\vec{t}_c,\right). \tag{17}$$

Here, μ_j is the kinetic friction coefficient for the pair of particles i and j, δ_{ij}^t is the tangential deformation, $\dot{\delta}_{ij}^t$ is the rate of tangential deformation, $\vec{t}_c$ is the tangential contact/collision vector and $k_{t,ij}$ stiffness and $c_{t,ij}$ damping constants [15].

After calculation all contacts between particles, the contact forces for each rigid body is given by

$$\vec{f}_n = \frac{1}{Nc}\sum_{j=1}^{Nc}\vec{f}_{n,ij}^r + \vec{f}_{n,ij}^d, \quad \vec{f}_t = \frac{1}{Nc}\sum_{j=1}^{Nc}\vec{f}_{t,ij} \tag{18}$$

where Nc is the number of particles that are in contact with particle i.

2.4 Contact/collision normal vector

The contact/collision normal vector $\vec{n}_c$ is computed from the particle features at the moment just before the collision. A feature can be a vertex, an edge or a face of the rigid body. In the present work, the geometry of rectangular parallelepiped is enough to model all rigid bodies, therefore the number of neighbor particles are used to identify the features of a particle i.

During the simulations, the contact/collision normal vector between a pair of particles i and j is defined by:

1. Particle i or j is face, the unit vector parallel to the face normal is used as $\vec{n}_c$.
2. Neither particles are face, the unit vector distance between particles is used as $\vec{n}_c$.

The direction of $\vec{n}_c$ is chosen such that the relative velocity of the rigid bodies at the collision point along the collision normal is negative, indicating that the bodies are moving towards each other [16].

3 RESULTS AND DISCUSSIONS

3.1 Contact friction model

In order to verify the present friction model, a simple case of a free solid sliding on a sloped surface was simulated. The free solid is modeled as a rectangular cuboid with a squared base (0.2 x 0.2 x 0.1 m³) and the surface is modeled as an inclined plane of length 10.2 m and the angle of 30 degrees with horizontal, as shown in Figure 1. The free solid has no initial velocity and only gravitational and friction forces act on its motion. The numerical parameters and material properties are given in Table 1.

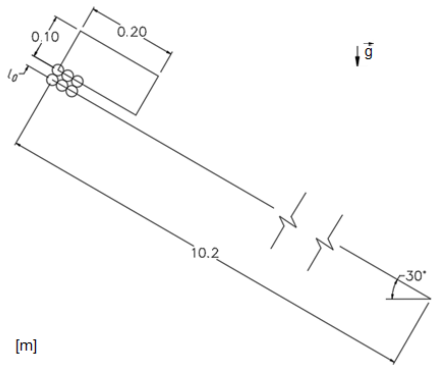

Figure 1: Main dimensions of the sloped surface and the sliding body.

Table 1: Sliding body. Numerical parameters and material properties.

Solid	*lo* (m)	*L/lo*	*ρ* (kg/m3)	*m* (kg)	*v*	*E* (MPa)	C_n (kg/s)
Body	0.025	8	780	3.12	0.3	50	1
Plane		-	∞	∞	0.3	50	-/-

Four cases with different numerical friction coefficients ($\mu_{num} = 0.15, 0.25, 0.35, 0.45$) were simulated and the equivalent analytical friction coefficient μ_{ana} were obtained by the computed accelerations of the free solid. The evolution of the body's position for both analytical and numerical results and the relation between the numerical and analytical friction coefficients are illustrated in Figure 2 (a) and Figure 2 (b), respectively. The computed positions of the free solid are very close to the analytical ones, although the numerical friction coefficients are related to the analytical ones by a factor of 1.22.

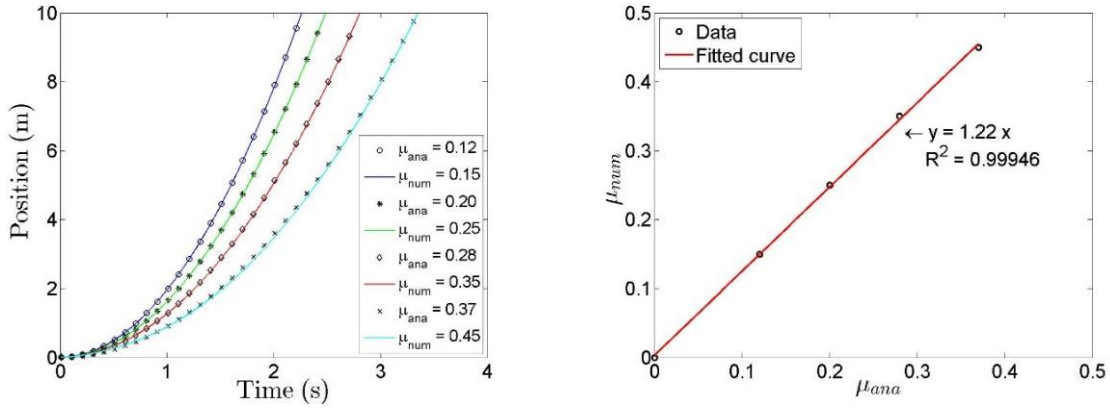

(a) (b)

Figure 2: (a) Position of the free solid. (b) Numerical and analytical friction coefficient relation.

3.2 3D dam breaking

To verify the contact-contact model in a case of high complexity, the model is applied to a case of free solid transport in free surface flow, modeled as a 3D experimental dam breaking event, which free cubic solids interact each other and fixed walls [6].

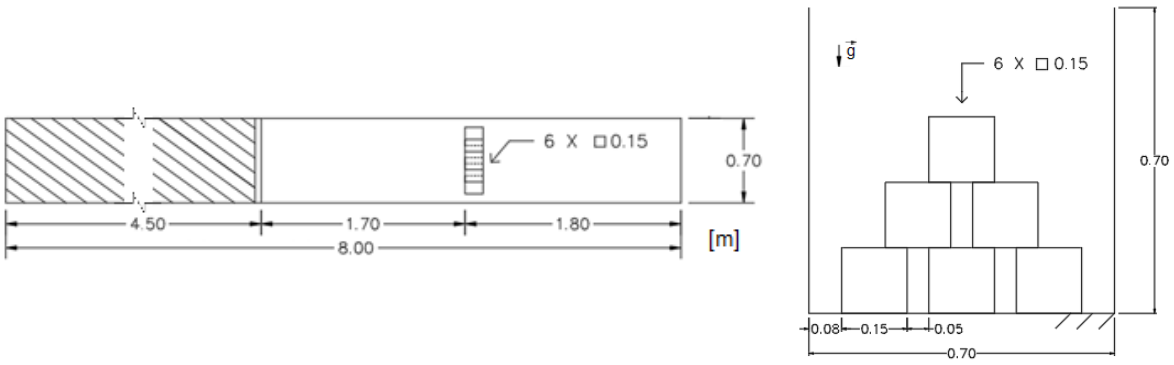

(a) (b)

Figure 3: (a) Main dimensions of the 3D dam breaking. (b) Triangular formation of cubes.

The experiment consists of a very long canal with dimensions 8.0 x 0.7 x 0.7 m³, a squared floodgate that holds water to the height of 0.4 m, installed at 4.50 m from the upstream wall, and 6 cubes of side 0.15 m arranged in a triangular formation. The cubes are placed 1.7 m away from the gate, where each cube is separated from its neighbor by 0.05 m. The central cube has its center of mass aligned with the central axis of the canal. Figure 3 shows the main dimensions of the geometry.

The floodgate ascends with a constant velocity of 1.9 m/s, to open completely in 0.21 s. The simulation is performed with time step $\Delta t = 5x10^{-4}s$, the coefficient of artificial

compressibility $\alpha = 10^{-8}$, the relaxation coefficient $\gamma = 0.05$ and free surface threshold values $\beta_1 = 0.97$ and $\delta_1 = 0.2$. The other parameters used can be observed in Table 2.

Table 2: 3D dam breaking. Numerical and materials properties.

Solid	***lo* (m)**	***L/lo***	**ρ (kg/m3)**	***m* (kg)**	***v***	***E* (GPa)**	**C_n (kg/s)**	**μ**
Cube	0.0125	12	800	2.7	0.3	3	0.1	0.15
Wall		-	∞	∞	0.3	210	-	0.25

Figure 4 shows a sequence of frames from the experiment, simulations obtained by SPH [6], and the simulation carried in the present study. At the instant 0.95 s, the water front begins transporting the cubes downstream. The cubes at the base are transported by the water front while the remaining cubes fall at the instant 1.15 s. After this, all the cubes are carried by the wave front, although the cubes at the base present a delay in the motion computed by the present simulation compared to experimental results and simulation obtained by SPH method.

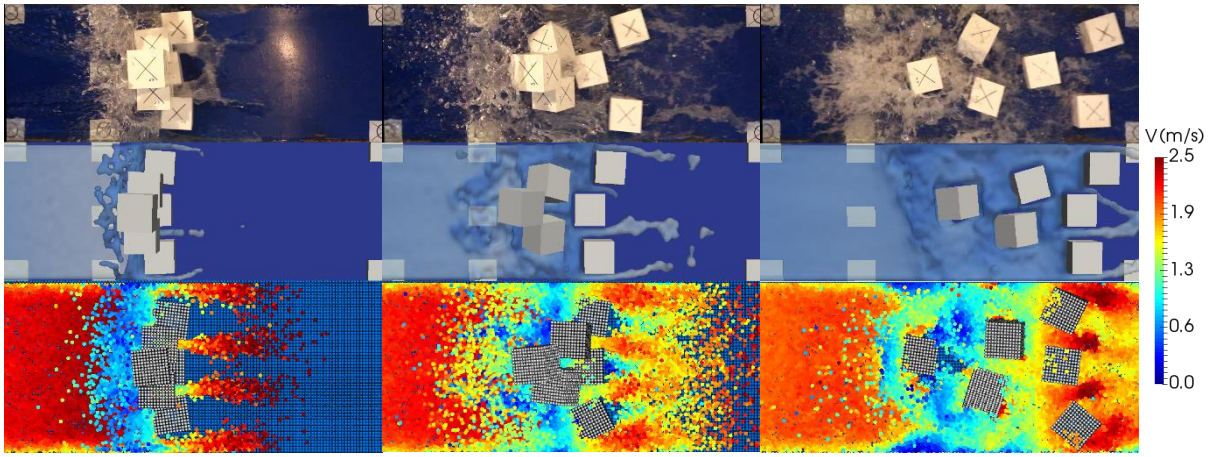

t = 0.95 s *t = 1.15 s* *t = 1.45 s*

Figure 4: Snapshots of the 3D dam breaking simulation. (top) Experiment, (middle) simulations obtained by SPH [6], and (bottom) the simulation carried in the present study.

The position of the center of mass of the cube at the top obtained by the present simulation, and experimental and numerical results are given in Figure 5. After the fluid hits the cubes at base, the cube at the top starts the motion along the longitudinal axis at the instant 0.85 s. The cube falls and is transported by wave front between the instants 1.07 and 1.40 s. Compared to experimental results, the cube presents a lower returning at the instant 1.30 s, and a faster fall between the instants 1.22 and 1.36 s. However, both computed motions along the x and z directions show a good agreement with experimental ones.

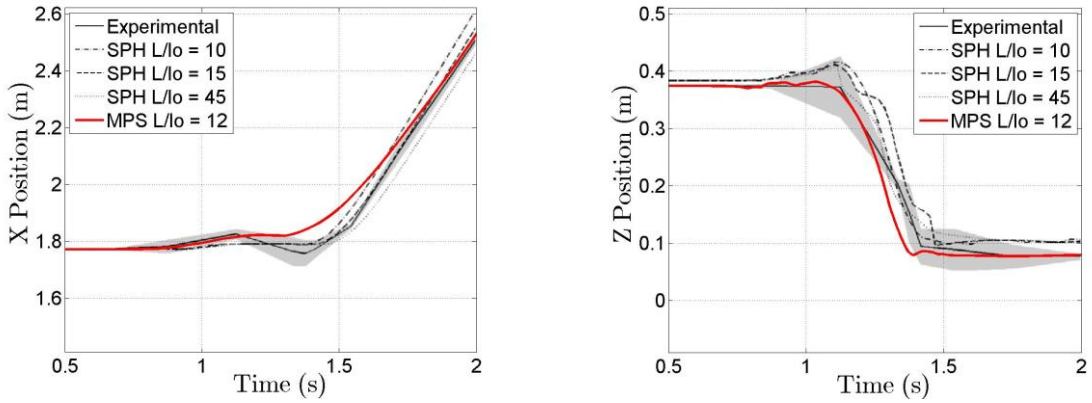

(a) (b)

Figure 5: Cube at the top. Motion along the (a) longitudinal and (b) vertical directions.

4 FINAL CONSIDERATIONS

A nonlinear spring and dashpot model for solid-solid contact and/or collision, based on contact mechanics theories, was investigated for Moving Particle Simulation (MPS) method in the present work. At first, the computed motion of a solid sliding on a sloped surface was compared to analytical motion, providing a linear relation between the numerical and analytical friction coefficients. After that, the model was applied to a case of solid transport in free surface flow, modeled as a dam breaking event with cubic solids interact each other and fixed walls. The positions of the solid obtained by the proposed model were compared with available numerical and experimental results. The comparisons of the results showed the effectiveness of the present approach to reproduce the main behaviors of free surface flow and multi-body interactions.

ACKNOWLEDGEMENTS

This work has financial support from CAPES and FDTE. The authors are grateful to Petrobras for financial support on the development of the MPS/TPN-USP simulation system based on MPS method.

REFERENCES

[1] Oh, S., Kim, Y. and Roh, B.S. Impulse-based rigid body interaction in SPH. *Computer Animation and Virtual Worlds* (2009) **20**:215-224.

[2] Amicarelli, A., Albano, R., Mirauda, D., Agate, G., Sole, A. and Guandalini, R. A Smoothed Particle Hydrodynamics model for 3D solid body transport in free surface flows. *Computers and Fluids* (2015) **37**:205-228.

[3] Harada, T., Tanaka, M., Koshizuka, S. and Kawaguchi, Y. Real-time coupling of fluids and rigid bodies. *In: APCOM 07 in conjunction with EPMESC XI* (2007).

[4] Ren, B., Jin, Z., Gao, R., Wang, Y.-X. and Xu, Z.-L. SPH–DEM modeling of the hydraulic stability of 2D blocks on a slope. *Journal of Waterway, Port, Coastal and Ocean Engineering*, **140** (2014).

[5] Asai, M. and Chandra, B. Numerical prediction of bridge wash-out during natural disaster by using a stabilized ISPH method. *In: Advances in Civil, Environmental and Materials Research* (2016).
[6] Canelas, R., Ferreira, R.M.L., Crespo, A.A.J.C. and Domínguez, J.M. A generalized SPH-DEM discretization for the modelling of complex multiphasic free surface flows. *In: 8th International SPHERIC Workshop* (2013).
[7] Koshizuka, S. and Oka, Y. Moving Particle Semi-implicit method for fragmentation of incompressible fluid. *Nuclear Science and Engineering* (1996) **123**:421-434.
[8] Tsukamoto, M.M., Cheng, L.-Y. and Nishimoto, K. Analytical and numerical study of the effects of an elastically-linked body on sloshing. Computers & Fluids (2011) **49**:1-21.
[9] Bellezi, C.A., Cheng, L.-Y. and Nishimoto, K. Particle based numerical analysis of green water on FPSO deck. *In: 32nd International Conference on Ocean, Offshore and Artic Engineering* (2013).
[10] Amaro Jr., R.A. and Cheng, L.-Y. Brittle fracture and hydroelastic simulations based on moving particle simulation. *Computer Modeling in Engineering & Sciences* (2013) **95**:87-118.
[11] Tsukamoto, M.M., Cheng, L.-Y. and Motezuki, F.K. Fluid interface detection technique based on neighborhood particles centroid deviation (NPCD) for particle methods. *International Journal for Numerical Methods in Fluids* (2016) **82**:148-168.
[12] Cundall, P.A. and Strack, O.D.L. A discrete numerical model for granular assemblies. *Geotechnique* (1979) **29**:47-65.
[13] Johnson, K.L. *Contact Mechanics*. Cambridge University Press, Cambridge (1985).
[14] Vetsch, D. *Numerical simulation of sediment transport with meshfree methods*. (Ph.D. thesis), ETH Zurich (2011).
[15] Hoomans, B. Granular dynamics of gas-solid two-phase flows. (Ph.D Thesis), University of Twente (2000).
[16] Coutinho, M.G. *Dynamic Simulations of Multibody Systems*. Springer-Verlag New York (2001).

V International Conference on Particle-based Methods – Fundamentals and Applications
PARTICLES 2017
P. Wriggers, M. Bischoff, E. Oñate, D.R.J. Owen, & T. Zohdi (Eds)

CALCULATION OF NITROGEN FLOW IN NICKEL MICRONOZZLE BASED ON NUMERICAL APPROACHES OF GAS AND MOLECULAR DYNAMICS

V. PODRYGA[1] AND S. POLYAKOV[1]

[1]Keldysh Institute of Applied Mathematics of Russian Academy of Sciences (KIAM RAS)
Miusskaya sq., 4, 125047 Moscow, Russia
E-mail: pvictoria@list.ru, web page: http://keldysh.ru/index.en.shtml/

Key words: Gas Flow, Micronozzle, Molecular Dynamics, Quasigasdynamic Equations, Nitrogen, Nickel, Macroparameters of Gas Area.

Abstract. The work is devoted to the modeling of gas flows in micronozzles. The complexity of studying such processes is connected both with the small sizes of technical system that makes it difficult to carry out the natural experiments and with the violation of hypothesis of continuity of the considered gas medium. An additional factor of complexity is the lack of information on the real processes taking place at the gas-metal boundary. An attempt to consider the features of gas flow in a micronozzle using a multiscale approach is made. The multiscale approach has two computational levels and uses the calculations by macroscopic quasigasdynamic model and microscopic model of molecular dynamics. In this approach the macromodel is supplemented by parameters and boundary conditions from database made in micromodel calculations. The flow of nitrogen in the nickel micronozzle is considered as an example. Previously the parameters of interacting the nitrogen molecules and atoms of the nickel surface were calculated and saved in database. In this paper they were used to form the material coefficients in the quasigasdynamic equations. The performed preliminary modeling has shown that at low flow velocities in calculations it is possible to obtain a flow with a profile of longitudinal velocity close to the Poiseuille flow profile. It shows the adequacy of the developed numerical techniques.

1 INTRODUCTION

Modern computer technology allows modeling very large systems and complex processes at the level of detailing that was previously not available. So relevance of studying the complex gasdynamical processes in technical micro- and nanosystems developed for the introducing nanotechnology in industry has increased. A feature of mathematical problems in this area is the simultaneous study of processes at many scales, including micro- and macrolevels. One of the modern and actively developing approaches to solving such problems is a multiscale approach that combines the methods of continuum mechanics and particle methods. This combination allows you to replace an expensive and difficult realized physical experiment with computer calculations.

In the paper, one of the aspects of modeling technical microsystems is considered. It is connected with calculating the parameters of gas microflows under technical vacuum

conditions. For a correct description of such processes, it is necessary to know the properties of real gases and to reproduce them in a numerical experiment. One way to obtain the missing information about the properties of a gas medium is molecular dynamics simulation [1, 2].

The formulation of the problem of gas flow through a micronozzle of a technical system is considered. In the practical part the calculations of the nitrogen flow moving from a chamber into a nickel micronozzle of cylindrical geometry and further into the field of a technical vacuum will be made. It is assumed that in the environment there is already a small amount of the same gas at a significantly lower pressure and at a temperature that coincides with the temperature of inhibition.

The problem was solved with the help of multiscale approach [3-5], that has two levels of detailing: macro- and microscopic. At the macrolevel of detailing, a description of the gas medium flows occurs. At the microlevel transport coefficients, parameters of the equations of state and the boundary conditions parameters are calculated. The macroscopic model of the flow is based on the quasigasdynamic (QGD) equations [6], the microscopic model – on the use of molecular dynamics (MD) methods [1, 2]. Modeling takes place at different levels in 2 basic stages: 1) calculations at the microlevel in order to accumulate a database on the flow characteristics in the temperature and pressure ranges of interest; 2) flow calculations at the macrolevel using the database obtained at the previous stage.

The main goal of this work is to perform the calculations for described problem, analyze the obtained calculated data and compare them with experiment data.

2 MATHEMATICAL MODELS

2.1 Microscopic model

In this work we consider the case of one type of the gas for the flow and one type of metal for the micronozzle. Then at the microlevel the gas-metal system is represented as a set of particles which behavior is described by Newton's equations:

$$m_{l,i}\frac{d\mathbf{v}_{l,i}}{dt}=\mathbf{F}_{l,i},\quad \mathbf{v}_{l,i}=\frac{d\mathbf{r}_{l,i}}{dt},\quad i=1,...,N_l,\quad l=a,b, \tag{1}$$

where i – particle number, $l=a,b$ – particle type (a – molecules of the gas, b – metal atoms), N_l –total particles number of type l, $m_{l,i}$ – particle mass of type l with number i, $\mathbf{r}_{l,i}=\left(r_{x,l,i},r_{y,l,i},r_{z,l,i}\right)$ and $\mathbf{v}_{l,i}=\left(v_{x,l,i},v_{y,l,i},v_{z,l,i}\right)$ – position vector and velocity vector of the i-th particle of type l, $\mathbf{F}_{l,i}=\left(F_{x,l,i},F_{y,l,i},F_{z,l,i}\right)$ – the total force acting on this particle.

The forces are the sum of the component of i-th particle interaction with the surrounding particles and the component responsible for external action:

$$\mathbf{F}_{l,i}=-\frac{\partial U\left(\mathbf{r}_{l,1},...,\mathbf{r}_{l,N_l}\right)}{\partial\mathbf{r}_{l,i}}+\mathbf{F}_{l,i}^{ext},\quad i=1,...,N_l,\quad l=a,b, \tag{2}$$

where U – total potential energy, $\mathbf{F}_{l,i}^{ext}$ – force of interaction with the environment.

Potential energy of the system depends on particles coordinates and describes the

interaction between them. The choice of interaction potential is based on comparison of mechanical properties of potential model and real material. For the solution of an objective it is necessary to consider interactions gas-gas, metal-metal and gas-metal:

$$U = U_{aa} + U_{bb} + U_{ab}, \tag{3}$$

$$U_{aa} = \sum_{i=1,\, j>i}^{N_a} \varphi_{aa}\left(\left|\mathbf{r}_{a,i} - \mathbf{r}_{a,j}\right|\right), \tag{4}$$

$$U_{bb} = \sum_{i=1}^{N_b}\left[\varphi_{1,bb}\left(\mathbf{r}_{b,i}\right) + \sum_{j>i}\varphi_{2,bb}\left(\left|\mathbf{r}_{b,i} - \mathbf{r}_{b,j}\right|\right)\right], \tag{5}$$

$$U_{ab} = \frac{1}{2}\sum_{i=1}^{N_a}\sum_{j=1}^{N_b}\varphi_{ab}\left(\left|\mathbf{r}_{a,i} - \mathbf{r}_{b,j}\right|\right). \tag{6}$$

Each type of interaction is described by the corresponding potential $\varphi_{ll'}$. For nitrogen molecules it was used Mi's potential in the form of "n-6" [7] adapted in work [8]. For interaction of nickel atoms among themselves it was used the form of EAM [9] potential which considers not only pair interactions $\varphi_{2,bb}$, but also the impact of the environment on a particular particle $\varphi_{1,bb}$. To account the gas-metal interactions a standard potential Lennard-Jones [10] was used.

The initial conditions at the microlevel include starting distribution of particle coordinates and velocities and are defined by an equilibrium thermodynamic state of particles system. Calculations of gas environment usually start with normal conditions or at first it is reduced to thermodynamic equilibrium at a given temperature and pressure. Metal parts of a microsystem must have at the start the lattice structure according to metal at given temperature. They should be no excessive stress. For more information about calculating the equilibrium state in metal-metal, gas-gas and gas-metal microsystems see [11-14].

The boundary conditions at the molecular level are selected depending on the simulated situation. In particular, when calculations are aimed on determining the properties of the medium, a certain allocated three-dimensional its volume is considered, out if which the periodic continuation medium unlimited distances in all three spatial directions is assumed. In this case, periodic boundary conditions are used.

If the calculations are made of real geometry microsystem, the one or more directions have a finite size. In this case as boundary conditions can be used or mirror boundary conditions (when particles interact with the specular reflection and don't leave thereof abroad), or a free exit of particles on one side of the allocated volume and an entrance of a particles flow – on another. For metal microsystems it is also characterized total absence of boundary conditions which are maintained in a view of the forces of a mutual attraction of atoms in a metal lattice.

In this work both periodic, and mirror boundary conditions, and also an entrance of a particles flow in environment and a free exit of particles from it were used. In addition separate parts of microsystems were thermostatted [15, 16].

The system of equations (1) is solved using Velocity Verlet Integration [17]:

$$\mathbf{r}^{n+1} = \mathbf{r}^n + \mathbf{v}^n \Delta t + \frac{\mathbf{F}^n}{m} \frac{(\Delta t)^2}{2}, \quad \mathbf{v}^{n+1} = \mathbf{v}^n + \frac{\mathbf{F}^{n+1} + \mathbf{F}^n}{2m} \Delta t \ , \tag{7}$$

here Δt – the integration step, n – the step number, $\mathbf{F}^{n+1}$ – the force value on the current step.

2.2 Macroscopic model

QGD equations in case of one type of the gas in invariant concerning system of coordinates with the constraint and the equations of state have the form:

$$\frac{\partial \rho_l}{\partial t} + \operatorname{div} \mathbf{W}_l^{(\rho)} = 0, \tag{8}$$

$$\frac{\partial \left(\rho_l u_{l,k} \right)}{\partial t} + \operatorname{div} \mathbf{W}_l^{(\rho u_k)} = 0, \ k = x, y, z, \tag{9}$$

$$\frac{\partial E_l}{\partial t} + \operatorname{div} \mathbf{W}_l^{(E)} = 0, \tag{10}$$

$$E_l = \frac{1}{2} \rho_l \left| \mathbf{u}_l \right|^2 + \rho_l \varepsilon_l, \quad \varepsilon_l = c_{V,l} T_l, \quad H_l = \frac{E_l + p_l}{\rho_l}, \quad p_l = Z_l \rho_l \Re_l T_l. \tag{11}$$

Here $l = a$, gas has numerical density (concentration) n_a and mass density $\rho_a = m_a n_a$, where m_a – mass of gas molecules a. Gas is characterized by its temperature T_l and macroscopic velocity $\mathbf{u}_l$. Other parameters: p_l – partial pressures, E_l – total energy densities, ε_l – specific internal energies, H_l – total enthalpies, $Z_l = Z_l \left(T_l \right)$ – compressibility coefficients, $c_{V,l} = c_{V,l} \left(T_l \right)$ – specific heat capacities at constant volume, $\Re_l = k_B / m_l$ – gas constants (k_B – Boltzmann constant). Vectors $\mathbf{W}_l^{(\rho)}$, $\mathbf{W}_l^{(\rho u_k)}$, $\mathbf{W}_l^{(E)}$ up to a sign are identical to the density flux of the corresponding components of the momentum density and energy density.

In [13] on the example of nitrogen molecule system the technique of specifying the equations of state was considered. In [18] three methods for determining the kinetic coefficients were presented, comparing methods were produced and examples of calculating the coefficients of nitrogen molecule system were given.

The system of equations (8)-(10) is closed by initial and boundary conditions. The initial conditions correspond to the equilibrium gas environment in the absence of interaction with external factors. The boundary conditions can be determined in the form of third-type boundary conditions describing an exchange of mass, momentum and energy components between the gas flow and the metal walls. In [14, 19] interaction of a gas flow with microchannel walls on the example of nitrogen-nickel system was considered. In [20] on an example of the same system the accommodation coefficients were obtained. These calculations represent a technique of obtaining the boundary conditions by direct MD computation.

For calculating the macroparameters on QGD equations the grid numerical method having a finite-volume method [21-23] in the basis is used. For this in the computational domain D the spatial grid Ω_D with cells C_m ($m = 1,...,M$) and time grid ω_t with variable step Δt was introduced. Grid Ω_D in general is a hybrid, that is, it includes several element types: tetrahedrons, pentahedrons, hexahedrons, octahedrons and heptahedrons. All parameters of gas components (density, pressure, temperatures, velocity vector components, etc.) have been carried to the centers of mass of grid elements, that is to the centers of cells. Stream variables have been set in the centers of cells sides. Spatial approximations of the main members have been executed by the technique presented in work [24]. The computing scheme on time was obvious.

3 NUMERICAL EXPERIMENTS

In this section, the results of calculating the nitrogen flow after exit from chamber to the nozzle and further into the free space are presented. The problem was chosen in connection with the existence of experimental data presented in the paper [25]. The geometry of the chosen model statement of the problem practically coincides with that described in [25] (see Figure 1). The cylindrical micronozzle has a diameter $D_0 \approx 310\,\mu m$, length $L_0 = 6D_0 \approx 1860\,\mu m$. It connects the chamber of nitrogen and the open space of the vacuum area, which was initially filled with the same highly diluted gas. The dimensions of the computational domain were chosen as follows. The diameters of the computational parts in the chamber and in the vacuum space were equal $D_1 = D_2 = 6D_0$. The length of the calculated part in the chamber was $L_1 = 10L_0$; the length of the considered part of the vacuum space was $L_2 = 50L_0$. At the initial time the gas does not move: $u_1 = u_2 = 0$. In this case, it is in the cylinder under standard normal conditions: $T_1 = 295.15\,K$, $p_1 = 101325\,Pa$; in the nozzle and the vacuum space it is at the same temperature, but at lower pressures: $T_2 = 295.15\,K$, $p_2 = \delta_0 p_1$, $\delta_0 \sim 10^{-3} \div 10^{-5}$ – pumping parameter. The nozzle on the left is blocked by a partition, which opens instantly at the beginning of the calculation.

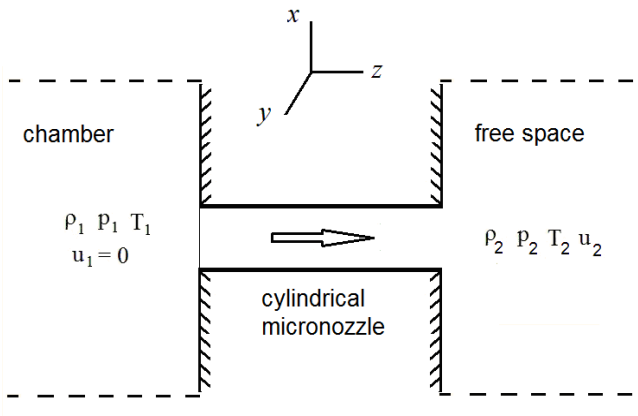

Figure 1: Geometry of a model problem for convenience presented in the form of a two-dimensional section

3.1 Calculations at microlevel

Calculations within this level consist of setting the initial state of the gas microsystem and carrying out a cycle of calculations according to the Verlet scheme (7). The initial calculation data assumes the assignment of the calculation area and its volume, the initial number of particles and their distribution on the volume, the velocity distributions on absolute values and directions, the parameters of the interaction potentials, the parameters of the final equilibrium state (for example, temperature and average momentum), parameters of the numerical integration scheme.

During calculating the properties of gas mixtures, the basic gas macroparameters were determined. These macroparameters are compressibility factor, heat capacities at constant volume and pressure, shear and bulk viscosities, thermal conductivity, diffusion coefficients. The motivation for choosing these macroparameters is determined by the fact that for a given temperature, pressure, and velocity vector, the base macroparameters make it possible to determine all other macroparameters of the gas.

Series of MD calculations of gas characteristics were performed in the temperature range from 80 to 400 K under pressure $p_0 = 101325\ Pa$. The obtained data were approximated by a set of dependencies and are shown in Figures 2-5 in comparison with the known experimental and theoretical data from. For the convenience of analysis the coefficients of shear viscosity μ_{N_2}, bulk viscosity μ_{b,N_2}, thermal conductivity κ_{N_2}, diffusion D_{N_2} are normalized to their values $\mu^0_{N_2} = 1.667 \cdot 10^{-5}\ Pa \cdot s$, $\mu^0_{b,N_2} = 1.288 \cdot 10^{-5}\ Pa \cdot s$, $\kappa^0_{N_2} = 2.419 \cdot 10^{-2}\ W/m \cdot K$, $D^0_{N_2} = 1.850 \cdot 10^{-5}\ m^2/s$ at a temperature $T_0 = 273.15\ K$.

As can be seen from the figures, the constructed approximations are generally agree well with the experiment data. An exception is the dependence of the specific heat in the low-temperature region (less than 100 K), where the nitrogen gradually passes into the liquid phase. For this zone, one must take into account the dependence of the specific heats c_{V,N_2} and c_{p,N_2} from the density (pressure). There is also some discrepancy in the curves of dynamic and bulk viscosities, which is also observed in the literature in connection with the difficulty in determining these quantities in theory and in experiments. The obtained data were used below in the calculation of the selected model problems.

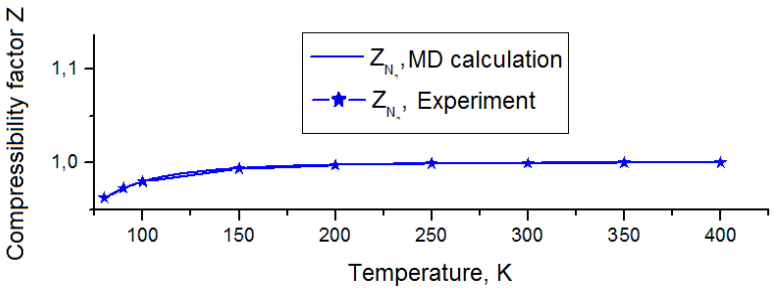

Figure 2: Compressibility factor Z_{N_2} of nitrogen as a function of temperature

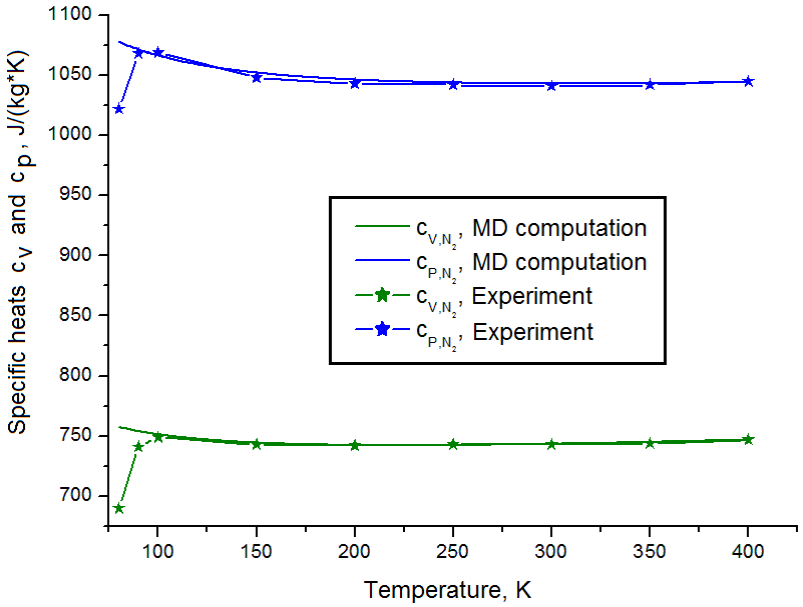

Figure 3: Dependences of the specific heats c_{V,N_2} and c_{p,N_2} of nitrogen on temperature

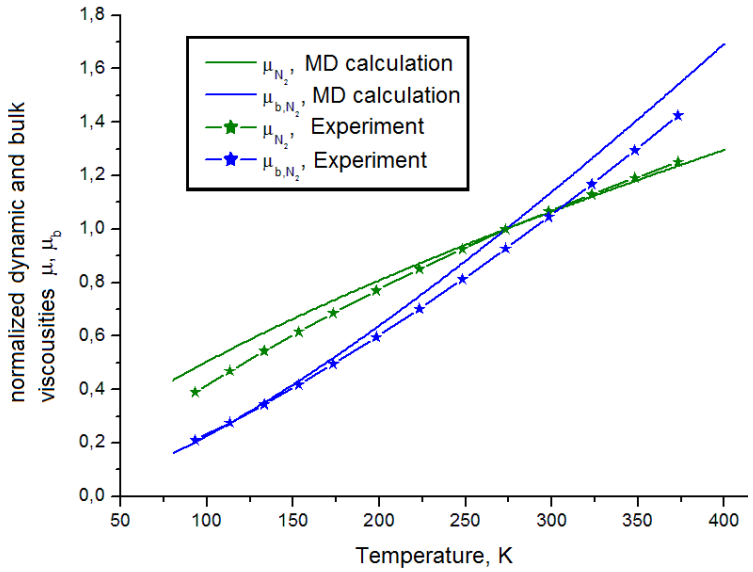

Figure 4: Coefficients of normalized dynamic $\mu_{N_2} / \mu^0_{N_2}$ and relative bulk $\mu_{b,N_2} / \mu^0_{b,N_2}$ viscosities of nitrogen as a function of temperature

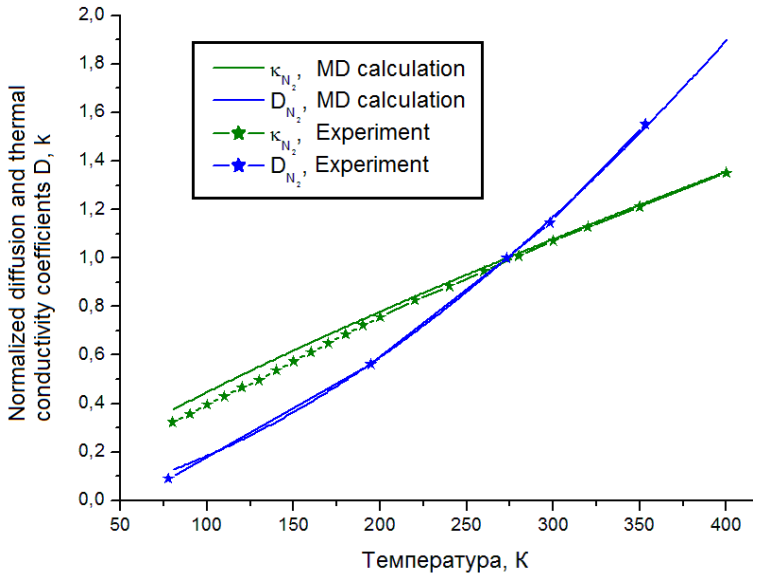

Figure 5: Normalized coefficients of thermal conductivity $\kappa_{N_2} / \kappa^0_{N_2}$ and diffusion $D_{N_2} / D^0_{N_2}$ of nitrogen as a function of temperature

3.2 Calculations at macrolevel

Calculations were carried out under conditions of two- and three-dimensional geometry. On Figure 6 two-dimensional distributions of the concentration of nitrogen molecules normalized by the value $10^{24} m^{-3}$, and the longitudinal velocity component are presented at different times.

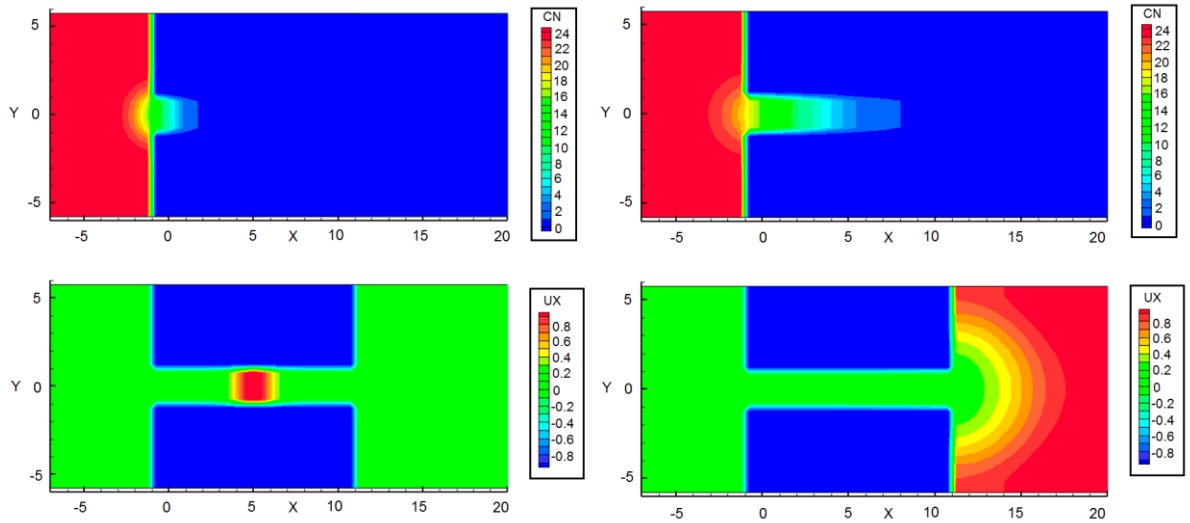

Figure 6: Distributions of the normalized concentration of nitrogen molecules (from above) and the longitudinal velocity component (from below) at time points $t = 0.0553, 0.553\ \mu s$

Normalization parameter on space is equal to $0.5D_0$. In dimensionless variables, the length of the region is $L_x = 732$, diameter is $D_y = D_z = 12$. In the two-dimensional case, the calculations were carried out in a rectangle $L_x \times D_y$, in the three-dimensional case, the calculations were carried out in a cylinder of square cross section with common dimensions $L_x \times D_y \times D_z$.

An analysis of the obtained data shows that the passage of gas into the micronozzle is implemented symmetrically and corresponds to the physics of the process.

Three-dimensional calculations confirmed the results obtained in the two-dimensional case, namely, the dynamics of distributions of the main gasdynamic parameters. The difference between the three-dimensional calculations and the two-dimensional ones was expressed in the difference in the times when specific distributions were formed. In particular, the times of thermal wave output from the micronozzle differed approximately by 1.3 times that can be connected with the chosen square form of a micronozzle.

Figure 7 shows the profiles of normalized nitrogen concentration on the axis of the vacuum space. As can be seen from the figure, the main behavior of the concentration coincides with the experimental data. Thus, with the help of the developed algorithms, it is possible to obtain information about real physical processes.

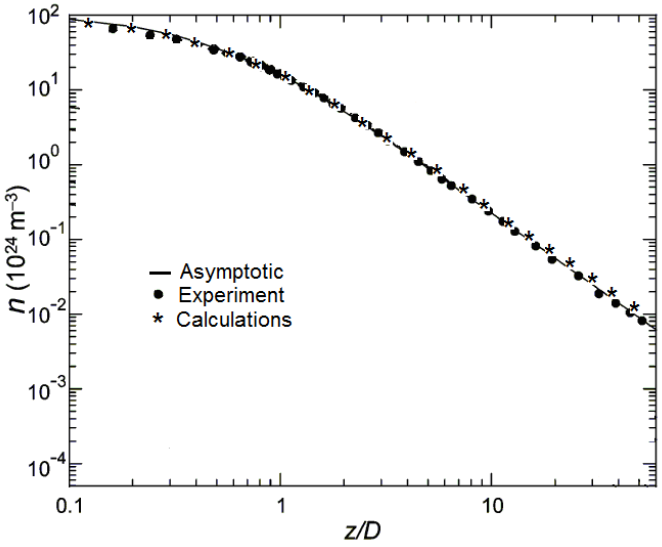

Figure 7: Established profiles of the normalized nitrogen concentration obtained in the natural experiment [25] and in the numerical calculation

Direct MD calculations of nitrogen flow in a thin channel with a thickness about 500 nm were also carried out. They showed that for flow velocities of the order of 1 nm/ns or less, at the exit from the microchannel the velocity profile is formed close to the Poiseuille profile. However, the final conclusion about the parameters of such flow requires additional investigation.

4 CONCLUSIONS

- Multiscale numerical approach to three-dimensional modeling of nonlinear interaction of gas with metal in microsystems was performed.
- Parallel realization of the approach using hybrid parallel computing technology was developed.
- Verification of numerical approach and validation of parallel software were fulfilled.
- Proposed numerical approach allows simulating qualitatively the behavior of gas - metal complex microsystems under the real conditions.

REFERENCES

[1] Rapaport, D.C. *The art of molecular dynamics simulations.* Second Edition, Cambridge University Press, (2004).

[2] Frenkel, D. and Smit, B. *Understanding molecular simulation. From algorithm to applications*. New-York: Academic Press, (2002).

[3] Podryga, V.O. Multiscale Approach to computation of three-dimensional gas mixture flows in engineering microchannels. *Dokl. Math.* (2016) **94**:458-460.

[4] Podryga, V.O. Computational technology of multiscale modeling the gas flows in microchannels. *IOP Conf. Ser.: Mater. Sci. Eng.* (2016) **158**:012078.

[5] Podryga, V.O., Karamzin, Yu.N., Kudryashova, T.A., and Polyakov, S.V. Multiscale simulation of three-dimensional unsteady gas flows in microchannels of technical systems. *Proc. VII ECCOMAS Congress*, M. Papadrakakis, V. Papadopoulos, G. Stefanou, V. Plevris (eds.), Crete Island, Greece, 5–10 June 2016, (2016) **2**:2331-2345.

[6] Elizarova, T.G. *Quasi-Gas Dynamic Equations*. Computational Fluid and Solid Mechanics, Springer, Dordrecht, (2009).

[7] Von Mie, G. Zur kinetischen theorie der einatomigen korper. *Ann. Phys. Leipzig* (1903) **8:**657-697.

[8] 8 14 Fokin, L.R. and Kalashnikov, A.N. The transport properties of an N2-H2 mixture of rarefied gases in the EPIDIF database. *High Temp.* (2009) **5:**643-655.

[9] Zhou, X.W., Johnson, R.A., and Wadley, H.N.G. Misfit-energy-increasing dislocations in vapor-deposited CoFe/NiFe multilayers. *Phys. Rev. B* (2004) **69:**144113.

[10] Lennard-Jones, J.E. Cohesion. *Proc. Phys. Soc.* (1931) **5**:461-482.

[11] Podryga, V.O. Molecular dynamics method for simulation of thermodynamic equilibrium. *Math. Models Comput. Simul.* (2011) **3**:381-388.

[12] Podryga, V.O. and Polyakov, S.V. Molecular dynamics simulation of thermodynamic equilibrium establishment in nickel. *Math. Models Comput. Simul.* (2015) **5:**456-466.

[13] Podryga, V.O. and Polyakov, S.V. Correction of the gas flow parameters by molecular dynamics. *Proc. Fourth International Conf. on Particle-Based Methods–Fundamentals and Applications (PARTICLES 2015)*, ed. by E. Onate and etc. CIMNE, (2015) 779-788.

[14] Podryga, V.O., Polyakov, S.V., and Puzyrkov, D.V. Supercomputer molecular modeling of thermodynamic equilibrium in gas-metal microsystems. *Vychislitel'nye metody i programmirovanie* (2015) **1:**123-138.

[15] Berendsen, H.J.C., Postma, J.P.M., Gunsteren, W.F., et al. Molecular dynamics with coupling to an external bath. *J. Chem. Phys*. (1984) **81:**3684-3690.

[16] Heerman, D.W. *Computer simulations methods in theoretical physics*. Springer, (1986).
[17] Verlet, L. Computer «experiments» on classical fluids. I. Thermodynamical properties of Lennard-Jones molecules. *Phys. Rev*. (1967) **159:**98-103.
[18] Podryga, V.O. Calculation of kinetic coefficients for real gases on example of nitrogen. In: Dimov I., Faragó I., Vulkov L. (eds) *Numerical Analysis and Its Applications. NAA 2016. Lecture Notes in Computer Science. Cham: Springer*, (2017) **10187**:542-549.
[19] Podryga, V.O., Polyakov, S.V., and Zhakhovskii, V.V. Atomistic calculation of the nitrogen transitions in thermodynamic equilibrium over the nickel surface. *Mat. Model*. (2015) **7:**91-96.
[20] Podryga, V.O. and Polyakov, S.V. Molecular dynamic calculation of gas macroparameters in the stream and on the boundary. *Keldysh Institute Preprints,* 80**, (**2016).
[21] Fryazinov, I.V. Balance method and variational-difference schemes. *Differentsial'nye uravneniya* (1980) **7:**1332-1343.
[22] Samarskiy, A.A., Koldoba, A.V., Poveshchenko, Yu.A., Tishkin, V.F., Favorskiy, A.P. *Difference schemes on irregular grids*. Minsk: Publishing of Closed Joint Stock Company "Criterion", (1996).
[23] Eymard, R., Gallouet, T.R., and Herbin, R. The finite volume method. *Handbook of Numerical Analysis, Amsterdam, North Holland* (2000) **7**:713-1020.
[24] Popov, I.V. and Fryazinov, I.V. Method of adaptive artificial viscosity for the equations of gas dynamics on triangular and tetrahedral grids. *Math. Models Comput. Simul.* (2013) **1:**50-62.
[25] Ramos, A., Tejeda, G., Fernandez, J.M., Montero, S. Nonequilibrium processes in supersonic jets of N2, H2, and N2 + H2 mixtures: (I) Zone of silence. *J. Phys. Chem. A* (2009) **113**:8506-8512.

V International Conference on Particle-based Methods – Fundamentals and Applications
PARTICLES 2017
P. Wriggers, M. Bischoff, E. Oñate, D.R.J. Owen, & T. Zohdi (Eds)

CHARACTERIZING GAS FILM CONDUCTION FOR PARTICLE-PARTICLE AND PARTICLE-WALL COLLISIONS

Andrew M. Hobbs*‡ and Jin Y. Ooi†

* Astec, Inc.
4101 Jerome Ave.
Chattanooga, Tennessee, 37407, USA
e-mail: ahobbs@astecinc.com, web page: http://www.astecinc.com

†‡ School of Engineering, The University of Edinburgh
William Rankine Building, The King's Buildings
Thomas Bayes Road, Edinburgh, EH9 3FG, United Kingdom
e-mail: j.ooi@ed.ac.uk, web page: http://www.eng.ed.ac.uk/research/institutes/iie

Abstract

Heat transfer in granular media is an important mechanism in many industrial applications. For some applications conduction is an important mode of heat transfer. Several models have been proposed to describe particle scale conduction both between particles (particle-particle) and with walls (particle-wall). Within these conduction models are several distinct modes: conduction through physical contact (macro-contact), conduction through surface roughness (micro-contacts), and conduction through the stagnant gas film surrounding each particle (particle-fluid-particle or particle-fluid-wall). While these models have been developed and verified in literature, the relationship between the conduction heat transfer coefficient and key parameters is not immediately obvious. This is especially true for gas film conduction. In this work we investigate gas film conduction for particle-particle and particle-wall collisions via DEM simulations using a well-established gas film model to determine the behavior of the heat transfer coefficient as a function of the separation distance and particle size. With a better understanding of the gas film heat transfer coefficient, we propose a simplified model that captures the same response but is easier to understand and significantly more computationally efficient.

Keywords: Conduction, Discrete element method, gas film conduction, granular heat transfer

INTRODUCTION

Heat transfer in granular materials is a common occurrence in many industrial applications. In many instances hot gases are used to convectively heat the particles. However, there are some applications where conductive heat transfer is the dominant mode. One such application is the heating of recycled asphalt product (RAP). RAP is the millings from road surfaces and is comprised of aggregates and bitumen coating. For RAP to be reused in new road surface mixes, it must be heated and any moisture evaporated. Since the bitumen coating is flammable, a flame cannot be used to directly heat the RAP. A common method is to mix hot, uncoated (virgin) aggregate with the cold, wet RAP. In such a process conductive heat transfer between the virgin and RAP is dominant.

Numerical techniques used to simulate particle systems are now well established and increasing computational power means more industrial scale processes are accessible via methods such as the discrete element method (DEM) [1,2,3]. Since heat transfer is common in many industrial processes, particle models have been extended beyond simple contact mechanics to include thermal effects [4,5]. Coupling to a fluids solver permits convective heat transfer between the fluid and particle phase to be calculated [6,7] but this is expensive and unnecessary where convection is not dominant. A common approach where conduction is dominant is DEM particle scale simulation using the Hertzian soft sphere contact model. Conductive heat transfer was added to this approach by Batchelor and O'Brien [8]. This model assumes that heat flows through the physical contact (or macro-contact) between particles given by the Hertzian contact radius:

$$Q_{MC} = 2k^* \left[\frac{3F_N R^*}{4E^*}\right]^{1/3} \Delta T \tag{1}$$

where k^* is the effective thermal conductivity, F_N is the normal force, R^* is the effective radius, E^* is the effective Youngs modulus, and ΔT is the temperature difference.

Rong et al. [9] postulated that in addition to physical contact, conduction could occur through a stagnant gas layer surrounding each particle. As the gas film surrounding a particle touches an adjacent surface (particle or wall), conduction occurs through the gas film. The heat rate can be calculated according to Fourier's Law:

$$Q_{film} = \int \frac{dA}{\Delta L} k_f \Delta T \tag{2}$$

where k_f is the fluid thermal conductivity, A is the surface area , and ΔL is the separation distance.
It follows that the conductive heat transfer rate through particle-fluid-particle Q_{pfp} and through particle-fluid-wall Q_{pfw} can be described as follows:

$$Q_{pfp} = \int_{r_{in}}^{r_{out}} \frac{2\pi k_f}{\max(l,s)} dr\, \Delta T \tag{3}$$

$$Q_{pfw} = \int_{r_{in}}^{r_{out}} \frac{2\pi k_f r}{\max(l,s)} dr\, \Delta T \tag{4}$$

where the linear distance between particle surfaces is defined by the variable l, the radial dimension by the variable r, and the upper and lower bounds of the integral r_{out} and r_{in} are illustrated for the particle-fluid-particle contact in Figure 1. To prevent a singularity at the point of contact, a minimum limit s=2.75 x 10^{-8} m is assumed to be related to the mean free path of gas.

Rong [10] assumed that the macro-contact was analogous to the contact area separated by the mean free path of gas equation (9).

$$Q_{MC=} \frac{k_f A_c}{4.0 \times 10^{-10}} \Delta T \tag{5}$$

This approach was implemented by Bu et al. (2013) to include micro-contact surface roughness, the macro-contact and gas film model by Rong as well as the interior thermal resistance of the particle. For Biot numbers less than one, the particle can be assumed to be isothermal and the interior resistance neglected.

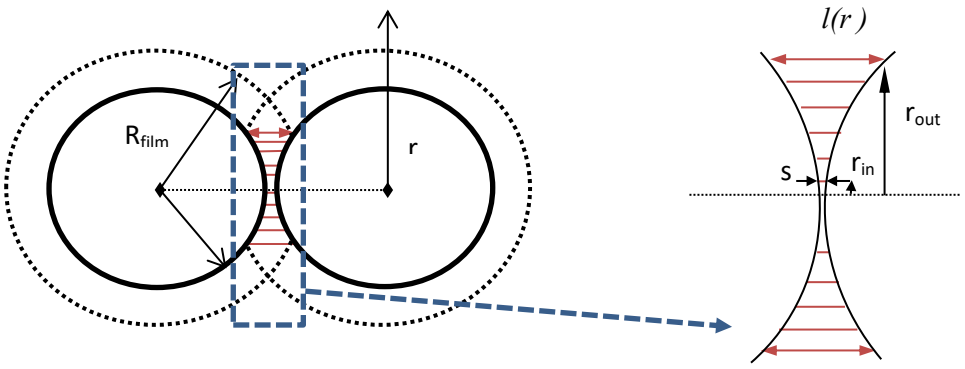

Figure 1 *Illustration of particle-fluid-particle conduction*

Morris et al. [12] combined the Rong's gas film model with the Batchelor and O'Brien's macro-contact model from Equation 1. Morris et al. also determined that for materials with a low thermal conductivity the gas film could be as much as two orders of magnitude more than the physical contact. The authors proposed a ratio to determine the effect of the gas film relative to the macro-contact, given by:

$$\frac{R_P k_f}{R_c k_P} \geq 1 \tag{6}$$

where R_P is the particle radius and R_c is the contact radius and k_f and k_p are the thermal conductivity of the fluid and particle, respectively. For values greater than one, the gas film conduction is dominant.

In this study we focus on gas film conduction for particle-particle and particle-wall collisions. Internal resistance is neglected as the effect is deemed negligible in the specific application of RAP processing. The analytic solution to the integral of Fourier's equation for sphere-sphere and sphere-wall was implemented according to the algorithm by Morris in the MFIX code. The analytic solution to particle-fluid-wall heat transfer coefficient $\widehat{H}$ is given in Equation 7 below, where the normalized particle overlap $\widehat{\delta}$ is greater or equal to zero when physical contact occurs. When $\widehat{\delta}$ is less than zero there is only gas film contact. A similar set of equations provides the solution for particle-fluid-particle contacts. The variables previously described in equations 3 and 4 are made dimensionless by dividing by the particle radius and denoted in Equation 7 by the ^ symbol.

$$\widehat{H} = \begin{cases} \frac{\pi}{\hat{s}}\left[\left(1-\hat{\delta}\right) - A^2\right] + 2\pi\left[B - A + \left(1-\hat{\delta}\right) ln\left(\frac{1-\hat{\delta}-B}{\hat{s}}\right)\right], & \hat{\delta} \geq 0 \\ 2\pi\left[\frac{\hat{r}_s^2}{2\hat{s}} + B - C + \left(1-\hat{\delta}\right) ln\left(\frac{1-\hat{\delta}-B}{1-\hat{\delta}-C}\right)\right], & \hat{\delta} < 0 \end{cases} \tag{7}$$

where

$$A = 1 - \hat{\delta} - \hat{s}$$
$$B = \sqrt{1 - \hat{r}_{out}^2}$$
$$C = \sqrt{1 - \hat{r}_s^2}$$

and

$$\hat{r}_{out} = \begin{cases} \sqrt{\hat{R}_{film}^2 - (1 - \hat{\delta})}, & \hat{\delta} < 1 - \sqrt{\hat{R}_{film}^2 - 1} \\ 1, & \hat{\delta} \geq 1 - \sqrt{\hat{R}_{film}^2 - 1} \end{cases}$$
$$\hat{r}_s = \begin{cases} \sqrt{1 - A^2}, & \hat{\delta} > -\hat{s} \\ 0, & \hat{\delta} \leq -\hat{s} \end{cases}$$

Whilst these models have been developed and verified to a limited extent, the relationship between the conduction heat transfer coefficient and the key parameters is rather obscure. This is especially true for gas film conduction which is dominant in many industrial processes where the industrial solids are poor conductors such as in this study on RAP and road aggregates. In this study we investigate the gas film conduction for particle-particle and particle-wall collisions via DEM simulations to determine the behavior of the heat transfer coefficient as a function of the separation distance and particle size.

Gas Film Conduction For Poly-dispersed Particle Systems

The Rong gas film conduction model assumes that the gas film thickness is roughly 50% of the particle radius. Morris showed that the solution is not especially sensitive to this value and proposed a value of 42%. In this work we use a gas film thickness that is 40% of the particle radius. Because the integral solution to Fourier's equation is dependent on the linear distance from one particle surface to the other particle (or wall) surface, the minimum size ratio for this to remain valid is 0.4 (see Figure 2). The means the smaller particle's radius cannot be smaller than the larger particle's film thickness, otherwise the film thickness could enclose some surface area of the smaller particle not in direct line with the larger particle. With this limitation in mind and assuming fixed material properties for spherical particles, the gas film heat transfer coefficient should be related only to the particle size ratio and separation distance.

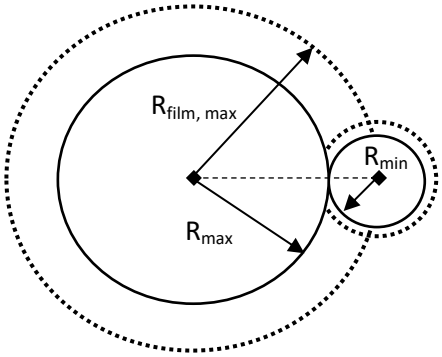

$$R_{min} \geq R_{film,max} - R_{max}$$

Figure 2 *Illustration of minimum size ratio where $R_{min} \geq$ film thickness*

NUMERICAL METHODS: DEM SIMULATIONS

Particle-Particle Collisions

The Rong gas film model as implemented by Morris in the open source multiphase code MFIX [12,13] was implemented as a custom contact model in the commercial DEM code EDEM [14]. Care was taken to use as near to the original Morris algorithm as possible although some minor changes were necessary due to differences in which variables were directly accessible from each DEM solver. Particle-particle and particle wall collisions were investigated using the Rong/Morris models for a range of particle size ratios varying from 1 to 0.4. Table 1 shows the material properties and simulation settings. Two particles with the same material properties were slowly brought into contact. The simulated velocities were very low and the resulting minimal collision force meant that the influence of physical contact could be neglected. The gas film heat transfer coefficient was calculated from the predicted heat flux and temperature difference. Figure 3 shows some representative results at the point of contact.

Table 1 Material properties and simulation settings used in DEM simulation

Density	2500 kg/m^3
Young's Modulus	5.0 x 10^{10} Pa
Poisson's Ratio	0.3
Thermal Conductivity	0.96 W/m K
Specific Heat	472 J/kg K
Coefficient of Restitution	1 x 10^{-7}
Coefficient of Static Friction	0.5
Particle Radius	2 to 5 mm
Initial Particle Velocity	0.01 m/s
Initial Particle Temperature	20 C min, 100 C max
Initial Wall Temperature	100 C
Simulation Time Step	1 x 10^{-6}s

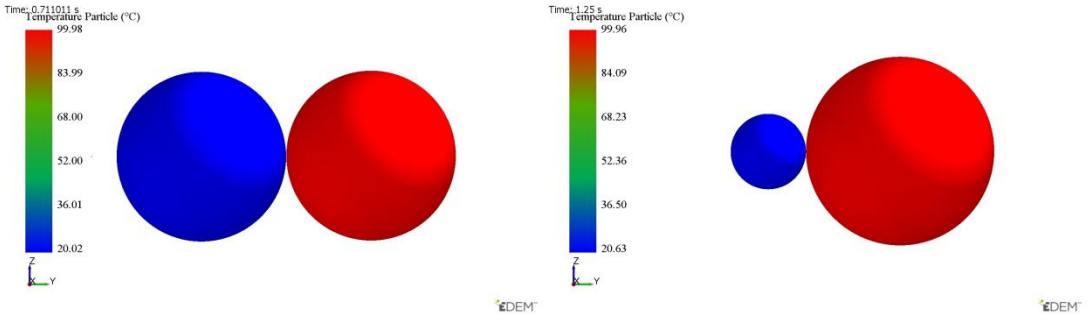

Figure 3 DEM results at the point of physical contact for size ratios 1 and 0.4

Particle-Wall Collisions

A similar simulation was used to investigate particle-wall collisions. A single particle collision at low velocity with a fixed surface was simulated for different particle sizes. Again, because the collision force was minimal the physical contact could be neglected. The gas film coefficient was calculated from the predicted heat flux and temperature difference.

RESULTS

Particle-Particle Collisions

The heat transfer coefficient (HTC) computed from the DEM simulations can be plotted as a function of the particle surface to surface distance normalized by the film thickness. The result is shown in Figure 4a. For a normalized separation distance of 1 there is no gas film contact and the coefficient is 0 for gas film conduction as expected. For values less than 1 the heat transfer coefficient increases logarithmically until the point of contact when the normalized separation distance is 0. For particle-particle collisions a set of curves was generated for the different particle size ratios. As the ratio approaches 0.4 the log curve becomes more acute nearest to the point of physical contact. At the point of contact a similar curve can be generated using the results for each particle size (Figure 5a). The response surface as a function of particle size and separation distance is shown in Fig 5b. The logarithmic relationship of the HTC to normalized separation distance is easily recognizable and the relationship between size ratio at the point of contact can also be seen.

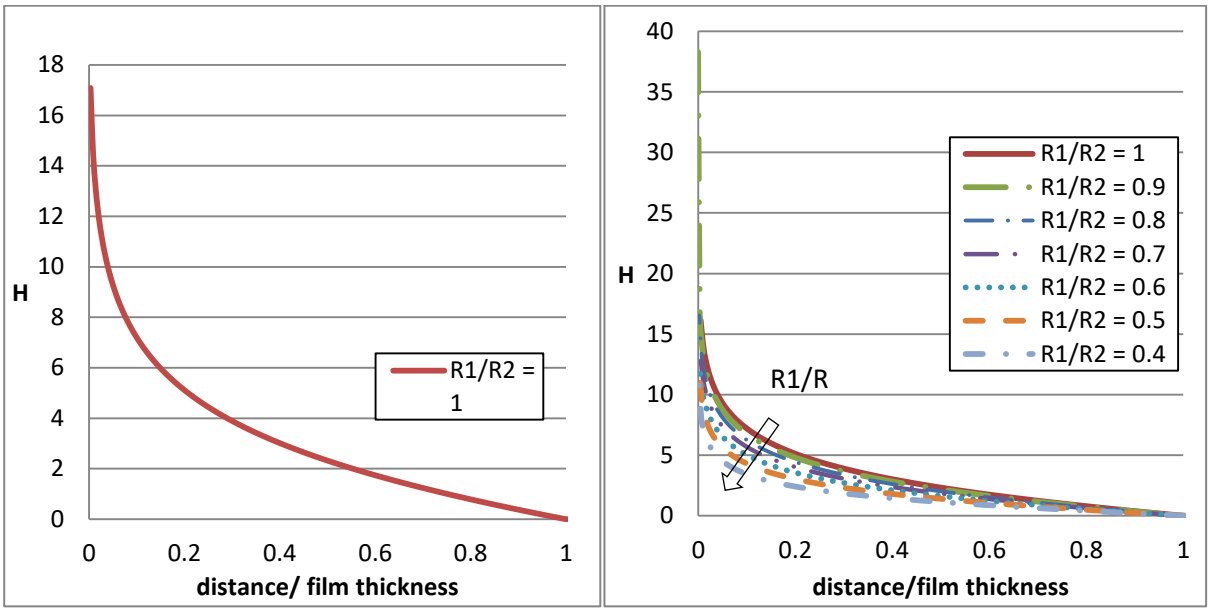

Figure 4a (left) Plot of the gas film coefficient vs the normalized separation distance for particle-particle size ratio = 1. **Figure 4b** (right) Gas film coefficient for different particle size ratios

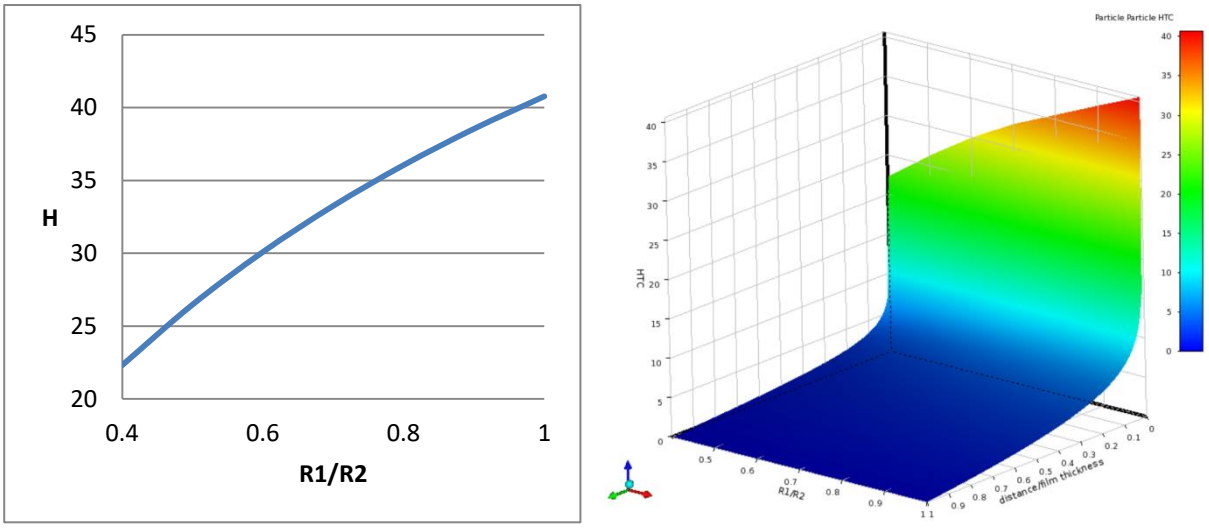

Figure 5a (left) Plot of gas film coefficient at the point of physical contact as a function of the particle size ratio. **Figure 5b** (right) Response surface for particle-particle gas film coefficient

This graphical representation of the HTC provides a much more intuitive description of the gas film heat transfer behavior involving particle-particle collisions. Curve fitting was used to describe the HTC relationships for film contact and physical contact in simple equations as follows:

Film Contact $$Q_{pfp} = \frac{R1/R2}{(R1/R2)^{0.2125}}\left[-3.161\ln\left(\frac{distance}{film\ thickness}\right) + 0.151\right]R_p k_f \Delta T \qquad (8)$$

Physical Contact $$Q_{pfp} = [20.22\ln(R1/R2) + 40.604]\, R_p k_f \Delta T \quad (9)$$

where a weighting function using the size ratio (R1/R2) was determined to provide the best fit to describe the whole domain.

Particle-Wall Collisions

For particle-wall collision the curve for the heat transfer coefficient is simply a function of the particle size and the separation distance. Because we assume that the wall is infinite the shape of the curve is not affected by the particle size as shown in Figure 6a, that is, the curves for all the particle sizes are identical except for at the point of physical contact. At point of contact, the HTC shows an increasing with the particle size (as shown in Figure 6b). Curve fitting to each of these curves leads to Equations 10 and 11 respectively:

Film Contact $$Q_{pfw} = \left[-6.101\ln\left(\frac{distance}{film\ thickness}\right) + 0.6015\right] R_p \mathrm{k}_f \Delta T \quad (10)$$

Physical Contact $$Q_{pfw} = \left[6.2831\ln(R_p) + 110.17\right] R_p k_f \Delta T \quad (11)$$

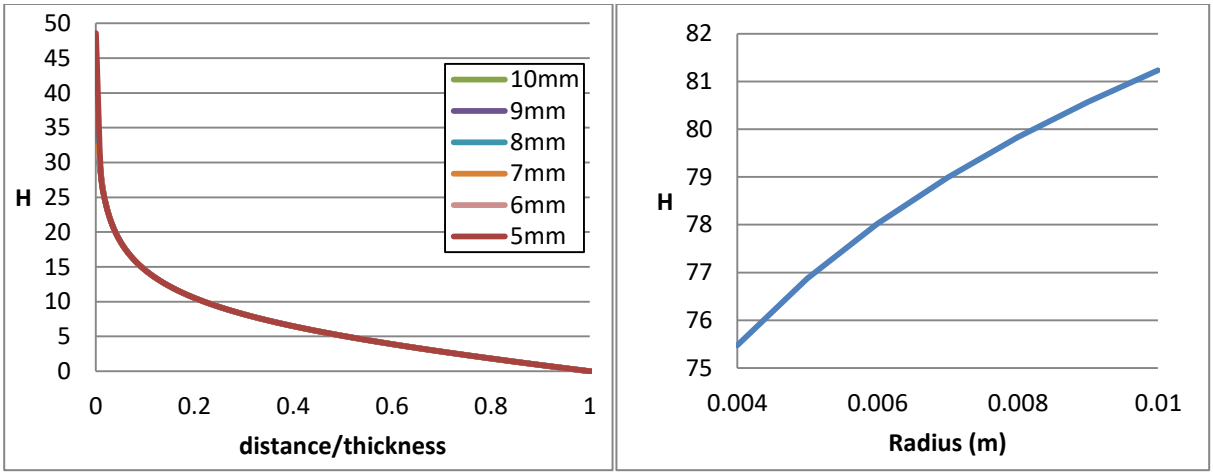

Figure 6a (left) Plot of particle-wall heat transfer coefficient for film contact. **Figure 6b** (right) Plot of particle-wall coefficient for physical contact as a function of particle radius.

Simplified Model for Gas Film Conduction Model

With the description of the heat transfer coefficient as a function of the normalized separation distance and particle size ratio, the gas film conduction model can be expressed in four simple equations 8-12. These equations were implemented in EDEM replacing the analytical solution to the

Rong integral. The computed HTC for particle-particle and particle-wall collisions using the simplified model are compared with the Rong/Morris full analytical mode in Figures 7 and 8 below which show an excellent agreement.

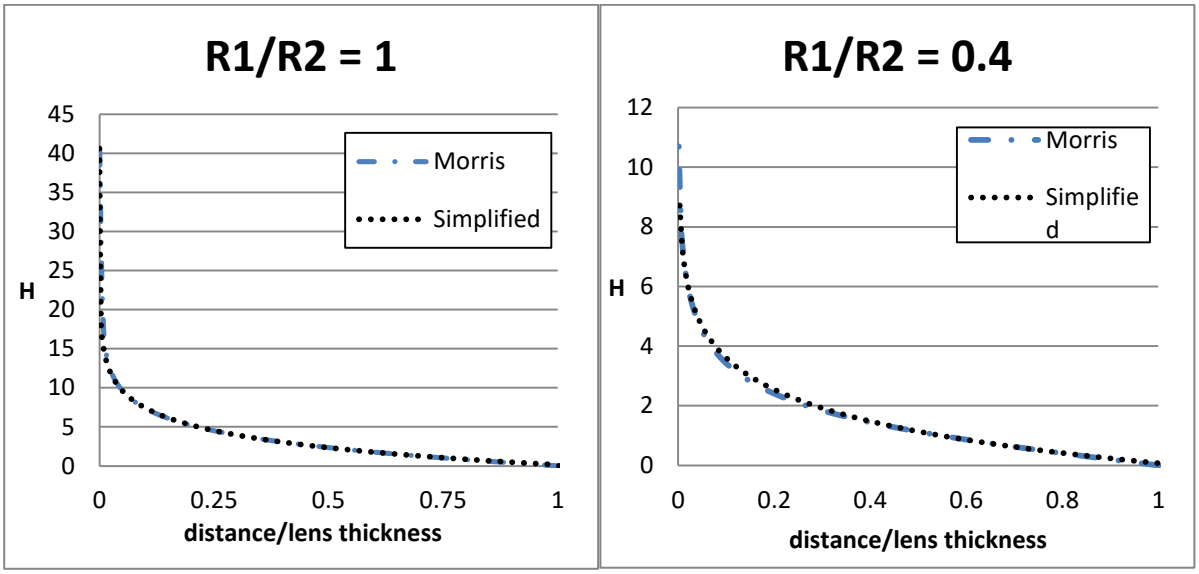

***Figure** 7 Comparison of particle-fluid-particle coefficient for size ratio of 1 (left) and 0.4 (right)*

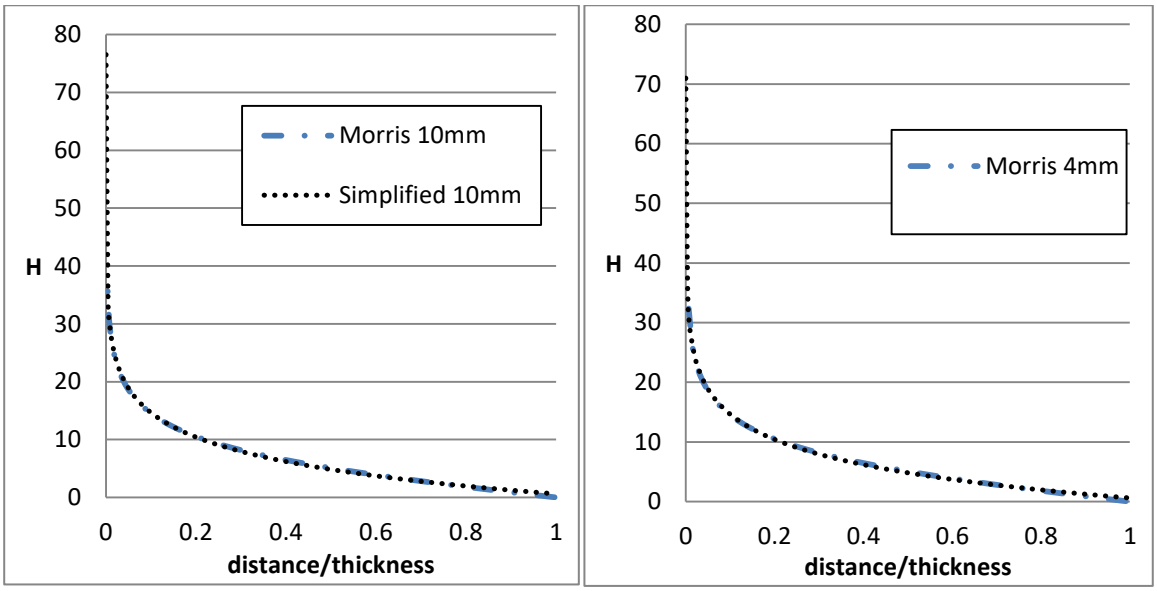

Figure 8 Comparison of particle-fluid-wall coefficient for size ratio of 10mm (left) and 4mm (right) particles

Further, comparing the computation time of the calculation for a single binary collision, the portion of time spent on the conduction calculation can be determined by subtracting the calculation time of the standard Hertz-Mindlin model with no conduction from the total time. Figure 9 shows that 27% of the total calculation time was spent on the Morris conduction calculation while only 19% of

the total time was spent on the simplified model. This represents an improvement of 33.4% of the conduction calculation. The net total improvement is approximately 9.0%. Further tests of an industrial scale problem with 250,000 particles have demonstrated speed improvements of 10% with near identical results for particle temperature (Figure 10). In this mill test case with heated walls, the maximum particle temperature after 10 second of simulation time for the simplified model is within 0.022% of the maximum value predicted by the Morris model and the maximum gas film heat flux within 0.0017% of the Morris model. The improvement in calculation time will depend on the individual simulation, but results for a range of simulations have been between 5 and 15% with simulations with more static contacts showing the least benefit.

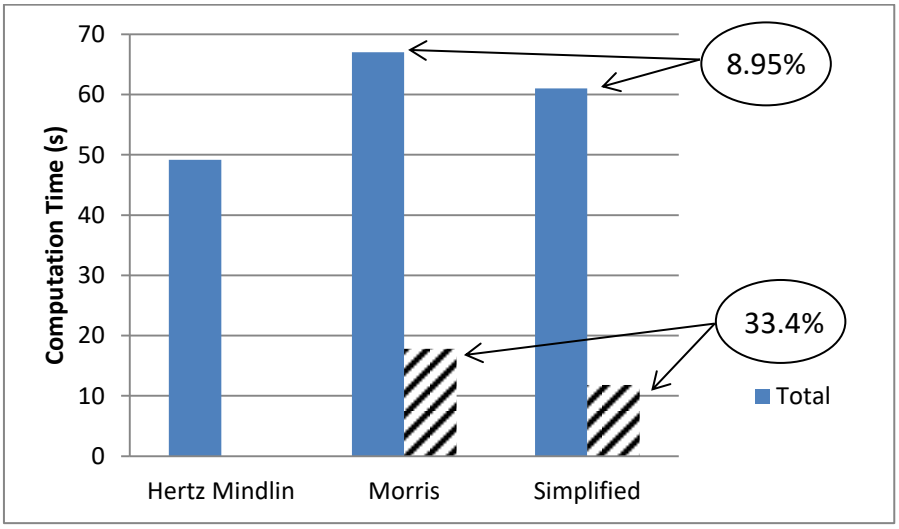

Figure 9 Computation time for standard Hertz Mindlin with no conduction, Morris gas film, and the Simplified conduction model for a binary collision

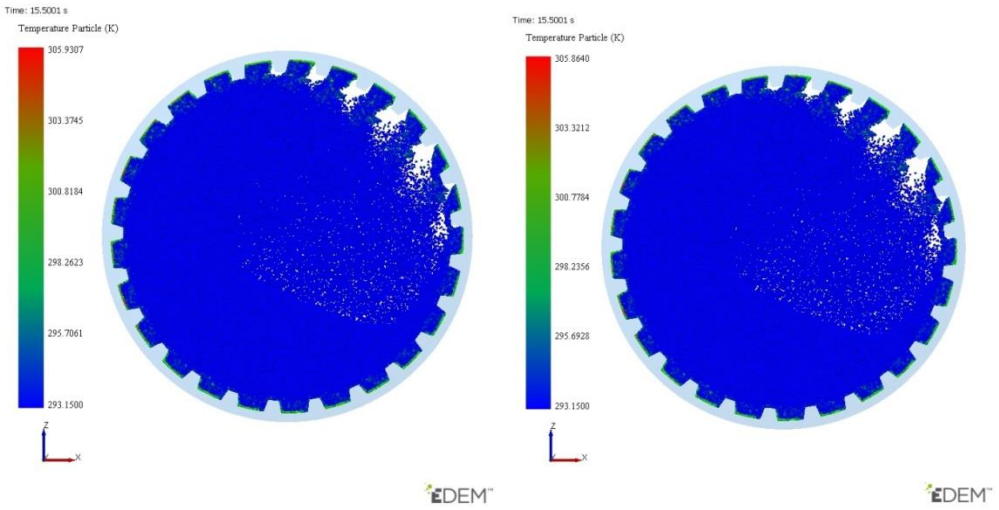

Figure 10. Particle temperature for mill test case with 250,000 particles. The Morris model is on the left, the simplified model on the right.

CONCLUSION

In this study we have investigated the behavior of particle scale gas film conduction for particle-particle and particle-wall contacts. Using a model proposed by Rong as implemented by Morris, DEM simulations were carried out for a binary collision and a single particle-wall collision using a range of particle sizes. The heat transfer coefficient was calculated based on the simulation results and plotted against normalized separation distance. The heat transfer coefficient is found to vary logarithmically with separation distance and simple models were proposed from best fit to the simulation results.

This simplified model was shown to reduce the total computation time of a range of flow regimes in the order of 5 to 15%. It should be noted that since the curve fits are based on results up to the point of contact with no overlap, this model is independent of particle overlap which is advantageous when a reduced material stiffness is used to speed up calculations. Beyond computational efficiency, the simpler expression for the relationship of the gas film coefficient will be useful in the next stage of work investigating scaling laws and the impact of the gas film model on multi-sphered particles.

Acknowledgements

The authors are grateful to Astec, Inc. for funding this research and to DEM Solutions staff, especially Christophe Le Dauphine and Carles Bosch Padros as well as to Aaron Morris whose work serves as the basis for this investigation.

REFERENCES

[1] Cundall, P.A. and Strack, O.D., 1979. A discrete numerical model for granular assemblies. Geotechnique, 29(1), pp.47-65.

[2] Kremmer, M. and Favier, J.F., 2001. A method for representing boundaries in discrete element modelling – part I: Geometry and contact detection, *Int. J. Numerical Methods in Engineering*, 51, 1407-1421.

[3] Kremmer, M. and Favier, J.F., 2001. A method for representing boundaries in discrete element modelling – part II: Kinematics, *Int. J. Numerical Methods in Engineering*, 51, 1423-1436.

[4] Brosh, T. and Levy, A., 2010. Modeling of heat transfer in pneumatic conveyer using a combined DEM-CFD numerical code. Drying Technology, 28(2), pp.155-164.

[5] Chaudhuri, B., Muzzio, F.J. and Tomassone, M.S., 2006. Modeling of heat transfer in granular flow in rotating vessels. Chemical Engineering Science, 61(19), pp.6348-6360.

[6] Li, J. and Mason, D.J., 2002. Application of the discrete element modelling in air drying of particulate solids. Drying Technology, 20(2), pp.255-282.

[7] Hobbs, A., 2009. Simulation of an aggregate dryer using coupled CFD and DEM methods. International Journal of Computational Fluid Dynamics, 23(2), pp.199-207.

[8] Batchelor, G.K. and O'brien, R.W., 1977, July. Thermal or electrical conduction through a granular material. In Proceedings of the Royal Society of London A: Mathematical, Physical and Engineering Sciences (Vol. 355, No. 1682, pp. 313-333). The Royal Society.

[9] Rong, D. and Horio, M., 1999, December. DEM simulation of char combustion in a fluidized bed. In Second International Conference on CFD in the Minerals and Process Industries CSIRO, Melbourne, Australia (pp. 65-70).

[10] D. Rong, DEM Simulation of Hydrodynamics, Heat Transfer and Combustion in Fluidized Beds, Ph.D. thesis, Tokyo University of Agriculture and Technology, Tokyo, Japan, 2000.

[11] Bu, C.S., Liu, D.Y., Chen, X.P., Liang, C., Duan, Y.F. and Duan, L.B., 2013. Modeling and Coupling Particle Scale Heat Transfer with DEM through Heat Transfer Mechanisms. *Numerical Heat Transfer, Part A: Applications*, *64*(1), pp.56-71.

[12] Morris, A.B., Pannala, S., Ma, Z. and Hrenya, C.M., 2015. A conductive heat transfer model for particle flows over immersed surfaces. *International Journal of Heat and Mass Transfer*, *89*, pp.1277-1289

[13] Syamlal, M., Rogers, W., & O'Brien, T. J. 1993. MFIX documentation: Theory guide. *National Energy Technology Laboratory, Department of Energy, Technical Note DOE/METC-95/1013 and NTIS/DE95000031*.

[14] DEM Solutions, Ltd., 2015 EDEM 2.7 Programming Guide, Online.

V International Conference on Particle-based Methods – Fundamentals and Applications
PARTICLES 2017
P. Wriggers, M. Bischoff, E. Oñate, D.R.J. Owen, & T. Zohdi (Eds)

IMPLEMENTATION OF MCA IN THE FRAMEWORK OF LIGGGHTS

NADIA SALMAN[1], MARK WILSON[1], ANNE NEVILLE[1] AND ALEXEY SMOLIN[2]

[1] University of Leeds
Centre of Doctoral Training in Integrated Tribology
Woodhouse Lane, LS2 9JT, Leeds, UK
email: mnnsa@leeds.ac.uk , webpage: https://www.leeds.ac.uk

[2] Institute of Strength Physics and Materials Science
Siberian Branch of Russian Academy of Sciences
pr. Akademicheskiy 2/4, 634021, Tomsk, Russia
email: asmolin@ispms.tsu.ru , webpage: http://www.ispms.ru

Key words: Movable Cellular Automata, LIGGGHTS, Plastic Deformation, Solid Behaviour.

Abstract. We describe the implementation of the Movable Cellular Automata Method (MCA) within the framework of the open-source code LIGGGHTS to simulate complex solid behaviour; most importantly plastic deformation, on different scales. The developed code extends the capabilities of the MCA method, as well as that of LIGGGHTS software; which simulates granular behaviour and is based on the discrete element method. The main difference between MCA and DEM is that the interaction between the particles is based on a many-body forces form of inter-automata interactions, similar to the embedded atom method used in molecular dynamics, because pair-wise interactions between elements used in DEM are insufficient to simulate irreversible strain accumulation (plasticity) in ductile consolidated materials. We first give an overview of the MCA method and its significance, followed by the implementation approach. The code has been successfully verified against analytical data.

1 INTRODUCTION

The Movable Cellular Automata Method (MCA) method was first introduced by Psakhie, Horie et al in 1995 [1] as a simulation tool within the framework of mesomechanics. MCA is a hybrid particle-based method based on the classical cellular automata (CA), discrete element (DEM) and molecular dynamics (MD) methods; combining their advantages. This method allows the modelling of complex materials behaviour and processes. Many developments in MCA have been made since 1995, and the latest description of the method can be found in [2]; where MCA is presented as a discrete approach to model the behaviour of materials on different length scales and is used as a multi-scale modelling approach.

MCA represents the medium as an ensemble of contacting or linked particles to simulate fracture and material deformation, as in the widely known discrete element methods. However, one of the fundamental problems with some particle-based methods, including DEM, is the correct representation of the inter-particle interaction forces, which is the most sensitive and time consuming part of any particle-based simulation [3]. The forces that describe the particle-particle interactions determine the physical and mechanical response of the system. In DEM, these take an approximated pair-wise form to describe materials on the

microscale. This form assumes that the total energy of the system is just the sum of the pair bonds, the same as in the Lennard-Jones potentials [4], which has been proven to often fail to describe the material on the macroscale and damage generation at scales lower than the size of the discrete element; that is why they are often coupled with continuum approaches.

Research showed that this problem can be solved by using a many-body interaction form which provides an accurate description of highly consolidated solids where elastic-plastic deformation occurs [2,3,5]. Hence, the authors of the MCA method applied the many-body interaction concept of the embedded atom method (EAM) [6,7], widely used in MD, to the MCA equations of motion. This allowed them to connect the average stresses and strains for the volume of each particle with the forces of interaction with its neighbouring particles. Meaning each automaton in the system follows the applied constitutive laws, leading to an accurate mechanical response of the whole system, and the capability of correct simulation of irreversible strain accumulation (plasticity) in ductile materials.

Since MCA is a particle-based method, it can be implemented within an MD or DEM code with some modifications as they have the same main functionalities. We chose LIGGGHTS as a framework for this task. LIGGGHTS [8] stands for LAMMPS Improved for General Granular and Granular Heat Transfer Simulations, which is a DEM open-source code, distributed under the GNU general public licence (GPL). LIGGGHTS was extended from LAMMPS [9], a powerful MD software developed at Sandia National Lab, to include the simulation of granular materials on larger scale levels. They are massive parallel computing software and designed for large scale simulations; by using spatial decomposition techniques to break down the simulation space into smaller 3D sub-domains; where each is assigned to a different processor. Message Passing Interface (MPI) exchange is used for communication between the processors allowing large simulation domains to be scaled in memory and speed.

In this paper we briefly describe the MCA methodology, more details can be found in [2,3,5], then present its implementation into the open-source code LIGGGHTS to enable the simulation of solid behaviour and plasticity in a 3D framework. This is done by adding our own commands and classes to the code, mainly a new atom style, pair style, bond style, and some fix styles, to implement MCA functionalities within LIGGGHTS; which is explained in section 3. LIGGGHTS source code, examples and documentation can be found at [10].

2 THEORETICAL BACKGROUND: THE MCA METHOD

MCA assumes that the simulated system is discretised into a series of small elements of finite size, known as the movable cellular automata. These automata are in contact and/or chemically linked (bonded) or unlinked (unbonded), and when an external load is applied they interact with each other, rotating and moving from one position to another. The interactive state between automata could be changed and they can form new automata pairs; describing mechanical deformation processes [5]. The motion of the automata is simulated according to their inter-automata interactions; using the Newton-Euler equations of motion; including the pair relationship, many-body forces and bond forces.

Hence, the simulation of automata motion is governed by the Newton-Euler equations to simulate the translational and rotational motion of pairs of automata:

$$\begin{cases} \boldsymbol{m_i \frac{d^2\vec{R}_i}{dt^2} = \sum_{j=1}^{N_i} \vec{F}_{ij}^{pair} + \vec{F}_i^{\Omega} = \sum_{j=1}^{N_i} \vec{F}_{ij}^{n} + \vec{F}_{ij}^{t} = \vec{F}_i} \\ \boldsymbol{\hat{J}_i \frac{d\vec{\omega}_i}{dt} = \sum_{j=1}^{N_i} \vec{M}_{ij}} \end{cases} \quad \textbf{(1)}$$

where $m_i, \vec{R_i}, \vec{\omega_i}, \hat{J}_i$ are the mass, location vector, rotation velocity and moment of inertia of automaton i respectively. $\vec{F}_i$ is the total force acting on i from its surrounding neighbours (N_i), and $\vec{M}_{ij}$ is the momentum of the system. This form for the inter-automata interaction forces is borrowed from the embedded atom method (EAM) [6,7]. By analogy, the total force $\vec{F}_i$ consists of a pair-wise component ($\vec{F}_{ij}^{pair}$) which depends on the displacement of i relative to j, and the volume-dependent component ($\vec{F}_i^{\Omega}$) which depends on the combined effects of all the neighbours of automata i. $\vec{F}_i$ can be described as the sum of the normal/central ($\vec{F}_{ij}^{n}$) and tangential/shear ($\vec{F}_{ij}^{t}$) components of interaction forces, and are characterized by the corresponding specific normal (σ_{ij}) and shear (τ_{ij}) response forces:

$$\begin{cases} \boldsymbol{\vec{F}_{ij}^{n} = \sigma_{ij} S_{ij}} \\ \boldsymbol{\vec{F}_{ij}^{t} = \vec{\tau}_{ij} S_{ij}} \end{cases} \quad \textbf{(2)}$$

where S_{ij} is the area of contact between automata i and j. Within the framework of multi-body interactions, forces acting on the automata are calculated using deformation parameters such as: elastic constants (shear modulus G_i and bulk modulus K_i), plastic constants (yield stress σ_y and work hardening ε_h), relative overlap (Δh_{ij}) for translational interaction, and tangential/shear displacement (Δl_{ij}^{shear}) for rotational interaction, as shown in Figure 1.

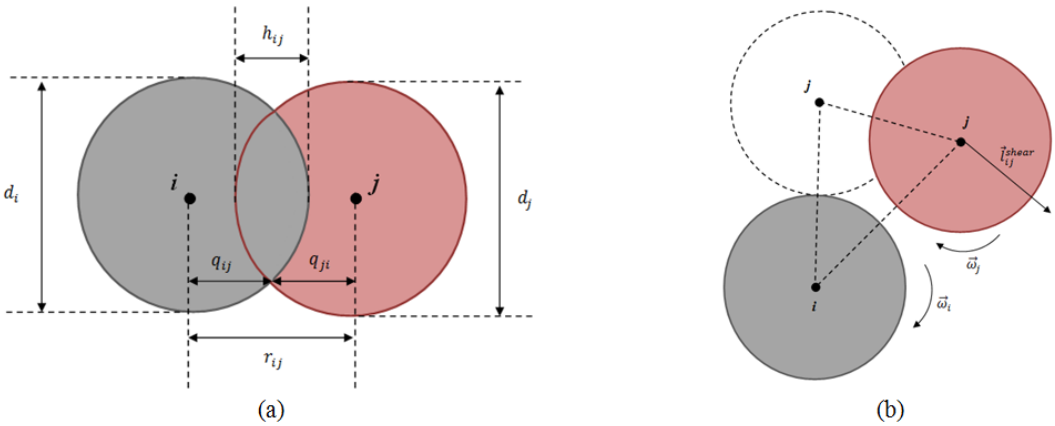

Figure 1: Schematic showing the (a) translational (b) rotational interactions between a pair of automata

$$\begin{cases} \boldsymbol{\Delta h_{ij} = \Delta \xi_{ij} d_i/2 + \Delta \xi_{ji} d_j/2} \\ \boldsymbol{\Delta \vec{l}_{ij}^{shear} = \Delta \vec{V}_{ij}^{shear} \Delta t / r_{ij} = \Delta \gamma_{ij} q_{ij} + \Delta \gamma_{ji} q_{ji}} \end{cases} \quad \textbf{(3)}$$

where normal strain (ξ_{ij}) and shear strain (γ_{ij}) are the parameters of deformation. Hence, the response of an isotropic elastic material can be described by the generalized Hooke's law:

$$\begin{cases} \boldsymbol{\Delta \sigma_{ij} = 2G_i \Delta \xi_{ij} + (1 - 2G_i/K_i) P_i} \\ \boldsymbol{\Delta \vec{\tau}_{ij} = 2G_i (\Delta \vec{\gamma}_{ij})} \end{cases} \quad \textbf{(4)}$$

where P_i is the pressure in volume (Ω_i) of automaton i, also known as the mean stress $\bar{\sigma}^i_{mean}$.

In 3D representation, bending and torsional deformation of the pair of automata also occur due to the difference in automaton rotation:

$$\Delta \boldsymbol{K_{ij}} = -\big(\boldsymbol{G_i} + \boldsymbol{G_j}\big)(\boldsymbol{\omega_j} - \boldsymbol{\omega_i})\Delta \boldsymbol{t} \tag{5}$$

where K_{ij} is the torque of automata pair, which is used to calculate the momentum in Eq. 1.

To calculate these parameters of deformation, in the many-body interaction form it is assumed that the stresses and strains are uniformly distributed in the volume of an automaton *i*. The average stresses and strains in the volume of *i* are determined by the average stress tensor ($\bar{\sigma}^i_{\alpha\beta}$) and average strain tensor ($\bar{\varepsilon}^i_{\alpha\beta}$), which are used to calculate mean stress P_i and the tensor invariants such as the equivalent stress ($\bar{\sigma}^i_{eq}$) and equivalent strain ($\bar{\varepsilon}^i_{eq}$) :

$$\begin{cases} \bar{\boldsymbol{\sigma}}^{\boldsymbol{i}}_{\boldsymbol{\alpha\beta}} = \frac{\mathbf{1}}{\Omega_i}\sum_{\boldsymbol{j=1}}^{\boldsymbol{N_i}} \boldsymbol{S_{ij} q_{ij}} (\vec{\boldsymbol{n}}_{\boldsymbol{ij}})_{\boldsymbol{\alpha}} \big[\boldsymbol{\sigma_{ij}} (\vec{\boldsymbol{n}}_{\boldsymbol{ij}})_{\boldsymbol{\beta}} + \boldsymbol{\tau_{ij}} (\vec{\boldsymbol{t}}_{\boldsymbol{ij}})_{\boldsymbol{\beta}}\big] \\ \boldsymbol{P_i} = -\bar{\boldsymbol{\sigma}}^{\boldsymbol{i}}_{\boldsymbol{mean}} = -\frac{\bar{\sigma}^i_{xx} + \bar{\sigma}^i_{yy} + \bar{\sigma}^i_{zz}}{3} \\ \bar{\boldsymbol{\sigma}}^{\boldsymbol{i}}_{\boldsymbol{eq}} = \frac{\mathbf{1}}{\sqrt{2}}\sqrt{(\bar{\boldsymbol{\sigma}}^{\boldsymbol{i}}_{\boldsymbol{xx}} - \bar{\boldsymbol{\sigma}}^{\boldsymbol{i}}_{\boldsymbol{yy}})^{\mathbf{2}} + (\bar{\boldsymbol{\sigma}}^{\boldsymbol{i}}_{\boldsymbol{yy}} - \bar{\boldsymbol{\sigma}}^{\boldsymbol{i}}_{\boldsymbol{zz}})^{\mathbf{2}} + (\bar{\boldsymbol{\sigma}}^{\boldsymbol{i}}_{\boldsymbol{zz}} - \bar{\boldsymbol{\sigma}}^{\boldsymbol{i}}_{\boldsymbol{xx}})^{\mathbf{2}} + \mathbf{6}\big[(\bar{\boldsymbol{\sigma}}^{\boldsymbol{i}}_{\boldsymbol{xy}})^{\mathbf{2}} + (\bar{\boldsymbol{\sigma}}^{\boldsymbol{i}}_{\boldsymbol{yz}})^{\mathbf{2}} + (\bar{\boldsymbol{\sigma}}^{\boldsymbol{i}}_{\boldsymbol{xz}})^{\mathbf{2}}\big]} \end{cases} \tag{6}$$

where $\alpha, \beta = X, Y, Z$ are the coordinates of the system, q_{ij} is the distance between the mass centre of *i* and its contact point with *j*, $(\vec{n}_{ij})_{\alpha,\beta}$ and $(\vec{t}_{ij})_{\beta}$ are the projections of unit-normal $(\vec{n}_{ij})$ and unit tangential $(\vec{\tau}_{ij})$, vectors on X,Y,Z coordinates. The average strain tensor in the automaton *i* can be computed by increments of elastic stress tensor at each time step [3]

The stress/strain tensor components are then used to realize the different elastic and plastic deformation models developed in continuum mechanics. This means that the forces of inter-automata interactions are directly obtained by the constitutive laws of the modelled medium.

For elastic-plastic behaviour, the von Mises model for plastic flow theory is used by adopting the Wilkins algorithm [11,12]. Here, if the stress intensity ($\bar{\sigma}^i_{eq}$) exceeds the plastic stress ($\bar{\sigma}^i_{pl}$) which is the radius of Von Misses yield circle, then the corrected stress for *i* is:

$$(\bar{\boldsymbol{\sigma}}^{\boldsymbol{i}}_{\boldsymbol{\alpha\beta}})' = (\bar{\boldsymbol{\sigma}}^{\boldsymbol{i}}_{\boldsymbol{\alpha\beta}} - \boldsymbol{P_i})\boldsymbol{M_i} + \boldsymbol{P_i} \tag{7}$$

where $(\bar{\sigma}^i_{\alpha\beta})'$ is the corrected (returned) average stress tensor, $\bar{\sigma}^i_{\alpha\beta}$ is the elastic stress tensor calculated before, and $\boldsymbol{M_i} = \bar{\sigma}^i_{pl}/\bar{\sigma}^i_{eq}$ is the coefficient of stress drop. Thus the corrected normal $(\boldsymbol{\sigma_{ij}})'$ and tangential $(\boldsymbol{\tau_{ij}})'$ forces are:

$$\begin{cases} (\boldsymbol{\sigma_{ij}})' = (\boldsymbol{\sigma_{ij}} - \boldsymbol{P_i})\boldsymbol{M_i} + \boldsymbol{P_i} \\ (\boldsymbol{\tau_{ij}})' = \boldsymbol{\tau_{ij}}\boldsymbol{M_i} \end{cases} \tag{8}$$

For fracture and bonding behaviour, a pair of automata can be considered to be linked or unlinked, and they can switch their state by using a switching criteria defined by the deformation of the material. These switching criteria could be a fracture or bonding criteria, and it is possible to apply any of the well known criteria used in continuum mechanics such as Mohr-Coulomb, Humber-Mises-Hencky, Drucker- Prager and others for this.

3 IMPLEMENTATION OF MCA IN LIGGGHTS: SOFTWARE DEVELOPMENT

Here we describe the implementation of the MCA 3D elastic-plastic model into LIGGGHTS and the relevant code parts that were added to describe MCA functionalities.

3.1 General data structure

LIGGGHTS is written in C++ using an object-oriented structure making it possible to modify and extend. The flowchart in

Figure 2 outlines the general structure of the LIGGGHTS program, which is quite similar to any general particle-based simulation program, showing their relevant functions in the source code in their order of execution.

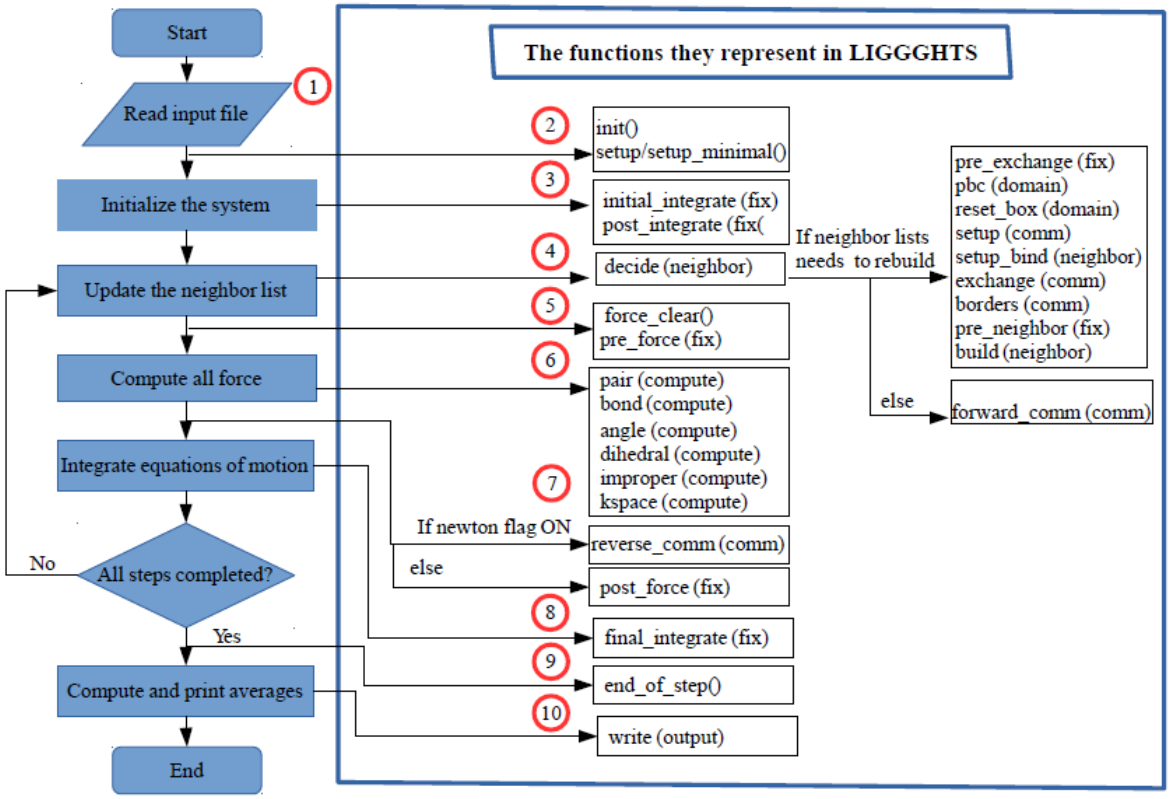

Figure 2: Flow chart of program structure and the relevant functions in LIGGGHTS

The system is first initialised using the input data which is defined in an input script by commands relevant to the acquired simulation. The initial positions and velocities are assigned to the particles. Then the time-stepping starts by integration; we use the Velocity-Verlet integration scheme [13], which is the most commonly used in MD and DEM simulations to calculate position and velocity as a function of time. According to the Velocity-Verlet integration scheme, as shown in Algorithm 1, the first step is to update the velocities by a half time-step and positions by one step. Then compute the interaction forces between the particles and their neighbours. Then update the velocities by another half-step.

Algorithm 1: Velocity-Verlet integration scheme

1- Calculate: $\vec{v}\left(t+\frac{1}{2}\Delta t\right)=\vec{v}(t)+\frac{1}{2}\vec{a}(t)\Delta t$
2- Calculate: $\vec{x}(t+\Delta t)=\vec{x}(t)+\vec{v}\left(t+\frac{1}{2}\Delta t\right)\Delta t$
3- Derive $\vec{a}(t+\Delta t)$ from the interaction forced using $\vec{x}(t+\Delta t)$
4- Calculate: : $\vec{v}(t+\Delta t)=\vec{v}\left(t+\frac{1}{2}\Delta t\right)+\frac{1}{2}\vec{a}(t+\Delta t)\Delta t$

LIGGGHTS works by calling the main functions in the order shown in the flowchart in Figure 2. Steps 1 and 2 in Algorithm 1 occur in the 'initial_integrate' function shown in the flowchart, step 3 by computing the forces (mainly 'pair' and 'bond' computes), and step 4 by 'final_integrate'. The calculation of the inter-particle forces is the most time consuming part of any particle-based simulation. The higher the number of particles, the relative distances and velocities between the neighbouring pairs, the higher the computational time to evaluate the forces between them. The computational time is reduced by using cut-off distance, neighbour lists and linked cell list algorithms to identify the nearby particles and only update and calculate the forces on the particles within the neighbour area within a given time step.

Each command in LIGGGHTS corresponds to a relevant class that defines that specific functionality. The following are the new commands added relevant to MCA implementation and examples of how they are defined in the input script:

```
atom_style    mca radius ${rp} packing fcc n_bondtypes ${bt} bonds_per_atom ${bpa}
pair_style    mca ${skin}
bond_style    mca
fix           integr nve_group nve/mca
fix           bondcr all bond/create/mca 1 1 1 ${cutoff} 1 ${bpa}
fix           topV_fix top mca/setvelocity 0 0 v_vel_up
```

Algorithm 2 shows the functions and the relevant MCA classes that were added to LIGGGHTS in the order of execution as shown in Figure 2, to implement our new commands by adding MCA functionalities to the source-code.

Algorithm 2: Programme structure with relevant new MCA implemented classes

1- init( ) / setup( )	[AtomVecMCA],[FixBondCreateMCA],[FixMCASetvel]
2- initial_integrate( )	[FixNVEMCA]
3- post_integrate( )	[FixBondCreateMCA]
4- pre_exchange( )	[FixBondExchangeMCA]
5- pre_force( )	[FixMeanStressMCA]
6- pair_compute( )	[PairMCA]
7- bond_compute( )	[BondMCA]
8- post_force( )	[FixMCASetvel]
9- final_integrate( )	[FixNVEMCA]

The main features that were added/implemented and their relevant classes according to Algorithm 2 are explained below. For the sake of ease of writing, the terms 'automata' and 'atoms' are used interchangeably having the same meaning.

3.2 Initialization

3.2.1 Initialise atom positions: AtomVecMCA

Before time-stepping begins the atoms are generated, the necessary structures are allocated in their memory locations and each atom is assigned with a position and velocity. In MCA, same as MD, the particles are placed in an appropriate lattice structure (SC, FCC, HCP).

Although the size of an automaton is characterized by a diameter (d_i), the shape of the automaton is not always a sphere. The real shape is determined by the area of its contact with its neighbor (S_{ij}), they have face-face interactions. This equivalent shape is characterized by a new radius parameter which is calculated from the initial volume of the automata.

Thus, some new automata parameters need to be defined in LIGGGHTS, which is done in a new class called 'AtomVecMCA'. These parameters are: mca radius, orientation vector, inertia, contact area, contact distance, volume, mean stress, equivalent stress, equivalent strain and number of bonded automata. Initial contact area and volume of automata are also defined and computed here based on the radius and packing.

3.2.2 Create bonds between atoms: FixBondCreateMCA

Each automaton forms bonds with its neighbours, and the maximum number of bonds of an automaton depends on the coordination number; 6 bonds for SC and 12 bonds for FCC/HCP. Each two neighboring automata form an automata pair, and are considered to be in contact. Initially, if the simulated specimen is a consolidated solid, then the contacts are assumed to be linked (bonded). If there are damages or cracks, then they are assumed to be unlinked (unbonded). This is implemented in the new class 'FixBondCreateMCA'.

3.2.3 Initialise atom velocities: FixMCASetvel

Atoms should also be initialised with a velocity before the time stepping begins. It is also sometimes useful to set boundary conditions or loading via velocity. This can be done in the new class 'FixMCASetvel'.

3.2.4 Initial integration: FixNVEMCA

Here the time stepping (run) begins and, as explained, according to the Velocity Verlet integration scheme, the first step is to update the velocities by a half time-step and positions by one step. In MCA, we also update the rotation velocity $\vec{\omega}$ by half-step.

3.2.5 Post integration: FixBondCreateMCA

After the first half of integration, the bond list and number of bonds need to be updated. This is also done in the class 'FixBondCreateMCA'.

3.3 Neighbour list generation and update

As explained, neighbour lists are produced and /or checked at every time step to exclude computing the interaction forces for any far away automata. This also includes checking the bonds between automata at every time step, erasing any broken bonds from this list and

adding any new bonds created. This is done in a new fix called 'FixExchangeBondMCA' is to exchange data of MCA bonds across processors at every time step.

3.4 Force calculation

3.4.1 Mean stress predictor: FixMeanStressMCA

Before starting the force calculation on each automaton, the predictor for $\bar{\sigma}^i_{mean}$ estimation should be calculated because the specific forces of interaction between the automata at the current time step is calculated using $\bar{\sigma}^i_{mean}$ as shown in Eq. 4. This is done by the 'pre_force' function in the FixMeanStressMCA' class. Usually for elastic behaviour, there is no need for a predictor corrector, while for accurate elasto-plastic behaviour two cycles are usually enough.

3.4.2 Pair and many-body force interactions: PairMCA

Algorithm 3 shows how the forces on the atoms are calculated, which is done in the new class 'PairMCA'. The elastic specific forces are calculated first, then the corrector for plasticity is calculated using the equivalent stress as described before, and the new total forces are obtained. Rotation is also taken into consideration and added to the code.

Algorithm 3: MCA forces computation algorithm - calculation in every time step

1- Calculate σ_{ij}, $\vec{\tau}_{ij}$ and K_{ij} at current time step (n+1), from equations 3,4 and 5.

2- Calculate corresponding values of $\bar{\sigma}^i_{xx}$, $\bar{\sigma}^i_{yy}$, $\bar{\sigma}^i_{xy}$, $\bar{\sigma}^i_{zz}$, $\bar{\sigma}^i_{mean}$ and $\bar{\sigma}^i_{eq}$, from equation 6.

3- Examine the value of $\bar{\sigma}^i_{eq}$, then calculate M_i if required.

4- Calculate σ'_{ij} and τ'_{ij}, from equations 7 and 8.

5- Calculate the forces and torques of automata, from equations 2,4 and 5.

3.4.3 Bond forces: BondMCA

In this class the breaking of bonds is implemented. To do so the contact distances between automata are calculated, then using the equivalent stress criterion it checks if any bonds have broken using the Drucker- Prager criterion or any new bonds have been created.

3.5 Final integration

Before the final integration step, boundary conditions are added if needed which is done in the new 'FixMCASetVel' class. Then according to the velocity Verlet integration, the last step is updating the velocity and rotations for another half step, as shown in Algorithm 1, to obtain the final location and velocities of the automata. This is also implemented in 'FixNVEMCA' and this is then the end of the current time step. If it is not the last time-step of the simulation, the cycle is repeated starting from step 4 in the flowchart of Figure 2.

4 VERIFICATION OF ELASTIC-PLASTIC MODEL

To verify the elastic-plastic MCA developed model in LIGGGHTS, 3D samples under uni-axial compression/tension and shear were modeled. The response function parameters of the material were checked to demonstrate correct macroscopic mechanical response. The simulated samples are 3D Aluminum samples, with equal-sized FCC packed automata as shown in Figure 3. The internal structure is assumed to be homogenous and free of discontinuities (damages or cracks), and all automata are assumed to be initially bonded. The material parameters are: Young's modulus $E = 70\,GPa$, Poisson's ratio $\mu = 0.3$, density $\rho = 2700\,kg/m^3$, yield stress $\sigma_y = 2\,MPa$ and work hardening modulus $\varepsilon_h = 10\,GPa$. The bottom layer of particles are fixed (velocity = 0) and the upper layer moves vertically (tension/compression) or horizontally (shear) with a low constant velocity to simulate quasi-static deformation regime. Both layers are free in the horizontal direction.

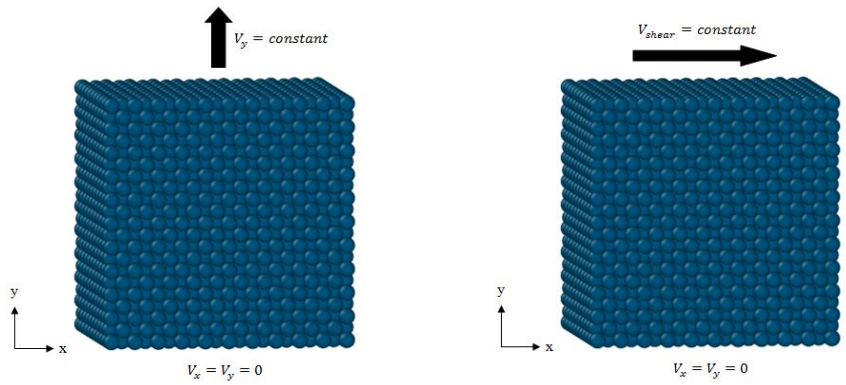

(a) (b)

Figure 3: Initial structure of MCA 3D model sample simulated in LIGGGHTS under (a) tension (b) shear

To study fracture behaviour, uni-axial tension/compression and shear tests were simulated with the setup shown in Figure 3. Their stress/strain curves (blue curves) are plotted against the analytical solution (red line) of Young's modulus for tension/compression and shear modulus for shear behaviour in Figure 4.

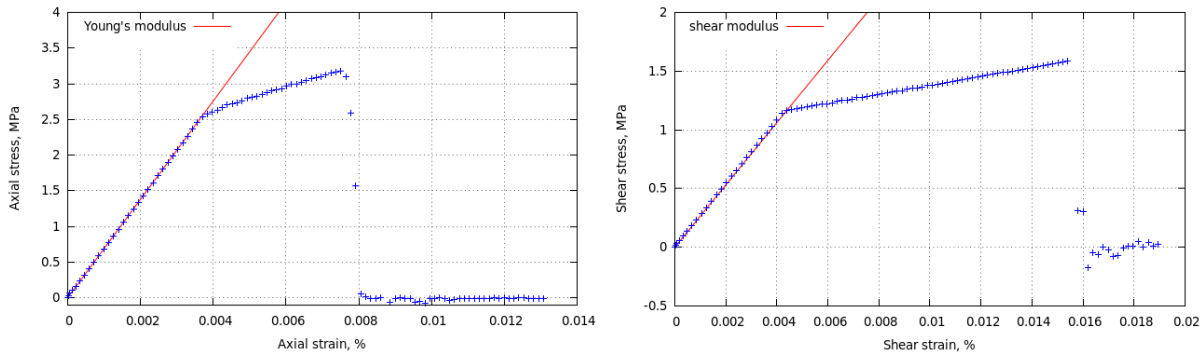

(a) (b)

Figure 4: Stress/strain curves of uni-axial (a) tension and (b) shear compared to analytical solution (red line).

Both tension and compression showed correct macroscopic response and very close agreement with the analytical solution as shown in Figure 4(a). It is important to mention that here we only tested with large automata sizes because MPI exchange has not been implemented yet to allow for parallel processing. More accurate results are obtained by decreasing the automata size relatively to the required behaviour. However, still the results show how the implementation of the many-body interaction forces form resulted in correct macroscopic response; which is not possible when only pair-wise interactions are considered. The same is shown by the shear behaviour in Figure 4(b). The results show the possibility of modelling fracture under tension/compression and shear loading as the material fails after reaching a critical value.

Furthermore, to test correct plasticity behaviour, uni-axial loading/unloading was also simulated for tension and shear as shown in Figure 5. The results show a typical loading-unloading curve, which means the model is capable of modelling correct elasto-plastic behaviour.

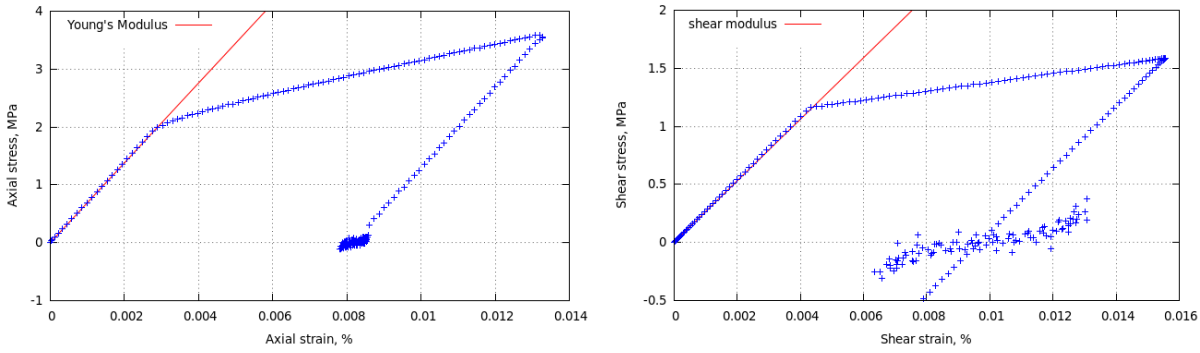

(a) (b)

Figure 5: Stress/strain curves of uni-axial loading/unloading by (a) tension and (b) shear compared to analytical solution (red line).

5 CONCLUSIONS

- A new elastic-plastic model was developed within LIGGGHTS open-source code. The model is based on the MCA particle-based method.
- This implementation allows for the modelling of correct fracture and elasto-plastic behaviour, as shown by the verification tests.
- The current limitation of the code is that it does not allow MPI exchange for parallel processing, however this will still be implemented within the code.
- Further work will also include testing the bond breaking of the particles, as well more complex materials systems, with smaller automata size and different boundary conditions.

REFERENCES

[1] S.G. Psakhie, Y. Horie, S.Y. Korostelev, A.Y. Smolin, A.I. Dmitriev, E. V. Shilko, S. V. Alekseev, Method of movable cellular automata as a tool for simulation within the framework of mesomechanics, Russ. Phys. J. 38 (1995) 1157–1168.

[2] E. V. Shilko, S.G. Psakhie, S. Schmauder, V.L. Popov, S. V. Astafurov, A.Y. Smolin, Overcoming the limitations of distinct element method for multiscale modeling of materials with multimodal internal structure, Comput. Mater. Sci. 102 (2015) 267–285.
[3] S.G. Psakhie, E. V Shilko, A.S. Grigoriev, S. V Astafurov, A. V Dimaki, A mathematical model of particle – particle interaction for discrete element based modeling of deformation and fracture of heterogeneous elastic – plastic materials, Eng. Fract. Mech. 130 (2014) 96–115.
[4] S. Plimpton, Fast Parallel Algorithms for Short–Range Molecular Dynamics, J. Comput. Phys. 117 (1995) 1–19.
[5] S. Psakhie, E. Shilko, A. Smolin, S. Astafurov, V. Ovcharenko, Development of a formalism of movable cellular automaton method for numerical modeling of fracture of heterogeneous elastic-plastic materials, Frat. Ed Integrita Strutt. 24 (2013) 26–59.
[6] M.S. Daw, M.I. Baskes, Embedded-atom method: Derivation and application to impurities, surfaces, and other defects in metals, Phys. Rev. B. 29 (1984) 6443–6453.
[7] M.S. Daw, S.M. Foiles, M.I. Baskes, The Embedded-Atom Method: A Review of Theory and Applications, Elsevier Sci. Publ. N/A (1993) 251–310.
[8] C. Kloss, C. Goniva, LIGGGHTS: a new open source discrete element simulation software, in: Proc. Fifth Int. Conf. Discret. Elem. Methods, London, UK, 2010: pp. 25–26.
[9] S.J. Plimpton, Large-scale Atomic/Molecular Massively Parallel Simulator, LAMMPS, (n.d.). http://lammps.sandia.gov.
[10] Christoph Kloss, LIGGGHTS, (n.d.). https://github.com/CFDEMproject/LIGGGHTS-PUBLIC.
[11] M.L. Wilkins, Calculations of elastic-plastic flow, Academic Press, New York, 1964.
[12] M.L. Wilkins, Computer simulation of dynamic phenomena, 1999.
[13] N. Martys, R.D. Mountain, Velocity Verlet algoritm for dissipative-particle-dynamics-based models for suspensions, Phys. Rev. E. 59 (1999) 3733–3736.

V International Conference on Particle-based Methods – Fundamentals and Applications
PARTICLES 2017
P. Wriggers, M. Bischoff, E. Oñate, D.R.J. Owen, & T. Zohdi (Eds)

MOLECULAR DYNAMICS STUDY OF SLIDING MECHANISMS OF NI, AMORPHOUS NI-P AND NANOCRYSTALLINE NI FILMS

ANDREY I. DMITRIEV[1,2], ANTON YU. NIKONOV[1,2] AND WERNER ÖSTERLE[3]

[1]Institute of Strength Physics and Materials Science (ISPMS), Russian Academy of Science
Akademichesky pr. 2/4, 634021 Tomsk, Russia
e-mail: dmitr@ispms.tsc.ru, http://www.ispms.ru/

[2]National Research Tomsk State University (TSU)
Lenin pr. 36, 634050 Tomsk, Russia
http://www.tsu.ru

[3] Federal Institute for Materials Research and Testing
Unter der Eichen 87, Berlin, D-12200, Germany
http://www.bam.de

Key words: Amorphous film, nanocrystalline nickel, sliding simulation, molecular dynamics, deformation mechanism.

Abstract. In the paper by using molecular dynamics method we investigate the sliding feature of different nano-scale specimens: single-crystal nickel evolving from amorphous pure Ni during shear deformation, Ni-P a layer and nanocrystalline nickel. Special attentions are paid to the value of resistance stresses and plastic deformation mechanisms manifested during sliding simulations. The study is performed at an ambient temperature. The analysis showed that Ni-P amorphous structure is characterized by lowest resistance stresses and smooth sliding provided by the bond-switching mechanism between pairs of atoms due to shear loading. Similar low resistance stress was also observed for an amorphous pure Ni layer, but only at an early stage of sliding before crystallization occurred. The highest shear resistance was confirmed for single-crystal nickel caused by classical deformation mechanisms like stacking fault formation and dislocation movement. Sliding simulations of a nanocrystalline specimen show both, crystal defect driven deformation in the bulk and sliding along quasi-amorphous grain boundaries. Thus, it was shown that nickel-phosphorous coating in amorphous-like state may exhibit low friction properties, and, therefore, serve as the solid lubricant material.

1 INTRODUCTION

Pure metal coatings are highly appreciated in many technical applications due to relatively simple manufacturing technologies that allow adjusting the film properties depending on customers' needs, controlling the processing parameters. Compared to copper and tin coatings nickel is a hard coating which often is used to increase the load carrying capacity of a substrate and thus improve its wear resistance [1]. Frequently, the improvement of hardness and wear resistance could be attributed to a reduction of grain size of electro-plated nickel coatings [2]. Taking into account that the effect of grain size reduction on hardness and wear

resistance is described by the Hall-Petch relationship [3], the effect of the grain size on the coefficient of friction (COF) has not been sufficiently studied. Considering electro-plated nickel coatings, the above mentioned authors have observed a decrease of the COF with decreasing grain size [2]. Fan et al. explained the peculiar mechanical behavior of nanocrystalline materials by assuming a certain grain boundary (GB) layer adopting an amorphous structure [4]. Since interesting results were obtained recently by using MD-modeling for sliding simulations of amorphous silica and carbon films [5], the idea was born to study the sliding behavior of amorphous nickel films supported by nickel crystals on both sides in a similar way. With this model setup we hoped to find an explanation for the experimentally observed decrease in COF with decreasing grain size during the transition from the micrometer to the nanometer range [2].

Similar as nanocrystalline nickel coatings, completely amorphous films can also be used to reduce the friction coefficient of several tribological couples [6]. The amorphous structure is stabilized by adding a second element to the system that can interstitially dissolve in the matrix. Since this happens on the atomic scale at high temperature followed by rapid quenching, the metastable amorphous phase is preserved at ambient temperature. A well-known technical coating system is Ni-P which is produced by electro-less deposition from an electrolyte containing nickel salts and NaH2PO2 as reducing agent. The distinctive characteristics of the Ni-P coating include wear resistance, high hardness, excellent lubricating properties, and others. It is widely applied in aviation machine, chemical industry, electronic manufacturers and etc. [1]. Moreover, it was found recently [2] that the hardness of Ni-P coating depends on P content and crystallization time at the given temperature. According to experimental observations high P (P>6 % vol.) coating has amorphous microstructure and it's characterized by high corrosion resistance and low friction properties.

The present paper focuses on a comparison of the sliding behavior of amorphous and nanocrystalline nickel films determined on the basis of MD modelling results. This study is related to interesting technical materials, namely the electro-less fully amorphous Ni-P coating and the electro-plated nanocrystalline glossy nickel coating. The objective of the work was to find correlations between the microstructure of different types of electro-plated nickel coatings and the friction forces evolving when coated parts were subjected to sliding.

2 EXPERIMENTAL BACKGROUND

The technical application of the considered tribological system is a plug-socket interconnects, where the plug is made of copper-Sn alloy coated with nickel and the socket is a printed circuit coated with copper. Since plug-in and plug-out forces have to fulfill certain requirements the tribological system has to be optimized. The first step into this direction is to determine coefficients of friction of different variants of nickel coatings sliding against copper by applying pin-on-disc tests in the laboratory. This was done in the meantime, and the results are shown in Fig.1.

Increasing friction forces are observed while sliding occurs in positive direction especially for nanocrystalline, but also for micron-sized and submicron-sized Ni after some cycles, but not for the amorphous Ni-P coating. Simultaneously observed friction force fluctuations and acoustic signals provide evidence that local cold welding with subsequent de-bonding has occurred between pin and disc material. The amorphous material on the other hand seems to

be not prone to cold welding with the counter body. Thus it turned out that understanding the different mechanisms of sliding of the amorphous and nanocrystalline material are key factors for optimization of the friction couple towards desired functional properties of the envisaged application, a plug-socket connection.

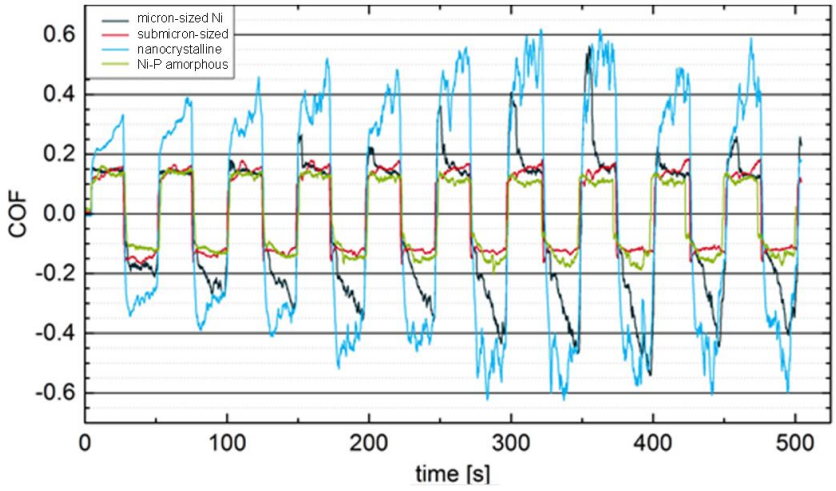

Figure 1: Results of reciprocating pin-on-disc tests; copper pins sliding against various nickel coatings.

3 THE NUMERICAL MODEL

Simultaneously with described above experimental studies a certain progress was made in sliding simulations of amorphous films by applying molecular dynamics modelling (MD) [7–9]. By the following a description of the numerical model is given in short. The MD simulation model of sliding test was consisted of three parts: the central part is a specimen under loading in shape of parallelepiped and two supports (loaded blocks) on top and bottom having an ideal single crystalline Ni structure. Each of the loaded blocks in turn was divided in an inner layer with Newtonian atoms and thin outer boundary layer with atoms through which the loading conditions were implemented. The vertical dimension of each loaded block was identical and was about 8 nm including the boundary layer thickness of approximately 1 nm as shown in Fig. 2a and Fig. 3a. The total dimensions of the specimen with both loaded blocks were 7 x 10 x 30 nm along Z-, X- and Y-axes respectively. Thus, the total number of atoms within the framework of a micro-canonical ensemble NVE was about 200000. Three different structures of the central part were considered: Ni in amorphous state and amorphous Ni-P. The simulation model for sliding test of nanoscale polycrystalline nickel had a slightly different structure and will be described later separately.

The modeled structure, situated between two stiff support layers, was subjected to a sliding simulation with constant velocities +15 and -15 m/s applied to the upper and lower boundary layers, respectively. Furthermore, additional compression forces along the Y direction corresponding to normal pressures of 350 MPa were applied to boundary atoms while the temperature of the whole specimen was kept in the acceptable range from 250 K to 350 K.

A periodic boundary condition is prescribed in the X- and Z-directions of the specimen to reduce the simulation scale effect. The atomic interactions between nickel atoms as well as between Ni and P atoms are described by the embedded atom method (EAM) potential [10].

All MD calculations were implemented using the LAMMPS [11] molecular dynamics code with a time step of 1×10-15 s. The common neighbor analysis (CNA) is adopted to identify the structural allocation of each atom during sliding simulation [12]. According to CNA, a single hexagonal-close-packed (hcp) coordinated-layer means a coherent twin boundary, the two hcp-coordinated-layers with a face-centered-cubic (fcc) coordinated-layer between them denote an extrinsic stacking fault, and the two adjacent hcp-coordinated-layers indicate an intrinsic stacking fault. Atoms with unidentified structure are denoted separately and indicate the amorphous-like structure. In this study, we track the microstructural evolution to reveal the features of shear deformation of specimens with different inner structure.

3 RESULTS FOR SPECIMENS WITH AN AMORPHOUS INTERLAYER

3.1 Sliding Simulation of Ni

A thin layer of amorphous nickel was produced by virtual heating and further quenching to 300 K of the middle part of an initially defect-free single crystal nickel specimen. Before start of loading, the specimen was relaxed to equilibrium configurations with minimum potential energy. Due to atoms rearrangement during melting and subsequent quenching procedures a few structural defects like nanopores and vacancy clusters were created in the amorphous layer as shown in Fig 1a where the initial structure is shown.

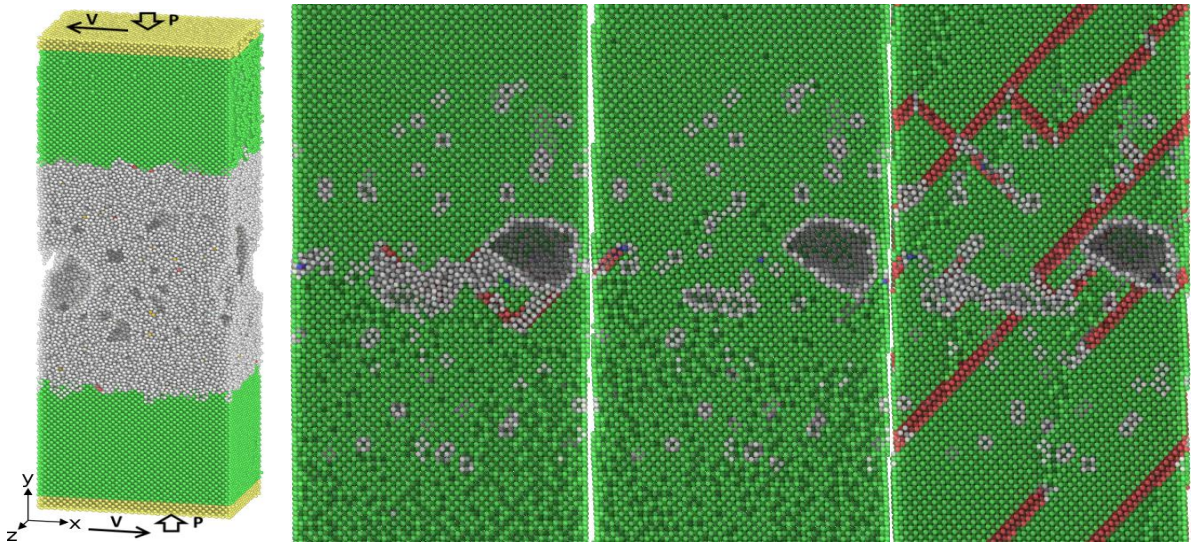

(a) (b) (c) (d)

Figure 2: (a) The loading scheme and the initial structure of the modeled specimen before simulation of sliding. Structure (projection on XY plane) of an amorphous nickel layer at different moments of time: (b) after 30 ps; (c) after 70 ps; and (d) after 100 ps. Atoms are colored on the basis of values calculated by CNA. Green: fcc, red: hcp, gray: unidentified (amorphous). Yellow atoms shown in figure (a) belong to loaded layers.

Figure 2 also presents some snapshots of XY-projections of the microstructural evolution of the modeled specimen during the sliding simulation. For a clearer visualization of the microstructure evolution the central part of the modeled specimen initially containing an amorphous layer is shown only. Surprisingly, but anyway plausibly, the amorphous structure

did not remain stable during the sliding simulation. The onset of crystallization leads to an increase in resistance stress, as shown in Fig. 4a. This process is taking place during the first 30 ps for our specimen (see Fig. 2b). As shown in Fig. 2c, the crystallization of the amorphous layer can lead to formation of residual structural defects. Most atoms and their neighbors correspond to the fcc structure, but there are also some nano-pores, vacancies and nano-sized twins and intrinsic stacking faults corresponding to the hcp structure. The number of structural defects (nano-twins and stacking faults) increases with further loading (Fig. 2d).

3.2 Sliding Simulation of an Amorphous Ni-P Film

To study the features of sliding of an amorphous Ni-P film we extended the modeling system by adding 20 at. % P (11,65 wt. % P) to Ni amorphous interlayer. Similar to previous calculations we simulate a layered sample where two Ni crystals were separated by the central part, where atoms of Ni were initially mixed with atoms of P. An amorphous state of Ni-P layer was reached by virtual heating and further quenching to 300 K of that part of the modeled specimen. The resulting structure is shown in Fig. 3a. The thickness of the amorphous layer was about 14 nm.

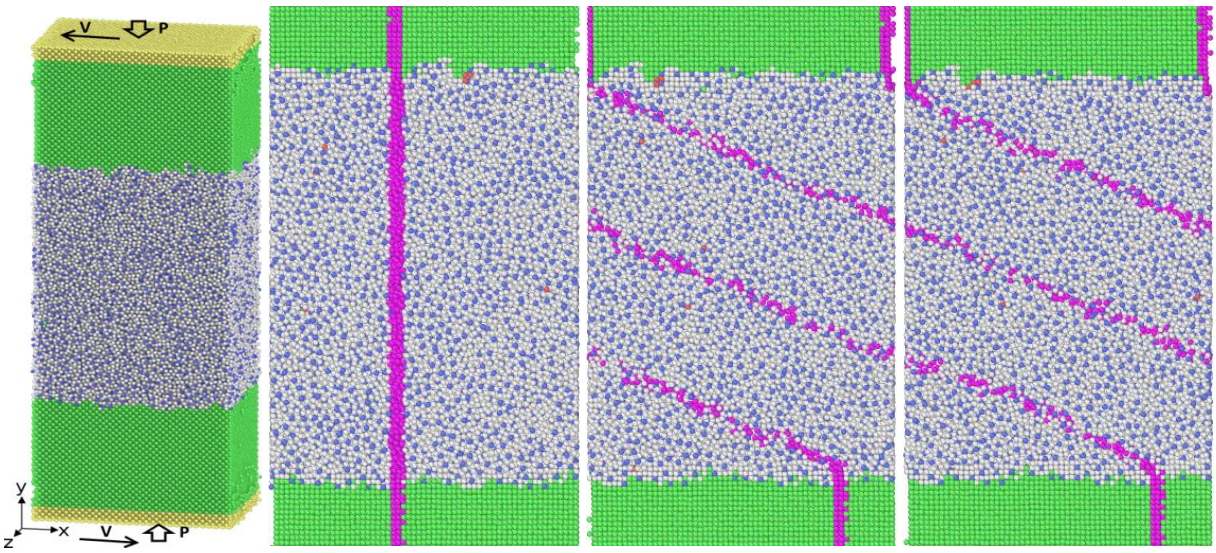

(a) (b) (c) (d)

Figure 3: (a) The loading scheme and the initial structure of the modeled specimen before simulation of sliding. Structure (projection on XY plane) of a central fragment containing an amorphous Ni-20 at. % P layer at different moments of time (b) 0 ps; (c) after 500 ps and (d) after 1 ns. CNA values are used for atoms' colorization. Green: fcc Ni-atoms, blue: P-atoms, gray: undefined (amorphous) Ni atoms. A magenta marking is used to visualize atomic displacements in the specimen after corresponding time of sliding. The formation of several parallel lines is caused by the action of periodic boundary conditions along the direction of shear loading.

According to the results of simulation the structure evolution always show homogeneous shearing within the amorphous Ni-P interlayer, irrespective of the applied normal pressure. This is confirmed by the snapshots with atomic configurations at different time steps shown in the Fig. 3b-d. Thus, the results of MD-modeling predict smooth sliding and a low COF for the amorphous Ni-P layer.

4 SIMULATION RESULTS FOR NANOSCALE POLYCRYSTALLINE NI

4.1 Model Description

A further objective of our study was to estimate tangential stresses occurring during sliding simulations of nickel layers with nanocrystalline structure. The motivation was to explain significant differences of the tribological behavior observed experimentally for electro-plated nickel coatings and electroless deposited Ni-P coatings [13]. The modelled sample consisted of more than 1.5 million atoms with the following geometry: 40,5×40,5×10,5 nm along X, Y and Z axis, respectively. To create the initial nanocrystalline nickel structure the Voronoi partition method was used [14]. In our simulation the crystallographic orientation of each Voronoi cell (grain) was chosen stochastically. The resulting polycrystalline Ni specimen has an average grain size of 8 nm. The structure after the relaxation stage is shown in the Fig. 5a where atoms are colored according to the values calculated by common neighbor analysis (CNA). For a clearer visualization of the defect structures atoms with local topology different from the fcc structure are depicted only. As a consequence of residual stresses due to polycrystallization after relaxation stage mostly all nano-grains contain structural defects like ensembles of vacancies or different planar defects as depicted in figure 4a. Phenomena like recrystallization and grain boundary curvature are also taking place.

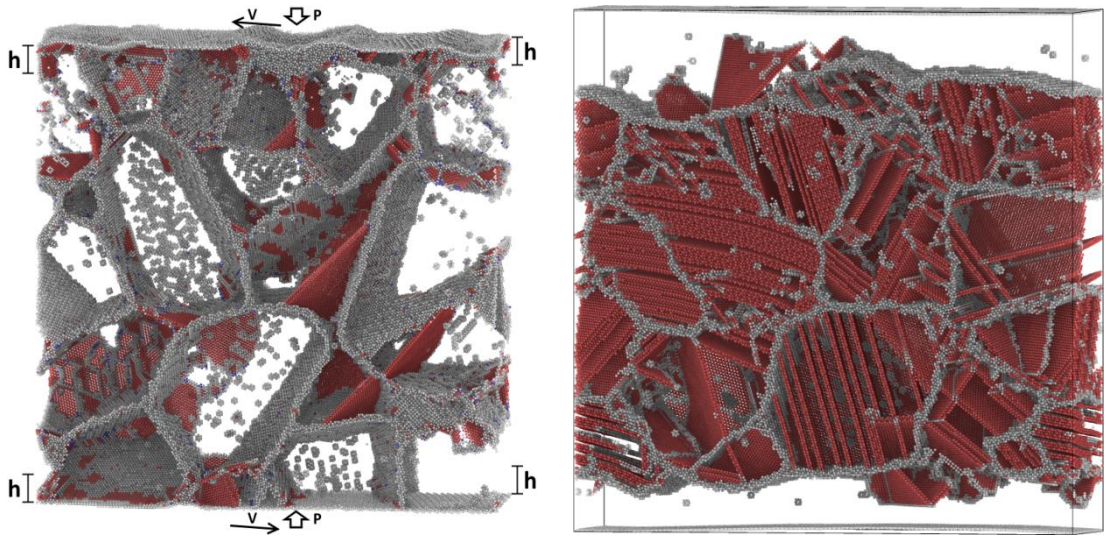

(a) (b)

Figure 4: Structure of the modeled polycrystalline Ni specimen (a) after the relaxation stage and (b) after 750 ps of sliding. Atoms are colored on the basis of values calculated by CAN: Red atoms – hcp lattice; gray – unidentified configurations (border atoms, grain boundaries, vacancies and so on). Fcc atoms are not shown.

The loading scheme was implemented in the following manner. The atoms of the polycrystalline specimen belonging to top or bottom border layers with the thickness h of about 2 nm from each side were substituted by atoms of single-crystal nickel with defect-free structure of the same thickness. All atoms of these two layers were subjected to lateral motion with constant velocity. The velocity was oriented along X direction. Furthermore, top and bottom layers move in opposite directions with 15 m/s each. Thus the total relative velocity

was 30 m/s. The Z projections of atoms velocities in border layers were fixed to zero. Similar to amorphous Ni sliding simulation additional compression loading along Y direction of about 350MPa was applied to atoms belonging to boundary layers. Periodic boundary conditions were simulated along Z and X directions. The initial temperature was 300 K and during loading the temperature was controlled within the acceptable range from 250 K to 350 K.

4.2 Sliding Simulation of a Nanocrystalline Ni Layer

Figure 4b shows the nanocrystalline Ni structure after 750 ps of sliding simulation. Obviously, a lot of structural defects are formed within nano-gains as a consequence of shearing between the upper and lower boundary layers. Note however, that a major part of the stacking faults is just an expansion of "original" defects caused by the action of periodic boundary conditions and a particular crystallographic orientation of that nano-grain. During our sliding simulations two further structural changes are observed. Firstly, grains are rotated in a way that the number of horizontal GBs lying parallel to the sliding direction is increased. Secondly, the interface between monocrystalline loading blocks and the central nanocrystalline structure is changed. With increasing simulation time, corresponding to increasing sliding distance, the load bearing single crystal blocks grow by consuming nearest atoms of the inner polycrystalline structure. Thus stress-driven interface migration in the direction perpendicular to the lateral motion of the single crystalline support layers occurs.

5 COMPARISON OF TANGENTIAL STRESSES

In Fig. 5 tangential resistance stresses are compared for all three specimens considered above (single-cristal nickel evolving from amorphous pure Ni during the sliding simulation, Ni-P amorphous layer and nanocrystalline nickel). The resistance stress was calculated as a ratio of resistance force and contact area of the loaded layer whereas the resistance force was computed as resulting tangential force acting on all loaded atoms in that layer. As expected, the average value of resistance stress in case of the polycrystalline nickel specimen is lower than the corresponding parameter for the single-crystal case and about twice as high as for the Ni-P amorphous structure. In all cases an averaging consisted of calculation of the mean value of 100 neighbouring points.

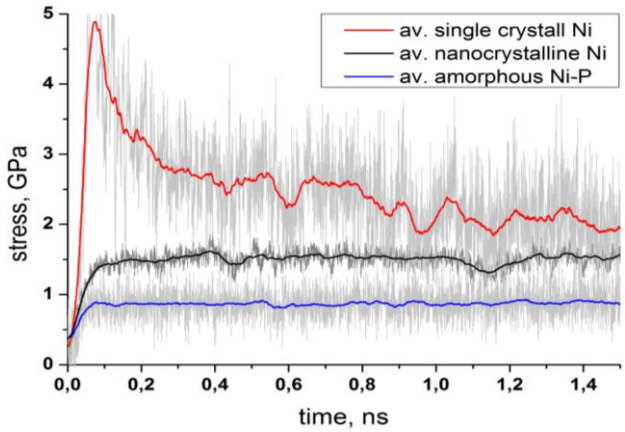

Figure 5: Time dependencies of resistance stress for the three modeled specimens. Light grey peaks denote instantaneous values and coloured curves represent the corresponding mean values.

6 CONCLUSIONS

Sliding simulations based on molecular dynamics modeling provided interesting insights into elementary friction mechanisms of amorphous and nanocrystalline nickel films which are widely used in numerous tribological applications. The experimentally observed low friction performance of an amorphous Ni-P coating [13] was confirmed by MD modeling. This behavior could be attributed to homogenous shearing of the amorphous film without defect formation. Smooth sliding is provided most likely by the bond-switching mechanism, which means that after breaking a bond between a pair of atoms due to shear loading, both atoms move a short distance in opposite directions before they are bound again to other atoms.

It has been shown that grain boundary atoms which could not be assigned to a crystallographic structure and thus can be considered as amorphous layers, play an important role during sliding simulations of nanocrystalline nickel. In that case, most of the shear deformation needed for accommodation of opposing sliding velocities is concentrated in horizontal grain boundaries. Both, grain boundary alignment and interface roughening increase with increasing sliding time. Since these mechanisms exert opposing effects on friction force, higher stresses are needed for initiating sliding of the nanocrystalline sample than for the amorphous structure stabilized with 20 at% P. Nevertheless, good tribological performance (low friction and wear) can also be expected for nanocrystalline nickel coatings because of the evidenced crucial role of GB-sliding. It should be mentioned here that the grain boundaries of the nanocrystalline sample, actually consisted only of an array of single unidentified atoms, and not of a several nanometer thick amorphous layer, as assumed by Fan et al. [4]. Even after plastic deformation, the grain boundary structure did not change. Only in the presence of certain alloying atoms a thickening of amorphous GB-layers was observed.

ACKNOWLEDGEMENTS

Investigations have been carried out with financial support from Program for Basic Scientific Research of the State Academy of Science on 2013–2020. The numerical simulations have been carried out with supported by Tomsk State University competitiveness improvement program.

REFERENCES

[1] Wänstrand, O., Larsson, M., Kassman-Rudolphi, A. Mechanical and tribological properties of vapour deposited low friction coatings on Ni plated substrates. *Tribol. Int.* (2000) **33**:737-742.

[2] Jeong, D.H., Gonzalez, F., Palumbo, G., Aust, K.T., Erb, U. The effect of grain size on the wear properties of electrodeposited nanocrystalline nickel coatings. *Scripta mater.* (2001) **44**:493-499.

[3] Hall, E.O. Variation of hardness of metals with grain size. *Nature* (1954) **173**:948-949.

[4] Fan G.J., Cho H., Liaw P.K., Lavernia E.J. A model for the inverse Hall–Petch relation of nanocrystalline materials. *Mater. Sci. Eng. A* (2005) **409**:243-248.

[5] Dmitriev, A.I., Nikonov, A.Yu., Österle, W. MD sliding simulations of amorphous tribofilms consisting of either SiO2 or carbon. *Lubricants* (2016) **4**(24):1-12, doi:10.3390/lubricants4030024.

[6] Ebrahimian-Hosseinabadi, M., Azari-Dorcheh, K., Moonir Vaghefi, S.M. Wear behavior

of electroless Ni–P–B4C composite coatings, *Wear* (2006) **260**:123-127.
[7] Nikonov, A.Yu., Konovalenko, Iv.S., Dmitriev, A.I. Molecular dynamics study of lattice rearrangement under mechanically activated diffusion. *Phys. Mesomech.* (2016) **19**(1):77–85.
[8] Dmitriev, A.I. Nikonov, A.Yu., Psakhie, S.G. Atomistic mechanism of grain boundary sliding with the example of a large-angle boundary Σ=5. Molecular dynamics calculation. Phys. Mesomech. 2011 **14**(1-2):24-31.
[9] Dmitriev, A.I., Nikonov, A.Yu., Österle W. Molecular dynamics sliding simulations of amorphous Ni, Ni-P and nanocrystalline Ni films. *Comput. Mater. Sci.*, (2017) **129**:231-238
[10] Sheng, H.W., Ma, E. and Kramer, M.J. Relating dynamic properties to atomic structure in metallic glasses, *JOM* (2012) **64**:856-881.
[11] Plimpton, S. Fast Parallel Algorithms for Short-Range Molecular Dynamics, *J. Comput. Phys.* (1995) **117**(1):1-19.
[12] Honeycutt, J. and Andersen H. Molecular dynamics study of melting and freezing of small Lennard-Jones clusters. *J. Phys. Chem.* (1987) **91**:4950–4963.
[13] Österle W., Dörfel I., Wollschläger N., et al., Potential of different nickel coatings for optimizing the sliding behavior of electrical connectors, *Tribol. Int.* (2017) submitted.
[14] Van Swygenhoven, H., Derlet, P.M. and Hasnaoui, A. Atomistic Modeling of Strength of Nanocrystalline Metals. *Adv. Eng. Mater.* (2003) **5**:345–350.

V International Conference on Particle-based Methods – Fundamentals and Applications
PARTICLES 2017
P. Wriggers, M. Bischoff, E. Oñate, D.R.J. Owen, & T. Zohdi (Eds)

MOLECULAR DYNAMICS STUDY OF THE ACOUSTIC EMISSION DURING NANOINDENTATION OF IRON CRYSTAL

ANTON YU. NIKONOV[1,2], ANDREY I. DMITRIEV[1,2], ANDREY V. FILLIPOV[1,3], VALERIY E. RUBTSOV[1,3], SERGEY YU. TARASOV[1,3]

[1] Institute of Strength Physics and Materials Science (ISPMS)
2/4, pr. Akademicheskii, Tomsk, 634021, Russia
e-mail: sp@ms.tsc.ru, web page: http://www.ispms.ru/en/

[2] Tomsk State University (TSU)
36, Lenina Avenue, Tomsk, 634050, Russia
e-mail: rector@tsu.ru, web page: http://tsu.ru/english/

[3] Tomsk Polytechnic University (TPU)
30, Lenin Avenue, Tomsk, 634050, Russia
e-mail: tpu@tpu.ru, web page: http://tpu.ru/en/

Key words: acoustic emission, structure defects, molecular dynamics, indentation.

Abstract. In the paper simulation of the indentation of iron crystal was carried out using the method of molecular dynamics. We investigated the effect of vibrations on the AE under the impact of a single element (indenter) with a certain amount of material. Fluctuations of the forces acting on the sensor, changing of the system energy and the formation of defects during loading were analyzed. The force signal showed the increase in its amplitude and power spectrum as well as the median frequency drop under loading by vibrating indenter. The rationale behind all these changes may be dependence between the vibration amplitude and full system energy.

1 INTRODUCTION

Analysis of acoustic emission (AE) is one of the most common methods for monitoring of mechanical systems. A distinctive feature of this approach is the ability to identify different structure changes by the generated acoustic signals without the active intervention and change the properties of the material, since AE relates to traditional methods of non-destructive testing. At present, the use of the AE method is gaining popularity as a monitoring of the state of mechanical systems (gearboxes and bearing friction units) and detection of vibrations. Also, this approach is used in the manufacture of machine parts, for example, in metal cutting machinery, where AE is used to monitor the state of the cutting tool or the type of chip formation. The appearance of vibrations during processing of this kind is highly undesirable, because they lead to a decrease in the quality of the obtained parts. Analysis of AE makes it possible to detect vibrations, but it is necessary to separate signals that arise both a result of the tribological contact of the workpiece with the tool and during intensive plastic deformation of the material. In view of the complex internal structure of polycrystalline materials and the multitude of processes occurring during plastic deformation in the volume

of the billet, it is difficult to interpret the sources of acoustic emission. The relevance of this problem is confirmed by a large number of experimental and theoretical works, the main results of which are published in high-ranking periodicals, for example, Physical review letters, Physical review, Tribology International, Engineering Fracture Mechanics, Materials Science and Engineering and other. So, Pawełek in [1] showed the Frank-Read source can be a source of AE. Chung and Kannatey-Asibu [2] notes, that initial and harmonic dislocation movement during plastic deformation of crystal (grains) can also be a source of emission AE. The harmonic motion of dislocations promote to reduce the frequency of AE as the degree of deformation increases. In [3], the authors associated low-amplitude continuous AE signals with the low-magnitude stress-strain curve serrations caused by the propagation of the Porteven-Le Chatelier bands. The high-magnitude burst-like AE signals were correlated to the high-magnitude stress-strain serrations generated by nucleating Portevin–Le Chatelier bands. Salje et. al. in [4] using molecular dynamics have shown, that on the atomic scale AE is determined by both potential and kinetic energy levels changes. The aim of present work is to study the influence of generated structure defects and change of internal energy of sample on AE signals during nanoindentation.

2 NUMERICAL MODEL

The study was conducted in the framework of molecular dynamics method using the software package LAMMPS [5]. The interaction between atoms is described within the embedded atom method [6]. The physical correctness of the used software package and interatomic potential was verified based on a comparison of the calculated values of the energy of vacancy formation and packing defect with similar experimental data. In both cases, the deviation amounted to less than 1%. The iron model sample was 18×18×9 nm rectangular parallelepiped. The total number of atoms exceeded 200000. A schematic representation of the sample is shown in Fig. 1. Along the Z axis of the laboratory coordinate system, periodic boundary conditions were specified. The four lower atomic layers were fixed, forming a substrate. The simulations were carried out for 0K and 300K temperatures. The zero temperature was used to evaluate the effect of heat motion on the system dynamics. A "combined" indenter was used to load the system. Such an indenter was an absolutely rigid cylinder of atoms with a radius of 2 nm and a field cylindrical indenter with a radius of 2.2 nm. The indenter axes coincided and were oriented along the Z axis. The material indenter prescribes adhesion properties due to the mutual attraction of atoms. The atoms of the sample entering the interior of the field indenter region were acted upon by forces from the axis of the cylinder. The magnitude of the force is described by $F(r) = -K(r - R)^2$, where K – constant, r – distance from cylinder axis to atom and R – cylinder radius, at r > R F(r) = 0. Thus, the field indenter reduced the adhesion forces between the atoms of the sample and the indenter. The indentation simulation was carried out in two stages when the first one was indenting the iron sample at the constant rate 0.1Å/ps. The second stage was that when the indenter penetrated 1 nm into the iron sample it began oscillating with an amplitude increment A(t)=0.05 Å/ps and frequency $\omega=1/3ps^{-1}$. The position of the cylinder axis as a function of time is shown in Fig. 2.

The acoustic response to indenting was evaluated as forces acting on the atomic area sensor located on the sample's right face (as shown by gray fragment in Fig.1).

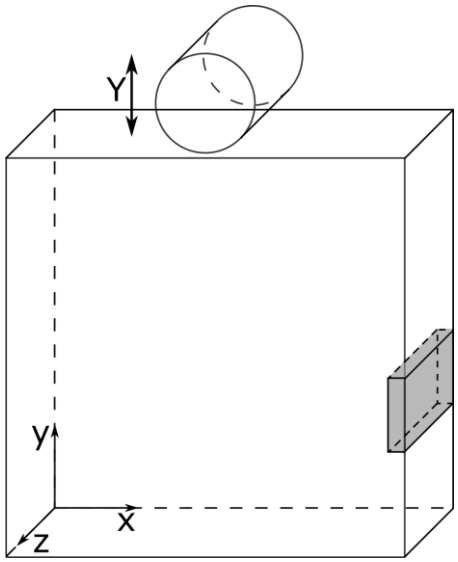

Figure 1: Schematic representation of the simulated sample.

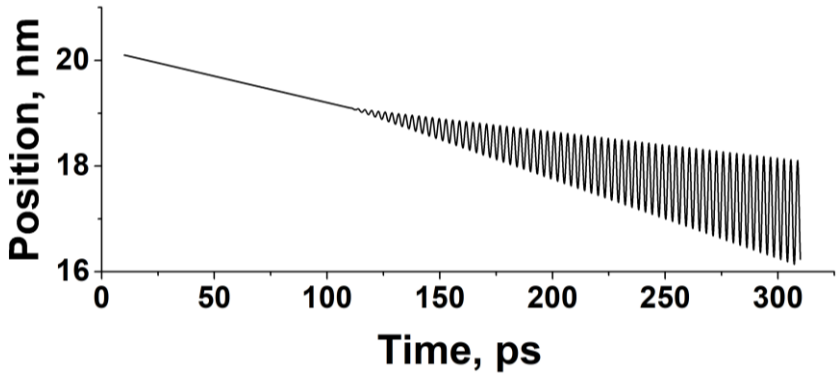

Figure 2: Time dependence of indenter's center position in case of vibrational loading.

3 SIMULATION RESULTS

3.1 Acoustic response to static indenter

Constant loading rate indentation produces atomic displacements and defects that generate elastic waves received by the sensor in the form of a force directed along the X-axis. This force is oscillating around its constant value with time (Fig.3a) thus simulating the acoustic emission response to indentation. Median frequency of such a signal reveals the above observed type of behavior, i.e. irregular oscillations around mean value F_{med}~7 THz (Fig.3b). Power spectrum shows signal frequencies in the range 0 to 8 THz. The maximum power spectrum value is found in the low frequency range (Fig.3c). It is reasonable to suggest that the non-zero temperature is the reason for oscillations in Fig.3a.

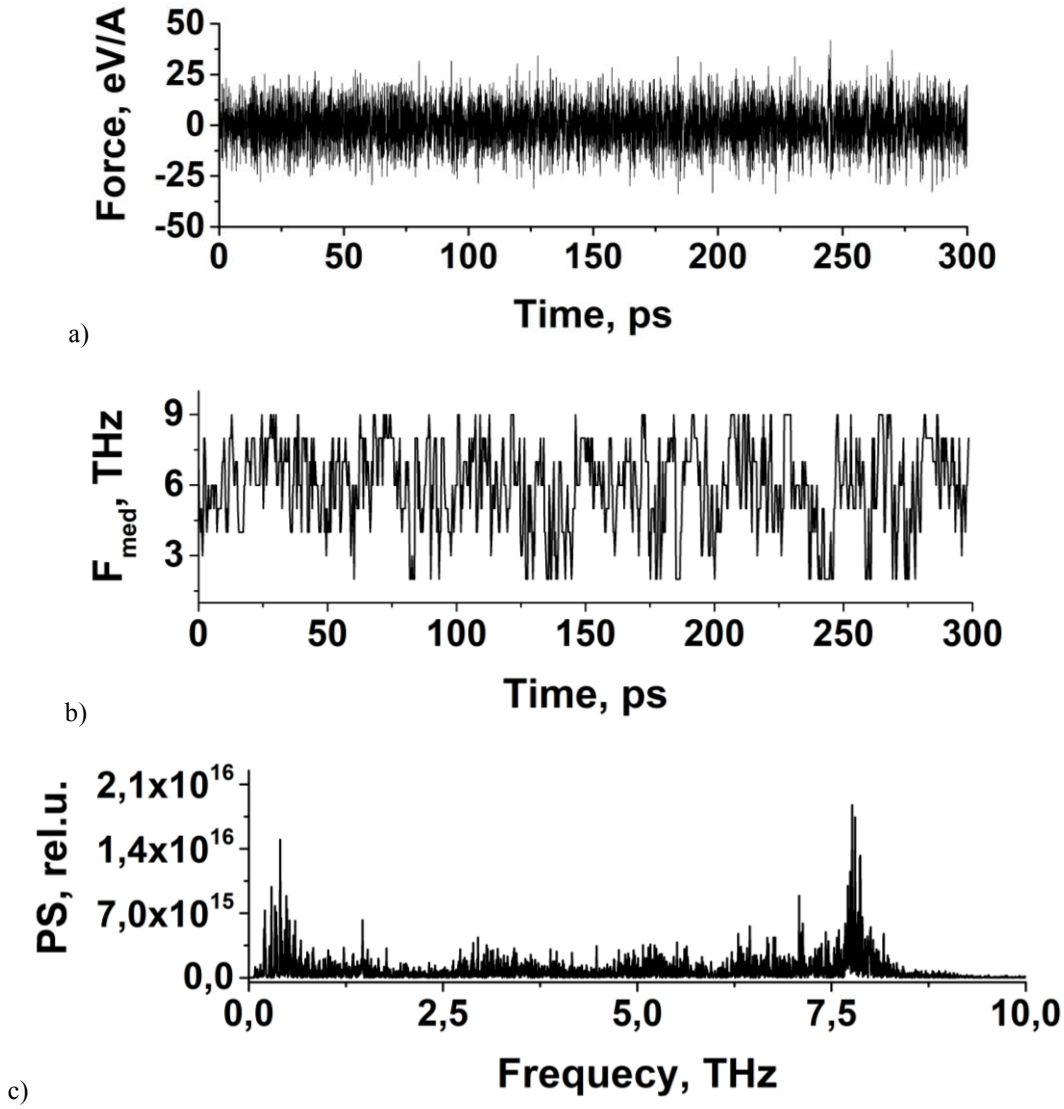

Figure 3: Force signal (a), median frequency (b) and power spectrum (c) in static loading

3.2 Acoustic response to vibrating indenter

The effect of vibrations on the acoustic response is shown in Fig.4 where at least three types of the acoustic response could be found. The first one (Fig.4a) corresponds to a static vibration-free loading stage and it is identical to the force oscillations in Fig.3a obtained under similar type of loading. Also both median frequency and power spectrum (Fig.4b, c) show the same type of behavior as shown in Fig.3b, c.

The second type of behavior is a transition from a vibration-free loading to loading when the vibration amplitude has just started growing. The median frequency immediately started falling from 7 to 1.7 THz (Fig. 4b). The maximum power spectrum value grew to 0.7×10^{16} (Fig.4c).

The third type of behavior is characterized by the high amplitude force oscillations. In

addition, the force amplitude shows some long period oscillations but generally continues growing. The median frequency is still in the low frequency range (Fig.4b) with only ten up to 3.1 THz peaks. The power spectrum shows only some peaks with the maximums in low frequency range.

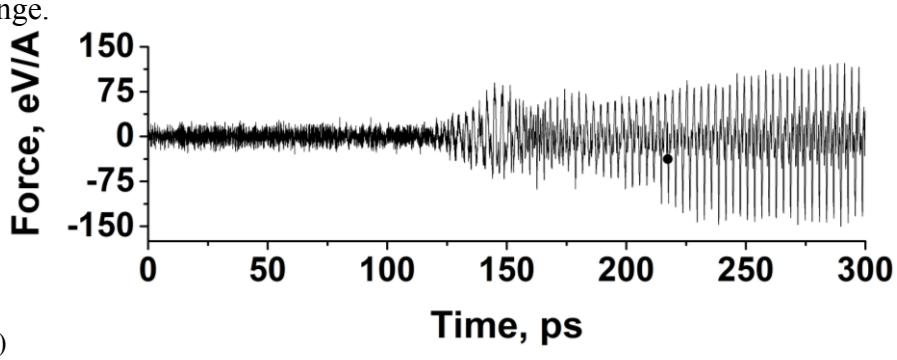

a)

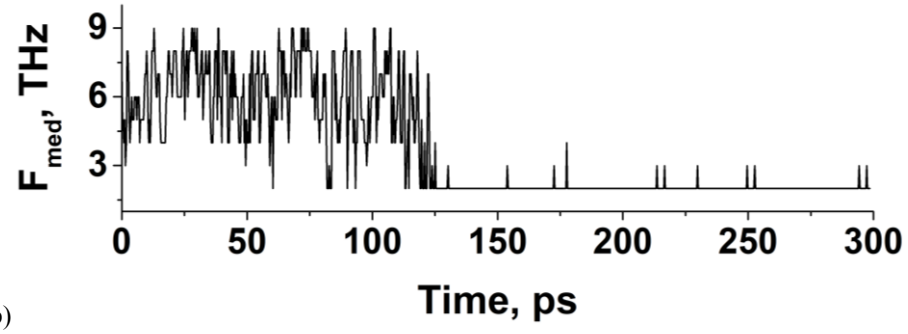

b)

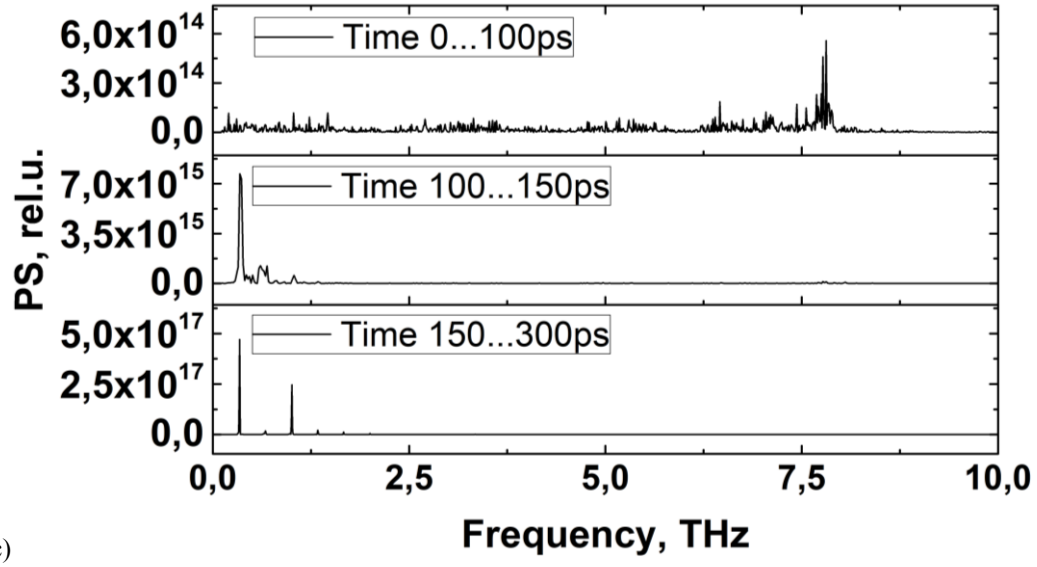

c)

Figure 4: Force signal (a), median frequency (b) and power spectrum (c) in vibration loading

According to the results force received by the sensor grows with the vibration amplitude. The spectral characteristics show dependence between the median frequency and vibrations on the one side and between power spectrum and vibrations on the other. The rationale behind

such a relationship may be a redistribution of energy inside the system modeled.

By computing the full energy of the modeled system for both cases we can see that indentation without vibrations gives the full energy value oscillating around some mean level whereas the imposed vibrations cause its growth on the background of high amplitude oscillations (Fig. 5). This growth is achieved mainly due to increasing the potential energy, i.e. due to increased amplitudes of atom displacements. The kinetic energy changes may be evaluated from the temperature changes caused by vibrations (Fig.6). One can see that mean temperature is only slightly varied with time thus confirming our suggestion that potential energy is a main contributor to the full energy. If so then it becomes understandable why median frequency reduced due to vibrations. Interatomic distances increase together with a number of defects formed whose relaxation is retarded by enhanced elastic stress fields. The number of crystalline lattice defects produced during indentation without and with vibrations increases with time in both cases (Fig.7).

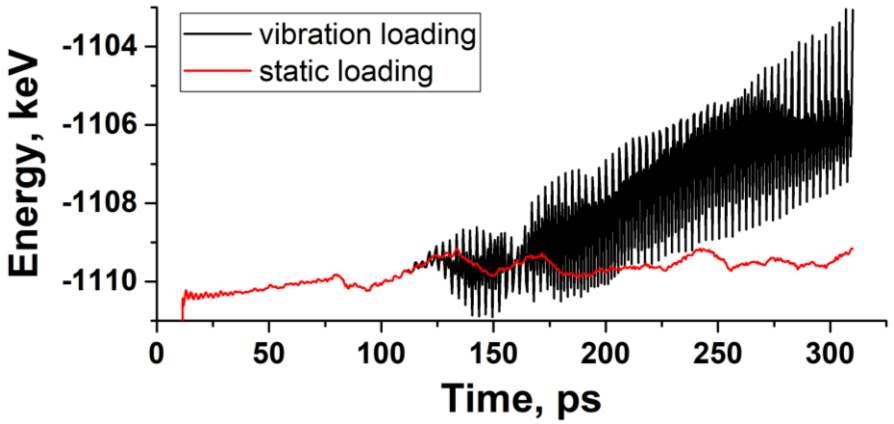

Figure 5: Full energy of the model system

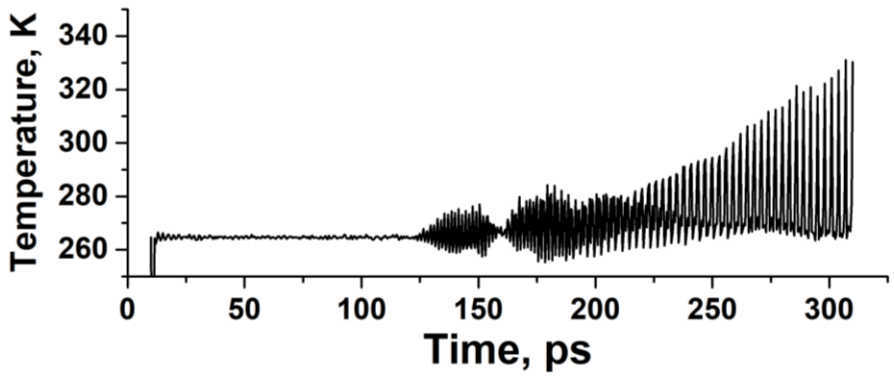

Figure 6: Time dependence of temperature of the model system in case of vibrational loading

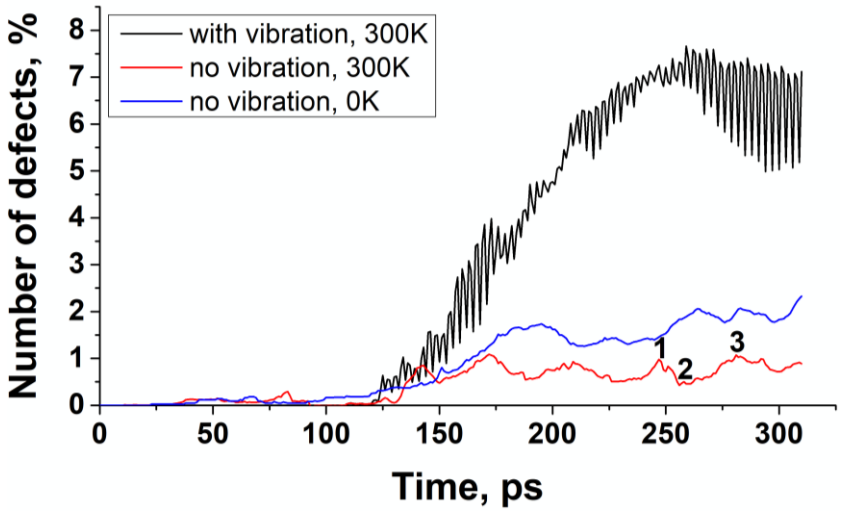

Figure 7: The number of atomic structure defects generated during vibration and static indentation

This suggestion has been confirmed by the results of crystalline structure analysis carried out using the Common Neighbor Analysis (CNA) developed by Honeycutt and Andemen [7]. This method allows determining the local topology of interatomic structure corresponding to bcc, fcc and hcp crystal lattices [8-9]. In the present work, such a procedure was applied to count atoms belonging to crystalline structures other than the initial bcc during indentation, i.e. to determine the number of atoms forming the defect configurations.

The dependencies in Fig.7 show how the number of atoms changes with time for vibrating indenter at 300K and static indenter at 0K and 300K. The number of atoms belonging to defect configurations shows a growth with time at 0K together with some periodicity. This tendency may have been explained by the fact that the defect atomic configurations are produced and accumulated because of low atom mobility at 0K. On the contrary, the number of defect configurations at 300K shows only periodic minimums and maximums without a tendency to accumulate. One can see in Fig.7 that the defect nucleation stages 1 and 3 correspond to high defect number peaks while stage 2 corresponds to local minimum when previously formed defects have already relaxed by emerging on the sample's surface. The situation is quite different during vibrational loading when the defects number grows sharply starting from the moment of time when vibrations have been imposed.

Comparing the full energy dependence in Fig.5 to the number of defects in Fig.7 one can state that potential energy of the system is determined by the number of unrelaxed defect configurations.

4 CONCLUSIONS

The AE signal was simulated in framework of molecular dynamics method by the force obtained on the lateral face of the sample and resulted from deforming the sample by an indenter. The results show that the full system energy grows with the vibration amplitude mainly by means of the potential energy component, which means that atoms become more widely separated from each other and form more of defect configurations, i.e we have higher

volume of material involved in deformation. The resulting AE signal will be composed of different components possessing different frequencies and amplitudes. High AE signal amplitude gives low frequency components so that power spectrum migrates to the low frequency end and median frequency shows a drop. The rationale behind all these changes may be dependence between the vibration amplitude and the system full energy. Obtained results are in good agreement with experimental data on the acoustic emission response to vibration loading in the course of peakless tool turning [10].

ACKNOWLEDGMENTS

Work was supported by The Tomsk State University competitiveness improvement program.

REFERENCES

[1] Pawełek, A. Possibility of a soliton description of acoustic emission during plastic deformation of crystals. *J. Appl. Phys.* (1988) **63**:5320-5325.

[2] Chung, J.B., Kannatey-Asibu, E. Acoustic emission from plastic deformation of a pure single crystal. *J. Appl. Phys.* (1992) **72**:1812-1820.

[3] Chmelík, F., Klose, F.B., Dierke, H., Šachl, J., Neuhäuser, H., Lukáč, P. Investigating the Portevin-Le Chatelier effect in strain rate and stress rate controlled tests by the acoustic emission and laser extensometry techniques. *Mater. Sci. Eng. A.* (2007) 462:53-60.

[4] Salje, E.K.H., Wang, X., Ding, X., Sun, J. Simulating acoustic emission: The noise of collapsing domains. *Phys. Rev. B.* (2014) 90:64103.

[5] Plimpton, S.J. Fast parallel algorithms for short-range molecular dynamics. *J. Comp. Phys.* (1995) 117(1):1-19.

[6] Mendelev, M.I., Han, S., Srolovitz, D.J., Ackland, G.J., Sun, D.Y., Asta, M. Development of new interatomic potentials appropriate for crystalline and liquid iron. *Philos. Mag.* (2003) **83**:3977-3994.

[7] Honeycutt, J.D., Andemen, H.C. Molecular dynamics study of melting and freezing of small Lennard-Jones clusters. *J. Phys. Chem.* (1987) **91**:4950-4963.

[8] Nikonov, A.Y., Konovalenko, I.S., Dmitriev, A.I. Molecular dynamics study of lattice rearrangement under mechanically activated diffusion. *Phys. Mesomech.* (2016) **19**: 77-85.

[9] Dmitriev, A.I., Nikonov, A.Y., Österle, W. Molecular dynamics sliding simulations of amorphous Ni, Ni-P and nanocrystalline Ni films. *Comput. Mater. Sci.* (2017) **129**:231-238.

[10] Filippov, A.V., Nikonov, A.Y., Rubtsov, V.E., Dmitriev, A.I., Tarasov, S.Y. Vibration and acoustic emission monitoring the stability of peakless tool turning: Experiment and modeling. *J. Mater. Process. Technol.* (2017) **246**:224-234.

V International Conference on Particle-based Methods – Fundamentals and Applications
PARTICLES 2017
P. Wriggers, M. Bischoff, E. Oñate, D.R.J. Owen, & T. Zohdi (Eds)

TREATMENT VOLUME OF AEDES ALBOPICTUS WITH X RAYS GENERATED FROM ELECTRONS

M. VADRUCCI[1]*, F. BORGOGNONI[1], M. CALVITTI[2], R. MORETTI[2], L. PICARDI[1]

[1] ENEA - Development of Particle Accelerators and Medical Applications Laboratory, Via E. Fermi, 45, 00044 Frascati (RM), Italy
monia.vadrucci@enea.it

[2] ENEA, Biotechnologies and Agroindustry Division, Via Anguillarese 30, 00123, S.M. di Galeria (RM), Italy

Key words: electron accelerator, X Rays irradiation, Aedes albopictus, Sterile Insect Technique, sterilization technologies.

Abstract. Irradiation is a common method used for sterilizing objects in several fields. In the entomology sector, insects are sterilized through irradiation and released in to the wild to sexually compete with the population at large reducing the chance for reproduction. This practice is the Sterile Insect Technique (SIT). Traditionally irradiation sources for SIT purpose are radioisotopes but many reasons compelled to getting efforts to develop other radiative technologies. Since gamma rays and electrons have similar sterilizing effects, the choice of source for SIT irradiation is based on considerations about penetration and environmental factors.

Gamma irradiators are usually simpler to operate, and less expensive, than electron accelerators, at least within the range of power required for SIT applications. Currently, the increased difficulties to manage and ship radioisotopes is being successfully resolved by the introduction of novel X-ray irradiators that enable a safer use of irradiator machines and procedures for SIT applications.

In the ENEA Frascati research center we developed irradiators for clinical radiotherapy consisting in a radiation converter from electrons to X-rays. Since X-rays penetrate deeper than the electrons from which they are generated, we used this technology in a configuration that delivers a uniform dose on large targets to irradiate insects for SIT aim.

In this topic, we gained practical experience working with Aedes albopictus, a mosquito vector of various tropical diseases such as dengue and zika. Several dosimetric studies have been conducted to achieve male sterility without affecting male mating competitiveness in comparison with untreated males. Lower doses have been also tested on an Ae. albopictus strain modified with the bacterium Wolbachia, which also determines male sterility, to sterilize the females eventually escaping the sexing procedures preliminary to the releases of the males.

1 INTRODUCTION

The Particle Accelerators and Medical Applications Laboratory (APAM) at ENEA Frascati research center, develops particle accelerators for medical, industrial and research applications [1-3]. Some electron accelerators were developed as stand alone accelerators or as parts of a larger facility.

A 4.8 MeV 180 mA S-band electron on-axis coupled linear accelerator (linac) was completely designed and built inside the accelerator laboratory. This design was used as a basis for the IORT accelerator development with industry [4].

This medium energy linac offers some suitable services to scientific community in the several applications fields in which e-beam and X rays are useful and often it has been used as a test facility for material processing. Examples of test of radiations already carried out are in the following table 1.

Table 1: Examples of irradiations with the 4.8 MeV linac at ENEA Frascati research center.

Crosslinking of polymers
Degradation of pesticides
Degradation of phenols in waters of washing of the olives
Degradation of policlorobiphenols (PCB) present in oils of isolation of the transformers
Cracking of oil products
Water sterilization infected by pathogenic agents
Control of the effects of the on the functionality of the cells of the blood
Production of color centers in alkaline crystals in presence of drugging for employs in solid state laser
Generation from metallic targets of x-rays radiation
Damage tests of hard materials for nuclear fusion applications

The APAM laboratory unit dedicated to the electron accelerator system studies the physics parameters and the dosimetry of the particle beam up to the "radiation effects" investigating the whole chain of processes starting from the elementary interactions between ionizing radiation in matter up to the formation of the effect (eg, radiation damages to soft and hard materials [5]).

Monte Carlo methods are developed and employed for the simulation of radiation field and the induced processes for radiation response studies and radiobiological experiments.

Recently, within the COBRA project [6], a new irradiation chamber for treatment volume in order to remove biodegradation of artistic and cultural assets [3] has been realized. Investigations in this topic have led to the interest in the generation and characterization of radiation fields for radiobiological experiments with X-rays produced by the accelerated electrons. On this line we have devoted a study to the effects of radiation on insects.

Aedes albopictus is a mosquito vector of various severe diseases including dengue, zika, yellow fever and chikungunya. Insecticides did not show the ability to obtain the suppression of this dangerous insect species on the long term, mainly due to the development of resistant populations. Thus, innovative strategies of control are required to supplement the existing means to maintain this population's population density below the epidemic risk threshold. The production and release of sterile males capable of reducing the fertility of the wild-type population is proving to be a suitable approach to achieving this goal. ARwP Ae. Albopictus

is a line capable of producing sterile males due to infection of a specific strain of the endosymbiotic Wolbachia bacterium. Herein, we tested various X-ray dosages as a mean to achieve the sterilization of females eventually escaping the sexing procedures which could be undesired during releases in the field.

The present work was mainly aimed at the definition of a radiation protocol for the treatment volume of Aedes albopictus with X rays generated by electrons.

LINEAR ACCELERATOR

The linear accelerator employed in this work is an S-band standing wave on-axis coupled machine delivering 900 W maximum average power at 4.8 MeV and operating in the π/2 mode. The operating parameters are given in table 2. In figure 1 a drawing of the on-axis coupled accelerator and a picture of the brazed structure are given.

Table 2: 4.8 MeV linac parameters.

Mode Frequency	2999 Hz
Q0 factor	12000
Coupling Coefficient	1.9
Shunt Impedance ZS	72.7 MΩ/m
Number of accelerating cavities	7+2 halves
Number of Coupling Cavities	8
Cavity Length	48 mm
Pulse Duration (FWHM)	3.5 μs
Current at 4.8 MeV	200 mA
Frequency Repetition Rate	100 Hz (max)

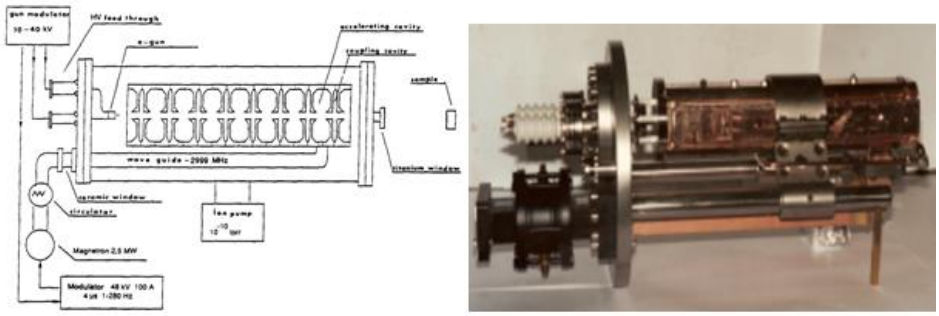

Figure 1. Left: drawing of the linear accelerator; right: the 4.8 MeV on-axis coupled linear accelerator.

Figure 2 shows the irradiation facility consisting on the described linear electron accelerator and the irradiation chamber.

The energy of electrons is determined by measuring the electrons range in aluminum: the obtained energy depends on whether the transmitted beam is measured in peak current from the beginning of pulse or measuring the average current and by transforming it to peak value using duty cycle of beam pulse.

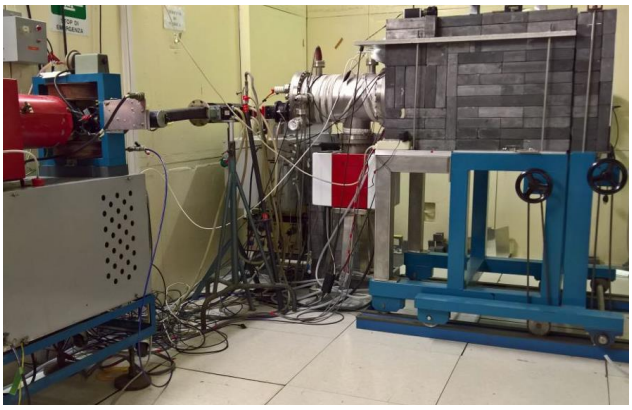

Figure 2. View of the e-beam/X-ray irradiation facility.

X-RAY IRRADIATION

Several set-ups are available using the e-beam irradiation facility described above.

The irradiation campaigns for the treatment volume of Aedes Albopictus depicted before were performed with X-rays.

The accelerated electrons exiting from the linac were collimated by stainless steel flange with an aperture of 5.5 mm and then shoot a target to generate X-rays through the bremsstrahlung effect. The produced X-rays passes through a lead conic collimator with 30 mm diameter as shown in figure 3.

Figure 3. Left: view of the e-beam exit. Right: X-rays lead collimator in front of the e-beam exit.

The MCNPX6 Monte Carlo Method was used to find the best thickness and material of target with biggest conversion efficiency. A simulation with the single material target model for scanning parameters calculates the conversion efficiency and estimates the dose rate. By the optimized calculation we choose a tungsten conversion target 1.64 mm thick [7] with a further aluminum, 0.5 mm thick, to block both any remaining primary electrons and the secondary ones produced.

Figure 4 shows the X-rays source, tungsten converter, housed between the electron collimator, just outside the linac exit window, and the X-ray beam lead collimator.

The insect sterilization protocol, afterward outlined, was developed working with the operational parameters summarized in Table 3.

Figure 5 shows the X-ray source spectrum calculated by MCNPX6.

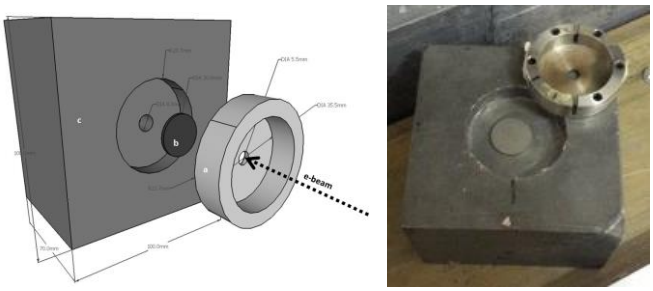

Figure 4. Schematic view (left) and photo (right) of the e-beam collimator (a); tungsten converter for X-rays (b); lead collimator (c).

Table 3: 4.8 MeV linac operational parameters set for the insect sterilization protocol.

Cathode Current	4 mA
Cathode Voltage	2 kV
High Voltage (power supply)	19 kV
Mean Current Accelerated Electrons	140 mA
Repetition Frequency	14 Hz
Pulse length	3 μs

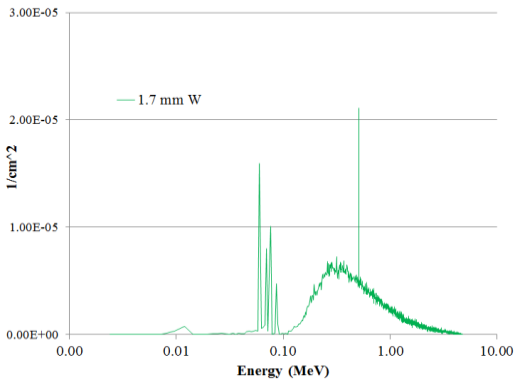

Figure 5. X-ray fluence distributions for source particles: the peak at 511 keV due to the pairs production and the characteristic fluorescence X-ray peak at 1.02 MeV are visible. [7]

The shield used for X-ray irradiation is a lead chamber positioned after the linac vacuum chamber (figure 2) and encloses both the electrons output terminal and the X-ray source as shown in figure 6. The internal volume of this irradiation chamber is: 410 x 810 x 400 mm^3.

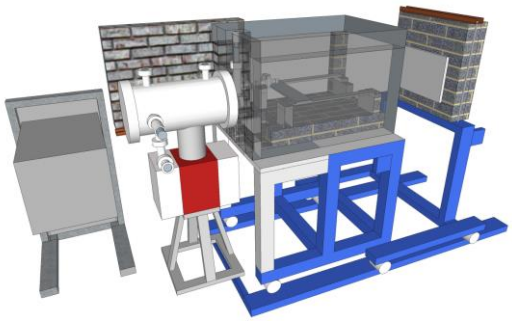

Figure 6. Sketch of the irradiation setup with the lead shielding room (410 x 810 x 400 mm^3) for the X-rays tests.

The half-value layer (HVL) method (effective up to 3 MeV photons) was used to measure the X-ray spectrum using thicker copper layers and also a Monte Carlo simulation was carried out interposing the filters on the previously calculated photonic spectrum.

The dosimetric control measurements were executed in the volume of the shielding room by a FWT IC-17A ionization chamber having an active volume of 1 cm3, suitable for high dose rates, calibrated at the LAT-231 calibration center with 60-Co, 137-Cs [7]. This dosimeter has a linear calibration factor in the energy region between 50 keV and 1.25 MeV showing a maximum, acceptable, variability of 10%. The calculated uncertainties are associated as follows: 1.5% the calibration factor, 5% the measurements, 3% the positioning. These should also add to the variability of the irradiation intensity of the converter due to variability of the e-beam cathodic emission.

The ionization chamber, powered by 300 V, was connected to a Keithley 6514 electrometer with a feedback capacity of 400.97 nF.

AEDES ALBOPICTUS

Female pupae (46±2 hour old) of the ARwP Ae. albopictus line were irradiated at various doses. The emerging adults were then mated with fertile males and then allowed to lay eggs to check for their fertility.

IRRADIATION MODALITY

A preliminary X rays dose and dose rate measurements campaign allowed to assess the distribution of dose inside the irradiation chamber. An ionization chamber sensor (model PPC05 from IBA) coupled to a reference class electrometer for measurements of absorbed dose (model Dose 1 from IBA-Wellhofer-Scanditronix) has been used to measure the dose rate in several points inside the lead shielded room. The sensor inside the irradiation chamber was moved by a remote handling system. In order to have a relatively low dose rate and, at the same time, a greater homogenous dose distribution, we decide to move far from the beam source point. In particular, for the insects sterilization process a distance of 30 cm from the X rays exit window has been considered. In this position, the measured dose rate is 0.952 Gy/min.

Then, a Petri dish containing water and the ARwP Ae. albopictus pupae has been placed perpendicularly at X rays beam axis, as shown in figure 7. Two Petri dishes have been irradiated for 31’30” and two other samples for 20’50”

Figure 7: Petri dish with Aedes albopictus pupae inside the irradiation room.

CONCLUSIONS

Currently we're going to run the way of experimental campaigns to define the best irradiation protocol in the entomology sector of the Sterile Insect Technique (SIT), to sterilize the dangerous insects Ae. albopictus that released into the wild sexually compete with the population at large reducing the chance for reproduction.

The reason of the interest in this X-rays application is related to the conditions of both radiation field and penetration improving sterilizing effects with simpler and safer process.

To evaluate the absorbed dose appropriate for male and female specimens of Ae. albopictus modified with the Wolbachia bacterium, as described above, we're setting up the right X-ray exposure procedure also performing the photon beam simulations using the EGSnrc Monte Carlo code. This system, available for non-commercial purposes, of radiation transport, is a code specifically designed to model the transport of radiation. It includes BEAMnrc software component can meet the requirements for modeling beams traveling through consecutive material components ranging from a simple to a complex geometry of the linac head terminal. Also the EGS tool is used to estimate the dose distribution on the sample target and the data will be compared with Fluka simulations. In this way, we are simulating the fluency profile on our sample within the irradiation chamber, described in the above paragraphs, to optimize the delivering of the prescribed radiation dose to the sample and new several experimental tests are foreseeing.

REFERENCES

[1] M. Vadrucci, A. Ampollini, F. Borgognoni, P. Nenzi, L. Picardi, C. Ronsivalle, V. Surrenti, E. Trinca - *Irradiation activity with the top-implart proton linear accelerator* - accepted by Radiation & Application Journal (2017).

[2] M. Vadrucci, A. Ampollini, G. Bazzano, L. Picardi, C. Ronsivalle, *The low-energy proton beam for radiobiology experiments at the top-implart facility,*Biophysics & Bioeng. Letters (2015) **8** (1).

[3] F. Borgognoni, M. Vadrucci, G. Bazzano, P. Ferrari, S. Massa, R. Moretti, M. Calvitti, C. Ronsivalle, A. Moriani, L. Picardi, *X-ray sterilization of insects and microorganisms for cultural heritage applications*, Nuclear Instruments and Methods in Physics Research Section B: Beam Interactions with Materials and Atoms. In press, Available online 18 March 2017, https://doi.org/10.1016/j.nimb.2017.03.033

[4] http://www.soiort.com/en/iort-eng/

[5] F. Borgognoni, M. Mayer, L. Picardi, M. Vadrucci, M. Zibro, *MeV electron-beam irradiation of tungsten for vacancy creation*, submitted to EUROMAT 2017 conference, 17-22 September 2017, Thessaloniki, Greece.

[6] http://www.soiort.com/en/iort-eng/

[7] F. Mariotti, P. Ferrari, M. Vadrucci, F. Borgognoni, L. Campani, *Charecterization of the REX Bremsstrahlung source,* submitted to AIRP 2017 8-10 November 2017, Salerno Italy.

V International Conference on Particle-based Methods – Fundamentals and Applications
PARTICLES 2017
P. Wriggers, M. Bischoff, E. Oñate, D.R.J. Owen, & T. Zohdi (Eds)

COMPARISON OF PARTICLE-RESOLVED DIRECT NUMERICAL SIMULATION AND 1D MODELLING OF CATALYTIC REACTIONS IN A CYLINDRICAL PARTICLE BED

ARPIT SINGHAL[1, 2*], SCHALK CLOETE[3], ROSA QUINTA-FERREIRA[2] AND SHAHRIAR AMINI[1, 3]

[1] NTNU: Norwegian University of Science and Technology
Department of Energy and Process Engineering,
Kolbjørn hejes v 1B, NO-7491,
Trondheim, Norway
arpit.singhal@ntnu.no

[2] University of Coimbra
Department of Chemical Engineering
Rua Sílvio Lima, Polo II, 3030-790
Coimbra, Portugal
rosaqf@eq.uc.pt

[3] SINTEF Materials and Chemistry
Flow Technology Department
S. P. Andersens veg 15 B, NO-7031
Trondheim, Norway
schalk.cloete@sintef.no and
shahriar.amini@sintef.no

Key words: Direct numerical simulation (DNS), CFD-DEM, packed bed, catalytic gas-solid reaction, reaction rate, heat transfer, multiscale.

Abstract. This work presents a comparative study of reactive flow in a realistically packed array of cylindrical particles on two widely different scales: particle-resolved direct numerical simulation (PR-DNS) and 1D modelling. PR-DNS directly simulates all transfer phenomena in and around the cylindrical particles, while 1D modelling utilizes closure models to predict system behaviour at a computational cost several orders of magnitude lower than PR-DNS.

PR-DNS is performed on a geometry of ~100 realistically packed cylindrical particles generated using the discrete element method (DEM). Simulations are performed over a range of Thiele moduli, Prandtl numbers and reaction enthalpies. The geometry with particles of aspect ratio four is meshed with fine polyhedral elements both inside and outside the particles. Hence, we obtain accurate results for combined internal and external heat and mass transfer in the cylindrical particle array.

These results are compared with a 1D packed bed reactor model incorporating appropriate models for intra particle diffusion and for external heat and mass transfer (applicable to cylindrical particles). Results document a good comparison for the heterogeneous first order

catalytic simple reaction. Therefore, recommendations are made to guide future 1D modelling works involving reactive flows in packed beds of cylindrical particles.

NOMENCLATURE

Greek Symbols

α	Volume fraction
ε	Void fraction
ϕ	Thiele modulus (Th)
η	Effectiveness factor

Latin Symbols

a	Characteristic length of cylinder particle ($r_p/2$)
C_p	Specific heat capacity of fluid [J/kg.K]
C_A	Concentration of species A [mol/m^3]
D	Molecular diffusivity [m^2/s]
d_p	Diameter of the cylindrical particle [m]
E	Activation energy [J/mol]
h	Heat transfer coefficient [W/m^{2}K]
k_0	Arrhenius constant [1/s]
K_f	Thermal Conductivity of fluid [W/m.K]
Nu	Nusselt number (hd_p/K_f)
Pr	Prandtl number ($\mu C_p/K_f$)
R	Gas constant [8.314 J/mol/K]
R_{cat}	Catalytic reaction rate [mol/m^{3}s]
r	Radius [m]
Re	Reynolds number ($\rho u_s d_p/\mu$)
Sc	Schmidt number ($\mu/\rho D$)
Sh	Sherwood number (hd_p/D)
T	Temperature [K]
u_s	Superficial velocity of the fluid [m/s].

Sub/superscripts

f	Fluid
p	Particle.

1 INTRODUCTION

Cylindrical particles are often utilized in gas-solid packed bed systems, with application from process to pharmaceutical industry. Therefore, a wide range of closure models is available for gas-solid reaction systems. The closure models are segregated depending upon the application of the particles in either catalytic or non-catalytic role.

There are several important works describing the non-catalytic gas-solid systems [1, 2]. While, for the heterogeneous catalytic system the most important parameter of effectiveness factor is given for intra particle diffusion in spherical porous particle by [3]. The correct expression for the effectiveness factor with the cylindrical particle can be found in [4-6].

The recent work from the authors [7, 8] used the analytical expressions for effectiveness factor of general catalytic reaction forms in 1D packed bed models. The validity of these 1D packed bed models when combined with appropriate closure models for external heat and mass transfer in dense packed beds of cylindrical particle motivates the current work.

The objective of our work is to evaluate the predictions of gas-solid reaction systems on two distinct scales. Firstly, a PR-DNS on a geometry of ~100 densely packed cylindrical particles (aspect ratio four; $\varepsilon = 0.468$) [9] is used to give insight into the intra-particle diffusion and heat transfer phenomenon. Then the 1D packed bed model based on the closure for effectiveness factor [6] and external heat and mass transfer [9] is used to approximate this solution at a much lower computational cost. The comparison of the results for species concentration and temperature variation from both approaches are then documented.

2 METHODOLOGY

2.1 PR-DNS Simulation Setup

The realistically packed cylindrical particle bed of aspect ratio four ($\varepsilon = 0.468$) is generated using discrete element method (DEM) integrated in Star CCM+ 11.02. It is explained in more detail in Singhal et al. [9]. Such a geometry obtained is free from wall effects, which has been proved in [10]) hence giving confidence in the numerical accuracy of the methodology. The geometry is meshed with polyhedral elements with resolution $d_e/30$ using FLUENT meshing on particle surfaces both inside and outside the particle to account for intra particle diffusion. Subsequently a growth rate of 20% is allowed from the particle surface to fill up the void (Figure 1).

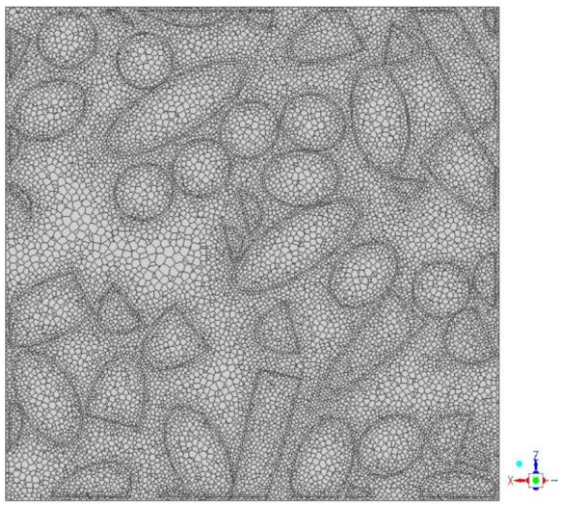

Figure 1: A section (y = 0) through the geometry of cylindrical particles meshed with polyhedral elements.

Steady state DNS with SIMPLE algorithm for pressure-velocity coupling and 2nd order spatial discretization for solver equations using ANSYS FLUENT is used to provide solution to the problem at hand. Steady state DNS is found to be accurate for the type of geometry solved, as transient fluctuations in the small spaces are negligible [10]. The final rendered geometry has a velocity inlet, pressure outlet and a non-slip condition on the wall. The solid particles are considered to be porous (the grain model [11]), where the reaction modelled by Eq. (1) takes place. Table 1 describes the simulation parameters used in the DNS.

$$A\ (g) + B\ (s) \rightarrow C\ (g) + B\ (s) \tag{1}$$

The reaction rate is defined by Eq. (2) and (3):

$$R_{cat} = \alpha_s k C_A \tag{2}$$

$$k = k_0 exp\left(\frac{-E}{RT}\right) \tag{3}$$

PR-DNS was performed for different combinations of heat transfer resistance (Prandtl number) and mass transfer resistance (Thiele modulus). In total, nine combinations of Thiele modulus and Prandtl number were used to obtain the results (Table 1). Different mass and heat transfer mechanisms are obtained by varying the molecular diffusivity and thermal conductivity of the gas phase using Thiele modulus (Th) and Prandtl number (Pr) definition given in Table 1. Using an appropriate pre-exponential factor (Eq. (3)), the value for reaction rate constant of 10000 1/s at temperature 1000 K is obtained. Similarly, a high value for activation energy is assumed to create a strong coupling between heat and mass transfer.

Table 1: Simulation parameters for PR-DNS

Parameters	**Value**
Eq. Particle diameter (d_e) (m)	0.001
Packed bed voidage	0.468
Particle void fraction (internal)	0.3
Density (kg/m^3)	*Fluid* :1 *Particles* :2500
Fluid velocity (m/s)	1
Inlet mole fraction (A)	0.1
Specific heat capacity (C_p) (J/kg/k)	1000
Arrhenius constant (k_0) (1/s)	1673603814
Activation energy (E) (J/mol)	100000
Thermal conductivity (Solid) (W/m.K)	0.1
Thiele moduli (Th)	5, 10, 20
Prandtl numbers (Pr)	0.50, 0.75, 1
Heat of reaction (kJ/mol)	100, 10, 0, -10

2.2 Thiele Modulus and Effectiveness Factor

The effectiveness factor and Thiele modulus [12] definition is similar to the previous work with spherical particle [8] defined for heterogeneous catalytic gas-solid reactions of first order. It is defined as the effect of intra particle diffusion on reaction rate [3, 13].

$$\eta = \frac{actual\ reaction\ rate}{reaction\ rate\ without\ diffusion\ limitations} \tag{4}$$

$$\phi \approx \frac{reaction\ rate}{diffusion\ rate} \tag{5}$$

2.3 1D Packed Bed Model

An outline of the 1D model setup can be seen in detail in the earlier work of the authors [7, 8]. The 1D packed bed model domain consists of 100 cells in one direction. The model is simulated using a Two Fluid Model approach in ANSYS FLUENT 17.2. The velocity of the solid phase in all 100 cells is fixed to zero. Subsequently, the conservation for mass, momentum, energy and specie are solved to obtain the solution.

In the 1D-model approach, appropriate closure models applicable to cylindrical particle beds have to be used to account for heat and mass transfer limitations. The closure models for effectiveness factor to model intra particle mass transfer limitations are given by Levenspiel [3], these closures are modified as suggested by [6], to be now applicable for cylindrical particles. Moreover, the external heat and mass transfer limitations are modelled using the closure models developed for cylindrical particles [9]. The effectiveness factor closures considered in this work are given below in Eq. (6)-(8):

$$\eta = \frac{1}{\phi}\left(\frac{1}{tanh(3\phi)} - \frac{1}{3\phi}\right) \tag{6}$$

$$\phi = a\sqrt{\frac{k}{D_e}} \tag{7}$$

$$D_e = \frac{D\varepsilon}{\tau} \tag{8}$$

The Thiele modulus (ϕ) represents the ratio of kinetic rate to diffusion rate, so higher values represent greater mass transfer limitation. The effective diffusivity (D_e) is composed of the molecular diffusivity (D), the void fraction of porous particles $(\varepsilon = 0.3)$ and the tortuosity $(\tau = 1)$. The correlation for external heat (Pr) and mass transfer (Sc) from Singhal et al. [9] is written as shown in Eq. (9).

$$\begin{aligned} Nu &= (0.81 + 0.0652\varepsilon^{-3.55}Re^{0.644}Pr^{0.456}) \\ Sh &= (0.81 + 0.0652\varepsilon^{-3.55}Re^{0.644}Sc^{0.456}) \end{aligned} \tag{9}$$

The domain dimensions and the boundary conditions are identical to the PR-DNS simulations. In addition, the solid volume fraction is set as the mean volume fraction of the solid in the PR-DNS domain (0.532) times the solid volume fraction in the particles (0.7).

3 RESULTS AND DISCUSSIONS

3.1 Heat and Mass Transfer in Densely Packed Cylinders

PR-DNS is performed over a range of Thiele moduli (Th 5-20) and Prandtl numbers (Pr 0.5-1) for a densely packed bed of cylindrical particles of aspect ratio four (ε = 0.468). The results for typical variation of gas temperature and specie concentration (of specie A) for an

endothermic reaction (at dH_{rxn} = 10 kJ/mol) are shown in Figure 2 and Figure 3. Figure 2 shows temperature variation over Pr 0.50 to Pr 1 (top to bottom). As the gas thermal conductivity decreases, the particle temperature decreases (Pr 1 has colder particles than at Pr 0.50). This is due to increase in heat transfer resistance with increasing Prandtl number that limits the influx of heat consumed by the endothermic reaction. Also, for a fixed heat transfer resistance (Figure 2 (right to left)), a lower mass transfer resistance results in colder particles due to a faster endothermic reaction.

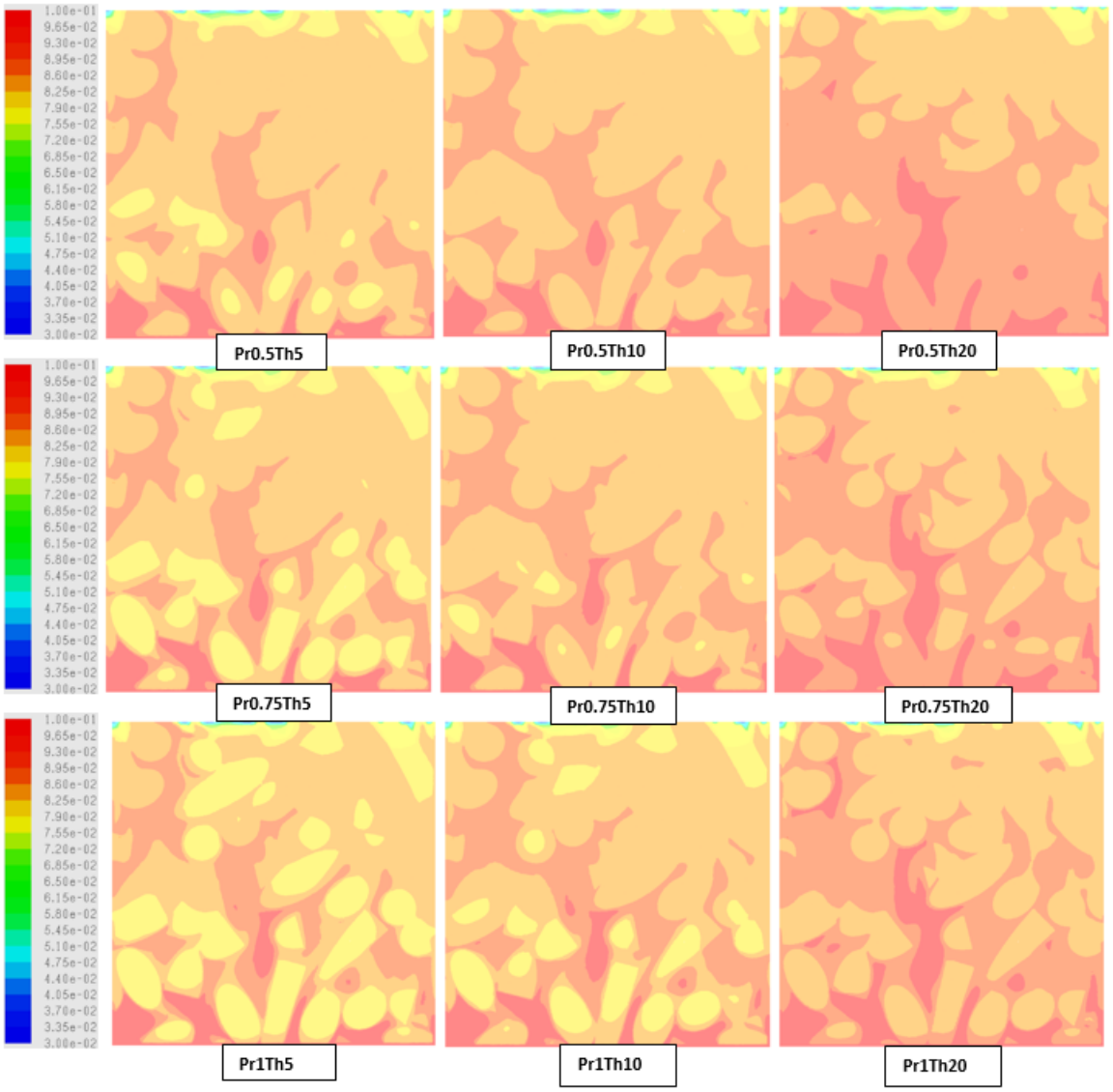

Figure 2: PR-DNS results (plane y= 0) for the temperature variation in the packed bed of cylindrical particles of aspect ratio four for different Prandtl numbers (Pr) and Thiele moduli (Th) at dHrxn = 10 KJ/mol.

The mass transfer limitations can be seen appropriately in Figure 3. It is evident from Figure 3 (left to right), that the concentration of specie A inside the particle decreases. This is because

of the increase in the mass transfer resistance, i.e. the gas mass diffusivity decreases with increase in Thiele modulus. More details are given in the subsequent sections.

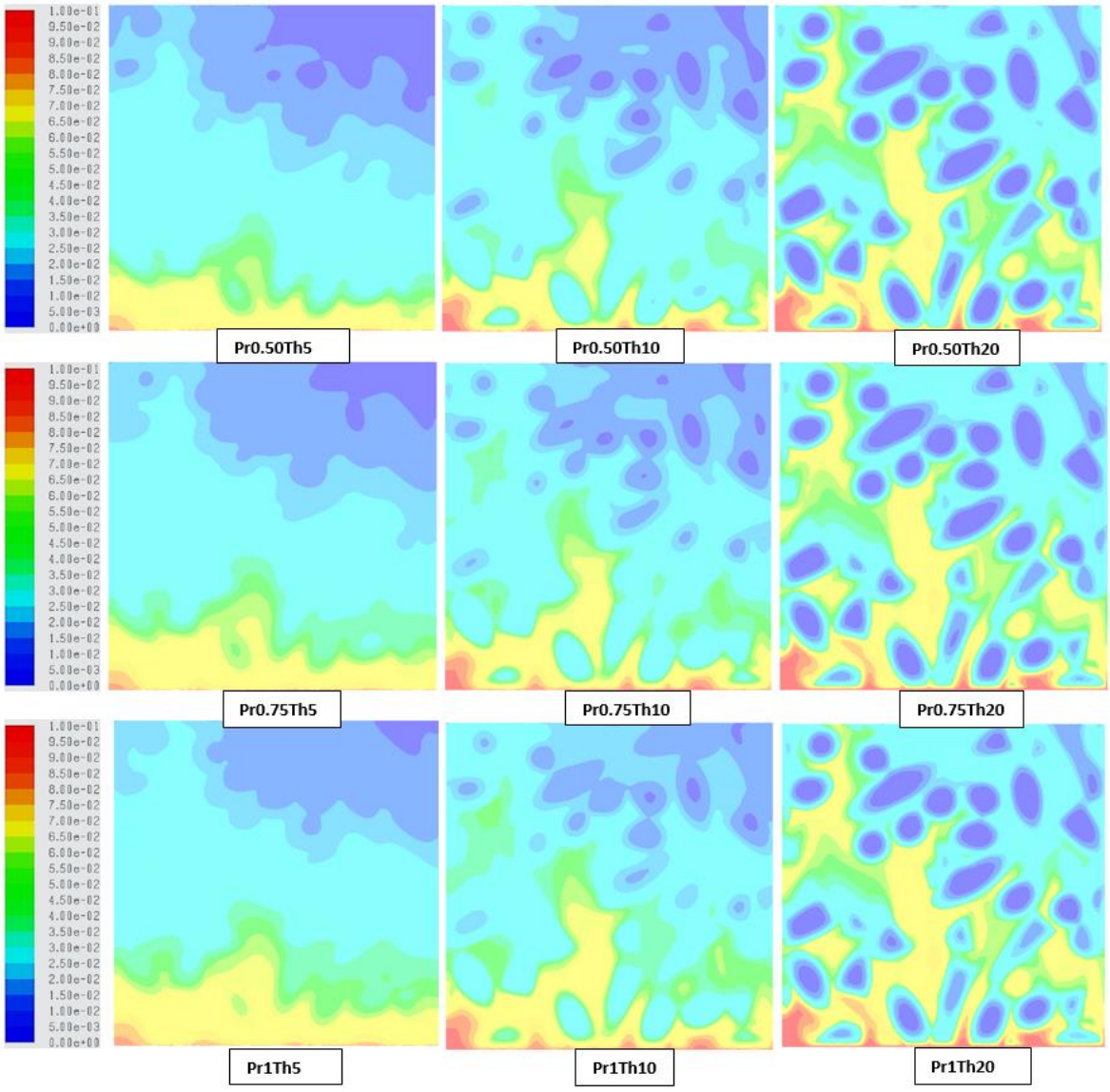

Figure 3: PR-DNS results for the reactant (A) mole fraction in the packed bed of cylindrical particles of aspect ratio four for different Prandtl numbers (Pr) and Thiele moduli (Th) at dHrxn = 10 KJ/mol.

The effect of heat of reactions (dH_{rxn}) on specie concentration (of A) is shown in Figure 4. Four different dH_{rxn} (= 100, 10, 0, -10 kJ/mol) are assessed for the Pr1T20 case, including one exothermic reaction. The specie concentration (of specie A) inside the particle decreases as we decrease the dH_{rxn}. This is because an exothermic reaction is self-strengthening (faster reaction ➔ higher temperature ➔ faster reaction), whereas the opposite is true for an endothermic reaction. The exothermic reaction strengthens itself by increasing the temperature, while the endothermic reaction extinguishes itself by decreasing the temperature.

3.2 1D Model Predictions

The comparison between the PR-DNS data and the 1D model predictions are presented in this section. In the first comparison, the 1D model data is compared with the PR-DNS data for bulk fluid specie concentration and temperature (over a range of Prandtl number and Thiele modulus). The bulk fluid [9, 10, 14-16] properties are used for PR-DNS data to generalise any effect of the location of the planes [9, 10] in the geometry in the calculation of the temperature and specie concentration. Secondly, the effect of change in reaction enthalpies are compared. Also note that for the 1D model all the heat of reaction source term is implemented in the solid phase as suggested in our previous work [8].

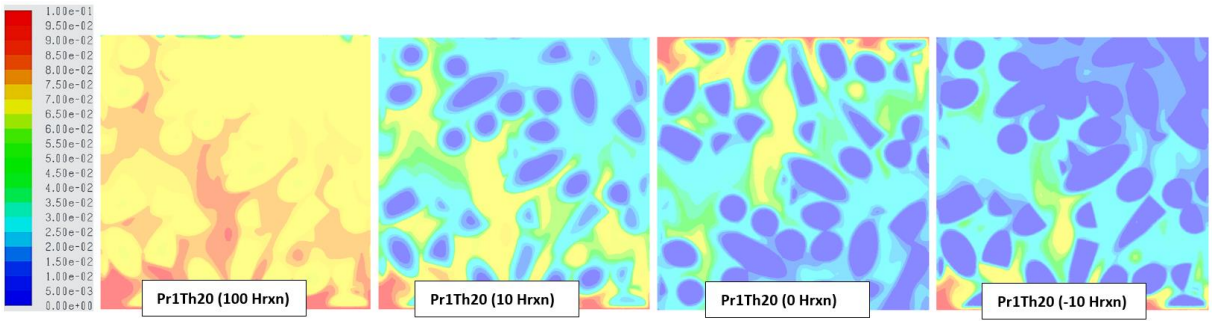

Figure 4: PR-DNS results for the reactant (A) mole fraction for (Pr = 1; Th = 20) case. The variation in specie concentration with different heat of reactions (dH_{rxn} = 100, 10, 0, -10) is shown from left to right.

3.2.1 Variation of Prandtl number and Thiele modulus

Figure 5 shows the axial specie concentration (for specie A) profiles for nine combinations of Thiele modulus and Prandtl number. The results agree well with the PR-DNS results suggesting that mass transfer limitations are defined with appropriate closures for 1D model. Figure 6 shows the axial profiles for the difference between the bulk gas temperature and the average particle temperature. The amount of reaction in an endothermic system decreases as Pr is increased by decreasing the gas phase thermal conductivity. A lower thermal conductivity implies greater gas-particle heat transfer resistance, thereby allowing less heat to enter and sustain the highly endothermic reaction. The temperature variation inside each particle should be very small given the solids phase thermal conductivity (Table 1) implemented. In general, good agreement between PR-DNS and 1D results is obtained with a moderate discrepancy at Pr = 1.

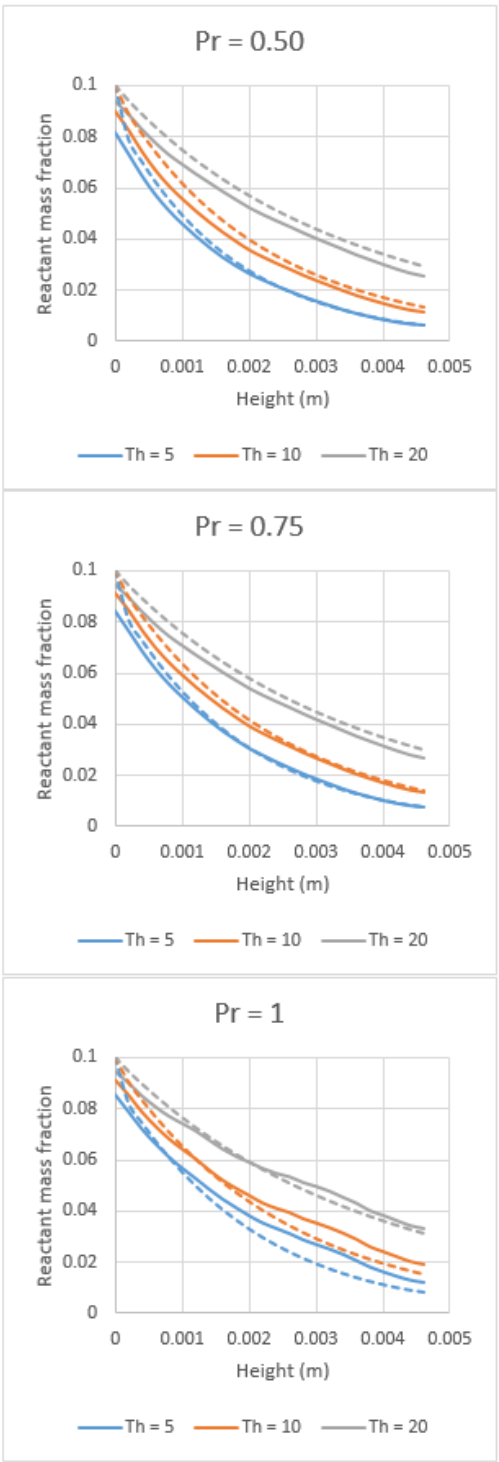

Figure 5: Comparison of axial species profiles (for specie A) between PR-DNS (solid lines) and 1D simulations (dashed lines) for different Prandtl numbers (Pr) and Thiele moduli (Th) at dHrxn = 10 kJ/mol..

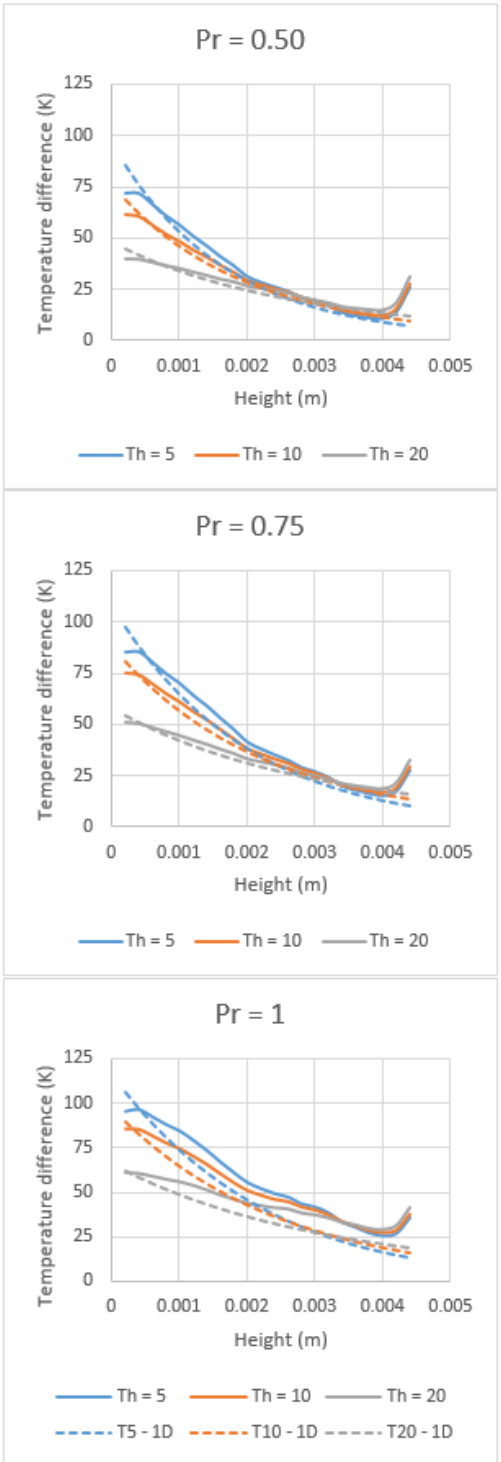

Figure 6: Comparison of axial gas-particle temperature difference between PR-DNS (solid lines) and 1D simulations (dashed lines) for different Prandtl numbers (Pr) and Thiele moduli (Th) at dHrxn = 10 kJ/mol.

3.2.2 Variation of reaction enthalpy

In the previous sections, the heat of reactions used is ($dH_{rxn} = 10$ kJ/mol) signifying an endothermic reaction. In order to monitor the effect of dH_{rxn} on the reactant conversion, three additional heat of reactions (including an exothermic reaction) are evaluated for the case (Pr1T20) with greatest heat and mass transfer limitations.

It can be seen from Figure 7 that the 1D model predicts PR-DNS results accurately and the reactant conversion increases with a decrease in the reaction enthalpies. In the two cases with the fastest reaction rates, the inclusion of the external mass transfer limitation becomes important to achieve a good match with PR-DNS results.

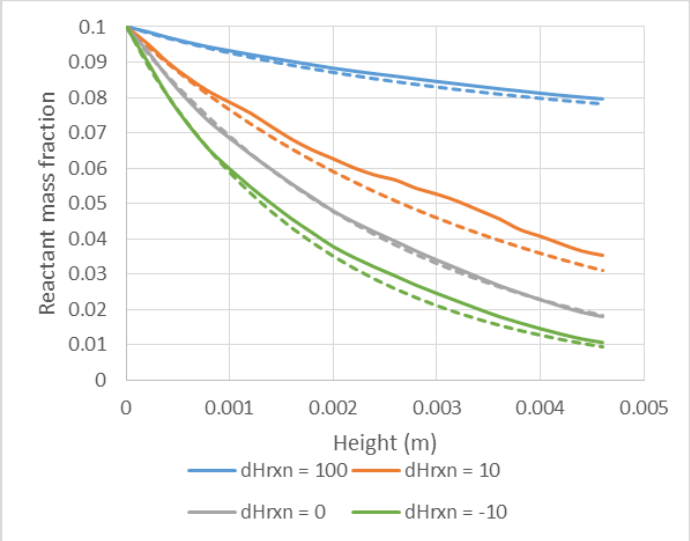

Figure 7: Comparison of axial species profiles (for specie A) between PR-DNS (solid lines) and 1D simulations (dashed lines) for Pr1T20 case and different reaction enthalpies (dH_{rxn} in kJ/mol).

11 CONCLUSIONS

This work presented a comparison of particle-resolved direct numerical simulations (PR-DNS) with 1D packed bed model for a densely packed bed of cylindrical particles of aspect ratio four ($\varepsilon = 0.468$) in a gas-solid first order catalytic reaction system.

Existing closures for 1D packed bed model for spherical particles modified appropriately for cylindrical particles predicts well against the result for resolved simulations (PR-DNS) over a range of Thiele moduli, Prandtl numbers and reaction enthalpies. Recently proposed closures for external heat and mass transfer from cylindrical particles were important to ensure good performance of the 1D model. Future works will assess whether this good performance is maintained in systems with multiple reactions with different reaction orders.

12 ACKNOWLEDGEMENT

This work is a part of a European Union project under Seventh research framework program (FP7/2007-2013) under grant agreement n° 604656 - A multi-scale Simulation based design platform for Cost effective CO_2 capture Processes using Nano-structured materials (NanoSim).

The authors are grateful to European Research Council for its support. Additionally, the computational resources at NTNU provided by NOTUR, http://www.notur.no, were used during this project.

REFERENCES

[1] Nashtaee, P.S.b. and B. Khoshandam, Noncatalytic gas-solid reactions in packed bed reactors: a comparison between numerical and approximate solution techniques. *Chemical Engineering Communications*, 2014. **201**(1): p. 120-152.

[2] Ramachandran, P.A. and L.K. Doraiswamy, Modeling of noncatalytic gas-solid reactions. *AIChE Journal*, 1982. **28**(6): p. 881-900.

[3] Levenspiel, O., *Chemical Reaction Engineering, 3rd ed*. Vol. 3rd ed. 1999: John Wiley & Sons, New York.

[4] Asif, M., Efficient Expressions for Effectiveness Factor for a Finite Cylinder. *Chemical Engineering Research and Design*, 2004. **82**(5): p. 605-610.

[5] Gunn, D.J., Diffusion and chemical reaction in catalysis and absorption. *Chemical Engineering Science*, 1967. **22**(11): p. 1439-1455.

[6] Rawlings, J.B.a.E., John G, *Chemical reactor analysis and design fundamentals*. 2002: Nob Hill Pub, Madison, Wis.

[7] Cloete, S., et al., Gas Switching as a Practical Alternative for Scaleup of Chemical Looping Combustion. *Energy Technology*, 2016. **4**(10): p. 1286-1298.

[8] Singhal, A., et al., *Comparison of Particle-Resolved Direct Numerical Simulation and 1D modelling of catalytic reactions in a packed bed*, in *12th International Conference on CFD in Oil & Gas, Metallurgical and Process Industries*. 2017: Trondheim, Norway.

[9] Singhal, A., et al., Heat transfer to a gas from densely packed beds of cylindrical particles (under review). *Chemical Engineering Science*, 2017.

[10] Singhal, A., et al., Heat transfer to a gas from densely packed beds of monodisperse spherical particles. *Chemical Engineering Journal*, 2017. **314**: p. 27-37.

[11] Szekely, J., Evans, J.W., Sohn, H.Y.,, *Gas-solid reactions*. 1976: Academic Press, New York. 612-612.

[12] Thiele, E.W., Relation between Catalytic Activity and Size of Particle. *Industrial & Engineering Chemistry*, 1939. **31**(7): p. 916-920.

[13] Ishida, M. and C.Y. Wen, Comparison of kinetic and diffusional models for solid-gas reactions. *AIChE Journal*, 1968. **14**(2): p. 311-317.

[14] Deen, N.G., et al., Direct numerical simulation of flow and heat transfer in dense fluid–particle systems. *Chemical Engineering Science*, 2012. **81**: p. 329-344.

[15] Deen, N.G., et al., Review of direct numerical simulation of fluid–particle mass, momentum and heat transfer in dense gas–solid flows. *Chemical Engineering Science*, 2014. **116**: p. 710-724.

[16] Sun, B., S. Tenneti, and S. Subramaniam, Modeling average gas–solid heat transfer using particle-resolved direct numerical simulation. *International Journal of Heat and Mass Transfer*, 2015. **86**: p. 898-913.

V International Conference on Particle-based Methods – Fundamentals and Applications
PARTICLES 2017
P. Wriggers, M. Bischoff, E. Oñate, D.R.J. Owen, & T. Zohdi (Eds)

MODELLING OF CHEMICAL REACTIONS IN METALLURGICAL PROCESSES

MUSTAFA E. KINACI[1], THOMAS LICHTENEGGER[2,3] AND SIMON SCHNEIDERBAUER[1,3]

[1] Christian Doppler Laboratory for Multi-Scale Modelling of Multiphase Processes
4040 Linz, Austria
mustafa_efe.kinaci@jku.at

[2] Linz Institute of Technology (LIT), Johannes Kepler University
4040 Linz, Austria
thomas.lichtenegger@jku.at

[3] Department of Particulate Flow Modelling, Johannes Kepler University
4040 Linz, Austria
simon.schneiderbauer@jku.at

Key words: CFD-DEM, Iron-ore reduction, Chemical models, Particle shrinkage, Unreacted-core model, Diffusion coefficients

Abstract. Since the last three decades, the study of reduction of iron-ore has gained much attention as it is considered a core process for the steel industry. Fluidized bed and moving bed reactors are utilized to reduce the iron-ore efficiently. As reducing agents coal, coke or natural gases are used, which are released as CO_2 gas, or sometimes in small amounts as H_2O to the environment. The conditions in these reactors are harsh and provide limited accessibility, therefore computational tools are used to investigate them. One such tool is the CFD-DEM method, where the reacting gas species and the governing equations for the gas flow are calculated in the Eulerian (CFD) side, whereas the particle reactions and equation of motion are calculated in the Lagrangian (DEM) side.

In the current work, the CFD-DEM method is extended to cover the most dominant types of models for heterogeneous reactions between submerged solids and fluids. One of these models is the Shrinking Particle Model (SPM), which is used to verify the communication framework between the CFD and DEM sides by running preliminary test cases. Another model is the Unreacted Shrinking Core Model (USCM), which is considered as a good model for a reality like iron-ore reduction modelling.

1 INTRODUCTION

The deterioration of the quality of ore and coal due to high costs and low availability related with the shortage of resources has led to increase in research of iron ore reduction. The practical importance of being used as a feedstock for steel-making processes has also played an important role [1, 2].

The leading process used in iron-making is the blast furnace. These furnaces consists of a moving bed reactor with countercurrent flow of the solid reactants against a reducing gas. In the blast furnace process, the iron ore fines which built up around 80% of iron ores, need to go through a pelletizing or sintering process [3]. In some cases, such as the fluidized bed technology, fine ores can directly be charged into the reduction process making it highly advantageous. Such fluidized bed reactors are used in the pre-reduction stage of the FINEX® process [4, 5]. The FINEX® process, which was jointly developed by POSCO (Korea) and Primetals Technologies (Austria), produces hot metal in the same quality as traditional blast furnaces, without the need for sintering and coke making. The iron-ores that are charged into the process go through fluidized bed reactors where they are heated and reduced to Direct Reduced Iron (DRI). The DRI is then charged into the melter gasifier where the final reduction and melting as well as the production of reducing gas by gasification of coal with oxygen takes place. Another advantage of the FINEX® process is the exhaust gas, which can be used for various other applications such as heating within a steel plant, power generation and so forth [6].

The main reactions for the reduction of metallic oxide with a gaseous reductant (CO or H_2) can be expressed with the following reaction steps:

$$3\,Fe_2O_3 + CO/H_2 \longrightarrow 2\,Fe_3O_4 + CO_2/H_2O \tag{1}$$

$$Fe_3O_4 + CO/H_2 \longrightarrow 3\,FeO + CO_2/H_2O \tag{2}$$

$$FeO + CO/H_2 \longrightarrow Fe + CO_2/H_2O \tag{3}$$

The conditions inside the reactors limit accessibility thereby complicating the physical investigation of the processes. Thus, simulation methods and computational tools are used to improve the iron-making processes. One such tool is the Two-Fluid Model (TFM), which is an Euler-Euler approach that treats the solid and the fluid phases as a continuum. However, this model lacks the proper representation of particle size description and the related physical phenomena. In order to represent micro-scale phenomena, the TFM would require a fine spatial grid, which would make the computation unaffordable for industrial scale utilization. If coarse-graining is carried out there would be a loss of unresolved (small) scales and might lead to errors [8, 7]. Another tool uses the coupling of Computational Fluid Dynamics (CFD) for the continuous fluid phase (i.e. the reduction gas) and the Discrete Element Method (DEM) for the discrete particles

such as iron-ore and coal. These methods are coupled in a CFD-DEM approach based on the open source software packages OpenFOAM (OpenCFD Ltd. 2009) and LIGGGHTS (LIGGGHTS, 2011) [9]. DEM provides an easier way to evaluate the per-particle chemistry such as the shrink/growth of particles due to reactions and it does not require to transfer these reactions to a continuum representation. However, to tackle industrial scale operations with the CFD-DEM, coarse-graining needs to be carried out in order to reduce the computational demands. Another method that can be thought of would be the hybrid Lagrangian-Eulerian model that combines the Lagrangian Discrete Phase Model (DPM) and a coarse-grained TFM such as in the works of Schneiderbauer et al. [10].

2 REACTION KINETICS

The most common types of representation models for the non-catalytic reactions of solids submerged in fluids are the shrinking particle model (SPM) and the unreacted shrinking core model (USCM) [11]. In the SPM, only the surface of the particle reacts with the surrounding fluid therefore there is no layer formation due to the reaction and the products diffuse directly into gas. As the reaction progresses, the particle shrinks and eventually disappears completely. In the USCM, as the particle surface reacts and shrinks it forms a layer behind. The reductant gas has to diffuse through this layer in order to react with the core.

The main reactions for the direct reduction of iron with a gaseous reductant, CO/H_2, can be expressed in three reaction steps as shown in reaction equations 1 - 3. The three layer USCM developed by Philbrook, Spitzer and Manning [12] is able to represent the three interfaces of hematite/magnetite, magnetite/wustite and wustite/iron adequately. The reduction of iron-oxide to produce metallic iron follows these steps [12];

- The reducing gas is transported through the gas film onto the particle surface.
- The reductant gas then diffuses through the porous iron layer.
- Part of the reductant reacts with wustite at the wustite/iron interface producing iron and gaseous product.
- Rest of the reducing gas diffuses through the wustite layer onto the wustite/magnetite interface.
- A portion of the gas reacts with magnetite at layer surface producing wustite and gaseous product.
- The balance gas diffuses through the magnetite layer onto the magnetite/hematite interface.
- Chemical reaction of the leftover gas occurs at the hematite core and produces magnetite and a gaseous product.

- The gaseous product diffuses outwards through the pores of the pellet.

Since each step poses a resistance to the total reduction of the pellet, the reduction pattern of a single pellet can be considered to follow a resistance network such as an electrical resistance circuit network as illustrated in Fig. 1.

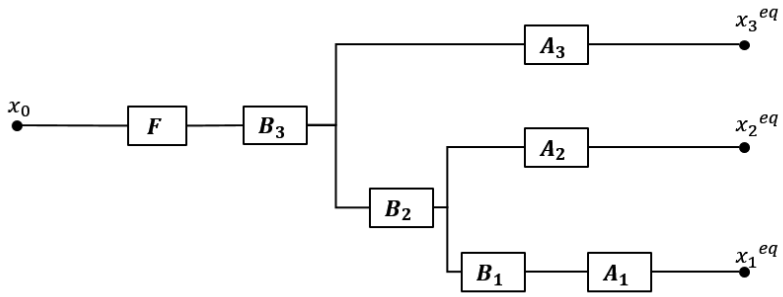

Figure 1: Resistance network diagram that illustrates the resistance of an iron-ore pellet that goes through in the reduction process.

The solution of the resistance network yields the reaction flow rate $\dot{Y}_{i,j}$ for every layer that can be defined as

- from hematite to magnetite

$$\begin{aligned}\dot{Y}_{i,h} = [([A_3(A_2+B_2+B_3+F)+(A_2+B_2)(B_3+F)](x_0 - x^{eq}_{CO,1}) \\ - [A_3(B_2+B_3+F)+B_2(B_3+F)](x_0 - x^{eq}_{CO,2}) \\ - [A_2(B_3+F)](x_0 - x^{eq}_{CO,3}))\frac{1}{W}]_i\end{aligned} \tag{4}$$

- from magnetite to wustite

$$\begin{aligned}\dot{Y}_{i,m} = [([(A_1+B_1+B_2)(A_3+B_3+F)+A_3(B_3+F)](x_0 - x^{eq}_{CO,2}) \\ - [B_2(A_3+B_3+F)+A_3(B_3+F)](x_0 - x^{eq}_{CO,1}) \\ - [(A_1+B_1)(B_3+F)](x_0 - x^{eq}_{CO,3}))\frac{1}{W}]_i\end{aligned} \tag{5}$$

- from wustite to iron

$$\begin{aligned}\dot{Y}_{i,w} = [([(A_1+B_1)(A_2+B_2+B_3+F)+A_2(B_2+B_3+F)] \\ (x_0 - x^{eq}_{CO,3}) - [A_2(B_3+F)](x_0 - x^{eq}_{CO,1}) \\ - [(A_1+B_1)(B_3+F)](x_0 - x^{eq}_{CO,2}))\frac{1}{W}]_i\end{aligned} \tag{6}$$

in which $A_{i,j}$ represents the relative chemical reaction resistance term, $B_{i,j}$ the relative diffusivity resistance term, j represents the layers hematite, magnetite and wustite and i the reducing gas species. F is the mass transfer resistance term, which is defined with $1/k_f$. x_0 is the bulk gas mole fraction and $x_{i,j}^{eq}$ the relative layer equilibrium mole fractions. The denominator W is expressed as

$$\begin{aligned} W = &[(A_1 + B_1)(A_3(A_2 + B_2 + B_3 + F) + (A_2 + B_2)(B_3 + F)) \\ &+ A_2(A_3(B_2 + B_3 + F) + B_2(B_3 + F))]_i \end{aligned} \tag{7}$$

The equilibrium mole fractions of the reducing gas species can be defined with the equilibrium constant. The equilibrium constant Keq_j, is the ratio of product to reactant equilibrium mole fractions, and represented as

$$\frac{x_{prod,j}^{eq}}{x_{reac,j}^{eq}} = Keq_{\mathrm{Fe_xO_y,CO}}. \tag{8}$$

With the help of the reaction flow rate $\dot{Y_{i,j}}$, the reactant gas mass change for every layer is calculated as

$$\frac{dm_{i,j}}{dt} = \dot{Y}_{i,j}\rho_g 4\pi r^2, \tag{9}$$

where i is the reactant gas species such as CO or H_2, ρ_g is the gas density, r is the particle radius. With the help of the reactant gas mass change, one is able to calculate the mass change of every layer and the product gas as

$$\frac{dm_{k,j}}{dt} = \frac{dm_{i,j}}{dt}\frac{\upsilon_k}{\upsilon_j}\frac{M_k}{M_j}, \tag{10}$$

in which k is either the layer species of the iron-ore pellet Fe_2O_3, Fe_3O_4, FeO, Fe or the product gas of H_2O or CO_2. The υ is the stoichiometric coefficient of the relative species, and M is the molar mass of relative species.

The chemical reaction resistance term $A_{i,j}$ can be expressed as

$$A_{i,j} = \left[\frac{1}{(1-f_j)^{\frac{2}{3}}}\frac{1}{k_j\left(1-\frac{1}{Keq_j}\right)}\right]_i \tag{11}$$

in which j represents the reduction layer, i the reducing gas,. k_j is the reaction rate constant for layer j and is determined as

$$k_j = k_0 \exp(\frac{-E_a}{RT}), \tag{12}$$

the values for the pre-exponential factor k_0, and the activation energy E_a can be found in literature[13]. f_j is the local fractional reduction of the relative layer that is calculated as

$$f_j = 1 - \left(\frac{r_j}{r_p}\right)^3. \tag{13}$$

The diffusivity resistance term $B_{i,j}$ can be calculated for the relative iron oxide component as [13]

$$B_{i,h} = \left[\frac{(1-f_m)^{\frac{1}{3}} - (1-f_h)^{\frac{1}{3}}}{(1-f_m)^{\frac{1}{3}}(1-f_h)^{\frac{1}{3}}} \frac{r_g}{D_h^{eff}}\right]_i, \tag{14}$$

$$B_{i,m} = \left[\frac{(1-f_w)^{\frac{1}{3}} - (1-f_m)^{\frac{1}{3}}}{(1-f_w)^{\frac{1}{3}}(1-f_m)^{\frac{1}{3}}} \frac{r_g}{D_m^{eff}}\right]_i, \tag{15}$$

$$B_{i,w} = \left[\frac{1-(1-f_w)^{\frac{1}{3}}}{(1-f_w)^{\frac{1}{3}}} \frac{r_g}{D_w^{eff}}\right]_i, \tag{16}$$

in which D_j^{eff} represents the effective diffusion coefficient of the relative layer.

2.1 Diffusion Coefficients

The diffusion of a gas through a porous medium, in this case the porous iron-ore pellet, depends on the molecular and Knudsen diffusions. If the Knudsen number, the ratio of the mean free path of the gas molecules to the pore diameter, is smaller than 0.1 molecular diffusion becomes predominant. If the Knudsen number is larger than 10, then Knudsen diffusion becomes prevalent [14, 15].

The Knudsen diffusion for diffusing species i, $D_{i,K}$ can be determined with [14, 15, 16]

$$D_{i,K} = \frac{\phi_{pore}}{3}\sqrt{\frac{8k_BNT}{\pi M_i}}. \tag{17}$$

where $k_B = 1.38066 \times 10^{-16 g \cdot cm/s^2 K}$ is the Boltzmann constant, and $N = 6.023 \times 10^2 3^{molecules/mol}$ is the Avogadro's constant, ϕ_{pore} is the pore diameter and M_i represents the molar mass of species i.

The effective Knudsen diffusion can be defined as a function of porosity, ε , and tortuosity, τ for layer j of the iron-ore particle with

$$D_{j,K}^{eff} = \frac{\varepsilon_j}{\tau_j} D_{i,K} \tag{18}$$

There are various diffusion coefficient correlations for binary molecular diffusion. The most common method is the *Chapman-Enskog* correlation, which is derived from the particle collision diameters and the Lennard-Jones potentials. Since for some gases the estimates for collision diameters or Lennard-Jones parameters are not available [14, 17], other empirical correlations have been proposed. A slightly better correlation

$$D_{i,j} = \frac{10^{-3} T^{1.75} \left(\frac{1}{M_i} + \frac{1}{M_j}\right)^{(1/2)}}{p \left[\left(\sum_i \nu_i\right)^{(1/3)} + \sum_j \nu_j^{(1/3)}\right]^2} \tag{19}$$

where M is the relative gas molar mass, and ν the diffusion volume of the specified species has been proposed by Fuller, Schettler and Giddings [16, 17]. The values for the diffusion volumes are defined in Table 1.

Table 1: Diffusion volumes for various species [17]

Atomic and Structural Diffusion Volume Increments			
C	16.5	H	1.98
O	5.48	N	5.69
Diffusion Volume of Simple Molecules			
H_2	7.07	N_2	17.9
O_2	16.6	Air	20.1
CO	18.9	CO_2	26.9
N_2O	35.9	H_2O	12.7

The diffusion coefficient in multicomponent mixtures is then calculated as [18, 19]

$$D_{i,m} = (1 - x_i) \left(\sum_{i \neq j} \frac{x_j}{D_{i,j}}\right)^{-1}, \tag{20}$$

in which x is the mole fraction. Just like the effective Knudsen diffusion coefficient, the effective diffusion coefficient for multicomponent mixtures is determined by multiplying the diffusion term with the ratio of porosity to tortuosity as

$$D_{j,m}^{eff} = \frac{\varepsilon_j}{\tau_j} D_{i,m}. \tag{21}$$

The total effective diffusion can thus be defined as

$$\frac{1}{D_j^{eff}} = \frac{1}{D_{j,m}^{eff}} + \frac{1}{D_{j,K}^{eff}}. \tag{22}$$

3 RESULTS

The CFD-DEM coupling library is extended to cover the SPM. This model is used to verify if the communication framework between the Eulerian and the Lagrangian sides. The communication of DEM and CFD works by first initializing the particles on the DEM side and transferring their information such as the locations and velocities to the CFD

side. This information is then used to localize the particles and determine the voidfraction, fluid density, temperature, drag force and the species concentration (mass fractions) at particle locations. These data are communicated back to the DEM side. The newly transferred data is then used to determine the particle movement, the change in particle size and change of gas concentrations for the new time step. After DEM calculations, the new data is transferred back to CFD side. This process continues until a specified amount of time steps have been computed.

A simple test case is developed, consisting of a single carbon particle that reacts with the reactant gas of O_2 with a user defined reaction rate constant. The test case results are verified by comparing the species mass balances. The particle reacts only with the O_2 present, and stops after the total amount of O_2 has been depleted. The mass change of the reactant and product gas species is investigated in relation to particle shrinking. The simulation results are compared with theoretical data that is calculated with the same species concentration as the simulation, which prove to be in a good agreement. The mass change of the gas species is illustrated depending on the time in Fig. 2.

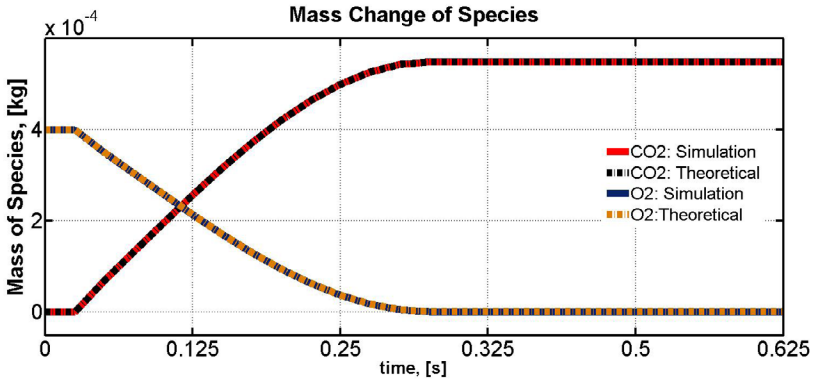

Figure 2: The change of mass of reacting gas species O_2 and product gas CO_2 depending on time.

After the communication framework has successfully been established, the USCM is implemented. At first, only the reaction resistance terms A_j is considered. An iron-ore pellet with diameter of 0.2 dm is placed in a rectangular domain with a volume of 375 m^3 and a cell volume of 1.80 m^3. The relative radii for hematite, magnetite and wustite layers are set to $0.3, 0.5$ and 0.6 respectively. The reactant gas CO reacts with the particle to produce CO_2. The fractional reduction of the relative layers with only the reaction resistance term is illustrated in Fig. 3a, and the shrinking of radii is illustrated in Fig. 3b.

The simulation is run for 3 seconds, however as the fluid velocity is practically zero, to make the reduction process faster the mass changes of the reactant gas, the pellet layer, and product gas are increased numerically with 10^4. As there is no flow, the Eulerian side is not affected by this scale up. As, the reduction of the layers with only the reaction

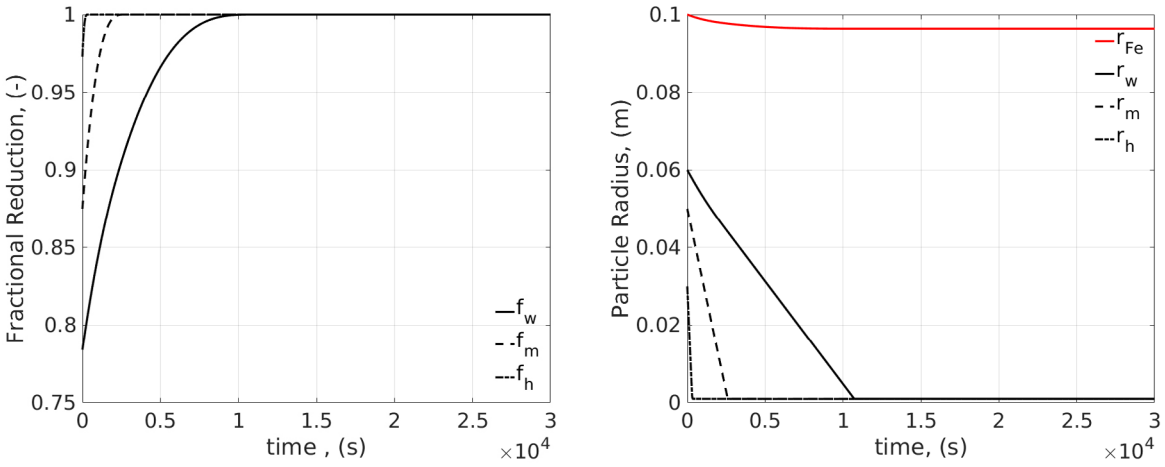

(a) The fractional reduction.

(b) The layer radii shrink.

Figure 3: The reduction of an iron-ore pellet with only the reactions resistance term.

resistance term proved successful results, the previously defined diffusion coefficient of FSG, Knudsen diffusion and the effective total diffusion coefficient is also added to the model. The particle properties that have been defined for the test case are defined in Table 2.

Table 2: The particle properties used in test case.

Parameter	Symbol	Value	Unit
Porosity	ϵ_p	15	%
Tortuosity	τ_p	3	(-)
Pore Diameter	d_p	3.61×10^{-9}	m

It is clear that the time of layer reduction increases drastically with the activation of the diffusion coefficient resistance term. With the same amount of upscaling not even the hematite core is reduced as illustrated in Fig. 4a. An upscaling of 10^8 is carried out, to see the total fractional reduction with the diffusion resistance term. It can be seen that the particle totally reduces first when at 2.7×10^8 seconds real time as illustrated in Fig. 4b.

4 CONCLUSION AND OUTLOOK

The mathematical models representing the fluid-solid chemical reactions have been implemented into the DEM library, so that the CFD-DEM method can be used to investigate the reduction of iron-ore inside the fluidized bed reactors. First, the SPM has been

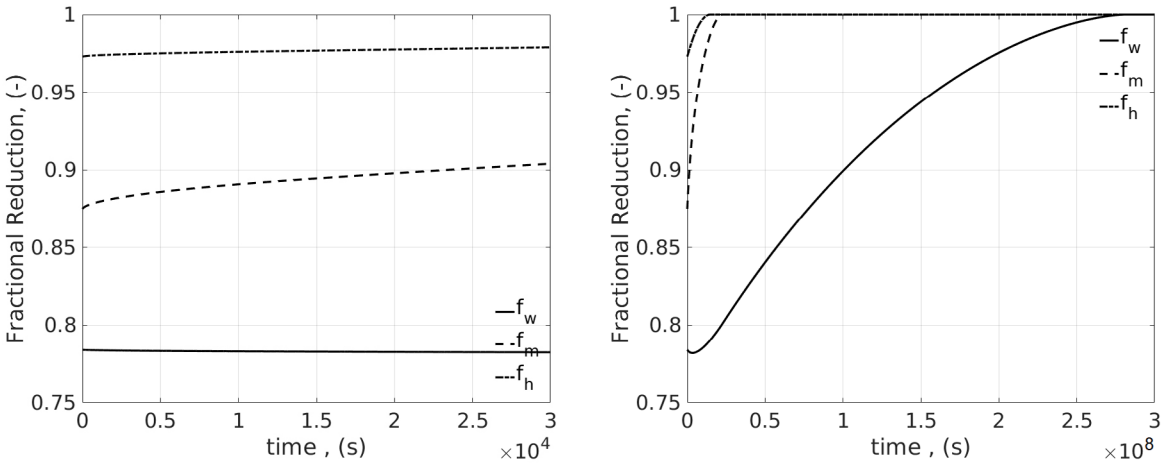

(a) Scale up of 10^4. (b) Scale up of 10^8.

Figure 4: The fractional reduction of an iron-ore pellet with the diffusion resistance term and various scale up factors.

implemented and verified. A test case is constructed to check the communication framework between CFD and DEM sides. As the communication was successfully established, the framework was expanded to cover the three-layered USCM. The USCM is considered as a valid model to represent the reduction of iron-ore. Simulations have been carried out that considered only the reaction resistance terms. It has been seen that the particle layers reduce in a reasonable manner. Afterwards, the diffusion resistance term has been added to the equations. With the addition of the diffusion resistance term, the time it took for the layers to shrink increased greatly.

Further research involves implementing the mass transfer coefficient to the coupling library, considering the effects of different pore diameters, particle porosities and tortuosities. After a thorough investigation and comparison with literature, a coarse-graining of the CFD-DEM approach will be carried out and even maybe a combination of the TFM and DPM for industrial scale simulations.

REFERENCES

[1] Donskoi, E., and McElwain, D. L. Estimation and modeling of parameters for direct reduction in iron ore/coal composites: Part I. Physical parameters. *Metallurgical and Materials Transactions B.* **34(1)**:93–102. (2003).

[2] Turkdogan, E. T., and R. J. Fruehan. Fundamentals of iron and steelmaking. *The Making, Shaping and Treating of Steel, Steelmaking and Refining Volume, 11th ed., RJ Fruehan, ed., AISE Steel Foundation, Pittsburgh* **11**:125–126.

[3] Schenk , J. L. Recent status of fluidized bed technologies for producing iron input materials for steelmaking. *Particuology.* **9(1)**:14–23. (2011).

[4] Habermann, A., Winter, F., Hofbauer, H., Zirngast, J., and Schenk, J. L. An experimental study on the kinetics of fluidized bed iron ore reduction. *ISIJ international* **40**:935–942.

[5] POSCO and Primetals Technologies. *The FINEX Process.* (2015).

[6] Plaul, F. J., C. Bhm, and J. L. Schenk. Fluidized-bed technology for the production of iron products for steelmaking. *Journal of the Southern African Institute of Mining and Metallurgy* **109.2**:121–128. (2009).

[7] Schneiderbauer, S. and Pirker, S. Filtered and Heterogeneity-Based Subgrid Modifications for Gas-Solid Drag and Solid Stresses in Bubbling Fluidized Beds. *American Institute of Chemical Engineers.* **3**: 839–854. (2014).

[8] van der Hoef, M. A. et al. Multiscale Modeling of Gas-Fluidized Beds. *Advances in Chemical Engineering* **31**:65–149. (2006).

[9] Goniva, C., et al. Influence of rolling friction on single spout fluidized bed simulation. *Particuology.* **10**:582–591. (2012)

[10] Schneiderbauer, S. et al. A Lagrangian-Eulerian Hybrid Model for the Simulation of Poly-disperse Fluidized Beds: Application to Industrial-scale Olefin Polymerization. *submitted to Powder Technology.* (2016).

[11] Levenspiel, O. *Chemical Reaction Engineering.* Oregon State University Book Stores, Inc. (1989).

[12] Tsay, Q. T., Ray, W. H. and Szekley, J. The modeling of hematite reduction with hydrogen plus carbon monoxide mixture. *AIChE J* **22**:1064–1076. (1976).

[13] Valipour, M.S. and Hashemi,M.Y. Motamed and Saboohi, Y. Mathematical modeling of the reaction in an iron ore pellet using a mixture of hydrogen, water vapor, carbon monoxide and carbon dioxide: an isothermal study. *Advanced Powder Technology* (2006) **17**:277–295.

[14] Cussler, E.L. *Diffusion: mass transfer in fluid systems*. Cambridge University Press. (2009).

[15] He, W. Lv, W. and Dickerson, J. *Gas Transport in Solid Oxide Fuel Cells*. Springer. (2014).

[16] Welty, J. R., Wicks, C. E., Rorrer, G. and Wilson, R. E. *Fundamentals of Momentum, Heat, and Mass Transfer*. John Wiley & Sons. (2009).

[17] Fuller, E. N., Schettler, P. D. and Giddings, J. C. A new method for prediction of binary gas-phase diffusion coefficients.*Industrial and Engineering Chemistry* (1966) **16**: 18-27.

[18] Elnashaie, S. S. *Modelling, simulation and optimization of industrial fixed bed catalytic reactors*. Vol. 7. CRC Press, 1994.

[19] Wilke, C. R., and Pin, C. Correlation of diffusion coefficients in dilute solutions. *AIChE Journal* (1955) **1**:264–270.

V International Conference on Particle-based Methods – Fundamentals and Applications
PARTICLES 2017
P. Wriggers, M. Bischoff, E. Oñate, D.R.J. Owen, & T. Zohdi (Eds)

IDENTIFICATION OF BLOCK-LIKE MOVEMENT IN COHESIVE AND NON-COHESIVE SPOUTED BED OPERATIONS

ALIJA VILA[1], THOMAS LICHTENEGGER[2], STEFAN PUTTINGER[2] AND STEFAN PIRKER[2]

[1] K1-MET Metallurgical Competence Center (K1-MET)
4020 Linz, Austria
alija.vila@k1-met.com, www.k1-met.com

[2] Department of Particulate Flow Modelling (PFM), Johannes Kepler University (JKU)
4040 Linz, Austria
www.jku.at/pfm

Key words: Gas-solid flows, Spouted bed, Cohesive particles, CFD-DEM

Abstract. Spouted beds are widely used in the chemical and process industries for a large variety of processes. Good understanding of the transport phenomena in these systems is of great importance to improve the design and scale-up procedure [1]. Gas-solid flow heterogeneities, such as particle clustering can have a significant impact on interphase transport properties. The focus of the research is on the interaction between solid particles and interstitial gas. The investigation is realized by means of non-resolved CFD-DEM simulation and the experimental measurement of the spouted bed.

Experimental measurements are conducted in a lab-scale pseudo-2D spouted bed test facility. The cohesive material is substituted by non-cohesive particles with an added moister. With wet particles, it is expected to observe the effects related to the particle cohesion, such as channeling and formation of particle clusters. The main purpose of the experiment is to obtain the information on the overall dynamics of the spouted bed in cohesive and non-cohesive flow regimes. The recorded images were processed with DaVis Particle Image Velocimetry (PIV) post-processing tool.

Numerical CFD-DEM model is developed to investigate the behavior of non-cohesive particles in a spouted bed. Particles are modeled with the Discrete Element Method (DEM), where one integrates Newton's law of motion for each particle under the forces due to the surrounding particles. This method is based on the use of an explicit numerical scheme in which the interaction of the particles is monitored contact by contact [2, 3]. Coupled CFD-DEM simulations allow the incorporation of single-particle properties and modifications of their interaction and as such are suitable for this study. Numerical simulation can be validated by the experimental measurement. Future work will deal with cohesive forces between the particles.

1 INTRODUCTION

Fluidized and spouted beds have a wide industrial application such as drying, combustion, granulation, gasification, coating etc. These applications take advantage of useful properties such as good solid-fluid contact characteristics. While the conventional fluidized bed uses a porous plate distributor, typical spouted bed generally involves a single central orifice. A narrow jet is injected through the orifice which leads to a flow pattern with two distinct regions: a dilute region with upward fluid and particle movement and a dense region including slower downwards moving particles. A spouted bed can operate with larger particle size and more predictable particle circulation compared to a fluidized bed [4].

In industrial applications, cohesion between the particles is a very common occurrence. Cohesive effects lead to the formation of heterogeneities in the particle distribution. In rapid distortion regime of non-cohesive powders with instantaneous inter-particle collisions, such heterogeneities might establish in the form of particle clusters. In cohesive powders where long enduring inter-particle contacts prevail, it might lead to a formation of block-like structures divided by gas tunnels.

Experimental studies conducted by a number of researchers had shown liquid bridge forces having considerable effects on the flow behavior. These studies found that effects of liquid phase include a decrease of the minimum spouted velocity, changes of flow patterns and pressure drop [5, 6, 7].

Due to the difficulties in measurement and control of the cohesive force experimentally, there is a motivation to approach the issue by means of numerical simulation. Coupled approach of CFD and DEM can provide detailed information about behavior on the particle scale. As such, numerical simulations can give valuable information in the analysis of the cohesive effects and their influence on highly dynamic particulate flows [1, 2, 3].

2 PHYSICAL MODELING

Experimental measurements are conducted in a lab-scale pseudo-2D spouted bed test facility. The bed column has a cross section of 150 mm x 20 mm. To allow flow visibility, the column is made of glass front and back plates with aluminum side walls. Air inlet in located in the center of the bed with the width over the whole bed depth. Particles used in the experiment are soda-lime glass spheres, with 2 mm mean diameter and bulk density of 1.5 kg/dm^3. Thus, they belong to particle type D of Geldart classification. Background illumination is achieved with five fluorescent tubes behind the diffusing plate and it provides a good contrast between the particles and the gas phase.

Images are recorded with a Photron Fastcam at 250 frames per second at the resolution of 640 x 928 pixels and exposure time of 1/500 s. The setup allows 9.66 seconds of measurement and results in 2403 images before the internal memory of the camera is full. For each experimental run, an initial snapshot of the bed is captured and initial bed height is calculated. For more details on the set-up, one can refer to the previous work

on flow regime detection in spout-operated fluidized beds [8].

Deionized water is added and mixed with the particles prior to the insertion in the column. Such practice can not ensure the information about the exact amount of the moisture, or the distribution inside the bed. Due to the unsteady nature of the experiment, the water drops would have to be continually added to achieve a steady state. However, this setup should be sufficient as the measurement time is less than 10 seconds, so the change in the moisture content is negligible.

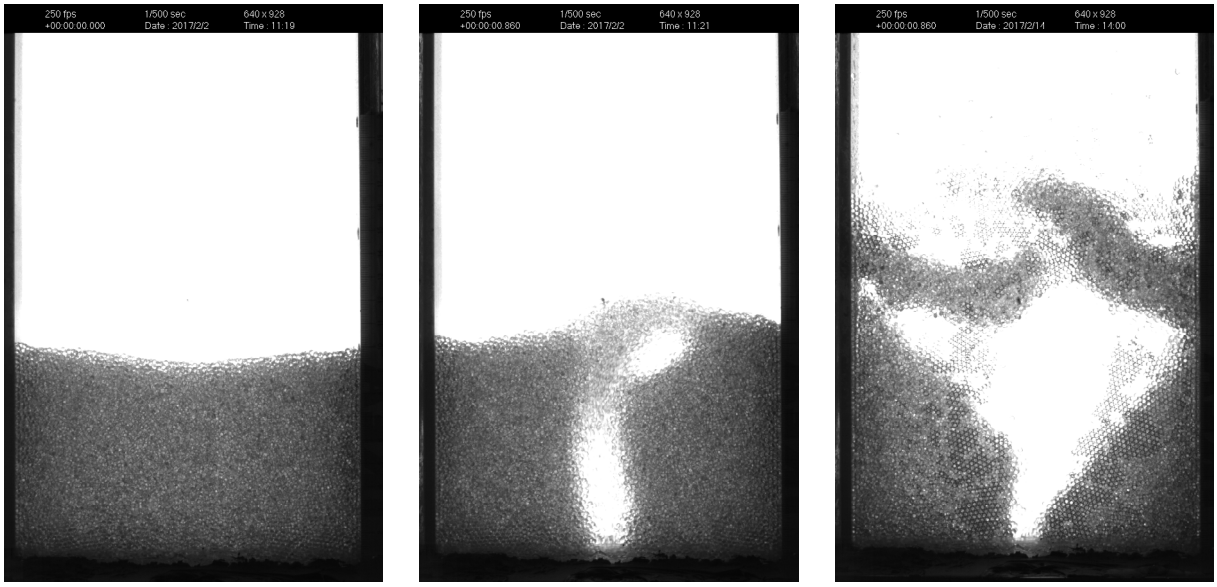

(a) Initial bed configuration (b) After 0.86 s with dry particles (c) After 0.86 s with wet particles

Figure 1: High-speed camera snapshots

Digital image post-processing is done in MATLAB to obtain the mean image and pixel variance image from the series of recorded snapshots. These images provide a reproducible result that can be compared with previous measurements. Image processing also allows the identification of different zones inside the bed. In the mean images, it is possible to observe central spout, blurred moving annulus region, and sharp dead zones.

Since the particles in question are of type D, with relatively large diameter, PIV method can be applied to investigate the particle phase dynamics. The results of tracking algorithm represent the velocity field of the particles phase [9]. Multi-pass PIV time series operation was performed on a windows sizes of 128x128 and 32x32 with an overlap of 50% and 70%, respectively. The geometric mask is defined to avoid the unphysical vectors appearance on the edges and algorithmic thresholding mask to increase the contrast between the fluid and particle phase.

3 NUMERICAL MODELING

In the CFD-DEM model, the gas-phase dynamics are obtained from the volume-averaged Navier-Stokes equations in Computational Fluid Dynamics (CFD) method. The motion of every individual particle is calculated from Newton's second law in the Discrete Element Method (DEM) [1].

3.1 Fluid phase

The equation for mass and momentum conservation are used to compute the motion of the fluid and are given by:

$$\frac{\partial}{\partial t}(\varepsilon\rho_f) + \nabla\cdot(\varepsilon\rho_f\vec{u}_f) = 0 \tag{1}$$

$$\frac{\partial}{\partial t}(\varepsilon\rho_f\vec{u}_f) + \nabla\cdot(\varepsilon\rho_f\vec{u}_f\vec{u}_f) = -\varepsilon\nabla p + \nabla\cdot(\varepsilon\bar{\bar{\tau}}) + \vec{F}_d + \varepsilon\rho_f\vec{g} \tag{2}$$

where ε is the void fraction, ρ_f is the fluid density, $\vec{u}_f$ is the fluid velocity, p is the static pressure, $\bar{\bar{\tau}}$ is the fluid viscous stress tensor, $\vec{F}_d$ is the drag force between the particles and fluid and $\vec{g}$ is the gravitational acceleration. Correlation obtained from Lattice-Boltzmann Method (LBM) was used for the drag force [10].

3.2 Particle phase

Newton's second law of motion is solved for each particle separately in the DEM calculation. Particles are modeled as spheres that interact with each other and the surrounding fluid:

$$m_i\frac{d\vec{v}_{p,i}}{dt} = \vec{F}_i^{(p-p)} + \vec{F}_i^{(p-f)} + \vec{F}_i^{e} \tag{3}$$

where $\vec{F}_i^{(p-p)}$ is the particle-particle contact force, $\vec{F}_i^{(p-f)}$ is the force related to the interaction of particles with a fluid, as the drag force and the pressure gradient.

The force on the particle i due to the surrounding particles j have normal $\vec{F}_{i,j}^{(n)}$ and tangential $\vec{F}_{i,j}^{(t)}$ component described with spring-dashpot model [2].

$$\vec{F}_i^{(p-p)} = \sum_{j\neq 1}(\vec{F}_{i,j}^{(n)} + \vec{F}_{i,j}^{(t)}) \tag{4}$$

Granular hooke/stiffness model is included to describe contact forces between particles. When the distance between the particles is less than their contact distance (sum of two particle diameters), the correlation for the frictional force between two granular particles is used.

$$\vec{F} = (k_n\vec{\delta}_{n_{ij}} - \gamma_n\vec{v}_{n_{ij}}) + (k_t\vec{\delta}_{t_{ij}} - \gamma_t\vec{v}_{t_{ij}}) \tag{5}$$

where $\delta_{n_{ij}}$ is the overlap distance of two particles, k_n the elastic constant for normal contact, k_t the elastic constant for tangential contact, γ_n the viscoelastic damping constant for normal contact, γ_t the viscoelastic damping constant for tangential contact, $\delta_{t_{ij}}$ the tangential displacement vector between two spherical particles, $v_{n_{ij}}$ the normal component of the relative velocity of the two particles and $v_{t_{ij}}$ is the tangential component of the relative velocity of the two particles. The coefficients k_n, k_t, γ_n, γ_t are calculated from the material properties.

3.3 Model setup

The simulation is set up with the geometry and conditions similar to the one in the experiment. The geometry of the modeled pseudo-2D spouted bed matches the test facility cross-section of 150 mm x 20 mm, and a cross-section of 2 mm x 20 mm. The size of the grid must be sufficiently fine to obtain accurate fluid field, but also coarse enough since non-resolved CFD-DEM requires cell larger than particles [13, 14, 15, 16]. The width of the orifice matches the size of the smallest cell in the domain with 2 mm, what is also the size of a single particle. Due to the limitations of the CFD-DEM method, it is not possible to use a finer grind on the inlet for the particles in question. The domain is discretized into 35 x 110 x 6 cells with expansion ratios, as shown in Figure 1.

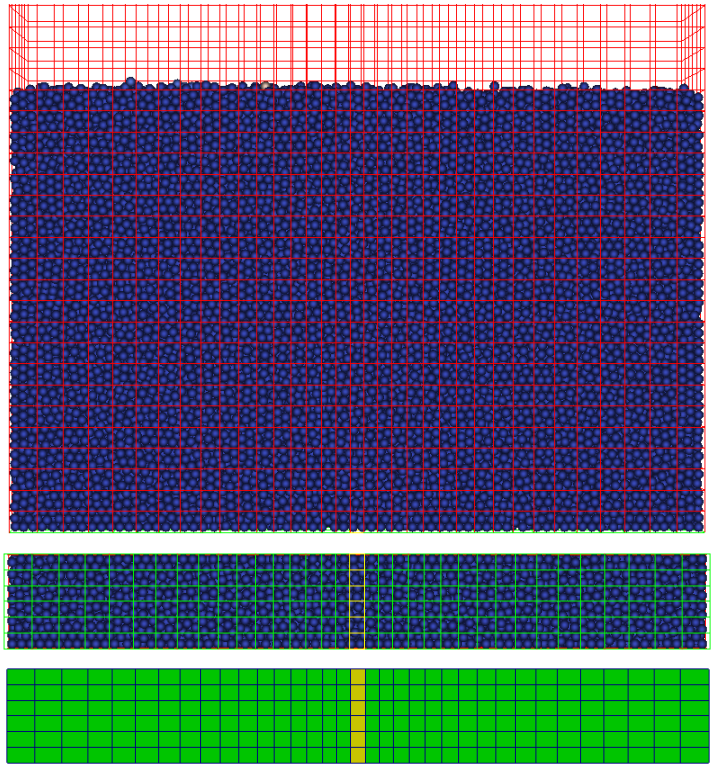

Figure 2: Numerical grid. Front wall and inlet views.

Physical and numerical parameters are defined for two types of the wall so that the particle-wall properties can be modified for sapphire glass front and back wall and aluminum side walls. For additional details on simulation parameters and operating conditions, one can refer to a previous work on CFD-DEM fluidized bed simulation [13].

For particle Reynolds number over 1000, the minimum fluidization velocity can be expressed as [4]:

$$U_{mf}^2 = \frac{d_p(\rho_p - \rho_f)g}{24.5\rho_f} \tag{6}$$

Equations (1), (2) are solved with the PISO algorithm [11] for incompressible flow. Equation (3) is solved with Verlet integration [12] with DEM.

Solid particles are randomly generated with an established mass rate and allowed to settle under gravity to initial bed height $H_0 = 100$ mm. The total number of inserted particles is 42016. With the insertion done, the restart file is created and coupled CFD-DEM simulation can be run. A gas flow is introduced from the inlet with a velocity of $U_{in} = 85$ m/s. On the walls, zero pressure gradient boundary condition is applied, with velocities fixed at 0 m/s. Fixed atmospheric pressure is applied to the outlet. Coupled CFD-DEM simulation of the spouted bed is carried out for 10 seconds of real time what matches the experimental investigation.

4 RESULTS

There is a noticeable visual difference between the results obtained for cohesive and non-cohesive particle-gas flow regimes. Dry particle experiment showed spouted bed behavior with periodic jet fluctuations. Interstitial liquid adds cohesion to the particles, what leads to the formation of channels and fluid flows through preferred path. The movement of the spout it very limited compared to the case with dry particle and observed velocities are lower. The height of the expanded bed is larger with wet particles and bigger void can be observed inside the bed.

It should be noted that particles moving in the dilute spout region might not be detected with the camera, even with chosen low exposure time. Vector values obtained by the post-processing PIV multi-pass time series operation show the dynamics of the dense annular region, fountain and bed surface regions.

Every fourth recorded image is exported to DaVis PIV post-processing tool and the time-step between images is adjusted accordingly. The software gives values for 8960 vectors in each of the 600 frames, resulting in a 3D matrix with dimensions 80x112x600. The results are exported to MATLAB where further post-processing is done in order to find a quantifiable difference between cohesive and non-cohesive particle-gas flows.

The results are analyzed with histogram distribution divided into 100 bins. Values outside of the particle bed are filtered out in order to reduce a redundant number of zero velocity vectors. However, most of the values fall into low-velocity range and in Figure 5. bar graphs are plotted with logarithmic y-axis for better transparency. Histograms

are standardized with a total number of obtained values to compare the two cases. The comparison is made for two parameters: total magnitude and the horizontal component of velocity vectors. Measurements of the dry particle-gas flow gave a wider range of the velocities and more uniform distribution.

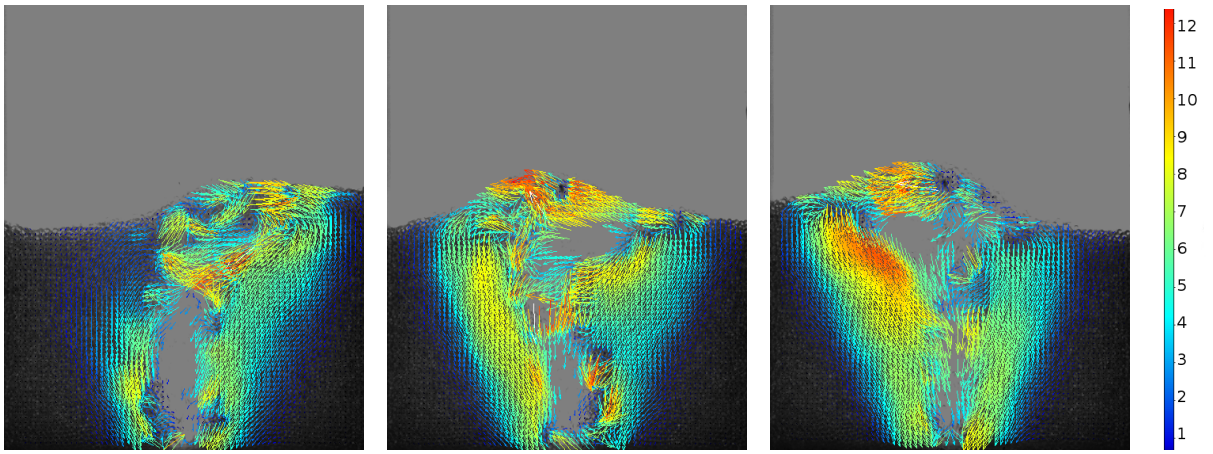

Figure 3: PIV post-processing snapshots for dry particle experiment. The observed pixel displacement range is shown in the scale.

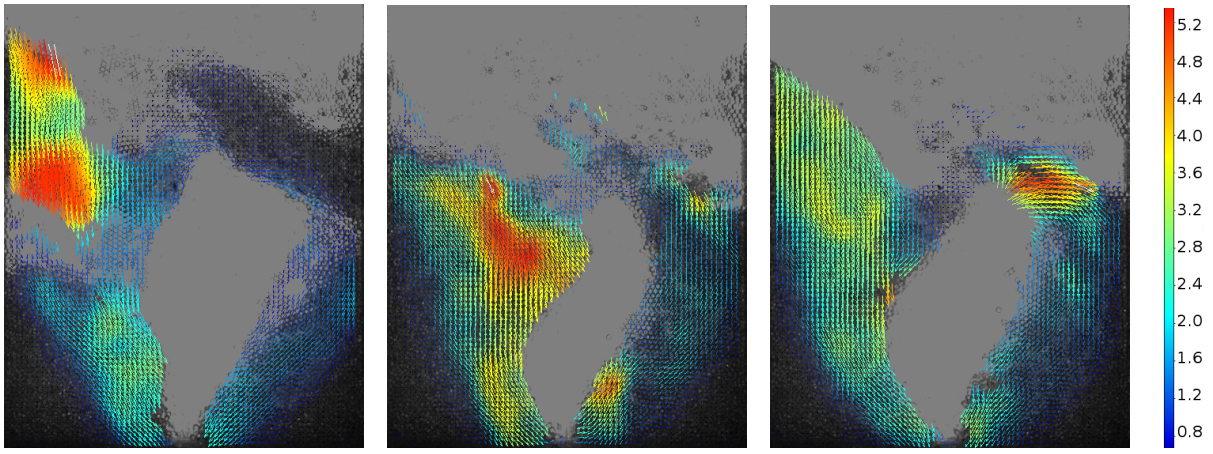

Figure 4: PIV post-processing snapshots for wet particle experiment. The observed pixel displacement range is shown in the scale.

The histogram distribution is made for total velocity magnitude U and horizontal component of the velocity U_x. One bin represents the values in range of 0 - 1.4 px/s and 0 - 0.75 px/s, respectively. The number of vectors inside each bin is tracked for all the processed frames. Autocorrelation process is applied to vector count function for further investigation of the distinct regimes. It was expected to detect a significantly

different time lag of the function before crossing the 0 value. The manner in which the autocorrelation function approaches the 0 value shows some distinctive features for both regimes. However, the difference between sample autocorrelation of the function through the first bin is not too prominent. It should be noted that the investigated function of vector count in the middle of the range for dry particle bed has very strong fluctuations, so autocorrelation process does not result in a clear figure.

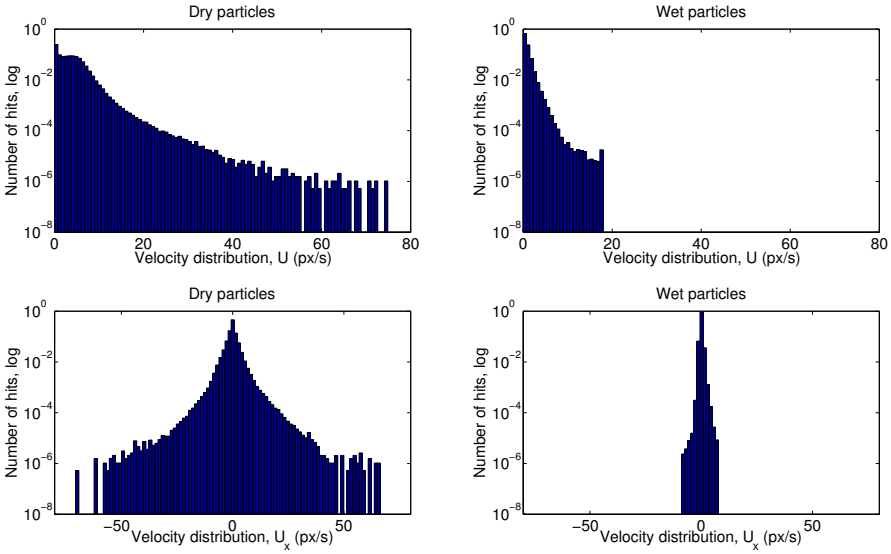

Figure 5: Histogram distribution of the velocity ranges for both regimes.

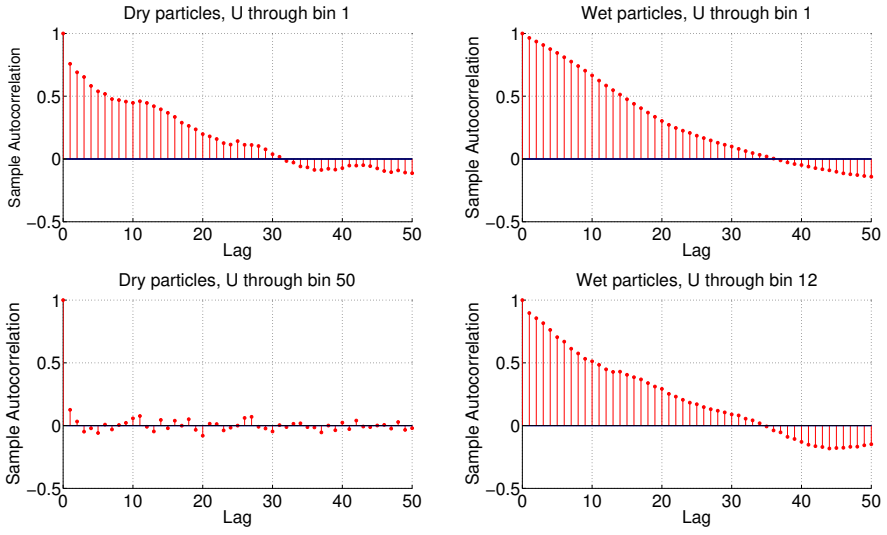

Figure 6: Autocorrelation function of the vector number through 50 frames.

With autocorrelation function not showing a sufficiently clear difference between the cohesive and non-cohesive experiment, a different method has to be applied. Intersections between two functions are tracked to better capture the parameters related to cohesive flow structures. One function being the mean number of vectors in the chosen bin and the other one a number of vectors per frame.

A number of consecutive frames between the intersections can be related with a block-like movement. There is a noticeable difference in chosen parameters obtained from dry and wet particle experiment. A relative number of intersections between referred functions was significantly lower in the cohesive particle-gas flow, with a higher mean number of consecutive frames between intersections.

Table 1: Parameteres related to a block-like movement.

Function	Relative number of intersections	Frames between intersections (mean)
Vectors in first bin (dry)	0.18	5.52
Vectors in middle bin (dry)	0.42	2.36
Vectors in first bin (wet)	0.035	26.14
Vectors in middle bin (wet)	0.12	8.28

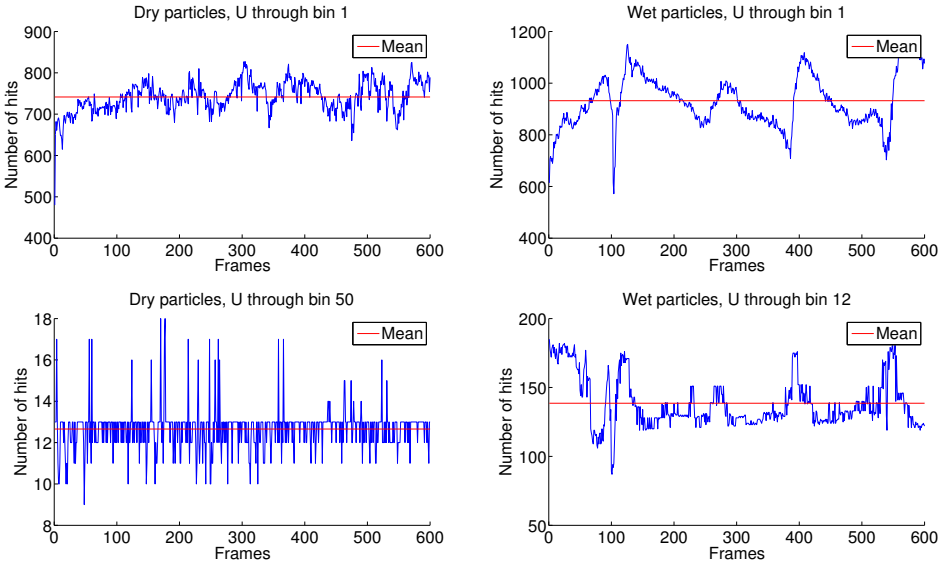

Figure 7: Number of vectors inside the first and the middle bin through the processed frames. Middle of velocity range is represented by the bin number 50 for the dry particles and the bin number 12 for the wet particles.

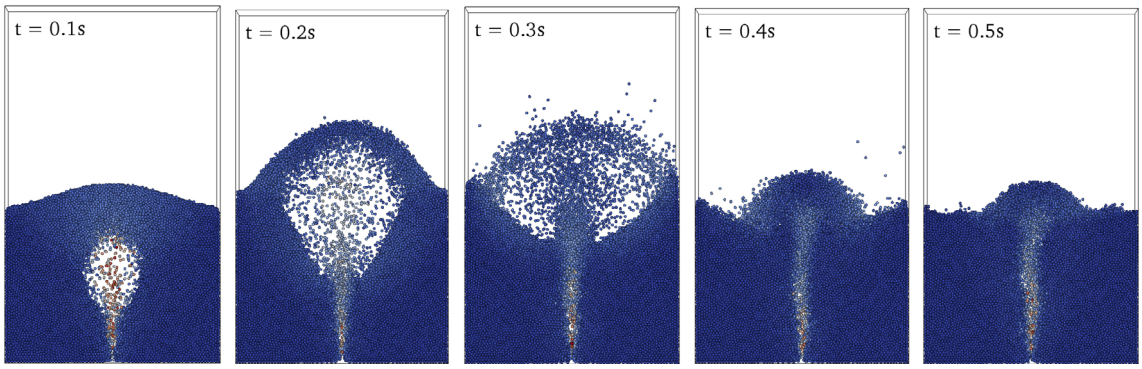

Figure 8: Expansion of a spouted bed predicted by the numerical simulation.

Dry particle experiment can serve as a good validation of the described CFD-DEM model since it is conducted under very similar conditions. The snapshots in Figures 8. and 9. show values of the void fractions inside the bed and the particle velocities. The simulated flow pattern is in good agreement with experimental measurement. As demonstrated, current simulation can predict the behavior of non-cohesive particles in the spouted bed.

Previously described post-processing procedure was applied to images obtained by the numerical simulation. Processed data were compared with the experimental results and good agreement can be found with similar parameters related to a block-like movement.

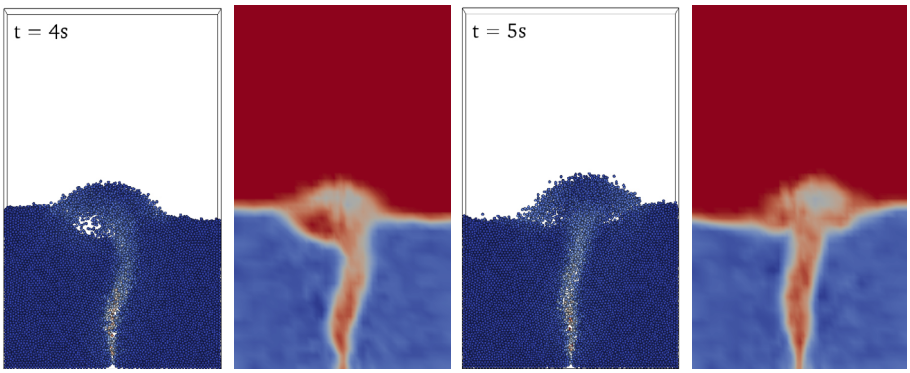

Figure 9: Development of a spouted bed predicted by the numerical simulation.

5 CONCLUSION AND OUTLOOK

In the paper, experimental set-up and post-processing methods are described, together with a developed CFD-DEM spouted bed simulation. The goal of the experiment was to investigate the influence of particle cohesion on the flow behavior. In order to obtain an indicator for block-like movement related to particle cohesion, a new methodology was developed. Non-cohesive particle experiment also serves as a validation of the numerical model.

The experimental measurement showed a significant difference in the solid-gas flow dynamics between the setups with cohesive and non-cohesive particles. Particle image velocimetry operation provided velocity vector values that show the difference between the regimes. Block-like movement of the cohesive particles was detected with PIV method and quantified with post-processing scripts.

The developed CFD-DEM numerical model showed a good agreement with the experimental results. Future work will deal with cohesive forces between the particles. There have been some proposed models to quantify the cohesive interaction [17]. Furthermore, the goal is to develop a new drag model to address the phenomena of the block-like movements and formation of gas tunnels. Such model should provide realistic results that can give a better comparison with measurements.

6 ACKNOWLEDGEMENT

The authors want to acknowledge the financial support from Austrian Federal Ministry of Economy, Family and Youth, and the Austrian National Foundation for Research, Technology and Development.

REFERENCES

[1] Deen, N.G., Van Sint Annaland, M., Van der Hoef, M.A. and Kuipers, J.A.M. Review of discrete particle modeling of fluidized beds. *Chemical Engineering Science*, 62: 28 44, 2007.

[2] Cundall, P.A. and Strack, O.D.L. A discrete numerical model for granular assemblies. *Geotechnique*, 29(1): 4765, 1979.

[3] Tsuji, Y., Kawaguchi, T. and Tanaka, T. Discrete particle simulation of two-dimensional fluidized bed. *Powder Technology*, 77: 79-87, 1993.

[4] Epstein, N. and Grace, J.R. Spouted and Spout-Fluid Beds: Fundamentals and Applications. *Cambridge University Press*, 2010.

[5] Nagahashi, Y., Epstein, N, Grace. J.R., Asako, Y. and Yokogawa A. Effect of cohesive forces on fluidized and spouted beds of wet particles. *Can. J. Chem. Engi.*, 84: 527-531, 2006.

[6] Passos, M.L. and Mujumdar, A.S. Spouting Enhancement by Addition of Small Quantities of Liquid to Gas-Spouted Beds. *Powder Technology*, 110: 222-238, 2000.

[7] Bacelos, M.S., Passos, M.L. and Freire, J.T. Effect of interparticle forces on the conical spouted bed behavior of wet particles with size distribution. *Powder Technology*, 174: 114-126, 2007.

[8] Puttinger, S., von Berg, L., Schneiderbauer S. and Pirker, S. Bed zone and flow regime detection in spout-operated fluidized beds by digital image processing and pressure probes. *8th World Conference on Experimental Heat Transfer, Fluid Mechanics, and Thermodynamics*, 16-20, 2013.

[9] Puttinger, S., Holzinger, G. and Pirker, S. Investigation of highly laden particle jet dispersion by the use of a high-speed camera and parameter-independent image analysis. *Powder Technology*, 234: 46-57, 2013.

[10] Beetstra, R., Van der Hoef, M.A. and Kuipers, J.A.M. Drag force of intermediate Reynolds number flow past mono- and bidisperse arrays of sphere. *AIChE J.*, 53: 489-501, 2007.

[11] Issa, R.I. Solution of the implicitly discretised fluid flow equations by operator-splitting. *J. Comput. Phys.*, 62: 40-65, 1986.

[12] Verlet, L. Computer "experiments" on classical fluids. I. Thermodynamical properties of Lennard-Jones molecules. *Phys. Rev.*, 159: 98, 1967.

[13] Lichtenegger, T., Peters, E.A.J.F., Kuipers, J.A.M. and Pirker, S. A recurrence CFD study of heat transfer in a fluidized bed. *Chemical Engineering Science*, 2017.

[14] Lichtenegger, T. and Pirker, S. Extremely fast simulations of heat transfer in fluidized beds. *Proceedings of the 12th International Conference on CFD in the Oil & Gas, Metallurgical and Process Industries, Trondheim* , 2017.

[15] Hoomans, B.P.B., Kuipers, J.A.M., Briels, W.J. and van Swaaij, W. Discrete particle simulation of bubble and slug formation in a two-dimensional gasfluidised bed: a hard-sphere approach. *Chemical Engineering Science*, 51: 99-118, 1996.

[16] Link, J., Cuypers, L.A., Deen, N.G. and Kuipers, J.A.M. Flow regimes in a spoutfluid bed: A combined experimental and simulation study. *Chemical Engineering Science*, 60: 3425-3442, 2005.

[17] Xu, H., Zhong, W., Yuan, Z. and Yu, A.B. CFD-DEM study on cohesive particles in a spouted bed. *Powder Technology*, 314: 377-386, 2017.

V International Conference on Particle-based Methods – Fundamentals and Applications
PARTICLES 2017
P. Wriggers, M. Bischoff, E. Oñate, D.R.J. Owen, & T. Zohdi (Eds)

NUMERICAL ANALYSIS OF DEBRIS-FLOW INTERACTION WITH OPEN BARRIERS

MADDALENA MARCHELLI[1], ALESSANDRO LEONARDI[2] AND MARINA PIRULLI[1]

[1] Polytechnic University of Turin
Corso Duca degli Abruzzi, 24 - 10129 Torino, Italy
maddalena.marchelli@polito.it - marina.pirulli@polito.it

[2] Idrostudi Srl
Area Science Park, Loc. Padriciano 99, 34149 Trieste, Italy
alessandro.leonardi.ing@gmail.com

Key words: Granular Materials, DEM, Debris Flow, Barrier, Slit Dam

Abstract. Debris flows are fast gravity-driven flows consisting of multiple interacting phases. Due to their rapid movement and destructive power, structural mitigation measures have become essential in order to prevent extensive damage to property and life. Among these structures, rigid barriers constitute an efficient system of mitigation, which induces sediment deposition in case of an event. The optimal design of these structures requires the impact force estimation, which has recently become a crucial issue. Because of this, numerous experimental and numerical investigations have been carried out in recent years concerning debris flow and their impact energy on rigid closed barriers [1]. However, there is a lack of information in the framework of rigid open barriers, especially for what concerns the influence of the outlet geometry. In this regard, many studies have examined the jamming of a single-outlet silo [2], where the mass discharges in the direction of gravity, but the jamming of particles on an inclined slope has not been sufficiently investigated yet. The present numerical study investigates the formation of arching behind an open barrier that partially arrests the flow of particles on an inclined channel. The nature of jamming, and the impact energy on the barrier are examined using DEM simulations for a fixed discharged mass, using different outlet sizes and inclines. The applied model is an improvement of the LBM-DEM code developed by Leonardi et al. [3]. Static friction is implemented with the spring-dashpot linear model and a directional constant torque model is included in order to describe rolling resistance due to elastic deformation and the effect of non-spherical particle shape. The resulting force and momentum at the flow base are analysed in detail together with the kinetic energy and the distribution of particles in the slit. The dynamic impact of the solid component alone is analysed in order to rationalize the design of open barriers. Indeed numerical examples show that a single

outlet could jam with a probability that decreases with the slope and the outlet size, but two adjacent outlets do not necessarily jam in the same configuration.

1 INTRODUCTION

Much research in recent years focuses on debris flow, recognizing it as one of the most devastating landslide phenomenon, in terms of loss of life and damage to structures and infrastructures. Debris flows are a mixture of water and non-plastic coarse material that flow in a steep channel [4]. Their destructive potential is due to the absence of premonitory signs, the extremely high velocity ($0.05 - 20$ m/s), the erosive capability and the long travel distance even on gentle slopes. In this perspective, the design of mitigation structures as countermeasures has become of great interest. Among these structures, the present study focuses on open rigid barriers, which constitute as efficient system for reducing kinetic energy, trapping sediment, and causing material deposition. Recently, more and more numerical and experimental investigations have been carried out in the frame of studying debris flow impact on rigid closed barrier [5, 1, 6]. Nevertheless, insufficient informations are available on open rigid barriers. In particular the influence of the outlet size on the trapping efficiency remains almost unstudied [7]. In this regard, many studies have examined the jamming of a single-outlet silo [8, 9, 2, 10, 11, 12], or a granular pile [13, 14], where the mass discharges in the direction of gravity. In those cases the granular material can generate bridges or arches, i.e. stable collective structures comprising several grains which can sustain the weight above them [15]. Arches can cause granular jamming in a fixed configuration that is mechanically stable, which results in a temporary or permanent clogging of the outlets of a barrier thus trapping the material behind it. Notwithstanding its importance for the retainment mechanism, the jamming of particles, and the formation of arches behind barriers built along an inclined plane, have not been sufficiently investigated yet.

The purpose of this work is to study arch formation behind a barrier, which in turn is a key factor for determining its trapping capability, and the impact energy exerted on the barrier itself. To achieve such goals, simulations are performed using a DEM model, using a fixed discharging mass treated as an assembly of rigid spheres with deformable contacts.

Real debris flows have a complex multi-phase nature, where sediments are mixed with an ambient fluid [4]. A complete description of this is outside of the scope this paper, which instead focuses on the different role played by the barrier outlet size and the slope inclination. The model is an improvement of the LBM-DEM code developed by Leonardi et al. [3], and a new and more sophisticated friction model is tested. Static friction is implemented with the spring-dashpot linear model and a directional torque model is included to consider both elastic deformation effect and non-spherical particle shape.
This paper is organized as follows. A brief description of the model applied is introduced

in Sect. 2. In this section, constitutive parameters, initial condition and geometry of the analyses are specified. In Sect. 3 the main features of numerical results are illustrated. In Sect. 4 the role played by the variables and the outcomes are discussed. Finally in Sect. 5. conclusions and future perspectives on multiple outlets barrier are proposed.

2 THE DEM APPROACH AND SIMULATIONS

2.1 The DEM approach

Numerical simulations have been performed by employing the LBM-DEM code developed by Leonardi et al. [3]. This code has been improved by introducing rolling and static sliding friction, i.e. the resisting forces to sliding motion between two surface in contact. In the DEM model framework these forces arise when a particle-particle or particle-wall collision occurs. The linear dashpot model idealizes the contact as a parallel connection with a spring of stiffness k and a damper with viscous coefficient α. The tangential force $\mathbf{F^T}$ is capped by the normal force $\mathbf{F^N}$ through Coulomb's law $|\mathbf{F}^{\mathrm{T}}| \leq \mu_{\mathrm{s}}\mathbf{F}^{\mathrm{N}}$. For the sliding case the dynamic friction is $\mathbf{F}^{\mathrm{T}} = \mu_{\mathrm{d}}\mathbf{F}^{\mathrm{N}}$. The static ($\mu_{\mathrm{s}}$) and the dynamic ($\mu_{\mathrm{d}}$) friction coefficients follow the relation $\mu_{\mathrm{d}} \leq \mu_{\mathrm{s}}$. In DEM simulations the static situation requires an elastic spring to allow a restoring force, i.e. a non-zero remaining tangential force in static equilibrium due to the activated Coulomb friction. This spring represents the distance between the first contact point between two particles and the actual contact point, and is active as long as a contact is present. The model implemented in the code follows the solution proposed by Luding [16].

The present DEM model has been expanded by including a rolling resistance model, which consider the elastic and plastic contact deformation of the material and the effect of non-spherical shapes. In fact, the contact between two particles creates a deformation of the two bodies, whose contact forces no longer act on a single point, but over an area. Furthermore, a sort of rolling resistance arises also from the effect of a non-spherical particle shape. The employed DEM uses simple spheres to represent a real granular material, thus requiring a rolling resistance to take non-sphericity into account. A directional constant torque model has been adopted: a constant torque is applied, always contrasting the relative rotation between the two contacting bodies. The torque $\mathbf{M}^{\mathrm{R}}$ is applied to each pair of particles in contact [17], as follows.

$$\mathbf{M}_i^{\mathrm{R}} = -\mu_{\mathrm{r}} F^{\mathrm{N}} \frac{\boldsymbol{\omega}_{\mathrm{rel}}}{|\boldsymbol{\omega}_{\mathrm{rel}}|} A_{\mathrm{r}} \tag{1}$$

$$\mathbf{M}_j^{\mathrm{R}} = +\mu_{\mathrm{r}} F^{\mathrm{N}} \frac{\boldsymbol{\omega}_{\mathrm{rel}}}{|\boldsymbol{\omega}_{\mathrm{rel}}|} A_{\mathrm{r}} \tag{2}$$

where i, j denote two generic particles, F^{N} is the modulus of the normal component of the particle-particle force, $\boldsymbol{\omega}_{\mathrm{rel}} = \boldsymbol{\omega}_i - \boldsymbol{\omega}_j$ is the relative angular velocity, $A_{\mathrm{r}} = (r_i r_j)/(r_i + r_j)$ the rolling radius, r the particle radius, and μ_{r} the rolling friction coefficient. This parameter is dimensionless, and is only a function of shape, material roughness, and of the rolling speed.

Following the approach proposed for implementing sliding and rolling resistance, a simple linear contact model, characterized by a normal and a tangential stiffness (k_{N} and k_{S} respectively) is chosen for the following simulations.

2.2 Simulations

The model geometry is illustrated in Fig. 1, where both the granular mass and the single-outlet rigid barrier are shown. The model is confined within a cubic domain, enclosed by walls with their own friction coefficient. The flow width is equal to 18 times

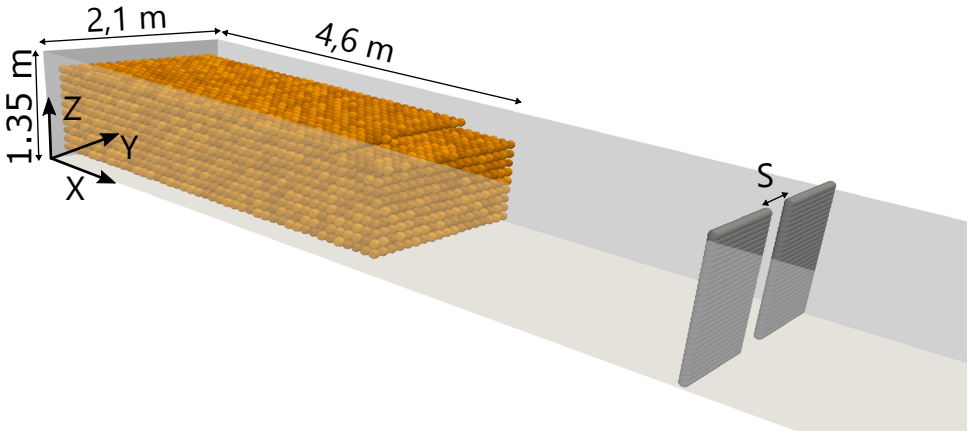

Figure 1: DEM Model, initial condition of the monodisperse spherical discharged mass and position of the barrier.

the average grain diameter D, so that the influence of the lateral boundary is minimized. The barrier width spans the whole transversal size of the domain, except for the outlet, positioned in the center of the barrier, and its height is equal to the domain height. For the sake of simplicity, the simulations consider a monodisperse granular flow modeled using rigid spherical grains. The geometrical characteristics as well as the constitutive parameters are reported in Table 1.

The initial velocity for the granular mass is set to zero, and the flow is driven by gravity. The obstacle is orthogonal to the sliding plane. Four different slopes θ are considered: $10°, 20°, 30°, 35°, 40°$, with the purpose of simulating inclinations smaller or greater than the internal friction angle ϕ_{i}, equal to 30°, a typical value for soils. The wall-particle and the barrier-particle friction coefficients are here equal.

Generally, rigid open barrier are built in the fan apex area, where the slope is much lower than 30°. However debris flow events are characterized also by the presence of water, which reduces the internal friction angle and increases mass mobility. In this view, the choice of simulating an inertial flow, in which frictional forces do not contrast and halt the motion, is essential in order to correctly estimate the trapping efficiency. Generally it is assumed that if $\theta \leq \phi_{\mathrm{i}}$ the flow regime is frictional, while if $\theta \leq \phi_{\mathrm{i}}$ it is mainly inertial. Furthermore, finding multiple barrier is not unusual, and is often required to

Table 1: Parameters considered in the numerical model. For the description of all parameters not defined here please refer to [3]

Number of particles	7640
Diameter D [m]	0.1
Density [kg/m^3]	2500
k_{N} [N/m]	10^6
k_{S} [N/m]	$\frac{2}{7}k_{\mathrm{N}}$
Restitution coefficient ζ [-]	0.2
$\mu_{\mathrm{s,particle\text{-}particle}}$, $\mu_{\mathrm{s,particle\text{-}wall}}$ [-]	0.577
$\mu_{\mathrm{r,particle\text{-}particle}}$ [-]	0.0678
$\mu_{\mathrm{r,particle\text{-}wall}}$ [-]	$2\mu_{\mathrm{r,particle\text{-}particle}}$
Domain size (XYZ) [m]	$20.00 \times 2.10 \times 1.35$
Mass discharge size (XYZ) [m]	$4.60 \times 1.90 \times 1.00$
Position of the front(X) [m]	4.725
Position of the filter barrier (X)[m]	8.00

catch material from high-energy supercritical flows rather than allowing the free saltation of grains downstream [7].

In addition to the slope inclination, also the outlet size S, (written as a multiple of the characteristic radius of the grains r), is varied, with the purpose of finding a critical S/r ratio above which no clogging occurs. For $\theta = 10°$ and $\theta = 20°$, the investigated S/r varies from 2 to 10. For the whole range an arching effect is always observed. Critical S/r is instead investigated for slope angles greater than internal friction angles, simulating until $S/r \leq 9 - 10$, depending on the considered slope. The study of both inclinations and S/r is in the perspective that the grain-trapping efficiency depends on both outlet width and flow condition.

3 RESULTS

In the perspective of a proper design of open rigid barriers, jamming occurrence and characteristics, as well as the maximum impact forces, need to be investigated. The numerical simulations carried out are analyzed in this view and in this section the numerical results are presented in detail. The formation of arching is examined analyzing the following parameters for each incline: (1) the ratio between the height of the arch H_{arch} and the height of the barrier H_{bar} with respect to the time of arching t_{stop}, referring to the first arrival time t_0. (Figs.2, 3), (2) the fraction of the material that is not retained $\%_{nr}$ with respect to the outlet width of the barrier, after a complete stop of the discharging mass is occurred (Fig. 4) . To compute the height of the arch, the outlet height has been subdivided in ten intervals, within which, for all outlet width, the kinetic energy of particles $E_{\mathbf{K,p}}$ has been calculated. If $\sum_{\mathbf{interval}} E_{\mathbf{E,p}} < 10^{-5}$ the particles are considered

halted. Figs. 2,3 plot with markers the center of each interval, when the mass halts and only if there is any retained mass inside.
Considering each slope angle θ, it is observed that:

- $\theta = 10°$: frictional forces prevail and the discharging mass is halted before it impacts against the barrier. Permanent arching occurs for each outlet dimension, but with a height far lower than the barrier height. Clogging time with respect to the first impact time is very short, around $2 - 5$ s, reaching a maximum value of 24 s by increasing the outlet width (Fig. 2 (A));

- $\theta = 20°$: frictional forces prevails as for $\theta = 10°$. Arching occurs for all outlet sizes with a greater height, but is not always rapid. For $S/r = 6$ stable clogging occurs progressively in time and for $S/r > 7$ formation is rapid but only later in time and involving only few layers of grains, (Fig. 2 (B));

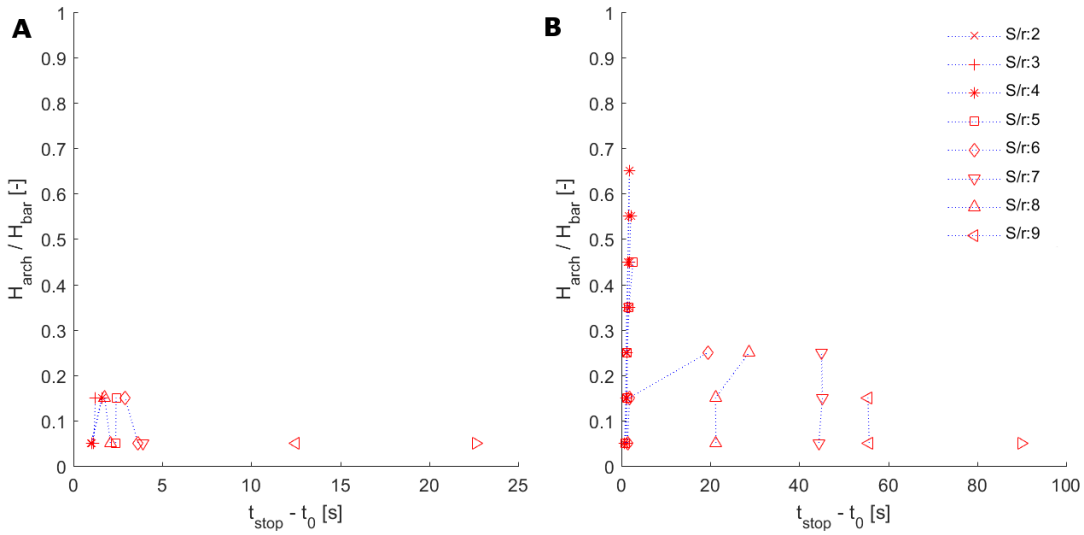

Figure 2: Ratio between the height of the arch and the height of the barrier with respect to the time of arching for $\theta = 10°$ (A) and $\theta = 20°$ (B)

- $\theta = 30°$: frictional forces balance inertial ones. Stable clogging occurs up to $S/r < 9$. For $S/r < 5$ jamming verifies almost instantaneously, and after this value clogging involves only few layers of grains (Fig. 3 (A));

- $\theta = 35°$: inertial forces prevail. Jamming occurs rapidly up to $S/r \leq 4$; for $S/r = 5$ clogging occurs progressively and a a stable configuration is reached at 70 s from the first impact against the barrier. For $S/r > 5$ until $S/r = 9$ clogging involves only one or two layers of grains and verifies later in time (Fig. 3 (B));

- $\theta = 40°$ inertial forces prevail. The same trend as for $\theta = 35°$ is observed. Arching occurs up to $S/r = 8$ (Fig. 3 (C)). This result is in agreement with [12], who stated that for an inclined plane of 40° the probability that an arch is destabilized is around 0.3 for $S/D = 5$.

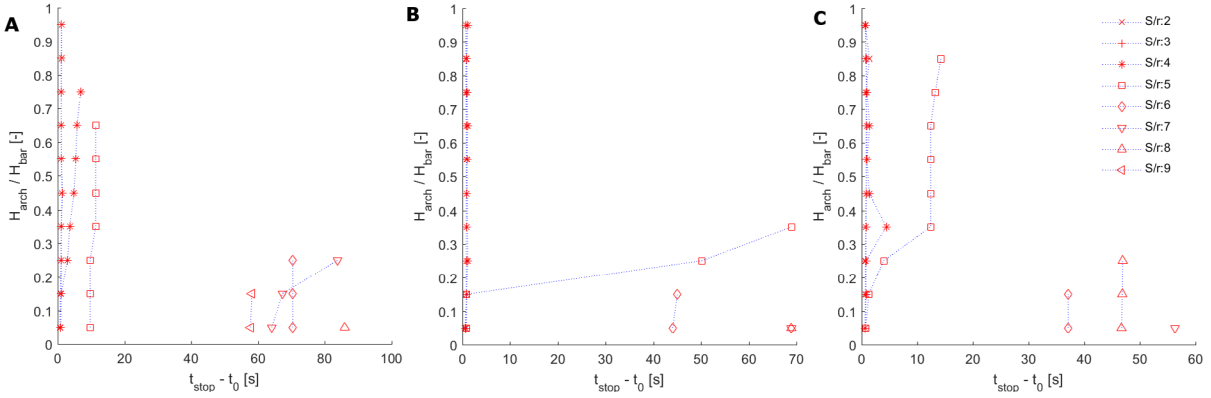

Figure 3: Ratio between the height of the arch and the height of the barrier with respect to the time of arching for $\theta = 30°$ (A), $\theta = 35°$ (B) and $\theta = 40°$ (C)

Fig. 4 shows how the amount of material flowing through the barrier varies with respect to the outlet size. A negligible amount of material passes through the outlet of the barrier for $S/r \leq 4$. Almost the whole material is retained for $\theta = 10°$ independently from the outlet width. A substantial material retainment is observed also for $\theta = 20°$. For $\theta \geq 30°$ an increasing amount of grains flows through the barrier by raising S/r (starting from $S/r = 5$) and a stable configuration is reached with about $90 - 95\%$ of the material fully retained. Concerning the impact forces on the barrier, the results examine the following variables for each outlet size S/r and slope θ: (1) the maximum value of the normal impact force $\mathbf{F}^{\mathrm{N}}_{\mathrm{max}}$ exerted against the barrier (Fig. 5 (A)), (2) the maximum value of the x torque $\mathbf{M}^{x}_{\mathrm{max}}$ exerted to the barrier (Fig. 5 (B)), (3) the ratio between the maximum value of the normal force and the maximum value that would have been registered if the barrier had been completely closed $\mathbf{F}^{\mathrm{N}}_{0}$ (Fig. 6 (A)), (4) the ratio between the maximum value of the normal force and its value in static condition $\mathbf{F}^{\mathrm{N}}_{\mathrm{st}}$ (Fig. 6 (B)), (5) the maximum normal force exerted against the barrier versus the time lag between first arrival and the time at which the maximum force is registered t_{lag} (Fig. 7). Considering Fig. 5 (A), the results collapse on a narrow envelope, with no evidence of a specific trend for varying S/r. A significant increase of the maximum value is registered by increasing slope incline. The same trend occurs for the momentum exchange (Fig. 5 (B)). Fig. 6 (A) shows the influence of the presence of an outlet in the barrier in term of forces exerted to the barrier itself. For $\theta \geq 20°$ an appreciable reduction $(40 - 60\%)$ is observed, almost irrespective of slope incline and outlet size. Only for $\theta = 10°$ no reduction is, as here the maximum value is due to the single-grain impact, which is the same for both open and close barrier. The

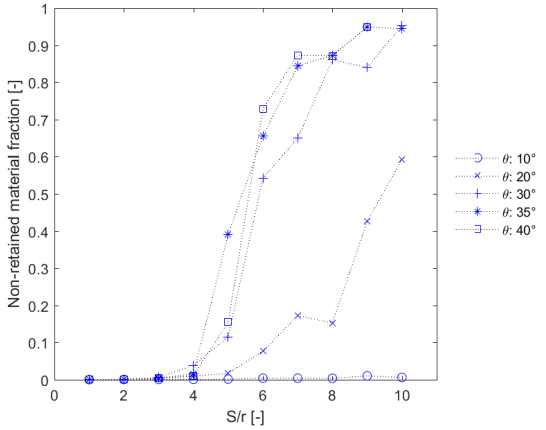

Figure 4: Non retained material fraction with respect to the outlet size of the barrier at complete stop of the discharging mass

plot of Fig. 6(B) highlights that for $S/r \leq 6$ a considerable amount of mass $(75 - 95\%)$ flows through the outlet and thus the static force is far lower the maximum one. Finally, the graph in Fig. 7 shows a considerable scattering of data and a high t_{lag} for $\theta = 20°$. For greater slopes, t_{lag} reduces. For equal slope angle, the data scattering varying the outlet size reduces when increasing the slope angle, with no evident trend considering S/r variation. For $\theta = 10°$ all results converge to the same value, as for all simulations at this slope the maximum value is reached at the same time and corresponds to a single grain impact.

4 DISCUSSION

Results of the simulations allow some preliminary conclusions for what concerns the dynamics of arching and impact against the barrier.

Concerning the arching for a slope angle lower to the internal friction angle ($\theta < \phi_i$), it is recognized that the steeper the slope is, the higher the arch will be, with jamming occurring more rapidly. Conversely, for $\theta \geq \phi_i$ the steeper the inclined plane is, the less promptly a permanent clogging occurs, and the height of the arch decreases. This might be due to an increase of the flow velocity and thus of the collisional forces which grow at the expense of the frictional ones. Nevertheless, the increment in velocity seems to result in higher arches for lower slopes, as frictional forces still prevail on inertial ones. Here arching originates with progressive clogging (that is the sequence of jamming and unjamming situations until a stable configuration is reached) and lower stable arches form for steepness grater than internal friction angle. This implies that the critical outlet size decreases with increasing slope. It may be inferred that for inertial regimes, in which the collisional dynamics prevails, stable clogging occurs for an outlet size lower or equal to $3 - 4D$. These results are comparable with those found for 3D laboratory experiments

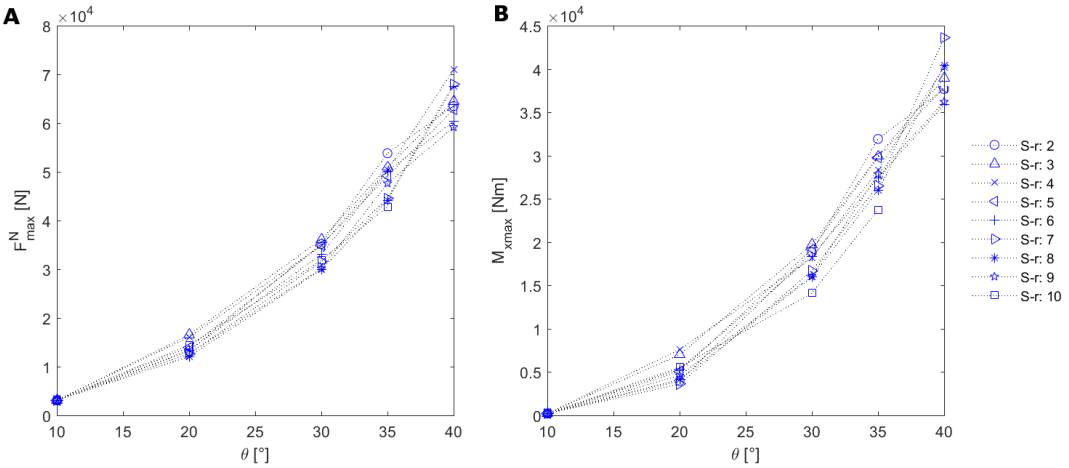

Figure 5: Maximum normal force (A) and maximum momentum in x direction (B) exerted by the discharged mass to the barrier.

on spherical steel beads discharged by a silo: [8] found a critical value $S = 4 - 5D$, while [2] $S = 3D$ and [10] $S = 4D$. Furthermore, for $S/r = 5$ progressive clogging is observed, creating a transitional state of jam and flows, until a stable arch forms. For $6 \leq S/r \leq 9$ arching verifies later in time and therefore stabilizes at a lower height. This tendency suggests that for this setting ore than 80% of the material should flow to allow resisting force to balance driving ones. The increase of slope (and thus velocity) in the collisional regime reduces the clogging time and the flowing of the mass through the outlet. For this reason, the situation for $\theta = 20°$ is equal to $\theta = 40°$, but the amount of retained material and the halt mechanisms are quite different.

The analysis shows that $\mathbf{F}^{\mathrm{N}}_{\mathrm{max}}$ increases by raising θ: velocity grows and the kinetic energy with it, resulting in a greater impact force. Collisions occur more frequently by increasing θ. It seems that this trend is almost independent from the outlet size dimension. For the same reason, the time at which $\mathbf{F}^{\mathrm{N}}_{\mathrm{max}}$ is registered decreases with increasing θ. Referring to Fig. 7, the data scattering for $\theta = 20°$, for which a great gradient among values in time for different outlet is observed, is attributed to great oscillations occurred before reaching a static value, without a specific peak value. It appears that for this inclination motion is considerably decelerated and delayed by frictional forces, preventing the reach of a clear peak value.

5 CONCLUSIONS AND FUTURE PERSPECTIVES

An appropriate modeling of the mechanical process that develops when a granular flow interacts with protection measures is of great concern and a crucial issue. Achieving a deeper understanding of the mechanisms is very important in the perspective of deriving a better structure design. In this context, the present study focuses on open rigid barriers, investigating the arching and the impact dynamics. The research is based on a series

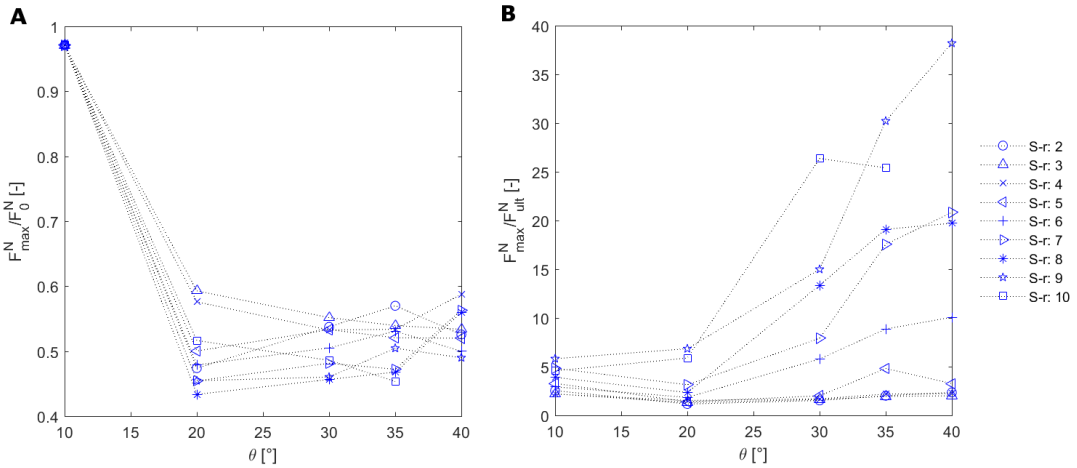

Figure 6: Ratio between maximum value of force for each outlet size and maximum value for a closed barrier with the same slope is plotted in respect to slope angle (A) and ratio between maximum value of the force and its value in static condition for each outlet size in respect to slope angle (B).

of numerical simulations where both outlet size and slope angle are varied in order to separately analyze their influence. The critical discussion of the numerical results has allowed to derive some significant considerations.

The slope incline remarkably affects the prevalent mechanism of motion and thus how arching evolves in time and in height. For a slope lower than the internal friction angle, frictional forces prevail and arching occurs for every outlet size, with a deposit height and clogging time that increase with the slope. For slope angles equal or higher than the internal friction angle, inertial forces prevail and stable arches are observed up to the outlet size $S \leq 3 - 4D$. Furthermore, for $S/r = 5$ a progressive clogging is observed and jamming is no more very rapid. For $6 \leq S/r \leq 8 - 9$ the jamming time increases, with few layers of grains involved in the process. In this configuration the retained mass value is around 5%. This implies that the amount of mass flowing downstream is considerable but the presence of the barrier still provides a significant reduction of kinetic energy. This aspect will be targeted by future works. The trapping efficiency is nevertheless proved for $S/r \leq 5$ for each inclines, with progressive clogging occurring for $S/r = 5$ for slope $\theta \geq \phi_i$. This allows to draw conclusions for what concerns the efficiency and maintenance cost of a barrier. Progressive clogging to some extent prevent a sudden filling of the barrier and thus a quick loss of effectiveness.

The nature of jamming is different if there are two or more adjacent outlet [18]. Stable and/or independent arches cannot form if the width of the racks in the barrier is lower than a certain value. This aspect requires further investigation, which is deferred to future works.

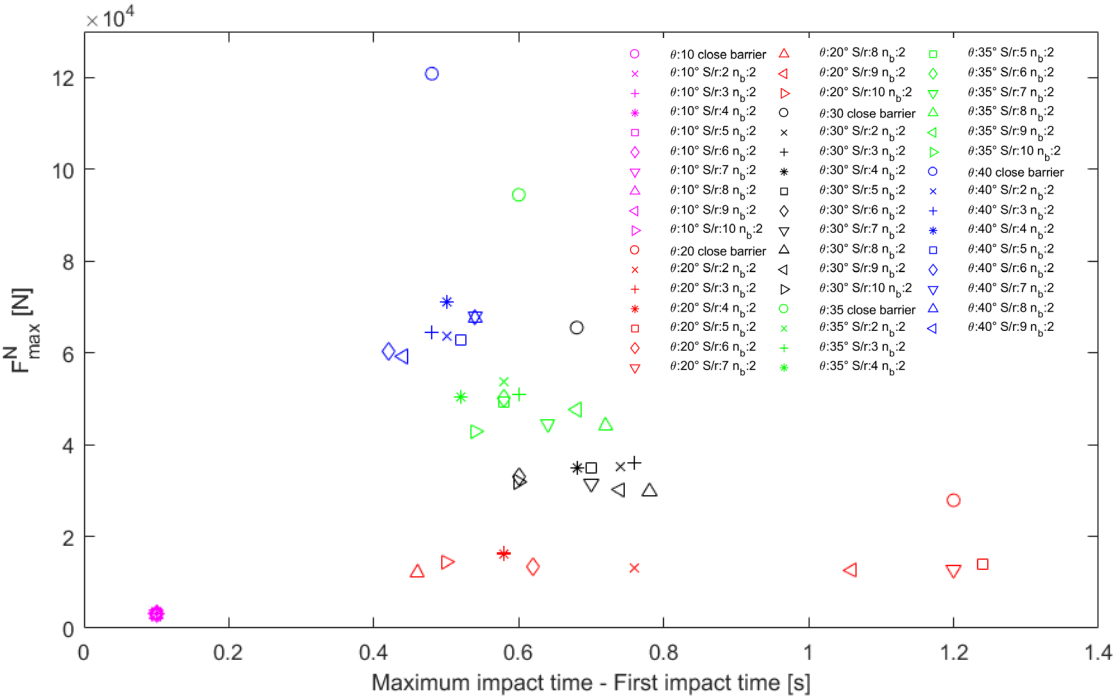

Figure 7: Maximum force exerted against the barrier versus time lag between first arrival and maximum value.

REFERENCES

[1] Albaba, A., Lambert, S.,Nicot, F., Chareyre, B. Relation between microstruscture and loading applied by granular flow to a rigid wall using DEM modeling. *Granular Matter* (2015) **17** (5):603–616.

[2] Pournin, L., Ramaioli, M., Folly, P., Liebling, Th. M. About the influence of friction and polydispersity on the jamming behavior of bead assemblies. *The European Physical Journal E* (2007) **23**:229–235.

[3] Leonardi, A., Wittel, F. K., Mendoza, M., Vetter, R., Herrmann, H. J. Particle-fluid-structure interaction for debris flow impact on flexible barrier. *Computer-Aided Civil and Infrastructure Engineering*, (2015) **31**:323–333.

[4] Hungr, O., Evans, S. G., Bovis, M. J., Hutchinson, J. N. A review of the classification of landslides of the flow type. *Environmental & Engineering Geoscience* (2001) **7** (3):221–238.

[5] Zanuttigh, B. and Lamberti, A. Experimental analysis of the impact of dry avalanches on structures and implication for debris flows. *Journal of Hydraulic Research* (2006) **44** (4):522–534.

[6] Calvetti, F., di Prisco, C., Vairaktaris, E. Impact of dry granular masses on rigid barriers. *IOP Conference Series: Earth and Environmental Science* (2015): doi:10.1088/1755-1315/26/1/012036.

[7] Choi, C. E., Goodwin, G.R., Ng, C. W. W, Cheung,D. K. H., Kwan, J, S. H., Pun, W. K. Coarse granular flow interaction with slit structures *Géotechnique Letters* (2016) **6**:267–274.

[8] Zuriguel, I., Garcimartín, A., Maza, D., Pugnaloni, L. A., Pastor, J. M. Jamming during the discharge of granular matter from a silo. *Physical Review E* (2005) **71**: doi: 10.1103/PhysRevE.71.051303.

[9] Chevoir, F., Gaulard, F., Roussel, N. Flow and jamming of granular mixtures through obstacles. *Europhysics Letters* (2007) **79**: doi: 10.1209/0295-5075/79/14001.

[10] Sheldon, H. G. and Durian, D. J. Granular discharge and clogging for tilted hoppers. *Granular Matter* (2010) **12**:579–585.

[11] Hidalgo, R. C., Lozano, C, Zuriguel, I., Garcimartn, A. Force analysis of clogging arches in a silo. *Granular Matter* (2013): doi: 10.1007/s10035-013-0451-7.

[12] Arvalo, R. and Zuriguel, I. Clogging of granular materials in silos: effect of gravity and outlet size. *Soft Matter* (2016) **12**:123–130.

[13] Magalhães, C. F. M., Moreira, J. G., Atman, A. P. F. Catastrophic regime in the discharge of a granular pile. *Physical Review E - Statistical, Nonlinear, and Soft Matter Physics* (2010) **84**:1–4.

[14] Magalhães, C. F. M., Moreira, J. G., Atman, A. P. F. Segregation in arch formation. *European Physical Journal E* (2012) **35 (5)**. doi 10.1140/epje/i2012-12038-5.

[15] Garcimartín, A., Zuriguel, I., Pugnaloni, L. A., Janda, A. Shape of jamming arches in two-dimensional deposits of granular materials. *Physical Review E - Statistical, Nonlinear, and Soft Matter Physics* (2010) **82**: doi 10.1103/PhysRevE.82.031306

[16] Luding, S. Introduction to discrete element methods: Basic of contact force models and how to perform the micro-macro transition to continuum theory. *European Journal of Environmental and Civil Engineering* (2008): 785–826.

[17] Girolami, L., Hergault, V., Vinay, G., Wachs, A. A three-dimensional discrete-grain model for the simulation of dam-break rectangular collapses: comparison between numerical results and experiments. *Granular Matter* (2012) **14**:381–392.

[18] Mondal, S., Sharma, M. M. Role of flying buttresses in the jamming of granular matter through multiple rectangular outlets. *Granular Matter* (2014) **16**:125–132.

V International Conference on Particle-based Methods – Fundamentals and Applications
PARTICLES 2017
P. Wriggers, M. Bischoff, E. Oñate, D.R.J. Owen, & T. Zohdi (Eds)

ON THE EFFECT OF STATIC AND DYNAMIC PARTICLE SIZE DISTRIBUTION ON FLOW TURBULENCE MODULATION

DERRICK O. NJOBUENWU[1] AND MICHAEL FAIRWEATHER[2]

School of Chemical and Process Engineering, University of Leeds
Leeds, LS2 9JT, United Kingdom
[1]d.o.njobuenwu@leeds.ac.uk; [2]m.fairweather@leeds.ac.uk

Key words: Large eddy simulation, Discrete particle simulation, Gravity, Turbulence modulation, Agglomeration, Particle size distribution.

Abstract. The effect of an evolving particle size distribution due to particle agglomeration and breakup, and the direction and absence of gravitational acceleration, on flow turbulence modulation is investigated using large eddy and discrete particle simulation of a turbulent channel flow. The results are compared with the case in which the particle size distribution is static and where only inter-particle collision is allowed. Due to the small particle Stokes number considered, inherent in a solid-liquid flow, and the small simulation time, only small effects were observed for the static versus dynamic particle size distribution on the fluid turbulence. For vertical channel flows, however, the influence of flow direction and gravity lead to different particle segregation patterns which, together with changes in wall shear stresses and mass flow rate due to buoyancy effects, do affect the flow turbulence and the evolution of inter-particle collisions, collision efficiency and agglomerate breakup.

1 INTRODUCTION

The structures in a turbulent flow are known to be highly complex, associated with time-dependent, three-dimensional phenomena covering a wide range of spatial and temporal scales. The degree of the complexity increases with the introduction of a dispersed particle phase. Additional effects include the interaction between phases in terms of mass, momentum and energy (as applicable) exchange, the interaction between particles and any walls, and the influence of gravity, particle collision, agglomeration and breakup. Since the system performance is a complex function of such underlying phenomena, a detailed knowledge regarding the hydrodynamics and the evolution of the dispersed phase is essential for understanding such systems. The governing features of the dispersed phase are its size and velocity distributions, both of which have a major influence on the flow turbulence.

Previous works have focused on the effect of particle size distribution (PSD) on fluid turbulence. These have been performed by studying two-way coupling and four-way coupling [1, 2], where the effects of two-way coupling between the particles and the flow, and inter-particle collisions, on fluid turbulence are considered. To the best of our knowledge, there has been no work on the effect of an evolving PSD due to particle agglomeration and breakup on turbulence modulation. Work to date therefore considered the effect of a static, poly-dispersed PSD on turbulence modulation. In this paper, an eddy-resolving simulation for prediction of

the fluid velocity distribution is adopted to improve confidence in the results. Large eddy simulation (LES) is preferred to direct numerical simulation (DNS) to benefit from LES's lower computational cost as compared to DNS. Discrete particle simulation (DPS) considering particle drag, shear-lift, pressure gradient, added mass and buoyancy forces, and sub-grid scale velocity fluctuation contributions to particle acceleration, is applied to treat the particle dynamics in the turbulent flow. The classical particle-in-cell technique is used to treat the two-way coupling.

Most numerical simulations exclude the gravitational force to study only turbulence-induced agglomeration. However, gravitational acceleration is inevitably present and hence must be included as one of the external forces that induce particle-particle interactions leading to agglomeration and sedimentation. The inclusion of gravitational acceleration does alter the fluid mass flow rate and the particle behaviour in a system, as shown in the literature [3-5].

In resolving four-way coupling aspects, the search for possible binary particle collisions is based on a deterministic method following domain decomposition. The outcome of all collisions is determined using a hard-sphere collision model while all collisions are subjected to an energy-balance agglomeration to test for possible agglomeration [6]. All agglomerates are subjected to hydrodynamic shear stresses in the flow for possible breakup of agglomerates [7]. Note that agglomerate breakup is due to agglomerate-agglomerate or primary particle-agglomerate collisions, and through impact with a wall or due to hydrodynamic shear [7].

The LES-DPS developed for predicting the dynamic PSD and turbulence modulation is tested on flows of relevance to the transport of nuclear waste sludge. Channel flow is the simulation domain while calcite particles suspended in water are the nuclear waste simulant. Results will be presented in terms of the PSD, and profiles of fluid and particle velocities, with simulation time, focussing on the impact of the evolving particle size distribution on the flow turbulence.

2 MATHEMATICAL FORMULATION

A four-way coupled Eulerian-Lagrangian approach is adopted since the suspension is dense with high particle volume fractions. In large eddy simulation, the continuity and Navier-Stokes equations are spatially filtered so that the energy-containing large-scale turbulent motions are solved while the sub-grid scales (SGS) are modelled. The filtered governing equations with the influence of the dispersed phase can be expressed as:

$$\frac{\partial \bar{u}_j}{\partial x_j} = 0 \tag{1}$$

$$\frac{\partial \bar{u}_i}{\partial t} + \frac{\partial \bar{u}_i \bar{u}_j}{\partial x_j} = -\frac{1}{\rho}\frac{\partial \bar{p}}{\partial x_i} + \frac{\partial}{\partial x_j}\left(\bar{\sigma}_{ij} - \tau_{ij}\right) + \frac{\Pi}{\rho} + \frac{S_{m,i}}{\rho} \tag{2}$$

where $\bar{\sigma}_{ij} = -2\nu\bar{S}_{ij}$ represents the viscous stress, $\bar{S}_{ij} = 0.5(\partial\bar{u}_i/\partial x_j + \partial\bar{u}_j/\partial x_i)$ is the filtered strain-rate tensor, ν is the kinematic viscosity, $\tau_{ij} = \overline{u_i u_j} - \bar{u}_i\bar{u}_j$ is the SGS tensor which represents the effect of the SGS motions on the resolved motions, t is time, x_j is the spatial co-ordinate directions, u_j is the velocity vector, p is the pressure, and ρ is the density. The SGS tensor is computed using the dynamic version of the Smagorinsky model proposed by Piomelli and Liu [8]. Its specific implementation has been presented in a recent paper [9]. $\Pi = -\rho u_\tau^2/h$ is the mean pressure constant imposed along the streamwise direction (z-axis)

that drives the flow. $S_{m,i}$ is a source term and accounts for the action on the fluid of the particles, given by the sum of all hydrodynamic forces in the momentum equation due to all particles in a fluid computational cell.

The motion of a particle in a turbulent flow field follows Newton's second law of motion:

$$\mathrm{d}\mathbf{v} = \left\{ \frac{(\overline{\mathbf{u}} - \mathbf{v})}{\tau_p} f_D + C_{SL} \frac{3\rho}{4\rho_p} [(\overline{\mathbf{u}} - \mathbf{v}) \times \overline{\boldsymbol{\omega}}] + \frac{\rho}{\rho_p} \frac{\mathrm{D}\overline{\mathbf{u}}}{\mathrm{D}t} + \frac{\rho}{2\rho_p} \left(\frac{\mathrm{d}\overline{\mathbf{u}}}{\mathrm{d}t} - \frac{\mathrm{d}\mathbf{v}}{\mathrm{d}t} \right) + \left(1 - \frac{\rho}{\rho_p} \right) \mathbf{g} \right\} \mathrm{d}t \tag{3}$$

$$\mathrm{d}\mathbf{x_p} = \mathbf{v}\mathrm{d}t \tag{4}$$

An important notation convention is that the derivatives $\mathrm{d}/\mathrm{d}t$ and $\mathrm{D}/\mathrm{D}t$ represent Lagrangian derivatives, following the particle and the containing fluid element respectively, so that boldface symbols denote the vector quantities, with $\mathrm{d}\overline{\mathbf{u}}/\mathrm{d}t = \partial\overline{\mathbf{u}}/\partial t + \mathbf{v} \cdot \nabla\overline{\mathbf{u}}$ and $\mathrm{D}\overline{\mathbf{u}}/\mathrm{D}t = \partial\overline{\mathbf{u}}/\partial t + \overline{\mathbf{u}} \cdot \nabla\overline{\mathbf{u}}$. The terms on the right-hand side of Eq. (3) are, respectively, contributions from the drag, shear lift, pressure-gradient, added-mass, and buoyancy forces. The particle properties are denoted by the subscript p, and fluid properties are either given without a subscript (for readability) or by the subscript f (where it enhances clarity). $\mathbf{v}$ and $\mathbf{x_p}$ are the particle instantaneous velocity and position; $\overline{\mathbf{u}}$ and $\overline{\boldsymbol{\omega}} = 0.5(\nabla \times \overline{\mathbf{u}})$ are known resolved fluid velocities and rotation interpolated at particle position. The term f_D is a non-linear correction due to the particles' finite Reynolds number, $Re_p = |\overline{\mathbf{u}} - \mathbf{v}| d_p/\nu$, taken from the Schiller and Naumann drag correlation, and expressed as $f_D = 1.0 + 0.15 Re_p^{0.687}$, with d_p as the particle diameter. $\tau_p = (\Phi_p d_p^2)/18\nu$ is the particle relaxation time and when normalised by the viscous time-scale $\tau_f = \nu/u_\tau^2$, gives the particle Stokes number, $\tau_p^+ = \tau_p/\tau_f$, which is then used to characterise the particle response time, with $\Phi_\rho = \rho_p/\rho$ being the particle to fluid density ratio. Hence, a superscript $(^+)$ denotes variables made dimensionless in wall (viscous) units using the fluid kinematic viscosity, ν, and the fluid shear velocity, u_τ. The shear lift force coefficient C_{SL} accounts for corrections due to small and large particle Reynolds numbers, as proposed by Mei [10].

The deterministic hard-sphere collision model [11] is adopted to treat the interactions between particles due to binary collisions. Agglomeration for the colliding particles is based on an expression which permits agglomeration if the elastic energy (i.e. the relative kinetic energy before the collision minus the dissipated energy) after the compression period of the collision is less than the work required to overcome the van der Waals' forces [12]:

$$\frac{(\mathbf{v}_2^- - \mathbf{v}_1^-)^2 - [(\mathbf{v}_2^- - \mathbf{v}_1^-) \cdot \mathbf{n}_\mathrm{c}]^2 (1 - e_n^2)}{|(\mathbf{v}_2^- - \mathbf{v}_1^-) \cdot \mathbf{n}_\mathrm{c}|} \leq \frac{H^*}{6\delta_0^{*2}} \left[(1 - e_n^2) \frac{6}{\pi^2 \rho_p^* \bar{p}^*} \frac{d_{p,1}^{*3} + d_{p,2}^{*3}}{d_{p,1}^{*2} d_{p,2}^{*2} (d_{p,1}^* + d_{p,2}^*)} \right]^{1/2} \tag{5}$$

where quantities with the superscript * are made dimensionless in the integral scale using the channel half-height h, bulk velocity, u_b and fluid density, ρ. H is the particle Hamaker constant, $\bar{p}$ is the maximum contact pressure at which plastic deformation occurs, δ_0 is the minimal contact distance and e_n is the normal restitution coefficient. Note the superscript $(^-)$ denotes quantities before the collision, and the subscripts 1 and 2 denote particles number one and two. The agglomerate size and structure are based on a volume-equivalent sphere.

Breakup is defined as a singular event in time, i.e. there is an exact moment in time when an agglomerate turns from being intact into being broken. We assume that this happens when the local hydrodynamic stress $\sigma \sim \mu(\epsilon/\nu)^{1/2}$ at the agglomerate position, acting on the

agglomerate, exceeds a critical stress, σ_{cr} [7]; where ϵ is the instantaneous turbulence kinetic energy dissipation rate at the position of the agglomerate, and μ and ν are the dynamic and kinematic viscosities. The critical stress σ_{cr} is a characteristic of the considered agglomerate, i.e. σ_{cr} is a function of the aggregate properties such as size, structure, type of the constituting particles, and the chemical environment. Among these variables, the size of the aggregate is most crucial. A large body of experimental, numerical and theoretical studies, see Babler et al. [7] and cited references, suggest a power law dependency of the form:

$$\sigma_{cr} \sim r^{-q} = N_{pp}^{-q/d_f} \tag{6}$$

where $N_{pp} \sim r^{d_f}$ is the number of primary particles constituting the agglomerate, d_f is the agglomerate fractal dimension, r is the radius of the primary particle, and $q = \left[9.2\left(3 - d_f\right) + 1\right]/2$ is a scaling exponent that depends on the agglomerate structure [7]. There are no exact models to effect breakup, and recent research [7] has been limited to detecting the moment break-up events are likely to occur. We adopt this model for detecting breakup events for small agglomerates and subsequently breakup the parent agglomerate into two daughter particles. This method of breaking an agglomerate into two parts is a popular modelling assumption mainly because of the lack of data for other types of breakup mode.

3 NUMERICAL SIMULATIONS

The BOFFIN-LES code [13] was used to solve the LES equations. The shear Reynolds number of the channel flow was $Re_\tau = u_\tau\, h/\nu = 300$ based on the properties of water ($\rho = 1000$ kg m^{-3}, $\nu = 10^{-6}$ m^2 s^{-1}). The computational domain, $2h \times \pi h \times 2\pi h$, was discretised using grid nodes of $129 \times 128 \times 128$ in the wall normal, spanwise and streamwise directions, respectively. Periodic boundary conditions are applied in the streamwise and spanwise directions and the no-slip condition is imposed on the walls.

Table 1: Calcite mechanical properties and influence of particle diameter, normal restitution coefficient and volume fraction on particle-particle interactions.

Parameter	Symbol	Unit	Value
Particle density	ρ_p	kg m^{-3}	2710
Hamaker constant	H	J	3.8×10^{-20}
Mean yield stress	$\bar{p}$	Pa	3.0×10^{8}
Minimal contact distance	δ_0	m	2.0×10^{-10}
Particle diameter	d_p	μm	60
Normal restitution coefficient	e_n	-	0.4
Particle volume fraction	α_p	-	1×10^{-3}

Particles are injected uniformly into the fully developed un-laden flow with their velocity set to the local fluid velocity and tracked by solving the particle equation of motion. A 4th-order Runge-Kutta scheme and a trilinear interpolation scheme are employed in the DPS code with time step equal to that of the LES. Periodic boundary conditions are applied in the streamwise and spanwise directions and perfect elastic collisions are imposed on the walls.

The particle simulation properties and the mechanical properties of calcite particles, a simulant for UK legacy waste sludge, used in these simulations are listed in Table 1. Particle-particle collisions are considered within a long dispersion phase to assure a proper mixing of the primary particles. Then, two-way coupling, inter-particle collision, agglomeration and breakup are considered. The instant in time at which the agglomeration and breakup models are applied is denoted $t^* = 0$ and then a dimensionless time interval of $\Delta t^* \sim 100$ is investigated.

4 RESULTS AND DISCUSSION

Figure 1 shows the population balance (growth and/or death) of the single, N_{pp}, and agglomerate particles, $N_{a,i\leq 5}$, defined as the ratio of the number of particle sizes to the initial number of total single particles, $N_0 = 2{,}748{,}100$, after a simulation time $t^* = tu_b/h = 100$. In this test case, agglomeration and breakup were monitored for primary particles with particle diameter, $d_p = 60$ μm, particle Stokes number, $\tau_p^+ = 5$, density ratio, $\rho_p/\rho \sim 100$ and agglomerate fractal dimension, $d_f = 2.0$.

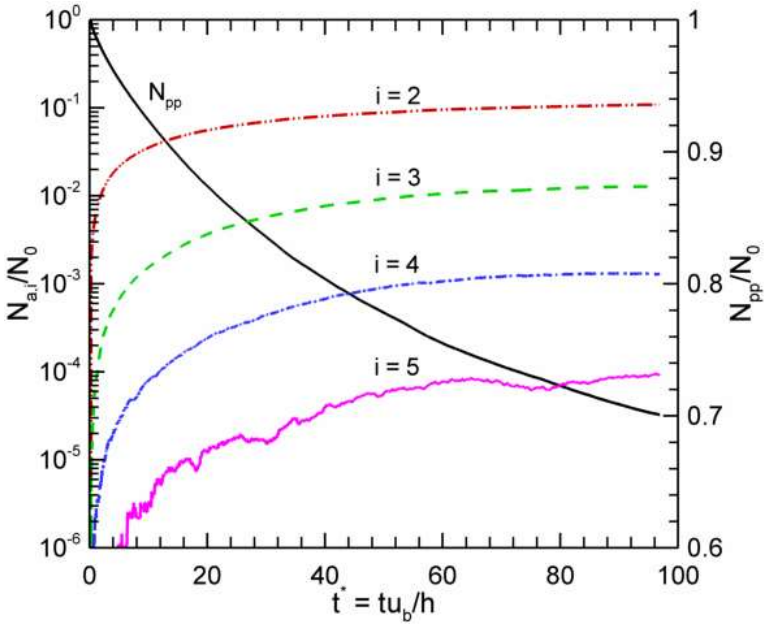

Figure 1: Time evolution of the population of single, N_{pp}, and agglomerate particles, $N_{a,i=2,3,\ldots}$. Lines are as follows: black (−) single; red (− ·· −) double; green (− −) triple; blue (− · −) quadruple; purple (−) quintuple

Figure 1 shows the particle size distribution at any time instance, t^*, and demonstrates that agglomerates of two particles, $N_{a,i=2}$, form first. With increasing time, large agglomerates begin to form through collisions between single particles and larger agglomerates, and between the agglomerates themselves, all constrained by de-agglomeration due to hydrodynamic shear stress acting on the agglomerate. The rate of formation and breakup of

the lower order agglomerates, e.g. $N_{a,i=2,3}$, ultimately tends to a steady state, while those of the higher order agglomerates, e.g. $N_{a,i=5}$, show an unsteady trend since the large agglomerates are susceptible to breakup.

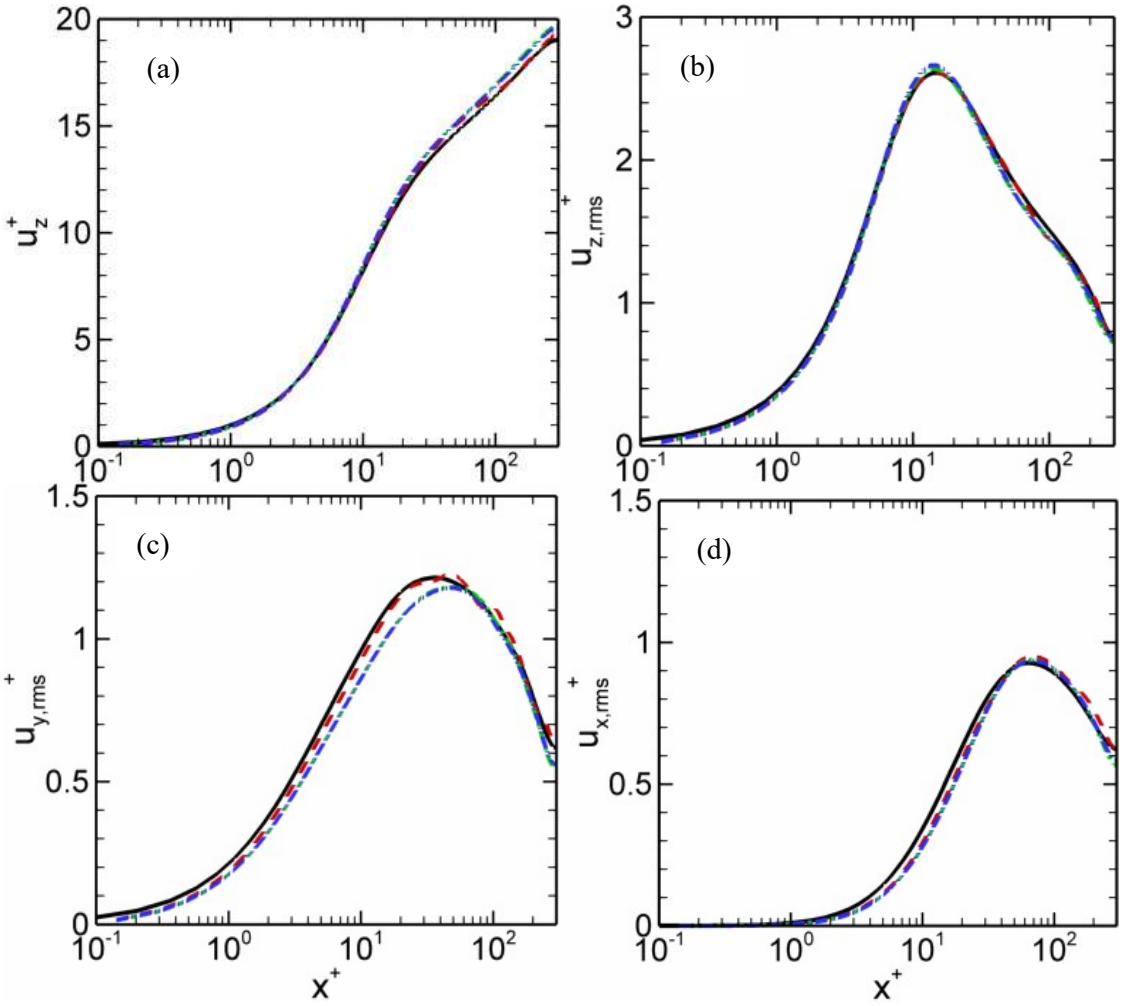

Figure 2: (a) Mean streamwise fluid velocity, u_z^+, and rms of fluid velocity fluctuations for (b) streamwise, $u_{z,\mathrm{rms}}^+$, (c) spanwise, $u_{y,\mathrm{rms}}^+$, and (d) wall-normal, $u_{x,\mathrm{rms}}^+$, components. Lines are as follows: black (−) unladen DNS; red (− −) unladen LES; green (− · −) four-way coupled LES, with collision only and blue (− ·· −) four-way coupled LES, with collision, agglomeration and breakup ($d_p = 60$ µm, $\rho_p/\rho \sim 100$, $\tau_p^+ = 5$, $d_f = 2.0$).

Following the test case presented in Figure 1 where four-way coupling including inter-particle collision, agglomeration and breakup are considered, the first and second statistical turbulent moments for the liquid phase are compared in Figure 2 with those obtained from unladen DNS [14], unladen LES and four-way coupled LES with inter-particle collision only, all computed at shear Reynolds number $Re_\tau = 300$. The four-way coupling case considering particle collision, agglomeration and breakup results in a dynamic particle size distribution,

while the four-way coupling case considering inter-particle collision only results in a static PSD, and in this case mono-dispersity.

Figure 2 gives profiles of the mean streamwise fluid velocity, u_z^+, and the root mean square (rms) of the fluid velocity fluctuations in the streamwise, $u_{z,\mathrm{rms}}^+$, spanwise, $u_{y,\mathrm{rms}}^+$, and wall-normal, $u_{x,\mathrm{rms}}^+$, directions. All show only small differences between the unladen flow and the four-way coupled case based on the static and dynamic PSDs. Although the presence of particles in the fluid flow does modulate the flow turbulence, therefore, the degree of this modulation depends on several factors as reviewed in Pang et al. [15]. Due to a small particle Stokes number, $\tau_p^+ = 5$, for this flow, and a small elapsed simulation time $\Delta t^* \sim 100$, the consideration of two-way coupling with static and dynamic PSD has little effect on the fluid statistical moments studied. This negligible effect of small particle Stokes number on fluid statistics has been observed in previous studies, e.g. [12].

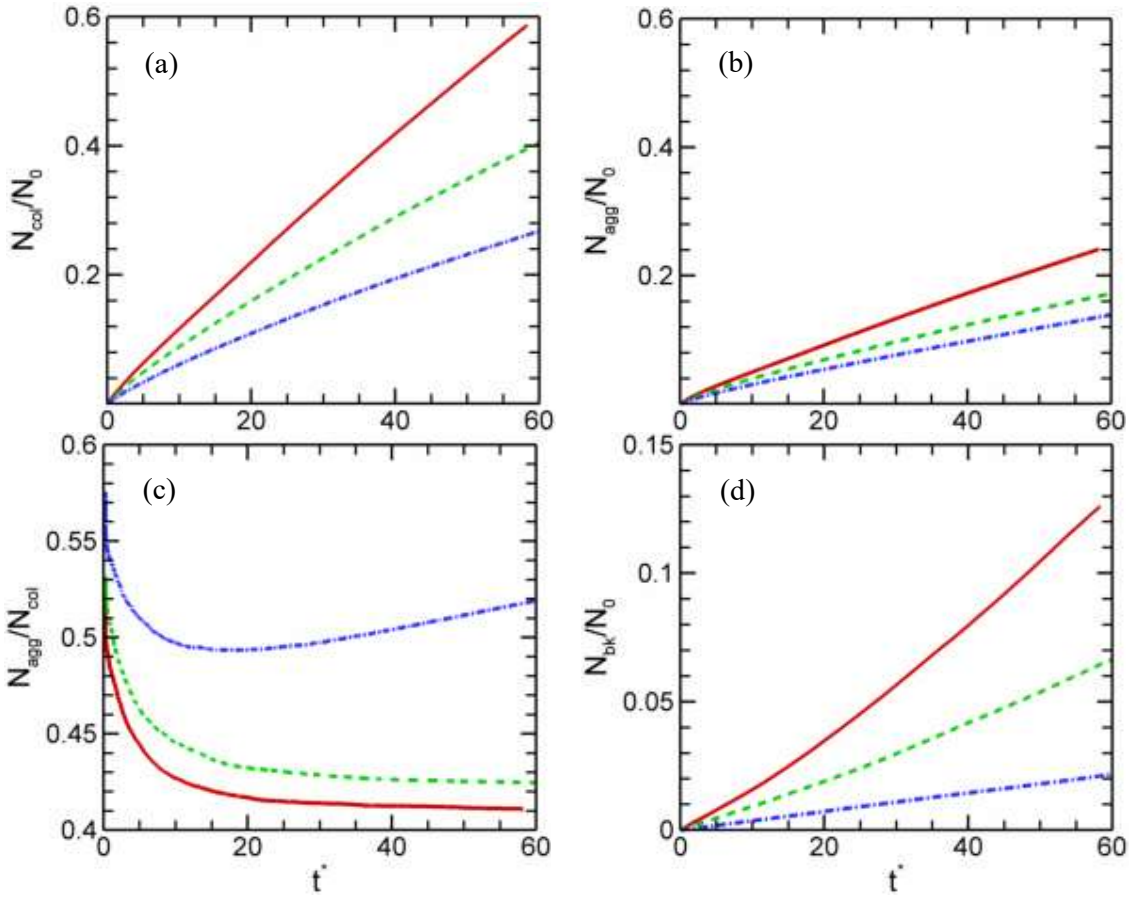

Figure 3: Time history of (a) the total number of the accumulated particle-particle collisions, N_{col}/N_0, (b) the total number of the accumulated particle-particle collisions leading to agglomeration, N_{agg}/N_0 , (c) the agglomeration rate, N_{agg}/N_{col}, and (d) the total number of the accumulated agglomerate breakups, N_{bk}/N_0; N_0 is the total number of primary particles $\left(d_p = 60\ \mu m,\ \rho_p/\rho = 2.71\right)$ initially injected into the domain. Lines are as follows: red (−) downward flow; green (− −) no-gravity flow; and blue (− · −) upward flow.

Figure 3 shows the evolution of the number of collisions, N_{col}, the number of collisions which satisfy the agglomeration criterion in Eq. (5), N_{agg}, the agglomeration rate, N_{agg}/N_{col}, and the number of breakups, N_{bk}, for the three flows considered, i.e. downward flow, no-gravity flow and upward flow, all normalised by the initial total number of primary particles, $N_0 = 2{,}748{,}100$. The effect of momentum exchange between the solid and liquid phases, the shear induced lift force and the direction of gravity all have an effect on particle segregation, inter-particle collision, particle agglomeration and agglomerate breakup. Subsequently, their combined effects influence the fluid first and second statistical moments.

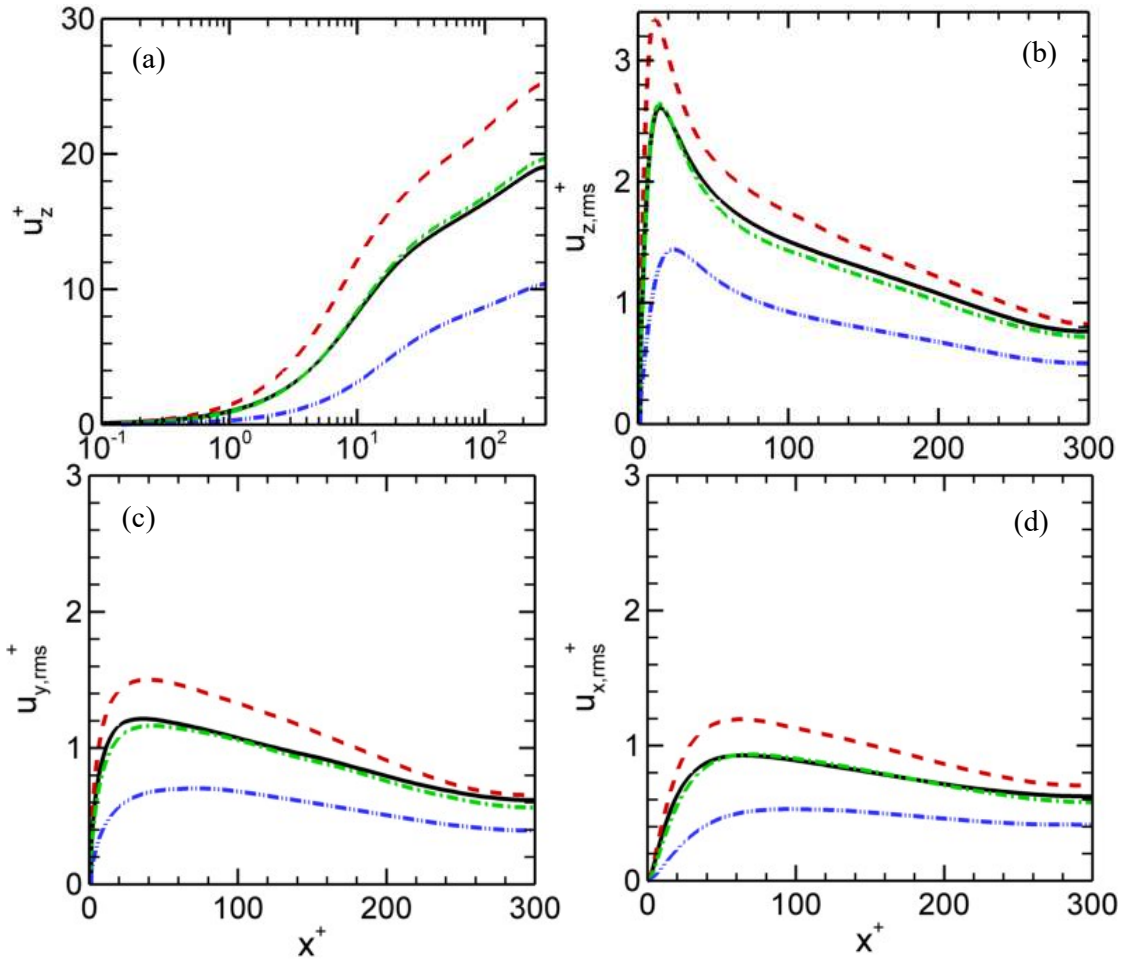

Figure 4: (a) Mean streamwise fluid velocity, u_z^+, and rms of fluid velocity fluctuations for (b) streamwise, $u_{z,\mathrm{rms}}^+$, (c) spanwise, $u_{y,\mathrm{rms}}^+$, and (d) wall-normal, $u_{x,\mathrm{rms}}^+$, components. Simulations based on particle diameter $d_p = 60$ µm and $\rho_p/\rho = 2.71$ Lines are as follows: black (−) unladen DNS; red (− −) downward flow; green (− · −) no-gravity flow; and blue (− ·· −) upward flow.

The particles in the downward flow (DF) and no-gravity flow (NG) accumulate at the wall, with the former showing more particle segregation at the wall compared to the flow without gravity. In contrast to both these flows, the particles in the upward flow (UF) are depleted in the near-wall region. Note the results that support this observation are not shown here, but this has been observed previously [2]. Due to presence of gravity, and also to local momentum exchange with the carrier fluid and to differences in particle segregation, we observe in Figure 4 significant increases (resp. decreases) of both the wall shear and liquid mass flow rate in downward (resp. upward) flows when compared to the no-gravity flow. Hence, in the three cases, the particles see significantly different turbulence intensities, as is evident in the evolution of the number of collisions, agglomerations, breakups and the agglomeration rate in Figure 3. With the largest wall shear stress and mass flow rate for the downward flow, the DF case showed the highest rate of particle collisions, N_{col}/N_0, agglomeration events, N_{agg}/N_0, and breakups, N_{bk}/N_0. In contrast, the DF case showed the lowest agglomeration rate, N_{agg}/N_{col}. These observations are consistent with theory and with our earlier observations reported in Njobuenwu and Fairweather [6], where particle collision, agglomeration and breakup, all increased, while the agglomeration rate (N_{agg}/N_{col}) decreased, with an increase in the carrier-phase mass flow rate (Reynolds number). Hence, the influence of the direction of gravity in a vertical flow on particle collision, agglomeration and breakup is like that of flow Reynolds number, i.e. equivalent to increased Reynolds number of DF, and decreased for UF. In the same vain, the UF showed the least particle collision, agglomeration and breakup, but the largest agglomeration rate.

5 CONCLUSIONS

The effect of the particle size distribution (static versus dynamic), and the direction and absence of gravitational acceleration, on particle collision, agglomeration and breakup, and fluid turbulence, in vertical channel flows has been investigated. Large eddy simulation, discrete particle simulation, deterministic hard-sphere collision and energy-balanced based agglomeration models, and breakup due to hydrodynamic shear stress, were all adopted for this study. Due to the small particle Stokes number considered, inherent in a solid-liquid flow and small simulation time $\Delta t^* \sim 100$, only small effects were observed for the static versus dynamic particle size distribution on the fluid turbulence. In the vertical channel flow case, particles in downward and zero gravity flows are transported towards the wall where they accumulate, while particles in upward flow migrate away from the wall. This segregation pattern, as well as changes in the wall shear stresses and mass flow rate due to buoyancy effects, do affect the flow turbulence and the evolution of inter-particle collisions and the collision efficiency, as well as agglomerate breakup rate.

6 ACKNOWLEDGEMENTS

The authors would also like to thank the EPSRC for their support of the DISTINCTIVE (Decommissioning, Immobilisation and Storage Solutions for Nuclear Waste Inventories) Consortium under grant EP/L014041/1 which supported the work described.

REFERENCES

[1] Yamamoto, Y., Potthoff, M., Tanaka, T., Kajishima, T. and Tsuji, Y. Large-eddy simulation of turbulent gas–-article flow in a vertical channel: Effect of considering inter-particle collisions. *J. Fluid Mech.* (2001) **442**:303-334.

[2] Njobuenwu, D.O. and Fairweather, M. Simulation of turbulent particulate flows for nuclear waste management: Agglomeration in vertical flows. In *Computer Aided Chemical Engineering* 38, Zdravko, K. and Miloš, B. (Eds). Elsevier (2016).

[3] Marchioli, C., Picciotto, M. and Soldati, A. Influence of gravity and lift on particle velocity statistics and transfer rates in turbulent vertical channel flow. *Int. J. Multiphase Flow* (2007) **33**:227-251.

[4] Molin, D., Marchioli, C. and Soldati, A. Turbulence modulation and microbubble dynamics in vertical channel flow. *Int. J. Multiphas. Flow* (2012) **42**:80-95.

[5] Njobuenwu, D.O. and Fairweather, M. Deterministic modelling of particle agglomeration in turbulent flow. In *Eighth International Symposium on Turbulence, Heat and Mass Transfer*, Sarajevo (2015), 587-590.

[6] Njobuenwu, D.O. and Fairweather, M. Simulation of deterministic energy-balance particle agglomeration in turbulent liquid-solid flows. *arXiv preprint arXiv:1701.02346* (2017).

[7] Babler, M.U., Biferale, L., Brandt, L., Feudel, U., Guseva, K., Lanotte, A.S., Marchioli, C., Picano, F., Sardina, G., Soldati, A. and Toschi, F. Numerical simulations of aggregate breakup in bounded and unbounded turbulent flows. *J. Fluid Mech.* (2015) **766**:104-128.

[8] Piomelli, U. and Liu, J. Large-eddy simulation of rotating channel flows using a localized dynamic model. *Phys. Fluids* (1995) **7**:839-848.

[9] Njobuenwu, D.O. and Fairweather, M. Simulation of inertial fibre orientation in turbulent flow. *Phys. Fluids* (2016) **28**:063307.

[10] Mei, R. An approximate expression for the shear lift force on a spherical particle at finite reynolds number. *Int. J. Multiphas. Flow* (1992) **18**:145-147.

[11] Sundaram, S. and Collins, L.R. Numerical considerations in simulating a turbulent suspension of finite-volume particles. *J. Comput. Phys.* (1996) **124**:337-350.

[12] Breuer, M. and Almohammed, N. Modeling and simulation of particle agglomeration in turbulent flows using a hard-sphere model with deterministic collision detection and enhanced structure models. *Int. J. Multiphas. Flow* (2015) **73**:171-206.

[13] Bini, M. and Jones, W. Particle acceleration in turbulent flows: A class of nonlinear stochastic models for intermittency. *Phys. Fluids* (2007) **19**:035104.

[14] Marchioli, C. and Soldati, A., Reynolds number scaling of particle preferential concentration in turbulent channel flow. In *Advances in Turbulence XI*. 117, Palma, J. M. L. M. and Lopes, A. S. (Eds). Springer (2007).

[15] Pang, M., Wei, J. and Yu, B. Effect of particle clusters on turbulence modulations in liquid flow laden with fine solid particles. *Braz. J. Chem. Eng.* (2011) **28**:433-446.

V International Conference on Particle-based Methods – Fundamentals and Applications
PARTICLES 2017
P. Wriggers, M. Bischoff, E. Oñate, D.R.J. Owen, & T. Zohdi (Eds)

PARTICLE CONCENTRATION AND STOKES NUMBER EFFECTS IN MULTI-PHASE TURBULENT CHANNEL FLOWS

L. MORTIMER, M. FAIRWEATHER AND D. O. NJOBUENWU

University of Leeds
School of Chemical and Process Engineering, University of Leeds, Leeds, LS2 9JT, UK
pmlfm@leeds.ac.uk

Key words: Direct numerical simulation, Lagrangian particle tracking, Particle-laden flow, Fluid dynamics, Concentration, Stokes number

Abstract. This investigation examines the effect that particle concentration has on the dynamics of two-phase turbulent channel flows at low and high density ratios. In the literature, little explanation is offered for the existence of high particle turbulence intensities in the buffer layer and viscous sublayer for particles with high Stokes number. The present study aims to explore particle dynamics in those regions. The spectral element method DNS solver, Nek5000, is used to model the fluid phase at a shear Reynolds number, $Re_\tau = 180$. Particles are tracked using a Lagrangian approach with inter-phase momentum exchange (two-way coupling). Mean fluid and particle velocity statistics are gathered and analysed to determine the effect of increasing both Stokes number and concentration. Results indicate that the system with the greater Stokes number (air) has a much larger impact on the mean streamwise velocity and turbulence intensity profiles. As the concentration is increased, the mean flow velocity and turbulence intensity are reduced in the bulk and increased very close to the wall. For the low Stokes system, there is negligible effect on the flow statistics at low concentration. One-way coupled solid-phase statistics indicate that particles in water follow the flow very closely. At the higher density-ratio, particles lag behind the flow in the bulk, but overtake the flow in the near-wall region, where the existence of increased streamwise turbulence intensities is also observed. To elucidate the dynamics, concentrations and fluxes are analysed. Particles are observed to be distributed more densely close to the wall in air, compared to a reasonably uniform distribution in water. Finally, contour plots indicate that particles in air tend to congregate in regions of low streamwise fluid velocity, and the extent to which this differs between the two systems is then quantitatively measured.

1 INTRODUCTION

The transport of solid particles by turbulent fluid flows is common in many natural and industrial processes. A detailed understanding of the dynamics of such systems is important in determining the properties of the flow, and in particular the dispersion, deposition and resuspension of particles. A knowledge of these mechanisms is vital to improving and optimising flow systems containing particulate suspensions. Nevertheless, due to the complex nature of particle-turbulence interaction, the dynamics and mechanisms underpinning the motion of particles in these flows is currently not fully understood. Previous work investigating

this kind of phenomena has demonstrated Stokes number-dependent particle behaviour in the near-wall region [1-3]. However, understanding of the physics of this behaviour is poor, with relatively few sources offering explanations for its existence. Preferential concentration of particles in low-velocity regions close to solid surfaces has also been observed [4], but the extent to which particles remain in these low speed streaks is unknown. The topic of turbulence modulation through two-way coupling is also of great interest, since the volume fraction of most industrial flows tends to be high. It has been shown that the addition of particles can either enhance or attenuate the turbulence depending on the properties of the solid phase [5]. This tends to depend on the size of the particles such that those with large diameters ($d_P > 500\mu m$) will increase the streamwise turbulence intensity [6] whilst the latter is attenuated for those with small diameters.

The purpose of this study is to compare the dispersive properties of particle-laden turbulent flows at two different Stokes numbers representing identical glass particles in water and air. By fixing the diameter of each set of particles, we can examine more closely the effect of density ratio. In order to assess the extent to which particle concentration affects the turbulence field, the air channel flow is also compared at low and high volume fractions.

The fluid phase is modelled using the direct numerical simulation code, Nek5000, at a shear Reynolds number, $Re_\tau = 180$. A two-way coupled Lagrangian point-particle tracking method is used to predict the dispersed solid phase. A non-dimensional particle equation of motion is introduced using solely solid phase properties, non-dimensionalised against bulk fluid length and timescales. This includes the effects of drag, lift, pressure gradient and added mass forces. A feedback force is included in the Navier-Stokes equations based on the sum of particle forces in a grid-cell to account for two-way coupling. In both low and high concentration situations, the volume fraction is high enough to cause turbulence modulation. To allow focus primarily on the two-way interaction of these systems, inter-particle collisions will not be considered.

2 METHODOLOGY

2.1 Fluid simulation

The carrier-fluid field representing a fully developed channel flow is obtained using direct numerical simulation. This allows for resolution of the smallest length and time scales associated with the dynamic turbulent structures of the flow. In this work the Eulerian-phase solver, Nek5000 [7], was used which utilizes a high-order spectral element method to simulate the fluid phase. This code was chosen due to its efficient parallelisation capabilities and extensive testing and validation history. In the code, the incompressible Navier-Stokes equations are solved to high accuracy on a discretized Cartesian grid consisting of $27 \times 18 \times 23$ 8^{th} order elements (i.e. 5.7M nodes). The elements are scaled such that the nodes closest to the wall are distributed more densely. The Navier-Stokes equations are non-dimensionalised using the channel half-height, δ, the bulk velocity, U_B, and the fluid phase density, ρ_F. From here on, a quantity with an asterisk (*) denotes a variable non-dimensionalised in this manner.

The equations are:

$$\boldsymbol{\nabla} \cdot \boldsymbol{u}^* = 0 \tag{1}$$

$$\frac{\partial \boldsymbol{u}^*}{\partial t^*} + \boldsymbol{u}^* \cdot \boldsymbol{\nabla} \boldsymbol{u}^* = -\boldsymbol{\nabla} \mathrm{p}^* + \frac{1}{Re_B} \boldsymbol{\nabla} \cdot \boldsymbol{\tau}^* + \boldsymbol{f}_C^* \tag{2}$$

where $\boldsymbol{u}^*$ is the fluid velocity, p^* is the fluid pressure, Re_B is the bulk Reynolds number defined as $Re_B = U_B \delta / \nu_F$, ν_F is the fluid kinematic viscosity and $\boldsymbol{\tau}^*$ is the viscous stress tensor. The additional term $\boldsymbol{f}_C^*$ is cell-dependent and accounts for the two-way momentum exchange between particles in that cell and the surrounding fluid.

For this study, the computational position domain (x, y, z) corresponds to a $12\delta \times 2\delta \times 6\delta$ channel. Here, x is the streamwise direction, y is the wall-normal direction, and z is the spanwise direction. Periodic boundary conditions are enforced in the streamwise and spanwise directions, whereas the wall-normal axis uses nonslip conditions at $y^* = \pm\delta$. The flow is driven and maintained by a constant pressure gradient. Using non-dimensional parameters this is:

$$\frac{\partial p^*}{\partial x^*} = \left(\frac{Re_\tau}{Re_B}\right)^2 \tag{3}$$

where Re_τ is the shear Reynolds number.

2.2 Particle dynamics

In order to model the transport of large numbers of particles through the fluid field, a Lagrangian particle tracker (LPT) was developed which interfaces concurrently with Nek5000. Each element of the solid phase is represented by a computational sphere. The LPT solves the non-dimensional Newtonian equations of motion for each particle in order to calculate trajectories. This equation is derived by considering the force-balance between the particle's inertia and the fluid. For this study, we have chosen to consider contributions from drag, lift, virtual mass and pressure gradient forces. The Basset history force has been neglected due to long computation times and previous evidence [8] showing little effect on the resulting motion.

The equations of motion are as follows:

$$\frac{\partial \boldsymbol{x}_P^*}{\partial t^*} = \boldsymbol{u}_P^* \tag{4}$$

$$\frac{\partial \boldsymbol{u}_P^*}{\partial t^*} = \underbrace{\frac{3 C_D |\mathbf{u}_\mathbf{s}^*|}{4 d_p^* \rho_P^*} \mathbf{u}_\mathbf{s}^*}_{Drag} + \underbrace{\mathbf{g}^* (1 - \rho^*)}_{Gravity} + \underbrace{\frac{3}{4} \frac{C_L}{\rho_P^*} (\mathbf{u}_\mathbf{s}^* \times \boldsymbol{\omega}_F^*)}_{Lift} + \underbrace{\frac{1}{2\rho_P^*} \frac{D' \mathbf{u}_\mathbf{F}^*}{Dt^*}}_{Virtual\ Mass} + \underbrace{\frac{1}{\rho_P^*} \frac{D \mathbf{u}_\mathbf{F}^*}{Dt^*}}_{Pressure\ Gradient} \tag{5}$$

In Equations (4) and (5), $\boldsymbol{x}_P^*$ represents the coordinates of the particle position, $\boldsymbol{u}_P^*$ is the particle velocity, $\boldsymbol{u}_S^* = \boldsymbol{u}_F^* - \boldsymbol{u}_P^*$ is the particle-fluid slip velocity, d_P^* is the diameter of the particle non-dimensionalised by the channel half-height, ρ_P^* is the particle-fluid density ratio and $\boldsymbol{\omega}_F^*$ is the fluid vorticity at the particle position given by $\boldsymbol{\omega}_F^* = \boldsymbol{\nabla} \times \boldsymbol{u}_F^*$. The drag coefficient, C_D, is taken from standard empirical observations [9, 10] and the lift term uses the Saffman-Mei [11, 12] coefficient. A fourth order accuracy Runge-Kutta scheme was applied (with a Δt equal to that of the continuous phase solver) for integration of the differential equations in order to obtain each particle's position and velocity at each fluid timestep. Each particle's inertial effect on the fluid phase was considered through the inclusion of an additional source term in the Navier-Stokes equations:

$$\boldsymbol{f}_C^* = \frac{1}{V_C}\sum_{P=1}^{N_P} \boldsymbol{F}_P^* \tag{6}$$

where V_C is the volume of a computational cell, N_P is the number of particles in that cell and $\boldsymbol{F}_P^*$ is the non-dimensional fluid force exerted on particle P. This is applied at each fluid timestep and uses the particle force calculation from the previous timestep.

Table 1: Simulation parameters (L: Low concentration, H: High concentration).

Parameter	Water (L)	Air (L)	Water (H)	Air (H)
Shear Reynolds number, Re_τ	180	180	180	180
Bulk Reynolds number, Re_B	2800	2800	2800	2800
Particle diameter, d_P^*	0.005	0.005	0.005	0.005
Number of particles, N_P	300,000	300,000	2,566,851	2,566,851
Shear Stokes number, St_τ	0.113	91.845	0.113	91.845
Bulk Stokes number, St_B	0.01	7.937	0.01	7.937
Density ratio, ρ_P^*	2.5	2041	2.5	2041
Volume fraction, Θ_P	10^{-4}	10^{-4}	10^{-3}	10^{-3}

The properties used in each simulation are presented in Table 1. Each simulation presented here was performed both one-way and two-way coupled, with the exception of the high-concentration water flow due to time constraints. The simulations were first run as a single-phase flow using a standard turbulent profile with added chaotic terms in the wall-normal and spanwise directions. Once turbulence was established, fluid statistics were monitored every 100 non-dimensional time units until the mean streamwise velocity and RMS velocity fluctuations had reached a statistically steady state.

Particles were then injected uniformly throughout the channel and given an initial velocity equal to that of the fluid. Particle statistical distributions across the wall-normal direction were obtained by splitting the domain into 120 cuboidal regions of equal size, and taking an average over all the particles in that zone. Once the particle number density near the wall had reached a stable value, considered later, particle data was collected and statistics were obtained. It was from this stable state that the two-way coupled runs were started, reducing the fluid and particle timestep initially to avoid divergences in the flow field due to high particle forces. The fluid velocity statistics were then tracked once again to determine whether the system had finished responding to the addition of momentum-coupling. Once satisfied, statistics were reobtained as previously.

3 RESULTS AND DISCUSSION

3.1 Fluid phase statistics

This section explores the effect of particle concentration and Stokes number on the dynamics of the fluid phase. All flow variables plotted here are normalised by the bulk properties of the flow. Figure 1 compares the mean streamwise velocity of the fluid for each simulation as well as for the unladen flow. Here, the difference between the unladen flow and the low

concentration two-phase flow in water is negligible. This is due to the low Stokes number, limiting the momentum coupling between the two phases. In the low concentration air simulation, the mean velocity profile is slightly reduced in the bulk flow region.

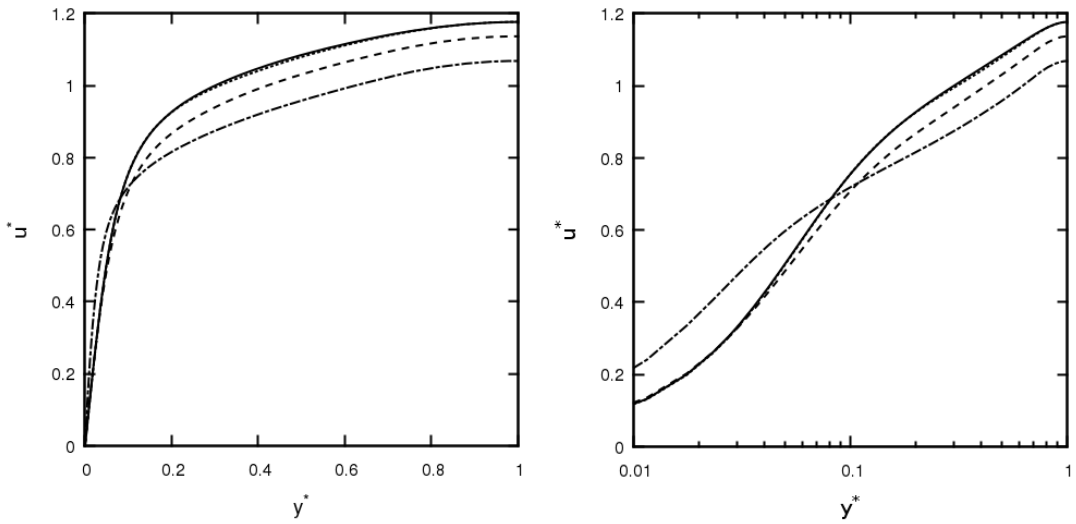

Figure 1: Mean streamwise fluid velocity comparison. — : unladen flow; - - - : two-way coupled air phase at low concentration; ..... : two-way coupled water phase at low concentration; – · – : two-way coupled air phase at high concentration.

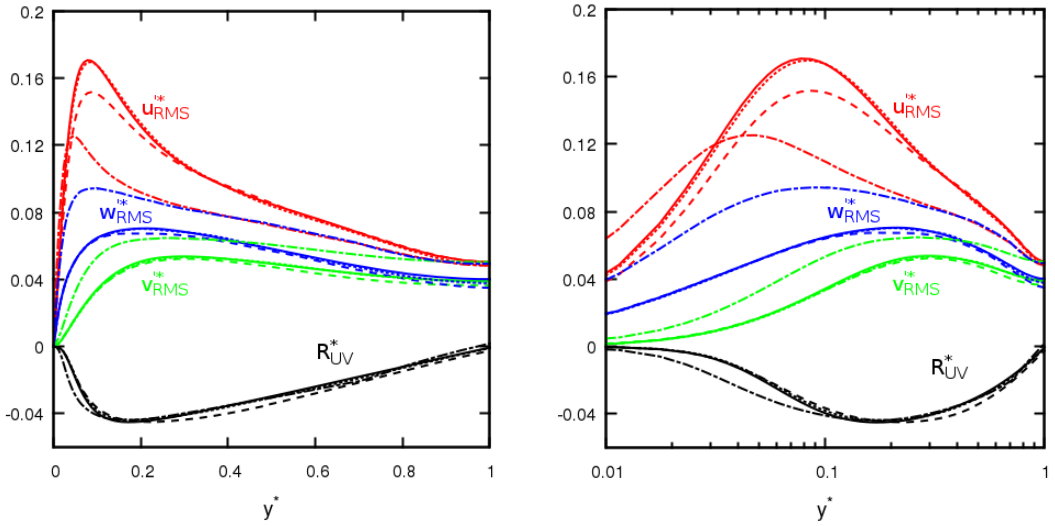

Figure 2: RMS fluid velocity fluctuations and shear stress comparison. — : unladen flow; - - - : two-way coupled air phase at low concentration; ..... : two-way coupled water phase at low concentration; – · – : two-way coupled air phase at high concentration.

This is further emphasised at high concentration, with an increase in fluid velocity found near the wall. This effectively reduces the thickness of the boundary layer and increases the

wall shear stress due to a higher wall-normal velocity derivative. The combination of both increased volume fraction and density ratio provides the particle phase with enough inertia to increase the fluid velocity close to the wall.

The fluid phase turbulent normal and shear stresses are presented in Figure 2. When compared to the unladen flow (solid lines), the particles once again show negligible impact on the water phase. With increased volume fraction, particles tend to reduce the streamwise turbulence intensities and increase the wall-normal and spanwise components. Close attention to the rightmost graph in Figure 2 indicates that the streamwise turbulence intensities are increased very close to the wall at $y^* < 0.035$.

3.2 Particle phase statistics

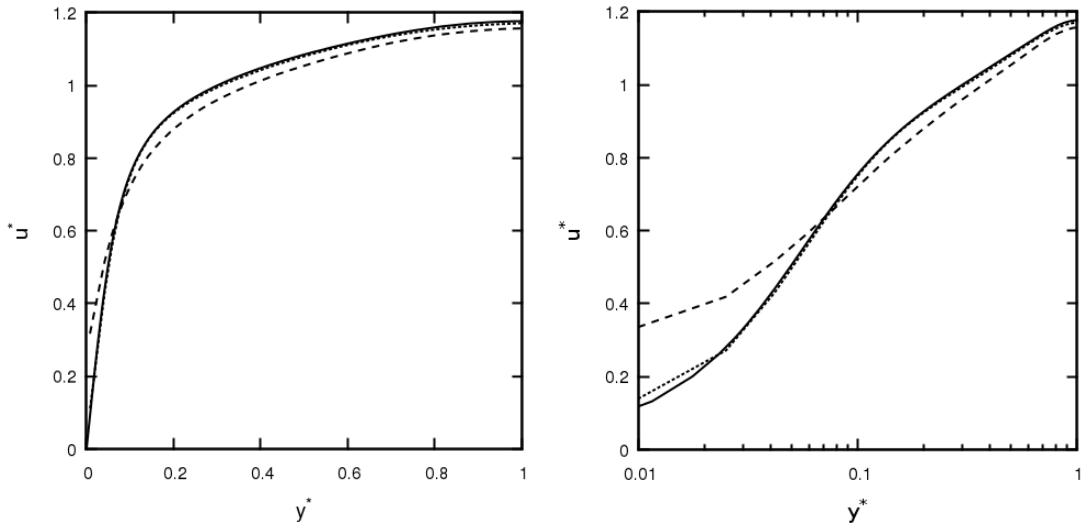

Figure 3: Mean streamwise particle velocity comparison. —— : unladen flow; - - - : one-way coupled particle phase at high concentration in air; ..... : one-way coupled particle phase at high concentration in water;

To explore the dynamics associated with the particle phase, mean velocity and RMS velocity fluctuation statistics were obtained. Figure 3 compares the one-way coupled particle mean velocities in the streamwise direction. Since one-way coupled flow statistics are concentration-independent, only the high concentration systems are considered here. For water, the particle profile is very similar to the fluid profile, with a slight increase towards the wall at $y^* < 0.02$. Particles in air generally lag behind the fluid in the bulk region, but travel faster than the fluid at $y^* < 0.08$.

Particle RMS velocities are plotted in Figure 4. There are slight deviations from all three fluid RMS components in the water channel. The spanwise and wall-normal components are all reduced slightly when compared to the unladen flow, which is most emphasised around $y^* = 0.2$ (i.e. on the boundary between the bulk and log-law regions). The streamwise component resides very close to the unladen flow except for very close to the wall where it increases somewhat. These effects are strongly emphasised at the higher Stokes number (air). A very notable feature is that the streamwise RMS velocity increases as the wall is approached and is

significantly larger than for the unladen flow profile. Large RMS values imply that particle slip velocities will also be high, since the particles are unlikely to be following the flow directly in that region due to their range of speeds. This is then directly linked to the magnitude of the coupling in that region, since the predominant forces (drag and lift) will be much greater. In this case it seems that the particles dampen the momentum, moving in a more turbulent manner themselves. In the spanwise and wall-normal direction, particles possess enough inertia to avoid being influenced by the fluid turbulence, and so their RMS velocity profiles are greatly reduced.

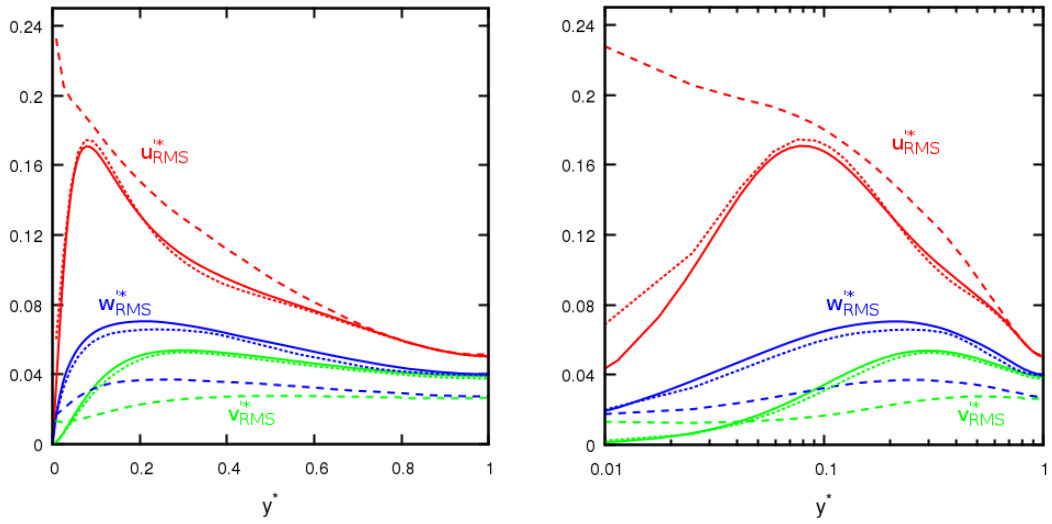

Figure 4: RMS particle velocity fluctuations comparison. —— : unladen flow; - - - : one-way coupled particle phase at high concentration in air; ..... : one-way coupled particle phase at high concentration in water;

The left plot in Figure 5 depicts the concentration of particles close to the wall over time which is used to establish whether the particle motion has reached stability. The concentration is normalised by the concentration at injection. Clearly particles in air take around 30 non-dimensional time units to reach this point, after which the gradient drops off greatly and the normalised concentration continues to deviate slightly around 2.7. The right plot shows the distribution of particles across the channel at $t^* = 150$. Here we can see more directly the effects of the increase in wall-region particle concentration for the air channel. The water channel profile remains very flat, aside from a slight increase and dip very close to the wall.

Table 2 defines the boundaries of the regions of the flow and provides the mean net flux of particles through those regions per timestep both up (towards the centre-line) and down (towards the wall). For water, it is evident that the flux (upwards and downwards) through each plane separating two regions is almost identical. This implies that there is no net 'flow' of particles in any particular direction, which is further validated by the right plot of Figure 5. This also seems to be true for air, however, there are far fewer particles moving between the log-law region and the buffer layer than there are in water. Conversely, there are more particles moving between the buffer layer and the viscous sublayer than there are in water, indicating more wall-normal motion in that region.

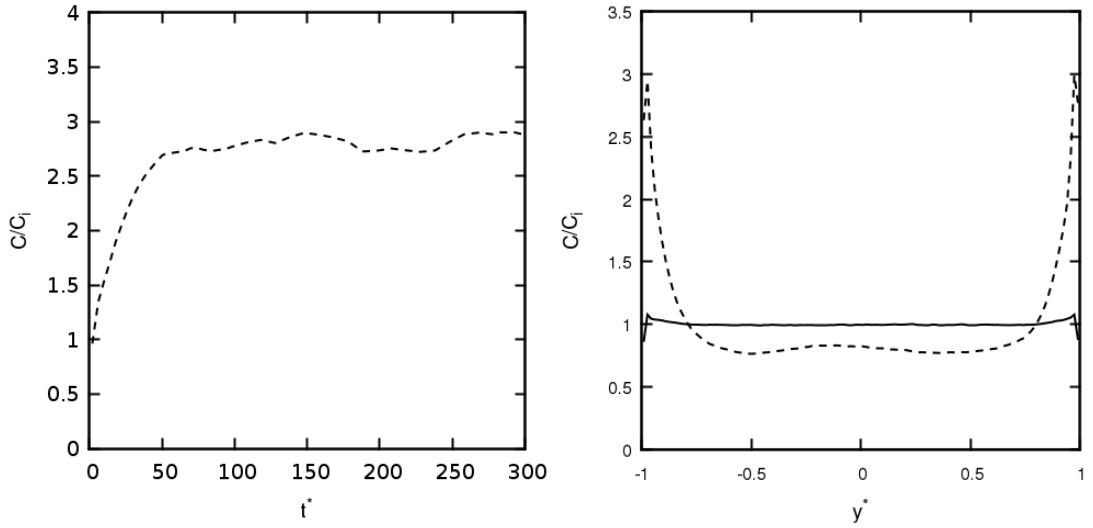

Figure 5: Instantaneous normalised particle concentration in near-wall region $y^* < 0.0083$ over time for air (left) and mean across the channel (right). —— : water; --- : air.

Table 2: Definition of flow layers in $y^*$and particle fluxes through those regions (W: Water, A: Air).

Region	Start	End	F up (W)	F up (A)	F down (W)	F down (A)
Bulk flow	0.200	1.000	-	-	994	449
Log-law	0.166	0.200	994	456	914	458
Buffer layer	0.027	0.166	914	463	137	576
Viscous sublayer	0.000	0.027	136	576	-	-

Figure 6 overlays one-way coupled particle positions on top of contour plots of the instantaneous streamwise fluid velocity on the plane $y^* = 0.0135$ for both the air and water channel flows. It is clear that for the air channel (upper plot), the particles reside predominantly in areas of low streamwise velocity (white regions). In an effort to compare the two flows more quantitatively we define a low velocity region such that the streamwise or magnitude $(u_x^*, |\boldsymbol{u}^*| < 0.75)$ and the wall-normal and spanwise components $\left(u_y^*, u_z^* < 0.025\right)$. Figure 7 shows the percentage of time a particle spends in our definition of a low velocity region for the air and water channels. The results of this analysis are also filtered by region. Comparing the two, it is notable that in all cases particles spend more time in low velocity regions in air than they do in water. In most cases, particles in air spend almost twice as much time in these regions. Note that the percentage will be strongly dependent on where we define a low-velocity region, so the emphasis of this analysis is on comparison between the two systems.

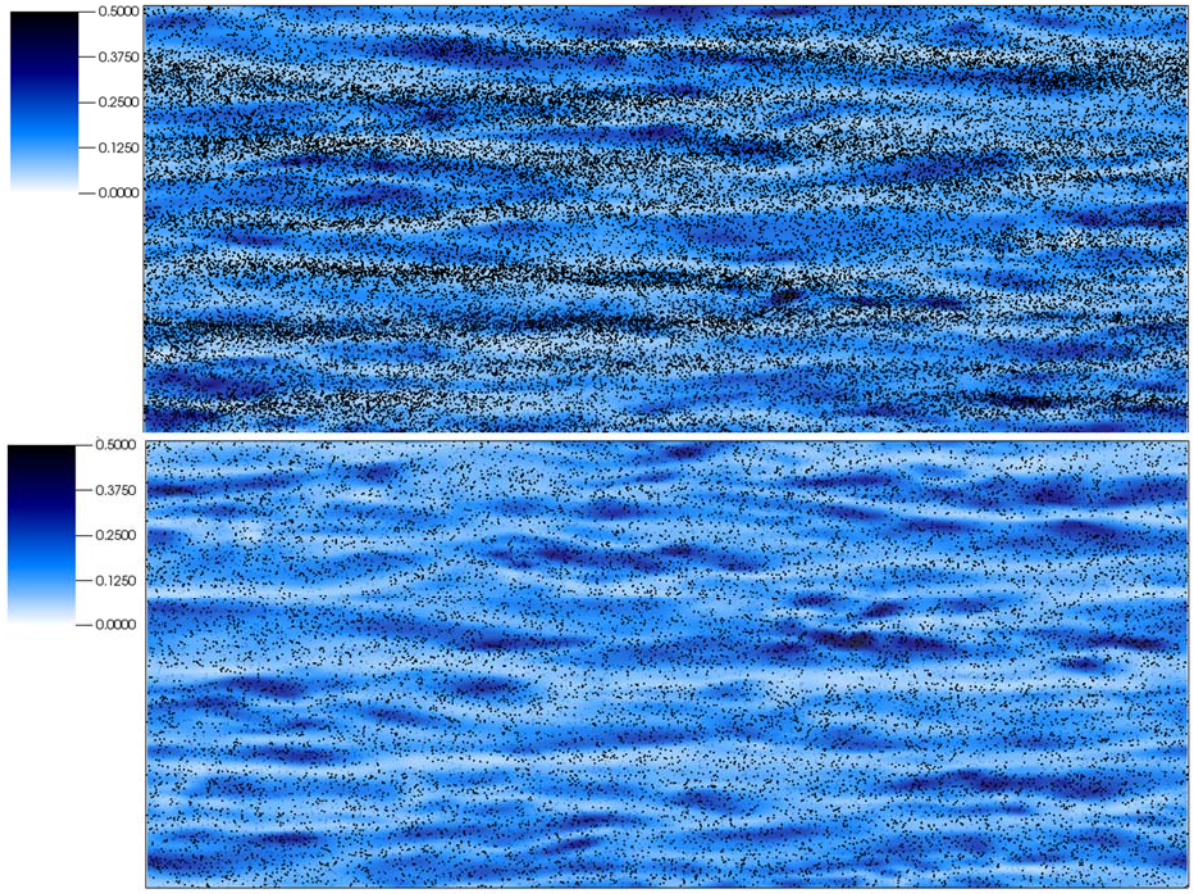

Figure 6: Particle distribution overlaid on contour plots of instantaneous fluid streamwise velocity in the viscous sublayer ($y^* = 0.0135$). Upper: Air; Lower: Water.

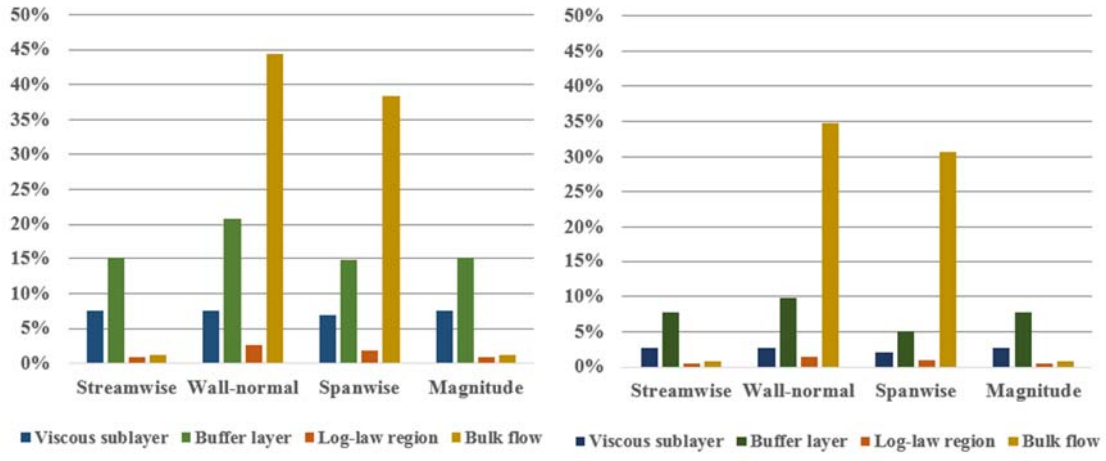

Figure 7: Percentage of time a particle spends in low velocity region for air (left) and water (right) channel flows.

4 CONCLUSIONS

This work aimed to expand the knowledge surrounding turbulence modulation and near-wall particle dynamics at high Stokes number by comparing the effects with that of a flow at low Stokes number.

It has been demonstrated that at for particles with high Stokes numbers there is a much greater impact on the turbulence, such that it dampens the streamwise component and enhances the wall-normal and spanwise components. In the near-wall region, mean particle streamwise velocity fluctuations were high for the large Stokes number system and tended to match the unladen flow for the low Stokes number system. The effect of momentum-exchange between particle and fluid and its relation to the RMS profiles for the particle phase was explored. It was speculated that the reduced fluid turbulence intensities could be due to the high particle RMS velocities in that region. It is certain that regions of high slip velocity will directly impact the magnitude of the coupling force term, but the nature of impact (attenuation or enhancement) is yet to be understood. Further work should be carried out comparing density ratios at higher particle diameters to try observe their effect on turbulence enhancement.

Particle distributions in the wall region were compared for low and high Stokes number. There was a notable increase in particle concentration near the wall during the stabilising period for the particles with greater inertia, which remained consistent for the remainder of the time considered. This was not apparent with the particles of low Stokes number, which was explained by the near identical streamwise and RMS velocity profiles. By tracing the fluid flow, the mass flux through planes in y^* must remain zero overall (as in the continuous phase), therefore there cannot be a buildup of particles in any one region. By considering particle fluxes in the wall region, we observe this to be true in the stable state for both air, and more so for water. It is also notable that the greatest amount of particle movement between one region and another takes place on the boundary between the buffer layer and the viscous sublayer for air, whereas in water this is from the bulk flow into the wall-region.

Finally, the extent to which particles remain in low velocity streaks is assessed both qualitatively and quantitively. It is indicated by considering particle distributions in the viscous sublayer that there is a tendency in air to show preference to low speed streaks, which is not apparent in water. This is confirmed and examined in further detail by partitioning the domain into regions. Results indicate that for a certain definition of a low velocity region, particles in air are around twice as likely to be found in a low speed streak than those in water. This could be further validated by considering the effect of increasing the cut-off point between ‘low’ and ‘high’ velocity regions, as particle distribution plots indicate congregation around the regions and sometimes not directly inside them.

After having observed how the turbulence is attenuated by high concentrations of small particles in high-density ratio systems, this work should be extended by performing similar simulations with larger particles. This should encourage turbulence enhancement, with the effect that density ratio and concentration has on the fluid turbulence of equal interest.

5 ACKNOWLEDGEMENTS

This work was supported by a UK Engineering and Physical Sciences Research Council grant at the University of Leeds from the EPSRC Centre for Doctoral Training in Nuclear Fission - Next Generation Nuclear.

REFERENCES

[1] Li, Y., McLaughlin, J.B., Kontomaris, K. and Portela, L. Numerical simulation of particle laden turbulent channel flow. *Phys. Fluids* (2001) **13**:2957-2967.

[2] Rouson, D.W. and Eaton, J.K. On the preferential concentration of solid particles in turbulent channel flow. *J. Fluid Mech.* (2001) **428**:149-169.

[3] Zhao, F., George, W. and Van Wachem, B. Four-way coupled simulations of small particles in turbulent channel flow: The effects of particle shape and Stokes number. *Phys. Fluids* (2015) **27**:083301.

[4] Rouson D.W.I. and Eaton, J.K. Direct numerical simulation of particles interacting with a turbulent channel flow. Proc. 7th Workshop on Two-Phase Flow Predictions, Ed. M. Sommerfeld (Erlangen, Germany, 1994).

[5] Vreman, A. Turbulence characteristics of particle-laden pipe flow, *J. Fluid Mech.* (2007) **584**:235-279.

[6] Elghobashi, S. and Truesdell, G.C. On the two-way interaction between homogeneous turbulence and dispersed solid particles. I: Turbulence modification. *Phys. Fluids* (1993) **5**:1790-1801.

[7] Fischer, P.F., Lottes, J.W. and Kerkemeier, S.G. Nek5000 Web Page. http://nek5000.mcs.anl.gov (2008).

[8] Fairweather, M. and Hurn, J.P. Validation of an anisotropic model of turbulent flows containing dispersed solid particles applied to gas-solid jets. *Comput. Chem. Eng.* (2008) **32**:590-599.

[9] Schiller, L. Neue quantitative versuche zur turbulenzentstehung. *ZAMM* (1934) **1**4:36-42.

[10] Clift, R., Grace, J.R. and Weber, M.E. *Bubbles, drops, and particles*. Courier Corporation, 2005.

[11] Saffman, P. The lift on a small sphere in a slow shear flow. *J. Fluid Mech.* (1965) **22**:385-400.

[12] Mei, R. and Klausner, J.F. Shear lift force on spherical bubbles. *Int. J. Heat Fluid Fl.* (1994) **15**:62-65.

V International Conference on Particle-based Methods – Fundamentals and Applications
PARTICLES 2017
P. Wriggers, M. Bischoff, E. Oñate, D.R.J. Owen, & T. Zohdi (Eds)

THE IMPACT OF COUPLING AND PARTICLE VOLUME FRACTION ON FLUID-PARTICLE INTERACTIONS IN A TURBULENT CHANNEL FLOW

DAVID A. RUPP, DERRICK O. NJOBUENWU AND MICHAEL FAIRWEATHER

University of Leeds
School of Chemical and Process Engineering, University of Leeds, Leeds, LS2 9JT, UK
pmdr@leeds.ac.uk

Key words: Direct numerical simulation, Particles, Concentration, Lagrangian particle tracking, Stochastic, Spectral element method

Abstract. Direct numerical simulation, facilitated by a spectral element method, is used to predict a multi-phase fluid flow through a channel at a shear Reynolds number of 300. Following validation of single- and multi-phase flow results against other DNS predictions available in the literature, a channel flow is simulated utilising a Lagrangian particle tracker to model 300,000 particles with a diameter of 100 μm, having a density ratio equivalent to that of water to glass, and a particle volume fraction of approximately 0.01%. This flow is calculated using multiple levels of coupling between the particles and the flow; one-way, two-way and four-way. The mean streamwise velocity of the fluid and the particles, along with the shear and normal stresses, are compared for the different coupling methods, with the differences between them analysed and, although small, they are found to be consistent across the channel. A second set of runs is performed using in excess of 2 million particles in order to facilitate a tenfold increase in the particle volume fraction, to 0.1%, with the particles expected in this case to have a greater impact upon the properties of the fluid. The statistics of the fluid and particles in these simulations are then compared with those from the simulation with a lower concentration of particles in order to determine the magnitude of the effect the particles have on the fluid in this flow. The effects of the different couplings on the flow are much greater in this case due to the increased number of particles affecting the flow. Also, the presence of the particles is seen to increase the turbulence levels of the fluid, especially in the streamwise direction. The accuracy of the simulations clearly increases with the level of coupling. However, the speed of the simulations decreases. One way of achieving decreased run times, for both volume fraction cases, is to use a faster stochastic version of the particle tracking code for four-way coupling. This is tested, replacing the Lagrangian collision mechanics in the four-way coupled simulations with a probabilistically-determined mechanistic model. For the lower volume fraction, the normal stresses of the particles are exaggerated somewhat using the stochastic method. The simulation time is decreased compared to the Lagrangian approach, although the results presented suggest that the stochastic method requires further refinement.

1 INTRODUCTION

Accurately simulating particle-laden flows is of fundamental importance in many industries

that, as part of their operations, are required to transport multi-phase flows, including waste. This includes industries in the chemical, nuclear, agriculture, pharmaceutical and minerals processing sectors. Without proper optimisation, these processes can be inefficient and the time between maintenance and/or replacement of equipment can be increased, with all of the associated costs.

Under complex turbulent conditions, it is laborious, if not impossible, to exactly predict how the dynamic interactions between the fluid and particles affect the flow as a whole using conventional mathematical methods, and experimentation often produces inconsistent results due to the difficulty in repeating initial conditions. Hence this work turns to computer modelling methods. Direct numerical simulation is a method which resolves the entire flow, over all length and time scales, and all of the turbulence effects within it and, when coupled to a particle tracking technique, offers the potential to provide basic understanding of particle-laden flows. However, it is also far more computationally expensive than the less inclusive, and accurate, large eddy simulation and Reynolds-averaged Navier-Stokes approaches.

By assessing the behaviour of particles within a multi-phase flow it is possible to set a useful benchmark which can be used to predict the behaviour of such flows. Depending on the scale of the change in the behaviour of the fluid when increasing its level of simulated coupling with the particles, it can be determined if the particle phase has a negligible effect or otherwise.

A number of previous works have simulated these flows in recent years [1-3]. Important findings include the fact that turbulence intensities grow more anisotropic as the particle mass loading is increased. Furthermore, qualitative descriptions have been offered [4] concerning the way particles affect the continuous phase at high concentrations. However, there is insufficient literature on the effect of various physical and flow properties of the fluid and particles in simulations of particle transport and interactions in turbulent flow. The present work, therefore, considers particle-laden channel flows using direct numerical simulation coupled to a Lagrangian particle tracking technique, with simulations performed using one-, two- and four-way coupling between the particles and the fluid flow. Two particle loadings are considered, equivalent to particle volume fractions of approximately 0.01% and 0.1%, to elucidate the effect of particle concentration on the continuous phase properties. Lastly, a stochastic method, replacing the Lagrangian collision mechanics in the four-way coupled simulations, is assessed in terms of its accuracy and potential to decrease simulation times.

2 METHODOLOGY

2.1 Fluid flow modelling

The fluid flow is simulated using a spectral element method, a hybrid of the finite-element method and the spectral method, which was developed by Patera [5]. The fluid domain is divided into elements with a resolution finer than 15 times the Kolmogorov scale, which Moser and Moin [6] have shown to be the minimum requirement to resolve the smallest turbulent structures.

$$\frac{\delta \boldsymbol{u}^*}{\delta t^*} + (\boldsymbol{u}^* \cdot \nabla)\boldsymbol{u}^* = -\nabla p^* + \frac{1}{Re}\nabla \cdot \tau^* + f_i \tag{1}$$

$$\nabla . \boldsymbol{u}^* = 0 \tag{2}$$

Equations (1) and (2) are the non-dimensional, incompressible Navier-Stokes and continuity equations solved, where $\boldsymbol{u}^*$is the fluid velocity vector, which has been non-dimensionalised using the bulk velocity U_B, and t^* is the non-dimensionalised time tU_B/δ, where δ is half the height of the channel. p^* is a non-dimensionalised pressure term equal to $p/\rho U_B^2$, where ρ is the density of the continuous phase. Re is the bulk Reynolds number given by $\delta U_B/\nu$, and τ^* is the non-dimensionalised deviatoric stress tensor given by $\tau^* = (\nabla \boldsymbol{u}^* + \nabla \boldsymbol{u}^{*\tau})$. f_i is an arbitrary forcing term that is only applied to flows with multiple phases.

The code used to simulate the fluid flow was Nek5000, an efficient DNS code developed by Fischer et al. [7].

2.2 Channel geometry

The fluid flow equations were solved for a turbulent flow in a channel with dimensions 12δ × 2δ × 6δ, with δ being the half-height of the channel, at a bulk Reynolds number of 4900, which translates to a shear Reynolds number of 300. The channel had periodic boundary conditions in the streamwise and spanwise directions, making its size arbitrary in those directions, with the channel wall having a significant effect on the flow. The computational domain was divided into 32 × 32 × 32 elements consisting of 8 × 8 × 8 nodes each, giving a total of ~16.8M nodes.

2.3 Multi-phase simulations

The first simulation considered below concerned validation of predictions of a single-phase channel flow against previous runs by Marchioli and Soldati [8]. Subsequent runs were for multi-phase flows with varying number of particles that were simulated using a highly versatile Lagrangian particle tracking code which synchronises with the Eulerian fluid flow model, time-step for time-step.

$$\frac{\partial \boldsymbol{x_P^*}}{\partial t^*} = \boldsymbol{u_P^*} \tag{3}$$

$$\frac{\partial \boldsymbol{u_P^*}}{\partial t^*} = \underbrace{\frac{3C_D|\mathbf{u_s^*}|}{4d_p^*\rho_P^*}\mathbf{u_s^*}}_{Drag} + \underbrace{\mathbf{g}^*(1-\rho^*)}_{Gravity} + \underbrace{\frac{3}{4}\frac{C_L}{\rho_P^*}(\mathbf{u_s^*} \times \boldsymbol{\omega}_F^*)}_{Lift} + \underbrace{\frac{1}{2\rho_P^*}\frac{D'\mathbf{u_F^*}}{Dt^*}}_{Virtual\ Mass} + \underbrace{\frac{1}{\rho_P^*}\frac{D\mathbf{u_F^*}}{Dt^*}}_{Pressure\ Gradient} \tag{4}$$

The tracking code solves Equations (3) and (4) for $\partial x_P^*/\partial t^*$, the change in non-dimensional position over non-dimensional time, of each particle using the fourth order Runge-Kutta method [9], although in this work gravitational effects were ignored. d_p^*, ρ_P^* and $\rho^*$are the non-dimensional particle diameter, density and fluid density, $\boldsymbol{u_s^*}$, $\boldsymbol{u_F^*}$, $\boldsymbol{\omega_F^*}$ are the slip velocity, fluid velocity and vorticity, and C_D, C_L and $\mathbf{g}^*$are coefficients of drag, lift and gravity, respectively.

The first set of particle runs used 300k 10.2 μm particles with a high density compared with that of the fluid, corresponding to fly ash with a density of 1500 kg m^{-3} in air of density 1.3 kg m^{-3}. These particles had a Stokes number of 1 and predictions were validated against the results of Marchioli and Soldati [8]. All subsequent results were collected from runs containing 100 μm particles with a density corresponding to glass, 2500 kg m^{-3}, in water, 1000 kg m^{-3}. These particles had a Stokes number of 0.3125.

The particles used for the validation noted were one-way coupled, such that the fluid applied a force on the particles but not vice-versa. In four-way coupling, the fluid is affected by the

particles and the particles are allowed to collide. The two-way coupling term in Equation (5) is added to the initial Navier-Stokes equations to account for the force the particles have on the fluid:

$$f_C = \frac{1}{V}\sum(P=1)^N F_P \tag{5}$$

Here, V is the volume of a computational cell, N is the number of particles it contains, and F_P is the force exerted on any particle P. In order to gauge the effect of neglecting higher levels of coupling, one-way coupled and four-way coupled 100 μm glass particles were run at volume fractions of 0.01% and 0.1%.

Inter-particle collisions were simulated by checking the radius of a particle and comparing it to each potential collision partner in the region, extrapolating backwards to find the time of collision and changing the particle velocity and position accordingly. In order to limit computer run times, the flow was divided into small segments and only those particles in the same segment of the flow were considered for collision. Despite this, the computational expense of this process rises drastically with the number of particles.

2.4 Stochastic method

Another way of decreasing the computational expense present in monitoring particle-particle interactions is to use the stochastic method as described by Sommerfeld [10], and forgo monitoring the colliding of particles altogether, instead treating them as probability distributions for the purpose of collision. The probability of a collision according to this method is given by first calculating the velocity $u'_{fict,i}$ of a fictional collider using Equation (6), which accounts for the Stokes number St in the form of a correlation function $R(St)$ which determines whether the fictional particle has a velocity closer to the real particle's velocity $u'_{real,i}$ or a random value calculated from the root mean squared velocity $\sigma_{p,i}$ and a Gaussian random number ξ.

$$u'_{fict,i} = R(St)u'_{real,i} + \sigma_{p,i}\sqrt{1-R(St)^2}\xi \tag{6}$$

$$R(St) = \exp(-0.55 \times St^{0.4}) \tag{7}$$

$$P_{coll} = f_c\Delta t = \frac{\pi}{4}\left(2D_\mathrm{p}\right)^2\left|\overrightarrow{u_{\mathrm{p},i}} - \overrightarrow{u_{\mathrm{p},J}}\right| n_\mathrm{p}\Delta t \tag{8}$$

Kinetic theory is then used to calculate the probability of the collision from Equation (8) based on the instantaneous relative velocity $|\overrightarrow{u_{p,i}} - \overrightarrow{u_{p,J}}|$ between the fictional and real particles, the number density n_p and the particle diameter D_p.

3 RESULTS AND DISCUSSION

3.1 Validation

Figure 1 shows the results of the single-phase validation runs against the predictions obtained by Marcholi and Soldati [8], and Morinishi and Tamano [11]. Few runs have been performed at a shear Reynolds of 300, and Morinishi and Tamano [11] only gave results for y^* values close

to the wall. Nevertheless, there is good agreement between the present results and those of these previous works. There is a slight discrepancy between the height of the peak of the stream-wise fluid normal stress, but this is at an acceptable level, and is most likely due to minor differences in the numerical methods employed.

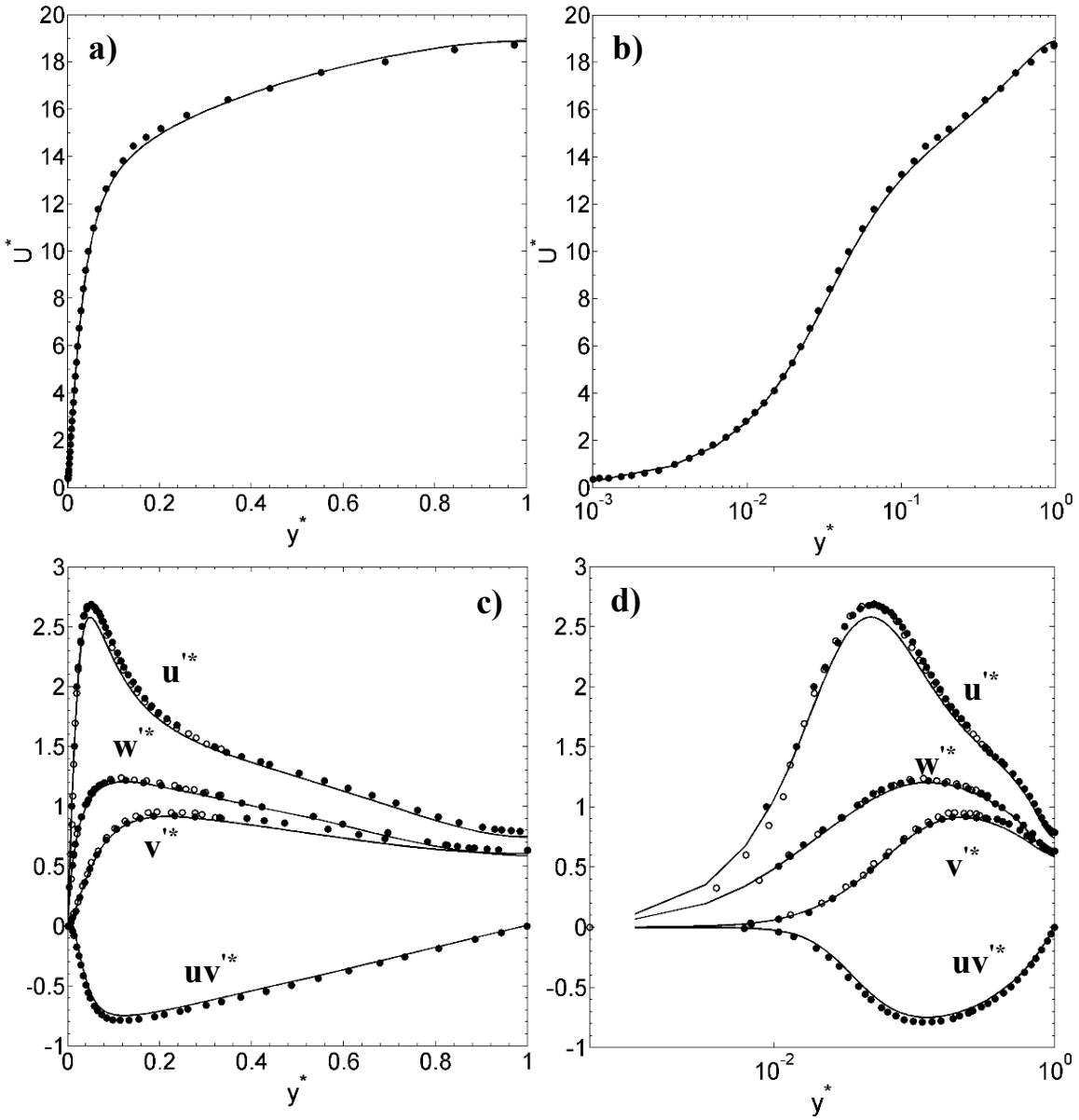

Figure 1: Validation of the mean streamwise fluid velocity U^* for a) linear scale and b) log scale, and the normal and shear stresses, u'^*, v'^*, w'^* and uv'^*, for c) linear scale and d) log scale of a single-phase flow at 300 shear Reynolds number. Present results as line, Marchioli and Soldati (2007) and Morinishi and Tamano (2005) as black and white points, respectively.

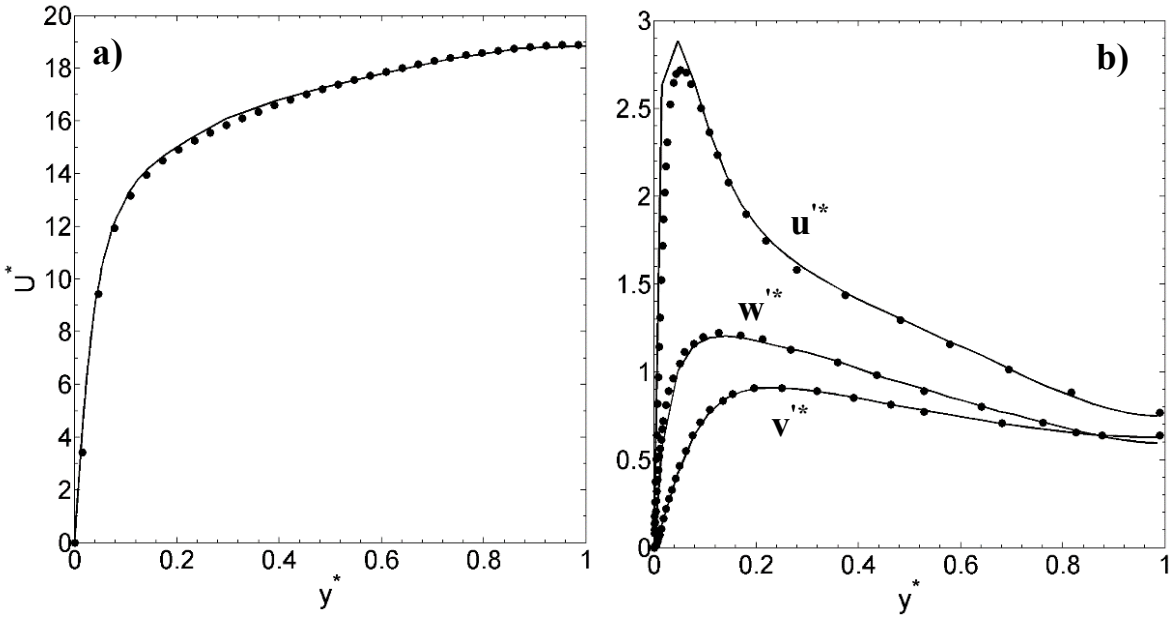

Figure 2: Validation of a) the mean streamwise particle velocity U^* and b) the normal stresses u'^*, v'^* and w'^* of a one-way coupled multiphase flow at 300 shear Reynolds numer. Present results as line, Marchioli and Soldati (2007) as points.

Figure 2 gives the results of a multi-phase validation run, plotting the mean streamwise velocity and the normal stresses for the particles. Since the flow was one-way coupled the fluid phase for this run is as in Figure 1. The particles again show mean streamwise velocity and normal stress values which are a good match to the predictions of Marchioli and Soldati [8].

3.2 Low concentration comparisons

The glass spheres were then run in a water flow at a volume fraction of 0.01% to compare the effects of one-way and four-way coupling between the fluid and particle phases at a Reynolds number of 300. The results are given in Figure 3. At first glance the difference in the fluid flow seems negligible, with the mean streamwise velocity unchanged between the two sets of results. There is a not imperceptible increase in the fluid and particle velocities towards the centre of the flow, however, and between $\pm 0.2\delta$ and $\pm 0.6\delta$, it is clear that the four-way coupled fluid flow has a slightly greater streamwise velocity fluctuation than for the one-way case.

In the region between $\pm 0.7\delta$ and $\pm\delta$, towards the centre of the flow, the streamwise velocity fluctuation of the four-way coupled run dips below the one-way case, but the spanwise and wall normal fluctuations increase slightly. In the region between $\pm 0.2\delta$ the peak shows a similar trend and this would appear to accord with energy conservation laws, namely, the kinetic energy from the streamwise direction is transferred to or from the other directions. The particle velocities and stresses show markedly similar responses .

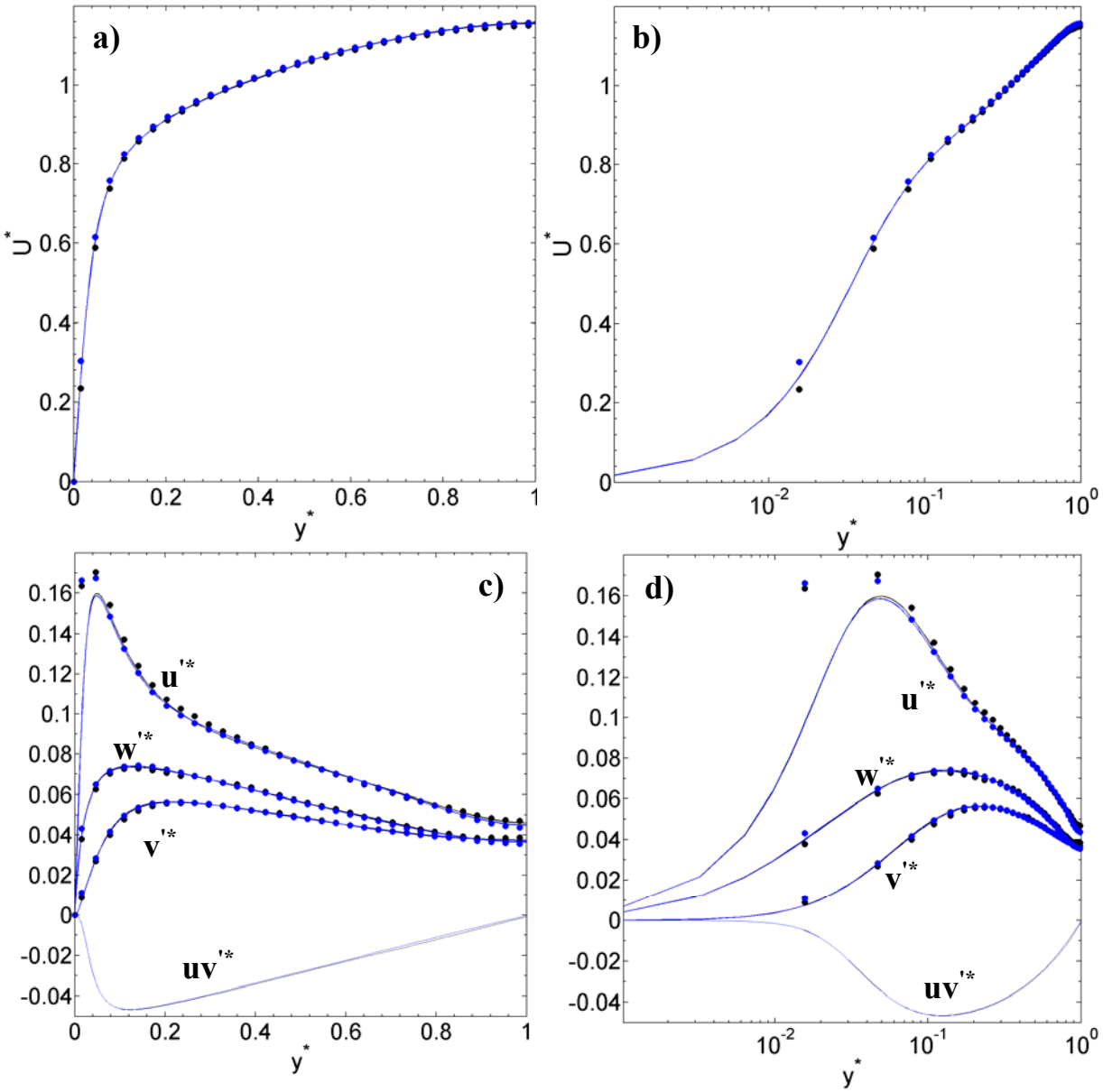

Figure 3: Mean streamwise velocities U^* for a) linear scale and b) log scale, and the normal and shear stresses u'^*, v'^*, w'^* and uv'^*, for c) linear scale and d) log scale of a multiphase flow with 100μm particles at a volume fraction of 0.01% and 300 shear Reynolds number. Fluid and particles as solid line and points, respectively, with one-way coupled in black and four-way coupled in blue.

3.3 High concentration comparisons

The particles at a volume fraction of 0.1% show a magnified difference between the effects of one-way and four-way coupling (Figure 4). The mean streamwise velocity and all of the normal stresses are greater in the latter case. The turbulence level in the fluid flow has thus seen

a noticeable increase. These effects are more pronounced away from the centre of the channel, as for the low concentration results.

Although increasing the number of particles does change the behaviour of the fluid, and increases the impact of the particles on the flow, the particles themselves show a strong tendency to follow the flow that does not change with concentration, despite the fact that they are affecting the medium in which they are carried. The low Stokes number of the particles makes this unsurprising.

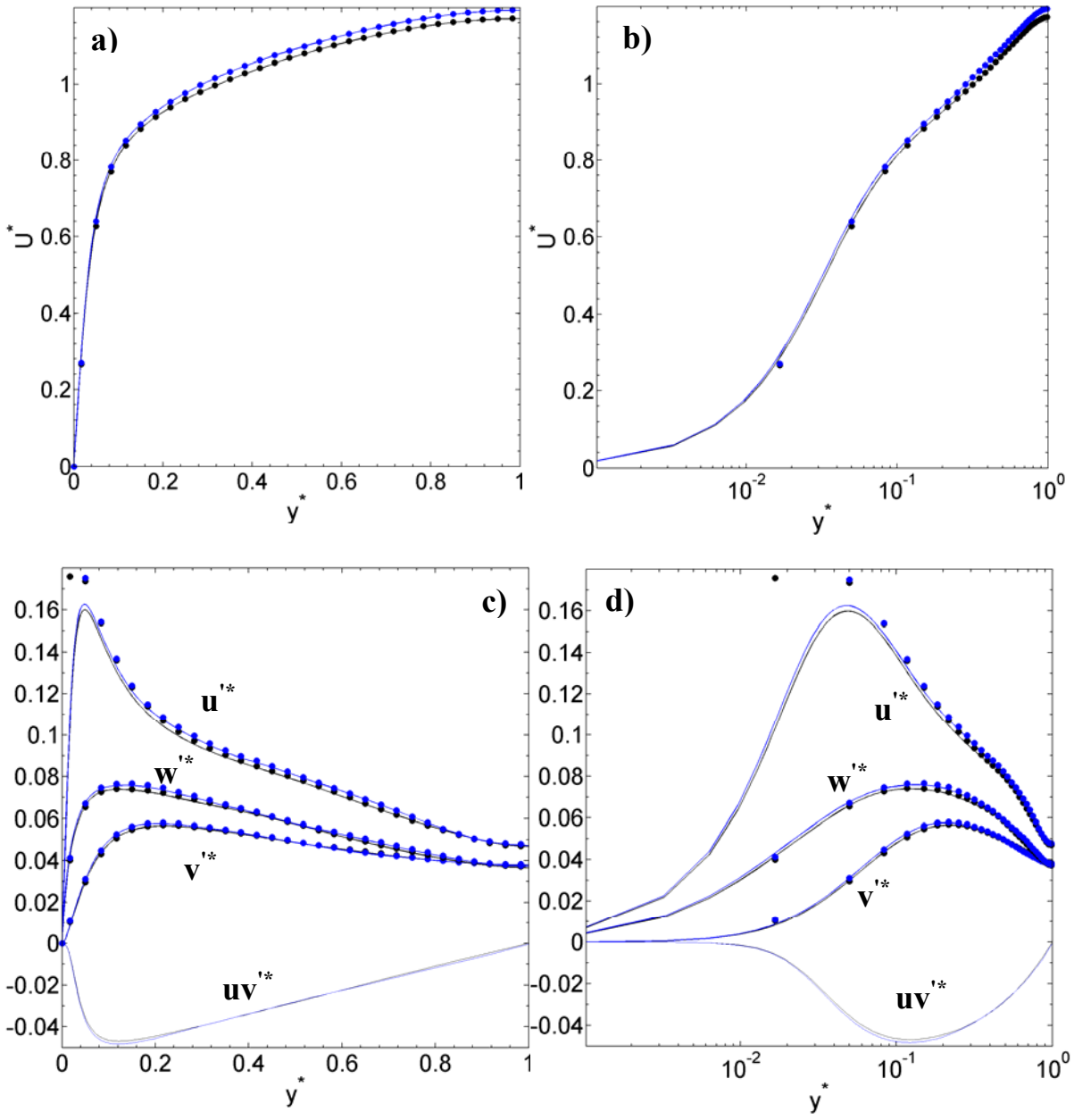

Figure 4: Mean streamwise velocities U^* for a) linear scale and b) log scale, and the normal and shear stresses u'^*, v'^*, w'^* and uv'^*, for c) linear scale and d) log scale of a multiphase flow with 100μm particles at a volume fraction of 0.1% and 300 shear Reynolds number. Fluid and particles as solid line and points, respectively, with one-way coupled in black and four-way coupled in blue.

3.4 Stochastic model

Under the same conditions as the previous low concentration runs, the results of which are given in Figure 3, the stochastic method was used with the aim of providing a suitably accurate set of predictions without the relatively slow computational speed of the Lagrangian collision mechanics that the regular four-way coupled approach used. The mean streamwise velocity, as before, varied only slightly due to the change in methodology, as shown in Figure 5, but the particle normal stresses now differ considerably from the fluid normal stresses in a way that suggests a methodical overprediction of these values, when compared to the results of Figure 3, especially considering the fact that the divergence in predictions increases considerably towards the centre of the flow. For the low volume fraction, therefore, the normal stresses of the particles are exaggerated somewhat using the stochastic method, although this was found to be less the case for the higher volume fraction (not shown). In both cases the simulation time was decreased compared to the Lagrangian approach, although the results suggest that the stochastic method requires further refinement.

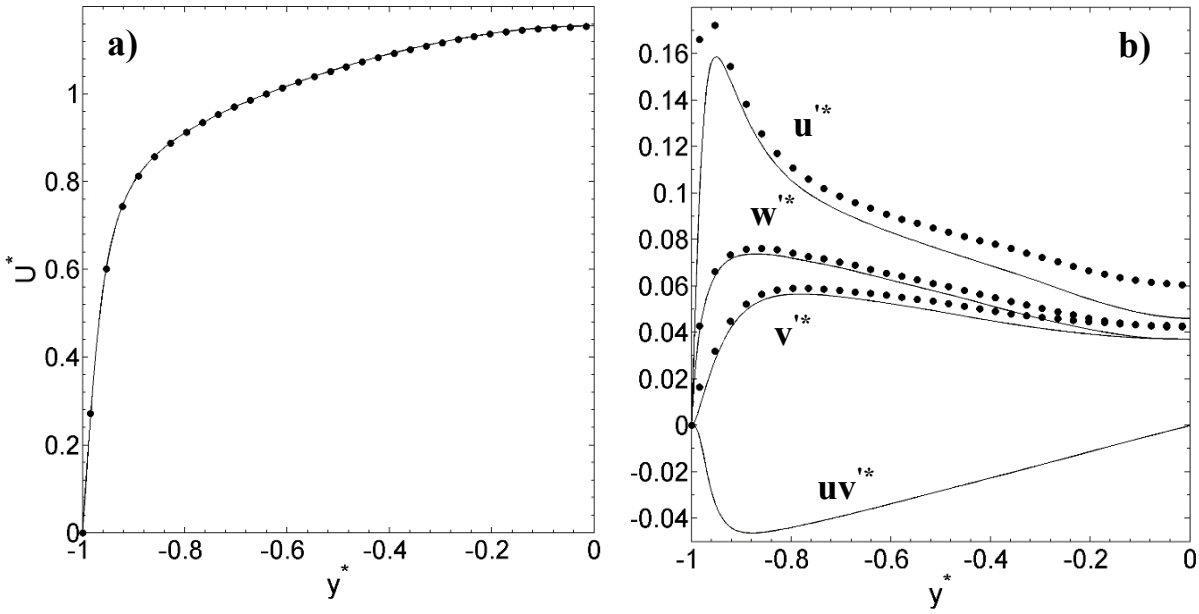

Figure 5: a) Mean streamwise velocity U^* and b) the normal and shear stresses u'^*, v'^*, w'^* and uv'^* for 100μm particles at a volume fraction of 0.01% and 300 shear Reynolds number using a stochastic collision metric. Fluid flow results as line, particles as points.

4 CONCLUSIONS

The study reported considered the effects of different particle-fluid coupling regimes on the turbulence statistics of a simulated multi-phase channel flow at a shear Reynolds number of 300. By performing direct numerical simulations, coupled to particle tracking, at different particle concentrations and differing levels of coupling, results have been established that demonstrate how particles affect the turbulent flow at this Reynolds number. Further work should consider investigating the impact of lower and higher volume fractions of particles than

considered herein, as well as different sizes of particles, to establish precisely those flows in which it is necessary to use higher order coupling and for which flows such coupling is unnecessary. For higher concentrations of particles, the implementation of a stochastic collision metric, rather than a full four-way coupling approach, becomes advantageous in terms of model run times, although the results presented suggest that the stochastic method used requires further refinement prior to its use in computing such flows.

REFERENCES

[1] Squires, K.D. and Eaton, J.K. Particle response and turbulence modification in isotropic turbulence. *Phys. Fluids* (1990) **A2**:1191-1203.

[2] Sundaram, S. and Collins, L.R. A numerical study of the modulation of isotropic turbulence by suspended particles. *J. Fluid Mech.* (1999) **379**:105-143.

[3] Li, Y., McLaughlin, J.B., Kontomaris, K. and Portela, L. Numerical simulation of particle-laden turbulent channel flow. *Phys. Fluids* (2001) **13**:2957-2967.

[4] Vreman, B., Geurts, B.J., Deen, N., Kuipers, J.A. and Kuerten, J.G. Two-and four-way coupled Euler-Lagrangian large-eddy simulation of turbulent particle-laden channel flow. *Flow Turbul. Combust.* (2009) **82**:47-71.

[5] Patera, A.T. A spectral element method for fluid dynamics: Laminar flow in a channel expansion. *J. Comput. Phys.* (1984) **54**:468-488.

[6] Moser, R.D. and Moin, P. Direct numerical simulation of curved turbulent channel flow. NASA TM 85974 (1984).

[7] Fischer, P.F., Lottes J.W. and Kerkemeier S.G. Nek5000 Web Page. http://nek5000.mcs.anl.gov (2008).

[8] Marchioli, C. and Soldati, A. Reynolds number scaling of particle preferential concentration in turbulent channel flow. In: Palma J., Lopes A.S. (Eds) Advances in Turbulence XI, Springer Proceedings Physics, 117, Springer, Berlin (2007).

[9] Süli, E. and Mayers, D. *An introduction to numerical analysis*. Cambridge University Press, 2003.

[10] Sommerfeld, M. Validation of a stochastic Lagrangian modelling approach for inter-particle collisions in homogeneous isotropic turbulence. *Int. J. Multiph. Flow* (2001) **27**: 1829-1858.

[11] Morinishi, Y. and Tamano, S. Study on differences in turbulence statistics between compressible and incompressible low-Reynolds number turbulent channel flows using semi-local scaling. *JSME Int. J. Ser. B* (2005) **48**:743-749.

V International Conference on Particle-based Methods – Fundamentals and Applications
PARTICLES 2017
P. Wriggers, M. Bischoff, E. Oñate, D.R.J. Owen, & T. Zohdi (Eds)

3D LASER SCANNING TECHNIQUE COUPLED WITH DEM GPU SIMULATIONS FOR RAILWAY BALLASTS

PATRICK PIZETTE[1], NICOLIN GOVENDER[1,2], DANIEL N. WILKE[3], BENJAMIN GOBE[1,4], NOR-EDINE ABRIAK[1] AND RAJ K. RAJAMANI[5]

[1] IMT Lille Douai, Univ. Lille, EA 4515 - LGCgE - Laboratoire de Génie Civil et géoEnvironnement, départment Génie Civil & Environnemental, F-59000 Lille, France
patrick.pizette@imt-lille-douai.fr and http://www.lgcge.fr

[2] Research Center Pharmaceutical Engineering, GmbH, Graz , Austria
govender.nicolin@gmail.com and http://www.rcpe.at

[3] Centre of Asset and Integrity Management, University of Pretoria, South Africa
wilkedn@gmail.com and http://www.up.ac.za/centre-for-asset-integrity-

[4] COLASRAIL, Maisons-Laffitte, France and http://www.colasrail.com

[5] University of Utah, Metallurgical Engineering Department, University of Utah, USA
rajkrajamani@gmail.com and faculty.utah.edu

Key words: Granular Materials, DEM, Ballast, Railway, 3-D laser scanning, large scale DEM simulation, polyedron

Abstract. Spheres with complex contact models or clumped sphere models are classically used to model ballast for railway applications with the Discrete Element Method (DEM). These simplifications omits the angularity of the actual ballast by assuming the ballast is either round or has rounded edges. This is done by necessity to allow for practically computable simulations that may consist of a few hundred particles. This study demonstrates that an experimentally validated DEM simulation environment, BlazeDEM-3DGPU, that computes on the graphical processing unit (GPU) is able to simulate railway ballast with a more realistic shapes that includes angularity for railway applications. In particular, a procedure is developed that extracts polyhedral shaped ballast geometries digitized from 3D-laser scanning for use in DEM simulations. The results show that much larger number of particles can be successfully modelled allowing for new possibilities offered by the GPUs to investigate model railway problems using DEM. Specifically, in this study a typical experimental ballast box that contains up to 60 000 polyhedral particles have been simulated with the BlazeDEM-3DGPU computing environment within reasonable computing times.

1 INTRODUCTION

France has the second largest European railway network that accounts for a total of 29 901 km of railway. The French railway network is comprised of 16 445 km of double track railway, 15 140 km electrified railway and 1 876 km can accommodate high-speed trains. The main track gauge and high-speed track gauge are both 1 435 mm. In 2014 a freight of 32 billion tonne-km was hauled and a passenger distance of 84 billion passenger-km serviced in France alone. The integrity of the railway relies significantly on the integrity of the railway ballast that supports the railway with failure proving disastrous [**?**, **?**]. The deterioration of superstructure ballast and sub-ballast is amplified by train-track vibrations of high speed trains inadequate water drainage that may cause subsidence of the superstructure ballast and track. As a consequence a number of countries have limited the maximum speed of high speed trains which include China that reduced speeds from 220 mph to 185 mph, Eurostar in Britain runs up to 185 mph and the TGV Est in France reaches only 200 mph.

Particle shape is a key parameters that influences the performance of railway ballast in particular the settling of railway ballast. Specifically, railway ballast depends strongly on the particle shape, surface roughness and wear characteristics of the ballast. As a consequence railway industries have imposed standards to define quality requirements regarding railway ballast.

In parallel, researchers are developing simulation methodologies to tackle the problematic settling of ballasts as freight is hauled within an infrastructure. In particular, the discrete element method (DEM) is classically used to better understand the settling of ballasts under repeated cyclic loading and train-track vibrations. The computational demands of DEM often limits these studies to 2D simulations [2] with limited 3D simulations that at most consider clumped spherical particles [2] with neglects the effect of particle angularity. This is unfortunate as one of the critical geometric aspects of ballast and ballast degradation is particle angularity. This is poorly represented using clumped spherical representations [2, 3] or using a modified rolling contact model adapted from simple individual spheres [4].

This study investigates the potential of BlazeDEM-3DGPU [5] code to model

1. realistic ballast particle shapes,
2. large number of particles in 3D ballast simulations,
3. ballast using GPU based simulations.

In this study preliminary simulation results are presented but in future studies aim to validate simulations against experimental results to assess the importance of accurate and realistic particle representations when modeling ballast. The GPU that makes highly efficient parallelized hardware available is essential for our study towards ii) increasing the number of particles in a ballast simulation within reasonable computing times on multiple

GPUs [5, 6, 7], while the specific DEM environment BlazeDEM-3DGPU [5] is crucial i) to model polyhedral convex and non-convex shaped particles that allows for accurate and efficient incorporation of both angularity and interlocking of the ballast. The GPU by design a highly parallelized hardware architecture as a typical CPU node can launch 12 threads per cycle, a GPU node can launch 53284 threads per cycle. This allows for particle scale simulation to be explored when modeling balast as parallelism at particle level allows one thread per particle which significantly decreases the computational times. In addition, to the particle shape the contact model in BlazeDEM-3DGPU [5] is based on the overlapping volume between particles for a better assessment of the strain energy involved between contacting particles.

The ballast particle shapes are captured using a 3-D laser scanner to obtain accurate digitized ballast particle shape representations of high-speed track ballast for use in the DEM simulations in this study. The detail of the digitized ballast particles are controlled by the number of vertices and faces used to approximate the ballast particle samples. A significant benefit of this approach is that the critical geometric features could be investigated by conducting DEM simulations using varying detailed ballast samples. In addition, the simplified the ballast samples allows for larger number of *angular particles* to be simulated during loading and unloading and vibration studies of the ballast.

The remainder of this study is dedicated towards demonstrating that the developed laser scanning strategy is effective, efficient and practical to quantify the shape properties of the ballasts towards constructing digitized ballast samples for use in DEM simulations. Secondly, that GPU-enabled DEM can efficiently model typical large scale box representative of a typical laboratory ballast experiments to test the cycling compressive loading.

Figure 1: Representative ballast samples from Fontaineriant quarry (Normandy France).

2 3D Laser Scanning Procedure

The 3D laser scanning procedure consists of mounting the particles appropriately to be accurately scanned as outlined in Section 2.1. Thereafter the particle is digitized by approximating the high resolution representation by fitting vertices and planes to cover the surface of the particle as discussed in Section 2.2. the process is repeated for all six selected ballast particles whereafter they are used in DEM simulations of ballast as detailed in Section 3.

The ballast considered in this study are from the ballast used for the new French high-speed rail LGV Bretagne-Pays de la Loire (LGV LN 10, to be completed in 2017). The ballast were extracted from Fontaineriant quarry (Normandy France) which is a quartzite (locally called also in French grès amoricain). The classical designation range for ballast used for French high-speed railway is 31.5/63. The 6 representative ballast samples used in this study are presented in Figure 1.

2.1 3D-Laser scanning device and initial digitization

The shape of ballast particles are classically obtained by particle image processing or X-ray computed tomography (CT). The particle image processing allows for fast and inexpensive processing of the ballast particles allowing for large numbers of particles to be processed. However, the 2-dimensional images obtained by image processing and stitched volume objects are sufficient for the overall particle geometry and aspect ratios while additional detail is seldom well resolved. Improved accuracy is obtained using X-ray CT that allows 3-D shapes to be captured more accurately as demonstrated by Ahmed et al. [11] for ballast applications. However, X-ray CT measurements are expensive, sophisticated and laborious which limits the number of particles that can be processed.

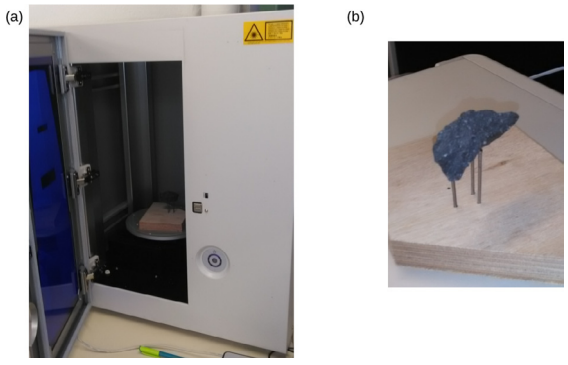

Figure 2: (a) 3D-laser scanning device (b) ballast with scan support

This study considers the 3D-Laser scanning device depicted in Figure 2(a), which can be considered intermediate to the particle image processing and X-ray CT scanning. A 3D-Laser scanning device has already been employed with sufficient accuracy to characterize aggregate shape [10]. In this study, a modern 3D-laser scanning device is used to obtain

a scan of the ballast. As shown in the Figure 2(b), the ballast samples are scanned sequentially with the sample being supported by wire supports. The samples are rotated as they are only scanned from the top, this allows for a full digitization of the particle geometry in which there is no effect of the wire supports. The 3-D laser scanning device requires several rotations to scan a sample to finally obtain a digitized ballast particle. The number of rotations to complete planar scans can reduce or increase the precision of the scanned sample. In our case, the times to scan and digitize a ballast sample varied between 10 and 20 minutes depending on the scanning parameters and selected representative planar element i.e. triangle or parallelogram. Table 1 shows that the number of initial polygons of the detailed digitized representations depend of the size and complexity of the ballast as the scanning parameters of the device are the same for each sample.

Table 1: Digitized ballast data before and after mesh reduction operation : number of geometrical elements

	After Scanning		After Mesh Reduction	
Ballast	Triangle	Point	Facet	Vertex
B1	24964	12470	12	8
B2	89980	44856	12	8
B3	25212	12606	12	8
B4	100246	50111	12	8
B5	69096	34517	12	8
B6	71876	35873	12	8

2.2 Ballast digitization to reduce geometrical detail

Once the ballast samples have been scanned they need to be digitized into DEM particles ready for simulation. The scanned particles are digitized with high detail and stored in the `STL` data format, which represents the the particle surfaces as triangles. The geometric detail of the highly detailed digitized samples are then reduced using MeshLab [12], which is open-source and freely available. In this study, the mesh reduction function was utilized to reduce the number of triangular facets to avoid excessive storage requirements as particles in the DEM simulation environment. For this study we chose number of final facets to be 12 for all particles as outlined in Table 1.

Future investigations will adapt the number of facets according to the complexity of the particle which was not the main objective of this study. The originally scanned high detailed particles (left) and digitized DEM particles (right) are depicted in Figure 3. The results highlights that the particle elongation and flatness are globally well represented, while the angularity could be more better defined using more detailed particle in future. The surface texture (roughness) captured by the detailed digitization as well as the non-convexity of the particles are not present in the final particle representations although

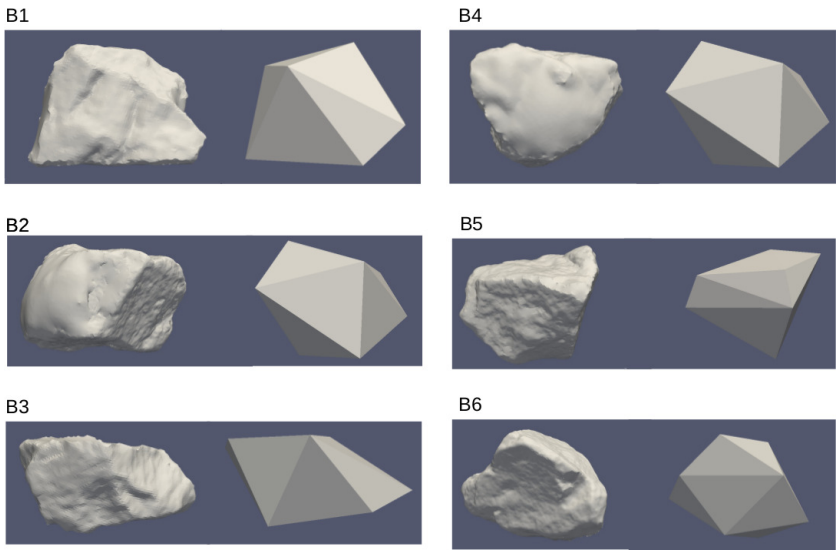

Figure 3: Detailed digitized ballast after the scanning (left) and after reducing the geometrical detail for DEM representation (right)

the detail reduction process is capable of generating both convex or non-convex particle shapes.

3 GPU Discrete Element Simulation

3.1 Ballast considerations during DEM

Both the time computational time and realistic particle shapes are currently the two main limiting factors to use DEM on a regular basis to tackle large scale ballast railway problems. Typically CPU based DEM environments simulate at most a few thousand of ballast particles using the clumped sphere representations that ignores the angularity of actual ballast [3, 4]. It is expected that this kind of DEM simulations can give qualitative assessments but the effect of angularity is expected to be a crucial factor for ballast simulations but this is yet to be investigated in greater detail.

3.2 BlazeDEM-3DGPU

As outlined previously this study considers uses the BLAZEDEM-3DGPU framework developed by Govender et al. [5, 6, 7, 8, 9]. This numerical framework has been validated for silo discharge and power consumption of milling operation simulations that allows for large number of particles to be simulated within reasonable computing time. BlazeDEM-3DGPU is able also to model more complex shapes that include regular and irregular polyhedra (non-convex particles) [8].

In the case of selected scanned ballasts, the `STL` file format is converted to the BlazeDEM-3DGPU format. In particular, the faces and vertices are extracted to define the polyhedral

geometries. Note also that the python library `numpy-stl` was used to obtain the Inertia tensor, volume and centre of mass for each digitized ballast particle. In particular, the inertia tensors plays an important effect for the stability of the final packing. The BlazeDEM-3DGPU depicted particle geometries are shown in Figure 4.

All simulations conducted in this study are done using a linear spring dashpot model and Coulomb Criterion are used : $COR_{pp} = 0.25$, $COR_{pw} = 0.1$, $\mu_{pp} = 0.6$, $\mu_{pw} = 0.5$, density $= 1.8g/cm^3$ for a time-step of $1.10^{-4}s$.

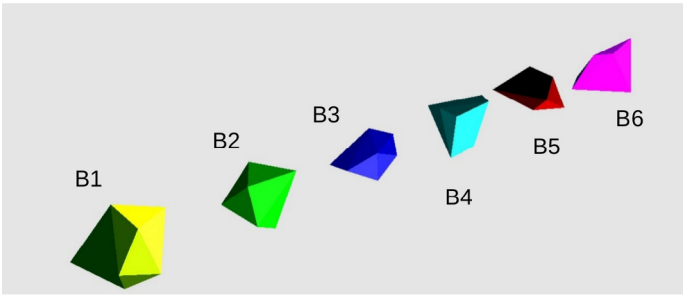

Figure 4: DEM Ballast particles for the 6 selected digitized ballasts

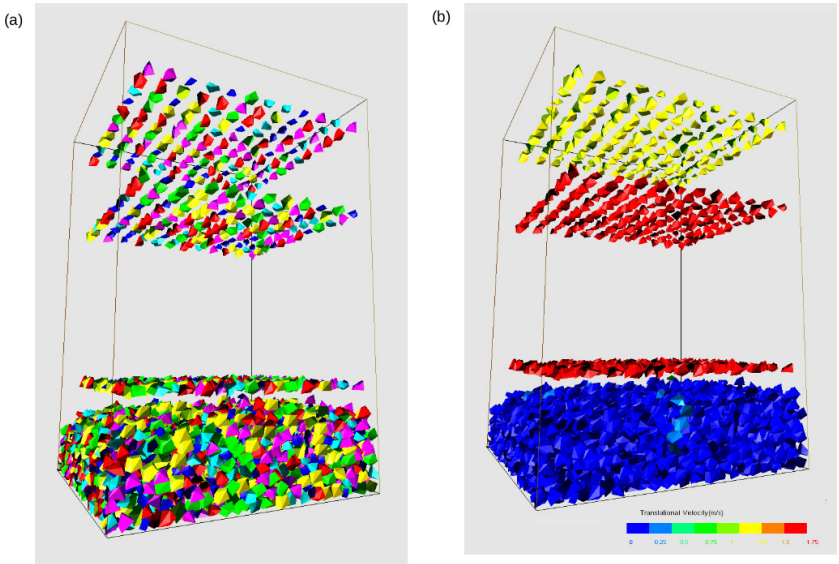

Figure 5: Filling stage of box BOX1 after 7.5 s of filling time (a) coloured by particle geometry and (b) coloured by linear velocity

3.3 Ballast box filling simulations

Two boxes were considered in this study. The first box is 128 cm by 128 cm (BOX1) and the second box is 248 cm by 248 cm (BOX2). These sizes have been chosen to be

similar at the scale of experimental devices used classically for the ballast studies during cyclic compaction tests. Figures 5 depicts the ballast filling stage of BOX1. As shown in Figure 5(a) the ballast particles were sequentially filled by slice with random packing of the different particle geometries as well as their orientations, since each colour represents a different geometry in Figure 5(a). The linear velocities in turn are depicted in Figure 5(b) depicting stability during ballast formation. In this study two ballast packings are filled as summarize in Table 2. The final packings are shown in the Figure 6 for the two boxes. The computing time for around 20 s of filling for the packing 1 is around 0.8 hour for two GPUs TITAN X cards.

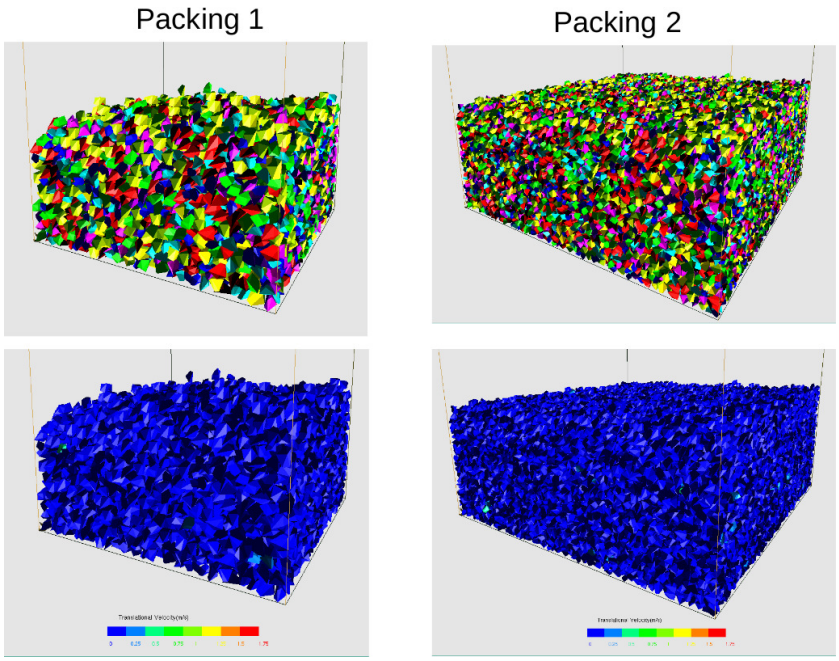

Figure 6: Ballast packings after the filling stage in box BOX1 (a) and box BOX2 (b) (top - coloured by particle geometry and down - coloured by linear velocity)

Table 2: Ballast packing characteristics

Number of ballasts	Total	B1	B2	B3	B4	B5	B6
Packing 1 (BOX1)	10000	2000	1500	1500	2000	1500	1500
Packing 2 (BOX2)	60000	12000	9000	9000	12000	9000	9000

4 Conclusions

Time computation and realistic particle shape (classically clumps of spheres) are actually the principal limitations to apply Discrete Element Method to large scale ballast railway problems. In this paper, two typical experimental ballast boxes were filled by up to 60 000 thousand convex polyhedral-shaped ballast particles using BlazeDEM-3DGPU that efficiently utilizes the GPU to conduct discrete element simulations within reasonable computing times. A simplified experimental procedure has been developed in this work to reduce detailed digitized ballast samples obtained scanning actual samples using 3-D laser scanner to typical polyhedron geometries that can be used in DEM simulations. This study highlights the promising prospects that GPUs can bring to model railway problems more precisely within reasonable time frames. One of the ambitious perspectives of this work will be to test the methodology developed here for the digitized ballasts for the non-convex polyhedra shape, a particle shape that has already been tested with the BlazeDEM-3DGPU platform [8].

Acknowledgements

We gratefully acknowledge the support of NVIDIA Corporation with the donation of the Titan X Pascal GPU used for this research.

REFERENCES

[1] Report for European Railway Agency, Assessment of freight train derailment risk reduction measures, Report No : BA000777/02 (2011)

[2] Hossain Z., Indraratna B, Darve F. and Kumar Thakur P., DEM analysis of angular ballast breakage under cyclic loading. *Geomech Eng.* (2007) **2**:175–181

[3] McDowell G. R., Li, H., Discrete element modelling of scaled railway ballast under triaxial conditions. *Granular Matter* (2016) 18:66

[4] Irazàbal J, Salazar F, Oñate E, Numerical modelling of granular materials with spherical discrete particles and the bounded rolling friction model. Application to railway ballast. *Computers and Geotechnics* (2017) **85**:220–229

[5] Govender N., Wilke D.N., Kok S., Blaze- DEMGPU Modular high performance DEM framework for the GPU architecture. *SoftwareX* (2016) **5**:62–66

[6] Govender N., Wilke D.N., Pizette P., Abriak N-E, A study of shape non-uniformity and poly-dispersity in hopper discharge of spherical and polyhedral particle systems using the BlazeDEM3D- GPU code. *Appl. Math. Comput* (in press)

[7] Govender N., Wilke D. and Kok S., Collision detection of convex polyhedral on the NVIDIA GPU architecture for the discrete element method. *Appl. Math. Comput.* (2014)**15**:810–829

[8] Wilke D.N., N. Govender N. , Pizette P., Abriak N-E, Computing with non-convex Polyhedra on the GPU, Proceedings of the 7th International Conference on Discrete Element Methods. *Springer Proceedings Phys.* (2017) **188**:1371–1377

[9] Pizette P., Govender N, Abriak NE, Wilke D.N, GPU DEM Simulations and Experimental Studies of Ball Milling Process for Various Particle Shapes, 7th International Conference on Discrete Element Method. *Springer Proceedings Phys.* (2017) **188**:1447–1455

[10] Kim H, Haas CT, Rauch AF, Browne C. 3D image segmentation of aggregates from laser profiling. *Computer-Aided Civil and Infrastructure Eng* (2003) **18**:254-263

[11] Ahmed, S. I., 2014. An investigation of fabric and of particle shape in railway ballast using X-ray CT and the discrete element method. PhD Thesis, University of Southampton

[12] Cignoni P., M. Callieri, M. Corsini, M. Dellepiane, F. Ganovelli, G. Ranzuglia MeshLab: an Open-Source Mesh Processing Tool Sixth Eurographics Italian Chapter Conference (2008) 129–136

V International Conference on Particle-based Methods – Fundamentals and Applications
PARTICLES 2017
K. Tazoe, H. Tanaka, M. Oka, & G. Yagawa (Eds)

AN ANALYSIS OF HALF ELLIPTICAL SURFACE CRACK PROPAGATION PHENOMENON WITH SMOOTHED PARTICLE HYDRODYNAMICS METHOD

KOKI TAZOE[1], HIROTO TANAKA[2], MASANORI OKA[3] AND GENKI YAGAWA[4]

[1] Research & Development Center, YANMAR CO., LTD.
2481, Umegahara, Maibara, Shiga, 521-8511, Japan
e-mail: koki_tazoe@yanmar.com

[2] Research & Development Center, YANMAR CO., LTD.
2481, Umegahara, Maibara, Shiga, 521-8511, Japan
e-mail: hiroto_tanaka@yanmar.com

[3] Research & Development Center, YANMAR CO., LTD.
2481, Umegahara, Maibara, Shiga, 521-8511, Japan
e-mail: masanori_oka@yanmar.com

[4] Emeritus Professor, The University of Tokyo and Toyo University
1-32-19, Akatsutsumi, Setagaya, Tokyo, 156-0044, Japan
e-mail: yagawag@gmail.com

Key words: SPH, Fatigue, Crack propagation, Fracture mechanics

Abstract. The smoothed particle hydrodynamics (SPH) method was applied to the problem of fatigue crack propagation. The stress singularity characteristics at the crack tip and the stress intensity factor were compared between the SPH results and the reference values. The result of half elliptical surface crack propagation analysis showed smooth crack propagation history and the shape of the analyzed fracture surface was close to that achieved by test. Accordingly, it is concluded that the SPH is a useful tool to analyze the linear elastic fracture mechanics and the fatigue crack propagation.

1 INTRODUCTION

The estimation of fatigue damage is essential to ensuring the safety of mechanical structures. Fatigue crack propagation is one of the dominant phenomenon of fatigue damage. Accordingly, some meshing numerical analyses for the crack propagation problem, represented by X-FEM [1], have been investigated. However, in general, it is difficult to use meshing numerical analyses to deal with some complex situations, such as the process of penetrating the thickness of a plate, or connecting multiple cracks or defects. On the other hand, mesh-less numerical analyses, like a particle method, can solve such problems easily.

In this study, smoothed particle hydrodynamics (SPH) method [2] was applied to linear elastic fracture mechanics and fatigue crack propagation. In order to investigate the way of handling linear elastic fracture mechanics with SPH, the stress singularity at the crack tip area in a single edge cracked specimen was analyzed and compared with past numerical results [3].

After that, the half elliptical surface crack propagation phenomenon, one of the fundamental fatigue crack propagation problems, was analyzed and compared with the fatigue crack propagation test results.

2 FRACTURE MECHANICS WITH SPH METHOD

2.1 Some equations of linear elastic fracture mechanics

The magnitude of load acting on a crack is defined as stress intensity factor K. For example, as seen in Fig. 1, in the case of a two-dimensional crack exposed to mean stress σ_0, the distribution of mode I direction stress at the crack tip area has the following singularity.

$$\sigma(r) = K / (2\pi r)^{1/2} \tag{1}$$

This equation regards all areas of the specimen as an elastic field. As seen in this equation, K is the coefficient of the stress distribution function at the crack tip. Namely, the K value is the magnitude of local stress field at the crack tip area, where the fracture really occurs. In the case of Fig. 1, K is defined as the function of crack length a and shape correcting coefficient F, as follows [4].

$$K = \sigma_0 F(\pi a)^{1/2} \tag{2}$$

In the case of fatigue load, as seen in Fig. 2, stress intensity factor range ΔK, which is the difference between maximum K and minimum K, rules the fatigue fracture phenomenon.

$$\Delta K = K_{max} - K_{min} = (1 - R)K_{max} \tag{3}$$

where stress ratio R is the proportion of the minimum load to maximum load. Generally, ΔK is related to fatigue crack growth rate da/dN, which is the increment of crack length per one fatigue cycle, as seen in Fig. 3. In the middle range, the relation has the following Paris-Erdogan law [5].

$$da / dN = C\Delta K^m \tag{4}$$

where C and m are material constant.

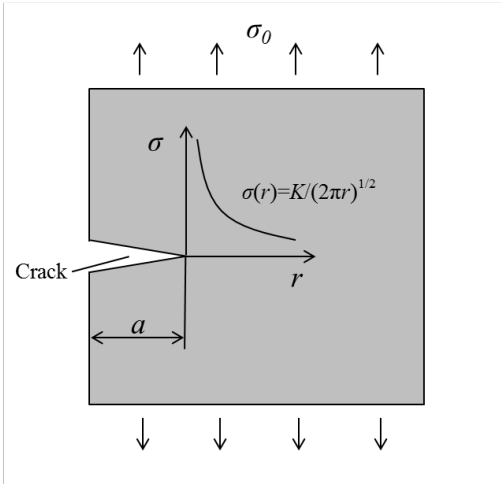

Figure 1 2D mode I crack

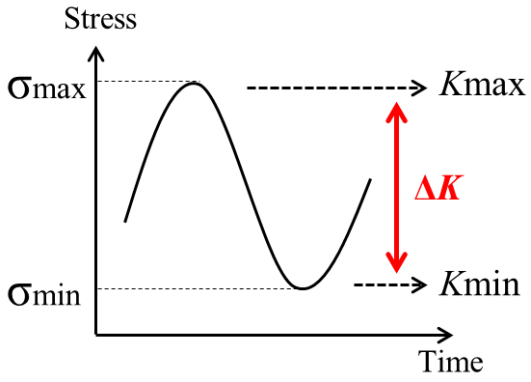

Figure 2 Stress vs. time

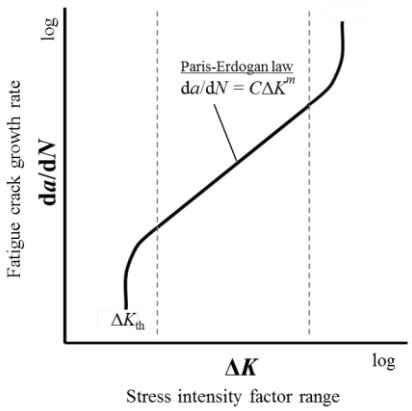

Figure 3 Fatigue crack growth curve

2.2 Stress intensity factor range

In the SPH fatigue crack propagation analysis, K values in all crack tip particles must be calculated. In this study, K values are calculated simply as follows.

$$K = \sigma_1(\pi A)^{1/2} \tag{5}$$

where σ_1 is the principal stress of the crack tip particle and A is the particle size. This equation is derived from substitution σ_1 and 1/2 A for equation (1). This program is used for constant range fatigue load, then, ΔK is calculated by substituting R and equation (5) for equation (3). To verify the validity of this method, stress singularity at the crack tip in a single edge cracked model, which is one of the fundamental crack problems, is analyzed and compared with past numerical analysis.

2.3 Fatigue crack propagation model

Generally, crack propagation analysis with a meshing numerical method can define crack tips in any position. However, SPH analysis cannot be used in the same way because the positions of the particles are restricted by particle size. Therefore in this study, the following damage model is applied to the crack tip particles, and the fracture is defined for every crack tip particle.

$$\Delta D_{i,n} = (\mathrm{d}a / \mathrm{d}N|_{i,n})\Delta N_n / A \tag{6}$$

$$D_{i,n} = D_{i,n-1} + \Delta D_{i,n} \tag{7}$$

where ΔD is the increment of damage, ΔN is the increment of fatigue cycle and D is the total damage value of the particle. D is the dimensionless quantity and the remaining life L for each crack tip particle is defined as follows

$$L_{i,n} = 1 - D_{i,n} \tag{8}$$

ΔN in each analysis step is calculated by equations (5), (4) and (8). After ΔN is obtained, ΔD is calculated by equation (6). The damage in step n $D_{i,n}$ is calculated by the sum of $D_{i,n-1}$ and $\Delta D_{i,n}$. Fracture occurs in the crack tip particle when D is equal to 1, namely L is equal to zero. The fracture particle is removed from the crack tip and a new crack tip is redefined. After that, the next analysis step is calculated.

3 FATIGUE TEST

3.1 Model of cracked specimen

Fig. 4 shows cracked models for SPH analysis. Fig. 4 (a) is a single edge cracked plate model for the stress singularity analysis. Particle sizes are 0.1 mm, 0.05 mm and 0.02 mm, and the numbers of particles are 19,950, 79,900 and 449,750, respectively. Fig. 5 shows a half elliptical surface cracked model for fatigue crack propagation analysis. The particle size is 0.1 mm and the number of particles is 154,810. The cracked areas are modeled by removing particles. Accordingly, the distance between upper crack surface and lower the surface is one particle size. The half elliptical surface cracked model has a triangle shaped initial crack on one of its corners. The support domain size of each analysis is twice the particle size.

3.2 Specimen for fatigue test and material

Fig. 5 shows the geometry of the half elliptical surface crack specimen. The specimen has the same initial slit as the model in Fig.4 (b). The initial slit was made by a wire electric discharge machine.

The material used in this study was low carbon steel JIS-S50C. Table 1 and Table 2 show the chemical compositions and mechanical properties of the material respectively. Fig. 6 shows the fatigue crack growth curve of the material. C value is 2.0×10^{-12} and m value is 3.2443.

3.3 Crack propagation test

To compare with the result of the SPH crack propagation analysis, a fatigue crack propagation test with a half elliptical surface crack was carried out. In this study, to visualize the crack shape history, beach marks were introduced to the fracture surface. The marks were introduced by increasing the stress ratio as seen in Fig. 7.

In this test, the fatigue life was not obtained because the stress ratio and load level were changed during the test. The comparison of fatigue life will be carried out with constant loaded fatigue test results in the future.

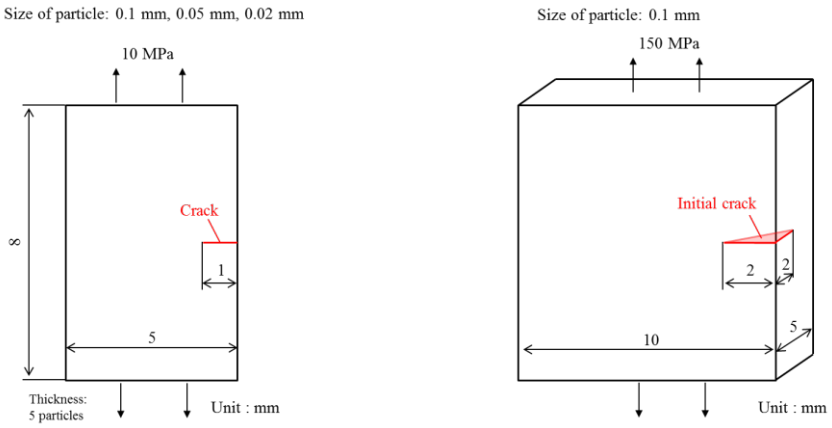

(a) Single edge cracked plate model (b) Half elliptical surface cracked model

Figure 4 Models for SPH

Table 1: Chemical Compositions of JIS-S50C [mass. %]

C	Si	Mn	P	S	Cu	Ni	Cr	Mo	V
0.48	0.18	0.63	0.014	0.002	0.12	0.07	1.04	0.15	0.01

Table 2: Mechanical propaties of JIS-S50C

Yield stress [MPa]	Tensile stress [MPa]	Elongation [%]	Reduction of area [%]	Vickers hardness*
353	681	33.6	12.6	195

*Force:2 [kgf], Time:30 [sec]

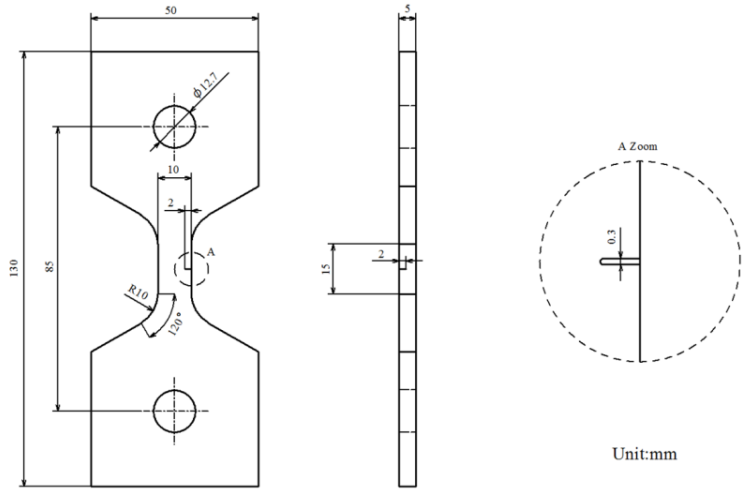

Figure 5 Half elliptical surface cracked specimen

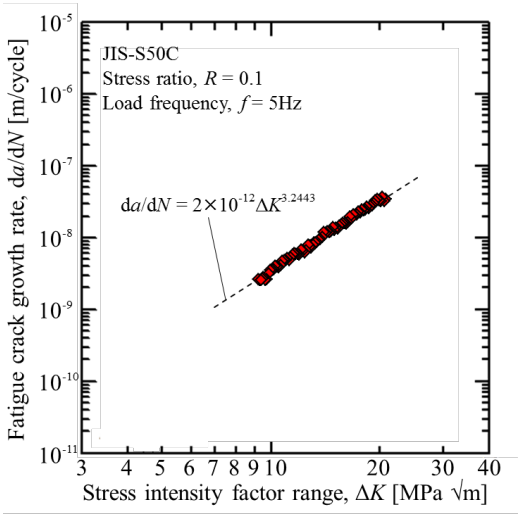

Figure 6 Fatigue crack growth curve of JIS-S50C

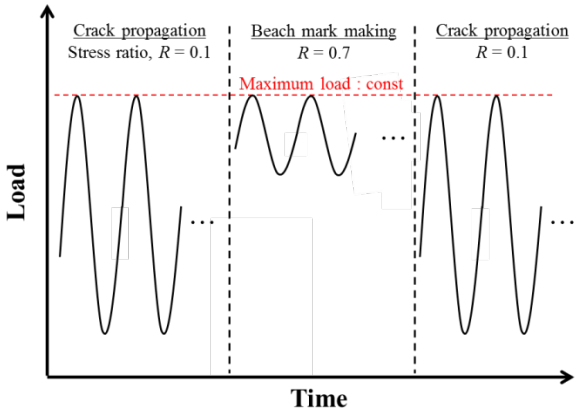

Figure 7 Load vs. time in fatigue crack propagation test

4 ANALYSIS RESULTS

4.1 Stress singularity

Fig. 8 shows the distributions of stress at the crack tip of a single edge cracked model (see Fig. 1), where the SPH results with three different particle sizes and that based on the reference [3] are rather well compared. The K value calculated from the SPH result of particle size 0.02 mm using equation (5) is 0.90 MPa√m, whereas that of the reference [3] is 0.77 MPa√m.

4.2 Fatigue crack propagation

Fig. 9 shows the results of half elliptical surface crack propagation. Fig. 9 (a) shows the crack shape history analyzed by the SPH method. The SPH results show the crack propagation history of a half elliptical surface crack penetrate the plate thickness smoothly. Fig. 9 (b)-(i) shows the original image of the tested fracture surface. In the fracture surface, the beach marks, namely the real crack shape history, are observed clearly. The results of SPH analysis almost trace the tested results, as seen in Fig. 9 (b)-(ii) and Fig. 9 (b)-(iii).

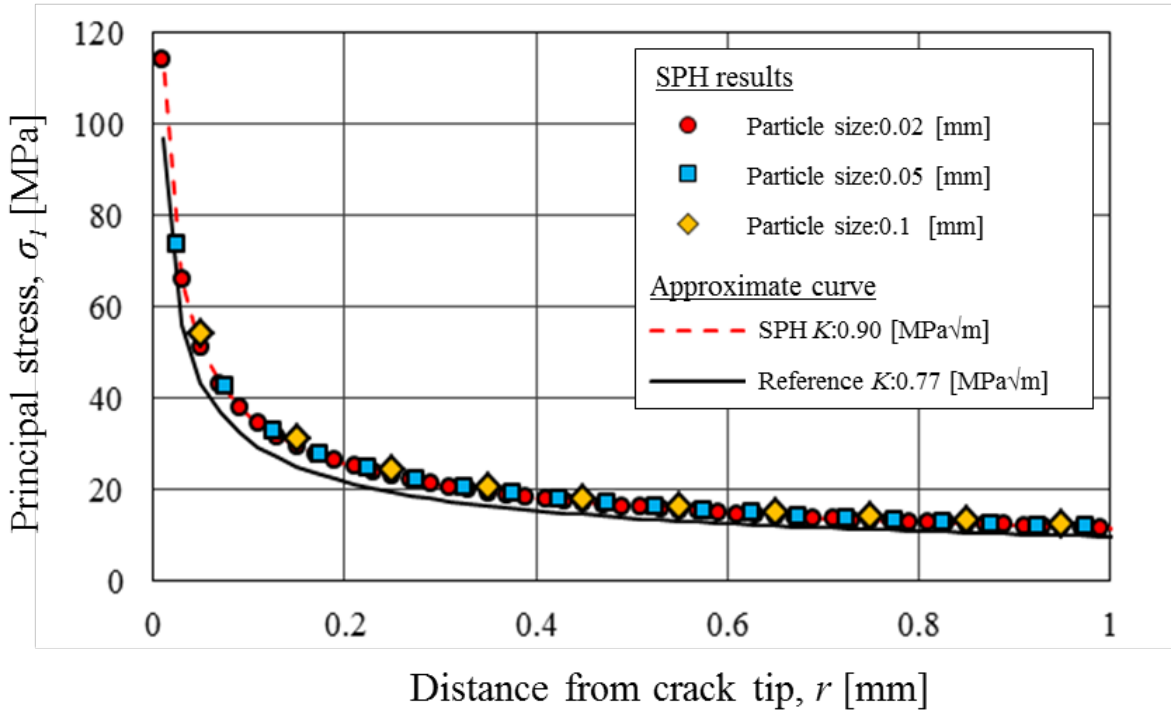

Figure 8 Stress distributions at crack tip

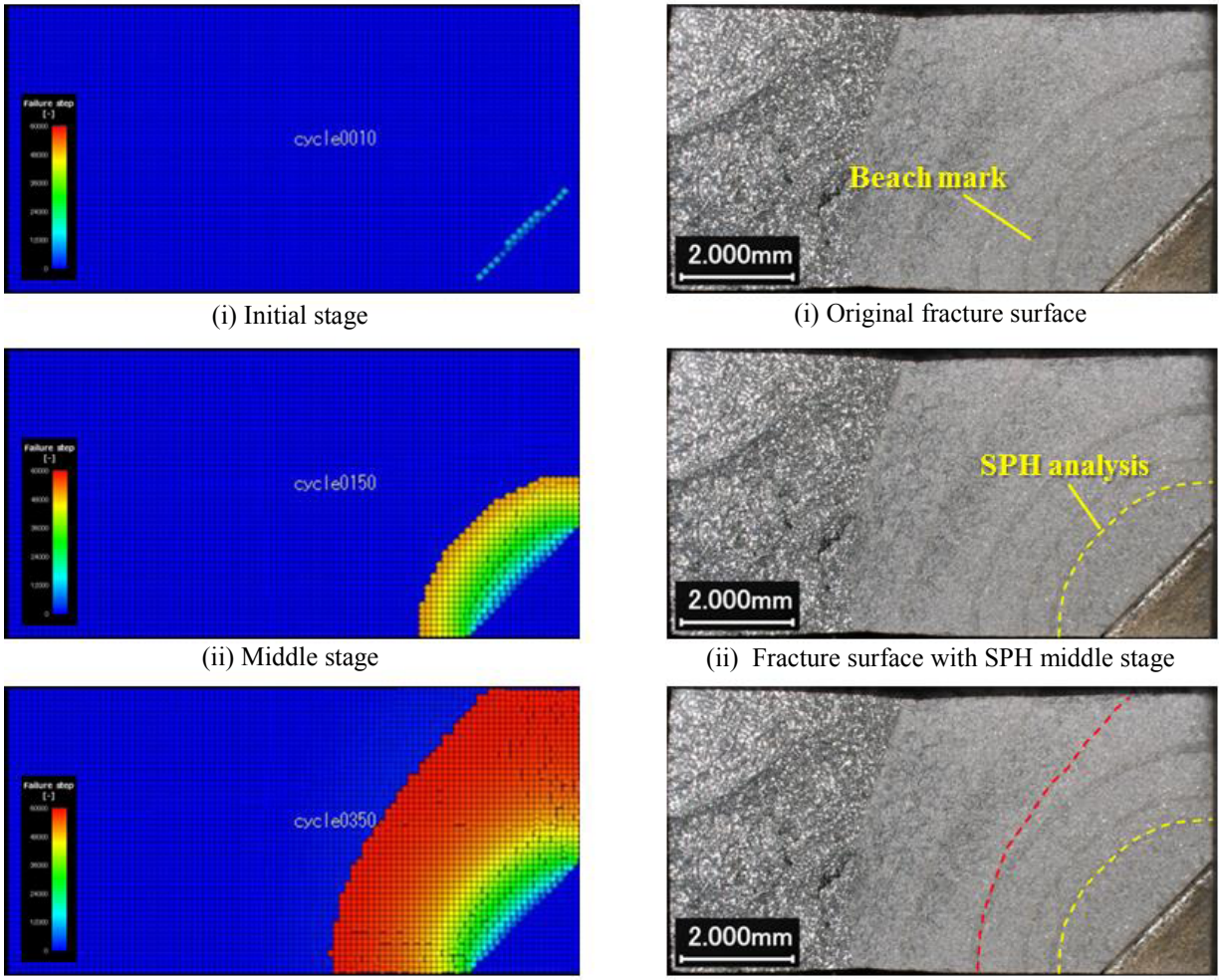

(i) Initial stage (i) Original fracture surface

(ii) Middle stage (ii) Fracture surface with SPH middle stage

(iii) Final stage (iii) Fracture surface with SPH final stage

(a) SPH fatigue crack propagation analysis (b) Fatigue crack propagation test

Figure 9 Fracture surfaces

5 CONCLUTIONS

The following results were obtained.

(a) The SPH is able to calculate stress singularity at the crack tip rather well.

(b) K value by SPH analysis tends to be higher than the reference value.

(c) The half elliptical surface crack propagation is simulated in a smooth manner.

(d) The results of the SPH analysis trace well the beach marks observed at tested fracture specimen.

It is concluded that the SPH method is considered to be useful for analysis of linear elastic fracture mechanics and fatigue crack propagation. The difference of the K values between the SPH result and the reference value as well as the predictions of the fatigue life will be studied in the future.

REFERENCES

[1] Moës, N. Dolbow, J. and Belytschko, T. A fine element method for crack growth without remeshing. *Int. J. Num. Meth. Engng* (1999) **46-1**:131-150

[2] Lucy, L. B. A numerical approach to the testing of the fission hypothesis. *Astronom. J.* (1977) **8**:1013-1024

[3] Brown, W. F. Jr. and Srawley, J. E. Plane strain crack toughness testing of high strength metallic materials. *ASTM STP* (1966) **410**:12

[4] Irwin, G. R. Analysis of stresses and strains near the end of a crack traversing a plate. *Journal of applied mechanics* (1957) **24**:361-364

[5] Paris, P. and Erdogan, F. A critical analysis of crack propagation laws, *Journal of basic engineering*, *Transactions of the American society of mechanical engineer*s (1963) 528-534

V International Conference on Particle-based Methods – Fundamentals and Applications
PARTICLES 2017
P. Wriggers, M. Bischoff, E. Oñate, D.R.J. Owen, & T. Zohdi (Eds)

A SPH MODEL FOR PREDICTION OF OIL SLICK DIAMETER IN THE GRAVITY-INERTIAL SPREADING PHASE

C.A.D. FRAGA FILHO

Development, Implementation and Application of Computational Tools for
Problem Solving in Engineering Research Group
Federal Institute of Education, Science and Technology of Espírito Santo
Campus Vitória, Mechanical Engineering Coordination
Av. Vitória, 1729, 29040-780, Jucutuquara, Vitória–ES, Brazil
email: cadff1@gmail.com
web page: http://dgp.cnpq.br/dgp/espelhogrupo/8154537003018313

Key words: Gravity-inertial spreading phase, Lagrangian particle method, SPH, oil slick diameter prediction, energy restitution coefficient, collisions detection and response.

Abstract. This paper presents the implementation of the SPH Lagrangian method for the prediction of the oil slick diameter in the gravity-inertial spreading. Computer codes that predict the slick diameter generally use hybrid models (Eulerian-Lagrangian), and simulations start from the end of the first phase (gravity-inertial), in which the oil slick diameter is given by Fay's equations [1, 2]. Fay adjusted curves to oil spreading experimental data on a calm sea condition aiming to estimate the oil slick diameter as a time function, after the spill occurrence. The mathematical modelling in this work is based on the Navier-Stokes equations, for incompressible Newtonian fluids. In the boundary treatment, a model for the collisions between the particles has been used, with the definition of an energy restitution coefficient [10]. At the end of the first stage of the spill, the numerical results obtained by SPH simulations show agreement with the solution obtained from Fay's equations.

1 INTRODUCTION

The spreading is due to the pollutant's tendency to flow over itself. It's the most significant transport process in the first few hours of the spill. Its understanding and quantification are of great importance to the preservation of the environment.

The curves adjusted by Fay [1,2] to oil spreading experimental data are still used in prediction models for oil slick reaching. The researcher estimated the oil slick diameter based on mathematical equations, dividing the phenomenon in three distinct stages, in which the gravitational, inertial and viscous forces and superficial tension are held accountable for the movement of the oil over the water. The shear stress on the surface of the oil was not considered due to the wind action, the advective forces and the turbulent diffusion. Due to the inexistence of winds, currents and waves, the oil spread in a circular shape, in a displacement that presented radial symmetry. Field data was employed in the attainment of proportionality coefficients for the equations proposed in the three stages of the spreading. It is known that the oil spreading, in real-life conditions, cannot be fully explained by these equations; however, through modifications, like considering the shear effects caused by the wind on the surface of the oil

(which explain the elliptical shape of the oil slick in an actual spreading), the equations can be applied nowadays.

The first stage of the oil spreading is not usually taken into consideration in the numerical study of the phenomenon because it is very short (about an hour for a 10,000 ton oil spill – according to Fay's results, [1]). An estimate of the oil slick diameter at the end of this stage, which is necessary for algorithms that simulate the longer lasting stage of the spreading (gravity-viscous), is, in general, obtained with a prediction based on Fay's adjusted curves to experimental data. Most of the software are hybrids and utilize meshes (in the Eulerian modelling of the water) and particles in the discretization of the oil. The prediction of the oil particle's position over time is based on the solution of Langevin's equation, according to reference [3]. However, the employment of Eulerian modelling in the simulation of oil on the water surface is not a good choice, for the need of updating meshes (remeshing), after each numerical iteration, making the process expensive and complicated.

During the last few years, the meshless Lagrangian methods have been more and more employed. The particle methods are included in this category, providing stable and accurate numerical solutions to integral equations or partial differential equations. The Smoothed Particle Hydrodynamics method is an alternative to the solution of problems modelled by the equations of conservation of mass, momentum balance and energy transport.

Particle methods, which address the spreading problem with a Lagrangian view for the two phases involved (oil and water), are incipient in the scientific study of spreading. Violeau [4] and Yang and Liu [5] presented their model and results employing this approach to the study of oil spill containment using floating devices.

The present work presents the implementation of a purely Lagrangian particle model, based on the equations of conservation of mass and momentum balance for the oil, in a calm sea condition. The Smoothed Particle Hydrodynamics (SPH) method is employed in the solution of those equations. The study is directed towards the understanding of the first stage of the spreading (gravity-inertial), independent of the other physical and chemical processes that occur during the spill, presented in references [6,7]. Employment of purely Lagrangian methods in the diameter prediction of the oil slick can not be found in literature. An algorithm was developed and implemented, using Fortran Language, and the numerical results were verified with the curves adjusted by Fay.

This paper is organized in sections as follows. In Section 2, the Lagrangian mathematical modelling employed in this work is briefly presented. Section 3 presents the methodology of the prediction of the oil slick diameter in the gravity-inertial spreading of oil and numerical aspects. The results and discussion of the results are in Section 4. Finally, the conclusions of this study are presented in Section 5.

2 SMOOTHED PARTICLE HYDRODYNAMICS (SPH) METHOD

Originally, the SPH method was developed in the end of the 70s of the 20th century, by Lucy [8] and Gingold and Monaghan [9], for the modelling of astrophysics phenomena. After some time, it was employed in the field of solid and fluid mechanics with a wide range of applications, due to its ability to incorporate the complexity of physical problems. Especially due to the complex geometries involving free surface fluids and fluid-structure interaction, the method has attracted a great number of researches.

For the solution of conservation differential equations, the SPH method discretizes the domain in a finite number of particles. The values of the physical properties in the reference particles are obtained by the interpolation of the properties of neighbouring particles with the use of smoothing functions (kernels). The particles are delimited by an influence domain (at a maximum distance $\mathrm{k}h$ from the fixed particle considered) that defines an area of influence in which there is the contribution of the neighbouring particles to approach the physical property in the reference particle.

In the SPH method, different kernels can be used, and so that they are considered suitable for interpolation, it is necessary that each one follows certain properties: smoothness, positivity, symmetry, convergence, decay, compact support, and normalization within the domain of influence. Common kernels used in the interpolations are presented in [10].

SPH provides approximations to the physical properties (such as density), gradients (such as pressure gradients), divergents (such as velocity divergents) and Laplacians (such as temperature and velocity Laplacians) related to fluid flow, with a second order error.

2.1 SPH Approximations for the Conservation Equations

Modelling of fluid flows and energy transport is performed by the conservation (mass and energy) and momentum balance equations. For an incompressible Newtonian fluid, the Navier-Stokes equations are employed. Table 1 shows the SPH approximations for these equations, written in a Lagrangian description, Eqs. (1)–(3).

Table 1. Differential Equations and SPH Approximations

Differential Equation (Continuum)	SPH Approximation (Domain discretised by particles)	
Mass conservation: $\dfrac{\mathrm{d}\rho}{\mathrm{dt}} = -\rho\nabla.\mathbf{v}$	$\dfrac{\mathrm{d}\rho_a}{\mathrm{dt}} = \sum_{b=1}^{n} m_b \mathbf{v}_{ab}.\nabla W\left(\boldsymbol{X}_a - \boldsymbol{X}_b, h\right)$	(1)
Momentum balance: $\dfrac{\mathrm{d}\mathbf{v}}{\mathrm{dt}} = -\dfrac{\nabla P}{\rho} + \upsilon\nabla^2\mathbf{v} + \mathbf{g}$	$\dfrac{\mathrm{d}\mathbf{v}_a}{\mathrm{dt}} = \sum_{b=1}^{n} m_b \left(\dfrac{P_a}{\rho_a^2} + \dfrac{P_b}{\rho_b^2}\right)\nabla W\left(\boldsymbol{X}_a - \boldsymbol{X}_b, h\right) + +2\upsilon_a \sum_{b=1}^{n} \dfrac{m_b}{\rho_b} \mathbf{v}_{ab} \dfrac{(\boldsymbol{X}_a - \boldsymbol{X}_b)}{\left\lvert \boldsymbol{X}_a - \boldsymbol{X}_b \right\rvert^2}.\nabla W\left(\boldsymbol{X}_a - \boldsymbol{X}_b, h\right) + \mathbf{g}$	(2)
Energy conservation: $\dfrac{\mathrm{de}}{\mathrm{dt}} = \dfrac{1}{\rho}(-P\nabla.\mathbf{v} + \varepsilon_{\mathrm{v}} + \nabla.\mathbf{q} + q_H)$	$\dfrac{\mathrm{de}_a}{\mathrm{dt}} = \dfrac{1}{\rho}\left[-P_a \sum_{b=1}^{n} m_b \mathbf{v}_{ab}.\nabla W\left(\boldsymbol{X}_a - \boldsymbol{X}_b, h\right) + +\varepsilon_{\mathrm{v}} + \nabla.\mathbf{q} + q_H\right]$	(3)

where ρ is the fluid density, t is the time, ∇ is the mathematical vector operator nabla, $\mathbf{v}$ is the fluid velocity, $\mathbf{g}$ is the acceleration due to gravity, υ is the kinematic fluid viscosity, P is the absolute pressure, e is the specific internal energy, ε_{v} is the energy dissipation per unit volume, $\mathbf{q}$ is the conduction heat flux, q_H is the heat generated by other sources per unit volume, W is the kernel, $\boldsymbol{X}$ is the particle spatial position, h is the support radius, a and b are subscripts that refer to fixed and neighbouring particles, respectively and $\mathbf{v}_{ab} = \mathbf{v}_a - \mathbf{v}_b$.

2.2 Consistency

In the SPH method, the consistency depends not only on the function approximation employed but also on the influence domain, the number of particles, and their distribution within the domain. If the influence domain is continuous and complete, there is a uniform distribution of particles inside it, and the support radius has been properly defined, the conditions for the consistencies of zeroth and first orders are met due to the properties of normalization and symmetry of the kernel. The influence of the support radius in the approximations obtained by SPH therefore needs to be properly analysed [11].

In regions near the boundaries, the truncation of the influence domain occurs, leading to less accuracy in approximations. This phenomenon is known as particle inconsistency.

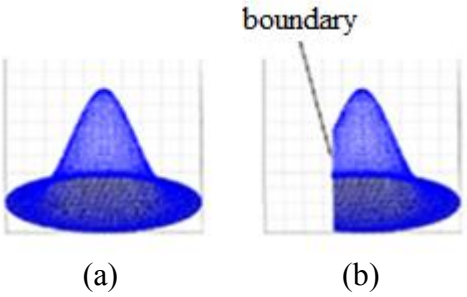

Figure 1. Influence domain: (a) complete and (b) incomplete or truncated.
It is possible see that the kernel is not defined in a whole domain.

Chen et al. [12] proposed the application of the Corrected Smoothed Particle Method (CSPM) for the particles inconsistency treatment, by introducing a correction factor. The particle density is corrected from the use of given expression in Eq. (4):

$$\rho_a{}^* = \sum_{b=1}^{n} m_b W(X_a - X_b, h) \Big/ \sum_{b=1}^{n} W(X_a - X_b, h) \frac{m_b}{\rho_b} \tag{4}$$

where $\rho_a{}^*$ is the corrected density of the particle.

Similar expressions are obtained for the pressure gradient Cartesian components [10].

2.3 Numerical aspects of SPH for dynamic fluid flows

2.3.1 Variable Smoothing Length

The length of the influence domain is very important in the SPH method. It influences the efficiency of the calculations and the accuracy of the solutions. If the length of the influence domain is too small or too large, the results will not be consistent with the studied physical problem. The need to apply support radius compensation occurs, for example, in the simulation of dam breaking. In this work the following form correction proposed in [13]:

$$\frac{Dh}{Dt} = -\frac{1}{n_d}\frac{h}{\rho}\frac{D\rho}{Dt} \tag{5}$$

where n_d is the number of domain dimensions.

2.3.2 Artificial Viscosity

The transformation of kinetic energy into heat takes place in problems involving mainly shock waves and needs to be measured, which does not happen when Eqs. (1)-(3) are employed. The artificial viscosity application in the simulations aims to avoid numerical instabilities and the interpenetration between particles [13]. The formulation used is shown in Eq. (6):

$$\pi_{ab} = \begin{cases} \dfrac{-\alpha_\pi \chi_{ab} c_{ab} + \beta_\pi \chi_{ab}^{\,2}}{\rho_{ab}}, & \left(\mathbf{v}_a - \mathbf{v}_b\right).\left(\boldsymbol{X}_a - \boldsymbol{X}_b\right) < 0, \\ 0, & \left(\mathbf{v}_a - \mathbf{v}_b\right).\left(\boldsymbol{X}_a - \boldsymbol{X}_b\right) \geq 0. \end{cases} \tag{6}$$

$$\chi_{ab} = \frac{h_{ab}\left(\mathbf{v}_a - \mathbf{v}_b\right).\left(\boldsymbol{X}_a - \boldsymbol{X}_b\right)}{\left|\boldsymbol{X}_a - \boldsymbol{X}_b\right|^2 + 0{,}01\varphi^2}, \quad c_{ab} = \frac{c_a + c_b}{2}, \quad \rho_{ab} = \frac{\rho_a + \rho_b}{2}, \quad h_{ab} = \frac{h_a + h_b}{2}.$$

where π_{ab} is the artificial viscosity, α_π and β_π are coefficients used in the calculation of artificial viscosity, c_a and c_b are the velocities of sound in the fixed and neighbouring particles, respectively, h_a and h_b are the support radii of the fixed and neighbouring particles, respectively, φ^2 is a factor that prevents numerical differences when two particles approach one another. The factor φ^2 was set to $0.01{h_{ab}}^2$.

The term related to artificial viscosity is added to the terms of pressure in the SPH approximations for the momentum balance and energy conservation equations.

2.3.3 Temporal Integration

The Euler method (First Order Runge-Kutta) was employed in the update of particle properties over time. The integration stability depends on the time period choice. The CFL (Courant-Friedrichs-Lewy condition) numeric stability criterion was applied to guarantee the convergence of the results [14].

2.3.4 Boundary Conditions

In this work, the geometrical boundary conditions have been implemented. The collisions of the particles of fluid against the solid walls (considered as being well-defined planes) have been studied. The inter-particle collisions were not considered.

An algorithm for the study of collisions and trajectories of the particles that collide against the solid walls of the domain has been implemented. After the temporal integration and obtaining of the position of the center of mass of each fluid particle by the SPH method (in the situation in which there are not walls delimiting the domain), the collision algorithm, based on mathematical and geometry fundaments, brought the particles back into the domain. This is based on the fact that the fluid particles could not escape the domain due to the presence of the predefined geometrical planes. The degree of elasticity of the collisions was measured by a coefficient of restitution of kinetic energy (CR).

When a collision of a particle against a plane was detected, and the particle's velocity was obtained by the SPH method, there was a correction of the magnitude of its velocity component perpendicular to the collision plane, immediately after the impact as follows [10]:

$$(v_{col})_i = CR \times (v_p)_i \tag{7}$$

where $(v_p)_i$ and $(v_{col})_i$ are the magnitude of the particle's velocity component perpendicular to the collision plane at the i direction, before and after the collision, respectively; $i \in (x, y)$.

After the collision, the sense of the particle's velocity component and mass centre coordinate perpendicular to the wall is altered. The sense and magnitude of the velocity component parallel to the wall remains unaltered.

The coordinate of the particle's mass centre perpendicular to the plane is corrected, as show Eq. (8).

$$(C_f)_i = (C_1)_i + (1.00 + CR)(r - d) \tag{8}$$

where:

$(C_1)_i$ and $(C_f)_i$ and are the coordinates of the mass centre position at the time instant $(t_o + \Delta t)$ and after the reflection, respectively,

r is the particle radius,

d is the distance between the particle's mass centre and the collision plane.

Figure 2 shows the initial and final mass centres positions (C_o and C_f) after colliding successively with two planes (A and B) in a numerical iteration. The point C_1 is the final position that would be achieved by the particle mass center if there were no walls delimiting the field.

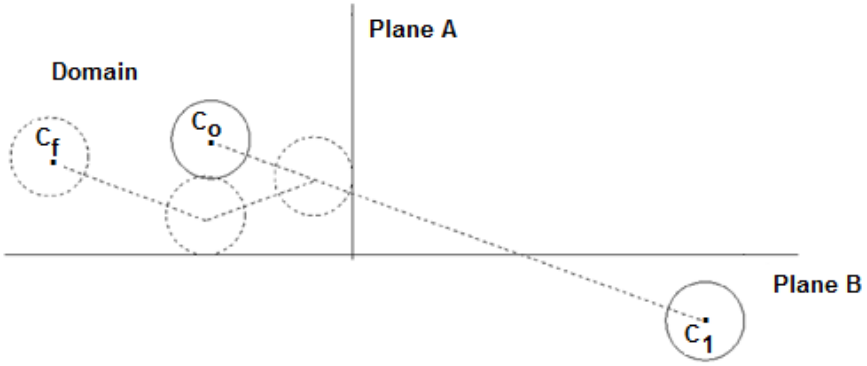

Figure 2. Collisions experienced by a particle in a time step.

3 PREDICTION OF OIL SLICK DIAMETER IN THE GRAVITY-INERTIAL SPREADING

3.1 Mathematical modelling and computer code

Fay [1, 2] adjusted curves to experimental data of the spreading of oil, considering a calm sea condition. These adjusted curves, defined for idealized theoretical conditions are still used, with some modifications. Mass losses, shear on the surface of the oil (caused by the wind), the advective forces and the turbulent diffusion were were not considered. After performing a physical analysis of the forces acting on the oil, he divided the process in three stages. In the first stage, the action of the gravity force predominates as driving, balanced by the force of inertia, resistant to movement. This stage has its duration as a function of the volume of the spilled oil, being called gravity-inertial spreading. The expression adjusted by Fay to the experimental results is presented by Eq. (8):

$$\mathrm{D} = 2k_1 \left(\Delta_\mathrm{w} g V t^2 \right)^{\frac{1}{4}} \tag{8}$$

$$\Delta_\mathrm{w} = \frac{\rho_\mathrm{w} - \rho_o}{\rho_\mathrm{w}} \tag{9}$$

where D is the oil slick diameter, ρ_w is the water density, ρ_o is the oil density, g is the magnitude of the gravitational acceleration, V is the volume of the oil spilled, $k_1 = 1.14$.

This stage of the spreading lasts until the time instant t_f given by Eq. (10):

$$t_f = \left(\frac{h_o}{g \Delta_w} \right)^{\frac{1}{2}} \tag{10}$$

where h_o is the initial oil height.

The initial movement of the spilled oil is analogous to that of a dam break [15]. The mass conservation and momentum balance equations, Eqs. (1) and (2), have been employed to obtain the solution using the SPH method. This solution is verified by comparison with the results from Fay's equation.

3.2 Computational Geometry, Initial and Boundary Conditions

The simulated domain consisted of a tank with a 20-meter length, 20-meter width and 1.5-meter height, with a water level of 0.50 meters, and an oil volume initially disposed, in the centre, in the form of a cylinder with a height and diameter of 1 meter. Figure 3 presents the tank and the initial particle disposition.

The study was carried out with a small volume of oil, which caused the first stage of the spreading to be short. A bigger volume of oil was used in Fay's experiments; however, there are no restrictions in his work regarding the volume of the oil spill and the use of his adjusted curves in the prediction of the oil slick diameter, making this research feasible, especially due to the specifications of the available hardware.

A bi-dimensional analysis of the problem was carried out. A longitudinal section of the volume was studied (Fig. 4). Figure 5 shows an upper view of the spreading and circular shape of the oil slick spreading on calm sea condition.

The oil particle positions along the horizontal direction were monitored at each numerical iteration. The initial lateral distance between the centres of mass of the particles was 2.00×10^{-2} m, being employed in the discretization of the domain 2,500 oil particles and 26,000 water particles (density of 1,000 kg/m^3 e absolute viscosity of 1.00×10^{-3} Pa.s). The oil was considered a homogeneous, uniform and isotropic fluid. The simulations were carried out for light-weight oil, with a density of 850.00 kg/m^3 and absolute viscosity of 3.32×10^{-3} Pa.s. The time period employed in all simulations, defined by the CFL stability criterion was 1.41×10^{-4} s. The water particles remained still during the simulations. Tait equation has been employed in predicting the dynamic pressure field of oil [16]. The modified pressure concept has been implemented [17]. The duration of the spreading in its first stage, obtained by Eq. (10) was 0.82 s, with a total of 5,815 numerical iterations.

A rigid plane was established, at water level, where the oil spreading occurred.

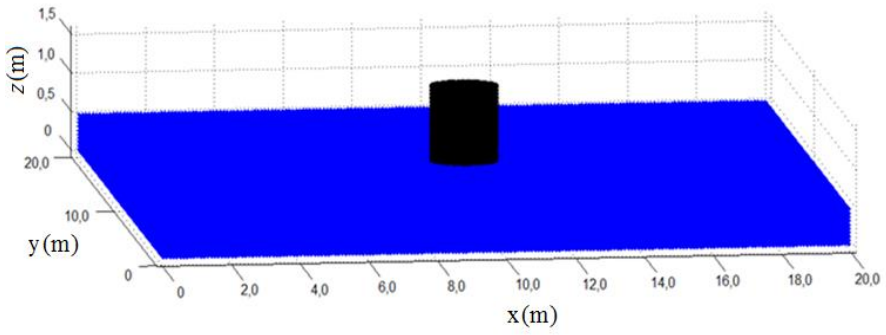

Figure 3. Simulated geometry.

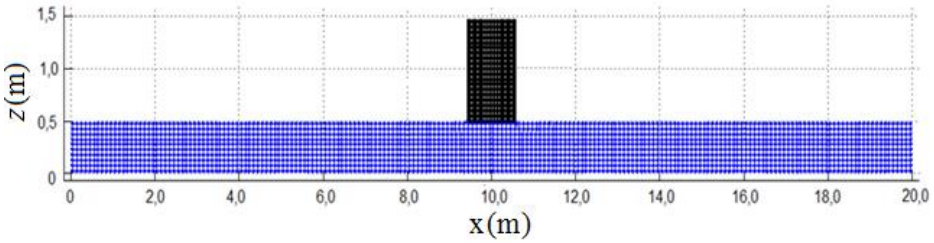

Figure 4. Longitudinal section of the oil at the initial time instant.

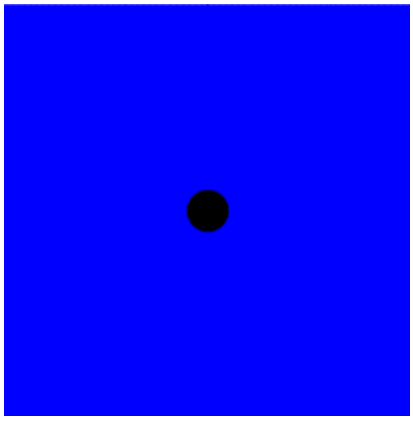

Figure 5. Upper view: the circular shape of the oil slick spreading on calm sea condition.

3.3 Numerical Simulations

In the simulations that were carried out, artificial viscosity was employed (with the coefficients $\alpha_\pi = 0.30$ and $\beta_\pi = 0.00$), a renormalization of the density of the oil was applied, the Tait equation was employed to predict the dynamic pressure fields of the oil (with the parameter B worth 0,85 x 10^5 Pa), a correction of the pressure gradients was made, the interpolations were carried out with the cubic spline kernel, the support radius varied over time, the boundary conditions were chosen (a plane fixed at water level) and the collisions against the boundaries were established as a result of the employment of energy restitution coefficients, temporal integration carried out by the Euler method.

After obtaining the velocity fields of the oil particles using the SPH method, the collisions that occurred against the horizontal plane defined at water level were detected with the analysis of the water particle trajectories. The direction of the velocity components of the particles that collided remained the same, however the sense of the vertical velocities of the particles changed. The sense of the velocity component in the x-axis remained unchanged. The positions of the particles' mass centres after the shocks also were corrected.

The oil particle evolution was monitored during the simulation. With the employment of radial symmetry, at each iteration, the circumferences were established with the radii defined by the longest horizontal distance between the positions of the oil particles and the position of the centre of the tank (10.00 m; 10.00 m; 0.50 m).

4 RESULTS AND DISCUSSION

In the beginning of the simulation using the SPH method, there was a bigger resistance to the oil movement with all the coefficients of restitution employed until the time period reached 0.04 s (Figure 7). In this time period, the oil slick diameter showed a tendency to remain constant. After this time period, the oil slick expanded until an inflection point in the curve (plotted in red) at around 0.12 s. From this moment until the end of the simulation, a positive growth rate was observed for the oil slick diameter.

Table 2 presents the oil slick diameters obtained by the SPH method (with the coefficient of restitution receiving values from 0.70 to 0.92) and by Fay's equation. The difference between the results is also presented.

Table 2. Oil Slick Diameter at the end of the Gravity-Inertial Stage

CR	Oil slick diameter (m)		Difference between the diameters - ΔD (m)
	SPH	Fay	
0.70	2.2583	3.0971	0.8388
0.80	2.2703	3.0971	0.8268
0.90	2.9824	3.0971	0.1147
0.92	3.0980	3.0971	-0.0009

It was verified that results obtained for the oil slick diameter obtained by the SPH method converged to results provided by the Fay's equation, as the CR increased. When the energy restitution coefficient reached 0.92, the results were coincident at the end of first stage of spreading. Figure 6 shows the agreement between the results (SPH and Fay's equation), at the end of the gravity-inertial phase, when using the CR with a value of 0.92.

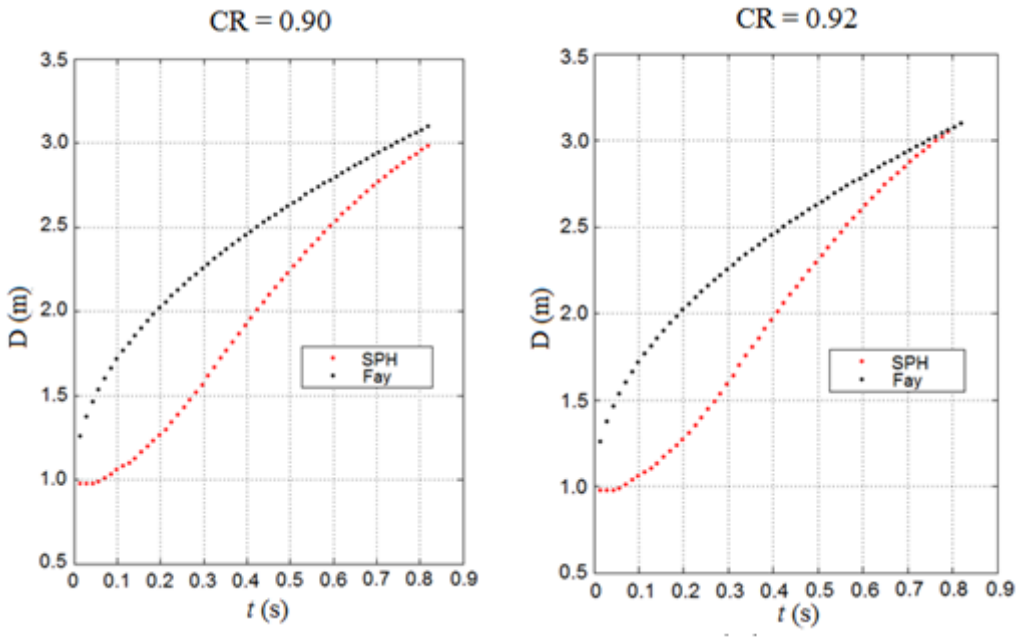

Figure 6. Evolution of the oil slick in the first stage of spreading.

The convergence of the numerical results (comparing to Fay's equation solution) occurred for low energy dissipation, but that needed to be correctly defined so that the correct diameter value was reached at the end of the first stage of the spreading.

Aiming to measure the computational efficiency, the CPU (central processing unit) processing time was measured. Table 3 presents the time period for different coefficients of restitution of energy, maintaining the same conditions and parameters for all simulations. All the simulations were carried out using Linux operating system, Intel i5-2450M processor (second generation) and 8 GB memory. The description of the sequential computational algorithm used in simulations is in [18].

Table 3. CPU processing time for different energy restitution coefficients

CR	CPU processing time
0.70	6 h 5 min 6 s
0.80	5 h 46 min 19 s
0.90	5 h 44 min 4 s
0.92	5h 43 min 31 s

5 CONCLUSIONS

In this work, with the employment of the Lagrangian SPH method in the discretization of the energy conservation and momentum balance equations, consistent numerical results were reached, in agreement with Fay's results, for the prediction of the oil slick diameter of light-weight oil, at the end of the first stage of the spreading.

The mathematical model used Navier-Stokes equations for Newtonian and incompressible fluids. While choosing the boundary conditions, a plane was fixed at water level and the coefficients of restitution of kinetic energy were employed to measure the interface effect on the oil movement. The energy restitution coefficient reflects the percentage of energy dissipated during the collision of the particle against the plane. The calibration of the proposed numerical model was done according to values attributed to the restitution coefficient (CR). Simulations were carried out for light-weight oil and, after employing different coefficients, a result for the oil slick diameter, in agreement with the solution of Fay's was obtained for a CR equal to 0.92.

The algorithm employed is capable of obtaining a solution for the first stage of the oil spreading, becoming a new tool to be used in the researches. For other types of oil, with specific physical properties (density, viscosity) another value for the coefficient of restitution can be found, so that there is an agreement between the oil slick diameter (found using the SPH method and Fay's equation) at the end of the gravity-inertial stage.

The numerical result obtained is important, for the oil slick diameter found is an input entry for the gravity-viscous stage simulation, the longest and the one that causes the greatest environmental impacts, not needing to employ Fay's adjusted curves for its prediction anymore.

The employed model, in its first stage, shows itself as a promising tool and can also be used in the study of the subsequent stages of oil spreading on a calm sea. It can be applied to real-life conditions (in which there are winds, currents and waves) with the attribution of the physical properties of the external agents to the particles that discretize the domain.

REFERENCES

[1] J. A. Fay, The Spread of Oil Slicks on a Calm Sea. Oil on the Sea, Plenum Press (1969) 53-64
[2] J. A. Fay, Physical Processes in the Spread of Oil on a Water Surface, International Oil Spill Conference Proceedings (1971) 463-467.
[3] M. Guo, P. Shi, X. Liu, *A Three Dimensional Transport Model for Oil Spills in Coastal Waters Based on Particle Approach.* Proceedings of the Sixth International Conference on Natural Computation (2010) 3773-3777.
[4] D. Violeau, C. Buvat, K. Abed-Meraim, Numerical Modelling of Boom and Oil Spill with SPH, Coastal Engineering (2007) (12): 895-913.
[5] X. Yang, M. Liu, Numerical Modeling of Oil Spill Containment by Boom using SPH, Physics, Mechanics & Astronomy (2013) 56 (2): 315-321.
[6] P. Sebastião, C. G. Soares, Modeling the Fate of Oil Spills at Sea. Spill Science and Technology Bulletin (1995) 2 (2-3): 121-131.
[7] M. L. Spaulding, State of the art review and future directions in oil spill modeling, Marine Pollution Bulletin (2017) (115): 7–19.
[8] L. B. Lucy, Numerical Approach to Testing the Fission Hypothesis. Astronomical Journal (1997) (82): 1013-1024.
[9] R. A. Gingold, J. J. Monaghan, Smoothed Particle Hydrodynamics: Theory and Application to Non-Spherical Stars, Monthly Notices of the Royal Astronomical Society (1997) (181): 375-387.
[10] C. A. D. Fraga Filho, Study of Gravity-Inertial Phase of Spreading of Oil on a Calm Sea employing the Lagrangian Particle Method Smoothed Particle Hydrodynamics, PhD Thesis, UFES, Brazil, (2014). Available: http://spheric-sph.org/sph-phds [Accessed 2 June 2016].
[11] M. B. Liu, G.R. Liu, Smoothed Particle Hydrodynamics (SPH): an overview and recent developments. Arch. Comput. Methods Eng. (2010) (17): 25-76.
[12] J. K. Chen, J. E. Beraun, T. C. Carney, A corrective smoothed particle method for boundary value problems in heat conduction. Int. J. Num. Meth. Engng. (1999) (46): 231–252.
[13] G. R. Liu, M. B. Liu. Smoothed Particle Hydrodynamics: a Meshfree Particle Method. World Scientific, Singapore, (2003).
[14] R. Courant, K. Friedrichs, H. Lewy. On the partial difference equations of mathematical physics, IBM Journal (1967) (11):215-234.
[15] K. D. Stolzenbach, O. S. Madsen, E. E. Adams, A. M. Pollack, C. K. Cooper, A Review and Evaluation of Basic Techniques for Predicting the Behavior of Surface Oil Slicks. Massachusets Institute of Technology, (1977).
[16] J. J. Monaghan, Simulating free surface flows with SPH. J. Comput. Phys. (1994) 110 (2): 399-406.
[17] Batchelor, G.K. *An Introduction to Fluid Dynamics.* Cambridge University Press, 3rd edition, (2000).
[18] C. A. D. Fraga Filho, Development of a computational instrument using a lagrangian particle method for physics teaching in the areas of fluid dynamics and transport phenomena. Rev. Bras. Ensino Fís. (2017), vol. 39, n. 4. Available: http://www.scielo.br/pdf/rbef/v39n4/1806-1117-rbef-39-04-e4401.pdf [Accessed 2 June 2017].

V International Conference on Particle-based Methods – Fundamentals and Applications
PARTICLES 2017
P. Wriggers, M. Bischoff, E. Oñate, D.R.J. Owen, & T. Zohdi (Eds)

COUPLING OF FINITE-VOLUME-METHOD AND INCOMPRESSIBLE SMOOTHED PARTICLE HYDRODYNAMICS METHOD FOR MULTIPHASE FLOW

CHRISTIAN A. WALTER, MANUEL HIRSCHLER AND ULRICH NIEKEN

Institute of Chemical Process Engineering, University of Stuttgart
Böblinger Straße 78, 70199 Stuttgart, Germany
christian.walter@icvt.uni-stuttgart.de, http://www.icvt.uni-stuttgart.de

Key words: SPH, FVM, coupling, multiphase, ISPH

Abstract. It is an intuitive way to use the advantages of two different simulation methods, such as the Finite-Volume (FV) and Smoothed Particle Hydrodynamics (SPH), to reduce the computational effort. Finite-Volume, like other grid-based methods, is advantageous for huge systems without fluid-fluid interfaces, whereas SPH is advantageous in the vicinity of fluid interfaces. We will present our first results for a combined simulation, including a moving SPH domain, in a simple Poiseuille flow and a more complex multiphase capillary rise scenario.

1 INTRODUCTION

Mesh-free simulation methods, as the Smoothed Particle Hydrodynamics method (SPH), are advantageous for simulating free-surface flows, solid-fluid interaction with deformations and multiphase applications. In contrast to grid-based methods, SPH doesn't require an expensive meshing or adaption of the grids. On the other hand, simulations of simple flow are very expensive. A way to reduce the computational effort of the SPH method is to use it only in parts of the problem domain where it is necessary. In other parts a more efficient calculation method, like the Finite-Volume method (FVM) may be used.
In the literature some work can be found for linking grid-based and grid-free simulation methods for solid-fluid systems [1] but there is a leak in coupling fluid-fluid systems [2]. Therefore, a new approach to combine both simulation methods for multiphase flow applications is presented. The coupling strategy is outlined using FVM and, in conformity, an incompressible SPH (ISPH) solver.

2 Coupling of Finite Volume Method an ISPH

2.1 ISPH Solver

At our institute, the ISPH solver "SiPER" is developed and used for different applications in multi-phase micro-flow in porous media and morphology evolution in fluid systems. We use the model described in detail in [4]. The coupling strategy is based on our previously published open boundary conditions as described in [3]. We basic algorithm is a Predictor-Corrector integration scheme, where we use a Bi-Conjugate Gradient method to solve the Pressure Poisson Equation (PPE) using the PETSc-library [7].

2.2 Finite Volume Solver

The FVM is implemented as 2D staggered grid solver according to [5] inside the existing SiPER code. It is implemented in the same structure as the SPH solver with a Predictor-Corrector integration scheme. The PPE is also solved using a Bi-Conjugate Gradient method of the PETSc-library. The code is limited to an equidistant grid.

2.3 Coupling Strategy

Set up of the simulation domain

The first step of the coupled simulation is to lay the equidistant grid of the FVM over the whole domain with the height H and length L. Inside of this domain the SPH domain is inserted on a random position x_{SPH} with its belonging length L_{SPH}. Due to the fact that the coupling is only done in one direction the height of the SPH domain is equal to the total domain height H. This setup can be seen in figure 1. The red lines indicate the coupling boundaries between the two simulation methods.
The FV grid cells behind the SPH domain will be deactivated, therefore we get two separated FV domains. In each domain we can calculate a fluid with different properties.

Coupling boundary condition

The relevant properties for the coupling are the velocity $\mathbf{v} = (u, v)$ and the pressure p. For a successful coupling the following four conditions at the interface between the methods have to be fulfilled

$$\mathbf{v}_I^{SPH} = \mathbf{v}_I^{FVM}, \quad (1) \qquad p_I^{SPH} = p_I^{FVM}, \quad (3)$$

$$\nabla\mathbf{v}_I^{SPH} = \nabla\mathbf{v}_I^{FVM}, \quad (2) \qquad \nabla p_I^{SPH} = \nabla p_I^{FVM}. \quad (4)$$

Terms of higher order are neglected. Due to the properties of the Navier-Stokes equations, a Dirichlet (Eq. (1) or (3)) and a Neumann (Eq. (2) or (4)) boundary condition is needed. The incompressibility of the fluid fulfills condition (2). As second boundary condition a Dirichlet boundary for the pressure is chosen. The pressure at the interface is unknown

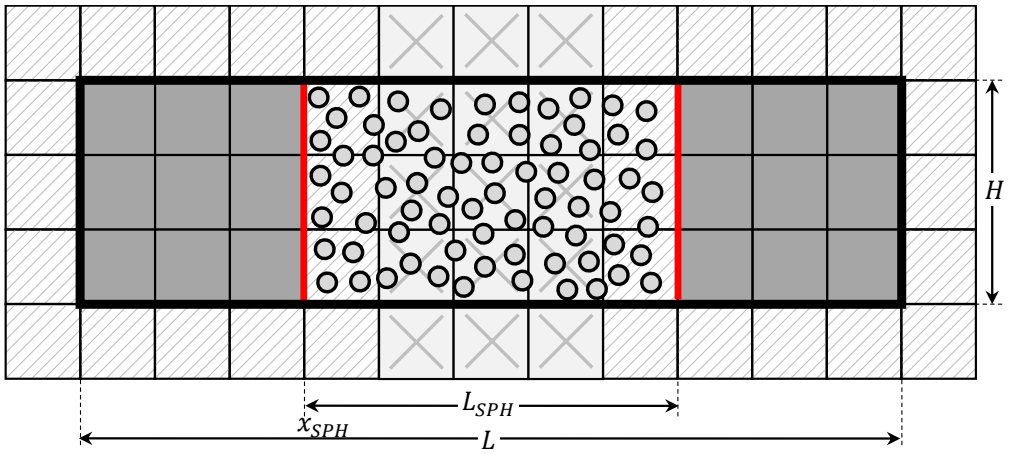

Figure 1: Setup of the simulation domain for the coupling of the FV ans SPH method.

a priori because of the random position of the SPH domain inside the whole simulation domain. Because of that we need to calculate the pressure for the Dirichlet boundary conditions iteratively.
At the interface in the SPH domain, the pressure p_I^{SPH} is calculated with an interpolation of the pressure values of the adjacent FV cells as shown in fig. 2 (right). At the interface in the FV domain, the pressure in the center of the boundary cells are needed. At this position a fictive SPH particle is inserted and with the SPH interpolation scheme the pressure can be calculated as shown in figure 2 (left). The pressure on the interface is calculated as

$$p_I^{FVM} = \frac{(p_r + p_i)}{2} \tag{5}$$

Obviously, with this approach the pressure on the interface has to be iterated until $p_I^{FVM} = p_I^{SPH}$. This pressure iteration takes part during the SPH corrector step.

Overlapping of the simulation domains

By using open boundary pressure conditions, small errors in the pressure solution are present. These errors prevent a convergence of the pressure iteration. To avoid this problem the simulation domains of SPH and FV will be slightly overlapped, as shown in fig. 3. The position of the interface is not equal to the boundary of each simulation domain but is defined as

$$x_I = \frac{x_{I,SPH} + x_{I,FVM}}{2}. \tag{6}$$

The pressure calculation for the FV boundary condition is now at a position with a negligible error. The iteration is aborted by two different criteria. First, the mean square

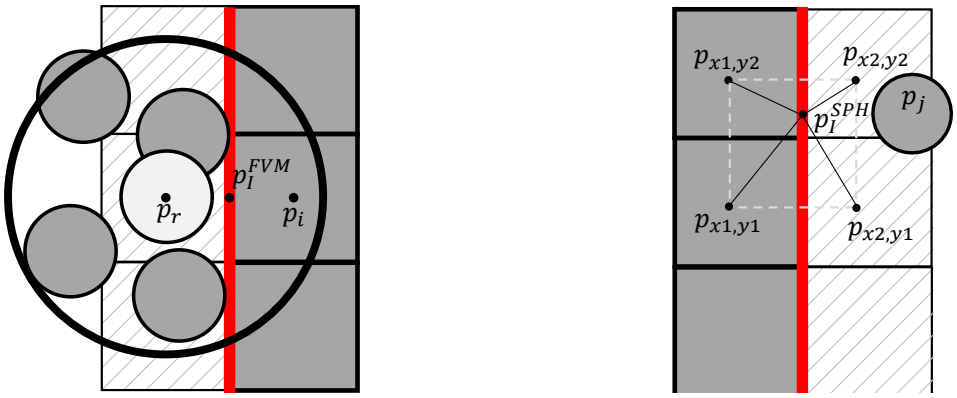

Figure 2: Pressure calculation at the interface for FV (left) with an SPH interpolation. Bilinear interpolation of the pressure on the grid cells for the SPH method (right)

deviation at the position of the interface x_I between the SPH and the FV pressure is used, second the variation of the pressure at the boundaries is used.

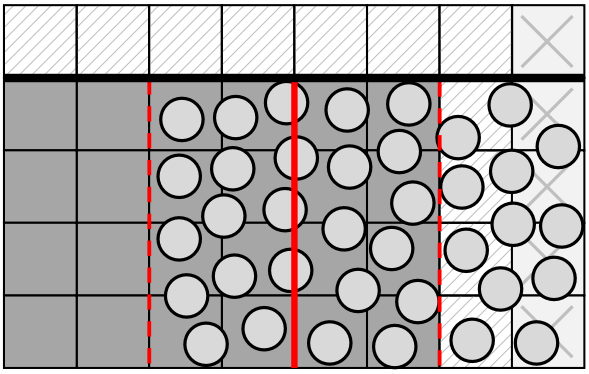

Figure 3: Interface with overlapping simulation methods.

Movement of the SPH domain

The aim of the coupling is to simulate e.g. bubbles in a bubble column where small, moving areas of multiphase flow are present. Therefore the SPH domain has to move inside the FV domain. To achieve this, the position of the SPH domain has to be calculated in every time step. This is done by identifying the phase boundary and then move the SPH domain in a way that the phase boundary is always in the center of the SPH domain. During this movement particles are generated or deleted as described for open boundary conditions in [4]. The FV grid will change due to the position of the SPH domain and grids will be deactivated or activated, applying the new fluid properties. The movement of the SPH domain is limited to one size of the grid cell per time step to avoid errors.

3 Results and discussion

3.1 Poiseuille Flow

A single-phase, two-dimensional Poiseuille flow is calculated for a viscous fluid with a density of $\rho = 1000\,\mathrm{kg/m^3}$, a dynamic viscosity $\mu = 0.01\,\mathrm{kg/s\,m}$ and a simulation domain with the height of $H = 1\,\mathrm{mm}$ and the length $L = 6\,\mathrm{mm}$. Dirichlet pressure conditions ($p_L = 180\,\mathrm{Pa}$, $p_R = 0\,\mathrm{Pa}$) are applied. A sketch up is shown in fig. 4.

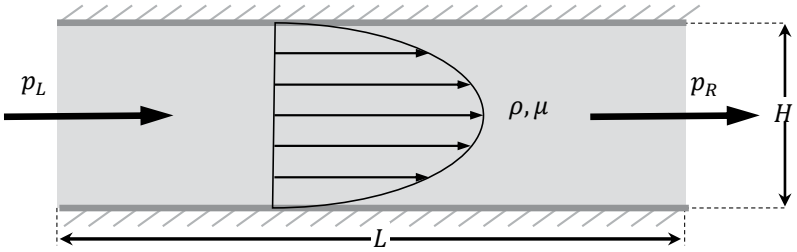

Figure 4: Visualization of the Poiseuille flow.

The solution of the velocity is compared to the analytic solution

$$u_x(y,t) = \frac{g_x\,\rho}{2\,\mu} y\,(y-H) + \sum_{n=0}^{\infty} \frac{4\,g_x\,\rho\,H^2}{\mu\,\pi^3}\,(2n+1)^3 \; sin\left(\frac{\pi\,y}{H}\,(2n+1)\right)\; exp\left(-\frac{(2n+1)^2\,\pi^2\mu}{\rho\,H^2}\,t\right). \tag{7}$$

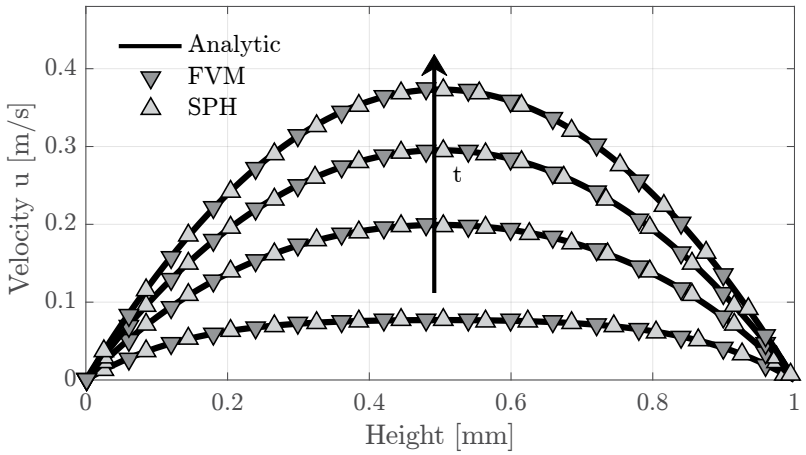

Figure 5: Comparison of the analytic velocity profile with the solution of the coupled simulation for four different points of time.

Figure 5 shows the calculated velocity at the left interface. The results are in good agreement with the analytic solution. The integrated error of pressure and velocity is below 0.1% at every time step.

3.2 Moving Poiseuille Flow

To evaluate the error of the moving SPH domain inside the FV domain, the SPH domain is moved multiple times from left to right and back again. This movement results in a triangle shaped pressure profile over the time as seen in fig. 6. The simulation

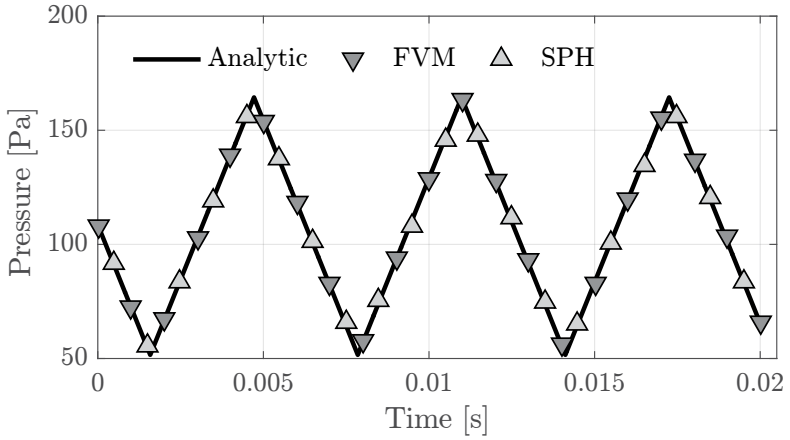

Figure 6: Pressure profile at the interface for a moving SPH domain.

represents the analytic solution very well. As seen in fig. 7, the error in the velocity through the movement is equally. In summary, it can be stated that the movement of the SPH domain does not result in a highly increasing error.

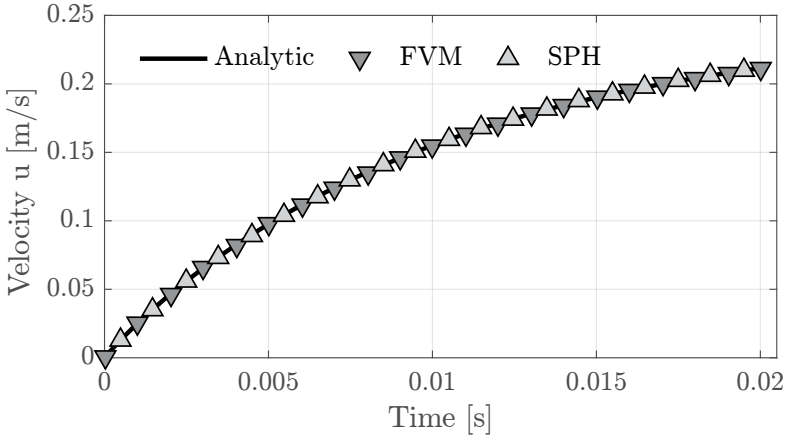

Figure 7: Temporal progress of the velocity at the interface.

3.3 Capillary Rise

A capillary rise between two flat parallel walls as shown in fig. 8 consists of a wetting fluid (w) ($\rho_w = 1800\,\mathrm{kg/m^3}$ $\mu_w = 0.0047\,\mathrm{kg/sm}$) and a non-wetting fluid (n) ($\rho_n = 1000\,\mathrm{kg/m^3}$ $\mu_n = 0.001\,\mathrm{kg/sm}$). The height of the simulation domain is $H = 9.3\,\mathrm{mm}$ and the distance between the two plates is $d = 1.55\,\mathrm{mm}$. The wetting fluid will move up through the capillary and stops on a stationary level (h_w) where the forces are in an equilibrium [6]. At the beginning the pressure sinks fast and ends on a stationary profile. Fig. 9 shows

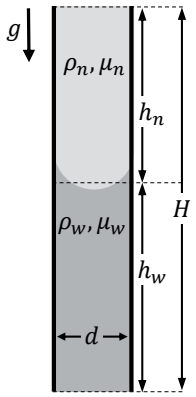

Figure 8: Visualization of the capillary rise.

the expected behavior for the pressure during the rise. Both interfaces between SPH and FV are shown, and the difference between both lines gives the pressure drop at the fluid fluid boundary. The results are in good agreement with capillary rise experiments [6].
We conclude that our coupling strategy leads to reasonable results. In future work, some minor issues at the interface between FVM and SPH need to be fixed. A promising alternative to match the interfaces is very recently presented by Napoli et al. [2].

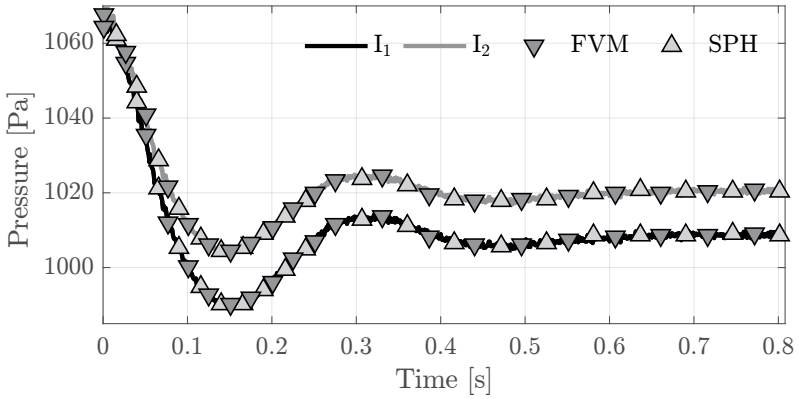

Figure 9: Temporal progress of the pressure for both interfaces.

REFERENCES

[1] Johnson, Gordon R. *Linking of Lagrangian particle methods to standard finite element methods for high velocity impact computations.* Nuclear Engineering and Design, 150(2):265 - 274, 1994.

[2] Napoli, E.; De Marchis, M.; Milice, B. and Monteleone, A. *A coupled Finite Volume-Smoothed Particle Hydrodynamics method for incompressible flows.* Computer Methods in Applied Mechanics and Engineering, 310:674 - 693, 2016.

[3] Kunz, P.; Hirschler, M.; Huber, M. and Nieken, U. *Inflow/outflow with Dirichlet boundary conditions for pressure in ISPH*, Journal of Computational Physics, Volume 326, 1 December 2016, Pages 171-187.

[4] Hirschler, M. et al. *Open boundary conditions for ISPH and their application to micro-flow*, Journal of Computational Physics, Volume 307, 15 February 2016, Pages 614-633.

[5] Griebel, M.; Dornseifer, T. and Neunhoeffer, T. *Numerical Simulation in Fluid Dynamics: A Practical Introduction.* SIAM e-books. Society for Industrial and Applied Mathematics (SIAM, 3600 Market Street, Floor 6, Philadelphia, PA 19104), 1997.

[6] Kunz, P.; Zarikos, I. M.; Karadimitriou, N. K.; Huber, M.; Nieken, U. and Hassanizadeh, S. M. (2016) *Transport in Porous Media*, volume 114, issue 2, pp. 581 - 600.

[7] Balay, S.; Abhyankar, S.; Adams, M. F.; Brown, J.; Brune, P.; Buschelman, K.; Dalcin, L.; Eijkhout, V.; Gropp, W. D.; Kaushik, D.; Knepley, M. G.; Curfman McInnes, L.; Rupp, K.; Smith, B. F.; Zampini, S. and Hong Zhang, H. (2016) *PETSc Web page*, http://www.mcs.anl.gov/petsc

V International Conference on Particle-based Methods – Fundamentals and Applications
PARTICLES 2017
P. Wriggers, M. Bischoff, E. Oñate, D.R.J. Owen, & T. Zohdi (Eds)

NUMERICAL SIMULATION OF THE SEDIMENTATION OF AN ELLIPTIC PARTICLE UNDER EXTERNAL ELECTRIC FIELD USING ISPH

NIMA TOFIGHI[1], MEHMET YILDIZ[2] AND AFZAL SULEMAN[1]

[1] Department of Mechanical Engineering, University of Victoria, Victoria, BC V8P 5C2, Canada
ntofighi@uvic.ca; suleman@uvic.ca

[2] Integrated Manufacturing Technologies Research and Application Center, Faculty of Engineering and Natural Sciences (FENS), Sabanci University, Tuzla, 34956 Istanbul, Turkey
meyildiz@sabanciuniv.edu

Key words: Smoothed Particle Hydrodynamics, Fluid-Structure Interaction, Electrohydrodynamics

Abstract. Incompressible smoothed particle hydrodynamics method has been used to simulate the sedimentation of a two-dimensional rigid elliptic disc in quiescent medium in presence of an external electric field. The motion of the elliptic disc in the absence of the electric field is compared to literature data and good agreement is observed. The results show that the trajectory of the elliptic disc in presence of the electric field is strongly affected by the electrical properties of fluid and solid.

1 Introduction

This study deals with the motion of a rigid elliptic particle sedimenting in a quiescent background fluid. At low Reynolds numbers, the particle tends to sediment lying flat on its major axis [1]. When placed in an external electric field, the electrical forces exerted on the particle may result in a moment that changes its orientation [2]. The electric field induced rotation in this case is of particular significance in particle orientation in sprays or microfluidic devices, to name a few [3, 4].

Electrohydrodynamics of multiphase flows have been successfully investigated using incompressible smoothed hydrodynamics (ISPH) method before [5]. Here, an isothermal two dimensional ISPH method is used to calculate velocity, pressure and electrical potential of the elliptic particle and its surrounding fluid. The sedimentation of an elliptic particle in the absence of the external electric field has been investigated before in [1, 6] and our method is validated in [7].

The sedimentation pattern of the elliptic particle is highly dependent on the electrical properties of the system and proximity of the boundaries. To investigate the long term

sedimentation patterns, a shifting boundary condition is implemented and tested without the electric field. Then, four sets of boundary conditions and two different sets of electrical properties are simulated and the behavior of the elliptic particle is investigated.

2 Governing Equations and Geometry

Equations governing an incompressible flow subject to an external electric field may be written in dimensionless form as

$$\boldsymbol{\nabla} \cdot \mathbf{u} = 0, \tag{1}$$

$$\rho \frac{\mathrm{D}\mathbf{u}}{\mathrm{D}t} = \boldsymbol{\nabla} p + \frac{1}{\mathrm{Re}} \boldsymbol{\nabla} \cdot \boldsymbol{\tau} + \frac{1}{\mathrm{Eg}} \mathbf{f}_{(e)}, \tag{2}$$

where $\mathbf{u}$ is the velocity vector, p is pressure, ρ is density, t is time and $\mathrm{D}/\mathrm{D}t = \partial/\partial t + \mathbf{u} \cdot \boldsymbol{\nabla}$ represents the material time derivative. Here, $\boldsymbol{\tau}$ is the viscous stress tensor,

$$\boldsymbol{\tau} = \mu \left[\boldsymbol{\nabla} \mathbf{u} + (\boldsymbol{\nabla} \mathbf{u})^{\dagger} \right], \tag{3}$$

where μ denotes viscosity and superscript $\square^{\dagger}$ represents the transpose operation. $\mathbf{f}_{(e)}$ is the electric force vector defined as [8]

$$\mathbf{f}_{(e)} = -\frac{1}{2} \mathbf{E} \cdot \mathbf{E} \boldsymbol{\nabla} \varepsilon + q^{v} \mathbf{E}. \tag{4}$$

Here ε denotes electric permittivity, q^{v} is is the volume charge density near the interface while $\mathbf{E}$ is the electric field vector. Assuming small dynamic currents and neglecting magnetic induction effects, the electric field is irrotational [8] and may be represented by gradient of an electric potential ϕ, $\mathbf{E} = -\boldsymbol{\nabla} \phi$. Further assumption of fast electric relaxation time compared to viscous relaxation time leads to the following relations for electric potential and charge density

$$\boldsymbol{\nabla} \cdot (\sigma \boldsymbol{\nabla} \phi) = 0, \tag{5}$$

$$q^{v} = \boldsymbol{\nabla} \cdot (\varepsilon \boldsymbol{\nabla} \phi), \tag{6}$$

where σ is the electrical conductivity.

Dimensionless values are formed using the following scales

$$\begin{aligned} &\mathbf{x} = \mathbf{x}^{*}/d, \quad \rho = \rho^{*}/\rho_{f}, \quad \mathbf{u} = \mathbf{u}^{*}/\sqrt{gd}, \\ &t = t^{*}\sqrt{g/d}, \quad \mathbf{E} = \mathbf{E}^{*}/E_{\infty}, \quad \phi = \phi^{*}/E_{\infty}H, \\ &p = (p - \rho \mathbf{g} \cdot \mathbf{x})^{*}/\rho_{f} g d, \quad \mathcal{D} = \rho_{s}/\rho_{f}, \quad \mathcal{V} = \mu_{s}/\mu_{f}, \\ &\mathcal{P} = \varepsilon_{s}/\varepsilon_{f}, \quad \mathcal{C} = \sigma_{s}/\sigma_{f}, \end{aligned} \tag{7}$$

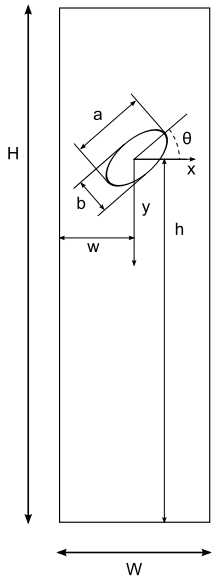

Figure 1: General schematic of the test cases

leading to Reynolds and Electrogravitational numbers defined as

$$\mathrm{Re} = \frac{\rho_f \sqrt{g d^3}}{\mu_f}, \quad \mathrm{Eg} = \frac{\rho_f g d}{\varepsilon_f E_\infty^2}. \tag{8}$$

Here E_∞ is the undisturbed electric field intensity, H is the distance between electrodes and $d = \sqrt{ab}$ denotes equivalent ellipse diameter. An asterisk marks dimensional variables whereas subscripts $\square_s$ and $\square_f$ denote fluid and solid phases, respectively.

Figure 1 shows the general geometry of the cases studied here. The elliptic particle is positioned at (w, h) in a $W \times H$ rectangular box at an angle θ with respect to the horizontal axis. Aspect ratio of the ellipse is set to $a/b = 2$. Gravitational acceleration acts in positive y direction. When electric field is present, an electric potential difference of $\Delta\phi = E_\infty H$ is imposed between horizontal walls, generating an undisturbed electric field parallel to side walls. Details of initial particle arrangement are given in [7].

3 Numerical Method

To distinguish between different phases, a color function $\hat{c}$ is defined such that it assumes a value of zero for one phase and unity for the other. The color function is then smoothed out across the phase boundaries as

$$c_{\mathrm{i}} = \sum_{\mathrm{j}=1}^{J_n} \frac{\hat{c}_{\mathrm{j}} W_{\mathrm{ij}}}{\psi_{\mathrm{i}}}, \tag{9}$$

to ensure smooth transition between the properties of each phase when used for their interpolation. Here, $\psi_{\mathrm{i}} = \sum_{\mathrm{j}=1}^{J_n} W_{\mathrm{ij}}$, is the number density of SPH particle i, calculated

as the sum of interpolation kernel of neighboring particles i and j over all neighbors of particle i, J_n. Interpolation kernel, $W(r_{\mathrm{ij}}, h)$, is a function of the magnitude of distance vector $\mathbf{r}_{\mathrm{ij}} = \mathbf{r}_{\mathrm{i}} - \mathbf{r}_{\mathrm{j}}$ and smoothing length h [9]. Interpolation of phase properties is carried out through

$$\frac{1}{\chi_{\mathrm{i}}} = \frac{c_{\mathrm{i}}}{\chi_s} + \frac{1 - c_{\mathrm{i}}}{\chi_f}, \tag{10}$$

where χ may denote density, viscosity, permittivity or conductivity.

The solid region is treated as a liquid with a viscosity ratio of $\mathcal{V} = 100$ [7]. Additionally, rigidity constraints are imposed by computing a center-of-mass velocity and angular velocity

$$\mathbf{u}_s = \frac{1}{J_s} \sum_{\mathrm{j}=1}^{J_s} \mathbf{u}_{\mathrm{j}}, \quad \omega_s = \frac{1}{I_s} \sum_{\mathrm{j}=1}^{J_s} \mathbf{u}_{\mathrm{j}} \times \mathbf{r}_{\mathrm{j}s}, \tag{11}$$

which are used to assign an individual velocity to each solid particle according to

$$\mathbf{u}_{\mathrm{i}} = \mathbf{u}_s + \omega_s \times \mathbf{r}_{\mathrm{i}s}. \tag{12}$$

Here, $\mathbf{r}_{\mathrm{i}s} = \mathbf{r}_{\mathrm{i}} - \mathbf{r}_s$ where $\mathbf{r}_s$ denotes the solid object's center of mass, J_s is the number of particles present in the solid phase and I_s is the solid object's moment of inertia about its center of mass.

A predictor-correcter scheme is employed to advance the governing equations in time with a variable timestep according to $\Delta t = 0.25h/u_{max}$, where u_{max} is the largest particle velocity magnitude [10]. In the predictor step, (5) and (6) are solved to obtain $\mathbf{f}_{(e)}^{(n)}$ through (4). Then positiona and velocity are advanced to their intermediate forms using the following relations,

$$\mathbf{r}_{\mathrm{i}}^{+} = \mathbf{r}_{\mathrm{i}}^{(n)} + \mathbf{u}_{\mathrm{i}}^{(n)} \Delta t + \boldsymbol{\delta}\mathbf{r}_{\mathrm{i}}^{(n)}, \tag{13}$$

$$\mathbf{u}_{\mathrm{i}}^{+} = \mathbf{u}_{\mathrm{i}}^{(n)} + \left(\frac{1}{\mathrm{Re}} \boldsymbol{\nabla} \cdot \boldsymbol{\tau}_{\mathrm{i}}^{(n)} + \frac{1}{\mathrm{Eg}} \mathbf{f}_{(e),\mathrm{i}}^{(n)} \right) \frac{\Delta t}{\rho_{\mathrm{i}}}, \tag{14}$$

where starred variables represent intermediate values and superscript (n) denotes values at the nth time step. Number density and fluid properties are calculated according to the intermediate position of the interface. The artificial particle displacement vector in (13), $\boldsymbol{\delta}\mathbf{r}_{\mathrm{i}}$, is defined as in [10] and a constant value of 0.06 is used.

Using intermediate values, pressure at the next time step is calculated and positions and velocities are advanced in time using the following equations

$$\boldsymbol{\nabla} \cdot \left(\frac{1}{\rho_{\mathrm{i}}^{+}} \boldsymbol{\nabla} p_{\mathrm{i}}^{(n+1)} \right) = \frac{\boldsymbol{\nabla} \cdot \mathbf{u}_{\mathrm{i}}^{+}}{\Delta t}, \tag{15}$$

$$\mathbf{u}_{\mathrm{i}}^{(n+1)} = \mathbf{u}_{\mathrm{i}}^{+} - \frac{1}{\rho_{\mathrm{i}}} \boldsymbol{\nabla} p_{\mathrm{i}}^{(n+1)} \Delta t, \tag{16}$$

Table 1: Configurations for testing the shifting boundary condition.

Case	A	B	C	D
Top and bottom	No-slip	Shifting	No-slip	Shifting
Side walls	No-slip	No-slip	Periodic	Periodic

$$\mathbf{r}_{\mathrm{i}}^{(n+1)} = \mathbf{r}_{\mathrm{i}}^{(n)} + \frac{1}{2}\left(\mathbf{u}_{\mathrm{i}}^{(n)} + \mathbf{u}_{\mathrm{i}}^{(n+1)}\right)\Delta t + \boldsymbol{\delta}\mathbf{r}_{\mathrm{i}}^{(n)}. \tag{17}$$

In these equations, the rigidity constraints ((11) and (12)) are implemented after each velocity update.

Details of the spatial discretization and enforcement of boundary conditions are given in [7].

4 Results

4.1 Shifting boundary condition

A sedimenting ellipse is likely to move in a periodic manner. However, the period of such motion may be very long and the effects of bounding walls may be substantial. As such, the long-term simulation of the sedimentation of the elliptic particle may be necessary for observing the periodic motion in some cases. To implement the shifting boundary, the ellipse is placed at the center of the computational domain. As its center of mass moves up by one particle spacing, all particles are shifted so that the ellipse is vertically centered. Any particles transfered out of the upper boundary are discarded and a new layer of particles are added at the bottom boundary. If the computational domain is high enough, the ellipse will continue its descent without limitation.

Since the motion of the ellipse without electric field is well studied, the method is tested in the absence of an external electric field [1, 6, 7]. The parameters are set as $\mathcal{D} = 1.1$, $\mathrm{Re} = 58.8$, $a/b = 2$, $W/a = 4$, $h/d = 34$ and $\theta = \pi/4$. Computational domain is discretized by 80035 particles. The combination of the boundary conditions used here are given in table 1.

In most cases, the effects of top and bottom walls should not contaminate the results and the simulations are terminated before wall effects appear. However, the effects of side walls are unavoidable in sedimentation in confined domains [1]. In this sense configurations A-B and C-D are paired for comparison. It is expected that cases B and D behave similar to cases C and D as long as the ellipse is far from the bottom wall. Figure 2 plots the horizontal position and orientation of the particle with respect to its vertical position. Cases A and C reach the bottom wall at $y^*/W = 6$ while cases B and D may continue indefinitely. The agreement between A-B and C-D pairs is excellent and this means that from a hydrodynamic point of view, the implementation of the shifting boundary has no effect on the sedimentation. It is worth mentioning that in all cases, the ellipse comes to a horizontal orientation while its position is dependent on the side wall boundary condition. With a no-slip wall, the hydrodynamic forces move the ellipse toward the center of the

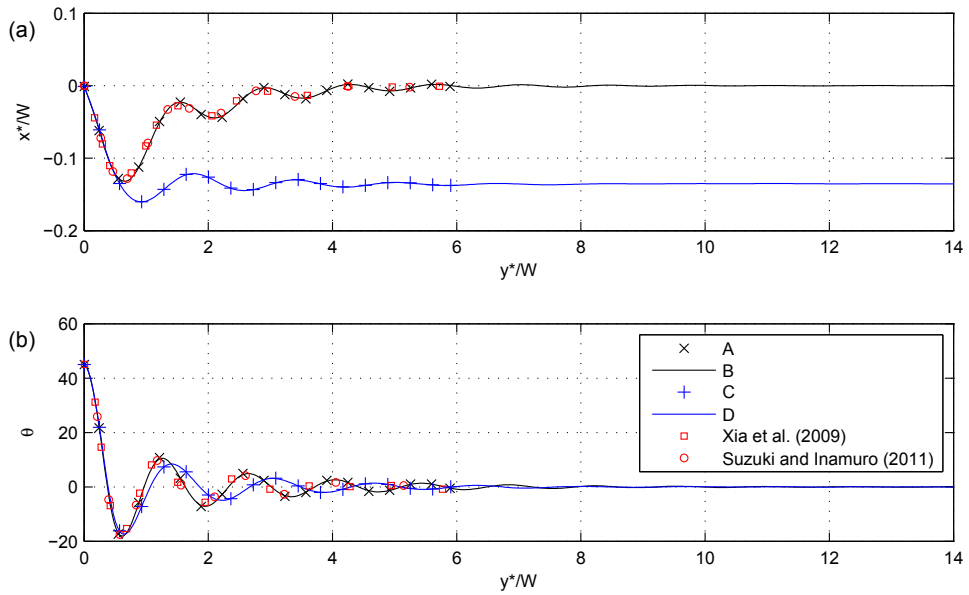

Figure 2: Horizontal position (a) and orientation (b) of the elliptic disc while sedimenting.

domain while in the periodic configuration, the ellipse settles further away from its starting horizontal position. The Reynolds numbers based on terminal velocity, $\mathrm{Re}_t = \rho_f u_t d/\mu_f$, is equal to 15.1 and 16.2 for A-B and C-D pairs, respectively. As expected, this shows that the ellipse descends slower in confined domain due to wall effects.

4.2 Boundary effects on sedimentation

The introduction of the electrical field may significantly alter the behavior of the ellipse sedimenting in quiescent fluid. Two sets of permittivity ratio and conductivity ratio pairs of $(10, 20)$ and $(20, 0.1)$ are used and will be referred to as cases S and U, respectively. The significance of the electrical parameters chosen is that the former has $\tau_s < \tau_f$ while the latter has $\tau_s > \tau_f$, where $\tau = \varepsilon/\sigma$. This means that the electrical forces resist rotation for case S while the situation for case U is more complex. Velocity boundary conditions are as given in table 2. For configurations A and B no electric field lines pass through the side walls while in configurations C and D, the side walls are periodic. Reynolds number is set to 58.8 while Electrogravitational number is equal to 27.7.

Figure 3 plots the horizontal position and orientation of the ellipse versus its vertical position for S cases. In all cases, the ellipse aligns itself with the electric field almost instantly, regardless of the boundary configuration, with cases A-B and C-D following the same trajectory. When side walls are present, *i.e.* configurations A and B, the ellipse moves slowly toward the center of the computational domain whereas in configurations C and D, the ellipse remains to the right of its starting horizontal position. It is worth noting that the early horizontal deviation in electrified cases is in the opposite direction

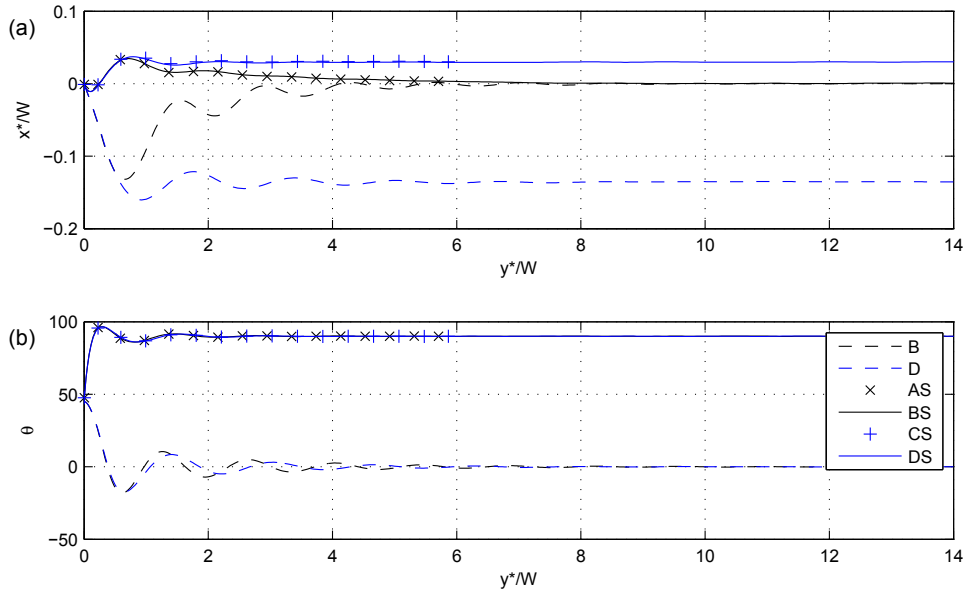

Figure 3: Horizontal position (a) and orientation (b) of the elliptic disc of case S while sedimenting in an external electric field.

of the cases without the electric field.

Figure 4 provides the horizontal position and orientation of the ellipse for case U. Unlike case S, case U shows remarkably different trajectories with different boundary configurations. While cases CU and DU behave similarly with a periodic motion, cases AU and BU are completely unrelated. This shows that the electrical boundaries have notable effects when there is a race between $\mathbf{f}_{(ep)} = -\mathbf{E}\cdot\mathbf{E}\boldsymbol{\nabla}\varepsilon/2$ and $\mathbf{f}_{(eq)} = q^v\mathbf{E}$ (equation (4)). Cases CU and DU follow a periodic trajectory to the left of their starting position and rotate up to ten degrees around the flat orientation. Case BU follows a periodic motion of equal horizontal distance and angular span to that of CU and DU at a higher frequency in the center of the channel. Unlike others, case AU does not follow a periodic trajectory and stays mostly in an upright orientation. It moves back and forth near the left wall before changing direction in $y^*/W = 4$ and heading toward the right wall.

Table 2 provides Re_t for all cases. For oscillating cases, the average vertical velocity is used instead of the terminal velocity in computation of Re_t. In agreement with the observations made above, cases AS-BS and CS-DS have similar terminal Reynolds numbers. For case U, the oscillatory motion reduces the descent velocity resulting in smaller Re_t. As expected, cases CU and DU have similar terminal Reynolds numbers while the largest Re_t belongs to AU which descends in a mostly upright orientation.

To explore the effects of the electrical forces on the motion of case U in more detail, figures 5 and 6 provide the torques and horizontal component of the forces applied to the ellipse during its descent. The electrical force and torque are computed directly from the electrical forces applied to particles of the solid phase. Since the FSI coupling technique

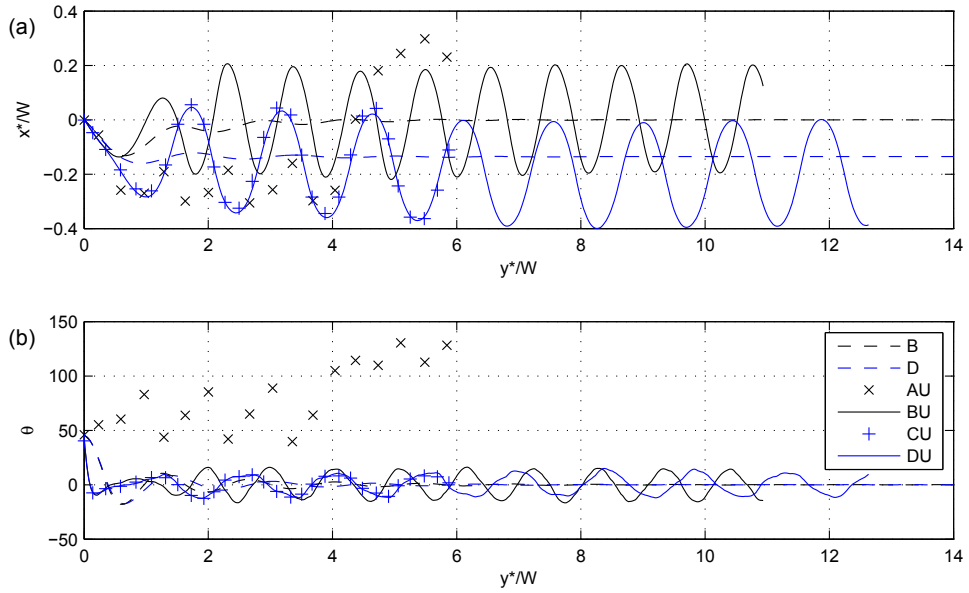

Figure 4: Horizontal position (a) and orientation (b) of the elliptic disc of case U while sedimenting in an external electric field.

Table 2: Terminal Reynolds number Re_t for cases S and U for different boundary configurations. When no electric field is applied $\mathrm{Re}_t = 15.1$ [7].

Case	A	B	C	D
S	22.1	21.9	22.8	22.8
U	19.7	9.6	11.1	11.2

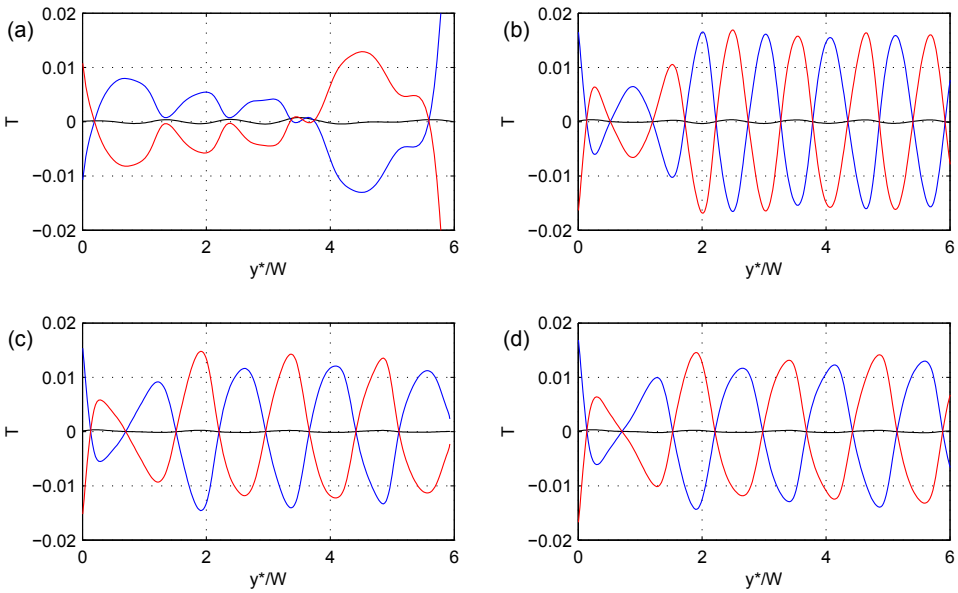

Figure 5: Hydrodynamic torque (blue), electric torque (red) and resultant torque applied to the ellipse of case U with boundary configurations of A (a), B (b), C (c) and D (d) while sedimenting in an external electric field. A positive value induces a counter-clockwise rotation.

used here does not provide an explicit interface for the solid body, the hydrodynamical parts are found by subtracting the electrical components from the resultant torque and force applied to the body. The resultant components are calculated using the position and orientation of the ellipse in time. The results are smoothed using a Gaussian filter to remove spurious oscillations.

The differences between case AU and other cases are apparent in both torque and forces exerted on it. Having both side and top boundaries in its vicinity, the initial electrical torque turns the ellipse in counter-clockwise direction to align it with the electric field. The hydrodynamic torque is comparable but smaller than the electrical counterpart and the ellipse maintains its orientation. This causes it to approach the left wall where it is deflected due to electrical forces ($y^*/W \approx 0.75$). While descending near the wall from $y^*/W \approx 1$ to 4, the electric torque encourages a flat orientation whereas the hydrodynamic torque opposes it. The ellipse gets closer to the left wall progressively with each approach and this reduces the hydrodynamic forces pushing it toward the wall. At $y^*/W \approx 4$, the ellipse breaks off the left wall and heads toward the opposing wall. While passing the middle of the channel, the electrical and hydrodynamical forces become negligible. At this position, electrical torque encourages a counter-clockwise rotation while a slightly larger hydrodynamical torque resists it. After $y^*/W \approx 5$, the bottom wall affects the simulation.

Despite sharing the same side wall configuration with case AU, replacing top and bottom boundaries with shifting walls changes the electrical effects exerted on case BU

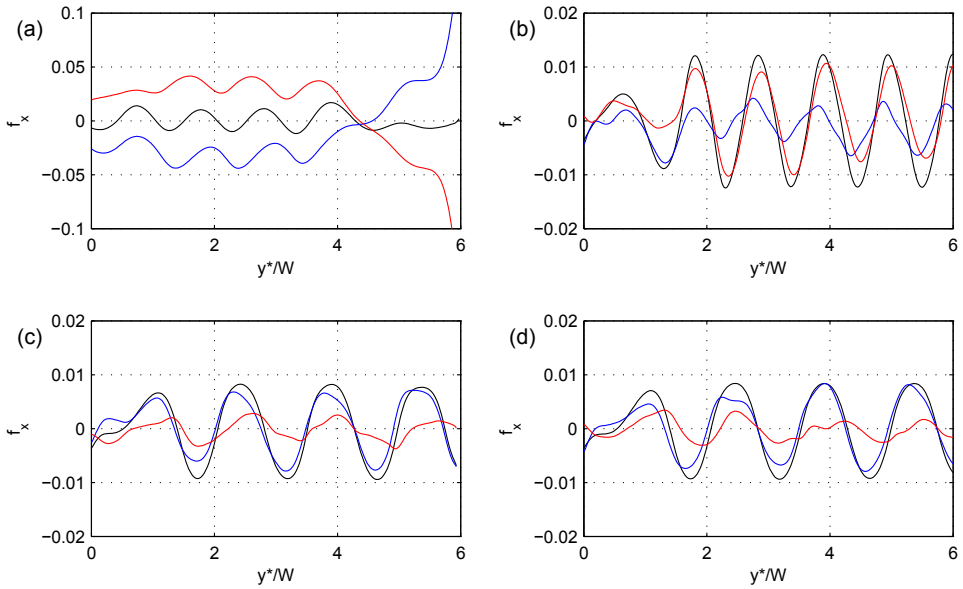

Figure 6: Horizontal component of hydrodynamic force (blue), electric force (red) and resultant force applied to the ellipse of case U with boundary configurations of A (a), B (b), C (c) and D (d) while sedimenting in an external electric field. A positive value moves the ellipse to the right.

significantly. Throughout its path, the electrical torque remains the dominant term and dictates both rotation and horizontal position. Initially, the electrical torque turns the ellipse toward a flat orientation while the hydrodynamic torque resists it. The electrical torque is clockwise for positive angles and counter-clockwise for negative angles. Electrical and hydrodynamic forces are in agreement and act to move the ellipse away from the wall. The period of both forces are similar while the electric component lags behind the hydrodynamic part.

Cases CU and DU act in a similar fashion. The electrical and hydrodynamical torques alternate as the ellipse pivots around its flat orientation. The torques oppose each other with the electrical torque as the dominant component. On the other hand, the dominant force term is the hydrodynamic component. Although there are no side walls to induce electrical forces in the horizontal direction, the domain width is small enough for the periodic boundary to have an effect. The ellipse interacts with itself through the periodic boundary and as the symmetry breaks a horizontal force is exerted on the ellipse. The electrical force points in the negative direction for positive angles and in positive direction for negative angels. This means that the ellipse is electrically forced to the left for positive angles and to the light for negative angles, which is also in line with hydrodynamic tendency of the ellipse. As a result, electrical and hydrodynamical forces have the same period while the electrical part slightly lags behind.

5 Conclusions

An ISPH method to simulate the sedimentation of an elliptic particle in quiescent flow under external electric field is presented here. A shifting boundary condition for long term simulation of the sedimentation is implemented and tested. It is seen that the shifting boundary condition has negligible effects in the absence of the electric field. The simulations in the presence of the electric field are carried out for two sets of electrical properties and four different boundary configurations. The results show that both electrical properties and the boundaries have significant effects on the trajectory of the sedimentation.

6 Acknowledgments

NT gratefully acknowledges financial support from Mitacs-Accelerate program grant number IT08354. MY acknowledges financial support provided by the Scientific and Technological Research Council of Turkey (TUBITAK) grant number 112M721. AS acknowledges the financial support provided by the Natural Sciences and Engineering Research Council (NSERC) for the Canada Research Chair in Computational and Experimental Mechanics.

REFERENCES

[1] Xia, Z., Connington, K.W., Rapaka, S., Yue, P., Feng, J.J. and Chen, S. Flow patterns in the sedimentation of an elliptical particle. *J. Fluid Mech.* (2009) **625**:249-272.

[2] Quincke, G. Ueber rotationen im constanten electrischen felde. *Ann. Phys.* (1896) **295**:417-486.

[3] Ai, Y., Beskok, A., Gauthier, D.T., Joo, S.W. and Qian, S. DC electrokinetic transport of cylindrical cells in straight microchannels. *Biomicrofluidics* (2009) **3**:044110.

[4] House, D.L., Luo, H. and Chang, S. Numerical study on dielectrophoretic chaining of two ellipsoidal particles. *J. Colloid Interface Sci.* (2012) **374**:141-149.

[5] Tofighi, N., Ozbulut, M., Feng, J.J. and Yildiz, M. The effect of normal electric field on the evolution of immiscible Rayleigh-Taylor instability. *Theor. Comput. Fluid Dyn.* (2016) **30**:469-483.

[6] Suzuki, K. and Inamuro, T. Effect of internal mass in the simulation of a moving body by the immersed boundary method. *Comput. Fluids* (2011) **49**:173-187.

[7] Tofighi, N., Ozbulut, M., Rahmat, A., Feng, J.J. and Yildiz, M. An incompressible smoothed particle hydrodynamics method for the motion of rigid bodies in fluids. *J. Comput. Phys.* (2015) **297**:207-220.

[8] Saville, D.A. Electrohydrodynamics: The Taylor-Melcher leaky dielectric model. *Annu. Rev. Fluid Mech.* (1997) **29**:27-64.

[9] Monaghan, J.J. Smoothed Particle Hydrodynamics and Its Diverse Applications. *Annu. Rev. Fluid Mech.* (2012) **44**:323-346.

[10] Zainali, A., Tofighi, N., Shadloo, M.S. and Yildiz, M. Numerical investigation of Newtonian and non-Newtonian multiphase flows using ISPH method. *Comput. Meth. Appl. Mech. Eng.* (2013) **254**:99-113.

AUTHORS INDEX

CIMNE

International Center
for Numerical Methods in Engineering